SECOND EDITION

TREATISE ON GEOPHYSICS

Volume 8

CORE DYNAMICS

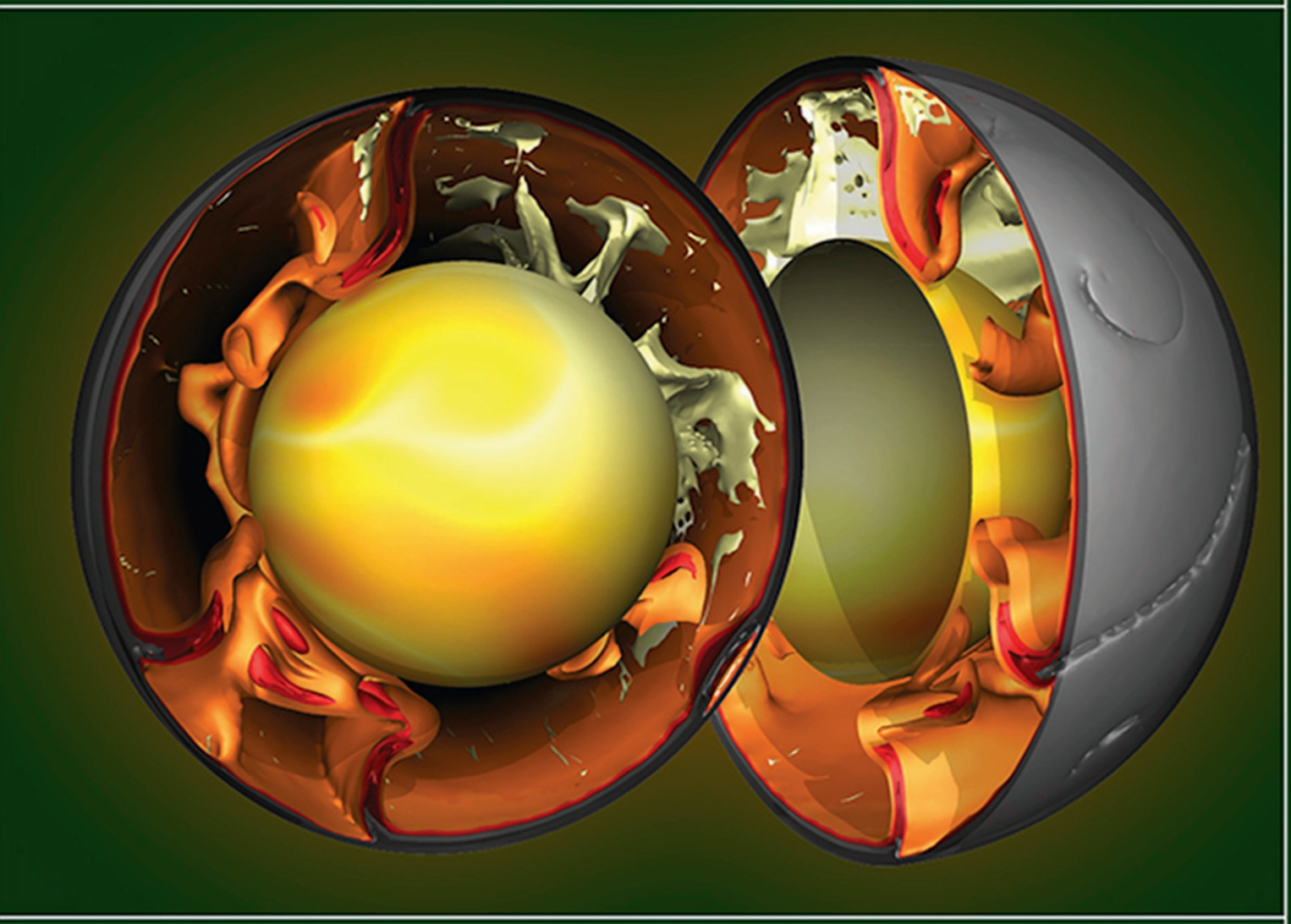

VOLUME EDITOR: PETER OLSON

EDITOR-IN-CHIEF: GERALD SCHUBERT

TREATISE ON GEOPHYSICS

SECOND EDITION

This page intentionally left blank

TREATISE ON GEOPHYSICS

SECOND EDITION

EDITOR-IN-CHIEF

Gerald Schubert

Distinguished Professor Emeritus, Department of Earth, Planetary and Space Sciences, University of California, Los Angeles

VOLUME 8

CORE DYNAMICS

VOLUME EDITOR

Professor Peter Olson

Department of Earth and Planetary Sciences, Johns Hopkins University

ELSEVIER AMSTERDAM • BOSTON • HEIDELBERG • LONDON • NEW YORK • OXFORD
PARIS • SAN DIEGO • SAN FRANCISCO • SINGAPORE • SYDNEY • TOKYO

Elsevier
Radarweg 29, PO Box 211, 1000 AE Amsterdam, The Netherlands
The Boulevard, Langford Lane, Kidlington, Oxford OX5 1GB, UK
30 Corporate Drive, Suite 400, Burlington MA 01803, USA

Copyright © 2015 Elsevier B.V. unless otherwise stated. All rights reserved.

Cover image created for this work by Fabio Crameri, University College London.
The figure depicts the temperature field from a convection calculation using the code STAG-YY, written by Paul Tackley.

The following chapters are US Government works in the public domain and not subject to copyright:

1.11 Crust and Lithospheric Structure - Global Crustal Structure; 3.09 Earth Rotation Variations – Long Period; 4.07 The Role of Fault-Zone Drilling; 5.11 The Time-Averaged Field and Paleosecular Variation; 10.21 Exoplanetary Geophysics: An Emerging Discipline; 11.12 Tools and Techniques: Gravitational Method.

No part of this publication may be reproduced or transmitted in any form or by any means, electronic or mechanical, including photocopying, recording, or any information storage and retrieval system, without permission in writing from the publisher. Details on how to seek permission, further information about the Publisher's permissions policies and our arrangements with organizations such as the Copyright Clearance Center and the Copyright Licensing Agency, can be found at our website: www.elsevier.com/permissions.

This book and the individual contributions contained in it are protected under copyright by the Publisher (other than as may be noted herein).

Notices
Knowledge and best practice in this field are constantly changing. As new research and experience broaden our understanding, changes in research methods, professional practices, or medical treatment may become necessary.

Practitioners and researchers may always rely on their own experience and knowledge in evaluating and using any information, methods, compounds, or experiments described herein. In using such information or methods they should be mindful of their own safety and the safety of others, including parties for whom they have a professional responsibility.

To the fullest extent of the law, neither the Publisher nor the authors, contributors, or editors, assume any liability for any injury and/or damage to persons or property as a matter of products liability, negligence or otherwise, or from any use or operation of any methods, products, instructions, or ideas contained in the material herein.

Library of Congress Cataloging-in-Publication Data
A catalog record for this book is available from the Library of Congress

British Library Cataloguing-in-Publication Data
A catalogue record for this book is available from the British Library

ISBN (print): 978-0-444-53802-4

For information on all Elsevier publications
visit our website at http://store.elsevier.com/

Editorial & Production: Gemma Tomalin, Richard Berryman, Marise Willis, Michael Nicholls, Ellen Bishop
Cover design: Matthew Limbert

Printed and bound in the United Kingdom

15 16 17 18 19 10 9 8 7 6 5 4 3 2 1

CONTENTS

Preface *vii*

Editor-in-Chief *ix*

Contributors *xi*

Contents of all Volumes *xiii*

8.01 Core Dynamics: An Introduction and Overview 1
P Olson

8.02 Energetics of the Core 27
F Nimmo

8.03 Theory of the Geodynamo 57
PH Roberts

8.04 Large-Scale Flow in the Core 91
R Holme

8.05 Thermal and Compositional Convection in the Outer Core 115
CA Jones

8.06 Turbulence in the Core 161
H-C Nataf and N Schaeffer

8.07 Rotational Dynamics of the Core 183
A Tilgner

8.08 Core–Mantle Interactions 213
BA Buffett

8.09 Waves in the Core and Mechanical Core–Mantle Interactions 225
D Jault and CC Finlay

8.10 Numerical Dynamo Simulations 245
UR Christensen and J Wicht

8.11 Magnetic Polarity Reversals in the Core 279
GA Glatzmaier and RS Coe

8.12 Inner Core Dynamics 297
I Sumita and M Bergman

8.13 Experiments on Core Dynamics 317
P Cardin and P Olson

This page intentionally left blank

PREFACE

The *Treatise on Geophysics* is a comprehensive and in-depth study of the physics of the Earth and of terrestrial-like planets residing both within and outside our solar system. Its breadth and detail of coverage are beyond what any single geophysics text can provide. The first edition of the *Treatise on Geophysics* was published in 2007, nearly a decade ago. Of course, there is much progress in science in that length of time and the field of geophysics has grown rapidly and developed new lines of inquiry. Accordingly, we have brought the *Treatise on Geophysics* up-to-date with this second edition. The new edition will continue to provide students and professionals with fundamental and state-of-the-art discussion of all aspects of geophysics. In this new edition, the reader will find updates to all the chapters contained in the first edition and new chapters that discuss topics missing from the first edition. In a few instances, chapters from the first edition have simply been reprinted in order to avoid gaps in coverage. Chapters that emphasized fundamental physics often required little updating.

A highlight of the second edition is a new volume on Resources in the Near-Surface Earth. The new volume discusses the role of geophysics in the exploitation and conservation of natural resources and the assessment of degradation of natural systems by pollution. The near surface is a zone where humans and natural systems interact. Understanding the effects of human impacts is a challenge particularly for the long term.

There are four new chapters in the volume on Deep Earth Seismology. One of them describes progress in seismic instrumentation in the last 30 years in the era of broadband digital sensor and recording systems. Another one addresses a new approach for the determination of crust and uppermost mantle structure, based on ambient noise cross-correlations. This has revolutionized the field, since it allows the study of regional structure at high resolution in areas where there are no earthquakes. The third new chapter is devoted to recent advances in characterizing the lithosphere–asthenosphere boundary under both oceans and continents. Finally, the last new chapter discusses the morphology of subducted slabs in the Earth's transition zone.

The Mineral Physics volume has new chapters on dynamic (shock-wave) compression methods, and on the mineralogy of the upper mantle and the D″ layer focusing on post-perovskite, and extrasolar super-Earths.

New material in the Geodesy volume expands the temporal resolution and latency of geodetic measurements to high-rate, real-time measurements and increases the spatial resolution to meter size pixels with optical and radar imaging systems. Application areas are extended with new material on the uses of Earth gravity measurements.

The Earthquake Seismology volume has a new chapter on rock mechanics that is a comprehensive account of modern rock mechanics with emphasis on the variation of frictional properties of rocks during an earthquake cycle. Many chapters have considerable updates reflecting the lessons from significant recent earthquakes (e.g., the 2011 Tohoku-Oki earthquake and the 2013 Okhotsk deep earthquake), new observations on slow slips and triggered earthquakes, and developments of new methods (e.g., back projection method). Some chapters are updated (e.g., paleoseismology and strong ground motion) with substantial new material.

Chapters in the Geomagnetism volume have been updated to include recent advances in the acquisition of larger data sets and higher quality data and in the construction of more reliable and sophisticated models. Improvements in data have occurred in areas such as magnetic anomalies, paleointensities, and planetary magnetism. Improvements in models of the present day field include so-called comprehensive models and models that incorporate data assimilation.

The Crustal and Lithosphere Dynamics volume has new contributions on mountain building and landscape evolution.

The Mantle Dynamics volume contains new chapters on the generation of plate tectonics from mantle convection and the core–mantle boundary region.

The Core Dynamics volume features a comprehensive update of this rapidly changing subject, including new chapters on turbulence and waves in the fluid outer core.

The volume on the Evolution of the Earth presents a new assessment on the role of volatiles in Earth evolution.

There are new chapters in the Physics of Terrestrial Planets and Moons volume on planetary atmospheres, planetary tectonics, extrasolar planets and asteroids and comets. The study of extrasolar planets has had explosive growth in the last decade and new spacecraft missions have significantly enhanced our knowledge of solar system planets and moons.

Finally, this is an opportunity for me to thank and acknowledge the editors of the individual volumes for their hard work, patience, dedication, and commitment in bringing this new edition of the Treatise to fruition. I am also indebted to Gemma Tomalin of Elsevier for her care and attention to the organization and production of the Treatise and to Deepa Arumugam for her careful coordination of the proofs from the copyeditor and typesetter. Of course, the authors of the individual chapters are the ones who are responsible for the excellence of the Treatise. We have all had some ups and downs in the process of producing the second edition of the Treatise but the final product is one that we can all view with pride.

Gerald Schubert
Editor-in-Chief

EDITOR-IN-CHIEF

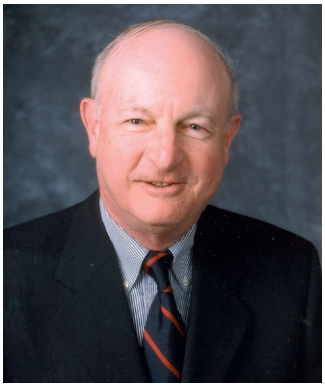

Gerald Schubert is Distinguished Professor Emeritus in the Department of Earth, Planetary and Space Sciences at the University of California, Los Angeles. His research interests encompass the physics of the interiors and atmospheres of the Earth, the Moon, and the other moons and planets of the solar system. He is co-author with Donald Turcotte of *Geodynamics* (ed. 3, Cambridge University Press, 2014) and with Turcotte and Peter Olson of *Mantle Convection in the Earth and Planets* (Cambridge University Press, 2001). He is the author of over 540 research papers. He has participated in a number of NASA's planetary missions, including Apollo, Pioneer Venus, Magellan, and Galileo, and has been editor and editorial board member of many journals, including *Icarus*, *Journal of Geophysical Research*, *Geophysical Research Letters*, and *Annual Reviews of Earth and Planetary Sciences*. Professor Schubert is a Fellow of the American Geophysical Union and a recipient of the Union's James B. MacElwane medal and the Harry H. Hess medal. He is a member of the National Academy of Sciences and the American Academy of Arts and Sciences.

This page intentionally left blank

CONTRIBUTORS

M Bergman
Bard College at Simon's Rock, Great Barrington, MA, USA

BA Buffett
University of California, Berkeley, CA, USA

P Cardin
University Grenoble Alpes/CNRS, Grenoble, France; Université Joseph-Fourier, Grenoble, France

UR Christensen
Max-Planck-Institut für Sonnensystemforschung, Göttingen, Germany

RS Coe
University of California, Santa Cruz, CA, USA

CC Finlay
DTU Space, Technical University of Denmark, Lyngby, Denmark

GA Glatzmaier
University of California, Santa Cruz, CA, USA

R Holme
University of Liverpool, Liverpool, UK

D Jault
University Grenoble Alpes/CNRS, Grenoble, France

CA Jones
University of Leeds, Leeds, UK

H-C Nataf
University Grenoble Alpes/CNRS, Grenoble, France

F Nimmo
University of California, Santa Cruz, CA, USA

P Olson
Johns Hopkins University, Baltimore, MD, USA

PH Roberts
University of California, Los Angeles, CA, USA

N Schaeffer
University Grenoble Alpes / CNRS, Grenoble, France

I Sumita
Kanazawa University, Kanazawa, Japan

A Tilgner
University of Göttingen, Göttingen, Germany

J Wicht
Max-Planck-Institut für Sonnensystemforschung, Göttingen, Germany

This page intentionally left blank

8.01 Core Dynamics: An Introduction and Overview

P Olson, Johns Hopkins University, Baltimore, MD, USA

© 2015 Elsevier B.V. All rights reserved.

8.01.1	**Introduction**	1
8.01.2	**The Scientific Journey to the Center of the Earth**	1
8.01.3	**State of the Core**	4
8.01.4	**The Search for a Dynamo Theory**	5
8.01.5	**Core Dynamics and the Geomagnetic Field**	9
8.01.6	**Core Energetics**	10
8.01.7	**Core Dynamics as a Heat Engine**	12
8.01.8	**Convection and Dynamo Action**	12
8.01.9	**Simulating the Geodynamo**	14
8.01.10	**Mantle Effects Within the Core**	15
8.01.11	**The Dynamical Inner Core**	16
8.01.12	**Future Prospects and Problems**	17
8.01.13	**Additional References**	18
8.01.14	**Summary of the Chapters in This Volume**	18
8.01.14.1	Energetics of the Core	18
8.01.14.2	Theory of the Geodynamo	18
8.01.14.3	Large-Scale Flow in the Core	19
8.01.14.4	Thermal and Compositional Convection in the Outer Core	19
8.01.14.5	Waves in the Core and Mechanical Core–Mantle Interactions	20
8.01.14.6	Turbulence in the Core	20
8.01.14.7	Rotational Dynamics of the Core	20
8.01.14.8	Numerical Dynamo Simulations	20
8.01.14.9	Magnetic Polarity Reversals in the Core	21
8.01.14.10	Inner Core Dynamics	22
8.01.14.11	Experiments on Core Dynamics	22
8.01.14.12	Core–Mantle Interactions	23
References		23

8.01.1 Introduction

The inaugural edition of the *Treatise on Geophysics* published in 2007 included for the first time a geoscience volume specifically devoted to the dynamics in the Earth's core. This Core Dynamics volume in the second edition of Treatise on Geophysics continues that tradition, offering an in-depth discussion of the dynamical processes that are active at the very heart of the Earth, some of which have impact far beyond the core itself. In the years since the first edition, there has been much in the way of progress, plus some revisions, as is inevitable in studying the most remote region of our planet. The overall trend is toward a more dynamical perspective of the core, in which energy production and dissipation are higher and the pulse of evolution is stronger, compared to our thinking just a few years ago. Evidence of this trend is found in the major new ideas, advances, concepts, and research directions that have appeared since the first edition, including the following:

- Inner core convection, including the proposed translation instability
- First-principles atomic structure calculations and high-pressure experiments indicating higher electric and thermal conductivity in the core than previously thought, altering our picture of its present-day state and its evolutionary history
- New approaches to imaging the structure of the large-scale core flow
- Identification of shorter-period torsional oscillation frequencies, providing new estimates of the average magnetic field strength inside the core
- Novel laboratory experiments including the von Kármán sodium dynamo experiment
- Application of broad-based scaling laws derived from numerical dynamos and laboratory experiments applied to the modern and the ancient geomagnetic field

The Core Dynamics volume in the second edition of Treatise on Geophysics includes updates of what appeared in the first edition plus accounts of the progress since then, such as the items listed earlier in the text. It also includes a new chapter on waves in the core and a newly authored chapter on outer core turbulence.

8.01.2 The Scientific Journey to the Center of the Earth

As long as man has speculated about the interior of the Earth, it has been presumed there exists a central core. Centuries before the rise of modern science, philosophers and theologians had

 http://dx.doi.org/10.1016/B978-0-444-53802-4.00137-8

concluded that the Earth has a hot core at its center, with properties that differ from all other parts of our planet. For nearly as long, it has been recognized that the Earth is also magnetic, but the origin of the Earth's magnetism remained just as mysterious as the nature of the deep interior.

Although the ancient Chinese made the first discoveries related to geomagnetism, scientific inquiries about the Earth's core began in the West in the Middle Ages. In 1269, Petrus Peregrinus de Maricourt's treatise *Epistola de magnete* offered explanations for magnetic attraction and repulsion, the operation of the compass, the properties of magnetized materials, and the concept of magnetic poles (Arnold, 1904). Peregrinus also reported an unsuccessful search for magnetic monopoles – breaking naturally magnetized lodestones into ever smaller fragments – and he even described in rudimentary terms the idea of a magnetic field reversal. Gilbert (1600) was the first to demonstrate that the compass needle is controlled by a force originating within the Earth, showing that the pattern of magnetic field lines near a uniformly magnetized sphere approximates the known directions of the compass needle over the Earth's surface (**Figure 1**). Three hundred and fifty years later, Sidney Chapman characterized Gilbert's demonstration as 'the only successful experiment in the history of geomagnetism!'

Early in the era of global exploration, navigators observed that the Earth's magnetic field slowly changes with time, a property now called the secular variation. In an attempt to explain the secular variation, Halley (1683, 1692) proposed that the geomagnetic field has its origin near the Earth's center, in a region separated from the solid crust by a cavernous, fluid-filled shell. Halley envisioned that both the crust and the central region or core rotate in the prograde sense but the core rotates slightly slower than the crust, causing the magnetic field to drift systematically westward as seen at the surface. Two important and long-lasting concepts were thus born: the basic three-layer model of the Earth's interior (solid crust and mantle, liquid outer core, and solid inner core) and the association between the geomagnetic drift and motion of the fluid outer core with respect to other parts of the Earth's system. Halley's model implicitly assumed that the magnetic field originated in a solid inner core (Evans, 1988), akin to Gilbert's uniformly magnetized sphere. Subsequently, it was shown that Halley's model is at variance with the ferromagnetic properties of Earth materials, which lose their permanent magnetization at the Curie temperature at depths of a few tens of kilometers beneath the surface. However, by then, the physical connection between magnetic fields and electric currents had been established, providing an alternative explanation for the geomagnetic field that relied on free electric currents rather than permanent magnetization (**Figure 2**).

The liquid (i.e., molten) state of the outer core was firmly established during the early part of the twentieth century, but the roots of the idea can be traced back into antiquity. Several independent lines of scientific evidence appeared in the middle of the nineteenth century in favor of high temperatures in the Earth's deep interior, including the steep geothermal gradient

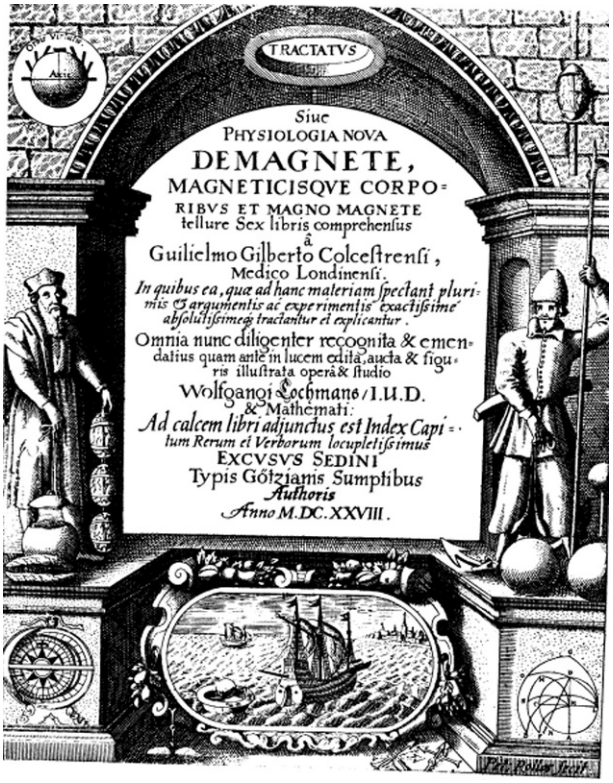
TRACTATVS

Siue
PHYSIOLOGIA NOVA
DEMAGNETE,
MAGNETICISQVE CORPO-
RIBVS ET MAGNO MAGNETE
tellure Sex libris comprehensus
à
Guilielmo Gilberto Colcestrensi,
Medico Londinensi.
In quibus ea, quæ ad hanc materiam spectant pluri-
mis & argumentis ac experimentis exactissimè
absolutissimeq; tractantur & explicantur.
Omnia nunc diligenter recognita & emen-
datius quam antè in lucem edita, aucta & figu-
ris illustrata operâ & studio
&
Wolfgangi Lochmans / I.U.D.
& Mathemati.
Ad calcem libri adjunctus est Index Capi-
tum Rerum et Verborum locupletissimus
EXCVSVS SEDINI
Typis Gōtzianis Sumptibus
Authoris
Anno M.DC.XXVIII.

Figure 1 Title page from Gilbert's (1600) treatise *De Magnete*.

Figure 2 Edmond Halley (1656–1742) interpreted the geomagnetic secular variation.

measured in deep mines and petrologic measurements that indicated very high temperatures are needed to form most igneous rocks. However, the early estimates of the actual temperature variation through the deep Earth varied wildly, preventing any firm conclusion about the state of matter in the core.

Toward the close of the nineteenth century, two competing models of the state of the Earth's deep interior emerged. One model assumed that the interior was solid (except small melt regions below volcanoes) and also elastic, with a very high shear modulus, 'as rigid as steel,' according to Kelvin's (1862) famous prescription. This model was supported by observations of the amplitudes of the tides (Darwin, 1879) and the period of the Earth's free nutation, the Chandler wobble (Newcomb, 1892). The competing model held that the interior was largely fluid, an idea that was popular with geologists at that time, although it had prominent adherents within the physics community as well, for example, Ritter (1878), Poincaré (1885), Arrhenius (1900), and, even earlier, Franklin (1793).

The terms of this debate underwent a permanent shift with the publication by Wiechert (1897) of the first quantitative model of the Earth's structure (**Figure 3**). Wiechert's Earth model was based on all available astronomical and geodetic data and featured a central metallic core surrounded by a rocky mantle. Wiechert is often given credit for being the first to attribute both chemical and physical differences to the core and mantle and the first to conclude that the core–mantle boundary, the most significant discontinuity in the planet's interior, represents a change from silicates to iron and a density jump. In any case, there is little doubt that his work launched the era of seismic exploration of the core. Within a decade, Oldham identified seismic P- and S-waves (1899) and interpreted the P-wave shadow as low velocity in a central core (Oldham, 1906). Shortly thereafter, Gutenberg (1912) determined the location of the core–mantle boundary, at a depth of 2900 ± 20 km, consistent within his calculated uncertainty with the present-day value.

Gutenberg's original Earth model included rigidity throughout the core, in spite of the fact that seismic shear wave transmission through the core had never been confirmed, a testimony to the lasting influence of Kelvin's ideas. Indeed, the fluidity of the core was not settled until Jeffreys (1926) showed it was possible to reconcile seismic wave speeds with tidal and Chandler wobble observations using an Earth model with a liquid core of radius 3471 km, essentially the same as in the Gutenberg model. As Brush (1996) pointed out in his history of the exploration of the Earth's interior, Jeffreys' reputation was somewhat tarnished by his refusal to accept continental drift and the concept of mantle convection (Jeffreys, 1929). Ironically, however, Jeffreys himself made several fundamental contributions to the theory of convection in viscous fluids that led to the basic model for mantle convection, and he also contributed importantly to the acceptance of the geodynamo theory by demonstrating the outer core is liquid.

The final piece of the main radial structure of the core was provided by Lehmann (1936), who discovered the inner core boundary, which she placed at 4970 km depth, or 1400 km radius (the currently preferred radius is about 1220 km) (**Figure 4**). Following Lehmann's discovery, seismologists have succeeded in demonstrating the crystalline nature of the inner core material. The study by Dziewonski and Gilbert (1971) of normal mode overtones excited by the 1964 Alaska earthquake provided an estimate of its average rigidity, and subsequent investigations have determined that the inner core

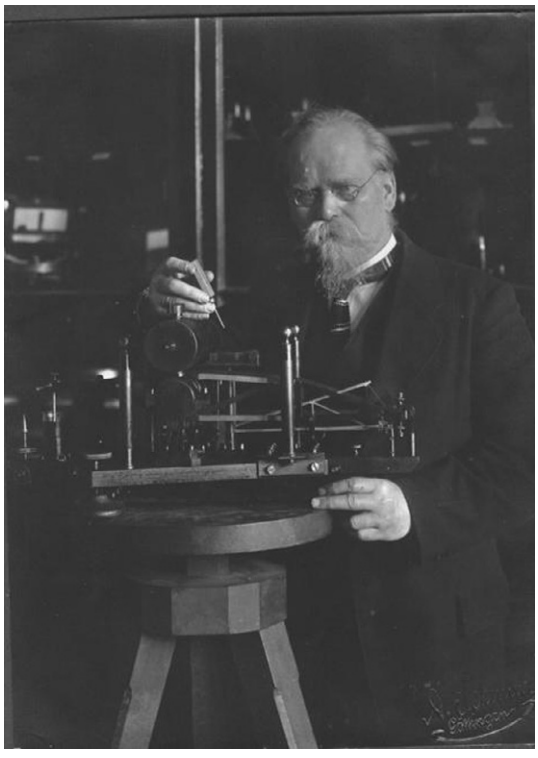

Figure 3 Emil Wiechert (1861–1928) constructed the first quantitative Earth model with a core.

Figure 4 Inge Lehmann (1888–1993) discovered the inner core.

Table 1 Chronology

Year	*Person(s)*	*Event*
1000	Chinese	Discovered lodestone south–north orientation
1269	P. Peregrinus	Defined magnetic poles
1600	W. Gilbert	Publication of *De Magnete*
1634	H. Gellibrand	Discovered geomagnetic secular variation
1683	E. Halley	Interpreted secular variation
1820	H. Ørsted, A. Ampere	Related magnetism to electric currents
1831	M. Faraday	Introduced disk dynamo
1834	C. F. Gauss	Measured magnetic intensity
1836	C. F. Gauss	Spherical harmonic analysis
1897	E. Weichert	Iron core Earth model
1906	R. Oldham	Observed core seismic waves
1906	B. Brunhes	Reversely magnetized rocks
1912	B. Gutenberg	Determined core radius
1919	J. Larmor	Proposed self-sustaining fluid dynamos
1936	I. Lehmann	Discovered inner core
1933	T. Cowling	Antidynamo theorems
1942	H. Alfvén	Magnetohydrodynamic waves
1946	W. Elsasser	First MHD dynamo theory
1952	F. Birch	Composition of the core
1953	J. Jacobs	Present-day inner core growth
1955	E. Parker	$\alpha\omega$-Dynamo effect
1958	A. Hertzenberg, G. Backus	Laminar kinematic dynamos
1961	J. Verhoogen	Inner core freezing as core energy source
1963	F. Lowes and I. Wilkinson	Laboratory dynamo
1963	J. B. Taylor	Rotational dynamo constraint
1966	M. Steenbeck et al.	α^2-Dynamo effect
1971	A. Dziewonski and F. Gilbert	Inner core rigidity
1976	S. Braginsky	Asymptotic dynamo model Z
1995	G. Glatzmaier and P. Roberts	Self-consistent reversing dynamo model
1995	A. Kageyama and T. Sato	Self-consistent compressible dynamo model
1996	Z. Song and P. Richards	Inner core superrotation
2001	A. Gailitis, U. Muller, and others	First laboratory fluid dynamos
2006	U. Christensen and J. Aubert	Scaling laws for planetary dynamos
2007	VKS team	von Kármán reversing laboratory dynamo
2010	T. Alboussiere, M. Monnereau, and others	Inner core translation

is also anisotropic and heterogeneous. Table 1 gives a chronology of important milestones in this scientific journey.

8.01.3 State of the Core

A full review of the composition of the core is found in Volume 2 of this treatise. Here, we provide a brief summary of the major constituents of the core, for purposes of this chapter. Table 2 lists some of the well-known physical properties of the core, Table 3 lists some important thermodynamic and transport properties (which are generally less well known), and Figure 5 shows its basic radial structure.

Table 2 Known physical properties

Property	*Notation*	*Units*	*Value*
Core radius (mean)	r_o	m	3.480×10^6
Inner core radius (mean)	r_i	m	1.22×10^6
Outer core thickness	d	m	2.26×10^6
Core–mantle boundary (CMB) area	A_o	m^2	1.52×10^{14}
Inner core boundary (ICB) area	A_o	m^2	1.87×10^{13}
Core–mantle boundary ellipticity	ε_o	nd	2.5×10^{-3}
Core volume	V	m^3	1.77×10^{20}
Inner core volume	V_i	m^3	7.6×10^{18}
Outer core volume	V_o	m^3	1.70×10^{20}
Core moment of inertia	I	kg m^2	9.2×10^{36}
Outer core mass	M_o	kg	1.835×10^{24}
Inner core mass	M_i	kg	9.68×10^{22}
Core density (mean)	ρ	kg m^{-3}	1.09×10^4
Inner core density (mean)	ρ_i	kg m^{-3}	1.29×10^4
Core–mantle boundary gravity	g_o	m s^{-2}	10.68
ICB gravity	g_i	m s^{-2}	4.40
Core–mantle boundary pressure	P_o	GPa	136
ICB pressure	P_i	GPa	323
P-wave velocity below CMB	v_p	km s^{-1}	8.07
P-wave velocity above ICB	v_p	km s^{-1}	10.36
Poisson ratio, inner core	ν_P	nd	0.44
Angular velocity of rotation	Ω	rad s^{-1}	7.292×10^{-5}
Free core nutation period	T_c	s	3.71×10^7
Magnetic dipole moment	m_d	A m^2	7.8×10^{22}
Magnetic dipole tilt	θ_d	deg	10.8
Magnetic intensity, CMB (rms)	B_{CMB}	mT	0.42
Magnetic intensity, outer core (rms)	B_{rms}	mT	2–4
Magnetic dipole intensity, CMB (rms)	B_{CMB}^{dip}	mT	0.263

The model of a predominantly iron core was firmly in place by the middle of the twentieth century and was well supported by evidence from seismology (Bullen, 1954) and mineral physics (Birch, 1952). One early argument that was often cited in support of an iron core was Birch's law (Birch, 1964), a linear relationship between density and bulk sound velocity with a coefficient proportional to the mean atomic weight of the material. Application of Birch's law revealed that the mean atomic weight of the outer core and inner core is both slightly less than iron but is far too large to be explained by a phase transformation of lower mantle material. Although it is now recognized that the theoretical basis for Birch's law is weak, it was historically important because it seemed to demand a metallic, rather than an oxide-rich or silica-rich composition. Other metals might also be present in the core. The abundance of nickel in iron meteorites was historically used to argue that the core contains substantial Fe–Ni alloy, but since many of the physical properties of nickel are indistinguishable from iron at core conditions, unambiguous detection of nickel in the core is problematic.

The presence of lighter elements is vitally important for the dynamics of the core. As described in Volume 2 of this treatise,

Table 3 Thermodynamic and transport properties

Property	*Notation*	*Units*	*Range*
Core–mantle boundary temperature	T_o	K	4100 ± 400
ICB temperature	T_i	K	5500 ± 600
Outer core temperature (mean)	T	K	4700 ± 500
Adiabatic temperature gradient, CMB	$-dT/dr_{ad}$	K km^{-1}	0.8 ± 0.2
Adiabatic temperature gradient, ICB	$-dT/dr_{ad}$	K km^{-1}	1.0 ± 0.3
Density jump, ICB	$\Delta\rho_i$	kg m^{-3}	750 ± 150
Light element concentration, outer core	C_o	%	8 ± 3
Light element concentration, inner core	C_i	%	3 ± 2
Thermal expansivity	α	K^{-1}	$1.2 \pm 0.5 \times 10^{-5}$
Light element expansivity	α_C	nd	0.8 ± 0.2
Specific heat	C_p	J kg^{-1} K^{-1}	850 ± 20
Latent heat, crystallization	L	J kg^{-1}	$1 \pm 0.5 \times 10^6$
Thermal conductivity	k	W m^{-1} K^{-1}	100 ± 30
Thermal diffusivity	κ	m^2 s^{-1}	$5 \pm 3 \times 10^{-6}$
Compositional diffusivity	D	m^2 s^{-1}	$1 \times 10^{-9\pm2}$
Kinematic viscosity, outer core	ν	m^2 s^{-1}	$1 \times 10^{-6\pm2}$
Kinematic viscosity, inner core	ν_i	m^2 s^{-1}	$1 \times 10^{10\pm3}$
Electric conductivity	σ	A^2 kg^{-1} m^{-3} s^3	$1–2 \times 10^5$
Magnetic diffusivity	λ	m^2 s^{-1}	1 ± 0.5

the abundance of the various candidate light elements has been a matter of intense controversy. Decades of high-pressure measurements and theory have convincingly demonstrated Birch's interpretation that the outer core is less dense than pure iron at in situ conditions, even allowing for the expected density decrease due to melting, and therefore requires the addition of light elements to reduce the density by 6–10%. Candidate light elements frequently proposed to reconcile this density deficit include oxygen, sulfur, silicon (MacDonald, 2003; Poirier, 1994), and, less frequently, hydrogen and even carbon. Sulfur has a known affinity for iron at low pressures, and high-pressure studies indicate that the oxygen is soluble in iron at core conditions (Alfe et al., 2003). Both sulfur and oxygen are known to affect the phase diagram of iron substantially, including the melting point. Somewhat less is known about the high-pressure effects of silicon in the core (Georg et al., 2007) and still less about hydrogen and carbon.

Most detailed information on the present-day structure of the core comes from seismology (see Volumes 1 and 4 of this treatise). The variation of seismic wave velocity and density with depth through the fluid outer core shown in **Figure 5(b)** are basically consistent with a homogeneous mixture of iron and the lighter alloying elements listed in the preceding text (Dziewonski and Anderson, 1981). Regions that deviate from this apparent homogeneity including a thin layer at the base of the outer core will be described later. Unfortunately, it has proven to be difficult to choose between the candidate light elements in the core on the basis of their seismic properties alone. Some dilution of the solid inner core by lighter elements is also indicated, as the predicted density of solid iron is a few percent greater than what the seismic properties indicate (Masters and Gubbins, 2003; Shearer and Masters, 1990). The actual density change at the inner core boundary is 600–900 Mg m^{-3} (Cao and Romanowicz, 2004), of which about one-third is due to solidification. The rest is likely due to differences in light element concentration between the inner core and outer core. This small density difference has profound implications for the driving mechanism for flow in the core and also for the power source of the geodynamo (Buffett, 2003). A related issue is the abundance of radioactive heat sources in the core. Among the possible radio isotopes, ^{40}K is the most likely to be energetically significant, because of its low-pressure affinity for iron sulfides, suggesting it may have partitioned into the core during the Earth's accretion. However, the amount of potassium in the core is still debated (Bouhifd et al., 2007; Gessmann and Woods, 2002; Rama Murthy et al., 2003). In addition to potassium, some uranium content has been proposed for the core, which could slightly augment the amount of internal heat production. As mentioned earlier in the text, the temperature distribution in the core appears to follow an adiabat. Based on melting point temperature measurements (Boehler, 1996) and shock wave data (Nguyen and Holmes, 2004), it is estimated that the temperatures at the core–mantle boundary and inner core boundary are approximately 4100 and 5500 K, respectively, as shown in **Table 3**.

8.01.4 The Search for a Dynamo Theory

Until rather late in the twentieth century, *core dynamics* was a rather narrowly defined subject, limited to a handful of topics drawn from classical mechanics, such as rotational and tidal deformation, pursued by a small number of theoretical physicists and applied mathematicians, G. Darwin, H. Poincaré, and H. Jeffreys, among them. The full range of core dynamics, the subject of this volume, has received widespread study only since the advent of the modern dynamo theory for the origin of the geomagnetic field.

After the time of Halley, relatively little attention was paid to the origin of the geomagnetic field, until well into the twentieth century. Gauss (1832, 1939) conjectured that geomagnetic secular variation was a consequence of solidification of the crust but evidently did not speculate much on the origin of the main field (**Figure 6**). Zollner (1871) constructed a model for geomagnetic secular variation that included several aspects of the present-day dynamo theory, including electric currents induced in a liquid core and interaction with the solid mantle. However, his ideas evidently were not taken up by others, and the subject continued to languish in obscurity. Even in the middle decades of the twentieth century, leading theorists showed only passing interest in the generation of the

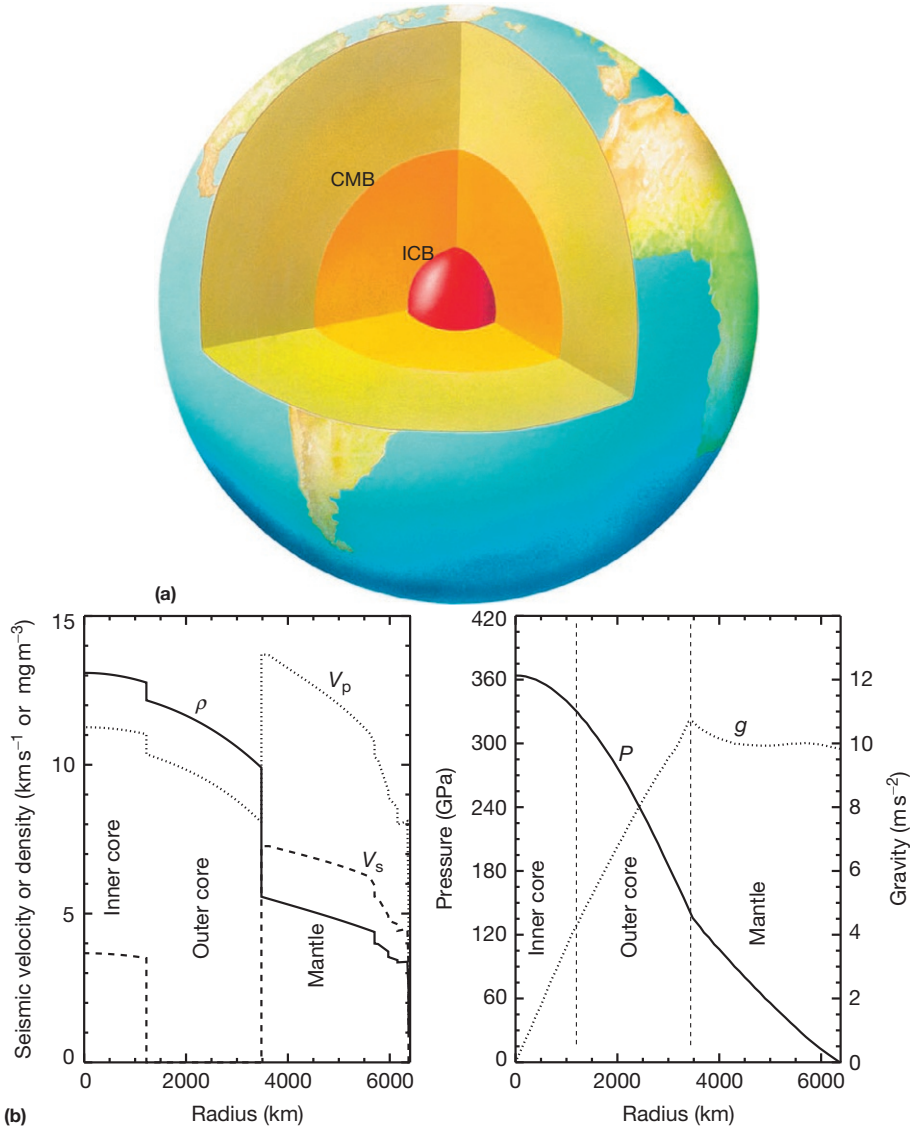

Figure 5 (a) Cutaway view showing the main layers of the Earth's interior, including the solid mantle (yellow), the liquid outer core (orange), the solid inner core (red), and the core–mantle boundary (CMB) and the inner–outer core boundary (ICB). (b) Seismic Earth model PREM. Reproduced from Dziewonski AM and Anderson DL (1981) Preliminary reference Earth model. *Physics of the Earth and Planetary Interiors* 25: 297–356.

geomagnetic field. For example, Chapman and Bartels' (1940) treatise *Geomagnetism* devotes portions of just seven pages (out of 1050 total) to this topic. They rejected permanent magnetization, ohmic decay of free electric currents, and gyromagnetism as primary causes. They also dismissed the self-sustaining dynamo mechanism, concluding, as did Schuster (1911), that the "difficulties which stand in the way of basing terrestrial magnetism on electric currents inside the Earth are insurmountable" (**Figure 7**).

Evidently, Chapman and Bartels were responding to the suggestion in a short paper by Larmor (1919), proposing that, because the circulation of a conducting fluid in the presence of a seed magnetic field would induce an electric field, if a suitable path for electric currents was created in the fluid, a stronger magnetic field might be maintained indefinitely. In short, Larmor had proposed a self-sustaining fluid dynamo (**Figure 8**). Although Larmor's suggestion was primarily intended for application to the Sun (his paper refers to Hale's discovery of magnetic fields in sunspots), the idea seemed equally applicable to the Earth. However, it did not result in immediate progress on the geodynamo, perhaps because of an influential paper by Cowling (1933), who showed that electromagnetic induction by a conducting fluid cannot maintain a steady axisymmetric magnetic field. This was the first of several antidynamo theorems that cast a shadow of doubt on the validity of the self-sustaining dynamo concept. In retrospect, it seems that Cowling's theorem was overinterpreted. A steady axisymmetric dynamo is probably an unphysical situation and is certainly not applicable to the Earth. Nevertheless, many theorists of that era concluded that Cowling's theorem implied that a general nonexistence proof of fluid dynamos would eventually be found.

Figure 6 Carl Friedrich Gauss (1777–1855) father of geomagnetism.

Figure 7 Henri Poincaré (1854–1912) developed the theory of rotating, precessing fluids.

The logjam started to break in the 1940s, beginning with a series of papers by Elsasser (1946, 1950) and Bullard et al. (Bullard and Gellman, 1954; Bullard et al., 1950), the first quantitative efforts to build a full magnetohydrodynamic (MHD) theory for the main geomagnetic field. Accomplishments in these early papers that have stood the test of time include the derivation of the magnetic induction equation for incompressible flow, representation of the magnetic field in terms of its poloidal and toroidal parts, amplification of toroidal field through the interaction of toroidal shear flow with a poloidal (i.e., dipolar-type) field, selection rules for interaction between toroidal magnetic fields and poloidal flows, identification of outer core convection as the main source of kinetic energy for the flow, and definitions of several of the key dimensionless parameters that govern self-sustaining fluid dynamos, including the ratio of Lorentz to Coriolis forces, now called the Elsasser number. In addition, these early papers offered an explanation for the observed geomagnetic westward drift, based on the conservation of angular momentum and core–mantle interaction (**Figures 9** and **10**).

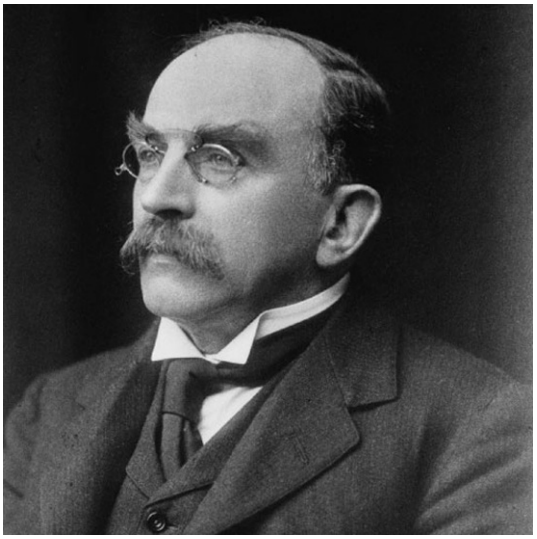

Figure 8 Joseph Larmor (1857–1942) proposed a self-sustaining fluid dynamo for the core.

The main shortcoming of these pioneering papers was that they failed to adequately prove the existence of self-sustaining fluid dynamos, even kinematic ones. Elsasser's (1946) attempt at a theoretical demonstration fell short of completeness, and the early numerical efforts by Bullard and Gellman (1954) to construct kinematic dynamos in terms of a series of spherical harmonics have subsequently been shown to diverge when the series is extended (Gubbins, 1973; Lilly, 1970). The first working theoretical examples of kinematic fluid dynamos were by Backus (1958) and Hertzenberg (1958). Although these were based on quite unrealistic flows (e.g., the Backus dynamo assumed periods of motion alternating with periods of stasis), they succeeded in demonstrating the existence of fluid dynamos and, with this, the limitations of Cowling's theorems. Several other examples of kinematic dynamos followed on their heels, in which the flow was assumed to consist of large-scale, laminar-type motions amenable to analytic or simple numerical investigation (see **Chapter 8.03**), including an important experimental dynamo by Lowes and Wilkinson (1963) that involved both fluid and solid conducting parts. Although these idealized dynamos provided only limited insight into the dynamics of the geodynamo, they nevertheless

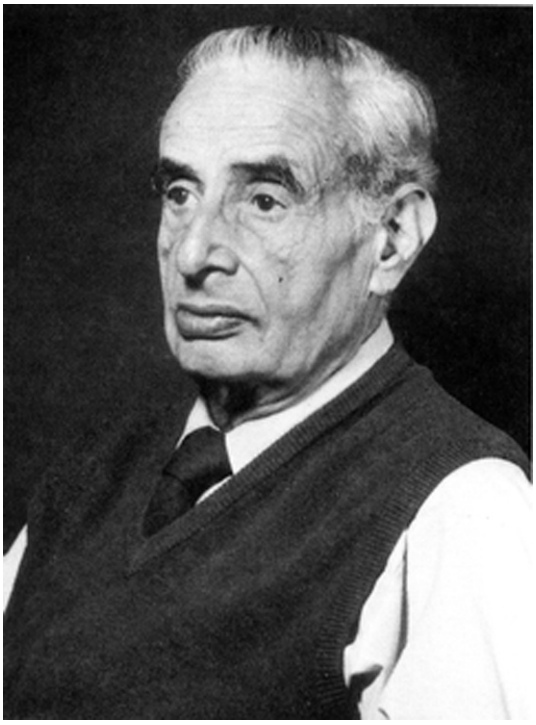

Figure 9 Walter M. Elsasser (1904–91) pioneer in the dynamo theory of geomagnetism.

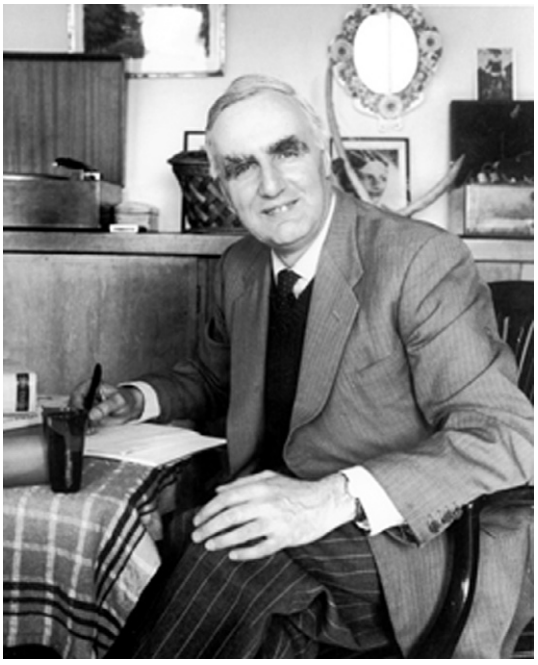

Figure 10 Edward C. Bullard (1907–80), leading twentieth-century geophysicist, the first to attempt numerical solution of the dynamo problem.

were valuable milestones, helping to define some of the conditions necessary for magnetic field generation in the core.

Just as these successes were being registered, the direction of dynamo research began to shift away from large-scale kinematic models, following the introduction of mean-field dynamo concepts. The first mean-field theory for dynamo action was an early model by Parker (1955), who proposed that polodial magnetic field is induced in the core by the statistical action of smaller-scale convective vortices acting on the large-scale toroidal magnetic field. Parker used the term *cyclonic* to describe the kinematics of convective flows in which the radial velocity correlates with the radial vorticity, a consequence of the Earth's rotation. The term now used to describe such motions is *helicity*, defined as the inner product of vorticity and velocity vectors.

Helical flows have the important property of twisting east–west-oriented toroidal magnetic field lines into meridional planes, thus inducing a poloidal magnetic field from the original toroidal one. This mechanism for inducing poloidal from toroidal magnetic field was recognized as a key ingredient that was missing from many of the failed efforts to produce kinematic dynamos. It became a particularly potent concept starting in the 1960s, with the introduction of *mean-field electrodynamics*, a formal approach for calculating the large-scale induction properties of complex, small-scale flows (see **Chapter 8.03**). Mean-field electrodynamics is implicit in the early work of Parker (1955), but the form in which it is used today came later, from astrophysics (Steenbeck and Krause, 1969; Steenbeck et al., 1967). The basic idea is to represent the fluid velocity and the magnetic field as consisting of a mean plus a fluctuating part, the latter part having zero average over some appropriately chosen length or timescales. Under the right conditions, the interaction between the small-scale velocity and magnetic fields generates a large-scale electric field that is parallel to the large-scale magnetic field. The proportionality between the induced electric field and the large-scale magnetic field is represented by the coefficient α, and the name given to this type of induction is the 'α-effect.' Dynamo action occurs if the α-coefficient is sufficiently large to overcome the inhibiting effects of magnetic diffusion.

Roberts (1972) produced an extensive set of numerical calculations that showed how self-sustaining kinematic dynamos could be generated in conducting fluid spheres using various distributions of the α-parameter, in combination with different types of large-scale flows. The nomenclature introduced by Roberts for the large-scale flows included ω for toroidal shear flows and m for meridional (poloidal) flows. Combinations of these parameters produced an assortment of dynamos, for example, α^2-dynamos, in which both the toroidal and poloidal magnetic fields are induced by the small-scale motion; $\alpha\omega$-dynamos, in which the poloidal field is induced by the small-scale flow through the α-effect, but the toroidal field is induced by the ω-effect; and $\alpha\omega m$-dynamos, where all three effects are active. One advantage of this formalism is that kinematic dynamos exhibiting a wide variety of characteristics could easily be constructed, without explicitly specifying the details of the fluid motion, in essence by lumping all of the flow properties into a few parameters. It was subsequently shown that the α-effect is proportional in many rotating systems to the fluid helicity (Moffatt, 1978; Rädler, 1978), so that the kinematics of these dynamos could be related, at least indirectly, to real fluid motions.

With the successes of mean-field electrodynamics, efforts to find dynamos driven entirely by large-scale flows waned in the

1970s, and around this same time, additional impetus for the study of mean-field dynamos was provided by experimental and theoretical developments on thermal convection in rapidly rotating fluids. As discussed earlier, it is generally accepted that the most important fluid motions in the outer core for maintaining the geodynamo are convection – flows driven by destabilizing thermal and compositional buoyancy forces. Convection in the core is surely affected by the Coriolis acceleration. Because of the small viscosity of liquid iron compounds, the Ekman number in the core is exceedingly small, perhaps as small as 10^{-15} (the Ekman number is the ratio of viscous to the Coriolis effects). In addition, the geomagnetic secular variation indicates that the fluid velocities in the core are of the order 10–20 km year^{-1}. Assuming a length scale of a few hundred kilometers for these motions, the Rossby number implied for these motions is also rather small (the Rossby number is the ratio of vorticity in the fluid motion to planetary vorticity). Busse et al. (Busse, 1970; Busse and Carrigan, 1976) developed theoretical and experimental techniques to study the structure of convection in this so-called rapidly rotating limit. They demonstrated that rapidly rotating convection takes the form of small-scale columns or vortices that are nearly two-dimensional (2D) and aligned parallel to the axis of rotation, as discussed in **Chapter 8.13**. Moreover, columnar convection is helical, with negative helicity in the northern hemisphere and positive helicity in the southern hemisphere (see Jones et al., 2000, and **Chapter 8.05**), and so is capable of dynamo action through the α^2-mechanism. Thus, the structure of rotating convection provides another important piece of the core dynamics puzzle.

While all of these advances in understanding the kinematics of dynamo action were taking place, only incremental progress was being made on the more difficult problem of dynamo equilibration. Dynamo equilibration involves the back-reaction of the magnetic field on the flow, through the Lorentz force. The Lorentz force is nonlinear in the magnetic field, and its action in the context of internally generated fields was a little-understood facet of MHDs. The main focus of efforts to understand dynamo equilibration mechanisms involved a theorem proved by Taylor (1963), showing that, for small Ekman and Rossby numbers, the torque exerted by the Lorentz force must vanish on cylinders coaxial with the rotation axis. This so-called Taylor constraint imposes some restrictions on the configuration and the strength of the internal magnetic field in such a dynamo. It was widely assumed that the Taylor constraint applies to the geodynamo, and therefore, it determines the strength and the symmetry of the geomagnetic field inside the core. An alternative model of the field equilibration process was proposed by Braginsky (1976), the so-called model Z, which assumed a nearly uniform magnetic field configuration in the core interior plus thin magnetic layers just below the core–mantle boundary.

The stumbling block for all magnetic field equilibration theories has been the lack of a full understanding of the Lorentz force in self-sustaining dynamos. The nonlinear character of the Lorentz force has precluded the development of full analytic solutions, except in a few, highly idealized theoretical cases, such as weakly nonlinear dynamo action in horizontally infinite plane layers. Convincing demonstrations of how dynamos in spherical geometry driven by fully developed convective flows subject to the Lorentz forces equilibrate had to await the advent of 3D numerical models.

Full 3D, spherical MHD simulations were pioneered by astrophysicists Gilman and Miller (1983) for application to the Sun and magnetic stars and by Zhang and Busse (1988) for application to the Earth. Two influential and highly publicized numerical dynamos were produced nearly simultaneously, one by Glatzmaier and Roberts (1995) and another by Kageyama and Sato (1995). Both of these models were driven by thermal convection, although the former used the Boussinesq approximation, whereas the latter included fluid compressibility. Quickly thereafter, these models were extended to include the buoyancy derived from the growth of the inner core, for example, the study by Glatzmaier et al. (1999) was based on the theory for thermochemical convection in a compressible fluid proposed by Braginsky and Roberts (1995). Since then, numerical dynamos have spread around the globe, with a wide variety of competing dynamo models now in use (see **Chapter 8.10**). Further experimental confirmation of the dynamo theory came in the form of the first successful self-sustaining, laboratory fluid dynamos by Gailitis et al. (2003), Müller et al. (2006), and Berhanu et al. (2010) using liquid sodium (see **Chapter 8.13**).

8.01.5 Core Dynamics and the Geomagnetic Field

The study of the geomagnetic field is a rich topic in its own right and is the subject of Volume 5 in this treatise. Extensive descriptions of the geomagnetic field and paleomagnetic field can also be found in Merrill et al. (1998) and in Gubbins and Herrero-Bervera (2007), and the full theory of the geomagnetic field is given in Backus et al. (1996). Here, it is appropriate to briefly list some of the main features of the geomagnetic field that we seek to explain in terms of the core's dynamics. First and foremost is the persistence of an internally generated geomagnetic field, not just the modern field, but a field sustained throughout most if not all of the Earth's history. The main geomagnetic field that originates in the core is at least 3.4 Ga, according to the rock record (Tarduno et al., 2010), and quite possibly is as old as the core itself. The present-day dipole moment, $7.8 \times 10^{22}\,\mathrm{Am}^2$, is probably somewhat larger than the long-term average value, which may be around $6 \times 10^{22}\,\mathrm{Am}^2$. Significantly, there is little evidence for a secular trend in the dipole moment over geologic time, although there is abundant evidence of fluctuations, as described in the succeeding text. For reference, the free decay time of the dipole field in the core is only 30–50 ky. The existence of an ancient field, the lack of evidence of a decreasing dipole moment, and the inadequacy of permanent magnetization as a source for the field are three facts that demand there be a regeneration mechanism, that is, a dynamo theory.

The dominance of the dipole component is evident in the present-day field, where its energy exceeds that in any other spherical harmonic component, and this remains the case even when the surface field is extrapolated to the core–mantle boundary. The dipole dominance becomes even stronger if time averages of the geomagnetic field are considered. The characteristic time constants of the nondipole terms in the spherical harmonic representation of the field are measured

in centuries, so that when the field is averaged over a millennium or more, it tends toward a dipolar state. Over somewhat longer time averages, of the order of 10–20 ky, the components of the dipole moment vector lying in the equatorial plane average out, and the field tends toward a geocentric axial dipole (GAD), an important reference configuration. The GAD presentation of the field is the basis of much of paleomagnetism (see Volume 5) and the actual time-averaged field conforms to GAD at about the 95% level. The main deviations from GAD in the time-averaged field in the last few million years are a small axial quadrupole term (with the same sign as the dipole) and a small 1–2% additional deviation that may be a nonaxial field, but is not fully resolved (Johnson and Constable, 1997).

Although it has long-term persistence, the geomagnetic field exhibits fluctuations on a wide range of timescales, which are fully described in Volume 5 of this treatise. Fluctuations that originate within the core include the so-called geomagnetic jerks at the high-frequency end of the spectrum – probably the shortest time signal capable of traversing the weakly conducting mantle and still producing a measurable signal at the surface – and decade timescale fluctuations in tilt and other core field parameters. The classic geomagnetic secular variation occurs on century timescales and includes the present-day dipole moment decrease, which has been a feature of the geomagnetic field ever since Gauss' intensity measurements in the 1830s. Large-amplitude, irregular dipole moment strength fluctuations occur on millennium timescales, and individual dipole polarity chrons have characteristic timescales of several hundred thousand years. The constant polarity chrons are separated by polarity reversals and are often subdivided into shorter subchrons, separated by brief dipole transitions called excursions. The duration of the polarity reversal process, typically 5–15 ky, defines another characteristic timescale of the dynamo. On the longest timescales, the frequency of polarity reversals changes with a 200 My time constant, the minimum in the cycle being marked by superchrons, lengthy intervals that are evidently devoid of polarity reversals. The relationship between these characteristics of polarity reversals and the dynamics of the core is the subject of Chapter 8.11.

8.01.6 Core Energetics

The sequence of events in the formation and evolution of the core is reasonably well established, even though the timing of events and important details of the processes remain uncertain (see Volume 9 of this treatise). It is widely accepted that the core began to form during or shortly after the accretion from the solar nebula (Kleine et al., 2002). Heat generated by large impacts during the accretion phase, some of these impactors having metallic protocores of their own, would have resulted in widespread melting in the near-surface (Rubie et al., 2011), allowing the metallic compounds to separate and sink to the center, as illustrated in Figure 11. The kinetic and gravitational energy released in this process probably raised the core temperature by several thousand degrees, enough to ensure that the early core was entirely molten, particularly in the case of a giant Moon-forming impact. Along with Fe, the protocore metal included Ni and some important light constituents,

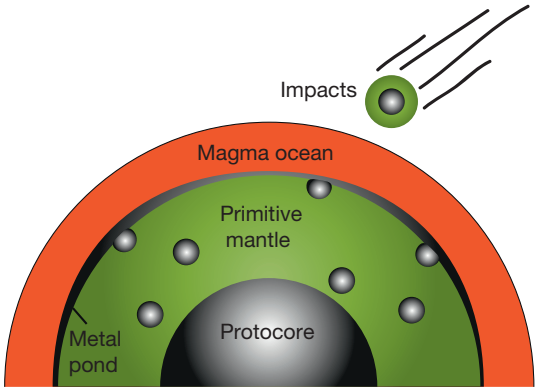

Figure 11 Schematic illustration of the mechanisms for gravitational separation of the core from the mantle during the magma ocean phase early in the Earth's history.

particularly S, O, and Si, and possibly Mg, C, and a few other abundant elements. Important heat-producing elements such as Th and U were likely partitioned into what became the mantle and crust, but some heat producers, most notably ^{40}K, may have dissolved into the iron compounds (Murthy et al., 2003) and been swept into the core. The exact processes by which the core segregated from the mantle remain uncertain, but regardless of their details, this was an extremely energetic event capable of completely mixing the early core and setting the stage for its later evolution, which was dominated by heat loss to the mantle and convection. Only much later, as the cooling of the Earth proceeded, the temperature in the core became low enough for the solid inner core to begin to nucleate by crystallization at the center.

As described in Chapters 8.07, 8.05, 8.06, and 8.09, the iron-rich outer core liquid has a small enough viscosity to permit strong convective flows, waves, turbulence, and other types of fluid motion with the present-day velocities in the range of 20 km year^{-1}. These fluid motions induce electric currents and magnetic fields in the core, which have persisted throughout the Earth's history in spite of the electric resistance of the iron and other core compounds. The set of processes by which magnetic fields and electric currents are produced and maintained by core dynamics are called the *geodynamo*. The geodynamo is fundamentally a MHD phenomenon, in which the kinetic energy of the outer core fluid is converted into electromagnetic energy. This energy conversion is promoted by the Earth's rotation, which structures the flow through the Coriolis acceleration, leading to sustained magnetic field production. The magnetic fields so produced exert forces back onto the core through the Lorentz forces, altering the fluid motion and allowing the geodynamo to attain an overall statistical equilibrium in the face of a host of fluctuations and instabilities.

Since the energy for the geodynamo is ultimately derived from the overall cooling of the Earth (possibly augmented by radioactive heating in the core), the history of the geodynamo is closely linked to the thermal and chemical evolution of the core and also to the thermal evolution of the mantle. The rejection of the light elements from the inner core as it crystallizes is now thought to be the major source of buoyancy for convection in the liquid outer core. The fluid enriched in light elements is expected to form ascending flows in the outer core,

while the fluid that is relatively depleted in light elements is expected to form descending flows. Thermal buoyancy is another important source of outer core convection. Thermal buoyancy originates near the core–mantle boundary, a consequence of the heat lost from the core to the cooler mantle. In addition, thermal buoyancy is also produced by inner core growth, through the release of latent heat of crystallization near the inner core boundary. The relative contributions of thermal and compositional buoyancy to convection in the outer core are uncertain, but recent upward revisions of the thermal conductivity of high-pressure iron compounds (de Koker et al., 2012) suggest that thermal buoyancy in the outer core is not as strong as compositional buoyancy. This was not always the situation, however. Earlier in the Earth's history, the inner core was likely smaller and played a proportionally smaller role in driving outer core convection, and prior to the nucleation of the inner core (which is variously estimated to have begun 0.3–1.0 Gy ago; see Chapter 8.02), convection in the outer core was probably driven by buoyancy forces originating at the core–mantle boundary.

An important factor in the energetics of the core is the control on the rate of core evolution imposed by the overlying mantle. The solid mantle has a larger thermal mass than the core, and its subsolidus convective overturn is much slower. Accordingly, heat transfer through the mantle is the rate-limiting process in the heat transfer out of the core, and for this reason, the mantle is the rate-limiter for convection in the core and inner core growth and also for the power available to the geodynamo. Estimates of the total heat flow from the core to the mantle have recently been revised upward and are now in the range of 8–16 TW (Lay et al., 2008; Wu et al., 2011), corresponding to 20–40% of the total heat flow at the Earth's surface (see Table 4). This would seem more than adequate to power convection in the outer core, except that the adiabatic gradient in the outer core is also quite large, nearly 0.9 K km^{-1}, and owing to the large thermal conductivity of liquid iron compounds, the heat conducted down the core adiabat is also large, comparable to the total core heat flow. The conducted heat flow makes little direct contribution to outer core convection and therefore represents a substantial tax on the geodynamo: The core must loose enough heat to maintain an adiabatic thermal profile in order to ensure that convection occurs throughout most of the outer core. In doing so, it uses up a relatively large fraction of its available energy.

Other complications in core–mantle thermal interactions arise because of the way the mantle draws heat from the core. The so-called D″ layer, the 200 km thick layer at the base of the lower mantle above the core–mantle boundary, is among the most heterogeneous regions in the Earth. As depicted in Figure 12, the lateral variations of seismic properties are larger in D″ than anywhere else in the lower mantle. In addition, the D″ layer is dynamically active. Its long-wavelength structure is related to, and probably dictated by, the large-scale pattern of flow, density, and viscosity variations in the lower mantle (Schubert et al., 2001). On shorter wavelengths, the internal dynamics in D″ shape its structure. The D″ layer is generally considered to be a source of mantle plumes, hot upwelling structures that produce volcanic hotspots on the surface. Thermal plumes are expected to form in D″ by virtue of the large superadiabatic thermal gradient there, estimated to be in the neighborhood of 5 K km^{-1}. The major volcanic hotspots – those with a large enough buoyancy flux to originate in D″ and traverse the whole mantle – are relatively small in number and are widely distributed over the Earth's surface. This suggests that the spacing of plumes near the core–mantle boundary may be controlled by the large-scale pattern of mantle flow, although the heat flow from the core to the mantle in the neighborhood of the plumes may be controlled by the dynamics of the plumes themselves. In any event, a strong theoretical case can be made that the local heat flux from the core to the mantle is spatially variable over the core–mantle boundary (Zhang and Zhong, 2011). It is likely that this pattern of heterogeneity and its amplitude have varied with time in concert with changes in the pattern of convection in the lower mantle and changes in location and intensity of mantle plumes. Just how fast or slow this pattern changes, how the core and the geodynamo respond to

Table 4 Dynamical properties

Property	*Notation*	*Units*	*Approximate range*
Total heat flux, CMB	Q	TW	12 ± 4
Adiabatic heat flux, CMB	Q_{ad}	TW	10 ± 3
Buoyancy flux, outer core	F	m^2 s^{-3}	$\sim 10^{-13}$
Core age	t_c	year	$> 4.4 \times 10^9$
Inner core age	t_i	year	$0.3–1.2 \times 10^9$
Inner core growth rate	dr_i/dt	m year^{-1}	$1–2 \times 10^{-3}$
Viscous diffusion time	t_ν	year	$\sim 10^{10}$
Thermal diffusion time	t_κ	year	$\sim 10^{11}$
Magnetic diffusion time	t_λ	year	$\sim 2 \times 10^5$
Dipole diffusion time	t_{dip}	year	$3–5 \times 10^4$
Circulation time	d/U	year	100–300

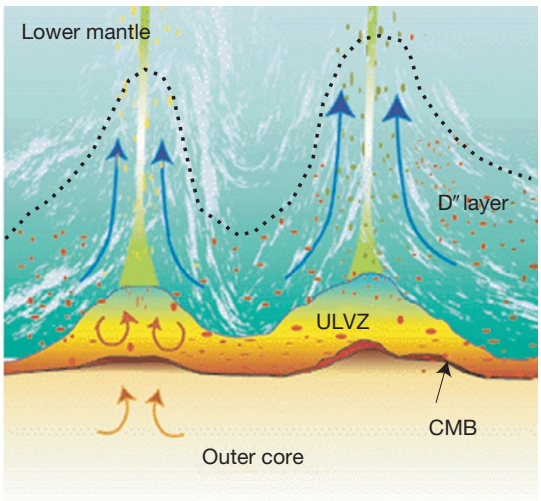

Figure 12 Schematic depiction of the D″ layer near the CMB, illustrating various types of core–mantle interaction and small-scale dynamical processes that have been proposed for this region. The seismic ultralow velocity zone consists of thin lenses of material directly above the CMB that may be partially molten and may have a composition intermediate between the mantle and the core. Courtesy of E. Garnero.

these mantle-induced perturbations, and what effects this coupling has on the Earth system as a whole are frontier research issues.

8.01.7 Core Dynamics as a Heat Engine

The overall operation of the dynamo can be thought of as a giant Carnot heat engine with several interacting parts. This analogy, which is fully described in **Chapter 8.02**, can also be found in several general treatments (Gubbins et al., 2003; Nimmo and Alfe, 2006; Roberts et al., 2003; Verhoogen, 1979). Heat is extracted from the core by the mantle, providing a source of kinetic energy in the core that maintains the geomagnetic field. The sources of buoyancy for convection in the outer core have already been mentioned – thermal buoyancy due primarily to the secular cooling of the core and compositional buoyancy derived from the growth of the solid inner core. Both of these sources are linked by the global energy flow in the core, whose path is the following: Secular cooling of the core results in solidification at the inner core boundary and growth of the inner core.

Fractionation of light elements and lighter compounds into the outer core reduces its mean density and lowers its gravitational potential energy with time (Lebrosse, 2003). Since the adjustment toward lower potential energy requires convection to redistribute the light elements throughout the outer core, production of kinetic energy of fluid motion is necessary for this process to occur fast enough to keep up with the overall cooling of the core. Part of this kinetic energy is then transformed into magnetic energy, the kinematic step in the dynamo process. This is called the gravitational dynamo mechanism if it only involves light element redistribution. There are additional energy sources available to help drive the geodynamo, including latent heat released by inner core crystallization (Verhoogen, 1961) and stirring of the core by tidal forces and by the precession of the Earth's spin axis (Lacaze et al., 2006; Malkus, 1968; Tilgner, 2005; see also **Chapter 8.07**). As discussed previously, thermocompositional buoyancy is probably the most important energy source now, but the rotational irregularities may have played a proportionally larger role at times in the past.

Another important aspect of the Carnot heat engine analogy is the concept of the efficiency of the geodynamo. Fluid dynamos have intrinsically low thermodynamic efficiency. The primary energy dissipation process within the core is ohmic dissipation – ordinary Joule heating by electric currents flowing in the imperfectly conducting core material. The efficiency of the geodynamo can be expressed as the ratio of the total Joule heating in the core to the total convective power delivered to the dynamo process. Theory indicates this ratio is about 0.1–0.2. Numerical dynamo models indicate that the amount of Joule heating necessary to maintain the present-day geomagnetic field is roughly 1.0 TW. Accordingly, the convective power in the core lies between about 5 and 10 TW; factoring in the heat flow down the core adiabat, which is 6–12 TW, gives a theoretical estimate for total heat loss from the core to maintain the geodynamo of 8–18 TW. The lower end of this range does not present problems for the current energy budget of the Earth and is well within the range of the present-day estimates, but the higher end begins to present problems, particularly because the energy demands on the geodynamo become more acute further back in time. For these reasons, one of the primary objectives in core dynamics is to derive tighter constraints on the energy budget and energy flow in the geodynamo today and in the past.

8.01.8 Convection and Dynamo Action

Based on recent estimates of the electric conductivity of the core, the internally generated dipolar part of the geomagnetic has an e-fold decay time of about 30–50 ky, and the persistence of a strong magnetic field over geologic time requires continual regeneration of the internal field on timescales shorter than this. Convection in the core has to be sufficiently vigorous to induce large-scale magnetic fields on this relatively short timescale. Since we can image only the largest scales of flow in the core, we rely on theoretical, experimental, and numerical studies of convection in rapidly rotating spherical shells to provide insight into how the induction process works. Planetary rotation affects core convection through the so-called Taylor–Proudman constraint, whereby the axes of the fluid vorticity tend to align parallel (or antiparallel) to the Earth's spin axis (Taylor, 1923). The resulting convective motion, shown in **Figure 13**, is referred to as columnar because the variation in flow structures measured along the spin axis is smaller than the variations measured in perpendicular planes, that is, planes parallel to the equator. The theory indicates that the Lorentz force due to the geomagnetic field within the core distorts the columns in the equatorial plane, as do inertia, the compressibility of the core fluid, and the curvature and roughness of the core–mantle and inner core boundaries. Columnar convection also includes secondary motions with velocity components parallel to the spin axis. The combination of these secondary motions and the primary geostrophic motion gives the convection the aforementioned property of helicity, in which the vorticity and velocity vectors are correlated on average, the helicity being generally negative in the northern hemisphere of the outer core and generally positive in the southern hemisphere. Helicity gives rise to the α-effect through which poloidal magnetic field is induced from toroidal magnetic field, and vice versa. The forward and backward transformation of magnetic energy between these two types of fields in the outer core is the key kinematic ingredient in the geodynamo. Helicity is not just a property of convection; other rotationally dominated flows, such as the flows induced by precession, are also helical and can therefore contribute to the geodynamo. Another induction mechanism is provided by large-scale toroidal flows, such as thermal wind flows. The shear in these nearly horizontal flows converts poloidal magnetic field lines into toroidal magnetic field lines, much like winding a ball of string, thereby providing the so-called ω-effect. The relative contributions of the α- and ω-effects in the geodynamo are uncertain, largely because the strength of the toroidal field in the core is unknown. If the toroidal field is only about as strong as the poloidal field in the core (1–10 mT), then the geodynamo is likely an α^2-type dynamo, and the ω-effect due to large-scale shear flows does not control the field strength in the core. Much stronger field strengths in the core would imply

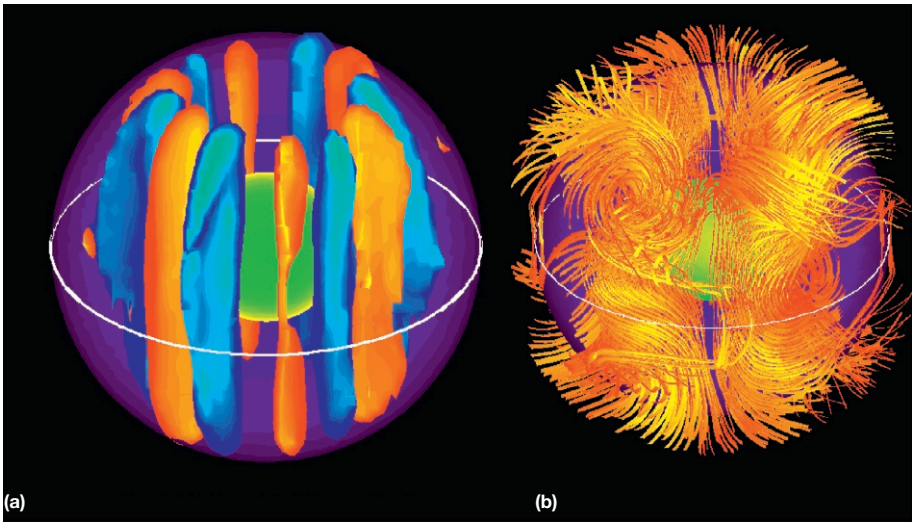

Figure 13 Numerical dynamo with columnar-style convection in a rotating spherical shell (purple) with a solid inner core (green). (a) Columnar concentrations of axial vorticity (red, positive; blue, negative vorticity); (b) magnetic field lines induced by the convection.

a larger role for the ω-effect, and the geodynamo would then be classified as $\alpha\omega$ or $\alpha^2\omega$. It is significant that both effects are functions of latitude, offering a fundamental explanation for why the geomagnetic field tends toward an axially symmetrical dipole time-averaged configuration.

An important dynamical issue concerns the process of magnetic field equilibration – that is, what controls the geomagnetic field strength. In this context, theorists distinguish between two extreme classes of dynamos, called weak and strong, respectively. In strong-field dynamos, the Lorentz force exerted by the magnetic field on the fluid is larger than the Coriolis acceleration, whereas in weak-field dynamos, the opposite relationship holds. In terms of dimensionless numbers, these two regimes correspond to the Elsasser number larger and smaller than one, respectively. An Elsasser number of one corresponds to rms field of about 2–4 mT in the core. The fluid motion in strong-field dynamos is sometimes called *magnetostrophic*, a term that implies the tendency for the fluid to circulate around magnetic field lines, rather than directly crossing them. Strong-field dynamos tend to equilibrate by trading off magnetic and kinetic energy. Increase in magnetic energy increases the Lorentz force, reducing the kinetic energy of the fluid, which ultimately causes the field to decrease back toward its equilibrium strength. Conversely, decrease in magnetic energy decreases the Lorentz force, allowing the kinetic energy to increase, which induces a stronger magnetic field. This situation would seem to provide a stable equilibrium field strength (assuming a constant driving force for the convection) and may explain why the geomagnetic dipole moment has been stable for much of the Earth's history. In fact, estimates of the internal geomagnetic field strength based on torsional oscillations place its rms intensity near 2–4 mT (Gillet et al., 2010), indicating that the Elsasser number in the core is close to one and implying that although the Lorentz forces are important, the geodynamo is not fully in the magnetostrophic regime.

The aforementioned simplified argument for the equilibration mechanism fails to account for the most dramatic geomagnetic field changes, polarity reversals. Volume 5 describes what is known of the polarity reversal process from paleomagnetism. In this volume, we discuss what is known about the reversal process in the core, from theory and from numerical models. Mathematically, a simple change in the sign of the magnetic field (a full reversal) makes no difference in the governing MHD equations for the geodynamo, since the Lorentz force is quadratic and the induction equation is homogeneous in the magnetic field. In other words, there is no bias for polarity in an MHD dynamo; both polarities are equally likely. That the paleomagnetic record shows no evidence for polarity bias and also shows no evidence for differences in field structure with polarity is a strong point in favor of a MHD origin for the geodynamo.

The existence of occasional geomagnetic reversals, widely spaced in time and yet short in duration, suggested to some early investigators that they might possibly have an external trigger. However, theory and numerical experiments have convincingly shown that polarity reversals occur in dynamos through internal processes, without any external influence needed. Some dynamos reverse periodically, most notably the $\alpha\omega$-dynamos, which often show wavelike or oscillatory magnetic field behavior. Other dynamos reverse more irregularly, a consequence of chaotic fluctuations in fluid motion. It is likely that several different mechanisms are capable of producing polarity reversals in the geodynamo. It is also likely there are many failed attempts at reversal, marked by events such as polarity excursions, for example. For these reasons, it is not clear that an individual reversal represents a very significant event in the history of the core.

Possibly more significant for core dynamics is the average frequency of reversals, which has changed appreciably through geologic time. The average rate of reversals is about 4 per million years during the past few million years, but this rate has increased systematically since the 40 My long Cretaceous Normal Superchron, which ended about 83 Ma. Because dynamo theory indicates that the important dynamical timescales intrinsic to the geodynamo should be substantially less than hundreds of millions of years, many geodynamicists have looked to the mantle for the cause of long-term polarity

reversal changes. As described in Chapter 8.10, it is now well documented that the frequency of polarity reversals is sensitive to the overall vigor of convection in the core and, in addition, spatial variations in core convection, both of which the mantle controls. Additional evidence for a mantle control on the geodynamo comes from the tendency for some transition fields to follow statistically preferred paths during polarity change. A full understanding of the ways the core and mantle interact and how these interactions affect the geodynamo and also the dynamics of the mantle remains an important goal for the future. Current ideas and possible new directions in this area are the topic of Chapter 8.08.

8.01.9 Simulating the Geodynamo

In addition to the discovery of new core structures from seismology, the identification of possible new compositions from high-pressure mineral physics, the delineation of the present-day and ancient geomagnetic field, and the progress in dynamo experimentation, the most important recent advances in understanding core dynamics have come from numerical simulations of the dynamo process. Chapters 8.10 and 8.11 describe the rapid development, considerable successes, inherent limitations, and future prospects of this approach. Here, it is appropriate just to summarize the basic ideas behind these models and comment on their overall objectives.

Numerical dynamo models solve the conservation equations for fluid motion and magnetic field induction in rotating spherical shell geometries with homogeneous magnetic boundary conditions, to ensure that any sustained magnetic field is internally generated and free of external sources. The field and the flow evolve through their mutual interaction. Primary goals are to produce magnetic fields resembling the geomagnetic field and to understand how the various interactions generate the observed properties of geomagnetic field. Other important goals are to explain the present-day stratification and heterogeneity of the inner and outer core and to chart the evolution of the core since earlier times.

As mentioned previously in the text, the numerical dynamo approach developed slowly at first and, then starting with the breakthrough simulations of Glatzmaier and Roberts (1995) and Kageyama and Sato (1995), quickly became a global activity. Numerical dynamos driven by thermochemical convection in thick, rotating fluid shells commonly produce magnetic fields similar to the geomagnetic field, with a strong axial dipole component, secular variation, and occasional polarity reversals (e.g., Christensen, 2011; Takahashi et al., 2005). Numerical dynamos with inner cores smaller than the present Earth predict only slightly different magnetic field intensity at early stages of inner core growth. These successes have led to the impression, in some quarters, that the geodynamo problem has actually been solved. In truth, however, many fundamental problems remain in applying numerical dynamo results directly to the Earth, not to mention the other magnetic planets, which have been swept under the rug, so to speak, in this burst of progress. Some of these problems stem from our limited knowledge of the properties, structure, and history of the core, but others arise because the dynamo models are far-removed in parameter space from the Earth. Specifically, numerical dynamos rotate too slowly, are less turbulent, and have far too large viscosity (relative to electric conductivity) compared to the core. In terms of the dimensionless parameters that control convective dynamos, this combination of factors means that the Rayleigh number is too small and the Ekman and magnetic Prandtl numbers are too large in the dynamo models. Estimates of these and other dimensionless parameters important to core dynamics are listed in Table 5. As demonstrated in Chapter 8.10, direct numerical simulation with realistic values of all of these parameters is still a remote prospect, because of the enormous temporal and spatial resolution such calculations would require.

As Chapter 8.10 describes, several different types of numerical models are now used for studying the geodynamo. Most dynamo models are driven by thermal or compositional convection, although there is substantial progress on mechanically driven dynamos (see Chapter 8.07). In nearly all of these models, the poloidal magnetic field is generated by what is essentially a mean-field effect, through helicity produced by the convection. A part of the toroidal field is also generated by the convection, and some is generated by large-scale shear flows, particularly in the neighborhood of the tangent cylinder of the inner core. Many numerical dynamos produce realistic large-scale magnetic fields: dominantly axial dipoles with the Elsasser number $\Lambda \simeq 1$, nearly flat spectra at the core–mantle boundary, and realistic velocities (magnetic Reynolds number $\mathrm{Rm} \simeq 500 - 2000$), even though the input Ekman number E, Rayleigh number Ra, Prandtl number Pr, and magnetic Prandtl number Pm are decidedly unrealistic. An example of an advanced dynamo model is shown in Figure 14. Some numerical dynamos have strong westward drift and large zonal velocities at low latitudes, although many do not have this feature. In some numerical dynamos, the most rapid westward drift is found at high latitudes, due to thermal wind-style flow within the inner core tangent cylinder.

Polarity reversals occur in numerical dynamos with large temporal fluctuations, particularly when the dipole field is weak and time-variable. In some cases, the polarity transition

Table 5 Dimensionless parameters

Parameter	*Notation*	*Definition*	*Approximate value*
Radius ratio	r^*	r_i/r_o	0.35
Prandtl number	Pr	ν/κ	0.05–0.2
Magnetic Prandtl number	Pm	ν/λ	$1–3 \times 10^{-6}$
Roberts number	q	ν/κ	$\sim 10^{-6}$
Ekman number	E	$\nu/\Omega d^2$	$1–5 \times 10^{-15}$
Magnetic Ekman number	E_λ	$\lambda/\Omega d^2$	$1–5 \times 10^{-9}$
Thermal Ekman number	E_k	$\kappa/\Omega d^2$	$\sim 10^{-15}$
Rayleigh number, ΔT	Ra_T	$\alpha g \Delta T d^3/\kappa\nu$	$\sim 10^{22}$
Rayleigh number, q	Ra_q	$\alpha g q d^4/k\kappa\nu$	$\sim 10^{28}$
Dissipation number	Di	$\alpha g d/C_p$	0.3
Elsasser number	Λ	$\sigma B^2_{rms}/\rho\Omega$	~ 1
Elsasser number, CMB	Λ_{cmb}	$\sigma B^2_{CMB}/\rho\Omega$	~ 0.05
Reynolds number	Re	Ud/ν	$\sim 10^7$
Rossby number	Ro	$U/\Omega d$	$2–5 \times 10^{-6}$
Local Rossby number	Ro_l	$Ul/\pi\Omega d^2$	~ 0.1
Magnetic Reynolds number	Rm	Ud/λ	600–2000
Péclet number	Pe	Ud/κ	$\sim 10^7$

is short, comparable to the timescale of the transitions in the paleomagnetic record. However, some reversals in dynamo models are characterized by extremely long transition periods. Two broad classes of reversals have been found. In convection-dominated dynamo models, large temporal fluctuations are usually found at high Rayleigh number where the flow is strongly chaotic. In these dynamos, the reversals are irregular (seemingly random) in time and often initiate from large patches of reversed magnetic flux. It has been shown that the frequency of these irregular reversals is sensitive to thermal boundary conditions (Glatzmaier et al., 1999; Kutzner and Christensen, 2004; Olson et al., 2010). Dynamo models with strong zonal flows also show polarity reversals, but at more regular intervals, suggesting that this type of reversal may be related to dynamo wave instabilities.

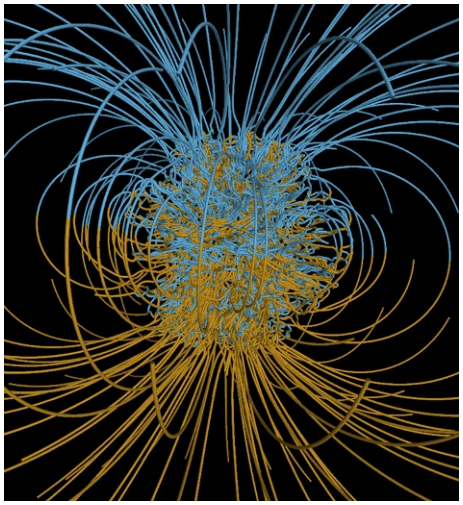

Figure 14 Magnetic field lines of force from a numerical dynamo model. Blue, inward directed; yellow, outward directed field. A dominantly dipolar magnetic field extends out from the core into the mantle. Complex magnetic field is induced inside the core by turbulent columnar convection. Courtesy of G. Glatzmaier.

8.01.10 Mantle Effects Within the Core

Many of the processes we associate with core dynamics and the geodynamo have timescales that are short compared to mantle dynamics timescales. Figure 15 summarizes the space and timescales that characterize some of the important core dynamical processes. As discussed in Chapters 8.07, 8.08, and 8.09, inertia, Alfvén, and buoyancy-driven waves have characteristic timescales ranging from 1 day to decades or centuries. The convective overturn time in the core is measured in centuries to millennia. The dipole free decay time is 30–50 ky, and the average duration of dipole polarity chrons over the past 5 My is about 240 ky.

In addition to the relatively short timescales connected with fluid dynamical processes in the core, the geodynamo shows evidence of much longer timescales. These more slowly evolving processes have often been attributed to the influence of the mantle on the core. The best-known example of this class of phenomena is the modulation in the frequency of magnetic polarity reversals seen in the record of seafloor magnetization (see Volume 5). A related phenomenon is the occasional magnetic superchron – lengthy intervals of time that appear to be devoid of reversal behavior. The reversal frequency modulation occurs on a 200 My timescale, which is very suggestive of the timescale for changes in mantle convection (see Volume 8 of this treatise). Additional but less certain evidence comes from the persistence of nondipole field components and the tendency

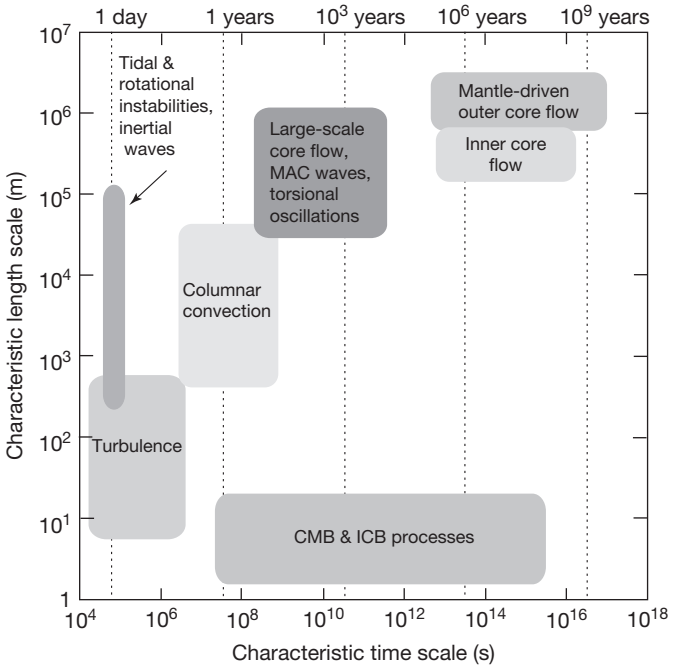

Figure 15 Spectra of characteristic length and timescales in core dynamics.

of the field to reverse polarity along paths that are confined in longitude. Since it seems unlikely on theoretical grounds that the core has such a long-term dynamical memory of its own, it is natural to look at the roles the mantle might play.

The lowermost region of the mantle is known to be among the most heterogeneous regions in the planet (see Volume 1 of this treatise). Mantle heterogeneity that could directly affect the geodynamo includes lateral variations of temperature and heat flow near the core–mantle boundary, topography on the core–mantle boundary, and lateral variations in other physical and chemical properties, possibly including melts. As discussed in **Chapter 8.08**, this heterogeneity has the potential to influence the core in multiple ways, although a full exploration of the ramifications of each type of heterogeneity is yet to be made.

Thermal interaction with the mantle is expected to influence the core on very long timescales. Temperature differences of several hundred degrees are expected in the lower mantle, and these will cause substantial heat flow heterogeneity over the core–mantle boundary. It is possible that there are regions on the core–mantle boundary where the heat flow is less than the heat conducted down the core adiabat, and stable thermal stratification will prevail in these areas. In spite of the very small lateral temperature differences this boundary heterogeneity produces in the core, the circulation in the core will be strongly modified, through the addition of thermal wind-type flows and the suppression of convection in the stable regions.

The dynamical response of the core to mantle thermal heterogeneity is a rich subject, one that has received considerable attention in the past decades (e.g., Olson et al., 2012; Zhang and Gubbins, 1992), but many basic questions are far from resolved. Numerical dynamo models indicate that mantle heterogeneity induces long-lasting, large-scale circulation in the outer core (see **Chapter 8.08**) and can influence the frequency and the character of polarity reversals (see **Chapter 8.11**). The fact that core–mantle boundary heterogeneity changes in both pattern and magnitude on 100–200 My timescales due to convection in the lower mantle and the possibility of true polar wander suggests a causal link between mantle structure and the long-term geodynamo variations, including reversal frequency modulation, superchrons, and low-frequency variations in the dipole field strength (Biggin et al., 2012).

How do mantle boundary conditions affect numerical dynamos? Fixed heat flow at the outer boundary generally yields a more strongly dipolar dynamo compared to fixed temperature boundary conditions and, in addition, is a better approximation to the actual thermal conditions at the core–mantle boundary. In terms of lateral heterogeneity, excessive variations in core–mantle boundary heat flow tend to produce hemispheric dynamos or actually kill dynamo action. Moderate variations in boundary heat flow generate departures from axisymmetry in the time-averaged magnetic field and also influence the frequency of polarity reversals. The so-called *tomographic* heat flow boundary condition assumes that core–mantle boundary heat flow variations are proportional to seismic velocity variations in the D″ layer. This boundary condition produces heterogeneity in numerical dynamos that can be compared with heterogeneity in the geomagnetic field, including concentrated flux spots at high latitudes, regions with westward drift, and regional differences in the time-averaged magnetic field and secular variation. In addition, calculations using this boundary condition indicate that thermal coupling between the mantle and the inner core is possible; the nonuniform heat flow at the core–mantle boundary is transmitted through the whole outer core, producing azimuthal variations in heat flow at the inner core boundary. These characteristics are not found in numerical dynamos with uniform core–mantle boundary heat flow, which generate time-averaged magnetic fields with axial symmetry.

Chemical exchange is another type of long-term core–mantle interaction and is even less well understood than thermal interactions. As discussed in **Chapter 8.08**, the seismic complexity of the core–mantle boundary region, which indicates heterogeneity over a wide range of spatial scales, is broadly consistent with the idea that chemical interactions with the mantle (Buffett and Seagle, 2010), sedimentation, infiltration, and compaction, and other processes that are known to be important in shaping the surface environment may have counterparts in the core–mantle boundary region. The challenge is how to identify these processes in terms of their seismic signatures and the fingerprints they leave in isotope and trace element chemistry.

Very different kinds of core–mantle interactions can occur on shorter timescales. Elevated electric conductivity near the base of the mantle permits the secular variation of the geomagnetic field to induce electric currents in the lower mantle that can couple the mantle and core electromagnetically (Holme, 1998; Rochester, 1962) and allow for exchange of angular momentum between the core and the mantle on decade and century timescales. Other short-term interactions include gravitational coupling between mantle density heterogeneity and density heterogeneity in the core, including the equatorial bulge of the inner core.

8.01.11 The Dynamical Inner Core

Perhaps the most unanticipated developments in core dynamics have come from the realization of the importance of the solid inner core. Long thought to be homogeneous and dynamically passive, it now is seen to play a much more significant role in the evolution of the core and the geodynamo process. The core was recognized to be seismically anisotropic about two decades ago, based on the travel times of seismic compressional waves, which travel a few percent faster along polar paths, compared with equatorial paths (see Volume 1 of this treatise). Initially, this anisotropy was seen as more or less uniform through the whole inner core, which led to an early suggestion that the inner core might be a single crystal, possibly aligned by the Earth's rotation. Subsequently, however, it has been shown that the anisotropy is not entirely rotationally aligned, and moreover, it is spatially heterogeneous through the inner core. In particular, anisotropy is weak or absent for a few hundred kilometers below the inner core boundary, and even more surprising, it appears to vary in strength between the eastern and western hemispheres of the inner core (Deuss et al., 2010).

Several explanations have been offered to explain the inner core anisotropy. The obvious one is textural anisotropy, the statistical alignment of crystals. Another possible explanation is partial melt fabric. Each of these explanations has its own merits, although both involve difficulties. There are also several competing theories for the origin of the anisotropy, which are

discussed fully in Chapter 8.12. Most of these explanations imply the ability of the inner core to deform on timescales of tens of millions of years, which requires the solid material to have a small yield strength and a finite viscosity.

One provocative interpretation of inner core dynamics is its anomalous rotation. Numerous studies have used observations of small, secular changes in the travel times of seismic P-waves traversing the inner core to infer that the inner core is rotating relative to the crust and mantle. The initial reports suggested a relatively fast superrotation, with the inner core rotating eastward relative to the crust by about one degree per year (Song and Richards, 1996). Subsequent investigations have demonstrated that this rate is too high. The observed splitting of certain normal modes that are sensitive to inner core structure indicates little or no anomalous rotation, whereas follow-up studies based on the original P-wave technique still indicate that superrotation is possible, but only at a fraction of a degree per year. Interestingly, the theoretical possibility of inner core superrotation had been known for more than a decade (Gubbins, 1981), and prograde anomalous inner core rotation was observed in several of the earliest numerical dynamo models. Indeed, the pattern of core convection predicted by numerical dynamo models is fully consistent with inner core superrotation (see Chapter 8.10). However, there are some unresolved basic issues. First, the uncertainty in the seismic observations does not entirely preclude an inner core co-rotating with the rest of the Earth. In addition, it is theoretically possible that gravitational coupling locks the inner core to the mantle (see Chapter 8.08). This question will ultimately be settled, as better seismic data accumulate.

Another recent and equally provocative interpretation of inner core dynamics involves the so-called translational instability, which has been proposed as a mechanism that links the hemispheric dichotomy of the inner core to the seismically anomalous F-layer above the inner core boundary. Figure 16 is a schematic showing the fundamentals of this instability. Because the inner core boundary is at the melting point of the core material, translation of the inner core relative to the Earth's center promotes melting on its leading edge and solidification on its trailing edge. It has been shown that this translation can proceed so long as it reduces the gravitational potential energy of the core as a whole (Alboussiere et al., 2010). Whereas solidification releases light elements, promoting convection in the outer core, melting of the inner core produces a dense iron-rich liquid that would tend to stratify the core. The anomalously low seismic velocities in the F-layer above the inner core boundary might be due to the accumulation of this iron-rich liquid.

8.01.12 Future Prospects and Problems

It is impossible to know if the pace of progress in core dynamics we have witnessed over the past decades will continue. In light of the unexpected discoveries in the short time since the publication of TOG1, predictions regarding areas of future progress would seem pointless. Instead, it is more useful to define important goals that could serve as focal points for future research. Most of the chapters in this volume have identified the key science questions particular to each area. The following is a partial list of broadly defined questions, by which progress in core dynamics might be judged:

- What is the present-day energy budget of the core?
- How old is the inner core?
- What processes account for the complex structure of the inner core?
- How has inner core formation affected the rest of the Earth?
- What is the strength of the geomagnetic field in the core, and what processes control its strength?
- How much energy is dissipated in maintaining the geodynamo?
- What is the relative importance of chemical versus thermal buoyancy in core convection?
- How important are radioactive heat sources in the core?
- Are there stably stratified regions in the outer core?

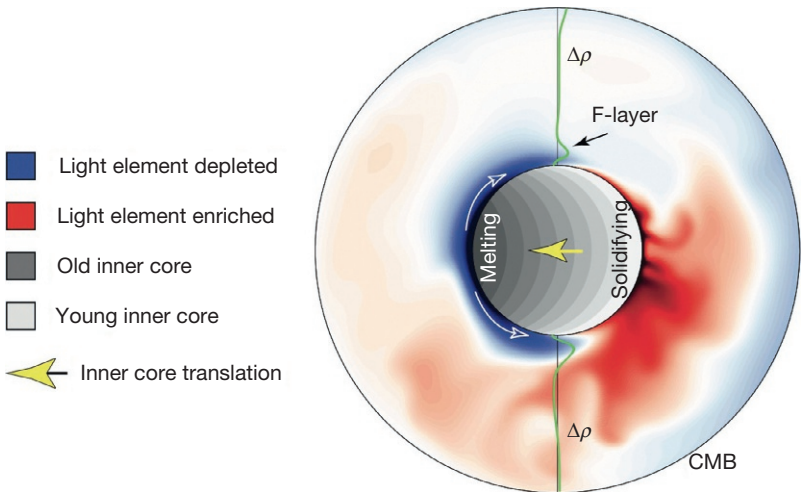

Figure 16 Schematic of the inner core translational instability with melting and solidification on opposite sides of the ICB and formation of the iron-enriched layer at the base of the outer core.

- What are the characteristic length and timescales of core convection?
- What is the nature of turbulence in the outer core, and how does turbulence influence core dynamics at larger scales?
- What roles do wave motions play in the geodynamo?
- What roles do precession, tides, and other mechanical forcings play in maintaining the geodynamo?
- How does dynamo action in numerical models differ from dynamo action in true liquid metals?
- What properties of numerical dynamos can be scaled to Earth conditions?
- What is the relationship between the flow at the top of the core inferred from geomagnetic observations and the geodynamo process?
- What are the contributions of rotational instabilities to the geodynamo?
- Is the inner core locked to the mantle, or does it differentially rotate?
- What are the critical processes that lead to magnetic polarity changes and other forms of geomagnetic variation?
- What is the nature of long-term mantle control on core and geodynamo processes, such as the chemical and thermal evolution of the core and the frequency of magnetic polarity reversals?
- What are the characteristics of shorter-term core–mantle interactions, such as those related to length-of-day variations?
- Which aspects of the Earth's core dynamics are applicable to the cores in other planets?

8.01.13 Additional References

Although there is no published book like this volume, with comparable breadth and focus on the dynamics of the core, there are numerous works that treat the specific foundations of this subject. Several of these deserve special mention here. Monographs by Verhoogen (1979) and Jacobs (1987) and the collected volumes edited by Dehant et al. (2003) and Jones et al. (2003) treat most aspects of core structure and energetics. Various aspects of the rotational dynamics of the core–mantle system are treated by Smylie (2013). The fundamentals of rotating fluid dynamics and geophysical turbulence can be found in Greenspan (1968) and Rhines (1979), respectively, and the fundamentals of dynamo theory in books by Moffatt (1978) and Davidson (2001). Stacey (1992) and Poirier (1988) are good sources of basic information on core properties, Schubert et al. (2001) and Kennett and Bunge (2008) give detailed accounts of the dynamics of the mantle, and Merrill et al. (1998), Backus et al. (1996), and Gubbins and Herrero-Bervera (2007) give comprehensive accounts of the geomagnetic and paleomagnetic fields as they relate to core dynamics. There have been numerous review papers on the advances in numerical dynamo models, including Dormy et al. (2000), Kono and Roberts (2002), Glatzmaier and Roberts (2002), and Christensen (2011). Braginisky and Roberts (1995) have developed a complete set of equations for the core convection including thermal and compositional buoyancy.

8.01.14 Summary of the Chapters in This Volume

8.01.14.1 Energetics of the Core

Chapter 8.02 analyzes the gross energetics of the core, a subject of long-standing and ongoing controversy. After reviewing the present state of the core, author Francis Nimmo derives the global balances of energy and entropy, which are critical to such basic issues as the growth rate of the solid inner core and the power necessary to maintain the geodynamo. Special attention is given in this chapter to the power requirements and the long-term consequences of inner core growth. Growth of the inner core results in compositional convection and latent heat release, and the author concludes that the former is likely the most important energy source for the geodynamo. Geophysical considerations indicate that the present-day heat loss from the core is in the range 10–16 TW. Nimmo shows how this heat flow translates into predictions of inner core age, which is in the neighborhood of 300–800 Ma. Even when the uncertainties in core properties are taken into account, thermal history calculations indicate that the inner core is far younger than the Earth as a whole. The lower end of the range of uncertainty puts the onset of inner core nucleation well within the Paleozoic Era, which would imply that the inner core has existed only for about one Wilson cycle of plate tectonics and that it postdates the explosion of advanced life forms over the Earth's surface. The author concludes by considering the possible alternatives to the young inner core scenario. One of these alternatives is a model in which the core contains appreciable radioactive heat sources, most notably radioactive potassium ^{40}K, and the power requirements of the geodynamo remain low throughout the inner core growth. Another possibility is the progressive removal of magnesium from the core. Resolution of this central yet controversial issue might come by detecting inner core formation in the record of the paleomagnetic field, new insight into core–mantle interactions, or some as yet unexploited geochemical evidence on the early core.

8.01.14.2 Theory of the Geodynamo

Long before there were 3D numerical dynamo simulations and long before self-sustaining experimental sodium dynamos, the theoretical foundations for understanding the geodynamo were laid by applied mathematicians and physicists. The accomplishments of this dedicated group are all the more noteworthy in light of the fact that they were working without the benefits of realistic numerical or laboratory examples of fluid dynamos.

The important elements of dynamo theory are set out by Paul Roberts in Chapter 8.03. Roberts begins by defining what a fluid dynamo is, what is meant when a dynamo is self-sustaining and self-generated, and the difference between kinematic dynamos, in which the fluid velocity is specified a priori and the magnetic field is then calculated, and MHD dynamos, in which the energy source is specified, and both the flow and the magnetic field are calculated simultaneously. Dynamo theory starts from the pre-Maxwell equations for electromagnetic induction in a moving, conducting fluid. An important limiting case that is often used for intuition and practical applications is Alfvén's frozen flux theorem, appropriate for a perfect electric conductor.

Roberts then presents the basis for kinematic dynamos in both Cartesian and spherical geometries. Important results include a lower bound for the critical magnetic Reynolds number for dynamo action, plus a set of antidynamo theorems, including the famous theorems by Cowling, that reveal some of the necessary conditions for fluid dynamos to become self-sustaining. Next up is a full account of the very influential mean-field electrodynamics, the statistical treatment of the induction effects of turbulent fluid motion. This leads to several types of mean-field dynamos, which derive their dynamo action from the α-effect, an induction property of convective turbulence, and the ω-effect, the induction property of large-scale shear flows. The chapter ends with a reduction of the full equations of MHDs in the limit of rapid rotation and low viscosity that lead to torsional oscillations and steady magnetostrophic flow.

Now that the study of the geodynamo has come to rely so heavily on large-scale numerical simulations, it is fair to ask what role dynamo theory plays in the present discussion. Roberts' summary provides a clear reply to this question. Existing dynamo models, be they numerical or experimental, offer limited insight into the geodynamo by virtue of the fact that they are inherently complex and, to make matters worse, are far-removed from the Earth's parameters. Accordingly, the results of numerical dynamos need to be skillfully interpreted, and the same is true for laboratory dynamo experiments. Dynamo theory provides the fundamental concepts for making such interpretations.

8.01.14.3 Large-Scale Flow in the Core

Multiple lines of evidence indicate that a broad spectrum of motions are likely in the fluid outer core, governed by a variety of possible force balances that include several possible driving mechanisms. In light of the inherent complexity in the geodynamo processes, there is little hope of deducing the nature of the flow in the core on the basis of theoretical considerations alone. For this reason, a substantial effort has been made over the past few decades to infer as many properties of the flow in the core as possible from other types of geophysical observations. By far, the most success in this regard has come from analyzing the secular variation of the geomagnetic field on the core–mantle boundary. There is a full description of the properties of geomagnetic secular variation in Volume 5 of the treatise.

In this volume, we are primarily concerned with interpreting the images of flow near the top of the core, obtained from the geomagnetic secular variation, in terms of the types of motion that are important for core dynamics in general and the geodynamo in particular. We are also interested in the evidence for interaction between the core and other parts of the Earth's system as revealed by these motions. In Chapter 8.04, Richard Holme summarizes what we know about the actual fluid motions in the core, both in the present-day and in the past, as far back in time as the geomagnetic record allows us to infer them. Holme points out that geomagnetic secular variation has been used to trace motions in the core over the past four centuries, starting with Halley's famous 1692 discovery of its westward drift, which Halley interpreted as the result of relative motion between magnetized regions in the Earth's interior. Holme shows how the early idea of a uniformly westward drifting core, based on a preferred westward shift of anomalies in the core field with time, has been replaced by a far more complex picture of the core flow, which includes westward motion mostly confined to the Atlantic Hemisphere. However, the long-standing controversy over the geomagnetic westward drift and its interpretation provided impetus to develop the modern techniques for imaging core flow, which are based on the concept of frozen magnetic flux. Holme first reviews the frozen flux hypotheses, including its assumptions and limitations, and then goes on to summarize the important aspects of the core flow that the applications of this technique have revealed. He shows how frozen flux reveals that an energetic, large-scale flow is present in the outer core, with characteristic velocities of 10–20 km year^{-1}. This motion appears to be most vigorous beneath the Atlantic and Indian Oceans (since it is proportional to the geomagnetic secular variation, which is greatest there), and it includes several large-scale vortices and jets that are suggestive of the large-scale quasi-geostrophic vortices and jets seen in the general circulation of the atmosphere and ocean. Smaller-scale motions are doubtless also present (see Chapters 8.05, 8.06, and 8.09) but are filtered from the geomagnetic secular variation by the electric conductivity of the mantle and by permanent magnetization in the crust and are therefore invisible at the surface. Wave motion in the core is another possible interpretation of the secular variation. Holme discusses several interesting interactions between the core and the mantle related to core flow, including the decade-scale variations in the rate of rotation. These variations involve angular momentum exchange between the core and mantle and appear as nearly periodic variations in the zonally averaged part of the core flow. In addition, the core flow shows some response to the abrupt, transient changes in the core field, the class of phenomena called geomagnetic jerks.

8.01.14.4 Thermal and Compositional Convection in the Outer Core

Convection in the liquid outer core is the primary energy source for the geodynamo and also the primary mechanism for heat and mass transfer through the core. In Chapter 8.05, author Christopher Jones examines the complex fluid mechanics involved in convection in the core. Both thermal convection and compositional convection are important in the outer core, thermal convection produced by temperature variations arising from the inner core boundary and especially from the core–mantle boundary and the compositional convection being a product of chemical fractionation of light elements such as sulfur and oxygen into the outer core fluid accompanying crystallization of the inner core.

After reviewing the recent evidence for increased core heat flow and conductivity, Jones introduces the basic physical principles involved in thermochemical convection in the core, deriving the equations governing convection with emphasis on the effects of compressibility, which are present in the outer core by virtue of the enormous ($\sim$200 GPa) increase in hydrostatic pressure between the core–mantle and inner–outer core boundaries. He then conducts a systematic tour of the physics of convection, starting with a model of high Rayleigh number convection in a nonrotating, electrically

insulating fluid, then progressively adding in the effects of rotation and magnetic fields, and ending up with a model of core convection in which all of the known physical ingredients are present and interacting with each other. The result is a model of core convection that is multiply anisotropic, with the flow jointly constrained by the Earth's rotation, by the Lorentz force due to interaction between the induced magnetic field and associated electric currents, and by other dynamical effects. Jones shows how the characteristic velocity, time, and length scales of this convection are all determined by internal dynamical balances involving subtle balances between Coriolis, Lorentz, buoyancy and inertial forces, and the spherical shell configuration of the outer core. He goes on to show how this rotating magnetoconvection model for the core dynamics fits into the numerical models of the geodynamo described in Chapter 8.10 on the large scale and, in the other extreme, how it fits with the concepts of smaller-scale core turbulence described in Chapter 8.06. Jones then considers how the particular deep Earth environment influences core convection, specifically, how mantle heterogeneity and the formation of stable layers near the core–mantle boundary affect convection in the core. Control of core convection by the mantle is barely understood and is among the priorities for future expansion of knowledge in this subject.

8.01.14.5 Waves in the Core and Mechanical Core–Mantle Interactions

Chapter 8.09 is a comprehensive review of theory for the higher-frequency dynamics in the fluid outer core, those with characteristic timescales that are shorter than the free decay time of the magnetic dipole, along with applications of this theory to the magnetic field inside the core and its coupling to the lower mantle. Included in the spectrum of processes in this chapter are Alfvén's waves, inertial waves including their low-frequency approach to geostrophy and their modifications due to compressibility and stratification, in particular internal gravity waves and waves of mixed types. There is a full derivation of the quasi-geostrophic equation of motion for the outer core that includes the Lorentz forces with boundary effects in the forms of topographic and magnetic coupling. Based on this equation, expressions for barotropic Rossby wave propagation in the outer core are derived and the axial average equations. Later sections of the chapter describe the classic approach to inviscid core dynamics due originally to J. B. Taylor, its modern extensions, and its time-dependent version that forms the theoretical basis for torsional oscillations in the core. The application of this theory to the interpretation of oscillatory geomagnetic secular variation is then used to provide constraints on the axial component of the magnetic field inside the core, which is followed by a discussion of angular momentum exchange between the core and the mantle.

8.01.14.6 Turbulence in the Core

In Chapter 8.06, authors Henri-Claude Nataf and Nathanael Schaeffer take on the challenge of characterizing the unseen (and possibly unseeable) short-lived, chaotic motions in the outer core that fall under the general heading of turbulence. Turbulence is found in fluids throughout the cosmos, and every careful analysis of the dynamical state of the outer core has concluded that it is present there as well, although hidden from direct observation. First, the authors offer a set of definitions for turbulence that are applicable to the special environment of the outer core. They then discuss why seemingly inconsequentially small motions can have large influence on the global behavior of the core and the dynamo process, by controlling the flow of energy and its dissipation, mixing of heat and constituents, and also the conversion of kinetic to magnetic energy. This is followed up with a cogent description of the classical turbulence concepts including energy cascades and coherent structures, with examples of turbulence drawn from numerical models of convection in the outer core. The final half of the chapter is a connected account of turbulence parameterizations that are applicable to the core, with the objective of representing the complex interplay between fluid inertia, viscous effects, buoyancy forces, the Coriolis acceleration, and the Lorentz forces derived from the magnetic field.

8.01.14.7 Rotational Dynamics of the Core

Convection is not the only type of motion in the fluid outer core. There are a host of instabilities that arise because of irregularities in the Earth's rotation. These are well documented in theory and experiments, for example, in Chapter 8.13. In Chapter 8.07, Andreas Tilgner summarizes the state of knowledge on rotation-induced core flows. He begins by deriving the equations of motion for a fluid rotating about a variable axis, in which the transverse or Poincaré acceleration appears in addition to the familiar Coriolis and centripetal accelerations. He summarizes the properties of inertial oscillations and the structure and transport properties of viscous Ekman layers.

The central problem in this subject is the flow induced by precession. Tilgner begins by presenting the classical solutions to the inviscid problem, including the Poincaré solution on which most subsequent studies were based. He then systematically introduces the complexities of a real fluid: first the effects of viscosity, then instabilities, tidal excitation, and finally nonlinear interaction with convective flows. A long-standing question is whether precession can support a planetary dynamo by itself, without assist from buoyancy-driven motions. Tilgner discusses the status of this debate and points out the directions future work must take to supply a definitive answer.

8.01.14.8 Numerical Dynamo Simulations

The use of first-principles numerical models of self-sustaining fluid dynamos has been the most significant technical development in the study of the geodynamo in decades. The enormous progress in this arena and the challenges for the future are the subjects of Chapter 8.10. Authors Ulrich Christensen and Johannes Wicht first review the governing equations for the geodynamo in their basic Boussinesq form, including the fundamental dimensionless parameters that control the system. They then define the critical dimensionless output parameters that characterize each dynamo model solution and provide the basis for comparison with the geodynamo. Attention is paid to the choices of boundary conditions appropriate for the core–mantle boundary and the inner–outer core boundary. The choice of boundary conditions is crucial for

modeling specific aspects of the geodynamo behavior, not only its interaction with the mantle but also its interaction with the solid inner core.

The challenges in dynamo modeling stem from the fact that the physics of the geodynamo are characterized by extreme values of the governing dimensionless parameters, which are not accessible to direct numerical simulation. This situation has guided both the development of numerical dynamos and the techniques used to apply them to the Earth. Each of these aspects is discussed in detail in Chapter 8.10. Christensen and Wicht first summarize the simplifying approximations that are sometimes used in the models, such as representing the buoyancy force in convection in terms of just a single variable, imposed symmetries, and modifications to the inertial and diffusive terms in the equations. In terms of the numerical techniques, Christensen and Wicht focus on the spectral (or semispectral) approach, which has been the workhorse method to date, although they point out its inherent limitations and the need to continue the development of alternative methods that will be more suitable for the massively parallel computer architectures in the future.

The authors then summarize the main classes of dynamo models found to date, describing their changes in structure as the main controlling parameters (Rayleigh and Ekman numbers) are systematically varied in the direction of the Earth's values. They point out that most convectively driven numerical dynamo models are basically of the α^2-type, although ω-effects from thermal wind flows are sometimes important contributors to the dynamo mechanics.

The rapid increase in the number of high-quality numerical dynamos in the literature has made it possible to derive scaling laws for the basic behavior of convective dynamos. This is an important development, since it provides a way to extrapolate numerical results with more modest input parameters to the extreme parameter regime of the geodynamo. Christensen and Wicht show a number of rather simple scaling laws for the numerical dynamo properties that project rather well to the geodynamo, providing additional evidence that dynamo models do capture important parts of the core's dynamics.

As for the future prospects in dynamo modeling, it may be that much of low-hanging fruit for the geodynamo has already been picked, and progress hinges on solving a number of thorny physical problems involving the complicating but interesting effects discussed in other chapters of this volume. Christensen and Wicht end the chapter with an assessment of these problems, where improvements to numerical dynamos should be made, and the challenges in applying numerical dynamos to other planets.

8.01.14.9 Magnetic Polarity Reversals in the Core

The fact that the geomagnetic field has stably persisted for most of the Earth's history, while exhibiting occasional polarity reversals, is among the strongest pieces of evidence in support of the dynamo theory. As discussed at length in Volume 5 of this treatise and as summarized in Chapter 8.11, both the existence and the known characteristics of magnetic polarity reversals offer general confirmation of the dynamo interpretation and severe challenges for any successful model of the geodynamo.

In Chapter 8.11, authors Gary Glatzmaier and Robert Coe examine the behavior of polarity reversals in numerical dynamo models in light of the evidence on the nature of reversals as seen in the paleomagnetic record. Key observations include the time required for polarity reversal (2 to about 12 ky), the characteristic duration of stable polarity chrons (100–1000 ky, but highly variable), the nature of the transition field, and the possibility of polarity bias, statistical differences between magnetic fields for normal (i.e., present-day-type) polarity and reverse polarity configurations. They argue that nearly all records of reversals indicate reduced intensity for the transition field, but that the actual transition field structure is complex and may differ substantially between individual reversals, as evidenced by the variety of VGP (virtual geomagnetic pole) paths. They also point to the significance of large directional excursions, which appear to be more frequent than full polarity switches and may represent failed reversals in the core.

Dynamo models have shown convincingly that it is not necessary to have an external trigger for polarity reversals. There are several mechanisms that operate in numerical dynamos that can produce spontaneous polarity reversals, either in a semiregular way (i.e., nearly periodic reversals) or in a chaotic way (in which the reversal sequence is seemingly random in time). Glatzmaier and Coe analyze some specific numerical examples of each of these types of reversals. Their general conclusion is that chaotic, nearly random reversing dynamos better approximate the observed reversal behavior as measured by the main geomagnetic polarity timescale (i.e., the reversals that define the major polarity chrons). However, they also find that the presence of more frequent, short reversals implied by excursions may indicate that a more regular reversal mechanism also operates in the geodynamo.

The authors examine the role of reversals in illuminating the interaction between the core and the mantle, a recurring theme in the other chapters of this volume. The transition field structure in some (but not all) reversals seems to indicate some mantle control on the process, in that the VGP paths for these reversals tend to cluster within one of two longitude belts. As mentioned earlier in this chapter, one interpretation of this phenomenon is that it represents the tendency for the transition field to configure itself in accord with the large-scale heterogeneity of the lower mantle. As Glatzmaier and Coe show, the transition fields in numerical dynamo models are indeed sensitive to large-scale boundary heterogeneity. Preferred reversal paths do emerge in the statistical behavior of dynamo models with heterogeneous thermal boundary conditions, for example. However, like nearly all aspects of core–mantle interaction, the paleomagnetic data are still ambiguous and the numerical dynamo models are still too rudimentary to yield a firm conclusion on this issue.

The evidence for very long timescales in the polarity record, as typified by magnetic polarity superchrons and the 200 My modulation of the reversal frequency record, is of considerable theoretical interest for properly interpreting the longer-term thermal interaction of the core and the mantle. Glatzmaier and Coe point to several numerical studies that demonstrate dynamo model sensitivity to mantle heterogeneity, particularly thermal heterogeneity at the core–mantle boundary. Reversal frequency seems to be a function of the total heat loss at the core–mantle boundary and also is sensitive to the pattern of

that heat loss. The authors demonstrate that dynamo models generally show more frequent reversals with increased total heat flow, a consequence of increased flow complexity. They also present some preliminary evidence, drawn from the few studies on this subject, that the pattern of core–mantle boundary heat flow affects reversal frequency. Sensitivity of reversal frequency to the pattern of mantle dynamics offers a way to link the history of the paleomagnetic field to the history of mantle convection and plate tectonics – an exciting prospect, but one that will require a large, sustained, and focused effort involving better paleomagnetic observations combined with substantial dynamo model improvements.

8.01.14.10 Inner Core Dynamics

Chapter 8.12 summarizes the wealth of new information on the inner core and discusses the various roles the inner core plays in core dynamics and the geodynamo. Authors Ikuro Sumita and Michael Bergman first describe the current understanding of the phase diagram of the core, which is critical for properly interpreting the effects of inner core growth and for estimating the present-day thermal regime of the core. They then use the information from the phase diagram as the basis for a discussion of the small-scale processes near the inner–outer core boundary that affect and are affected by the solidification. Solidification processes at the inner core boundary naturally lead to their next topic, estimating the grain size and creep viscosity of the inner core solid material. Viscosity and grain size are closely linked in the inner core (as they are in the crystalline mantle), and the value of inner core viscosity controls the rate of creep deformation in dynamical processes such as the relaxation that accompanies heterogeneous inner core growth and superrotation. It also affects the ability of the inner core to convect on its own. Sumita and Bergman then describe the various models that have been advanced to explain the recent and most perplexing observations of the inner core, its heterogeneity, anisotropy, and (possible) anomalous rotation and convection. These are linked, since the lateral heterogeneity and the anisotropy of the inner core serve as the basis for detecting (and correctly interpreting) its possible anomalous rotation, internal convection, and translation. They conclude that the evidence for anisotropy is unequivocal, the evidence for lateral heterogeneity is compelling (but likely subject to many future revisions), whereas the evidence on the internal dynamics of the inner core, although intriguing, remains too nebulous to draw firm conclusions.

8.01.14.11 Experiments on Core Dynamics

Laboratory experiments always play a crucial role in fluid dynamics research, and core dynamics is no different in this respect. In Chapter 8.13, Philippe Cardin and this author conduct a tour of the important experiments that have shaped our physical intuition about the flows in the core that produce the geodynamo and govern its evolution. Most if not all of the dynamical phenomena discussed elsewhere in this volume can be seen in their relatively pure forms in the framework of laboratory experiments. This chapter is possibly singular in all of geodynamics, in collecting photographic examples of all the types of flow thought to be significant in the core.

The chapter begins with a description of the fundamental flow structure in rotating fluids, the geostrophic column. Geostrophy is familiar in atmosphere and ocean dynamics, but this particular class of structures, the so-called Taylor columns, is especially important in the outer core because of its thick-shell geometry and the dominance of the Coriolis acceleration over the effects of viscosity. Where geostrophic columns touch the core–mantle and inner–outer core boundaries, the no-slip condition leads to various shear boundary layers, including Ekman boundary layers. Similarly, where distinct geostrophic columns meet, free shear layers called Stewartson layers form. The most prominent Stewartson-type shear layer in the core is formed along the inner core tangent cylinder – the imaginary cylinder parallel to the Earth's rotation axis and tangent to the inner core equator. The strength of the inner core tangent cylinder is an important element of the internal structure of the core, because the tangent cylinder wall tends to divide the outer core into dynamically separate fluid regions.

Complementing the theory of rotational instabilities in Chapter 8.07, this chapter discusses the experiments on precession-induced flows in spheres, spherical shells, and spheroids. These flows include the classic Poincaré-type flow (in which the outer core rotates about an axis that lags the mantle in precession) and the parametric instabilities that occur when precession effects reach finite amplitude. Experimental examples of the quasi-geostrophic turbulence discussed in Chapter 8.06 are shown in connection with these rotational instabilities.

Although rotational instabilities are likely in the core, the main source of energy for the geodynamo probably comes from thermochemical convection. The chapter includes a discussion of the clever experimental techniques that were developed to investigate thermal convection in rapidly rotating spherical shells, starting with the pioneering work by F. H. Busse et al. Subjects include the nature of rotating convection at onset and how the structures change as the convection becomes fully developed, rotating convection in liquid metals, and the differences between compositionally driven versus thermally driven flows.

Fluid mechanics in the core is strongly influenced by the geomagnetic field. As discussed in Chapter 8.05, the theoretical foundation here is classical MHDs of an electrically neutral but conducting fluid, subject to the combined effects of buoyancy, rotation, and its own internally generated magnetic field. An important simplification to this system uses an externally applied magnetic field in place of a self-sustained one; the resulting flow is called magnetoconvection. The fundamentals of rotating magnetoconvection as it occurs in laboratory fluid metals such as mercury, gallium, and molten sodium are described, with a focus on the differences between magnetic and nonmagnetic convection in a rotating fluid.

Lastly, an account is given of the recent successes and future prospects for laboratory self-sustaining fluid dynamos. The design and the results from the Riga and Karlsruhe sodium dynamos are reviewed, both of which achieved self-sustaining behavior within the same year, 2001. These two dynamos used mechanical forcing to reach supercritical Reynolds numbers and helical-shaped ducts and channels to get the proper feedbacks between poloidal and toroidal field components. Next, considerable successes of the cylindrical VKS sodium dynamo, including the identification of a host of dynamo states, some of which include spontaneous polarity reversals, are reviewed.

A future challenge is to produce a laboratory dynamo in an Earth-like geometry with rotation included. The authors discuss the technical difficulties associated with scale and power requirements associated with this type of experiment, some of which are now underway.

8.01.14.12 Core–Mantle Interactions

In Chapter 8.08, Bruce Buffett examines a wide range of possible ways the mantle can affect core dynamics and corresponding ways the core can affect the mantle. He separately considers the effects of thermal, mechanical, electromagnetic, and chemical interactions and how each of these might be detected at the Earth's surface. As Buffett points out, the possible inventory of core–mantle interactions is quite large, comparable to the number and scope of interactions between the lithosphere and the hydrosphere. In terms of timescales, they range from about 1 day for rotational interactions to hundreds of millions of years for thermal and chemical interactions. The basic elements of core–mantle thermal interaction were referred to earlier in this chapter. Mantle dynamics has a controlling influence on the heat loss from the core, and as Buffett argues, both the total heat flow and the pattern of heat flow at the core–mantle boundary are expected to have a major influence on core dynamics. Furthermore, this influence is time-dependent, because of the evolving thermal regime of the core–mantle system and also because the pattern and strength of mantle flow varies with time. During times when heat loss to the mantle is low, a thermally stable stratified layer might develop in the outer core fluid below the core–mantle boundary. This layer could be destroyed by an episode of increased boundary heat flow or through the accumulation of lower density, iron-depleted fluid rising up from the inner core boundary region. It is expected that high-frequency components of the geodynamo would be damped when the stable layer was present, resulting in a quieter geomagnetic field during those times. Conversely, at times when convection is vigorous below the core–mantle boundary, the geomagnetic field is expected to show more variability. The same reasoning applies to spatial variations of boundary heat flow, a consequence of the pattern of mantle convection. These variations produce lateral variations in the intensity of convection and also larger-scale thermal wind flows, both of which tend to destroy the rotational symmetry of the geomagnetic field. Dynamo models indicate that the frequency and the character of magnetic polarity reversals are sensitive to boundary heat flow heterogeneity, with some types of boundary heterogeneity acting to destabilize the dynamo (resulting in more frequent reversals) and other types of heterogeneity acting to stabilize it. The primary control on the character of reversals comes through longitudinal bias, that is, a tendency for the equatorial component of the dipole to amplify at longitudes where the heat flow is large, which in turn causes a statistical preference for the dipole to reverse along these longitudes. There is suggestive evidence for many of these thermal effects in the paleomagnetic and geomagnetic field behavior (see Volume 5 of this treatise), but as Buffett explains, unambiguous identification of these effects requires better resolution of the paleomagnetic field and a more thorough comparison with dynamo models.

Electromagnetic core–mantle interactions described in Chapter 8.08 include the electromotive force exerted by the core field on the mantle through its interaction with electric currents in the mantle. The strength of this interaction depends on the electric conductivity of the lower mantle, which is not very large unless it contains an appreciable amount of core material. The best-understood interaction of this type is the exchange of angular momentum between the core and mantle that produces decade-scale length-of-day variations. Less well understood are electromagnetic interactions arising from lateral variations in mantle electric conductivity. The effects of these interactions are expected to be most pronounced when the field is varying rapidly (as it is today) and particularly during polarity transitions. Mechanical interactions include the effect of core–mantle boundary topography and roughness on core dynamics, the large influence of seemingly small topographic variations being well known in ocean and atmosphere dynamics. Unfortunately, the core–mantle boundary topography has proven to be exceedingly difficult to image seismologically, so the importance of this interaction has yet to be quantified. Another class of mechanical interactions involves gravitational coupling between the solid inner core and the mantle, which limits the freedom of the inner core to rotate separately from the mantle.

Lastly, Buffett summarizes the evidence for and against chemical interaction between the mantle and the core, including mechanisms by which mass exchange across the core–mantle boundary might occur, the most likely components involved, and the prospects for their detection. There are multiple pathways for mass exchange, so the real issue here is to determine which – if any – are large enough to produce an observable chemical tracer or a signature in the seismic structure of the core.

References

Alboussiere T, Deguen R, and Melzani M (2010) Melting-induced stratification above the Earth's inner core due to convective translation. *Nature* 466(7307): 744–747.

Alfe D, Gillan MJ, and Price GD (2003) Thermodynamics from first principles temperature and composition of the Earth's core. *Mining Magazine* 67: 113–123.

Arnold B (1904) *Translation of "The Letter of Petrus Peregrinus on the Magnet A.D. 1269"*. New York: McGraw Publishing.

Arrhenius S (1900) Zur Physik des Volcanismus. *Geologiska Foreningens i Stockholm Forhandlingar* 22: 395–420.

Backus GE (1958) A class of self-sustaining spherical dynamos. *Annals of Physics* 4: 372–447.

Backus G, Parker R, and Constable C (1996) *Foundations of Geomagnetism*. Cambridge: Cambridge University Press.

Berhanu M, Verhille G, Boisson J, et al. (2010) Dynamo regimes and transitions in the VKS experiment. *European Physical Journal B* 77: 459–468.

Biggin AJ, Steinberger B, Aubert J, et al. (2012) Possible links between long term geomagnetic variations and whole mantle convection processes. *Nature Geoscience* 5(8): 526–533.

Birch F (1952) Elasticity and constitution of the Earth's interior. *Journal of Geophysical Research* 57: 227–286.

Birch F (1964) Density and composition of mantle and core. *Journal of Geophysical Research* 69: 4377–4388.

Boehler R (1996) Melting temperature of the Earth's mantle and core: Earth's thermal structure. *Annual Review of Earth and Planetary Sciences* 24: 15–40.

Bouhifd MA, Gautron L, Bolfan-Casanova N, et al. (2007) Potassium partitioning into molten iron alloys at high pressure: Implications for Earth's core. *Physics of the Earth and Planetary Interiors* 160(1): 22–33.

Braginsky SI (1964) Self-excitation of a magnetic field during the motion of a highly conducting fluid. *Soviet Physics – Journal of Experimental and Theoretical Physics* 20: 726–735.

Braginsky SI (1976) On the nearly axially-symmetrical model of the hydromagnetic dynamo of the Earth. *Physics of the Earth and Planetary Interiors* 11(3): 191–199.

Braginsky SI and Roberts P (1995) Equations governing convection in Earth's core and the geodynamo. *Geophysical and Astrophysical Fluid Dynamics* 79: 1–97.

Brush SG (1996) *Nebulous Earth*. Cambridge: Cambridge University Press.

Buffett BA (2003) The thermal state of Earth's core. *Science* 299: 1675–1677.

Buffett BA and Seagle CT (2010) Stratification of the top of the core due to chemical interactions with the mantle. *Journal of Geophysical Research* 115: B04407.

Bullard EC, Freedman C, Gellman H, and Nixon J (1950) The westward drift of the Earth's magnetic field. *Philosophical Transactions of the Royal Society of London, Series A* 247: 213–278.

Bullard EC and Gellman H (1954) Homogeneous dynamos and terrestrial magnetism. *Proceedings of the Royal Society of London A* 247: 213–278.

Bullen KE (1954) Composition of the Earth's outer core. *Nature* 174: 505.

Busse FH (1970) Thermal instabilities in rapidly rotating systems. *Journal of Fluid Mechanics* 44: 441–460.

Busse FH and Carrigan CR (1976) Laboratory simulation of thermal convection in rotating planets and stars. *Science* 191: 81–83.

Cao AM and Romowicz B (2004) Constraints on density and shear velocity contrasts at the inner core boundary. *Geophysical Journal International* 57: 1146–1151.

Chapman S and Bartels J (1940) *Geomagnetism*. Oxford: Clarendon Press.

Christensen UR (2011) Geodynamo models: Tools for understanding properties of Earth's magnetic field. *Physics of the Earth and Planetary Interiors* 187(3): 157–169.

Cowling TG (1933) The magnetic field of sunspots. *Monthly Notices of the Royal Astronomical Society* 94: 39–48.

Darwin GH (1879) On the bodily tide of viscous and semi-elastic spheroids, and on the ocean tides upon a yielding nucleus. *Philosophical Transactions* 170: 1–35.

Davidson PA (2001) *An Introduction to Magnetohydrodynamics*. Cambridge: Cambridge University Press.

de Koker N, Steinle-Neumann G, and Vlek V (2012) Electrical resistivity and thermal conductivity of liquid Fe alloys at high P and T, and heat flux in Earth's core. *Proceedings of the National Academy of Sciences* 109(11): 4070–4073.

Dehant V, Creager K, Karato S, and Zatman S (2003) *Earth's Core, Dynamics, Structure, Rotation*. *AGU Geodynamics Series*. vol. 31. Washington, DC: American Geophysical Union.

Deuss A, Irving JC, and Woodhouse JH (2010) Regional variation of inner core anisotropy from seismic normal mode observations. *Science* 328(5981): 1018–1020.

Dormy E, Valet JP, and Courtillot V (2000) Numerical models of the geodynamo and observational constraints. *Geochemical, Geophysics, Geosystems* 1.

Dziewonski AM and Anderson DL (1981) Preliminary reference Earth model. *Physics of the Earth and Planetary Interiors* 25: 297–356.

Dziewonski AM and Gilbert F (1971) Solidity of the inner core of the Earth inferred from normal model observations. *Nature* 234: 465–466.

Elsasser WM (1946) Induction effects in terrestrial magnetism. Part II. The secular variation. *Physical Review* 70: 202–212.

Elsasser WM (1950) The Earth's interior and geomagnetism. *Reviews of Modern Physics* 22: 1–35.

Evans ME (1988) Edmond Halley, geophysicist. *Physics Today* 41: 41–45.

Franklin B (1793) Conjectures concerning the formation of the Earth. *Transactions of the American Philosophical Society* 3: 1–5.

Gailitis A, Lielausis O, Platacis E, Gerbeth G, and Stefani F (2003) The Riga dynamo experiment. *Surveys in Geophysics* 24: 247–267.

Gauss CF (1832) Cited in "Carl Friedrich Gauss und die Erforschung des Erdmanetismus", by Schering, E., Abhand. *Gesellschaft Wissenschaften Gottingen* 34: 1–79.

Gauss CF (1839) Allgemeine Theorie des Erdmagnetismus. In: *Resultate aus den Beobachtungen des magnetischen Vereins*. Gottingen.

Georg RB, Halliday AN, Schauble EA, and Reynolds BC (2007) Silicon in the Earth's core. *Nature* 447: 1102–1106.

Gessmann C and Wood B (2002) Potassium in the earth's core? *Earth and Planetary Science Letters* 200: 63–78.

Gilbert W (1600) De Magnete.

Gillet N, Jault D, Canet E, and Fournier A (2010) Fast torsional waves and strong magnetic field within the Earth's core. *Nature* 465(7294): 74–77.

Glatzmaier G (2002) Geodynamo simulations – How realistic are they? *Annual Review of Earth and Planetary Science* 30: 237–257.

Glatzmaier G, Coe R, Hongre L, and Roberts P (1999) The role of the Earth's mantle in controlling the frequency of geomagnetic reversals. *Nature* 401: 885–890.

Glatzmaier G and Roberts P (1995) A three-dimensional self-consistent computer simulation of a geomagnetic field reversal. *Nature* 337: 203–209.

Glatzmaier G and Roberts P (2002) Simulating the geodynamo. *Contemporary Physics* 38: 269–288.

Greenspan H (1968) *The Theory of Rotating Fluids*. Cambridge: Cambridge University Press.

Gubbins D (1973) Numerical solution of the kinematic dynamo problem. *Philosophical Transactions A* 274: 493–521.

Gubbins D (1981) Rotation of the inner core. *Journal of Geophysical Research* 86(B12): 11695–11699.

Gubbins D, Alfe D, Masters G, Price GD, and Gillan MJ (2003) Can the Earth's dynamo run on heat alone? *Geophysical Journal International* 155: 609–622.

Gubbins D and Herrero-Bervera E (eds.) (2007) *Encyclopedia of Geomagnetism and Paleomagnetism*, pp. 495–497. Dordrecht: Springer.

Gutenberg B (1912) Uber Erdbebenwellen, VIIA. Gottingen Nachr., pp. 125–176.

Halley E (1683) A theory of the variation of the magnetical compass. *Philosophical Transactions* 13: 208–221.

Halley E (1692) An account of the cause of the change of the variation of the magnetical needle, with an hypothesis of the structure of the internal parts of the Earth. *Philosophical Transactions* 16: 563–578.

Hertzenberg A (1958) Geomagnetic dynamos. *Philosophical Transactions A* 250: 543–583.

Holme R (1998) Electromagnetic core-mantle coupling I: Explaining decadal changes in the length of day. *Geophysical Journal International* 132(1): 167–180.

Jacobs JA (1987) *The Earth's Core*, 2nd edn. New York: Academic Press.

Jeffreys H (1926) The rigidity of the Earth's central core. *Monthly Notices of the Royal Astronomical Society, Geophysical Supplement* (1): 371–383.

Jeffreys H (1929) *The Earth: Its Origin, History and Physical Constitution*, 2nd edn. Cambridge: Cambridge University Press.

Johnson CL and Constable CG (1997) The time-averaged geomagnetic field: Global and regional biases for 0–5 Ma. *Geophysical Journal International* 131(3): 643–666.

Jones CA, Soward AM, and Mussa AI (2000) The onset of convection in a rapidly rotating sphere. *Journal of Fluid Mechanics* 405: 157–179.

Jones C, Soward A, and Zhang K (eds.) (2003) *Earth's Core and Lower Mantle*. London: Taylor and Francis.

Kageyama A and Sato T (1995) Computer simulation of a magnetohydrodynamic dynamo II. *Physics of Plasmas* 2: 1421–1431.

Kelvin L (1862) On the rigidity of the Earth. *Philosophical Transactions* 153: 573–582.

Kennett BLN and Bunge HP (2008) *Geophysical Continua*. Cambridge: Cambridge University Press.

Kleine T, Mnker C, Mezger K, and Palme H (2002) Rapid accretion and early core formation on asteroids and the terrestrial planets from HfW chronometry. *Nature* 418(6901): 952–955.

Kono M and Roberts P (2002) Recent geodynamo simulations and observations of the geomagnetic field. *Reviews of Geophysics* 40: 1013.

Kutzner C and Christensen UR (2004) Simulated geomagnetic reversals and preferred virtual geomagnetic pole paths. *Geophysical Journal International* 157(3): 1105–1118.

Labrosse S (2003) Thermal and magnetic evolution of the Earth's core. *Physics of the Earth and Planetary Interiors* 140(1): 127–143.

Lacaze L, Herreman W, Le Bars M, Le Dizs S, and Le Gal P (2006) Magnetic field induced by elliptical instability in a rotating spheroid. *Geophysical and Astrophysical Fluid Dynamics* 100: 299–317.

Larmor J (1919) How could a rotating body such as the sun become a magnet? *British Association for the Advancement of Science* 87: 159–160.

Lay T, Hernlund J, and Buffett BA (2008) Core–mantle boundary heat flow. *Nature Geoscience* 1(1): 25–32.

Lehmann I (1936) P′. *Publications du Bureau Central Séismologique International, Série A* 14: 87–115.

Lilley FEM (1970) On kinematic dynamos. *Proceedings of the Royal Society of London, Series A* 316: 153–167.

Loper D (1978) Some thermal consequences of the gravitationally powered dynamo. *Journal of Geophysical Research* 83: 5961–5970.

Lowes FJ and Wilkinson I (1963) Geomagnetic dynamo: A laboratory model. *Nature* 198: 1158–1160.

MacDonald WF (2003) Composition model for the Earth's core. In: Holland HD and Turekian KK (eds.) *The Mantle and Core*. *Treatise on Geochemistry*, vol. 2, pp. 547–568. Oxford: Pergamon.

Malkus VWR (1968) Precession of the earth as the cause of geomagnetism. *Science* 160: 259–264.

Masters G and Gubbins D (2003) On the resolution of density within the Earth. *Physics of the Earth and Planetary Interiors* 140: 159–167.

Merrill RT, McElhinny MW, and McFadden PL (1998) *The Magnetic Field of the Earth*. San Diego, CA: Academic Press.

Moffatt HK (1978) *Magnetic Field Generation in Electrically Conducting Fluids*. Cambridge: Cambridge University Press.

Müller U, Stieglitz R, and Horanyi S (2006) Experiments at a two-scale dynamo test facility. *Journal of Fluid Mechanics* 552: 419–440.

Murthy VR, van Westrenen W, and Fei Y (2003) Experimental evidence that potassium is a substantial radioactive heat source in planetary cores. *Nature* 423: 163–165.
Newcomb S (1892) On the dynamics of the Earth's rotation, with respect to the periodic variation of latitude. *Monthly Notices of the Royal Astronomical Society* 52: 336–341.
Nguyen JH and Holmes NC (2004) Melting of iron at the physical conditions of the Earth's core. *Nature* 427: 339–342.
Nimmo F and Alfe D (2006) Properties and evolution of the Earth's core and geodynamo. In: Sammonds PR and Thompson JMT (eds.) *Advances in Science, Earth Science*. London: Imperial College.
Oldham RD (1906) The constitution of the Earth, as revealed by earthquakes. *Nature* 92: 684–685.
Olson PL, Coe RS, Driscoll PE, Glatzmaier GA, and Roberts PH (2010) Geodynamo reversal frequency and heterogeneous core–mantle boundary heat flow. *Physics of the Earth and Planetary Interiors* 180(1): 66–79.
Olson P, Deguen R, Hinnov LA, and Zhong S (2013) Controls on geomagnetic reversals and core evolution by mantle convection in the Phanerozoic. *Physics of the Earth and Planetary Interiors* 214: 87–103.
Parker EN (1955) Hydrodynamic dynamo models. *Astrophysical Journal* 122: 293–314.
Poincare H (1885) Sur l'equilibre d'une masse fluide animee d'un mouvement de rotation. *Comptes rendus de l'Académie des Sciences, Paris* 100: 346–348.
Poincare H (1910) Sur la precession des corps deformables. *Bulletin Astronomique* 27: 321–356.
Poirier JP (1988) Transport properties of liquid metals and viscosity of the Earth's core. *Geophysical Journal* 92: 99–105.
Poirier JP (1994) Light elements in Earth's outer core: A critical review. *Physics of the Earth and Planetary Interiors* 85: 319–337.
Rädler K-H (1978) *Zeitschrift für Naturforschung* 23a: 1851–1860.
Rama Murthy V, von Westrenen W, and Fei Y (2003) Experimental evidence that potassium is a substantial radioactive heat source in planetary cores. *Nature* 423: 163–165.
Rhines PB (1979) Geostrophic turbulence. *Annual Review of Fluid Mechanics* 11: 401–441.
Ritter A (1878) Untersuchungen uber die Hole der Atmosphare und die Constitution gasforminger Weltkorper. *Annalen der Physik, Series 3* 5: 405–445, 543–558.
Roberts PH (1972) Kinematic dynamo models. *Philosophical Transactions of the Royal Society of London, Series A* 272: 663–698.
Roberts PH, Jones CA, and Calderwood AR (2003) Energy fluxes and ohmic dissipation in the Earth's core. In: Jones C, Soward A, and Zhang K (eds.) *Earth's Core and Lower Mantle*. London: Taylor and Francis.
Rochester MG (1962) Geomagnetic core–mantle coupling. *Journal of Geophysical Research* 67: 4833–4836.
Rubie DC, Frost DJ, Mann U, et al. (2011) Heterogeneous accretion, composition and core-mantle differentiation of the Earth. *Earth and Planetary Science Letters* 301: 31–42.
Schubert G, Turcotte D, and Olson P (2001) *Mantle Convection in the Earth and Planets*. New York: Cambridge University Press.
Schuster A (1911) *The Progress of Physics During 33 Years (1875–1908)*. Cambridge: Cambridge University Press.
Shearer P and Masters G (1990) The density and shear velocity contrast at the inner core boundary. *Geophysical Journal International* 10: 491–498.
Smylie DE (2013) *Earth's Dynamics, Deformations and Oscillations of the Rotating Earth*. New York: Cambridge University Press.
Song X and Richards P (1996) Seismological evidence for differential rotation of the earth's inner core. *Nature* 382: 221–224.
Stacey F (1992) *Physics of the Earth*, 3rd edn. Brisbane: Brookfield Press.
Steenbeck M, Krause F, and Radler K-H (1967) A calculation of the mean electromotive force in an electrically conducting fluid in turbulent motion, under the influence of Coriolis forces. *Zeitschrift für Naturforschung* 21a: 369–376.
Takahashi F, Matsushima M, and Honkura Y (2005) Simulations of a quasi-Taylor state geomagnetic field including polarity reversals on the Earth simulator. *Science* 309: 459–461.
Tarduno JA, Cottrell RD, Watkeys MK, et al. (2010) Geodynamo, solar wind, and magnetopause 3.4 to 3.45 billion years ago. *Science* 327(5970): 1238–1240.
Taylor GI (1923) The motion of a sphere in a rotating liquid. *Proceedings of the Royal Society of London A* 102: 180–189.
Taylor JB (1963) The magneto-hydrodynamics of a rotating fluid and the Earth's dynamo problem. *Proceedings of the Royal Society of London A* 274: 274–283.
Tilgner A (2005) Precession driven dynamos. *Physics of Fluids* 17: 034104.
Verhoogen J (1961) Heat balance of the Earth's core. *Geophysical Journal of the Royal Astronomical Society* 4: 276–281.
Verhoogen J (1979) *Energetics of the Earth*. Washington, DC: National Academy of Science.
Wiechert E (1897) Uber die Massenvertheilung im Innern der Erde. Gottingen Nachr., pp. 221–243.
Wu B, Driscoll P, and Olson P (2011) A statistical boundary layer model for the mantle D region. *Journal of Geophysical Research* 116: B12112.
Zhang KK and Busse FH (1988) Finite amplitude convection and magnetic field generation in a rotating spherical shell. *Geophysical and Astrophysical Fluid Dynamics* 44(1–4): 33–53.
Zhang K and Gubbins D (1992) On convection in the Earth's core driven by lateral temperature variation in the lower mantle. *Geophysical Journal International* 108: 247–255.
Zhang N and Zhong S (2011) Heat fluxes at the Earth's surface and core-mantle boundary since Pangea formation and their implications for the geomagnetic superchrons. *Earth and Planetary Science Letters* 306(3): 205–216.
Zollner F (1871) Uber den Ursprung des Erdmagnetismus und die magnetischen Bezien-hungen der Weltkorper. *Gesellschaft der Wissenschaften, Mathematisch-Physikalische, Leipzig* 23: 479–575.

This page intentionally left blank

8.02 Energetics of the Core

F Nimmo, University of California, Santa Cruz, CA, USA

© 2015 Elsevier B.V. All rights reserved.

8.02.1	**Introduction**	29
8.02.2	**Core Structure and Magnetic Field Evolution**	29
8.02.2.1	Density	29
8.02.2.2	Composition	30
8.02.2.3	Temperature	31
8.02.2.4	Conductivity	31
8.02.2.5	Dynamo Behavior over Time	31
8.02.3	**Energy and Entropy Equations**	32
8.02.3.1	Preliminaries	33
8.02.3.2	Energy Balance	34
8.02.3.2.1	General expression	34
8.02.3.2.2	Core heat flow Q_{cmb}	35
8.02.3.2.3	Internal heating Q_R	35
8.02.3.2.4	Heat of reaction Q_H	35
8.02.3.2.5	Secular cooling and pressure heating Q_S, Q_P	36
8.02.3.2.6	Gravitational energy Q_g	36
8.02.3.2.7	Latent heat release Q_L	36
8.02.3.2.8	Pressure effect on freezing Q_{PL}	36
8.02.3.2.9	Summary	36
8.02.3.3	Entropy Terms	36
8.02.3.4	Example Core Structure	38
8.02.3.4.1	Specific heat (Q_s, E_s)	39
8.02.3.4.2	Radioactive heating (Q_R, E_R)	39
8.02.3.4.3	Latent heat (Q_L, E_L)	40
8.02.3.4.4	Gravitational contribution (Q_g, E_g)	40
8.02.3.4.5	Entropy of heat of solution (E_H)	40
8.02.3.4.6	Adiabatic contribution (Q_k, E_k)	40
8.02.3.4.7	Other contributions	40
8.02.3.5	Summary	40
8.02.4	**Present-Day Energy Budget**	40
8.02.4.1	Introduction	40
8.02.4.2	General Behavior	41
8.02.4.3	Core Properties	42
8.02.4.3.1	Density and gravity	42
8.02.4.3.2	Thermodynamic properties	42
8.02.4.3.3	Temperature and melting	43
8.02.4.3.4	Chemical properties	43
8.02.4.3.5	Ohmic Dissipation	43
8.02.4.3.6	Internal heating	43
8.02.4.3.7	Present-day CMB heat flow	44
8.02.4.3.8	Geochemical constraints on inner core age	44
8.02.4.3.9	Comparison with other models	44
8.02.4.4	Present-Day Behavior	45
8.02.5	**Evolution of Energy Budget through Time**	47
8.02.5.1	Introduction	47
8.02.5.2	Theoretical Models	47
8.02.5.3	Age of the Inner Core	49
8.02.5.4	Stable Stratification	51
8.02.6	**Summary and Conclusions**	52
Acknowledgments		52
References		52

 http://dx.doi.org/10.1016/B978-0-444-53802-4.00139-1

Abbreviations

CMB Core–mantle boundary

ICB Inner core boundary

Nomenclature

A	Characteristic core length scale
$\mathbf{B}$	Magnetic field
B	Characteristic core length scale
c	Mass fraction of light element
C	Characteristic core length scale
C_c	Constant relating light element release to core growth
C_p	Specific heat capacity
C_r	Constant relating core growth to temperature change
D	Length scale of adiabatic temperature variation
D_k	Length scale of thermal conductivity variation
e	Internal energy
E	Electric field
E_g	Entropy production rate due to potential energy
E_H	Entropy production rate due to chemical heating
E_k	Entropy production rate due to thermal conduction
E_L	Entropy production rate due to latent heat
E_P	Entropy production rate due to pressure heating
E_R	Entropy production rate due to internal heating
E_s	Entropy production rate due to secular cooling
E_α	Entropy production rate due to molecular diffusion
E_Φ	Entropy production rate due to ohmic dissipation
$\tilde{E}_T$	Total entropy production constant
f_{ad}	Ratio of T_i to T_c
G	Gravitational constant
g, g	Acceleration due to gravity
h	Internal heating rate
i	Flux vector of light element
I_s	$\int \rho T \, dV$
I_T	$\int \rho / T \, dV$
k	Thermal conductivity
K_0	Compressibility at zero pressure
k_c	Thermal conductivity at CMB
L	Length scale of density variations
L'_H	Latent heat incorporating pressure effect
L_H	Latent heats
M_c	Core mass
M_{oc}	Outer core mass
P	Pressure
P_c	Pressure at the CMB
ppm	Parts per million
P_T	Constant relating pressure change to temperature change
q	Heat flux
Q_{cmb}	CMB heat flow
Q_g	Heat flow due to potential energy
Q_H	Heat flow due to chemical reaction
Q_L	Heat flow due to latent heat
Q_P	Heat flow due to pressure heating
Q_R	Heat flow due to radioactive heating
Q_s	Heat flow due to secular cooling
$\overline{Q}_{cmb}$	Mean core heat flow
$\tilde{Q}_T$	Total heat flow constant
r	Radial distance
r_c	Core radius
r_e	Planetary radius
R_H	Heat of reaction
r_i	Inner core radius
s	Entropy
S	Outward normal vector
t	Time
T, T_a	Temperature, adiabatic temperature
T_c	Temperature at the CMB
T_i	Temperature at the ICB
T_m	Melting temperature
T_{m0},T_{m1},T_{m2}	Coefficients describing melting curve
TW	10^{12} W
$\mathbf{u}$	Core contraction velocity
$\mathbf{v}$	Local core fluid velocity
v_p,v_s	Seismic P-wave and S-wave velocities
W_g	Energy released since IC formation due to potential energy
W_L	Energy released since IC formation due to latent heat
W_R	Energy released since IC formation due to radioactive decay
W_s	Energy released since IC formation due to secular cooling
α	Thermal expansivity
α_c	Compositional thermal expansivity
γ	Grüneisen parameter
Δc	Compositional contrast across the ICB
ΔP	Pressure difference from ICB to the center of the Earth
$\Delta T'_c$	Change in T_c prior to IC formation
ΔT_c	Change in T_c since IC formation
$\Delta \rho_c$	Compositional density contrast
λ	Radioactive decay constant
μ	Chemical potential
μ_0	Permeability of free space
ρ	Density
ρ_0	Density at zero pressure
ρ_{cen}	Density at the center of the Earth
ρ_i	Density at the ICB

ρ_m	Mantle density	τ_i	Inner core age
σ	Electrical conductivity	Φ	Ohmic dissipation
τ'	Deviatoric stress	Ψ	Gravitational potential

8.02.1 Introduction

Understanding the energy budget of the Earth's core is important for at least four reasons. First, it is this energy budget that permits the present-day existence of the Earth's dynamo and magnetic field. Second, the persistence of this field for at least 3.5 Gyr places strong constraints on the thermal and energetic evolution of the core (and, particularly, the growth of the inner core). Third, whether or not a dynamo operates depends mainly on the rate at which heat is extracted from the core into the mantle; thus, the existence of a dynamo also places constraints on the evolution of the mantle. Finally, an improved understanding of the way the Earth's dynamo has evolved will help us to interpret the significance of extant or extinct dynamos in other planetary bodies, both in this solar system (e.g., Nimmo and Alfe, 2006; Stevenson, 2010) and perhaps even elsewhere (e.g., Gaidos et al., 2010).

The aims of this chapter are to summarize the contributing factors to the core's overall energy (and entropy) budgets, to quantify these factors and their likely uncertainties, and to demonstrate how these results may be used to evaluate the behavior of the core, both now and in the past. The development in the succeeding text should allow a reader to start from general thermodynamic equations and end up able to calculate the entropy and energy terms for an arbitrary core structure. Large parts of this chapter are based on previous works, particularly those of Braginsky and Roberts (1995), Buffett et al. (1996), Labrosse (2003), Roberts et al. (2003), Gubbins et al. (2003, 2004), Nimmo et al. (2004), Nimmo (2007), and Pozzo et al. (2012). Other relevant chapters in this treatise include those by Loper and in **Chapters 8.05**, **8.03**, **8.10**, **8.02**, **8.11**, and **8.08**. Such a treatment is inevitably lengthy; readers more interested in the application of the equations to the Earth than their derivation are advised to focus on **Sections 8.02.4** and **8.02.5**.

Most of this chapter has required little revision since the first edition of the Treatise of Geophysics (Nimmo, 2007). However, it has recently been argued that core thermal conductivities are roughly three times higher than previously thought (**Section 8.02.2.4**). This result has important implications for the present-day behavior and long-term evolution of the core, which are discussed in some detail in **Sections 8.02.4** and **8.02.5**. It also means that the conclusions of many modeling results published prior to 2012 may require some modification. A second discovery is of the complex structure of the inner core (see **Chapters 1.23** and **8.12**); disentangling the inner core's growth will ultimately help us to understand how the dynamo evolved. A third development is the ability to use geoneutrinos to infer the concentration of radiogenic elements in the Earth (Gando et al., 2011). While currently rather crude, these measurements may ultimately provide observational constraints on radiogenic heat production within the core.

Our main conclusions may be summarized as follows. The principal driving mechanism for the present-day dynamo is probably the release of one or more light elements at the inner core boundary (ICB) due to ongoing inner core solidification. In the absence of such solidification, the core would have had to cool roughly three times as fast in order to maintain the same rate of dissipation in the dynamo (**Section 8.02.4.4**). The rate at which the core cools is controlled by the mantle. Independent estimates of the present-day heat flow at the core–mantle boundary (CMB) of 7–17 TW are sufficient to maintain a present-day dynamo. However, prior to the onset of core solidification, a CMB heat flow of at least 15 TW is required to drive a dynamo. Such high heat flows imply that early core temperatures are likely to cause widespread lower mantle melting. These high initial temperatures are reduced if the core contains radioactive potassium, which acts as an extra energy source for the dynamo and allows slower core cooling and less rapid inner core growth. However, even with potassium present, the implied inner core age never exceeds 0.7 Gyr. The high heat fluxes required to sustain a dynamo prior to inner core solidification appear compatible with our understanding of mantle thermal evolution. These conclusions are based on the assumption that the core remains well mixed and unstratified. As discussed in **Section 8.02.5.3**, a partially stratified core is a distinct possibility, but the fluid dynamics and implications of this situation have not yet been satisfactorily resolved.

The rest of the chapter is arranged as follows. **Section 8.02.2** briefly summarizes core and dynamo parameters relevant to the later analysis. **Section 8.02.3** gives the general energy and entropy equations describing core thermal evolution and dynamo generation. It also gives specific expressions for each of the mechanisms (e.g., latent heat release) contributing towards dynamo generation for a simple analytic model of core structure. **Section 8.02.4** shows how these expressions may be used to establish general results for core and dynamo behavior. This section also derives specific results for the present-day energy and entropy budgets of the core, based on models of core and mantle structure. **Section 8.02.5** summarizes investigations of these budgets through time, focusing in particular on the age of the inner core and the role of stable stratification. Finally, **Section 8.02.6** summarizes and concludes the chapter.

8.02.2 Core Structure and Magnetic Field Evolution

8.02.2.1 Density

The density structure of the core may be derived directly from seismological observations (see **Chapter 1.23**). **Figure 1(a)** plots the density structure of the core as a function of depth and shows the increase with depth due to increasing pressure. The density discontinuity at the ICB arises because of two

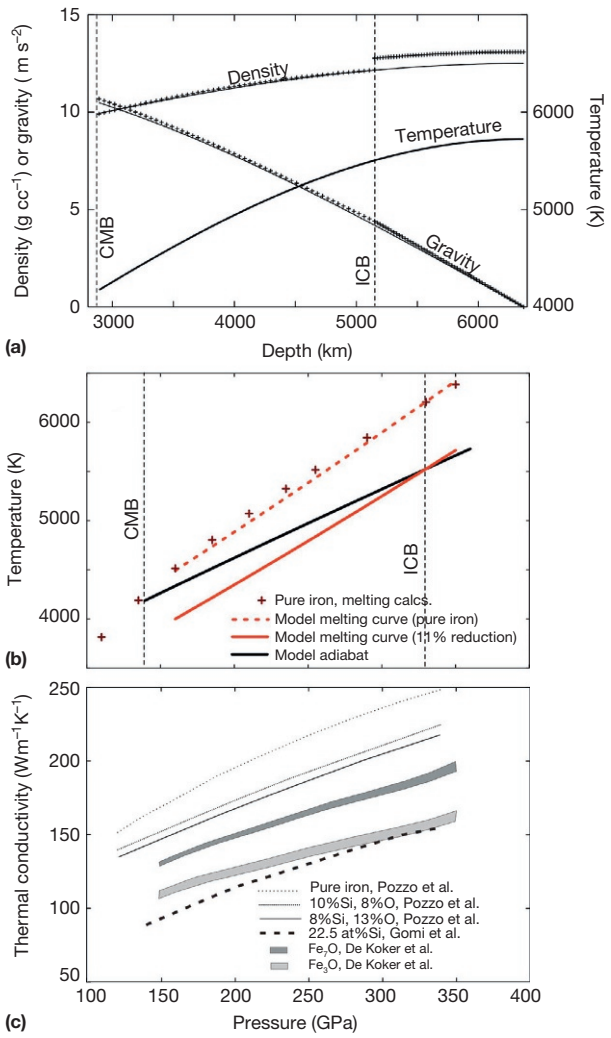

Figure 1 (a) Comparison of model calculations (solid lines) with PREM values (crosses; Dziewonksi and Anderson, 1981). Density, gravity, and adiabatic temperature are calculated using eqns [41], [45], and [46], respectively, and parameter values given in **Table 2**. (b) Melting behavior. Crosses are calculated values for pure iron from Alfè et al. (2004). Dashed red line is a model representation of this curve using eqn [53]. Solid red line is the same curve with an 11% reduction to account for the effect of impurities (see text). Black line is the adiabat replotted from (a). (c) Representative thermal conductivity profiles, redrawn from Pozzo et al. (2012), De Koker et al. (2012), and Gomi et al. (2013).

effects. Firstly, solid core material is inherently denser than liquid core material at the same pressure and temperature (P,T) conditions. Secondly, the outer core contains more of one or more light elements than the inner core (e.g., Poirier, 1994) and would therefore be less dense even if there were no phase change. This compositional density contrast has a dominant role in driving compositional convection in the core (see **Section 8.02.3.3**); unfortunately, its magnitude is uncertain by a factor of about 2.

Even the total density contrast across the ICB is somewhat uncertain. The two observations generally employed are normal mode data (e.g., Dziewonski and Anderson, 1981) and reflected body-wave amplitude ratios (e.g., Shearer and Masters, 1990). A normal mode study (Masters and Gubbins, 2003) gives a total density contrast at the ICB of 640–1000 kg m^{-3}, which agrees rather well with the result of 600–900 kg m^{-3} obtained using body waves (Cao and Romanowicz, 2004), but is somewhat higher than the value obtained by Koper and Dombrovskaya (2005).

The density contrast, based on first-principles simulations, between pure solid Fe and liquid Fe at the ICB is estimated at 1.6% (Laio et al., 2000). This value contrasts with the 5–8.3% density contrast inferred from seismology to exist at the ICB. These results imply a compositional density contrast of 3.2–6.7%, or ≈400–800 kg m^{-3}, and may in turn be used to estimate the difference in light element concentrations between the inner and outer cores.

8.02.2.2 Composition

Cosmochemical abundances leave no doubt that the bulk of the core is made of iron. However, it is also clear that the outer core is 6–10% less dense than pure liquid iron would be under the estimated P,T conditions (e.g., Alfè et al., 2002a; Poirier, 1994). The inner core also appears to be less dense than a pure iron composition would suggest (Jephcoat and Olson, 1987), though here the difference is smaller. Both the outer and inner cores must therefore contain some fraction of light elements, of which the most common suspects are sulfur, silicon, and oxygen (Poirier, 1994). Furthermore, the outer core must contain a greater proportion of such elements than the inner core. It is the expulsion of these light elements during inner core crystallization that, to a large extent, drives the dynamo.

Using first-principles computations, Alfè et al. (2002a) found that oxygen does not tend to be retained within crystalline iron. It therefore partitions strongly into the outer core and is most likely the element responsible for the compositional density contrast at the ICB. Conversely, S and Si have atomic radii similar to that of iron at core pressures and thus substitute freely for iron in the solid inner core. There is thus little difference between S and Si concentrations in the inner and outer cores. Based on an assumed total ICB density contrast of 4.5% (575 kg m^{-3}), Alfè et al. (2002a) concluded that 2.8% (360 kg m^{-3}) of this density contrast arose from compositional variations. They suggested that the inner core contains 8.5 ± 2.5% molar S/Si, while the outer core contains 10 ± 2.5% molar S/Si and 8 ± 2.5% molar O. A higher total density contrast would imply a higher molar fraction of O: for instance, a total density contrast of 7% would imply a compositional density contrast of 5.3% (650 kg m^{-3}) and 15% molar O in the outer core.

Which light elements were partitioned into the core during the Earth's formation depends on the conditions at the time, because partitioning is a strong function of pressure, temperature, and oxygen fugacity (e.g., Tsuno et al., 2013). As a result, some calculations favor Si as the dominant element (Ricolleau et al., 2011; Rubie et al., 2011), while others prefer O (Siebert et al., 2013). A comparison of experimental velocity and density determinations with seismologically derived values supports relatively low O concentrations (Huang et al., 2011) and a mix of S and Si (Morard et al., 2013). The identity of the light element(s) present in the core thus remains uncertain.

If the core last equilibrated with the silicate mantle at sufficiently high temperatures, species such as Mg could have dissolved in the core in substantial amounts (Nomura et al., 2012). As noted by Stevenson (2012), subsequent exsolution of these species as the core cooled could provide a potent additional mechanism to drive the dynamo and could also lead to a stably stratified layer at the top of the core (see Section 8.02.5.4).

8.02.2.3 Temperature

As long as the core is vigorously convecting, its mean temperature profile will closely approximate that of an adiabat, except in very thin top and bottom boundary layers. Since the temperature at the ICB must equal the melting temperature of the core at that pressure, the temperature elsewhere in the core may then be extrapolated from the ICB along an appropriate adiabat. The assumption of an adiabatic core will be adhered to throughout most of this chapter; the possibility of stably stratified regions will be discussed in Section 8.02.5.3.

The previously mentioned discussion shows that determining the melting behavior of core material is crucial to establishing the temperature structure of the core. This, however, is not easy to do: experiments at the P,T conditions required (e.g., Boehler, 1993; Brown and McQueen, 1986; Yoo et al., 1993) are challenging, and computational (first-principles) methods (e.g., Alfè et al., 2002b; Belonoshko et al., 2000; Laio et al., 2000) are time-consuming and hard to verify. Furthermore, the presence of the light element(s) likely reduces the melting temperature from that of pure iron, but by an uncertain amount. These issues are discussed in detail elsewhere in this volume. Here, we will simply summarize what appears to be the most convincing set of computational results to date.

Based on first-principles calculations, Alfè et al. (2003) obtained a melting temperature of 6350 ± 500 K for pure iron at ICB pressures (330 GPa). This agrees remarkably well with a recent static determination of pure iron melting temperature at ICB pressures of 6230 ± 500 K (Anzellini et al., 2013). Alfè et al. (2003) went on to use ideal solution theory to argue that the melting point depression due to the presence of oxygen is proportional to the oxygen concentration difference across the ICB and obtained a temperature reduction of 700 ± 100 K. The predicted temperature at the ICB is therefore 5650 ± 600 K. Extrapolating from this point to other locations within the core depends on the adiabat, which involves further unknowns discussed later in the text (Section 8.02.3.4).

The results of the calculations by Alfè et al. (2002a,b, 2003) differ from previous calculations by Belonoshko et al. (2000) and Laio et al. (2000). However, this discrepancy arises mainly because of the different molecular dynamics techniques adopted; correcting for these differences, the results obtained are very similar (Alfè et al., 2002a). The melting curve of Alfè et al. (2002a,b) agrees well with the low-pressure diamond anvil cell results of Shen et al. (1998) and Ma et al. (2004), though not those of Boehler (1993). Similarly, the curve agrees with the higher-pressure shock-wave results of Brown and McQueen (1986) and Nguyen and Holmes (2004), though not those of Yoo et al. (1993). Further discussion of the differing results may be found in Alfè et al. (2004).

Figure 1(b) shows the calculations of Alfè et al. (2002a,b) and two theoretical melting curves (eqn [53]), one including a temperature reduction of 11% to account for the presence of the light element(s). This line gives a temperature at the ICB ($P = 328$ GPa) of 5508 K. Figure 1(b) also shows a hypothetical adiabat and demonstrates that the temperature at the CMB, obtained by extrapolating down the adiabat, is 4180 K. Based on the ICB temperature uncertainty, the uncertainty at the CMB is ± 400 K.

8.02.2.4 Conductivity

The thermal and electrical conductivities of the core are related to each other by the Wiedemann–Franz law (e.g., Stacey and Anderson, 2001). A higher electrical conductivity would enhance magnetic field generation, other things being equal. However, a higher thermal conductivity increases the ability of the core to transport heat down the adiabat and thus reduces the convective vigor of the core circulation. Of these two effects, the latter is the more important in governing dynamo behavior.

Until recently, the main method of estimating thermal conductivity of core materials was by using shock-wave experiments and measuring electrical conductivity. Early shock-wave experiments were carried out by Keeler and Royce (1971) and Matassov (1977), with similar results. The latter data were used by Stacey and Anderson (2001) to conclude that k at the CMB was 46 W m^{-1} K^{-1}. A later study by Bi et al. (2002) gave lower conductivities.

Recently, two first-principles calculations of electronic structure and conductivity of iron under core conditions have been carried out (De Koker et al., 2012; Pozzo et al., 2012). These two studies are in reasonable mutual agreement (Figure 1(c)) and also agree well with the Keeler and Royce (1971) and Matassov (1977) data. They are also consistent with static determinations of iron conductivity at high pressures (Gomi et al., 2013). The implied thermal conductivities are very high (see Figure 1(c)): 90–150 W m^{-1} K^{-1} at the CMB, depending on the assumed temperature and composition, and up to 250 W m^{-1} K^{-1} at the center of the core. While some uncertainties remain, particularly regarding the effect of alloying elements, the overall conclusion of high thermal conductivity is unlikely to be reversed. This high conductivity has important implications for the evolution of the dynamo, as will be discussed later in the text.

8.02.2.5 Dynamo Behavior over Time

The behavior of the Earth's magnetic field over time bears directly on core energetics (see reviews by Jacobs, 1998; Chapter 5.13; Valet, 2003). In particular, one might expect that the long-term behavior of the field would provide information on the evolution of the dynamo and core. In practice, however, as discussed in the succeeding text, the information is limited to the following: (1) a reversing, predominantly dipolar field has existed, at least intermittently, for at least the last 3.5 Gyr, and (2) the amplitude of the field does not appear to have changed in a systematic fashion over time.

One reason for this paucity of constraints is that the measurable magnetic field at the Earth's surface differs considerably from the field within the core. Firstly, the short-wavelength

surface field is dominated by crustal magnetic anomalies, which obscure the components of the dynamo field at wavelengths shorter than about 3000 km (e.g., Langel and Estes, 1982). Moreover, the toroidal component of the core's magnetic field has field lines that are parallel to the surface of the core. Thus, the toroidal component is not observable at the Earth's surface, though it is probably at least comparable in magnitude to the observable poloidal component (e.g., Jackson, 2003). As a result, the magnetic field that we can measure at the surface is different in both frequency content and amplitude from the field within the core. In particular, ohmic heating is dominated by small-scale magnetic fields that are not observable at the surface.

Several other factors also make it difficult to relate the observed evolution of the geomagnetic field to the core's thermal evolution in any more detail. Firstly, although numerical simulations can now generate dynamos whose behavior resembles that of the Earth's magnetic field (see **Chapter 8.10**), the parameters employed by these models differ very significantly from those applicable to the real Earth. Although some very high-resolution models (Kageyama et al., 2008) result in dynamos that look less like the Earth's than lower-resolution models, this may be a result of the neglect of compositional convection. In any event, it is currently not clear how reliable a guide numerical models provide to interpreting the dynamo's evolution.

Second, these numerical models suggest that the details of dynamo behavior may be at least as sensitive to local factors (such as spatial variations in CMB heat flow) as to global factors (such as inner core size or core cooling rate). For instance, the frequency of model polarity reversals appears to depend on both total CMB heat flow and its spatial distribution (Olson et al., 2010). Conversely, the model mean field amplitude appears highly insensitive to inner core radius (Aubert et al., 2009). Effects such as these make it hard to relate measured changes in the surface field to core characteristics.

Third, the present-day amount of dissipation actually generated by dynamo activity (ohmic heating) is very uncertain, making a direct link between core thermal evolution and dynamo activity problematic (see **Section 8.02.4.3.5**). And finally, paleomagnetic observations are sparse at times prior to the oldest surviving oceanic floor (150 Myr BP). This makes identification of trends in field amplitude very difficult (see, e.g., Labrosse and Macouin, 2003).

Despite these difficulties, it is clear that, over timescales greater than a few thousand years, the mean position of the magnetic axis coincides with the rotation axis (Valet, 2003). Furthermore, the field appears to have remained predominantly dipolar over time (though see Bloxham, 2000) and has apparently persisted for at least 3.5 Gyr (McElhinny and Senanayake, 1980; Tarduno et al., 2010). There is some evidence that the degree to which the field departs from dipolarity may have changed (e.g., Pavlov and Gallet, 2010; Smirnov et al., 2011), while the earliest documented apparent paleomagnetic reversal is at 3.2 Gyr BP (Layer et al., 1996). The magnetic field intensity has fluctuated over time, with the present-day magnetic field being anomalously strong (Selkin and Tauxe, 2000) and the field during the Mesozoic anomalously weak (Prevot et al., 1990). The maximum field intensity appears never to have exceeded the present-day value by more than a factor of 5 (Dunlop and Yu, 2004; Valet, 2003), while Archean magnetic field strengths were comparable to present-day values (Tarduno et al., 2007, 2010). The pattern of magnetic reversals for the Proterozoic is well known, but not well understood. For instance, although reversals occur roughly every 0.25 Myr on average (Lowrie and Kent, 2004), there were no reversals at all in the period 125–85 Ma (e.g., Merrill et al., 1996), for reasons that are obscure but may well have to do with the behavior of the mantle over that interval (e.g., Glatzmaier et al., 1999).

In summary, the fact that a reversing dynamo has apparently persisted for >3.5 Gyr can be used to constrain the energy budget of the core over time (see **Section 8.02.5**). Unfortunately, other observations that might potentially provide additional constraints, such as the evolution of the field intensity or the frequency of reversals, are either poorly sampled or difficult to relate to the global energy budget or both.

8.02.3 Energy and Entropy Equations

The Earth's dynamo is ultimately maintained by convection (either compositional or thermal), with the convective motions being modified by electromagnetic and rotational forces (see, e.g., Roberts and Glatzmaier, 2000). Since the dynamo has persisted over 3.5 Gyr, convection must have likewise persisted in at least some portion of the core, which places constraints on its energy budget. In this section, the basic equations that allow the different terms in the energy balance to be estimated are derived. It will be demonstrated that the ohmic heating generated by dynamo activity does not appear in the energy equations. Thus, these equations are in general insufficient to determine whether or not a geodynamo will operate, though they do allow the evolution of parameters like the inner core radius to be calculated. However, by deriving the equivalent entropy equations, in which the ohmic heating term does appear, a criterion for geodynamo activity may be determined (see eqn [74]).

This section summarizes a large body of previous work on core thermodynamics. Pioneering works by Bullard (1950), Verhoogen (1961), and Braginsky (1963) were followed by studies focusing primarily on the entropy balance of the dynamo (Backus, 1975; Gubbins, 1977; Gubbins et al., 1979; Hage and Muller, 1979; Hewitt et al., 1975; Loper, 1978). Later works include the monumental Braginsky and Roberts (1995) and contributions by Lister and Buffett (1995), Buffett et al. (1996), Buffett (2002), Lister (2003), Labrosse (2003), Roberts et al. (2003), Gubbins et al. (2003, 2004), and Nimmo et al. (2004).

The derivations given in the succeeding text, though not especially difficult, are somewhat lengthy. Individual terms contributing to the geodynamo are summarized in **Table 1**. The most important equations, those that summarize the entropy and energy balances, are given in eqns [31] and [40], respectively. These equations also make the underlying physics relatively easy to understand. Briefly, the principal sources of buoyancy capable of driving convection and a dynamo are either thermal (core cooling, latent heat release at the ICB, and radioactive decay) or compositional (light element release at the ICB). The thermal sources are less efficient at driving a dynamo (they generate less entropy) than the compositional sources. Competing against these sources is the ability of the

Table 1 Summary of analytic expressions for entropy and energy terms

Term	*Energy*	*Entropy*
Secular cooling	$Q_s = -\int \rho C_p \frac{dT}{dt}\, dV$	$E_s = -\int \rho C_p \left(\frac{1}{T_c} - \frac{1}{T}\right)\frac{dT}{dt}\, dV$
Latent heat	$Q_L = -\frac{4\pi r_i^2 L_H T_i}{(dT_m/dP - dT/dP)g}\frac{1}{T_c}\frac{dT_c}{dt}$	$E_L = -\frac{4\pi r_i^2 L_H (T_i - T_c)}{(dT_m/dP - dT/dP)T_c g}\frac{1}{T_c}\frac{dT_c}{dt}$
Radioactive decay	$Q_R = \int \rho h\ dV$	$E_R = \int \rho h \left(\frac{1}{T_c} - \frac{1}{T}\right) dV$
Heat of reaction	$Q_H = \int \rho R_H \frac{Dc}{Dt}\, dV = 0$	$E_H = -\int \rho \left(\frac{\partial \mu}{\partial T}\right)_{P,c} \frac{Dc}{Dt}\, dV$
Compositional	$Q_g = \int \rho \psi \alpha_c \frac{Dc}{Dt}\, dV$	$E_g = (Q_g/T_c)$
Pressure heating	$Q_P = \int \alpha T P_T \frac{dT_c}{dt}\, dV$	$E_P = \frac{Q_P}{T_c} - \int \alpha P_T \frac{dT_c}{dt}\, dV$
Pressure freezing	$Q_{PL} = 4\pi r_i^2 L_H \frac{T'_m}{T'_m - T'}\frac{P_T}{g}\frac{dT_c}{dt}$	$E_{PL} = Q_{PL}\left(\frac{1}{T_c} - \frac{1}{T_i}\right)$

Note that the latent heat terms Q_L, E_L can incorporate the pressure freezing terms Q_{PL}, E_{PL} by substituting L'_H for L_H (eqn [30]). Also note that d/dt has been substituted for D/Dt (see text). Integrations are carried out over the entire core except for the compositional and heat of reaction terms.

core to lose heat by conduction along the adiabat. More rapid core cooling (higher CMB heat flux) provides more entropy available to drive a dynamo. On the other hand, a reduced core cooling rate or an increased thermal conductivity may cause convection to cease, because the core is then capable of losing its heat purely by conduction.

8.02.3.1 Preliminaries

The methods and notation adopted here are essentially reviews of Gubbins et al. (2003, 2004) and Nimmo et al. (2004), with the exception that the treatment of entropy of heat of reaction (**Section 8.02.3.3**) has had an error corrected. Alternative approaches that yield similar or identical results may be found in Buffett et al. (1996), Roberts et al. (2003), and Labrosse (2003). A useful set of simplified expressions is given by Lister (2003).

An important caveat in what follows is that the core is generally assumed to be adiabatic throughout. This assumption may not hold true if the heat flux out of the top of the core is subadiabatic (e.g., Gomi et al., 2013; Labrosse et al., 1997; Loper, 1978; Pozzo et al., 2012) or if the light element accumulates at the top of the core (e.g., Braginsky, 1999). Further discussion of stably stratified regions in the core may be found in **Section 8.02.5.4**. We also neglect exsolution of light elements (Stevenson, 2012) as a potential energy source; inclusion using the methods outlined in **Sections 8.02.3.2** and **8.02.3.3** is straightforward.

Assuming that convection throughout the outer core is vigorous, the core fluid will be well mixed outside thin boundary layers. This in turn implies that both the entropy and fraction of the light element are uniform in the fluid outer core. Over timescales longer than the convective transport timescale, the pressure field is assumed to average to hydrostatic:

$$\nabla P = \rho \nabla \Psi \qquad [1]$$

where P is the pressure, ρ is the density, and Ψ the gravitational potential. Although the hydrostatic balance is not precisely maintained (with important consequences for core convection), the difference from a hydrostatic reference state is negligible for globally averaged quantities. The nature of the reference state is discussed in more detail in Braginsky and Roberts (2002).

For an isentropic and isochemical outer core, the temperature gradient is adiabatic and obeys

$$\nabla T_a = \frac{\alpha \mathbf{g} T_a}{C_P} = \frac{\gamma \mathbf{g}}{\left(v_P^2 - \frac{4}{3}v_S^2\right)} \qquad [2]$$

where T_a is the temperature along an adiabat; α and C_P is the thermal expansivity and specific heat capacity, respectively; $\mathbf{g}$ is the acceleration due to gravity; γ is the Grüneisen parameter; and v_P and v_S are the seismic P- and S-wave velocities, respectively.

For a two-component mixture, the thermodynamic relationship between the three state variables P,T (temperature) and the mass fraction of the light element c is given by

$$T\,ds = de - \frac{P\,d\rho}{\rho^2} - \mu\,dc \qquad [3]$$

Here, de and ds are the differentials of the internal energy and entropy, respectively, and μ is the chemical potential, where

$$\left(\frac{\partial \mu}{\partial T}\right)_{P,c} = -\left(\frac{\partial s}{\partial c}\right)_{P,T} \qquad [4]$$

and

$$\left(\frac{\partial \mu}{\partial P}\right)_{T,c} = -\frac{1}{\rho^2}\left(\frac{\partial \rho}{\partial c}\right)_{P,T} = \frac{\alpha_c}{\rho} \qquad [5]$$

and α_c is a dimensionless coefficient that indicates the sensitivity of the core density to the presence of the light element (Gubbins et al., 2004; Roberts et al., 2003):

$$\alpha_c = -\frac{1}{\rho}\left(\frac{\partial \rho}{\partial c}\right)_{P,T} \approx \frac{\Delta \rho_c}{\rho_i \Delta c} \qquad [6]$$

Here, $\Delta\rho_c$ is the change in density across the ICB due to the change in light element concentration, Δc, across the same

interface and ρ_i is the density of the solid inner core at the ICB. The parameter α_c depends on the properties of the light element and is assumed to be independent of the light element concentration (mass fraction) c.

The continuity equation for the core can be written as

$$\frac{\partial \rho}{\partial t} + \nabla \cdot (\rho \mathbf{v}) = \frac{\mathrm{D}\rho}{\mathrm{D}t} + \rho(\nabla \cdot \mathbf{v}) = 0 \qquad [7]$$

where $\mathbf{v}$ is the local fluid velocity. Similarly, conservation of mass of the light element can be written as

$$\rho \frac{\partial c}{\partial t} + \rho \mathbf{v} \cdot \nabla c + \nabla \cdot \mathbf{i} = \rho \frac{\mathrm{D}c}{\mathrm{D}t} + \nabla \cdot \mathbf{i} = 0 \qquad [8]$$

where $\mathbf{i}$ is the flux vector of the light element. Both the compositional and heat flux vectors depend on the gradients of the three state variables, P,T and s according to the Onsager reciprocal relationships (Landau and Lifshitz, 1959):

$$\mathbf{q} = -k\nabla T + \mathbf{i}\left(\mu + \frac{\beta T}{\alpha_\mathrm{D}}\right) \qquad [9]$$

$$\mathbf{i} = -\alpha_\mathrm{D}\nabla\mu - \beta\nabla T \qquad [10]$$

where k is the thermal conductivity, α_D and β are material constants (defined in Gubbins et al., 2004), and μ is related to P,T and c via eqn [3]. These expressions are usually simplified to yield Fourier's and Fick's laws, respectively, but the full forms are retained here for use in Section 8.02.3.3.

Having established these preliminary expressions describing the reference state of the core, the individual terms in the core's energy and entropy budgets may now be derived.

8.02.3.2 Energy Balance

Although the individual terms in the core's energy budget can be quite complicated, the overall budget is actually quite simple to write down. The rest of Section 8.02.3.2 will demonstrate that the energy budget may be written as

$$Q_\mathrm{cmb} = Q_\mathrm{s} + Q_\mathrm{L} + Q_\mathrm{g} + Q_\mathrm{P} + Q_\mathrm{H} + Q_\mathrm{R} \qquad [11]$$

Here, Q_cmb is the heat flow across the CMB, the thermal energy extracted out of the core by the mantle. This energy arises from six main sources: Q_s, the secular cooling of the core; Q_L, the latent heat delivered as the inner core solidifies; Q_g, the gravitational potential energy (or more properly compositional energy) associated with the release of the light element during inner core solidification; Q_P, a small contribution due to the change in pressure during core cooling; Q_H, a contribution from chemical reactions, which turns out to be zero; and Q_R, a contribution from the decay of any radioactive elements within the core. The first four terms on the right-hand side of the equation are all proportional to the rate of core cooling $\mathrm{d}T_c/\mathrm{d}t$, where T_c is the core temperature at the CMB (Gubbins et al., 2003). Thus, in the absence of radioactive heating, the heat flow out of the core is directly proportional to the core cooling rate. Hence, a high CMB heat flow requires either a rapidly cooling core or a large contribution from radioactive elements. In a situation lacking an inner core, the only nonzero terms are Q_s, Q_P, and potentially Q_R. The same CMB heat flow would therefore require a more rapidly cooling core than a similar situation in which an inner core existed.

An important aspect of eqn [11] is that heating due to dynamo activity (Joule heating) or viscous dissipation does not appear. This is because the dissipation only involves the conversion of energy within the core (buoyancy forces generate kinetic energy and magnetic energy, which in turn are converted to heat via ohmic dissipation and viscous dissipation). As a result, the global energy balance is not affected. In order to investigate the effect of dissipation, it is necessary to consider the entropy budget of the core. This approach allows the investigation of the circumstances under which a dynamo will operate and is the subject of Section 8.02.3.3.

8.02.3.2.1 General expression

A very general expression for energy conservation within the core may be written as follows (Gubbins et al., 2003; see also Buffett et al., 1996):

$$\begin{aligned}\frac{\mathrm{d}}{\mathrm{d}t}\int \rho e \,\mathrm{d}V + \frac{\mathrm{d}}{\mathrm{d}t}\int \frac{1}{2}\rho \mathbf{v}^2 \,\mathrm{d}V + \int \frac{\partial}{\partial t}\frac{\mathbf{B}^2}{2\mu_0}\,\mathrm{d}V \\ = -\oint P\mathbf{v}\,\mathrm{d}\mathbf{S} - \oint \frac{\mathbf{E}\times\mathbf{B}}{\mu_0}\,\mathrm{d}\mathbf{S} + \oint \mathbf{v}\cdot\tau'\,\mathrm{d}\mathbf{S} - \oint \mathbf{q}\,\mathrm{d}\mathbf{S} + \int \rho h\,\mathrm{d}V \\ + \int \rho \mathbf{v}\cdot\nabla\Psi\,\mathrm{d}V \end{aligned} \qquad [12]$$

Here, ρ is the density, e is the internal energy, $\mathbf{v}$ is the core fluid velocity, $\mathbf{B}$ and $\mathbf{E}$ are the magnetic and electric fields, μ_0 is the permeability of free space, P is the pressure, $\mathbf{S}$ is an outward normal surface vector, τ' is the deviatoric stress, $\mathbf{q}$ is the CMB heat flux, h is the local volumetric heat generation, Ψ is the gravitational potential, and V denotes the volume of the whole core. The left-hand side of this equation gives the total rate of change of internal, kinetic, and magnetic energies, respectively. The surface integrals on the right-hand side give the work done on the surface by pressure and electromagnetic forces, surface tractions, and the heat flow across the boundary (Q_cmb). The final two volume integrals give the total heat generated and the work done against gravitational forces.

Several simplifications may be applied to this equation (Gubbins et al., 2003, 2004). For the Earth's core, there are two very different timescales implicit in eqn [12]: the short timescale (~10 years) associated with convective motions and the much longer timescale (~100 Myr) associated with cooling and contraction of the core as a whole. Let the velocity associated with core contraction be denoted by $\mathbf{u}$. Then, over timescales long compared to the convective timescale, but short compared to the core evolution timescale, the core will be well represented by the well-mixed, hydrostatic, and isentropic basic states (see Section 8.02.3.1) as long as stable stratification is not occurring. Over this intermediate timescale, the total fluid velocity $\mathbf{v}$ may be assumed to average to the slow contractional velocity $\mathbf{u}$ (Gubbins et al., 2003), while at the core boundary, it is always true that $\mathbf{v}\ \mathrm{d}S = \mathbf{u}\ \mathrm{d}S$. Over this same timescale, it is assumed that the time fluctuations of kinetic and magnetic energies are negligible (see Braginsky and Roberts, 1995), and thus, the second two terms on the LHS are zero.

Another simplification arises from the imposition of boundary conditions. By assuming that the Earth's mantle is a perfect insulator, the surface integral involving electromagnetic fluxes disappears. This is a good approximation even if the deep mantle were ever pervasively molten (see Section 8.02.5.2): iron is still a much better conductor than

liquid silicates. A similar assumption of stress-free boundary conditions allows the removal of the shear stress surface integral. This approach is convenient and will be followed here, although a no-slip boundary condition would be more realistic (see Roberts and Glatzmaier, 2000).

Equation [12] may thus be rearranged as follows:

$$\begin{aligned} Q_{\text{cmb}} &= \oint \mathbf{q}\ \mathrm{d}\mathbf{S} \\ &= \int \rho h\ \mathrm{d}V - \int \rho \frac{\mathrm{D}e}{\mathrm{D}t}\ \mathrm{d}V + \int \rho \mathbf{u}\cdot\nabla\Psi\ \mathrm{d}V - \int \nabla\cdot(P\mathbf{u})\ \mathrm{d}V \end{aligned} \quad [13]$$

where

$$\frac{\mathrm{D}}{\mathrm{D}t} = \frac{\partial}{\partial t} + \mathbf{u}\cdot\nabla \quad [14]$$

and each integral is taken over the whole core and is time-averaged. The term in $\mathbf{u}\cdot\nabla\Psi$ arises because the long-term evolution of the gravitational potential depends only on $\mathbf{u}$. It will later prove useful to convert $\rho\mathbf{u}\cdot\nabla\Psi$ to $\mathbf{u}\cdot\nabla P$ by using eqn [1]. The final term on the RHS is obtained by the application of the divergence theorem and substitution of $\mathbf{u}$ for $\mathbf{v}$ (see Gubbins et al., 2003). Note that Q_{cmb} is the amount of heat being extracted from the core and not the adiabatic heat flow.

Equation [13] shows that the long-term energy loss from the core may be estimated using integrals over the reference state, that is, the short-term convective velocity $\mathbf{v}$ is not important. To put it another way, the short-term convective velocity is responsible for maintaining the reference state, but the energy available to drive the dynamo depends only on the long-term evolution of the core. In the absence of an inner core, a further simplification arises: the application of eqn [3] causes the last two terms on the RHS of eqn [13] to disappear and the integral in $\frac{\mathrm{D}e}{\mathrm{D}t}$ is replaced by one in $T\frac{\mathrm{D}s}{\mathrm{D}t}$ (see Gubbins et al., 2003). However, in the case of a solidifying inner core, there is a significant contribution to the gravitational energy from the redistribution of the light element (see succeeding text).

Thermal contraction and inner core solidification both lead to a volume reduction in the core, which releases additional gravitational energy. Although it has been claimed (Hage and Muller, 1979) that this energy becomes available to drive the dynamo, Gubbins et al. (2003) showed that the actual contribution to the energy budget is very small.

Equation [13] is more directly applicable than eqn [12] to the Earth's core. In particular, it may be used to derive each of the terms given in eqn [11] in a relatively straightforward fashion. Each of these terms is derived in turn later in the text; readers wishing to avoid the details will find all terms summarized in **Table 1**.

8.02.3.2.2 Core heat flow Q_{cmb}

From eqn [13], the heat flow across the CMB is given by

$$Q_{\text{cmb}} = \oint \mathbf{q}\cdot\mathrm{d}\mathbf{S} \quad [15]$$

The heat flux $\mathbf{q}$ in the case of a solidifying inner core depends on the solute flux $\mathbf{i}$ (eqn [9]) and the temperature gradient in the boundary layer. However, assuming that no solute crosses the boundary, then $\mathbf{i}\cdot\mathrm{d}\mathbf{S} = 0$ and the CMB heat flow may be written as

$$Q_{\text{cmb}} = -\oint k\nabla T\cdot\ \mathrm{d}\mathbf{S} \quad [16]$$

8.02.3.2.3 Internal heating Q_R

Internal heat production may arise because of radiogenic elements or (less likely for the Earth) tidal dissipation (Greff-Lefftz and Legros, 1999) or core–mantle coupling (Touma and Wisdom, 2001). For the radiogenic case, it is reasonable to assume that heating is uniform since vigorous convection will homogenize the distribution of radiogenic elements. In such a case, the internal heating is given by

$$Q_{\text{R}} = \int \rho h\ \mathrm{d}V \quad [17]$$

where h is the volumetric heating rate. Note that this term does not include any contribution from ohmic heating.

8.02.3.2.4 Heat of reaction Q_H

In the presence of a solidifying inner core, the internal energy term in eqn [13] may be written with the help of eqn [3] as

$$\begin{aligned} \int \rho \frac{\mathrm{D}e}{\mathrm{D}t}\ \mathrm{d}V &= \int \rho T \frac{\mathrm{D}s}{\mathrm{D}t}\ \mathrm{d}V + \int \frac{P}{\rho}\frac{\mathrm{D}\rho}{\mathrm{D}t}\ \mathrm{d}V + \int \rho\mu\frac{\mathrm{D}c}{\mathrm{D}t}\ \mathrm{d}V \\ &= \int \rho T \frac{\mathrm{D}s}{\mathrm{D}t}\ \mathrm{d}V - \int P\nabla\cdot\mathbf{u}\ \mathrm{d}V + \int \rho\mu\frac{\mathrm{D}c}{\mathrm{D}t}\ \mathrm{d}V \end{aligned} \quad [18]$$

where the second equality makes use of eqn [7].

The rate of change of internal energy depends on the rate of change of entropy (which depends on P,T, and c), pressure, and concentration of the light element. The first term on the RHS of eqn [18] may be written as

$$\begin{aligned} \rho T\frac{\mathrm{D}s}{\mathrm{D}t} &= \rho T\left(\frac{\partial s}{\partial T}\right)_{P,c}\frac{\mathrm{D}T}{\mathrm{D}t} + \rho T\left(\frac{\partial s}{\partial P}\right)_{T,c}\frac{\mathrm{D}P}{\mathrm{D}t} + \rho T\left(\frac{\partial s}{\partial c}\right)_{P,T}\frac{\mathrm{D}c}{\mathrm{D}t} \\ &= \rho C_{\text{p}}\frac{\mathrm{D}T}{\mathrm{D}t} - \alpha T\frac{\mathrm{D}P}{\mathrm{D}t} - \rho T\left(\frac{\partial \mu}{\partial T}\right)_{P,c}\frac{\mathrm{D}c}{\mathrm{D}t} \end{aligned} \quad [19]$$

where Maxwell's relation (eqn [4]) has been used, the specific heat capacity C_{p} is defined by

$$C_{\text{p}} = T\left(\frac{\partial s}{\partial T}\right)_{P,c} \quad [20]$$

and the thermal expansivity α is given by

$$\alpha = -\rho\left(\frac{\partial s}{\partial P}\right)_{T,c} = -\frac{1}{\rho}\left(\frac{\partial \rho}{\partial T}\right)_{P,c} \quad [21]$$

The second term on the RHS of eqn [18] vanishes in conjunction with the last two terms on the RHS of eqn [13]. Combining the terms in eqn [18] which depend on c, we obtain

$$Q_{\text{H}} = \int \rho\left[\mu - T\left(\frac{\partial \mu}{\partial T}\right)_{P,c}\right]\frac{\mathrm{D}c}{\mathrm{D}t}\ \mathrm{d}V = \int \rho R_{\text{H}}\frac{\mathrm{D}c}{\mathrm{D}t}\ \mathrm{d}V \quad [22]$$

where R_{H} is the heat of reaction between iron and the light element. Here, Q_{H} represents the change in internal energy due to chemical reactions: for an exothermic reaction, heat is absorbed at the ICB and released throughout the liquid core. Note that as long as R_{H} remains constant, $Q_{\text{H}} = 0$, because removal of the light element at the ICB is balanced by the

increase in concentration throughout the outer core (see eqn. [37] of Gubbins et al., 2004).

8.02.3.2.5 Secular cooling and pressure heating Q_s, Q_P

Making use of eqn [19], we can identify two terms in the internal energy budget not associated with compositional variations. The first is the secular cooling term:

$$Q_s = -\int \rho C_p \frac{DT}{Dt}\, dV \qquad [23]$$

This term is simply the heat released as the core cools; it includes a small contraction term due to the Lagrangian derivative. Although the release of latent heat due to inner core solidification can be included in this term (by modifying the specific heat), greater transparency is retained by including the latent heat as a separate term (see succeeding text).

The second term gives the heating that arises from a change in pressure and is referred to as the pressure heating term by Gubbins et al. (2003). It is given by

$$Q_P = \int \alpha T P_T \frac{DT_c}{Dt}\, dV \qquad [24]$$

where P_T is a numerical coefficient that relates the change of pressure at the ICB with time to the rate of core cooling:

$$\frac{DP}{Dt} = P_T \frac{dT_c}{dt} \qquad [25]$$

where T_c is the core temperature at the CMB. A more extensive discussion of this small term is given in Gubbins et al. (2003).

8.02.3.2.6 Gravitational energy Q_g

The gravitational energy term arises due to the release of the light element at the ICB and is thus really a compositional energy term (Braginsky and Roberts, 1995; Lister and Buffett, 1995). Considering only the density changes arising due to these compositional changes, the gravitational potential term in eqn [12] may be written (Gubbins et al., 2004) as

$$Q_g = \int_\infty \rho \mathbf{v}\cdot\nabla\Psi\, dV = \int_\infty \Psi \left(\frac{\partial \rho}{\partial t}\right)_{P,T} dV = \int \rho \Psi \alpha_c \frac{Dc}{Dt}\, dV \qquad [26]$$

where the compositional expansion coefficient α_c is defined by eqn [6]. The gravitational energy contribution is proportional to the rate of expulsion of the light element, as parameterized by $\frac{Dc}{Dt}$.

8.02.3.2.7 Latent heat release Q_L

The latent heat released depends on the rate at which the inner core solidifies:

$$Q_L = 4\pi r_i^2 L_H \rho_i \frac{dr_i}{dt} \qquad [27]$$

where r_i is the inner core radius, ρ_i is the density at the ICB, and L_H is the latent heat (assumed constant). The rate at which the ICB advances is determined by the rate at which the ICB temperature changes and the relative slopes of the adiabat and melting curve (see Section 8.02.3.4). The rate at which T_i, the temperature at the ICB, changes may be directly related to the rate of change of the temperature T_c at the CMB, because both lie on the same adiabat. The quantity $\frac{dr_i}{dt}$ may therefore be rewritten in terms of $\frac{dT_c}{dt}$ (see Section 8.02.3.4).

8.02.3.2.8 Pressure effect on freezing Q_{PL}

If the pressure increases, the melting temperature of iron increases and thus the inner core grows. A pressure change ΔP causes the inner core radius to increase by a quantity Δr_i where

$$\Delta r_i = \frac{T'_m}{T'_m - T'} \frac{\Delta P}{\rho_i g} \qquad [28]$$

where T_m and T are the melting and adiabatic temperatures of the core at $r = r_i$, respectively, and T'_m and T' are their radial derivatives.

Making use of eqn [25], the additional latent heat released by this effect is given by

$$Q_{PL} = \frac{4\pi r_i^2 L_H T'_m}{T'_m - T'} \frac{P_T}{g} \frac{dT_c}{dt} \qquad [29]$$

The effect can also be included by modifying the usual latent heat as follows:

$$L'_H = L_H + \frac{dT_m}{dP} P_T \qquad [30]$$

In practice, the increase in latent heat due to this effect is only 10–20% (Gubbins et al., 2003).

8.02.3.2.9 Summary

Combining the results of Sections 8.02.3.2.2–8.02.3.2.8, the general energy budget for the core, eqn [13], may be rewritten as follows:

$$\begin{aligned} Q_{cmb} = -\oint k\nabla T\, d\mathbf{S} &= \int \rho h\, dV - \int \rho C_p \frac{DT}{Dt}\, dV \\ &+ \int \alpha T \frac{DP}{Dt}\, dV - \int \rho R_H \frac{Dc}{Dt}\, dV + \int \rho \Psi \alpha_c \frac{Dc}{Dt}\, dV + 4\pi r_i^2 L_{H'} \rho_i \frac{dr_i}{dt} \\ &= Q_R + Q_s + Q_P + Q_H + Q_g + Q_L \end{aligned} \qquad [31]$$

The utility of this equation is that it makes each of the mechanisms contributing towards the core's energy budget obvious: the total amount of energy being extracted from the core depends on radioactive heat production within the core, secular cooling and contraction of the core, and chemical, gravitational, and latent heat release as the inner core grows. With the exception of radioactive heating, all these terms turn out to be directly proportional to the rate of core cooling $\frac{dT_c}{dt}$ (see Section 8.02.3.4). This equation also demonstrates that neither the adiabatic heat flow, Q_k, nor ohmic heating plays any role in the global energy budget. Both these terms, however, do figure in the corresponding entropy balance, which is derived next.

8.02.3.3 Entropy Terms

As noted earlier in the text, the ohmic heating (dissipation) caused by the dynamo does not enter the global energy balance. However, dissipation is nonreversible and therefore a source of entropy. Thus, by considering the entropy budget of the core, criteria may be established for the operation (or failure) of the dynamo (see Section 8.02.4.2). In particular,

an equation analogous to eqn [31] may be derived that describes the entropy budget of the core. In particular, both entropy sinks (heat diffusion, ohmic dissipation, and molecular conduction) and sources (radioactive decay, secular cooling, latent heat release, pressure heating, chemical reactions, and compositional buoyancy) may be identified.

These entropy terms, derived in the succeeding text, are rates of entropy production. In general, each entropy term may be thought of as a heat flow, multiplied by some efficiency factor (<1) and divided by some characteristic operating temperature. Higher heat flows result in higher rates of entropy production.

The general equation corresponding to eqn [12] for the entropy terms is (Gubbins et al., 2004; Hewitt et al., 1975)

$$\rho\frac{\mathrm{D}s}{\mathrm{D}t}=-\frac{\nabla\cdot\mathbf{q}}{T}+\frac{\mu\nabla\cdot\mathbf{i}}{T}+\frac{\rho h}{T}+\frac{\Phi}{T} \qquad [32]$$

where the heat flux $\mathbf{q}$ depends on the solute flux $\mathbf{i}$ (eqn [9]) and the entropy s depends on P,T and c (eqn [3]). This equation summarizes the changes in entropy arising from both thermal and compositional effects. Here, Φ is the combined viscous dissipation and ohmic dissipation. The former is assumed to be negligible and the volumetric ohmic dissipation is given by

$$\Phi=\frac{\mathbf{J}^2}{\sigma}\approx\left(\frac{B^2}{\mu_0^2\sigma l^2}\right) \qquad [33]$$

where $\mathbf{J}$ is the electric current density; B and l are typical values for the magnetic field and the length scale at which dissipation occurs (e.g., Labrosse, 2003), respectively; and σ is the electrical conductivity. It is because of the appearance of this term that the entropy balance may be used to determine whether or not a dynamo can operate.

Making use of eqn [9], we may write

$$-\frac{\nabla\cdot\mathbf{q}}{T}+\frac{\mu\nabla\cdot\mathbf{i}}{T}=-\nabla\cdot\left(\frac{\mathbf{q}}{T}\right)+\mu\nabla\cdot\left(\frac{\mathbf{i}}{T}\right)-\frac{\beta}{\alpha_\mathrm{D}}\frac{\mathbf{i}\cdot\nabla T}{T}+k\left(\frac{\nabla T}{T}\right)^2 \qquad [34]$$

Integrating and making use of eqn [10], we then have

$$\int\left[\frac{-\nabla\cdot\mathbf{q}}{T}+\frac{\mu\nabla\cdot\mathbf{i}}{T}\right]= -\frac{Q_\mathrm{cmb}}{T_\mathrm{c}}+\int\left[\mu\nabla\cdot\left(\frac{\mathbf{i}}{T}\right)+\frac{\mathbf{i}^2}{\alpha_\mathrm{D}T}+\frac{\mathbf{i}}{T}\cdot\nabla\mu+k\left(\frac{\nabla T}{T}\right)^2\right] \qquad [35]$$

where we have used the divergence theorem to derive the $Q_\mathrm{cmb}/T_\mathrm{c}$ term. Assuming there is no light element flux out of the core, the integral of $\nabla\cdot\left(\frac{\mu\mathbf{i}}{T}\right)=0$ by the divergence theorem. So we can finally obtain

$$\int\left[-\frac{\nabla\cdot\mathbf{q}}{T}+\frac{\mu\nabla\cdot\mathbf{i}}{T}\right]=-\frac{Q_\mathrm{cmb}}{T_\mathrm{c}}+\int\left[\frac{\mathbf{i}^2}{\alpha_\mathrm{D}T}+k\left(\frac{\nabla T}{T}\right)^2\right] \qquad [36]$$

The LHS of eqn [32] may be expanded using eqn [19] as before. The RHS may be further simplified by making use of eqn [36]. The resulting expression is

$$\int\frac{\rho C_\mathrm{p}}{T}\frac{\mathrm{D}T}{\mathrm{D}t}\mathrm{d}V-\int\alpha\frac{\mathrm{D}P}{\mathrm{D}t}\mathrm{d}V-\int\rho\frac{\partial\mu}{\partial T}\frac{\mathrm{D}c}{\mathrm{D}t}\mathrm{d}V =-\frac{Q_\mathrm{cmb}}{T_\mathrm{c}}+\int k\left(\frac{\nabla T}{T}\right)^2\mathrm{d}V+\int\frac{\mathbf{i}^2}{\alpha_\mathrm{D}T}\mathrm{d}V+\int\frac{\rho h}{T}\mathrm{d}V+\int\frac{\Phi}{T}\mathrm{d}V \qquad [37]$$

where the terms on the LHS represent contributions to the entropy budget from core cooling, contraction, and chemical reactions.

The term in $\mathbf{i}^2$ is the entropy of molecular conduction, E_α, which turns out be negligible (see succeeding text). The terms involving ρh and Φ are the entropy contributions from internal heating and ohmic (and viscous) dissipation, respectively. The term in $(\nabla T/T)^2$ is the entropy of thermal diffusion, E_k. This quantity depends on the temperature gradient and is an entropy sink: it reduces the entropy available to drive the dynamo and if large enough will ensure a fully conductive core and thus an absence of dynamo activity.

Since Q_cmb contains contributions from the different sources (eqn [31]), most of these source terms occur twice in eqn [37]. For instance, the secular cooling contribution to the overall entropy budget is

$$\int\left(\rho C_\mathrm{p}\frac{\mathrm{D}T}{\mathrm{D}t}\right)\left(\frac{1}{T}-\frac{1}{T_\mathrm{c}}\right)\mathrm{d}V \qquad [38]$$

where the term in T_c is a consequence of the $Q_\mathrm{cmb}/T_\mathrm{c}$ term in eqn [37]. Similar equations may be derived for the contributions from latent heat, radioactive decay, and pressure heating. As before, the latent heat term may be incorporated into the secular cooling term.

The resulting expression for the entropy budget is as follows:

$$\int\left[\frac{1}{T}-\frac{1}{T_\mathrm{c}}\right]\left[\rho C_\mathrm{p}\frac{\mathrm{D}T}{\mathrm{D}t}-T\alpha\frac{\mathrm{D}P}{\mathrm{D}t}-\rho h\right]\mathrm{d}V+\left(\frac{1}{T_\mathrm{i}}-\frac{1}{T_\mathrm{c}}\right)4\pi r_\mathrm{i}^2L_\mathrm{H}'\rho_\mathrm{i}\frac{\mathrm{d}r_\mathrm{i}}{\mathrm{d}t} -\int\rho\left(\frac{\partial\mu}{\partial T}\right)_{P,c}\frac{\mathrm{D}c}{\mathrm{D}t}\mathrm{d}V+\frac{Q_\mathrm{g}}{T_\mathrm{c}}=\int k\left(\frac{\nabla T}{T}\right)^2\mathrm{d}V+\int\frac{\mathbf{i}^2}{\alpha_\mathrm{D}T}\mathrm{d}V+\int\frac{\Phi}{T}\mathrm{d}V \qquad [39]$$

which may be rewritten in an analogous form to eqn [31] as follows:

$$E_\mathrm{s}+E_\mathrm{P}+E_\mathrm{R}+E_\mathrm{L}+E_\mathrm{H}+E_\mathrm{g}=E_\mathrm{k}+E_\alpha+E_\Phi \qquad [40]$$

where here the pressure effect on melting has been included in the latent heat term, as before.

Note that this equation has a different heat of reaction expression to eqn [27] of Gubbins et al. (2004), owing to an error in that work. The correct expression is

$$E_\mathrm{H}=-\int\rho\left(\frac{\partial\mu}{\partial T}\right)_{P,c}\frac{\mathrm{D}c}{\mathrm{D}t}\mathrm{d}V$$

because the term Q_H contained within Q_cmb is zero (see eqn [22]). Thus, the entropy contribution from the heat of reaction depends only on $\partial\mu/\partial T$ and not μ. As discussed in **Section 8.02.4.3.4**, E_H is small and so this contribution may be neglected.

An important aspect of eqn [39] is the $(1/T_\mathrm{c}-1/T)$ terms. These terms give the thermodynamic (Carnot) efficiency of the various processes driving the dynamo and arise because the sources and sinks of buoyancy are operating at different temperatures. Buoyancy sources that are distributed throughout the core volume have a lower efficiency than those that arise at the ICB, because the mean operating temperature of the former is smaller and thus the efficiency term $(1/T_\mathrm{c}-1/T)$ is also smaller. Thus, the buoyancy forces due to radioactive

decay or secular cooling are intrinsically less efficient at driving a dynamo compared with latent heat release.

An important exception is the term that arises due to compositional convection. This term only occurs once in eqn [39] and has the form Q_g/T_c. Its efficiency is thus intrinsically higher than those of the other energy sources. Thus, as we will see in the succeeding text, although compositional convection has only a moderate effect on the core's energy budget, its contribution to the core's entropy budget (and thus the operation of the dynamo) is very significant.

Table 1 summarizes the expressions derived earlier in the text for the various entropy and energy terms.

8.02.3.4 Example Core Structure

The terms in energy and entropy derived previously and summarized in Table 1 are general in that they may be applied to any model of core structure. Some of the core properties required, such as density, compressibility, and gravitational acceleration, can be obtained from seismological observations (see Figure 1). Other properties, in particular the temperature structure, must be inferred from experimental studies or first-principles numerical calculations (see Section 8.02.4.3). Here, a model core structure is derived that allows analytic expressions for the terms in Table 1 to be obtained. These expressions give good agreement with numerical integrations carried out using the observed core density structure (see Nimmo et al., 2004). A comparison of these results with those using different parameter choices is given in Section 8.02.4.3.9.

Given the large uncertainties associated with various core parameters, it is acceptable to make simplifying assumptions that allow the energy and entropy integrals to be treated analytically. The first major simplification is to assume spherical symmetry, although lateral variations in properties like the CMB heat flux may sometimes have important effects on the detailed behavior of the dynamo (e.g., Bloxham, 2000).

A second simplification is to assume that certain core properties, such as compressibility, thermal expansivity, and specific heat capacity, are constant. While only an approximation, this makes the integrals tractable and results in density and gravity profiles that are similar to those inferred (Figure 1). Here, we describe the approach taken by Labrosse et al. (2001). Other authors, such as Buffett et al. (1996), Lister (2003), and Roberts et al. (2003), have adopted slightly different expressions.

The density within the Earth's core increases by about 35% from the CMB to the center of the planet (Figure 1). Following Labrosse et al. (2001), the variation of ρ with radial distance r from the center of the Earth is given approximately by

$$\rho(r) = \rho_{cen}\exp\left(\frac{-r^2}{L^2}\right) \quad [41]$$

where ρ_{cen} is the density at the center of the Earth and L is a length scale given by

$$L = \sqrt{\frac{3K_0\left(\ln\frac{\rho_{cen}}{\rho_0}+1\right)}{2\pi G\rho_0\rho_{cen}}} \quad [42]$$

Here, K_0 and ρ_0 are the compressibility and density at zero pressure, respectively; G is the universal gravitational constant; and $L \approx 7000$ km (see Section 8.02.4.3). From eqn [41], the mass of the core M_c is given by

$$\begin{aligned} M_c &= \int_0^{r_c}\rho(r)\mathrm{d}V \\ &= 4\pi\rho_{cen}\left[-\frac{L^2}{2}r\exp\left(\frac{-r^2}{L^2}\right)+\frac{L^3}{4}\sqrt{\pi}\,\mathrm{erf}\left(\frac{r}{L}\right)\right]_0^{r_c} \end{aligned} \quad [43]$$

where r_c is the core radius. Expanding $\mathrm{erf}(r/L)$ allows M_c to be written as

$$M_c = \frac{4}{3}\pi\rho_{cen}r_c^3\mathrm{e}^{-r_c^2/L^2}\left(1+\frac{2}{5}\frac{r_c^2}{L^2}+\cdots\right) \quad [44]$$

Similarly, the acceleration due to gravity g is given by

$$g(r) = \frac{4\pi}{3}G\rho_{cen}r\left(1-\frac{3r^2}{5L^2}\right) \quad [45]$$

This expression neglects the density jump $\Delta\rho$ across the ICB, introducing an error of order $r_i^4/L^4 \ll 1$, where r_i is the inner core radius (Labrosse et al., 2001). Note that the effect of this density jump is incorporated when considering compositional convection.

The adiabatic temperature T_a within the core is given by

$$T_a(r) = T_{cen}\exp\left(\frac{-r^2}{D^2}\right) \quad [46]$$

where T_{cen} is the temperature at the center of the Earth and D is another length scale given by

$$D = \sqrt{3C_p/2\pi\alpha\rho_{cen}G} \quad [47]$$

Here, C_p is the specific heat capacity, α the thermal expansivity, and $D \approx 6000$ km (see Section 8.02.4.3). Note that eqn [46] assumes that the ratio α/C_p or equivalently the ratio $\gamma/(v_p^2-(4/3)v_s^2)$ is constant. This issue is discussed further in Section 8.02.4.2. The adiabat will only be followed in regions that are not stably stratified; this issue is discussed briefly in Section 8.02.5.4.

The adiabatic profile (eqn [46]) allows the following useful simplification to be made (Gubbins et al., 2003):

$$\frac{1}{T_a}\frac{\mathrm{D}T_a}{\mathrm{D}t} = \frac{1}{T_c}\frac{\mathrm{d}T_c}{\mathrm{d}t} \quad [48]$$

where T_c is the temperature at the CMB. This approximation allows the term in $T^{-1}\mathrm{D}T/\mathrm{D}t$ to be taken out of all the integrals given in Table 1, assuming that the temperature profile is adiabatic. Furthermore, the rate of inner core growth $\mathrm{d}r_i/\mathrm{d}t$ and the rate of change of concentration in the light element $\mathrm{D}c/\mathrm{D}t$ may both be related to $\mathrm{d}T_c/\mathrm{d}t$ as follows.

Equation [48] shows that the rate of cooling at the ICB is directly proportional to the rate of cooling at the CMB. In addition, Figure 2 shows that the change in inner core radius δr_i for a change in core temperature δT_c depends on the relative slopes of the adiabat and the melting curve. We may therefore write

$$\frac{\mathrm{d}r_i}{\mathrm{d}t} = \frac{-1}{\left(\frac{\mathrm{d}T_m}{\mathrm{d}P}-\frac{\mathrm{d}T_a}{\mathrm{d}P}\right)}\frac{T_i}{\rho_i g}\frac{1}{T_c}\frac{\mathrm{d}T_c}{\mathrm{d}t} = C_r\frac{\mathrm{d}T_c}{\mathrm{d}t} \quad [49]$$

where the slopes of the adiabat and melting curve at the ICB are given by $\mathrm{d}T_a/\mathrm{d}P$ and $\mathrm{d}T_m/\mathrm{d}P$, respectively, and T_i and ρ_i are the ICB temperature and density, respectively.

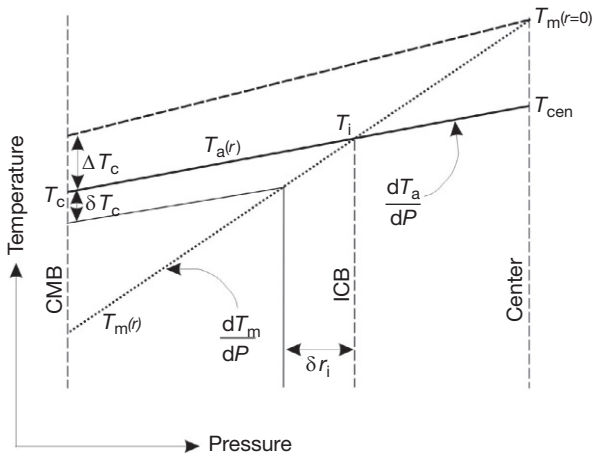

Figure 2 Schematic of melting and adiabatic temperature profiles. The inner core (temperature T_i) is defined by the intersection of the adiabat T_a and the melting curve T_m. The corresponding temperature at the CMB, T_c, is obtained by following the adiabat. Changing this CMB temperature by a small amount δT_c results in a change in inner core radius δr_i that depends on the relative slopes of the adiabat and melting curve, (dT_a/dP) and (dT_m/dP), respectively. The temperature drop at the CMB since the onset of inner core solidification is given by ΔT_c.

In a similar fashion, the rate of release of light material into the outer core may be written as

$$\frac{Dc}{Dt}=\frac{4\pi r_i^2\rho_i c}{M_{oc}}\frac{dr_i}{dt}=C_cC_r\frac{dT_c}{dt} \qquad [50]$$

where M_{oc} is the mass of the outer core and $C_c=4\pi r_i^2\rho_i c/M_{oc}=4\pi r_i^2\Delta\rho_c/M_{oc}\alpha_c$. Here, we are assuming that the concentration of light elements in the inner core is zero, that is, $\Delta c=c$. Note that the rate of light element release is directly proportional to the core cooling rate.

It should further be noted that integrals involving Dc/Dt consist of two contributions: one denoting the removal of light element from the inner core at the ICB and one involving the uniform redistribution of this material over the outer core. Assuming that the heat of reaction is constant, this conservation of species means that the energy term Q_H, but not the entropy term E_H, is identically equal to zero (see Gubbins et al., 2004).

The pressure is given by

$$P(r)=P_c+\frac{4\pi G\rho_{cen}^2}{3}\left[\left(\frac{3r^2}{10}-\frac{L^2}{5}\right)\exp\left(\frac{-r^2}{L^2}\right)\right]_r^{r_c} \qquad [51]$$

where P_c is the pressure at the CMB.

The dependence of the core melting temperature on pressure and composition is often approximated using Lindemann's law (e.g., Buffett et al., 1996; Labrosse et al., 2001; Roberts et al., 2003). For example, neglecting the compositional effects, one could write (Labrosse, 2003)

$$T_m(r)=T_{m0}\exp\left[-2\left(1-\frac{1}{3\gamma}\right)\frac{r^2}{D^2}\right] \qquad [52]$$

where T_{m0} is the melting temperature at zero pressure and γ is the Grüneisen parameter. Here, we adopt a slightly different approach, following that of Stevenson et al. (1983), and parameterize the core melting temperature T_m as

$$T_m(P)=T_{m0}\left(1+T_{m1}P+T_{m2}P^2\right) \qquad [53]$$

where T_{m1} and T_{m2} are constants and T_{m0} incorporates the reduction in melting temperature due to the light element(s). Note that this parameterization will only be valid over a limited pressure range, so that T_{m0} does not represent the zero-pressure melting temperature.

With the variation of ρ, g, and T within the core described by eqns [41], [45], and [46], respectively, analytic expressions for the entropy and energy terms are given later in the text.

8.02.3.4.1 Specific heat (Q_s, E_s)

Table 1 and eqn [48] may be used to show that both Q_s and E_s involve a term $I_s=\int\rho T\ dV$ given by (Labrosse et al., 2001)

$$I_s=4\pi T_{cen}\rho_{cen}\left(-\frac{A^2r_c}{2}e^{-r_c^2/A^2}+\frac{A^3\sqrt{\pi}}{4}\ \mathrm{erf}\left(\frac{r_c}{A}\right)\right) \qquad [54]$$

where

$$A^2=\left(\frac{1}{L^2}+\frac{1}{D^2}\right)^{-1} \qquad [55]$$

It will be useful to expand I_s as follows:

$$I_s=\frac{4}{3}\pi T_{cen}\rho_{cen}r_c^3e^{-r_c^2/A^2}\left(1+\frac{2}{5}\frac{r_c^2}{A^2}+\cdots\right) \qquad [56]$$

The temperature profile will depart from the adiabat in the inner core, but Labrosse (2003) argued that the integral may be taken over the entire core without introducing significant errors. The contributions Q_s and E_s may thus be written as

$$Q_s=-\frac{C_p}{T_c}\frac{dT_c}{dt}I_s,\quad E_s=\frac{C_p}{T_c}\left(M_c-\frac{I_s}{T_c}\right)\frac{dT_c}{dt} \qquad [57]$$

where M_c is the mass of the core and T_c the core temperature at the CMB.

8.02.3.4.2 Radioactive heating (Q_R, E_R)

For radioactive heating, the term involved $I_T=\int\rho/T\ dV$ is more complicated and depends on the relative sizes of D and L. Although complete analytic solutions may be derived (see Nimmo et al., 2004), it is more useful to carry out a series expansion, which yields

$$I_T=\frac{4\pi\rho_{cen}}{3T_{cen}}r_c^3\left(1-\frac{3}{5}\frac{r_c^2}{B^2}+\cdots\right) \qquad [58]$$

where

$$B^2=\left(\frac{1}{L^2}-\frac{1}{D^2}\right)^{-1} \qquad [59]$$

These equations allow the contributions Q_R and E_R to be determined:

$$Q_R=M_ch,\quad E_R=\left(\frac{M_c}{T_c}-I_T\right)h \qquad [60]$$

where h is the heat production per unit mass within the core.

8.02.3.4.3 Latent heat (Q_L, E_L)

The contributions Q_L and E_L given in Table 1 may be written as

$$Q_L = 4\pi r_i^2 L'_H \rho_i \frac{dr_i}{dt}, \quad E_L = Q_L \frac{(T_i - T_c)}{T_c T_i} \qquad [61]$$

where L'_H is the latent heat of fusion (incorporating the small pressure effect) and T_i is the temperature at the ICB.

8.02.3.4.4 Gravitational contribution (Q_g, E_g)

From eqn [45], the potential $\Psi(r)$ relative to zero potential at the CMB is given by

$$\Psi(r) = \left[\frac{2}{3}\pi G \rho_{cen} r'^2 \left(1 - \frac{3r'^2}{10L^2}\right)\right]_{r_c}^{r} \qquad [62]$$

Table 1 and eqn [50] give

$$\begin{aligned} Q_g &= \left[\int_{oc} \rho\Psi \, dV - M_{oc}\Psi(r_i)\right] \alpha_c C_c C_r \frac{DT_c}{Dt} \\ &= \left[\int_{oc} \rho\Psi \, dV - M_{oc}\Psi(r_i)\right] \Delta\rho_c \frac{c}{\Delta c} \frac{4\pi r_i^2}{M_{oc}} \frac{dr_i}{dt} \end{aligned} \qquad [63]$$

Here, $\Delta\rho_c$ is the compositional density drop across the ICB, M_{oc} is the mass of the outer core (oc denotes the outer core), α_c is the compositional expansion coefficient (eqn [6]), $C_r dT_c/dt = dr_i/dt$, and C_c is defined after eqn [50]. If the inner core completely excludes the light element(s), then $c = \Delta c$. Note that in this case, Q_g depends only on the compositional density contrast $\Delta\rho_c$ and not on c, the actual concentration.

The integral $\int_{oc} \rho\Psi \, dV$ is given by

$$\frac{8\pi^2 \rho_{cen}^2 G}{3}\left[\left(\frac{3}{20}r^5 - \frac{L^2}{8}r^3 - L^2C^2 r\right)e^{-r^2/L^2} + \frac{C^2}{2}L^3\sqrt{\pi}\,\mathrm{erf}\left(\frac{r}{L}\right)\right]_{r_i}^{r_c} \qquad [64]$$

where

$$C^2 = \frac{3L^2}{16} - \frac{r_c^2}{2}\left(1 - \frac{3r_c^2}{10L^2}\right) \qquad [65]$$

The mass of the outer core M_{oc} may be obtained from eqn [43] by changing the limits of integration. Equations [64] and [65] allow Q_g to be obtained; E_g is simply Q_g/T_c.

8.02.3.4.5 Entropy of heat of solution (E_H)

As discussed in the preceding text, the quantity $Q_H = 0$. The contribution E_H in Table 1 is given by

$$E_H = -\left[\int_{oc} \rho \frac{\partial\mu}{\partial T} \, dV\right] C_c \frac{dr_i}{dt} \qquad [66]$$

As discussed in Section 8.02.4.3.4, this term is small compared with the other terms of interest, and we generally ignore it.

8.02.3.4.6 Adiabatic contribution (Q_k, E_k)

The entropy change due to thermal diffusion is given by Table 1:

$$E_k = \int k\left(\frac{\nabla T}{T}\right)^2 dV \qquad [67]$$

where k is the core thermal conductivity.

Based on the results shown in Figure 1(c), the variation of k with radius can be approximated as a quadratic function:

$$k(r) = k_c \frac{\left(1 - \frac{r^2}{D_k^2}\right)}{\left(1 - \frac{r_c^2}{D_k^2}\right)} \qquad [68]$$

where k_c is the thermal conductivity at the CMB and D_k is a characteristic length scale.

From eqn [46], we have $\nabla T_a/T_a = -2r/D^2$; using eqns [67] and [68], it can therefore be shown that for an adiabatic core,

$$E_k = \frac{16\pi k_c r_c^5}{5D^4}\left(1 + \frac{2}{7}\frac{1}{(D_k^2/r_c^2) - 1}\right) \qquad [69]$$

while Q_k at the CMB is simply given by

$$Q_k = 8\pi r_c^3 k_c T_c / D^2 \qquad [70]$$

Note that both Q_k and E_k, unlike almost all the other terms in Table 1, are independent of the core cooling rate. Increasing conductivity with depth increases the total adiabatic entropy production rate and thus makes it harder to drive a dynamo. It also increases the propensity of the lower core to be stably stratified (see Section 8.02.5.4).

8.02.3.4.7 Other contributions

Gubbins et al. (2003, 2004) argued that the molecular diffusion term E_α and pressure heating term E_P in eqn [40] are negligible and may be ignored. The rate of change of the core temperature is governed by

$$\frac{DT_c}{Dt} = \frac{\partial T_c}{\partial t} + \mathbf{u}\cdot\nabla T_c \qquad [71]$$

where $\mathbf{u}$ is the core contraction velocity. Gubbins et al. (2003) stated that core contraction is negligible at the present day, in which case $DT_c/Dt = dT_c/dt$.

8.02.3.5 Summary

Table 1 gives the general expressions for each of the terms contributing to the core's energy (eqn [31]) and entropy (eqn [40]) budgets. Section 8.02.3.4 gives explicit expressions for these terms when the state of the core is described by a simple analytic model. Given a core cooling rate dT_c/dt, this allows the rates of heat transfer and entropy production for the core to be derived.

8.02.4 Present-Day Energy Budget

8.02.4.1 Introduction

Having derived approximate expressions for the individual terms in the energy and entropy equations, in this section, the magnitudes of these terms are estimated for the Earth. In order to do so, various properties of the Earth's core are required, some of which are still highly uncertain. Section 8.02.4.2 derives some general conclusions regarding the present-day budgets that are independent of the specific property values assumed. Section 8.02.4.3 summarizes the likely values and discusses their uncertainties. Section 8.02.4.4 shows how these values may be used to establish the present-day global energy and entropy budgets of the core and

compares these estimates with other constraints. For instance, the fact that a dynamo is operating at the present day places a constraint on the current CMB heat flow (eqn [74] and see succeeding text). This section draws heavily on previous works on the subject, as described later in the text, in particular those of Buffett et al. (1996), Roberts et al. (2003), Labrosse (2003), Gubbins et al. (2003, 2004), Nimmo et al. (2004), Nimmo (2007), Davies and Gubbins (2011), Pozzo et al. (2012), and Gomi et al., 2013 and in **Chapter 9.08**.

8.02.4.2 General Behavior

It is clear that the entropy budget within the core at the present day is capable of sustaining a dynamo. In this section, we review the constraints that this observation places on conditions in the core. In particular, we show how to calculate the rate at which the core must be cooling to sustain the dynamo and the balance between thermal and compositional contributions to the dynamo. Considerations of core cooling inevitably lead to the question of the energy/entropy budget of the core through time; this topic is the subject of **Section 8.02.5** and **Chapter 9.08**.

The entropy rate available to drive the dynamo is given by eqn [40] and, neglecting the small terms E_α and E_P, may be written as

$$\Delta E = E_R + E_s + E_L + E_H + E_g - E_k = E_R + \tilde{E}_T \frac{dT_c}{dt} - E_k \qquad [72]$$

where E_s, E_L, E_H, and E_g depend on the core cooling rate dT_c/dt (see **Table 1**), E_R depends on the presence of radioactive elements in the core, and E_k depends on the adiabat at the CMB. $\tilde{E}_T$ is simply a convenient way of lumping together the terms that depend on core cooling rate (see Gubbins et al., 2003) and is itself independent of dT_c/dt. This equation illustrates two important points. Firstly, as expected, a higher cooling rate or a higher rate of radioactive heat production increases the entropy rate available to drive a dynamo. Secondly, a larger adiabatic contribution reduces the available entropy.

The equivalent energy balance (eqn [9]), neglecting Q_P and $Q_H(=0)$, may be written as

$$Q_{cmb} = Q_R + Q_s + Q_g + Q_L = Q_R + \tilde{Q}_T \frac{dT_c}{dt} \qquad [73]$$

Again, $\tilde{Q}_T$ is simply a convenient way of lumping together those terms (Q_s, Q_g, and Q_L) that depend on the core cooling rate. By combining eqns [72] and [73], an expression may be obtained that gives the core heat flow required to sustain a dynamo characterized by a particular entropy production rate E_Φ:

$$Q_{cmb} = Q_R \left(1 - \frac{\tilde{Q}_T}{\tilde{E}_T}\frac{1}{T_R}\right) + \frac{\tilde{Q}_T}{\tilde{E}_T}(E_\Phi + E_k) \qquad [74]$$

where T_R is the effective temperature such that $T_R = Q_R/E_R$. This equation encapsulates the basic energetics of the dynamo problem.

Equation [74] shows that larger values of adiabatic heat flow or ohmic dissipation require a correspondingly higher CMB heat flow to drive the dynamo, as would be expected. In fact, in the absence of radiogenic heating, the CMB heat flow required is directly proportional to $E_k + E_\Phi$. Because the term $\left(1 - \left(\tilde{Q}_T/\tilde{E}_T\right)(1/T_R)\right)$ exceeds zero, a dynamo that is partially powered by radioactive decay will require a greater total CMB heat flow than the same dynamo powered without radioactivity. Alternatively, if the CMB heat flow stays constant, then an increase in the amount of radioactive heating reduces the entropy available to power the dynamo. These results are a consequence of the fact that radioactive heating has a lower thermodynamic efficiency than other methods of driving a dynamo (see **Section 8.02.3.3**).

Equation [74] also illustrates the fact that a dissipative dynamo can exist even if the CMB heat flow is subadiabatic – which may well be the case. For instance, anticipating the results of **Section 8.02.4.3** and using **Table 4**, we have $\tilde{Q}_T/\tilde{E}_T = 11\,500\,K$ for the present-day inner core size. If the CMB heat flow is set to the adiabatic value ($Q_{cmb} = 15$ TW; $E_k = 450$ MW K^{-1}), the application of eqn [74] shows that the entropy available to drive the dynamo, $E_\Phi = 850$ MW K^{-1}. Only if the CMB heat flow fell below 5 TW, strongly subadiabatic, would the entropy available become negative. Thus, a subadiabatic CMB heat flow can sustain a dynamo, as long as an inner core is present to drive compositional convection (e.g., Labrosse et al., 1997; Loper, 1978). It should be noted that these results assume the CMB heat flux does not vary in space; lateral variations in the heat flux may allow a dynamo to function even if the mean value of Q_{cmb} suggests the dynamo should fail (or vice versa). It should also be noted that a subadiabatic heat flow may result in portions of the core being stably stratified (see **Section 8.02.5.4**). In this case, the core temperature structure will not be adiabatic and the equations used to determine the entropy balance will no longer be accurate.

In the absence of an inner core, $\tilde{Q}_T(dT_c/dt) = Q_s$ and $\tilde{E}_T(dT_c/dt) = E_s$. Because the value of $\tilde{Q}_T/\tilde{E}_T$ increases when an inner core is absent, eqn [74] shows that driving the same dynamo purely by thermal convection requires a higher CMB heat flow than when an inner core is present. Again, this effect is a result of the higher efficiency of compositional convection (**Section 8.02.3.3**). Making use of eqns [44], [46], [55]–[57], [67], and [70], it can be shown that in the absence of an inner core,

$$\frac{\tilde{Q}_T}{\tilde{E}_T} \approx \frac{Q_k}{E_k} = \frac{5}{2}\frac{D^2}{r_c^2}T_c \qquad [75]$$

and in a similar fashion (eqns [44], [46], and [58]–[60]), it may also be demonstrated that for $L < D$,

$$T_R = T_c \frac{1 + \left(\frac{2}{5}\right)\left(\frac{r_c^2}{L^2}\right)}{\frac{2}{5}\left(\frac{r_c^2}{D^2}\right)} \qquad [76]$$

with a similar result for $L > D$.

In the absence of an inner core, eqn [74] may therefore be rewritten as

$$Q_{cmb} = \frac{Q_R}{1 + \left(\frac{5}{2}\right)\left(\frac{L^2}{r_c^2}\right)} + Q_k\left(1 + \frac{E_\Phi}{E_k}\right) \qquad [77]$$

If $Q_R = 0$ and ohmic heating is negligible ($E_\Phi = 0$), then eqn [77] shows that the heat flow at the CMB Q_{cmb} must exceed the adiabatic heat flow Q_k for a dynamo driven only by thermal

convection to function. This result is well known (e.g., Nimmo and Stevenson, 2000), but the utility of eqn [77] is that it allows dynamo dissipation to be taken into account explicitly: a more strongly dissipative core requires a more superadiabatic CMB heat flow to operate.

Equation [77] also illustrates the effect of radiogenic heating in the absence of an inner core. Because the term $(1+(5/2)(L^2/r_c^2))$ is of order 10, the CMB heat flow required to maintain a thermally driven dynamo at a constant dissipation rate is not very sensitive to an increase in radiogenic element concentrations (see Figure 3). This is because the efficiencies of radiogenic heating and secular cooling are comparable (see Section 8.02.3.3).

The presence of radiogenic elements is more influential on the core cooling rate and thus ultimately the age of the inner core (e.g., Labrosse et al., 2001). Rewriting eqn [73], we obtain a core cooling rate of

$$\frac{dT_c}{dt} = \frac{Q_{cmb} - Q_R}{\tilde{Q}_T} \qquad [78]$$

It is clear that the effect of the Q_R term is to reduce the rate of core cooling and hence prolong the life of the inner core. This is an issue we return to later in the text.

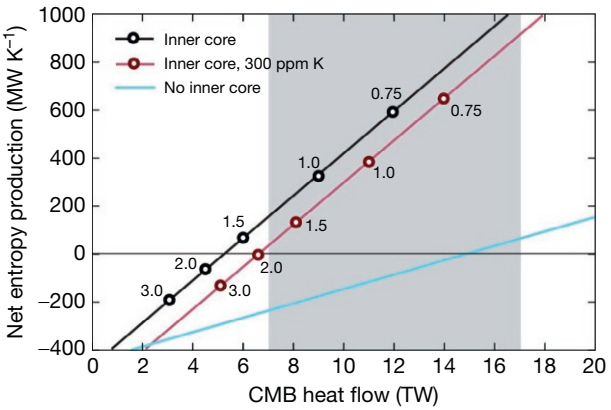

Figure 3 Rate of entropy production as a function of CMB heat flow. Calculations carried out using the expressions given in Section 8.02.3.4 and the parameter values given in Table 2. Dots give the inner core age in Gyr and are calculated assuming a constant heat flow. Shaded area denotes the estimated present-day CMB heat flow (see text).

8.02.4.3 Core Properties

Having made some general remarks, we now turn to the specific core properties we will assume for more detailed analysis. The temperature structure and physical and compositional nature of the core are described in detail elsewhere in this treatise. The values adopted here are summarized in Table 2. Only a brief discussion of these values is given in the succeeding text; further discussion of the effects of uncertainties in these values on model results may be found in Chapter 9.08 (this volume). Note that in general the values are assumed to be constant throughout the core; as discussed later in the text, such an assumption is incorrect, but unlikely to yield significant errors. The resulting theoretical profiles for density, temperature, and gravity are shown in Figure 1 and may be compared with the seismologically inferred values.

8.02.4.3.1 Density and gravity

Figure 1 shows the seismologically inferred density and gravity profiles and compares them with those obtained using the theoretical expressions given in Section 8.02.3.4 and the values given in Table 2. There is good agreement; the only difference is that the simple density model (eqn [41]) neglects the increase in density of the inner core. However, as noted in the preceding text, this error has a negligible effect on the results.

8.02.4.3.2 Thermodynamic properties

From the point of view of the entropy and energy budgets, the most important thermodynamic properties are those influencing the temperature profile and the CMB heat flow, that is, γ (or equivalently α and C_p) and k.

As discussed in Section 8.02.2.4, the thermal conductivity of core materials at the CMB is probably in the range 100–150 W m^{-1} K^{-1} and higher at greater pressures. Based on De Koker et al. (2012), the characteristic length scale over which k varies (eqn [68]) is $D_k \approx 5900$ km. Application of eqn [67] reveals that in this case, the assumption of constant conductivity results in a value of E_k that is 15% too small. For simplicity, we will generally ignore this correction and assume a constant thermal conductivity of 130 W m^{-1} K^{-1}. An exception is in our discussion of stable stratification (Section 8.02.5.4).

Thermodynamic arguments (e.g., Anderson, 1998) and molecular dynamics simulations (e.g., Alfè et al., 2002b)

Table 2 Values of quantities assumed for core calculations

Symbol	Value	Units	Equation number	Symbol	Value	Units	Equation number
ρ_{cen}	12 500	kg m^{-3}	[41]	ρ_0	7900	kg m^{-3}	[42]
r_c	3480	km	[43]	r_i	1220	km	[45]
K_0	500	GPa	[42]	P_c	139	GPa	[51]
L	7272	km	[42]	D	6203	km	[47]
T_c	4180	K	[57]	T_i	5508	K	[61]
P_{icb}	328	GPa	[51]	T_{cen}	5726	K	[46]
α	1.25	$\times 10^{-5}$ K^{-1}	[47]	C_p	840	J kg^{-1} K^{-1}	[47]
L_H	750	kJ kg^{-1}	[61]	α_c	1.1	–	[6]
k	130	W m^{-1} K^{-1}	[67]	$\Delta\rho_c$	560	kg m^{-3}	[6]
T_{m0}	2677	K	[53]	T_{m1}	2.95	$\times 10^{-12}$ Pa^{-1}	[53]
T_{m2}	8.37	10^{-25} Pa^{-2}	[53]	C_r	−10 100	m K^{-1}	[49]

The rationale for these values is given in Sections 8.02.2 and 8.02.4.3.

both suggest that the value of the Grüneisen parameter γ is close to a constant value of 1.5 throughout the core. Since the seismic velocities vary significantly across the core, this result in turn implies that α is variable (here, C_p is assumed constant). Labrosse (2003) derived an expression for α as a function of the core density and argued that α varies from 1.25×10^{-5} K^{-1} at the center to 1.7×10^{-5} K^{-1} at the CMB. Roberts et al. (2003) obtained a variation of $0.9–1.8 \times 10^{-5}$ K^{-1} by assuming a depth-dependent γ. Labrosse (2003) also pointed out, however, that to the third-order accuracy required, the temperature profile (eqn [46]) is not affected by the variation in α and simply depends on the value of this parameter at the center of the Earth. We follow Labrosse (2003) and adopt a constant value for α of 1.25×10^{-5} K^{-1} to determine $T_a(r)$.

Holding α constant means we will slightly underestimate the adiabatic CMB heat flow. This is a conservative approach, in that it means we will be slightly underestimating the heat flow required to drive a dynamo (eqn [77]). When considering stratification of the core, both the conductivity and the adiabatic gradient matter (Section 8.02.5.4). In reality, k increases with depth while α decreases with depth; as a result, an assumption of constant k and constant α is a reasonably good approximation.

8.02.4.3.3 Temperature and melting

Molecular dynamics simulations (see Section 8.02.4.3) suggest that the temperature at the ICB is 5650 ± 600 K once the presence of light elements is taken into account. Equally important, the pressure dependence of melting at ICB conditions is about 9.4 K GPa^{-1} (0.48 K km^{-1}). We can then derive the melting parameters in eqn [53]: $T_{m0} = 2677$ K, $T_{m1} = 2.95 \times 10^{-12}$ K Pa^{-1}, and $T_{m2} = 8.4 \times 10^{-25}$ K Pa^{-2}, where the pressure at the ICB is 328 GPa. This melting curve is plotted for comparison with the Alfè et al. (2004) molecular dynamics results in Figure 1(b).

Taking $T_i = 5508$ K, eqn [46] shows that the present-day CMB temperature is $T_c = 4180$ K. The melting temperature at the center of the core is 5800 K, so the equivalent adiabatic temperature at the CMB is 4240 K. These calculations show that the reduction in T_c since the onset of inner core solidification, referred to as ΔT_c, is about 60 K.

Equation [46] gives an adiabatic gradient at the ICB of 0.35 K km^{-1}. It is the difference between this gradient and the melting gradient that determines the rate of inner core growth as the core cools. For these particular parameters, the quantity C_r that relates core cooling and inner core growth (eqn [49]) is $-10\,100$ m K^{-1}. Note that this quantity is uncertain because it depends on the difference between two comparable terms.

8.02.4.3.4 Chemical properties

By far, the most important chemical property of the core is the compositional density drop $\Delta\rho_c$. The examination of eqn [64] demonstrates that it is this property, rather than the mass fraction of light element c, that actually determines the gravitational energy available. As noted in Section 8.02.2.1, the uncertainty in $\Delta\rho_c$ is probably a factor of 2, with a likely range of 400–800 kg m^{-3}; we adopt a value of 560 kg m^{-3}.

Molecular dynamics simulations give $\partial(\mu_O - \mu_{Fe})/\partial T = -0.45$ meV atom^{-1} K^{-1} and $\partial(\mu_{Si} - \mu_{Fe})/\partial T = +0.11$ meV atom^{-1} K^{-1} at 135 GPa and 4400 K (Alfe, personal communication). For the Fe–O system, this yields $\partial\mu/\partial T \approx -780$ J kg^{-1} K^{-1}, which is an order of magnitude smaller than the quantity $R_H/T_c \approx -6700$ J kg^{-1} K^{-1}. As a result, the (corrected) heat of reaction term E_H may be neglected, in agreement with Pozzo et al. (2012).

Other chemical properties of the core materials, such as the material constants α_D and β, may be determined from molecular dynamics simulations (Gubbins et al., 2004).

8.02.4.3.5 Ohmic Dissipation

The entropy production rate E_Φ required to power the dynamo is a critical parameter because it ultimately determines how rapidly the core must cool to maintain such a dynamo (eqn [74]). It in turn depends directly on the ohmic heating (eqn [33]), but this heating rate is currently very poorly constrained. The heating is likely to occur at length scales, which are sufficiently small that they can be neither observed at the surface nor resolved in numerical models (Roberts et al., 2003). Moreover, the toroidal field, which is undetectable at the surface, may dominate the heating.

The ohmic dissipation Q_Φ may be converted to an entropy production rate using $E_\Phi = Q_\Phi/T_D$ (Roberts et al., 2003), where the characteristic temperature T_D is unknown but intermediate between T_i and T_c and is here assumed to be 5000 K. Roberts et al. (2003) used the results of the Glatzmaier and Roberts (1996) simulation to infer that 1–2 TW is required to power the dynamo, equivalent to an entropy production rate of 200–400 MW K^{-1}. Buffett (2002) suggested 0.1–0.5 TW and Buffett and Christensen (2007) 0.7–1 TW. The dynamo model of Kuang and Bloxham (1997) gives an entropy production rate of 40 MW K^{-1}. Labrosse (2003) argued for a range 350–700 MW K^{-1}, and Gubbins et al. (2003) favored 500–800 MW K^{-1}. Christensen and Tilgner (2004) gave a range of 0.2–0.5 TW, but this range was later updated to 1.1–15 TW (Christensen, 2010) or 3–8 TW (Stelzer and Jackson, 2013). There is clearly little consensus on the dissipation rate required, but roughly 1 TW (equivalent to a few hundred MW K^{-1}) seems reasonable.

8.02.4.3.6 Internal heating

Section 8.02.4.2 shows that radioactive heat production (or, for that matter, tidal heating) in the core has a significant effect on the entropy and energy budgets. It has sometimes been suggested, for reasons explained later in the text, that radioactive potassium is present in the core. This isotope, ^{40}K, has a half-life of 1.3 Gyr and makes up 0.012% of naturally occurring potassium at the present day.

Samples of the Earth's crust and upper mantle produce ratios of lithophile, refractory elements very similar to those found in primitive (chondritic) meteorites and the solar photosphere. The constancy of these ratios allows the abundance of these elements (e.g., U and Th) in the bulk silicate Earth (BSE) to be established with some confidence (e.g., McDonough and Sun, 1995). However, it is also clear that Earth samples are generally depleted, relative to chondrites, in more volatile lithophile elements such as potassium. The

amount of depletion appears to be roughly correlated with condensation temperature. One estimate of potassium concentration in the BSE yields a range of 120–300 ppm (Lassiter, 2004) and a K/U ratio range of 7000–12 000. Chondrites typically have K/U ratios an order of magnitude higher, indicating the extent of the terrestrial depletion.

One possible explanation for the depletion in volatile elements is that the Earth either never accreted them in the first place (due to the elevated temperatures in the protoplanetary disk) or lost them early in its history (e.g., due to late, large impacts). However, the lack of variation in potassium isotope ratios across measured solar system bodies implies that no fractionation of potassium occurred (Humayun and Clayton, 1995), which places severe limits on the classes of mechanisms that could induce volatile loss. An alternative possibility is that some of the potassium was sequestered into the Earth's core (e.g., Lewis, 1971; Murthy and Hall, 1970). Potassium would presumably not be the only element sequestered: other alkali metals (e.g., Na and Rb) should follow suit. Whether the inferred concentrations of these metals in the BSE are compatible with such sequestration is unclear, though it does seem likely that neither U nor Th resides in the core. Given the existing uncertainties and the extent to which the BSE is depleted in potassium relative to the chondrites, it is hard to rule out ~100 ppm K in the core on cosmochemical grounds. Geoneutrinos (Gando et al., 2011) may ultimately resolve this issue, but current measurements are too crude to be helpful.

Laboratory experiments suggest that some K is likely to partition into Fe liquids, especially in the presence of S and/or Ni (Bouhifd et al., 2007; Gessmann and Wood, 2002; Lee et al., 2004; Murthy et al., 2003). However, there is not universal agreement on this issue (Corgne et al., 2007), and the extrapolations in pressure required are large. The highest-pressure experiments to date (Nomura et al., 2010) suggest minimal quantities of potassium in the core, but at these conditions, the compositional parameter space has yet not been thoroughly explored. Further arguments regarding the presence or absence of potassium in the core may be found in Roberts et al. (2003) and McDonough (2006).

8.02.4.3.7 Present-day CMB heat flow

The rate of entropy production within the dynamo ultimately depends on the CMB heat flow, that is, the rate at which heat is extracted from the core. The CMB heat flow, in turn, is determined by the ability of the mantle to remove heat. As reviewed by Lay et al. (2008), independent estimates on this cooling rate exist, based on our understanding of mantle behavior.

The most reliable approach to estimating CMB heat flow appears to be the seismological detection of the deep mantle phase transition from perovskite to postperovskite. Because this phase transition occurs at particular P, T conditions (Murakami et al., 2004; Oganov and Ono, 2004), seismic detection of the depth of the transition provides a temperature constraint. When a pair of transitions occur (a 'double-crossing'; Hernlund et al., 2005), the temperature gradient and thus the heat flux may be inferred. Two regions yield extrapolated global CMB heat flows of 9–17 TW (Lay et al., 2006) and 7–15 TW (Van der Hilst et al., 2007). Nakagawa and Tackley (2010) pointed out that these regions have higher than average heat flux, so that the globally averaged flow may be lower (around 9 TW).

A thermochemical boundary of spatially variable properties and thicknesses 150–300 km termed D″ exists at the base of the mantle, perhaps indicating the presence of partial melt (Lay et al., 1998). The temperature at the top of this layer may be obtained from extrapolating the mantle potential temperature inward along an adiabat and is about 2700 K. As discussed in **Section 8.02.2.3**, the temperature at the core side of the CMB is about 4200 K. Taking the (uncertain) lower mantle thermal conductivity to be $10\,\mathrm{W\,m^{-1}\,K^{-1}}$ (Ohta et al., 2012), the implied conductive heat flow across D″ is 8–16 TW. Wu et al. (2011) used a more sophisticated statistical approach to infer a range of 13 ± 3 TW. However, as pointed out by Buffett (2002) and Labrosse et al. (2007), the presence of significant quantities of radioactive materials in this layer could significantly reduce the heat flux out of the core.

Comparison of convection models with observations of mantle plumes yields a CMB heat flow ≈ 11 TW (Leng and Zhong, 2008). A recent convection study incorporating a weak postperovskite rheology yielded values in excess of 30 TW (Nakagawa and Tackley, 2011).

Based on these results, a reasonable estimate of CMB heat flow appears to be 12 ± 5 TW ($79 \pm 30\,\mathrm{mW\,m^{-2}}$). As will be seen later in the text, a CMB heat flow < 5 TW is inconsistent with the existence of a present-day dynamo; heat flow requirements become more stringent in epochs prior to inner core formation.

8.02.4.3.8 Geochemical constraints on inner core age

The age of the inner core is a particularly important parameter. Obtaining observational constraints on this age is therefore of great significance. Some publications (Brandon et al., 2003; Puchtel et al., 2005) have suggested that (1) coupled ^{186}Os–^{187}Os isotope anomalies found in surface lavas carry a signal from the core (via material entrained across the CMB) and (2) these anomalies were generated as a result of inner core formation, which began ~3.5 Gyr BP. These results, if correct, are of great significance; unfortunately, they are probably not correct (Meibom, 2008). Other studies have ascribed the osmium anomalies to mantle heterogeneities rather than a core contribution (Baker and Jensen, 2004; Hauri and Hart, 1993; Luguet et al., 2008; Schersten et al., 2004). Moreover, a corresponding signal should also be observed in tungsten and lead isotope anomalies; such signals appear to be lacking in Hawaiian lavas (Lassiter, 2006; Schersten et al., 2004) and Afar plume basalts (Rogers et al., 2010). Finally, measurements of Pt, Re, and Os partition coefficients at intermediate pressures and temperatures give values that are too small to explain the observed isotopic anomalies (Hayashi et al., 2009; Van Orman et al., 2008). Thus, although the proposed result is intriguing, it is not widely accepted and (as will be seen in the succeeding text) it is in serious conflict with the geophysical results.

8.02.4.3.9 Comparison with other models

Clearly, the choice of parameters presented in the preceding text involves considerable uncertainties. One reason for adopting the analytic model presented in **Section 8.02.3.4** is that the effect of varying individual parameters is relatively transparent. Estimated errors have been tabulated in several other works,

notably Labrosse (2003), Roberts et al. (2003), and Nimmo et al. (2004). Rather than going through a similar exercise here, Table 3 compares the parameter choices adopted by different groups, to highlight those parameters that are particularly uncertain and those that are in general agreement. Further discussion of the effects these uncertainties have on the model results may be found in Chapter 9.08. The parameters adopted in this study closely mimic those of Pozzo et al. (2012) to facilitate comparison with their results; in particular, to arrive at the same adiabatic CMB heat flow, we employ a slightly larger conductivity value than they do.

There is good general agreement on some parameters, in particular the specific heat capacity C_p, the Grüneisen parameter γ, and the compositional expansion coefficient α_c. As discussed in Section 8.02.2.4, the thermal conductivity has recently been revised sharply upward, resulting in an increase in estimated adiabatic heat flows in later works. The assumed compositional density contrast across the ICB $\Delta\rho_c$ also varies by a factor of 2. Thus, the gravitational entropy production estimated by Labrosse (2003) will be almost twice that of Roberts et al. (2003). Since the gravitational term is probably the dominant one in the overall entropy budget (see succeeding text), this kind of uncertainty can have potentially significant effects.

The assumed present-day temperature structure strongly affects the entropy estimates, because of terms having the form $(T^{-1})-(1/T_c)$. More recent estimates of T_i and T_c are higher than earlier estimates, mainly as a result of the recent molecular dynamics calculations (see Section 8.02.2.3). Estimates of the adiabatic temperature gradient have also increased in more recent works and appear to be converging on a value of roughly 0.8 K km^{-1} at the CMB. The slope of the melting curve is, however, still uncertain: current estimates vary by roughly a factor of 50%. Small uncertainties in the slopes of the adiabat and solidus lead to large variations in the growth history of the inner core. This issue is discussed further, and tabulations of inner core ages under different parameter choices are given in Section 8.02.5.3.

8.02.4.4 Present-Day Behavior

Having summarized the likely parameter values, this section applies the results of Section 8.02.3.4 to calculate the present-day energy and entropy budgets of the core. In what follows, we generally assume a CMB heat flow of either 12 TW (the best-guess present-day estimate) or 15.2 TW (the adiabatic value). Table 4 summarizes these results.

Figure 3 shows how the rate of entropy production available to drive a dynamo varies as a function of the heat flow out of the core, both for a set of core parameters appropriate to the present-day Earth and for a situation in which the inner core has not yet formed. As expected, higher core heat fluxes generate higher rates of entropy production; also, the same cooling rate generates more excess entropy when an inner core exists than when thermal convection alone occurs.

As discussed in the preceding text, when an inner core is present, positive contributions to entropy production arise from core cooling, latent heat release, and gravitational energy; the adiabatic contribution is negative (eqn [72]). For a present-day, radionuclide-free core, a CMB heat flow of <5 TW (cooling rate of 34 K/Gyr) results in a negative net entropy contribution and, therefore, no dynamo (Figure 3). This cooling rate would yield an inner core roughly 1.8 Gyr old, using the parameters adopted here. A higher core cooling rate generates a higher net entropy production rate; it also means that the inner core must have formed more recently.

For a present-day estimated CMB heat flow of 7–17 TW, the net entropy production rate available to drive the dynamo is 160–1030 MW K^{-1}, sufficient to generate roughly 0.8–5 TW of ohmic dissipation. This range may be compared with estimates of ohmic heating (Section 8.02.4.3.5), which are typically 2 TW or less. A heat flow of 7–17 TW also implies an inner core age of about 0.6–1.3 Gyr for the parameters given in Table 2. Note that we are neglecting exsolution as a possible energy source here.

Prior to the formation of an inner core, the CMB heat flow had to exceed the adiabatic value (>15 TW) in order to

Table 3 Comparison of parameter values assumed by five different studies

Quantity	*Units*	*Buffett*	*Roberts*	*Labrosse*	*Pozzo*	*This work*
α	$\times 10^{-5}$ K^{-1}	1.0	0.89–1.77	1.25–1.7	1.02–1.95	1.25
C_p	J kg^{-1} K^{-1}	800	819–850	850	715	840
γ	–	1.4	1.15–1.33	1.5	1.5	–
L_H	kJ kg^{-1}	600	1560	660[a]	750	750
k_c	W m^{-1} K^{-1}	35	46	50	100	130
$\Delta\rho_c$	kg m^{-3}	400	255	500	560[b]	560
α_c	–	0.93	1.0	–	1.1	1.1
T_i	K	4662	5100	5600	5500	5508
T_c	K	3724	3949	4186	4039	4180
$\frac{\partial T_m}{\partial r}\Big\vert_{ICB}$	K km^{-1}	0.51	0.34	0.54	0.48	0.48
$\frac{\partial T_a}{\partial r}\Big\vert_{ICB}$	K km^{-1}	0.24	0.24	0.37	0.34	0.35
$\frac{\partial T_a}{\partial r}\Big\vert_{CMB}$	K km^{-1}	0.54	0.88	0.75	1.0	0.76
Q_k	TW	2.8	5.9	3.0	15.2	15.0

The references are Buffett et al. (1996), Roberts et al. (2003), Labrosse (2003), and Pozzo et al. (2012).

[a]Assuming a present-day IC temperature of 5600 K.

[b]The quoted density contrast in Pozzo et al. (2012) includes a 0.24 g cc^{-1} contribution from solidification.

maintain a dynamo for reasons discussed earlier in the text (eqn [77]). For a dynamo requiring an entropy production rate of 200 MW K^{-1}, the core cooling rate had to be roughly three times as fast to maintain this rate before the onset of inner core solidification. This again illustrates the rapid core cooling required if thermal convection is the only buoyancy source.

Figure 3 also shows that, as discussed in the preceding text, a larger CMB heat flow is required for the same entropy production if radioactive heating is important in the present-day Earth. In this particular example, when there is 300 ppm potassium in the core, no dynamo can function if the CMB heat flow drops below 6.3 TW. However, the corresponding core cooling rate is 32 K/Gyr, less than the potassium-free equivalent, but still only yielding an inner core age of 2.0 Gyr. The effect of potassium is relatively modest because the radioactive heating rate is a small fraction of the total CMB heat flow.

Prior to the existence of the inner core, the effect of radioactive decay on the entropy production is small (Figure 3), because the prefactor for Q_R in eqn [77] is small. Again, however, the existence of radioactive potassium in the core has a significant effect on the cooling history of the core. The role of potassium in controlling the age of the inner core is more minor and is discussed further in Section 8.02.5.3.

Table 4 summarizes the individual contributions to the overall entropy and energy budgets for the present-day core, both with and without potassium. The CMB heat flow is specified to be either the present-day value (12 TW) or 15.2 TW. It is clear that the different driving mechanisms are associated with different thermodynamic efficiencies. In particular, while the gravitational term only contributes roughly one-fifth of the total heat budget when potassium is absent, it delivers three-fifths of the entropy budget. Similarly, the latent heat term delivers the same power, but twice as much entropy, as the secular cooling term.

Table 4 also makes the role of radioactive heating clear. Its efficiency is comparable to that of secular cooling; thus, for the same total CMB heat flow, adding radioactive elements reduces ΔE, the entropy available to drive the dynamo. The presence of radioactivity also reduces the core cooling rate and thus increases the age of the inner core. However, since the radioactive contribution (2.1 TW) is small compared to the assumed CMB heat flow, the increase in inner core age is relatively small.

Table 4 also compares our results with those of case 5 of Pozzo et al. (2012). Although the details differ, the overall answers are very similar. The main difference is that Pozzo et al. (2012) derived a younger inner core because they have a smaller value of ΔT_c (see Table 5).

In summary, Figure 3 shows that the minimum CMB heat flow that could allow a dynamo to persist at the present day is about 5 TW, somewhat below the lower bound based on

Table 4 Individual contributions to energy/entropy budgets for a present-day core with parameters given in Table 2 and a CMB heat flow of either 15.2 TW or 12 TW (estimated present-day value)

	Pozzo (K=0)		*This work (K=0)*		*This work (K=300 ppm)*		*This work (K=0)*	
	Q *(TW)*	E *(MW K^{-1})*	Q *(TW)*	E *(MW K^{-1})*	Q *(TW)*	E *(MW K^{-1})*	Q *(TW)*	E *(MW K^{-1})*
Q_s, E_s	5.9	212	6.1	183	5.3	159	4.8	144
Q_L, E_L	5.9	389	5.7	327	4.9	284	4.5	258
Q_g, E_g	3.4	830	3.4	809	2.9	701	2.7	639
Q_R, E_R	0	0	0	0	2.1	60	0	0
Q_k, E_k	15.2	−561	15.0	−450	15.0	−450	15.0	−450
Q_{cmb}, ΔE	15.2	870	15.2	869	15.2	753	12.0	591
dT_c/dt (K Gyr^{-1})	−115		−104		−90		−82	
r_i/dt (km Gyr^{-1})	1092		1050		909		829	
IC age (Gyr)	0.37		0.59		0.68		0.75	

Q and E refer to the energy and entropy contributions, respectively; ΔE is the entropy available to drive the dynamo, dT_c/dt is the core cooling rate, and dr_i/dt is the inner core growth rate. The small heat of reaction term E_H is neglected. Cases are shown with and without 300 ppm potassium (K) in the core. Inner core (IC) age is calculated assuming a constant CMB heat flow. Here, $C_r = -10100$ K and we compare our results with case 5 of Pozzo et al. (2012).

Table 5 Comparison of results obtained by different groups

Quantity	*Units*	*Buffett*	*Roberts*	*Labrosse*	*Pozzo*	*This work*
T_m ($r=0$)		5000	5379	5967	–	5800
ΔT_c	K	146	68	96	43	60
W_s	$\times 10^{28}$ J	23	8.7	18.2	7.0	11.6
W_g	$\times 10^{28}$ J	3.8	1.9	4.1	7.0	4.4
W_L	$\times 10^{28}$ J	5.6	15	7.0	4.0	6.9
W_{tot}	$\times 10^{28}$ J	36	26	29	18.0	23
IC age ($Q_{cmb}=10$ TW)	Gyr	1.13	0.83	0.92	0.55	0.73

The references are Buffett et al. (1996), Roberts et al. (2003), Labrosse (2003), and Pozzo et al. (2012), case 5. Inner core age assumes a constant heat flow of 10 TW. ΔT_c was taken from references rather than calculated from eqn [81] where possible.

mantle studies (Section 8.02.4.3.7). Even with this low heat flow, the inner core age would still be <2 Gyr. In reality, it is probably much younger than this, because heat fluxes in excess of 15 TW are required to drive a dynamo prior to inner core formation. Investigating the evolution of the dynamo and inner core in more detail is the subject of the next section.

8.02.5 Evolution of Energy Budget through Time

8.02.5.1 Introduction

From the previously mentioned text, it is evident that the energy and entropy budgets of the present-day active dynamo are consistent with the inferred CMB heat flow of ≈ 12 TW. On the other hand, a heat flow in excess of 15 TW appears required to drive the dynamo in the absence of an inner core.

Because a dynamo similar to the present-day one has apparently been operating for at least 3.5 Gyr, constraints can also be applied to the energy and entropy budgets over this time period. Attempting to do so introduces additional, large uncertainties, in particular the fact that the evolution of the CMB heat flow through time is unknown. Nonetheless, this problem has been investigated by several groups, notably Yukutake (2000), Buffett (2002), Labrosse (2003), Nimmo et al. (2004), Costin and Butler (2006), Davies (2007), and Nakagawa and Tackley (2010). Many of these groups reached similar conclusions. In particular, the inner core was commonly found to be a relatively young feature, with an age of ~ 1 Gyr; and early core temperatures tended to be very high, an effect that was somewhat mitigated if radioactive potassium was present in the core. As discussed later in the text, these conclusions are strengthened once the upward revision of core thermal conductivity is included.

Prior to inner core solidification, the CMB heat flow over time depends on the adiabatic and ohmic dissipation terms and is given by eqn [77]. Given a CMB heat flow, the core cooling rate, and hence the total core temperature drop prior to onset of inner core solidification, is simple to determine (eqn [78]). Let the inner core age be τ_{ic} and the age of the dynamo be τ_d. Then, making the simplifying assumption that the heat capacity of the core is simply MC_p, the reduction in core temperature T_c over the interval from the onset of dynamo activity to the start of core solidification is given by

$$\Delta T_c' \approx \left(T_c \frac{8\pi r_c^3 k}{D^2} \left[1 + \frac{E_\Phi}{E_k} \right] - \overline{Q}_R \frac{1}{\left(2r_c^2/5L^2\right) + 1} \right) \frac{[\tau_d - \tau_{ic}]}{MC_p} \quad [79]$$

where $\overline{Q}_R$ is the mean radiogenic heat flow over the interval of interest. Since the temperature at which inner core solidification starts is fixed, eqn [79] allows the initial temperature of the core to be calculated. Higher ohmic dissipation rates, later inner core formation, and higher thermal conductivities all imply a larger core temperature drop and a higher initial temperature (Buffett, 2002; Labrosse et al., 2001). On the other hand, radioactive heating reduces the amount by which the temperature drops. Using the values of Table 2 and assuming that $E_k \approx E_\Phi$, the core temperature drop over a 2 Gyr time interval is roughly 1100 K in the absence of radioactive heating. Mantle solidus temperatures at the CMB are estimated to be 4000–4300 K (Andrault et al., 2011; Fiquet et al., 2010). Thus, a significantly hotter early core implies widespread melting of the lowermost mantle. Such melts, which are probably dense (Mosenfelder et al., 2007), could strongly affect the thermal evolution of the core and perhaps delay the onset of dynamo activity (Labrosse et al., 2007).

The advantage of eqn [79] is that it provides a robust and relatively transparent estimate of how much core cooling occurred prior to inner core formation. However, in practice, the CMB heat flux is likely to have fluctuated with time, and the onset of inner core solidification raises additional complications. Thus, a fuller picture of core and dynamo evolution requires more sophisticated approaches, which are discussed in the succeeding text.

8.02.5.2 Theoretical Models

The CMB heat flow ultimately controls the thermal evolution of the core, but its evolution through time is not observationally constrained. Accordingly, theoretical arguments have to be adopted. One such argument is to employ a numerical model of the Earth's thermal evolution and predict the CMB heat flow through time. Models can be either relatively simple parameterized convection calculations (e.g., Nimmo et al., 2004) or more sophisticated (but two-dimensional) approaches in which the full fluid-dynamic equations are solved (e.g., Nakagawa and Tackley, 2010). These models illustrate the important point that the evolution of the CMB heat flow cannot be decoupled from the thermal evolution of the Earth's mantle. The rate at which heat is transported across the CMB depends on the temperature gradient at the base of the mantle, which ultimately depends on the rate at which the mantle itself is cooling. Thus, a successful model must accurately reproduce the behavior of the mantle through time in order to calculate the evolution of the CMB heat flow.

None of the models currently in existence are likely to meet this criterion. Firstly, the actual evolution of the mantle temperature through time is poorly known (see Davies). Secondly, the effect of mantle temperature on plate tectonic behavior is not well understood, with even the sign of the effect being disputed (e.g., Korenaga, 2003); similarly, the change in mean plate tectonic velocities over billions of years is unknown. Since it is plate tectonics that control the cooling rate of the mantle, these are important issues. Thirdly, it is not clear that any model incorporates all of the relevant physics. For instance, the postperovskite phase near the base of the mantle likely has an appreciable effect on the evolution of the CMB heat flow (e.g., Nakagawa and Tackley, 2011), as would dense chemical piles at the base of the mantle (McNamara and Zhong, 2004) or the presence of a partially molten zone (Labrosse et al., 2007).

Given these uncertainties, an alternative approach relying on fewer poorly known parameters is desirable. One such approach is to assume that the ohmic dissipation in the core, and thus the rate of entropy production required to drive the dynamo E_Φ, has been constant or varied in a prescribed manner, through time (e.g., Buffett, 2002; Labrosse, 2003). Since the rate of entropy production depends on the core cooling rate (eqn [72]), specifying this rate of production details the core cooling rate and thus the CMB heat flow over time. This in turn allows the core temperature T_c to be integrated backward

from the present day. A high rate of entropy production requires rapid cooling of the core and thus a young inner core and an early core that is very hot.

The CMB heat flow changes slowly, on timescales of several 100 Myr. It can therefore be seen from eqn [74] that the onset of inner core solidification will cause a large increase in the rate of entropy production available to drive the dynamo. This is because the heat flow Q_{cmb} is fixed in the short term, and the addition of latent heat and compositional driving forces (which are thermodynamically more efficient) reduces the value of $\tilde{Q}_T/\tilde{E}_T$. The specified rate of entropy production should therefore be appropriate to the situation just prior to the onset of inner core solidification.

The advantage of this approach – specifying an entropy production rate and deducing the resulting temperature evolution – is that it is simple: for instance, no knowledge of the mantle is required. Thus, parameter space can be explored rapidly, and the sensitivity of the results to uncertainties in different parameters can be determined. On the other hand, this technique requires a large assumption: that dissipation within the core has stayed constant over time. Furthermore, as discussed in the preceding text, the actual rate of dissipation involved in even the present-day dynamo is unknown. Finally, this approach neglects the possibility of stable core stratification, an issue discussed further in Section 8.02.5.4 and Chapter 9.08.

Figure 4 is an example of the results obtained by specifying an entropy production rate. It starts from the present-day structure discussed in Section 8.02.4.3 and integrates T_c backward in time such that the entropy production rate prior to inner core formation stays constant at 100 MW K^{-1}. It is assumed that the core heat flow subsequent to inner core formation remains constant, which is reasonable given the young inner core ages obtained.

Figure 4(a) shows the evolution of T_c and CMB heat flow, integrated backward from the present. An entropy production rate just prior to IC formation of 100 MW K^{-1} requires a CMB heat flow of 18.5 TW (Figure 3) and a core cooling rate of 315 K Gyr^{-1} in the absence of radioactive heating. The initial CMB temperature is 5760 K, enough to guarantee widespread lower mantle melting. The CMB heat flow is a significant fraction of the total global surface heat flow of 42 TW (Sclater et al., 1980) and exceeds the likely value deduced from present-day observations (Section 8.02.4.3.7). As a result, this scenario appears unrealistic.

Figure 4 shows that adding potassium reduces the initial temperature, as expected from eqn [79], to 5040 K. The magnitude of this effect is mainly due to the short half-life of potassium, which produces 15 times more heat at 3.5 Gyr BP than at the present day. However, the heat flux required to drive the dynamo at a particular entropy production rate is hardly changed (eqn [77]).

Figure 4(b) shows the evolution of the inner core radius and entropy production with time. The high core cooling rate means that the inner core is a young feature (0.5 Gyr old). As expected, the entropy production rate increases when inner core formation begins. While one might expect such an increase to have significant effects on the observed magnetic field, in practice, the observations are sufficiently sparse that no such effects have been detected (Section 8.02.2.4). Because of the high CMB heat flow, the presence of potassium has little effect on the age of the inner core, though it does affect the early core temperature as noted in the preceding text.

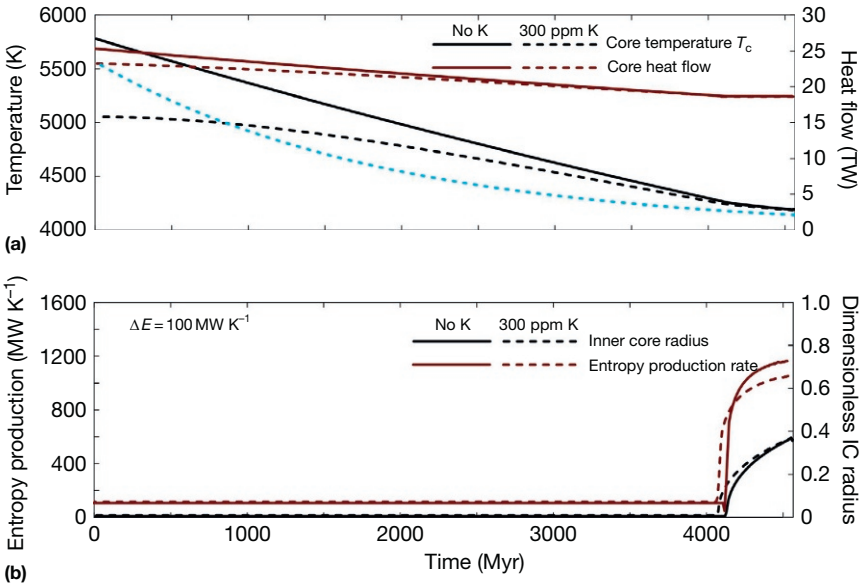

Figure 4 (a) Evolution of core temperature T_c (left-hand scale) and heat flow Q_{cmb} (right-hand scale) through time, assuming a constant rate of entropy production of 100 MW K^{-1} prior to inner core solidification. During inner core solidification, the heat flow is kept constant at 18.5 TW. Results were obtained by integrating backward in time using the present-day conditions and parameters specified in Table 2. Given a fixed heat flow or rate of entropy production and a radioactive heat production rate, the change in core temperature with time may be calculated. Thick lines denote case with no core potassium; thin lines denote case with 300 ppm potassium. In the latter case, the radioactive heat production is given by the dotted line. (b) Evolution of rate of entropy production and growth of inner core. Thick lines denote potassium-free case; thin lines have 300 ppm potassium in the core.

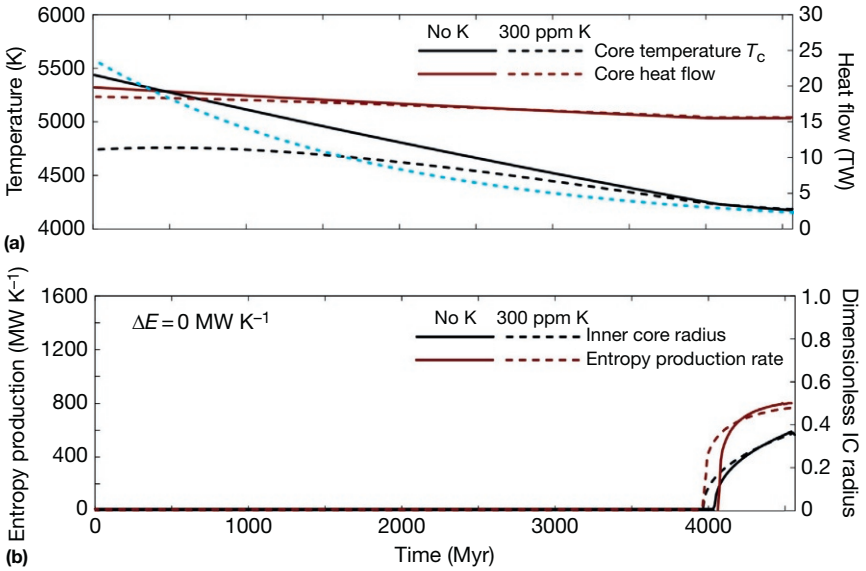

Figure 5 As for **Figure 4**, except that the rate of entropy production prior to inner core solidification is fixed at 0 MW K^{-1} and CMB heat flow following onset of solidification is fixed at 15 TW.

As noted by Buffett (2002) and Labrosse (2003) and shown in eqn [79], the dissipation required to drive the dynamo has a strong influence on the evolution of the core temperature. **Figure 5** shows an identical set of results to **Figure 4**, except assuming a constant (preinner core) entropy production rate of 0 MW K^{-1}, that is, a marginal dynamo in which dissipation is negligible. This provides a conservative set of results. As one would expect, the lower heat flow results in a slower core cooling rate and a somewhat older inner core (0.52–0.60 Gyr, depending on the potassium concentration). The resulting initial core temperatures are lower (4730–5440 K) but still imply widespread early mantle melting.

An interesting consequence of these two scenarios is that the CMB heat flow changes only by about 35 and 20%, respectively, over 4 Gyr. This is a result of the assumption of constant entropy production; nonetheless, it suggests that the CMB heat flow may be less sensitive to changes in mantle temperature than simple scaling arguments (e.g., Nimmo et al., 2004) would suggest. This issue is discussed in more detail in **Chapter 9.08**.

Figure 6 summarizes these results. **Figure 6(a)** plots the initial core temperature as a function of core potassium and entropy production rate. It demonstrates that, as expected, higher rates of entropy production require more core cooling and thus higher initial temperatures. Adding potassium to the core counteracts this effect. These effects are essentially identical to those found by Buffett (2002) and Labrosse (2003). Irrespective of the details of the calculations, widespread early melting of the lowermost mantle is anticipated to occur.

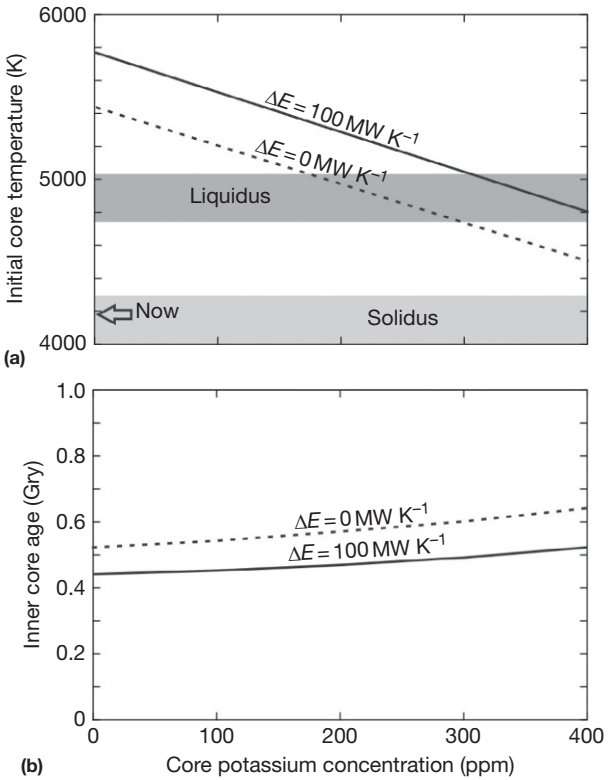

Figure 6 (a) Variation in initial CMB core temperature (at 4.56 Gyr BP) as a function of core potassium concentration and entropy production rate within the core. Calculations carried out as for **Figures 4** and **5**. Shaded regions indicate estimated solidus and liquidus temperatures for the lowermost mantle (Andrault et al., 2011); arrow indicates estimated present CMB core temperature. (b) Variation in inner core age as a function of core potassium concentration and entropy production rate.

8.02.5.3 Age of the Inner Core

Figures 3–5 make it clear that the initiation of inner core solidification significantly increases the entropy production available to drive the geodynamo, even though the consequences of this increase for the magnetic field intensity are unclear. If the inner core age could be established observationally, it would provide

an immediate constraint on the time-averaged CMB heat flow and hence on the mechanisms available to drive the geodynamo. Establishing the age of the inner core is therefore of great importance but, as outlined in Section 8.02.4.3.8, geochemistry does not appear to provide useful constraints.

Over the interval since inner core solidification began, the total amount of energy released W_{tot} has come from four main sources: secular cooling of the whole core (W_s), gravitational energy (W_g), latent heat release (W_L), and perhaps some radioactive decay (W_R). These quantities may be calculated by time integration of the corresponding heat flow terms given in Section 8.02.3.2; for the similar set of equations investigated by Buffett et al. (1996), analytic expressions for these terms may also be derived.

Letting the inner core age be τ_i and the mean CMB heat flow over this interval be $\overline{Q}_{cmb}$, then we have

$$\tau_i = \frac{W_s + W_g + W_L + W_R}{\overline{Q}_{cmb}} = \frac{W_s + W_g + W_L + \frac{Q_R}{\lambda}\left(e^{\lambda\tau_i} - 1\right)}{\overline{Q}_{cmb}} \quad [80]$$

where Q_R is the present-day radioactive heat production and λ is the decay constant. Note that this equation, unlike eqn [74], contains no information on whether a dynamo operates; in particular, if the mean CMB heat flow is too small, a dynamo will not occur.

The inner core age depends on the total energy released since solidification began and the CMB heat flow. Of the four energy terms, the first depends on the mean temperature drop ΔT in the core since solidification began ($W_s \approx M_c C_p \Delta T$); the others are independent of this quantity and depend on the same variables as their time derivatives Q_g, Q_L, and Q_R (see Section 8.02.3.4). The mean temperature drop ΔT in turn depends on the behavior of the solidus and the adiabat, as discussed in the succeeding text.

Since the inner core first began to solidify, the temperature at the ICB has dropped by an amount determined by the behavior of the melting curve and adiabat (see Figure 2). To achieve this growth in inner core size requires a corresponding change in the temperature at the CMB, ΔT_c. Making the approximation that the solidus and adiabat are both linear (with respect to pressure) within the inner core, then the change in CMB temperature since the onset of core solidification ΔT_c is given by (see Figure 2)

$$\Delta T_c = \frac{\Delta P}{f_{ad}}\left(\frac{dT_m}{dP} - \frac{dT_a}{dP}\right) = 23\,K\left(\frac{(dT_m/dP) - (dT_a/dP)}{1\,K/GPa}\right)\left(\frac{1.32}{f_{ad}}\right) \quad [81]$$

where ΔP is the pressure difference between the present ICB and the center of the Earth, T_a and T_m are the adiabatic and melting temperature profiles, f_{ad} is a factor converting the core temperature at the CMB to that at the ICB, and the numerical values are obtained by using the parameter values given in Table 2. Note that ΔT_c depends on the difference in slopes and is thus sensitive to small variations in these slopes.

For the parameters given in Table 2, $f_{ad} = 1.32$, $\Delta P = 30$ GPa, and the nominal difference in slopes at the ICB is 2.6 K GPa^{-1}. This indicates that the core has only cooled by approximately 60 K since the inner core began to solidify. However, as noted in the preceding text, the slopes of both the adiabat and the melting curve are subject to substantial uncertainties. In order to investigate these uncertainties, Table 5 compares the values adopted for relevant quantities by the same four groups shown in Table 4. There is a considerable range in the value of ΔT_c obtained, from 43 to 146 K. The amount of heat released by core cooling W_s has a correspondingly large range: it dominates all other contributions in most models but is of lesser importance in the model of Roberts et al. (2003). Similarly, the release of latent heat W_L can range from minor (Buffett) to dominant (Roberts). The uncertainty in the total amount of energy released since inner core solidification is uncertain by a factor of 2, ranging from 18 to 36×10^{28} J. This range will be adopted as representative of the likely uncertainties and may be used to estimate the inner core age. For a mean CMB heat flow range of 7–17 TW, eqn [80] shows that the resulting inner core age in the absence of radiogenic heating is 0.34–1.6 Gyr. Even for the extreme combination of low heat flow and high W_{tot}, the implied inner core age is much less than the age of the Earth.

Just prior to the onset of inner core formation, the CMB heat flow must have equaled or exceeded the adiabatic value, depending on the amount of ohmic dissipation (eqn [77]). Assuming that the heat flow has not decreased since, the mean heat flow since IC formation cannot have been less than the adiabatic value. Taking this value to be 15 TW and using the total energy release range of $18–36 \times 10^{28}$ J result in a maximum inner core age range of 0.38–0.76 Gyr from eqn [80]. This estimate is conservative and still results in an inner core only one-sixth the age of the Earth at most. An even lower CMB heat flow would allow an older inner core, but would not allow a dynamo to function prior to inner core formation. Furthermore, such a low CMB heat flow is not consistent with the available present-day observational constraints (Section 8.02.4.3.7).

Equation [80] shows that another way to increase the age of the inner core is to add radioactive heating. Figure 6(b) shows how the inner core age varies as a function of potassium concentration for different rates of ohmic dissipation, calculated using the same method as that shown in Figures 4 and 5. As expected, lower rates of entropy production and the addition of potassium both result in longer-lived inner cores. However, even 300 ppm potassium only results in very modest changes, because the CMB heat flow required to drive a dynamo greatly exceeds that due to radioactive decay. Figure 6(b) shows that for the parameters given in Table 2, an inner core age in excess of 0.7 Gyr is not permitted.

This result is robust to most uncertainties. Taking an upper bound on W_{tot} of 36×10^{28} J and a CMB heat flow of 12 TW, eqn [80] yields inner core ages of 0.95 and 1.25 Gyr, with and without 300 ppm potassium. If Q_{cmb} is set to the lower bound of 7 TW, the inner core age increases to 1.6 Gyr without potassium. In this case, the addition of 300 ppm would permit an inner core as old as the Earth. However, in addition to requiring extreme parameter choices, this scenario is unlikely to permit a dynamo to operate at earlier times, when the inner core was smaller and compositional buoyancy was less effective. We accordingly view the conclusion that the inner core must be young as robust. Similar studies (e.g., Buffett, 2002; Labrosse, 2003; Roberts et al., 2003) reached a similar conclusion assuming smaller core conductivities; the present much larger core conductivities only make the conclusion stronger.

One remaining uncertainty is the effect of a stably stratified layer. Because of the high thermal conductivity of iron, a stably stratified layer immediately below the CMB would have to be of order 10^3 km thick in order to significantly reduce the rate of core cooling (e.g., Labrosse et al., 1997). On the other hand, a thick stagnant layer is likely to make it harder to sustain a dynamo in the remaining convective region and to reduce the surface field strength. Quantitative investigation of these kinds of effects has barely begun (e.g., Nakagawa, 2011) and is likely to be a focus of much future work.

8.02.5.4 Stable Stratification

Stable stratification in the core can arise from two processes. A subadiabatic heat flow out of the top of the core can give rise to a stably stratified region (e.g., Loper, 1978). Where conductivity varies with depth, this region will be at the center of the core (Pozzo et al., 2012, and see succeeding text). Alternatively, light elements may accumulate in a buoyant layer immediately beneath the CMB (e.g., Braginsky, 2006).

The presence of stably stratified layers could be deduced from either seismological or geomagnetic observations. Helffrich and Kaneshima (2010) argued for a 300 km thick subadiabatic layer at the top of the outer core based on array seismology, while various groups (reviewed in Gubbins et al., 2008) have presented seismological evidence for a stratified layer immediately above the ICB. Gubbins (2007) used geomagnetic observations to argue that any stratified layer at the top of the core must be thin (<100 km), while Buffett (2010) argued for such a layer on the basis of the Earth's nutations.

Prior to the formation of an inner core, the presence of a deep, stably stratified layer seems probable (see later text), unless disrupted by lateral heat flux variations. Once inner core formation begins, however, the situation becomes more complicated. On the one hand, light element release can drive convection even in the presence of a subadiabatic heat flux (**Section 8.02.4.2**); on the other hand, if the light elements do not remain well mixed, then a buoyant stable layer will develop at the top of the core. Further discussion of the behavior of subadiabatic layers may be found in Labrosse et al. (1997) and Lister and Buffett (1998). A compositionally buoyant layer may also arise through core–mantle interactions (Buffett and Seagle, 2010).

Compositionally buoyant layers, once formed, are likely to be stable against disruption from convection beneath (Gomi et al., 2013), mainly because the thermal density contrast is much smaller than the compositional density contrast. However, such layers are likely to be unstable in the presence of lateral variations in CMB heat flux (Lister and Buffett, 1998; Pozzo et al., 2012).

Here, we will restrict ourselves to the simpler case, prior to inner core formation; the more complicated case is discussed in Pozzo et al. (2012). We adopt an approach similar to that of Pozzo et al. (2012) and Davies and Gubbins (2011) who calculated the net effective temperature gradient dT/dr, where a negative value indicates a stably stratified region. Here, we calculate instead the effective heat fluxes F as a function of radius. By making use of eqn [58], the effective heat flux due to radioactive heating may be shown to be

$$F_{\text{rad}} \approx \frac{\rho_{\text{cen}} hr}{3}\left[1-\left(\frac{3}{5}\right)\left(\frac{r^2}{L^2}\right)\right] \qquad [82]$$

Similarly, the effective heat flux due to secular cooling from eqn [56] is given by

$$F_{\text{s}} \approx \frac{T_{\text{cen}}}{T_{\text{c}}}\rho_{\text{cen}} C_{\text{p}}\left(\frac{dT_{\text{c}}}{dt}\right)\left(\frac{r}{3}\right)\left[1-\left(\frac{3}{5}\right)\left(\frac{r^2}{A^2}\right)\right] \qquad [83]$$

and the adiabatic contribution is simply

$$F_{\text{ad}} = \frac{2kr}{D^2}T(r) \qquad [84]$$

In the absence of an inner core, the net effective heat flux is $F_{\text{total}} = F_{\text{s}} + F_{\text{rad}} - F_{\text{ad}}$, and a negative value indicates a stably stratified region (cf. Pozzo et al., 2012).

Figure 7(a) shows how F_{s} and F_{ad} vary with radial position for a CMB heat flow of 20 TW. Bold lines are for variable

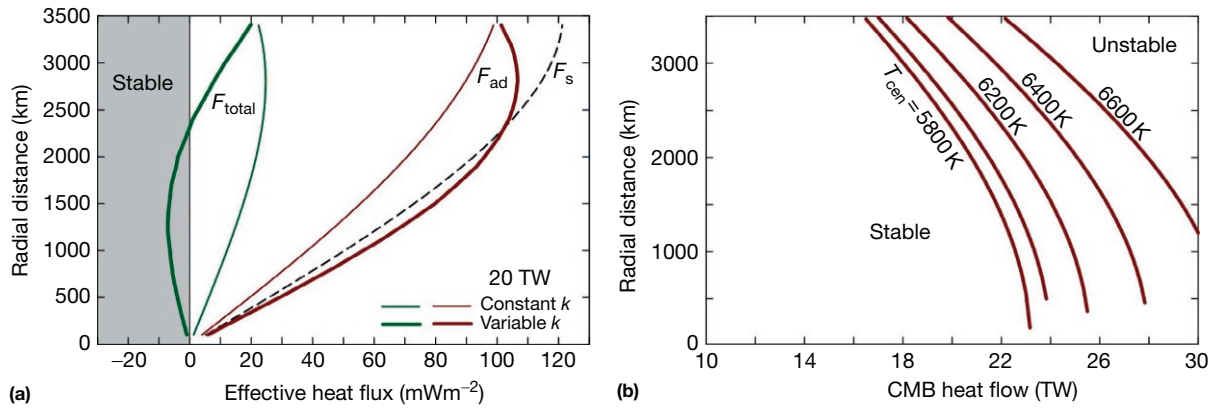

Figure 7 (a) Effective heat fluxes as a function of radial position prior to inner core formation. A negative value of F_{total} implies a stably stratified region. Contributions from secular cooling F_{s} and the adiabat F_{ad} are calculated using eqns [83] and [84], respectively. Bold lines and thin lines are for variable (eqn [68]) and constant (130 W m^{-1} K^{-1}) thermal conductivity, respectively. Parameter values are from **Table 2**. The CMB heat flow is 20 TW and the cooling rate dT_{c}/dt is 340 K/Gyr. In the constant conductivity case, the entire core is convective, while in the variable-conductivity case, the bottom two-thirds are stably stratified. (b) Radial extent of the stably stratified layer as a function of CMB heat flow and core central temperature T_{cen}. Here, variable thermal conductivity is assumed.

conductivity (eqn [68]) and thin lines are for constant conductivity. In the case of constant conductivity, the entire core remains convective. However, once the increase in conductivity with depth is taken into account, a stably stratified region is predicted to develop in the bottom two-thirds of the core. Potassium (not shown) has only a minor effect, because the radiogenic heat flow is small compared with the total. These calculations are not fully self-consistent, because the calculated conductivities assume an adiabat (and thus convection). Furthermore, the reduction in α with depth (**Section 8.02.4.3.2**) will somewhat reduce the stabilizing effect of the adiabat. Nonetheless, this example serves to illustrate that stable stratification may well have occurred prior to inner core formation.

Figure 7(b) shows how the radial extent of the stably stratified layer varies with heat flow and core central temperature. Higher heat flows result in a thinner stable layer, as expected, while higher central temperatures yield a thicker layer (because the adiabatic gradient is larger). Increasing the value of k at the CMB likewise increases the thickness of the stable layer. The location of the stable layer is deep, not shallow, mainly because of the strong radial variation in conductivity (Gomi et al., 2013). Pozzo et al. (2012) reached the opposite conclusion because they also included compositional and latent heat terms.

A deep, stably stratified layer will not strongly affect the thermal evolution of the core, but might alter the characteristics of the geodynamo (in a similar manner to the inner core). A stable layer at the top of the core will screen out short-wavelength and short-period magnetic signals and will also act as a thermal insulator (Gubbins et al., 1982; Labrosse et al., 1997), potentially reducing the rate of core cooling. Both kinds of layers may be destabilized by lateral heat flux variations at their boundaries. Further discussion of these issues may be found in **Chapter 9.08**.

8.02.6 Summary and Conclusions

Our current picture of the core is in some ways quite different from that at the time of the previous chapter (Nimmo, 2007). Driving a dynamo is now thought to require high CMB heat flows: >5 TW at the present day and >15 TW prior to inner core formation (**Figure 3**). Mantle simulations show that such high heat flows are achievable, especially if the viscosity of postperovskite is low (Nakagawa and Tackley, 2011) or the base of the mantle is molten (Labrosse et al., 2007). As a result of the high heat flows, the inner core is young, with an age probably <20% of the age of the Earth (**Figure 6(b)**). The lowermost mantle was likely pervasively molten for much of its history, irrespective of whether potassium was present or not (**Figure 6(a)**). How such a molten mantle affected heat transfer across the CMB is not yet thoroughly understood (Labrosse et al., 2007) and represents an interesting subject for future study.

Perhaps the most important remaining question is whether parts of the core were ever stably stratified. As discussed in **Section 8.02.5.4**, stable stratification is likely in the epoch before inner core formation. In situations where compositional convection matters, the extent to which a stably stratified layer will develop is unclear. So far, little attention has been paid to thermal evolution scenarios in which core stratification matters (though see Labrosse et al., 1997; Lister and Buffett, 1998). Equally, the behavior of dynamos under these conditions has received only limited attention (Christensen and Wicht, 2008; Nakagawa, 2011; Stanley and Mohammadi, 2008). Further theoretical work is certainly required. At the same time, it is likely that further seismological (e.g., Helffrich and Kaneshima, 2010) or geomagnetic (e.g., Buffett, 2010; Gubbins, 2007) measurements will help to establish whether stably stratified regions of the core currently exist.

Acknowledgments

Thanks to Manfred Gold for careful reading, Chris Davies for helpful discussions, Dario Alfe for calculating the chemical potentials, and Peter Olson for a thorough review.

References

Alfè D, Gillan MJ, and Price GD (2002) Ab initio chemical potentials of solid and liquid solutions and the chemistry of the Earth's core. *Journal of Chemical Physics* 116: 7127–7136.

Alfè D, Gillan MJ, and Price GD (2003) Thermodynamics from first principles: Temperature and composition of the Earth's core. *Mining Magazine* 67: 113–123.

Alfè D, Price GD, and Gillan MJ (2002) Iron under Earth's core conditions: Liquid-state thermodynamics and high-pressure melting curve from ab initio calculations. *Physical Review B* 65: 165118.

Alfè D, Price GD, and Gillan MJ (2004) The melting curve of iron from quantum mechanics calculations. *Journal of Physics and Chemistry of Solids* 65: 1573–1580.

Anderson OL (1998) The Gruneisen parameter for iron at outer core conditions and the resulting conductive heat and power in the core. *Physics of the Earth and Planetary Interiors* 109: 179–197.

Andrault D, Bolfan-Casanova N, Lo Nigro G, Bouhifd MA, Garbarino G, and Mezouar M (2011) Solidus and liquidus profiles of chondritic mantle: Implication for melting of the Earth across its history. *Earth and Planetary Science Letters* 304: 251–259.

Anzellini S, Dewaele A, Mezouar M, Loubeyre P, and Morard G (2013) Melting of iron at Earth's inner core boundary based on fast X-ray diffraction. *Science* 340: 464–467.

Aubert J, Labrosse S, and Poitou C (2009) Modelling the palaeo-evolution of the geodynamo. *Geophysical Journal International* 179: 1414–1428.

Backus GE (1975) Gross thermodynamics of heat engines in deep interior of Earth. *Proceedings of the National Academy of Sciences of the United States of America* 72: 1555–1558.

Baker JA and Jensen KK (2004) Coupled Os-186-Os-187 enrichments in the Earth's mantle – core–mantle interaction or recycling of ferromanganese crusts and nodules? *Earth and Planetary Science Letters* 220: 277–286.

Belonoshko AB, Ahuja R, and Johansson B (2000) Quasi – Ab initio molecular dynamic study of Fe melting. *Physical Review Letters* 84: 3638–3641.

Bi Y, Tan H, and Jin F (2002) Electrical conductivity of iron under shock compression up to 200 GPa. *Journal of Physics: Condensed Matter* 14: 10849–10854.

Bloxham J (2000) Sensitivity of the geomagnetic axial dipole to thermal core–mantle interactions. *Nature* 405: 63–65.

Boehler R (1993) Temperatures in the Earth's core from melting-point measurements of iron at high static pressures. *Nature* 363: 534–536.

Bouhifd MA, Gautron L, Bolfan-Casanova N, et al. (2007) Potassium partitioning into molten alloys at high pressure: Implications for Earth's core. *Physics of the Earth and Planetary Interiors* 160: 22–33.

Braginsky SI (1963) Structure of the F layer and reasons for convection in the Earth's core. *Doklady Akademii Nauk SSSR* 149: 1311–1314.

Braginsky SI (1999) Dynamics of the stably stratified ocean at the top of the core. *Physics of the Earth and Planetary Interiors* 111: 21–34.

Braginsky SI (2006) Formation of the stratified ocean of the core. *Earth and Planetary Science Letters* 243: 650–656.

Braginsky SI and Roberts PH (1995) Equations governing convection in Earth's core and the geodynamo. *Geophysical and Astrophysical Fluid Dynamics* 79: 1–97.

Braginsky SI and Roberts PH (2002) On the theory of convection in Earth's core. In: Ferriz-Mas A and Nunez M (eds.) *Advances in Nonlinear Dynamos*, pp. 60–82. London: Taylor & Francis.
Brandon AD, Walker RJ, Puchtel IS, Becker H, Humayun M, and Revillon S (2003) Os-186-Os-187 systematics of Gorgona Island komatiites: Implications for early growth of the inner core. *Earth and Planetary Science Letters* 206: 411–426.
Brown JM and McQueen RG (1986) Phase-transitions, Gruneisen parameter and elasticity for shocked iron between 77 GPa and 400 GPa. *Journal of Geophysical Research* 91: 7485–7494.
Buffett BA (2002) Estimates of heat flow in the deep mantle based on the power requirements for the geodynamo. *Geophysical Research Letters* 29: 1566.
Buffett BA (2010) Chemical stratification at the top of Earth's core: Constraints from observations of nutations. *Earth and Planetary Science Letters* 296: 367–372.
Buffett BA and Christensen UR (2007) Magnetic and viscous coupling at the core–mantle boundary: Inferences from observations of the Earth's nutations. *Geophysical Journal International* 171: 145–152.
Buffett BA, Huppert HE, Lister JR, and Woods AW (1996) On the thermal evolution of the Earth's core. *Journal of Geophysical Research* 101: 7989–8006.
Buffett BA and Seagle CT (2010) Stratification of the top of the core due to chemical interactions with the mantle. *Journal of Geophysical Research* 115: B04407.
Bullard EC (1950) The transfer of heat from the core of the Earth. *Monthly Notices of the Royal Astronomical Society* 6: 36–41.
Cao AM and Romanowicz B (2004) Constraints on density and shear velocity contrasts at the inner core boundary. *Geophysical Journal International* 157: 1146–1151.
Christensen UR (2010) Dynamo scaling laws and applications to the planets. *Space Science Reviews* 152: 565–590.
Christensen UR and Tilgner A (2004) Power requirements of the geodynamo from ohmic losses in numerical and laboratory dynamos. *Nature* 429: 169–171.
Christensen UR and Wicht J (2008) Models of magnetic field generation in partly stable planetary cores: Applications to Mercury and Saturn. *Icarus* 196: 16–34.
Corgne A, Keshav S, Fei YW, and McDonough WF (2007) How much potassium is in the Earth's core? New insights from partitioning experiments. *Earth and Planetary Science Letters* 256: 567–576.
Costin SO and Butler SL (2006) Modelling the effects of internal heating in the core and lowermost mantle on the Earth's magnetic history. *Physics of the Earth and Planetary Interiors* 157: 55–71.
Davies GF (2007) Mantle regulation of core cooling: A geodynamo without core radioactivity? *Physics of the Earth and Planetary Interiors* 160: 215–229.
Davies CJ and Gubbins D (2011) A buoyancy profile for the Earth's core. *Geophysical Journal International* 187: 549–563.
De Koker N, Steinle-Neumann G, and Vlcek V (2012) Electrical resistivity and thermal conductivity of liquid Fe alloys at high P and T, and heat flux in Earth's core. *Proceedings of the National Academy of Sciences of the United States of America* 109: 4070–4073.
Dunlop DJ and Yu Y (2004) Intensity and polarity of the geomagnetic field during Precambrian time. In: Channell JET, et al. (eds.) *Geophysical Monograph Series*, 145, pp. 85–100. American Geophysical Union.
Dziewonksi AM and Anderson DL (1981) Preliminary reference Earth model. *Physics of the Earth and Planetary Interiors* 25: 297–356.
Fiquet G, Auzende AL, Siebert J, et al. (2010) Melting of peridotite to 140 gigapascals. *Science* 329: 1516–1518.
Gaidos E, Conrad CP, Manga M, and Hernlund J (2010) Thermodynamic limits on magnetodynamos in rocky exoplanets. *The Astrophysical Journal* 718: 596–609.
Gando A, et al. (2011) Partial radiogenic heat model for Earth revealed by geoneutrino measurements. *Nature Geoscience* 4: 647–651.
Gessmann CK and Wood BJ (2002) Potassium in the Earth's core? *Earth and Planetary Science Letters* 200: 63–78.
Glatzmaier GA, Coe RS, Hongre L, and Roberts PH (1999) The role of the Earth's mantle in controlling the frequency of geomagnetic reversals. *Nature* 401: 885–890.
Glatzmaier GA and Roberts PH (1996) An anelastic evolutionary geodynamo simulation driven by compositional and thermal convection. *Physica D* 97: 81–94.
Gomi H, Ohta K, Hirose K, et al. (2013) The high conductivity of iron and thermal evolution of the Earth's core. *Physics of the Earth and Planetary Interiors* 224: 88–103.
Greff-Lefftz M and Legros H (1999) Core rotational dynamics and geological events. *Science* 286: 1707–1709.
Gubbins D (1977) Energetics of the Earth's core. *Journal of Geophysics* 43: 453–464.
Gubbins D (2007) Geomagnetic constraints on stratification at the top of the Earth's core. *Earth and Planetary Science Letters* 59: 661–664.
Gubbins D, Alfe D, Masters G, Price GD, and Gillan MJ (2003) Can the Earth's dynamo run on heat alone? *Geophysical Journal International* 155: 609–622.
Gubbins D, Alfe D, Masters G, Price GD, and Gillan MJ (2004) Gross thermodynamics of two-component core convection. *Geophysical Journal International* 157: 1407–1414.
Gubbins D, Masters TG, and Jacobs JA (1979) Thermal evolution of the Earth's core. *Geophysical Journal of the Royal Astronomical Society* 59: 57–99.
Gubbins D, Masters G, and Nimmo F (2008) A thermochemical boundary layer at the base of Earth's outer core and independent estimate of core heat flux. *Geophysical Journal International* 177: 71–80.
Gubbins D, Thomson CJ, and Whaler KA (1982) Stable regions in the Earth's liquid core. *Geophysical Journal of the Royal Astronomical Society* 68: 241–251.
Hage H and Muller G (1979) Changes in dimensions, stresses and gravitational energy of the Earth due to crystallization at the inner core boundary under isochemical conditions. *Geophysical Journal of the Royal Astronomical Society* 58: 495–508.
Hauri EH and Hart SR (1993) Re-Os isotope systematics of HIMU and EMII oceanic island basalts from the South Pacific ocean. *Earth and Planetary Science Letters* 114: 353–371.
Hayashi H, Ohtani E, Terasaki H, and Ito Y (2009) The partitioning of Pt–Re–Os between solid and liquid metal in the Fe–Ni–S system at high pressure: Implications for inner core fractionation. *Geochimica et Cosmochimica Acta* 73: 4836–4842.
Helffrich G and Kaneshima S (2010) Outer-core compositional stratification from observed core wave speed profiles. *Nature* 468: 807–809.
Hernlund JW, Thomas C, and Tackley PJ (2005) A doubling of the post-perovskite phase boundary and structure of the Earth's lowermost mantle. *Nature* 434: 882–886.
Hewitt J, McKenzie DP, and Weiss NO (1975) Dissipative heating in convective flows. *Journal of Fluid Mechanics* 68: 721–738.
Huang HJ, Fei YW, Cai LC, et al. (2011) Evidence for an oxygen-depleted liquid outer core of the Earth. *Nature* 479: 513–516.
Humayun M and Clayton RM (1995) Potassium isotopic constraints on nebular processes. *Meteoritics* 30: 522–523.
Jackson A (2003) Intense equatorial flux spots on the surface of the Earth's core. *Nature* 424: 760–763.
Jacobs JA (1998) Variations in the intensity of the Earth's magnetic field. *Surveys in Geophysics* 19: 139–187.
Jephcoat A and Olson P (1987) Is the inner core of the Earth pure iron. *Nature* 325: 332–335.
Kageyama A, Miyagoshi T, and Sato T (2008) Formation of current coils in geodynamo simulations. *Nature* 454: 1106–1109.
Keeler RN and Royce EB (1971) Electrical conductivity of condensed media at high pressures. In: Caldirola P and Knoepel H (eds.) *Physics of High Energy Density*, 48, pp. 106–125. New York: Academic Press.
Koper KD and Dombrovskaya M (2005) Seismic properties of the inner core boundary from PKiKP/P amplitude ratios. *Earth and Planetary Science Letters* 237: 680–694.
Korenaga J (2003) Energetics of mantle convection and the fate of fossil heat. *Geophysical Research Letters* 30: 1437.
Kuang WL and Bloxham J (1997) An Earth-like numerical dynamo model. *Nature* 398: 371–374.
Labrosse S (2003) Thermal and magnetic evolution of the Earth's core. *Physics of the Earth and Planetary Interiors* 140: 127–143.
Labrosse S, Hernlund JW, and Coltice N (2007) A crystallizing dense magma ocean at the base of the Earth's mantle. *Nature* 450: 866–869.
Labrosse S and Macouin M (2003) The inner core and the geodynamo. *Comptes Rendus Geoscience* 335: 37–50.
Labrosse S, Poirier JP, and Le Mouel JL (2001) The age of the inner core. *Earth and Planetary Science Letters* 190: 111–123.
Labrosse S, Poirier JP, and LeMouel JL (1997) On cooling of the Earth's core. *Physics of the Earth and Planetary Interiors* 99: 1–17.
Laio A, Bernard S, Chiarotti GL, Scandolo S, and Tosatti E (2000) Physics of iron at Earth's core conditions. *Science* 287: 1027–1030.
Landau LD and Lifshitz EM (1959) *Fluid Mechanics*. *Course of Theoretical Physics*, vol. 6. London: Pergamon Press.
Langel RA and Estes RH (1982) A geomagnetic field spectrum. *Geophysical Research Letters* 9: 250–253.
Lassiter JC (2004) Role of recycled oceanic crust in the potassium and argon budget of the Earth: Toward a resolution of the "missing argon" problem. *Geochemistry, Geophysics, Geosystems* 5: Q11012.
Lassiter JC (2006) Constraints on the coupled thermal evolution of the Earth's core and mantle, the age of the inner core, and the origin of the $^{186}Os/^{188}Os$ "core signal" in plume-derived lavas. *Earth and Planetary Science Letters* 250: 306–317.
Lay T, Hernlund J, and Buffett BA (2008) Core-mantle boundary heat flow. *Nature Geoscience* 1: 25–32.
Lay T, Hernlund J, Garnero EJ, and Thorne MS (2006) A post-perovskite lens and D" heat flux beneath the central Pacific. *Science* 314: 1272–1276.

Lay T, Williams Q, and Garnero EJ (1998) The core–mantle boundary layer and deep Earth dynamics. *Nature* 392: 461–468.

Layer PW, Kroner A, and McWilliams M (1996) An Archean geomagnetic reversal in the Kaap Valley pluton, South Africa. *Science* 273: 943–946.

Lee KKM, Steinle-Neumann G, and Jeanloz R (2004) Ab-initio high-pressure alloying of iron and potassium: Implications for the Earth's core. *Geophysical Research Letters* 31: L11603.

Leng W and Zhong S (2008) Controls on plume heat flux and plume excess temperature. *Journal of Geophysical Research* 113: B04408.

Lewis JS (1971) Consequences of the presence of sulfur in the core of the Earth. *Earth and Planetary Science Letters* 11: 130–134.

Lister JR (2003) Expressions for the dissipation driven by convection in the Earth's core. *Physics of the Earth and Planetary Interiors* 140: 145–158.

Lister JR and Buffett BA (1995) The strength and efficiency of thermal and compositional convection in the geodynamo. *Physics of the Earth and Planetary Interiors* 91: 17–30.

Lister JR and Buffett BA (1998) Stratification of the outer core at the core–mantle boundary. *Physics of the Earth and Planetary Interiors* 105: 5–19.

Loper DE (1978) The gravitationally powered dynamo. *Geophysical Journal of the Royal Astronomical Society* 54: 389–404.

Lowrie W and Kent DV (2004) Geomagnetic polarity timescales and reversal frequency regimes. In: Channell JET, et al. (eds.) *Timescales of the Paleomagnetic Field*. *Geophysical Monograph Series*, 145, American Geophysical Union.

Luguet A, Pearson DG, Nowell GM, et al. (2008) Enriched Pt–Re–Os isotope systematics in plume lavas explained by metasomatic sulfides. *Science* 319: 453–456.

Ma YZ, Somayazulu M, Shen GY, Mao HK, Shu JF, and Hemley RJ (2004) In situ X-ray diffraction studies of iron to Earth-core conditions. *Physics of the Earth and Planetary Interiors* 143: 455–467.

Masters G and Gubbins D (2003) On the resolution of density within the Earth. *Physics of the Earth and Planetary Interiors* 140: 159–167.

Matassov G (1977) *The Electrical Conductivity of Iron–Silicon Alloys at High Pressures and the Earth's Core*. PhD Thesis, Lawrence Livermore Laboratory, University of California, CA.

McDonough W (2006) Core composition. In: Gubbins D and Herrero-Bervera E (eds.) *Encyclopedia of Geomagnetism and Paleomagnetism*. Netherlands: Springer.

McDonough W and Sun SS (1995) The composition of the Earth. *Chemical Geology* 120: 223–253.

McElhinny MW and Senanayake WE (1980) Paleomagnetic evidence for the existence of the geomagnetic field 3.5 Ga ago. *Journal of Geophysical Research* 85: 3523–3528.

McNamara AK and Zhong SJ (2004) Thermochemical structures within a spherical mantle: Superplumes or piles? *Journal of Geophysical Research* 109: B07402.

Meibom A (2008) Geochemistry – The rise and fall of a great idea. *Science* 319: 418–419.

Merrill RT, McElhinny MW, and McFadden PL (1996) *The Magnetic Field of the Earth, Paleomagnetism, the Core and the Deep Mantle*. London: Academic Press.

Morard G, Siebert J, Andrault D, et al. (2013) The Earth's core composition from high pressure density measurements of liquid iron alloys. *Earth and Planetary Science Letters* 373: 169–178.

Mosenfelder JL, Asimow PD, and Ahrens TJ (2007) Thermodynamic properties of Mg_2SiO_4 liquid at ultra-high pressures from shock measurements to 200 GPa on forsterite and wadsleyite. *Journal of Geophysical Research* 112: B06208.

Murakami M, Hirose K, Kawamura K, Sata N, and Ohishi Y (2004) Post-perovskite phase transition in $MgSiO_3$. *Science* 304: 855–858.

Murthy VR and Hall HT (1970) The chemical composition of the Earth's core: Possibility of sulfur in the core. *Physics of the Earth and Planetary Interiors* 2: 276–282.

Murthy VR, van Westrenen W, and Fei YW (2003) Experimental evidence that potassium is a substantial radioactive heat source in planetary cores. *Nature* 323: 163–165.

Nakagawa T (2011) Effect of a stably stratified layer near the outer boundary in numerical simulations of a magnetohydrodynamic dynamo in a rotating spherical shell and its implications for Earth's core. *Physics of the Earth and Planetary Interiors* 187: 342–352.

Nakagawa T and Tackley PJ (2010) Influence of initial CMB temperature and other parameters on the thermal evolution of Earth's core resulting from thermochemical spherical mantle convection. *Geochemistry, Geophysics, Geosystems* 11: Q06001.

Nakagawa T and Tackley PJ (2011) Effects of low-viscosity post-perovskite on thermo-chemical mantle convection in a 3D spherical shell. *Geophysical Research Letters* 38: L04309.

Nguyen JH and Holmes NC (2004) Melting of iron at the physical conditions of the Earth's core. *Nature* 427: 339–342.

Nimmo F (2007) Energetics of the core. *Treatise on Geophysics* 8: 31–66.

Nimmo F and Alfe D (2006) Properties and evolution of the Earth's core and geodynamo. In: Sammonds PR and Thompson JMT (eds.) *Advances in Science: Earth Science*. London: Imperial College Press.

Nimmo F, Price GD, Brodholt J, and Gubbins D (2004) The influence of potassium on core and geodynamo evolution. *Geophysical Journal International* 156: 363–376.

Nimmo F and Stevenson D (2000) The influence of plate tectonics on the thermal evolution and magnetic field of Mars. *Journal of Geophysical Research* 105: 11969–11980.

Nomura R, Hirose K, Ozawa H, Ohishi Y, and Hirao N (2012) Partitioning of potassium into the Earth's core and implications for thermal history of the Earth. *American Geophysical Union Fall Meeting* DI33A-2411.

Oganov AR and Ono S (2004) Theoretical and experimental evidence for a post-perovskite phase of $MgSiO_3$ in Earth's D" layer. *Nature* 430: 445–448.

Ohta K, Yagi T, Taketoshi N, et al. (2012) Lattice thermal conductivity of $MgSiO_3$ perovskite and post-perovskite at the core–mantle boundary. *Earth and Planetary Science Letters* 349: 109–115.

Olson PL, Coe RS, Driscoll PE, Glatzmaier GA, and Roberts PH (2010) Geodynamo reversal frequency and heterogeneous core–mantle boundary heat flow. *Physics of the Earth and Planetary Interiors* 180: 66–79.

Pavlov V and Gallet Y (2010) Variations in geomagnetic reversal frequency during the Earth's middle age. *Geochemistry, Geophysics, Geosystems* 11: Q01210.

Poirier J-P (1994) Light elements in the Earth's core: A critical review. *Physics of the Earth and Planetary Interiors* 85: 319–337.

Pozzo M, Davies C, Gubbins D, and Alfe D (2012) Thermal and electrical conductivity of iron at Earth's core conditions. *Nature* 485: 355–359.

Prevot M, Derder ME, McWilliams M, and Thompson J (1990) Intensity of the Earth's magnetic field – Evidence for a Mesozoic dipole low. *Earth and Planetary Science Letters* 97: 129–139.

Puchtel IS, Brandon AD, Humayun M, and Walker RJ (2005) Evidence for the early differentiation of the core from Pt–Re–Os isotope systematics of 2.8 Ga komatiites. *Earth and Planetary Science Letters* 237: 118–134.

Ricolleau A, Fei YW, Corgne A, Siebert J, and Badro J (2011) Oxygen and silicon contents of Earth's core from high pressure metal-silicate partitioning experiments. *Earth and Planetary Science Letters* 310: 409–412.

Roberts PH and Glatzmaier GA (2000) Geodynamo theory and simulations. *Reviews of Modern Physics* 72: 1081–1123.

Roberts PH and Glatzmaier GA (2001) The geodynamo, past, present and future. *Geophysical and Astrophysical Fluid Dynamics* 94: 47–84.

Roberts PH, Jones CA, and Calderwood A (2003) Energy fluxes and ohmic dissipation in the Earth's core. In: Jones CA, et al. (ed.) *Earth's Core and Lower Mantle*, pp. 100–129. London: Taylor & Francis.

Rogers NW, Davies MK, Parkinson IJ, and Yirgu G (2010) Osmium isotopes and Fe/Mn ratios in Ti-rich picritic basalts from the Ethiopian flood basalt province: No evidence for core contribution to the Afar plume. *Earth and Planetary Science Letters* 296: 413–422.

Rubie DC, Frost DJ, Mann U, et al. (2011) Heterogeneous accretion, composition and core–mantle differentiation of the Earth. *Earth and Planetary Science Letters* 301: 31–42.

Schersten A, Elliott T, Hawkesworth C, and Norman M (2004) Tungsten isotope evidence that mantle plumes contain no contribution from the Earth's core. *Nature* 427: 234–237.

Sclater JG, Jaupart G, and Galson D (1980) The heat flow through oceanic and continental crust and the heat loss of the Earth. *Reviews of Geophysics and Space Physics* 18: 269.

Selkin PA and Tauxe L (2000) Long-term variations in palaeointensity. *Philosophical Transactions of Royal Society of London, Series A* 358: 1065–1088.

Shearer P and Masters G (1990) The density and shear velocity contrast at the inner core boundary. *Geophysical Journal International* 102: 491–498.

Shen GY, Mao HK, Hemley RJ, Duffy TS, and Rivers ML (1998) Melting and crystal structure of iron at high pressures and temperatures. *Geophysical Research Letters* 25: 373–376.

Siebert J, Badro J, Antonangeli D, and Ryerson FJ (2013) Terrestrial accretion under oxidizing conditions. *Science* 339: 1194–1197.

Smirnov AV, Tarduno JA, and Evans DAD (2011) Evolving core conditions ca. 2 billion years ago detected by paleosecular variation. *Physics of the Earth and Planetary Interiors* 187: 225–231.

Stacey FD and Anderson OL (2001) Electrical and thermal conductivities of Fe–Ni–Si alloy under core conditions. *Physics of the Earth and Planetary Interiors* 124: 153–162.

Stanley S and Mohammadi A (2008) Effects of an outer thin stably stratified layer on planetary dynamos. *Physics of the Earth and Planetary Interiors* 168: 179–190.

Stelzer Z and Jackson A (2013) Extracting scaling laws from numerical dynamo models. *Geophysical Journal International* 193: 1265–1276.

Stevenson DJ (2010) Planetary magnetic fields: Achievements and prospects. *Space Science Reviews* 152: 651–664.

Stevenson DJ (2012) How to keep a dynamo running in spite of high thermal conductivity. *American Geophysical Union Fall Meeting*. DI11C-03.

Stevenson DJ, Spohn T, and Schubert G (1983) Magnetism and thermal evolution of the terrestrial planets. *Icarus* 54: 466–489.

Tarduno JA, Cottrell RD, Watkeys MK, and Bauch D (2007) Geomagnetic field strength 3.2 billion years ago recorded by single silicate crystals. *Nature* 446: 657–660.

Tarduno JA, Cottrell RD, Watkeys MK, et al. (2010) Geodynamo, solar wind and magnetopause 3.4 to 3.45 billion years ago. *Science* 327: 1238–1240.

Touma J and Wisdom J (2001) Nonlinear core–mantle coupling. *The Astronomical Journal* 122: 1030–1050.

Tsuno K, Frost DJ, and Rubie DC (2013) Simultaneous partitioning of silicon and oxygen into the Earth's core during early Earth differentiation. *Geophysical Research Letters* 40: 66–71.

Valet JP (2003) Time variations in geomagnetic intensity. *Reviews of Geophysics* 41: 1004.

Van der Hilst RD, De Hoop MV, Wang P, Shim SH, Ma P, and Tenorio L (2007) Seismostratigraphy and thermal structure of Earth's core–mantle boundary region. *Science* 315: 1813–1817.

Van Orman JA, Keshav S, and Fei YW (2008) High pressure solid/liquid partitioning of Os, Re and Pt in the Fe–S system. *Earth and Planetary Science Letters* 274: 250–257.

Verhoogen J (1961) Heat balance of the Earth's core. *Geophysical Journal of the Royal Astronomical Society* 4: 276–281.

Wu B, Driscoll P, and Olson P (2011) A statistical boundary layer model for the mantle D" region. *Journal of Geophysical Research* 116: B12112.

Yoo CS, Holmes NC, Ross M, Webb DJ, and Pike C (1993) Shock temperatures and melting of iron at Earth core conditions. *Physical Review Letters* 70: 3931–3934.

Yukutake T (2000) The inner core and the surface heat flow as clues to estimating the initial temperature of the Earth's core. *Physics of the Earth and Planetary Interiors* 121: 103–137.

This page intentionally left blank

8.03 Theory of the Geodynamo

PH Roberts, University of California, Los Angeles, CA, USA

© 2015 Elsevier B.V. All rights reserved.

8.03.1	**Introduction**	57
8.03.1.1	Dynamos and Self-Excited Dynamos	57
8.03.1.2	The Geodynamo Hypothesis	58
8.03.1.3	Plan of Chapter: Notation	59
8.03.2	**Basic Electrodynamics**	59
8.03.2.1	Pre-Maxwell Theory	59
8.03.2.2	Constitutive Relations	60
8.03.2.3	Induction Equation: Magnetic Reynolds Number	61
8.03.2.4	Electromagnetic Energy and Stress	61
8.03.2.5	The Perfect Conductor: Alfvén's Theorem	62
8.03.2.6	The Imperfect Conductor: Reconnection	63
8.03.2.7	The Low Conductivity Approximation	67
8.03.3	**Kinematic Dynamos**	67
8.03.3.1	The Dynamo Condition	67
8.03.3.2	The Torpol Representation	68
8.03.3.3	The Eigenvalue Problem for Steady Flows	70
8.03.3.4	Bounds on the Magnetic Reynolds Number	71
8.03.3.5	Anti-dynamo Theorems (ADTs)	71
8.03.4	**Laminar Dynamos**	73
8.03.4.1	Early Successful Models	73
8.03.4.2	One-Dimensional Models	73
8.03.4.3	Two-Dimensional Models	74
8.03.4.4	Three-Dimensional Models	75
8.03.5	**Turbulent Kinematic Dynamos**	75
8.03.5.1	Field Creation by Cyclonic Turbulence: MFE	75
8.03.5.2	Mean Field Dynamo Models	77
8.03.5.3	Saturation: Intermediate Models	78
8.03.6	**MHD Dynamos**	79
8.03.6.1	Basic Equations and Boundary Conditions: Energetics	79
8.03.6.2	Classical Theory of Rotating Fluids	80
8.03.6.3	Coriolis Magnetohydrodynamics (CMHD)	82
8.03.6.4	MAC Waves and Torsional Waves	84
8.03.6.5	Magnetostrophy	85
8.03.7	**Final Remarks**	87
References		87

8.03.1 Introduction

8.03.1.1 Dynamos and Self-Excited Dynamos

'Dynamo' is the name given to any device that 'induces' electric current to flow through the motion of an electrical conductor in an 'inducing' magnetic field. Dynamos were constructed first in the early nineteenth century, but the first really significant technological advance was made by Siemens (1867). Siemens conceived of, constructed, and in 1866 publically demonstrated the first self-excited dynamo, in which the inducing magnetic field was created by the induced currents; previously, it had been supplied by permanent magnets.

The physical principles governing dynamos are illustrated in Figure 1, where the homopolar dynamo is shown. Here, D is a solid electrically conducting disk rotating with angular velocity $\boldsymbol{\Omega}$ about an axis of symmetry A′A, parallel to which we first suppose (see Figure 1(a)) that there is a uniform externally produced 'inducing field' $\mathbf{B}_0$, such as might be produced by permanent magnets. Through the velocity $\mathbf{u}=\boldsymbol{\Omega}\times\mathbf{x}$ of the conductor, an electromotive force (emf) $\mathbf{u}\times\mathbf{B}_0$ is induced that would, if there were a closed electric circuit, drive a current radially outward from A′A towards the rim R. (Here, $\mathbf{x}$ is the position vector from an origin on A′A.) Instead, positive charges (P) build up on R, and negative charges (N) are set up on the electrically conducting axle. In this way, an electric field $\mathbf{E}$ is created that cancels out the induced emf, as of course is necessary since no current flows.

Now, let a conducting wire W join A′A to R, electrical contact being maintained by sliding contacts (or 'brushes') at S_1 and S_2; see Figure 1(b). Electric charges that in Figure 1(a) were trapped on the rim can now be 'drawn off' as an electric current I flowing along W and across D; the electric circuit has

 http://dx.doi.org/10.1016/B978-0-444-53802-4.00144-5

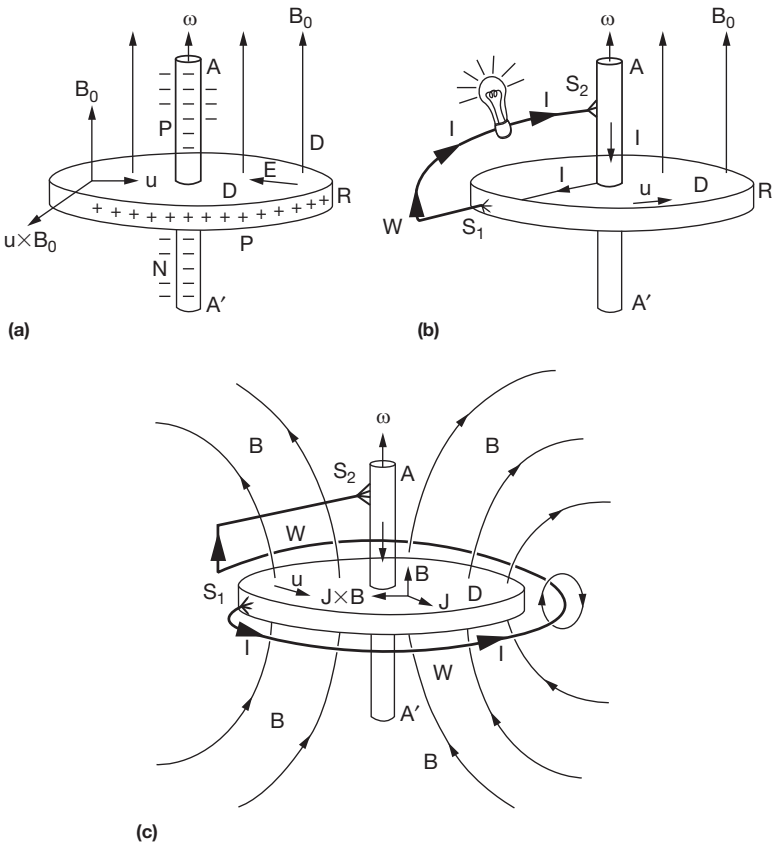

Figure 1 The homopolar dynamo; see text for explanation.

been completed and the electromotive force has become motive! This 'induced current' I can be directed to perform a useful task, such as powering the electric light bulb shown in Figure 1(b), the concomitant expenditure of energy being provided by the energy source that maintains the rotation of D. It is this conversion of mechanical energy into electrical energy that is the essence of the dynamo, in this case a pre-Siemens, non-self-exciting dynamo.

Siemens' idea was to make use of the magnetic field that always accompanies the flow of electric current. Suppose that instead of taking the shortest route between S_1 and S_2, the wire W is wound round and in the plane of D, just outside R and making almost one complete loop around R before being led to the two brushes (Figure 1(c)). The direction of the winding is such that the 'induced magnetic field' $\mathbf{B}$ produced by the current I in the loop reinforces the applied magnetic field $\mathbf{B}_0$. In the plane of D, both fields are perpendicular to the disk, in the same sense $A' \rightarrow A$. Unlike $\mathbf{B}_0$, the magnetic field $\mathbf{B}$ is not uniform across D, so that the emf $\mathbf{u} \times \mathbf{B}$ it creates from the motion does not depend on $\mathbf{x}$ in the same way that $\mathbf{u} \times \mathbf{B}_0$ does, but it can perform the same function. If Ω exceeds some critical value Ω_c, the 'seed magnetic field' $\mathbf{B}_0$ can be removed and the dynamo will continue to operate, the current I being induced by the emf $\mathbf{u} \times \mathbf{B}$ alone. Thereafter, the device will create a magnetic field for as long as an angular velocity greater than Ω_c is maintained. The dynamo has become 'self-excited.'

If we persist in looking only at the electrodynamics of the dynamo, we would believe that if Ω is increased beyond Ω_c, then $\mathbf{B}$ will grow without limit because the rotation of D would create magnetic energy faster than it is destroyed by the electrical resistance of the circuit. This absurdity is removed when we consider the mechanics of the device. A Lorentz force, $\mathbf{J} \times \mathbf{B}$ per unit volume, opposes the rotation $\mathbf{u} = \boldsymbol{\Omega} \times \mathbf{x}$ of the disk; see Figure 1(c). In the marginal state, $\Omega = \Omega_c$, this creates a magnetic torque Γ_B about A′A that is equal and opposite to the applied torque Γ_A that keeps the disk in rotation. An increase in Γ_A makes Ω bigger, but this results in a larger $\mathbf{B}$ and a greater Γ_B. Soon, a new balance between Γ_A and Γ_B is set up with a larger Ω_c.

8.03.1.2 The Geodynamo Hypothesis

The suggestion that the magnetic fields of the Earth and the Sun are produced by self-excited dynamos was first made by Larmor (1919). He visualized that the solid disk in Figure 1 is replaced in the Earth and the Sun by the movement of electrically conducting fluid. His idea gained ground as every other explanation of terrestrial and solar magnetism became increasingly implausible. Paleomagnetic studies found that there are no discernible differences between the normal and reversed polarity states of the geomagnetic field. This is particularly hard to reconcile with any other explanation of geomagnetism but is required of a self-excited dynamo because if $\mathbf{B}(\mathbf{x},t)$ satisfies the governing equations, so does $-\mathbf{B}(\mathbf{x},t)$. Once the seed

field of the homopolar dynamo is removed, magnetic field of either sign can be sustained equally well. The idea that the main geomagnetic field is produced by a dynamo operating in the Earth's fluid core became known as 'the geodynamo hypothesis.'

It is clear from the homopolar dynamo that the geodynamo hypothesis demands answers to two questions. First, without seeking an origin for the fluid motion, can one find a motion that self-generates magnetic field? The answer to this is the 'kinematic dynamo' question is not obvious. The homopolar dynamo has a specially contrived lack of symmetry so that its electric current follows a path that enhances regeneration of magnetic field. In contrast, the Earth's core is a nearly spherically symmetrical mass of electrically conducting material in which no current path is preferred. A dynamo that regenerates magnetic field in such circumstances is called a 'homogeneous dynamo,' but do they exist? Theoreticians were challenged either to prove the answer is 'No' or to create a working model. Nearly four decades elapsed before this challenge was met. During this time, and subsequently, it became increasingly well understood how structural asymmetry in the homopolar dynamo could be mimicked in a homogeneous dynamo by fluid motions that lack mirror symmetry.

Once the kinematic dynamo question had been answered in the affirmative, attention became increasingly focused on different questions: How is the driving motion $\mathbf{u}$ produced? How is it modified by the presence of the magnetic field $\mathbf{B}$ that it itself creates? These are the concerns of 'magnetohydrodynamic dynamo' theory, or 'MHD dynamo theory.' Obviously, the kinematic theory is 'contained' in the MHD theory and is an essential part of it.

8.03.1.3 Plan of Chapter: Notation

The objective of this chapter is to provide the basics of kinematic and MHD dynamo theory. In Section 8.03.2, the basic electromagnetic theory is briefly reviewed, and in Section 8.03.3, the kinematic theory is formulated. Dynamo models driven by laminar and turbulent flows are described in Sections 8.03.4 and 8.03.5. In Section 8.03.6, the ideas behind MHD dynamos are outlined. Discussion is everywhere slanted towards the geophysical application. SI units are used.

To simplify the presentation, some verbal abbreviations will usually be employed: 'velocity' = fluid velocity, 'density' = mass density, 'field' = magnetic field, 'current' = 'electric current density,' 'conductor' = conductor of electricity, 'potential' = electric potential, 'core' = the Earth's core, 'FOC' = fluid outer core, 'SIC' = solid inner core, 'CMB' = core–mantle boundary (radius r_o), 'ICB' = 'inner core boundary' (radius r_i), 'emf' = electromotive force, and 'EM' = either electromagnetism or electromagnetic.

Script letters, $\mathcal{L}$, $\mathcal{T}$, $\mathcal{U}$, $\mathcal{B}$, $\mathcal{J}$, $\mathcal{E}$, …, will indicate typical magnitudes of length, time, velocity, field, current, electric field, …. The angular velocity of the reference frame, $\mathbf{\Omega}$, will be that of the Earth's mantle; it will be assumed to be constant and in the z-direction. Sometimes cylindrical coordinates (s, ϕ, z) will be used and sometimes spherical coordinates (r, θ, ϕ). 'Zonal' will mean 'in the ϕ-direction' and 'meridional' will mean 'lying in meridional planes,' that is, in the planes ϕ = constant. Except for the unit normal $\mathbf{n}$ to surfaces, unit vectors will be denoted by $\mathbf{1}_q$, where the q is the coordinate concerned, ∂_q being short for ∂/∂_q. An exception is ∂_t, which stands for the (Eulerian) time derivative, ∂/∂_t. Except in Section 8.03.5, $\overline{Q}$ denotes the average over ϕ of a quantity Q, and Q' will be short for $Q - \overline{Q}$. The ϕ-averages of the spherical or cylindrical components of a vector $\mathbf{Q}$ define $\overline{\mathbf{Q}}$. A similar notation will be used when turbulence is considered in Section 8.03.5, but there and briefly in Section 8.03.2.6, $\overline{Q}$ denotes the ensemble average of Q in a turbulent environment, and the ϕ average of the ensemble average is denoted by $\overline{\overline{Q}}$.

8.03.2 Basic Electrodynamics

8.03.2.1 Pre-Maxwell Theory

Magnetohydrodynamics is the study of the flow of electrically conducting fluids in the presence of magnetic fields. It has significant applications in technology and in the science of planets, stars, and galaxies. In this volume, its main focus is on its role in explaining the origin and properties of the geomagnetic field.

MHD is based on the equations governing fluid motion in the presence of magnetic fields and the equations governing EM fields in moving fluids. Nearly always, and invariably in geomagnetic studies, the nonrelativistic form of MHD is employed. This is appropriate when conditions are changing slowly, that is, when the characteristic velocity $\mathcal{U}$ of the conductor is small compared with the velocity of light c and when the time $\mathcal{L}/c$ taken by light to cross the system is small compared with all timescales $\mathcal{T}$ of interest. The EM fields are governed by the equations that were in use before Maxwell introduced displacement currents and are therefore called the 'pre-Maxwell equations.' Unlike full Maxwell theory, in which the electric field $\mathbf{E}$ and the magnetic field $\mathbf{B}$ are on an equal footing, $\mathbf{E}$ plays a subsidiary role in pre-Maxwell theory. This is why the magnetic field is usually referred to simply as 'the field.' The aim of this subsection is to review pre-Maxwell theory briefly.

The point-wise form of the pre-Maxwell EM equations is, in SI units,

$$\nabla \times \mathbf{H} = \mathbf{J} \qquad [1a]$$

$$\nabla \times \mathbf{E} = -\partial_t \mathbf{B} \qquad [1b]$$

$$\nabla \cdot \mathbf{B} = 0 \qquad [1c]$$

$$\nabla \cdot \mathbf{D} = \vartheta \qquad [1d]$$

where $\mathbf{J}$ is the current density, $\mathbf{D}$ is the electric displacement, and ϑ is the volume charge density. Equations [1a] and [1b] are, respectively, Ampère's law and Faraday's law. The sources on the right-hand sides of [1a] and [1d] must satisfy charge conservation, and, in pre-Maxwell theory, this requires

$$\nabla \cdot \mathbf{J} = 0 \qquad [1e]$$

which is consistent with [1a]. If [1c] holds for any t, it holds for all t by [1b].

The CMB, and the ICB too, is represented by a 'discontinuity surface,' s, across which material properties change abruptly. The same integral laws that led to [1a]–[1e] imply that

$$\langle \mathbf{n} \times \mathbf{H} \rangle = \mathbf{C} \quad \text{on s} \qquad [2a]$$

$$\langle \mathbf{n} \times (\mathbf{E} + \mathbf{u} \times \mathbf{B}) \rangle = \mathbf{0} \quad \text{on s} \qquad [2b]$$

$$\langle \mathbf{n} \cdot \mathbf{B} \rangle = 0 \quad \text{on s} \qquad [2c]$$

$$\langle \mathbf{n} \cdot \mathbf{D} \rangle = \Theta \quad \text{on s} \qquad [2d]$$

$$\langle \mathbf{n} \cdot \mathbf{J} \rangle = -\nabla_s \cdot \mathbf{C} \quad \text{on s} \qquad [2e]$$

Here, Θ is the surface charge density, $\mathbf{C}$ is the surface current density, ∇_s is the two-dimensional surface divergence, $\mathbf{n}$ is the unit vector to s, and $\langle Q \rangle$ is the difference in limiting values of a quantity Q at P, evaluated on opposite sides of s; $\mathbf{u} \times \mathbf{B}$ appears in [2b] because $\mathbf{u}$, the velocity of point P on s, may be discontinuous on s. Simplifications of conditions [2] will be derived in Section 8.03.2.6.

Geodynamo theory is mainly concerned with timescales much shorter that those over which the Earth evolves. It is then a good approximation to take $\mathbf{n} \cdot \mathbf{u} = 0$ on the CMB and ICB and to assume that these surfaces are spherical, of radii r_o and r_i, on which $\mathbf{n}$ $(=1_r)$ is radial.

8.03.2.2 Constitutive Relations

The pre-Maxwell equations must be supplemented by relations that define the physical nature of the medium in which they are applied. We shall suppose that every medium is isotropic and homogeneous so that at a point P within it and in a reference frame moving with the constant uniform velocity $\mathbf{u}_P = \mathbf{u}(\mathbf{x}_P)$ of P,

$$\mathbf{H}' = \mathbf{B}'/\mu_P \qquad [3a]$$

$$\mathbf{D}' = \varepsilon_P \mathbf{E}' \qquad [3b]$$

$$\mathbf{J}' = \sigma_P \mathbf{E}' \qquad [3c]$$

where μ, ϵ, and σ are the permeability, permittivity, and electrical conductivity of the medium. Except in the crust, the temperature within the Earth everywhere exceeds the Curie point, at which permanent ferromagnetism ceases to exist. We shall usually ignore the crust (see the succeeding text) and assume that everywhere $\mu = \mu_0 = 4\pi \times 10^{-7}$ H m^{-1}, the vacuum permeability; ϵ may differ from the vacuum permittivity ϵ_0 $(=1/c^2\mu_0)$.

To apply [3], it is necessary to relate $\mathbf{B}'$, $\mathbf{E}'$, $\mathbf{H}'$, $\mathbf{D}'$, and $\mathbf{J}'$ to $\mathbf{B}$, $\mathbf{E}$, $\mathbf{H}$, $\mathbf{D}$, and $\mathbf{J}$. To relate them at $\mathbf{x}_P$, the Lorentz transformation is approximated by its nonrelativistic (Galilean) form, appropriate for $\mathcal{U} \ll c$:

$$\mathbf{x} = \mathbf{x}' + \mathbf{u}_P t' \qquad [4a]$$

$$t = t' \qquad [4b]$$

The EM fields and sources in the two reference frames are related by

$$\mathbf{B}' = \mathbf{B} \qquad [5a]$$

$$\mathbf{E}' = \mathbf{E} + \mathbf{u}_P \times \mathbf{B} \qquad [5b]$$

$$\mathbf{H}' = \mathbf{H} \qquad [5c]$$

$$\mathbf{D}' = \mathbf{D} + \mathbf{u}_P \times \mathbf{H}/c^2 \qquad [5d]$$

$$\mathbf{J}' = \mathbf{J} \qquad [5e]$$

$$\vartheta' = \vartheta - \mathbf{u}_P \cdot \mathbf{J}/c^2 \qquad [5f]$$

Since $\nabla' = \nabla$ and $\partial_t' = \partial_t + \mathbf{u}_P \nabla$ according to [4a], [4b], it follows from [5] that [1] also hold in the primed frame of reference, that is, the pre-Maxwell equations are frame-indifferent. According to [5], only $\mathbf{E}$, $\mathbf{D}$, and ϑ are frame-dependent. When translated back to the original frame, [3] are

$$\mathbf{H} = \mathbf{B}/\mu_0 \qquad [6a]$$

$$\mathbf{D} = \varepsilon \mathbf{E} + (\varepsilon - \varepsilon_0)\mathbf{u} \times \mathbf{B} \qquad [6b]$$

$$\mathbf{J} = \sigma(\mathbf{E} + \mathbf{u} \times \mathbf{B}) \qquad [6c]$$

The suffix P has been removed since these relations hold for every P. After its removal, $\mathbf{u}$, σ, and ϵ in [6] may be functions of $\mathbf{x}$.

Wherever $\mathbf{H}$ occurs, we shall now use [6a] to remove it, in favor of $\mathbf{B}$. Equation [6c] is the generalization of 'Ohm's law' to a moving conductor and is centrally important. By [1a], [6a], and [6c],

$$\mu_0 \mathbf{J} = \nabla \times \mathbf{B} \qquad [6d]$$

$$\mathbf{E} = -\mathbf{u} \times \mathbf{B} + \eta \nabla \times \mathbf{B} \qquad [6e]$$

where $\eta = 1/\mu_0\sigma$ is the 'magnetic diffusivity.' The form [6e] of Ohm's law provides a convenient way of removing $\mathbf{E}$ in favor of $\mathbf{B}$; as mentioned earlier, $\mathbf{E}$ plays a subsidiary role in MHD as do $\mathbf{D}$ and ϑ. Nevertheless, it is worth observing that by [1d], [1e] and [6b], [6c],

$$\vartheta = -\varepsilon_0 \nabla \cdot (\mathbf{u} \times \mathbf{B}) + \mathbf{J} \cdot \nabla(\varepsilon/\sigma) \qquad [6f]$$

Unlike the case of a stationary conductor for which an initial ϑ flows to the boundaries in a time of order $\epsilon_0/\sigma = O(\eta/c^2)$ (i.e., instantaneously according to pre-Maxwell theory), the free charge density in a moving conductor is given by [6f] and is generally nonzero.

Because of uncertainty in the magnitude of σ in the core, it is usual to suppose that it is the same everywhere, a typical estimate being $\sigma = 4 \times 10^5$ S m^{-1} so that $\eta = 2$ m^2 s^{-1}. We shall assume this value in the succeeding text. A recent first-principles calculation has however given, for an iron mixture under core conditions, $\sigma = 1.1 \times 10^6$ S m^{-1}, and therefore, $\eta = 0.7$ m^2 s^{-1} (Pozzo et al., 2012). Some implications of this very different η, and our continued use of $\eta = 2$ m^2 s^{-1} in this chapter, are topics discussed in Section 8.03.5.1. In other planets, such as the gas giants Jupiter and Saturn, σ depends strongly on depth into the planet, and the assumption of uniform η may lead to significant errors.

Because of its permanent magnetization, [6a] does not hold in the Earth's crust where the permeability exceeds μ_0 and depends on $\mathbf{x}$; as in [3a], $\mathbf{H} = \mathbf{B}/\mu$ applies with $\mu = \mu(\mathbf{x})$. The presence of crustal magnetization prevents the harmonic parts of the observed $\hat{\mathbf{B}}$ at the Earth's surface from being extrapolated to the CMB; see Section 8.03.3.1. Only the dipole, quadrupole, and fields of harmonic number $n \lesssim 13$ are accessible at the CMB. This 'magnetic curtain,' as Roberts and King (2014) christened it, hides all knowledge of variations in $\hat{\mathbf{B}}$ over the CMB of wavelength less than about 300 km. The electrical conductivity of the mantle, $\hat{\sigma}$, is apparently small. Its inductive effect shields, from observation at the Earth's surface, only fields at the CMB whose timescales are of order 1 year or shorter. Such fields are associated with short wavelength variations of $\mathbf{B}$ over the CMB, which cannot be observed at the Earth's surface because of crustal magnetization. Although this encourages one to set $\hat{\sigma} = 0$, the mantle can then hold a permanent charge whose density, $\hat{\vartheta}$, is unrelated to the dynamo but which makes an irrelevant

contribution to the electric field, $\hat{\mathbf{E}}$, in the mantle. We shall therefore also assume that $\hat{\vartheta}=0$, so that $\hat{\mathbf{E}}$ is solely created by the charge density, Θ, on the CMB.

8.03.2.3 Induction Equation: Magnetic Reynolds Number

The elimination of $\mathbf{E}$ between [1b] and [6e] shows that $\mathbf{B}$ obeys the 'induction equation':

$$\partial_t \mathbf{B} = \nabla \times (\mathbf{u} \times \mathbf{B}) - \nabla \times (\eta \nabla \times \mathbf{B}) \qquad [7]$$

For uniform η, [1c] shows that [7] can be rewritten as

$$\partial_t \mathbf{B} = \nabla \times (\mathbf{u} \times \mathbf{B}) + \eta \nabla^2 \mathbf{B} \qquad [8]$$

Another useful form of the induction equation is

$$d_t \mathbf{B} = (\mathbf{B} \cdot \nabla)\mathbf{u} - \mathbf{B}\nabla \cdot \mathbf{u} + \eta \nabla^2 \mathbf{B} \qquad [9a]$$

which follows from [8], [1c], and the vector identity

$$\nabla \times (\mathbf{u} \times \mathbf{B}) = (\mathbf{B} \cdot \nabla)\mathbf{u} - (\mathbf{u} \cdot \nabla)\mathbf{B} + \mathbf{u}\nabla \cdot \mathbf{B} - \mathbf{B}\nabla \cdot \mathbf{u} \qquad [9b]$$

Here, $d_t = \partial_t + \mathbf{u}\nabla$ is the motional or 'Lagrangian' derivative, that is, the derivative following the motion of the conductor. Sometimes, the term 'the dynamo equation' is applied to one or other of these three forms of the induction equation, but this is a misnomer, since they apply in many contexts totally unrelated to dynamo theory.

MHD processes in a rotating body such as the core are usually most readily studied using a reference frame rotating with the body. With the understanding that $\mathbf{u}$ is the velocity relative to the rotating frame, the same relations [6] hold and lead to the same induction equations. In what follows, the reference frame rotates with the mantle.

Equation [8] exposes the evolution of $\mathbf{B}$ as a competition between EM induction (through $\nabla \times (\mathbf{u} \times \mathbf{B})$) and ohmic diffusion (through $\eta \nabla^2 \mathbf{B}$). The relative importance of these effects is quantified by

$$\mathrm{Rm} = \mathcal{U}\mathcal{L}/\eta = \mu_0 \sigma \mathcal{U}\mathcal{L} \qquad [10a]$$

The values $\mathcal{U} = 2 \times 10^{-4}\,\mathrm{m\,s^{-1}}$, $\mathcal{L} = 2 \times 10^{6}\,\mathrm{m}$, and $\eta = 2\ \mathrm{m^2\,s^{-1}}$ lead to Rm=200. In analogy with the familiar (kinetic) Reynolds number $\mathrm{Re} = \mathcal{U}\mathcal{L}/\nu$ used in fluid mechanics to quantify the effects of the (kinematic) viscosity ν, Rm is called the 'magnetic Reynolds number.' It can also be written as the ratio

$$\mathrm{Rm} = \mathcal{T}_\eta / \mathcal{T}_u \qquad [10b]$$

of the 'electromagnetic diffusion time' $\mathcal{T}_\eta = \mathcal{L}^2/\eta$ to the 'fluid advection time' $\mathcal{T}_u = \mathcal{L}/\mathcal{U}$. The former quantifies the time in which a current system of scale $\mathcal{L}$ in a conductor will decay ohmically, unless some agency maintains it. For the Earth, $\mathcal{T}_\eta \approx 2 \times 10^5$ years, if we take $\mathcal{L} = r_o$. The Earth is known to have possessed a field for at least 3.4×10^9 years (Kono and Tanaka, 1995). Thus, the Earth's magnetic field is not a 'legacy of the past'; an agency is required to maintain the current system, and, according to the geodynamo hypothesis, this is electromagnetic induction created by the term $\mathbf{u} \times \mathbf{B}$ in eqn [8]. For the dynamo to be successful, this term must create new flux as rapidly as, or more rapidly than, it is destroyed by the $\eta \nabla^2 \mathbf{B}$ term. This implies that $\mathcal{T}_u < \mathcal{T}_\eta$ and $\mathrm{Rm} > 1$. Most kinematic dynamo models require that $\mathcal{T}_\eta$ exceeds $\mathcal{T}_u$ by at least one, but more probably two, order of magnitude.

Although a unique value of Rm for a system may be defined by choosing values of $\mathcal{U}$ and $\mathcal{L}$ characteristic of the system as a whole, it is often useful (as in Section 8.03.2.6) to regard Rm as a function of $\mathbf{x}$ defined by, for example, $\mathcal{U} = |\mathbf{u}(\mathbf{x})|$ and a typical length, $\mathcal{L}_0$, such as a typical inverse gradient of the field, for example, $\mathcal{L}_0 = |\mathbf{B}(\mathbf{x})|/\mu_0|\mathbf{J}(\mathbf{x})|$, as suggested by Ohm's law [6e], or $\mathcal{L}_0$ might be the radius of curvature of the field line through $\mathbf{x}$. (A field line is a curve that is everywhere parallel to the magnetic field $\mathbf{B}$.) Writing Rm as

$$\mathrm{Rm}(\mathbf{x}) = \mathcal{U}/\mathcal{U}_\eta \qquad [10c]$$

where

$$\mathcal{U}_\eta = \eta/\mathcal{L}_0 \qquad [10d]$$

exposes $\mathcal{U}_\eta$ as a speed with which field lines diffuse through the conductor, this being large compared with the fluid velocity wherever $\mathrm{Rm}(\mathbf{x}) \ll 1$, as happens where field gradients are large. The westward drift velocity on the CMB of recognizable features of the geomagnetic field is of order $4 \times 10^{-4}\ \mathrm{m\,s^{-1}}$. It is likely that part of this motion is due to the diffusion of the features relative to the fluid (see Section 8.03.2.6). Then the westward drift velocity would tend to overestimate the flow speed $\mathcal{U}$.

Tobias et al. (2011) suggest that the scales mainly responsible for generating the geomagnetic field are those for which $\mathrm{Rm}(\mathbf{x}) \approx 1$, i.e., $\mathcal{L}_0 = \eta/\mathcal{U} \approx 10^4\,\mathrm{m}$. This represents a compromise: larger scale fields are mainly advected by the flow (see Section 8.03.2.5), while fields of smaller scale are heavily damped ohmically (see Section 8.03.2.7). When the length scale of $\mathbf{u}$ is 10^4 m, the induction eqn [7] can be readily solved for $\mathbf{B}$. The solution of the momentum equation governing $\mathbf{u}$ presents severe difficulties however. The FOC is a liquid metal of small viscosity, ν, and its magnetic Prandtl number, $\mathrm{Pm} = \nu/\eta$, is only about 10^{-6}. Hence $\mathrm{Rm}(\mathbf{x}) \approx 1$ implies that the corresponding kinetic Reynolds number, $\mathrm{Re}(\mathbf{x}) = \mathrm{Rm}(\mathbf{x})/\mathrm{Pm} \approx 10^6$. Plausibly the FOC is in turbulent motion mainly operating in the computationally inaccessible sub-grid scales. For convenience, the turbulence is often taken as isotropic though, in reality, it is likely to be highly anisotropic because of Coriolis, Lorentz, and buoyancy forces. It is unknown whether turbulence in the FOC creates a significant secondary source of large-scale magnetic field, as it can in large bodies of plasma such as the solar convection zone. Section 8.03.5 below is devoted to turbulent induction.

Kinematic dynamo theory rests on the induction eqn [8] and Gauss's law [1c]. It assumes that $\mathbf{u}$ is given, but it would make no sense to study physically meaningless flows. We shall restrict ourselves to 'eligible flows' that, for example, have no point sources or sinks and that are everywhere and at all times bounded. Some models will involve discontinuous $\mathbf{u}$, that is, 'tearing' of the fluid, but these models can be simply modified so that the tearing is replaced by a large but finite shear (see Section 8.03.2.6). For simplicity, it will usually be assumed that the fluid is incompressible:

$$\nabla \cdot \mathbf{u} = 0 \qquad [11]$$

Some results will apply to compressible fluids too.

8.03.2.4 Electromagnetic Energy and Stress

It follows from [1a], [1b] that

$$\partial_t e^B + \nabla \cdot \mathbf{I}^B = -\mathbf{E} \cdot \mathbf{J} \qquad [12a]$$

where e^B is the EM energy per unit volume and $\mathbf{I}^B$ is the EM energy flux (or 'Poynting vector'):

$$e^B = B^2/2\mu_0 \qquad [12b]$$

$$\mathbf{I}^B = \mathbf{E}\times\mathbf{B}/\mu_0 \qquad [12c]$$

When integrated over a volume v bounded by a surface s, [12a] states that magnetic energy in v diminishes through its outward flow across s and by the rate at which the EM field transfers its energy to the material contents of v. By [6c], the latter has two parts:

$$-\mathbf{E}\cdot\mathbf{J} = -q^J - \mathbf{u}\cdot\mathbf{L} \qquad [12d]$$

where

$$\mathbf{L} = \mathbf{J}\times\mathbf{B} \qquad [12e]$$

$$q^J = J^2/\sigma \geq 0 \qquad [12f]$$

Here, $\mathbf{L}$, the 'Lorentz force,' is the force per unit volume that the EM field exerts on the conductor and q^J, which is necessarily nonnegative, is the rate per unit volume at which EM energy is converted into heat through electrical resistance. This is called the 'Joule dissipation' or 'ohmic dissipation.'

On combining [12a], [12d] and integrating over v, it follows that

$$\frac{\mathrm{d}\mathcal{M}}{\mathrm{d}t} = -\mathcal{Q}_J - \mathcal{F} - \oint_s (\mathbf{I}^B\cdot\mathbf{n})\,\mathrm{d}^2x \qquad [13a]$$

where

$$\mathcal{M} = \int_v e^B \mathrm{d}^3x \qquad [13b]$$

is the magnetic energy contained in v,

$$\mathcal{Q}_J = \int_v \frac{J^2}{\sigma}\,\mathrm{d}^3x \qquad [13c]$$

is total Joule dissipation, and

$$\mathcal{F} = \int_v \mathbf{u}\cdot\mathbf{L}\,\mathrm{d}^3x \qquad [13d]$$

is the rate of working of the Lorentz force. The Poynting flux, $\mathbf{n}\cdot\mathbf{I}^B$, is continuous across discontinuity surfaces such as the CMB or ICB. (For $\eta \neq 0$, this follows from [23a], [23b].) Assuming that $\hat{\mathbf{B}}$ vanishes at infinity, the total magnetic energy in all space is $\mathcal{M} + \hat{\mathcal{M}}$ where

$$\hat{\mathcal{M}} = \int_{\hat{v}} \hat{e}^B \mathrm{d}^3x \qquad [13e]$$

is the magnetic energy in $\hat{v}$, for which

$$\frac{\mathrm{d}\hat{\mathcal{M}}}{\mathrm{d}t} = \oint_s (\mathbf{I}^B\cdot\mathbf{n})\,\mathrm{d}^2x \qquad [13f]$$

The evolution of the total magnetic energy

$$\mathcal{M}_{\mathrm{tot}} = \mathcal{M} + \hat{\mathcal{M}} = \int_{v+\hat{v}} e^B \mathrm{d}^3x \qquad [13g]$$

is therefore governed by

$$\frac{\mathrm{d}}{\mathrm{d}t}\mathcal{M}_{\mathrm{tot}} = -\mathcal{Q}_J - \mathcal{F} \qquad [13h]$$

In an electric motor, $\mathcal{F}$ is positive and represents the conversion rate of EM energy into mechanical energy. In a dynamo, the opposite is true: Kinetic energy is transformed into EM energy, and the last term in [13h] is large enough to make good the integrated ohmic losses $\mathcal{Q}_J$. This chapter, and indeed this entire volume, focuses on negative $\mathcal{F}$ and dynamo action.

The EM force and torque (about the origin of $\mathbf{x}$) on the contents of v are

$$\mathbf{f} = \int_v \mathbf{L}\,\mathrm{d}^3x = \int_v \mathbf{J}\times\mathbf{B}\,\mathrm{d}^3x \qquad [14a]$$

$$\mathbf{\Gamma} = \int_v \mathbf{x}\times\mathbf{L}\,\mathrm{d}^3x = \int_v \mathbf{x}\times(\mathbf{J}\times\mathbf{B})\,\mathrm{d}^3x \qquad [14b]$$

By using [1a], [1c], and [12e], it is possible, and often useful, to express $\mathbf{f}$ and $\mathbf{\Gamma}$ as surface integrals. This is achieved by reexpressing $\mathbf{L}$ as the divergence of the EM stress tensor $\overleftrightarrow{\pi}^B$:

$$L_i = \nabla_j \pi^B_{ij} \qquad [15]$$

$$\pi^B_{ij} = \frac{B_iB_j}{\mu_0} - \frac{B^2}{2\mu_0}\delta_{ij} = \pi^B_{ji} \qquad [16a]$$

The first term on the right-hand side of [16a] represents tension in a field line; the final term in [16a] represents an isotropic magnetic pressure, $P_m = B^2/2\,\mu_0$, which is about 4 atm for a field of 1 T. These interpretations will be useful in Sections 8.03.2.5 and 8.03.2.6.

By using [16a], $\mathbf{f}$ and $\mathbf{\Gamma}$ may be replaced by surface integrals:

$$f_i = \oint_s \pi^B_{ij} n_j \mathrm{d}^2x \qquad [16b]$$

$$\Gamma_i = \oint_s \epsilon_{ijk} x_j \pi^B_{kl} n_l \mathrm{d}^2x \qquad [16c]$$

Equivalently,

$$\mathbf{f} = \oint_s \left[\frac{\mathbf{B}(\mathbf{B}\cdot\mathbf{n})}{\mu_0} - \frac{B^2}{2\mu_0}\mathbf{n}\right]\mathrm{d}^2x \qquad [16d]$$

$$\mathbf{\Gamma} = \oint_s \mathbf{x}\times\left[\frac{\mathbf{B}(\mathbf{B}\cdot\mathbf{n})}{\mu_0} - \frac{B^2}{2\mu_0}\mathbf{n}\right]\mathrm{d}^2x \qquad [16e]$$

According to the pre-Maxwell theory, the magnetic field alone determines the electric force on the conductor, the electric stresses, and the electric energy. The corresponding contributions made by the electric field are smaller by a factor of order $(\mathcal{U}/c)^2$.

8.03.2.5 The Perfect Conductor: Alfvén's Theorem

A 'perfect conductor' is one of infinite electrical conductivity σ, that is, $\eta = 0$. Since $\mathbf{J}$ must be finite even though $\sigma = \infty$, Ohm's law [6e] implies that

$$\mathbf{E} = -\mathbf{u}\times\mathbf{B} \quad (\text{if } \sigma = \infty) \qquad [17]$$

The induction equations [8] and [9a] can be written as

$$\partial_t\mathbf{B} = \nabla\times(\mathbf{u}\times\mathbf{B}) \quad (\text{if } \sigma = \infty) \qquad [18]$$

or as

$$d_t\mathbf{B} = \mathbf{B}\cdot\nabla\mathbf{u} - \mathbf{B}\nabla\cdot\mathbf{u} \quad (\text{if } \sigma = \infty) \qquad [19]$$

In a perfect conductor, the magnetic Reynolds number, Rm, is infinite by [10a]. While $\mathrm{Rm} \gg 1$ in many applications of

MHD (including some considered here), $\mathrm{Rm}=\infty$ is an idealization that is never achieved. It is however often helpful because of

Alfvén's theorem: Magnetic flux tubes move with a perfect conductor as though frozen to it.

A flux tube is a 'bundle' of field lines. It is defined by a 'cross section' Σ, the tube being the volume occupied by all the field lines intersecting Σ. The surface, M, of the tube is therefore a 'magnetic surface,' that is, a surface composed of field lines and on which $\mathbf{n}\cdot\mathbf{B}=0$. The net magnetic flux through Σ is

$$F=\int_{\Sigma}\mathbf{B}\cdot\mathbf{n}\,\mathrm{d}^2x \qquad [20]$$

and is called the 'strength' of the tube. It follows from [1c] that F is the same for every cross section of the tube.

Alfvén's theorem can be proved by appealing to the kinematic result

$$d_t(\mathbf{dS})=\mathbf{dS}(\boldsymbol{\nabla}\cdot\mathbf{u})-dS_j\boldsymbol{\nabla}u_j \qquad [21]$$

This describes the change in area and orientation of an element $\mathbf{dS}=\mathbf{n}\mathrm{d}^2x$ of surface area as it is advected with the flow. Combining this with [19], it follows that

$$d_t(\mathbf{B}\cdot\mathbf{dS})=0 \quad (\text{when} \quad \sigma=\infty) \qquad [22a]$$

Therefore (for $\sigma=\infty$),

$$\mathbf{B}\cdot\mathbf{dS}=0 \ \text{ at } \ t=0 \ \text{ implies } \ \mathbf{B}\cdot\mathbf{dS}=0 \ \text{ for all } t \qquad [22b]$$

so that if M is initially a magnetic surface, it is always a magnetic surface. Thus, a flux tube remains a flux tube for all time. Further, [22a] shows that the flux tube preserves its strength F as it moves.

The following examples illustrate how the frozen flux picture, coupled with the concepts of stress and energy developed in Section 8.03.2.4, help in visualizing MHD processes:

- Conversion of kinetic energy into magnetic energy occurs in an incompressible fluid when motions stretch or bend flux tubes; conversely, shortening or straightening field lines creates kinetic energy from magnetic energy. The stretching of field lines stores magnetic energy in much the same way as a rubber band stores elastic energy when it is stretched. If a flux tube of cross-sectional area A_0 containing field B_0 is lengthened from L_0 to L, its cross section will, according to [11], decrease in the same proportion ($A=A_0L_0/L$) and the field within it will increase by the same factor ($B=B_0L/L_0$). The magnetic energy it contains, which is proportional to B^2, is therefore enhanced by a factor of $(L/L_0)^2$ from $(B_0^2/2\mu_0)L_0A_0$ to $(B^2/2\,\mu_0)LA=(B^2/2\,\mu_0)L_0A_0=[(B_0^2/2\mu_0)L_0A_0](L/L_0)^2$. If $L=L_0+\delta$ where $\delta\ll L_0$, the increase in magnetic energy is $(B_0^2/2\mu_0)A_0\delta$. This is the work done by the applied force in stretching the tube by δ in opposition to the magnetic tension $(B_0^2/2\mu_0)A_0$ of the field lines.
- *Alfvén waves* are the result of field line tension. The mass per unit length and the tension of a flux tube of unit cross-sectional area are ρ and B^2/μ_0 so that, as in a taut string, a wave can travel nondispersively in either direction along the flux tube with speed $\sqrt{[(B^2/\mu_0)/\rho]}=B/\sqrt{(\mu_0\rho)}$. This defines the 'Alfvén velocity,' $\mathbf{V}_\mathrm{A}=\mathbf{B}/\sqrt{(\mu_0\rho)}$. It is approximately 1 cm s^{-1} for $B=1$ mT and $\rho=10^4$ kg m^{-3}; the Alfvénic timescale $\mathcal{T}_\mathrm{A}=\mathcal{L}/\mathcal{V}_\mathrm{A}$ is about a decade for $\mathcal{L}=r_o$. In a system such as the core that is rotating with an angular velocity Ω that is large compared with $\mathcal{V}_\mathrm{A}/\mathcal{L}$, Alfvén waves lose much (but not all) of their significance, which is subsumed by 'slow waves,' with velocity $\mathcal{V}_\mathrm{s}=\mathrm{O}(\mathcal{V}_\mathrm{A}^2/2\Omega\mathcal{L})\ll\mathcal{V}_\mathrm{A}$ and timescale $\mathcal{T}_\mathrm{s}=\mathrm{O}(2\Omega\mathcal{L}^2/\mathcal{V}_\mathrm{A}^2)\gg\mathcal{T}_\mathrm{A}$; see Section 8.03.6.4.

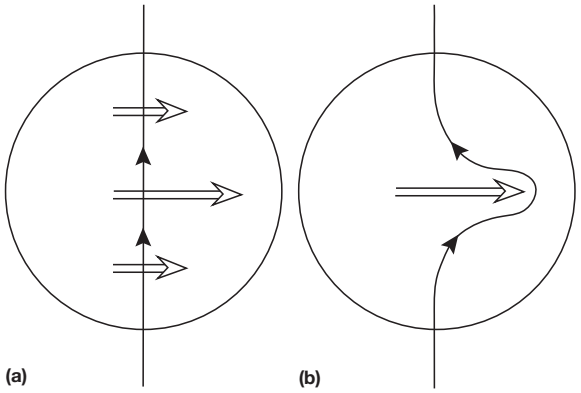

Figure 2 The ω-effect. (a) A field line in a meridian plane (single arrow) is sheared by a zonal flow (double arrows). (b) As a result of the shearing, the field line is bent, so creating a ϕ-component of **B**.

- A zonal shearing motion $\zeta=\overline{u}_\phi/s$ can drag the lines of force of a meridional field $\overline{\mathbf{B}}_\mathrm{M}$ out of the meridional planes, that is, it can create a zonal component $\overline{B}_\phi$ in $\overline{\mathbf{B}}$ (see Figure 2). Dating from a time when ζ was frequently denoted by ω or Ω, this is often called the 'omega-effect' (ω-effect); in the astrophysical literature, it is more often referred to as the 'Omega-effect' (Ω-effect). Taking Alfvén's theorem literally, $\overline{u}_\phi$ will continue to wind the field lines around the symmetry axis for as long as the motion can be sustained, and $\overline{B}_\phi$ and e^B will increase monotonically. The magnetic stresses grow as the field lines become increasingly stretched in the ϕ-direction until eventually the agency that creates $\overline{u}_\phi$ can no longer maintain it and growth of $\overline{B}_\phi$ ceases. This marks the end of the kinematic regime (in which fluid motion is prescribed a priori and the field grows) and the start of the MHD regime in which the field quenches its own further growth.
- The intermittent character of MHD turbulence is reflected by the existence of flux tubes in which **B** is more intense than in their surroundings. Frequently, **B** is visualized as being discontinuous across the surface M of the tube, which is therefore a current sheet, by [2a]. Because of the field line tension, a closed flux tube will tend to collapse in much the same way as a stretched elastic band contracts when released. If there is no compensating stretching process, the collapse will continue until **B** has subsided to the level of the field in its environment. Similarly, a bent flux tube tends to straighten, returning some of its magnetic energy to the kinetic energy of the fluid frozen onto it; an example is given in the next subsection.

8.03.2.6 The Imperfect Conductor: Reconnection

Strictly speaking, a field line passes through every point in space, but only a finite number of lines can be shown in

sketches of field line topology, where the crowding together of field lines indicates a more intense field. In these sketches, field lines may appear to disconnect and reconnect in a new topology as the field evolves. This phenomenon is called 'reconnection,' the prior disconnection being tacitly assumed.

According to Alfvén's theorem, field line topology is immutable. Fluid lying on a field line always remains on that field line; reconnection of field lines is impossible. This makes the dynamo problem meaningless; the magnetic flux trapped in the conductor can never be lost; it can only be rearranged. One cannot even ask how the conductor acquired its flux originally. Flux can be gained, retained, or lost only by its diffusion relative to the conductor, and diffusion happens only when σ and Rm are not infinite. Every successful dynamo relies on reconnection processes.

When $\eta \neq 0$, the boundary conditions [2] simplify. From a physical standpoint, it is clear that an infinitely thin concentration of current, even if it could be set up initially, would instantly diffuse into a layer of finite thickness, in which $\mathbf{J}$ (though possibly large) is finite. This layer would instantaneously replace the surface current $\mathbf{C}$ by a thin layer of high current density. When $\eta \neq 0$, the conditions [2] reduce to

$$\langle \mathbf{n} \times \mathbf{B} \rangle = \mathbf{0} \quad \text{on s} \qquad [23a]$$

$$\langle \mathbf{n} \times \mathbf{E} \rangle = \mathbf{0} \quad \text{on s} \qquad [23b]$$

$$\langle \mathbf{n} \cdot \mathbf{B} \rangle = 0 \quad \text{on s} \qquad [23c]$$

$$\langle \mathbf{n} \cdot \mathbf{J} \rangle = 0 \quad \text{on s} \qquad [23d]$$

$$\langle \mathbf{n} \cdot \mathbf{D} \rangle = \Theta \quad \text{on s} \qquad [23e]$$

Condition [23d] is superfluous since, according to [1a] and [6a], it is satisfied when [23a] holds. Similarly, [23c] implies that $\langle \mathbf{n} \cdot \partial_t \mathbf{B} \rangle = 0$, so that one (linear combination) of the 2 scalar conditions [23b] is automatically obeyed by [23c]. Thus, only 4 of the 6 scalar conditions [23a]–[23d] are independent. The usual choice is

$$\langle \mathbf{B} \rangle = \mathbf{0} \quad \text{on s} \qquad [24]$$

together with one condition from [23b]. This is often of slight interest, as [23b] merely determines the surface charge density, Θ, in terms of $\langle \mathbf{n} \times \mathbf{u} \rangle$ and $\langle \sigma \rangle$; see Section 8.03.3.1.

Regarding Rm as a function of $\mathbf{x}$ as in Section 8.03.2.3, Alfvén's theorem and the ideas of the last subsection are useful in picturing MHD processes wherever $\mathrm{Rm}(\mathbf{x}) \gg 1$ (i.e., wherever $\mathcal{U} \gg \mathcal{U}_\eta$). Reconnection is, however, likely to be significant wherever $\mathcal{U} \ll \mathcal{U}_\eta$ (i.e., $\mathrm{Rm}(\mathbf{x}) \ll 1$).

The following examples illustrate this idea and reconnection processes:

The ω-Effect. As well as the dynamical process described in the last subsection, there is a kinematic process that halts the production of zonal field by the ω-effect. As $\overline{B}_\phi$ is amplified by the shear ζ, the curvature of the field lines (depicted in Figure 2(b)) grows, and diffusion increasingly acts to straighten them out. They move with the conductor less and less, drifting in the opposite direction with a velocity $\mathcal{U}_\eta$ of order $\varpi\eta$ relative to the conductor, where ϖ is the maximum field line curvature. When $\overline{B}_\phi$ becomes of order $\mathrm{Rm}\overline{\mathbf{B}}_\mathrm{M}$ where $\mathrm{Rm} = \zeta/\eta\varpi^2$, amplification of $\overline{B}_\phi$ ceases, the stretching process being offset by an equal but opposite resistive drift of the field lines through the conductor.

A similar example will be of interest in Section 8.03.3.5: Suppose that $\mathbf{B}$ is created by currents flowing in a spherical conductor. If the radial component of $\mathbf{u}$ vanishes, the collapse of the magnetic field cannot be prevented; resistive drift inexorably carries the field lines inward.

Flux Expulsion. A simple illustration of this phenomenon is provided by a solid sphere of radius a, embedded in a solid conductor with which it is in perfect electrical contact. A uniform magnetic field $\mathbf{B}_0$ is applied, and the sphere is set into rotation with angular velocity $\boldsymbol{\omega}$ about an axis perpendicular to $\mathbf{B}_0$. The appropriate magnetic Reynolds number is $\mathrm{Rm} = \omega a^2/\eta$ and is assumed to be large. To an observer on the surface s of the sphere and rotating with it, the applied field seems to be oscillatory and, since $\mathrm{Rm} \gg 1$, it ultimately penetrates only a short distance, of order $\delta_m = \mathrm{Rm}^{-1/2} a = (\eta/\omega)^{1/2}$, into the sphere. This phenomenon is well known in the EM of solid conductors and is called the 'skin effect,' because the induced currents are confined to a thin 'skin' on s. These currents create a dipolar magnetic field, $\mathbf{b}$, that almost completely excludes $\mathbf{B}_0$ from the interior of the sphere $\mathbf{n} \cdot (\mathbf{B}_0 + \mathbf{b}) \approx 0$ on s. During the time the system evolves into this steady state, the field lines within the sphere gradually diffuse out of it and reconnect in the skin and in the vicinity of the sphere. This process, called 'flux expulsion,' is sketched in Figure 3.

Field lines tend to be similarly expelled from circulating flows in fluid conductors and to be crowded together in EM boundary layers at the edges of the circulations, so forming flux ropes and flux sheets. It might seem at first sight that this can only be detrimental to dynamo action, but this is not necessarily the case. Consider induction by a steady flow. An X-type stagnation point may exist between one circulation and its neighbor. (An example is given in Section 8.03.4.3.) The expelled flux surrounds this point, and, since the streamlines separate there, the field lines almost frozen to them are 'exponentially stretched.' This is an efficient way of transforming kinetic energy into magnetic energy. Even more efficient are flows with chaotic streamlines, that is, flows in which a finite volume of space is filled by only a finite number of streamlines (i.e.,

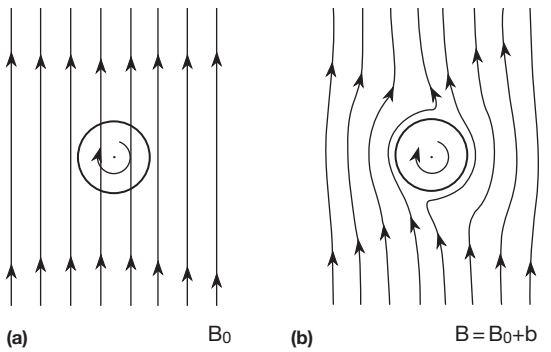

Figure 3 Flux expulsion. (a) A conducting sphere embedded in a similarly conducting, stationary medium lies in a uniform magnetic field $\mathbf{B}_0$ and is set in rotation. (b) The field is ultimately expelled from the sphere.

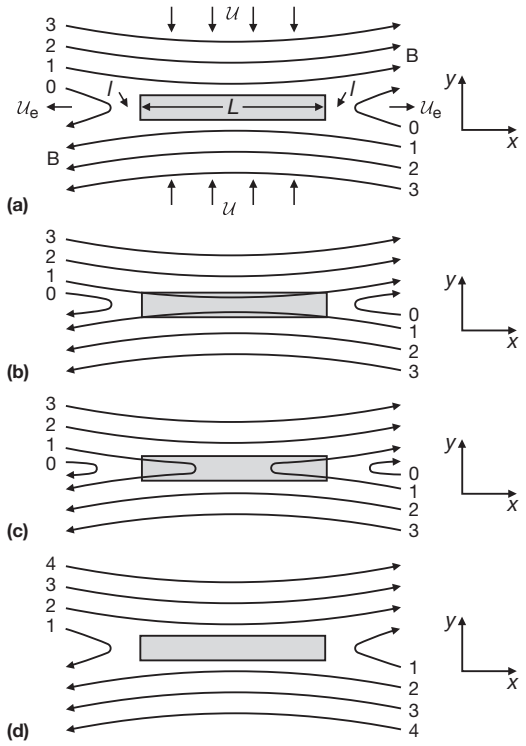

Figure 4 The Sweet–Parker reconnection machine: see text for explanation.

the streamlines do not lie on stream surfaces but fill a volume). Exponential stretching can be even more efficient when the chaos includes time, as in a turbulent flow.

The Sweet–Parker Mechanism (SPM). This, the simplest and most fundamental process of magnetic reconnection, is sketched in Figure 4. A steady flow, $\mathcal{U}$, of a weakly resistive fluid in the $\pm y$-directions forces together two 'slabs' of oppositely directed field $\pm B$ (Figure 4(a)). The slabs are of length $\mathcal{L}$ and the field is approximately in the $\pm x$-directions. As the fluid is incompressible, $\mathbf{u}$ must have nonzero x-components, $\pm\mathcal{U}_e$, as indicated in Figure 4(b). This figure shows (shaded) the formation of a reconnection region $\mathcal{R}$, which has such a small thickness ℓ that it resembles a current sheet. Because $\ell = O(\mathrm{Rm}^{-1/2})\mathcal{L} \ll \mathcal{L}$, ohmic diffusion can break the topological constraint of Alfvén's theorem and allow the field lines in $\mathcal{R}$ to reconnect (Figure 4(c)), even though field lines elsewhere are advected with the flow. The reconnected lines exit from $\mathcal{R}$ in the $\pm x$-directions. A field line labeled 'n' in Figure 4(c) is replaced by a field line '$n+1$' in Figure 4(d). The entire process is then repeated.

Many MHD phenomena appear to be explicable only through 'fast' reconnection, that is, reconnection on the ideal timescale $\mathcal{T}_u$. This is especially true of solar and astrophysical phenomena such as solar flares, but it is widely believed that reconnection in the Earth's core is slow, with a timescale of order $\mathcal{T}_\eta$. Between these two extremes are reconnection processes that are 'intermediate,' that is, operate on a timescale that is short compared with $\mathcal{T}_\eta$ but long compared with $\mathcal{T}_u$. The SPM, which operates on the timescale $(\mathcal{T}_\eta \mathcal{T}_u)^{1/2}$, is of intermediate type.

The SPM is a kinematic reconnection machine, but some dynamical aspects are clear, for example, the curvature of the reconnected field lines in Figure 4(c) assists in ejecting them from $\mathcal{R}$ (Section 8.03.2.5).

The Stretch–Twist–Fold (STF) Dynamo. Start with the flux tube shown in Figure 5(a). As described in Section 8.03.2.4, the field lines in the tube are in tension, and this tension may be systematically increased by a 3-step, stretch–twist–fold process:

Stretch the rubber band to double its length.

Twist it into a Figure 8.

Fold the loops of the 8 on top of one another to form two linked loops of the same size as the original band.

These steps are illustrated in Figure 5(a)–5(c), in which panel (a) depicts the initial flux tube, panel (b) sketches it when it is stretched and twisted, and panel (c) shows it after it is subsequently folded. The energy within and the tension of the flux tube are increased by a factor of 4 in step (i). Steps (ii)–(iii) can in principle be repeated over and over again, the sense of twist in step (ii) being always the same. This gives the tube the sense of 'handedness' of a screw motion, an idea associated in the succeeding text with the concept of 'helicity' and the notion of broken reflection symmetry that is crucial to the success of this dynamo. The tension in the tube increases progressively if steps (i)–(iii) are repeated, and at some stage, the mechanism that is performing those steps can no longer overcome the growing tension in the tube. This marks the end of the kinematic regime (in which fluid motion is prescribed a priori and the field grows) and the start of the MHD regime (in which the field quenches its own further growth). If the band is released at any stage, it will relax back to its initial state (Figure 5(a)). This illustrates the crucial importance of stage (iv) in which ohmic diffusion acts and Alfvén's theorem no longer applies. Reconnection occurs near the point marked 'R' in the flux tube (see Figure 5(c)), where the field gradients are greatest. The result of the reconnection, two separate rings when steps (i)–(iii) are performed only once, is shown in Figure 5(d). Reconnection has 'locked in' the field that was amplified in steps (i)–(iii). Said another way, magnetic reconnection provides the crucial element of irreversibility in the dynamo.

The STF dynamo, originally proposed by Vainshtein and Zeldovich (1972), has become the paradigm for 'fast dynamos,' which are defined as processes of field amplification that operate on timescales independent of $\mathcal{T}_\eta$ in systems where Rm is large; see Childress and Gilbert (1995). Clearly, a fast dynamo necessarily requires fast reconnection, in order to lock in the dynamo-generated field as fast as it is produced (Figure 5).

Parker's α-Effect Mechanism. Alfvén's theorem is useful in visualizing what happens when a helical eddy meets a flux rope. Helical motions are those in which the velocity $\mathbf{u}$ is correlated to the vorticity $\boldsymbol{\zeta}$ so that the 'helicity'

$$H = \mathbf{u}\cdot\boldsymbol{\zeta} \qquad [25a]$$

where

$$\boldsymbol{\zeta} = \nabla \times \mathbf{u} \qquad [25b]$$

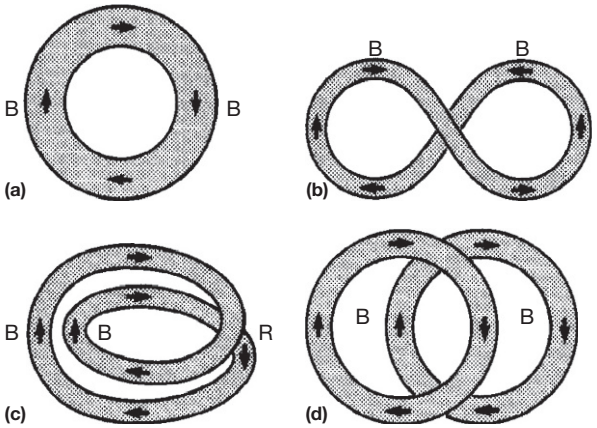

Figure 5 Stretch–twist–fold. (a) A closed flux tube is (b) stretched, twisted, and (c) folded over onto itself, so creating large field gradients near R where one loop detaches from the other, as indicated in (d).

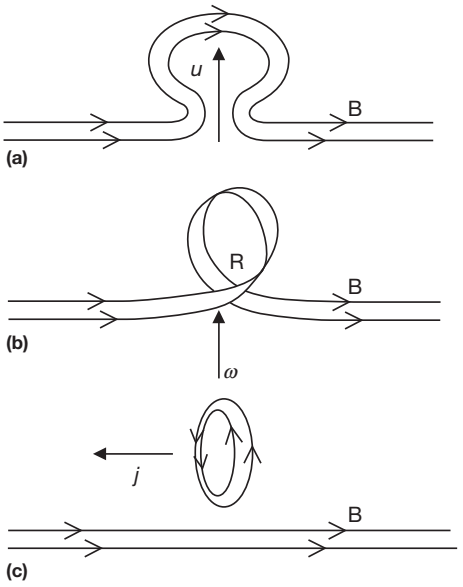

Figure 6 The alpha-effect mechanism. (a) A flux rope bent by the velocity **u** of a cyclonic eddy (b) is twisted by the vorticity $\boldsymbol{\omega}$ of the eddy, creating large field gradients near R where the flux loop detaches as indicated in (c).

is the vorticity. Helicity is the simplest manifestation of a lack of mirror symmetry, and the destruction of this symmetry is often called 'symmetry breaking.' Other helicities that break mirror symmetry are the magnetic helicity $H_B = \mathbf{A}\cdot\mathbf{B}$, where $\mathbf{A}$ is a vector potential of $\mathbf{B}$ (i.e., $\mathbf{B} = \nabla\times\mathbf{A}$); the current helicity $H_J = \mathbf{B}\cdot\mathbf{J}$; and the cross helicity $H_X = \mathbf{u}\cdot\mathbf{B}$. All these felicities have significance in dynamo theory but will not be considered here, apart from a brief reference in Section 8.03.5.1 where magnetic and current felicities are generated by a flow possessing (kinetic) helicity, H.

Helicity is a pseudoscalar, that is, a scalar that changes sign under a reflection of coordinates, either in a plane (e.g., $z\rightarrow -z$) or through the origin ($\mathbf{x}\rightarrow -\mathbf{x}$). It arises naturally in a rotating, convecting system. A helical eddy may be pictured as a screw motion in which a blob of fluid twists around the direction in which it moves. Although the inductive effects of $\mathbf{u}$ and $\boldsymbol{\zeta}$ act simultaneously, it is convenient to consider them successively. The 'vertical' motion $\mathbf{u}$ creates an Ω-shaped indentation on the flux rope, as sketched in Figure 6(a). The twisting motion associated with $\boldsymbol{\zeta}$ turns this Ω out of the plane of the paper. In Figure 6(b), the plane of the Ω is now perpendicular to the initial direction of the flux rope. The field gradients are large near the point marked 'R' in Figure 6(b). Here, diffusion can rapidly detach the Ω as an independent flux loop that, in the idealization depicted here, lies in the plane perpendicular to the flux rope; see Figure 6(c).

Parker (1955) visualized multiple zonal flux tubes and multiple helical eddies producing multiple independent flux loops in the meridian plane, which coalesced to create a meridional field, $\mathbf{B}_M$. This is a field that, according to standard EM theory, could be created by an emf antiparallel to $\mathbf{B}_M$. To describe this phenomenon when the flow is turbulent, we temporarily redefine the overbar to mean the statistical average over the ensemble of states, so that $\mathbf{u} = \overline{\mathbf{u}} + \mathbf{u}'$ where $\mathbf{u}'$ represents the multiple helical eddies, [6e] is replaced by

$$\overline{\mathbf{E}} = -\overline{\mathbf{u}}\times\overline{\mathbf{B}} - \alpha\overline{\mathbf{B}} + \eta\nabla\times\overline{\mathbf{B}} \qquad [26]$$

where α is a pseudoscalar and the presence of $\alpha\overline{\mathbf{B}}$ is called the 'alpha-effect' (α-effect). This is an emf unknown in standard EM theory and gave birth to a new subject called 'mean field electrodynamics.' When the twisting shown in Figure 6(b) is right-handed with respect to the direction of $\overline{\mathbf{u}}$, the helicity [25a] is positive and α in [74] is negative. Similarly, if $H<0$, then $\alpha>0$.

A convecting compressible fluid provides a simple example of [26]: Imagine that the sequence shown in Figure 6 concerns a cold, sinking 'blob' of fluid at high southern latitudes, the top of each panel being nearer than the bottom to the center of the fluid body. As the eddy shown sinks, it compresses under the increasing pressure of its environment but attempts to conserve its angular momentum relative to the inertial frame. This translates, in the reference frame rotating with the fluid body, to an increase in the angular velocity ω of the eddy about the rotation axis, as indicated in Figure 6(b). The sense of helicity is the same for a hot, buoyant blob expanding as it rises through the fluid. This example also indicates a preference for 'right-handed' helicity, $H>0$, in the southern hemisphere of a rotating, convecting, compressible fluid body and 'left-handed' helicity, $H<0$, in its northern hemisphere. In the associated alpha-effect, $\alpha<0$ in the southern hemisphere and $\alpha>0$ in the northern hemisphere. It is clear from [25a] that $|H|\le|\mathbf{u}||\boldsymbol{\zeta}| = O(\mathcal{U}^2/\mathcal{L})$; a 'maximally helical flow' is one in which $|H| = |\mathbf{u}|\,|\boldsymbol{\zeta}|$.Turbulent dynamos, mean field electrodynamics, and the alpha-effect are topics taken further in Section 8.03.5. Meanwhile, we resume using the overbar to denote averages over ϕ.

Alfvén's Twisted Kink (ATK) Dynamo. Take a piece of taut rope and start twisting its ends, as in Figure 7(a). As the result of

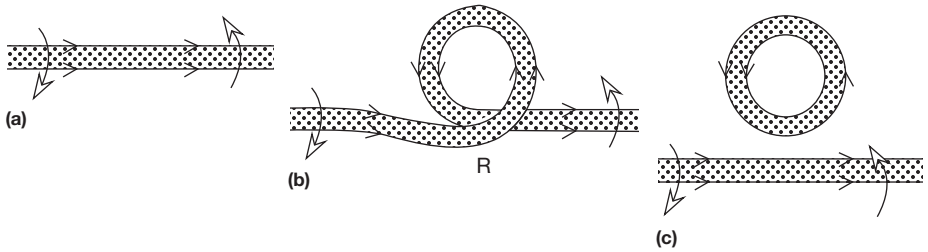

Figure 7 Alfvén's twisted kink dynamo. (a) A flux rope is twisted and (b) becomes unstable to the formation of kinks. The large field gradients near R allow the kink to detach from the rope, as indicated in (c).

an instability, it will develop kinks like those often seen on the cord joining a telephone handset to its cradle (Figure 7 (b)). A magnetic flux rope twisted in the same way will also develop a kink and, because of the large field gradients near the crossing point R in the figure, a tube will detach (Figure 7(c)) and move away from the flux rope. Simultaneously, the torsion of the rope is released but increases again as the twisting continues until further loops detach. The flux rope has become a machine for generating flux tubes. A sufficiently large twisting rate creates a fast dynamo (Alfvén, 1950).

8.03.2.7 The Low Conductivity Approximation

Alfvén's theorem and the ideas just presented in Sections 8.03.2.5 and 8.03.2.6 are useful when $\mathrm{Rm} \gg 1$. We now consider the opposite extreme, the 'low conductivity approximation' in which $\mathrm{Rm} \ll 1$. Since then $\mathcal{T}_\eta \ll \mathcal{T}_u$, the EM field adjusts almost instantaneously to changes in $\mathbf{u}$ so that [1], [2], and [6e] give, to leading order in Rm,

$$\mathbf{E} = -\boldsymbol{\nabla}\Psi \qquad [27a]$$

$$\sigma^{-1}\mathbf{J} = \eta\boldsymbol{\nabla}\times\mathbf{B} = -\boldsymbol{\nabla}\Psi + \mathbf{u}\times\mathbf{B} \qquad [27b]$$

just as though $\mathbf{B}$ were time-independent. By [27b], the Lorentz force [12e] is

$$\mathbf{L} \equiv \mathbf{J}\times\mathbf{B} = \sigma\mathbf{B}\times\boldsymbol{\nabla}\Psi - \sigma B^2\mathbf{u}_\perp \qquad [27c]$$

where $\mathbf{u}_\perp = \mathbf{u} - (\mathbf{u}\cdot\mathbf{B})\mathbf{B}/B^2$ is the component of $\mathbf{u}$ perpendicular to $\mathbf{B}$. This demonstrates that the field opposes the motion in part through an anisotropic 'magnetic friction,' $-\sigma B^2\mathbf{u}_\perp/\rho$ per unit mass. Comparison with the fluid acceleration $\partial_t\mathbf{u}$ shows the importance of $\mathcal{T}_\mathrm{m} = \rho/\sigma B^2 = \eta/V_\mathrm{A}^2$, which is often called the 'magnetic damping time,' not to be confused with the magnetic diffusion time $\mathcal{T}_\eta = \mathcal{L}^2/\eta$. The magnetic damping time is significant in MHD turbulence theory for liquid metals such as the Earth's core. It is independent of $\mathcal{L}$ and, for $\eta = 2\ \mathrm{m^2\ s^{-1}}$ and $V_\mathrm{A} = 1\ \mathrm{cm\ s^{-1}}$, it is the shortest timescale relevant to core dynamics: $\mathcal{T}_\mathrm{m} \approx 6$ h.

The integrated rate of working of the leading-order Lorentz force [27c] is

$$\mathcal{F} \equiv \int_v \mathbf{u}\cdot\mathbf{L}\ \mathrm{d}^3x = -\int_v \mathbf{J}\cdot(\mathbf{u}\times\mathbf{B})\mathrm{d}^3x = -\mathcal{Q}_J - \int_s \Psi\mathbf{J}\cdot\mathbf{n}\ \mathrm{d}^2x \qquad [27d]$$

which is $-\mathcal{Q}_J$ when no current flows across s. The Lorentz force then merely satisfies the ohmic demands of v. In the approximation [27b], the magnetic energy density e^B does not change since, by [27a], $\boldsymbol{\nabla}\cdot\mathbf{I}^B = -\mathbf{E}\cdot\boldsymbol{\nabla}\times\mathbf{B}/\mu_0 = -\mathbf{E}\cdot\mathbf{J}$. When an external source creates a field $\mathbf{B}_0$, motions in v induce a field, $\mathbf{b} = \mathbf{B} - \mathbf{B}_0$, that is of order Rm $\mathbf{B}_0$, which is tiny compared with the field $\mathbf{B}_0$ created by currents flowing outside v. Nevertheless, the currents $\mathbf{J}$ $(=j)$ induced in v, which are $\mathrm{O}(\sigma\mathcal{U}B_0)$, create a Lorentz force of order $\sigma B_0^2\mathcal{U}$, which may significantly alter $\mathbf{u}$. If $\mathrm{Ha} \gg 1$, $\mathbf{L}$ dominates the viscous force $\rho\nu\nabla^2\mathbf{u} = \mathrm{O}(\rho\nu\mathcal{U}/\mathcal{L}^2)$; if $\mathrm{I} \gg 1$, it dominates the inertial force $\rho\mathbf{u}\cdot\boldsymbol{\nabla}\mathbf{u} = \mathrm{O}(\rho\mathcal{U}^2/\mathcal{L})$. Here, Ha is the 'Hartmann number' and I is the 'interaction parameter':

$$Ha = \mathcal{B}\mathcal{L}\left(\frac{\sigma}{\rho\nu}\right)^{1/2} = \frac{\mathcal{V}_A\mathcal{L}}{\sqrt{(\nu\eta)}} \qquad [28]$$

$$I = \frac{\sigma\mathcal{B}^2\mathcal{L}}{\rho\mathcal{U}} = \frac{\mathcal{V}_A^2\mathcal{L}}{\eta\mathcal{U}} \qquad [29]$$

Approximations [27] are commonly applied to laboratory experiments involving liquid metals for which EM induction processes are usually insignificant. It is perhaps surprising though true that, even when the low conductivity approximation is appropriate, it is sometimes helpful to use the concept of frozen-in fields when picturing the evolution of $\mathbf{B}$. This is because, even when $\mathrm{Rm} \ll 1$, there is usually a slight tendency for the field to evolve as it would in a perfect conductor.

When [27] hold, the EM field depends only parametrically on t, but an improved solution may be obtainable as an expansion in Rm, the leading term obeying [27a]. Of course, steady-state solutions of the induction equation for any Rm must satisfy [27b]; see Section 8.03.3.3.

8.03.3 Kinematic Dynamos

8.03.3.1 The Dynamo Condition

The STF and ATK models in Section 8.03.2.6 are heuristic and remote from geophysical needs. This subsection derives more explicitly the condition of self-excitation. We do this in a framework relevant to the core, which we take to be a conducting fluid sphere v surrounded by an insulator $\hat{v}$; see Section 8.03.2.2. Since $\hat{\sigma} = 0$, it follows from [1a]–[1c] and [6a] that outside the core,

$$\boldsymbol{\nabla}\times\hat{\mathbf{B}} = \mathbf{0} \qquad [30a]$$

$$\boldsymbol{\nabla}\cdot\hat{\mathbf{B}} = 0 \qquad [30b]$$

$$\boldsymbol{\nabla}\times\hat{\mathbf{E}} = -\partial_t\hat{\mathbf{B}} \qquad [30c]$$

These imply that $\hat{\mathbf{B}}$ is a potential field:

$$\hat{\mathbf{B}} = -\nabla\hat{V} \qquad [31a]$$

where the 'geopotential,' $\hat{V}$, obeys Laplace's equation

$$\nabla^2\hat{V} = 0 \qquad [31b]$$

In the case of the Earth, [31b] led Gauss to his well-known representation of $\hat{\mathbf{B}}$ at and above the Earth's surface $r = a$:

$$\hat{V} = a\sum_{n=1}^{\infty}\sum_{m=0}^{n}\left[\left(\frac{a}{r}\right)^{n+1}\left(g_n^m\cos m\phi + h_n^m\sin m\phi\right) + \left(\frac{r}{a}\right)^{n}\right.$$
$$\left.\left(\hat{g}_n^m\cos m\phi + \hat{h}_n^m\sin m\phi\right)\right]P_n^m(\theta) \qquad [31c]$$

where $P_n^m(\theta)$ is the (Schmidt-normalized) Legendre function, for which the rms of $P_n^m(\theta)\begin{matrix}\cos\\ \sin\end{matrix} m\phi$ over any sphere of constant r is $4\pi/(2n+1)$. Because the mantle is assumed insulating, we adopt Gauss's expansion everywhere for all $r \geq r_o$.

'Gauss's coefficients' g, h, $\hat{g}$, and $\hat{h}$ in [31c] are time-dependent; the g and h coefficients describe the field produced within v and decreasing with distance from it, while the $\hat{g}$ and $\hat{h}$ coefficients correspond to the fields created by external sources that, according to [31c], are 'at infinity.' The 'dynamo condition' expresses the absence of field sources outside v:

$$\text{Dynamo condition: form 1:}\quad \hat{g}_n^m \equiv 0,\quad \hat{h}_n^m \equiv 0 \qquad [32]$$

When this is enforced, the magnetic field is produced totally by sources within v, and [31c] becomes

$$\hat{V} = r_o\sum_{n=1}^{\infty}\left(\frac{r_o}{r}\right)^{n+1}Y_n(\theta,\phi) \qquad [33a]$$

so that

$$\hat{\mathbf{B}} = \sum_{n=1}^{\infty}\left(\frac{r_o}{r}\right)^{n+2}\left[(n+1)Y_n\mathbf{1}_r - \frac{\partial Y_n}{\partial\theta}\mathbf{1}_\theta - \frac{\partial Y_n}{\sin\theta\,\partial\phi}\mathbf{1}_\phi\right] \qquad [33b]$$

where $Y_n(\theta, \phi)$ is the surface harmonic

$$Y_n(\theta,\phi) = \left(\frac{a}{r_o}\right)^{n+2}\sum_{m=0}^{n}\left(g_n^m\cos m\phi + h_n^m\sin m\phi\right)P_n^m(\theta) \qquad [33c]$$

Equation [33b] shows that the field becomes increasingly dipolar with increasing r, and an alternative way of expressing the dynamo condition is

$$\text{Dynamo condition: form 2:}\quad \hat{\mathbf{B}} = \mathrm{O}\left(r^{-3}\right)\ \text{ for }\ r\to\infty \qquad [34]$$

The three $n = 1$ terms in [33a] define the Earth's centered dipole moment $\mathbf{m}$. This is customarily expressed in terms of $\mathbf{H}$ rather than $\mathbf{B}$ so that $\hat{V}_{\text{dipole}} = \mu_0\mathbf{m}\cdot\mathbf{r}/4\pi r^3$ (the 4π being there because SI are rationalized units). Since $P_1(\theta) = \cos\theta$ and $P_1^1(\theta) = \sin\theta$, it therefore follows that $\mathbf{m} = (4\pi a^3/\mu_0)[g_1^1\mathbf{1}_x + h_1^1\mathbf{1}_y + g_1^0\mathbf{1}_z]$, where $4\pi a^3/\mu_0 \approx 2.580\times\ 10^{27}\,\text{A m}^{-1}\,\text{T}^{-1}$; the z-component of $\mathbf{m}$ defines the 'axial dipole,' and the x- and y-components, the 'equatorial dipole.' The direction of $\mathbf{m}$ and its magnitude m have fluctuated in the geological past, particularly its direction that has undergone polarity reversals; see Kono (2007). The time average of m is $7.8\times10^{22}\,\text{A m}^2$ according to Kono and Tanaka (1995). This is close to its present strength, although m is currently decreasing. Because $g_1^0 < 0$ at present, the angle between $\mathbf{m}$ and Oz, commonly called the 'tilt' of the dipole axis, is large: $\cos^{-1}(m_z/m) \approx 170°$, but more usually, it is expressed as $\cos^{-1}(-m_z/m) \approx 10°$. The five $n = 2$ terms in [33a] represent the quadrupolar part of $\hat{\mathbf{B}}$.

According to [31a] and [33b], the magnetic energy stored outside the core is

$$\hat{\mathcal{M}} = \frac{1}{2\mu_0}\int_{\hat{v}}\hat{B}^2\,\mathrm{d}^3x = \frac{1}{2\mu_0}\int_{\text{CMB}}\hat{V}\hat{B}_r\mathrm{d}^2x = \frac{2\pi r_o^3}{\mu_0}\sum_{n=1}^{\infty}\frac{M_n}{2n+1} \qquad [35a]$$

where

$$M_n = (n+1)\left(\frac{a}{r_o}\right)^{2n+4}\sum_{m=0}^{n}\left[\left(g_n^m\right)^2 + \left(h_n^m\right)^2\right] \qquad [35b]$$

is the Mauersberger–Lowes field spectrum at the CMB, which is B^2 for the nth harmonic averaged over the CMB. This can be computed from observation for $n \lesssim 13$ and is remarkably constant for $n \geq 3$. The constancy of M_n cannot hold for all n, as this would give infinite $\hat{M}$, by [35a].

Since $\mathbf{B} = \hat{\mathbf{B}}$ on the CMB by [24], the dynamo conditions [32] and [34] restrict the solutions of the induction equation on s and therefore in v. They are rather inconvenient conditions as they stand; a simpler, third form will be derived in Section 8.03.3.2. It is important to realize that the boundary conditions [23b], [23e] on $\mathbf{n}\times\mathbf{E}$ and $\varepsilon\mathbf{n}\cdot\mathbf{E}$ at the ICB and CMB do not similarly restrict solutions of the induction equation in v. It was seen in Section 8.03.2.6 that one of the two scalar conditions $\langle\mathbf{n}\times\mathbf{E}\rangle = \mathbf{0}$ could be absorbed into [24] while the other defined Θ on the discontinuity surfaces. This merely gives, through the discontinuity in $\epsilon\mathbf{n}\cdot\mathbf{E}$, the charge density needed to ensure continuity of the normal component of the current flow across these surfaces. In the mantle and beyond, $\hat{\mathbf{E}}$ is uniquely determined by Θ on the CMB, as noted at the end of Section 8.03.2.2. This charge reflects the currents generated in the core and prevents them from entering the mantle.

8.03.3.2 The Torpol Representation

Nearly all investigations of dynamos in the Earth, planets, and stars make use of a simple way of representing the magnetic field $\mathbf{B}$ in a spherical conductor. This automatically satisfies [1c] and separates $\mathbf{B}$ into 'toroidal' and 'poloidal' parts:

$$\mathbf{B} = \mathbf{B}_T + \mathbf{B}_P = \nabla\times(T\mathbf{r}) + \nabla\times\nabla\times(S\mathbf{r}) \qquad [36a]$$

where $T(r, \theta, \phi, t)$ is the 'toroidal scalar' and $S(r, \theta, \phi, t)$ is the 'poloidal scalar.' Obviously, according to [1a] and [36a], the toroidal field $\mathbf{B}_T = \nabla\times(T\mathbf{r})$ is created solely by poloidal currents. A particularly pleasant feature is the reverse: the poloidal field $\mathbf{B}_P = \nabla\times\nabla\times(S\mathbf{r})$ is created solely by toroidal currents, since

$$\mu_0\mathbf{J} = \nabla\times\mathbf{B} = \nabla\times\left(\left[-\nabla^2 S\right]\mathbf{r}\right) + \nabla\times\nabla\times(T\mathbf{r}) \qquad [36b]$$

A second curl shows that $\nabla^2\mathbf{B} = \nabla\times([\nabla^2 T]\mathbf{r}) + \nabla\times\nabla\times([\nabla^2 S]\mathbf{r})$.

In spherical polar components, $\mathbf{B}_T$ and $\mathbf{B}_P$ are

$$\mathbf{B}_T = -\mathbf{r}\times\nabla T = \frac{1}{\sin\theta}\frac{\partial T}{\partial\phi}\mathbf{1}_\theta - \frac{\partial T}{\partial\theta}\mathbf{1}_\phi \qquad [36c]$$

$$\begin{aligned}\mathbf{B}_P &= \boldsymbol{\nabla}\left[\frac{\partial(rS)}{\partial r}\right] - \mathbf{r}\boldsymbol{\nabla}^2 S \\ &= \frac{L^2 S}{r}\mathbf{1}_r + \frac{1}{r}\frac{\partial}{\partial\theta}\left[\frac{\partial(rS)}{\partial r}\right]\mathbf{1}_\theta + \frac{1}{r\sin\theta}\frac{\partial}{\partial\phi}\left[\frac{\partial(rS)}{\partial r}\right]\mathbf{1}_\phi\end{aligned} \quad [36d]$$

where

$$\begin{aligned}L^2 S &= r\frac{\partial^2(rS)}{\partial r^2} - r^2\nabla^2 S \\ &= -\left\{\frac{1}{\sin\theta}\frac{\partial}{\partial\theta}\left[\sin\theta\frac{\partial S}{\partial\theta}\right] + \frac{1}{\sin^2\theta}\frac{\partial^2 S}{\partial\phi^2}\right\}\end{aligned} \quad [36e]$$

The salient characteristic of [36c] is that toroidal fields have no radial components.

The simplest examples of toroidal and poloidal fields are the axisymmetric fields $\overline{\mathbf{B}}_\phi$ and $\overline{\mathbf{B}}_\mathrm{M}$ defined by $T = \overline{T}(r, \theta, t)$ and $S = \overline{S}(r, \theta, t)$. It may be seen from [36c], [36d] that $\overline{\mathbf{B}}_\phi$ is 'zonal' (has only a ϕ-component) and $\overline{\mathbf{B}}_\mathrm{M}$ is meridional (has no ϕ-component):

$$\overline{\mathbf{B}} = \overline{\mathbf{B}}_\phi + \overline{\mathbf{B}}_\mathrm{M} = \overline{B}_\phi\mathbf{1}_\phi + \boldsymbol{\nabla}\times\left(\overline{A}_\phi\mathbf{1}_\phi\right) \quad [37]$$

where $\overline{A}_\phi = -\partial_\theta\overline{S}$ and $\overline{B}_\phi = -\partial_\theta\overline{T}$.

The usefulness of the representation [36] depends partly on the ease with which T and S can be 'projected' from a given $\mathbf{B}$ by solving

$$L^2 T = r(\boldsymbol{\nabla}\times\mathbf{B})_r = \mu_0 r J_r \quad [38a]$$

$$L^2 S = rB_r \quad [38b]$$

Since $L^2 S = f(r)$ $(\neq 0)$ has no solutions, fields having monopolar components (if they existed) could not be represented by [36], but since magnetic monopoles do not exist, [38a], [38b] are easily solved through their spherical harmonic components, using the fact that

$$L^2 Y_n = n(n+1)Y_n. \quad [38c]$$

For example, by [38b],

$$B_r = \sum_{n=1}^{\infty} B_{r,n}(r, t)Y_n(\theta, \phi) \quad [38d]$$

implies

$$S = r\sum_{n=1}^{\infty}\frac{B_{r,n}(r, t)}{n(n+1)}Y_n(\theta, \phi) \quad [38e]$$

and T can be similarly extracted from [38a].

By using this projection method, partial differential equations governing $T_n(r,t)$ and $S_n(r,t)$, equivalent to the induction equation, can be derived. A further attraction is the ease with which the dynamo condition [34] can be applied. In $\hat{\mathrm{v}}$, [36b] implies

$$\hat{T} = 0 \quad [39a]$$

$$\boldsymbol{\nabla}^2\hat{S} = 0 \quad [39b]$$

Equations [36c], [36d] then show that

$$\hat{\mathbf{B}} = -\boldsymbol{\nabla}\hat{V} \quad [39c]$$

where

$$\hat{V} = -\partial_r\left(r\hat{S}\right) \quad [39d]$$

As in [31b], $\hat{S}$ satisfies Laplace's equation and, as in [33b], the dynamo condition [34] shows that

$$\hat{S} = \sum_{n=1}^{\infty}\hat{S}_n(r, t)Y_n(\theta, \phi) \quad [39e]$$

$$\hat{S}_n(r, t) = \hat{S}_n(r_o, t)\left(\frac{r_o}{r}\right)^{n+1} \quad [39f]$$

This, together with [39a], means that everywhere in $\hat{\mathrm{v}}$ and in particular on the CMB,

$$\hat{T}_n = 0 \quad [39g]$$

$$\frac{\partial\hat{S}_n}{\partial r} + \frac{(n+1)\hat{S}_n}{r} = 0 \quad [39h]$$

According to [36c], [36d], and [24] is equivalent to

$$\langle T_n\rangle = 0 \quad \text{on s} \quad [39i]$$

$$\langle S_n\rangle = 0 \quad \text{on s} \quad [39j]$$

$$\langle\partial S_n/\partial r\rangle = 0 \quad \text{on s} \quad [39k]$$

implying, by [39g]–[39k],

$$\text{Dynamo condition: form 3:} \quad T_n = 0,$$

$$\frac{\partial S_n}{\partial r} + \frac{(n+1)S_n}{r} = 0 \text{ at } r = r_o \quad [40]$$

These are boundary conditions on the solutions for $\mathbf{B}$ in v. Using these, the induction equation can be solved without reference to the exterior $\hat{\mathbf{B}}$ of v. From the resulting $\mathbf{B}$, one can, but only if desired (perhaps for presentational purposes), extract $S_n(r_o,t)$ and determine the field $\hat{\mathbf{B}}$ in the form [39c], with

$$\hat{V} = \sum_{0}^{\infty} nS_n(r_o, t)\left(\frac{r_o}{r}\right)^{n+1}Y_n(\theta, \phi) \quad [41]$$

that satisfies the dynamo condition and the continuity requirement [24].

The simplicity of the third form of the dynamo condition partly explains the current popularity of spectral methods in solving both kinematic and MHD dynamo problems. To illustrate this simplicity, we derive the 'decay modes' for a spherical conductor such as the Earth's core. These are solutions of the induction eqn [8] when $\mathbf{u} \equiv \mathbf{0}$, so that

$$\partial_t T = \eta\nabla^2 T \quad [42a]$$

$$\partial_t S = \eta\nabla^2 S \quad [42b]$$

The solutions that are nonsingular at $r = 0$ are proportional to

$$T_n(r) = j_n\left(k_n^T r\right)Y_n(\theta, \phi)\exp\left(-\eta\, k_n^{T2} t\right) \quad [42c]$$

$$S_n(r) = j_n\left(k_n^S r\right)Y_n(\theta, \phi)\exp\left(-\eta\, k_n^{S2} t\right) \quad [42d]$$

where j_n is the spherical Bessel function of order n. They obey [40] provided

$$j_n\left(k_n^T r_o\right) = 0 \quad [42e]$$

$$j_{n-1}\left(k_n^S r_o\right) = 0 \quad [42f]$$

These equations are satisfied by an infinite set of positive admissible k_n^T and k_n^S, the smallest of which we denote by

k_{n1}^T and k_{n1}^S. The e-folding times over which T_n and S_n disappear through ohmic diffusion are therefore $(\eta\, k_{n1}^{T2})^{-1}$ and $(\eta\, k_{n1}^{S2})^{-1}$. The longest of these times is given by the smallest number in the combined sets of k_{n1}^T and k_{n1}^S, which belongs to the poloidal dipole mode for which $k_{S1}=\pi/r_o$; we denote this by $k_{\min}$. In units of r_o^2/η, the e-folding times of the first five dipole modes are approximately 0.101321, 0.025330, 0.011258, 0.006333, and 0.004053; for the quadrupole modes and for the toroidal $n=1$ modes, they are 0.049528, 0.016756, 0.008410, 0.005054, and 0.003372; and for the toroidal $n=2$ modes, they are 0.030105, 0.012089, 0.006585, 0.004154, and 0.002863. Other cases can be obtained from Table 10.6 of Abramowitz and Stegun (1964).

The decay modes provide the basis for what is called a 'variational inequality,' which will be useful in Section 8.03.3.4. This exploits the fact that the modes form a complete orthogonal set, in terms of which an arbitrary magnetic field **B** satisfying [24] and the dynamo condition, but not necessarily the induction equation, can be expanded. Since every other mode in that sum decays more rapidly than the longest-lived poloidal $n=1$ mode, it follows that

$$\int_v (\nabla\times\mathbf{B})^2 \mathrm{d}^3x \geq k_{\min}^2 \int_{v_\infty} B^2 \mathrm{d}^3x \qquad [43a]$$

where $v_\infty (=v+\hat{v})$ denotes all space. This may be rewritten in terms of the total magnetic energy $\mathcal{M}_{\mathrm{tot}}$ of the dynamo and its ohmic dissipation $\mathcal{Q}_J$, defined in [13c], [13g]. It then becomes a lower bound on the ohmic losses:

$$\mathcal{Q}_J \geq 2\eta\, k_{\min}^2 \mathcal{M}_{\mathrm{tot}} \qquad [43b]$$

The 'efficiency' of a dynamo, if defined as

$$\widetilde{E} = k_{\min}^2 \int_{v_\infty} B^2 \mathrm{d}^3x \Big/ \int_v (\nabla\times\mathbf{B})^2 \mathrm{d}^3x \qquad [44a]$$

can therefore not exceed 1 (Gubbins et al., 2000a). The value of $k_{\min}$ provides an improved estimate of $\mathcal{T}_\eta = (\eta k_{\min}^2)^{-1} = r_o^2/\pi^2\eta$, or about 10^4 years, an order of magnitude smaller than our previous estimate r_o^2/η. Nevertheless, it refers only to the longest-lived mode, not to the entire **B** spectrum. An appropriately smaller $\mathcal{T}_\eta$, more representative of the ohmic losses, is

$$\mathcal{T}_\eta = \widetilde{E}(\eta k_{\min}^2)^{-1} = \int_{v_\infty} B^2 \mathrm{d}^3x \Big/ \eta \int_v (\nabla\times\mathbf{B})^2 \mathrm{d}^3x \qquad [44b]$$

Both $\widetilde{E}$ and $\mathcal{T}_\eta$ can be assessed from any geodynamo simulation, but this is not possible for the Earth since $\mathbf{B}_T$ is unknown and only the $n \lesssim 13$ harmonics of $\hat{\mathbf{B}}_P$ are available.

8.03.3.3 The Eigenvalue Problem for Steady Flows

In studying kinematic dynamo action, it is often convenient to keep the form of **u** fixed but to vary its amplitude. This is most easily done by writing the induction equation in nondimensional form by the transformation $\mathbf{r}\to\mathcal{L}\mathbf{r}$ and $t\to(\mathcal{L}/\mathcal{U})t$. Then [8] and [1c] are

$$\partial_t \mathbf{B} = \nabla\times(\mathbf{u}\times\mathbf{B}) + \mathrm{Rm}^{-1}\nabla^2\mathbf{B} \qquad [45a]$$

where

$$\nabla\cdot\mathbf{B} = 0 \qquad [45b]$$

Time-dependent **u** will be briefly considered at the end of Section 8.03.4.4, but we now focus on the easier case $\partial_t\mathbf{u}=\mathbf{0}$ for which normal mode solutions of [45a] exist of the form

$$\mathbf{B}\propto e^{\lambda t} \qquad [46]$$

Equation [45a] becomes

$$\lambda\mathbf{B} = \nabla\times(\mathbf{u}\times\mathbf{B}) + \mathrm{Rm}^{-1}\nabla^2\mathbf{B} \qquad [47]$$

The boundary conditions and the equations governing $\hat{\mathbf{B}}$ are unaltered. Together, they define an eigenvalue problem of a type commonly encountered in fluid stability theory. The eigenvalue is the growth rate λ, and Rm is the 'control parameter.'

For bounded volumes v, the eigenfunctions, $\mathbf{B}_\alpha$, form a complete set, in terms of which an arbitrary solution of [45a] can be expanded:

$$\mathbf{B} = \sum_\alpha \mathbf{B}_\alpha(\mathbf{x})\exp(\lambda_\alpha t) \qquad [48a]$$

and the spectrum of λ_α is discrete, with limit point at $-\infty$. The eigenvalue problem is not self-adjoint in general. The growth rates λ_α may be complex, although they then occur in conjugate complex pairs, so that the corresponding eigenfunctions can ensure the reality of the sum [48a]. Greatest interest attaches to the λ_α (or λ_αs] having the greatest real part, because these dominate the solution for large t; for presentational simplicity, we suppose that only one such eigenvalue exists and denote it by $\lambda_{\max}$.

The eigenvalues are continuous functions of the control parameter. As Rm varies, mode crossing may occur, and a complex eigenvalue pair may become real or conversely. If

$$\mathrm{Re}(\lambda_{\max}) \geq 0 \qquad [48b]$$

the corresponding term in [48a] will persist for all time, showing that the flow Rm **u** is dynamo. In fact, if $\mathrm{Re}(\lambda_{\max}]>0$, the field grows without bound, a physical absurdity that arises from the linearity of the kinematic dynamo problem. It is removed by the nonlinear Lorentz force in the MHD dynamo problem. If [48b] does not hold, all terms in [48a] disappear as $t\to\infty$, and the motion Rm **u** is not a dynamo for this Rm.

As in fluid stability theory, the 'marginal' or 'critical' mode is of special interest. This is defined by the smallest value Rm_c of Rm for which

$$\mathrm{Re}(\lambda_{\max}) = 0 \qquad [48c]$$

The critical mode may not exist, in which case the postulated **u** is not a dynamo for any Rm, no matter how large. When the critical mode exists, it is of one of two types:

$$\begin{cases} \mathrm{Im}(\lambda_{\max}) = 0, & \text{called a DC mode} \\ \mathrm{Im}(\lambda_{\max}) \neq 0, & \text{called an AC mode} \end{cases} \qquad [48d]$$

Here, 'AC' and 'DC' follow everyday usage of these abbreviations: AC for alternating current and DC for direct current. The DC case is a 'direct bifurcation'; the AC case is often called a 'Hopf bifurcation' (although such bifurcations had earlier been studied by Eddington, who called the bifurcation 'overstability').

It will be shown in Section 8.03.3.4 that $\mathrm{Re}(\lambda_{\max})$ is bounded above so that, in the original dimensional variables, $\mathrm{Re}(\lambda_{\max})$ is at most of order $1/\mathcal{T}_u$, which is independent of η. It might be supposed that a limit of this order is necessarily attained as $\mathrm{Rm}\to\infty$, but this is not so. As the dimensional $\mathbf{u}$ is increased, flux expulsion as described in Section 8.03.2.6 becomes more effective and regeneration is increasingly confined to current sheets of diminishing thickness. As a result, the dimensional $\mathrm{Re}(\lambda_{\max})$, after reaching a maximum, may decrease.

Three types of kinematic dynamo are usually distinguished: If the dimensionless $\mathrm{Re}(\lambda_{\max})$ tends to a 'positive' limit as $\mathrm{Rm}\to\infty$, the dynamo is 'fast.' In this limit, the dimensional $\mathrm{Re}(\lambda_{\max})$ is independent of η and of order $\mathcal{T}_u^{-1}$. If the dimensional $\mathrm{Re}(\lambda_{\max})$ is of order $\mathcal{T}_\eta^{-1}$ (though positive), the dynamo is 'slow'; if it is positive and lies between $\mathcal{T}_\eta^{-1}$ and $\mathcal{T}_u^{-1}$, it is an 'intermediate dynamo.' Plausibly, the geodynamo is slow (Section 8.03.5.3).

If $\mathbf{u}(-\mathbf{x})=-\mathbf{u}(\mathbf{x})$, the MHD equations admit solutions of two distinct parities: either $\mathbf{B}(-\mathbf{x})\equiv\mathbf{B}(\mathbf{x})$ or $\mathbf{B}(-\mathbf{x})\equiv-\mathbf{B}(\mathbf{x})$. But it is not generally true that if $\mathbf{u}(\mathbf{x})$ regenerates field, so will $-\mathbf{u}(\mathbf{x})$; in general, $\lambda(-\mathrm{Rm})\neq\lambda(\mathrm{Rm})$. A striking example of this is the homopolar dynamo in Section 8.03.1.1, where reversing $\mathbf{u}$ destroys regeneration and actually hastens the demise of $\mathbf{B}$. The eigenvalue problem for λ is not self-adjoint. (The adjoint dynamo problem was first derived by Roberts (1960). It has the same eigenvalues as [47] but different eigenfunctions. See Gibson and Roberts (1966), Proctor (1977a), Kono and Roberts (1991), and Sarson and Gubbins (1996).)

When the dynamo is of DC type, the critical mode can be found by setting $\lambda=0$ in [47]. This transfers the eigenvalue problem from finding λ to determining Rm_c:

$$0=\mathrm{Rm}_c\boldsymbol{\nabla}\times(\mathbf{u}\times\mathbf{B})+\boldsymbol{\nabla}^2\mathbf{B} \qquad [49a]$$

8.03.3.4 Bounds on the Magnetic Reynolds Number

The discussion following [10b] indicates that dynamo action is possible only if Rm is big enough. Lower bounds on Rm have been derived by Backus (1958), Childress (1969a,b), and Roberts (1967). We rederive only the first of these here, in dimensional units.

The Backus and Childress bounds follow from the evolution equation for the total magnetic energy, given by [13h]:

$$\frac{\mathrm{d}}{\mathrm{d}t}\mathcal{M}_{\mathrm{tot}}=-\mathcal{Q}_J-\int_v\mathbf{u}\cdot(\mathbf{J}\times\mathbf{B})\mathrm{d}^3x \qquad [49b]$$

The Backus bound requires that $\mathbf{u}=\mathbf{0}$ on s. Then, by [16a], [16b] and the divergence theorem,

$$\int_v\mathbf{u}\cdot(\mathbf{J}\times\mathbf{B})\mathrm{d}^3x=\int_v\pi_{ij}^B\nabla_j u_i\mathrm{d}^3x=\frac{1}{\mu_0}\int_v d_{ij}B_iB_j\mathrm{d}^3x \qquad [50a]$$

where $d_{ij}=\frac{1}{2}\left(\nabla_i u_j+\nabla_j u_i-\boldsymbol{\nabla}\cdot\mathbf{u}\delta_{ij}\right)$ reduces to the rate of strain tensor when the fluid is incompressible. Evidently,

$$\int_v d_{ij}B_iB_j\mathrm{d}^3x\le\zeta_{\max}\int_v\mathbf{B}^2\mathrm{d}^3x\le 2\mu_0\zeta_{\max}\mathcal{M}_{\mathrm{tot}} \qquad [50b]$$

where $\zeta_{\max}$ is the largest absolute value taken by any eigenvalue of d_{ij} anywhere in v. It now follows from [49], [50a], [50b] and the variational inequality [43b] that

$$\frac{\mathrm{d}}{\mathrm{d}t}\mathcal{M}_{\mathrm{tot}}\le 2\left(\zeta_{\max}-\eta\,k_{\min}^2\right)\mathcal{M}_{\mathrm{tot}} \qquad [50c]$$

In terms of the magnetic Reynolds number $\mathrm{Rm}_\mathrm{B}=\zeta_{\max}/\eta\,k_{\min}^2$, [50c] shows that a necessary condition for dynamo action is $\mathrm{Rm}_\mathrm{B}>1$. It also demonstrates that the maximum growth rate of $\mathbf{B}$ is $\zeta_{\max}-\eta\,k_{\min}^2$. The result [50c] was first established by Backus (1958) for the incompressible case [11]; see also Proctor (1977b).

The Childress bound,

$$\frac{\mathrm{d}}{\mathrm{d}t}\mathcal{M}_{\mathrm{tot}}\le 2k_{\min}(u_{\max}-\eta\,k_{\min})\mathcal{M}_{\mathrm{tot}} \qquad [51]$$

is also obtained from the energy equation without assuming that $\mathbf{u}\equiv\mathbf{0}$ on s. In terms of the magnetic Reynolds number $\mathrm{Rm}_\mathrm{C}=u_{\max}/\eta\,k_{\min}$, [51] shows that a necessary condition for dynamo action is $\mathrm{Rm}_\mathrm{C}>1$. It also demonstrates that the maximum growth rate of $\mathbf{B}$ is $k_{\min}(u_{\max}-\eta k_{\min})$. In any specific situation, the bound Rm_C may be lowered by rotating the reference frame to reduce $u_{\max}$ since, as noted in Section 8.03.2.3, the induction equation is invariant under rotation of frame.

It was recognized in Section 8.03.2.6 that if $u_r\equiv 0$ in a sphere (i.e., if $\mathbf{u}_P\equiv\mathbf{0}$), $\mathbf{B}$ collapses as the field lines diffuse inexorably inward with a velocity of order $\mathcal{U}_\eta=\eta/r_o$. This can be countered by a sufficiently large u_r, and the bigger the u_r, the larger the ratio $\mathcal{B}_P/\mathcal{B}_T$ for the $\mathbf{B}_P$ created from $\mathbf{B}_T$. It is therefore plausible that to maintain the dynamo for the specified $\mathcal{B}_P/\mathcal{B}_T$, u_r must exceed $\mathrm{O}([\mathcal{B}_P/\mathcal{B}_T]\mathcal{U}_\eta)$. This idea was made precise by Busse (1975), who showed that if $\mathcal{M}_{\mathrm{tot,P}}$ and $\mathcal{M}_T$ are the magnetic energies of the poloidal and toroidal fields, a necessary condition for dynamo action is

$$\mathcal{M}_{\mathrm{tot},P}\equiv\frac{1}{2\mu_0}\int_{v_\infty}\mathbf{B}_P^2\mathrm{d}^3x\le\frac{1}{2}\mathrm{Rm}_r^2\mathcal{M}_T \qquad [52a]$$

where

$$\mathcal{M}_T\equiv\frac{1}{2\mu_0}\int_v\mathbf{B}_T^2\mathrm{d}^3x \qquad [52b]$$

and $\mathrm{Rm}_r=(|ru_r|)_{\max}/\eta$; see also Roberts (1987).

Proctor (2004) derived a similar but stronger result. He showed that a necessary condition for dynamo action is

$$\mathrm{Rm}_P\ge\left(\frac{1}{2}\mathrm{Rm}_T+\sqrt{2}\right)^{-1} \qquad [52c]$$

where $\mathrm{Rm}_P=u_{P_{\max}}r_o/\eta$ and $\mathrm{Rm}_T=u_{T\max}r_o/\eta$ are the magnetic Reynolds numbers based on the maxima of the poloidal and toroidal flow speeds.

8.03.3.5 Anti-dynamo Theorems (ADTs)

The bounds of the last subsection provide precise necessary conditions for dynamos to exist, but these conditions are not sufficient. This was first recognized by Cowling (1934) who announced an unexpected and negative result that was the first of so many other 'antidynamo theorems' (ADTs) that it was widely believed it would only be a matter of time before a general ADT was proved prohibiting homogeneous dynamos in general:

Cowling's theorem: Axisymmetric magnetic fields cannot be maintained by a dynamo.

By [8], a flow $\mathbf{u}$ that has ϕ-dependent components necessarily creates from an axisymmetric $\mathbf{B}$, a field with ϕ-dependent components. The theorem therefore presupposes that $\mathbf{u}$ $(=\overline{\mathbf{u}})$ is axisymmetric. It may be particularly noticed that Cowling's theorem does not rule out dynamos driven by axisymmetric motions, but forbids such dynamos from maintaining the axisymmetric part of a field; see **Section 8.03.4.3**.

In the steady state envisaged by Cowling (1934), in which [27a], [27b] hold, the axisymmetry of $\overline{\Psi}$ means that $\overline{E}_\phi = 0$, so that

$$\eta\nabla\times\overline{\mathbf{B}}_M = \overline{\mathbf{u}}_M\times\overline{\mathbf{B}}_M \qquad [53]$$

Cowling reversed the dynamo problem. Instead of seeking $\mathbf{B}$ for given $\mathbf{u}$, he sought $\mathbf{u}$ for given $\mathbf{B}$. He noticed that an axisymmetric field satisfying the dynamo condition possesses at least one singular latitude circle C (in v or on s) where $\overline{\mathbf{B}}_M = \mathbf{0}$. In general, $\nabla\times\overline{\mathbf{B}}_M \neq \mathbf{0}$ on C (or if it vanishes then, $\overline{\mathbf{B}}_M$ vanishes to higher order) so that [53] requires $\overline{\mathbf{u}}_M = \infty$; in the terminology in **Section 8.03.2.3**, the flow is ineligible. There is only one escape: $\overline{\mathbf{B}}_M \equiv \mathbf{0}$, that is, $\overline{\mathbf{B}} = \overline{B}\mathbf{1}_\phi$, but this too can be ruled out by geometrical reasoning; see Roberts (1967).

Cowling's argument applied to both compressible and incompressible fluid motions (though it had an irritating and not easily removed imperfection noted by Roberts (1967)). Backus and Chandrasekhar (1956) and Braginsky (1965a) provided more robust proofs that applied to incompressible, but not necessarily steady, fields and motions. Ivers and James (1984) gave a proof that is valid for both compressible and incompressible unsteady motions. These results generalize the theorem beyond what Cowling had envisaged.

Braginsky's (1965a) proof, which applies to unsteady $\overline{\mathbf{B}}$ and incompressible $\overline{\mathbf{u}}$, is useful here. It starts by extracting from [8] the equations governing the functions $\overline{A}_\phi(s,z,t)$ and $\overline{B}_\phi(s,z,t)$ defining the general axisymmetric field [37]:

$$\partial_t\overline{A}_\phi + s^{-1}\overline{\mathbf{u}}_M\cdot\nabla\left(s\overline{A}_\phi\right) = \eta\Delta\overline{A}_\phi \qquad [54a]$$

$$\partial_t\overline{B}_\phi + s\overline{\mathbf{u}}_M\cdot\nabla\left(s^{-1}\overline{B}_\phi\right) = \eta\Delta\overline{B}_\phi + s\overline{\mathbf{B}}_M\cdot\nabla\zeta \qquad [54b]$$

where $\Delta = \nabla^2 - s^{-2}$ and ζ is the zonal shear $\overline{u}_\phi/s$. The last term in [54b] is a source that can create zonal field from meridional field by the ω-effect (**Sections 8.03.2.5** and **8.03.2.6**). There is however no corresponding source in [54a] to generate meridional field from the zonal field; the left-hand side of [54a] merely represents the advection of $s\overline{A}_\phi$ by $\overline{\mathbf{u}}_M$ and not its creation. Braginsky's proof consists in showing that $\overline{A}_\phi \to 0$ as $t\to\infty$, whereupon the last term in [54b] vanishes also, so that $\overline{B}_\phi$, having lost its source, disappears too. It is interesting to realize that the magnetic energy of an initially specified $\overline{\mathbf{B}}_M$ may at first grow enormously through the ω-effect, and yet the entire field must eventually become arbitrarily small. It is true quite generally in dynamo theory that a demonstration that a flow initially amplifies a field does not establish that it is a dynamo. This is a consequence of the non-self-adjointness of the dynamo problem; see **Section 8.03.3.3**.

- The Cartesian analog of Cowling's theorem is due to Cowling (1957):

Two-dimensional field theorem: Two-dimensional magnetic fields cannot be maintained by a dynamo.

Here, 'two-dimensional' (2-D) means that all three components are independent of one Cartesian coordinate; it does not mean that any particular component is identically zero. A three-dimensional (3-D) velocity $\mathbf{u}$ necessarily induces a 3-D field from a 2-D field. The theorem therefore presupposes that $\mathbf{u}$ is 2-D. It should be particularly noticed that the theorem does not rule out dynamos driven by 2-D motions, but forbids such dynamos from maintaining a field that has a 2-D part; see **Section 8.03.4.3**.

- Perhaps, the ADT next in significance to Cowling's theorem is the

Toroidal velocity theorem The toroidal motion of an incompressible fluid in a spherical conductor cannot maintain a magnetic field by dynamo action.

Following the discussion in **Section 8.03.2.6**, this ADT is hardly a surprise. Its proof has points of similarity with Braginsky's proof of Cowling's theorem, with S and T taking over the roles of $\overline{A}_\phi$ and $\overline{B}_\phi$, respectively. It is more convenient to work with $Q\equiv\mathbf{r}\cdot\mathbf{B}$ $(=\mathrm{L}^2S)$ and T rather than S and T. The induction eqn [8] implies that

$$\partial_t Q + \mathbf{u}\cdot\nabla Q = \eta\nabla^2 Q + \mathbf{B}\cdot\nabla(\mathbf{r}\cdot\mathbf{u}) \qquad [55a]$$

The final term in [55a] is the only source that can maintain Q and is absent if the motion is purely toroidal $(\mathbf{r}\cdot\mathbf{u}\equiv\mathbf{0})$. Then Q, and therefore S and $\mathbf{B}_P$, disappear in a time of order $\mathcal{T}_\eta$. When neither poloidal field nor poloidal flow is present, the induction equation reduces to

$$\partial_t T + \mathbf{u}\cdot\nabla T = \eta\nabla^2 T \qquad [55b]$$

This resembles the heat conduction equation with T being temperature. There is no source of T within v and $T=0$ on s. Therefore, $\mathbf{B}_T$ disappears in a time of order $\mathcal{T}_\eta$.

The toroidal velocity ADT is due to Elsasser (1947) and Bullard and Gellman (1954); see also Cowling (1957). There is no analogous poloidal velocity ADT; Love and Gubbins (1996a,b) had constructed a dynamo maintained by a purely poloidal flow.

- The Cartesian analog of the toroidal velocity theorem (Zeldovich, 1956) is

Planar velocity theorem: Motions in a plane layer that everywhere lack a component perpendicular to the boundaries cannot maintain a magnetic field by dynamo action.

Bachtiar et al. (2006) recently pointed out that the shape of v is important: in a sphere, planar motions can maintain a dynamo.

- Kaiser et al. (1994) established a result that follows from Proctor's theorem [52c]:

Toroidal field theorem: A purely toroidal field cannot be maintained by a dynamo.

This is also called the 'invisible dynamo theorem' since it shows that a dynamo necessarily signals its existence magnetically outside the conductor. (A dynamo generally produces an external electric field since charges Θ on s must be present to prevent electric currents from leaving v.)

For other ADTs, see Namikawa and Matsushita (1970), Hide (1979), Hide and Palmer (1982), Ivers and James (1981, 1986, 1988a,b), and Zeldovich and Ruzmaikin (1980).

8.03.4 Laminar Dynamos

8.03.4.1 Early Successful Models

The difficulty faced by early dynamo theorists is apparent from the last subsection: It was necessary either to prove a general ADT or to construct an explicit working model. As the computers then available were incapable of deriving convincing numerical solutions of the partial differential equations posed by the induction eqn [8], the explicit model could emerge only from mathematical analysis, perhaps supplemented by sufficiently undemanding numerical work. At first, there seemed to be little hope of finding simple, exact solutions of [8] satisfying the dynamo condition, and thoughts naturally turned to approximate procedures, but a convincingly converged result required expansion in a small parameter. The bounds in Section 8.03.3.4 show that Rm is certainly not that parameter! Eventually, two successful models were produced (Backus, 1958; Herzenberg, 1958). These provided the first, and much needed, mathematical demonstrations that homogeneous dynamos exist, so establishing that a search for a general ADT would be fruitless. The Herzenberg flow $\mathbf{u}$ is steady. It inspired the first homogeneous dynamo experiments (Lowes and Wilkinson, 1963, 1968) and further theoretical studies. See, for example, Gibson (1968) and, most recently, Brandenberg et al. (1998).

A step closer to geophysical reality was taken by Braginsky (1965a), who based an asymptotic model on a simple idea: if the magnetic Reynolds number $\mathrm{Rm}=\overline{u}_\phi r_o/\eta$ based on the zonal core motion $\overline{u}$ is large, even a small deviation $\mathbf{u}'$ from axisymmetry may suffice to produce (from the $\overline{B}_\phi$ created from $\overline{\mathbf{B}}_M$ by the ω-effect) the $\overline{\mathbf{B}}_M$ necessary to defeat Cowling's theorem. To achieve this, $\overline{\mathbf{u}}$ and $\overline{\mathbf{B}}$ are expanded in powers of $\mathrm{Rm}^{-1/2}$, the leading terms being $\overline{u}_\phi\mathbf{1}_\phi$ and $\overline{B}_\phi\mathbf{1}_\phi$. At the next order, $\mathbf{u}'$ of order $\mathrm{Rm}^{-1/2}\overline{u}_\phi$ induces from $\overline{B}_\phi$ an asymmetrical $\mathbf{B}'$ of order $\mathrm{Rm}^{-1/2}\overline{B}_\phi$ that in turn generates an emf $\overline{\varepsilon}_\phi=\overline{(\mathbf{u}'\times\mathbf{B}')}_\phi$ of order $\mathrm{Rm}^{-1}\overline{B}_\phi$. This is a source that must be added to the right-hand side of [54a]. It may maintain a meridional field $\overline{\mathbf{B}}_M$ of order $\mathrm{Rm}^{-1}\overline{B}_\phi$, which is precisely the strength necessary to create $\overline{B}_\phi$ by the ω-effect. This regenerative loop, $\overline{B}_\phi\leftrightarrow\overline{\mathbf{B}}_M$, parallels the one that maintains a turbulent dynamo in Section 8.03.5.2.

Implementation of Braginsky's idea is intricate, but its results are simplified by the introduction of 'effective fields' that replace $\overline{\mathbf{u}}_M$ and $\overline{\mathbf{B}}_M$ and are also of order Rm^{-1}. Our discussion here ignores that complication. See Soward and Roberts (2014) for a recent discussion. To leading order, the emf that maintains dynamo action is

$$\overline{\varepsilon}_\phi=\alpha\overline{B}_\phi\mathbf{1}_\phi, \qquad [56]$$

where α is $\mathrm{O}(\mathrm{Rm}^{-1})$ and can be calculated explicitly from $\mathbf{u}'$ and $\overline{u}_\phi$, though the recipe is rather complicated. Soward (1972) showed how α is linked to the helicity of $\mathbf{u}$.

After the source [56] has been inserted into the right-hand side of [54a], Cowling's theorem is no longer a threat; self-excited $\overline{\mathbf{B}}$ may exist and may be found by solving [54a], [54b] for $\overline{\mathbf{B}}$ numerically, a task that is far less challenging than integrating the 3-D induction eqn [8] for $\mathbf{B}$. Braginsky (1964a,b) successfully solved three such axisymmetric models. One of these even contains a dynamical element: the rotation rate, Ω_i, of the SIC was found in response to the magnetic torque $\Gamma_{z,\mathrm{i}}$ that the FOC exerts on it. Two features of Braginsky's asymptotic analysis are of special geophysical interest. First, since $\mathbf{B}'/\overline{\mathbf{B}}_M=\mathrm{O}(\mathrm{Rm}^{1/2})\gg 1$, it might seem at first sight that his expansion is geophysically irrelevant. Because $\mathrm{Rm}\gg 1$ however, the largest terms in his expansion of $\mathbf{B}'$ are frozen to the fluid and do not escape from the core. In fact, $\hat{\mathbf{B}}'=\mathrm{O}(\mathrm{Rm}^{-1/2}\overline{\mathbf{B}}_M)$, consistent with the small tilt of the centered dipole. Second, as is clear from his generalization (Braginsky, 1965b), $\mathbf{u}'$ and $\mathbf{B}'$ should be attributed mainly to large-scale, longitudinally moving planetary waves that ride on the axisymmetric state $\overline{u}_\phi$ and $\overline{B}_\phi$, creating as they do so the α that sustains $\overline{\mathbf{B}}_M$. This attractive idea adds new significance to the westward drift of the observed geomagnetic field.

8.03.4.2 One-Dimensional Models

The existence of simple solutions of [8] satisfying the dynamo condition was overlooked until 1973 when Ponomarenko devised a one-dimensional model that is one in which $\mathbf{u}$ depends solely on one coordinate s and is independent of ϕ, z (and t), so that [46] simplifies to

$$\mathbf{B}=\mathbf{B}_1(s)\exp(lm\phi+lkz+\lambda t) \qquad [57a]$$

Cowling's theorem demands that $m\neq 0$ and the 2-D field ADT that $k\neq 0$.

In the model of Ponomarenko (1973), the conductor fills all space but is stationary outside a cylinder C of radius a. See Figure 8. As in [34], the dynamo condition requires that $\mathbf{B}_1(s)$ be exponentially small for $s\to\infty$. Within C, $\mathbf{u}$ is a 'solid-body' motion, which is a motion that C can execute even if solid. The velocity of C is helical, a combination of a uniform velocity U along the axis Oz and a rotation about Oz with uniform angular velocity ω:

$$\mathbf{u}=\begin{cases}s\omega\mathbf{1}_\phi+U\mathbf{1}_z & \text{if } s<a\\ \mathbf{0} & \text{if } s>a\end{cases} \qquad [57b]$$

If $U=0$, the motion has no component in the z-direction and the dynamo fails by the planar velocity ADT in Section 8.03.3.6. Clearly, there is an infinity of possible

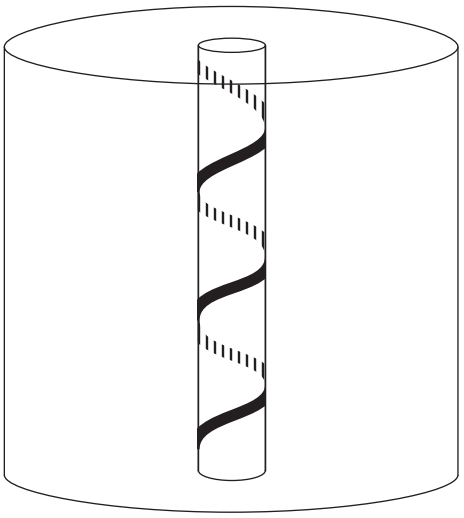

Figure 8 The Ponomarenko dynamo.

models, distinguished by the value of $p = a\Omega/U$ where $-\infty < p < \infty$. For $p \neq 0$, the motion [57b] is non-mirror-symmetrical, the positive helicity of a model with $p > 0$ being mirrored by the negative helicity of the model of opposite p.

The magnetic Reynolds number is defined as $\mathrm{Rm} = u_{\max} a/\eta$ where $u_{\max} = \sqrt{(U^2 + \omega^2 a^2)}$. The eigenvalue problem for $\lambda(m,k)$ only requires that ordinary differential equations for $\mathbf{B}_1(s)$ be solved, and that can be done analytically, leading to a dispersion relationship for λ that can be solved even on a pocket calculator! As described in **Section 8.03.3.3**, the smallest value of Rm for which $\mathrm{Re}(\lambda) = 0$ is minimized over m and k to give Rm_c, and since $\mathrm{Im}(\lambda_c) \neq 0$, the dynamo is of AC type. The minimum of Rm_c over $|p|$ gives the most efficient generator, and $\mathrm{Rm}_c \approx 17.7$ for this model.

The Ponomarenko dynamo spawned a number of similar 'screw dynamos': Ruzmaikin et al. (1988, 1989a,b), Solovyev (1985a,b, 1987), Sokoloff et al. (1989), Lupian and Shukurov (1992) and Léorat (1995). Because of the infinite shear on $s = a$, the Ponomarenko dynamo is fast (Gilbert, 1988). Screw dynamos, in which the infinite shear is smoothed out in a narrow layer, are also efficient generators, but, in the terminology in **Section 8.03.3.3**, they are 'intermediate.' A Ponomarenko-type dynamo of finite z-length (Gailitis, 1990) developed into a homogeneous dynamo successfully demonstrated in laboratory experiments; see **Chapter 8.13** and Roberts and King (2013).

8.03.4.3 Two-Dimensional Models

As noted in **Section 8.03.3.5**, the 2-D field ADT does not exclude models driven by 2-D motions, that is, flows independent of one Cartesian coordinate, z. For these, [46] simplifies to

$$\mathbf{B} = \mathbf{B}_2(x, y)\exp(lkz + \lambda t). \qquad [58]$$

The 2-D field ADT merely requires that $k \neq 0$.

The earliest 2-D model was the spatially periodic dynamo of Roberts (1972a,b), in which

$$\mathbf{u} = \mathbf{1}_x \sin y + \mathbf{1}_y \sin x + \mathbf{1}_z(\cos x - \cos y) \qquad [59a]$$

The projection onto an xy-plane of this flow is sketched in **Figure 9(a)**. There is, in addition to the xy-components of motion shown, a z-component into (out of) the paper for each clockwise-turning (counterclockwise-turning) 'cell.' Although the model predates Ponomarenko's, each cell resembles a Ponomarenko dynamo, adjacent cells moving in opposite z-directions but having the same positive helicity H.

From the real part of [58], the xy-average of $\mathbf{B}$ at $t = 0$ is

$$\overline{\mathbf{B}} = B_0(\mathbf{1}_x \cos kz + \mathbf{1}_y \sin kz) \quad \text{where} \quad k > 0 \qquad [59b]$$

It is exponentially stretched where it crosses the dividing streamlines at the stagnation points shown in **Figure 9(a)**. This makes the motion [59a] an efficient generator (see **Section 8.03.2.6**). Strictly, it is an intermediate dynamo although it would be fast but for a logarithmic factor (Soward, 1987). It is the basis of successful laboratory experiments demonstrating homogeneous dynamo action; see **Chapter 8.13** and Roberts and King (2013).

The way in which the flow [59a] generates $\overline{\mathbf{B}}$ is sketched in **Figure 9(b)**, where three constant z-'decks' are shown spanning one quarter of a z-wavelength. On the 'lower' deck, the flow has an 'upward' component in the shaded patches and the mean field (in the direction indicated) is 'lifted upward' and twisted by the 'vertical' vorticity so that it is roughly in the direction Ox of the mean field on the center deck. On the upper deck ($z = \pi/4\,k$), the flow has a 'downward' component in the unshaded patches and the mean field (in the direction indicated) is 'depressed' to the center deck and twisted by the vorticity so that it too is roughly in the x-direction of $\overline{\mathbf{B}}$. The same process reinforces $\overline{\mathbf{B}}$ on every z-section of the flow. The mean field [59b] is helical, in the sense that $\nabla \times \overline{\mathbf{B}} = -k\overline{\mathbf{B}}$; the current helicity $H_J = \overline{\mathbf{B}} \cdot \nabla \times \overline{\mathbf{B}}$ is negative, as is the magnetic helicity $H_B = \overline{\mathbf{A}} \cdot \nabla \times \overline{\mathbf{A}} = \overline{\mathbf{A}} \cdot \overline{\mathbf{B}}$.

In addition to [59a], Roberts (1972a,b) investigated three other dynamos driven by spatially periodic flows; see also Roberts (1969) and Childress (1969a,b, 1970). Since then, there have been several other studies of such systems, most recently by Tilgner and Busse (1995), Zheligovsky and Galloway (1998), and Demircan and Seehafer (2002).

The term 'two-dimensional' can be generalized to cover motions 'independent of one coordinate,' either z as in the Cartesian 2-D models described in the preceding text or ϕ as in the spherical 2-D dynamos described next. As noted in **Section 8.03.3.5**, Cowling's ADT does not exclude models driven by axisymmetric motions $\overline{\mathbf{u}}$. For these, [46] simplifies to

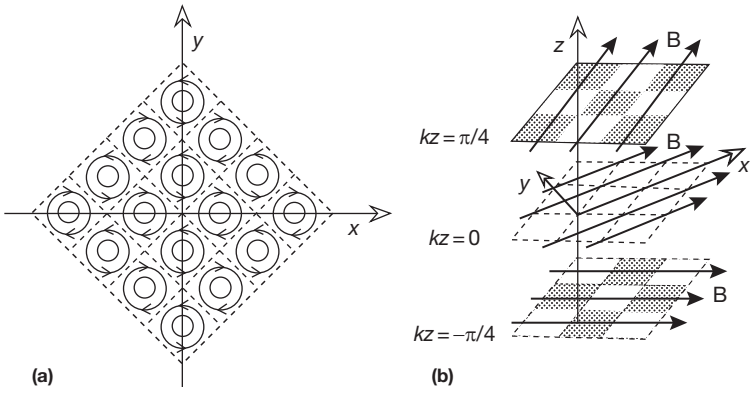

Figure 9 The G. O. Roberts dynamo. (a) The xy-projection of the periodic pattern of motion that fills all space. (b) The effect of the motion on the mean field (see text).

$$\mathbf{B} = \mathbf{B}'(r, \theta)\exp(lm\phi + \lambda t) \qquad [60]$$

Cowling's ADT merely requires that $m \neq 0$. When $\mathrm{Im}(\lambda_c) \neq 0$, the field [60] moves longitudinally as a 'dynamo wave,' regenerating itself as it goes; see also **Section 8.03.5.2**.

Although spherical 2-D models were first proposed more than four decades ago, perhaps the first convincing model was that of G. O. Roberts, reported by Roberts (1971a,b), which was solved numerically. It is driven by an adaptation of a Cartesian periodic motion such as [59a] that forces it into a sphere; see also Childress (1970). A simpler flow was employed by Gubbins (1973). Three models devised by Dudley and James (1989) deserve special notice. They explore symmetries with simple $\overline{\mathbf{u}}$ and have proved useful in interpreting laboratory experiments; see **Chapter 1.13** and Roberts and King (2013).

Gailitis (1993, 1995) investigated several spherical 2-D models, in which the conductor fills all space but is stationary outside a sphere. Although electric currents now leak into $\hat{V}$, the dynamo condition still imposes [34]. Gailitis made an interesting comparison between two similar flows, one having helicity and one without it. Both regenerated field but Rm_c was much smaller for the helical model. He concluded that 'helicity is favorable but not indispensible' for dynamo action.

8.03.4.4 Three-Dimensional Models

When $\mathbf{u}$ depends on all three coordinates, separable solutions of the form [57a], [58], or [60] do not exist, so that [46] is the only simplification in solving [8]. We classify these 'three-dimensional models' as cylindrical, Cartesian, or spherical.

The cylindrical 3-D class consists of the models of Lortz (1968). As for the Ponomarenko model, these operate in a conductor filling all space. They capitalize on the effectiveness of helicity in field generation, and they can be solved analytically. They will not be described here. Their theory has been developed most recently by Eltayeb and Loper (1988), Lortz (1990), and Soward (1990).

The Cartesian class of 3-D dynamos is exemplified by the Beltrami flow, which is a spatially periodic motion in which $\mathbf{u}$ and $\boldsymbol{\zeta}$ are proportional, so that it is a maximally helical flow (i.e., $|H| = |\mathbf{u}|\ |\boldsymbol{\omega}|$; see **Section 8.03.2.6**). Most famous is the Arnold–Beltrami–Childress (ABC) flow:

$$\mathbf{u} = (C\sin z + B\cos y)\mathbf{1}_x + (A\sin x + C\cos z)\mathbf{1}_y + (B\sin y + A\cos x)\mathbf{1}_z \qquad [61]$$

Depending on the choice of the constants A, B, and C, this flow possesses chaotic streamlines and may be a fast dynamo. See Galloway and Frisch (1986). The G. O. Roberts dynamo [59a] is a 2-D Beltrami flow.

The earliest example of the spherical class of 3-D dynamos was that of Herzenberg (1958). The first successful computational models were those of Pekeris et al. (1973) and Kumar and Roberts (1975). The latter aimed at comparing 3-D models with corresponding 2-D models derived from Braginsky's asymptotic analysis (**Section 8.03.4.1**). Four independent parameters define this model, one for the zonal flow, one for the meridional flow, and two for the asymmetrical (poloidal) flow. This 4-D parameter space has been thoroughly investigated in papers by Love and Gubbins (1996a,b), Sarson and Gubbins (1996), Holme (1997), Gubbins et al. (2000a,b), and Gubbins and Gibbons (2002). They found few regenerating solutions, prompting Gubbins et al. (2000a) to opine that 'Dynamo action might, therefore, be quite unusual, at least for a large-scale flow.' The particular case in which the zonal flow parameter is zero led to the successful poloidal field model referred to in **Section 8.03.3.5**; see Love and Gubbins (1996a).

Two further issues about spherical kinematic models should be mentioned. The first concerns the paradoxical result of Bullard and Gubbins (1977): it appeared that, contrary to intuition, Rm_c can be reduced by bringing to rest the outermost layer of fluid; see also Serebrianya (1988), Sarson and Gubbins (1996), and Liao et al. (2005). This enhancement of dynamo action is welcome news for those who believe on other grounds that the uppermost layers of the FOC are stably stratified; see, for example, Braginsky (1984). The reduction of Rm_c is attributed by Hutcheson and Gubbins (1994) to the diffusion (into the stagnant layer) of toroidal field that would otherwise concentrate more intensely near the boundary and produce a larger ohmic loss.

The second issue concerns a case in which even [46] does not apply: dynamos driven by periodic time-dependent $\mathbf{u}$, such as those produced by precessional or librational forcing. See Wu and Roberts (2009, 2012) and Zhang et al. (2011). Then $\mathbf{B}$ oscillates within an envelope that grows or diminishes in amplitude, corresponding, respectively, to regeneration or nonregeneration; Floquet theory can decide which. See Willis and Gubbins (2004), who study a model in which $\mathbf{u}$ has the same spatial form as the Kumar–Roberts dynamo but oscillates sinusoidally in time. The success of the Backus (1958) dynamo depended on the choice of a time-dependent $\mathbf{u}$ that is periodic but far from sinusoidal.

8.03.5 Turbulent Kinematic Dynamos

8.03.5.1 Field Creation by Cyclonic Turbulence: MFE

In this section, we again use the overbar to denote averages over a turbulent ensemble. We represent a turbulent flow traditionally as $\mathbf{u} = \overline{\mathbf{u}} + \mathbf{u}'$, where $\overline{\mathbf{u}}$ is the turbulent (ensemble) average of $\mathbf{u}$ and $\mathbf{u}'$ is the fluctuating remnant. A possible confusion arises because our principal application of turbulent dynamo theory is to axisymmetric flows and fields. We therefore denote these by $\overline{\overline{\mathbf{u}}}$ and $\overline{\overline{\mathbf{B}}}$, writing $\overline{\mathbf{u}} = \overline{\overline{\mathbf{u}}} + \mathbf{u}''$ and $\overline{\mathbf{B}} = \overline{\overline{\mathbf{B}}} + \mathbf{B}''$ where $\overline{\overline{\mathbf{u}}} = \overline{\overline{u}}_\phi \mathbf{1}_\phi + \overline{\overline{\mathbf{u}}}_M$ and $\overline{\overline{\mathbf{B}}} = \overline{\overline{B}}_\phi \mathbf{1}_\phi + \overline{\overline{\mathbf{B}}}_M$.

The importance of helicity in promoting dynamo action was first realized by Parker (1955) in the context of solar magnetism. He argued that the Coriolis forces make solar turbulence 'cyclonic.' He visualized that through the process idealized in **Section 8.03.2.6**, each turbulent eddy generates a flux loop in the plane perpendicular to the inducing field (represented by the flux rope in **Figure 6**). He pointed out that a large-scale mean field is then produced in that plane through the diffusive merging of each loop with those created by neighboring cyclonic eddies. Similarly in spherical geometry, a mean zonal field $\overline{\overline{B}}_\phi \mathbf{1}_\phi$ creates through the α-effect a mean meridional field $\overline{\overline{\mathbf{B}}}_M$, leaving the ω-effect in **Section 8.03.2.5** to complete the regenerative cycle $\overline{\overline{B}}_\phi \leftrightarrow \overline{\overline{\mathbf{B}}}_M$, so defeating Cowling's theorem.

Substitution of $\mathbf{u} = \overline{\mathbf{u}} + \mathbf{u}'$ and $\mathbf{B} = \overline{\mathbf{B}} + \mathbf{B}'$ into [6e] and averaging leads to

$$\eta\nabla\times\overline{\mathbf{B}}=\overline{\mathbf{E}}+\overline{\mathbf{u}}\times\overline{\mathbf{B}}+\overline{\boldsymbol{\varepsilon}} \qquad [62a]$$

where

$$\overline{\boldsymbol{\varepsilon}}=\mathbf{u}'\times\mathbf{B}' \qquad [62b]$$

Attention focuses on the new term $\overline{\varepsilon}$ in the Ohms law [62a] for the mean field $\overline{\mathbf{B}}$. Out of the recognition of the existence and importance of this term, a new subject was born, 'mean field electrodynamics' or 'MFE.' To evaluate $\overline{\boldsymbol{\varepsilon}}$, it is necessary to find, or at least evaluate approximately, the solution of the equation governing $\mathbf{B}'$. This equation is derived from [6e] and [62a] by subtraction:

$$\eta\nabla\times\mathbf{B}'=\mathbf{E}'+\mathbf{u}'\times\overline{\mathbf{B}}+\overline{\mathbf{u}}\times\mathbf{B}'+\boldsymbol{\varepsilon}' \qquad [62c]$$

(The possibility that a dynamo operates with $\mathbf{B}'$ alone, that is from solutions of [62c] with $\overline{\mathbf{B}}\equiv\mathbf{0}$, is irrelevant to MFE and is not considered here.)

Consider induction by homogeneous turbulence, that is, turbulence whose statistical properties are the same for all points $\mathbf{x}$ so that, for example, the correlation between the velocity at two different points depends only on t and their separation $\mathbf{x}$, that is,

$$Q_{ij}(\mathbf{x},t)=\overline{u_i(\mathbf{x}_1,t)u_j(\mathbf{x}_1+\mathbf{x},t)}=Q_{ji}(-\mathbf{x},t), \qquad [63]$$

is independent of $\mathbf{x}_1$; similarly, $\overline{\mathbf{u}}$ is constant, assumed zero by choice of reference frame.

Suppose that $\mathrm{Rm}'\ll 1$, where $\mathrm{Rm}'=\mathcal{U}'\mathcal{L}'/\eta$ is the magnetic Reynolds number of the fluctuating part, $\mathbf{u}'$, of the flow. Two simplifications are immediate. First, the emf $\mathbf{u}'\times\overline{\mathbf{B}}$ produces a field at most of order $\mathrm{Rm}'\overline{\mathbf{B}}$, and this in turn creates a contribution to $\boldsymbol{\varepsilon}'$ of order $\mathrm{Rm}'\mathbf{u}'\times\overline{\mathbf{B}}$, which is negligible compared with $\mathbf{u}'\times\overline{\mathbf{B}}$ in [62c]. We may therefore set $\boldsymbol{\varepsilon}'=\mathbf{0}$, a step usually called 'first-order smoothing' and here justified. Second, we recall from **Section 8.03.2.6** that when $\mathrm{Rm}'\ll 1$, $\nabla\times\mathbf{E}'=\mathbf{0}$ to leading order. By [9b], [11], and [62c], we therefore have

$$\eta\nabla^2\mathbf{B}'=\mathbf{u}'\cdot\nabla\overline{\mathbf{B}}-\overline{\mathbf{B}}\cdot\nabla\mathbf{u}'. \qquad [64a]$$

The sources of $\mathbf{B}'$ on the right-hand side of [64a] make two contributions to $\overline{\boldsymbol{\varepsilon}}$:

- The first source creates $\mathbf{B}'$ of order $\mathcal{L}'\mathrm{Rm}'\nabla\overline{\mathbf{B}}$. This generates an $O(\eta\mathrm{Rm}'^2\nabla\overline{\mathbf{B}})$ part of $\overline{\boldsymbol{\varepsilon}}$ that may be written as $\overline{\varepsilon}_i^{(s)}=-\beta_{ijk}\nabla_j\overline{B}_k$ where β_{ijk} depends only on the symmetrical part $Q_{ij}^{(s)}=\frac{1}{2}(Q_{ij}+Q_{ji})$ of Q_{ij}. If the turbulence is isotropic, that is, has statistical properties independent of direction, $\beta_{ijk}=\beta\epsilon_{ijk}$ with $\beta>0$. Then, $\overline{\boldsymbol{\varepsilon}}=-\beta\nabla\times\overline{\mathbf{B}}$, and if this term is transferred to the left-hand side of [62a], it is immediately seen that its effect on $\overline{\mathbf{B}}$ is purely diffusive, just as though the molecular diffusivity η were enhanced by a 'turbulent diffusivity' β of order $\mathcal{U}'^2\mathcal{T}'_\eta$ giving a total diffusivity of $\overline{\eta}=\eta+\beta$.
- The second source in [64a] creates $\mathbf{B}'$ of order $\mathrm{Rm}'\overline{\mathbf{B}}$. This generates an $O(\mathcal{U}'\mathrm{Rm}'\overline{\mathbf{B}})$ part of $\overline{\boldsymbol{\varepsilon}}$ that may be written as $\overline{\boldsymbol{\varepsilon}}_i^{(a)}=\alpha_{ij}\overline{B}_k$ where α_{ij} depends only on the antisymmetric part $Q_{ij}^{(a)}=\frac{1}{2}(Q_{ij}-Q_{ji})$ of Q_{ij}. The classic theory of turbulence supposes mirror symmetry, which means that its statistical properties are unchanged by the coordinate reflection $\mathbf{x}\to-\mathbf{x}$, so that $Q_{ij}^{(a)}=0$, by [63]. Cyclonic turbulence lacks mirror symmetry and $Q_{ij}^{(a)}\neq 0$. The simplest case is 'pseudo-isotropic turbulence,' which is statistically independent of direction but possesses mean helicity $\overline{H}=\overline{\mathbf{u}'\cdot\boldsymbol{\omega}'}$. Then, $\alpha_{ij}=\alpha\delta_{ij}$ and $\overline{\boldsymbol{\varepsilon}}=\alpha\overline{\mathbf{B}}$, where $\alpha=O\left(\mathcal{T}'_\eta\overline{H}\right)$. In agreement with the earlier heuristic arguments, α and $\overline{H}$ have opposite signs. The creation of the large-scale emf $\alpha\overline{\mathbf{B}}$ parallel to $\overline{\mathbf{B}}$ is called the α-effect, for no better reason than the choice made by Steenbeck et al. (1966) for the constant of proportionality. The α-effect is a classic example of 'inverse cascade' or what is sometimes called an 'up-the-spectrum process,' where the small-scale turbulence does not merely provide through β an energy sink for the large scales but also profoundly affects them.

The theory so far has led for pseudo-isotropic turbulence to

$$\overline{\mathbf{E}}=-\overline{\mathbf{u}}\times\overline{\mathbf{B}}-\alpha\overline{\mathbf{B}}+\overline{\eta}\nabla\times\overline{\mathbf{B}} \qquad [64b]$$

This form for $\overline{\boldsymbol{\varepsilon}}$ ignores significant questions, such as how an isotropic $Q_{ij}^{(a)}$ can be created and maintained. Although the α-effect and helicity arise naturally in rotating convective turbulence, Coriolis, buoyancy, and Lorentz forces make the turbulence nonisotropic, possibly strongly so. When the turbulence is inhomogeneous, that is, when its statistical properties depend on $\mathbf{x}$, a more general form of $\overline{\mathbf{E}}$ generally approximates $\overline{\mathbf{E}}$ better:

$$\overline{E}_i=-\varepsilon_{ijk}\overline{u}_j\overline{B}_k-\alpha_{ij}\overline{B}_j+\beta_{ijk}\nabla_j\overline{B}_k \qquad [64c]$$

where α_{ij} is a skew tensor that changes sign under coordinate reflection and β_{ink} is a polar tensor that does not. Nevertheless, modelers have often preferred the simpler choice [64b] because it contains the essence while involving fewer *ad hoc* parameters. (But see, e.g., Roberts (1972a,b) and Krause and Rädler (1980)).

The case $\mathrm{Rm}'\ll 1$ is the easiest to analyze, but the least interesting since $\overline{\boldsymbol{\varepsilon}}$ has little effect on $\overline{\mathbf{B}}$; for example, the turbulent diffusivity β is of order $\mathcal{U}'^2\mathcal{T}'_\eta=\mathrm{Rm}'^2_{\mathrm{m}}\eta\ll\eta$. A more interesting and challenging case is $\mathrm{Rm}'\gg 1$. It is more interesting because $\overline{\boldsymbol{\varepsilon}}$ in [62a] now plays a very significant role in the electrodynamics. It is more challenging because there is no simple route to [64b] and [64c]; indeed, these expressions are oversimplifications because first-order smoothing is unjustified. On the assumption that [64b] is nevertheless an acceptable approximation, it is often argued that, because of fast reconnection (**Section 8.03.2.6**), α and β are nearly independent of η. Replacing therefore $\mathcal{T}'_\eta$ by $\mathcal{T}'_u$ in the small-Rm' estimates for α and β, we obtain $\alpha=O\left(\mathcal{T}'_u\overline{H}\right)$ and $\beta=\mathrm{O}\left(\mathcal{U}'^2\mathcal{T}'_u\right)=\mathrm{O}(\mathcal{U}'\mathcal{L}')\gg\eta$. The diffusive timescale of $\overline{\mathbf{B}}$ is $\overline{\mathcal{L}}^2/\beta=\mathrm{Rm}'^{-1}\left(\overline{\mathcal{L}}^2/\eta\right)$ rather than $\overline{\mathcal{L}}^2/\eta$. In the case of the Sun, $\overline{\mathcal{L}}^2/\eta$ may be billions of years but Rm' may exceed 10^9 so that $\overline{\mathcal{L}}^2/\beta$ may be the decadal timescale of the solar cycle of magnetic activity, the time during which the Sun cleanses itself of old flux and makes new reversed flux. The dynamo efficiency, $\widetilde{E}$, defined by [44a], is plausibly reduced by a factor of order η/β by the ohmic losses of the turbulence. In order of magnitude, the ratio $\alpha\overline{\mathbf{B}}/\beta\nabla\times\overline{\mathbf{B}}$ of the two sources on the right-hand sides of [64b] is $\alpha\overline{\mathcal{L}}/\beta=\mathrm{O}(\overline{H}\overline{\mathcal{L}}/\mathcal{U}'^2)$. Because $\mathcal{L}'\ll\overline{\mathcal{L}}$, the first dominates the second if $\overline{H}$ takes its maximum possible value of order $\mathcal{U}'^2/\mathcal{L}'$. Even a helicity much smaller than this maximum can create a significant α-effect when $\mathrm{Rm}'\gg 1$.

The value of Rm' for turbulence in the Earth's core is uncertain but is likely to be much less than in the solar convection zone. Assuming η and β are comparable, a better estimate of

the timescale, $\overline{\mathcal{T}}$, of the mean field, $\overline{\mathbf{B}}$, is $\overline{\mathcal{L}}^2/\overline{\eta}$, where $\overline{\eta}=\eta+\beta$. If, similar to the Sun, this is typical of the time, $\mathcal{T}_{\rm rev}$, taken for the geomagnetic field to reverse its polarity, it provides a possible explanation of a difficulty implied by the small value of η recently derived by Pozzo et al. (2012): $\eta=0.7\ \mathrm{m^2\ s^{-1}}$ (Section 8.03.2.3). This gives the diffusive time constant of the core is $\mathcal{T}_\eta=\overline{\mathcal{L}}^2/\eta=6\times10^5$ year for $\overline{\mathcal{L}}=r_o$. This may be compared with the estimate of $\mathcal{T}_{\rm rev}=2-8\times10^4$ year made by Clement (2004). If $\mathcal{T}_{\rm rev}$ is determined by the mean field, $\overline{\mathbf{B}}$, as $\overline{\mathcal{L}}^2/\overline{\eta}$, then $\beta/\eta\approx2$–7, giving a β that is larger than but comparable with η. One should perhaps interpret $\eta=2\ \mathrm{m^2\ s^{-1}}$, which was preferred pre-Pozzo as being the value of $\overline{\eta}$. This is of course speculative because the spectrum of $\mathbf{B}$ in the core is unknown. If $\beta\gg\eta$ as for the Sun, the spectrum peaks at wavenumbers much larger than $\overline{\mathcal{L}}^{-1}$, but when β and η are comparable as is apparently the case for the Earth's core, the spectrum at the smallest wavenumbers, of order $\overline{\mathcal{L}}^{-1}$, cannot be expected to increase rapidly with wavenumber. Unfortunately (see Section 8.03.3.1), the spectrum of $\hat{\mathbf{B}}_P$ is known at $r=r_o$ and for only the very limited range, $n\lesssim13$, of harmonic wavenumbers, in which it seems rather flat. Where it peaks is unknown but it might be at larger n.

This discussion of MFE merely touches the fringes of what has become a massive subject. Further details can be found in Roberts and Stix (1971), Moffatt (1978), Krause and Rädler (1980), and Dormy and Soward (2007).

8.03.5.2 Mean Field Dynamo Models

The impact of MFE and especially the α-effect has been enormous, particularly in astrophysics. In reviewing what has been done, we adopt the simpler [64b] of the two expressions for the emf. This, combined with [62a] and the ensemble averages of [1b] and [1c], gives the simplest form of the 'mean field induction equation':

$$\partial_t\overline{\mathbf{B}}=\boldsymbol{\nabla}\times\left(\alpha\overline{\mathbf{B}}+\overline{\mathbf{u}}\times\overline{\mathbf{B}}\right)+\overline{\eta}\boldsymbol{\nabla}^2\overline{\mathbf{B}} \qquad [65]$$

Self-sustaining solutions satisfying the dynamo conditions are called 'mean field dynamos.' These have been proffered as models of planetary, stellar, and galactic magnetism.

The additional source $\alpha\overline{\mathbf{B}}$ in [65] means that Cowling's theorem (Section 8.03.3.5) does not prevent $\overline{\mathbf{B}}$ from having an axisymmetric part $\overline{\overline{\mathbf{B}}}$. We concentrate mainly on this part, using the representation [37] and obtaining, in place of [54],

$$\partial_t\overline{\overline{A}}_\phi+s^{-1}\overline{\overline{\mathbf{u}}}_{\rm M}\cdot\boldsymbol{\nabla}\left(s\overline{\overline{A}}_\phi\right)=\overline{\eta}\Delta\overline{\overline{A}}_\phi+\alpha\overline{\overline{B}}_\phi \qquad [66a]$$

$$\partial_t\overline{\overline{B}}_\phi+s\overline{\overline{\mathbf{u}}}_{\rm M}\cdot\boldsymbol{\nabla}\left(s^{-1}\overline{\overline{B}}_\phi\right)=\overline{\eta}\Delta\overline{\overline{B}}_\phi+s\overline{\overline{\mathbf{B}}}_{\rm M}\cdot\boldsymbol{\nabla}\zeta-\alpha\Delta\overline{\overline{A}}_\phi \qquad [66b]$$

As already noted in Section 8.03.2.6, dynamical considerations favor the equatorial symmetry

$$\begin{aligned}&\alpha(-z)=-\alpha(z),\qquad &&\overline{\overline{u}}_s(-z)=\overline{\overline{u}}_s(z)\\&\overline{\overline{u}}_\phi(-z)=\overline{\overline{u}}_\phi(z),\qquad &&\overline{\overline{u}}_z(-z)=-\overline{\overline{u}}z(z)\end{aligned} \qquad [66c]$$

applying for each s. In this case, there are two distinct types of solutions:

$$\begin{aligned}&\text{dipole family:}\qquad &&\overline{\overline{B}}_s(-z)=-\overline{\overline{B}}_s(z)\\&\overline{\overline{B}}_\phi(-z)=-\overline{\overline{B}}_\phi(z),\qquad &&\overline{\overline{B}}_z(-z)=\overline{\overline{B}}_z(z)\end{aligned} \qquad [66d]$$

$$\begin{aligned}&\text{quadrupole family:}\quad &&\overline{\overline{B}}_s(-z)=\overline{\overline{B}}_s(z)\\&\overline{\overline{B}}_\phi(-z)=\overline{\overline{B}}_\phi(z),\qquad &&\overline{\overline{B}}_z(-z)=-\overline{\overline{B}}_z(z)\end{aligned} \qquad [66e]$$

These imply $\overline{\overline{A}}_\phi(-z)=\overline{\overline{A}}_\phi(z)$ for the dipolar family and $\overline{\overline{A}}_\phi(-z)=-\overline{\overline{A}}_\phi(z)$ for the quadrupolar family. When [66a] does not hold, the solutions must generally involve both symmetry types.

The concept of equatorial symmetry applies to general $\mathbf{B}$ after the overbars have been removed from [66], and the MHD equations again allow solutions of a single parity provided $\mathbf{u}$ is quadrupolar. To avoid confusion, however, the words 'dipolar' and 'quadrupolar' are usually then replaced by 'antisymmetric' and 'symmetrical,' respectively, since the equatorial dipole actually belongs to the symmetrical family. There has been considerable interest in the equatorial symmetry of the paleofield; see Merrill et al. (1996).

Both the final term in [66a] and at least one of the last two terms in [66b] are needed to maintain $\overline{\mathbf{B}}$. We first suppose that $\overline{\mathbf{u}}_{\rm M}$ is negligible or zero. There are three possibilities:

- If $\alpha\gg\overline{\overline{u}}_\phi$, the α-effect provides the dominating source in [66b] and creates from $\overline{\overline{A}}_\phi$ a zonal field of strength $\overline{\overline{B}}_\phi=\mathrm{O}\left(\mathrm{Rm}_\alpha\overline{\overline{A}}_\phi/\overline{\mathcal{L}}\right)$, where $\mathrm{Rm}_\alpha=\alpha\overline{\mathcal{L}}/\overline{\eta}$ is the α-effect Reynolds number; the α-source in [66a] produces $\overline{\overline{A}}_\phi=\mathrm{O}\left(\mathrm{Rm}_\alpha\overline{\overline{B}}_\phi\overline{\mathcal{L}}\right)$ from $\overline{\overline{B}}_\phi$. Clearly, regeneration requires that Rm_α exceeds some critical value $\mathrm{Rm}_{\alpha c}$. Such a dynamo that operates through the 'product' of two α-effects is called an α^2-dynamo.
- If $\overline{\overline{u}}_\phi\gg\alpha$, the ω-effect provides the dominating source in [66b] and creates from $\overline{\overline{A}}_\phi$ a zonal field of strength $\overline{\overline{B}}_\phi=\mathrm{O}\left(\mathrm{Rm}_\omega\overline{\overline{A}}_\phi/\overline{\mathcal{L}}\right)$, where $\mathrm{Rm}_\omega=\zeta\overline{\mathcal{L}}^2/\overline{\eta}$ is the ω-effect Reynolds number. The α-source in [66a] produces $\overline{\overline{A}}_\phi=\mathrm{O}\left(\mathrm{Rm}_\alpha\overline{\overline{B}}_\phi\overline{\mathcal{L}}\right)$ from $\overline{\overline{B}}_\phi$, as before. Clearly, regeneration requires that the 'dynamo number,' $D=\mathrm{Rm}_\alpha\mathrm{Rm}_\omega=\alpha\zeta\overline{\mathcal{L}}^3/\overline{\eta}^2$, exceed some critical value D_c. Such a dynamo that operates through the 'product' of α- and ω-effects is called an $\alpha\omega$-dynamo.
- If α and $\overline{\overline{u}}_\phi$ are comparable, the two sources in [66b] are equally effective and must be retained, giving an $\alpha^2\omega$-dynamo. This will not be considered here.

Many solutions of each type have been generated. The α^2-dynamos satisfy [65] with $\overline{\overline{\mathbf{u}}}\equiv\mathbf{0}$ and are usually of DC type. This is so for the very simple spherical solutions that exist when α ($\neq0$) is a constant. These can be readily found by the technique in Section 8.03.3.2, which when applied to [65] gives

$$\partial_t\overline{\overline{T}}=\overline{\eta}\nabla^2\overline{\overline{T}}-\alpha\nabla^2\overline{\overline{S}} \qquad [67a]$$

$$\partial_t\overline{\overline{S}}=\overline{\eta}\nabla^2\overline{\overline{S}}+\alpha\overline{\overline{T}} \qquad [67b]$$

Marginal solutions are of DC type and satisfy (in nondimensional variables) $\nabla^2\overline{\overline{T}}+\mathrm{Rm}_{\alpha c}^2\overline{\overline{T}}=0$, where $\mathrm{Rm}_\alpha=\alpha r_o/\overline{\eta}$. Instead of [42c] and [42d], we have

$$\overline{\overline{T}}=\mathrm{Rm}_{\alpha c}j_n(\mathrm{Rm}_{\alpha c}r)Y_n(\theta,\phi) \qquad [67c]$$

$$\overline{\overline{S}}=[j_n(\mathrm{Rm}_{\alpha c}r)-C_nr^n]Y_n(\theta,\phi) \qquad [67d]$$

If $C_n=\mathrm{Rm}_{\alpha c}\,j'_n(\mathrm{Rm}_{\alpha c})/(2n+1)$ and $j_n(\mathrm{Rm}_{\alpha c})=0$, the dynamo condition [40] is satisfied. Again, $n=1$ is the critical mode and

$\mathrm{Rm}_{\alpha c} = 4.493$. (This constant α-model does not satisfy the symmetry condition [66a].)

The $\alpha\omega$-dynamos are usually of AC type and involve a particularly interesting phenomenon: the 'dynamo wave.' Parker, who invented the $\alpha\omega$-dynamo, also exhibited dynamo waves for the first time using a simple planar model in which the α-effect creates $\overline{\overline{B}}_x(y,t)\mathbf{1}_x$ from $\overline{\overline{B}}_z(y,t)\mathbf{1}_z$ and a shearing motion $\zeta x\mathbf{1}_z$ does the reverse; α and ζ are constants. Equation [65] gives

$$\partial_t \overline{\overline{B}}_x = \overline{\eta}\partial_y^2 \overline{\overline{B}}_x + \alpha\partial_y \overline{\overline{B}}_z \qquad [68a]$$

$$\partial_t \overline{\overline{B}}_z = \overline{\eta}\partial_y^2 \overline{\overline{B}}_z + \zeta \overline{\overline{B}}_x \qquad [68b]$$

These equations admit solutions of the form

$$\overline{\overline{\mathbf{B}}} \propto \exp[l(ky - \omega t)] \qquad [68c]$$

provided that

$$\left(l\omega - \overline{\eta}k^2\right)^2 = l\alpha\zeta k \qquad [68d]$$

Only one root of this equation can be regenerative, namely,

$$\omega = -l\overline{\eta}k^2 - \left(\frac{1}{2}|\alpha\zeta k|\right)^{1/2}[\mathrm{sgn}(\alpha\zeta \mathrm{k}) - l] \qquad [68e]$$

This gives growing $\overline{\overline{\mathbf{B}}}$ if $\mathrm{Im}(\omega) > 0$, that is, if $D > D_c = 2$, where $D = |\alpha\zeta k^{-3}|/\overline{\eta}^2$ is the dynamo number. In the critical state $D = D_c$, the frequency $\omega\ [= -\overline{\eta}k^2\mathrm{sgn}(\alpha\zeta k)]$ is nonzero, so the dynamo is of AC type. Magnetic activity progresses as a wave moving with phase velocity $-\overline{\eta}|k|\mathrm{sgn}(\alpha\zeta)\mathbf{1}_y$. As in Section 8.03.2.6, the drift speed $\mathcal{U}_\eta$ of $\overline{\overline{\mathbf{B}}}$ relative to the conductor is of order $\eta/\mathcal{L}$, where $\mathcal{L}$ is the wavelength.

Parker (1957) used dynamo waves to explain the solar activity cycle, which progresses from the poles of the Sun to its equator. The timescale is consistent with its 22-year period provided β is sufficiently large, so that $\overline{\overline{T}}_\eta$ is sufficiently small; see Section 8.03.5.1. Parker visualized that (x, y, z) in the planar model correspond to (r, θ, ϕ), in that order, for spherical $\alpha\omega$-dynamos. The planar model then indicates that if $\zeta < 0$ and if $\alpha > 0$ in the northern hemisphere, a dynamo wave originating near the North Pole will progress towards the equator. The symmetry conditions [66a] show that one starting near the South Pole will also move towards the equator. Subsequently, numerous integrations of [66] in spherical geometry confirmed this; see, for example, Roberts (1972a,b). More recently, as mentioned in Section 8.03.4.4, Gubbins et al. (2000a,b) found similar solutions in a 3-D kinematic model. As Section 8.03.2.6 has shown, $\alpha > 0$ ($\alpha < 0$) in the northern (southern) hemisphere is plausible, but advances in helioseismology did not support $\zeta < 0$, and this led to the abandonment of Parker's model of the solar cycle in the simple form in which he originally conceived it. Dynamo waves may nevertheless be significant for the geodynamo (Section 8.03.6.4). In the 3-D MHD geodynamo simulation of Glatzmaier and Roberts (1996a,b), waves of magnetic activity progress westward through the core even though the fluid itself, together with the SIC, moves predominantly eastward. It is tempting to believe that these are dynamo waves, responsible for maintaining the $\overline{\overline{\varepsilon}}_\phi$ that the dynamo requires, the relative motion of field and conductor being the resistive drift $\mathcal{U}_\eta\ (= \eta/\mathcal{L})$ described in Section 8.03.2.6.

Some vestiges of Cowling's theorem infect models based on [64b]. As pointed out in Section 8.03.3.5, every regenerative $\overline{\overline{\mathbf{B}}}$ has at least one singular latitude circle C, in v or on s, where $\overline{\overline{\mathbf{B}}}_\mathrm{M} = \mathbf{0}$ and only ineligible, infinite $\overline{\overline{\mathbf{u}}}$ can maintain $\overline{\overline{\mathbf{B}}}$. Cowling's argument also excludes MF dynamos based on [64b] that have a singular C on any zero α-surface, such as the equatorial plane for the symmetry [66a]. This means that not only $\overline{\overline{\mathbf{B}}}$ of the quadrupolar family [66c] but also $\overline{\overline{\mathbf{B}}}$ of the dipole family [66b] must possess at least two singular Cs, one in each hemisphere. This tends to make each hemisphere act as a dynamo, independently of the other, so that reversing the sign of $\overline{\overline{\mathbf{B}}}$ in one hemisphere almost creates an acceptable solution of the opposite symmetry. This means that $\mathrm{Rm}_{\alpha c}$ for α^2-dynamos or D_c for $\alpha\omega$-dynamos is numerically nearly the same for one symmetry as for the other. See also Proctor (1977a). The more general mean field dynamos based on [64c] can in principle maintain the $\overline{\overline{\varepsilon}}_\phi(-z) = -\overline{\overline{\varepsilon}}_\phi(z)$ symmetry of the dipole family without excluding C from the equatorial plane.

Some of the DC models create $\overline{\overline{\mathbf{B}}}$ remarkably similar to those produced by 3-D MHD dynamo simulations. Perhaps, this is not too surprising since (even though this tends to be hidden beneath its greater complexity) an MHD model must still create an $\overline{\overline{\varepsilon}}_\phi$ large enough to sustain the axisymmetric part of its field.

This discussion of the α^2- and $\alpha\omega$-models has so far supposed that $\overline{\overline{\mathbf{u}}}_M \equiv \mathbf{0}$. We now consider $\alpha\omega$M-dynamos in which $\overline{\overline{\mathbf{u}}}_M \neq \mathbf{0}$. It was observed in Section 8.03.3.5 that $\overline{\overline{\mathbf{u}}}_M$ advects $\overline{\overline{A}}_\phi$ and $\overline{\overline{B}}_\phi$ but does not enable them to defeat Cowling's theorem. Nevertheless, $\overline{\overline{\mathbf{u}}}_M$ can change the character of mean held dynamos by carrying $\overline{\overline{B}}_\phi$ to regions where the α-source is particularly effective and by advecting $\overline{\overline{A}}_\phi$ to places where the ω-effect is especially potent or it can do the reverse. This can reduce or increase D_c considerably and can transform the AC dynamo to a DC dynamo. This is what happens to the Braginsky models described in Section 8.03.4.1. These do not create α at a point through helical turbulence in the neighborhood of that point. Instead, they produce α through the helicity of planetary waves of global scale. Nevertheless, they are mean field dynamos, where the mean refers to an average over ϕ. As shown in [56], their α-effect is confined to the production of $\overline{\overline{A}}_\phi$, so they are $\alpha\omega$-dynamos or more precisely $\alpha\omega$M-dynamos, since $\overline{\overline{\mathbf{u}}}_M$ is large enough and of the right sign to reduce D_c significantly and to create a steady $\overline{\overline{\mathbf{B}}}$.

8.03.5.3 Saturation: Intermediate Models

Nonlinear generalizations of mean field dynamos provide comparatively simple ways of exploring dynamical issues. By assigning α, Cowling's theorem is defeated and the collapse of $\overline{\overline{\mathbf{B}}}$ is prevented, leaving the investigator free to study nonlinear processes such as 'saturation,' in which the Lorentz force equilibrates $\overline{\overline{\mathbf{B}}}$ at some statistically constant amplitude.

The only mechanism that can equilibrate an α^2-dynamo is a $\mathbf{B}$-dependent α. The heuristic discussion of Parker's α-effect in Section 8.03.2.6 makes it clear that the larger the $\mathbf{B}$ in the flux tube, the more it will resist deformation by a cyclonic eddy. This motivates the commonly used but *ad hoc* ansatz

$$\alpha = \frac{\alpha_0(\mathbf{x})}{1 + (\mathbf{B}/B_0)^2} \qquad [69]$$

where B_0 is a constant. The question of whether the full $\mathbf{B}$ or its statistical mean, $\overline{\mathbf{B}}$, should feature in [69] is of considerable interest in solar physics and astrophysics but may be less significant for the geodynamo (see Section 8.03.5.4). Additionally, it is reasonable to include a dependence of α on the current helicity H_J, in recognition of the decreased angle through which the Ω in **Figure 6(a)** is turned by ζ when $\mathbf{B}$ is increased (Roberts, 1971a,b).

Nonlinear $\alpha\omega$-models can saturate by a different route: $\mathbf{B}$ dependence of the ω-effect. The energy source powering these dynamos is usually assumed to be pole–equator temperature differences produced by convection. In a rotating system, this creates a thermal wind, $\overline{u}^T(s,z)\mathbf{1}_\phi$; see **Section 8.03.6.2**. In addition, Lorentz and viscous forces make two other contributions to the ω-effect: a magnetic wind $\overline{u}^M(s,z)\mathbf{1}_\phi$ of order $\overline{B}_\phi^2/2\Omega\mu_0\rho r_o$ that tends to suppress the zonal differential rotation and a geostrophic wind $\overline{u}^G(s)\mathbf{1}_\phi$ that depends only on distance s from the polar axis (and t); see **Section 8.03.6.2**. In total,

$$\overline{u}_\phi = \overline{u}^T(s,z) + \overline{u}^M(s,z) + \overline{u}^G(s) \qquad [70]$$

Because the α-effect and thermal wind are specified, these 2-D, nonlinear α^2- and $\alpha\omega$-models cannot properly be called 'MHD dynamos,' but, as they take an important step in that direction, they are often termed 'intermediate dynamos.' No attempt will be made here to review the, by now, extensive literature on intermediate dynamo models; interested readers will find Soward (1991) and Dormy and Soward (2007) informative. Despite significant progress, perplexing issues remain unresolved, a state of affairs that is unlikely to improve quickly now that fully 3-D MHD geodynamo simulations have become commonplace.

8.03.6 MHD Dynamos

8.03.6.1 Basic Equations and Boundary Conditions: Energetics

This section has two aims, the first of which is to survey the basics of MHD dynamo theory. The addition of the equations of fluid dynamics is a major step demanding more than a greater computational commitment; it requires also a deeper insight when interpreting numerical results. The second objective (**Section 8.03.6.5**) is to focus on an aspect of the MHD theory that is little considered elsewhere in this book: magnetostrophy. As we shall have no occasion to make further use of toroidal scalars, T will henceforth denote temperature.

The discussion will focus on dynamos driven by thermal buoyancy alone, compositional buoyancy being ignored. We assume that $\mathbf{u}$ obeys

$$\partial_t\mathbf{u} + \mathbf{u}\cdot\nabla\mathbf{u} + 2\boldsymbol{\Omega}\times\mathbf{u} = -\nabla\Pi + g_o\gamma T\mathbf{r}/r_o + \mathbf{J}\times\mathbf{B}/\rho + \nu\nabla^2\mathbf{u} \qquad [71a]$$

This is the usual Navier–Stokes equation for a rotating Boussinesq fluid with an added Lorentz force. In the Boussinesq approximation, ρ is uniform, so that mass conservation reduces to the condition [11] of incompressibility:

$$\nabla\cdot\mathbf{u} = 0 \qquad [71b]$$

Also, since ρ is uniform, the gravitational acceleration $\mathbf{g}$ is $-g_o\mathbf{r}/r_o$, so that the thermal buoyancy force per unit mass is, as shown in [71a], $-\mathbf{g}\gamma T = g_o\gamma\, T\mathbf{r}/r_o$ where γ is the thermal expansion coefficient. Momentum conservation in [71a] is expressed in the reference frame that corotates with the mantle at a constant angular velocity $\boldsymbol{\Omega}$. The resulting Coriolis acceleration, $2\boldsymbol{\Omega}\times\mathbf{u}$, appears on the left-hand side of [71a]. The centrifugal acceleration, $\boldsymbol{\Omega}\times(\boldsymbol{\Omega}\times\mathbf{x})$, has been combined with the kinetic pressure, P, to form the 'reduced pressure,' $\Pi = P/\rho - \frac{1}{2}(\boldsymbol{\Omega}\times\mathbf{x})^2$. The last two terms in [71a] represent the Lorentz and viscous forces per unit mass. Because of its small moments of inertia, the Earth's SIC would respond readily to torques exerted by the mantle and FOC, but for simplicity, we suppose that a torque exists that keeps the SIC corotating with the mantle ($\boldsymbol{\Omega}_i = \boldsymbol{\Omega}$). Then, the no-slip condition gives

$$\mathbf{u} = \mathbf{0} \quad \text{on the CMB and ICB} \qquad [71c]$$

When viscous forces are ignored, the differential order of [71a] is reduced, and it is possible to satisfy only one scalar condition on $\mathbf{u}$ at each boundary; then [71c] is replaced by

$$\mathbf{n}\cdot\mathbf{u} = 0 \quad \text{on the CMB and ICB when } v = 0 \qquad [71d]$$

Most MHD geodynamo simulations are based on [71a] and [71b], although a geophysically more realistic approach was initiated by Glatzmaier and Roberts (1996a,b) whose simulations replaced the Boussinesq by the anelastic approximation, which allows for the compressibility of the core; see Braginsky and Roberts (1995).

The magnetic field obeys the kinematic theory developed in **Sections 8.03.2–8.03.5**. The temperature T is governed by an energy equation of the form

$$\partial_t T + \mathbf{u}\cdot\nabla T = \kappa\nabla^2 T \qquad [72]$$

where we have neglected three volumetric sources of heat: dissolved radioactivity, the viscous dissipation rate per unit volume, and the ohmic dissipation rate per unit volume. Convection is maintained by a constant applied temperature difference, $\Delta T = T_i - T_o$, between the ICB and CMB, which are held at temperatures T_i and T_o.

Equations [71a] and [71b] imply

$$\frac{d\mathcal{K}}{dt} = \mathcal{P} - \mathcal{Q}_v - \mathcal{F} \qquad [73a]$$

where

$$\mathcal{K} = \int_v \tfrac{1}{2}\rho\mathbf{u}^2 d^3x \qquad [73b]$$

is the kinetic energy,

$$\mathcal{P} = \int_v \rho g_o\gamma T(\mathbf{r}\cdot\mathbf{u}/r_o)d^3x \qquad [73c]$$

is the buoyant power input,

$$\mathcal{Q}_v = \int_v \rho\nu\boldsymbol{\zeta}^2 \mathrm{d}^3x \qquad [73d]$$

is the rate of viscous heating, and $\mathcal{F}$ is the rate at which the flow loses kinetic energy to magnetic energy by working against the Lorentz force, $\mathbf{L}$ (see [12e]). When the total energy, kinetic and magnetic, is summed, the $\mathcal{F}$ terms cancel, so that [13h] and [73a] give

$$\frac{\mathrm{d}}{\mathrm{d}t}(\mathcal{K} + \mathcal{M}_{\mathrm{tot}}) = \mathcal{P} - \mathcal{Q}_v - \mathcal{Q}_\eta \qquad [73e]$$

Equation [73e] is the energy budget of the convective dynamo. Although $\mathcal{K} + \mathcal{M}_{\mathrm{tot}}$ is usually time-dependent, a successful MHD dynamo on average maintains $\mathbf{u}$ and $\mathbf{B}$ over a time long compared with the diffusion time, $\mathcal{T}_\eta$. We call such a dynamo 'steadily operating.' By [73e], its power balance is

$$\mathcal{P}^{\mathrm{mean}} = \mathcal{Q}_v^{\mathrm{mean}} + \mathcal{Q}_\eta^{\mathrm{mean}} \qquad [73f]$$

which expresses the fact that buoyancy makes good the viscous and ohmic losses.

8.03.6.2 Classical Theory of Rotating Fluids

In this subsection, we shall suppose that $\mathbf{B} \equiv \mathbf{0}$, and at first, we exclude buoyancy too ($\mathbf{g} \equiv \mathbf{0}$). We give a rudimentary account of relevant concepts in the theory of rotating fluids. For a more complete treatment, see Greenspan (1968), Dormy and Soward (2007).

Two dimensionless numbers quantify the importance of viscosity and inertia relative to the Coriolis force, the 'Ekman number,' E, and the 'Rossby number,' Ro:

$$\mathrm{E} = \nu/2\Omega\mathcal{L}^2 \qquad [74a]$$

$$\mathrm{Ro} = \mathcal{U}/2\Omega\mathcal{L} \qquad [74b]$$

The viscosity of the FOC is commonly estimated to be about $10^{-6}\,\mathrm{m^2\,s^{-1}}$ so that, for $\mathcal{L} = 2 \times 10^6\mathrm{m}$, $\mathrm{E} \approx 10^{-15}$, i.e., the FOC is very rapidly rotating:

$$\mathrm{E} \ll 1 \qquad [74c]$$

Smaller $\mathcal{L}$ gives larger E, a fact we can recognize by introducing a scale-dependent Ekman number, $\mathrm{E}(\mathrm{x}) = \nu/2\Omega\mathcal{L}_0$, analogous to the local magnetic Reynolds number, $\mathrm{Rm}(\mathrm{x}) = \mathcal{U}\mathcal{L}_0/\eta$, of Section 8.03.2.3. The most important, field-creating scale was there found to be $\mathcal{L}_0 \approx 10^4\mathrm{m}$. The corresponding $\mathrm{E}(\mathrm{x}) \approx 10^{-10}$, so that [74c] holds for this scale too. Apparently viscosity does not significantly affect the dynamics for the scales that generate the geomagnetic field.

The Rossby number quantifies the importance of the inertial force relative to the Coriolis force for motions of scale $\mathcal{L}$. For $\mathcal{U} = 2 \times 10^{-4}\,\mathrm{m\,s^{-1}}$, we have $\mathrm{Ro} \sim 10^{-5}$ so that

$$\mathrm{Ro} \ll 1 \qquad [74d]$$

and the Coriolis force again dominates: $|2\boldsymbol{\Omega} \times \mathbf{u}| \gg |\mathbf{u} \cdot \boldsymbol{\nabla}\mathbf{u}|$. The remaining inertial term, $\partial_t\mathbf{u}$, in [71a] is significant only for timescales $\mathcal{T}$ much less than $\mathcal{L}/\mathcal{U}$. These arise for 'inertial waves,' which in their simplest form are governed by the abbreviated [71a]:

$$\partial_t\mathbf{u} + 2\boldsymbol{\Omega} \times \mathbf{u} = -\boldsymbol{\nabla}\Pi \qquad [75]$$

The waves are dispersive. If $\mathbf{u}$ is proportional to $\exp(l\omega t)$ and obeys [71b], [71d], the spectrum of possible ω is discrete, with infinitely many possible eigenvalues ω, all in the range $|\omega| \le 2\Omega$; see Dormy and Soward (2009). The closer $|\omega|$ is to zero, the denser the packing of eigenvalues and the more two-dimensional the eigenfunctions are with respect to $\boldsymbol{\Omega} = \Omega\mathbf{1}_z$. The extreme case, $\omega = 0$, is relevant for timescales of order $\mathcal{L}/\mathcal{U}$ and larger. These belong to a single, infinitely degenerate eigenfunction called the 'geostrophic mode.' For this mode, $\partial_t\mathbf{u} = \mathbf{0}$ so that [75] becomes

$$2\boldsymbol{\Omega} \times \mathbf{u} = -\boldsymbol{\nabla}\Pi \qquad [76a]$$

By [71b], this gives $2\boldsymbol{\Omega} \cdot \boldsymbol{\nabla}\mathbf{u} = \mathbf{0}$, that is,

$$\mathbf{u} = \mathbf{u}(x, y, t) \qquad [76b]$$

Stated in words:

Proudman–Taylor theorem: The slow steady motion of a rotating inviscid fluid is two-dimensional with respect to the rotation axis (Proudman, 1916; Taylor, 1916).

Since the CMB and ICB are assumed axisymmetric (and in fact spherical), [71d] and [76b] imply $\mathbf{u} = \overline{\mathbf{u}}^G$, where

$$\overline{\mathbf{u}}^G = \overline{u}^G(s, t)\mathbf{1}_\phi \qquad [76c]$$

The function $\overline{u}^G(s, t)$ is arbitrary; this is the infinite degeneracy referred to in the preceding text. The 'geostrophic flow' $\overline{\mathbf{u}}^G$ is axisymmetric, zonal, and constant on 'geostrophic cylinders,' $\mathcal{C}(s)$. These cylinders are of radius s and, if $s \ge r_i$ have length $2z_1(s)$, where $z_1(s) = \sqrt{(r_o^2 - s^2)}$. (For $s < r_i$, their length is $z_1(s) = -\sqrt{(r_i^2 - s^2)}$). Figure 10 shows a typical geostrophic cylinder and also the particular one, $\mathcal{C}_i = \mathcal{C}(r_i)$, that touches the SIC on its equator and is therefore called the 'tangent cylinder.' The arbitrariness of $\overline{u}^G$ expresses the fact that the Coriolis force created by $\overline{\mathbf{u}}^G$ is ineffective, because

$$2\boldsymbol{\Omega} \times \overline{\mathbf{u}}^G = \boldsymbol{\nabla}\Upsilon \qquad [76d]$$

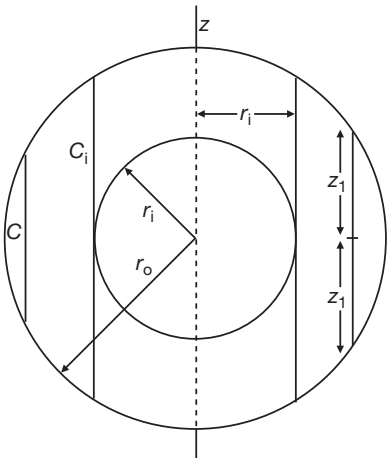

Figure 10 Geostrophic cylinders. A meridional section of the core is shown. One geostrophic cylinder, $\mathcal{C}(s)$, of radius $s > r_i$ appears in cross section as two lines parallel to Oz of length $2z_1$, where $z_1 = \sqrt{(r_o^2 - s^2)}$. The tangent cylinder, $\mathcal{C}_i$, is also shown; this is the geostrophic cylinder of radius r_i that touches the SIC on its equator.

where $\Upsilon = -2\Omega\int \overline{u}^G(s,t)\mathrm{d}s$. Thus, the Coriolis force can be absorbed into $\nabla\Pi$. This means that for $\nu = 0$, each geostrophic cylinder can turn about its axis Oz without disturbing, or being disturbed by, its neighbors.

Two nondimensional parameters are commonly used in describing convection, the 'Rayleigh number,' Ra, and the (thermal) 'Prandtl number,' Pr:

$$\mathrm{Ra} = g_o\gamma\Delta T d^3/\nu\kappa \qquad [77a]$$

$$\mathrm{Pr} = \nu/\kappa \qquad [77b]$$

where $d = r_o - r_i$ is the fluid depth. The Rayleigh number is a measure of how effective the buoyancy force is in overcoming the diffusive processes that oppose convection. Clearly this motion does not assist the core to cool; heat can still leave the core only by thermal conduction. However, convection, not conduction, is needed to power the dynamo.

A popular way to gain insight into convective processes, popular because the theory is relatively tractable, is to study the onset of convection. A motionless 'conductive state' is defined in which heat is carried across the system by thermal conduction. The linear stability of this state is then analyzed. It is found that when the 'control parameter,' Ra, reaches some 'critical' or 'marginal' value, Ra_c, the conduction solution becomes convectively unstable. The eigenfunction corresponding to Ra_c gives the structure of the marginal state. In the absence of the Coriolis and Lorentz forces, Ra_c is typically of order 10^3 and the marginal mode is a pattern of overturning convection cells, each having about the same horizontal scale $\mathcal{H}_c$ as the depth d of the fluid. When the Coriolis and Lorentz forces are significant, $\mathcal{H}_c$ and Ra_c may be greatly altered; see the succeeding text.

While studies of marginal convection provide insight into convective flows, they clearly have limited value. They predict that when $\mathrm{Ra} > \mathrm{Ra}_c$, the convective motions increase without limit, though in reality, the nonlinearities $\mathbf{u}\cdot\nabla\mathbf{u}$ and $\mathbf{J}\times\mathbf{B}$ in [71a] prevent this and cause the solution to 'saturate.' The enhanced amplitudes and modified structure of the convective motions as Ra is increased beyond Ra_c are topics discussed in other chapters in this volume. We shall merely use the results of linear theory to obtain clues about how the Coriolis and Lorentz forces affect thermal convection.

Consider next the dynamical effect of a buoyancy force produced by an axisymmetric temperature distribution $\overline{T}$. The steady linearized inviscid form of [71a] is then

$$2\boldsymbol{\Omega}\times\overline{\mathbf{u}} = -\nabla\overline{\Pi} - \gamma\overline{T}\mathbf{g} \qquad [78a]$$

Since $\nabla\times\mathbf{g} = \mathbf{0}$, this implies, in place of [76a],

$$2\boldsymbol{\Omega}\cdot\nabla\overline{\mathbf{u}} = -\gamma\mathbf{g}\times\nabla\overline{T} \qquad [78b]$$

Because $\mathbf{g}$ $(=-g_o\mathbf{r}/r_o)$ is radial, this reduces to $\partial_z\overline{u}_\phi = (g_o\gamma/2\Omega r_o)\partial_\theta\overline{T}$, which integrates to

$$\overline{\mathbf{u}} = \left[\overline{u}^T(s,z) + \overline{u}^G(s)\right]\mathbf{1}_\phi \qquad [78c]$$

The flow $\overline{u}^T$ is called the 'thermal wind.' Its magnitude is O $(g\gamma\delta T/2\Omega)$, and if this is comparable with the assumed characteristic velocity $\mathcal{U} = 2\times10^{-4}\,\mathrm{m\,s^{-1}}$, the pole–equator temperature difference δT on the CMB is of order 10^{-4} K for $\gamma\sim10^{-5}\,\mathrm{K^{-1}}$. This may be regarded as typical of the temperature differences between rising and falling convective streams in the core though, more precisely, when the compressibility of the core is properly allowed for, it is typical of the excess or deficit of the temperature relative to the adiabat.

There is clearly some arbitrariness in [78c], since all or any part of $\overline{u}^G$ can be absorbed into $\overline{u}^T$. A convenient way of removing this arbitrariness is by introducing a 'geostrophic average,' which, for a scalar field $Q(\mathbf{x},t)$, is defined for $s > r_i$ by

$$Q^G(s,t) = \frac{1}{A(s)}\int_{\mathcal{C}(s)} Q(\mathbf{x},t)\mathrm{d}^2x = \frac{1}{2z_1}\int_{-z_1}^{z_1}\overline{Q}(s,Z,t)\mathrm{d}Z \qquad [79a]$$

Here, $\pm z_1(s) = \pm\sqrt{(r_o^2 - s^2)}$ are the z-coordinates of the latitude circles where the geostrophic cylinder $\mathcal{C}(s)$ meets the CMB, $A = 4\pi s z_1(s)$ is the area of the cylinder, and $\mathrm{d}^2x = s\mathrm{d}\phi\mathrm{d}z$; see Figure 10. The geostrophic part, $\mathbf{Q}^G(s,t)$, of a vector field $\mathbf{Q}(\mathbf{x},t)$ is defined from its zonal component by

$$\mathbf{Q}^G(s,t) = Q_\phi^G(s,t)\mathbf{1}_\phi \qquad [79b]$$

These definitions apply only when $s > r_i$. Inside the TC, there are a geostrophic average for the fluid to the north of the SIC and another for the fluid to the south, but we shall often avoid this complication by ignoring the SIC entirely. The 'ageostrophic' part of $Q(\mathbf{x},t)$ is what is left over after the geostrophic part has been removed, for example,

$$\mathbf{u}(\mathbf{x},t) = \mathbf{u}^G(s,t) + \mathbf{u}^A(\mathbf{x},t) \qquad [79c]$$

This separation of $\mathbf{u}$ into its geostrophic and ageostrophic parts is important in highly rotating systems because the otherwise dominating Coriolis force of $\mathbf{u}^G$ becomes a gradient absorbed into the pressure and therefore ineffective; see [76d]. Other forces, particularly the inertial force, then assume an importance they would not otherwise possess. It is therefore often necessary to make the separation [79c] precise by insisting that

$$\left(\mathbf{u}^A\right)^G = 0 \qquad [79d]$$

The thermal wind is illustrative of a more general situation: the response of a rotating fluid to forcing; $\mathbf{u}$ is sought satisfying

$$2\boldsymbol{\Omega}\times\mathbf{u} = -\nabla\Pi + \mathbf{F} \qquad [80a]$$

where $\mathbf{F}(\mathbf{x},t)$ is the forcing. The geostrophic part of [80a] is

$$2\Omega u_s(s,t) = F_\phi^G \qquad [81b]$$

The left-hand side is a function of only s and t because the right-hand side is, but it is not geostrophic according to the definition [79b], which involves only the ϕ-component of $\mathbf{u}$. Clearly, u_s in [81b] is proportional to the mass flux across, and out of, $\mathcal{C}$. By [71d], the mass flux through the spherical caps, $\mathcal{N}(s)$ and $\mathcal{S}(s)$, is zero; see Figure 11. Therefore, denoting by $\mathcal{V}(s)$ the volume surrounded by the surface $S = \mathcal{C}(s) + \mathcal{N}(s) + \mathcal{S}(s)$, we have

$$u_s \equiv \frac{1}{A(s)}\int_{\mathcal{C}(s)}(\mathbf{u}\cdot\mathbf{n})\mathrm{d}^2x = \frac{1}{A(s)}\oint_S(\mathbf{u}\cdot\mathbf{n})\mathrm{d}^2x$$
$$= \frac{1}{A(s)}\int_{\mathcal{V}(s)}\nabla\cdot\mathbf{u}\,\mathrm{d}^3x = 0 \qquad [81c]$$

by [71b]. Equation [81b] therefore simplifies to

$$F_\phi^G = 0 \qquad [81d]$$

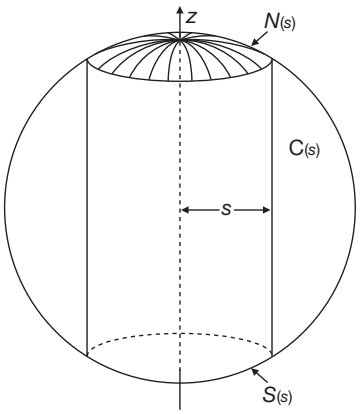

Figure 11 Spherical caps, $\mathcal{N}(s)$ and $\mathcal{S}(s)$, on the CMB provide the ends of the geostrophic cylinder $\mathcal{C}(s)$. The volume enclosed by $\mathcal{S}=\mathcal{C}(s)+\mathcal{N}(s)+\mathcal{S}(s)$ is denoted by $\mathcal{V}(s)$ in the text. (For simplicity, the existence of the SIC is ignored in this figure.)

When $\mathbf{F}$ is the buoyancy force $-\gamma T\mathbf{g}$ alone, [81d] is satisfied because $\mathbf{g}$ has no ϕ-component. In the next section, however, where $\mathbf{F}$ contains the Lorentz force, [81d] is a restriction on B.

One way of resolving the $F_\phi^G \neq 0$ difficulty is to restore the inertial force, $\partial_t \mathbf{u}$, to [80a]

$$\partial_t \mathbf{u} + 2\boldsymbol{\Omega}\times\mathbf{u} = -\boldsymbol{\nabla}\Pi + \mathbf{F} \qquad [82a]$$

from which the geostrophic part of [82a] is

$$\partial_t \mathbf{u}^G = -\boldsymbol{\nabla}(\Pi + \Upsilon) + \mathbf{F}^G \qquad [82b]$$

which gives

$$\partial_t u_\phi^G = F_\phi^G \qquad [83]$$

The consequences are considered in **Sections 8.03.6.3–8.03.6.5**.

Another way of resolving the $F_\phi^G \neq 0$ difficulty is by re-introducing viscous forces. Then the smallness [74c] of E encourages an asymptotic approach. Conceptually, the core is divided into boundary layers, in which viscosity is significant, and the remaining 'mainstream' in which viscosity does not act at leading order. Then,

$$\mathbf{u} = \mathbf{u}^{ms} + \mathbf{u}^{bl} \qquad [84a]$$

The most important boundary layer in rotating fluids is the Ekman layer at a boundary, the thickness of which is of order $\delta_\nu = (\nu/2\Omega)^{1/2} = \mathrm{E}^{1/2}\mathcal{L} \sim 0.1\,\mathrm{m}$. In [84a], $\mathbf{u}^{bl}$ vanishes rapidly with distance $r_o - r$ from the boundary; here, $r = r_o$. It is convenient to scale this distance with d_ν by defining $\xi = (r_o - r)/\delta_\nu$. In spherical coordinates, $\mathbf{u}^{bl}$ is then $\mathbf{u}^{bl}(\xi, \theta, \phi)$, where $\xi = 0$ is the boundary $r = r_o$ and $\xi \to \infty$ is commonly called the 'edge of the boundary layer,' at which

$$\mathbf{u}^{bl} \to \mathbf{0} \quad \text{as} \quad \xi \to \infty \qquad [84b]$$

Expanding $\mathbf{u}^{ms}$ as $\mathbf{u}^{ms} = \mathbf{u}_1 + \mathbf{u}_2 + \ldots$, the leading-order part, $\mathbf{u}_1$, obeys the inviscid equation [80a] and the boundary condition $\mathbf{n}\cdot\mathbf{u}_1 = 0$; see [71d]. This determines $\mathbf{u}_1$ but gives a nonzero $\mathbf{n}\times\mathbf{u}_1$ on $r = a$. The main task of the Ekman layer is to remedy this by finding the solution of the equations governing the Ekman layer such that $\mathbf{n}\times\mathbf{u}^{bl}_{\xi=0} + \mathbf{n}\times\mathbf{u}_{1,r=r_o} = 0$. Then, as $\partial_r = -\delta_\nu^{-1}\partial_\xi$, [71b] shows that u_ξ^{bl} is $\mathrm{O}(E^{1/2})$, so that [71d], that is, $\mathbf{n}\cdot\mathbf{u}^{bl}_{\xi=0} + \mathbf{n}\cdot\mathbf{u}_{2,r=r_o} = 0$, requires that $\mathbf{u}_2$ be $\mathrm{O}(E^{1/2})$ also. At the edge of the boundary layer ($\xi = \infty$) where [84b] applies, $\mathbf{n}\cdot\mathbf{u} = \mathbf{n}\cdot\mathbf{u}_2 + \ldots$ is nonzero. This is called the 'Ekman pumping' (if $\mathbf{u}_2$ is away from the boundary) or the 'Ekman suction' (if towards the boundary). It drives an order $E^{1/2}$ mainstream flow $\mathbf{u}_2$ throughout $\mathcal{V}(s)$. Therefore, on repeating the integration [81c] for the mainstream flow alone, the left-hand side of [81b] is

$$u_s(s,t) = -\frac{1}{A(s)}\oint_{\mathcal{N}+\mathcal{S}} (\mathbf{u}_2\cdot\mathbf{n})\mathrm{d}^2x \qquad [84c]$$

The right-hand side of [84c] is nonzero, of order $E^{1/2}$, and determined from $\mathbf{u}_1$ by the Ekman layer analysis outlined in the preceding text; for full details, see Dormy and Soward (2009). Through [81b], eqn [84c] establishes a relationship between the nonzero F_ϕ^G and the mainstream flow $\mathbf{u}_1$.

When $\mathbf{B} = \mathbf{0}$, viscosity strongly influences the onset of convection when $E \ll 1$. For simplicity, we suppose that $\mathrm{Pr} > 1$ and again ignore the SIC, supposing that convection is driven by dissolved heat sources. The flow in the marginal state, $\mathrm{Ra} = \mathrm{Ra}_c$, is asymmetrical, consisting of a 'cartridge belt' of two-dimensional cells, often called 'Taylor cells,' parallel to the axis of rotation and regularly spaced round that axis in a sequence of cyclonic and anticyclonic vortices, their vorticity being, respectively, parallel and antiparallel to $\boldsymbol{\Omega}$ (Busse, 1970; Dormy et al., 2004; Jones et al., 2000; Roberts, 1968). Their name 'Taylor cells' is a useful reminder of the Proudman–Taylor theorem, which the flow is trying to obey by being as two-dimensional as possible, consistent with allowing convection to occur at all. We have already seen that if $\nu = 0$, small-amplitude motions must be geostrophic. But geostrophic motions have no radial components to carry heat outward. Convection can occur only if viscous forces are large enough to break the rotational constraint of the theorem. Viscous forces are most effective at small $\mathcal{L}$, but such motions viscously dissipate energy rapidly and therefore require a strong buoyancy force to maintain them. This explains why when $E \ll 1$, the width $\mathcal{H}_c$ of the cells in the marginal state is small, of order $E^{1/3}r_o$, and why Ra_c is large, of order $E^{-4/3}$.

8.03.6.3 Coriolis Magnetohydrodynamics (CMHD)

This subsection focuses on MHD but only in the form relevant to core dynamics where the Coriolis forces are strong and drastically transform classical MHD, so much so that the subject deserves its own name and acronym. The obvious choice is 'rotating MHD,' but 'RMHD' is an abbreviation that is often used for either 'relativistic MHD' or 'reduced MHD.' Here, it will be called the 'Coriolis magnetohydrodynamics,' or 'CMHD.' For simplicity, the SIC is again almost completely ignored.

The 'Alfvén number' (aka the 'magnetic Mach number') is defined by

$$\mathrm{Al} = \mathcal{U}/\mathcal{V}_A \qquad [85a]$$

With $\mathcal{U} = 2\times10^{-4}\,\mathrm{m\,s^{-1}}$ and $\mathcal{V}_\mathrm{A} = 1\,\mathrm{cm\,s^{-1}}$ as before, $\mathrm{Al} \approx 0.02$. Even though this is not very small, we write for simplicity

$$\mathrm{Al} \ll 1 \qquad [85b]$$

for it is Al^2 ($\approx 4\times10^{-4}$) that is significant. Not only is it the ratio of kinetic and magnetic energy densities, but also it quantifies the importance of the inertial force $\rho\mathbf{u}\cdot\boldsymbol{\nabla}\mathbf{u} = \mathrm{O}(\rho\mathcal{U}^2/\mathcal{L})$ relative to the Lorentz force $\mathbf{J}\times\mathbf{B} = \mathrm{O}(\mathcal{B}^2/\mu_0\mathcal{L})$.

The Lorentz force can equilibrate the system in two main ways, the first of which has already been noted in Section 8.03.2.7. In the 'weak field regime,' the Lorentz and viscous forces are equipotent and

$$\mathcal{B} = \sqrt{(\mu_0\rho\nu\eta)}/\mathcal{L} \qquad [86a]$$

or

$$\mathrm{Ha} = \mathrm{O}(1) \qquad [86b]$$

where Ha is the Hartmann number defined in [28]. Alternatively, equilibration may occur when the Lorentz and Coriolis forces are comparable, the 'strong field regime':

$$\mathcal{B} = \sqrt{(2\Omega\mu_0\rho\eta)} \qquad [87a]$$

or

$$\Lambda = \mathrm{O}(1) \qquad [87b]$$

where Λ is the 'Elsasser number,' a parameter that is independent of both $\mathcal{L}$ and $\mathcal{U}$:

$$\Lambda = \frac{\sigma\mathcal{B}^2}{2\Omega\rho} = \frac{\mathcal{V}_A^2}{2\Omega\eta} \qquad [87c]$$

The adjectives 'weak' and 'strong' are appropriate since $\mathcal{B}_{\mathrm{weak}}/\mathcal{B}_{\mathrm{strong}} = \mathrm{O}(E^{1/2}) \ll 1$.

Magnetic parameters analogous to [74a] and [74b] are the 'magnetic Ekman number,' E_m, and 'magnetic Rossby number,' Ro_m:

$$E_\mathrm{m} \equiv \eta/2\Omega\mathcal{L}^2 \ll 1 \qquad [88a]$$

$$\mathrm{Ro}_\mathrm{m} \equiv \mathcal{V}_\mathcal{A}/2\Omega\mathcal{L} \ll 1 \qquad [88b]$$

where the smallness of these parameters is added to their definitions. To verify that they are small for $\mathcal{L} = 10^6$ m, take $\overline{\eta} = 2\ \mathrm{m}^2\ \mathrm{s}^{-1}$, and $\mathcal{V}_\mathcal{A} = 1\,\mathrm{cm\,s}^{-1}$ as before. Then, $E_\mathrm{m} \approx 3\times10^{-7}$ and $\mathrm{Ro}_\mathrm{m} \approx 2\times10^{-4}$, the first of which follows from [74d] since $E_\mathrm{m} = \mathrm{Ro}/\mathrm{Rm}$ and $\mathrm{Rm} \gg 1$. Because $\mathrm{Al}^2 = \mathrm{Pm}^{-1}(\mathrm{Rm}/\mathrm{Ha})^2$ and $\mathrm{Pm} \approx 10^{-6}$ for a liquid metal, the magnetic energy in a weak field dynamo operating in the core would be necessarily much less than the kinetic energy of the motions that sustain it. For a strong field dynamo, the kinetic energy is less than the magnetic energy by a factor of order $\mathrm{Al}^2 \approx 10^{-4}$.

Although the asymptotic analyses of Childress and Soward (1972) and Soward (1974) for $E \to 0$ establish unequivocally that weak field dynamos exist, the geodynamo is not one of them. Equation [87c] implies $\mathcal{B}_{\mathrm{strong}} \approx 1$ mT, which is typical of the observed field strength, but, even taking ν to be as large as η, [86a] gives only $\mathcal{B}_{\mathrm{weak}} \approx 0.1$ μT. Moreover, as Soward (1974) showed, there is a limit to the value of Ha beyond which weak field dynamos do not exist. The analysis of Fautrelle and Childress (1982) indicates that beyond this termination, there are strong field dynamos.

The effect of a uniform magnetic field, $\mathbf{B}_0$, on the onset of convective instabilities was first examined by Chandrasekhar; see Chapter V of his treatise on linear stability problems (Chandrasekhar, 1961). For a horizontal plane layer where $\mathbf{B}_0$ and $\boldsymbol{\Omega}$ are vertical, he showed that the $\mathcal{H}_c = \mathrm{O}(E^{1/3}d)$ preferred convective mode, which arises when $\mathbf{B}_0 \equiv \mathbf{0}$ and E is small (see Section 8.03.6.2), is replaced when Λ exceeds $\mathrm{O}(E^{1/3})$ by a different preferred mode for which $\mathcal{H}_c = \mathrm{O}(d)$ and $\mathrm{Ra}_c = \mathrm{O}(E^{-1})$, that is, Ra_c is reduced by an $\mathrm{O}(E^{-1/3})$ factor that is 10^5 for $E = 10^{-15}$. This is because the system no longer relies on small $\mathcal{H}$, and the associated large viscous dissipation, to break the rotational constraint. It defeats the constraint through the Lorentz force, which does not require a small $\mathcal{H}$ and an associated large ohmic dissipation. Subsequent research has shown that these findings are typical for marginal convection in CMHD; similar results hold for other orientations of $\mathbf{B}_0$ and $\boldsymbol{\Omega}$ and for spherical systems; see Fearn (1998) and Roberts and King (2014).

A question that has long been asked but is currently unanswered is whether these results from stability theory (where $\mathbf{B}$ is externally applied as a uniform $\mathbf{B}_0$) have any validity in geodynamo theory (where $\mathbf{B}$ is created by electric currents flowing in the core). Section 8.03.6.5 will examine the current status of attempts to answer this question.

Henceforward, the forcing function, $\mathbf{F}$ in Section 8.03.6.3, is assumed (see [80a]):

$$\mathbf{F} = -\gamma T\mathbf{g} + \mathbf{J}\times\mathbf{B}/\rho \qquad [89a]$$

so that [81d] becomes

$$(\mathbf{J}\times\mathbf{B})_\phi^G \equiv \frac{1}{A(s)}\int_{\mathcal{C}(s)} (\mathbf{J}\times\mathbf{B})_\phi \mathrm{d}^2x = 0 \qquad [89b]$$

This important result (Taylor, 1963) is called the 'Taylor condition' or the 'Taylor constraint.' A field obeying [89d] is called a 'Taylor state.' Here, we express [89b] through the 'Taylor integral,' $T(s,t)$:

$$T(s,t) = s\int_{\mathcal{C}(s)} (\mathbf{J}\times\mathbf{B})_\phi \mathrm{d}^2x \qquad [89c]$$

writing [89b] as

$$T(s,t) = 0 \quad \text{for all} \quad 0 \le s \le a \qquad [89d]$$

The torque about Oz exerted by the Lorentz force on the interior $\mathcal{V}(s)$ of $\mathcal{C}(s)$ is

$$\Gamma_z(s,t) \equiv \int_{\mathcal{V}(s)} s(\mathbf{J}\times\mathbf{B})_\phi \mathrm{d}^3x \qquad [90a]$$

and by [89c],

$$T(s,t) = \partial_s\Gamma_z(s,t) \qquad [90b]$$

From the absence of a singularity in $\mathbf{B}$ at $s = 0$, it follows that the Taylor condition [89d] implies $\Gamma_z(s,t) = 0$ for all s (and clearly the converse is true). According to [14f], $\Gamma_z(s,t)$ may also be written an integral over the surface $\mathcal{C}(s) + \mathcal{N}(s) + \mathcal{S}(s)$ of $\mathcal{V}(s)$:

$$\Gamma_z(s,t) = \frac{1}{\mu_0}\oint_{\mathcal{C}+\mathcal{N}+\mathcal{S}} sB_\phi(\mathbf{B}\cdot\mathbf{n})\mathrm{d}^2x \qquad [90c]$$

In the axisymmetric case, $\overline{B}_\phi = 0$ on the spherical caps of $\mathcal{V}(s)$, so that the magnetic torques exerted by these caps on $\mathcal{V}(s)$ are zero, leaving only the torque from $C(s)$. Then [89d] and [90b] imply

$$\int_{-z_1}^{z_1} \overline{B}_\phi \overline{B}_s \mathrm{d}z = 0 \qquad [90d]$$

This is the form of the Taylor condition for intermediate mean field dynamos (Section 8.03.5.3). For general **B**, the integrals over the caps in [90c] do not vanish and represent the part of $\Gamma_z(s,t)$ that the exterior of $\mathcal{V}(s)$ exerts on $\mathcal{V}(s)$ itself via the asymmetrical part of the vacuum field $\hat{\mathbf{B}}$. This torque is small for the Earth's core (e.g., Roberts and Aurnou, 2012) and will be discarded in deriving [93b] in the succeeding text.

8.03.6.4 MAC Waves and Torsional Waves

Section 8.03.6.2 noted that one way of dealing with a field that does not obey [89d] is by restoring the inertial force, replacing [80a] by

$$\partial_t \mathbf{u} + 2\boldsymbol{\Omega} \times \mathbf{u} = -\boldsymbol{\nabla}\Pi + \mathbf{F} \qquad [91a]$$

It is helpful to consider $\mathbf{u}^G$ and $\mathbf{u}^A$ separately, writing $\mathbf{u} = \mathbf{u}^G + \mathbf{u}^A$ and $\mathbf{F} = \mathbf{F}^G + \mathbf{F}^A$, as in [76d]. Section 8.03.6.2 showed that $F^G_\phi = \rho^{-1}(\mathbf{J}\times\mathbf{B})^G_\phi$ so that the geostrophic part of [91a] is

$$s\partial_t \zeta^G = \rho^{-1}(\mathbf{J}\times\mathbf{B})^G_\phi \qquad [91b]$$

where $\zeta^G(s,t) = u^G_\phi(s,t)/s$ is the angular velocity of the geostrophic cylinder $\mathcal{C}(s)$. This 'modified Taylor condition' was also given by Taylor (1963), but not pursued. We return to it later.

The ageostrophic part of [91a] is

$$\partial_t \mathbf{u}^A + 2\boldsymbol{\Omega} \times \mathbf{u}^A = -\boldsymbol{\nabla}\Pi^A + \mathbf{F}^A \qquad [91c]$$

where $\Pi^A = \Pi + \Upsilon$; see [76a]. The essential difference between [75] and [91c] is the presence of $\mathbf{F}^A$, which contains the Lorentz and buoyancy forces. The evolution of the Lorentz force, $\rho_0^{-1}\mathbf{J}\times\mathbf{B}$, is determined from that of $\mathbf{J} = \mu_0^{-1}\boldsymbol{\nabla}\times\mathbf{B}$ and **B**, which is decided by [8], [1c], and the dynamo condition [40]. The evolution of the buoyancy force, $-\gamma T\mathbf{g}$ (see [71a]), is determined by that of T (see [72]) and its boundary conditions.

Because of the addition of the Lorentz and buoyancy forces, the inertial waves in Section 8.03.6.3 have to be reconsidered. Time-independent solutions of [91a], [8], and [72] are perturbed by $\delta\mathbf{u}^A$, $\delta\mathbf{B}$, and δT. Because three time derivatives are involved in the evolution of $\delta\mathbf{u}^A$, $\delta\mathbf{B}$, and δT, three families of dispersive waves emerge. Braginsky (1964b, 1967) found that because $\mathrm{Ro_m} \ll 1$ (see [88b]), one family is essentially the same as the inertial waves in Section 8.03.6.3. Analyzing the other two families of waves through a planar model (Braginsky, 1964b) and a spherical model (Braginsky, 1967), he identified the dynamical timescale of the other two families:

$$\mathcal{T}_{\mathrm{MAC}} = 2\Omega\mathcal{L}^2/\mathcal{V}_A^2 = \mathrm{O}\left(3\times10^4 \mathrm{years}\right) \qquad [91d]$$

He christened these 'MAC waves,' standing for the three principal controlling forces, 'magnetic,' 'Archimedean' (buoyancy), and 'Coriolis,' 'inertia' being conspicuous by its absence. In fact, the relative sizes of the inertial and Coriolis forces in [91c] are of order $\mathrm{Ro}_m^2 \approx 4\times10^{-8}$, so that the discard of $\partial_t\mathbf{u}^A$ in [91c] is justified. The MAC wave timescale, $\mathcal{T}_{\mathrm{MAC}}$, is comparable with the reversal time, $\mathcal{T}_{\mathrm{rev}}$, of the geomagnetic field (Section 8.03.5.1). The corresponding velocity, $\mathcal{V}_{\mathrm{MAC}} = \mathcal{L}/\mathcal{T}_{\mathrm{MAC}} = \mathcal{V}_A^2/2\Omega\mathcal{L}$, is of order 10^{-6} m s^{-1}. (Another name for MAC waves, commonly used when buoyancy is unimportant as in Section 8.03.2.5, is 'slow waves.')

MAC waves are characteristically large-scale planetary waves, which are ϕ-dependent. Therefore, if they have finite amplitude, they are potentially able to create an emf $\overline{\mathcal{E}}_\phi = \left(\overline{\delta\mathbf{u}^A \times \delta\mathbf{B}}\right)_\phi$ that evades Cowling's theorem, allowing a MAC wave dynamo that maintains itself by drawing its power from buoyancy. In a perfect conductor, the phase relationship between $\delta\mathbf{u}^A$ and $\delta\mathbf{B}$ is unfavorable for creating the necessary emf, but in an imperfect conductor, $\overline{\mathcal{E}}_\phi \neq 0$. The diffusivity, η, of the field is much greater than both ν and the diffusivity, κ, of T, so that it not only creates the emf but also determines the decay rate of MAC waves. See Roberts and Aurnou (2012). The development of the MAC wave dynamo idea requires that the theory of diffusive, finite amplitude MAC waves be advanced, a task scarcely less challenging than that of studying the MHD dynamo in full! (But see Section 8.03.6.5.)

The assertion made above, that MAC and slow waves evolve on a long timescale (10^4–10^5 years), depends on the FOC being close to neutral stratification. It has been widely speculated however that a layer exists at the top of the FOC that is stably stratified. Braginsky (1993) assumed that the buoyancy frequency, N, of this 'hidden ocean at the top of the core' is Ω. He realized that this stratification would introduce MAC waves of much shorter timescales, of the order of decades. Buffett (2014) modeled these waves and showed how observations of the secular variation of B could be used to deduce physical properties of the hidden ocean. This led him to a striking confirmation of Braginsky's concept. Buffett inferred that N is slightly larger than Ω and that the primary MAC wave period is about 60 years. It should be emphasized that insofar as $\mathrm{Ro}_m \ll 1$, the MAC wave in CMHD subsumes every role of the Alfvén wave in MHD, with the important exception of the torsional wave, to be considered next.

The geostrophic part [91b] of the momentum eqn [91a] is responsible for a wave very different from the MAC wave. The magnetic field removes the geostrophic degeneracy of the inertial waves discussed in Section 8.03.6.2. The geostrophic cylinders $\mathcal{C}(s)$ shown in Figure 10 are no longer free to turn about Oz independently; each is threaded to its neighbors by the s-component of **B**. Thus, $\mathbf{u}^G$ is no longer arbitrary but is controlled by B_s. It was seen in Section 8.03.6.2 that the Coriolis force associated with geostrophic motions can be absorbed into the pressure gradient. Since this otherwise dominating force is then effectively removed, the remaining forces become influential, including the inertial term $\rho\partial_t\mathbf{u}^G$. This results in 'torsional waves,' which resemble Alfvén waves and have the same timescale, $\mathcal{T}_{\mathrm{As}} = r_o/\mathcal{V}_{\mathrm{As}}$, where V_{As} is now based on the rms strength of B_s on the geostrophic cylinder $\mathcal{C}(s)$:

$$\left(B_s^2\right)^G(s,t) = \frac{1}{A(s)}\int_{\mathcal{C}(s)} B_s^2(s,\phi,z,t)\mathrm{d}^2x = \mu_0\rho V_{\mathrm{As}}^2(s,t) \qquad [92a]$$

Even if $\mathcal{V}_{\mathrm{As}}$ is as small as 1 cm s^{-1}, $\mathcal{T}_{\mathrm{As}}$ is less than a decade. This may be compared with the timescale, $\mathcal{T}_{\mathrm{MAC}}$, of the ageostrophic waves. It is also short in comparison with the timescales, $\mathcal{T}_\nu$, $\mathcal{T}_\kappa$, and $\mathcal{T}_\eta$, of the diffusive processes. This means that over periods much less than these timescales, the time dependence of the meridional fields, $\mathbf{B}_{\mathrm{M}}$ and $\mathbf{u}_{\mathrm{M}}$, and all diffusive processes may

be ignored when studying torsional waves in the Earth, although they are heavily damped by viscosity in current numerical simulations; see Wicht and Christensen (2010).

In the case of axisymmetry, $\left(B_s^2\right)^G = \left(\overline{B}_s^G\right)^2$ with $\overline{\mathbf{B}}_M \left(= \overline{\mathbf{B}}_M^A\right)$ unchanged by the wave, so that the ideal induction eqn [54b] shows that $\overline{B}_\phi \left(= \overline{B}_\phi^G\right)$ satisfies

$$\frac{\partial \overline{B}_\phi}{\partial t} = s\overline{B}_s \frac{\partial \zeta^G}{\partial s} \qquad [92b]$$

If [89d] does not hold initially, a torsional wave is launched by the ζ^G in [91b]. In the absence of diffusion, ζ^G is nonzero for ever after. From [90b] and [90c], the time derivative of [91b] is

$$s\frac{\partial^2 \zeta^G}{\partial t^2} = \frac{1}{\mu_0 \rho s A(s)} \frac{\partial}{\partial s} \int_{\mathcal{C}(s)} \left(s\overline{B}_s \frac{\partial \overline{B}_\phi}{\partial t} \right) \mathrm{d}^2 x \qquad [93a]$$

It follows from [92b] that

$$\frac{\partial^2 \zeta^G}{\partial t^2} = \frac{1}{s^2 A} \frac{\partial}{\partial s} \left(s^2 A V_{\mathrm{As}}^2 \frac{\partial \zeta^G}{\partial s} \right) \qquad [93b]$$

This is the equation governing torsional waves when $\mathbf{B}$ is axisymmetric (Braginsky, 1970). In this case, V_{As} in [92a] involves only $\overline{B}_s$. For general $\mathbf{B}$, the asymmetrical part of B_s also contributes to V_{As}, and, since $\mathbf{B}'$ does not vanish on $r = r_o$, [93b] has an additional (though small) term arising from the torque transmitted through the CMB by the vacuum field (see the preceding text and Roberts and Aurnou, 2012):

$$\frac{\partial^2 \zeta^G}{\partial t^2} = \frac{1}{s^2 A} \frac{\partial}{\partial s} \left(s^2 A V_{\mathrm{As}}^2 \frac{\partial \zeta^G}{\partial s} \right) + Ns \frac{\partial \zeta^G}{\partial s} \qquad [93c]$$

where

$$N(s,t) = \frac{r_o}{\mu_0 \rho A z_1} \oint \left[(B_s B_r)^{\mathcal{N}} + (B_s B_r)^{\mathcal{S}} \right] \mathrm{d}\phi \qquad [93d]$$

Torsional waves transport the z-component of the angular momentum density to and fro across the core but do not change the total angular momentum about Oz:

$$m_{\mathrm{FOC}} = \int_{\mathrm{FOC}} \rho s^2 \zeta^G \mathrm{d}^3 x = \rho \int_0^{r_o} s^2 \zeta^G A \, \mathrm{d}s \qquad [93e]$$

In this simplest application of [93b], the SIC is ignored. The ordinary differential equation obtained by substituting $\zeta^G(s,t) = Z(s) \exp(l\omega t)$ into [93b] has regular singularities both at $s = 0$ and at $s = r_o$, where $A = 0$. The implicit requirement that ζ^G be bounded at both these points transforms [93b] into an eigenvalue problem for the torsional wave frequencies, ω. Similar conclusions hold if the SIC is included. More generally still, if coupling between the FOC, SIC, and mantle is introduced, the sum, $m_{\mathrm{FOC}} + m_{\mathrm{SIC}} + m_{\mathrm{mantle}}$, of their angular momenta is conserved. A torsional wave, initiated by a turbulent fluctuation in the FOC, then creates an increase (or decrease) in the length of day that correlates with an increase (or decrease) in $m_{\mathrm{FOC}} + m_{\mathrm{SIC}}$. By estimating $\overline{u}_G(s,t)$ from $\hat{\mathbf{B}}$ on the CMB and comparing with the known variation in length of day, Jault et al. (1988) inferred that such a correlation exists; see also Jackson et al. (1993).

If ohmic dissipation is restored, it is plausible that it will slowly restore ζ^G to a Taylor state and that as the system evolves on the MAC wave timescale, $\mathcal{T}_{\mathrm{MAC}}$, it will remain close to a Taylor state. Then, ζ^G may be expected to evolve on the MAC wave timescale also, so that $s\partial_t \zeta^G$ in [91b] is negligible, and the torsional waves are 'filtered out.' This explains why the Taylor condition and the Taylor states occupy such a prominent place in MHD dynamo theory. In what is sometimes called the 'Malkus–Proctor scenario' (Malkus and Proctor, 1975), solutions of the MHD equations continuously satisfying [89d] are sought.

Knowledge of $\hat{\mathbf{B}}$ on the CMB tells little about $\mathbf{B}_P$ and nothing about $\mathbf{B}_T$ in the core. The torsional wave potentially provides badly needed information about $\mathbf{B}$ via $(B_s^G)^2$, a quantity to which not only $\mathbf{B}_P$ but also $\mathbf{B}_T'$ contributes. This thought has motivated several models of torsional waves, for example, Braginsky (1970) and Zatman and Bloxham (1997). Extrapolation of $\mathbf{B}_P$ to the CMB and comparisons with geodynamo simulations indicate that $\mathcal{T}_{As}$ is about a decade (Gillet et al. 2010). The analysis of Abarca del Rio et al. (2000) of variations in length of day and the angular momentum of the atmosphere revealed a periodicity of about 5 years. This is usually interpreted as being due to torsional waves. Long before the torsional wave was detected in this way, a periodicity of about 60 years in the length of day and in the geomagnetic field was tentatively identified and hotly disputed. Its existence became more plausible as methods of data analysis improved; see Roberts et al. (2007). Because of the advance made by Buffett (2014) described above, the 60-year period is today identified with that of a MAC wave created by a stable layer at the top of the core. It is very strong evidence that such a layer exists.

8.03.6.5 Magnetostrophy

The existence and properties of numerical dynamo simulations dominate several chapters in this book, and it is obviously inappropriate to say much more about them here. The fact that current simulations have to assume that E exceeds typically 10^{-5} raises concerns about whether they realistically simulate the geodynamo, for which $E \approx 10^{-15}$. These concerns are highlighted in the recent geodynamo review of Roberts and King (2014). For large E, solutions to the dynamo equations are 'viscously dominated,' and the power balance [73f] is $\mathcal{P}^{\mathrm{mean}} = \mathcal{Q}_\nu^{\mathrm{mean}}$, very approximately. What happens for small E is conjectural, since numerical solutions of the MHD equations are unavailable, but **Section 8.03.6.3** provides strong hints. It was reported there that although weak field dynamos exist, for which the Elsasser number, Λ, is $\mathrm{O}(E^{1/3})$, this branch of solutions terminates before the hypothetical strong field branch $\Lambda = \mathrm{O}(1)$ is reached. Nevertheless, a weak field dynamo that is strongly perturbed is unstable, presumably transitioning to a strong field state where $\Lambda = \mathrm{O}(1)$. Also, the magnetoconvective stability theory in **Section 8.03.6.3** provides a hint why $\mathrm{E} = \mathrm{O}(1)$ may express geophysical reality better than viscously dominated simulations and why the power balance [73f] should be $\mathcal{P}^{\mathrm{mean}} = \mathcal{Q}_\eta^{\mathrm{mean}}$, very approximately. Perhaps, the relevant solutions of the dynamo equations are 'magnetically dominated,' that is, controlled much more by the Lorentz force than the viscous force?

These provocative questions have maintained interest in small E dynamos for more than 50 years. It is presumed that these can be solved by asymptotic methods in which

$$\mathbf{u} = \mathbf{u}^{(0)} + \mathrm{E}^{1/3}\mathbf{u}^{(1)} + \cdots \qquad [94]$$

and $\mathbf{u}^{(0)}$, $\mathbf{u}^{(1)}$, ... are independent of E. The leading-order term, $\mathbf{u}^{(0)}$, the associated magnetic field, $\mathbf{B}^{(0)}$, and temperature $T^{(0)}$, define the 'magnetostrophic dynamo.' This is all that will be considered here, and the superfix$^{(0)}$ will be omitted, as will the G on ζ^G. The stable layer at the top of the core will be ignored.

The hypothetical magnetostrophic dynamo (MS dynamo) is based on the full induction equation and associated dynamo condition on s, but the momentum equation has the truncated form [76a]:

$$2\boldsymbol{\Omega}\times\mathbf{u} = -\boldsymbol{\nabla}\Pi + \mathbf{F}^* \qquad [95a]$$

where $\mathbf{F}^* = \mathbf{F} - s\partial_t\zeta\mathbf{1}_\phi$ and $\mathbf{F} = -\gamma T\mathbf{g} + \rho^{-1}\mathbf{J}\times\mathbf{B}$ as defined by [89a]. Only the geostrophic part of the inertial force is included in [95a] because its ageostrophic part is negligible compared with the ageostrophic part of the Coriolis force; see **Section 8.03.6.4**. Mass conservation requires

$$\boldsymbol{\nabla}\cdot\mathbf{u} = 0 \qquad [95b]$$

The temperature T obeys [72] and associated boundary conditions; see **Section 8.03.6.1**. The solutions of [76a] and [76b] are required to satisfy [71d] on the spherical caps $\mathcal{N}$ and $\mathcal{S}$:

$$u_r^{\mathcal{N}} = u_r^{\mathcal{S}} = 0 \qquad [95c]$$

where $^{\mathcal{N}}$ and $^{\mathcal{S}}$ denote values on the rims of the spherical caps of radius s, so that in spherical coordinates, $u_r^{\mathcal{N}} = u_r(r_o, \theta, \phi)$ and $u_r^{\mathcal{S}} = u_r(r_o, \pi-\theta, \phi)$. The formulation of the MS dynamo problem is now complete. It includes both MAC waves and torsional waves. As in **Section 8.03.6.3**, [95a] and [95b] imply that the modified Taylor condition [89c], [89d] holds:

$$F_\phi^{*G} \equiv F_\phi^G - s\partial_t\zeta = 0 \qquad [95d]$$

which determines the evolution of ζ when the Taylor condition, $F_\phi^G = 0$, is not obeyed.

From [95a] and [95b], the vorticity equation follows:

$$2\Omega\partial_z\mathbf{u} = -\boldsymbol{\nabla}\times\mathbf{F}^* \qquad [96a]$$

By geometrical reasoning, Taylor (1963) deduced that the meridional components of $\mathbf{u}$ obeying [95c] are given by

$$2\Omega u_s = -\frac{1}{2}\left[\left(\int_{-z_1}^{z} - \int_{z}^{z_1}\right)(\boldsymbol{\nabla}\times\mathbf{F}^*)_s\,\mathrm{d}z - \frac{z_1}{s}\int_{-z_1}^{z_1}(\boldsymbol{\nabla}\times\mathbf{F}^*)_z\,\mathrm{d}z\right] \qquad [96b]$$

$$2\Omega u_z = \frac{1}{2}\left[\left(\int_{-z_1}^{z} - \int_{z}^{z_1}\right)(\boldsymbol{\nabla}\times\mathbf{F}^*)_z\,\mathrm{d}z - \frac{s}{z_1}\int_{-z_1}^{z_1}(\boldsymbol{\nabla}\times\mathbf{F}^*)_s\,\mathrm{d}z\right] \qquad [96c]$$

The corresponding expression for u_ϕ is more complicated and contains, as a part of $\overline{u}_\phi$, the geostrophic flow $u_\phi^G(s, t)$, which has to be determined. For more detail, see Roberts and Wu (2014).

Next, we determine on the evolution of u_ϕ^G from the evolution of B. Since $\mathbf{u} = \mathbf{u}^A + \mathbf{u}^G = \mathbf{u} + s\zeta\mathbf{1}_\phi$, the induction eqn [8] can be written as

$$\partial_t\mathbf{B} = B_s s\partial_s\zeta\mathbf{1}_\phi - \zeta\partial_\phi\mathbf{B} + \mathbf{C} \qquad [97a]$$

where $\mathbf{C}$ depends only on $\mathbf{B}$ and the $\mathbf{u}^A$ determined in the preceding text:

$$\mathbf{C} = \boldsymbol{\nabla}\times\left(\mathbf{u}^A\times\mathbf{B}\right) + \eta\boldsymbol{\nabla}^2\mathbf{B} \qquad [97b]$$

It is now possible to use [97a] and $\mathbf{J} = \mu_0^{-1}\boldsymbol{\nabla}\times\mathbf{B}$ to evaluate, following Taylor (1963),

$$\partial_t F_\phi^G = \rho^{-1}[\mathbf{J}\times\partial_t\mathbf{B} + (\partial_t\mathbf{J})\times\mathbf{B}]_\phi^G \qquad [97c]$$

An alternative but equivalent method was adopted by Roberts and Aurnou (2012), who made use of the torque integral [90c]

$$\Gamma_z(s, t) = \frac{1}{\mu_0}\frac{\partial}{\partial s}\left[s^2\int_{\mathcal{C}(s)} B_s B_\phi\,\mathrm{d}^2x\right] - \frac{r_o^2 s^2}{\mu_0 z_1}\oint\left[\left(B_r'B_\phi'\right)^{\mathcal{N}} + \left(B_r'B_\phi'\right)^{\mathcal{S}}\right]\mathrm{d}\phi \qquad [97d]$$

where the first term on the right-hand side is from the magnetic stress exerted on $\mathcal{C}(s)$ by the adjacent geostrophic cylinders and the second term is due to the stresses from remote cylinders transmitted through the CMB by the vacuum field. They give rise, respectively, to the first and second terms on the right-hand side of [97d]. Both methods lead to

$$\partial_t F_\phi^G = \frac{1}{sA}\frac{\partial}{\partial s}\left(s^2 A V_{\mathrm{As}}^2\frac{\partial\zeta}{\partial s}\right) + s^2 N\frac{\partial\zeta}{\partial s} - R(s, t) \qquad [97e]$$

where $N(s)$ is defined in [93c], $A(s)$ is as before the area of $\mathcal{C}(s)$, and

$$\mu_0\rho s R(s, t) = \left[\mathbf{C}_M\cdot\boldsymbol{\nabla}\left(sB_\phi\right) + \mathbf{B}_M\cdot\boldsymbol{\nabla}\left(sC_\phi\right)\right]^G \qquad [97f]$$

In combination with [95d], that is,

$$\partial_t\zeta = s^{-1}F_\phi^G \qquad [97g]$$

this yields the inhomogeneous wave equation

$$\frac{\partial^2\zeta}{\partial t^2} - \frac{1}{s^2 A}\frac{\partial}{\partial s}\left(s^2 A V_{\mathrm{As}}^2\frac{\partial\zeta}{\partial s}\right) + Ns\frac{\partial\zeta}{\partial s} = R \qquad [97h]$$

Comparing this with [93c], it is apparent that, when inertia is included (an approximation we term 'modified Taylor theory' or MTT), so are inertial waves. When inertia is abandoned, we term the approximation 'original Taylor theory' or OTT, because it follows the plan Taylor (1963) first proposed. Then the left-hand side of [97g] and consequently the first term in [97h] are lost, so that torsional waves are eliminated. It may be seen, more easily from OTT than from MTT, that the vanishing of Γ_z is equivalent to Taylor's condition [89d], and that its time derivative determines the unknown u_ϕ^G. This completes the derivation of u from B. Mean field solutions have been presented by Wu and Roberts (2015).

We now come to the reason why magnetostrophic models enjoy an immense potential advantage over contemporary numerical simulations of the geodynamo. The latter are limited by the demands of numerical stability to values of E that are so large that their geophysical relevance can be queried. Although this situation will be rectified through the progressive development of computer hardware, this is unlikely to make geophysically realistic E accessible for a few decades; see, for example, Davies et al. (2011) and Roberts and King (2013). In contrast, the magnetostrophic dynamo requires only the numerical integration of a one-dimensional wave equation

(in the case of MTT) or an ordinary differential equation (for OTT). Neither appears to present insuperable obstacles, and they promise solutions for $E=0$! This explains why, ever since Taylor wrote his landmark paper, persistent attempts have been made to implement the solution he planned. Nevertheless, progress in solving the MS dynamo has been slow. Early attempts by Fearn and Proctor (1987) failed, and the recent initiative by Livermore et al. (2011) has yet to bear fruit. (See these papers for allied publications by these authors.) Successful integrations of the magnetostrophic system should help to answer some perplexing questions about geodynamo modeling. Prominent among these is why current numerical simulations are consistently of α^2-type. The suggestion is strong that the excessive core viscosity needed by the simulations has suppressed the ω-effect. Some modelers have replaced the no-slip boundary condition [71c] with stress-free conditions, and this has promoted zonal flows and associated zonal magnetic fields; for example, see Busse and Simitev (2006). Whichever boundary condition is used, the suppression of internal shear by the excessive E remains. Zonal shear, and indeed the MS dynamo itself, is driven by the buoyancy term included in F_s and F_z in [95a]. The future will tell whether or not MS models are $\alpha\omega$-dynamos.

Finally, we make a few comparisons between OTT and MTT. The former demands that an integration of the magnetostrophic dynamo system always obeys the Taylor constraint [89d], but the latter does not. If the Taylor condition is not obeyed at the starting point, [97h] determines the initial $\partial_t\zeta$, and this launches a torsional wave. The presumption is that through the induction eqn [8], the wave will be damped on the timescale, $\mathcal{T}_\eta$, of magnetic diffusion, though a counterexample is known (Roberts and Stewartson, 1975). Ohmic damping of torsional waves is analyzed by Roberts and Aurnou (2012). While $s\zeta$ is large compared with $\mathbf{u}^A$, [97h] reduces to [93c] because the right-hand side of [97h] is then negligible. Ohmic damping may cause an initially large ζ to diminish in amplitude so that $R(s, t)$ becomes effective. If this happens, it is plausible that ζ becomes nearly locked to the ageostrophic state, which evolves on the MAC wave timescale, $\mathcal{T}_{\mathrm{MAC}}$. When that happens, MTT is little different from OTT in practical terms, though the fact that ζ evolves in OTT means, in philosophical terms, that $\partial_t\zeta$ in [97h] is nonzero and should be retained, so making MTT more relevant. In the dynamics of OTT, t is merely a parameter carried along in the analysis, and it is unnecessary to insist that the entire geostrophic part of $\mathbf{u}$ is contained in $\mathbf{u}^G$. The resulting $\mathbf{u}^A$ and $\mathbf{u}^G$ are then different but their sum, $\mathbf{u}=\mathbf{u}^A+\mathbf{u}^G$, is the same. In MTT, the condition $(\mathbf{u}^A)^G=\mathbf{0}$ must be enforced since otherwise $\mathbf{u}^G$ cannot be identified with $s\zeta$. For further details about modified Taylor theory, see Wu and Roberts (2014).

8.03.7 Final Remarks

This chapter has focused on the basic electromagnetic theory as applied to electrically conducting fluids and on the associated kinematic dynamo problem in which the fluid motion is specified and a self-exciting magnetic field is sought. These topics are contained within the larger MHD dynamo problem in which an energy source for the fluid motions is specified and both the fluid motion and a self-excited magnetic field are sought. Fundamentals of convective MHD dynamos have been described in Section 8.03.6; more details will be given in later chapters.

Hopefully, the reader of this chapter will realize that kinematic theory has brought important concepts and significant understanding to field generation by homogeneous dynamos, that is, dynamos that operate in simply connected, homogeneous masses of electrically conducting fluids. Among its successes, recognition of the importance of broken symmetry, including helicity, stands out. The kinematic theory has also provided motivation for laboratory experiments that study electromagnetic induction and dynamo action in liquid metals.

Geodynamo theory is now so dominated by MHD simulations that the reader may wonder whether kinematic theory has any useful further role to play. One may argue however that the purpose of such simulations is not merely to produce numerical analogs of the geodynamo. It is also to decipher their message, and this daunting objective requires a good understanding of kinematic theory. Unfortunately, it also demands proper treatment of core turbulence. The question of how to incorporate the turbulent transport of momentum, heat, and composition into geodynamo theory is the most severe challenge faced by geodynamo theory today. Large increases in ν and κ are currently necessary to ensure that numerical simulations are adequately resolved. They can be, and often are, advertised as turbulent diffusivities representing the effect of the small scales (i.e., the 'subgrid scales' that cannot be resolved in numerical simulations) on the large (resolved) scales. But it is questionable whether scalar turbulent diffusivities can adequately describe transport by a turbulence that, because of the dominance of the Coriolis, Lorentz, and buoyancy forces, must surely be highly anisotropic; see Roberts and King (2014). In view of these major obstacles, it is truly remarkable how successful numerical simulations of the geodynamo have been: the main features of the observed geomagnetic field have been replicated, leading some commentators to assert that the geodynamo problem has been solved. Others see the success as so unexpected that they call it the 'geodynamo paradox.' Its resolution is the main target of geodynamo theory today.

References

Abarca del Rio R, Gambis R, and Salstein DA (2000) Interannual signals in length of day and atmospheric angular momentum. *Annales Geophysicae* 18: 347–364.

Abramowitz M and Stegun IA (eds.) (1964) *Handbook of Mathematical Functions with Formulas, Graphs and Mathematical Tables*. Washington, DC: National Bureau of Standards.

Alfvén H (1950) Discussion of the origin of the terrestrial and solar magnetic fields. *Tellus* 2: 74–82.

Bachtiar AA, Ivers DJ, and James RW (2006) Planar velocity dynamos in a sphere. *Proceedings of the Royal Society of London A* 462: 2439–2456.

Backus G (1958) A class of self-sustaining dissipative spherical dynamos. *Annals of Physics (NY)* 4: 372–447.

Backus G and Chandrasekhar S (1956) On Cowlings theorem on the impossibility of self-maintained axisymmetric dynamos. *Proceedings of the National Academy of Sciences Washington* 42: 105–108.

Braginsky SI (1964a) Kinematic models of the Earth's hydromagnetic dynamo. *Geomagnetism and Aeronomy* 4: 572–583.

Braginsky SI (1964b) Magnetohydrodynamics of the Earth's core. *Geomagnetism and Aeronomy* 4: 698–712.

Braginsky SI (1965a) Self-excitation of a magnetic field during the motion of a highly conducting fluid. *Journal of Experimental and Theoretical Physics of the Academy of Sciences of the USSR* 20: 726–735.

Braginsky SI (1965b) Theory of the hydromagnetic dynamo. *Soviet Physics Journal of Experimental and Theoretical Physics* 20: 1462–1471.

Braginsky SI (1967) Magnetic waves in the Earth's core. *Geomagnetism and Aeronomy* 7: 851–859.

Braginsky SI (1970) Torsional magnetohydrodynamic vibrations in the Earth's core and variations in day length. *Geomagnetism and Aeronomy* 10: 1–8.

Braginsky SI (1993) MAC-oscillations of the hidden ocean of the core. *Journal of Geomagnetism and Geoelectricity* 45: 1517–1538.

Braginsky SI and Meytlis VP (1990) Local turbulence in the Earth's core. *Geophysical and Astrophysical Fluid Dynamics* 55: 71–87.

Braginsky SI and Roberts PH (1995) Equations governing convection in the Earth's core and the geodynamo. *Geophysical and Astrophysical Fluid Dynamics* 79: 1–97.

Brandenburg A, Moss D, and Soward AM (1998) New results for the Herzenberg dynamo: Steady and oscillatory solutions. *Proceedings of the Royal Society of London A* 454: 1283–1300, erratum, p. 3275.

Buffett BA (2014) Geomagnetic fluctuations reveal stable stratification at the top of the Earth's core. *Nature* 507: 484–487.

Bullard EC and Gellman H (1954) Homogeneous dynamos and terrestrial magnetism. *Philosophical Transactions of the Royal Society of London A* 247: 213–255.

Bullard EC and Gubbins D (1977) Generation of magnetic fields of global scale. *Geophysical and Astrophysical Fluid Dynamics* 8: 43–56.

Busse FH (1970) Thermal instabilities in rapidly rotating systems. *Journal of Fluid Mechanics* 44: 441–460.

Busse FH (1975) A necessary condition for the geodynamo. *Journal of Geophysical Research* 80: 278–280.

Busse FH and Simitev RD (2006) Parameter dependences of convection-driven dynamos in rotating spherical fluid shells. *Geophysical and Astrophysical Fluid Dynamics* 100: 341–361.

Chandrasekhar S (1961) *Hydrodynamic and Hydromagnetic Stability*. Oxford, UK: University Press, Reprinted by Dover publications.

Childress S (1969a) A class of solutions of the magnetohydrodynamic dynamo problem. In: Runcorn SK (ed.) *The Application of Modern Physics to the Earth and Planetary Interiors*, pp. 629–648. New York: Wiley.

Childress S (1969b) Théorie magnetohydrodynamique de lUeffet dynamo. Technical report, Departement Méchanique de la Faculté des Sciences, Université de Paris.

Childress S (1970) New solutions of the kinematic dynamo problem. *Journal of Mathematical Physics* 11: 3063–3076.

Childress S and Gilbert AD (1995) *Stretch, Twist, Fold: The Fast Dynamo*. Heidelberg: Springer.

Childress S and Soward AM (1972) Convection-driven hydromagnetic dynamo. *Physical Review Letters* 29: 837–839.

Clement BM (2004) Dependence of the duration of geomagnetic polarity reversals on site latitude. *Nature* 428: 637–640.

Cowling TG (1934) The magnetic field of sunspots. *Monthly Notices of the Royal Astronomical Society* 94: 39–48.

Cowling TG (1957) The dynamo maintenance of steady magnetic fields. *Quarterly Journal of Mechanics and Applied Mathematics* 10: 129–136.

Davies CJ, Gubbins D, and Jimack PK (2011) Scalability of pseudospectral methods for geodynamo simulations. *Concurrency and Computation: Practice and Experience* 23: 38–56.

Demircan A and Seehafer N (2002) Dynamo in asymmetric square convection. *Geophysical and Astrophysical Fluid Dynamics* 96: 461–479.

Dormy E and Soward AM (eds.) (2007) Mathematical Aspects of Natural Dynamos. In: *The Fluid Mechanics of Astrophysics and Geophysics*, vol. 13, pp. 142–145. Baton Rouge, FL: Chapman & Hall/CRC Taylor and Francis Group.

Dormy E, Soward AM, Jones CA, Jault D, and Cardin P (2004) The onset of thermal convection in rotating spherical shells. *Journal of Fluid Mechanics* 501: 43–70.

Dudley ML and James RW (1989) Time-dependent kinematic dynamos with stationary flows. *Proceedings of the Royal Society of London A* 425: 407–429.

Elsasser WM (1947) Induction effects in terrestrial magnetism. Part III. Electric modes. *Physical Review* 72: 831–833.

Eltayeb IA and Loper DE (1988) On steady kinematic helical dynamos. *Geophysical and Astrophysical Fluid Dynamics* 44: 259–269.

Fautrelle Y and Childress S (1982) Convective dynamos with intermediate and strong fields. *Geophysical and Astrophysical Fluid Dynamics* 22: 235–279.

Fearn DR (1998) Hydromagnetic flows in planetary cores. *Reports on Progress in Physics* 61: 175–235.

Fearn DR and Proctor MRE (1987) On the computation of steady, self-consistent spherical dynamos. *Geophysical and Astrophysical Fluid Dynamics* 38: 293–325.

Gailitis A (1990) The helical MHD dynamo. In: Moffatt HK and Tsinober A (eds.) *Topological Fluid Mechanics*, pp. 147–156. Cambridge, UK: Cambridge University Press.

Gailitis AK (1993) Magnetic field generation by axisymmetric flows of conducting liquids in a spherical stationary conductor cavity. *Magnetohydrodynamics* 29: 107–115.

Gailitis AK (1995) Magnetic field generation by the axisymmetric conducting fluid flow in a spherical cavity of a stationary conductor. 2. *Magnetohydrodynamics* 31: 38–42.

Galloway D and Frisch U (1986) Dynamo action in a family of flows with chaotic streamlines. *Geophysical and Astrophysical Fluid Dynamics* 36: 53–83.

Gibson RD (1968) The Herzenberg dynamo II. *Quarterly Journal of Mechanics and Applied Mathematics* 21: 257–267.

Gibson RD and Roberts PH (1966) Some comments on the theory of homogenous dynamos. In: Hindmarsh W, Lowes FJ, Roberts PH, and Runcorn S (eds.) *Magnetism and the Cosmos*, pp. 108–120. Edinburgh: Oliver and Boyd.

Gilbert AD (1988) Fast dynamo action in the Ponomarenko dynamo. *Geophysical and Astrophysical Fluid Dynamics* 44: 241–258.

Gillet N, Jault D, Canet E, and Fournier A (2010) Fast torsional waves and strong magnetic field within the Earth's core. *Nature* 465. http://dx.doi.org/10.1038/nature09010.

Glatzmaier GA and Roberts PH (1996a) An anelastic evolutionary geodynamo simulation driven by compositional and thermal convection. *Physica D* 97: 81–94.

Glatzmaier GA and Roberts PH (1996b) On the magnetic sounding of planetary interiors. *Physics of the Earth and Planetary Interiors* 98: 207–220.

Greenspan H (1968) *The Theory of Rotating Fluids*. Cambridge, UK: Cambridge University Press.

Gubbins D (1973) Numerical solution of the kinematic dynamo problem. *Philosophical Transactions of the Royal Society of London A* 274: 493–521.

Gubbins D, Barber CN, Gibbons S, and Love JJ (2000a) Kinematic dynamo action in a sphere. I. Effects of differential rotation and meridional circulation on solutions with axial dipole symmetry. *Proceedings of the Royal Society of London A* 456: 1333–1353.

Gubbins D, Barber CN, Gibbons S, and Love JJ (2000b) Kinematic dynamo action in a sphere. II. Symmetry selection. *Proceedings of the Royal Society of London A* 456: 1669–1683.

Gubbins D and Gibbons S (2002) Three dimensional dynamo waves in a sphere. *Geophysical and Astrophysical Fluid Dynamics* 96: 481–498.

Herzenberg A (1958) Geomagnetic dynamos. *Philosophical Transactions of the Royal Society of London A* 250: 543–583.

Hide R (1979) Dynamo theorems. *Geophysical and Astrophysical Fluid Dynamics* 14: 183–186.

Hide R and Palmer TN (1982) Generalisation of Cowlings theorem. *Geophysical and Astrophysical Fluid Dynamics* 19: 301–309.

Holme R (1997) Three-dimensional kinematic dynamos with equatorial symmetry: Application to the magnetic fields of Uranus and Neptune. *Physics of the Earth and Planetary Interiors* 102: 105–122.

Hutcheson KA and Gubbins D (1994) Kinematic magnetic field morphology at the core mantle boundary. *Geophysical Journal International* 116: 304–320.

Ivers DJ and James RW (1981) On the maintenance of magnetic fields by compressible flows and the Nernst–Ettingshausen effect. *Geophysical and Astrophysical Fluid Dynamics* 16: 319–323.

Ivers DJ and James RW (1984) Axisymmetric anti-dynamo theorems in non-uniform compressible fluids. *Philosophical Transactions of the Royal Society of London A* 312: 179–218.

Ivers DJ and James RW (1986) Extension of the Namikawa Matsushita anti-dynamo theorem to toroidal fields. *Geophysical and Astrophysical Fluid Dynamics* 36: 317–324.

Ivers DJ and James RW (1988a) An anti-dynamo theorem for partly symmetric flows. *Geophysical and Astrophysical Fluid Dynamics* 44: 271–278.

Ivers DJ and James RW (1988b) Antidynamo theorems for nonradial flows. *Geophysical and Astrophysical Fluid Dynamics* 40: 147–163.

Jackson A, Bloxham J, and Gubbins D (1993) Time-dependent flow at the core surface and conservation of angular momentum in the coupled core–mantle system. In: Le Mouël J-L, Smylie D, and Herring T (eds.) *Dynamics of the Earth's Deep Interior and Earth Rotation*. *Geophysical Monograph*, 72, pp. 97–107. Washington, DC: AGU.

Jault D, Gire G, and Mouël J-L (1988) Westward drift, core motions and exchanges of angular momentum between core and mantle. *Nature* 333: 353–356.
Jones C, Soward A, and Mussa A (2000) The onset of thermal convection in a rapidly rotating sphere. *Journal of Fluid Mechanics* 405: 157–179.
Kaiser R, Schmitt BJ, and Busse FH (1994) On the invisible dynamo. *Geophysical and Astrophysical Fluid Dynamics* 77: 93–109.
Kono M (ed.) (2007) *Geomagnetism*. In: Schubert G (ed.) (2007) *Treatise on Geophysics*, vol. 5. Amsterdam: Elsevier.
Kono M and Roberts PH (1991) Small amplitude solutions of the dynamo problem: 1. The adjoint system and its solution. *Journal of Geomagnetism and Geoelectricity* 43: 839–862.
Kono M and Tanaka H (1995) Intensity of the geomagnetic field in geological time: A statistical study. In: Yukutake T (ed.) *The Earth's Central Part: Its Structure and Dynamics*, pp. 75–94. Tokyo, Japan: Terra Scientific Publishing Co.
Krause F and Rädler K-H (1980) *Mean-field Magnetohydrodynamics and Dynamo Theory*. Berlin: Academic Press.
Kumar S and Roberts PH (1975) A three-dimensional kinematic dynamo. *Proceedings of the Royal Society of London A* 414: 235–258.
Larmor J (1919) How could a rotating body such as the Sun become a magnet? Report of the British Association for the Advancement of Science, pp 159–160.
Léorat J (1995) Linear dynamo simulations with time-dependent helical flows. *Magnetohydrodynamics* 31: 367–373.
Liao X, Zhang K, and Gubbins D (2005) A multilayered kinematic dynamo model: Implications of a stratified upper layer in the Earth's core. *Geophysical and Astrophysical Fluid Dynamics* 99: 377–395.
Livermore P, Ierley G, and Jackson A (2011) The evolution of a magnetic field subject to Taylor's constraint using a projection operator. *Geophysical Journal International* 187: 690–704. http://dx.doi.org/10.1111/j.1365246X.2011.05187.x.
Lortz D (1968) Exact solutions of the hydromagnetic dynamo problem. *Plasma Physics* 10: 967–972.
Lortz D (1990) Mathematical problems in dynamo theory. In: Brinkmann W, Fabian AC, and Giovannelli F (eds.) *Physical Processes in Hot Cosmic Plasmas*, pp. 221–234. Dordrecht: Kluwer.
Love JJ and Gubbins D (1996a) Dynamos driven by poloidal flow exist. *Geophysical Journal International* 23: 857–860.
Love JJ and Gubbins D (1996b) Optimized kinematic dynamos. *Geophysical Journal International* 124: 787–800.
Lowes FJ and Wilkinson I (1963) Geomagnetic dynamo: A laboratory model. *Nature* 198: 1158–1160.
Lowes FJ and Wilkinson I (1968) Geomagnetic dynamo: An improved laboratory model. *Nature* 219: 717–718.
Lupian EA and Shukurov AM (1992) The screw dynamo in realistic flows. *Magnetohydrodynamics* 28: 234–240.
Malkus WVR and Proctor MRE (1975) The macrodynamics of α-effect dynamos in rotating fluid systems. *Journal of Fluid Mechanics* 67: 417–443.
Merrill R, McElhinny M, and McFadden P (1996) The Magnetic Field of the Earth. Paleomagnetism, the Core and the Deep Mantle. In: 2nd edn, p. xii+527. San Diego CA: Academic Press.
Moffatt HK (1978) *Magnetic Field Generation in Electrically Conducting Fluids*. Cambridge, UK: Cambridge University Press, 264 pp.
Namikawa T and Matsushita S (1970) Kinematic dynamos problem. *Geophysical Journal of the Royal Astronomical Society* 19: 319–415.
Parker EN (1955) Hydromagnetic dynamo models. *Astrophysical Journal* 121: 293–314.
Parker EN (1957) The solar hydromagnetic dynamo. *Proceedings of the National Academy of Sciences Washington* 43: 8–14.
Pekeris CL, Accad Y, and Schkoller B (1973) Kinematic dynamos and the Earth's magnetic field. *Philosophical Transactions of the Royal Society of London A* 275: 425–461.
Ponomarenko YB (1973) On the theory of the hydromagnetic dynamo. *Journal of Applied Mechanics and Technical Physics* 14: 775–778.
Pozzo M, Davies C, Gubbins D, and Alfé D (2012) Thermal and electrical conductivity of iron at Earth's core conditions. *Nature* 485: 355–358.
Proctor MRE (1977a) On Backus necessary condition for dynamo action in a conducting sphere. *Geophysical and Astrophysical Fluid Dynamics* 9: 89–93.
Proctor MRE (1977b) The role of mean circulation in parity selection by planetary magnetic fields. *Geophysical and Astrophysical Fluid Dynamics* 8: 311–324.
Proctor MRE (2004) An extension of the toroidal theorem. *Geophysical and Astrophysical Fluid Dynamics* 98: 235–240.
Proudman J (1916) On the motion of solids in liquids possessing vorticity. *Proceedings of the Royal Society of London A* 92: 408–424.
Roberts GO (1969) Dynamo waves. In: Runcorn SK (ed.) *The Application of Modern Physics to the Earth and Planetary Interiors*, pp. 602–628. New York: Wiley.
Roberts GO (1972a) Dynamo action of fluid motions with two dimensional periodicity. *Philosophical Transactions of the Royal Society of London A* 271: 411–454.
Roberts PH (1960) Characteristic value problems posed by differential equations arising in hydrodynamics and hydromagnetics. *Journal of Mathematical Analysis and Applications* 1: 195–214.
Roberts PH (1967) *An Introduction to Magnetohydrodynamics*. London: Longmans, Green and Co., p. 264.
Roberts PH (1968) On the thermal instability of a rotating-fluid sphere containing heat sources. *Philosophical Transactions of the Royal Society of London A* 263: 93–117.
Roberts PH (1971a) Dynamo theory. In: Reid WH (ed.) *Lectures in Mathematics 14: Mathematical Problems in the Geophysical Sciences. 2. Inverse Problems, Dynamo Theory and Tides*, pp. 129–206. Providence, RI: American Mathematical Society.
Roberts PH (1971b) Dynamo theory of geomagnetism. In: Zmuda AJ (ed.) *World Magnetic Survey 1957–1969*, pp. 123–131. Paris: IUGG.
Roberts PH (1972b) Kinematic dynamo models. *Philosophical Transactions of the Royal Society of London A* 271: 663–697.
Roberts PH (1987) Dynamo theory. In: Nicolis C and Nicolis G (eds.) *NATO ASI Series 192: Irreversible Phenomena and Dynamical Systems Analysis in Geosciences*, pp. 73–133. Dordrecht: Reidel.
Roberts PH and Aurnou JM (2012) On the theory of core–mantle coupling. *Geophysical and Astrophysical Fluid Dynamics* 2012: 106157–106230.
Roberts PH and King EM (2013) On the genesis of the Earth's magnetism. *Reports on the Progress of Physics* 76: 096801.
Roberts PH and Stewartson K (1975) On double roll convection in a rotating magnetic system. *Journal of Fluid Mechanics* 68: 447–466.
Roberts PH and Stix M (1971) The turbulent dynamo. A translation of a series of papers by F. Krause, K.-H. Rädler, and M. Steenbeck. NCAR technical note TN/IA-60. Available from http://www.library.ucar.edu/uhtbin/hyperion-image/DR000045.
Roberts PH and Wu C-C (2014) On the Modified Taylor Constraint. *Geophysical and Astrophysical Fluid Dynamics* 108: 696–715.
Roberts PH, Yu ZJ, and Russell CT (2007) On the 60-year signal from the core. *Geophysical and Astrophysical Fluid Dynamics* 101: 11–35.
Ruzmaikin AA, Sokoloff DD, Solovev AA, and Shukurov AM (1989) Couette–Poiseuille flow as a screw dynamo. *Magnetohydrodynamics* 25: 6–11.
Sarson GR and Gubbins D (1996) Three-dimensional kinematic dynamos dominated by strong differential rotation. *Journal of Fluid Mechanics* 306: 223–265.
Serebrianya PM (1988) Kinematic stationary geodynamo models with separated toroidal and poloidal motions. *Geophysical and Astrophysical Fluid Dynamics* 44: 141–164.
Siemens W (1867) Über die Uwandlung von Arbeitskraft in electrischen Strom ohne Anwendlung permanenter Magnete. *Monatsberichte König. Preuss, Akademie Wissenschaften:* 55–58.
Sokoloff DD, Shukurov AM, and Shumkina TS (1989) The second approximation in the screw dynamo problem. *Magnetohydrodynamics* 25: 1–6.
Solovyev AA (1985a) Couette spiral flows of conducting fluids consistent with magnetic field generation. *Physics of Solid Earth* 12: 40–47.
Solovyev AA (1985b) Magnetic field generation by the axially symmetric flow of conducting fluid. *Physics of Solid Earth* 12: 101–103.
Solovyev AA (1987) Excitation of a magnetic field by the movement of a conductive liquid in the presence of large values of the magnetic Reynolds number. *Physics of Solid Earth* 23: 420–423.
Soward AM (1972) A kinematic theory of large magnetic Reynolds number dynamos. *Proceedings of the Royal Society of London A* 275: 611–651.
Soward AM (1974) A convection-driven dynamo 1. Weak-field case. *Philosophical Transactions of the Royal Society of London A* 275: 611–646.
Soward AM (1987) Fast dynamo action in a steady flow. *Journal of Fluid Mechanics* 180: 267–295.
Soward AM (1990) A unified approach to a class of slow dynamos. *Geophysical and Astrophysical Fluid Dynamics* 53: 81–107.
Soward AM (1991) The Earth's dynamo. *Geophysical and Astrophysical Fluid Dynamics* 62: 191–209.
Soward AM and Roberts PH (2014) Eulerian and Lagrangian means in rotating, magnetohydrodynamic Flows II. Braginsky's nearly axisymmetric dynamo. *Geophysical and Astrophysical Fluid Dynamics* 108: 269–322.
Steenbeck M, Krause F, and Rädler K-H (1966) Berechnung der mittleren LorentzFeldstärke befür ein elektrisch leitendendes Medium in turbulenter, durch CoriolisKräfte beeinflußter Bewegung. *Zeitschrift für Naturforschung* 21a: 369–376.
Taylor GI (1916) Motion of solids in fluids when the flow is not irrotational. *Proceedings of the Royal Society of London A* 93: 99–113.
Taylor JB (1963) The magnetohydrodynamics of a rotating fluid and the earths dynamo problem. *Proceedings of the Royal Society of London A* 274: 274–283.

Tilgner A and Busse FH (1995) Subharmonic dynamo action of fluid motions with two-dimensional periodicity. *Proceedings of the Royal Society of London A* 448: 237–244.

Tobias SM, Cattaneo F, and Boldyrev S (2011) MHD dynamos and turbulence. In: Davidson P, Kaneda Y, Moffatt K, and Sreenivasan KR (eds.) *A Voyage Through Turbulence*. Cambridge, UK: Cambridge University Press.

Vainshtein SI and Zeldovich YB (1972) Origin of magnetic fields in astrophysics. *Soviet Physics Uspekhi* 15: 159–172.

Wicht J and Christensen UR (2010) Torsional oscillations in dynamo simulations. *Geophysical Journal International* 181: 1367–1380.

Willis AP and Gubbins D (2004) Kinematic dynamo action in a sphere: Effects of periodic time dependent flows on solutions with axial dipole symmetry. *Geophysical and Astrophysical Fluid Dynamics* 98: 537–554.

Wu C-C and Roberts PH (2009) On a dynamo driven by topographic precession. *Geophysical and Astrophysical Fluid Dynamics* 103: 467–501. http://dx.doi.org/10.1080/03091920903311788.

Wu C-C and Roberts PH (2012) On a dynamo driven topographically by longitudinal libration. *Geophysical and Astrophysical Fluid Dynamics* http://dx.doi.org/10.1080/03091929.2012.682990.

Wu C-C and Roberts PH (2014) On solving magnetostrophic dynamo equations. *Geophysical and Astrophysical Fluid Dynamics*, submitted for publication.

Wu C-C and Roberts PH (2015) On magnetostrophic mean-field solutions of the geodynamo equations. *Geophysical and Astrophysical Fluid Dynamics* 109: to appear.

Zatman S and Bloxham J (1997) Torsional oscillations and the magnetic field within the Earth's core. *Nature* 388: 760–763.

Zeldovich YB (1956) The magnetic field in the two-dimensional motion of a conducting fluid. *Soviet Physics Journal of Experimental and Theoretical Physics* 31: 154–156.

Zeldovich YB and Ruzmaikin AA (1980) Magnetic field in a conducting fluid in two dimensional motion. *Soviet Physics Journal of Experimental and Theoretical Physics* 51: 493–497.

Zhang K, Chan KH, and Liao X (2011) On fluid motion in librating ellipsoids with moderate equatorial eccentricity. *Journal of Fluid Mechanics* 673: 468–479. http://dx.doi.org/10.1017/S002211-2011000735.

Zheligovsky VA and Galloway DJ (1998) Dynamo action in Christopherson hexagonal flow. *Geophysical and Astrophysical Fluid Dynamics* 88: 277–293.

8.04 Large-Scale Flow in the Core

R Holme, University of Liverpool, Liverpool, UK

© 2015 Elsevier B.V. All rights reserved.

8.04.1	**Introduction**	91
8.04.2	**Surface Core Flow from Observed Secular Variation**	92
8.04.2.1	Westward Drift	92
8.04.2.2	The Frozen-Flux Hypothesis	92
8.04.2.3	Poloidal–Toroidal Decomposition	93
8.04.2.4	Boundary Conditions	94
8.04.2.5	Nonuniqueness	94
8.04.2.6	The Large-Scale Approximation	94
8.04.2.7	Steady Flows	95
8.04.2.8	Toroidal Flows	95
8.04.2.9	Tangentially Geostrophic Flows	96
8.04.2.10	Comparison of Solutions Constructed with Different Nonuniqueness Reducing Assumptions	96
8.04.2.11	Other Flow Modeling Assumptions	97
8.04.2.11.1	Flow in a drifting reference frame	98
8.04.2.11.2	Helical flow	98
8.04.2.11.3	Columnar flow	98
8.04.2.12	Limitations in Resolution of Nonuniqueness	98
8.04.2.13	The Horizontal Field Components	99
8.04.2.14	Effects of Diffusion	99
8.04.2.15	Uncertainty of Field Magnitude	100
8.04.3	**Higher-Resolution Flows from Detailed Models of SV from Satellite Observations**	101
8.04.4	**Angular Momentum–LOD Variation and Correlation with Core-Angular Momentum**	103
8.04.5	**Torsional Oscillations as a Probe of Core Structure**	104
8.04.5.1	Probing the Magnetic Field Interior to the Core	104
8.04.5.2	Coupling of Torsional Oscillations to the Outer and Inner Core	105
8.04.5.3	Quasigeostrophy	106
8.04.5.4	Geomagnetic Jerks and Links to Earth Rotation	106
8.04.6	**Wave Motion as an Explanation for Secular Variation**	106
8.04.7	**Polar Vortices**	107
8.04.8	**Modeled Core-Surface Flow and the Dynamics of the Core**	108
8.04.8.1	Data Assimilation	109
8.04.8.2	Inverse Geodynamo Modeling	110
8.04.9	**Conclusions**	110
References		110

8.04.1 Introduction

Timescales of processes in the Earth tend in general to be very short, for example, the rupture associated with an earthquake, or very long (millions of years or longer), for example, the movement of the tectonic plates. The geomagnetic field provides the primary example of intermediate timescales. The internal magnetic field, with origin in the Earth's fluid core, varies on timescales from yearly or less (the so-called geomagnetic jerks) to decadal variation, secular change over centuries, to more significant variations (excursions and reversals) on timescales of millennia. These changes are named the secular variation. This chapter is concerned with variations on timescales of years to centuries and what can be deduced about the interior of the Earth and processes in the core from such changes. This subject has a long history: the first attempt to infer motion in the Earth's interior from geomagnetic secular variation was by Halley (1692). Modern analysis interprets the secular variation as being primarily due to advection of magnetic field at the top of the core and so uses magnetic observations to constrain flow there.

In Section 8.04.2, we begin by outlining how neglect of diffusion in the core allows the simplification of the magnetic induction equation to a form that can be used to solve for flow. This solution is highly nonunique: we review the approaches that have been taken to deal with this nonuniqueness and discuss to what extent they influence the resulting models of flow. We also discuss some attempts to allow for diffusional effects. In Section 8.04.3, we consider recent fine-scale flow models that have attempted to take advantage of new, detailed models of the magnetic field and (particularly) secular variation from satellite data. Effective modeling of flow from such models is proving difficult.

In Section 8.04.4, we consider the link between flow modeling and an important independent geophysical observable, the variation in length of day (LOD). Decadal variations in LOD almost certainly originate from the exchange of angular momentum between the fluid core and solid Earth, and simple models of whole-core flow constrained by surface flow modeling provide strong support for this. The existence of this correlation, and the underlying theory of torsional oscillations, provides an opportunity to probe physical processes not only at the surface of the core but also at depth: this is described in Section 8.04.5. There is increasing evidence that torsional processes are also linked to the most rapid feature seen in the internal secular variation, the so-called geomagnetic jerks (Section 8.04.5.4), promising a probe of core processes on timescales as little as a year or even less.

Large-scale flow provides one paradigm for secular variation, but another, hydromagnetic waves, is considered briefly in Section 8.04.6. In Section 8.04.7, we focus in detail on a particular small-scale structure in the flow, in the polar regions north and south of the inner core, the so-called polar vortices. Finally, in Section 8.04.8, we discuss briefly attempts to unify the kinematics of flow modeling with more dynamic approaches, including data assimilation, for further understanding of core processes.

8.04.2 Surface Core Flow from Observed Secular Variation

8.04.2.1 Westward Drift

The time variation (secular variation) of the magnetic field was first recognized in the late 17th century. In attempting to provide a theory to explain it; Halley (1692) noticed that a large part of the secular variation could be explained in terms of a 'westward drift' of the field. When maps of the field are produced over the Earth's surface at different epochs, there is a clear westward movement of features in the field. This apparent motion is seen particularly clearly if lines of zero declination (the so-called agonic lines) are plotted at different epochs (e.g., Langel, 1987). Halley estimated that a full revolution of the field would take about 700 years, giving a rotation rate of just over $0.5^\circ\,\text{year}^{-1}$. To explain the drift, he posited a model of the interior of the Earth consisting of concentric shells of magnetic material rotating at varying rates with respect to its surface. While much of his theory was unavoidably flawed (the interior of the Earth is too hot to support permanent magnetization at depths greater than about 100 km, and there are no large void spaces within the Earth and in particular no people living in them awaiting religious conversion!), the fundamental insight of the magnetic secular variation resulting from large-scale differential motion between different components of the Earth remains fully valid. In many ways, his theory has remarkable similarities to our current understanding. The Earth does consist of different layers, one of which (the fluid outer core) gives rise to the secular variation, of which a large part can indeed be represented by westward motions at the surface of the core.

With the advent of dynamo theory and the understanding that the magnetic field originates from fluid motions in the molten iron core, the first 'modern' theory of westward drift was proposed by Bullard et al. (1950). They argued that the cooling of the Earth would lead to a pattern of large-scale convection in the core. As a parcel of fluid rose, it would move further from the Earth's rotation axis. Therefore, to conserve angular momentum, the angular velocity of the parcel would reduce. Similarly, a sinking fluid parcel would reduce its moment arm and so need to increase its angular velocity. Bullard et al. suggested that this would lead to a net eastward flow with respect to the solid Earth at the base of the core near the inner core boundary and westward flow at the core surface, which would then carry the magnetic field in a westerly direction, giving rise to westward drift. While the basic physical ideas of this theory are very attractive, modeling of rotating convection has shown that the interaction of convection and rotation is much more complicated, and this pleasingly simple explanation for the drift is not physically viable.

Further, westward drift is an oversimplification of the magnetic secular variation. Estimates of westward drift obtained vary depending on the precise definition: Should it involve a fit to the whole field, just the equatorial dipole, the secular variation, or some combination? The value of Bullard et al. (1950) of $0.2^\circ\,\text{year}^{-1}$ has entered the geomagnetism consciousness as a standard, but estimates have varied from 0.08° eastward per year up to 0.733° westward (for a summary, see Langel (1987)). What this range of values demonstrates is that the picture of westward drift is much too simplistic. Even in the eighteenth century, it was realized that some features of the field drift northward rather than westward, and once Gauss had developed a method for measuring magnetic intensity, the observed decay of the dipole could clearly not be explained by drift alone. Further, westward drift is much more clearly visible in Europe and North America than in Asia and the Pacific hemisphere. Yukutake and Tachinaka (1969) argued that other features in the field did not move at all and proposed a division of the field into drifting and standing components, while Yukutake (1979) further suggested that the equatorial dipole field could be separated into two components, drifting in opposite directions, a process reminiscent of wave motion.

With the advent of detailed time-dependent models of the magnetic field at the core–mantle boundary (CMB) (described in the chapter by Jackson and Finlay in Volume 5 of this treatise), the idea of simple westward drift has been superseded, although as we shall see, westward motion is still a major component of most models of core-surface flow. It is these models that are the primary focus of this treatise chapter.

8.04.2.2 The Frozen-Flux Hypothesis

We turn therefore to a more detailed mathematical description of the generation of the secular variation. The evolution of the magnetic field in the core is governed by the magnetic induction equation

$$\frac{\partial \mathbf{B}}{\partial t} = \nabla \wedge (\mathbf{u} \wedge \mathbf{B}) + \eta \nabla^2 \mathbf{B} \qquad [1]$$

where $\mathbf{B}$ is the magnetic field, $\mathbf{u}$ the fluid velocity, and $\eta = 1/(\mu_0 \sigma)$ is the magnetic diffusivity, defined in terms of the permeability of free space μ_0 and the electric conductivity σ of the core fluid. For the derivation of this equation, see the discussion of secular variation by Jackson and Finlay in volume 5 and the dynamo theory in chapter by Roberts in this volume. Using this kinematic description of the system, we will derive and apply methods to determine the flow at the top of the core from time-varying models of the magnetic field.

For a full description of the flow in the core, we must also consider the dynamics, governed by the Navier–Stokes equations (in the Boussinesq approximation):

$$\rho_0\left(\frac{\partial \mathbf{u}}{\partial t}+\mathbf{u}\cdot\nabla\mathbf{u}+2\Omega\wedge\mathbf{u}\right)=-\nabla p+\rho' g+\mathbf{J}\wedge\mathbf{B}+\rho_0\nu\nabla^2\mathbf{u} \quad [2]$$

where ρ_0 is the hydrostatic density, ρ' is the departure of density from the hydrostatic state, Ω is the Earth's rotation vector, p is the nonhydrostatic pressure, g is the acceleration due to gravity, and $\mathbf{J}=(1/\mu_0)\nabla\wedge\mathbf{B}$ is the current density. Although the dynamics are not a primary focus of this chapter, the dynamic equation will be used in a simplistic way to provide additional constraints on flow and initial work to incorporate dynamics into flow modeling will also be described. For more details on the full dynamic system, see the chapters by Roberts and by Jones in this volume.

The primary tool for observational constraint of core fluid motions is the radial component of the induction equation at the CMB. The CMB is approximated as spherical, and because it is a material boundary, the radial component of the flow there is zero. Then, the radial component of eqn [1] can be written as

$$\dot{B}_r=-\nabla_H\cdot(\mathbf{u}_H B_r)+\frac{\eta}{r}\nabla^2(rB_r) \quad [3]$$

where $\mathbf{u}_H$ are the flow components in the horizontal directions and ∇_H is the horizontal part of the divergence operator. In words, the rate of change of the magnetic field at the CMB is the sum of the contributions from the advection of the radial field (the first term) and its diffusion (the second term). A simple scaling analysis of this equation allows estimation of the relative importance of advection to diffusion in the generation of the secular variation. Typical scales in the core might be $U\simeq 5\times10^{-4}\,\mathrm{m\,s^{-1}}$, $L\simeq 1000$ km, $\eta\simeq 1\,\mathrm{m^2 s^{-1}}$ giving $R_m\approx 500$, suggesting that advection dominates diffusion. If we neglect diffusion, then eqn [3] becomes

$$\dot{B}_r+\nabla_H(\mathbf{u}B_r)=0 \quad [4]$$

This equation is the starting point for modeling of flow at the core surface, as originally proposed by Roberts and Scott (1965). It is named the frozen-flux induction equation, because it can be shown (see, e.g., chapter by Jackson and Finlay in Volume 5) that the magnetic field is carried along passively with the flow and so provides a tracer of that flow. The justification for dropping diffusion is not particularly strong: Bloxham and Jackson (1991) among others discussed many of the factors that might make this assumption fail. Perhaps most obviously, the estimate of length scale may be inadequate: it is motivated by possible horizontal length scales of the magnetic field. It is likely that the radial length scale for magnetic field variation at the CMB may be shorter, due to the formation of hydromagnetic boundary layers, strongly increasing the importance of the diffusion term. Unfortunately, the radial dependence of the magnetic field cannot be constrained by observations. Even neglect of the diffusion term in the horizontal directions may be inappropriate, a point to which we will return later. Nevertheless, eqn [4] provides the primary tool for the modeling of core-surface flow. Given a model of the radial field B_r and either a model of secular variation $\dot{B}_r$ or direct estimates at the Earth's surface (e.g., from yearly differences of magnetic observatory annual means (e.g., Waddington et al., 1995)), it is possible to model (or at least constrain) the surface flow $\mathbf{u}$.

8.04.2.3 Poloidal–Toroidal Decomposition

For a spherical geometry, it proves useful to consider both the magnetic field and flow in terms of a poloidal–toroidal decomposition (see, e.g., Gubbins and Roberts, 1987, and the chapter by Roberts in this volume). Because of Gauss' theorem for magnetic field (and the absence of magnetic monopoles) and the incompressibility condition for flow from the Boussinesq approximation, it follows that both the field and flow are divergence-free:

$$\nabla\cdot\mathbf{B}=0 \quad [5]$$

$$\nabla\cdot\mathbf{u}=0 \quad [6]$$

As a result, we may write field and flow as

$$\mathbf{B}=\nabla\wedge(T\mathbf{r})+\nabla\wedge\nabla\wedge(S\mathbf{r}) \quad [7]$$

$$\mathbf{u}=\nabla\wedge(t\mathbf{r})+\nabla\wedge\nabla\wedge(s\mathbf{r}) \quad [8]$$

where T, t and S, s are toroidal and poloidal scalars, respectively, and $\mathbf{r}$ is the position vector. This leads to expressions for the flow in spherical coordinates (r, θ, ϕ) (radius, colatitude, and longitude) of

$$\mathbf{u}_T=\left(0,\frac{1}{\sin\theta}\frac{\partial t}{\partial\phi},-\frac{\partial t}{\partial\theta}\right) \quad [9]$$

$$\mathbf{u}_S=\left(\frac{L^2 s}{r},\frac{1}{r}\frac{\partial(rs)}{\partial r\partial\theta},\frac{1}{r\sin\theta}\frac{\partial(rs)}{\partial r\partial\phi}\right) \quad [10]$$

and similar expressions for the field, where

$$L^2=-\left\{\frac{1}{\sin\theta}\frac{\partial}{\partial\theta}\left(\sin\theta\frac{\partial}{\partial\theta}\right)+\frac{1}{\sin^2\theta}\frac{\partial^2}{\partial\phi^2}\right\} \quad [11]$$

is the angular momentum operator from quantum mechanics. (Note that this expansion for the poloidal–toroidal decomposition is by no means unique: often, e.g., the unit vector $\hat{\mathbf{r}}$ replaces the position vector r in eqns [7]–[8].)

We must consider the boundary conditions for both field and flow. As already noted, defining an impenetrable, spherical CMB gives zero radial velocity there, leading to an alternative form for the flow decomposition. From eqn [10], zero radial flow requires that $s=0$, but $\partial s/\partial r$ is nonzero. Writing $\mathcal{T}=t$, $\mathcal{S}=(1/r)((\partial(rs))/\partial r)$, we obtain an expression for the horizontal flow

$$\mathbf{u}_H=\nabla\wedge(\mathcal{T}r)+\nabla_H r\mathcal{S} \quad [12]$$

To solve for the flow, each of the scalars is further expanded on a basis of spherical harmonics, most commonly real, Schmidt-normalized harmonics, defining

$$\begin{aligned}\mathcal{T} &= \sum_{l=1}^{\infty}\sum_{m=0}^{l}P_l^m(\cos\theta)\left[\mathcal{T}_l^{mc}\cos m\phi+\mathcal{T}_l^{ms}\sin m\phi\right]\\ \mathcal{S} &= \sum_{l=1}^{\infty}\sum_{m=0}^{l}P_l^m(\cos\theta)\left[\mathcal{S}_l^{mc}\cos m\phi+\mathcal{S}_l^{ms}\sin m\phi\right]\end{aligned} \quad [13]$$

where $P_l^m(\cos\theta)$ are associated Legendre functions of degree l and order m (see, e.g., Langel, 1987). These expansions are then substituted into eqn [4], along with expressions for field and secular variation derived from spherical harmonic models of the potential magnetic field at the Earth's surface. Spherical harmonic orthogonality is used to derive a linear system of

equations for $\{\mathcal{T}_l^m, \mathcal{S}_l^m\}$. The solution for this set of flow coefficients provides a solution for the flow (e.g., Whaler, 1986).

8.04.2.4 Boundary Conditions

In order to estimate the flow near the surface of the core, we must consider the boundary conditions in detail. One boundary condition has already been discussed, which is that no penetration of the CMB requires zero radial velocity. However, as the CMB is a rigid boundary, considerations of hydrodynamics also require that the horizontal components of velocity there are zero. Clearly, therefore, determining the flow precisely at the CMB is trivial, but not very informative – it is zero there! When we speak of obtaining the flow at the top of the core, we are generally referring to the flow at the top of the 'free stream' – the region just below the hydromagnetic boundary layers at the CMB. The jump in the radial component of the field across this layer is constrained by a scaling analysis of the condition $\nabla \cdot \mathbf{B} = 0$, which gives

$$\frac{\partial B_r}{\partial r} \sim \nabla_H \cdot \mathbf{B}_H \qquad [14]$$

As the radial length scale of the boundary layer is much smaller than the horizontal length scale of the whole core, it follows that the change in B_r is small. Therefore, we may adopt the radial field at the CMB as appropriate for the radial field at the top of the free stream. Analysis of the perpendicular field components is less clear, particularly concerning the toroidal magnetic field (eqn [7]), but as we shall not use these perpendicular components here, we will pass over these problems.

8.04.2.5 Nonuniqueness

Equation [4] provides the fundamental tool with which it is possible to determine a surface core flow from observations. Its use was first attempted by Kahle et al. (1967), but problems soon became apparent. An ambiguity in part of the flow was noticed by Roberts and Scott (1965) and later quantified by Backus (1968). Backus wrote the product of the flow and radial field in the form

$$\mathbf{u}B_r = \nabla_H \Phi - \hat{\mathbf{r}} \wedge \nabla_H \Psi \qquad [15]$$

Substituting this decomposition into eqn [4] leads to

$$\dot{B}_r + \nabla_H^2 \Phi = 0 \qquad [16]$$

eliminating the scalar Ψ. Thus, the part of the flow corresponding to this scalar does not contribute to secular variation and is not constrained by field observations except for some weak continuity conditions at null-flux curves (lines of $B_r = 0$). (In other words, Ψ defines the *null-space* of the flow.) This problem is also clear from a very simple argument: even given the assumed zero radial velocity, there remain two components of flow to be determined (e.g., northward and eastward) over the surface of the core. Equation [4] provides only one equation with which to do this, so with fewer equations than unknowns, nonuniqueness should be no surprise. By expanding eqn [4] as

$$\dot{B}_r + B_r \nabla_H \cdot \mathbf{u} + \mathbf{u} \cdot \nabla_H B_r = 0 \qquad [17]$$

Backus (1968) observed that a component of the flow is only determined independently at points on the core surface on the null-flux curves and, even at these locations, only that component of the flow perpendicular to the curve.

Clearly, a second equation for the flow (at least) is required: while this does not guarantee a formally unique solution, clearly, two equations for two unknown flow components are better than just one. Such an equation can be obtained by considering various dynamic approximations; we discuss the most frequently used in the succeeding text but begin with a 'hidden' assumption of at least equal importance.

8.04.2.6 The Large-Scale Approximation

The most important condition required for flow calculation does not provide an additional equation and is often overlooked, because it is so ingrained in the methods of solution. The so-called large-scale approximation is the assumption that the flows that generate the observed SV are large scale at the surface of the core. It would always be possible to fit observed SV exactly by taking a flow of arbitrarily small scale. However, such small scales are not required to explain the observations and therefore cannot be reliably recovered from them. Two approaches have been used to apply this condition. The simpler approach is to limit the small scales of the flow by truncation of the spherical harmonic series in eqn [14] (e.g., Voorhies, 1986): by not parameterizing small scales, they are required to be zero. This approach requires no additional physical assumptions about the flow, but is arbitrary and mathematically unattractive, similar to applying Fourier methods without any tapering, leading to possible 'ringing.' A more common approach is to apply some form of regularization or 'damping.' One physically motivated form of damping is to minimize the mean-square velocity in the flow integrated over the area of the CMB:

$$\int_{CMB} \left(v_\theta^2 + v_\phi^2 \right) dS \qquad [18]$$

limiting its kinetic energy (Madden and Le Mouël, 1982). Problems from the implementation of this norm (essentially due to the lack of convergence of the flow and its implications for other physical constraints) led Bloxham (1988) to propose what has become known as the strong norm, which can be written as

$$\int_{CMB} \left(\left(\nabla_H^2 v_\theta \right)^2 + \left(\nabla_H^2 v_\phi \right)^2 \right) dS \qquad [19]$$

Physical interpretation of this norm can be attempted, but it is probably best to regard it merely as penalizing small-scale structure (roughness) more severely than condition [18]. Expanding the flow into its toroidal and poloidal parts following eqn [14], then damping condition [18] becomes to minimize

$$\sum_{l,m} \left(\frac{l(l+1)}{2l+1} \right) \left(\mathcal{T}_l^{m2} \mathcal{S}_l^{m2} \right) \qquad [20]$$

while damping condition [19] minimizes

$$\sum_{l,m}\left(\frac{l^3(l+1)^3}{2l+1}\right)\left(\mathcal{T}_l^{m2}\mathcal{S}_l^{m2}\right) \quad [21]$$

Hence, the strong norm increases the penalty on higher-degree flow components.

We emphasize that all of the more physical (and 'higher profile') approximations that follow are useful only because of the inherent assumption that the flow is large scale.

8.04.2.7 Steady Flows

The first a priori assumption adopted was to model the flow as steady (Gubbins, 1982) – that is, $\mathcal{T}$, $\mathcal{S}$ in eqn [14] are independent of time. This was motivated partially by computational convenience – considering a flow that is steady rather than time-dependent greatly reduces the number of free parameters that must be considered. However, more physical justification is also possible. The steady part of the secular variation accounts for a large fraction of its power, which can be related to a steady flow (consider eqn [4]). Further, many features of the field at the CMB change approximately uniformly with time: for example, the close-to-uniform westward progression of flux patches in the equatorial region under the Atlantic hemisphere suggests they are being carried along by a broadly steady flow.

Steady flows have been determined in two ways: firstly, a simple approach of fitting estimates of the secular variation at a range of epochs, given the magnetic field at those epochs and, secondly, and more consistently, the nonlinear problem posed by advecting an initial field model over the period of interest using a steady flow (e.g., Bloxham, 1992). Both methods produce similar-looking flows that can explain a large fraction of the secular variation, particularly its steady component – variance reductions of over 98% being perfectly possible (Bloxham, 1992).

The resolution of the flow nonuniqueness relies on sufficient change of the field over the time of analysis to allow for view of the flow in the null-space. This requirement was given in a determinant condition by Voorhies and Backus (1985) and yields a minimum time over which data must be considered for the flow to be formally unique. However, whatever the mathematical conditions imposed, the important factor is whether the assumption is physically sensible: Is the flow really steady (or sufficiently slowly varying) over the time period for which it is solved for? Bloxham (1992) demonstrated that even with very high variance reductions, such flows do not well explain fine-scale detail in the SV, particularly the 60-year oscillation in the axial dipole and other more rapid variations in field coefficients. Voorhies (1993) argued that such small variations are well below the error budget imposed by unmodeled physical processes relating to core flow (such as the influence of variations in mantle conductivity, core conductivity, and core asphericity), but nonetheless, these features of the SV appear to be robust and have the potential to provide much information about the dynamics of the top of the core (see, e.g., the description of geomagnetic jerks in **Section 8.04.5.4**). In particular, time variations can be correlated against variations in Earth rotation, and as described in **Section 8.04.4**, this correlation provides perhaps the only independent confirmation that core-surface flow modeling is meaningful. In this respect, assuming a simple steady flow is unsatisfactory, despite its success in explaining the observed secular variation in a very compact way.

8.04.2.8 Toroidal Flows

A toroidal motion is one in which upwelling of the flow is suppressed, so that there is no radial motion of the fluid, giving $u_r = 0$ not only at the CMB but also within the free stream. Various workers, particularly Braginsky (1999) and references therein, have suggested that the top of the core could be stably stratified, which might justify this assumption. Therefore, the radial derivative of the radial component of the flow is zero. The continuity equation gives

$$\frac{1}{r}\frac{\partial(ru_r)}{\partial r} + \nabla_H\cdot\mathbf{u}_H = 0 \quad [22]$$

giving the condition for no upwelling as

$$\nabla_H\cdot\mathbf{u}_H = 0 \quad [23]$$

implying no horizontal divergence in the surface flow. Substituting from eqn [12] gives

$$\nabla_H^2 r\mathcal{S} = 0 \quad [24]$$

and hence the condition that $\mathcal{S} = 0$ over the core surface, requiring no poloidal component to the motion: hence the name toroidal flow.

The additional constraint on the flow provided by eqn [23] reduces the formal nonuniqueness in the flow determination, but does not eliminate it. Combining eqn [23] with eqn [17] leads to

$$\dot{B}_r + \mathbf{u}\cdot\nabla_H B_r = 0 \quad [25]$$

Therefore, flow along contours of B_r (in the direction in which $\nabla_H B_r = 0$) generates no secular variation and so is unconstrained by observations. A particularly important such contour is the geomagnetic equator, meaning that under the toroidal flow assumption, the net flow around the equator is not constrained. As already discussed, Backus (1968) demonstrated that flow can always be determined uniquely perpendicular to null-flux contours; the toroidal flow assumption extends this result to include all contours of B_r. With additional physical assumptions, a toroidal flow can be considered as being determined fully uniquely: Lloyd and Gubbins (1990) demonstrated that, in the case of a completely insulating mantle, a toroidal flow is unique if calculated using both radial and horizontal components of the induction equation. However, even if the mantle is only a weak conductor, the horizontal components of the induction equation are no longer useful, and so, this result is not applied in current flow modeling.

Whaler (1980) provided observational support for the toroidal flow assumption from a local analysis of the geomagnetic field. She observed, following Roberts and Scott (1965), that at local extrema in B_r, where $\nabla_H B_r = 0$, eqn [25] requires

$$\dot{B}_r = 0 \quad [26]$$

She tested this condition against geomagnetic field models (choosing available International Geomagnetic Reference Field

(IGRF) models) and found evidence that this condition holds within observational uncertainties. However, because the field is downward continued from surface observations, no such test can be conclusive, because only 'patch averages' of the field can be determined from surface observations: the formal error on a point estimate of the field at the CMB is infinite (e.g., Backus et al., 1996). This was confirmed by Whaler and Holme (2007) who demonstrated that flows obtained by standard inversion were consistent with the conditions at extrema, given the large inherent uncertainties.

Toroidal flows have been calculated by several authors (e.g., Bloxham, 1992; Voorhies, 1984; Whaler, 1986). They fit the secular variation less well than flows with both toroidal and poloidal components, but this is not surprising as they possess half the number of free parameters for a given spherical harmonic truncation. While interest has moved on to other flow constraints, recent results, both direct seismological observations (Helffrich and Kaneshima, 2010) and an increase in the estimated electric conductivity of the core (Gomia et al., 2013; Pozzo et al., 2012), imply a strong likelihood of stable stratification at the top of the core, suggesting toroidal flow may be worth revisiting.

8.04.2.9 Tangentially Geostrophic Flows

An alternative dynamic assumption, and the one that has been used most frequently in flow modeling for several decades, is that of tangential geostrophy, independently proposed by Hills (1979) and Le Mouël (1984). An assumption is made that the dynamics of the flow at the top of the core is dominated by a balance between pressure gradients, rotation (via the Coriolis force), and buoyancy. Because the mantle is approximately an electric insulator (at least compared with the core), the Lorentz force is assumed to be small. Justification for this assumption is well summarized by Bloxham and Jackson (1991). In this approximation, the dynamic eqn [2] reduces to

$$2\rho(\Omega\wedge\mathbf{u}) = -\nabla p + \rho' g \qquad [27]$$

Curling this equation eliminates the pressure term, giving the *thermal wind equation*

$$2\rho(\Omega\cdot\nabla)\mathbf{u} = \mathbf{g}\wedge\nabla\rho' \qquad [28]$$

Assuming that gravity is fully radial, the radial component of eqn [28] implies

$$\nabla_{\mathrm{H}}\cdot(\mathbf{u}\cos\theta) = 0 \qquad [29]$$

(compare with the equivalent expression for toroidal flow, eqn [23]). As for toroidal flow, this assumption reduces, but does not eliminate, the formal nonuniqueness in flow determination. Substituting eqn [29] into the frozen-flux induction eqn [4] yields

$$\dot{B}_{\mathrm{r}} + \cos\theta\mathbf{u}\cdot\nabla_{\mathrm{H}}\cdot(B_{\mathrm{r}}/\cos\theta) = 0 \qquad [30]$$

It follows that flow is undetermined along contours of $B_{\mathrm{r}}/\cos\theta$. However, this remaining nonuniqueness is less severe than that for toroidal flow, as realized by Backus and Le Mouël (1986). Many of these contours intersect the geographic equator at points where $B_{\mathrm{r}} = 0$. The flow along such contours is not undetermined: it is only closed contours of $B_{\mathrm{r}}/\cos\theta$ around which the flow is ambiguous. These depend on the morphology of the main field and so differ slightly from epoch to epoch, but typically make up ~40% of the core surface. Such areas have been named 'ambiguous patches.' The tangential geostrophic approximation must also fail close to the geographic equator. In this region, the radial component of the Coriolis term is identically zero, and so the thermal wind balance [28] must break down (Backus and Le Mouël, 1986). Numerically, eqn [29] still applies a constraint on flow at the equator, giving $u_\theta = 0$ there, equatorial flow is entirely east–west, but this constraint is not physically well posed.

Two methods have been used to implement the tangentially geostrophic approximation. First, the flow can be expanded in terms of allowed geostrophic functions, the non-orthogonal geostrophic basis (e.g., Backus and Le Mouël, 1986; Gire and Le Mouël, 1990; Jackson, 1997; Le Mouël et al., 1985). This conditions the flow to be precisely tangentially geostrophic. An alternative approach is to damp nongeostrophic components of the flow numerically, for example, by minimizing the norm

$$\int_{\mathrm{CMB}} (\nabla_{\mathrm{H}}\cdot(\mathbf{u}\cos\theta))^2 \mathrm{d}\Omega \qquad [31]$$

(e.g., Holme, 1998; Le Mouël et al., 1985; Pais et al., 2004; Voorhies, 1993). If this integral is identically equal to zero, then the flows are constrained to be identically tangentially geostrophic. An advantage of this second approach, pursued in detail by Pais et al. (2004), is that it is possible to study the effects of small departures from geostrophy. Such a study seems appropriate, because the tangential geostrophic assumption is derived depending on other terms in the force balance being small, not zero, and so it is important to check that forcing the flow to be exactly tangentially geostrophic does not impose artifacts on the solution.

8.04.2.10 Comparison of Solutions Constructed with Different Nonuniqueness Reducing Assumptions

Bloxham and Jackson (1992) presented a comparison of flows derived by several groups with each of the previously mentioned assumptions (steady, toroidal, and tangentially geostrophic). Here, we present flows of each type derived in the same way from the same field models, so as to focus on the different physical features of the resulting flows, rather than potential methodological differences. We consider the field and secular variation around 1980, calculated from the model gufm1 of Jackson et al. (2000). This is a continuous, time-dependent model of the Earth's magnetic field, regularized to be smooth at the CMB. For more details of this model, see **Chapter 5.05**. We present toroidal and geostrophic flows calculated for 1980 (the epoch of the MagSat mission, at which the model is expected to be best constrained by the data) and a steady flow, using field and secular variation in 1970, 1980, and 1990, a sufficiently long interval to ensure formal uniqueness. Each flow is regularized with the strong norm (eqn [19]) and with damping parameters chosen to produce similar flow strength. We see not only some similarities but also some differences between the flows. The three models have similar maximum and root-mean-square flow speeds. There is a strong westward flow under the Atlantic hemisphere in all three cases. Under the Pacific, the steady and

toroidal flows show little flow (the secular variation in this region is small, requiring little flow), but the tangentially geostrophic flow shows in places a strong eastward flow. This flow is not required to explain the observations, but arises from the combination of the large-scale and tangential geostrophic assumptions. Furthermore, it is strongest at the equator, where the latter assumption does not necessarily hold and so should be viewed with suspicion. All three flows show some evidence of flow circulation in the southern hemisphere under Africa and the South Atlantic (christened the southern gyre by Voorhees) and weaker common circulation under North America. In all cases, flow is generally weaker in the Pacific hemisphere, due to the weaker secular variation there. All three flows show some evidence of large-scale symmetry between the northern and southern hemispheres and are dominated by toroidal components, particularly zonal toroidal modes (Bloxham, 1992; Hulot et al., 1990). However, the differences in detail between the flow models demonstrate how any conclusions drawn from a particular model depend on the validity of the underlying physical assumptions used to derive it.

8.04.2.11 Other Flow Modeling Assumptions

More recently, other assumptions have been tested to further constrain flow modeling. In Section 8.04.2.14, we discuss briefly modeling with diffusion, but within the framework of frozen flux, some additional methods have been proposed (Figure 1).

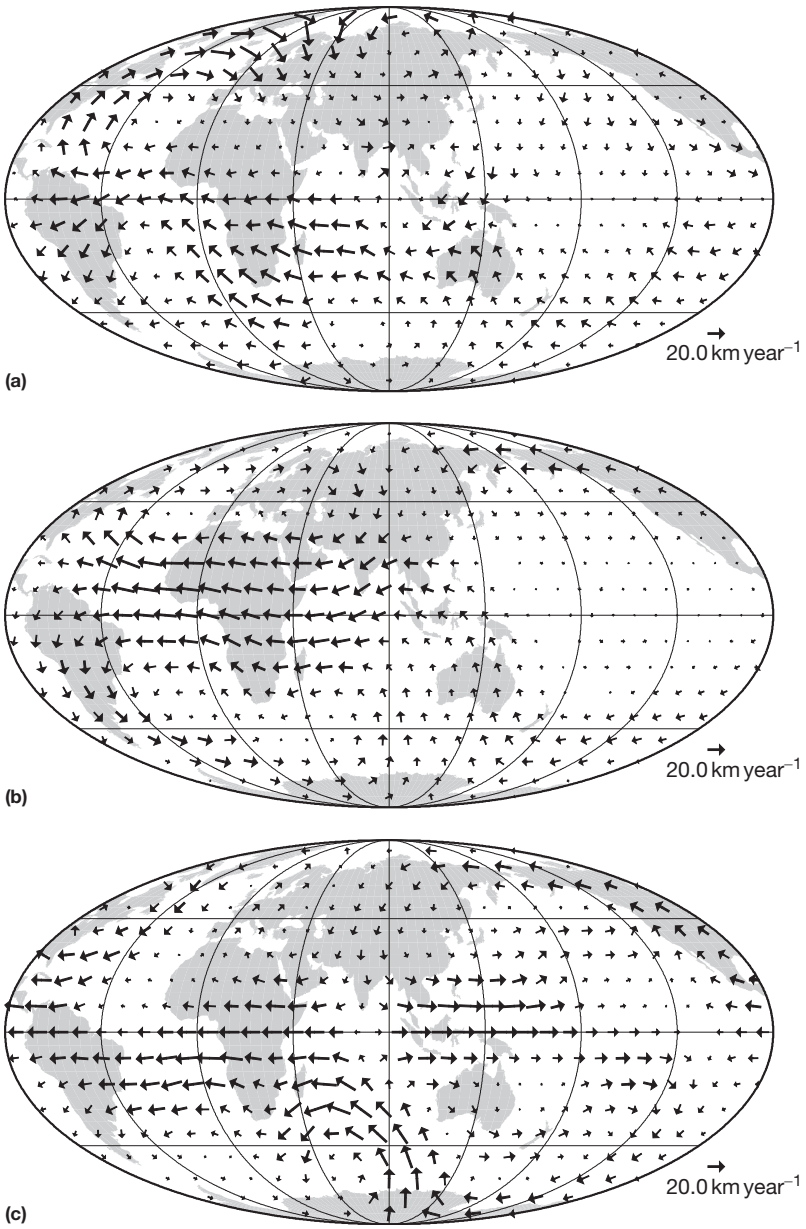

Figure 1 (a) Steady, (b) toroidal, and (c) tangentially geostrophic flows for 1980 calculated from the field model gufm1 (Jackson et al., 2000). Maximum/root-mean-square flow speeds in kilometer per year are (a) 31.0/12.2, (b) 29.6/12.6, and (c) 31.2/14.3.

8.04.2.11.1 Flow in a drifting reference frame

Voorhies and Backus (1985) suggested examination of flows that were steady in a drifting reference frame – a steady flow pattern rotating around the Earth's rotation axis. This could be conceived of as a crude solid body rotation of the whole outer core, of the core near-surface, or as a phase propagation of wave motion at the top of the core. Such flows provide a parsimonious fit to the observed secular variation (Davis and Whaler, 1997; Holme and Whaler, 2001), in the sense that the addition of one further free parameter to a steady flow, the drift rate, results in a large reduction in the misfit to the secular variation, largely by a better fit to variations in the axial dipole field. Allowing a time-dependent drift does not greatly further reduce secular variation misfit, but the variations in drift rate show good correlation with decadal variations in LOD (see **Section 8.04.4**).

8.04.2.11.2 Helical flow

Helical flow is one of two types of a priori information introduced by Amit and Olson (2004). Dynamos are known to operate well in the presence of helicity (giving rise to the so-called α-effect), and therefore, helicity is a sensible choice of a physical quantity with which to constrain flow structure. Amit and Olson (2004) assumed that

$$\nabla_{\mathrm{H}}\cdot\mathbf{u}_{\mathrm{H}} = k_0\zeta \qquad [32]$$

where k_0 is a constant to be chosen and ζ is the radial component of the vorticity $\nabla \wedge \mathbf{u}$. Using the toroidal–poloidal decomposition, the condition on the flow components is

$$\Delta_{\mathrm{H}}^2\mathcal{S} = k_0\nabla_{\mathrm{H}}^2\mathcal{T} \qquad [33]$$

The negative sign applies in the northern hemisphere and the positive sign, in the southern hemisphere. Note that k_0 is considered constant, for which there is some evidence from some dynamo simulations. Amit and Olson (2004) showed that a formulation that combines any amount of helical flow (any nonzero constant value of k_0) with the tangential geostrophic assumption produces a flow solution that is formally unique everywhere.

8.04.2.11.3 Columnar flow

The second assumption provided by Amit and Olson (2004) is columnar flow, which assumes that the flow internal to the dynamo is organized dominantly in columns; then, because these columns must make contact with the slanted spherical surface of the CMB, the surface flow is constrained such that

$$\nabla_{\mathrm{H}}\cdot\mathbf{u}_{\mathrm{H}} = \frac{2\tan\theta}{c}u_\theta \qquad [34]$$

where c is the core radius. The columnar assumption is closely related to the tangentially geostrophic approximation – eqn [29] can be rewritten as

$$\nabla_{\mathrm{H}}\cdot\mathbf{u}_{\mathrm{H}} = \frac{\tan\theta}{c}u_\theta \qquad [35]$$

differing only by a factor of 2 from eqn [34]. Equivalently, eqn [34] can be rewritten as

$$\nabla_{\mathrm{H}}\cdot\left(\mathbf{u}\cos^2\theta\right) = 0 \qquad [36]$$

closely related to eqn [29] and allowing easy implementation by application of a norm to damp noncolumnar contributions.

Some observational evidence for columnar flow is provided by very detailed models of the core-surface field constrained using maximum entropy techniques (Jackson, 2003). This approximation has become of particular interest from its central role in quasigeostrophy, discussed later in the text.

8.04.2.12 Limitations in Resolution of Nonuniqueness

Considerable effort has been expended on investigating the reduction or elimination of formal nonuniqueness by the various dynamic flow assumptions. This has led to a perception that, for example, constraining a flow to be tangentially geostrophic yields a unique result that can be applied to examine other physical problems. Such confidence is misplaced, as even in the case where a formally unique flow can be obtained; in practice, the flow is obtained by a fit to noisy 'data.' As in all data modeling problems, the 'data' (here, the radial field secular variation at the Earth's surface) are not fit exactly, but instead to within a given tolerance, generally to about one standard deviation defined by the expected error. The field models used are uncertain because of sparse, unevenly distributed, noisy data and contributions to the field from sources other than the core, particularly from the long-wavelength lithospheric field. Nevertheless, for convenience, the uncertainty in the large-scale field structure is usually ignored: the consequences of this are considered formally by Jackson (1995). The secular variation models can be even less certain. Direct estimates of magnetic secular variation from observatory data (e.g., Whaler, 1986) should allow better quantification of noise, but Beggan et al. (2009) showed highly correlated residuals to the estimated secular variation that matched the signature expected from the magnetospheric ring current external to the Earth. Using models of the SV from internal field modeling eliminates or reduces this effect, although secular variation in the internal field from induction in the conducting mantle, particularly related to the solar cycle, remains. Numerically, a model fit provides a unique solution (the flow that fits the data to within a given error tolerance, subject to additional physical information, and smoothness defined by the chosen form of damping – the large-scale approximation); however, there are an infinite number of flows that fit the data to such a given tolerance while allowing perhaps only slightly greater complexity (a slight relaxation of the damping). Thus, there is an infinite space of flows that explain the observed secular variation. This is particularly the case as the errors on the field coefficients are formally unbounded (or rather, any rigorous formal bound is so weak as to be practically useless (Backus, 1988)), due to the need to downward continue the field from the Earth's surface to the CMB, an operation that is mathematically unstable. An example of the pitfalls of overestimating the uniqueness of the flow was given by Holme (1998) in a study of electromagnetic core–mantle coupling. While forward modeling of the electromagnetic torque of the core on the mantle from a calculated field model displays little similarity with that torque required to explain observed variations in LOD, inverse models calculated to explain both the secular

variation and the torque do so with little additional flow complexity, showing that this core–mantle coupling mechanism cannot be ruled out on observational (flow modeling) grounds alone. Pais et al. (2004) took such ideas further by exploring the effects of relaxing the numerical implementation of the tangential geostrophic constraint, rather than applying it exactly. Physically, this is sensible: while we might believe that tangential geostrophy is a good approximation to the physics at the top of the core – for example, that the influence of the Lorentz force is weaker than the Coriolis force and pressure gradients – this is far from stating that the Lorentz force must be exactly zero. A small Lorentz force could give rise to a large change in the physical behavior of the flow. This is further investigated by Asari and Lesur (2011) who generalize the tangentially geostrophic condition to a tangentially magnetostrophic alternative, allowing for the direct influence of magnetic field on the force balance.

A particularly instructive example of the influence of the nonuniqueness reducing assumption is given by Beggan and Whaler (2008), who, in parallel to considering toroidal-only flows, also considered flows with poloidal-only components. There is no physical justification for such a flow, but nevertheless, solutions were obtained that fit the observed secular variation well, perhaps even better for comparable flow magnitude than the physically justifiable toroidal-only flow. We should therefore be very careful in interpreting the flows modeled, because in the Earth, the nonuniqueness reducing assumptions will not apply exactly – essentially, the flows obtained are only as good as the physics used as a constraint. This is particularly of concern when flow models are further analyzed to determine other physical properties, for example, in deriving torsional oscillation structure or constraining core–mantle coupling.

8.04.2.13 The Horizontal Field Components

The analysis thus far has focused entirely on the radial component of the induction equation; what can be determined from the perpendicular components of the equation? Sadly, the answer appears to be not very much. The horizontal field components include contributions from the toroidal field, which, in the assumption that the mantle is an insulator, is totally contained within the core. The mantle is not a perfect insulator, and in principle, it should be possible to obtain an estimate of the toroidal field at the top of the core by the measurement of global-scale electric currents at the Earth's surface, for example, in abandoned telecommunications cables (Lanzerotti et al., 1985). However, the effects are very small and very difficult to distinguish from other sources of electric currents, especially oceanic motional induction (see, e.g., Shimizu et al., 1998; Shimizu and Utada, 2004). This leaves the toroidal parts of the horizontal field, as given in eqn [12], essentially unknown. At the top of the free stream, it is likely that the toroidal field is at least as large as the poloidal field in the horizontal directions.

Nevertheless, Bloxham and Jackson (1991) attempted to use the horizontal components of the poloidal part of the magnetic field to map the vertical shear of the flow. They generated maps of the shear, but these were contested by Le Mouël (1991). Further investigation of the effects unearthed several unfortunate surprises: in particular, in inverting for shear from synthetic flows with shears of opposite signs, the same shear sign was obtained in both (as reported in Whaler and Davis (1997)). Therefore, the determination of shear at the top of the core does not appear to be robust and will not be discussed further. Gubbins (1996) had further considered the influence of shear in deriving methodology for including diffusion in flow modeling.

8.04.2.14 Effects of Diffusion

The analysis developed earlier in the text, particularly questions of flow uniqueness, has relied fundamentally on the neglect of magnetic diffusion, assuming that secular variation is dominated by advection, in particular on decadal timescales. However, this is by no means certain. In particular, eqn [3] allows an alternative self-consistent scaling interpretation: rather than the dominant term balance being the match of the secular variation against advection, the largest terms could instead be the advection and diffusion, almost canceling, with the secular variation a result of small departures from this equilibrium. Support for such a state was provided by analysis of kinematic dynamo output by Gubbins and Kelly (1996): they argued that a steady flow will evolve to just such a balance, with secular variation tending to zero over time. Love (1999) argued this point with vigor, suggesting that because we expect the dynamo process to be close to steady on decadal timescales, this is precisely the type of state we should expect in the core. If this physical picture truly holds, then clearly flow models neglecting diffusion are in serious error.

Some studies suggest that this problem may be less severe than at first glance. Voorhies (1993) argued for just such a state and solved for a steady flow and parameterized steady diffusion. Interestingly, he found that the form of the steady flow did not change greatly with the additional allowance for diffusion, even at quite low magnetic Reynolds numbers (when diffusion is in principle dominant over advection). This result is supported by the study of Rau et al. (2000), who conducted synthetic experiments based on the output of dynamo codes. They took the synthetic secular variation generated by the dynamo model, solved for a flow based on this secular variation, and compared their solution with the true flow at the dynamo surface. Despite the diffusive contribution to the flow being of the same order of magnitude as the advective contribution, the modeled flow recovered well many features of the true flow. A contrasting estimate of the effect of diffusion has been provided through data assimilation studies (see **Section 8.04.8.1**), for which the output of a dynamo code is constrained to match geomagnetic observations. A model that reproduces the field for the twentieth century suggests a diffusive contribution to secular variation of the order of 2.5% (Kuang et al., 2009), very much consistent with frozen flux.

Many workers have continued to ignore diffusion in modeling for core flow, perhaps encouraged by the result of Rau et al. (2000) or perhaps motivated at least in part by convenience: The flow inversion is already a severely underdetermined inverse problem, and adding additional parameterization for diffusion only makes this problem worse. The method of Voorhies (1993) relied on the steady flow assumption, together with steady diffusion, which makes the number of

parameters tractable. However, it does not allow for time-dependent flow. Voorhies argued that part of the secular variation that must be explained by nonsteady flows is small, particularly in comparison with errors resulting from neglect of other effects (such as diffusion or a noninsulating mantle). Bloxham (1992) made a similar point. Nevertheless, direct comparison with observations from magnetic observatories shows that a steady flow is unable to explain clear features in the observed secular variation (see, e.g., the results of Bloxham et al. (2002), who solve for a particularly detailed steady flow, which is nevertheless unable to explain notable features of the secular variation). Further, these parts of the secular variation are among the most interesting and provide the one independent test that the flow models are in any way meaningful (see **Section 8.04.4**). Therefore, it is unfortunate to ignore them. Gubbins (1996) had provided a methodology for solving for both time-dependent flow and diffusion, but this has not yet been implemented. An alternative approach is to work with models of the secular variation that obey the frozen-flux condition and therefore do not require diffusion. Jackson et al. (2007) provided such a model, while Lesur et al. (2010) solved simultaneously for field and flow models, thus ensuring that the secular variation can be explained without recourse to diffusion. These approaches are very interesting, although if it is accepted that diffusion is likely to act in the core, it is not clear whether better flow models will be obtained if it is eliminated (producing a field model that is likely not physical) or incorporated as an error that is not easy to quantify.

Alternative treatments of diffusion have been proposed. Olson et al. (2002) appealed to mean-field analysis, which has been useful in dynamo theory, to consider the different scales on which diffusion can act. They separate both field and flow into large and small scales

$$B_r = B + b \quad [37]$$

$$\mathbf{u}_H = \mathbf{U} + \mathbf{u} \quad [38]$$

yielding after some analysis a relation matching the upwelling of the small-scale flow to the diffusion of the small-scale field

$$B(\nabla_H \cdot \mathbf{u}) = \frac{\eta}{r}\nabla^2(rb) \quad [39]$$

where these smaller-scale magnetic field features are in advective–diffusive equilibrium in a frame moving with the large-scale velocity (not dissimilar to the concept of steady flow in a drifting frame described earlier in the text). The diffusive term still depends on unknown radial derivatives of the magnetic field at or within the free stream, but Olson et al. (2002) argued that, at least away from the equator, horizontal diffusion should be dominant, supporting this contention with examples from dynamo simulations.

The effects of diffusion are usually considered to be most important at small scales, but Holme and Olsen (2006) instead considered the influence of diffusion on the observed secular variation at large scales. Decomposing the field into its spherical harmonic constituents, the secular variation from diffusion might be expected to increase with harmonic degree, a simple scaling argument giving perhaps

$$\dot{B}_r(l) \sim l^2 B_r(l) \quad [40]$$

But the strength of the observed secular variation also increases with degree as a function of the field strength, approximately

$$\dot{B}_r(l) \sim l^{3/2} B_r(l) \quad [41]$$

(see also Holme et al., 2011). Thus, the observed secular variation power increases almost as rapidly with degree as the simple scaling argument for diffusion would predict, leaving the predictive fractional diffusive power in the observed SV only a weak function of harmonic degree. Holme and Olsen (2006) obtained crude estimates on the possible magnitude of diffusion at each harmonic degree using the well-defined magnetic free-decay modes (e.g., Gubbins and Roberts, 1987) to match the observed field. With this analysis, the largest contribution of diffusion to the observed secular variation occurs at low degrees (large scales) rather than the usually assumed high degrees (small scales). In particular, the strength of the axial dipole coefficient of the field is so dominant at the Earth's surface (where the geomagnetic field is observed) that the action of diffusion on this field component may be the most important diffusional element in the observed secular variation. Interestingly, some tangentially geostrophic flows, for example, the flows of Jackson (1997) and even more clearly flows of the same author reported by Whaler and Davis (1997), underfit the decay of the axial dipole by 5–10 nT year^{-1}. However, applying diffusional estimates as uncertainties on flow determination from the frozen-flux assumption gives surprisingly little change in flow from conventional error estimates, perhaps because the flow is unable to easily explain such secular variation and so does not.

8.04.2.15 Uncertainty of Field Magnitude

Flow modeling has concentrated on the period post 1840. The method for determining absolute field strength was devised by Gauss in 1838; prior to this, absolute measurements of the magnetic field do not exist. Earlier field models can still be constructed, but with an uncertain magnitude. Models from historical data typically match the current average decay of the axial dipole field with time (e.g., Jackson et al., 2000). The uncertainty in the assumption is well demonstrated by the claims of Gubbins et al. (2006), who scaling with available archaeomagnetic data claimed a uniform dipole strength from 1590 to 1840, and Suttie et al. (2011), who with more careful error treatment argued that the constant decay rate is more appropriate. Nonetheless, Le Huy et al. (2000) modeled flows prior to 1590–1840, but this approach was criticized by Jackson (2000), particularly emphasizing the variability of the dipole secular variation since 1840. However, Whaler and Holme (2011) showed that flow models are very weakly dependent on assumed intensity; other uncertainties (such as from the choice of a priori information and the large-scale smoothness/fit to data) produce far more variation in the flow models. Therefore, if flows are valid for the period post 1840, it is possible to extend analysis for the whole period for which historical models can be well calculated.

What about further back in time? Time-dependent field models have been constructed for the archaeomagnetic time period (up to the last 10 000 years; Korte et al., 2011); from

these, core-flow models have been determined for archaeomagnetic timescales (Dumberry and Bloxham, 2006; Wardinski and Korte, 2008). Arguments have been made concerning the prediction of core-angular momentum over these timescales (see succeeding text), but we note that many of the assumptions on the construction of core flow, not least the neglect of diffusion, rely upon timescales being shorter than those modeled in these cases.

8.04.3 Higher-Resolution Flows from Detailed Models of SV from Satellite Observations

Even within the constraints of nonuniqueness and unmodeled diffusion, a model of the core-surface flow can be no better than the models of the radial field and secular variation used to calculate it. Recent models of the secular variation in particular have a considerable improvement in resolution arising from data from recent satellite missions: the Danish Ørsted satellite (Neubert et al., 2001), the German CHAMP satellite (Reigber et al., 2002), and the Argentine SAC-C mission. These have provided effectively continuous data coverage from early 1999 to 2010, with global three-component vector measurements of the magnetic field allowing the construction of high-quality models of the global magnetic field and some additional scalar data from the Ørsted up until the time of writing (2013). 2013 saw the launch of the ESA Swarm mission, which will further extend and enhance this coverage. For more details of these missions, see Olsen and Stolle (2012) and **Chapter 5.02**. Only one earlier mission, the MagSat satellite, that flew for 6 months in 1979–80 (Langel et al., 1982) provided data quality and coverage even approaching the current period. These data allow models of secular variation to be constrained to smaller scales: for example, the CHAOS model of Olsen et al. (2006), which shows coherent signal in secular variation to at least spherical harmonic degree 14 (Holme et al., 2011).

Hulot et al. (2002) made the first attempt to use these higher-resolution models to calculate detailed flow models. They estimated a 20-year time-averaged secular variation from the difference between the fields in 1980 and in 2000 and used this to model the mean flow for the intervening period, centered on 1990, presented in the upper panel of **Figure 2**. This flow model included finer-scale features than previous models, in particular many small vortices in

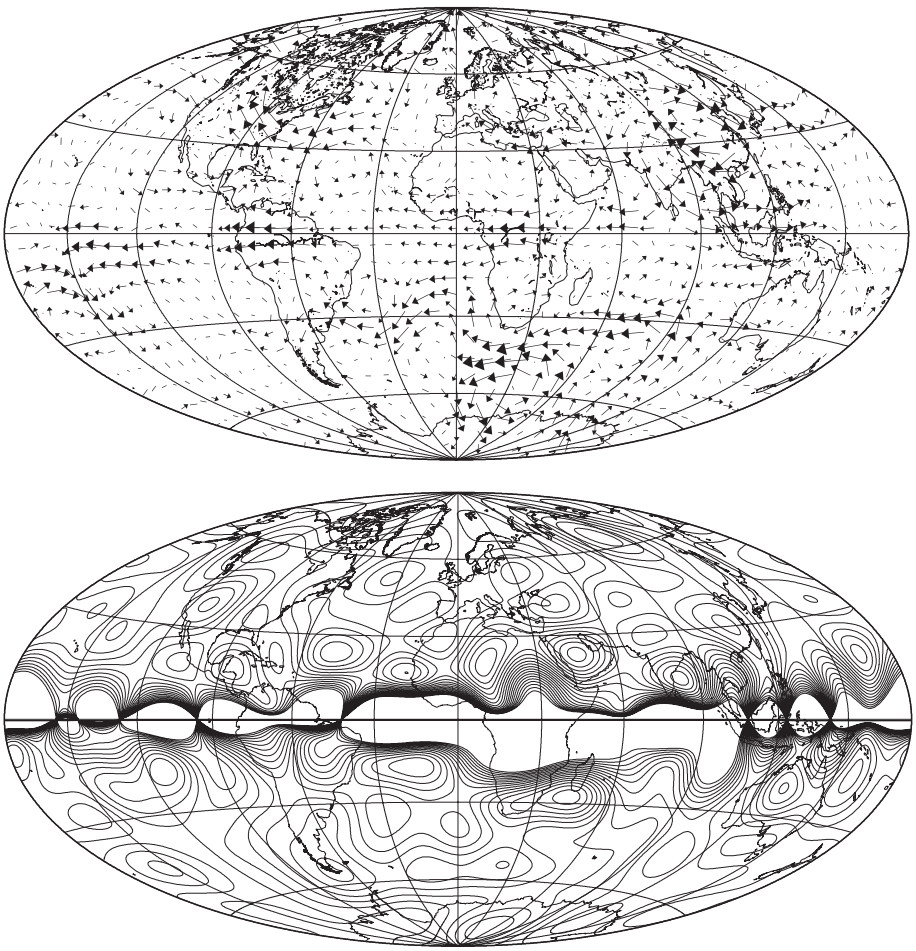

Figure 2 Flow of Hulot et al. (2002), plotted above the contours of the geostrophic nonuniqueness. Many of the small vortices that can be identified in the upper panel coincide with closed contours of the nonuniqueness in the lower panel. Upper panel adapted from Figure 1 of Hulot G, Eymin C, Langlais B, Mandea M, and Olsen N (2002) Small-scale structure of the geodynamo inferred from Oersted and MAGSAT satellite data. *Nature* 416: 620–623, with permission.

midlatitudes. Such features are characteristic of some geodynamo simulations (e.g., Olson et al., 1999). In contrast, Holme and Olsen (2006) calculated flows based on the secular variation from 4 years of data from the satellite missions. **Figure 3** presents possible flows calculated with both the toroidal and tangentially geostrophic assumptions for these epochs. Fine-scale detail is seen that varies greatly between the two flow approximations and even more compared with the flow of Hulot et al. (2002), particularly lacking the many midlatitude vortices. The differences between the flows are a consequence of their construction. The vortices observed by Hulot et al. (2002) are dominant flows along closed contours around field maxima and minima; this corresponds closely to the nonuniqueness described in **Section 8.04.2.9** and shown in the lower panel of **Figure 2**, and so these flows produce no secular variation. Such flows might be expected precisely from the balance between advection and diffusion described in **Section 8.04.2.14** and predicted by, for example, Gubbins and Kelly (1996). The vortex flows suggested by Hulot et al. (2002) are not required by the observations, but neither can they be ruled out by them.

Previous flow models had shown broad agreement between different methods and authors (see, e.g., the survey provided by Bloxham and Jackson (1991) and the flows shown in **Figure 1**); now, clearly, this agreement is breaking down. The reason for the emergence of this problem (compared with earlier, larger-scale flows) can be understood quite simply. The nonuniqueness for tangentially geostrophic flows, for example, is along closed contours of $B_r/\cos\theta$. These contours are themselves small scale, and only now, with attempts to fit higher-resolution secular variation, is the inversion able to generate flows of fine-enough scale to match them. The flows of Holme and Olsen (2006) do not show obvious evidence of the resulting vortices; however, this by no means proves that such features are not present in the real core flow. Their flows are damped so as to minimize the overall magnitude of the flow. Therefore, the nonunique flow around these closed contours will be chosen so as to minimize the global strength of

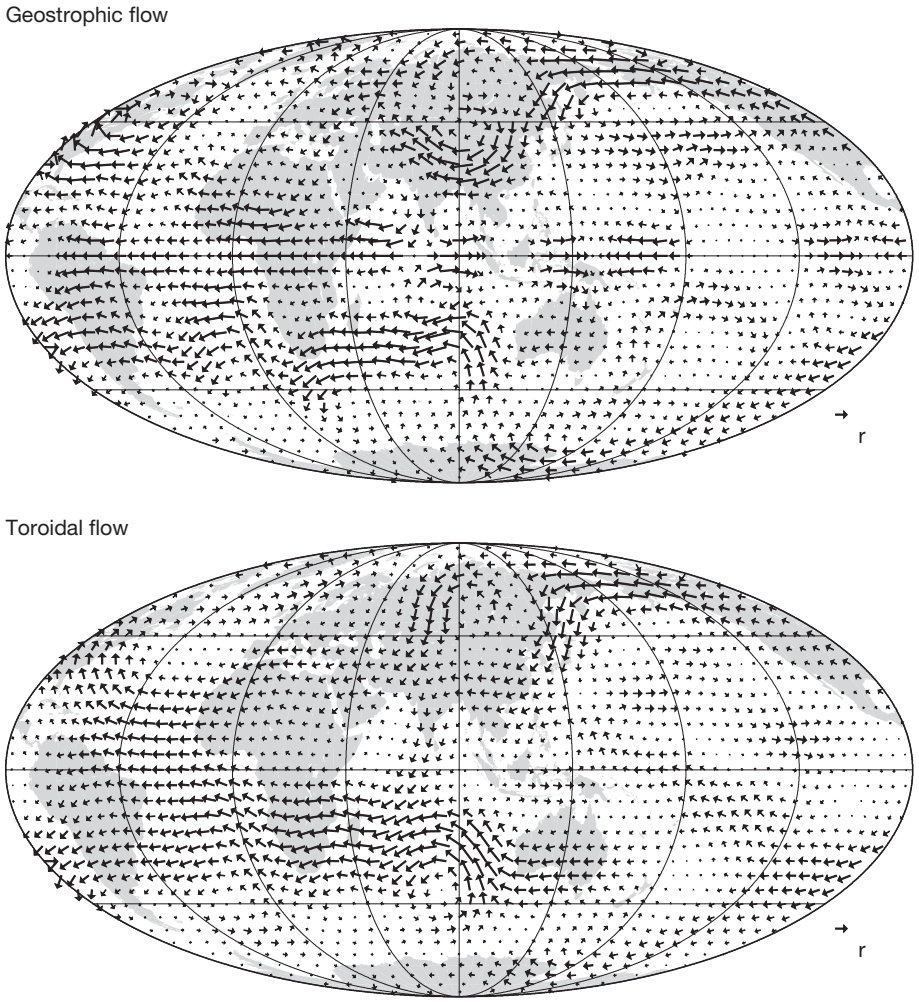

Figure 3 A toroidal and a tangentially geostrophic flow fit from a model derived from high-quality magnetic satellite data for the period 1999–2004 (reproduced from Holme R and Olsen N (2006) Core surface flow modelling from high-resolution secular variation. *Geophysical Journal International* 166: 518–528, with permission). Note circulation foci that might be evidence for columnar flow (northern and southern hemisphere vortices at matching latitudes and opposite rotational sense), although these features are not robust to variations in inversion parameters. Maximum/root-mean-square flow speeds in kilometer per year are 35.0/15.2 and 36.4/13.6, respectively.

the flow. The flow models are equally influenced by the presence of the nonuniqueness, if less obviously than the flows of Hulot et al. (2002).

An even greater problem for resolution of small-scale flow may be the limits to field resolution. Even with more detailed secular variation estimates, the new field models cannot resolve details in the core field smaller than spherical harmonic degree 13, because of the presence of the lithospheric field that screens out these scales. Eymin and Hulot (2005) demonstrated that flow models were strongly compromised by missing knowledge of the main field, supporting the earlier contention of Hulot et al. (1992). The problem arises because field and flow interact with each other at all scales: therefore, the modeled large-scale flow will generate large-scale secular variation from the unknown small-scale field. Eymin and Hulot (2005) considered a suite of field models with varied 'unknown' small-scale field and concluded that this lack of knowledge critically impairs modeling of the true flow from modeled secular variation.

Rau et al. (2000) arrived at similar conclusions when analyzing the output of dynamo simulations. They found that neglect of diffusion did not critically damage the integrity of the flows obtained, but that lack of knowledge of the smaller-scale features in the field was much more damaging. A filter on the field chosen to mimic the effects of the crustal field took a fine-scale field with no clear large-scale westward drift and produced a larger-scale field with apparent large westward drift. In effect, they argue (at least for their model) that a wave mechanism (see **Section 8.04.6**) is made to appear as if it were generated by large-scale flow.

Two approaches have been investigated to take account of these problems. The first, and most straightforward, has been to estimate the uncertainty introduced by small-scale fields and include it as part of the uncertainty budget in the modeling of core flows. Pais and Jault (2008) adopted this approach; the unfortunate implication is that the new high-resolution magnetic satellite data and models add little to our understanding of large-scale core flow. A more direct approach has been to consider ensemble inversion of core flows (Gillet et al., 2009). Models of the unknown small-scale field are generated randomly, and flows are calculated based on the advection of both the observed large-scale field and this additional structure; the proposed average flow solution is the average of the many flows generated with these different small-scale fields. A slightly counterintuitive result is that while each of the individual flows with its associated small-scale field well explains the observed secular variation, the average of the flows (and therefore suggested best representation of core flow) does not. This follows from eqn [4]; because the product of the flow and the field yields the secular variation, although the unknown field is simulated to be zero mean over the ensemble, the calculated flow is a function of this field, and the mean of the flow and field is nonzero.

8.04.4 Angular Momentum–LOD Variation and Correlation with Core-Angular Momentum

Core-surface flows can be calculated using the methodology described in **Section 8.04.2**, but without independent verification, they cannot be confirmed as meaningful. Fortunately, there is another piece of geophysical information against which at least part of the flow model can be tested: the variation in Earth's LOD. The rotation period of the Earth is not a uniform 86 400 s, but varies on timescales of days to millennia, due to the action of external torques and exchanges of angular momentum between different parts of the Earth system. Much more detail is presented in the chapter by Gross in Volume 3 of this treatise. Over the longest timescales, the tidal drag of the Moon and Sun on the rotating Earth is known to produce a secular slowing of rotation (increase in LOD), currently of order 1.4 ms per century. On yearly and subyearly timescales, the angular momentum variation predicted from models of the atmospheric global circulation explains most of the observed LOD variation, and a further part of the signal can also be predicted from oceanic general circulation models (see, e.g., Marcus et al., 1998) and hydrology (Chen, 2005). However, there are further variations of a couple of milliseconds in LOD over several decades that are not easily explained by surface processes. It was realized as early as the 1950s that the missing angular momentum was likely to be being taken up by the core: There was a good correlation between variations in declination at some magnetic observatories and LOD, and in particular, Vestine (1953) demonstrated a good correlation between bulk core rotation predicted from westward drift of the magnetic field and the LOD signal. The observation was put on a much stronger footing by Jault et al. (1988), based on the concept of Braginsky (1970) that angular momentum in the core on decadal timescales should be carried by torsional oscillations, rotation of fluid on concentric cylinders coaxial with the Earth's rotation axis. Jault et al. (1988) realized that if such motions were important, they would be manifest in variations in surface flow patterns (see **Figure 4**). Therefore, using surface flow models, the angular momentum of the whole core could be approximated and compared with observed LOD. Perhaps surprisingly, for uniform flow on cylinders, only two surface flow harmonics are required to calculate the change in angular momentum of the core, the zonal toroidal harmonics of degrees 1 and 3. The angular momentum (in the direction of the rotation axis) is given by (Jault et al., 1988)

$$J_z = \frac{8\pi c^4 \rho}{15}\left(\mathcal{T}_1^0 + \frac{12}{7}\mathcal{T}_3^0\right) \qquad [42]$$

where c and ρ are the radius and mean density of the core, respectively. Conservation of angular momentum between the solid Earth and core leads to a prediction for changes in observed LOD δT (measured in milliseconds) of

$$\delta T = 1.138\left(\delta\mathcal{T}_1^0 + \frac{12}{7}\delta\mathcal{T}_3^0\right) \qquad [43]$$

where the toroidal flow coefficients are measured in units of kilometer per year. Using this formulation, Jault et al. (1988) obtained a promising correlation between observed and predicted variations in LOD for the previous 40 years determined from a sequence of tangentially geostrophic flow models, especially the rate of change, convincing support followed from the work of Jackson et al. (1993), who provided an excellent correlation between predicted core-angular momentum changes and observed LOD variations for the past century. Prior to this period, the correlation is poorer, in particular with an apparent

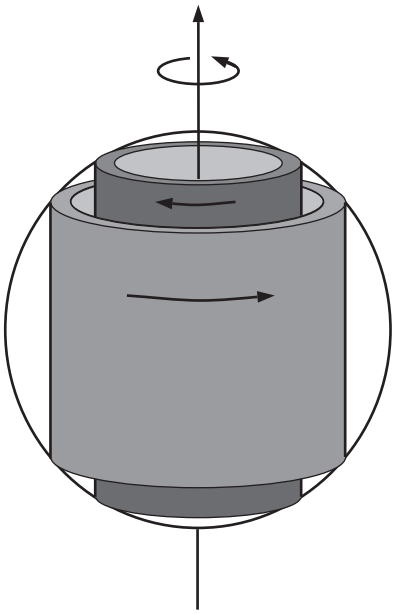

Figure 4 Schematic diagram of the structure of torsional oscillations. The vertical axis coincides with the Earth's rotation axis, and core flow moves on uniform cylinders. The expression in the surface flow in the northern and southern hemispheres should be the same. Courtesy of Dr. Stephen Zatman.

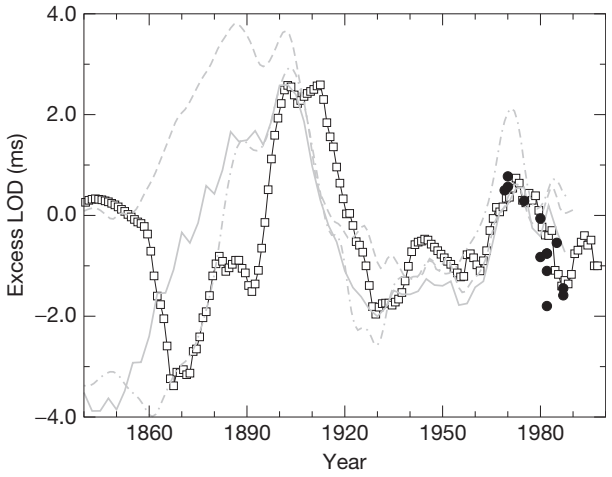

Figure 5 Comparison of observed variation in length of day (squares, from McCarthy and Babcock (1986)) and prediction from core-flow models: Jault et al. (1988) (circles), Pais and Hulot (2000) (dashed line), Jackson et al. (1993) (solid line), and Holme and Whaler (2001) (dot-dashed line). Reproduced from Ponsar S, Dehant V, Holme R, Jault D, Pais A, and van Hoolst T (2003) The core and fluctuations in the Earth's rotation. In: Dehant V, Creager KC, Karato S-I, and Zatman S (eds.) *Earth's Core*: *Dynamics*, *Structure*, *Rotation*, *Geodynamics Series*, vol. 31, pp. 251–261. Washington, DC: AGU, with permission.

phase shift, but the general pattern is still provocative. Pais and Hulot (2000) argued that the misfit of ΔLOD prior to 1900 is not significant compared with model uncertainty. The results of Jault et al. (1988), Jackson et al. (1993), and some other flow calculations are presented in **Figure 5**, taken from Ponsar et al. (2003). The way in which the correlation with LOD changes is achieved is also interesting. Jackson et al. (1993) showed that the two relevant toroidal harmonics $\mathcal{T}_1 0$ and $\mathcal{T}_3^0$ are approximately anticorrelated for much of the period. The flow giving rise to the LOD signal is a small part of the overall flow, and the secular variation generates a small part of the total secular variation, making the observed correlation with the variation in LOD even more impressive.

Other assumptions for flow dynamics also produce a good correlation with variations in LOD. Toroidal and even unconstrained motions (flow constrained to fit the secular variation without further dynamic assumptions) show evidence of the correlation, although weaker than for geostrophic flow. This could be regarded as support for the assumption that flow at the top of the core is approximately tangentially geostrophic. However, estimating core-angular momentum from a toroidal flow is more subject to uncertainty from nonuniqueness, because part of the toroidal nonuniqueness involves flow along contours of B_r that encircle the Earth and can make strong contributions to the calculated angular momentum. (Note that uncertainty for geostrophic flows arising from the failure of the approximation near the equator is not significant because although the moment arm from the rotation axis is maximum, the amount of fluid in the cylinder touching the equator is small because it is short, and so, little angular momentum is carried related to surface flows at this latitude.) Drifting flows with time-dependent drift (Holme and Whaler, 2001) show a correlation with ΔLOD that is almost as good as that from tangentially geostrophic flows and arguably better prior to 1900, as shown in **Figure 5**. A yet better correlation prior to 1900 is probably given by the original Vestine (1953) analysis of westward drift! The greater success of simpler flow parameterization from 1870 to 1900 may be due to the field and secular variation models: over this period, a major improvement in data quality and quantity was achieved, particularly the establishment of a global network of magnetic observatories. The improvement in data allows increasing resolution (to smaller scales) of secular variation in the field models, which a fit by a flow model attempts to explain by core processes. It may be that more parsimonious representations of flow are less influenced by this change.

8.04.5 Torsional Oscillations as a Probe of Core Structure

In the previous section, torsional motions have been introduced as an important contributor to the secular variation, even if amplitude of the resulting secular variation signal is small. Further consideration of torsional oscillations provides a direct probe of processes within the core, rather than just at its surface.

8.04.5.1 Probing the Magnetic Field Interior to the Core

If torsional oscillations are excited and assuming that core–mantle coupling is sufficiently weak that they can oscillate freely, then the characteristics of such oscillations can constrain magnetic field structure in the core. The coupling force between the cylinders arises primarily from their linkage by the magnetic field, in particular its cylindrical radial component B_s. The

work of Zatman and Bloxham (1997, 1998) was pioneering in this respect. They examined the structure of a time-dependent flow model and identified at least one and possibly two separate torsional waves within the structure of the oscillations, shown in Figure 6. Both the frequency and decay rate of these oscillations provide useful constraints, suggesting a value for B_s from 0.2 mT rising to over 1 mT at the inner core boundary in models including boundary friction at the CMB and inner core boundary. Note, however, that caution is necessary: it would be possible to construct a range of possible flow models from the observations that provide a sufficient fit to decadal LOD variation but differ in their fine-scale temporal structure. Because this analysis is of a model of a flow generated from a model of secular variation constrained by field observations, there is much scope for uncertainties to arise depending on the precise nature of the models chosen at each stage.

8.04.5.2 Coupling of Torsional Oscillations to the Outer and Inner Core

Using the framework of torsional oscillations, observed variations in LOD can also be used directly to probe core–mantle interaction. Drawing on a detailed theory giving the normal modes of oscillation including the inner core, coupled

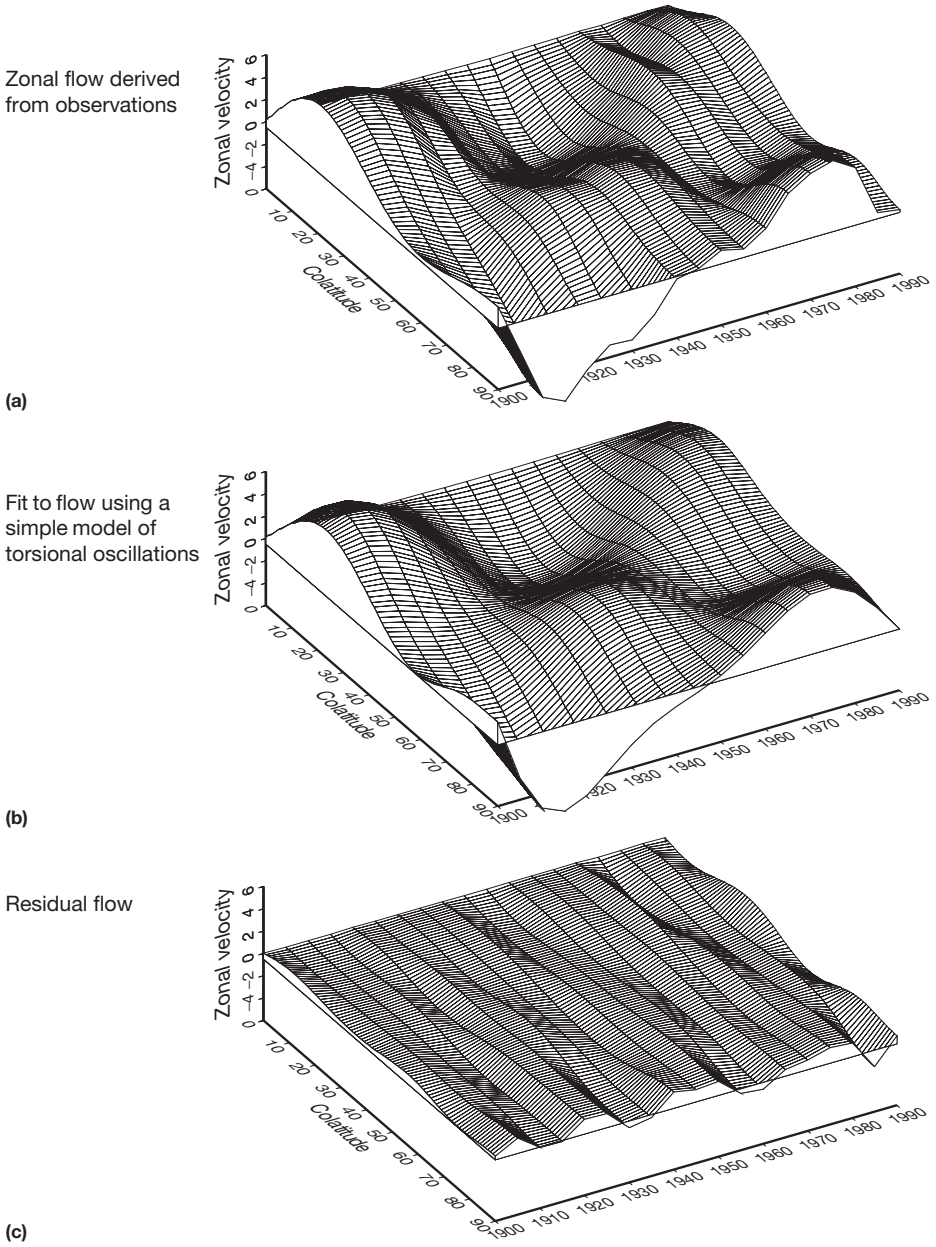

Figure 6 Explanation of torsional oscillation structure over the last 100 years in terms of torsional waves. (a) is the waves calculated from the flow model, (b) is the prediction from a fit of two torsional waves, and (c) is the residual to the fit. Adapted from Zatman S and Bloxham J (1997) Torsional oscillations and the magnetic field within the Earth's core. *Nature* 388: 760–763, with permission.

electromagnetically to the outer core and gravitationally to the mantle (Buffett and Mound, 2005; Mound and Buffett, 2003, 2005), Mound and Buffett (2006) focused on a variation with ~6-year period detected by Abarco del Rio et al. (2000) and quantified more directly and precisely by Holme and de Viron (2013). They argued that the 6-year oscillation is a natural consequence of the coupling of the modes with motion of the inner core (gravitationally coupled to the mantle). By matching their model to the LOD time series, they are able to constrain the strength of gravitational coupling between the inner core and the mantle and place a lower bound on the viscosity of the inner core. An alternative interpretation of the 6-year period in terms of fast torsional waves propagating in a strong (several mT) ambient field is given by Gillet et al. (2010).

8.04.5.3 Quasigeostrophy

The analysis presented thus far relies on assuming a balance of forces within the core, which on timescales of interest is geostrophic, and thus ignores the influence of other forces including buoyancy and Lorentz forces. Motivated by the highly successful approach in meteorology (e.g., Pedlosky, 1987), Jault (2008) and Pais and Jault (2008) had relaxed the geostrophic assumption of rigid motion in the direction of the rotation axis, introducing a quasigeostrophic (QG) formalism. Magnetic forcing is still ignored, and flow is assumed to be broadly columnar, as suggested by numerical dynamo simulations. Variations along the rotation axis are large scale, so that horizontal variations are much larger than vertical ones. For further details, see the review by Finlay et al. (2010a,b). For individual epochs, the internal flow is calculated from a core-surface flow that can satisfy the QG conditions: the flows have equatorial symmetry outside of the inner core tangent cylinder, do not cross this cylinder, and are columnar or tangentially geostrophic at the core surface. The latter is not consistent with incompressible flows (Amit and Pais, 2013), and therefore, much of this work has focused instead on columnar flows.

8.04.5.4 Geomagnetic Jerks and Links to Earth Rotation

Geomagnetic jerks are sharp changes in the rate of change of geomagnetic secular variation (in other words, close to a discontinuity in the second time derivative of the geomagnetic field) at points on the Earth's surface, first identified by Courtillot and Le Mouël (1984) (see the treatise chapter on secular variation or, e.g., Mandea et al. (2010) and references therein). They are seen particularly clearly in the eastward (Y) field component magnetic observatory records in Europe, although some jerks are seen globally. As an important detail in the secular variation, it is sensible to interpret their generation in terms of core-surface flow. Bloxham et al. (2002) had provided a particularly attractive interpretation. They modeled the background (almost) steady secular variation with a steady (if complex) flow and showed that for the 1969 geomagnetic jerk, the magnetic field variation could be well fit by flows consisting only of odd-degree, zonal toroidal, harmonics: the surface expression of torsional oscillations. Unfortunately, the mechanism does not explain some other jerks as effectively (e.g., southern hemisphere jerk features in 1971 and better-resolved jerks measured from satellite data (Silva and Hulot, 2012; Wardinski et al., 2008)), although all workers agree that torsional-like modes (specifically the zonal toroidal component of the surface flow) have an important role to play in explaining geomagnetic jerks through core-surface flow. Direct examination of the variation in LOD provides additional evidence for a link between geomagnetic jerks and Earth rotation (and so perhaps torsional oscillations in the core). Equation [4] implies that any sharp change in secular variation will be matched by a similarly sharp change in core flow and therefore in LOD. Holme and de Viron (2013) demonstrated such a feature, a strong link between the 6-year variation in LOD and geomagnetic jerks, and further suggested a possible discontinuity in the LOD itself. The jerk signatures and LOD variations are concurrent, and their link provides a tantalizing possibility of probing core processes on a very short timescale (a year or less).

8.04.6 Wave Motion as an Explanation for Secular Variation

The analysis presented so far has assumed that the secular variation is primarily a result of large-scale flow at the top of the core. The correlation between predicted core-angular momentum and observed variations in LOD suggests that at least part of the flow can be represented in this way. However, for much of the secular variation, there is another alternative, originating from a suggestion by Hide (1966) of an alternative mechanism to explain westward drift. Whereas Bullard et al. (1950) had argued for an origin of westward drift in large-scale flow, Hide instead suggested that it could arise as a result of wave motion. Magnetic waves called Alfvén waves were known to be supported in a fluid penetrated by a magnetic field. Adding the effect of rotation, additional families of diffusionless magnetohydrodynamic waves were shown to exist, some with periods of order days (similar to inertial waves), but others, named magnetic Rossby waves or planetary waves, with much longer periods, for reasonable estimates of the magnetic field strength perhaps 300 years. Initial analysis based on propagation in a thin shell (similar to analysis for the atmosphere) unfortunately suggested that these waves would propagate eastward, not westward! Hide provided an intuitive argument, later confirmed by more detailed analysis, as to why in the core (a thick shell) such waves would propagate westward instead. Further examination has suggested that westward motion will dominate when the toroidal field is stronger than the poloidal field, as is thought to be the case within the core (Hide and Roberts, 1979).

There are a number of tantalizing observations that suggest that a wave origin for much of the secular variation may be appropriate. When dividing the observed surface field into its standing and drifting components, Yukutake (1979) further suggested that the equatorial dipole field could be separated into two components, drifting in opposite directions; such a process is reminiscent of wave motion, consistent with Hide's ideas. Holme and Whaler (2001) parameterized the large-scale flow into a steady flow in a drifting frame and derived optimal solutions with equal and opposite drift rate, which if added together (the solutions are linear) give rise to a standing wave.

Finlay and Jackson (2003) had provided a detailed analysis of the variation of the nonaxisymmetric part of the field as revealed by the model gufm1 of Jackson et al. (2000). They revealed evidence of uniform westward motion of field near the core equator over all longitudes (although much less clear in the Pacific hemisphere), suggesting that the difference in secular variation between the Atlantic and Pacific hemispheres could have more to do with the morphology and strength of the background field than with any significant difference in physical processes in the two areas. Hydromagnetic waves provide one possible explanation for this signal.

Wave theory can also explain some level of complexity in the secular variation very concisely, as the local 'drift rate' of any feature can vary with location, as the wave velocity is a function of the background field strength, which will vary over the core's surface. Many features of the core field could be explained by a wave-based interpretation: for example, the westward motion of equatorial flux patches under the Atlantic hemisphere has been suggested to be due to trapped barotropic and baroclinic modes in a thin, stably stratified equatorial band (Bergman, 1993). Some numerical dynamo results (e.g., Rau et al., 2000) also show the motion of fine-scale field structure in ways that could be interpreted in terms of waves, but which if viewed through the 'crustal filter' (in other words, only the long-wavelength parts) appear to be large-scale westward drift, not dissimilar from that we see in models from the historical record.

How is a wave explanation for secular variation consistent with induction through flow (and specifically with eqn [4])? If a part of SV can be explained through a wave process, then this equation must still be justified, but the flows that satisfy it may be small scale, in particular too small scale to be resolved by the limit we have on the observed secular variation (and particularly the observed field). Evidence from the correlation with LOD suggests that at least one feature of the flow, the torsional oscillations, is large scale, although they themselves are now interpreted in terms of wave processes! While interpretations of secular variation in terms of large-scale flow are currently dominant, it is certainly not impossible that wave processes have an important role. This is particularly the case given recent reconsideration of a stably stratified layer at the top of the core (**Section 8.04.2.8**), which could support such wave motions. If this is supported, it opens up new avenues for constraining the physical processes in the core: for example, the nature of the propagation is likely to be a function of the structure of the unseen toroidal field.

8.04.7 Polar Vortices

If, as has been argued for torsional oscillations, models of core-surface flow reflect processes deeper within the core, then it might be expected that flow near the poles should differ in structure from flow elsewhere. The theory of torsional oscillations relies on the Taylor–Proudman theorem and that motions are uniform on cylinders throughout the core. However, inside the 'tangent cylinder' defined by the region of the core along the rotation axis above and below the solid inner core, the Taylor cylinders cannot extend from top to bottom of the core. The possible expression in surface flow of the region is small: The two caps at north and south poles make up $<7\%$ of the total core-surface area, but the analysis of the differences between flow in these caps and flow over the rest of the core surface offers the tantalizing prospect of probing the different dynamics in the different regions of the core. Flow in the tangent cylinder is particularly of interest, as it might reflect rotation of the inner core, controversially claimed to have been observed seismically (Song and Richards, 1996; Souriau and Poupinet, 2000; Zhang et al., 2005). Olson and Aurnou (1999) first identified the possible presence of a polar vortex from examination of the field model ufm of Bloxham and Jackson (1992) over more than 100 years. They identified a rotation of field features with time and, using a local (rather than global) flow modeling algorithm, a finite difference scheme regularized by horizontal diffusion, derived an average westward drift rate within the tangent cylinder of nearly a degree per year. They were aware of the inherent nonuniqueness of their flow model and solved for a flow that was cylindrically symmetrical about the rotation axis, which they argued would yield a unique flow field (**Figure 7**).

Further support for polar vortices has come from the analysis of field models from recent satellite data. Hulot et al. (2002) identified vortices in the flow not only in the north polar region but also in the south polar region. **Figure 8** shows the calculated axially averaged flow from the model of Hulot et al. (2002), based on the difference in field between 1980 and 2000. This profile shows a remarkably uniform profile in axisymmetric velocity outside the tangent cylinders, but with vortex-like profiles within them. Further support is provided by results of Holme and Olsen (2006) for both tangentially geostrophic and toroidal flows for the period 1999–2004. However, Eymin and Hulot (2005) cast some doubt on the robustness of these conclusions, arguing that the polar vortices determined are poorly resolved, echoing other earlier (unpublished) criticism. The root of this controversy is (once again) nonuniqueness of the flow determination. Tangentially geostrophic flows are nonunique to flows along contours of $B_r/\cos\theta$ (eqn [30]). The contours are shown for the north polar region in **Figure 9**. Because they encircle the pole, the net circulation of flow around the north pole could take any value, positive or negative.

Olson and Aurnou (1999) tried to bypass these difficulties by solving for an axially symmetrical component of the flow, which they argued can then be determined uniquely. Exact axial symmetry excludes all of the flows around the contours of geostrophic degeneracy, because they themselves are not axially symmetrical. However, such a claim of uniqueness is only valid if the physical assumption is truly valid, which at best is difficult to prove. Nevertheless, if the flow near the poles is large scale (or has a strong large-scale component), then the results of Hulot et al. (2002) and Holme and Olsen (2006) may be robust, because such large-scale flow cannot closely follow the contours of nonuniqueness, because small-scale structure cannot be matched.

Examination of dynamo simulations may provide some insight. In dynamo simulations of Sreenivasan and Jones (2005), flow occurs around a local field maximum and so would be poorly resolved in a flow determination from secular variation, as flows around such contours are close to the null-space of the inversion. However, this field area itself

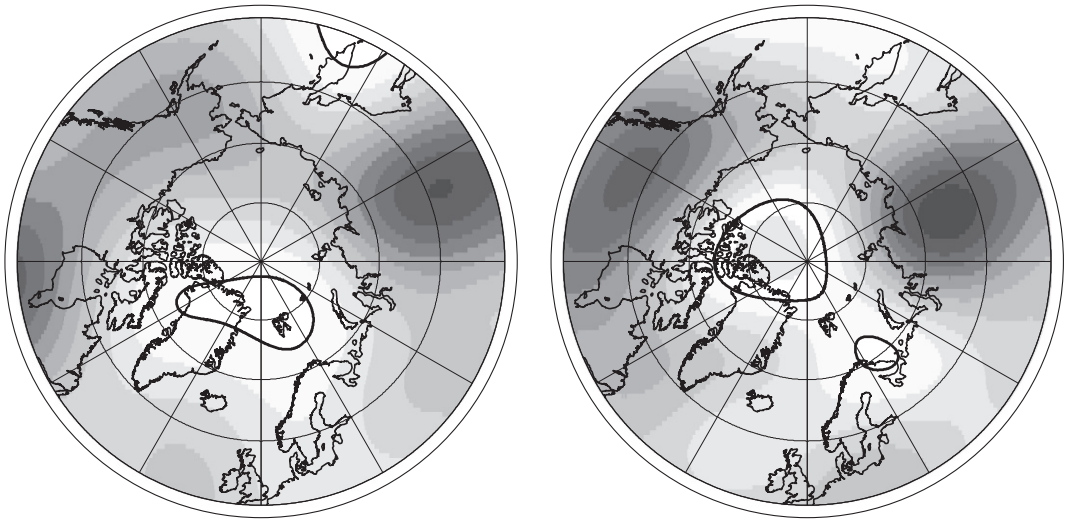

Figure 7 Evolution of the radial field of the model gufm1 in the polar region, left in 1970 and right in 1990, following Olson and Aurnou (1999). The movement of the null-flux curve (included as a thick contour) shows the direction of fluid motion of the vortex.

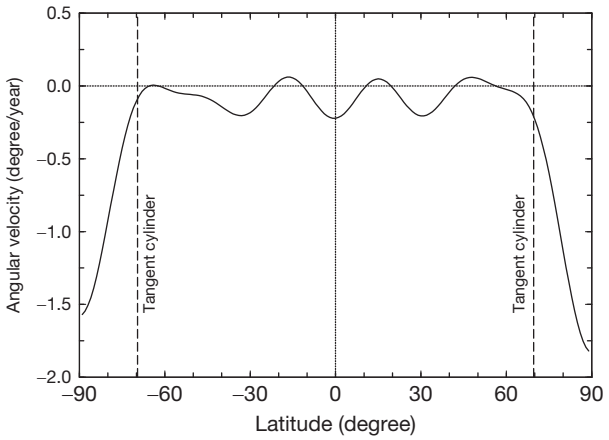

Figure 8 Axisymmetric flows from the model of Hulot et al. (2002) suggesting evidence for polar vortices in both northern and southern hemispheres. Reproduced from Hulot G, Eymin C, Langlais B, Mandea M, and Olsen N (2002) Small-scale structure of the geodynamo inferred from Oersted and MAGSAT satellite data. *Nature* 416: 620–623, with permission.

migrates around the pole. Thus, the flow models may reflect both these processes, with the Olson and Aurnou (1999) observation primarily sensitive to the long-term drift of the field maximum and with the models from satellite data more sensitive to possible flow around this maximum.

Given an observed polar vortex, what further can be deduced? Voorhies (1999) argued that from observation of the vortex, it was possible to constrain a rate of inner core rotation, obtaining a maximum bound of $1.5^\circ\,\text{year}^{-1}$. However, the simulations of Sreenivasan and Jones (2005) yield a polar vortex with a stationary inner core, gravitationally coupled to the mantle, so it is clear that observational measurements of geomagnetic secular variation cannot constrain possible inner core motion until the physics is much better understood. As with many questions as to the core flow, more rigorous statements await a better understanding of the flow regime at the top of the core, leading to better physical constraints on core motion.

8.04.8 Modeled Core-Surface Flow and the Dynamics of the Core

Except in very general terms, this review has so far avoided discussions of flow dynamics. The calculation of the flow models has been kinematic (from the induction equation), and while dynamic information has been included to reduce the nonuniqueness of this determination, dynamic implications of the flow models have not been considered in detail. This is in part due to the uncertainties in the models: There are large differences between calculated flow models, and it is difficult to argue objectively which model to accept. However, the introduction of dynamics into flow modeling is an area that has grown substantially over the last decade.

Initial work focused on how the flow models can be fitted into the dynamic framework, particularly with the ever-growing number of numerical dynamo models. One method is to examine the range of behavior that comes from relaxing nonuniqueness assumptions and whether this can provide any dynamic information. To this end, Pais et al. (2004) considered the relaxation of the tangential geostrophic approximation, modeling the required departure from equilibrium as being due to the magnetic Lorentz force. The equation for the current density that they solved is essentially identical to the flow modeling eqn [4], and so subject to the same issues of nonuniqueness. Nonetheless, it is possible to seek current distributions that minimize, for example, the energy dissipation required; they found that substantial departures from tangential geostrophy required an electric dissipation inconsistent with the energy budget of the core. This methodology may be applicable more broadly, to test whether the Lorentz forces required to support a particular flow are physically possible. Asari and Lesur (2011) investigated this directly by

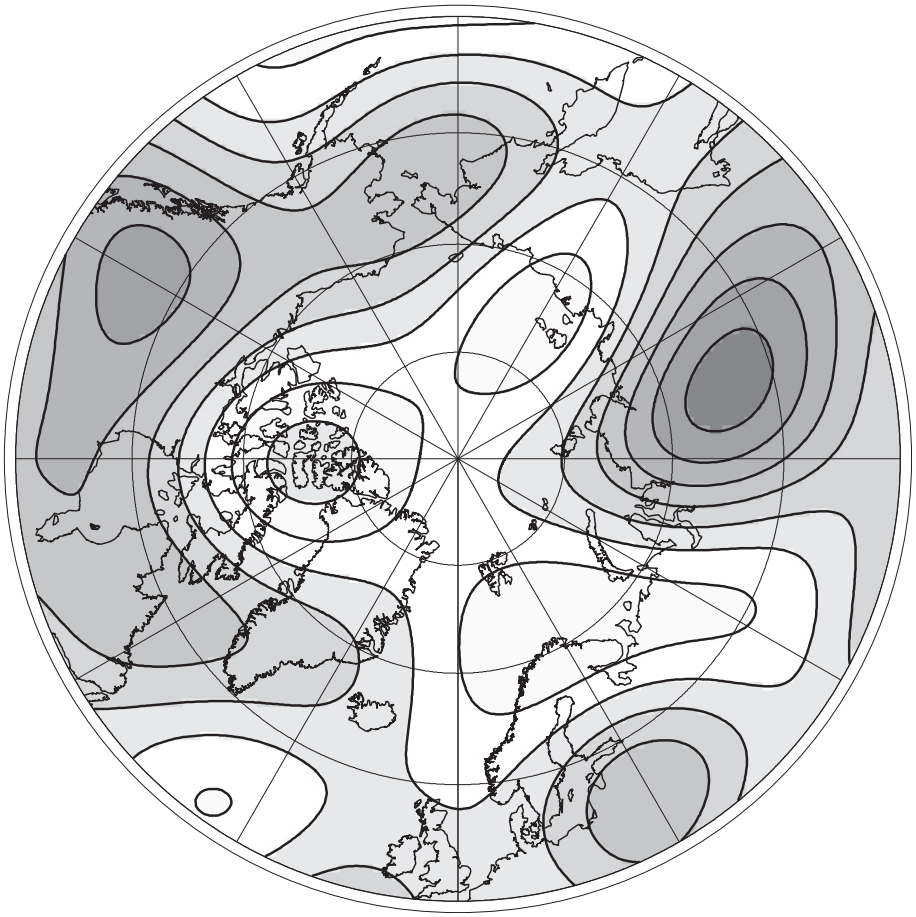

Figure 9 Contours of tangentially geostrophic degeneracy in the region of the north pole for 2000 from the model CO2003 (reproduced from Holme R and Olsen N (2006) Core surface flow modelling from high-resolution secular variation. *Geophysical Journal International* 166: 518–528, with permission). Note that the north pole is contained within a local maximum of such contours, and so, the net flow around the north pole can take any value.

generalizing the tangentially geostrophic approach to seek tangentially magnetostrophic flows.

It is of particular interest to consider what might control the long-term structure of the flow and, in particular, whether any features are likely to demonstrate coherence on long timescales. For this to occur, the most likely mechanism is thermal core–mantle coupling (Bloxham and Gubbins, 1987), with the thermal regime at the base of the mantle having a strong influence on the dynamo and so the flow patterns observed. Assuming that Lorentz forces are weak near the CMB, the thermal wind eqn [28] can in principle be used to constrain the buoyancy and so the temperature field. However, in order to do this, information is required on the flow shear. To construct the temperature field, either a thin-layer approximation must be used for flow at the top of the core (as applied by Kohler and Stevenson (1990) looking at topographic rather than thermal coupling) or the shear must be determined (Bloxham and Jackson, 1990), which as already mentioned is problematic. Instead, progress is being made through comparison with the results of dynamo codes (e.g., Amit and Olson, 2006), although as always using such methods, a significant caveat remains when interpreting the results as to the usefulness of simulations running in a physical regime far from that of the Earth.

The reader may ask, given the existence of output from dynamo codes, why the dynamics is not included directly in the calculation of flow. The answer to this is that all dynamo simulations work in a regime far from that of the Earth, and therefore, direct interpretation is not sensible. Even dynamos that at first glance look quite 'Earth-like' may be far from this when considered in more detail; an instructive example is given by Kuang et al. (2009). It is clearly useful to find some linkage in which the observed data influence the form of the numerical dynamo or the dynamic information constrains the output of the flow inversion.

8.04.8.1 Data Assimilation

Such a problem is common to many disciplines and is probably most developed in meteorology. In generating a weather forecast, the aim is to take current and past observations of atmospheric variables such as temperature, pressure, and wind speed and use dynamic equations to propagate the system forward in time. However, simple forward modeling generates solutions that rapidly diverge from observations. The real atmospheric flow is close to geostrophic, but that modeled from observations is likely to depart from this state, resulting

in the numerical generation of unrealistically strong gravity waves, causing rapid deviation of modeled flow from that observed. It is necessary to initialize the system with a state, determined iteratively, that both fits the observed data to within their uncertainties and also is consistent with an appropriate dynamic balance. This process is called *data assimilation*. We provide a brief introduction to the topic here; for more details, the reader is referred to the review of Fournier et al. (2010) and the chapter by Hulot et al. in Volume 5 of this treatise.

Three recent strands of work consider data assimilation in geomagnetism. At one extreme, Beggan and Whaler (2009) considered assimilation in the calculation of a kinematic steady core flow towards forecasting future secular variation. While using the tools of data assimilation, its dynamics are limited and so are most interesting in this context for the application of a Kalman filter to the flow modeling framework already described. At the other extreme, Kuang et al. (2009) had considered a fully dynamic dynamo and changed its output so as to match the observed field. This must be done repeatedly, as the system naturally evolves away from observations, leading to questions as to the usefulness of the output. An intermediate approach has been introduced through quasigeostrophy (Canet et al., 2009): flows are determined over a range of times, which are consistent with QG dynamics (**Section 8.04.5.3**). Implementation has been supported by successful prediction of the 6-year variation in the core contribution to LOD (Gillet et al., 2010).

Whether such techniques are useful can be measured in terms of their true predictive power – Can models predict the flow and field structure into the future? This is of far more than academic interest: in real-world problems (e.g., exploration and navigation), it is necessary to know the morphology of the field not in the past, from when detailed data are available, but now. The current standard for this is the IGRF (e.g., Finlay et al., 2010a,b), a field model calculated every 5 years, including a constant estimate of the secular variation for estimating the field into the future. In principle, it should be possible to better predict the secular variation using a flow model, but results have been equivocal (see, e.g., Maus et al., 2008). However, assimilated steady flows show more promise (Beggan and Whaler, 2010), while Kuang et al. (2010) submitted a candidate model for IGRF-11 secular variation from dynamo model assimilation that was adopted as part of the finally selected model. It will be interesting to compare each prediction with the observed field in 2015!

8.04.8.2 Inverse Geodynamo Modeling

A parallel approach has also been developed to model core flow not directly with a dynamo model, but constrained to follow the statistical properties of a collection of dynamo models with Earth-like output (Aubert, 2013; Fournier et al., 2011). Results are encouraging: in particular, similar features are seen to those derived with QG models, but without formally applying a QG constraint. While the results will still be sensitive to dynamo models far from the regime of the true Earth, it might be useful to paraphrase Charles Babbage – errors made using inadequate models are likely much less than those using no models at all!

8.04.9 Conclusions

What overall conclusions can be drawn with regard to the nature of large-scale flow in the core? If we wish to be able to make fully rigorous statements, then unfortunately, very few conclusions can be drawn. The still-uncertain role of diffusion, the uncertainty as to the validity of the assumptions made to reduce nonuniqueness, and the screening influence of the lithospheric field mean that almost any conclusion has to come with a caveat. Nonetheless, if we are willing to accept the assumptions as reasonable, we may make some general statements. The correlation of predicted core-angular momentum from flow models with observed variations in LOD, particularly recent results recovering an observed 6-year variation, suggests that at the very least, the large-scale time-varying flow is being recovered well by our flow modeling. The steady component of flow is less certain, but given the results of testing output from dynamo simulations, it is likely that at least the gross features of flow are being successfully recovered. RMS flow speed has not increased greatly with the higher-resolution models calculated from satellite data (compare the values in **Figures 1** and **3**) and so a general RMS flow speed of $\sim$20 km year^{-1} seems reasonable. The flow is probably well defined under the Atlantic hemisphere, where the secular variation is strong and regular, but less so under the Pacific hemisphere, where the secular variation is weaker, and models with different a priori information differ greatly. Until recently, the success of the tangentially geostrophic assumption in fitting observed and modeled secular variation and its comparatively strong theoretical underpinnings meant that it remains the most attractive form of a priori information for flow modeling; however, it is starting to face competition from the columnar flow assumption. In this case, thermal winds seem a probable driving mechanism for surface flows, at least over periods of centuries or so. Some finer features of core flow are likely to be robust: in particular, the modeled polar vortices are likely to be present and should provide a constraint on the dynamics in the tangent cylinder, although constraining inner core rotation is likely to be overambitious. The future will be strongly influenced by dynamo modeling; only through such modeling can the flow ambiguity described in this chapter be addressed; it is also the most promising avenue for direct constraint of dynamic processes from observed secular variation and inferred core flow. However, we must also not lose track of the observations themselves, which must take priority over any modeling assumptions.

References

Abarco del Rio R, Gambis D, and Salstein DA (2000) Interannual signals in length of day and atmospheric angular momentum. *Annals of Geophysics* 18: 347–364.

Amit H and Olson P (2004) Helical core flow from geomagnetic secular variation. *Physics of the Earth and Planetary Interiors* 147: 1–25.

Amit H and Olson P (2006) Time-average and time-dependent parts of core flow. *Physics of the Earth and Planetary Interiors* 155: 120–139.

Amit H and Pais MA (2013) Differences between tangential geostrophy and columnar flow. *Geophysical Journal International* 194: 145–157.

Asari S and Lesur V (2011) Radial vorticity constraint in core flow modeling. *Journal of Geophysical Research* 116, B11101.

Aubert J (2013) Flow throughout the Earth's core inverted from geomagnetic observations and numerical dynamo models. *Geophysical Journal International* 192: 537–556.

Backus GE (1968) Kinematics of geomagnetic secular variation in a perfectly conducting core. *Philosophical Transactions of the Royal Society of London A* 263: 239–266.
Backus GE (1988) Bayesian inference in geomagnetism. *Geophysical Journal* 92: 125–142.
Backus GE and Le Mouël J-L (1986) The region on the core-mantle boundary where a geostrophic velocity field can be determined from frozen flux magnetic data. *Geophysical Journal of the Royal Astronomical Society* 85: 617–628.
Backus G, Parker R, and Constable C (1996) *Foundations of Geomagnetism*. New York: Cambridge University Press.
Beggan C and Whaler K (2008) Core flow modelling assumptions. *Physics of the Earth and Planetary Interiors* 167: 217–222.
Beggan CD and Whaler KA (2009) Forecasting change of the magnetic field using core surface flows and ensemble Kalman filtering. *Geophysical Research Letters* 36, L18303.
Beggan C and Whaler K (2010) Forecasting secular variation using core flows. *Earth, Planets and Space* 62: 821–828.
Beggan CD, Whaler KA, and Macmillan S (2009) Biased residuals of core flow models from satellite-derived 'virtual observatories'. *Geophysical Journal International* 177: 463–475.
Bergman MI (1993) Magnetic rossby waves in a stably stratified layer near the top of the earth's outer core. *Geophysical and Astrophysical Fluid Dynamics* 68: 151–175.
Bloxham J (1988) The determination of fluid flow at the core surface from geomagnetic observations. In: Vlaar NJ, Nolet G, Wortel MJR, and Cloetingh SAPL (eds.) *Mathematical Geophysics, a Survey of Recent Developments in Seismology and Geodynamics*, pp. 189–208. Dordrecht: Reidel.
Bloxham J (1992) The steady part of the secular variation of the Earth's magnetic field. *Journal of Geophysical Research* 97: 19,565–19,579.
Bloxham J and Gubbins D (1987) Thermal core-mantle interactions. *Nature* 325: 511–513.
Bloxham J and Jackson A (1990) Lateral temperature variations at the core-mantle boundary deduced from the magnetic field. *Geophysical Research Letters* 17: 1997–2000.
Bloxham J and Jackson A (1991) Fluid flow near the surface of the Earth's outer core. *Reviews of Geophysics* 29: 97–120.
Bloxham J and Jackson A (1992) Time-dependent mapping of the magnetic field at the core-mantle boundary. *Journal of Geophysical Research* 97: 19537–19563.
Bloxham J, Zatman S, and Dumberry M (2002) The origin of geomagnetic jerks. *Nature* 420: 65–68.
Braginsky SI (1970) Torsional magnetohydrodynamic vibrations in the Earth's core and variations in day length. *Geomagnetism and Aeronomy* 10: 1–8.
Braginsky SI (1999) Dynamics of the stably stratified ocean at the top of the core. *Physics of the Earth and Planetary Interiors* 111: 21–34.
Buffett BA and Mound JE (2005) A green's function for the excitation of torsional oscillations in the earth's core. *Journal of Geophysical Research* 110, B08105.
Bullard EC, Freeman C, Gellman H, and Nixon J (1950) The westward drift of the Earth's magnetic field. *Philosophical Transactions of the Royal Society of London A* 243: 61–92.
Canet E, Fournier A, and Jault D (2009) Forward and adjoint quasi-geostrophic models of the geomagnetic secular variation. *Journal of Geophysical Research* 114, B11101.
Chen J (2005) Global mass balance and the length-of-day variation. *Journal of Geophysical Research* 110: B08404. http://dx.doi.org/10.1029/2004JB003474.
Courtillot V and Le Mouël J-L (1984) Geomagnetic secular variation impulses. *Nature* 311: 709–716.
Davis RG and Whaler KA (1997) The 1969 geomagnetic impulse and spin-up of the earth's liquid core. *Physics of the Earth and Planetary Interiors* 103: 181–194.
Dumberry M and Bloxham J (2006) Azimuthal flows in the Earth's core and changes in length of day at millennial timescales. *Geophysical Journal International* 165: 32–46.
Eymin C and Hulot G (2005) On core surface flows inferred from magnetic satellite data. *Physics of the Earth and Planetary Interiors* 152: 200–220.
Finlay CC, Dumberry M, Chulliat A, and Pais MA (2010a) Short timescale core dynamics: Theory and observations. *Space Science Reviews* 155: 177–218.
Finlay CC and Jackson A (2003) Equatorially dominated magnetic field change at the surface of Earth's core. *Science* 300: 2084–2086.
Finlay CC, Maus S, Beggan CD, et al. (2010b) International geomagnetic reference field: The eleventh generation. *Geophysical Journal International* 183: 1216–1230.
Fournier A, Aubert J, and Thebault E (2011) Inference on core surface flow from observations and 3-D dynamo modelling. *Geophysical Journal International* 186: 118–136.
Fournier A, Hulot G, Jault D, et al. (2010) An introduction to data assimilation and predictability in geomagnetism. *Space Science Reviews* 155: 247–291.
Gillet N, Jault D, Canet E, and Fournier A (2010) Fast torsional waves and strong magnetic field within the earths core. *Nature* 465: 74–77.
Gillet N, Pais MA, and Jault D (2009) Ensemble inversion of time-dependent core flow models. *Geochemistry, Geophysics, Geosystems* 10, Q06004.
Gire C and Le Mouël J-L (1990) Tangentially geostrophic flow at the core-mantle boundary compatible with the observed geomagnetic secular variation: The large-scale component of the flow. *Physics of the Earth and Planetary Interiors* 59: 259–287.
Gomia H, Ohtaa K, Hirosea K, et al. (2013) The high conductivity of iron and thermal evolution of the Earth's core. *Physics of the Earth and Planetary Interiors* 224: 88–103.
Gubbins D (1982) Finding core motions from magnetic observations. *Philosophical Transactions of the Royal Society of London A* 306: 247–254.
Gubbins D (1996) A formalism for the inversion of geomagnetic data for core motions with diffusion. *Physics of the Earth and Planetary Interiors* 98: 193–206.
Gubbins D, Jones AL, and Finlay CC (2006) Fall in Earth's magnetic field is erratic. *Science* 312: 900–902.
Gubbins D and Kelly P (1996) A difficulty with using the frozen flux hypothesis to find steady core motions. *Geophysical Research Letters* 23: 1825–1828.
Gubbins D and Roberts PH (1987) Magnetohydrodynamics of the Earth's core. In: Jacobs JA (ed.) *Geomagnetism*, vol. 2. San Diego, CA: Academic, Chapter 1.
Halley E (1692) On the cause of the change in the variation of the magnetic needle; with an hypothesis of the structure of the internal parts of the earth. *Philosophical Transactions of the Royal Society of London A* 17: 470–478.
Helffrich G and Kaneshima S (2010) Outer-core compositional stratification from observed core wave speed profiles. *Nature* 468: 807–810.
Hide R (1966) Free hydromagnetic oscillations of the Earth's core and the theory of the geomagnetic secular variation. *Philosophical Transactions of the Royal Society of London A* 259: 615–650.
Hide R and Roberts PH (1979) How strong is the magnetic field in the Earth's liquid core? *Physics of the Earth and Planetary Interiors* 20: 124–126.
Hills RG (1979) *Convection in the Earth's Mantle due to Viscous Shear at the Core-Mantle Interface and due to Large-Scale Buoyancy*. PhD Thesis, New Mexico State University, Las Cruces.
Holme R (1998) Electromagnetic core-mantle coupling I: Explaining decadal variations in the Earth's length of day. *Geophysical Journal International* 132: 167–180.
Holme R and de Viron O (2013) Characterization and implications of intradecadal variations in length of day. *Nature* 499: 202–204.
Holme R and Olsen N (2006) Core surface flow modelling from high-resolution secular variation. *Geophysical Journal International* 166: 518–528.
Holme R, Olsen N, and Bairstow FL (2011) Mapping geomagnetic secular variation at the core-mantle boundary. *Geophysical Journal International* 186: 521–528.
Holme R and Whaler KA (2001) Steady core flow in an azimuthally drifting reference frame. *Geophysical Journal International* 145: 560–569.
Hulot G, Eymin C, Langlais B, Mandea M, and Olsen N (2002) Small-scale structure of the geodynamo inferred from Oersted and MAGSAT satellite data. *Nature* 416: 620–623.
Hulot G, Le Mouël JL, and Jault D (1990) The flow at the core-mantle boundary-symmetry properties. *Journal of Geomagnetism and Geoelectricity* 42: 857–874.
Hulot G, Le Mouël JL, and Wahr JA (1992) Taking into account truncation problems and geomagnetic model accuracy in assessing computed flows at the core mantle boundary. *Geophysical Journal International* 108: 224–246.
Jackson A (1995) An approach to estimation problems containing uncertain parameters. *Physics of the Earth and Planetary Interiors* 90: 145–156.
Jackson A (1997) Time dependency of geostrophic core surface motions. *Physics of the Earth and Planetary Interiors* 103: 293–311.
Jackson A (2000) Comment on 'Time evolution of the fluid flow at the top of the core. Geomagnetic jerks' by M. Le Huy, M. Mandea, J.-L. Le Mouël and A. Pais. *Earth, Planets and Space* 52: 649.
Jackson A (2003) Intense equatorial flux spots on the surface of the earth's core. *Nature* 424: 760–763.
Jackson A, Bloxham J, and Gubbins D (1993) Time-dependent flow at the core surface and conservation of angular momentum in the coupled core-mantle system. In: Le Mouël J-L, Smylie DE, and Herring T (eds.) *Dynamics of the Earth's Deep Interior and Earth Rotation*, pp. 97–107. Washington, DC: AGU/IUGG.
Jackson A, Constable CG, Walker MR, and Parker RL (2007) Models of Earth's main magnetic field incorporating flux and radial vorticity constraints. *Geophysical Journal International* 171: 133–144.
Jackson A, Jonkers ART, and Walker MR (2000) Four centuries of geomagnetic secular variation from historical records. *Philosophical Transactions of the Royal Society of London A* 358: 957–990.
Jault D (2008) Axial invariance of rapidly varying diffusionless motions in the Earth's core interior. *Physics of the Earth and Planetary Interiors* 166: 67–76.

Jault D, Gire C, and Le Mouël JL (1988) Westward drift, core motions and exchanges of angular momentum between core and mantle. *Nature* 333: 353–356.

Jault D and Le Mouël JL (1991) Physical properties at the top of the core and core surface motions. *Physics of the Earth and Planetary Interiors* 68: 76–84.

Kahle AB, Vestine EH, and Ball RH (1967) Estimated surface motions of the Earth's core. *Journal of Geophysical Research* 72: 1095–1108.

Kohler MD and Stevenson DJ (1990) Modelling core fluid motions and the drift of magnetic field patterns at the CMB by use of topography obtained by seismic inversion. *Geophysical Research Letters* 17: 1473–1476.

Korte M, Constable C, Donadini F, and Holme R (2011) Reconstructing the holocene geomagnetic field. *Earth and Planetary Science Letters* 312: 497–505.

Kuang W, Tangborn A, Wei Z, and Sabaka T (2009) Constraining a numerical geodynamo model with 100 years of surface observations. *Geophysical Journal International* 179: 1458–1468.

Kuang W, Wei Z, Holme R, and Tangborn A (2010) Prediction of geomagnetic field with data assimilation: A candidate secular variation model for IGRF-11. *Earth, Planets and Space* 62: 775–785.

Langel RA (1987) The main field. In: Jacobs JA (ed.) *Geomagnetism*, vol. 1. San Diego, CA: Academic, Chapter 4.

Langel RA, Ousley G, Berbert J, Murphy J, and Settle M (1982) The MAGSAT mission. *Geophysical Research Letters* 9: 243–245.

Lanzerotti LJ, Medford LV, Maclennan CG, Thomson DJ, Meloni A, and Gregori GP (1985) Measurements of the large-scale direct-current Earth potential and possible implications for the geomagnetic dynamo. *Science* 229: 47–49.

Le Huy M, Mandea M, Le Mouël J-L, and Pais A (2000) Time evolution of the fluid flow at the top of the core. Geomagnetic jerks. *Earth, Planets and Space* 52: 163–173.

Le Mouël J-L (1984) Outer core geostrophic flow and secular variation of Earth's magnetic field. *Nature* 311: 734–735.

Le Mouël J-L, Gire C, and Madden T (1985) Motions at the core surface in the geostrophic approximation. *Physics of the Earth and Planetary Interiors* 39: 270–287.

Lesur V, Wardinski I, Asari S, Minchev B, and Mandea M (2010) Modelling the earth's core magnetic field under flow constraints. *Earth, Planets and Space* 62: 503–516.

Lloyd D and Gubbins D (1990) Toroidal fluid motion at the top of the Earth's core. *Geophysical Journal International* 100: 455–467.

Love JJ (1999) A critique of frozen-flux inverse modelling of a nearly steady geodynamo. *Geophysical Journal International* 138: 353–365.

Madden T and Le Mouël J-L (1982) The recent secular variation and the motions at the core surface. *Philosophical Transactions of the Royal Society of London* 306: 271–280.

Mandea M, Holme R, Pais A, Pinheiro K, Jackson A, and Verbanac G (2010) Geomagnetic jerks: Rapid core field variations and core dynamics. *Space Science Reviews* 155: 147–175.

Marcus SL, Chao Y, Dickey JO, and Gregout P (1998) Detection and modelling of nontidal oceanic effects on Earth's rotation rate. *Science* 281: 1656–1659.

Maus S, Silva L, and Hulot G (2008) Can core-surface flow models be used to improve the forecast of the Earth's main magnetic field? *Journal of Geophysical Research* 113, B08102.

McCarthy DD and Babcock AK (1986) The length of day since 1656. *Physics of the Earth and Planetary Interiors* 44: 281–292.

Mound JE and Buffett BA (2003) Interannual oscillations in length of day: Implications for the structure of the mantle and core. *Journal of Geophysical Research* 108: 2334.

Mound JE and Buffett BA (2005) Mechanisms of core-mantle angular momentum exchange and the observed spectral properties of torsional oscillations. *Journal of Geophysical Research* 110, B08103.

Mound JE and Buffett BA (2006) Detection of a gravitational oscillation in length-of-day. *Earth and Planetary Science Letters* 243: 383–389.

Neubert T, Mandea M, Hulot G, et al. (2001) Ørsted satellite captures high-precision geomagnetic field data. *Eos, Transactions American Geophysical Union* 82: 81–88.

Olsen N, Luhr H, Sabaka TJ, et al. (2006) CHAOS – A model of the Earth's magnetic field derived from CHAMP, Ørsted, and SAC-C magnetic satellite data. *Geophysical Journal International* 166: 67–75.

Olsen N and Stolle C (2012) Satellite geomagnetism. *Annual Review of Earth and Planetary Sciences* 40: 441–465.

Olson P and Aurnou J (1999) A polar vortex in the earth's core. *Nature* 402: 170–173.

Olson P, Christensen U, and Glatzmaier GA (1999) Numerical modeling of the geodynamo: Mechanisms of field generation and equilibration. *Journal of Geophysical Research* 104: 10383–10404.

Olson P, Sumita I, and Aurnou J (2002) Diffusive magnetic images of upwelling patterns in the core. *Journal of Geophysical Research* 107: 2348.

Pais A and Hulot G (2000) Length of day decade variations, torsional oscillations and inner core superrotation: Evidence from recovered core surface zonal flows. *Physics of the Earth and Planetary Interiors* 118: 291–316.

Pais MA and Jault D (2008) Quasi-geostrophic flows responsible for the secular variation of the Earth's geomagnetic field. *Geophysical Journal International* 173: 421–443.

Pais MA, Oliveira O, and Nogueira F (2004) Nonuniqueness of inverted core–mantle boundary flows and deviations from tangential geostrophy. *Journal of Geophysical Research* 109: B08105. http://dx.doi.org/10.1029/2004JB003012.

Pedlosky J (1987) *Geophysical Fluid Dynamics*, 2nd edn. New York: Springer-Verlag.

Ponsar S, Dehant V, Holme R, Jault D, Pais A, and van Hoolst T (2003) The core and fluctuations in the Earth's rotation. In: Dehant V, Creager KC, Karato S-I, and Zatman S (eds.) *Earth's Core: Dynamics, Structure, Rotation*. *Geodynamics Series*, vol. 31, pp. 251–261. Washington, DC: AGU.

Pozzo M, Davies C, Gubbins D, and Alfé D (2012) Thermal and electrical conductivity of iron at earth's core conditions. *Nature* 485: 355–358.

Rau S, Christensen U, Jackson A, and Wicht J (2000) Core flow inversion tested with numerical dynamo models. *Geophysical Journal International* 141: 485–497.

Reigber C, Liihr H, and Schwintzer P (2002) CHAMP mission status. *Advances in Space Research* 30: 129–134.

Roberts PH and Scott S (1965) On analysis of the secular variation, 1, A hydromagnetic constraint: Theory. *Journal of Geomagnetism and Geoelectricity* 17: 137–151.

Shimizu H, Koyama T, and Utada H (1998) An observational constraint on the strength of the toroidal magnetic field at the CMB by time variation of submarine cable voltages. *Geophysical Research Letters* 25: 4023–4026.

Shimizu H and Utada H (2004) The feasibility of using decadal changes in the geoelectric field to probe earth's core. *Physics of the Earth and Planetary Interiors* 142: 297–319.

Silva L and Hulot G (2012) Investigating the 2003 geomagnetic jerk by simultaneous inversion of the secular variation and acceleration for both the core flow and its acceleration. *Physics of the Earth and Planetary Interiors* 198: 28–50.

Song XD and Richards PG (1996) Seismological evidence for differential rotation of the Earth's inner core. *Nature* 382: 221–224.

Souriau A and Poupinet G (2000) Inner core rotation: A test at the worldwide scale. *Physics of the Earth and Planetary Interiors* 118: 13–17.

Sreenivasan B and Jones CA (2005) Structure and dynamics of the polar vortex in the Earth's core. *Geophysical Research Letters* 32: L20301. http://dx.doi.org/10.1029/2005GL023841.

Suttie N, Holme R, Hill MJ, and Shaw J (2011) Consistent treatment of errors in archaeointensity implies rapid decay of the dipole prior to 1840. *Earth and Planetary Science Letters* 304: 13–21.

Vestine EH (1953) On variations of the geomagnetic field, fluid motions, and the rate of Earths rotation. *Journal of Geophysical Research* 58: 127–145.

Voorhies CV (1984) *Magnetic Location of Earth's Core-Mantle Boundary and Estimates of the Adjacent Fluid Motion*. PhD Thesis, University of Colorado, Boulder.

Voorhies CV (1986) Steady flow at the top of Earth's core derived from geomagnetic field models. *Journal of Geophysical Research* 91: 12444–12466.

Voorhies CV (2013) Geomagnetic estimates of steady surficial core flow and flux diffusion: Unexpected geodynamo experiments. In: Le Mouël J-L, Smylie DE, and Herring T (eds.) *Dynamics of the Earth's Deep Interior and Earth Rotation*, pp. 113–125. Washington, DC: American Geophysical Union.

Voorhies CV (1999) Inner core rotation from geomagnetic westward drift and a stationary spherical vortex in Earth's core. *Physics of the Earth and Planetary Interiors* 112: 111–123.

Voorhies CV and Backus GE (1985) Steady flows at the top of the core from geomagnetic-field models – The steady motions theorem. *Geophysical and Astrophysical Fluid Dynamics* 32: 163–173.

Waddington R, Gubbins D, and Barber N (1995) Geomagnetic-field analysis.5. Determining steady core-surface flows directly from geomagnetic observations. *Geophysical Journal International* 122: 326–350.

Wardinski I, Holme R, Asari S, and Mandea M (2008) The 2003 geomagnetic jerk and its relation to the core surface flows. *Earth and Planetary Science Letters* 267: 468–481.

Wardinski I and Korte M (2008) The evolution of the core-surface flow over the last seven thousands years. *Journal of Geophysical Research* 113, B05101.

Whaler KA (1980) Does the whole of the Earth's core convect? *Nature* 287: 528–530.

Whaler KA (1986) Geomagnetic evidence for fluid upwelling at the core-mantle boundary. *Geophysical Journal of the Royal Astronomical Society* 86: 563–588.

Whaler KA and Davis RG (1997) Probing the Earth's core with geomagnetism. In: Crossley DJ (ed.) *Earth's Deep Interior*, pp. 114–166. Amsterdam: Gordon and Breach.

Whaler KA and Holme R (2007) Consistency between the flow at the top of the core and the frozen-flux approximation. *Earth, Planets and Space* 59: 1219–1229.

Whaler KA and Holme R (2011) The axial dipole strength and flow in the outer core. *Physics of the Earth and Planetary Interiors* 188: 235–246.

Yukutake T (1979) Review of the geomagnetic secular variations on the historical time scale. *Physics of the Earth and Planetary Interiors* 20: 83–95.

Yukutake T and Tachinaka H (1969) Separation of the earth's magnetic field into drifting and standing parts. *Bulletin of the Earthquake Research Institute* 47: 65.

Zatman S and Bloxham J (1997) Torsional oscillations and the magnetic field within the Earth's core. *Nature* 388: 760–763.

Zatman S and Bloxham J (1998) A one-dimensional map of B_S from torsional oscillations of the Earth's core. In: Gurnis M, Wysession ME, Knittle E, and Buffett BA (eds.) *The Core-Mantle Boundary Region*, pp. 83–196. Washington, DC: American Geophysical Union.

Zhang J, Song X, Li Y, Richards PG, Sun X, and Waldhauser F (2005) Inner core differential motion confirmed by earthquake doublets. *Science* 309: 1357–1360.

This page intentionally left blank

8.05 Thermal and Compositional Convection in the Outer Core

CA Jones, University of Leeds, Leeds, UK

© 2015 Elsevier B.V. All rights reserved.

8.05.1	**Introduction to Core Convection**	116
8.05.1.1	The Need for a Dynamo	116
8.05.1.2	Velocities in the Core	116
8.05.1.3	The Heat Flux and Core Cooling	117
8.05.1.4	Stably Stratified Layers	118
8.05.1.5	The Dynamics of Core Convection	118
8.05.2	**Equations Governing Convection**	120
8.05.2.1	Compressible and Anelastic Equations	120
8.05.2.2	Adiabatic Reference State	122
8.05.2.3	Equations for the Convective Perturbations	123
8.05.2.4	Boundary Conditions	123
8.05.2.5	The Boussinesq Limit	124
8.05.2.6	Formulation of the Equations for Numerical Solution	126
8.05.3	**Convection in the Absence of Rotation and Magnetic Field**	126
8.05.3.1	Thermal Convection	126
8.05.3.2	Compositional Convection	128
8.05.3.3	Translation of the Inner Core	128
8.05.4	**Effect of Rotation on Convection**	129
8.05.4.1	The Proudman–Taylor Theorem	129
8.05.4.2	The Onset of Instability	130
8.05.4.3	The Onset of Instability in the Rapidly Rotating Limit	131
8.05.4.4	The Ekman Boundary Layers	134
8.05.4.5	The Busse Annulus	135
8.05.4.5.1	Linear properties of the annulus model	136
8.05.4.5.2	Weakly nonlinear theory and the annulus model	136
8.05.4.5.3	Zonal flows and multiple jets	137
8.05.4.6	The Quasi-geostrophic Approximation	137
8.05.4.7	Thermal Wind	138
8.05.4.8	Scaling Laws and Heat Transport in Nonlinear Rapidly Rotating Convection	138
8.05.4.8.1	The inertial theory of rapidly rotating convection	139
8.05.4.8.2	Heat transport in rapidly rotating convection	139
8.05.4.9	Rapidly Rotating Rayleigh–Bénard Convection	140
8.05.5	**Convection With and Without Rotation in the Presence of Magnetic Field**	142
8.05.5.1	Flux Expulsion and Flux Rope Formation	142
8.05.5.2	Linear Theory of Magnetoconvection in Plane Geometry	143
8.05.5.2.1	Nonrotating magnetoconvection	143
8.05.5.2.2	Onset of plane-layer rotating magnetoconvection	144
8.05.5.2.3	Waves in the core	144
8.05.5.2.4	Small-scale dynamics and the Braginsky–Meytlis theory of platelike motion	145
8.05.5.2.5	Boundary layers in rotating magnetic fluids	145
8.05.5.3	Onset of Rotating Magnetoconvection in Spherical Geometry	146
8.05.5.4	Magnetic Instabilities	147
8.05.5.5	Taylor's Constraint	147
8.05.5.6	Numerical Simulations of Nonlinear Convection-Driven Dynamos	148
8.05.5.6.1	Convection outside the TC: Picture from numerical simulations	150
8.05.5.6.2	Convection inside the TC: Picture from numerical simulations	151
8.05.5.7	Scaling Laws and Dynamo Simulations	151
8.05.6	**Heterogeneous Boundary Conditions and Stable Layers near the CMB**	152
8.05.7	**Conclusions and Future Developments**	154
Appendix		155
References		156

 http://dx.doi.org/10.1016/B978-0-444-53802-4.00141-X

8.05.1 Introduction to Core Convection

8.05.1.1 The Need for a Dynamo

The basic structure of the Earth's interior has been deduced from seismic observations. It is known from these data that there is a high-density core surrounded by a lower-density mantle, with the transition occurring at the core–mantle boundary (CMB), which is located 3480 km from the center of the Earth. The high-density core, which is believed to be composed mainly of iron, is divided into a fluid outer core and a solid inner core, with the inner core boundary (ICB) having a radius of 1220 km. There is a density jump across the ICB of roughly 500 kg m^{-3} (Masters and Gubbins, 2003), the density of the inner core itself being around 12 000 kg m^{-3}. The fluid nature of the outer core is deduced from its inability to support transverse seismic waves (*S*-waves), which can only propagate in a solid.

The basic structure of the Earth's interior was mainly worked out in the first half of the twentieth century. It had been known much earlier that the Earth's magnetic field varies slowly with time; indeed, this secular variation was known to Henry Gellibrand in 1635; and Edmond Halley noticed that the field appeared to drift westward. He suggested that the Earth might have a layered concentric shell structure, with the magnetic field being carried along with one of the interior shells. Larmor (1920) proposed that the magnetic fields of the Earth and the Sun might be generated by a dynamo, driven by motion in an electrically conducting fluid in the core, which is the basis of the modern geodynamo theory of the Earth's magnetic field. The physical principles behind the dynamo theory are the laws of electromagnetism (Maxwell's equations) and the laws of fluid motion (the Navier–Stokes equations). These equations were well known in Larmor's time, but finding useful solutions of them has proved difficult, though it is now possible to find numerical solutions.

The iron in the outer core has an electrical conductivity now believed to be around 1.4×10^6 S m^{-1} (Pozzo et al., 2012), a significant increase on previous estimates. It now appears that the very high pressure of iron in the core leads to an increase rather than a decrease of electrical conductivity. It is not difficult to show that with this conductivity, the geomagnetic field would decay on a 50 000-year timescale (see, e.g., Moffatt, 1978) if the fluid in the core is not actively driven. Core material has electrical resistance that leads to ohmic dissipation, giving rise to heating. Unless fluid motion is continuously driven, the current systems that maintain the field in the core decay away. The amount of ohmic heating is a measure of the power input required to maintain the dynamo. Since the geomagnetic field induced magnetism in rocks laid down 3.5 Gy ago (e.g., Usui et al., 2009), soon after the Earth's formation, it is clear that a long-term energy source is needed to maintain the Earth's field. Many alternative theories to the dynamo mechanism have been proposed for maintaining the geomagnetic field, but none has stood the test of time. Gauss (1839) showed that the nature of the field is such that the main field must have an internal rather than an external origin. Chemical inhomogeneity (the battery effect) and thermoelectricity have been considered as possible sources, but while they can generate very small fields, they cannot plausibly provide the substantial energy needed to maintain the observed field.

While the dynamo origin of the geomagnetic field has been largely accepted, there is much less agreement on the nature of the energy source driving it. Thermal convection and compositional convection have been explored in considerable detail as possible energy sources, but precession and tidal forcing have also been considered seriously (e.g., Malkus, 1994, and **Chapter 8.07**). The gravitational torques on the nonspherical Earth make the polar axis precess around the ecliptic pole approximately once every 26 000 years. The liquid outer core of the Earth will therefore be forced at its boundary by this motion, and consequently, fluid motion is induced inside the outer core. The rotation axis of the fluid outer core will lag a little behind the rotation axis of the mantle, and the resulting torque will extract energy from the Earth's rotation, eventually bringing the rotation axis into its minimum energy configuration parallel to the ecliptic pole. Oceanic and solid Earth tides cause the Earth to gradually rotate more slowly, and stresses at the CMB transmit this angular momentum loss down to the fluid outer core by generating fluid motion there. These precessional and tidal energy sources for core motion ultimately derive from the rotational energy of the Earth. There is somewhat less energy in the Earth's rotation than there is in the gravitational and thermal energy that drives convection, but sufficient rotational energy exists to maintain a dynamo provided that the conversion of kinetic energy to magnetic energy is reasonably efficient. It seems likely that the fluid motions induced by precession or tides can drive a dynamo (Tilgner, 2005). The difficulty is that the forcing provided by these mechanisms has the diurnal frequency, while the dynamo operates on a much longer timescale, so whether the geodynamo can be powered by these mechanisms is still unknown. Here, we adopt the hypothesis that the dynamo is driven by convection, which provides an adequate power source on a suitable timescale.

8.05.1.2 Velocities in the Core

Direct evidence for core motions comes from the temporal behavior of the geomagnetic field, the secular variation. To a first approximation, fluid carries magnetic field with it as it moves. The change in the field is therefore due partly to the velocity just under the CMB. Magnetic diffusion allows the field to move through the fluid, but even if this is neglected, we cannot specify the velocity solely from magnetic field observations (Roberts and Scott, 1965). For example, if we monitor the radial component of the field B_r at the CMB, there will be no change in the field if the flow is parallel to lines of constant B_r, so the component of the flow velocity parallel to lines of constant B_r is invisible to secular variation measurements. Additional assumptions have to be made in order to specify the core flow. Two common assumptions are either that the flow is tangentially geostrophic or that it is toroidal, just below the CMB. Tangential geostrophy implies that $\nabla_H \cdot \cos\theta \mathbf{u} = 0$, while toroidal flow implies that $\nabla_H \cdot \mathbf{u} = 0$. Here, θ is the co-latitude and $\mathbf{u}$ is the fluid velocity just below the CMB. ∇_H means the horizontal part of the divergence is taken, so for toroidal flow,

$$\frac{1}{r\sin\theta}\frac{\partial(\sin\theta u_\theta)}{\partial\theta} + \frac{1}{r\sin\theta}\frac{\partial u_\phi}{\partial\phi} = 0 \qquad [1]$$

(for further details, see Holme and Olsen, 2006; **Chapter 8.04**). When either of these assumptions is made, it is possible to reconstruct the flow field (Bloxham and Jackson, 1991).

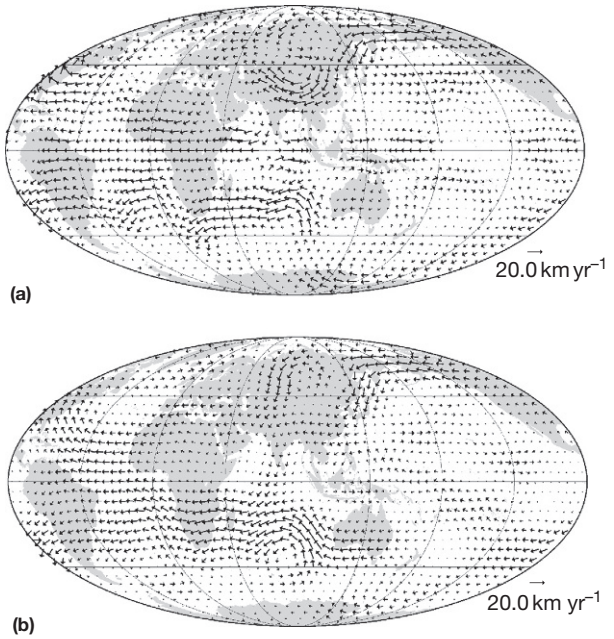

Figure 1 Core flows inferred from secular variation observations. (a) Using the geostrophic flow assumption. (b) Using the toroidal flow assumption. Reproduced from Holme and Olsen (2006) Core surface flow modelling from high-resolution secular variation. *Geophysical Journal International* 166: 518–528.

Figure 1, which is based on data from the Ørsted and CHAMP magnetic satellite observations, is reproduced from Holme and Olsen (2006).

The figure shows that some features are universal even if different assumptions are made, and the typical velocity of 15 km year^{-1}, which is 5×10^{-4} m s^{-1}, is a measure of the faster moving flows that are transporting the magnetic field. Of course, this is just the flow beneath the CMB, and the flow at larger depths may be different. Also, small-scale flows are invisible because only large-scale field structures can be seen. Small-scale field structures, those corresponding to spherical harmonics of degree greater than around 12, are obscured by crustal magnetism. The flow speeds may be somewhat larger if there is a significant small-scale contribution (Finlay and Amit, 2011). Nevertheless, flow speeds of this order are what is predicted from our understanding of core convection, and we will adopt the point of view that convective velocities of the order of 5×10^{-4} m s^{-1} are present in the core.

8.05.1.3 The Heat Flux and Core Cooling

It is likely that a great deal of heat was released when the iron differentiated from the mantle to the core of the Earth. The Earth has therefore been cooling down ever since its birth. The current rate of loss of heat from the Earth is around 47 TW. The fraction of this 47 TW that comes from the core is controversial, with estimates ranging from 3 (Sleep, 1990) to 15 TW (Roberts et al., 2003). Since the temperature increases as we approach the Earth's center, heat can be transmitted outward by thermal conduction. If all the heat flux coming from the core can be so transmitted, there will be no thermal convection. Thermal convection occurs when there is more heat to be transmitted than can be carried by conduction. As we shall see in the succeeding text, the criterion for the onset of core convection is essentially that the actual temperature gradient is steeper than the adiabatic temperature gradient. The key question is therefore whether the required heat flux can be carried down the adiabatic temperature gradient entirely by conduction. The adiabatic temperature gradient can be estimated reasonably well (see, e.g., Anufriev et al., 2005). The thermal conductivity is related to the electrical conductivity through the Wiedemann–Franz law $k = L\sigma T$, where the Lorenz constant L is about 2.5×10^{-8} W S^{-1} K^{-2}. Recent estimates of the electrical conductivity of iron at high pressure derived from both theory and experiment are somewhat larger than the estimates in the literature 5 years ago. In consequence of the Wiedemann–Franz law, this implies a similar increase in thermal conductivity so that the old value $k = 46$ W m^{-1} K^{-1} (Stacey and Anderson, 2001) has been replaced by $k = 130$ W m^{-1} K^{-1} (e.g., Pozzo et al., 2012). This is a very active area of research at present, but if these higher conductivities are confirmed as relevant to core conditions, this change has a strong influence on the energetics of the core (see the chapter by Nimmo in this volume). The estimated heat flux conducted down the adiabat is about 1 TW near the ICB and 15 TW near the CMB. Models suggest that a large fraction of the core heat flux comes from latent heat released at the ICB as the inner core grows. If this is the case, even with a low estimate of CMB heat flux, there is more than 1 TW to be carried outward near the ICB, and convection must occur there. Near the CMB, the situation is much less clear; only very high estimates of CMB heat flux give convection throughout the core, so there is likely to be a convectively stable region in the core near the CMB where the heat is being extracted solely by conduction down the adiabat. It is even possible that near the CMB, the temperature gradient is well below the adiabatic value.

If the core is cooling, the solid inner core must be slowly growing in size as the iron gradually freezes out. It might seem surprising that the core freezes first near the center, where it is hottest, rather than at the CMB where it is coolest. This is due to the rapid increase in pressure as we move toward the center of the core, pressure raising the melting point temperature. Because $(dT/dp)_{liq} > (dT/dp)_{ad}$, where the subscript 'liq' denotes variation along the melting point curve and the subscript 'ad' denotes variation along the adiabat, freezing first occurred at the center of the Earth as the core gradually cooled. As the inner core grows, light material is released, the iron content of the inner core being higher than that of the outer core. The exact nature of this light material is uncertain, but 'ab initio' quantum calculations of the properties of materials at core temperatures and pressures suggest that a mixture of several different light elements, oxygen, sulfur, and silicon, forms the light component (Alfè et al., 2003). This light material is buoyant and drives compositional convection. The rate of growth of the inner core is therefore directly related to the buoyancy flux of light material driving compositional convection. The density jump across the ICB can be measured directly by seismic observations. Estimates (Masters and Gubbins, 2003) give the density of the inner core to be about 5% greater than that of the outer core at the ICB. Some of this is due to the fact that iron (unlike water) contracts as it freezes, so there would be a density jump even if there was no light material; after this jump is subtracted off, the remaining part of the

density jump relates the compositional buoyancy flux to the rate of growth of the inner core. Knowledge of the melting point curve allows us to relate the rate of growth of the inner core to the rate of cooling of the outer core, which in turn relates to the heat flux passing through the CMB. The latent heat released at the ICB is also related to the rate of growth of the inner core.

While the basic physics governing inner core growth, compositional buoyancy flux, latent heat release, and core cooling rate is understood, unfortunately, the key physical properties of materials at very high pressure and temperature are not well known. They are measured by a combination of experiments and theory, but different authors give estimates that can vary by a factor 2 or more, which means that the estimated rate of growth of the inner core can vary considerably. A further complication is the uncertainty over whether radioactive elements occur in the core. They are believed to be responsible for most of the heat coming out of the mantle, but it is uncertain whether radioactive elements such as potassium (^{40}K) are present in the core material or not (see the chapter by Nimmo). ^{40}K is strongly depleted in the mantle from the value expected from the primordial composition, but this could be because it evaporated into space when the Earth formed. Alternatively, it could have alloyed with elements such as nickel and hence entered the core; our knowledge of geochemistry is not currently sufficient to be certain which scenario occurred. If ^{40}K and other radioactive elements are present in significant quantities, the whole heat budget of the core is changed dramatically. The core might not be cooling at all, with the radioactive heat released balancing the heat coming out of the CMB. The inner core would then not be growing, so there would be no compositional convection and no latent heat released at the ICB. The dynamo would then have to be driven entirely by thermal convection or some other source such as precession.

There are a number of different scenarios for the strength of compositional and thermal convection, and these have been significantly altered if the new thermal conductivity of 130 W m^{-1} K^{-1} (Pozzo et al., 2012) is adopted. The two major unknowns are the heat flux through the CMB and the rate of radiogenic heating in the core. With no radiogenic heating, a low CMB heat flux of, say, 6 TW leads to a rate of release of buoyant material of about 10^5 kg s^{-1} (rate of volume release multiplied by the inner core–outer core density change), corresponding to an inner core age of around 1 billion years. However, in most of the core, heat would be transported by conduction, and the resulting temperature gradient would be well below the adiabatic value. Any dynamo could only exist relatively close to the ICB. With a larger CMB heat flux, say, 15 TW, the amount of convection increases, and so does the rate of release of buoyant material, leading to an inner core age of 0.3 billion years only. Radiogenic heating could allow a 15 TW CMB heat flux with little inner core growth. Convection occurs throughout most of the core, except for a relatively thin layer just below the CMB.

Physically, the CMB heat flux is determined by mantle convection. There appears to be a thermal boundary layer at the base of the mantle, the D'' layer, through which heat is conducted into the mantle, but in the absence of reliable information about mantle convection, we have to accept that there is a wide range of plausible estimates for the CMB heat flux, and we need to consider what happens in both high and low CMB heat flux models.

8.05.1.4 Stably Stratified Layers

A number of authors have proposed that the top of the core might be stably stratified. Fearn and Loper (1981) suggested that light fluid released at the ICB might not fully mix in the outer core, but form plumes that would deposit the light material in a layer 80 km thick below the CMB. Braginsky (1993) described such a layer as an 'inverted ocean' trapped by the CMB, and he discussed possible wave motions in such a layer. More recently, barodiffusion has been proposed as a possible mechanism for creating a stably stratified layer (Braginsky, 2006; Gubbins and Davies, 2013). Barodiffusion occurs because light materials diffuse away from high-pressure regions. Layers of order 100 km thick could form by this mechanism. The density anomaly proposed in these layers is typically of order 1 part in 10^4, hugely greater than that needed to drive convection. Such a layer could support internal gravity waves, with a buoyancy frequency of the order of hours. Once formed, such a layer would be very strongly stably stratified and so might resist being destroyed by convection penetrating from below, and also, it might be stable to other instabilities. It might of course be difficult to form such a layer from an initially convecting region. Another issue is whether such a layer would be stable to double-diffusive instability. Braginsky (2006) argued that the layer would be thermally superadiabatic, and hence, weak turbulence could be driven by oscillatory instability (Turner, 1973). However, Gubbins and Davies (2013) suggested the layer would be stable to double diffusion, as recent estimates of the thermal conductivity suggest that the required heat flux in this region could be carried by conduction with a subadiabatic temperature gradient. The dynamics of such a region is discussed in **Section 8.05.6**. Would such a layer be detectable by seismology? A decrease in seismic velocity in a layer suggested to be 300 km thick below the CMB was noted by Helffrich and Kaneshima (2010), but the light layer proposed from these theoretical results might be expected to raise the velocity rather than lower it, by a similar amount.

A 150 km thick stably stratified layer near the ICB has also been proposed (Gubbins et al., 2008). The main motivation for this layer comes from seismology. The essence of the idea is that instead of a sharp jump in density from the higher-density inner core to the lower-density outer core, the transition is gradual over the 150 km layer. As with the CMB layer, the ICB layer if it exists will likely be strongly stably stratified and hence affect the convection near the ICB.

8.05.1.5 The Dynamics of Core Convection

It is clear from the earlier-mentioned discussion that while we do not know the exact amounts of heat flux and compositional flux that are being convected in the core, it is very likely these processes are occurring. Thermal convection is essentially a process by which hot parcels of fluid move outward, while cold parcels of fluid move inward. Natural questions are the following: What is the temperature difference between the warm and cool fluid parcels? How fast are they moving?

The heat flux transported constrains the product of these two quantities, but does not on its own specify either the velocity or the temperature perturbations individually. For example, suppose thermal convection at a radius $r_0=(r_{icb}+r_{cmb})/2$ convects 1 TW of heat. Suppose also that exactly one-half of the fluid at $r=r_0$ is moving radially outward at speed u_r and has temperature T'_* greater than the remaining fluid, which moves radially inward at speed u_r. If we take the density as the mean density 11 340 kg m^{-3} and the specific heat as 860 J kg^{-1} K^{-1}, then to transport one terawatt of heat requires $T'_*u_r=3.7\times10^{-8}$ ms^{-1} K. From the arguments in Section 8.05.1.2, the typical core velocity can be estimated from the typical speed with which flux patches move, say, 5×10^{-4} m s^{-1}. Then, $T'_*\sim7\times10^{-5}$ K, a surprisingly small value. However, it might be that radial motion is a factor 10 less, in which case we could transport the same amount of heat by increasing T'_* by a factor 10. Of course, this example assumed that the hot fluid was perfectly correlated with rising fluid. This might not be the case, in which a slightly higher T'_* would be required to transport the required heat flux at a given velocity. Now that very small horizontal temperature perturbations have been proposed for thermal convection in the core, one might ask whether such small temperatures can actually drive motions at this speed. As we shall see in the succeeding text, this is indeed possible, and core speeds of the order of 5×10^{-4} m s^{-1} emerge naturally from convection models. This is of course strong evidence for the existence of core convection. We can repeat these estimates for compositional convection. Again, we find that very small density perturbations of the order of 10^{-9} of the actual density are capable of delivering the required mass fluxes.

Our very small estimate for T'_* raises an issue that it is important to understand. The actual temperature difference between the ICB and the CMB is over 1000 K. So how can the temperature differences driving the convection be so much less? The answer is that in a convecting region, the core is almost adiabatically stratified, and it is only the difference between the actual temperature gradient and the adiabatic gradient that drives the convection. This difference is called the superadiabatic temperature gradient, and it is more than a million times smaller than the adiabatic gradient. So in a compressible fluid such as the Earth's core, we call ΔT_s the superadiabatic temperature difference across the core. T'_* is of the same order as ΔT_s, which is much less than 1000 K. This is illustrated in Figure 2.

Convection in the core will be influenced by rotation and magnetic field. Since the velocities are so slow, the dimensionless Rossby number $Ro=U_*/d\Omega$, taking $d=r_{cmb}-r_{icb}$ as a typical length scale and U_* as a typical velocity, is very small. It is therefore natural to work in the rotating frame and introduce Coriolis and centrifugal forces. The centrifugal force is small compared with that of gravity and it is usually ignored in core convection. Note that for constant density, the centrifugal force is the gradient of a potential, $\nabla\rho\Omega^2s^2/2$, so it can be exactly balanced by the pressure. Only when the very small variations due to density are taken into account does centrifugal force contribute, and then, it is dominated by the corresponding terms involving the gravitational acceleration, g. It is therefore through the Coriolis force that rotation makes an impact. In crude terms, we might expect this to happen when the magnitude of the Coriolis acceleration $|2\boldsymbol{\Omega}\times\mathbf{u}|$ exceeds the magnitude of the inertial acceleration $|(\partial\mathbf{u}/\partial t+\mathbf{u}\cdot\nabla\mathbf{u})|$. If we estimate the inertial acceleration as U_*^2/d, we see that Coriolis acceleration dominates inertial acceleration provided the Rossby number Ro is small, and the velocity changes on timescales longer than the rotation rate. If we accept the estimate of $|\mathbf{u}|\sim5\times10^{-4}$ m s^{-1} suggested in the preceding text, then $Ro\sim3\times10^{-6}$, so that from this crude estimate, Coriolis force completely dominates inertia in the core, and so we expect rotation to be very influential in the core. On the timescales we are interested in for core convection, which are much longer than a day, we therefore expect inertia to be small, so that the core is always in equilibrium, and changes occur in the core by evolving slowly through a sequence of equilibrium states. We do need to be careful, however, because there are a number of ways in which this estimate can be radically altered. If the fluid motion is geostrophic, this means that the Coriolis force is a potential force, and so it can be balanced entirely by pressure. Flows that are geostrophic are then controlled by the smaller terms in the equation of motion after the pressure force and the Coriolis force have canceled each other out. So for geostrophic flows, inertial terms can be more important than our crude estimate implies. The condition for geostrophy is that $\nabla\times(\rho\boldsymbol{\Omega}\times\mathbf{u})=0$. Motions in the Earth's atmosphere and oceans are mainly geostrophic, and this is likely to be true in the core too. However, because the Rossby number is so small in the core, any significant departure from exact geostrophy will lead to a large Coriolis force that cannot be pressure balanced, which will normally be balanced by buoyancy and magnetic forces. An example of geostrophic core motion is the torsional oscillation (see Chapter 8.04), where the fluid moves azimuthally only and the velocity is constant on cylinders. For this motion, the balance is between the magnetic Lorentz force and inertia, since the large Coriolis and pressure forces exactly cancel at all times. There is another way in which inertia can be

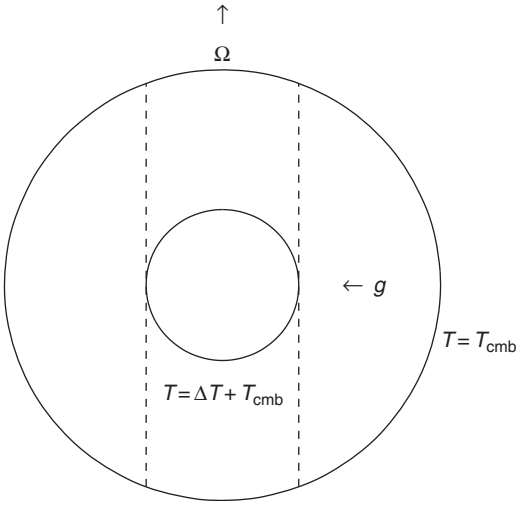

Figure 2 Geometry of convection between spherical shells. The dashed lines mark the position of the tangent cylinder (TC). For a Boussinesq liquid, ΔT is the total temperature difference across the outer core, but for compressible convection $\Delta T=\Delta T_{ad}+\Delta T_s$, and the superadiabatic temperature difference ΔT_s is much less than the adiabatic temperature difference ΔT_{ad}.

important for slow core flows; the length scale for the gradient in $\mathbf{u}\cdot\nabla\mathbf{u}$ may be much less than the core size, making inertia relatively more important. We shall return to this important issue of the effect of inertia in rotating convection later in the text.

If variations of density are ignored, the condition for geostrophy reduces to $\partial\boldsymbol{u}/\partial z=\mathbf{0}$. The requirement that slow steady motions with negligible ageostrophic forces (such as buoyancy and magnetic field) must be geostrophic, and hence satisfy this equation, is known as the Proudman–Taylor theorem, predicted by Proudman (1916) and verified experimentally by Taylor (1923). Core motions driven by convection are indeed slow and are steady on timescales corresponding to the rotation timescale, so we expect the velocity generally to be independent of z, that is, the motion is columnar, with whole columns of fluid moving together. Within the geometry of the Earth's core, there is then going to be an important distinction between the behavior inside and outside the tangent cylinder (TC) (see Figure 2). The TC is the imaginary cylinder whose axis is parallel to the rotation axis and that touches the inner core. Outside the TC, columns of fluid can extend from one hemisphere right through to the other hemisphere. Inside the TC, fluid columns can only reach from the CMB down to the ICB. Furthermore, a column of fluid moving outside the TC will have to change its length (and hence induce ageostrophic motion) quite slowly as it changes its distance from the rotation axis. A column of fluid moving from outside to inside the TC is cut in two and undergoes a very rapid change in length as it crosses the TC. Strongly ageostrophic motion is required to do this, so it is not very likely to happen; although there is no physical barrier at the TC, the dynamics of rapidly rotating fluids makes it unlikely that there is much fluid transport across the TC.

Convection inside and outside the TC is likely to be rather different in character, for geometric reasons. Outside the TC, columnar motions can transport heat effectively outward in the s-direction (using cylindrical polar coordinates s, ϕ, z with z parallel to the rotation axis). A relatively small amount of ageostrophic motion in the z-direction is required to transport the heat perpendicular to the axis of the columns. Inside the TC, convection faces more difficulties, because to get heat from the ICB to the CMB inside the TC requires mainly motion in the z-direction, which must vary with z because there can be no penetration through the ICB or CMB. Even though there is no penetration through the ICB and CMB, there can be a thin boundary layer, the Ekman layer, inside which there is some horizontally diverging flow. This leads to Ekman suction, that is, a small flow in the radial direction into the boundary layer (see Section 8.05.4.4). This Ekman suction may affect the flow in the core, but it is too small to carry much heat outward. Not surprisingly, convection inside the TC is harder to get going and will rely more strongly on ageostrophic forces such as the Lorentz force to control it. Nevertheless, at Rayleigh numbers well above critical, convection inside the TC can be as vigorous as that outside the TC, because the buoyancy forces are strong enough to maintain the ageostrophic part of the flow. Indeed, the heat transport inside the TC can even exceed that outside the TC (Busse and Simitev, 2006; Tilgner and Busse, 1997).

Magnetic fields influence core flow to some extent everywhere in the core. In a dynamo-generated field, this is inevitable, because the induction equation is linear in the magnetic field $\mathbf{B}$. For a dynamo, there must be growing modes that can potentially increase the field without limit. Magnetic field saturation occurs by the field altering the dynamo properties of the flow so that magnetic growth no longer occurs. However, the ability to generate magnetic field from a flow is a fairly subtle process, and small changes in the flow may be sufficient to prevent further field growth. We can try estimating the magnitude of the Lorentz force $|\mathbf{j}\times\mathbf{B}|$ and comparing it with the crude estimate of Coriolis force. From geomagnetic observations, the radial field at the CMB is typically 0.5 mT, and if we assume the field inside the core is slightly larger at 1 mT, then the current density $|\mathbf{j}|=|\nabla\times\mathbf{B}|/\mu\sim|\mathbf{B}|/\mu d$ is around 4×10^{-4} A m^{-2}, giving $|\mathbf{j}\times\mathbf{B}|\sim4\times10^{-7}$ N m^{-3}. The comparable estimate for $|2\rho\boldsymbol{\Omega}\times\mathbf{u}|$ is 8×10^{-4} N m^{-3}, considerably larger. However, it would be wrong to conclude that the magnetic field has no dynamical influence in the core. First, the field in the core may be considerably larger than the observed radial field at the CMB. There may be 'invisible' toroidal components that contribute to the core field but never emerge at the CMB. Even if 1mT is a fair estimate of the field, we must remember that the field will be important in the dynamics even if it balances only the ageostrophic part of the Coriolis force (that part not balanced by pressure), which may be considerably smaller than our 8×10^{-4} N m^{-3} estimate. Finally, the scale of variation of the magnetic field might be considerably smaller than d. Indeed, a crude balance between the generation term and the diffusion term in the induction equation suggests that the length scale for evaluating the current should be $dR_m^{-1/2}$, roughly a factor 40 less than d. Numerical dynamo simulations give a rather mixed picture of the importance of magnetic fields on the convection. Soderlund et al. (2012) found that the columnar pattern of convection is similar in both magnetic and nonmagnetic simulations. On the other hand, Sakuraba and Roberts (2009) and Takahashi and Shimizu (2012) changed the thermal boundary conditions and the input parameters and found that the flow pattern was significantly altered by the magnetic field. The effects of magnetic field on the convection pattern (and hence on the dynamo) are not yet fully understood. However, magnetic fields are certainly important in some respects. In particular, it is believed that the small-scale dissipation that balances the convective energy input comes primarily from magnetic (ohmic) dissipation.

8.05.2 Equations Governing Convection

8.05.2.1 Compressible and Anelastic Equations

Much of our information about core convection has come from numerical simulations based on the governing equations. The full equations are quite complicated, and a wide range of simplifications have been used to study particular aspects of convection. In this section, we consider some of the most commonly used approximations and the assumptions on which they are based. Since magnetic fields can influence convection, we include them in our discussion. In consequence, these equations can be used for dynamo simulations and for convection calculations. We shall assume that we are dealing with a two-component fluid with a light component, sometimes called a binary fluid. The mass fraction of a small

volume of fluid that is light is denoted by ξ. This is already a simplification of the situation in the core, as the material properties of the core are better described by a mixture of light components (Alfè et al., 2003). The heavy component is usually identified with iron (mass fraction $1-\xi$) and the light component with sulfur, though we are really lumping together all the different light elements in the core into one component. The density of the inner core near the ICB is greater than that of the outer core near the ICB, and this difference is greater than that due to the density change on solidification. So the value of ξ is lower in the inner core, and excess ξ is released at the ICB during the freezing process. This gives rise to buoyant compositional convection. The variable ξ is usually called the composition. We also allow for variations of temperature to drive thermal convection.

The momentum conservation equation can be written as

$$\rho\frac{\mathrm{D}\mathbf{u}}{\mathrm{D}t}+2\rho\boldsymbol{\Omega}\times\mathbf{u}=-\nabla p+\rho\mathbf{g}+\mathbf{j}\times\mathbf{B}+\rho\mathbf{F}^{v},\quad \frac{\mathrm{D}}{\mathrm{D}t}=\frac{\partial}{\partial t}+\mathbf{u}\cdot\nabla \qquad [2]$$

Here, the density ρ is the averaged density of both fluid components, $\mathbf{u}$ is the fluid velocity, and t is the time. $\boldsymbol{\Omega}$ is the Earth's rotation vector, so the second term on the left is the Coriolis force. Strictly speaking, it is an acceleration times a density, but it is convenient to consider it as a force per unit volume in the rotating frame.

A list of numerical values for the parameters used in core convection is given in **Table 1**, taken mostly from Anufriev et al. (2005), but updated taking into account the higher electrical and thermal conductivities (Pozzo et al., 2012). Note that there is uncertainty about many of these numbers. For example, while the value given for the kinematic viscosity is that usually adopted, Palmer and Smylie (2005) argued for a value five orders of magnitude larger, giving an Ekman number also five orders of magnitude greater than that quoted in **Table 1**. Some quantities, such as the rotation rate, are known to very high accuracy, but others are little more than informed guesses. The centrifugal force has not been included explicitly as it is added into the gravitational acceleration term. In core convection, it is usually omitted altogether, so gravity is radial. Note that in some experiments, centrifugal force dominates over gravity, so in these cases, $\mathbf{g}$ is perpendicular to the rotation axis. The oblateness of the core due to rotation may be important in studies of precession and tidal forcing but is usually omitted for simplicity in convection studies.

Table 1 Definitions and numerical values of core quantities

r_{cmb}	Outer core radius	3.48×10^{6} m
r_{icb}	Inner core radius	1.22×10^{6} m
d	Gap width $r_{cmb}-r_{icb}$	2.26×10^{6} m
ρ_0	Mean core density	11 340 kg m^{-3}
g	Gravitational acceleration	7.8 m s^{-2}
Ω	Earth rotation rate	7.29×10^{-5} s^{-1}
α	Thermal expansion coefficient	1.5×10^{-5} K^{-1}
c_p	Specific heat at constant pressure	860 J kg^{-1} K^{-1}
L_H	Latent heat energy per unit mass	$\sim10^{6}$ J kg^{-1}
$\Delta\xi$	Jump in ξ across the ICB	$\sim$ 0.05
γ	Grüneisen parameter	1.5
η	Magnetic diffusivity	$\sim$0.6 m^2 s^{-1}
κ	Thermal diffusivity	$\sim1.3\times10^{-5}$ m^2 s^{-1}
ν	Kinematic viscosity	$\sim5\times10^{-7}$ m^2 s^{-1}
U_*	Typical core velocity	$\sim5\times10^{-4}$ m s^{-1}
T'_*	Typical superadiabatic temperature perturbation	$\sim10^{-4}$ K
Ro	Rossby number $U_*/\Omega d$	$\sim3\times10^{-6}$
R_m	Magnetic Reynolds number U_*d/η	$\sim$1800
E	Ekman number $\nu/\Omega d^2$	$\sim10^{-15}$ (laminar) $\sim2\times10^{-9}$ (turbulent)

Where the quantity varies over the core, a typical value is given.

The pressure is denoted by p, and the magnetic term $\mathbf{j}\times\mathbf{B}$ is usually called the Lorentz force, sometimes the Laplace force. $\mathbf{j}$ is the current density (units A m^{-2}), and B is the magnetic field, measured in tesla (T). Older papers often used Gauss as the unit of magnetic field, 1 Gauss $=10^{-4}$ T. Most estimates of the core field strength lie in the range 1–10 mT. We include in eqn [2] the viscous force $\rho\mathbf{F}^{v}$. All estimates of the viscosity in the core suggest that viscous forces are very weak when acting over length scales the size of the core, so it is strange that we include them in our discussion. The reason is that it has not yet proved possible to devise stable numerical schemes with no viscosity. Schemes that do not include viscosity explicitly invariably contain numerical diffusion that provides an effective viscosity. Viscous forces act to smooth out very sharp variations in the flow, particularly in boundary layers. There have been attempts to solve the equations with no viscosity (e.g., Livermore et al., 2011; Walker et al., 1998), but none as yet has been particularly successful. The most fruitful approach has been to include viscosity but to reduce its magnitude as much as possible using high-resolution numerical schemes. In a compressible flow, the viscosity is often written as

$$F_i^{v}=\partial_j\left[\overline{\rho}\nu_T\left(\partial_j u_i+\partial_i u_j-\frac{2}{3}\delta_{ij}\nabla\cdot\mathbf{u}\right)\right] \qquad [3]$$

where ν_T is the turbulent kinematic viscosity (see **Chapter 8.06**).

The mass conservation equation is

$$\frac{\partial\rho}{\partial t}=-\nabla\cdot(\rho\mathbf{u}) \qquad [4]$$

The time-dependent perturbations in density are small, and the scale of time variations in the core is long. In consequence, the term $\partial\rho/\partial t$ in this equation is extremely small compared with the other terms. It is helpful to introduce the convective turnover time, $t_{conv}=d/U_*$, where $d=r_{cmb}-r_{icb}$ and U_* is a typical speed of convection. The turnover time is then the time an element of convecting fluid takes to travel a distance d. Following the arguments given in **Section 8.05.1.5**, the typical density perturbation driving core convection is only $10^{-9}\,\rho$, so the magnitude of the term $\partial\rho/\partial t$ is $10^{-9}\rho/t_{conv}$, whereas the magnitude of the other terms is ρ/t_{conv}, estimating the divergence operator as $1/d$. The term $\partial\rho/\partial t$ is therefore a factor 10^{-9} smaller than the other terms in eqn [4]. This argument is of course very crude, but a factor 10^{9} is so huge that the errors incurred by our rough approximations are negligible in comparison. It can also be shown that neglecting $\partial\rho/\partial t$ is equivalent to assuming that the sound travel time is small compared with the convective turnover time. We therefore immediately replace eqn [4] by

$$\nabla\cdot(\rho\mathbf{u})=0 \qquad [5]$$

The approximation of neglecting $\partial\rho/\partial t$ in the continuity equation is known as the anelastic approximation.

The density across the core varies by about 20% only, and many authors ignore this variation. This is part of the Boussinesq approximation, which will be systematically derived from the full equations in the succeeding text. Crudely speaking, the Boussinesq approximation neglects variations of density everywhere except in the buoyancy term. Density perturbations are retained in the buoyancy term because although they are a very small fraction of the total density, they are multiplied by g, which is a very large acceleration compared to U_*/t_{conv}.

The electromagnetic equations governing $\mathbf{j}$ and $\mathbf{B}$ are the pre-Maxwell equations of MHD (e.g., Davidson, 2001; Moffatt, 1978):

$$\frac{\partial \mathbf{B}}{\partial t} = \nabla \times (\mathbf{u} \times \mathbf{B}) - \nabla \times (\eta \nabla \times \mathbf{B}) \qquad [6]$$

$$\mu \mathbf{j} = \nabla \times \mathbf{B}, \quad \nabla \cdot \mathbf{B} = 0 \qquad [7a,b]$$

Here, μ is the magnetic permeability. Because the core is hot, well above the Curie point, the magnetic permeability is essentially that of free space, $\mu = 4\pi \times 10^{-7}$ H m^{-1}. The magnetic diffusivity η is defined by $\eta = 1/(\mu\sigma)$, where σ is the electrical conductivity measured in siemens per meter or equivalently in some papers ohm^{-1} m^{-1} (Ω^{-1} m^{-1}). The units of η are m^2 s^{-1}. Equation [6] is known as the induction equation. It is derived from Maxwell's equations, together with Ohm's law in a moving medium:

$$\mathbf{j}/\sigma = \mathbf{E} + \mathbf{u} \times \mathbf{B} \qquad [8]$$

The composition equation, or mass transport equation, is

$$\rho \frac{\mathrm{D}\xi}{\mathrm{D}t} = \nabla \cdot \left(k^{\xi} \nabla \xi\right) \qquad [9]$$

The coefficient k^{ξ} is the mass diffusion coefficient. It is very small in the core, and mass diffusion will be negligible in the core unless it is strongly enhanced by turbulence (see **Chapter 8.06**). In simulations, a much larger eddy diffusion value of k^{ξ} is usually assumed. The heat transport equation is

$$\rho T \frac{\mathrm{D}S}{\mathrm{D}t} = \nabla \cdot (k \nabla T) + H\rho \qquad [10]$$

where T is the temperature and S is the entropy. k is the thermal conductivity. It is often argued that turbulent transport will dominate thermal conductivity on the convection length scales. It is then more appropriate to replace $\nabla \cdot (k \nabla T)$ by $\nabla \cdot (\rho T \kappa_T \nabla S)$, an entropy diffusion term, since small-scale motions will mix entropy rather than temperature. H is the rate of release of heat per unit mass. One source for this could be radioactivity in the core. As we see later in the text, this term must also include the heating from viscous and ohmic dissipation.

To complete the equations, we need an equation of state giving the density in terms of pressure, temperature, and composition and an equation for the entropy, also in terms of pressure, temperature, and composition:

$$\rho = \rho(p, T, \xi), \quad S = S(p, T, \xi) \qquad [11a,b]$$

Equations [2]–[11a,b] could be used in principle to solve numerically for convection inside the core. In practice, they are almost always simplified much further before numerical solution is attempted. The perturbations of density that drive the convection are a tiny fraction of the full density, so errors of even one part in a million for the density would overwhelm the true density perturbations. Any practical scheme must separate out the perturbations in the thermodynamic variables from the reference state variables, a procedure sometimes called thermodynamic linearization.

8.05.2.2 Adiabatic Reference State

We must first specify the reference state about which we linearize the thermodynamic quantities.

We write

$$p = p_a + p_c, \quad \rho = \rho_a + \rho_c, \quad T = T_a + T_c, \quad \xi = \xi_a + \xi_c, \quad S = S_a + S_c \qquad [12a\text{–}e]$$

where the subscript a refers to the reference state values and c to the small perturbations associated with the convection. A number of different choices of reference states are possible. When Boussinesq convection experiments are performed, the natural reference state is the conduction state. Thus, for convection in a horizontal layer of liquid, where the only source of heat is from the boundary planes, the reference state has $T_a = T_0 - cz$, which is a solution of $\nabla^2 T_a = 0$. The equation of state is taken as $\rho_a = \rho_0(1 - \alpha T)$, α being the expansion coefficient, and the reference state pressure is the solution of the hydrostatic equation $\mathrm{d}p_a/\mathrm{d}z = -g\rho_a$, which is $p_a = p_0 - \rho_0 g(1 - \alpha T_0)z - 0.5\rho_0 g \alpha c z^2$. In a spherical Boussinesq system with no heat sources, the equivalent reference state temperature is a solution of $\nabla^2 T_a = 0$ in spherical polar coordinates, $T_a = T_0 + c/r$, which corresponds to a uniform heat flux of $4\pi kc$ passing from the ICB to the CMB.

The core is believed to be in a well-mixed state and close to adiabatic stratification. In consequence, a reference state in which the composition is uniform, ξ_a independent of position, and uniform entropy, S_a independent of position, is adopted (e.g., Braginsky and Roberts, 1995). The argument in favor of the well-mixed, near-adiabatic state is that when convection occurs, it can transport the required heat flux with a temperature gradient only very slightly greater than the adiabatic value, so to a first approximation, the basic state will be close to adiabatic. This argument does not apply if there is no convection. The temperature gradient will then adjust to that determined by Fourier's heat conduction law, which will not in general be an adiabatic state. We note that constant entropy in the core does not imply constant temperature and indeed defines the reference state temperature gradient. This will therefore not in general satisfy the heat conduction law. This leads to effective additional heat sources in the core as detailed in the succeeding text.

We now need some thermodynamic relations to express the change in entropy in terms of other variables:

$$\begin{aligned} \mathrm{d}S &= \left(\frac{\partial S}{\partial T}\right)_{p,\xi} \mathrm{d}T + \left(\frac{\partial S}{\partial p}\right)_{T,\xi} \mathrm{d}p + \left(\frac{\partial S}{\partial \xi}\right)_{p,T} \mathrm{d}\xi \\ &= \frac{c_p}{T}\mathrm{d}T - \frac{\alpha}{\rho}\mathrm{d}p + \frac{h^{\xi}}{T}\mathrm{d}\xi \end{aligned} \qquad [13]$$

(see, e.g., Braginsky and Roberts (1995), eqn. (D6)). The first of these relations expresses the chain rule, using the fact

that the entropy is a function of the three variables p, T, and ξ. c_p is the specific heat at constant pressure $c_p = T(\partial S/\partial T)_{p,\xi}$. The relation $(\partial S/\partial p)_{T,\xi} = (1/\rho^2)(\partial\rho/\partial T)_{p,\xi}$ is one of Maxwell's thermodynamic relations, and $\alpha = -\rho^{-1}(\partial\rho/\partial T)_{p,\xi}$ is the coefficient of thermal expansion. h^ξ is known as the heat of reaction, the heat released (or absorbed) when the composition changes.

Since the entropy and composition are assumed constant in the reference state, it follows that

$$\frac{\mathrm{d}p_a}{\mathrm{d}r} = -g\rho_a, \quad \frac{d}{T_a}\frac{\mathrm{d}T_a}{\mathrm{d}r} = -D, \quad \frac{d}{\rho_a}\frac{\mathrm{d}\rho_a}{\mathrm{d}r} = -\frac{D}{\gamma}, \quad D = \frac{g\alpha d}{c_p} \qquad [14a\text{–}d]$$

where the dimensionless parameter $D \approx 0.3$ in the core is called the dissipation parameter (see, e.g., Schubert et al., 2001) and γ is a dimensionless parameter called the Grüneisen parameter. As we see later in the text, D also measures the importance of ohmic and viscous dissipation in a planetary core. The equation for $\mathrm{d}p_a/\mathrm{d}r$ is simply the hydrostatic equation, and since $\mathrm{d}S$ and $\mathrm{d}\xi$ are zero for the chosen reference state, the equation for $\mathrm{d}T_a/\mathrm{d}r$ follows from eqn [13]. The equation for $\mathrm{d}\rho_a/\mathrm{d}r$ then follows from the definition of the Grüneisen parameter, $\gamma = (\rho/T)(\partial T/\partial\rho)_{S\xi}$. The numerical value of γ is discussed in Alfè et al. (2002).

The reference state equations can be solved either using the values from a reference Earth model such as PREM (Dziewonski and Anderson, 1981) constructed from seismic data or using a simple model such as that of Nimmo, described in this volume. The temperature has to be specified at either the ICB or CMB. In principle, the melting point of iron determines the ICB temperature, but in practice, there is uncertainty about how much the melting point is depressed by the chemical impurity; Nimmo takes $T_{\mathrm{icb}} = 5,520$ K. The models suggest a temperature drop across the outer core of ~ 1300 K.

8.05.2.3 Equations for the Convective Perturbations

We can now formulate the anelastic equations for convection in the Earth's core. The treatment here follows that of Anufriev et al. (2005), though here we ignore any perturbations in gravity induced by the perturbations ρ_c, though these are formally the same order as the other terms. The convective density perturbation ρ_c can be written in three parts in terms of the entropy, pressure, and composition perturbations:

$$\begin{aligned}\rho_c &= S_c\left(\frac{\partial\rho}{\partial S}\right)_{p,\xi} + p_c\left(\frac{\partial\rho}{\partial p}\right)_{S,\xi} + \xi_c\left(\frac{\partial\rho}{\partial\xi}\right)_{p,S} \\ &= -\frac{\rho_a\alpha T_a}{c_p}S_c - \frac{p_c}{g\rho_a}\frac{d\rho_a}{dr} - \rho_a\alpha^\xi\xi_c\end{aligned} \qquad [15]$$

Here, $a^\xi = -\rho^{-1}(\partial\rho/\partial\xi)_{p,S}$ is the adiabatic compositional expansion coefficient; because the light element has very low density compared to iron, it is nearly unity. We can now write the momentum equation in a form close to that of Braginsky and Roberts (1995):

$$\frac{\mathrm{D}\mathbf{u}}{\mathrm{D}t} + 2\boldsymbol{\Omega}\times\mathbf{u} = -\boldsymbol{\nabla}\left(\frac{p_c}{\rho_a}\right) + \mathbf{1}_r g\left(\frac{\alpha T_a}{c_p}S_c + \alpha^\xi\xi_c\right) + \frac{\mathbf{j}\times\mathbf{B}}{\rho_a} + \mathbf{F}^\nu \qquad [16]$$

This form of the equation of motion makes it convenient to eliminate the pressure perturbation by taking the curl. We then need the equations for the composition and entropy perturbation. The composition equation is

$$\frac{\partial\xi_c}{\partial t} + \mathbf{u}\cdot\boldsymbol{\nabla}\xi_c = \frac{1}{\rho_a}\boldsymbol{\nabla}\cdot\rho_\alpha\kappa^\xi\boldsymbol{\nabla}\xi_c - \dot{\xi}_a \qquad [17]$$

where $k^\xi = k^\xi/\rho_a$ is mass diffusivity. The term $\dot{\xi}_a$ arises because light material is continually being introduced at the ICB, and there is no way of getting rid of it. If we assume that in time, the material becomes well mixed, so that from the point of view of the convective composition component, the effect is equivalent to having a uniform sink of composition that averaged over the core exactly balances the input of ξ from the ICB.

The entropy equation is usually taken as

$$\rho_a T_a\frac{\mathrm{D}S_c}{\mathrm{D}t} = T_a\boldsymbol{\nabla}\cdot\rho_a\kappa_T T_a\boldsymbol{\nabla}S_c + \boldsymbol{\nabla}\cdot k\boldsymbol{\nabla}T_a - \rho_a T_a\dot{S}_a + \rho_a H \qquad [18]$$

Here, κ_T is the turbulent diffusivity of entropy. The reasoning behind this expression is that the turbulence makes elements of fluid move isotropically carrying their entropy, which then dissolve into the ambient fluid releasing that entropy. Braginsky and Meytlis (1990) pointed out that such elements will probably not move isotropically, so this form of diffusion might only be a crude model of the actual turbulent diffusion process. The term $\boldsymbol{\nabla}\cdot k\boldsymbol{\nabla}T_a$ is the heat flux deficit (Anufriev et al., 2005) that comes from the heat being conducted along the adiabat. This is a large term in the core, and since this conducted heat flux increases rapidly from the ICB to the CMB, the heat flux transported by the convection has to fall rapidly, possibly even going negative as the CMB is approached. This term is therefore a strong heat sink. The core is likely to be cooling (unless radioactivity is very significant), and so $\rho_a T_a\dot{S}_a$ is negative, so core cooling is equivalent to a heat source. The final term

$$\rho_a H = Q_\nu + Q_j + \rho_a H^{\mathrm{R}} \qquad [19]$$

gives the heat sources, Q_ν being the viscous dissipation, Q_j being the ohmic dissipation, and H^{R} the heat released by radioactivity.

Anufriev et al. (2005) pointed out that for a liquid, where $\alpha T \ll 1$, the entropy is dominated by the temperature term, that is, if in eqn [13], we replace $\mathrm{d}S$ by S_c, $\mathrm{d}T$ by T_c, etc., then the terms involving p_c and ξ_c are small compared with the term involving T_c. So we have the anelastic liquid approximation (ALA):

$$S_c = \frac{c_p}{T_a}T_c \qquad [20]$$

In the core, $\alpha T \sim 6\times10^{-2}$, so the errors arising from the ALA will be small. The advantage of the ALA is that the boundary conditions are more naturally formulated in terms of the temperature, not the entropy. Furthermore, the uncertainty about whether entropy dissipation or temperature dissipation should be used disappears, because the entropy fluctuation becomes equivalent to the temperature perturbation. Note that for a perfect gas, $\alpha T = 1$, and the ALA is not appropriate.

8.05.2.4 Boundary Conditions

The mechanical boundary conditions in the core are that there is no flow through the ICB and CMB, and there is no slip at

these boundaries. The growth rate of the inner core is so slow it can be ignored on the convective timescale. If the inner core is rotating relative to the mantle (whose rotation defines $\mathbf{\Omega}$), then separating the core flow into radial and tangential components, $\mathbf{u} = u_r \mathbf{1}_r + \mathbf{u}_t$:

$$u_r = 0, \quad \mathbf{u}_t(\mathbf{r}) = \mathbf{\Omega}_{IC} \times \mathbf{r}, \quad \text{at} \quad r = r_{icb}, \quad \text{and} \quad \mathbf{u} = 0 \quad \text{at} \quad r = r_{cmb} \qquad [21]$$

where $\mathbf{\Omega}_{IC}$ is the rotation vector of the inner core relative to the mantle. Kuang and Bloxham (1997) suggested that since the Ekman layer is so thin (see Section 8.05.4.4), it should be ignored and a stress-free condition applied instead (see also Section 8.05.5.6).

The electromagnetic boundary conditions at the ICB are that $\mathbf{B}$ is continuous across the ICB and the continuity of tangential $\mathbf{E}$ implies that $\eta \mathbf{j}_t$ is also continuous. Denoting the jump in a quantity across the boundary by square brackets [ ],

$$[\mathbf{B}] = 0, \quad [j_r] = 0, \quad [\eta \mathbf{j}_t] = 0, \quad \text{at} \quad r = r_{icb} \qquad [22a]$$

where r denotes the radial component and t the tangential component. Note that if the electrical conductivity of the inner and outer cores is different, tangential current is not continuous. Assuming that the electrical conductivity of the mantle is much less than that of the core, there is negligible current in the mantle, and the core field has to match to a potential field at the CMB. This implies

$$[\mathbf{B}] = 0, \quad [j_r] = 0 \qquad [22b]$$

This assumption does, of course, rule out any electromagnetic coupling between the core and mantle, which might be important for length-of-day models.

We also need a condition on the temperature and the composition at both the ICB and CMB. At the ICB, there are two contributions to the input heat flux per unit area into the outer core, the heat conducted out of the inner core, and the latent heat, released as a consequence of inner core freezing. If $r_{icb}(\theta, \phi, t)$ is the location of the ICB, the rate of release of latent heat energy there is $L_H \rho \dot{r}_{icb}$ per unit area (see the chapter by Nimmo), and the rate of release of light material is $\rho \Delta\xi \dot{r}_{icb}$ also per unit area. Here, L_H is the latent heat energy per unit mass and $\Delta\xi$ is the jump in ξ across the ICB; numerical values are given in Table 1.

The location of the ICB, $r = r_{icb}$, is determined by the melting point of iron, which is a function of p and ξ. Braginsky and Roberts (1995) and Roberts et al. (2003) showed that its rate of change at the ICB is governed by

$$\dot{S}_a = -c_p \Delta_2 \dot{r}_{icb} / r_{icb} \qquad [23]$$

$\Delta_2 \sim 0.04$ being a parameter dependent on the variation of the melting point with pressure (see Roberts et al., 2003, eqn [82], and Chapter 8.02). Assuming that the heat conducted out of the inner core balances the heat conducted along the adiabat near the base of the outer core, and using the ALA [20], the rate of release of latent heat at the ICB balances the heat flux conducted in the thermal boundary layer,

$$\frac{L_H \rho_a r_{icb}}{\Delta_2 c_p T_a} \left(T_a \dot{S}_a + c_p \frac{\partial T_c}{\partial t} \right) = \rho_a c_p k_T \frac{\partial T_c}{\partial r} \quad \text{on} \quad r = r_{icb} \qquad [24]$$

which is the thermal boundary condition on the ICB at $r = r_{icb}$. In general, there will be a jump in the temperature gradient at the ICB, and the thermal conductivity may be different across the ICB also. Nevertheless, Buffett et al. (1992) and Labrosse et al. (2001) pointed out that only small errors arise in assuming the inner core is adiabatically stratified, so the assumption that the conducted heat flux is the same on both sides of the ICB is reasonable. Note that $\dot{S} = \dot{S}_a + c_p \dot{T}_c / T_a$, and both terms are of comparable magnitude, as the very large S_a changes only very slowly on the core evolution timescale, while the much smaller $c_p T_c / T_a$ changes more rapidly on the convective turnover timescale. Similarly, the rate of release of light material at the ICB gives

$$\frac{\Delta\xi \rho_a r_{icb}}{\Delta_2 c_p T_a} \left(T_a \dot{S}_a + c_p \frac{\partial T_c}{\partial t} \right) = \rho_a \kappa_T \frac{\partial \xi_c}{\partial r} \quad \text{on} \quad r = r_{icb} \qquad [25]$$

which is the boundary condition on ξ at the ICB. Although both eqns [24] and [25] contain time derivatives of T_c, Glatzmaier and Roberts (1996) found them to be numerically stable, though most work on core convection uses simplified boundary conditions, such as $T_c = 0$ or $\partial T_c / \partial r$ constant at the ICB.

On the CMB, the heat flux is determined by mantle convection. It may be possible to get information about the distribution of the heat flux through the CMB, I_{cmb}, from seismic measurements (see Section 8.05.6 and, e.g., Olson (2003)), but in principle, it should be determined by mantle convection calculations. Assuming that this total heat flux is greater than the heat conducted down the adiabat at the CMB, if we adopt as a simple model a uniform distribution of CMB heat flux,

$$\rho_a c_p \kappa_T \frac{\partial T_c}{\partial r} = -I_{cmb} + I_{ad}(r_{cmb}) \quad \text{on} \quad r = r_{cmb} \qquad [26]$$

where I_{cmb} is the heat flux per unit area passing through the CMB and $I_{ad}(r_{cmb})$ is the heat flux conducted along the adiabat near the CMB. There has been a substantial amount of work on models with a nonuniform heat flux across the CMB, reviewed by Olson (2003). Since there can be no flux of light material across the CMB,

$$\frac{\partial \xi_c}{\partial r} = 0 \quad \text{on} \quad r = r_{cmb} \qquad [27]$$

This completes the anelastic boundary conditions. Common choices for the magnetic boundary conditions are either to assume an insulating inner core and mantle or to give a more accurate representation of the field inside the core by solving the magnetic diffusion problem in the solid inner core.

8.05.2.5 The Boussinesq Limit

The Boussinesq limit is found by letting the dissipation number $D = g\alpha d / c_p$ go to zero. It can therefore be thought of as a 'thin layer' approximation, since it is equivalent to $d \ll c_p / g\alpha$. As noted, it is only marginally satisfied in the core, but nevertheless, most studies of core convection are based on the Boussinesq equations. There are several reasons for this. First, Boussinesq convection is a well-studied problem, and so a wealth of intuition about it has built up, so that Boussinesq studies are built on a firm foundation. Second, the Boussinesq

equations are significantly simpler to solve numerically and have fewer free parameters than the full anelastic equations. Since the convection equations are numerically demanding, particularly in three-dimensional (3-D) calculations, this simplicity is a major advantage. A third reason is that much of our understanding has come from the study of laboratory experiments, which are all in the $\nabla\cdot\mathbf{u}=0$ regime. So simulations designed to make contact with this work are naturally Boussinesq.

We start with the anelastic mass conservation eqn [5]. Combining with eqn [14c], we get

$$\nabla\cdot(\rho_a\mathbf{u})=\rho_a\nabla\cdot\mathbf{u}-\frac{u_r D\rho_a}{\gamma d}=0 \qquad [28]$$

so in the limit $D\to 0$,

$$\nabla\cdot\mathbf{u}=0 \qquad [29]$$

The entropy equation can be reduced to a temperature equation by substituting in the ALA [20]. A large number of terms arise that involve ∇T_a and ∇c_p, but in the limit $D\to 0$, they all vanish because of [14b] and [14c]. Then, eqn [18] becomes

$$\rho_a c_p\frac{\mathrm{D}T_c}{\mathrm{D}t}=\rho_a c_p\kappa_T\nabla^2 T_c+\nabla\cdot k\nabla T_a-\rho_a T_a\dot{S}_a+\rho_a H \qquad [30]$$

In the Boussinesq limit, the expression for H, eqn [19], simplifies because the viscous dissipation and ohmic dissipation are proportional to D and so drop out (see Anufriev et al., 2005 for details). The basic reason for this is that in the Boussinesq limit, the thermal energy is much larger than the kinetic energy or the magnetic energy. The heat transport equation then becomes a temperature equation, because the dominant form of energy is the temperature-dependent internal heat energy. This is rather a drawback for the Boussinesq approximation, because the ohmic dissipation might be a significant player in the overall heat budget. In consequence, the last three terms on the right-hand side of eqn [30] can be bundled into a single space-dependent heat source term

$$\widehat{H}=\frac{\nabla\cdot k\nabla T_a}{\rho_a c_p}-\frac{T_a\dot{S}_a}{c_p}+\frac{H}{c_p} \qquad [31]$$

to get

$$\frac{\mathrm{D}T_c}{\mathrm{D}t}=\kappa_T\nabla^2 T_c+\widehat{H} \qquad [32]$$

which is the Boussinesq form of the heat transport equation. Equation [31] shows that the effective heat source for Boussinesq models is considerably more complicated than is sometimes appreciated. The first term on the right is the heat flux deficit term arising from the fact that more and more heat is conducted down the adiabat as we move outward from the ICB to the CMB. From the point of view of the convection, this is a large, almost uniform, heat sink. The second term on the right is the core cooling term, which is a source term, but probably not as large as the sink term. The third term is radioactive heating and is a source that is currently completely unknown. It could be zero or it could dominate the other two sources. Note that if it is small, $\hat{H}$ will be a net heat sink, and convection is then driven by the heat input at the ICB.

The composition equation [17] becomes

$$\frac{\partial\xi_c}{\partial t}+\mathbf{u}\cdot\nabla\xi_c=k^\xi\nabla^2\xi_c-\dot{\xi}_a \qquad [33]$$

The Boussinesq momentum equation is not very different from eqn [16], the entropy being replaced by the temperature according to eqn [20], and the viscous term simplifies to give

$$\frac{\mathrm{D}\mathbf{u}}{\mathrm{D}t}+2\boldsymbol{\Omega}\times\mathbf{u}=-\nabla\left(\frac{p_c}{\rho_a}\right)+\mathbf{1}_r g\left(\alpha T_c+\alpha^\xi\xi_c\right)+\frac{\mathbf{j}\times\mathbf{B}}{\rho_a}+\nu_T\nabla^2\mathbf{u} \qquad [34]$$

Of course, ρ_a is now a constant. Equations [29] and [32]–[34] constitute the Boussinesq equations for convection in the core. The boundary conditions are not affected by taking the Boussinesq limit, so the thermal and compositional equations (eqns [24]–[27]) can be applied, though in practice, much simpler conditions are usually adopted. Another frequent simplification is to bundle together the composition and temperature variables by multiplying eqn [32] by α and eqn [33] by α^ξ and defining the codensity $C=\alpha T_c+\alpha^\xi\xi_c$. This device only works if both composition and temperature have the same diffusion coefficient and the same boundary conditions (see **Section 8.05.3.2**).

Both the equations and the boundary conditions contain inhomogeneous forcing terms. In some codes, these equations are handled directly, but sometimes, the inhomogeneous terms are eliminated. This procedure is detailed in Anufriev et al. (2005); here, we illustrate with the composition equation. We define $\xi_c=\xi_0+\xi'$, and choose the basic distribution ξ_0 to be a function of r only and to satisfy

$$k^\xi\nabla^2\xi_0-\dot{\xi}_a=0 \qquad [35]$$

with boundary conditions

$$\frac{\mathrm{d}\xi_0}{\mathrm{d}r}=\frac{\Delta\xi r_{\mathrm{icb}}}{\Delta_2 c_p T_a k_T}T_a\dot{S}_a \quad\text{on}\quad r=r_{\mathrm{icb}} \quad\text{and}\quad \frac{\mathrm{d}\xi_0}{\mathrm{d}r}=0 \quad\text{on}\quad r=r_{\mathrm{cmb}} \qquad [36]$$

Now, ξ' satisfies

$$\frac{\partial\xi'}{\partial t}+\mathbf{u}\cdot\nabla\xi'=-\frac{\mathrm{d}\xi_0}{\mathrm{d}r}u_r+k^\xi\nabla^2\xi' \qquad [37]$$

Similarly, we define $T_c=T_0+T'$ and $T'_0=\partial T_0/\partial r$. Because they are spherically symmetrical and constant in time, these basic state contributions do not affect the momentum equation significantly, because the extra terms can be balanced by a pressure gradient. The homogeneous Boussinesq equations are then eqn [29] with

$$\frac{\mathrm{D}\mathbf{u}}{\mathrm{D}t}+2\boldsymbol{\Omega}\times\mathbf{u}=-\nabla\left(\frac{p'}{\rho_a}\right)+\mathbf{1}_r g\left(\alpha T'+\alpha^\xi\xi'\right)+\frac{\mathbf{j}\times\mathbf{B}}{\rho_a}+\nu_T\nabla^2\mathbf{u} \qquad [38]$$

$$\frac{\mathrm{D}T'}{\mathrm{D}t}=-\frac{\mathrm{d}T_0}{\mathrm{d}r}u_r+\kappa_T\nabla^2 T' \qquad [39]$$

$$\frac{\mathrm{D}\xi'}{\mathrm{D}t}=-\frac{\mathrm{d}\xi_0}{\mathrm{d}r}u_r+\kappa^\xi\nabla^2\xi' \qquad [40]$$

with the same mechanical and electromagnetic boundary conditions as in the inhomogeneous Boussinesq equations, but with thermal and compositional boundary conditions,

$$\frac{\partial T'}{\partial r}=\frac{L_H r_{\mathrm{icb}}}{\Delta_2 c_p\kappa_T T_a}\frac{\partial T'}{\partial t},\quad \frac{\partial\xi'}{\partial r}=\frac{\Delta\xi r_{\mathrm{icb}}}{\Delta_2\kappa_T T_a}\frac{\partial T'}{\partial t} \quad\text{on}\quad r=r_{\mathrm{icb}} \qquad [41]$$

$$\frac{\partial T'}{\partial r}=0,\quad \frac{\partial \xi'}{\partial r}=0\ \text{ on }\ r=r_{\text{cmb}} \qquad [42]$$

Since only derivatives of T' and ξ' are specified, they are arbitrary up to a constant. This degeneracy can be removed by specifying that the averages of T' and ξ' are zero over the ICB. This completes the specification of the homogeneous Boussinesq equations, but it should not be forgotten that T_0 and ξ_0 must be added on to reconstruct the actual temperature and composition perturbations. The homogeneous Boussinesq equations can be linearized in a natural way, in both the nonmagnetic and magnetic cases (in which case, the induction equation is needed), to give an eigenvalue problem for the critical Rayleigh number and wave frequency at the onset of convection.

8.05.2.6 Formulation of the Equations for Numerical Solution

It is useful to see how the full anelastic equations could be approached (see, e.g., Glatzmaier, 1984). One method (many others are possible) would be to take **u**, **B**, ξ_c, and S_c as the primary variables that are advanced at every time step using eqns [6], [16]–[18]. Because of eqns [5] and [7b], there are only two independent scalar fields in **u** and **B**, but this can be taken into account by writing **B** in terms of toroidal and poloidal scalar fields $\mathbf{B}=\nabla\times\mathcal{U}_{\mathbf{r}}+\nabla\times\nabla\times\mathcal{V}_{\mathbf{r}}$, with a similar expansion for $\rho\mathbf{u}$. This expansion means that eqns [5] and [7b] are automatically exactly satisfied. Two equations for $\mathcal{U}$ and $\mathcal{V}$ can be conveniently obtained by taking the radial component and the radial component of the curl of eqn [6] and similarly for ρ times [16]. It is then the toroidal and poloidal scalar fields for the magnetic field and momentum density that are time-stepped forward, along with S_c and ξ_c. At each time step, the pressure p_c can be found by taking the divergence of ρ times [16] and solving the resulting time-independent Poisson equation for p_c. Equation [15] and the equation of state then give the temperature and density perturbations. At this stage, every term on the right-hand sides of eqns [6], [16]–[18] is known at the current timestep, so we can advance to the next timestep. An appropriate set of boundary conditions would of course be needed to complete the numerical solution.

8.05.3 Convection in the Absence of Rotation and Magnetic Field

8.05.3.1 Thermal Convection

The thermal diffusivity in the core is estimated at $\kappa\sim1.3\times10^{-5}$, with the kinematic viscosity a factor 25 smaller at $\nu\sim5\times10^{-7}$ and the compositional diffusion coefficient another factor 10^3 smaller. In consequence, the dimensionless Rayleigh number $g\alpha\Delta T d^3/\kappa\nu$ is very large in the core, much greater than the critical value for the onset of convection in the absence of rotation, which is typically $Ra\sim10^3$. The onset of convection is discussed in considerable detail for the case of both a plane layer and a spherical shell, in **Chapters 1.03** and **1.07** of Chandrasekhar (1961). As we shall see, convection in the core is strongly influenced by rotation and magnetic field, and much useful information about the onset of convection in the presence of these constraints is given in the same book. It is nevertheless of interest to examine what form convection in the core might take if these constraints are ignored. One advantage of this approach is that unconstrained Boussinesq plane layer convection has been extensively studied both theoretically and experimentally up to quite high Rayleigh numbers, so that far more is known about the strongly nonlinear behavior in this case. Much less is known about the corresponding problems when rotation and magnetic field are important.

Experiments typically measure the heat flux in terms of the Nusselt number:

$$Nu=\frac{Fd}{\rho c_p\kappa\Delta T} \qquad [43]$$

which is the ratio of the total convective plus conductive heat flux per unit area, F, to the heat flux that would occur in the absence of convection, $\rho c_p\kappa\Delta T/d$. When comparing with the Earth's core, there is a potential for confusion here, because there are two possible definitions for the conducted heat flux. If this is taken as the heat conducted down the adiabat, then the Nusselt number in the Earth's core turns out to be of order unity. We denote the Nusselt number defined in this way, with $\Delta T=\Delta T_a$ the adiabatic temperature drop across the core (~1300 K) as $N=Fd/\rho c_p\kappa\Delta T_a$. However, for comparison with Boussinesq convection models, $\Delta T=\Delta T_s$, the superadiabatic temperature drop across the core. This is much smaller, probably $<10^{-3}$ K. We denote the Nusselt number defined in this way as $Nu=Fd/\rho c_p k\Delta T_s$, and its typical value in the core is about 10^6. Note that no direct numerical simulation (DNS) of rotating spherical convection has ever achieved Nu values this large, and there is no prospect of ever doing so.

At Rayleigh numbers just above critical, weakly nonlinear theory (described in more detail in **Section 8.05.4**) can be used to predict the Nusselt number in terms of the Rayleigh number. Weakly nonlinear theory is valid when the pattern of nonlinear convection is still close to that given by the linear theory of the onset of convection. It is no longer valid when convection is turbulent. It predicts that $Nu-1\propto Ra-Ra_c$, Ra_c being the critical Rayleigh number for the onset of convection. Initially, as Ra is increased above critical, this is what is found experimentally, but if the Rayleigh number is further increased, it is found that the Nusselt number starts to grow more slowly with Ra than this. Experiments at very large Ra usually find $Nu\sim Ra^n$, and in the range of Ra up to 10^{17}, which is about the largest value that has been tested experimentally (Niemela et al., 2000), n is typically about 0.3. As we see later in the text, theories exist for both $n=1/3$ and $n=2/7$, but it is conjectured that at $Ra\gg10^{17}$, n may rise to 0.5 (see, e.g., Grossmann and Lohse, 2000). Note that this experimental value of $Ra\sim10^{17}$ is much larger than that that can be obtained with 3-D numerical experiments, $Ra\sim10^7$ (note that for rapidly rotating convection, where the critical Rayleigh number is much larger than 10^3, considerably higher Ra can be achieved), though 2-D simulations can reach significantly larger Ra, up to 10^{12} (Rogers et al., 2003). The Rayleigh number in the Earth's core is probably around 10^{23} (Christensen and Aubert, 2006).

Since we cannot measure the temperature difference ΔT_s directly, it is more appropriate to work in terms of the convective heat flux per unit area, F_{conv}. Even this is not well known, but a total of 2 TW near the CMB (giving 0.013 W m^{-2} for the flux per unit area) for the *convective* heat flux (ignoring that

carried by conduction down the adiabat) is a reasonable order of magnitude estimate. Note that the actual convective heat flux varies considerably across the core (see Section 8.05.2) and may even be negative on average at the CMB, but nevertheless, we adopt 0.013 W m^{-2} for the purpose of estimation here. Since

$$Ra = \frac{g\alpha \Delta T_s d^3}{\kappa \nu}, \quad F_{\text{conv}} = (Nu - 1)\frac{\rho c_p \kappa \Delta T_s}{d} \qquad [44]$$

eliminating ΔT_s gives

$$Ra(Nu - 1) = \frac{g\alpha F_{\text{conv}} d^4}{\rho c_p \kappa^2 \nu} \qquad [45]$$

A simple early estimate for Nu in plane layer Boussinesq convection at large Ra was given by Priestley (1959) and Kraichnan (1962) (see Siggia (1994) for a more complete discussion than that given here). They suppose thermal boundary layers of thickness δ occur at the top and bottom boundaries, across which most of the temperature drop takes place. Since the temperature drop across each boundary is approximately $\Delta T_s/2$ and all the heat is transported by conduction in the boundary layer,

$$Nu \approx \frac{0.5d}{\delta} \qquad [46]$$

They further assume that the Rayleigh number for the boundary layer is close to critical. This gives

$$\frac{g\alpha \Delta T_s \delta^3}{2\kappa \nu} \approx 1000 \qquad [47]$$

assuming that the critical Rayleigh number is around 10^3, which linear theory calculations suggest is reasonable. Eliminating δ between eqns [46] and [47] gives $Nu \propto Ra^{1/3}$. Goldstein et al. (1990) found

$$Nu \approx 0.066 Ra^{1/3} \qquad [48]$$

from experimental data, where the coefficient 0.066 is not far from the $16\,000^{-1/3} \approx 0.04$ expected from eqns [46] to [47].

The interior velocity and temperature perturbations are obtained by balancing inertia and buoyancy, the mixing-length balance, together with a simple estimate of the convective heat flux. The mixing-length balance can be thought of as an element of fluid being accelerated by buoyancy for a turnover time d/U_*, where U_* is a typical velocity. The acceleration is therefore

$$U_*^2/d \approx g\alpha T_*' \qquad [49]$$

where T_*' is the typical temperature perturbation in the fluid interior. The convective heat flux is carried by blobs of hot fluid moving upward, with cold fluid descending, so

$$F_{\text{conv}} \approx \rho c_p U_* T_*' \qquad [50]$$

This gives the Deardorff velocity and temperature scale (Deardorff, 1970):

$$U_* = \left(\frac{g\alpha d F_{\text{conv}}}{\rho c_p}\right)^{1/3}, \quad T_*' = \left(\frac{F_{\text{conv}}}{\rho c_p}\right)^{2/3}\left(\frac{1}{g\alpha d}\right)^{1/3} \qquad [51a,b]$$

Note that the Deardorff velocity and temperature scale are independent of the diffusion coefficients. Experiments indicate that U_* is close to the rms velocity in the interior of the fluid; we therefore do not need a numerical scaling factor in [51a].

Putting in the standard values for the core for g, α, d, and c_p from Table 1 together with our estimate of $F_{\text{conv}} = 0.013$ W m^{-2} gives the Deardorff velocity $U_* = 7 \times 10^{-3}$ m s^{-1}. The faster moving magnetic features at the CMB move with a speed of about 5×10^{-4} m s^{-1}, about ten times slower than this, so our velocity estimate has turned out ten times too big. The overestimate is due to neglecting the inhibiting forces of rotation and magnetic field. While our estimate is clearly too large, it is nevertheless of interest to pursue this nonrotating nonmagnetic plane layer model a little further. Using eqns [45] and [48] with the standard values in Table 1 and our estimate for F_{conv}, we obtain $Ra \sim 10^{23}$ and $Nu \sim 3 \times 10^6$. $\Delta T_s \sim 2 \times 10^{-4}$, which is substantially larger than the Deardorff temperature. This must be the case for model consistency as the Deardorff temperature is the internal temperature perturbation, but the main temperature drop is across the boundary layer. Note that $Nu\Delta T_s \sim 600$ K, the same order of magnitude as $\Delta T_a \sim 1300$ K, consistent with N being of order unity. The thermal boundary layer thickness $\delta = 0.4$ m only. We have, of course, no way of telling whether the core boundaries are sufficiently smooth for such a thin boundary layer to be physically plausible.

Experiments indicate that the exponent in the $Nu \sim Ra^n$ relation is somewhat $< 1/3$. Castaing et al. (1989) suggested $n = 2/7$, but Grossmann and Lohse (2000) argued that there was not a single exponent, but rather a transition between different exponents corresponding to different regimes. The regime depends on whether dissipation is primarily occurring in a boundary layer or in bulk of the fluid and on whether the viscous boundary layers are thicker or thinner than the thermal boundary layers (Ahlers et al., 2009). Experiments covering a large range of Rayleigh number often gradually cross from one regime to another, so that $n \approx 2/7$ may be a good fit while moving from a $n = 1/4$ to an $n = 1/3$ regime.

Kraichnan (1962) pointed out that at very large Ra, even thin boundary layers like this might be shear unstable and hence turbulent. If so, this undermines the assumption of a quiescent boundary layer in which heat transfer is by conduction. Indeed, the basis of eqn [47] is that it is a laminar layer that thickens due to thermal diffusion until it becomes unstable due to local convection. With our estimates, the local Reynolds number of the boundary layer is $U_*\delta/\nu \sim 5000$, probably large enough to expect a turbulent boundary layer. The boundary layer then starts to change its character, becoming passive rather than active. This means that the temperature drop across the boundary layer becomes the same as the Deardorff temperature, so that it is the interior that controls the heat flux, not the boundary layer. F_{conv} then becomes independent of the diffusivities, since the Deardorff velocity and temperature are independent of diffusivities. We get

$$\Delta T_s \sim T_*' \qquad [52]$$

and using eqns [49] and [50] gives

$$Nu \approx \frac{U_* d}{\kappa} \sim (RaPr)^{1/2} \qquad [53]$$

A more precise treatment of the boundary layer (e.g., Siggia, 1994) suggests

$$Nu \approx \frac{U_* d}{\kappa} \sim (RaPr)^{1/2}/(\ln Ra)^{3/2} \quad [54]$$

Note, however, that experiments even at $Ra \sim 10^{17}$ show no sign of the $Ra^{1/2}$ dependence, the exponent typically being $n \approx 0.3$ (Niemela et al., 2000). As we expect that rotation and magnetic field will inhibit heat transport and, for nonmagnetic nonrotating convection, the interior is already beginning to take over the control of the heat transport at the Earth's core Rayleigh numbers, it is likely that the interior will be in control in the rotating magnetic Earth's core.

8.05.3.2 Compositional Convection

It was suggested by Braginsky (1963) that the gravitational energy released by the growth of the inner core might help to power the geodynamo. The density jump at the ICB suggests that the outer core must contain less dense elements than iron, so that the freezing process allows buoyant material to float upward, supplementing the buoyancy from thermally driven convection (Fearn, 1998). Most analyses of the energy balance in the core suggest that compositional convection does a similar amount of work as thermal convection, though the exact ratio is model-dependent (see **Chapter 8.02**). Unlike heat, the light material cannot escape from the outer core. There are two possibilities: the usual assumption is that the light material mixes in the outer core, so that the density of the outer core is a slowly decreasing function of time, the term $\dot{\xi}_a$ in eqn [17]. Because this rate of change of density is very slow compared to the flow turnover time, this is equivalent to having a uniform sink of buoyancy distributed throughout the core. A second possibility is that the light material forms a sediment at the top of the core (Buffett et al., 2000), near the CMB. If this is the case, there is a release of heavy material (compositionally closer to pure iron) near the CMB, which would give an additional convective driving, increasing the amount of gravitational power to drive the geodynamo.

Compositional convection can be seen in the laboratory using a saturated solution of ammonium chloride (e.g., Chen et al., 1994). If the container is strongly cooled from below (e.g., placing it on dry ice), ammonium chloride comes out of solution releasing relatively fresh water, which is less dense than its surroundings, and so rises. When the experiment is performed, the ammonium chloride does not crystallize as a solid block on the bottom of the container, but instead forms a dendritic structure with a 'mushy zone' consisting partly of crystallized ammonium chloride and partly of liquid. The lower-density solution released in the neighborhood of the crystallization process rises rapidly in thin 'chimneys' formed inside the mushy zone. Typically, the chimneys are narrow and spaced quite far apart, so there is a strong asymmetry between the narrow upwelling plumes coming out of the chimneys and the slowly sinking fluid being sucked back into the mushy zone (Aussillous et al., 2006). There is also evidence that mushy zones form when liquid iron freezes in metallurgical processes.

These observations have led to the suggestion that there may be a mushy zone at the ICB (Fearn et al., 1981), though this is controversial (Morse, 2002). There may even be chimneys of light material emerging from the mushy zone. Loper et al. (2003) explored the dynamics of such plumes, though it is uncertain whether such plumes can remain stable and maintain their identity (Classen et al., 1999) or whether the action of rotation and magnetic field might make the plumes mix into the core fluid. A further complication is that seismology indicates there is a stable layer surrounding the ICB (Gubbins et al., 2008). How light material released at the ICB penetrates through this layer is not yet clear.

While the physical origins of thermal and compositional convection are different, it is not so clear that the dynamics of the two phenomena are very different, and indeed, modelers often lump compositional and thermal convection together, the codensity C as mentioned in **Section 8.05.2.5**. Admittedly, the composition and temperature have different diffusion coefficients, but both are so low that small-scale turbulence is probably responsible for mixing both heat and composition. The main difference is in the boundary conditions at the CMB; the light material cannot escape the core, eqn [27], but heat can, eqn [26]. If fluid cannot easily pass across the TC (see also **Sections 8.05.5.6.1** and **8.05.5.6.2**), light material released at the ICB might have difficulty escaping outside the TC and hence give rise to a higher concentration inside the TC. This has been proposed as a possible explanation for the anticyclonic polar vortices (Olson and Aurnou, 1999; see also **Section 8.05.5.6.2**).

Anufriev et al. (2005) argued that the natural model of compositional convection consisting of a source at the ICB and a uniformly distributed sink of equal strength distributed throughout the core may be a reasonable model for the thermal convection too, because the heat flux deficit term arising from conduction down the adiabat is so large (eqn [18]).

8.05.3.3 Translation of the Inner Core

There is seismic evidence (Niu and Wen, 2001; Tanaka and Hamaguchi, 2001) that the inner core has an east–west asymmetry, that is, the wave velocities and attenuation are different in that part of the core that lies underneath the Earth's eastern and western hemispheres. To explain this surprising asymmetry, Alboussière et al. (2010) and Monnereau et al. (2010) proposed that the inner core is steadily translating sideways, that is, from west to east. Of course, this means that to maintain the inner core in place, the eastern hemisphere must be continually melting and the western hemisphere continually crystallizing. This means that the western hemisphere is younger than the eastern hemisphere, which might explain the seismic asymmetry, as the eastern half may have been crushed as it passed through the highest-pressure region near the center of the Earth. The melted material from the eastern hemisphere might also form a stable layer in the outer core near the ICB, hence explaining the seismic anomaly found close to the ICB (Gubbins et al., 2008).

Why should the inner core be undergoing such a translation? To understand this, we need to consider a small displacement of the inner core from west to east (see **Figure 3**). If there were no melting, the center of mass would be displaced to the point C' and when released would fall back to the center of the Earth at O. It would then overshoot and oscillate. This mode of oscillation is known as a Slichter (1961) mode and has a period of 4–8 h. However, if the displacement has a long timescale, because the eastern hemisphere moves into a

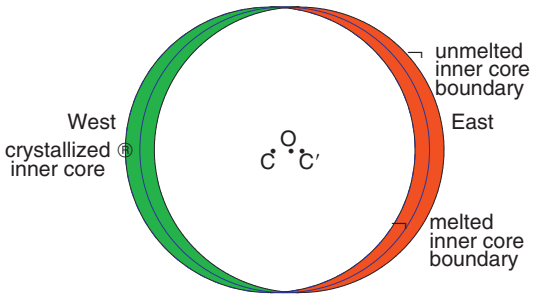

Figure 3 Translation of the inner core viewed from above the north pole. With no melting, if the center of mass of the inner core is moved to *C*', it will fall back under gravity towards *O*, the center of the Earth. If the red material has melted, and the green material has just crystallized, the center of mass of the inner core is at *C*, and the whole solid inner core will continue to move from west to east.

lower-pressure zone, it will melt, and the western hemisphere will recrystallize. The center of mass of this 'new' inner core will be at C, not C'. If C lies on the other side of O from C', the center of mass of the inner core in falling from C to O will be traveling west–east, that is, in the same direction as the initial displacement. This means that the inner core will be continuously freezing underneath the Americas and continuously melting underneath Indonesia, as proposed by Alboussière et al. (2010) and Monnereau et al. (2010). The mechanism itself has no preference for the direction of travel; it is only the seismic evidence that suggests west–east travel. Indeed, Aubert et al., 2013 proposed the direction of travel is east to west, as this might explain the enhanced westward drift of the geomagnetic field in the western hemisphere.

For this mechanism to work, it is clearly necessary that after melting, C lies west of the point O. It turns out (Alboussière et al., 2010) that this requires the temperature gradient in the inner core to exceed the adiabatic value, which is the same criterion as is required for convection to occur in the outer core. Thus, this mechanism can be thought of as an unusual form of convection, in which instead of small fluid parcels moving through the action of buoyancy, the whole inner core moves as a large solid parcel. It is not easy to determine the required temperature gradients, but estimates show that the criterion for instability could plausibly be satisfied.

8.05.4 Effect of Rotation on Convection

In this section, we consider how rotation affects convection in the absence of magnetic field. As we shall see later, magnetic fields do affect rotating convection very significantly, but it is necessary first to consider how rotation alone can affect convection before the additional complications of the magnetic field are considered. We will use two coordinate systems: cylindrical polars (s, ϕ, z), z being parallel to the rotation axis, and spherical polar coordinates (r, θ, ϕ), θ being the colatitude. Cylindrical coordinates turn out to be more natural for understanding the dynamics of rotating fluids, but spherical polar coordinates are preferred for numerical simulations in spherical shells.

8.05.4.1 The Proudman–Taylor Theorem

Slow steady flows in homogeneous rotating fluids have the remarkable property that the velocity is independent of the rotation axis. This result, known as the Proudman–Taylor theorem, can be demonstrated in the laboratory by towing a small obstacle along the bottom of a rotating tank; the whole column of fluid above the obstacle moves along with it as though the fluid column was a rigid body. This surprising result can best be understood in terms of the vorticity equation. Taking coordinates with $\boldsymbol{\Omega} = \Omega \mathbf{1}_z$, the curl of the Boussinesq momentum equation [38] with the magnetic field and composition set to zero gives

$$\frac{\partial \boldsymbol{\zeta}}{\partial t} + \mathbf{u}\cdot\nabla\boldsymbol{\zeta} - (2\boldsymbol{\Omega} + \boldsymbol{\zeta})\cdot\nabla\mathbf{u} = \nabla \times g\alpha T' \mathbf{1}_r + \nu\nabla^2\boldsymbol{\zeta} \qquad [55]$$

$\boldsymbol{\zeta}$ being the vorticity. For simplicity, we drop the subscript on ν_T; in this section, the viscosity can be thought of either as the molecular value when discussing low Ra convection or as a turbulent value for very high Ra convection. Taking U_* as the typical magnitude of the velocity, slow flows are those for which the Rossby number

$$Ro = \frac{U_*}{\Omega d} \ll 1 \qquad [56]$$

The Rossby number in the Earth's core is about 3×10^{-6}.

To understand the Proudman–Taylor theorem, it is helpful to first consider flows for which the length scale of variation in all directions (including the z-direction) is of order d. Then, the vorticity has magnitude U_*/d, and small Rossby number implies that $|\mathbf{u}\cdot\nabla\boldsymbol{\zeta} - \boldsymbol{\zeta}\cdot\nabla\mathbf{u}| \ll |2\Omega\partial\mathbf{u}/\partial z|$. Since $\boldsymbol{\Omega}$ is constant, eqn [55] can be thought of as an equation for $2\boldsymbol{\Omega} + \boldsymbol{\zeta}$. In oceanography and atmospheric sciences, the part $2\boldsymbol{\Omega}$ is called the planetary vorticity, because it is due to the rotation of the Earth rather than the behavior of the fluid. We are therefore assuming that the planetary vorticity is much greater than the fluid vorticity when we make this small Rossby number approximation. Given the slow flows, this will only break down for vortices with radii less than a few tens of meters in the core. The steady flow approximation requires that $|\partial\boldsymbol{\zeta}/\partial t| \ll |2\Omega\partial\mathbf{u}/\partial z|$, which will generally be the case provided that the timescale over which the velocity varies is much longer than a day. Since the convective turnover time d/U_* is several hundred years, such short timescales are unlikely to be of much significance in the dynamics of convection. The dominant term on the left-hand side of eqn [55] is therefore the term $2\Omega\partial\mathbf{u}/\partial z$. Of the terms on the right-hand side, viscosity is small except on very short length scales. The dimensionless ratio of viscous to Coriolis force is measured by the Ekman number $E = \nu/\Omega d^2 \sim 10^{-15}$ in the core. Buoyancy forces (and Lorentz forces) are significant in the core, but do not occur in homogeneous nonmagnetic fluids. The Proudman–Taylor theorem then arises because there is no term on the right-hand side to balance $2\Omega\partial\mathbf{u}/\partial z$. In consequence, the z-derivative of $\mathbf{u}$ must be zero, and fluid has to move in columns. If the time-dependent vorticity term is restored, but the forces on the right-hand side are ignored, we obtain

$$\frac{\partial \boldsymbol{\zeta}}{\partial t} - 2\boldsymbol{\Omega}\cdot\nabla\mathbf{u} = 0 \qquad [57]$$

Taking the curl of this and eliminating $\boldsymbol{\zeta}$ using eqn [57], we derive the inertial wave equation

$$\frac{\partial^2}{\partial t^2}\nabla^2\mathbf{u} = -4\Omega^2\frac{\partial^2}{\partial z^2}\mathbf{u} \qquad [58]$$

This shows that if a z-dependent flow is set up initially, the fluid responds by oscillating on a timescale of days. In the absence of any dissipation mechanism, these oscillations would go on ringing forever. In the core, however, these fast oscillations would excite rapid changes in the magnetic field, which would lead to a rapid damping through ohmic dissipation. Inertial waves may well exist in the core, but they are likely to have a small amplitude only and we will ignore any such oscillations. There are, however, a class of inertial waves that have much smaller frequencies, namely, those with a short wavelength ℓ in the plane perpendicular to z. These waves have frequency $2\Omega\ell/d$ and are considered in more detail in the succeeding text.

Another way of thinking of the Proudman–Taylor theorem is that in z-independent motion, the pressure force is in balance with the Coriolis acceleration. This is geostrophic motion. While the buoyancy force and the magnetic field can induce some z-dependence, many numerical models and laboratory experiments indicate that the motion is mostly in the form of almost 2-D columnar rolls. This is not to say, however, that the ageostrophic parts of the motion are unimportant.

The spherical geometry means that convection inevitably involves some z-dependent motion. The only purely geostrophic motion in a sphere is azimuthal flow $\mathbf{u} = u_\phi(s)\mathbf{1}_\phi$, which cannot transport any heat radially. If the CMB is bumpy, the geostrophic contours are those on which the length of fluid columns is preserved. In general, therefore, flow along geostrophic contours might have a weak radial dependence and hence permit convective heat transport (Bell and Soward, 1996; Westerburg and Busse, 2003). In a perfect sphere, any column moving in the s-direction changes its length. To avoid excessive changes of length of fluid columns, which inevitably involve z-dependent motion, tall thin columns are preferred. These can transport heat while minimizing the departure from geostrophy. If there is no magnetic field and the velocity is small enough for the nonlinear terms to be negligible, no balance between pressure, Coriolis force, and buoyancy is possible. Viscosity must be included for convection to occur at all. Viscous forces are very small in the core, so columns that are viscously controlled are very thin indeed. In the presence of magnetic field, this problem is alleviated, because an inviscid balance is possible by replacing the viscous force with Lorentz force.

There is one further consequence of the difficulty fluid columns have changing their length in rapidly rotating fluid, which is that there is unlikely to be much fluid motion across the TC. Inside the TC, the inner core cuts the fluid columns in half. Any motion in the s-direction across the TC will therefore involve strong z-dependence and so will need correspondingly strong thermal or magnetic forcing to occur. Another factor tending to divide the regions inside and outside the TC into two distinct parts is that columns inside the TC increase their length as they move outward in s, but columns outside the TC decrease in length as they move outward in s. As we see in the succeeding text, this means that the Rossby waves propagate eastward (i.e., prograde, in the same direction as the rotation) outside the TC but westward (retrograde) inside the TC. This discontinuity in the phase speed of the waves is another reason why convection in the two regions has to be considered separately.

8.05.4.2 The Onset of Instability

We are therefore led to study two types of linear problem for the onset of convection in a rotating sphere or spherical shell. The first is the nonmagnetic viscous problem, and the second is the equivalent magnetic problem in which a simple imposed magnetic field is specified. The nonmagnetic problem can be solved either numerically at finite (possibly small) E or asymptotically in the limit $E \to 0$. The magnetic problem can be solved numerically or asymptotically in the weak field limit (see **Section 8.05.5**). We start by describing the nonmagnetic problem.

Numerical solutions were obtained by Gilman (1975), Zhang and Busse (1987), Zhang (1992), Jones et al. (2000), and Dormy et al. (2004), with later workers generally reaching lower E, due to the increase in computer speeds. An accurate method for obtaining solutions is to expand the velocity in toroidal and poloidal scalars

$$\mathbf{u} = \nabla \times \mathcal{T}\,\mathbf{r} + \nabla \times \nabla \times \mathcal{S}\mathbf{r} \qquad [59]$$

which automatically satisfies the continuity equation and reduces the velocity field to two independent scalars. The equations are nondimensionalized taking the unit of time as r_{cmb}^2/ν, the viscous decay time, the unit of length as the sphere radius r_{cmb}, and the unit of temperature as $-Pr\, r_{\mathrm{cmb}} \mathrm{d}T_0/\mathrm{d}r$ where T_0 is the basic-state temperature. The discussion later in the text is in terms of temperature, but this could be replaced by composition. In this case, the boundary conditions adopted should be those appropriate for compositional convection (see eqns [41] and [42]), but otherwise, nothing is significantly changed. Note that the length scale used for nondimensionalization in this problem is r_{cmb} rather than the gap width d. This affects the definition of the Ekman number and Rayleigh number, so care must be exercised when comparing results from these stability problems with numerical dynamo simulations, which often use d as the length scale.

Two cases are commonly studied: a uniformly heated sphere where $\mathrm{d}T_0/\mathrm{d}r$ is proportional to r, appropriate for a strongly radioactive heat source, and differential heating where $\mathrm{d}T_0/\mathrm{d}r$ is proportional to $1/r^2$, suitable for a model where all the heat (or composition flux) is input at the ICB. In the differential heating model, the total input heat flux at the ICB equals the heat flux coming out of the CMB, so no account is taken of the variable amount of heat conducted down the adiabat. The gravity field is $-g\mathbf{r}$.

The linearized vorticity equation [55], which omits the advection of vorticity and the stretching of fluid vorticity (but not the much larger stretching of planetary vorticity), can be written as

$$\frac{\partial \boldsymbol{\zeta}}{\partial t} - 2\boldsymbol{\Omega}\cdot\nabla\mathbf{u} = \nabla \times g\alpha T'\mathbf{1}_r + \nu\nabla^2\boldsymbol{\zeta} \qquad [60]$$

and the scalar equations used are the radial components of eqn [60] and its curl

$$\mathcal{E}\left(\frac{\partial}{\partial t}-\nabla^2\right)\mathcal{L}^2\mathcal{T}-\frac{\partial \mathcal{T}}{\partial \phi}+\mathcal{C}\mathcal{S}=0 \qquad [61]$$

$$\mathcal{E}\left(\frac{\partial}{\partial t}-\nabla^2\right)\mathcal{L}^2\nabla^2\mathcal{S}-\frac{\partial}{\partial \phi}\nabla^2\mathcal{S}-\mathcal{C}\mathcal{T}+\mathcal{E}Ra\mathcal{L}^2T'=0 \qquad [62]$$

where (r, θ, ϕ) are spherical polar coordinates, the temperature perturbation is T', and

$$\mathcal{L}^2=-\frac{1}{\sin\theta}\frac{\partial}{\partial\theta}\left(\sin\theta\frac{\partial}{\partial\theta}\right)-\frac{1}{\sin^2\theta}\frac{\partial^2}{\partial\phi^2} \quad \text{and}$$

$$\mathcal{C}=\mathbf{1}_z\cdot\boldsymbol{\nabla}-\frac{1}{2}\left(\mathcal{L}^2\mathbf{1}_z\cdot\boldsymbol{\nabla}+1_z\cdot\boldsymbol{\nabla}\mathcal{L}^2\right) \qquad [63]$$

The temperature equation [39] becomes

$$Pr\frac{\partial T'}{\partial t}=\mathcal{Q}\mathcal{L}^2S+\nabla^2T' \qquad [64]$$

where $\mathcal{Q}=1$ for internal heating and $\mathcal{Q}=1/r^3$ for differential heating. The dimensionless parameters are the Ekman number, the Rayleigh number, and the Prandtl number:

$$\mathcal{E}=\frac{\nu}{2\Omega r_{\mathrm{cmb}}^2},\quad Ra=\frac{g\alpha r_{\mathrm{cmb}}^5}{\kappa\nu}\frac{\mathrm{d}T_0}{\mathrm{d}r},\quad Pr=\frac{\nu}{\kappa} \qquad [65]$$

Note that many nonlinear convection and dynamo codes use the same basic formulation of the equations as this, with a further toroidal and poloidal expansion of the magnetic field and the radial components of induction equation and its curl giving the two scalar equations for the field. Note also the factor 2 in this definition of the Ekman number. Unfortunately, there is no consistency in the literature over the definition of the Ekman number. In dynamo simulations, $E=\nu/\Omega d^2$ is often used. This gives $\mathcal{E}=E(1-r_{\mathrm{icb}}/r_{\mathrm{cmb}})^2/2$ so at radius ratio 0.35, $\mathcal{E}=0.21E$. Similarly, care is needed with Ra; although the same symbol is used in many papers, the definitions are frequently different, so suitable conversion factors must be worked out if numerical results from one paper are used in another.

The quantities $\mathcal{S}$, $\mathcal{T}$, and T' are then expanded in spherical harmonics, taking account of the symmetry about the equator. Busse (1970) showed that solutions with u_r, u_ϕ, and ζ_z symmetrical about the equator and u_θ and u_z antisymmetric about the equator are preferred, in that they have the lowest critical Rayleigh number. The expansion for $\mathcal{S}$ is then

$$\mathcal{S}=\sum_{l=0}^{L}\mathcal{S}_l(r)P_{2l+m}^m(\cos\theta)\exp\mathrm{i}(m\phi-\omega t) \qquad [66]$$

the other expansions being found in Jones et al. (2000). The radial dependence can be dealt with, for example, either by expanding $\mathcal{S}_l(r)$ in the Chebyshev polynomials and using collocation to derive the equations for the coefficients or by finite difference methods. In either case, a key point is that there is no coupling between modes with different azimuthal wave number m. The operators $\mathcal{L}^2$ and ∇^2 are particularly convenient in this representation, as $\mathcal{L}^2P_{2l+m}^m=-(2l+m+1)(2l+m)P_{2l+m}^m$ so they do not couple spherical harmonics, and the operator $\mathcal{C}$ only couples adjacent spherical harmonics, that is, $\mathcal{C}P_{2l+m}^m$ can be written as a simple linear combination of P_{2l+m+1}^m and P_{2l+m-1}^m. In consequence, the matrix equations arising from the expansion or discretization of the radial structure can be written in banded form, with each m value treated separately and only the blocks corresponding to $l-1$, l, and $l+1$ having nonzero elements. The eigenvalue ω is the frequency and the value of the Rayleigh number Ra_c, which makes ω real, the neutral mode condition, can then be found simply using a variety of different methods, for example, inverse iteration.

The Rayleigh number Ra_c is then minimized over m, to determine m_c, ω_c, and Ra_c as a function of $\mathcal{E}$, Pr, and the radius ratio $r_{\mathrm{icb}}/r_{\mathrm{cmb}}$. Calculations using a variety of boundary conditions, either stress-free or rigid and with fixed temperature and fixed heat flux, have been performed. Values of $\mathcal{E}$ down to 10^{-7} can be reached without excessive computational resources, which is sufficiently small to get excellent agreement with the asymptotic methods described in the succeeding text.

The results show that as $\mathcal{E}$ is reduced, the azimuthal wave number increases with $m_c\sim\mathcal{E}^{-1/3}$, the Rayleigh number increases as $Ra_c\sim\mathcal{E}^{-4/3}$, and frequency increases as $\omega_c\sim\mathcal{E}^{-2/3}$. This means that at small $\mathcal{E}$, the horizontal wavelength gets small, and in the limit of zero viscosity, the critical Rayleigh number goes to infinity, showing that no convection can happen without viscosity in this problem. Numerical simulations at four different Ekman numbers are shown in Figure 4, which is for the case of no internal heating, so convection onsets first close to the TC. The roll structures seen in these numerical calculations are also found in laboratory experiments (Busse and Carrigan, 1976) where the gravity is replaced by centrifugal acceleration arising from the very rapid rotation. In these experiments, the sphere has to be cooled from within. With $\mathcal{E}\sim10^{-15}$ in the core, these results suggest $m\sim3\times10^4$, giving a typical roll diameter of about 300 m only (there is a cyclonic and an anticyclonic roll in each wavelength). Tall thin columns stretching all the way to the boundaries are seen in experiments, but it seems unlikely that structures with such a large aspect ratio exist in the core. As we see in Sections 8.05.4.8.1 and 8.05.5.3, magnetic fields and nonlinear inertial effects can thicken the columns, and time-dependent motions may break the columns up. Having said that, it is possible that tall thin columns with a large (but $<10^4$) aspect ratio are present in the core. Dynamo simulations, especially those in the most Earth-like regimes, often show columnar convection. Interestingly, convection columns are particularly good at generating dipolar magnetic fields.

8.05.4.3 The Onset of Instability in the Rapidly Rotating Limit

The asymptotic $\mathcal{E}\to0$ theory of convection was developed by Roberts (1968) and Busse (1970), but the distinction between the local theory and the global theory of the onset of convection was elucidated more recently (Dormy et al., 2004; Jones et al., 2000). We use cylindrical polar coordinates (s, ϕ, z) and make an axial poloidal and toroidal decomposition:

$$\mathbf{u}=\boldsymbol{\nabla}\times\psi\mathbf{1}_z+\boldsymbol{\nabla}\times\boldsymbol{\nabla}\times\Phi\mathbf{1}z \qquad [67]$$

Since all the components of velocity are of similar order of magnitude (the boundary conditions ensure u_r and u_z are the same order), Φ is $O(\mathcal{E}^{1/3})$ smaller than ψ and so to leading order

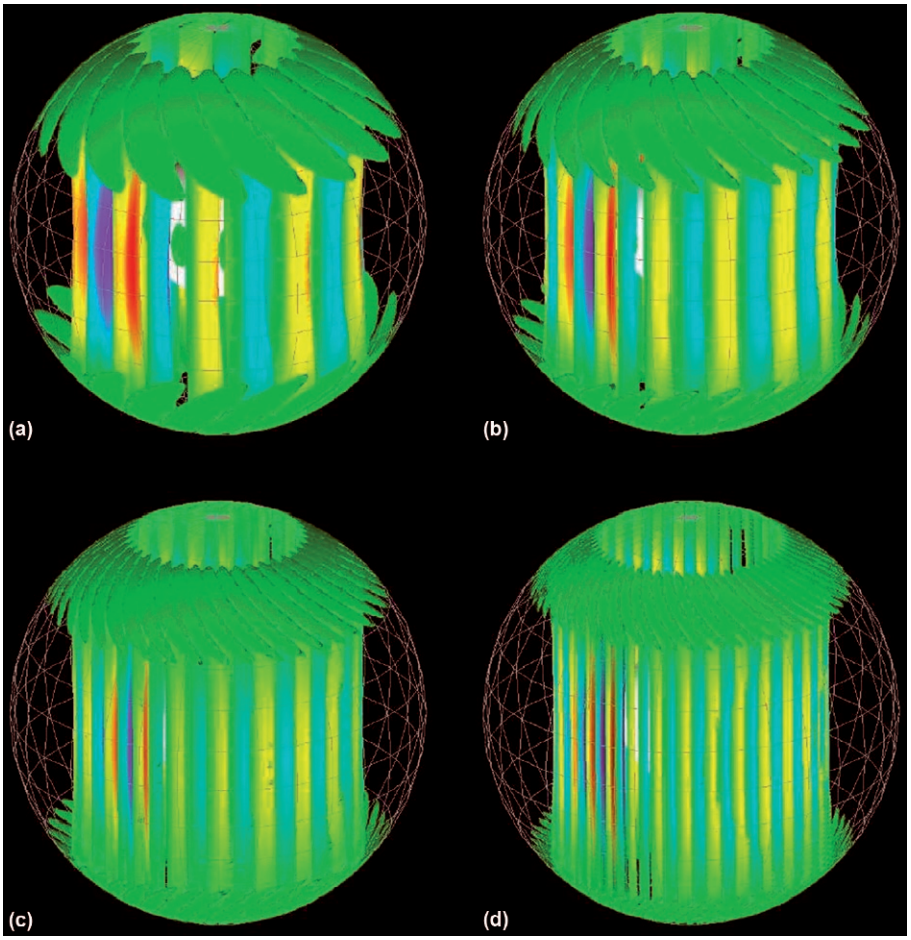

Figure 4 Contours of axial vorticity, colored according to the temperature perturbation, at the onset of convection in a spherical shell,radius ratio 0.35. (a) $\mathcal{E} = 3\times10^{-5}$, (b) $\mathcal{E} = 10^{-5}$, (c) $\mathcal{E} = 3\times10^{-6}$, (d) $\mathcal{E} = 10^{-6}$. This figure appeared in Dormy (1997).

$$\boldsymbol{u} = \nabla\times\psi\mathbf{1}_z + u_z\mathbf{1}_z \qquad [68]$$

Inserting this equation into the z-components of the linearized eqn [60] and its curl, the temperature equation [39], we obtain

$$\mathcal{E}\left(\frac{\partial}{\partial t}-\nabla^2\right)\nabla_H^2\psi + \frac{\partial u_z}{\partial z} = \mathcal{E}Ra\frac{\partial T'}{\partial\phi} \qquad [69]$$

$$\mathcal{E}\left(\frac{\partial}{\partial t}-\nabla^2\right)\nabla^2 u_z - \frac{\partial}{\partial t}\left(\nabla_H^2\psi\right) = \mathcal{E}Ra\left[z\nabla_H^2 T' - \frac{1}{s}\frac{\partial}{\partial s}\left(s^2\frac{\partial T'}{\partial z}\right)\right] \qquad [70]$$

$$\left(Pr\frac{\partial}{\partial t}-\nabla^2\right)T' = \mathcal{Q}\left(\frac{\partial\psi}{\partial\phi} + zu_z + s\frac{\partial^2\Phi}{\partial s\partial z}\right),$$
$$\nabla_H^2\Phi = -u_z, \qquad \nabla_H^2 = \frac{1}{s}\frac{\partial}{\partial s}s\frac{\partial}{\partial s} + \frac{1}{s^2}\frac{\partial^2}{\partial\theta^2} \qquad [71]$$

The local theory starts by seeking solutions with dependence $\exp\mathrm{i}\left(\tilde{k}s + \tilde{m}\phi - \tilde{\omega}t\right)$ and assuming that the wavelengths perpendicular to the z-direction are $O(\mathcal{E}^{1/3})$, and the Rayleigh number and frequency follow the scalings mentioned above. We write

$$Ra = \mathcal{E}^{-4/3}\mathcal{R},\quad \tilde{\omega} = \mathcal{E}^{-2/3}\omega,\quad \tilde{m} = \mathcal{E}^{-1/3}m,\quad \tilde{k} = \mathcal{E}^{-1/3}k,\quad a^2 = \frac{m^2}{s^2} + k^2 \qquad [72]$$

Some terms drop out, and the leading-order equation for u_z then becomes a second-order equation for z, known as the Roberts–Busse equation,

$$\mathcal{F}\frac{\mathrm{d}}{\mathrm{d}z}\frac{1}{\mathcal{F}}\frac{\mathrm{d}u_z}{\mathrm{d}z} + \left[\left(a^2-\mathrm{i}\omega\right)\mathcal{G} - \frac{\mathrm{i}m}{a^2-\mathrm{i}Pr\omega}\mathcal{F}\frac{\mathrm{d}}{\mathrm{d}z}\left(\frac{\mathcal{R}\mathcal{Q}z}{\mathcal{F}}\right)\right]u_z = 0 \qquad [73]$$

following the notation of Dormy et al. (2004), where

$$\mathcal{F} = \frac{m^2\mathcal{R}\mathcal{Q}}{a^2-\mathrm{i}Pr\omega} - a^2\left(a^2-\mathrm{i}\omega\right),$$
$$\mathcal{G} = \frac{\left(m^2+a^2z^2\right)\mathcal{R}\mathcal{Q}}{a^2-\mathrm{i}Pr\omega} - a^2\left(a^2-\mathrm{i}\omega\right) \qquad [74]$$

The stress-free boundary conditions are

$$\frac{\mathrm{d}u_z}{\mathrm{d}z} - \frac{\mathrm{i}a^2}{m}\left(a^2-\mathrm{i}\omega\right)zu_z = 0 \quad \text{at} \quad z = \pm\left(1-s^2\right)^{1/2} \qquad [75]$$

and for no-slip conditions

$$\frac{\mathrm{d}u_z}{\mathrm{d}z} - \frac{\mathrm{i}a^2}{m}\left(a^2-\mathrm{i}\omega\right)zu_z = \mathcal{E}^{1/6}\sqrt{\frac{r}{2z}}\frac{m^2+a^2z^2}{m^2}\mathcal{F}u_z$$
$$\text{at } z = \pm\left(1-s^2\right)^{1/2} \qquad [76]$$

from which it is clear that in the low $\mathcal{E}$ limit, the distinction between stress-free and no-slip boundary conditions is not

crucial. Physically, this is because the rolls are so thin that most of the dissipation is occurring in the bulk of the fluid and not in the boundary layer. Note that if these thin rolls excite a large-scale zonal flow, the bulk dissipation for that zonal flow will be very small, so then the dissipation in the boundary layer is crucial in determining the strength of the zonal flow. Just because the boundary conditions do not affect the linear rolls very much does not imply that boundary conditions are unimportant in nonlinear rotating convection.

The Roberts–Busse equation [73] can be solved numerically subject to the boundary conditions [75] or [76] as an eigenvalue problem, using any standard ODE eigenvalue numerical method. The real and imaginary parts determine the complex frequency ω for any given Rayleigh number $\mathcal{R}$. The imaginary part of the frequency is the exponential growth rate of the linear mode. The output of the eigenvalue solver is then the dispersion relation

$$\omega = \omega(s, k, m, \mathcal{R}) \qquad [77]$$

The difference between the original local theory of Roberts and Busse and the newer global theory lies entirely in how this dispersion relation is treated. The same equation (and hence the same dispersion relation) is used in both approaches. The local theory derives the equations for the five unknowns ω_L, s_L, k_L, m_L, and $\mathcal{R}_L$ from the five imaginary part conditions

$$\mathfrak{F}\{\omega\} = 0,\ \mathfrak{F}\left\{\left(\frac{\partial\omega}{\partial m}\right)_L\right\} = 0, \mathfrak{F}\left\{\left(\frac{\partial\omega}{\partial\mathcal{R}}\right)_L\right\} = 0,$$
$$\mathfrak{F}\left\{\left(\frac{\partial\omega}{\partial k}\right)_L\right\} = 0, \mathfrak{F}\left\{\left(\frac{\partial\omega}{\partial s}\right)_L\right\} = 0 \qquad [78]$$

which are that the scaled growth rate (the imaginary part of ω) should be zero and that the growth rate should be a local maximum of $\mathcal{R}$, m, k, and s. s_L is then the location of the local convective instability, that is, where the rolls first become unstable. For internal heating, the critical s_L is typically about $0.5r_{\mathrm{cmb}}$. The differential heating case does not have an internal local maximum for the growth rate (equivalently, a minimum critical Rayleigh number) but is maximized on the ICB.

In the differentially heated case, the local theory prediction for the critical Rayleigh number agrees with the fully 2-D spherical coordinate results, in the sense that as $\mathcal{E}$ is reduced, the results steadily approach the asymptotic results. However, in the internally heated case, where s_L is in the interior rather than at a boundary, there is no such agreement. In either case, the local solution must be part of a WKBJ expansion:

$$u_z(s, \phi, z) \sim \mathcal{W}(x) u_z(z) \exp\left(\mathrm{i}\int k\,\mathrm{d}s\right) \exp \mathrm{i}(m\phi - \omega t) \qquad [79]$$

In the differentially heated case, $k = 0$ at the ICB and k varies on an $(s - s_c)^{1/2}$ length scale near the ICB, so we introduce a scaled variable x given by

$$x = (s - s_{\mathrm{icb}})/\mathcal{E}^{2/9} \qquad [80]$$

Then, $\mathcal{W}(x)$ describes the variation in the s-direction, while the z-dependence comes from the Roberts–Busse equation [73]. The equation for the amplitude of the envelope, $\mathcal{W}(x)$, is derived by inserting eqn [79] into the governing equations, and with the differential heating case scaling for x, we obtain

$$-\frac{1}{2}\left(\frac{\partial^2\omega}{\partial k^2}\right)_L \frac{\mathrm{d}^2\mathcal{W}}{\mathrm{d}x^2} + \left(\frac{\partial\omega}{\partial s}\right)_L x\mathcal{W} + \left[\left(\frac{\partial\omega}{\partial\mathcal{R}}\right)_L \mathcal{R}_1 - \omega_1 + \left(\frac{\partial\omega}{\partial m}\right)_L m_1\right]\mathcal{W} = 0 \qquad [81]$$

where

$$\mathcal{R} = \mathcal{R}_L + \mathcal{E}^{2/9}\mathcal{R}_1, \quad m = m_L + \mathcal{E}^{2/9} m_1, \quad \omega = \omega_L + \mathcal{E}^{2/9}\omega_1 \qquad [82]$$

The Airy equation [81] can be solved subject to the boundary conditions

$$\mathcal{W} = 0 \ \text{ at } \ x = 0\,(s = s_{\mathrm{icb}}) \ \text{ and } \ \mathcal{W} \to 0 \ \text{ as } \ x \to \infty \qquad [83]$$

The Airy function solution therefore gives the leading-order asymptotic behavior in the radial direction, together with the z-dependence from the local Roberts–Busse equation. The leading-order critical Rayleigh number and frequency are therefore $\mathcal{R}_L$ and ω_L, and the first-order corrections come from the solution of eqn [81], which is an eigenvalue problem for $\mathcal{R}_1$ and $\omega_1 - m_1 \mathrm{d}\omega/\mathrm{d}m$. How ω_1 and m_1 are found individually is described in Dormy et al. (2004). In **Figure 5** (reproduced from Dormy et al., 2004), we see the planform of the rolls at onset for $\mathcal{E} = 10^{-7}$, $Pr = 1$. In the top row of **Figure 5**, numerical solution of the full equations has been used, while in the bottom row, the asymptotic theory was used. There is no great difference, suggesting that the asymptotic method works very well at $\mathcal{E} = 10^{-7}$ or less. The variation with radius ratio at onset was studied by Al-Shamali et al. (2004), using the numerical method rather than the asymptotic method.

The natural way to deal with the internally heated case would be to solve eqn [81] subject to the boundary conditions

$$\mathcal{W} \to 0 \ \text{ as } \ x \to \pm\infty \qquad [84]$$

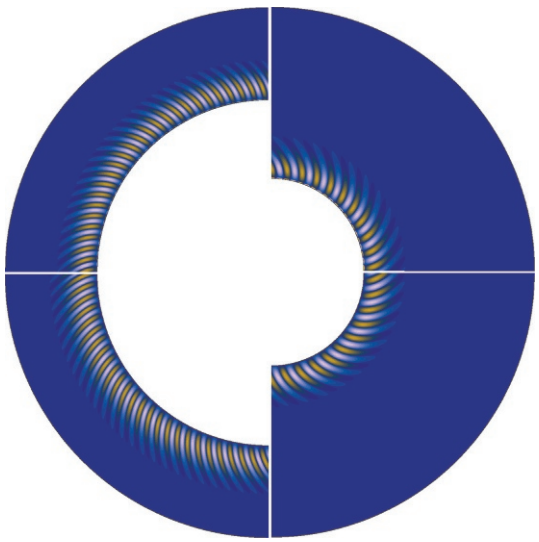

Figure 5 Comparison between equatorial cross-sections of the axial vorticity in the full numerics for $\mathcal{E}=10^{-7}$ (top row) and the asymptotic eigenfunction ψ for the same Ekman number (bottom row). Internal heating with large aspect ratio $r_{\mathrm{icb}}/r_{\mathrm{cmb}}$ on the left, differential heating with aspect ratio 0.35 on the right. Reproduced from Dormy E, Soward AM, Jones CA, Jault D, and Cardin P (2004) *Journal of Fluid Mechanics* 501: 43–70.

Unfortunately, no solution of eqn [81] satisfying eqn [84] exists, because of the term proportional to $(\partial\omega/\partial s)_L$. This means that when the onset of convection occurs away from the boundary, the local solution cannot be embedded in a consistent WKBJ solution. The solution to this difficulty is quite radical (Jones et al., 2000) and consists of abandoning the s_L found by local theory. Instead we seek a point in the complex s-plane, s_c, at which the real part

$$\Re\{\partial\omega/\partial s\} = 0 \qquad [85]$$

as well as the imaginary part being zero. We therefore solve eqn [78] together with eqn [85], so with s-complex, we now have six equations for six unknowns to find the global instability criteria. The coefficient of the term proportional to x in the amplitude equation [81], which is the term that makes it impossible to satisfy the boundary conditions [84], is now zero. The scaling for x now changes to

$$x = (s - s_c)/\mathcal{E}^{1/6} \qquad [86]$$

in the neighborhood of s_c and the amplitude equation becomes

$$-\frac{1}{2}\left(\frac{\partial^2\omega}{\partial k^2}\right)_c \frac{\mathrm{d}^2\mathcal{W}}{\mathrm{d}x^2} + \frac{1}{2}\left(\frac{\partial^2\omega}{\partial s^2}\right)_c x^2\mathcal{W} + \left[\left(\frac{\partial\omega}{\partial\mathcal{R}}\right)_c \mathcal{R}_1 - \omega_1 + \left(\frac{\partial\omega}{\partial m}\right)_c m_1\right]\mathcal{W} = 0 \qquad [87]$$

all derivatives being evaluated at the complex s_c. This now has a satisfactory solution in parabolic cylinder functions satisfying eqn [84].

Since the equations used to find the critical Rayleigh number and frequency are different from the local theory (six equations, not five), the results are different. The critical Rayleigh number is significantly higher (typically 25% higher at $Pr \sim 1$ or greater, but with a much larger difference at low Prandtl number) for this global theory than for local theory. The ways in which the solutions for complex $s = s_c$ are converted into real eigenfunctions and how the value of s_c (the point where the disturbance has maximum amplitude) is determined are detailed in Jones et al. (2000). In physical terms, this surprising result can be understood in terms of phase mixing. Disturbances that try to grow at the local critical Rayleigh number are sheared apart by the variation of ω with s. Because of the increasing slope of the boundaries with s in spherical geometry, waves at larger s travel with faster phase speed. It is therefore more difficult to get a disturbance inside an envelope where each part has to travel at the same speed when each part wants to travel at a different speed. At low Prandtl number, the disturbance occupies a much greater range of s, and the problem of 'orchestration' is more difficult, which is why the global critical Rayleigh number has to be much greater than the local critical Rayleigh number.

8.05.4.4 The Ekman Boundary Layers

In eqns [75] and [76], we noted that the boundary condition in the Roberts–Busse equation was affected by whether the boundary was no-slip or stress-free. This difference comes about because of the presence of Ekman layers near the boundary. Ekman layers are the thin boundary layers of thickness $O((\Omega/\nu)^{1/2})$ over which the velocity changes from its interior value to the value at the rigid boundary, usually taken to be zero. In this respect, the boundary layer is similar to the thin layers in nonrotating flow, for example, over aircraft wings. There are, however, some important differences. Ekman layers have an unusual *suction* property. At the boundary itself, the velocity is zero, while at the 'edge' of the boundary layer, the velocity parallel to the wall merges into its interior value. Somewhat surprisingly, at the edge of the boundary layer, there is a nonzero component of velocity perpendicular to the wall, called the Ekman suction. This velocity can be either outward or inward, depending on the sign of the interior fluid vorticity. If the horizontal length scale of this external vorticity is d, we can define an Ekman number $E = \nu/\Omega d^2$, and then, this suction velocity is $O(E^{1/2})$ times the parallel velocity components. This might seem negligibly small, but in fact, it can have quite a significant effect on the dynamics.

The Ekman suction affects the spin-up (or spin-down) time of rotating fluid, that is, the time taken for fluid initially at rest in a rotating frame to achieve rigid body rotation, subsequent to a sudden change in the container rotation speed. Naively, one might expect the spin-up time to be $O(d^2/\nu) \sim 10^{11}$ years for the core, this being the typical time for momentum to diffuse through the fluid by internal friction. Actually, the time is $O(E^{1/2})$ times this value, or about 5000 years, because all the fluid in the sphere is pumped into the boundary layer, where it acquires the boundary velocity much more rapidly. Recent experiments (Brito et al., 2004) have measured the spin-up time and found good agreement with the times predicted by the Ekman layer theory. They also find that if low Prandtl number fluid is convecting, the spin-up time is significantly shortened, suggesting that the convective turbulence is affecting the Ekman layer. The usual theory assumes a laminar Ekman layer.

The Ekman layer is studied by assuming E is small and considering the thin layer in which viscous forces, pressure forces, and Coriolis forces are in balance:

$$2\boldsymbol{\Omega} \times \mathbf{u} = -\frac{1}{\rho}\nabla p + \nu\nabla^2\mathbf{u} \qquad [88]$$

Because the layer is thin, the gradient of $\mathbf{u}$ in the direction perpendicular to the boundary is much larger than gradients in other directions, and these can therefore be ignored by comparison. Greenspan (1968) showed that the Ekman suction is

$$\mathbf{u}\cdot\mathbf{1}_n|_{z=\pm H} = \mp\frac{1}{2}\left(\frac{\nu}{\Omega}\right)^{1/2} \mathbf{1}_n\cdot\nabla\times\left[\frac{1}{(\mathbf{1}_n\cdot\mathbf{1}_z)^{1/2}}(\mathbf{1}_n\times\mathbf{u}+\mathbf{u})\right] \qquad [89]$$

where $\mathbf{1}_n$ is the unit vector normal to the wall pointing out of the fluid. Here, $\mathbf{u}\cdot\mathbf{1}_n|_{z=H}$ denotes the asymptotic value of the normal velocity at the northern hemisphere boundary ($-H$ for southern hemisphere boundary) as we move out of the boundary layer into the interior.

The simplest case is when the boundary is normal to the rotation axis, as near the poles. For the south pole, $\mathbf{1}_n = -\mathbf{1}_z$, when [89] reduces to $u_z = (\nu/\Omega)^{1/2}\zeta_z/2$, so that the suction is proportional to the z-component of the interior vorticity just above the boundary layer. Anticyclonic vorticity gives suction into the boundary at either pole, cyclonic (in the same sense as the rotation) vorticity to motion away from the boundary. We take the z-component of the curl and double curl of eqn [88] to get

$$-2\Omega\frac{\partial u_z}{\partial z}=\nu\frac{\partial^2\zeta_z}{\partial z^2},\quad 2\Omega\frac{\partial\zeta_z}{\partial_z}=\nu\frac{\partial^4 u_z}{\partial z^4} \qquad [90a,b]$$

which can be combined to give

$$\frac{\partial u_z}{\partial z}=-4E^2d^4\frac{\partial^5 u_z}{\partial z^5} \qquad [91]$$

We can add on H to z without changing these formulas, thus bringing the wall to the level $z=0$. The solution then consists of a constant plus four exponential terms corresponding to the four complex fourth roots of -4 ($\pm1\pm i$). The two with positive real part correspond to solutions that grow as we move out of the boundary layer and are therefore unacceptable. We are left with

$$u_z=u_z^i+\exp\left(-\frac{z}{d\sqrt{E}}\right)\left(A\cos\frac{z}{d\sqrt{E}}+B\sin\frac{z}{d\sqrt{E}}\right)$$
$$\zeta_z=\zeta_z^i+\exp\left(-\frac{z}{\sqrt{2E}}\right)\left(\frac{A+B}{d\sqrt{E}}\cos\frac{z}{d\sqrt{E}}+\frac{B-A}{d\sqrt{E}}\sin\frac{z}{d\sqrt{E}}\right) \qquad [92a,b]$$

and the boundary conditions are that $u_z=0$, $\partial u_z/\partial z=0$, and $\zeta=0$ at the wall, $z=0$. The last two follow from the fact that $u_x=u_y=0$ at the wall, so horizontal derivatives are zero, and $\nabla\cdot\mathbf{u}=0$. Inserting these into eqn [92a,b] gives $A=B=-u_z^i$, $\zeta_z^i=2E^{-1/2}u_z^i/d$, consistent with eqn [89]. Since the A and B terms in eqn [92a,b] vanish as we move up into the interior, the constants of integration ζ_z^i and u_z^i have a natural interpretation as the interior vorticity just after leaving the boundary layer and the Ekman suction, respectively. The Ekman layer in the core is <1 m thick, and so any roughness at the CMB or ICB may lead to a thickening of the layer.

The effect of Ekman suction on the onset of convection was investigated by Zhang and Jones (1993). They found that at high Prandtl numbers, it is stabilizing, but at low Prandtl numbers, it can be destabilizing. At low E, the effect of Ekman suction on the tall thin columns is small, and then, the most important effect of the Ekman suction is on the zonal flow.

8.05.4.5 The Busse Annulus

The discussion in Sections 8.05.4.1–8.05.4.3 showed that the sloping boundaries are crucial when considering the onset of rotation in convecting spherical geometry. Busse (1970) pointed out that a simplified model for the convection in a sphere is to consider a cylindrical annulus with sloping top and bottom boundaries (see Figure 6). The gravity is assumed to act in the $-\mathbf{i}_s$-direction.

If we now take the limit in which the angle of slope of the annulus, $\chi\ll1$, then the motion is almost geostrophic. The z-component of the velocity is now small compared with the other two components, and so we can write

$$\mathbf{u}=\nabla\times\psi(s,\phi)\mathbf{1}_z+u_z\mathbf{1}_z \qquad [93]$$

because the horizontal part of the flow is much larger and 2-D flow with zero divergence must be the curl of a scalar. There is a distinction between eqns [68] and [93] because in eqn [68], we retained the z-dependence of ψ, whereas in the annulus model, this disappears because of the small slope assumption. The annulus is also assumed to be thin, so that the curvature terms can be neglected, which means that the ϕ coordinate is replaced by a Cartesian x-coordinate, that is, $(1/s)\partial/\partial\phi$ becomes $\partial/\partial x$, and s is replaced by $-\gamma$.

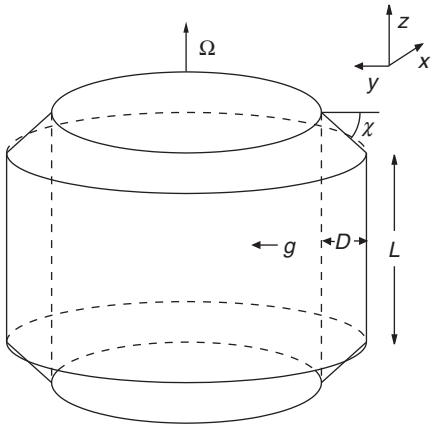

Figure 6 Geometry of the Busse annulus. The angle χ is assumed small, as is the gap-width to depth ratio, D/L. The x direction corresponds to the ϕ direction, and the y direction to the $-s$ direction in spherical geometry.

Our fundamental equation is [55], the vorticity equation. We assume small Rossby number so the planetary vorticity dominates the fluid vorticity, so the term $\boldsymbol{\zeta}\cdot\nabla\mathbf{u}$ is omitted. The z-component of the vorticity equation [55] is then

$$\frac{\partial\zeta}{\partial t}+\mathbf{u}\cdot\nabla\zeta-2\Omega\frac{\partial u_z}{\partial z}=-g\alpha\frac{\partial T'}{\partial x}+\nu\nabla^2\zeta \qquad [94]$$

Although the z-component of velocity u_z is small, $O(\chi)$, compared with the other components in [93], the rotation is large, so that the stretching of the planetary vorticity is important. Integrating over z and applying the boundary conditions $u_z=\pm\chi u_y$ on $z=\pm L/2$ give

$$\frac{\partial\zeta}{\partial t}+\frac{\partial(\psi,\zeta)}{\partial(x,\gamma)}-\frac{4\chi\Omega}{L}\frac{\partial\psi}{\partial x}=-g\alpha\frac{\partial T'}{\partial x}+\nu\nabla^2\zeta \qquad [95]$$

Note that in assuming this boundary condition, we have discarded any Ekman layer contribution from the endwalls. We are therefore assuming implicitly that they are stress-free. Nondimensionalizing on the gap between the cylinders D, timescale D^2/ν, and temperature $\nu\Delta T/\kappa$, ΔT being the temperature drop between the cylindrical boundaries, we get

$$\frac{\partial\zeta}{\partial t}+\frac{\partial(\psi,\zeta)}{\partial(x,\gamma)}-\beta\frac{\partial\psi}{\partial x}=-Ra\frac{\partial T'}{\partial x}+\nabla^2\zeta,\quad \zeta=\nabla^2\psi \qquad [96a,b]$$

The z-vorticity can be written in terms of the stream function ψ from eqn [93]. The temperature equation [39] becomes

$$Pr\left[\frac{\partial T'}{\partial t}+\frac{\partial(\psi,T')}{\partial(x,\gamma)}\right]=-\frac{\partial\psi}{\partial x}+\nabla^2T' \qquad [97]$$

where

$$Ra = \frac{g\alpha\Delta T D^3}{\kappa\nu}, \quad \beta = \frac{4\chi\Omega D^3}{L\nu} \qquad [98]$$

The rotation enters these equations explicitly only through the β-parameter; apart from this term, the equations are identical to those of 2-D Rayleigh–Bénard convection. Rotation has been invoked implicitly, though to justify the two-dimensionality of the flow. Equation [96a,b] is commonly used in the atmospheric sciences community where it is known as the beta-plane equation.

8.05.4.5.1 Linear properties of the annulus model

If we linearize these equations, by dropping the Jacobian terms in eqns [96a,b] and [97], and adopt the convenient no-penetration, stress-free, constant temperature boundary conditions at the sidewalls,

$$\psi = \frac{\partial^2\psi}{\partial\gamma^2} = 0, \quad T' = 0, \quad \text{on} \quad \gamma = \pm\frac{1}{2} \qquad [99]$$

then there is a simple solution

$$\psi = \exp \mathrm{i}(kx - \omega t)\cos\pi\gamma, \quad T' = \frac{-\mathrm{i}k}{k^2 + \pi^2 - \mathrm{i}\omega Pr}\psi \qquad [100a,b]$$

provided

$$\omega = \frac{\beta k}{(1+Pr)(\pi^2+k^2)}, \quad Ra = \frac{(\pi^2+k^2)^3}{k^2} + \frac{Pr^2\beta^2}{(\pi^2+k^2)(1+Pr)^2} \qquad [101a,b]$$

The equation for ω is the dispersion for thermal Rossby waves, and the expression for Ra is the critical Rayleigh number for the onset of convection. If $\beta = 0$, the onset of convection is steady, but the presence of the rotation means that convection onsets in the form of traveling waves. The critical wave number k for the onset of instability is found by setting

$$\frac{\mathrm{d}Ra}{\mathrm{d}k} = 0 \qquad [102]$$

Note also that if $\beta = 0$, we recover Rayleigh's famous result for the onset of convection $Ra_c = 27\pi^4/4$ with $k = \pi/\sqrt{2}$.

The thermal Rossby waves travel with phase speed c_s and group velocity c_g

$$c_s = \frac{\omega}{k} = \frac{\beta}{(1+Pr)(\pi^2+k^2)}, \quad c_g = \frac{\mathrm{d}\omega}{\mathrm{d}k} = \frac{\beta(\pi^2-k^2)}{(1+Pr)(\pi^2+k^2)^2} \qquad [103a,b]$$

If β is positive, the phase speed is positive, so the waves propagate eastward. This will be the case outside the TC. Inside the TC, the integration over z leads to a negative β, so waves travel westward there. From [100b], we see that rotation delays the onset of convection, as we expect. The rapid rotation limit $\beta \to \infty$ is the most instructive; we find

$$k = \frac{\beta^{1/3}Pr^{1/3}}{2^{1/6}(1+Pr)^{1/3}}, \quad \omega = \frac{\beta^{2/3}2^{1/6}}{Pr^{1/3}(1+Pr)^{2/3}}, \quad Ra = \frac{3\beta^{4/3}Pr^{4/3}}{2^{2/3}(1+Pr)^{4/3}} \qquad [104a,b,c]$$

Since β is essentially $1/E$ multiplied by factors to account for the particular geometry of the annulus, it is comforting to note that these are the same scalings found for Ra, ω, and k in Sections 8.05.4.2 and 8.05.4.3 in the rapid rotation limit. It is also interesting to note that although the phase speed is always eastward, the group velocity is westward for rapid rotation. Note also that it follows from the dispersion relation that the larger wavelengths have a higher-phase speed than the smaller 'tall thin column' modes.

8.05.4.5.2 Weakly nonlinear theory and the annulus model

Equations [96a,b] and [97] can also be solved in the nonlinear regime to investigate rapidly rotating convection at large Ra. One method is to solve these 2-D equations numerically using the pseudo-spectral method, and this is described in Section 8.05.4.5.3. It is also possible to use weakly nonlinear theory to investigate nonlinear behavior in rotating (and magnetic) systems at Rayleigh numbers just above critical.

The fundamental idea of weakly nonlinear theory is that just above critical, the spatial form of the convection is still approximately that given by linear theory. It can be shown that for Rayleigh numbers sufficiently close to critical, this will always be true, but in some situations, weakly nonlinear theory still gives a reasonable picture of behavior well above critical, while in other situations, it breaks down quite quickly. The great advantage of weakly nonlinear theory is that it avoids the solution of multidimensional partial differential equations. This means that although the theory may be quite hard to formulate, once that task is done, the parameter space can be covered much more thoroughly than is possible for DNS simulations. Weakly nonlinear theory is most useful for suggesting possible behavior and developing understanding of rotating convection. Because its domain of validity cannot be determined a priori, results using it do need to be checked against DNSs.

Weakly nonlinear theory for fluid problems was developed in the late 1950s, but the theory for the annulus model was given by Busse and Or (1986). The velocity is expanded in a power series

$$\psi = \varepsilon\psi_1 + \varepsilon^2\psi_2 + \varepsilon^3\psi_2 + \cdots \qquad [105]$$

with a similar expansion for the temperature perturbation

$$T' = \varepsilon T'_1 + \varepsilon^2 T'_2 + \varepsilon^3 T'_3 + \cdots \qquad [106]$$

Here, ε is the small parameter, and the Rayleigh number and the frequency must also be expanded in ε:

$$Ra = Ra_c + \varepsilon R_1 + \varepsilon^2 R_2 + \cdots, \quad \omega = \omega_c + \varepsilon\omega_1 + \varepsilon^2\omega_2 + \cdots \qquad [107]$$

We insert these expansions into eqns [96a,b] and [97] and equate like powers of ε. At first order in ε, there are no contributions from the nonlinear terms, and we just recover the linear theory. The solution then determines Ra_c and ω_c just as above, and ψ_1 and T'_1 are the standard linear eigenfunctions. The nonlinear terms start to appear at $O(\varepsilon^2)$. In the annulus problem, these nonlinear terms can be balanced by second-order terms in ψ and T'; for example, the nonlinear terms in the temperature equation give rise to a term proportional to $\varepsilon^2 \sin \pi\gamma \cos \pi\gamma$, which leads to a T'_2 term also proportional to $\sin 2\pi\gamma$. However, at the next order, $O(\varepsilon^3)$, some nonlinear terms have the same x- and γ-dependence as the linear solution, $\exp \mathrm{i}kx \cos \pi\gamma$. These are called resonant terms, and they cannot be allowed, because no finite terms in ψ and T' can balance them. We must arrange that these resonant terms have

a zero coefficient, and this gives equations that determine R_2 and ω_2. The absence of resonant terms at $O(\varepsilon^2)$ in this problem, which is symmetrical about $\gamma=0$, means that $R_1=\omega_1=0$. This procedure can be extended to higher orders, and at third order, a mean flow appears, that is, a flow u_x that does not average to zero in the x-direction. These flows are called zonal flows and have been much studied recently because large zonal flows are seen in the atmospheres of giant planets.

The idea of weakly nonlinear theory can be extended to the case of the rapidly rotating annulus (Abdulrahman et al., 2000). Now, we have two small parameters, the amplitude ε and the small horizontal wavelength $O(\beta^{-1/3})$. The behavior depends on the relative size of these small quantities, but the most interesting case is when $\varepsilon\sim\beta^{-1/3}$. It is then possible to derive nonlinear partial differential equations in γ and t only. In this system, the x-dependence is given by a wavy mode with the linear critical wave number, but the γ-dependence can vary from its onset form. This makes it possible to analyze the bifurcations that occur as the Rayleigh number is increased. Interestingly, all these bifurcations occur in a range of Rayleigh number for which Ra/Ra_c is only $O(\beta^{-2/3})$ above critical, so that the transition from steady rolls to chaotic convection takes place when the Rayleigh number is only slightly supercritical. Because the curvature is neglected in the annulus model, the system is symmetrical about the midplane in γ, that is, if the sidewalls are at $\gamma=\pm d/2$, there is a symmetry about $\gamma=0$. The zonal flow driven by the convection initially has this symmetry and has an approximately parabolic form. However, as the Rayleigh number is increased, a symmetry-breaking bifurcation occurs, and the zonal flow becomes asymmetrical about $\gamma=0$ (Abdulrahman et al., 2000; Or and Busse, 1987). With no curvature, there is nothing to distinguish the two asymmetrical zonal flow patterns corresponding to eastward or westward flow at the outer boundary, but if small curvature is introduced, then the zonal flow, which is eastward on the outer boundary, is preferred, corresponding to a prograde equatorial zonal flow in spherical shell geometry.

8.05.4.5.3 Zonal flows and multiple jets

The 2-D nonlinear equations [96a,b] and [97] can be integrated forward in time very efficiently, using fast Fourier transforms in Cartesian geometry with a pseudo-spectral method in which ψ and T' have expansions of the form

$$\psi=\sum_{l=-(N_x-1)}^{N_x-1}\sum_{m=1}^{N_\gamma}\psi_{lm}\exp^{(2\pi l x/L_x)}\sin m\pi\gamma \qquad [108]$$

This means that values of $\beta\sim10^6$ (low E) can be achieved (see Abdulrahman et al., 2000; Brummell and Hart, 1993; Teed et al., 2012). This makes the annulus model a powerful tool for the study of zonal flows. Zonal flow strength can be significantly affected by Ekman suction, which we omitted when we set $u_z=\pm\chi u_\gamma$ on $z=\pm L/2$. If we now include the Ekman suction term [89], remembering that χ is small, there is now a boundary term when we integrate eqn [94] over z, and eqn [96a,b] becomes

$$\frac{\partial\zeta}{\partial t}+\frac{\partial(\psi,\zeta)}{\partial(x,\gamma)}-\beta\frac{\partial\psi}{\partial x}=-Ra\frac{\partial T'}{\partial x}-C|\beta|^{1/2}\zeta+\nabla^2\zeta \qquad [109]$$

(details being given in Abdulrahman et al. 2000). The extra term proportional to the geometric constant of order unity, C, represents a damping due to the Ekman boundary layer. In experiments, this term can often be larger than the internal friction $\nabla^2\zeta$, for the zonal flow.

Strong zonal flow can affect the convection that sustains it. Indeed, the shear can suppress convection, so that the zonal flow can bite the hand that feeds it. This leads to a range of interesting dynamical behavior, for example, convection may become localized in space or in time, so that convection does not occur continuously, but only in bursts when the zonal flow is particularly weak (Busse, 2002; Rotvig and Jones, 2006; Teed et al., 2012).

In the Earth's core, zonal flows can be strongly affected by magnetic fields (Aubert, 2005), but the formation of zonal flow patterns is an important feature of rotating convecting flows. Simulations show that these east–west flows can build up to a very large amplitude, so that the kinetic energy in the jets can be much larger that the kinetic energy of the nonaxisymmetric rolls that are transporting the heat. An issue that has attracted much attention recently is the formation of multiple jets. The giant planets, particularly Jupiter, have a zonal flow pattern that has an alternating pattern of eastward and westward jets as the latitude varies. Numerical simulations of spherical convection at moderate Rayleigh number and Ekman number show a much simpler pattern, with a prograde (eastward) flow near the equator and a retrograde flow near the poles. The Sun has a differential rotation pattern of this form. In terms of the annulus model, the zonal flow comes from the $l=0$ mode in eqn [108], and a multiple jet solution is one on which this $l=0$ mode is dominated not by $m=1$ but by a higher m value. The boundary conditions have some effect on the appearance of multiple jets. If there is a no-slip boundary on the sloping boundaries, an Ekman layer is created, which leads to Ekman suction and hence damping in the interior. This reduces the magnitude of the zonal flows, which makes multiple jets more common. Increasing β to very high values also favors the formation of multiple jets. However, in the core, the pattern of the zonal flow is determined by the magnetic field, so we will not pursue these interesting nonmagnetic problems further here.

8.05.4.6 The Quasi-geostrophic Approximation

The Busse annulus model is a 2-D model that captures many of the essential features of rapidly rotating convection in spherical geometry found in experiments (see **Chapter 8.13**): convection occurs in the form of tall thin columns, it onsets as thermal Rossby waves propagating prograde, and large zonal flows develop that may have a multiple jet structure. The annulus model can only be rigorously derived when the slope of the boundaries is small, and it is limited because it does not take into account the strong variation of the boundary slope χ that occurs in spherical geometry (see **Figure 5**). The key property of the annulus model is that the axial vorticity is z-independent, thus reducing the problem from three to two dimensions. Both the linear theory of convection and experiments suggest that the axial vorticity does not vary strongly with z even in spherical geometry (Gillet and Jones, 2006). There is some variation with z but it is numerically small, suggesting that

assuming axial vorticity is z-independent may be a good approximation, even though it cannot be rigorously derived in any limit. If this is done, it follows that u_s and u_ϕ are also z-independent and that u_z is only linearly dependent on z. This is the essence of the quasi-geostrophic approximation (QGA) for rapidly rotating fluids. Detailed discussions of this approximation are given in Aubert et al. (2003) and numerical results using it in Morin and Dormy (2004) and Gillet and Jones (2006). Another way of viewing the QGA is that the terms omitted by assuming χ is small are not very important even when χ is $O(1)$, so that the QGA behavior is qualitatively similar to that of full spherical convection provided the rotation is very large. Note that one of these omitted terms is the z-component of gravity. In the experiments, where gravity is replaced by centrifugal acceleration (see **Chapter 8.13**), there is no z-component of gravity, so the QGA may be particularly appropriate. The QGA will certainly break down if the Rossby number becomes $O(1)$ or larger, because then the convection will no longer be columnar. The QGA gives useful results that can be compared with experiments (Gillet and Jones, 2006) and has the great advantage that because it is relatively easier to solve 2-D problems, the heat transport and the zonal flow can be explored over a wide range of parameter space. The zonal flow $\bar{u}_\phi$ is the ϕ average of u_ϕ, and it is found by taking the ϕ average of the ϕ component of eqn [38], remembering that the z average has already been taken, so we are effectively averaging over cylinders of radius s,

$$\left(\frac{\partial}{\partial t}-\nu\left[\nabla_H^2-\frac{1}{s^2}-\frac{E^{-1/2}r_{\mathrm{cmb}}^{1/2}}{\mathrm{d}H^{3/2}}\right]\right)\bar{u}_\phi=-\overline{\mathbf{u}\cdot\nabla_{\mathbf{u}_\phi}} \qquad [110]$$

where H is the height of the CMB above the equatorial plane, $H=(r_{\mathrm{cmb}}^2-s^2)^{1/2}$. On the left-hand side, the viscous force splits into two parts, the bulk friction and the Ekman suction, and in a steady state, these must balance the driving by the Reynolds stresses on the right-hand side. Frequently, the driving is quite strong and the viscosity is small, so a large zonal flow is needed to bring this equation into balance. However, even quite weak Lorentz forces will upset this balance, so we can expect zonal flows to be radically different in the magnetic case. The QGA cannot be used (at least in its present form) for convection inside the TC because the axial vorticity there does depend quite strongly on z; indeed, it can change sign as z varies. It is also unlikely to do well near the CMB equatorial regions, where the boundary slope is large.

8.05.4.7 Thermal Wind

Perhaps the least satisfactory feature of the QGA is that it is necessary to assume the temperature has no variation perpendicular to gravity. This may not be true in the core; it certainly is not true in the Earth's atmosphere where the poles are much colder than the equator. The ϕ component of eqn [55], omitting viscosity, time-dependence, and assuming small Rossby number, gives

$$2\Omega\frac{\partial u_\phi}{\partial z}=\frac{g\alpha}{r}\frac{\partial T'}{\partial\theta} \qquad [111]$$

This is the thermal wind equation. Note that now we have omitted the Reynolds stress term on the right-hand side of eqn [110] and internal friction and Ekman suction, so this is a very different balance from that envisaged in eqns [109] and [110], but it may be more realistic in the core. In the northern hemisphere of the Earth's atmosphere, where cold arctic air comes close to warm equatorial air, there is a strong positive $\partial T'/\partial\theta$ and hence the zonal east–west flow increases rapidly upward from eqn [111]. At ground level, the atmosphere is constrained to rotate at the same speed as the Earth, but at great heights, the resulting jet stream significantly shortens airplane travel times going from west to east. In the core, there is evidence from the secular variation that there are anticyclonic vortices near the poles in the Earth's core (Olson and Aurnou, 1999). If the origin of these vortices is a thermal wind (Aurnou et al., 2003; Sreenivasan and Jones, 2005), then the polar regions inside the core must be warmer (less dense) than the equatorial regions. Order of magnitude estimates show that even very small latitudinal temperature variations, of the order of 10^{-3} K, can give rise to the observed anticyclonic vortices. As mentioned in **Section 8.05.4.1**, the motion across the TC is likely to be small in the core, so a buildup of light material and hot material released from the inner core may accumulate inside the TC.

Since the thermal wind produces a variation of zonal flow with z, the flow not only may be anticyclonic near the CMB but also may be cyclonic (eastward) near the ICB. This could lead to a superrotation of the inner core, that is, an inner core rotating faster than the mantle. There is some seismological evidence that the inner core is rotating faster than the mantle, by about 0.3° per year (Collier and Helffrich, 2001; Song, 1996; Zhang et al., 2005), but it is controversial (Souriau et al., 2003; see also the **Chapter 1.23**). If the inner core and the mantle are both slightly nonaxisymmetric, gravitational coupling (Buffett and Glatzmaier, 2000) may lock the inner core to the mantle, allowing only an oscillation between the two rather than a continuous relative rotation.

8.05.4.8 Scaling Laws and Heat Transport in Nonlinear Rapidly Rotating Convection

The weakly nonlinear theory of **Section 8.05.4.5.2** can be used to predict behavior just above critical, but when the flow becomes turbulent, we would not expect a theory based on convection having the same pattern as it has near onset to be appropriate. In particular, at low Prandtl number, the flow speed and the heat transport grow only slowly with Ra/Ra_c-1 when Ra is very close to Ra_c, but simulations indicate that much more rapid growth of heat transport and flow speed occurs when Ra/Ra_c-1 is $O(1)$ (Gillet and Jones, 2006; Plaut and Busse, 2002). A turbulent 2-D flow is one where columnar eddies grow and decay continually throughout the fluid. They typically last a turnover time, which means their lifetime is about ℓ/U_*, where ℓ is the typical length scale transverse to the rolls ($\ell\ll d$, where d is the integral length scale, either the radius of the sphere or the gap width as appropriate) and U_* is the typical fluid velocity. Near onset, we expect $\ell\sim\mathrm{d}E^{1/3}$, but in a strongly nonlinear regime, we might expect that ℓ becomes independent of ν as a turbulent cascade develops. The usual situation in

turbulence is that the very small value of ν only affects the very small length scale at which the viscous dissipation occurs, and the only effect of reducing ν further is to extend the cascade so that the dissipation length becomes even smaller, without significantly affecting the behavior at the larger length scales. Note that here, we are only discussing rapidly rotating convection, by which we mean that the velocity is small enough so the Rossby number is small, and so the convection remains columnar. As we increase the Rayleigh number, the typical velocity will increase, so we must also increase the rotation rate in order to remain in the rapidly rotating regime. If the Rayleigh number is increased at fixed rotation rate, eventually the Rossby number will become order unity and a different regime is entered. Because the Earth's core has low Rossby number, we focus here only on the rapidly rotating regime and do not discuss what happens at intermediate Rossby number.

8.05.4.8.1 The inertial theory of rapidly rotating convection

A scaling independent of viscosity was proposed by Ingersoll and Pollard (1982) and developed by Aubert et al. (2001). The key idea is that there is a three-term balance in the axial vorticity equation [55] between vorticity advection, vortex stretching, and vorticity generation by buoyancy. We cannot give exact results without detailed numerical simulation, but here, we simply try to identify the dominant terms in the equations and hence to see how quantities such as the typical velocity scale. In this spirit, we denote the typical vorticity by ζ_* and the typical temperature perturbation by T_*' to get

$$\zeta_* \sim \frac{U_*}{\ell}, \quad U_*\zeta_*/\ell \sim \Omega U_*/d \sim g\alpha T_*'/\ell \qquad [112]$$

We have omitted the factor 2 in the vortex stretching term, because it can be absorbed in the definition of the typical length scales, and we are only interested in the scalings. Note however that it is d not ℓ that appears in the vortex stretching term, because the axial velocity only varies on the long length integral scale in columnar convection. The balance of inertial advection against buoyancy in nonrotating convection, eqn [49], would be the same as in eqn [112] if ℓ is taken as the mixing length. In rapidly rotating convection, the vorticity constraint impedes movement in the s-direction (the Proudman–Taylor constraint) because of the sloping endwalls, so we can view eqn [112] as a mixing-length balance but with the mixing length much reduced from d to ℓ. Another way of viewing this is that as a hot fluid column attempts to move outward in the s-direction, the Coriolis force turns it sideways in a distance ℓ.

The temperature perturbation is determined by the convective heat flux per unit area as in eqn [50]

$$F_{\text{conv}} \sim \rho c_p U_* T_*' \qquad [113]$$

where ρ is the fluid density and c_p the specific heat at constant pressure and F_{conv} a typical value of the convective heat flux per unit area. To complete the theory, we need a relation giving the convective heat flux in terms of the superadiabatic temperature difference between the ICB and the CMB. We discuss this in the succeeding text, but for geophysical (and astrophysical) applications, usually more is known about the heat flux than about temperature differences, so eqns [112] and [113] are often all that is needed. Eliminating T_*' and U_* between them gives

$$\ell \sim \left(\frac{g\alpha F_{\text{conv}} d^3}{\Omega^3 \rho c_p}\right)^{1/5} \qquad [114]$$

and then we get

$$U_* \sim \left(\frac{d}{\Omega}\right)^{1/5}\left(\frac{g\alpha F_{\text{conv}}}{\rho c_p}\right)^{2/5}, \quad g\alpha T_*' \sim \left(\frac{\Omega}{d}\right)^{1/5}\left(\frac{g\alpha F_{\text{conv}}}{\rho c_p}\right)^{3/5} \qquad [115a,b]$$

It is interesting to compare these with the Deardorff velocity and temperature scalings [51a,b]. The exponents in the scalings with F_{conv} are different, but not that different! In the inertial theory, we have $U_* \sim F_{\text{conv}}^{0.4}$, whereas for the Deardorff scaling, $U_* \sim F_{\text{conv}}^{1/3}$. The small difference arises because of the weak power of 1/5 in eqn [114]. This length scale ℓ is sometimes called the Rhines scale (Rhines, 1975) and it arises from the balance of vorticity advection and vortex stretching. For the inertial theory to be valid, this length scale must be larger than the thickness of the rolls at onset $\ell_c \sim d^{1/3}(\nu/\Omega)^{1/3}$. Of course, at sufficiently small ν, the Rhines length will be larger than the onset length, but E has to be very small before this is achieved. In the core, if we take the usual estimate of $E \approx 10^{-15}$ and $d = 2.26 \times 10^6$ m, then ℓ_c is only 20 m (but numerical factors from simulations can increase this to 300 m), but the Rhines scale $(U_* d/\Omega)^{1/2} \approx 4$ km, assuming a typical velocity of 5×10^{-4} m s^{-1}.

In simulations and experiments, it is quite hard to achieve such a low viscosity, and then an alternative viscous scaling

$$\Omega U_*/d \sim g\alpha T_*'/\ell_c, \quad \ell_c \sim d\left(\frac{E(1+P)}{P}\right)^{1/3} \qquad [116]$$

together with eqn [113] may give better results (Gillet and Jones, 2006).

The convective heat flux may be estimated in terms of the Nusselt number

$$F_{\text{conv}} \sim (Nu - 1)\rho c_p \kappa \Delta T_s/d \qquad [117]$$

exact in plane layer geometry but only an estimate in spherical geometry. Here, ΔT_s is the superadiabatic temperature gradient across the layer. If we define the Rayleigh number as $Ra = g\alpha \Delta T_s d^3/\kappa\nu$, the Ekman number as $E = \nu/\Omega d^2$, and the convective flux Rayleigh number as $Ra_Q = Ra(Nu - 1)$, then eqns [114] and [115a,b] can be expressed in dimensionless form as

$$\frac{\ell}{d} \sim E^{3/5} Pr^{-2/5} Ra_Q^{1/5} \qquad [118]$$

$$\frac{U_* d}{\kappa} \sim (EPr)^{1/5} Ra_Q^{2/5} \qquad [119]$$

$$Ra\frac{T_*'}{\Delta T_s} \sim (EPr)^{-1/5} Ra_Q^{3/5} \qquad [120]$$

8.05.4.8.2 Heat transport in rapidly rotating convection

We noted in the preceding text that both the inertial scaling and the viscous scaling are incomplete, because the Nusselt–Rayleigh number relation is undetermined. In nonrotating convection, this relationship is determined by the formation of boundary layers, the interior outside these boundary layers being almost isothermal, because convection is very efficient

there. In rapidly rotating convection, the formation of boundary layers is delayed, because the vorticity constraint makes convection less efficient. As the Rayleigh number is raised, eventually boundary layers form, and we expect that the Nu–Ra relationship will become like that in nonrotating convection. The experiments of Sumita and Olson (2000, 2003), where very high Rayleigh numbers were achieved, showed this behavior. For moderate Ra, $Nu-1$ is almost proportional to Ra/Ra_c-1 but $d\ \log(Nu-1)/d\ \log(Ra/Ra_c-1)$ dropped down to 0.41 at the highest Rayleigh numbers they could achieve.

A natural extension to the scaling laws in the absence of boundary layers is to balance nonlinear advection of heat with transport down the mean gradient:

$$\overline{(\mathbf{u}\cdot\boldsymbol{\nabla})T'}\sim u_s\frac{\mathrm{d}\overline{T}}{\mathrm{d}s},\quad \text{or}\quad T'_*\sim\frac{\ell}{d}\Delta T_s \qquad [121]$$

Fluid elements carry their temperature until they break after a distance ℓ and merge into their surroundings, which have temperature differing by $\ell\Delta T_s/d$.

With the inertial scaling formulas [114], [115b], and [117], this gives

$$Nu-1\sim\frac{(g\alpha\Delta T_s)^{3/2}d^{1/2}}{\Omega^2\kappa},\quad \text{or}\quad Nu-1\sim E^2Ra^{3/2}Pr^{-1/2},$$
$$\text{or}\quad Nu-1\sim E^{4/5}Pr^{-1/5}Ra_Q^{3/5} \qquad [122]$$

The viscous scaling [116] gives

$$Nu-1\sim\frac{g\alpha\Delta T_s d^{1/3}}{\Omega^{4/3}}\frac{(\nu+\kappa)^{1/3}}{\kappa}\sim Ra\left(\frac{1+Pr}{Pr}\right)^{1/3}E^{4/3}$$
$$\sim\left(\frac{1+Pr}{Pr}\right)^{1/6}E^{2/3}Ra_Q^{1/2} \qquad [123]$$

Both these formulas, which apply only when thermal boundary layers are negligible, show that the heat transport is strongly reduced at low E, the effect of the vorticity constraint blocking the convection, but $Nu-1$ increases much more rapidly with Ra than in nonrotating convection. Eventually, boundary layers develop and eqn [121] is replaced by a formula in which ΔT_s is not the total superadiabatic temperature drop across the layer but the drop across the interior region outside the boundary layers (see Gillet and Jones (2006) for details).

The inertial scaling suggests that viscosity is unimportant in determining the velocity and heat transport. Christensen (2002) made a numerical study of convection in a rotating spherical shell and concluded that the results could be better represented in terms of a modified Rayleigh number and Nusselt number:

$$Ra^*=\frac{g\alpha\Delta T_s}{\Omega^2 d},\quad Nu^*=\frac{F_{\mathrm{conv}}}{\rho c_p\Delta T_s\Omega d}\quad\text{and}\quad Ra_Q^*=Nu^*Ra^* \qquad [124a,b]$$

This has the advantage that it is independent of all diffusivities. Note that Ra^* is very small in the core, unlike the usual definition, which is very large in the core. Now assuming that $Nu\gg1$, eqns [119] and [122] can be written

$$\frac{U_*}{\Omega d}=Ro\sim\left(Ra_Q^*\right)^{2/5},\quad Nu^*\sim\left(Ra_Q^*\right)^{3/5} \qquad [125]$$

showing explicitly that the velocities and the convective heat transport are completely independent of diffusion. Christensen (2002) had compared these formulas with the output from numerical simulations. He found that they fit fairly well to the data. When there is no internal heating, the total convective flux across any spherical surface of radius r is constant, so $F_{\mathrm{conv}}\sim1/r^2$. At large Ra, the distinction between Nu and $Nu-1$ is unimportant, and he defines

$$Ra_Q^*=\frac{r_{\mathrm{icb}}g\alpha F}{r_{\mathrm{cmb}}\rho c_p\Omega^3d^2} \qquad [126]$$

where F is the heat flux per unit area on the outer boundary. The Rossby number is measured by taking the typical velocity as the root mean square poloidal velocity averaged over the outer core. The poloidal velocity is a measure of the convective velocity, as it excludes the zonal flow, which can be much larger. He then finds a good fit for the relations

$$Ro=0.54\left(Ra_Q^*\right)^{2/5},\quad Nu^*=0.077\left(Ra_Q^*\right)^{5/9} \qquad [127a,b]$$

The typical velocity therefore agrees well with the inertial scaling, and the power of 5/9 is between the 1/2 of eqn [123] and the 3/5 of eqn [122]. These results are encouraging, though some caution is needed in applying them. Gillet and Jones (2006) found that the viscous scaling gives rather similar power laws to the inertial scaling, and at moderate Ra, these may give a better fit to simulation data. Also, at fixed E and large Ra, thermal boundary layers become important and [127b] will break down. However, the core may well be in a regime where E is so small that diffusion is unimportant, and Ra is large but not so large that thermal boundary layers determine the heat transport.

8.05.4.9 Rapidly Rotating Rayleigh–Bénard Convection

Although spherical geometry is the most natural for studies of core convection, the Rayleigh–Bénard configuration of convection between parallel plates, with gravity and the rotation axis perpendicular to the walls has some advantages. Laboratory experiments (e.g., King et al., 2012; Rossby, 1969) can be performed conveniently, and the possibility of using fast Fourier transforms in all three coordinate directions speeds up numerical simulations. Furthermore, the geometry allows an asymptotic approach to be developed much more easily than in spherical geometry (Julien et al., 1998, 2006).

The onset of convection in this geometry is also delayed by rotation (Chandrasekhar, 1961), but the heat transport as measured by the Nusselt number rises more rapidly than for nonrotating convection (see **Figure 7**, a combination of laboratory and numerical experiments, reproduced from King et al., 2012). At fixed E, the plot of Nusselt number against Rayleigh number therefore eventually joins up with the nonrotating case. This is an important result, as it shows that although the Rayleigh number is very large in the core, it is not sensible to make it very large in simulations at fixed Ekman number, because the effects of rotation are then completely lost. A better procedure is to take the Rayleigh number large, but not so large that the rotational effects are lost, so effectively the numerical limitation on the achievable Ekman number also limits the achievable Rayleigh number.

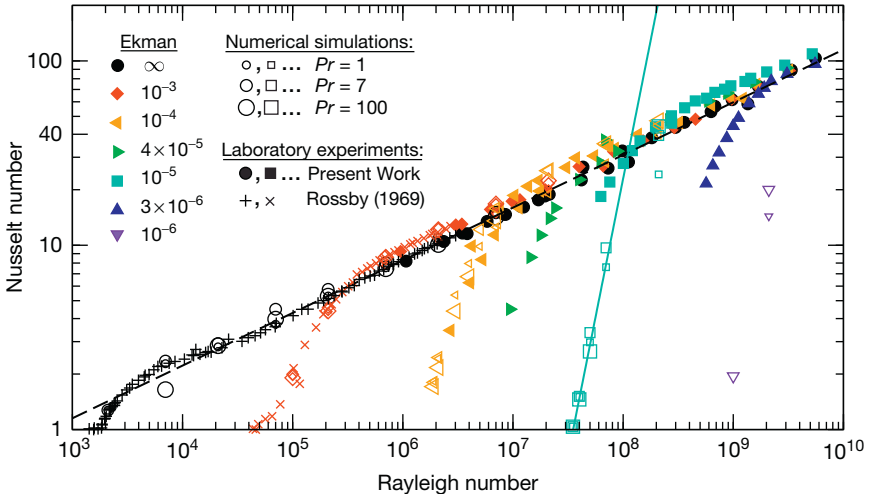

Figure 7 Nusselt number plotted versus Rayleigh number. Seven different Ekman numbers are explored, indicated by various symbol shapes. Solid symbols indicate measurements from laboratory experiments. Open symbols indicate results from numerical simulations, with symbol size corresponding to *Pr*. The Ekman number values are approximate for laboratory experiments, which vary due to changes in fluid viscosity. Data from Rossby (1969) are also shown for comparison for non-rotating (C) and $E \approx 10^{-3}$ cases. The dashed black line represents the non-rotating scaling $Nu = 0.16\, Ra^{2/7}$. The solid line illustrates the rapidly rotating scaling of eqn [132] for $E = 10^{-5}$. Reproduced from King et al. (2012) *Journal of Fluid Mechanics* 691: 568–582.

The issue of how the heat transport in rotating convection depends on Rayleigh number, Ekman number, and Prandtl number is currently an active research area, and no consensus has yet been achieved. We can write

$$Nu \sim Ra^{\alpha} E^{\beta} Pr^{\gamma} \qquad [128]$$

and attempt to find theoretical, numerical, and experimental evidence to determine the exponents α, β, and γ. We know from the work of Grossmann and Lohse (2000) in the non-rotating case that there may well be different regimes with different exponents, so a 'one-size-fits-all' approach may fail. We know for sure that at *Ra* just above critical weakly nonlinear theory applies (see, e.g., Gillet and Jones, 2006) and the exponent $\alpha = 1$ there. We also know that at large *Ra*, *Nu* joins the nonrotating curve so an exponent of $0.25 < \alpha < 1/3$ is expected. There may be a regime in which the convection is limited by the thin columns in the bulk rather than the boundary layers. If so, it is likely that the convected heat flux *F* will be independent of viscous or thermal diffusion. From the definition of *Nu*, eqn [43], and using eqn [128] and the definitions of *Ra*, *E*, and *Pr*, independence of ν and κ gives, respectively,

$$-\alpha + \beta + \gamma = 0, \quad -\alpha - \gamma = -1 \qquad [129]$$

We know from linear theory that as $E \to 0$, $Ra_{\mathrm{crit}} \sim E^{-4/3}$, so if the heat flux depends only on the combination Ra/Ra_{crit}, we must have $\beta = 4\alpha/3$. Then, eqn [129] gives the unique solution

$$\alpha = 3/2, \quad \beta = 2, \quad \gamma = -1/2, \quad Nu \sim Ra^{3/2} E^{2} Pr^{-1/2} \qquad [130]$$

Interestingly, this is the same relation as the inertial theory of convection gives (see eqn [123]). This is not so surprising when you consider that the inertial theory ignored the viscous and thermal diffusion terms in drawing up the balances. Julien et al. (2012) derived equation [130] from a consideration of the 'balance' equations believed to be valid in the limit of low Ekman number. Julien et al. (2012) argued that in the limit of low *E*, the boundary layers will not control the heat transport, but this has been debated by King et al. (2012) (see also King et al., 2013). King et al. (2012) gave a rotating version of the argument leading to eqn [48]. We suppose there is a thermal boundary layer of thickness δ. The criterion that this should be marginally stable to rotating convection is that

$$\frac{g\alpha \Delta T \delta^3}{\nu\kappa} = Ra_{\mathrm{crit}} = A\left(\frac{\nu}{\Omega \delta^2}\right)^{-4/3} \qquad [131]$$

Now, using the definition equation [44], the large-scale Ekman number $E = \nu/\Omega d^2$, and assuming that the temperature drop across the layer occurs primarily in the top and bottom boundary layers so that eqn [46] holds, we obtain the Nusselt number scaling

$$Nu \sim Ra^{3} E^{4} \qquad [132]$$

which fits the data in **Figure 7** reasonably well. A fundamental difference between eqns [132] and [130] is that in deriving equation [132], we assumed that the mean temperature drop occurred over the boundary layers, with the interior being nearly isothermal, whereas in the argument leading to eqn [130], boundary layers and their associated thermal diffusion are absent. It is possible there are some regimes where eqn [130] hold and others where eqn [132] is appropriate.

Another issue of interest is where the steep rotating *Nu*–*Ra* relation is replaced by the much shallower nonrotating *Nu*–*Ra* law. Schmitz and Tilgner (2009) investigated this by means of numerical simulations and concluded that the transition takes place when $RePrE^{1/2} \approx 2$. They plotted $\log((Nu-1)E^{1/3})$ against $\log(RePrE^{1/2})$ and found that all their data at varying *E* and *Pr* nearly collapsed onto one curve, which consisted of a straight line segment of slope 2 for low values of $RePrE^{1/2}$ and a straight line of slope 2/3 for high values of $RePrE^{1/2}$, which corresponds to the expected law for nonrotating convection

$(Nu-1)\sim(RePr)^{2/3}$. The transition between these two linear laws occurs at $RePrE^{1/2}\approx 2$, which is identified with the point at which the heat transport ceases to be affected by rotation. We can write this criterion in terms of the flux Rayleigh number, using the inertial theory of convection equation [119] as $Ra_Q = Ra(Nu-1)\sim 2^{5/2}E^{-7/4}Pr^{-1/2}$, showing that the transition flux Rayleigh number increases as E decreases. Note that the Schmitz and Tilgner criterion $RePrE^{1/2}\approx 2$ is not the same as $Ro\sim 1$, where we would expect columnar convection to break down, but instead where $Ro\sim 2Pr^{-1}E^{1/2}$. The transition in the heat transport law is occurring in the strongly columnar regime and presumably has to do with the formation of controlling thermal boundary layers rather than the breakdown of columnar convection.

8.05.5 Convection With and Without Rotation in the Presence of Magnetic Field

The Earth's core is made up of electrically conducting fluid permeated by magnetic field. These magnetic fields affect convection in many different ways. To simplify the different effects, theoreticians have studied simplified models that highlight the behavior in various circumstances. From the intuition developed by these studies, we hope to be able to understand the interplay of the many different forces at work in core convection. We first distinguish between the dynamo process, which addresses the question of how the field is generated, described in Chapter 8.03, and the back-reaction that the created field has on the convection. In this section, we do not attempt to describe the dynamo process, but instead assume that a field has been generated by a dynamo, and we study the interaction of this given field with the convection. The study of convection in the presence of an imposed field is usually known as magnetoconvection, whereas the full problem, including the generation of field from only a small seed field, is called the hydromagnetic dynamo problem. The imposed field can be applied by specifying that there is a nonzero magnetic field at the boundaries. Sometimes, this field is fixed at the boundaries; sometimes, there is a specified amount of flux passing through the boundary that can be moved around but not destroyed. While it is convenient to split the problem into magnetoconvection and dynamo action, there are of course connections between these two problems. The dynamo-generated field saturates when the back-reaction of the created field alters the flow pattern into something that no longer generates large quantities of field, so that the field strength is determined by magnetoconvection processes.

The issues we concentrate on here are as follows: (i) If we start with a uniform field, how is the field altered by the flow? (ii) If we impose a uniform magnetic field, how is the pattern of convection at onset changed? (iii) What magnetic field structures emerge in a fully convecting conducting fluid? The first two questions are essentially linear problems, and so analytic progress is possible. The third question is nonlinear and so much harder; we have to rely on a relatively small number of computer simulations.

While much of our understanding is based on the effect of a simple large-scale field on convection, it should be remembered that the field inside the core is not necessarily like this. Indeed, dynamo simulations usually show a rather complex field pattern inside the core, not just the simple dipolar-type field seen at the Earth's surface. Indeed, a much more complex pattern emerges even when the external potential field is extrapolated down to the CMB. In consequence, although our intuition is based on the effect of uniform fields, this may not always give us a reliable picture, so we should not be too surprised if dynamo simulations give a rather different picture from that predicted by magnetoconvection.

8.05.5.1 Flux Expulsion and Flux Rope Formation

We start by assuming that an initially uniform magnetic field permeates a fluid layer. At time $t=0$, a specified velocity field is switched on, and the magnetic field is moved around. What happens to the field? This is called the kinematic flux expulsion problem (Weiss, 1966). It is kinematic because the flow is assumed inexorable, unaffected by the field itself. It is flux expulsion because that is what happens: the flux is expelled from regions where the flow is vigorous into regions where very little shear occurs. The simplest case is that of 2-D roll flow, in a square box of height and width d,

$$\mathbf{u}=\boldsymbol{\nabla}\times\psi\mathbf{1}_z=\left(-U\sin\frac{\pi x}{d}\cos\frac{\pi y}{d},U\cos\frac{\pi x}{d}\sin\frac{\pi y}{d},0\right) \quad [133]$$

with a magnetic field

$$\mathbf{B}=\boldsymbol{\nabla}\times A\mathbf{1}_z=\left(\frac{\partial A}{\partial y}-\frac{\partial A}{\partial x},0\right),\ \text{with}$$
$$A=0\ \text{on}\ x=0,\ A=B_0 d\ \text{on}\ x=d \quad [134]$$

The initial field is a uniform vertical field, $A=B_0x$. Note that the boundary conditions on A ensure that the total amount of vertical flux is conserved, so there is no possibility of the field disappearing. The equation for A is the induction equation, which can be written in two dimensions as

$$\frac{\partial A}{\partial t}+\frac{\partial(\psi,A)}{\partial(x,y)}=R_m^{-1}\nabla^2 A \quad [135]$$

Here, the magnetic Reynolds number $R_m=Ud/\eta$, where η is the magnetic diffusivity. If R_m is small, the magnetic field is not disturbed much from its initial state, as the diffusion term dominates and the initial field satisfies $\nabla^2 A=0$. If R_m is large, flux expulsion occurs, and a typical solution is shown in Figure 8, based on Galloway and Weiss (1981). The figure shows behavior in a square box at a sequence of times in units of the turnover time d/U with $R_m=1000$.

The concentrated fields that develop at $x=0$ and $x=d$ are called flux sheets. At large R_m, their thickness scales as $\mathrm{d}R_m^{-1/2}$ (Galloway et al., 1977). This represents a balance of advection and diffusion in the flux sheet, advection into the sheet being at a rate U/d and diffusion out being at a rate η/δ_B^2, δ_B being the sheet thickness. In three dimensions, an axisymmetric convective flow produces a rope at the center of the cell rather than a flux sheet, but the thickness is still approximately $\mathrm{d}R_m^{-1/2}$, though logarithmic factors can enter (Galloway et al., 1977). The magnetic Reynolds number in the core is in the range 10^2–10^3, so we expect flux expulsion to be significant. There is evidence from geomagnetic field observations that flux patches exist, most notably under Alaska and Siberia in the present field.

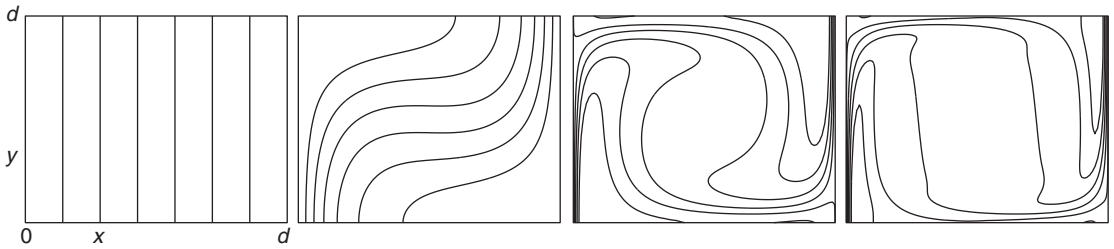

Figure 8 Flux expulsion. The field is initially vertical, and the turnover time is d/U. Four plots shown are at times 0, 0.5, 2.0, and 20.0 turnover times from left to right. The flux is expelled into ropes near the sides of the box.

Unfortunately, the width of the patches is rather uncertain, because crustal magnetism prevents us seeing small-scale structures, and it may be that the patches are thinner but more intense than is apparent from the necessarily smoothed out published CMB fields. This is certainly suggested by geodynamo simulations. On the surface of the Sun, the intense turbulence just below the photosphere sweeps the flux into sunspots, which are relatively quiescent regions. Since the convection is reduced in the spots, they appear cooler and hence dark in comparison with the rest of the solar surface.

8.05.5.2 Linear Theory of Magnetoconvection in Plane Geometry

We now consider the classic problem of the onset of magnetoconvection in a plane layer of electrically conducting fluid confined between horizontal boundaries at $z=\pm d/2$. The imposed field is uniform, but the convection generally produces a small induced field that can significantly affect the convection. Chandrasekhar (1961) described in great detail the case where the imposed magnetic field and the rotation axis are parallel to gravity. Many other cases have been studied. Convection near the equator in the presence of a strong azimuthal field might be best modeled by having gravity, rotation, and the magnetic field mutually perpendicular (Jones and Roberts, 2000; Roberts and Jones, 2000).

8.05.5.2.1 Nonrotating magnetoconvection

We start with the nonrotating case, to isolate the effects of magnetic field alone. If the imposed magnetic field is horizontal, then the convection onsets in the form of 2-D rolls with their axes aligned with the magnetic field. This resembles the alignment of convection rolls with the rotation axis in rotating convection. The magnetic alignment can be simply understood, because if $\mathbf{B}_0$ is the imposed field and $\mathbf{b}$ is the induced field created by the motion, eqn [6] implies

$$\frac{\partial \mathbf{b}}{\partial t} = \mathbf{B}_0 \cdot \nabla \mathbf{u} + \eta \nabla^2 \mathbf{b} \qquad [136]$$

so if the flow does not vary in the field direction, $(\mathbf{B}_0 \cdot \nabla)\mathbf{u} = 0$, and there is no source term and hence $\mathbf{b} = 0$. There is then no Lorentz force, and so convection proceeds as though there was no magnetic field, and the critical Rayleigh number at onset is the same as in the absence of magnetic field.

In contrast, if the field is vertical, then the magnetic field restrains the convection, as indeed occurs in a sunspot. Because of the horizontal boundaries, rising hot fluid has to turn over and so cannot be z-independent, so $(\mathbf{B}_0 \cdot \nabla)\mathbf{u}$ is nonzero, and there is an induced field. This gives rise to a perturbed current $\mathbf{j} = \nabla \times \mathbf{b}/\mu$ and hence a Lorentz force $\mathbf{j} \times \mathbf{B}_0$ in the linearized equation of motion:

$$\frac{\partial \mathbf{u}}{\partial t} = -\nabla\left(\frac{p'}{\rho}\right) + \mathbf{1}_z g \alpha T' + \frac{\mathbf{j} \times \mathbf{B}_0}{\rho} + \nu \nabla^2 \mathbf{u} \qquad [137]$$

The linearized temperature equation (we assume compositional convection behaves similarly) is

$$\frac{\partial T'}{\partial t} = -T_0' u_z + \kappa_T \nabla^2 T' \qquad [138]$$

In addition to the velocity components being zero at the boundaries, we also need additional boundary conditions for the magnetic field. The simplest case is for a perfect conductor, as then $b_z = 0$ on the horizontal boundaries, and the horizontal components of the current are zero, which since the current is divergence-free implies that $\mathrm{d}j_z/\mathrm{d}z = 0$ on the boundaries (Chandrasekhar, 1961). Together with a condition on the temperature, $T' = 0$ on the boundaries being the usual choice, this provides a convenient set of conditions. Somewhat more realistic for the core are insulating boundary conditions, that is, the material outside the core is assumed to be an insulator. This is a sensible condition for the CMB (though some iron could have leaked into cracks in the mantle, giving a finite conductivity). Then, there is no current out of the fluid, so $j_z = 0$, and the horizontal components of $\mathbf{b}$ must match onto an external potential field. In the case where the field on the boundary is naturally decomposed into Fourier modes $\sim \exp(\mathrm{i}k_x x + \mathrm{i}k_y y)$, this is straightforward to apply, because the external potential field has the form $\exp(-az + \mathrm{i}k_x x + \mathrm{i}k_y y)$, where $a = \pm(k_x^2 + k_y^2)^{1/2}$, the plus sign for the field above the layer and the minus sign for the field below. From $\nabla \cdot \mathbf{b} = 0$, it follows that $\mathrm{d}b_z/\mathrm{d}z = \mp a b_z$ on the top and bottom boundaries, respectively. A similar trick works for spherical geometry, but the cases of rectangular or cylindrical containers are much harder, as there is then no simple solution for the external field, which must therefore be calculated numerically.

The Lorentz force opposes the convection, so that the onset of convection is delayed, that is, the critical Rayleigh number is increased. Details are given in Chandrasekhar (1961). The dimensionless parameter that measures the importance of magnetic field is now called the Chandrasekhar number:

$$Q = \frac{B_0^2}{\mu \rho \nu \eta} \qquad [139]$$

If this parameter is large, the onset of convection is delayed until $Ra \sim Q^{1/2}$, and when convection occurs, it takes the form

of tall thin cells, which minimizes the bending of the field lines. The Lorentz force for a general nonuniform field is

$$\frac{1}{\mu}(\nabla\times\mathbf{B})\times\mathbf{B}=\frac{1}{\mu}(\mathbf{B}\cdot\nabla)\mathbf{B}-\frac{1}{2\mu}\nabla\mathbf{B}^2 \qquad [140]$$

the first term being the curvature and the second, the magnetic pressure. The magnetic pressure is not so important in Boussinesq convection, since it merely adds to the fluid pressure and has no curl. It is the curvature force that impedes convection by opposing the convection rolls so that stronger buoyancy forces are needed to maintain the convection. If the field is oblique to gravity, the horizontal component lines the convection rolls up with the field, while the vertical component raises the critical Rayleigh number.

8.05.5.2.2 Onset of plane-layer rotating magnetoconvection

Magnetic field on its own either opposes convection or is neutral to it in the case of horizontal field. However, in the presence of rotation, it is possible for the magnetic field to break the Proudman–Taylor constraint and hence lower the critical Rayleigh number. The linearized equation of motion is now

$$\frac{\partial\mathbf{u}}{\partial t}+2\boldsymbol{\Omega}\times\mathbf{u}=-\nabla\left(\frac{p'}{\rho}\right)+\mathbf{1}_z g\alpha T'+\frac{\mathbf{j}\times\mathbf{B}_0}{\rho}+\nu\nabla^2\mathbf{u} \qquad [141]$$

where again $\mathbf{B_0}$ is a uniform magnetic field and $\mathbf{j}$ is the small current induced by the small velocity. The case where the gravity, rotation, and applied field are all vertical (appropriate for the polar regions in the core) was studied by Chandrasekhar (1961). The rapid rotation limit was examined by Eltayeb (1972). The case where the rotation, applied field, and gravity are mutually perpendicular was studied by Roberts and Jones (2000) and Jones and Roberts (2000). When the field and rotation are in the same direction, not surprisingly, the convection rolls have their axes parallel to this direction. In the case where there is an angle between the rotation and magnetic field vectors, it is possible for the rolls either to line up with the rotation or the magnetic field or in some circumstances to be oblique to both (see Roberts and Jones (2000) for details).

It is most useful to consider the case of rapid rotation, that is, small E, with the field gradually increasing in strength. A key parameter is the Elsasser number:

$$\Lambda=\frac{B_0^2}{\mu\rho\eta\Omega} \qquad [142]$$

At the onset of convection, the induction equation gives a relation between the typical perturbed field b_* and the velocity U_*

$$\frac{B_0U_*}{d}\sim\frac{\eta b_*}{d^2} \qquad [143]$$

which means that the typical values of the Coriolis force and the Lorentz force balance when $\Lambda\sim1$. Note that this is not necessarily the case far from onset.

In the polar regions, where gravity, rotation, and applied field are all approximately parallel, a nonmagnetic mode onsets first until the Elsasser number reaches $\Lambda_c=2^{1/3}\pi^{2/3}E^{1/3}$ in the case of stress-free, thermally conducting and electrically insulating boundaries. Note that at small E, this is a very weak field, because $E^{1/3}$ is small. For $\Lambda<\Lambda_c$, these nonmagnetic modes have the form of tall thin columns with wavelength $O(E^{1/3})$ perpendicular to the rotation axis. However, as Λ is increased past Λ_c, there is a sudden transition to a magnetic mode of convection, which has horizontal wavelength the size of the layer depth. If Λ is increased further, the horizontal wavelength starts to decrease again, as in the nonrotating case, and the critical Rayleigh number starts to rise. There is therefore an optimum field strength that minimizes the Rayleigh number and has critical wavelengths of order d. The case of a vertical field is slightly exceptional, because with more general field orientations, the optimum Rayleigh number occurs when the Elsasser number is of order unity (Eltayeb, 1972).

8.05.5.2.3 Waves in the core

Equations [136]–[138] can be used to study wave motion in the core and convection. We ignore the boundary conditions, assume a uniform field, and look for solutions of the form $\exp\mathrm{i}(\mathbf{k}\cdot\mathbf{x}-\omega t)$ that represent traveling waves. Substituting this form into the equations gives the dispersion relation between $\mathbf{k}$ and ω. If the temperature gradient is stabilizing (subadiabatic), then real values of ω are found if diffusion is neglected. If diffusion is retained, ω is complex with a negative imaginary part corresponding to damped oscillations. If the temperature gradient is superadiabatic, growing waves (instabilities) are found provided the diffusion is not too large.

The full dispersion relation is complicated, but it can be simplified when, as in the Earth's core, different types of waves have very different frequencies (Fearn et al., 1988). It also helps to ignore diffusion in the first analysis. Finlay et al. (2010) have recently reviewed shorter timescale waves in the core. The fastest waves are inertial waves that balance the Coriolis and inertial accelerations as in eqn [58], and the inertial wave frequency is given by

$$\omega_c=2(\boldsymbol{\Omega}\cdot\mathbf{k})/|\mathbf{k}| \qquad [144]$$

The typical period is therefore of the order of a day, though for columnar modes with $\mathbf{k}$ almost perpendicular to $\boldsymbol{\Omega}$, they are slower. These waves have not yet been observed in the core, but they are expected to be driven by tidal forcing. It is useful to think of these waves in terms of vortex stretching. A rapidly rotating fluid has vorticity $2\boldsymbol{\Omega}$, and waves with $\boldsymbol{\Omega}\cdot\mathbf{k}\neq0$ bend the vortex lines, which act like stretched strings giving a restoring force leading to oscillations. The fast timescale of order hours arises because the Coriolis force is very strong in the core. To avoid these rapid oscillations, motion has to have $\boldsymbol{\Omega}\cdot\mathbf{k}\approx0$, that is, it has to be columnar.

Alfvén waves result from a balance of inertia and Lorentz force in the equation of motion, when combined with the induction equation. It is again useful to think of the magnetic field lines as stretched strings, with magnetic curvature forces, eqn [140], providing a restoring force whenever the field lines are bent. These waves have frequency

$$\omega_M=(\mathbf{B_0}\cdot\mathbf{k})/(\mu\rho)^{1/2} \qquad [145]$$

and they travel at the Alfvén speed, $|\mathbf{B_0}|/(\mu\rho)^{1/2}$. An important class of Alfvén waves are those corresponding to azimuthal motion constant on cylinders, which are called torsional oscillations (Braginsky, 1967). These have $\boldsymbol{\Omega}\cdot\mathbf{k}=0$ and so do not

excite the strong Coriolis force and therefore have periods much longer than a day. These torsional oscillations are believed to be important in the core and are probably responsible for decadal length-of-day variations (Jackson, 1997; Jault, 2003; Jault et al., 1988) and possibly shorter period elements of the geomagnetic secular variation, such as the so-called geomagnetic jerks. Early estimates gave their period as around 60 years (Braginsky, 1967), but recently, Gillet et al., 2010 suggested that the core field may be as strong as 4 mT, in which case a radial field of 2 mT is plausible, and the period of torsional oscillations may be as short as 6 years.

If we consider both Coriolis force and a uniform magnetic field $\mathbf{B_0}$, but still ignore buoyancy and all diffusive processes, the resulting dispersion relation is

$$\omega_{MC} = \pm\frac{\mathbf{\Omega}\cdot\mathbf{k}}{k} \pm \left[\frac{(\mathbf{\Omega}\cdot\mathbf{k})^2}{k^2} + \frac{(\mathbf{B_0}\cdot\mathbf{k})^2}{\rho\mu_0}\right]^{1/2} \qquad [146]$$

Generally, waves have the inertial frequency, but there is a slow wave when the two plus/minus signs are opposite. Physically, this case occurs when the Lorentz and Coriolis forces balance, so that the inertial term in the equation of motion is small. Magnetostrophic equilibrium is maintained throughout the oscillation. These slow waves have a timescale (e.g., Finlay et al., 2010)

$$\tau \sim \frac{\Omega\rho\mu_0 L^2}{\pi B_0^2} \sim \frac{\pi L^2}{\Lambda\eta} \qquad [147]$$

where L is the typical wavelength. For an internal field of 2 mT, this gives about 2000 years for a length scale of 1000 km.

Another timescale comes from the temperature gradient, from the balance of buoyancy and inertia in the equation of motion, combined with the temperature equation [138] with $\kappa = 0$. The frequency of internal gravity waves is $\omega_A = (g\alpha T_0')^{1/2} k_H/|\mathbf{k}|$, where T_0' is the subadiabatic temperature gradient and k_H is the component of $\mathbf{k}$ perpendicular to gravity. In a convectively unstable region, $T_0' < 0$, the temperature gradient is superadiabatic. Then, ω_A is imaginary, which corresponds to an exponentially growing unstable mode, with $|\omega_A|$ being the growth rate. With an estimate of 10^{-4} K for a typical superadiabatic temperature perturbation, $-T_0' \sim 10^{-4}/d$, giving a typical growth rate of about 5 months.

When all the nondiffusive terms in the equations are present, the dispersion relation gives a fast inertial wave and a slow wave in which only the time-derivative terms in the induction and temperature equations are important, inertia being negligible. These slow waves are known as MAC waves and have frequency

$$\omega_{\mathrm{MAC}} = \omega_{MC}\left(1 + \omega_A^2/\omega_M^2\right)^{1/2}, \quad \text{where} \quad \omega_{MC} = \frac{\omega_M^2}{\omega_C} \sim \frac{B_0^2}{\mu\rho\Omega d^2} \qquad [148]$$

In the superadiabatic case, when $|\omega_A| > |\omega_M|$, ω_{MAC} is imaginary, corresponding to a growing convective mode. The rate of growth is slow, since $\tau_{MC} = 2\pi/\omega_{MC}$ is of the order of some thousands of years. It is comparable with the magnetic diffusion time, since the ratio $\tau_{\mathrm{diff}}/\tau_{MC} = B_0^2/\mu\rho\Omega\eta = \Lambda$ and the Elsasser number Λ has a value of $O(1)$ in the core. The MAC growth rate will be a little larger than $1/\tau_{MC}$ because $|\omega_A| > \omega_M$, but these slow growth times are consistent with the time taken for the typical convective velocity to take fluid across the core, 200 years, so the dynamical picture does seem to be self-consistent.

8.05.5.2.4 Small-scale dynamics and the Braginsky–Meytlis theory of platelike motion

Although for general wave vectors $\mathbf{k}$ the MAC wave timescale is slow, it is much faster if $\mathbf{k}$ and $\mathbf{\Omega}$ are perpendicular. This is the case for columnar motion independent of z, the coordinate parallel to the rotation axis. For these motions, ω_{MC} is singular, and we have to restore inertia, leading to the much faster torsional wave frequency. It is also possible for $\mathbf{k}$ to be perpendicular to both $\mathbf{\Omega}$ and $\mathbf{B_0}$. This type of motion does not bend the field lines and so has no Alfvén wave behavior. For these motions with $\mathbf{k}$ in the direction $\mathbf{\Omega}\times\mathbf{B_0}$, neither magnetic field nor rotation can impede the growth of convective instability. In a Boussinesq fluid, waves have $\mathbf{k}\cdot\mathbf{u} = 0$, so such waves have motion only along 'plates,' planes containing the rotation vector and the magnetic field vector. If there is an unstable temperature gradient in a direction parallel to these planes, instability will grow on the much shorter ω_A timescale. Large-scale motion along plates may be blocked by the boundary curvature and therefore 'feel' the rotation, but small-scale convection in the core will be preferentially in the form of platelike motions aligned with the rotation and magnetic field. Since small-scale turbulence in the core is driven primarily by convective instability rather than turbulent cascade, Braginsky and Meytlis (1990) argued that this would mean that turbulence is likely to be highly anisotropic. This is a cause for concern, because most dynamo simulations assume an isotropic eddy diffusion. Introducing an anisotropic diffusion adds considerably to the computational cost of a dynamo code, though some work has been done (e.g., Matsushima, 2005).

A promising approach to the problem of how to include small-scale behavior into dynamo models is subgrid-scale modeling. A number of approaches have been tried (Buffett, 2003), but the similarity method is perhaps currently the most successful (Chen and Glatzmaier, 2005). The idea is to filter simulation runs at two different filter scales in order to estimate the effect of the smallest scales present in the run. Then, a similarity assumption is made, which comes down to assuming that the unresolved scales behave similarly to the smallest resolved scales. This allows an extrapolation to be made that takes into account the unresolved scales; details are given in Chen and Glatzmaier (2005). The advantage of this method is that if the smallest resolved scales are anisotropic, then the correction from the unresolved scales will also be anisotropic, so the Braginsky–Meytlis ideas could be captured by this approach. On the downside, if there are new modes entering the problem at the subgrid-scale level, they will not be detected by the similarity method, and so any effect they have will be missed in the simulation. The application of subgrid-scale methods to core convection is very recent, and it will be interesting to see how successful they are.

8.05.5.2.5 Boundary layers in rotating magnetic fluids

The presence of magnetic field affects the Ekman boundary layer structure discussed in Section 8.05.4.4. The simplest problem is to consider the boundary layer just above a plane wall $z = 0$ with rotation and an imposed magnetic field B_0 in the z-direction. The horizontal flow in the boundary layer then induces horizontal

field there. We seek a steady solution, $\partial \boldsymbol{B}/\partial t = 0$, so by Maxwell's equations, $\boldsymbol{\nabla} \times \mathbf{E} = 0$, and we assume no externally imposed electric field, so $\mathbf{E} = 0$. Then, from Ohm's law,

$$\mathbf{j} = \frac{1}{\mu\eta}\mathbf{u} \times \mathbf{B} \qquad [149]$$

There is some velocity normal to the wall in an Ekman layer (see Section 8.05.4.4) but it is small, $O(E^{1/2})$, and so to leading order, the horizontal components of $\mathbf{j}$ are

$$\mathbf{j} = \frac{u_y B_0}{\mu\eta}\mathbf{1}_x - \frac{u_x B_0}{\mu\eta}\mathbf{1}_y \qquad [150]$$

The curl of the steady momentum equation is

$$-2\Omega\frac{\partial \mathbf{u}}{\partial z} = \frac{1}{\rho}B_0\frac{\partial \mathbf{j}}{\partial z} + \nu\frac{\partial^2 \zeta}{\partial z^2} \qquad [151]$$

since the term involving $(\mathbf{j}\cdot\boldsymbol{\nabla})\mathbf{B}$ is negligible, because the boundary layer is thin (formally this requires the boundary layer to be thinner than $R_m^{-1/2}$ where $\mathrm{R_m}$ is the magnetic Reynolds number based on the large horizontal length scale). The x and y components of eqn [151] give

$$-2\Omega\frac{\partial}{\partial z}(u_x + \mathrm{i}u_y) = -\frac{\mathrm{i}B_0^2}{\rho\mu\eta}\frac{\partial}{\partial z}(u_x + \mathrm{i}u_y) + \mathrm{i}\nu\frac{\partial^3}{\partial z^3}(u_x + \mathrm{i}u_y) \qquad [152]$$

Seeking solutions of the form $\mathrm{u_x} + \mathrm{iu_y} \sim \exp \lambda z$ gives a zero root (allowing matching to the interior flow) and roots satisfying

$$\lambda^2 = \frac{B_0^2}{\rho\mu\eta\nu} + \frac{2\mathrm{i}\Omega}{\nu} \qquad [153]$$

When $B_0 = 0$, this gives an Ekman layer of thickness $(\nu/\Omega)^{1/2}$, and when $\Omega = 0$, it gives a Hartmann layer of thickness $(\rho\mu\eta\nu)^{1/2}/B_0$. These layers are of comparable thickness when the Elsasser number (see eqn [142]) is order unity. In this case, the layer thickness is determined by eqn [153] and the layer is called an Ekman–Hartmann layer.

The stability of Ekman–Hartmann layers has been analyzed (see, e.g., Desjardins et al., 1999). An analysis of Ekman–Hartmann layers in spherical geometry was given by Loper (1970).

8.05.5.3 Onset of Rotating Magnetoconvection in Spherical Geometry

The onset of instability in the presence of a magnetic field is studied by techniques similar to those described in Section 8.05.4.2. Most work has been done for magnetic fields of the form $\mathbf{B} = B_0 s \mathbf{1}_\phi$, the so-called Malkus field (Fearn, 1979a,b; Jones et al., 2003a,b; Malkus, 1967), and the case of a uniform field parallel to the spin axis (Sakuraba, 2002). In addition to expanding the velocity in toroidal and poloidal scalars, eqn [59], we also expand the magnetic field as

$$\mathbf{b} = \nabla \times \mathcal{U}\mathbf{r} + \nabla \times \nabla \times \mathcal{V}\mathbf{r} \qquad [154]$$

As usual, the dynamical equations are treated by taking the r components of the curl and double curl of the momentum equation, giving equations for the toroidal and poloidal components of $\mathbf{u}$. We take the radial components of the induction equation and its curl to get equations for $\mathcal{U}$ and $\mathcal{V}$. The temperature equation completes the set. Details are given in Zhang (1995). Although at first sight this formulation seems to involve a great many curl operations, the resulting equations are surprisingly straightforward, particularly if expansion in spherical harmonics P_l^m is adopted, so that the horizontal part of the $\boldsymbol{\nabla}^2$ operator reduces to multiplication by $-l(l+1)$. The Malkus form of the field is particularly attractive because it only couples adjacent spherical harmonics together, as does the Coriolis term. This means that the equation for P_l^m only involves the coefficients in front of P_{l-1}^m, P_l^m, and P_{l+1}^m. In consequence, the matrices for the linear eigenproblem have a banded structure, which makes it much easier to find their eigenvalues. If a more general form of the field is adopted, all the different l components are coupled, so the eigenvalues of a dense matrix must be found. Of course, if a nonaxisymmetric field were considered, the problem would be even worse, because then modes with different m are coupled. Solving such a problem would be as hard as the full nonlinear dynamo, and so it is not surprising that little is known about magnetoconvection in fields with complex geometries.

The effect of the magnetic field is measured by the Elsasser number, Λ (see eqn [142]). If Λ is very small, the magnetic field has little effect, and the convection onsets in the usual manner for rotating convection, that is, columnar modes are preferred. The first noticeable effect is when Λ is $O(E^{1/3})$. This is a rather small value, and core values of Λ must certainly be greater than this. For values in the weak field range, $O(E^{1/3}) < \Lambda < O(1)$, the convection is still columnar, but the critical value of m is significantly reduced; indeed, the preferred value drops from $O(E^{-1/3})$ down to $O(1)$ in this range. So we still have columnar convection, but the rolls are now much fatter due to the presence of the magnetic field. In this range, the critical Rayleigh number typically first increases with Λ and then reaches a maximum after which it falls significantly (Fearn, 1979b). This shows that magnetic field can break the Proudman–Taylor constraint and hence be favorable for convection.

The influence of magnetic field on convection in dynamo models has been discussed recently by Soderlund et al. (2012). They found that the linear theory based on the Elsasser number overestimates the role of the magnetic field on convection. A possible explanation is that linear theory is based on the effect of a uniform field permeating the convection rolls, but in fact, flux expulsion means that the field penetrating the rolls may be much weaker. Even the local magnetic Reynolds number based on the roll width length scale is sufficiently high for flux expulsion to occur. Based on this idea, they propose that the effect of magnetic field on convection in a high R_m fluid is better measured by a dynamic Elsasser number $\Lambda_d = \Lambda d/R_m \ell$, where ℓ is the (small) length scale associated with the intermittent magnetic field. They find situations where Λ is almost a hundred, but Λ_d is around unity, and the effect of magnetic field on the convection is only moderate, in the sense that rolls are not greatly thickened. Of course, the magnetic field must be affecting the field in some regard at Λ of order unity, because this is the value at which dynamos generally saturate (though there is some variation in saturated Elsasser numbers depending on boundary conditions and heating mechanisms of the dynamo). However, it is possible that saturation occurs through a change in the flow's stretching properties, and two convection rolls may look broadly similar but have rather

different stretching properties. Most of the dynamo simulations have been done at moderate magnetic Prandtl number. At Earth-like values of $Pm=\nu/\eta$, it seems likely that very thin rolls can occur for which the magnetic diffusion time is short compared to the timescale of roll formation. For such very thin rolls, of width a few kilometers, the field must permeate the roll and linear magnetoconvection will apply.

Another feature of magnetoconvection is that the frequency at onset drops rapidly as Λ increases (Fearn, 1979b), that is, the phase speed of propagation is much slower in the presence of magnetic field. It is also possible for the waves to propagate westward, rather than eastward, as generally seems to be the case in the core. The westward drift is not, though, a universal feature of the secular variation, as the Pacific hemisphere has no strong westward tendency, whereas the Atlantic hemisphere has. The phase frequency actually drops to the inverse thermal diffusion time in magnetoconvection for the main thermal mode of convection (Fearn, 1979b), but there are other modes where the phase speed is the inverse magnetic diffusion time (Zhang and Jones, 1996). At small $q=\kappa/\eta$, these timescales are very different. Quite surprisingly, the Malkus field can be unstable for negative Rayleigh number (Roberts and Loper, 1979). The instability is driven by magnetic field energy being converted into fluid motion, and it is these magnetic modes that have a frequency corresponding to the inverse magnetic diffusion time.

If magnetic field is increased into the $\Lambda\sim O(1)$ regime, the critical Rayleigh number typically has a minimum and then starts to increase when Λ becomes large. There are however exceptions to this behavior when the applied field is more complicated: Thus, if the applied toroidal field is antisymmetric about the equator (as may well be the case in the core), at large Λ, the critical Rayleigh number continues to decrease as Λ increases (Zhang and Jones, 1994), and Ra_c goes negative because convection is then driven by magnetic instability (see **Section 8.05.5.4**) rather than by thermal or compositional buoyancy, so these unstable modes have the character of the magnetic modes mentioned in the preceding text.

In the weak field case, it is possible to use the same asymptotic techniques as discussed in **Section 8.05.4.3** to find solutions at very low E (Jones et al., 2003a,b). This also provides a check on the numerical codes. As in nonmagnetic rotating convection, the corrections to the critical Rayleigh number due to the formation of boundary layers are small, but they can be calculated.

If the applied field is nonuniform, there is an additional effect besides the thickening of the rolls and the change of frequency. Sreenivasan and Jones (2011) noted that magnetic field can lead to strong axial flows through the convection columns. This is of interest to the dynamo process, because the helicity $\mathbf{u}\cdot\boldsymbol{\zeta}$ is an important quantity helping to generate magnetic field. Columnar convection naturally has a strong z-component of vorticity $\boldsymbol{\zeta}$, so if in addition there is an axial u_z flow, helicity results. Fluid elements spiral on corkscrew paths in a helical flow. The fact that magnetic field enhances helicity promotes subcritical behavior in dynamos. If there is only weak magnetic field, there is weak helicity and the dynamo may be unable to grow. If on the other hand there is a substantial magnetic field in the initial condition of a simulation, it generates the necessary helicity to maintain itself and will not decay away. Sreenivasan and Jones (2011) showed that a dipolar magnetic field structure is particularly good at generating the preferred type of helicity, but a quadrupolar field is much less effective. This then gives a reason why dipolar fields can be preferred to quadrupolar fields.

In the case where the applied magnetic field is axial and uniform, Sakuraba (2002) found broadly similar behavior to that found in the Malkus field, though here the broadening of the columns only occurs at $\Lambda\sim O(1)$ rather than at $\Lambda\sim O(E^{1/3})$, probably because in this model, magnetic field and rotation are parallel. In addition to the almost geostrophic columnar modes, another polar mode of convection was found, which has the opposite equatorial parity to the geostrophic mode, that is, the axial vorticity is antisymmetric about the equatorial plane while the axial velocity is symmetrical. This mode tends to be strongest in the polar regions (see also **Section 8.05.5.6.2**).

8.05.5.4 Magnetic Instabilities

It is well known that magnetic instabilities make it very difficult to confine plasma in fusion devices, and we might also expect that magnetic instabilities are significant in the core. A valuable review on magnetic instabilities is given in Fearn (1998). Magnetic instabilities require a nonuniform field, so the simple uniform field models usually employed for convection models are not subject to them, though as noted in the preceding text, even the very simple Malkus field can be destabilized by the addition of a stable thermal gradient. The simplest models with magnetic instability are those where the basic field is assumed to be azimuthal. The two cases that have received most attention are (i) $\mathbf{B}=B(s)\mathbf{1}_\phi$ and (ii) $\mathbf{B}=B(s,z)\mathbf{1}_\phi$. The first of these is often studied in cylindrical geometry, using various profiles $B(s)$ (e.g., Fearn, 1988). The advantage of this is that the linearized stability problem has coefficients that are functions of s only, so that disturbances of the form $\exp \mathrm{i}(k_z z+m\phi-\omega t)$ can be assumed, leading to a simple 1-D eigenvalue problem in s for the complex eigenvalue ω. The disadvantage of this simple model is that the toroidal field of the Earth is most likely to be antisymmetric about the equator and so must be a function of z. These models become magnetically unstable at lower values of the Elsasser number than models in which B is only a function of s, typically $\Lambda\sim O(10)$ rather than $O(100)$ (see Zhang and Fearn, 1994, 1995). These instabilities can interact with thermal convection and, as noted earlier in the text, can have a significant effect in magnetoconvection models (Zhang and Jones, 1994). Some magnetic instabilities can function in the absence of diffusion, and these are known as ideal instabilities, while the so-called resistive instabilities require diffusion and typically have a slower growth rate. In the core, where the magnetic diffusion time is similar to the inverse ideal MAC wave frequency, the distinction between these modes is not so clear-cut. It is also possible for differential rotation to provide a source of instability, and as one might expect, differential rotation can interact with magnetic instabilities to affect the critical Elsasser numbers for onset (Fearn, 1998).

8.05.5.5 Taylor's Constraint

In **Section 8.05.5.2.3**, we noted that torsional waves in the core have a period of around 6 years for a moderate 2 mT core

poloidal field. This is much faster than the rate of evolution of the large-scale field, so that if we average over this longer timescale, we expect the forces that excite geostrophic torsional oscillations to be in equilibrium. Assuming that the velocities in the core are of order those given by the secular variation, the Reynolds stresses are comparatively small in the core, and we ignore them here. Then, we integrate the ϕ-component of eqn [38] over cylinders of radius s. The Coriolis term reduces to an integral of $2\Omega u_s$ over the cylinder, which is zero because in a Boussinesq fluid ($\nabla\cdot\mathbf{u}=0$), there can be no net flow through these cylinders. The ϕ-component of the pressure also integrates to zero, and the buoyancy has no ϕ-component, so we get

$$\frac{\partial}{\partial t}\int_{C(s)}\rho u_\phi \,\mathrm{d}S = \int_{C(s)}\mathbf{j}\times\mathbf{B}\cdot 1_\phi \mathrm{d}S + \nu\int_{C(s)} 1_\phi\cdot\nabla^2\mathbf{u}\,\mathrm{d}S \qquad [155]$$

The viscous term is usually dominated by the contribution from the Ekman boundary layers shown in eqn [110] and is small in the core compared with the Lorentz force term. On the dynamo timescale, we expect the time-dependent term to average to zero, so we expect Taylor's constraint (Taylor, 1963)

$$\int_{C(s)}\mathbf{j}\times\mathbf{B}\cdot 1_\phi \mathrm{d}s = 0 \qquad [156]$$

to be satisfied. The essential point is that this constraint depends on the form of the magnetic field. It is not satisfied by $\mathbf{B}$ being small, but rather by positive and negative parts of the integrand exactly canceling each other out. The magnetic fields arising from the linear solutions of the dynamo equations or the induced fields from magnetoconvection problems will not in general satisfy Taylor's constraint. A state in which Taylor's constraint is not satisfied is called an *Ekman state* (see, e.g., Fearn, 1998), and in such a state, the magnetic field strength has to be small, controlled by the Ekman suction. Malkus and Proctor (1974) suggested that a geostrophic flow would develop that alters the induction process until a field satisfying Taylor's constraint is generated; this type of field is called a *Taylor state*. The Malkus–Proctor scenario was shown to occur in the context of α-effect dynamos by Soward and Jones (1983), with Taylor states emerging. However, for a plane layer magnetoconvection problem, Jones and Roberts (1990) were able to show that no Taylor state emerged as the Rayleigh number was increased so the Malkus–Proctor scenario is not necessarily universal, while Hollerbach et al. (1992) found some evidence of an approach to an inviscid state, but no true Taylor state emerged. In numerical dynamo simulations, it is difficult to obtain solutions at low E, so that the viscous term is often still significant in eqn [155]. The measure of whether a Taylor state has been achieved is called the Taylorization (Anufriev et al., 1995):

$$\mathrm{Tay} = \frac{\int_{C(s)}\mathbf{j}\times\mathbf{B}\cdot 1_\phi \mathrm{d}S}{\int_{C(s)}\left|\mathbf{j}\times\mathbf{B}\cdot 1_\phi\right|\mathrm{d}S} \qquad [157]$$

In an Ekman state, Tay is of order unity, but when a Taylor state is achieved, Tay is small (see also Livermore et al., 2011). Strong evidence that Taylorization occurs in a convectively driven plane layer dynamo was given by Rotvig and Jones (2002), and Aubert (2005) reported that at $E=10^{-4}$, the cylindrical average of $\mathbf{j}\times\mathbf{B}\cdot\mathbf{1}_\phi$ was only one-seventh of its maximum value, suggesting that spherical dynamo simulations are approaching a Taylor state too.

As mentioned in **Section 8.05.5.2.3**, torsional oscillations are believed to occur in the core. These can be thought of as oscillations about the Taylor state, but it is not currently known what is exciting them. In dynamo models, Reynolds stresses (see eqn [110]) are significant, and these give rise to some torsional oscillations (Dumberry and Bloxham, 2003), so that at any instant in time, a dynamo model will not exactly obey Taylor's condition, though it should do if averaged over time. In the core, Reynolds stresses are thought to be small, but Dumberry and Bloxham (2003) argued that they may nevertheless play a role in exciting torsional oscillations.

8.05.5.6 Numerical Simulations of Nonlinear Convection-Driven Dynamos

The next natural step after considering linear magnetoconvection is nonlinear magnetoconvection. However, the equations that need to be solved for this problem are the same as for numerical simulations of the convection-driven dynamos, namely, eqns [6], [7a,b], [29], [38], and [39]. Usually, compositional effects are assumed to give similar results to thermal effects, so ξ' is set to zero in eqn [38]. Most recent work has concentrated on the full dynamo problem rather than the nonlinear magnetoconvection problem. Indeed, the only essential difference is that in the magnetoconvection problem, an imposed magnetic field is added at the boundaries, so that it is not necessary to have a configuration that has growing dynamo modes. However, it transpires that in convecting rotating spherical shells, dynamo action is surprisingly easy to achieve, so the incentive for doing magnetoconvection calculations is correspondingly reduced. The ease with which rotating spherical convection models produce dynamo action came as somewhat of a surprise, given that many simple flows do not give dynamo action even at large R_m (see **Chapter 8.03**). However, spherical geometry is not the easiest configuration in which to study either magnetoconvection or dynamo action, and so the Busse annulus geometry has also been used for understanding nonlinear convection in the presence of a magnetic field (see, e.g., Kurt et al., 2004, and references contained therein).

The four basic parameters needed to define a convective dynamo are the Rayleigh number, the Ekman number, the Prandtl number, and the magnetic Prandtl number ν/η. The parameter range in which it is feasible to run convective dynamo simulations is restricted. Currently, simulations are restricted to $E>10^{-6}$, $\kappa/\eta>0.05$, and $R/R_c<100$ (R_c being the critical value in the absence of magnetic field), though these values are being improved all the time due not only to faster computers but also partly to improved numerical methods. Note that the definition of E has different numerical factors in different papers, so some calculations with $E<10^{-6}$ have been reported, but these are equivalent to $E\sim10^{-6}$ using our definition. The first successful self-consistent dynamo models were designed for solar and stellar convection (Gilman, 1983; Gilman and Miller, 1981; Glatzmaier, 1984). Zhang and Busse (1989) found steady drifting roll solutions that sustained a

magnetic field. The first fully time-dependent low Ekman number dynamos made use of hyperdiffusion (Glatzmaier and Roberts, 1995, 1997) or had very restricted resolution in ϕ (Jones et al., 1995), but with increasing computer speed, these drawbacks are no longer necessary. Models have been reviewed by Jones (2000, 2011), and they have been surprisingly successful at reproducing many features of the observed field. Models are frequently dipole-dominated, they can give occasional reversals rather reminiscent of the behavior of the actual Earth, the field strength produced is the right order of magnitude, and the secular variation is broadly similar to geomagnetic secular variation. Of course, varying the input parameters gives different results, but it is nevertheless rather encouraging that it is possible to make contact with geophysical observations from first-principle solutions of the fundamental equations. Conditions on the parameters needed to give 'Earth-like' geodynamo models were given by Christensen et al. (2010). Although there is much still to discover about the relation between the mathematical solutions of the equations and the geophysical observations, it does appear that much of the fundamental physics behind the models is correct.

A particularly simple convective dynamo, at a rather modest set of parameter values, has been adopted as a benchmark (Christensen et al., 2001) against which to test dynamo codes. This is necessary, as the dynamo computer programs are very complex, allowing many possibilities for coding error. A snapshot of the field and flow produced by a typical dynamo code is shown in **Figure 9(a)** and **9(b)**. Details of the boundary conditions and definitions of the parameters are in Sreenivasan and Jones (2006a). A modified Rayleigh number, often used in dynamo simulations and defined as $R = g\alpha\Delta T_s d/\eta\Omega$, is used. These simulations are for a fairly modest value of $R = 750$.

The flow pattern is columnar, not very different from that shown in **Figure 4**, which is for the linear onset of nonmagnetic convection. **Figure 9(a)** and **9(b)** is for $E = 10^{-4}$; reducing E gives more, thinner columns. The pattern drifts westward. The magnetic field seems to be primarily generated in the convection columns (Olson et al., 1999), and indeed, the strongest field is found near the TC, coming out of the tops of the rolls. Magnetic field near the equator is concentrated in the anticyclonic rolls (Kageyama and Sato, 1997), which then expands the anticyclonic rolls leading to westward flow near the CMB and eastward flow near the ICB (Sakuraba and Kono, 1999). Models in which the driving is from the boundaries only (with no internal heat source) (e.g., Christensen et al., 1999) differ in a systematic way from models with a uniform heat source (e.g., Busse, 2002; Grote and Busse, 2000). Models with no internal heating are typically much more dipolar, while with internal heating, quadrupolar dynamos are almost as common as dipolar ones. Generally, when the convective columns are concentrated close to the TC, dipolar dynamos are more common, whereas with distributed heating, convective columns can occur well away from the TC and the resulting dynamos are much less dipole-dominated.

Another interesting issue is the importance of inertia in dynamo models. At the modest values of E possible, if the Prandtl number is small, inertia plays a significant role in the dynamo process (Christensen and Aubert, 2006; Simitev and Busse, 2005; Sreenivasan and Jones, 2006a). The dynamo-generated field is then typically weaker, much more complex, and no longer dipole-dominated. Velocity estimates from the secular variation suggest inertia is not important at large scales in the core, and the dynamo simulations also suggest that the dipolar structure of the Earth is more easily reproduced in the low-inertia regime. Having said that, it should be noted that the low inertia, strongly dipole-dominated models show no sign of reversing. To get reversals, it is generally necessary to increase the Rayleigh number (and not to have E too small) to produce a more strongly time-dependent and less dipole-dominated field. Although dynamo models give rise to reversals (Glatzmaier and Roberts, 1995; Kutzner and Christensen, 2002; Sarson and Jones, 1999), there is no general agreement about how they are achieved. Sarson and Jones (1999) noted that the reversal typically takes place first in one hemisphere, suggesting the growth of a time-dependent quadrupolar mode, canceling out the dipolar field in one hemisphere and strengthening it in the other. The field can then reverse in one hemisphere, and this reversed flux can lead to a complete reversal. They also suggested that meridional circulation might be important in controlling the reversal process.

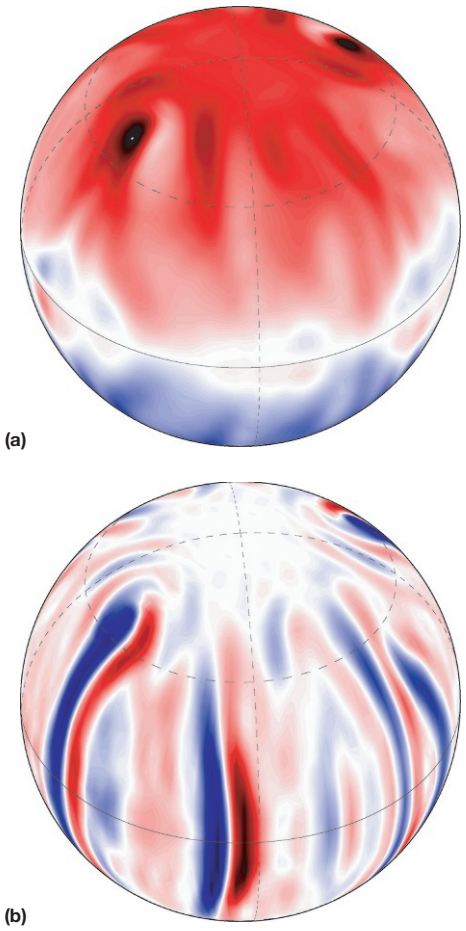

Figure 9 Contour plots from a dynamo simulation with $R = 750$, $E = 10^{-4}$, $Pr = Pm = 1$.(a) Shaded contours of B_r at the CMB. (b) Shaded contours of u_r at $r = 0.8r_{cmb}$. Reproduced from Sreenivasan B and Jones CA (2006a) *Geophysical Journal International* 164: 467–476.

As we learn more about convective dynamos, models that might be suitable for simulating the magnetic fields found on other planets are being developed (Jones, 2003, 2011; Stanley and Glatzmaier, 2010; Stevenson, 2003). There is considerable variety in the types of magnetic fields found on other planets. For example, the field on Mercury is particularly weak, while the fields on Uranus and Neptune are not dipolar-dominated but appear to be a mixture of dipolar and quadrupolar fields with no strongly preferred parity (Holme and Bloxham, 1996; Stanley and Bloxham, 2006). Developing planetary dynamo models is an area likely to develop rapidly over the next few years.

8.05.5.6.1 Convection outside the TC: Picture from numerical simulations

The inner core appears to have an important effect on the dynamics of convection, and the behavior of convection outside the TC is rather different from that inside the TC. As mentioned in Section 8.05.1.5, the large amount of vortex stretching required makes it difficult for fluid to cross the TC, though magnetic field may help to allow some transport. Dynamo simulations suggest that the pattern of convection outside the TC is not strongly influenced by magnetic field, the columnar pattern found in nonmagnetic simulations persisting, and the rolls have the same parity, that is, axial vorticity symmetrical and axial velocity antisymmetric about the equator (see Figure 9(b)). The magnetic field slows down the drift rate, as expected from magnetoconvection calculations, but the roll width is not increased as much as would be expected from linear magnetoconvection theory. Indeed, the roll thickness seems to go down with E according to the $E^{1/3}$ scaling.

Figure 10(a) and 10(b) shows outputs from a dynamo simulation run by Dr. B. Sreenivasan, where the Ekman number $E=3\times10^{-6}$. Comparing Figures 10(b) and 9(b), we can see that the columnar structures are indeed much thinner in the lower E case, despite the fact that both have fields with Elsasser number of order unity. Possibly this is due to the field being quite nonuniform. It is known that in nonlinear magnetoconvection without rotation that once convection starts, flux expulsion occurs from the convecting region and the heat transport is then relatively unimpeded by the field. Nevertheless, we should remember that in the simulations, it is not possible to get to the very thin roll regime and that on small scales, when the local magnetic Reynolds number gets small, we expect the magnetic field to be smooth, so it may be that magnetic field does thicken the rolls at very low Ekman number. It is also found that when fixed flux boundary conditions (rather than fixed temperature boundary conditions), and internal heating rather than basal heating is applied, magnetically dominated regions with larger coherent structures are found, together with regions of thin rolls (see, e.g., the review of Jones, 2011).

As the Rayleigh number is increased, the velocities increase and the flow becomes more chaotic. The Earth's core has low $q=Pm/Pr$, so it is of interest to see what happens to the convection pattern at low q. This is a hard regime to reach, because the magnetic Reynolds number has to be greater than about 50 to get dynamo action, but low q then implies very high Péclet number U_*d/κ, which makes it hard to get resolved simulations. Nevertheless, at sufficiently low E (typically about 10^{-6}), it is possible to get dynamos with $q\sim0.1$ (Christensen and Aubert, 2006) and see also Figure 10(a) and 10(b), which are for $Pr=1$, $Pm=0.1$. Note that although the Rayleigh number here is fifty times critical, because of the low E, the magnetic Reynolds number $R_m\approx125$, low for the core. This indicates that we need higher Ra, but unfortunately this is very expensive computationally. Note that these low E dynamos are remarkably dipole-dominated (Figure 10(a)), even more so than the field shown in Figure 9(a). Higher Ra would introduce a more chaotic flow, which helps to reduce this strong dipole dominance, allowing reversals to occur (Christensen et al., 2010).

Figure 10(a) and 10(b) shows that at small q, the flow structure is finer than the field structure, as we expect in the core. It is unfortunate, though, that this does not happen until very low E is reached, because the very long CPU time required to perform the simulations in this regime make it very hard to explore the parameter space. If the value of Pr is reduced, then inertial effects become important, while if Pr is increased, the roll thickness becomes even smaller, as predicted by linear nonmagnetic theory. The actual value of Pr is probably not

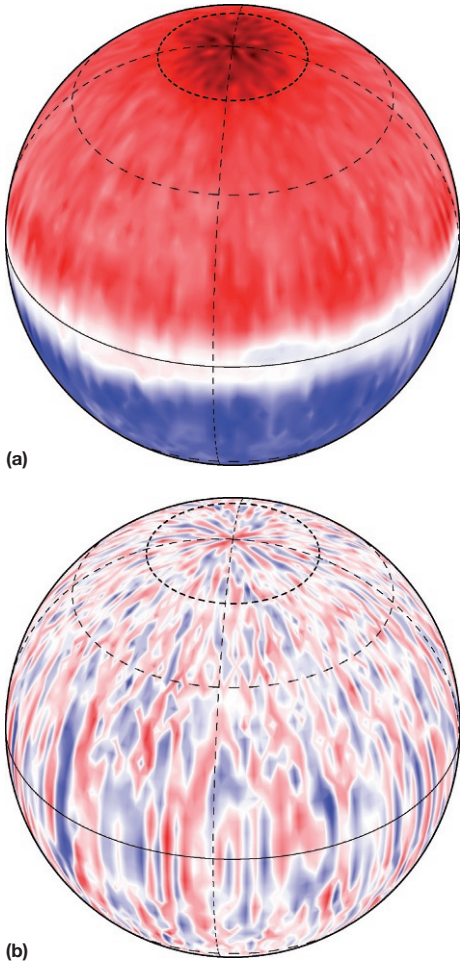

Figure 10 Contour plots from a dynamo simulation with $R=50R_c$, $E=3\times10^{-6}$, $Pr=1$, $Pm=0.1$. (a) Shaded contours of B_r at the CMB. (b) Shaded contours of u_r at $r=0.8r_{cmb}$. These figures were supplied by Binod Sreenivasan.

very relevant in the core, because both thermal diffusion and viscous diffusion are so small it can only operate on very short length scales on dynamo timescales.

The mechanism by which the convective rolls generate magnetic field by dynamo action in simulations was discussed by Olson et al. (1999). The toroidal field is mostly generated by twisting of the poloidal field, as in α^2-dynamos and unlike $\alpha-\omega$ dynamos, where toroidal field is generated by the stretching out of poloidal field by differential rotation. Low Ekman number dynamo simulations driven by rolls appear not to have very large differential rotation. In the QGA, it is assumed that u_z varies linearly with z, but in the numerical simulations, u_z changes more rapidly near the equator than at the boundary. Olson et al. (1999) pointed out that this variation is significant for dynamo action, so it is not clear that quasi-geostrophic flows will necessarily have the same dynamo properties as fully 3-D simulations give.

8.05.5.6.2 Convection inside the TC: Picture from numerical simulations

The linear theory of nonmagnetic convection in a sphere (Busse, 1970) suggests that the onset occurs at substantially high Rayleigh number inside the TC than outside the TC. This result is verified by numerical simulations (e.g., Dormy et al., 2004). Whereas the s-component of gravity predominates in convection outside the TC, it is the z-component that is most significant inside the TC. Indeed, of the standard idealized geometric convection models, the one most relevant to convection inside the TC is the plane horizontal parallel layer with vertical rotation and gravity (Sreenivasan and Jones, 2006b; discussed in **Section 8.05.5.2.2**). In this model, the first mode to onset has vertical velocity symmetrical about the midplane and vertical vorticity antisymmetric, so the axial vorticity will not be even approximately constant for convection inside the TC.

Magnetic field appears to affect the onset of convection much more radically inside the TC than outside it (Sreenivasan and Jones, 2005, 2006b). In particular, nonmagnetic convection has the tall thin column configuration both inside and outside the TC, but whereas magnetic field has only a limited impact outside the TC, inside the TC, the convection columns are much thicker with magnetic field, and magnetic field enhances the vigor of convection inside the TC (Olson and Glatzmaier, 1996). In the plane horizontal layer geometry, the effect of magnetic field is not gradual, but onsets at a specific value of the Elsasser number as noted in **Section 8.05.5.2.2**. In a study of behavior inside the TC in dynamo simulations, Sreenivasan and Jones (2005, 2006b) found anticyclonic vortices just below the CMB when inertial effects are small and cyclonic vortices when they are large. These vortices are associated with the large-scale magnetic mode of convection, and their horizontal scale can be predicted surprisingly accurately using the Chandrasekhar linear theory. Since there is evidence from secular variation that there are anticyclonic polar vortices (Olson and Aurnou, 1999), this supports the view that the geodynamo is in a low-inertia regime. They also found that the polar vortices are not actually centered on the pole but are in fact typically 10° off-axis, with the vortex patches drifting slowly westward round the pole.

The magnetic mode of convection in a plane layer has a somewhat different physical character from conventional nonmagnetic, nonrotating convection. In the simple case, hot fluid rises directly because of its buoyancy. In rotating magnetic-mode convection, hot fluid rotates about the convection column axis, because of the local thermal wind that results from the horizontal temperature gradient between the hot interior and relatively cool surroundings. This local rotation, or vertical vorticity, winds up the field lines to produce a current and a corresponding Lorentz force. This Lorentz force breaks the Proudman–Taylor constraint and allows a u_z that varies with z. It is then possible for fluid to rise in the interior.

There is still much that is uncertain about convection inside the TC. Simulations up to ten times critical generally have stronger convection outside the TC, because the delay in onset inside the TC is still having an effect. At very large Ra, the large-scale magnetic mode may eventually give rise to convection inside the TC more vigorous than outside it. There is also some uncertainty about how the field inside the TC is created. On the Earth, there is evidence that the poles have weaker field than the region where the TC intersects the CMB (about latitude 70°). This may be due either to weak convection failing to generate much field or to vigorous convection expelling flux from the polar regions.

8.05.5.7 Scaling Laws and Dynamo Simulations

In order to overcome the problem of the inaccessibility of the geodynamo parameter regime, there has been recent work on how the more important outputs from geodynamo simulations scale with the input parameters. If an asymptotic regime in which the role of the small diffusion coefficients can be identified, it may be possible to extrapolate to the very small values that occur in the Earth. Two approaches have been tried: Starchenko and Jones (2002) used results from plane-layer models and the general understanding of rotating magnetoconvection to estimate typical velocities and magnetic field strengths expected from very low E, low q dynamos. An alternative approach (Christensen and Aubert, 2006) is to analyze the data from a large number of dynamo simulations and see whether asymptotic trends are evident in the data. In practice, these two approaches are not so different, as theoretical ideas inevitably affect the way the dynamo simulation data are analyzed.

Starchenko and Jones started by assuming that at very low E, the Coriolis and buoyancy forces would be in balance and that the magnetic field would bring the horizontal length scale ℓ appearing in eqn [112] to a fixed ratio with $d=r_{\mathrm{cmb}}-r_{\mathrm{icb}}$. The idea here is that as E is reduced, the magnetic field prevents the roll width reducing as $E^{1/3}$. Then, eqn [112] is replaced simply by

$$\Omega U_*/d \sim g\alpha T'_*/\ell \qquad [158]$$

Then, eliminating the temperature perturbation using eqn [113],

$$U_* \sim \left(\frac{g\alpha F_{\mathrm{conv}}}{\rho c_p \Omega}\right)^{1/2}\left(\frac{d}{\ell}\right)^{1/2},$$

$$g\alpha T'_* \sim \Omega^{1/2}\left(\frac{g\alpha F_{\mathrm{conv}}}{\rho c_p}\right)^{1/2}\left(\frac{\ell}{d}\right)^{1/2} \qquad [159a,b]$$

If the ratio d/ℓ tends to a fixed limit at small E due to magnetic field, as postulated by Starchenko and Jones, U_* is

proportional to $F_{\rm conv}^{1/2}$. Interestingly, Christensen and Aubert (2006) found that the exponent of 2/5 gives a better fit to their data than the exponent of 1/2 in eqn [159]. Of course, the difference is not that great, but it may be connected with the observation made in Section 8.05.5.6.1 that in dynamo simulations, there is not much evidence of the magnetic field controlling the roll width, as suggested by Starchenko and Jones (2002). It remains possible, though, that this control will start to occur at $E < 10^{-6}$. Christensen and Aubert (2006) suggested replacing eqn [159a] by

$$U_* \sim (\Omega d)\left(\frac{g\alpha F_{\rm conv}}{\rho c_p \Omega^3 d^2}\right)^{2/5} \qquad [160]$$

which is the same formula as in the nonmagnetic case, eqn [115]. They noted that the best fit with their simulation data can be expressed in dimensionless variables

$$\mathrm{Ro} = \frac{U_*}{\Omega d}, \quad Ra_Q^* = \frac{g\alpha Q_{\rm adv}}{4\pi r_{\rm icb} r_{\rm cmb} \rho c_p \Omega^3 d^2} \qquad [161]$$

by

$$\mathrm{Ro} = 0.83 Ra_Q^{*0.41} \qquad [162]$$

very close to eqn [160]. Here, $Q_{\rm adv}$ is the total convective heat flux over a spherical surface of radius r, assumed constant with r throughout the core. Note that with this assumption, the convective heat flux $F_{\rm conv}$ in eqns [158]–[160] is best taken as

$$F_{\rm conv} = \frac{Q_{\rm adv}}{4\pi r_{\rm icb} r_{\rm cmb}} \qquad [163]$$

The Rayleigh number Ra_Q^* introduced by Christensen and Aubert is the Ra_Q^* defined in eqn [126]. Equation [162] therefore expresses the independence of the velocity scaling on any diffusion coefficient. The emergence of eqn [162], with no dependence on any Prandtl numbers, expresses the fact that the simulations do appear to be approaching an asymptotic regime, which is independent of diffusion, a very encouraging result.

Christensen and Aubert (2006) also went on to estimate the typical magnetic field strength in dynamo simulations. The rate of working of the buoyancy forces is $g\alpha F/c_p$, and assuming that the dissipation is primarily ohmic, this must balance the rate of ohmic dissipation, so

$$\eta\mu\mathbf{j}^2 \sim \frac{g\alpha F_{\rm conv}}{c_p} \qquad [164]$$

To convert this into a formula for $\mathbf{B}^2$, we need to know the magnetic dissipation time, that is,

$$\tau_{diss} = \frac{\int_V \mathbf{B}^2/2\mu \,\mathrm{d}v}{\int_V \eta\mu\mathbf{j}^2 \,\mathrm{d}v} \qquad [165]$$

or equivalently the magnetic dissipation length scale

$$\delta_B = \left(\frac{\tau_{\rm diss}}{\eta}\right)^{1/2} \qquad [166]$$

Christensen and Tilgner (2004) argued that $\delta_B \sim d R_m^{-1/2}$, again on the basis of an analysis of numerical simulations. This is consistent with nonrotating flux expulsion arguments (Galloway et al. (1977)). Then, eqn [164] becomes

$$\eta\mu\mathbf{j}^2 \sim \eta\frac{(\nabla\times\mathbf{B})^2}{\mu} \sim \frac{\eta\mathbf{B}^2}{\mu\delta_B^2} \sim \frac{g\alpha F_{\rm conv}}{c_p} \qquad [167]$$

giving

$$B_* \sim \left(\frac{g\alpha F_{\rm conv}\mu d}{U_* c_p}\right)^{1/2} \qquad [168]$$

With the Starchenko and Jones scaling [159], this gives

$$B_* \sim \mu^{1/2}\left(\frac{g\alpha F_{\rm conv}\rho\Omega\ell d}{c_p}\right)^{1/4} \qquad [169]$$

and with the Christensen and Aubert scaling [160], we get

$$B_* \sim \mu^{1/2} d^{2/5} \rho^{1/5} \Omega^{1/10}\left(\frac{g\alpha F_{\rm conv}}{c_p}\right)^{3/10} \qquad [170]$$

Note that the small difference in the velocity scalings has led to a significant difference in the scaling of B_* with Ω, because the Christensen and Aubert scaling has a remarkably weak scaling of B_* with Ω. Indeed, their best fit of the simulation data is close to

$$L_{\rm o} = 0.87 f_{\rm ohm}^{1/2} Ra_Q^{*0.33} \qquad [171]$$

where $L_{\rm o} = B_*/(\mu\rho)^{1/2}\Omega d$ and $f_{\rm ohm}$ is the fraction of the total dissipation (ohmic + viscous), which is ohmic. This gives, assuming as expected $f_{\rm ohm} \sim 1$ in the core,

$$B_* \approx 0.9\mu^{1/2}\rho^{1/6}\left(\frac{g\alpha Q_{\rm adv} d}{4\pi r_{\rm icb} r_{\rm cmb} c_p}\right)^{1/3} \qquad [172]$$

so that B_* is completely independent of the rotation.

When compositional convection is present, in the previously mentioned formulas, the thermal buoyancy flux $g\alpha Q_{\rm adv}$ is replaced by the compositional buoyancy flux $gQ_{\rm buoy}$ where $Q_{\rm buoy}$ is the mass of light material released per unit time.

The scalings [162] and [171] can be used to find the ratio of kinetic to magnetic energy, which is close to $Ra_Q^{*\,0.15}$. Since Ra_Q^* is very small in the core, this implies that magnetic energy is indeed larger than kinetic energy in the core, but the weak power shows that it is not surprising that in simulations, the two forms of energy have similar magnitudes. Also, although ohmic dissipation is predicted to dominate over viscous dissipation at very low E, simulations have great difficulty getting down to this regime (at $Pr = 1$), and generally, at $Pr = 1$, they show comparable ohmic and viscous dissipations.

8.05.6 Heterogeneous Boundary Conditions and Stable Layers near the CMB

Because the departure from an adiabatic temperature gradient is so small in the core, the CMB will be maintained at an almost uniform temperature. However, it is believed that in the mantle, cold descending slabs may reach close to the CMB, and the locations where this happens may have an anomalously high CMB heat flux, while in regions where the mantle has been relatively static, the temperature gradients, and hence the heat flux, may be lower. It is therefore likely that there are substantial

lateral variations of heat flux at the CMB (e.g., Schubert et al., 2001). If so, this lateral heterogeneity may well have an impact on core convection (for a review, see Olson, 2003). It is now possible to measure the velocity of shear waves near the CMB, using seismic tomography (e.g., Kuo et al., 2000). The simplest interpretation is that high velocity zones are associated with colder material and hence with higher heat flux (e.g., Nataf, 2000; Nakagawa and Tackley, 2008). A natural assumption is then that the heat flux is simply proportional to the seismic velocity variation. If this is correct, then the lowest heat fluxes are found under the central Pacific and the eastern Atlantic and Africa, while high heat flux is found under Australia and the Gulf of Mexico. This distribution is often modeled as a spherical harmonic P_2^2 pattern of variation.

As mentioned in **Section 8.05.1.3** and **Chapter 8.02**, there is no general agreement about the total heat flux coming out of the core. It is also difficult to estimate the percentage variation of any lateral heat flux, though there might even be variations of a factor two between different locations. One possible effect of laterally inhomogeneous heat flux would be to lock core convection to the mantle, that is, prevent any systematic westward or eastward drift. This could in turn lock the dynamo to the mantle. This could explain the preferred paths for the direction of the dipole field during reversals. There seems to be a preference for the virtual geomagnetic pole to track through the Americas or through East Asia (Laj et al, 1991), but the results are controversial (see, e.g., the review of Dormy et al. (2000) for a discussion). Another possible effect is that long-term changes in mantle convection might affect the reversal rate (e.g., Olson et al., 2009). It is well established that during certain eras, the geomagnetic field has not reversed, an extreme example being the Cretaceous superchron, during which the field maintained the same polarity for about 35 million years. The current reversal rate is about 4.5 reversals per million years. It is hard to explain why the reversal rate should vary on such a long timescale, because the magnetic diffusion time and the turnover time are much shorter. It is tempting to identify these long timescales with mantle convection timescales (see, e.g., Biggin et al., 2012) and therefore that mantle convection and hence the CMB heat flux distribution control dynamo reversal rates.

The issue of whether heterogeneities in heat flux on the boundary can lock the pattern of convection has been the subject of a number of theoretical studies (Davies et al., 2009; Gibbons and Gubbins, 2000; Zhang and Gubbins, 1996). Convection in a rapidly rotating sphere has a columnar structure, and the columns usually progress eastward if there is no magnetic field. With inhomogeneous boundary conditions, there is no critical Rayleigh number; even if Ra is small, there is still a weak motion that is driven by the inhomogeneous heat flux and therefore aligned with it. At very high Rayleigh number, one expects that the convection will be controlled by its internal dynamics and will move independently of the boundary conditions and so move eastward. However, in between these two extremes, a great variety of dynamical behavior can occur. Davies et al. (2009) did indeed find that at moderate E and Ra, locking can occur, but it becomes less common at small E and larger Ra. Nevertheless, even if the convection is not truly locked, it may be the case that the boundary still influences the flow, as might be expected from the columnar character of the convection. One interesting possibility found by Davies et al. (2009) is that convection occurs in nests, localized clusters of convection rolls, with the location of the nests depending on the boundary heterogeneity. Localized convection was noted by Grote and Busse (2000) even with homogeneous boundaries, and localized nests of convection have been found in compressible rotating convection models of stellar dynamos (Brown et al., 2008). The formation of nests is believed to be connected with the suppression of convection in regions of strong differential rotation, but the details are not yet understood.

It has also been noticed that downwelling fluid tends to concentrate radial magnetic flux into patches (Bloxham and Gubbins, 1987). Downwelling fluid occurs where the CMB temperature is coolest, and the outward temperature gradient is largest there (e.g., see **Figure 10** of Sarson et al., 1997) so the heat flux is a local maximum. So according to this argument, there should be long-term local maxima in the radial flux where the CMB heat flux is strongest, under Australia and the Gulf of Mexico, while upwelling fluid giving weaker field should be associated with relatively low, or negative, CMB heat flux. There is some evidence at least for a long-term excess field under Australia and relatively low field in the central Pacific (see Olson, 2003, for a review of the paleomagnetic evidence).

Since seismic tomography indicates where the regions of high and low heat flux occur at the CMB, it is possible to study whether the core flows derived from rotating convection give flows consistent with the secular variation. This was studied by Gibbons and Gubbins (2000). A steady-state convection pattern was found, locked to the inhomogeneous boundary condition. The downwelling regions generally coincide with regions of enhanced heat flux, but at low Ekman number, there is a tendency for maximum downwelling to occur to the east of the peak heat flux. Sarson et al. (1997), using a truncated dynamo model, also found locked solutions, this time with a steady dynamo, and again the downwelling broadly coincides with enhanced heat flux, this time associated with concentrated field patches, as predicted by Bloxham and Gubbins (1987). However, Sarson et al. (1997) found a tendency for the downwelling to be slightly west of the maximum heat flux. Glatzmaier et al. (1999) worked at a higher (and more realistic) value of the Rayleigh number and found that the solution was not locked, but time-dependent. A similar result was found earlier in a magnetoconvection calculation by Olson and Glatzmaier (1996). They found that though some locking occurs near CMB, at deeper levels, the flow and field drifted just as they do with spherically symmetrical CMB conditions. However, even though the Glatzmaier et al. (1999) solutions were not locked, a heterogeneous heat flux distribution gave enhanced field where the heat flux is maximal when averaged over time, so there is clearly a tendency for strong magnetic flux patches to form over regions of strong heat flux even when the solution is not completely locked. Kutzner and Christensen (2004) used a reversing numerical dynamo model with an imposed heterogeneous CMB heat flux to study whether reversal paths were systematically correlated with the heat flux distribution. They found that although individual reversal paths had considerable variation, there was a tendency for reversal paths to cluster around the regions of high heat flux on the CMB.

More recently, Aubert et al. (2007) suggested that CMB locking might affect the flow throughout the core, even down

to the ICB. The inner core is seismically inhomogeneous, and it is possible this could be explained by persistent east–west asymmetry in the core convection pattern induced by heterogeneous CMB heat flux. The CMB heat flux has a dominant $m=2$ pattern, which is not obviously consistent with the $m=1$ inner core asymmetry, but the convection is strongly nonlinear, so a range of azimuthal modes are excited. Gubbins et al. (2011) pursued this idea and found that it is possible for hotter regions of fluid induced by the CMB variation to descend to the ICB and lead to melting. This is an alternative explanation to that of Alboussière et al. (2010) and Monnereau et al. (2010) for the origin of stably stratified regions near the ICB.

Given the growing evidence for a stably stratified region just below the CMB, a natural question is as follows: What is the effect of lateral heat flux inhomogeneity on stably stratified fluid? This was examined by Lister (2003). If the stably stratified layer is unstirred, the subadiabatic temperature gradient will be of the same order as the adiabatic gradient itself, which implies a very strong stable stratification. Lister found that a vertical magnetic field makes a very substantial difference to the resulting flows. With no magnetic field, even a 5% lateral variation in heat flux could lead to a horizontal temperature difference of $T_*^{'}\sim 1\mathrm{K}$, which would drive a thermal wind of order $g\alpha T_*^{'}/2\Omega\sim 1\ \mathrm{m\,s^{-1}}$ through a layer of depth 200 km, which is far too big to be consistent with secular variation observations. Note that because of the strong stable stratification, $T_*^{'}\sim 1\,\mathrm{K}$ is much larger than the usual estimate of the temperature perturbation in a convecting core. However, with a magnetic field, the estimate is reduced by a factor that scales with $E^{1/4}$. Even if a turbulent value of $E\sim 10^{-8}$ is adopted, this gives a huge reduction in flow speed, and with a radial field of order 0.5 mT, he found a velocity of 7 mm $\mathrm{s^{-1}}$ in a layer 35 km deep. With a molecular Ekman number, the velocity drops to 0.3 mm $\mathrm{s^{-1}}$, which is compatible with the secular variation observations. Given the uncertainties in the estimates of the strength of the stable stratification, it seems that stably stratified layers below the CMB cannot be ruled out on the grounds that they would produce too strong a thermal wind.

In summary, at the present time, it seems that inhomogeneous thermal boundary conditions, with the heat flux varying by an $O(1)$ amount, can certainly affect the flow near the CMB, and this is of course where the secular variation field and inferred flow are measured. It is still uncertain whether the whole convection pattern and dynamo are also locked to the boundary inhomogeneities. It is certainly possible for some parameter regimes, but the larger Ra and low E regimes where the more Earth-like geodynamo models exist are convecting too strongly for the boundary conditions to affect the whole flow. However, we must keep in mind that geodynamo models are not operating in the correct region of parameter space, so it may still be possible for heterogeneous boundary conditions to play a significant role throughout the core.

8.05.7 Conclusions and Future Developments

While uncertainties about the physical properties of material at high pressure mean that we cannot be absolutely certain that convection occurs in the core, the evidence strongly suggests that both thermal convection and compositional convection are present at least in some parts of the core. It is also likely that convection is driving the geodynamo, though we cannot rule out the possibility that tides and precession might make a contribution in the Earth and other planets. The form that core convection takes is more uncertain. The linear theory of rotating, magnetic convection at onset is now fairly well understood, but core convection is strongly supercritical. Numerical simulations have carried our understanding into the nonlinear regime, and a picture that is consistent with our knowledge about the linear problem is beginning to emerge. However, numerical simulations cannot at present reach the true parameter regime for the core, and there is no prospect of doing so using our current techniques. Nevertheless, the combination of numerical simulations, asymptotic analysis, and physical intuition is a powerful one, and rapid progress is being made.

The most fruitful approach to date has been through geodynamo simulations, using the constraint that the pattern of convection must be consistent with the known facts of the secular variation and the paleomagnetic data. Recent analyses of how the properties of convection scale with the parameters have been particularly encouraging. This has given strong support to the notion that at least outside the TC, columnar convection dominates. This type of motion not only is expected on theoretical grounds but also generates fields consistent with those of the Earth in a robust manner, without the need for any special tuning of the parameters. The size of the rolls is however still controversial. Some believe that the large-scale flux patches seen in geomagnetic data are directly connected with the convection roll size; others believe that the roll size is much thinner and that the observed flux patches are the result of organized larger-scale flows.

Generally, our lack of understanding of small-scale convection is a matter for some concern. The regime where $\eta\gg\kappa$ is a difficult one, and simulations always use a hugely enhanced value of κ to avoid it. This means that the small-scale motions that must be present to transport the heat at very large Péclet number are not present in the simulations, and we do not know what effect they have. The current assumption, which is made for computational reasons rather than for physical reasons, is that these small-scale motions act to produce an enhanced isotropic eddy diffusion. This assumption may not be correct.

Even more controversial is whether the whole core is convecting or whether the regions near the CMB are at least partly stably stratified. Recent developments such as the revised enhanced thermal conductivity (Pozzo et al., 2012) favor the existence of such stable layers. The existence of the stable layer below the CMB depends on the uncertain value of the heat flux passing through the CMB. Large heat flux estimates favor whole-core convection, but lower estimates (though possibly as high as 10 TW) give rise to a stably stratified layer. Bound up with this uncertainty is the age of the inner core.

Also difficult is the issue of a stably stratified layer above the ICB. This is suggested by seismological considerations and could potentially be explained either by a translating inner core or by strongly heterogeneous CMB heat fluxes carrying hot material right through the outer core. However, many issues remain unresolved about how the light material released at the ICB can make its way through a strongly stably stratified layer.

Another exciting development is the growth of experimental programs studying the dynamics of rotating magnetic fluids. Like the simulations, these cannot reach core conditions either, but they do extend the parameter range in useful directions, particularly low magnetic Prandtl number. In combination with numerical experiments, they provide a very useful weapon in the fight to gain understanding of the fundamental processes. Crucial understanding of how small-scale and large-scale flows interact can be gained from laboratory experiments, while DNS has great difficulty with this issue, because of the very large resolution required to study it.

Finally, the geophysical data available are continually improving. New satellites are providing more information about the core field and its secular variation, though masking by the crustal field does limit what is possible. Seismic measurements are giving more information about the inner core and its structure and rotation, which are directly connected with flow patterns in the core. Length-of-day measurements and the torsional oscillations are also a potentially important source of information about the core. The detection of the short-period oscillations of the inner core about its mean position (the Slichter modes) is currently controversial but nevertheless could provide very valuable evidence about the state of the core, as indeed can nutation and precession data. In the longer term, there is even the possibility that the detection of the Earth's core neutrinos (Araki et al., 2005) could give us direct window into the core. In an age when the furthest reaches of the universe are being explored, it is perhaps surprising that what is going on beneath our feet is still a mystery. Solving this mystery is an outstanding scientific challenge and one that is being actively addressed by scientists from many different fields. We must hope that this simultaneous attack on the problem from such a large number of fronts will eventually prove decisive.

Appendix

Papers dealing with the Earth's core frequently use many different symbols. Here, we give a list of those used, together with their dimensions (blank for dimensionless quantities). Subscripts r, θ, ϕ refer to spherical coordinate components, while s, ϕ, z to cylindrical coordinate components. s is the perpendicular distance to the rotation axis. Subscript a denotes the adiabatic reference state value; subscript c, the much smaller departure from the adiabatic value due to convection.

Dimensionless mathematical expressions, such as $\mathcal{F}$ in the Roberts–Busse equation, are not defined here, as such quantities only have meaning in their immediate context.

Definition of symbols

Symbol	*Meaning*	*Units*
A	Magnetic potential	T m
α	Coefficient of thermal expansion	K^{-1}
α^{ξ}	Adiabatic compositional expansion coefficient	
$\mathbf{B}$	Magnetic field	T
B_*	Typical core field strength	T
β	Rotation parameter in the annulus model $4\chi\Omega D^3/L\nu$	
C	Coriolis operator in toroidal–poloidal expansion equations	m^{-1}
c_p	Specific heat at constant pressure	J kg^{-1} K^{-1}
χ	Endwall slope angle in the annulus model	
d	$r_{cmb} - r_{icb}$	m
D	Dissipation number	
δ	Thermal boundary layer thickness	m
δ_B	Magnetic dissipation length scale	m
Δ_2	Dimensionless quantity derived from melting point curve	
$\mathbf{E}$	Electric field	V m^{-1}
E, $\mathcal{E}$	Ekman number	
η	Magnetic diffusivity	m^2 s^{-1}
F_{conv}	The convective part of the heat flux	W m^{-2}
$\mathbf{F}^{\nu}$	Viscous force density	N m^{-3}
g	Acceleration due to gravity	m s^{-2}
γ	Grüneisen parameter	
H	Internal heat source	W kg^{-1}
h^{ξ}	Heat of reaction	J kg^{-1}
I_{ad}	Heat flux per unit area conducted down the adiabat	W m^{-2}
I_{cmb}	Heat flux per unit area passing through CMB	W m^{-2}
$\mathbf{j}$	Current density	A m^{-2}
k	Thermal conductivity	W m^{-1} K^{-1}
$\mathbf{k}$	Vector wave number	m^{-1}
k^{ξ}	Mass diffusion coefficient	kg m^{-1} s^{-1}
κ	Thermal diffusivity	m^2 s^{-1}
κ^{ξ}	Mass diffusivity	m^2 s^{-1}
ℓ	Typical width of convection rolls	m
L	Height of Busse annulus	m
L_H	Latent heat per unit mass	J kg^{-1}
$\mathcal{L}^2$	r^2 times the angular part of the Laplacian operator	
Λ	Elsasser number $B_0^2/\mu\rho\eta\Omega$	
m	Azimuthal wave number (exp $im\phi$)	
μ	Magnetic permeability	H m^{-1}
ν_T	Turbulent kinematic viscosity	m^2 s^{-1}
Nu	Nusselt number based on the superadiabatic temperature gradient	
N	Nusselt number based on the adiabatic temperature gradient	
$\mathbf{\Omega}$	Rotation rate of mantle (assumed constant)	s^{-1}
$\mathbf{\Omega}_{IC}$	Rotation rate of inner core	s^{-1}
ω_A	Buoyancy frequency (internal wave frequency)	s^{-1}
ω_C	Inertial wave frequency	s^{-1}
ω_M	Alfvén frequency (torsional wave frequency)	s^{-1}
P	Pressure (fluctuating pressure)	Pa
Pm	Magnetic Prandtl number ν/η	
Pr	Prandtl number ν/κ	
ψ	Stream function	m^2 s^{-1}
q	Roberts number κ/η	
Q	Chandrasekhar number $B_0^2/\mu\rho\nu\eta$	
Q_j	Ohmic dissipation	W m^{-3}
Q_ν	Viscous dissipation	W m^{-3}
r	Distance from the Earth's center	m
r_{cmb}	Radius of the CMB	m
r_{icb}	Radius of the ICB	m
ρ, ρ_a	Density of reference state	kg m^{-3}
ρ_c	Density perturbation	kg m^{-3}
Ra	Rayleigh number $g\alpha\Delta T_s d^3/\kappa\nu$	
Ra^*	Nondiffusive Rayleigh number $g\alpha\Delta T_s/\Omega d^2$	
Ra_Q	Convective flux Rayleigh number $Ra(Nu-1)$	
$\mathcal{R}$	Scaled Rayleigh number $\mathcal{E}^{4/3}$ Ra	
R_m	Magnetic Reynolds number $U_* d/\eta$	

Ro	Rossby number $U_*/\Omega d$	
S, (S_c)	Specific entropy (entropy perturbation)	J K^{-1} kg^{-1}
σ	Electrical conductivity	S m^{-1}
$\mathcal{S}$	Poloidal scalar for velocity	m^3 s^{-1}
t	Time	s
T	Temperature	K
T_a	Temperature of adiabatic state	K
T_c	Temperature perturbation due to convection	K
T'	$T_c - T_0$, T_0 being the static temperature distribution	K
T'_0	$\partial T_0/\partial r$	K m^{-1}
T'_*	Typical temperature perturbation in the core	K
ΔT_a	Adiabatic ICB–CMB temperature difference	K
ΔT_s	Superadiabatic ICB–CMB temperature difference	K
τ_{diss}	Magnetic dissipation time (energy/dissipation rate)	S
$\mathcal{T}$	Toroidal scalar for velocity	m^2 s^{-1}
$\mathbf{u}$	Velocity	m s^{-1}
U_*	Typical core velocity	m s^{-1}
$\mathcal{U}$	Toroidal scalar for magnetic field	T m
$\mathcal{V}$	Poloidal scalar for magnetic field	T m^2
ξ	Mass fraction of light element	
$\Delta\xi$	Jump of ξ across the ICB	
$\boldsymbol{\zeta}$	Vorticity	s^{-1}

References

Abdulrahman A, Jones CA, Proctor MRE, and Julien K (2000) Large wavenumber convection in the rotating annulus. *Geophysical and Astrophysical Fluid Dynamics* 93: 227–252.

Ahlers G, Grossmann S, and Lohse D (2009) Heat transfer and large scale dynamics in turbulent Rayleigh-Benard convection. *Reviews of Modern Physics* 81: 503–537.

Alboussière T, Deguen R, and Melzani M (2010) Melting-induced stratification above the Earth's inner core due to convective translation. *Nature* 466: 744–747.

Alfè D, Gillan MJ, and Price GD (2003) Thermodynamics from first principles: Temperature and composition of the Earth's core. *Mineralogical Magazine* 67: 113–123.

Alfè D, Price GD, and Gillan MJ (2002) Iron under Earth's core conditions: Liquid-state thermodynamics and high-pressure melting curve from ab initio calculations. *Physical Review B* 65, Art. No. 165118.

Al-Shamali FM, Heimpel MH, and Aurnou JM (2004) Varying the spherical shell geometry in rotating thermal convection. *Geophysical and Astrophysical Fluid Dynamics* 98: 153–169.

Anufriev AP, Cupal I, and Hejda P (1995) The weak Taylor state in an alpha-omega dynamo. *Geophysical and Astrophysical Fluid Dynamics* 79: 125–145.

Anufriev AP, Jones CA, and Soward AM (2005) The Boussinesq and anelastic liquid approximations for convection in the Earth's core. *Physics of the Earth and Planetary Interiors* 152: 163–190.

Araki T, et al. (2005) Experimental investigation of geologically produced antineutrinos with kamLAND. *Nature* 436: 499–503.

Aubert J (2005) Steady zonal flows in spherical shell dynamos. *Journal of Fluid Mechanics* 542: 53–67.

Aubert J, Amit H, and Hulot G (2007) Detecting thermal boundary control in surface flows from numerical dynamos. *Physics of the Earth and Planetary Interiors* 160: 143–156.

Aubert J, Brito D, Nataf HC, Cardin P, and Masson J-P (2001) A systematic experimental study of rapidly rotating spherical convection in water and liquid gallium. *Physics of the Earth and Planetary Interiors* 128: 51–74.

Aubert J, Finlay CC, and Fournier A (2013) Bottom-up control of geomagnetic secular variation by the Earth's inner core. *Nature* 502: 219.

Aubert J, Gillet N, and Cardin P (2003) Quasigeostrophic models of convection in rotating spherical shells. *Geochemistry, Geophysics, Geosystems* 4: Art. No. 1052.

Aurnou J, Andreadis S, Zhu L, and Olson P (2003) Experiments on convection in the Earth's core tangent cylinder. *Earth and Planetary Science Letters* 212: 119–134.

Aussillous P, Sederman AJ, Gladden LF, Huppert HE, and Worster MG (2006) Magnetic resonance imaging of structure and convection in solidifying mushy layers. *Journal of Fluid Mechanics* 552: 99–125.

Bell PI and Soward AM (1996) The influence of surface topography on rotating convection. *Journal of Fluid Mechanics* 313: 147–180.

Biggin AJ, Steinberger B, Aubert J, et al. (2012) Possible links between long-term geomagnetic variations and whole-mantle convection processes. *Nature Geoscience* 5: 526–533.

Bloxham J and Gubbins D (1987) Thermal core–mantle interactions. *Nature* 325: 511–513.

Bloxham J and Jackson A (1991) Fluid flow near the surface of the Earth's outer core. *Reviews of Geophysics* 29: 97–120.

Braginsky SI (1963) Structure of the F layer and reasons for convection in the Earth's core. *Soviet Physics—Doklady* 149: 8–10.

Braginsky SI (1967) Magnetic waves in the Earth's core. *Geomagnetism and Aeronomy* 7: 851–859.

Braginsky SI (1993) MAC-oscillations of the hidden ocean of the core. *Journal of Geomagnetism and Geoelectricity* 45: 1517–1538.

Braginsky SI (2006) Formation of the stratified ocean of the core. *Earth and Planetary Science Letters* 243: 650–656.

Braginsky SI and Meytlis VP (1990) Local turbulence in the Earth's core. *Geophysical and Astrophysical Fluid Dynamics* 55: 71–87.

Braginsky SI and Roberts PH (1995) Equations governing convection in the Earth's core and the geodynamo. *Geophysical and Astrophysical Fluid Dynamics* 79: 1–97.

Brito D, Aurnou J, and Cardin P (2004) Turbulent viscosity measurements relevant to planetary core–mantle dynamics. *Physics of the Earth and Planetary Interiors* 141: 3–8.

Brown B, Browning MK, Brun AS, Miesch MS, and Toomre J (2008) Rapid rotation, active nests of convection and global-scale flows in solar-like stars. *Astronomische Nachrichten* 328: 1002–1007.

Brummell NH and Hart JE (1993) High Rayleigh number beta convection. *Geophysical and Astrophysical Fluid Dynamics* 68: 85–114.

Buffett BA (2003) A comparison of subgrid-scale models for large-eddy simulations of convection in the Earth's core. *Geophysical Journal International* 153: 753–765.

Buffett BA, Garnero EJ, and Jeanloz R (2000) Sediments at the top of the Earth's core. *Science* 290: 1338–1342.

Buffett BA and Glatzmaier GA (2000) Gravitational braking of inner-core rotation in geodynamo simulations. *Geophysical Research Letters* 27: 3125–3128.

Buffett BA, Huppert HE, Lister J, and Woods AW (1992) Analytical model for solidification of the Earth's core. *Nature* 356: 329–331.

Busse FH (1970) Thermal instabilities in rapidly rotating systems. *Journal of Fluid Mechanics* 44: 441–460.

Busse FH (2002) Convective flows in rapidly rotating spheres and their dynamo action. *Physics of Fluids* 14: 1301–1314.

Busse FH and Carrigan CR (1976) Laboratory simulation of thermal convection in rotating planets and stars. *Science* 191: 81–83.

Busse FH and Or AC (1986) Convection in a rotating cylindrical annulus: Thermal Rossby waves. *Journal of Fluid Mechanics* 166: 173–187.

Busse FH and Simitev RD (2006) Parameter dependences of convection-driven dynamos in rotating spherical fluid shells. *Geophysical and Astrophysical Fluid Dynamics* 100: 341–361.

Castaing B, Gunaratne G, Heslot F, et al. (1989) Scaling of hard thermal turbulence in Rayleigh–Bénard convection. *Journal of Fluid Mechanics* 204: 1–30.

Chandrasekhar S (1961) *Hydrodynamic and Hydromagnetic Stability*. Oxford: Clarendon Press.

Chen Q and Glatzmaier GA (2005) Large eddy simulations of two-dimensional turbulent convection in a density-stratified fluid. *Geophysical and Astrophysical Fluid Dynamics* 99: 355–375.

Chen FL, Lu JW, and Yang TL (1994) Convective instability in ammonium chloride solution directionally solidified from below. *Journal of Fluid Mechanics* 276: 163–187.

Christensen UR (2002) Zonal flow driven by strongly supercritical convection in rotating spherical shells. *Journal of Fluid Mechanics* 470: 115–133.

Christensen UR and Aubert J (2006) Scaling properties of convection-driven dynamos in rotating spherical shells and application to planetary magnetic fields. *Geophysical Journal International* 166: 97–114.

Christensen UR, Aubert J, and Hulot G (2010) Conditions for Earth-like geodynamo models. *Earth and Planetary Science Letters* 296: 487–496.

Christensen U, Olson P, and Glatzmaier GA (1999) Numerical modelling of the geodynamo: A systematic parameter study. *Geophysical Journal International* 138: 393–409.

Christensen UR and Tilgner A (2004) Power requirement of the geodynamo from ohmic losses in numerical and laboratory dynamos. *Nature* 429: 169–171.

Christensen UR, et al. (2001) A numerical dynamo benchmark. *Physics of the Earth and Planetary Interiors* 128: 25–34.

Classen S, Heimpel M, and Christensen U (1999) Blob instability in rotating compositional convection. *Geophysical Research Letters* 26: 135–138.
Collier JD and Helffrich G (2001) Estimate of inner core rotation rate from United Kingdom regional seismic network data and consequences for inner core dynamical behaviour. *Earth and Planetary Science Letters* 193: 523–537.
Davidson PA (2001) *An Introduction to Magnetohydrodynamics*. Cambridge: Cambridge University Press.
Davies CJ, Gubbins D, and Jimack PK (2009) Convection in a rapidly rotating spherical shell with an imposed laterally varying thermal boundary condition. *Journal of Fluid Mechanics* 641: 335–358.
Deardorff JW (1970) Convective velocity and temperature scales for unstable planetary boundary layer and for Rayleigh convection. *Journal of Atmospheric Science* 27: 1211.
Desjardins B, Dormy E, and Grenier E (1999) Stability of mixed Ekman–Hartmann boundary layers. *Nonlinearity* 12: 181–199.
Dormy E (1997) *Modélisation numérique de la dynamo terrestre*. PhD Thesis, I.P.G.P.
Dormy E, Soward AM, Jones CA, Jault D, and Cardin P (2004) The onset of thermal convection in rotating spherical shells. *Journal of Fluid Mechanics* 501: 43–70.
Dormy E, Valet J-P, and Courtillot V (2000) Numerical models of the geodynamo and observational constraints. *Geochemistry, Geophysics, Geosystems* 1: 62–103, Art. No. 200GC000062.
Dumberry M and Bloxham J (2003) Torque balance, Taylor's constraint and torsional oscillations in a numerical model of the geodynamo. *Physics of the Earth and Planetary Interiors* 140: 29–51.
Dziewonski AM and Anderson DL (1981) Preliminary reference Earth model. *Physics of the Earth and Planetary Interiors* 25: 297–356.
Eltayeb IA (1972) Hydromagnetic convection in a rapidly rotating fluid layer. *Proceedings of the Royal Society of London A* 326: 229–254.
Fearn DR (1979a) Thermally driven hydromagnetic convection in a rapidly rotating sphere. *Proceedings of the Royal Society of London A* 369: 227–242.
Fearn DR (1979b) Thermally and magnetic instabilities in a rapidly rotating fluid sphere. *Geophysical and Astrophysical Fluid Dynamics* 14: 103–126.
Fearn DR (1988) Hydromagnetic waves in a differentially rotating annulus. 4. Insulating boundaries. *Geophysical and Astrophysical Fluid Dynamics* 44: 55–75.
Fearn DR (1998) Hydromagnetic flow in planetary cores. *Reports on Progress in Physics* 61: 175–235.
Fearn DR and Loper DE (1981) Compositional convection and stratification of the Earth's core. *Nature* 289: 393–394.
Fearn DR, Loper D, and Roberts PH (1981) Structure of the Earth's inner core. *Nature* 292: 232–233.
Fearn DR, Roberts PH, and Soward AM (1988) Convection, stability and the dynamo. In: Galdi GP and Straughan B (eds.) *Energy, Stability and Convection*, pp. 60–324. London: Longman.
Finlay CC and Amit A (2011) On flow magnitude and field-flow alignment at Earth's core surface. *Geophysical Journal International* 186: 175–192.
Finlay CC, Dumberry M, Chulliat A, and Pais MA (2010) Short timescale core dynamics: Theory and observations. *Space Science Reviews* 155: 177–218.
Galloway DJ, Proctor MRE, and Weiss NO (1977) Formation of intense magnetic fields near the surface of the Sun. *Nature* 266: 686–689.
Galloway DJ and Weiss NO (1981) Convection and magnetic fields in stars. *Astrophysical Journal* 243: 945–953.
Gauss CF (1839) Allgemeine Theorie des Erdmagnetismus. In: *Resultate aus den Beobachtungen des magnetischen Vereins*. Germany: Göttingen.
Gibbons SJ and Gubbins D (2000) Convection in the Earth's core driven by lateral variations in the core–mantle boundary heat flux. *Geophysical Journal International* 142: 631–642.
Gillet N, Jault D, Canet E, and Fournier A (2010) Fast torsional waves and strong magnetic field within the Earth's core. *Nature* 465: 74–77.
Gillet N and Jones CA (2006) The quasi-geostrophic model for rapidly rotating spherical convection outside the tangent cylinder. *Journal of Fluid Mechanics* 554: 343–369.
Gilman PA (1975) Linear simulations of Boussinesq convection in a deep rotating spherical shell. *Journal of Atmospheric Science* 32: 1331–1352.
Gilman PA (1983) Dynamically consistent nonlinear dynamos driven by convection in a rotating spherical shell. 2. Dynamos with cycles and strong feedbacks. *Astrophysical Journal Supplement* 53: 243–268.
Gilman PA and Miller J (1981) Dynamically consistent nonlinear dynamos driven by convection in a rotating spherical shell. *Astrophysical Journal Supplement* 46: 211–238.
Glatzmaier GA (1984) Numerical simulations of stellar convective dynamos. 1. The model and the method. *Journal of Computational Physics* 55: 461–484.
Glatzmaier GA, Coe RS, Hongre L, and Roberts PH (1999) The role of the Earth's mantle in controlling the frequency of geomagnetic reversals. *Nature* 401: 885–890.
Glatzmaier GA and Roberts PH (1995) A 3-dimensional self-consistent computer simulation of a geomagnetic field reversal. *Nature* 377: 203–209.
Glatzmaier GA and Roberts PH (1996) An anelastic evolutionary geodynamo simulation driven by compositional and thermal convection. *Physica D* 97: 81–94.
Glatzmaier GA and Roberts PH (1997) Simulating the geodynamo. *Contemporary Physics* 38: 269–288.
Goldstein RJ, Chiang HD, and See DL (1990) High-Rayleigh number convection in a horizontal enclosure. *Journal of Fluid Mechanics* 213: 111–126.
Greenspan H (1968) *The Theory of Rotating Fluids*. Cambridge: Cambridge University Press.
Grossmann S and Lohse D (2000) Scaling in thermal convection: A unifying theory. *Journal of Fluid Mechanics* 407: 27–56.
Grote E and Busse FH (2000) Hemispherical dynamos generated by convection in rotating spherical shells. *Physical Review E* 62: 4457–4460.
Gubbins D and Davies CJ (2013) The stratified layer at the core–mantle boundary caused by barodiffusion of oxygen, sulphur and silicon. *Physics of the Earth and Planetary Interiors* 215: 21–28.
Gubbins D, Masters G, and Nimmo F (2008) A thermochemical boundary layer at the base of Earth's outer core and independent estimate of core heat flux. *Geophysical Journal International* 174: 1007–1018.
Gubbins D, Sreenivasan B, Mound J, and Rost S (2011) Melting of the Earth's inner core. *Nature* 473: 361–363.
Helffrich G and Kaneshima S (2010) Outer-core compositional stratification from observed core wave speed profiles. *Nature* 468: 807–809.
Hollerbach R, Barenghi CF, and Jones CA (1992) Taylor's constraint in a spherical $\alpha\omega$-dynamo. *Geophysical and Astrophysical Fluid Dynamics* 67: 3–25.
Holme R and Bloxham J (1996) The magnetic fields of Uranus and Neptune: Methods and models. *Journal of Geophysical Research: Planets* 101: 2177–2200.
Holme R and Olsen N (2006) Core surface flow modelling from high-resolution secular variation. *Geophysical Journal International* 166: 518–528.
Ingersoll AP and Pollard D (1982) Motions in the interiors and atmospheres of Jupiter and Saturn: Scale analysis, anelastic equations, barotropic stability criterion. *Icarus* 52: 62–80.
Jackson A (1997) Time-dependency of tangentially geostrophic core surface motions. *Physics of the Earth and Planetary Interiors* 103: 293–311.
Jault D (2003) Electromagnetic and topographic coupling, and LOD variations. In: Jones A, Soward AM, and Zhang K (eds.) *Earth's Core and Lower Mantle*, pp. 56–76. London: Taylor & Francis.
Jault D, Gire C, and Lemouel JL (1988) Westward drift, core motions and exchanges of angular-momentum between core and mantle. *Nature* 333: 353–356.
Jones CA (2000) Convection driven geodynamo models. *Philosophical Transactions of the Royal Society of London A* 358: 873–897.
Jones CA (2003) Dynamos in planets. In: Thompson MJ and Christensen-Dalsgaard JC (eds.) *Stellar Astrophysical Fluid Dynamics*, pp. 159–176. Cambridge: Cambridge University Press.
Jones CA (2011) Planetary magnetic fields and fluid dynamos. *Annual Review of Fluid Mechanics* 43: 583–614.
Jones CA, Longbottom AW, and Hollerbach R (1995) A self-consistent convection driven geodynamo model, using a mean field approximation. *Physics of the Earth and Planetary Interiors* 92: 119–141.
Jones CA, Mussa AI, and Worland SJ (2003a) Magnetoconvection in a rapidly rotating sphere: The weak-field case. *Proceedings of the Royal Society of London A* 459: 773–797.
Jones CA and Roberts PH (1990) Magnetoconvection in rapidly rotating Boussinesq and compressible fluids. *Geophysical and Astrophysical Fluid Dynamics* 55: 263–308.
Jones CA and Roberts PH (2000) The onset of magnetoconvection at large Prandtl number in a rotating layer. II. Small magnetic diffusion. *Geophysical and Astrophysical Fluid Dynamics* 93: 173–226.
Jones CA, Rotvig J, and Abdulrahman A (2003b) Multiple jets and zonal flow on Jupiter. *Geophysical Research Letters* 30, Art. No. 1731.
Jones CA, Soward AM, and Mussa AI (2000) The onset of convection in a rapidly rotating sphere. *Journal of Fluid Mechanics* 405: 157–179.
Julien K, Knobloch E, Milliff R, and Werne J (2006) Generalized quasi-geostrophy for spatially anisotropic rotationally constrained flows. *Journal of Fluid Mechanics* 555: 233–274.
Julien K, Knobloch E, Rubio AM, and Vasil GM (2012) Heat transport in low-Rossby number Rayleigh–Bénard convection. *Physical Review Letters* 109: Art. No. 254503.
Julien K, Knobloch E, and Werne J (1998) A new class of equations for rotationally constrained flows. *Theoretical and Computational Fluid Dynamics* 11: 251–261.
Kageyama A and Sato T (1997) Velocity and magnetic field structures in a magnetohydrodynamic dynamo. *Physics of Plasmas* 4: 1569–1575.

King E, Stellmach S, and Aurnou J (2012) Heat transfer by rapidly rotating Rayleigh–Bénard convection. *Journal of Fluid Mechanics* 691: 568–582.

King E, Stellmach S, and Buffett B (2013) Scaling behaviour in Rayleigh–Bénard convection with and without rotation. *Journal of Fluid Mechanics* 691: 568–582.

Kraichnan RH (1962) Turbulent thermal convection at arbitrary Prandtl number. *Physics of Fluids* 5: 1374–1389.

Kuang W and Bloxham J (1997) An Earth-like numerical dynamo model. *Nature* 389: 371–374.

Kuo B-Y, Garnero EJ, and Lay T (2000) Tomographic inversion of S-SKS times for shear velocity heterogeneity in D'': Degree 12 and hybrid models. *Journal of Geophysical Research* 105: 28138–28157.

Kurt E, Busse FH, and Pesch W (2004) Hydromagnetic convection in a rotating annulus with an azimuthal magnetic field. *Theoretical and Computational Fluid Dynamics* 18: 251–263.

Kutzner C and Christensen UR (2002) From stable dipolar towards reversing numerical dynamos. *Physics of the Earth and Planetary Interiors* 131: 29–45.

Kutzner C and Christensen UR (2004) Simulated geomagnetic reversals and preferred virtual geomagnetic pole paths. *Geophysical Journal International* 157: 1105–1118.

Labrosse S, Poirier JP, and LeMouel JL (2001) The age of the inner core. *Earth and Planetary Science Letters* 190: 111–123.

Laj C, Mazaud A, Weeks R, Fuller M, and Herrero-Bervera E (1991) Geomagnetic reversal paths. *Nature* 351: 447.

Larmor J (1920) How could a rotating body such as the Sun become a magnet? In: *Report of 87th Meeting of the British Association for the Advancement of Science, September, 1919*. London: John Murray.

Lister JR (2003) Thermal winds forced by inhomogeneous boundary conditions in rotating, stratified hydromagnetic fluid. *Journal of Fluid Mechanics* 505: 163–178.

Livermore PW, Ierley G, and Jackson A (2011) The evolution of a magnetic field subject to Taylor's constraint using a projection operator. *Geophysical Journal International* 187: 690–704.

Loper DF (1970) General solution for the linearized Ekman–Hartmann layer on a spherical boundary. *Physics of Fluids* 13: 2995–2998.

Loper DE, Chulliat A, and Shimizu H (2003) Buoyancy-driven perturbations in a rapidly rotating, electrically conducting fluid. Part 1. Flow and magnetic field. *Geophysical and Astrophysical Fluid Dynamics* 97: 429–469.

Malkus WVR (1967) Hydromagnetic planetary waves. *Journal of Fluid Mechanics* 28: 793–802.

Malkus WVR (1994) Energy sources for planetary dynamos. In: Proctor MRE and Gilbert AD (eds.) *Lectures on Solar and Planetary Dynamos*, pp. 161–179. Cambridge: Cambridge University Press.

Malkus WVR and Proctor MRE (1974) The macrodynamics of α-effect dynamos in rotating fluids. *Journal of Fluid Mechanics* 67: 417–443.

Masters G and Gubbins D (2003) On the resolution of density within the Earth. *Physics of the Earth and Planetary Interiors* 140: 159–167.

Matsushima M (2005) A scale-similarity model for the subgrid-scale flux with application to MHD turbulence in the Earth's core. *Physics of the Earth and Planetary Interiors* 153: 74–82.

Moffatt HK (1978) *Magnetic Field Generation in Electrically Conducting Fluids*. Cambridge: Cambridge University Press.

Monnereau M, Calvet M, Margerin L, and Souriau A (2010) Lopsided growth of Earth's inner core. *Science* 328: 1014–1017.

Morin V and Dormy E (2004) Time dependent β convection in a rapidly rotating spherical shell. *Physics of Fluids* 16: 1603–1609.

Morse SA (2002) No mushy zones in the Earth's core. *Geochimica et Cosmochimica Acta* 66: 2155–2165.

Nakagawa T and Tackley PJ (2008) Lateral variations in CMB heat flux and deep mantle seismic velocity caused by a thermal–chemical-phase boundary layer in 3D spherical convection. *Geochemistry, Geophysics, Geosystems* 9: Art. No. Q06011.

Nataf H-C (2000) Seismic imaging of mantle plumes. *Annual Review of Earth and Planetary Sciences* 28: 391–417.

Niemela JJ, Skrbek L, Sreenivasan KR, and Donnelly RJ (2000) Turbulent convection at very high Rayleigh numbers. *Nature* 404: 837–840.

Niu F and Wen L (2001) Hemispherical variations in seismic velocity at the top of the Earth's inner core. *Nature* 410: 1081–1084.

Olson P (2003) Thermal interaction of the core and the mantle. In: Jones CA, Soward AM, and Zhang K (eds.) *Earth's Core and Lower Mantle*, pp. 1–38. London: Taylor & Francis.

Olson P and Aurnou J (1999) A polar vortex in the Earth's core. *Nature* 402: 170–173.

Olson P, Christensen UR, and Glatzmaier GA (1999) Numerical modeling of the geodynamo: Mechanisms of field generation and equilibration. *Journal of Geophysical Research* 104: 10383–10404.

Olson P, Coe RS, Driscoll PE, Glatzmaier GA, and Roberts PH (2009) Geodynamo reversal frequency and heterogeneous core–mantle boundary heat flow. *Physics of the Earth and Planetary Interiors* 180: 66–79.

Olson P and Glatzmaier GA (1996) Magnetoconvection and thermal coupling of the Earth's core and mantle. *Philosophical Transactions of the Royal Society of London A* 354: 1413–1424.

Or AC and Busse FH (1987) Convection in a rotating cylindrical annulus. Part 2. Transitions to asymmetric and vacillating flow. *Journal of Fluid Mechanics* 174: 313–326.

Palmer A and Smylie DE (2005) VLBI observations of free core nutations and viscosity at the top of the core. *Physics of the Earth and Planetary Interiors* 148: 285–301.

Plaut E and Busse FH (2002) Low Prandtl number convection in a rotating cylindrical annulus. *Journal of Fluid Mechanics* 464: 345–363.

Pozzo M, Davies C, Gubbins D, and Alfè D (2012) Thermal and electrical conductivity of iron at Earth's core conditions. *Nature* 485: 355–358.

Priestley CHB (1959) *Turbulent Transfer in the Lower Atmosphere*. Chicago: University of Chicago Press.

Proudman J (1916) On the motion of solids in a liquid possessing vorticity. *Proceedings of the Royal Society of London A* 92: 408–424.

Rhines PB (1975) Wave and turbulence on a beta-plane. *Journal of Fluid Mechanics* 122: 417–443.

Roberts PH (1968) On the thermal instability of a rotating fluid sphere containing heat sources. *Philosophical Transactions of the Royal Society of London A* 263: 93–117.

Roberts PH and Jones CA (2000) The onset of magnetoconvection at large Prandtl number in a rotating layer. I. Finite magnetic diffusion. *Geophysical and Astrophysical Fluid Dynamics* 92: 289–325.

Roberts PH, Jones CA, and Calderwood A (2003) Energy fluxes and ohmic dissipation. In: Jones CA, Soward AM, and Zhang K (eds.) *Earth's Core and Lower Mantle*, pp. 100–129. London: Taylor & Francis.

Roberts PH and Loper DE (1979) On the diffusive instability of some simple steady magnetohydrodynamic flows. *Journal of Fluid Mechanics* 90: 641–668.

Roberts PH and Scott S (1965) On the analysis of the secular variation. 1. A hydromagnetic constraint: Theory. *Journal of Geomagnetism and Geoelectricity* 17: 137–151.

Rogers TM, Glatzmaier GA, and Woosley SE (2003) Simulations of two-dimensional turbulent convection in a density-stratified fluid. *Physical Review E* 67: Art. No. 026315.

Rossby HT (1969) A study of Bénard convection with and without rotation. *Journal of Fluid Mechanics* 36: 309–335.

Rotvig J and Jones CA (2002) Rotating convection driven dynamos at low Ekman number. *Physical Review E* 66: 056308.

Rotvig J and Jones CA (2006) Multiple jets and bursting in the rapidly rotating convecting two-dimensional annulus model with nearly plane-parallel boundaries. *Journal of Fluid Mechanics* 567: 117–140.

Sakuraba A (2002) Linear magnetoconvection in rotating fluid spheres permeated by a uniform axial magnetic field. *Geophysical and Astrophysical Fluid Dynamics* 96: 291–318.

Sakuraba A and Kono M (1999) Effect of the inner core on the numerical solution of the magnetohydrodynamic dynamo. *Physics of the Earth and Planetary Interiors* 111: 105–121.

Sakuraba M and Roberts PH (2009) Generation of a strong magnetic field using uniform heat flux at the surface of the core. *Nature Geoscience* 2: 802–805.

Sarson GR and Jones CA (1999) A convection driven geodynamo reversal model. *Physics of the Earth and Planetary Interiors* 111: 3–20.

Sarson GR, Jones CA, and Longbottom AW (1997) The influence of boundary region heterogeneities on the geodynamo. *Physics of the Earth and Planetary Interiors* 101: 13–32.

Schmitz S and Tilgner A (2009) Heat transport in rotating convection without Ekman layers. *Physical Review E* 80: 015305.

Schubert G, Turcotte DL, and Olson P (2001) *Mantle Convection in the Earth and Planets*. Cambridge: Cambridge University Press.

Siggia ED (1994) High Rayleigh number convection. *Annual Review of Fluid Mechanics* 26: 137–168.

Simitev R and Busse FH (2005) Prandtl-number dependence of convection-driven dynamos in rotating spherical fluid shells. *Journal of Fluid Mechanics* 532: 365–388.

Sleep NH (1990) Hot spots and mantle plumes: Some phenomenology. *Journal of Geophysical Research* 95: 6715–6736.

Slichter LB (1961) The fundamental free mode of the Earth's inner core. *Science* 47: 186–190.

Soderlund KM, King EM, and Aurnou JM (2012) The influence of magnetic fields in planetary dynamo models. *Earth and Planetary Science Letters* 333: 9–20.

Song XD (1996) Seismological evidence for differential rotation of the Earth's inner core. *Nature* 382: 221–224.
Souriau A, Garcia R, and Poupinet G (2003) The seismological picture of the inner core: Structure and rotation. *Comptes Rendus Geoscience* 335: 51–63.
Soward AM and Jones CA (1983) α^2-dynamos and Taylor's constraint. *Geophysical and Astrophysical Fluid Dynamics* 27: 87–122.
Sreenivasan B and Jones CA (2005) Structure and dynamics of the polar vortex in the Earth's core. *Geophysical Research Letters* 32: Art. No. L20301.
Sreenivasan B and Jones CA (2006a) The role of inertia in the evolution of spherical dynamos. *Geophysical Journal International* 164: 467–476.
Sreenivasan B and Jones CA (2006b) Azimuthal winds, convection and dynamo action in the polar region of planetary cores. *Geophysical and Astrophysical Fluid Dynamics* 100: 319–339.
Sreenivasan B and Jones CA (2011) Helicity generation and subcritical behaviour in rapidly rotating dynamos. *Journal of Fluid Mechanics* 688: 5–30.
Stacey FD and Anderson OL (2001) Electrical and thermal conductivities of Fe-Ni-Si alloy under core conditions. *Physics of the Earth and Planetary Interiors* 124: 153–162.
Stanley S and Bloxham J (2006) Numerical dynamo models of Uranus' and Neptune's magnetic fields. *Icarus* 184: 556–572.
Stanley S and Glatzmaier GA (2010) Dynamo models for planets other than Earth. *Space Science Reviews* 152: 617–649.
Starchenko S and Jones CA (2002) Typical velocities and magnetic field strengths in planetary interiors. *Icarus* 157: 426–435.
Stevenson DJ (2003) Planetary magnetic fields. *Earth and Planetary Science Letters* 208: 1–11.
Sumita I and Olson P (2000) Laboratory experiments on High Rayleigh number thermal convection in a rapidly rotating hemispherical shell. *Physics of the Earth and Planetary Interiors* 117: 153–170.
Sumita I and Olson P (2003) Experiments on highly supercritical thermal convection in a rapidly rotating hemispherical shell. *Journal of Fluid Mechanics* 492: 271–287.
Takahashi F and Shimizu H (2012) A detailed analysis of a dynamo mechanism in a rapidly rotating spherical shell. *Journal of Fluid Mechanics* 701: 228–250.
Tanaka S and Hamaguchi H (2001) Degree one heterogeneity and hemispherical variation of anisotropy in the inner core from PKP(BC)–PKP(DF) times. *Journal of Geophysical Research* 102: 2925–2938.
Taylor GI (1923) The motion of a sphere in a rotating liquid. *Proceedings of the Royal Society of London A* 102: 180–189.
Taylor JB (1963) The magneto-hydrodynamics of a rotating fluid and the Earth's dynamo problem. *Proceedings of the Royal Society of London A* 274: 274–283.
Teed RJ, Jones CA, and Hollerbach R (2012) On the necessary conditions for bursts of convection within the rapidly rotating cylindrical annulus. *Physics of Fluids* 24, Art. No. 066604.
Tilgner A (2005) Precession driven dynamos. *Physics of Fluids* 17: Art. No. 034104.
Tilgner A and Busse FH (1997) Finite-amplitude convection in rotating spherical fluid shells. *Journal of Fluid Mechanics* 332: 359–376.
Turner JS (1973) *Buoyancy Effects in Fluids*. Cambridge: Cambridge University Press.
Usui Y, Tarduno JA, Watkeys M, Hofmann A, and Cottrell RD (2009) Evidence for a 3.45-billion-year-old magnetic remanence: Hints of an ancient geodynamo from conglomerates of South Africa. *Geochemistry, Geophysics, Geosystems* 10: Art. No. Q09Z07.
Walker MR, Barenghi CF, and Jones CA (1998) A note on dynamo action at asymptotically small Ekman number. *Geophysical and Astrophysical Fluid Dynamics* 88: 261–275.
Weiss NO (1966) The expulsion of magnetic flux by eddies. *Proceeding of the Royal Society of London* 293: 310.
Westerburg M and Busse FH (2003) Centrifugally driven convection in the rotating cylindrical annulus with modulated boundaries. *Nonlinear Processes in Geophysics* 10: 275–280.
Zhang K (1992) Spiralling columnar convection in rapidly rotating spherical shells. *Journal of Fluid Mechanics* 236: 535–556.
Zhang K (1995) Spherical shell rotating convection in the presence of a toroidal magnetic field. *Proceedings of the Royal Society of London A* 448: 245–268.
Zhang K and Busse FH (1987) On the onset of convection in rotating spherical shells. *Geophysical and Astrophysical Fluid Dynamics* 39: 119–147.
Zhang K and Busse FH (1989) Convection driven magnetohydrodynamic dynamos in rotating spherical shells. *Geophysical and Astrophysical Fluid Dynamics* 49: 97–116.
Zhang K and Fearn DR (1994) Hydromagnetic waves in rapidly rotating spherical shells generated by magnetic toroidal decay modes. *Geophysical and Astrophysical Fluid Dynamics* 77: 133–157.
Zhang K and Fearn DR (1995) Hydromagnetic waves in rapidly rotating spherical shells generated by poloidal decay modes. *Geophysical and Astrophysical Fluid Dynamics* 81: 193–209.
Zhang K and Gubbins D (1996) Convection in a rotating spherical fluid shell with an in-homogeneous temperature boundary condition at finite Prandtl number. *Physics of Fluids* 8: 1141–1158.
Zhang K and Jones CA (1993) The influence of Ekman boundary layers on rotating convection. *Geophysical and Astrophysical Fluid Dynamics* 71: 145–162.
Zhang K and Jones CA (1994) Convective motions in the Earth's fluid core. *Geophysical Research Letters* 21: 1939–1942.
Zhang K and Jones CA (1996) On small Roberts number magnetoconvection in rapidly rotating systems. *Proceedings of the Royal Society of London A* 452: 981–995.
Zhang J, Song XD, Li YC, Richards PG, Sun XL, and Waldhauser F (2005) Inner core differential motion confirmed by earthquake waveform doublets. *Science* 309: 1357–1360.

This page intentionally left blank

8.06 Turbulence in the Core

H-C Nataf and N Schaeffer, University Grenoble Alpes / CNRS, Grenoble, France

© 2015 Elsevier B.V. All rights reserved.

8.06.1	**Introduction**	162
8.06.1.1	What Is Turbulence?	162
8.06.1.1.1	An attempt to define turbulence	162
8.06.1.1.2	Is the earth's core turbulent?	162
8.06.1.2	Why Care?	162
8.06.1.2.1	Small scales contribute to secular variation	162
8.06.1.2.2	Small scales and dynamo action	163
8.06.1.2.3	Dissipation and efficiency	163
8.06.1.2.4	Mixing	163
8.06.2	**Fundamentals of Turbulence**	163
8.06.2.1	Energy Density Spectra and Energy Cascade	163
8.06.2.2	Structures	164
8.06.3	**Tools for Turbulence**	164
8.06.3.1	Direct Numerical Simulations	164
8.06.3.2	Laboratory Experiments	165
8.06.3.3	Observations	166
8.06.3.4	Shell Models	167
8.06.3.5	Plume Model	167
8.06.4	**Parameterization of Turbulence**	167
8.06.4.1	Hyperdiffusivities or Eddy Diffusivities	168
8.06.4.2	Large Eddy Simulations	168
8.06.5	**Equations, Timescales, and Length Scales**	168
8.06.5.1	Equations	168
8.06.5.2	Ordering of Forces in the Earth's Core	169
8.06.5.2.1	Coriolis force	169
8.06.5.2.2	Magnetic induction	170
8.06.5.2.3	Lorentz versus Coriolis	170
8.06.5.3	Waves and Transients	170
8.06.5.4	What Should Be Considered a Small Scale?	171
8.06.6	**Turbulent Regimes for the Core**	171
8.06.6.1	τ–ℓ Regime Diagrams	171
8.06.6.2	Turbulent Convection	172
8.06.6.2.1	The Rayleigh number	172
8.06.6.2.2	Density perturbation	173
8.06.6.2.3	Injection and dissipation scales	173
8.06.6.3	Turbulence in a Rotating Sphere	173
8.06.6.3.1	Bidimensionalization and Rossby waves	174
8.06.6.3.2	Zonal flows and potential vorticity	175
8.06.6.3.3	Possible turbulent regimes	175
8.06.6.3.4	Below the injection scale	175
8.06.6.4	MHD Turbulence	176
8.06.6.4.1	Mechanisms of MHD turbulence	176
8.06.6.4.2	Two scenarios of MHD turbulence	176
8.06.6.4.3	A highly dissipative scenario	177
8.06.6.4.4	A more realistic scenario	177
8.06.6.5	Turbulence in Planetary Cores	177
8.06.7	**Summary and Perspectives**	178
Acknowledgments		179
References		179

8.06.1 Introduction

In this chapter, we have the difficult task of describing the invisible part of the core: turbulent structures that we cannot detect but have to be there. Indeed, nonlinear interactions in the liquid core lead to the formation of velocity, temperature, and magnetic structures on a large range of scales. Their roles are important: they transfer energy between large and small length scales, and in the end, they control the dissipation of the geodynamo. Turbulence is at work everywhere and has been studied for decades. Our first step is to define turbulence and show why one should care about turbulence in the core. Then, we review a few fundamental features of hydrodynamic turbulence. Many tools are needed to decipher turbulence: we present key results obtained from numerical simulations, laboratory experiments, and observations of natural systems. Unfortunately, no observations of the internal geomagnetic field are possible at small scales, mostly because of the crustal field that overprints the small-scale core field. Observations of turbulence in other systems are thus welcome to gain insight in what could happen in the Earth's core. We also devote one section to the parameterization of turbulence in numerical simulations.

The last two sections focus on the core. Turbulence implies a range of timescales and length scales. We define dimensionless numbers depending on the length scale ℓ. They measure the relative weight of the various terms in the governing equations. Using the known properties of the core and its large-scale velocity and magnetic field, we evaluate these various numbers. We introduce τ–ℓ-diagrams that help us identify the scales at which turbulent regimes change. Step by step, we explore the suite of plausible turbulent regimes for the core, introducing successively the effects of rotation and magnetic field. Our analysis emphasizes the crucial role of rotation in limiting the dissipation of the geodynamo and points out the need for dedicated studies.

8.06.1.1 What Is Turbulence?

8.06.1.1.1 An attempt to define turbulence

Turbulence is difficult to define precisely, but we can list a few elements that characterize turbulent motion. The most prominent feature of turbulence is that the motion of the fluid involves a wide range of spatial and temporal scales. These scales cannot be treated independently and there is no scale separation between small and large scales, although different regimes can be identified.

In order for the various scales to interact, the nonlinear terms of the evolution equation must be important. In the case of pure hydrodynamic turbulence, this is ensured by a large Reynolds number $Re = UL/\nu \gg 1$, ratio of the diffusive time L^2/ν to the advection time L/U (L is a characteristic length, U a typical velocity, and ν the kinematic viscosity of the fluid). However, in a self-magnetized conducting fluid driven by thermochemical convection, there are other nonlinear terms that allow interaction of different scales.

A flow executing turbulent motion often exhibits eddies of various scales, but this may not be the case when a strong magnetic field and background rotation are present, as it is the case for the Earth's core. Turbulence is not chaos, but all turbulent flows exhibit fluctuations that call for a statistical description, rather than a deterministic one. If the precise details of the flow are controlled by initial conditions or small perturbations that we cannot measure, global quantities such as the energy dissipation rate, the average velocity field, and the amplitude of fluctuations are of great interest and are expected to be well defined and measurable.

As opposed to laminar motion, where the fluid particles follow a pattern controlled by the viscosity, with little change from one fluid particle to its neighbor, a turbulent motion involves complex time dependence and spatial dependence.

8.06.1.1.2 Is the earth's core turbulent?

Due to the low viscosity of molten iron, the Reynolds number is certainly very large – $Re \sim 10^8$ – meaning that the viscous term (which is the only isotropic dissipation term) acts mainly at small scale. Furthermore, the nonlinear terms associated with the Lorentz force are in fact much larger than the inertial term at large scale, leading to a ratio of nonlinear to viscous force of about 10^{12}.

However, the importance of the magnetic field and the global rotation rate make the turbulence rather peculiar. It is sometimes advocated that the flow variations along the rotation axis or magnetic field lines are inhibited, leading to sheet-like (laminar) motion that cannot be turbulent anymore (because velocity is now mostly perpendicular to its gradient). These are a lot of constraints for an incompressible vector field that has only two degrees of freedom.

We shall see in the following sections that not all these constraints have the same strength. In an attempt to describe the dynamics of the system, we will discuss how it can organize itself on a broad range of timescales and length scales in several different regimes.

8.06.1.2 Why Care?

Turbulent small-scale fields within the core will not be observed. So, why care? They can have a collective or average effect that has a direct measurable consequence on the large-scale flow and magnetic field, which we investigate. They also control the dissipation, which we need to assess in order to know how much power is needed to drive the dynamo.

8.06.1.2.1 Small scales contribute to secular variation

Much of what we know about flow and magnetic field within the core is deduced from the analysis of the secular variation of the magnetic field observed at the surface of the Earth (see Chapter 8.04). The magnetic field at the core–mantle boundary is determined only up to degree 13 of the spherical harmonics (corresponding to a wavelength of about $2\pi \times 3500/13 = 1700$ km at the top of the core). Its time derivative is known up to degree 10 for the most recent epoch. One aims at reconstructing the large-scale velocity $\mathbf{u}$ by inverting the frozen flux induction equation of the radial component of the magnetic field B_r at the core–mantle boundary:

$$\partial_t B_r + \nabla_H \cdot (\mathbf{u} B_r) = 0 \qquad [1]$$

where ∇_H is the horizontal part of the divergence operator (see Chapter 8.04). The problem is that unresolved small-scale motions can interact with unresolved small-scale magnetic field to contribute to the large-scale induction term of this

equation. Eymin and Hulot (2005) showed that realistic amplitudes of these two unresolved fields produce representation errors that largely exceed the observational errors. Better models are obtained when these representation errors are taken into account in core flow inversions (Pais and Jault, 2008). It is therefore of interest to get some constraints on the evolution of the velocity and magnetic field with harmonic degree beyond what can be inferred from the observations.

8.06.1.2.2 Small scales and dynamo action

Mean-field dynamo theories developed in the 1960s (Moffatt, 1961; Steenbeck et al., 1966) have demonstrated that the interaction of the small scales of a turbulent flow in a conducting fluid with the small scales of the magnetic field they induce can produce a large-scale magnetic field (see Moffatt, 1978, for a review). This mechanism is nicely illustrated by the success of the two-scale dynamo experiment in Karlsruhe (Stieglitz and Müller, 2001). Liquid sodium was forced to flow up and down in helicoid motions in an array of pipes set up to mimic the two-dimensional periodic paving of the G. O. Roberts dynamo (Roberts, 1972). Induction was clearly taking place at the scale of each of the 52 individual 0.21 m diameter pipes. Nevertheless, a large-scale magnetic field was produced at the scale of the complete 1.7 m diameter assembly.

The simplest forms of mean-field dynamo theory predict that isotropic homogeneous turbulent motions in a conducting fluid produce a large-scale electromotive force $\varepsilon = \boldsymbol{\alpha} : \langle \boldsymbol{B} \rangle + \boldsymbol{\beta} : \boldsymbol{\nabla} \times \langle \boldsymbol{B} \rangle$, where $\langle \boldsymbol{B} \rangle$ is the large-scale magnetic field; $\boldsymbol{\alpha}$ and $\boldsymbol{\beta}$ are two tensors, which depend upon the turbulent characteristics of the flow; and ':' is the tensorial dot product. In this view, the α-effect is crucial for enabling the large-scale magnetic field to grow, while the β-effect can increase or decrease the magnetic diffusivity. Parameterized numerical dynamo models relying on these ideas have had a crucial role in explaining the solar cycle, and they are still very useful (see Charbonneau, 2005, for a review). However, the lack of scale separation and the expected deviations from isotropy and homogeneity can strongly impact the relevance of this theory for the geodynamo.

8.06.1.2.3 Dissipation and efficiency

In the so-called inertial range of classical turbulence, energy is transferred from the large scales to the small scales, with almost no energy loss. The dissipation of energy occurs at the smallest scales, where velocity gradients become large enough for viscous forces to balance nonlinear inertial terms. The smaller this scale, the higher the dissipation. We examine several alternative scenarios for turbulence in **Section 8.06.6** and show that they yield extremely diverse dissipation rates. The efficiency of convective motions for producing a dynamo therefore strongly depends on the organization of the turbulent velocity and magnetic fields.

8.06.1.2.4 Mixing

Turbulence affects the mixing of fluid parcels and of what they transport. It has therefore received considerable attention in atmospheric and oceanic sciences, where the transport of pollutants or nutrients has an important socioeconomic impact. This question has not yet been tackled in studies of core dynamics. However, seismology reveals that layers at the bottom and at the top of the liquid core may have a slightly different composition. How much mixing takes place between these layers and the rest of the core has important geodynamic implications (Alboussière et al., 2010). The observation of the atmospheres of Jupiter and Saturn reveals that zonal bands with alternating wind directions are able to maintain a strikingly different chemical signature, yielding contrasting colors, despite a very active turbulence. We should keep this in mind when considering the fluid inside the cylinder tangent to the inner core.

8.06.2 Fundamentals of Turbulence

Identified by Feynman as 'the most important unsolved problem of classical physics,' turbulence has been the subject of numerous studies over a large part of the twentieth century. Unsolved fundamental issues remain, but an impressive corpus of results and models has been acquired (see Frisch, 1995, for a review and more). We give here a simple overview of some fundamental aspects of hydrodynamic turbulence (i.e., in the absence of global rotation and magnetic field).

8.06.2.1 Energy Density Spectra and Energy Cascade

While all turbulent fields undergo large fluctuations in time and space, it has been found that energy density spectra of the flows are robust and universal in hydrodynamic turbulence. In addition, these spectra nicely summarize the scaling properties of the flow and the energy transfer that takes place. Defining k as the (scalar) wave number of the flow in the Fourier space, the energy density $E(k)$ is defined by

$$\widetilde{E} = \frac{1}{2}\langle u^2 \rangle = \int_0^\infty E(k)\,\mathrm{d}k \qquad [2]$$

where $\widetilde{E}$ is the energy of the fluctuations per unit mass. The theory of 'universal turbulence' was established by Kolmogorov (1941a). The basic idea is that there should be a wave number k_0 above which turbulence does not depend upon how energy is fed to the flow. The only thing that counts is the mean power per unit mass ε it provides and that is also dissipated in the stationary regime. In this idealized view, universal turbulence should thus be isotropic and homogeneous, and it should have a self-similar character.

The smaller length scale at which dissipation operates is called Kolmogorov's scale, with wave number k_D. It depends upon ε and the kinematic viscosity ν. Viscous dissipation per unit mass can be written as $\nu(\boldsymbol{\nabla u})^2$, which we express as $\nu k_\mathrm{D}^2 (u(k_\mathrm{D}))^2$ at the k_D wave number. The typical velocity $u(k_\mathrm{D})$ is obtained by stating that the Reynolds number at this scale should be about 1 for dissipation to occur, yielding $u(k_\mathrm{D}) \sim \nu k_\mathrm{D}$. We thus obtain

$$k_\mathrm{D} = \left(\frac{\varepsilon}{\nu^3}\right)^{1/4} \qquad [3]$$

The main assumption of Kolmogorov is then that, in the wave number range between the injection scale and the dissipation scale ($k_0 \ll k \ll k_\mathrm{D}$), all statistically averaged quantities at wave number k are a function of k and ε only. Dimensional analysis then commands

$$E(k) = C_K \varepsilon^{2/3} k^{-5/3} \quad [4]$$

which is the famous $k^{-5/3}$ law derived by Obukhov (1941), where C_K is a dimensionless constant called 'Kolmogorov's constant.' It has been found that a wide class of actual turbulent flows follow this law, sometimes over many decades in wave number, and C_K has been measured to lie between 1.5 and 2.

The k power-law dependence of $E(k)$ is a signature of self-similarity in this wavenumber range, called the inertial range, along which energy cascades from the injection length scale down to the dissipation scale. Self-similarity extends to higher-order 'structure functions' $S_p(\ell)$, which are defined as $S_p(\ell) = \langle \delta u^p(\ell) \rangle$, where $\langle\rangle$ denotes a statistical average and $\delta u(\ell)$ is the velocity difference measured between two points separated by a distance ℓ. Longitudinal velocity differences are usually considered (i.e., difference in the projection of velocity on the line that links the two points). The measurements yield

$$S_p(\ell) \sim \ell^{\zeta_p} \quad [5]$$

where the exponents ζ_p appear to be universal. $E(k)$ is directly related to $S_2(\ell)$, so that $\zeta_2 = 2/3$ for Kolmogorov's $E(k)$ spectra. In fact, under Kolmogorov's hypotheses, one gets $\zeta_p = p/3$ for all p. The measurements indicate that the actual ζ_p exponents clearly deviate from this prediction as p increases (Anselmet et al., 1984). The high-order structure functions are related to the tails of the probability distribution function of velocity differences. For small separation distances ℓ, these distributions strongly deviate from normal distributions, showing a larger influence of intermittent 'rare' events.

8.06.2.2 Structures

The apparition of flow structures is an unavoidable consequence of the break of symmetry that characterizes the instabilities at the origin of turbulence. Anyone who has looked at turbulent flows in a river or in the air will retrieve the image – nicely illustrated by Leonardo da Vinci – that vortices or eddies are the building bricks of hydrodynamic turbulence. Eddies come in a large range of sizes. They are usually longer than wide and can even stretch into vorticity filaments. The core of an eddy has a strong but relatively homogeneous vorticity $\boldsymbol{\omega} = \nabla \times \boldsymbol{u}$, while the opposite holds on its edges. There, the shear between eddies nucleates smaller eddies. Long filaments can also break into shorter filaments. In this way, energy cascades down to small scales, where dissipation occurs.

With this in mind, it does not seem obvious that, even if vortices can take all sizes and orientations, the embedding of essentially one-dimensional structures (vorticity filaments) into three-dimensional space will have no influence on the statistically averaged quantities at wave number k, as originally assumed by Kolmogorov. This idea is the starting point of She and Leveque (1994). They showed that vorticity filaments dissipate the available surrounding energy very efficiently by forcing the lower-intensity eddies into an essentially bidimensional flow around them. Vorticity filaments are relatively rare, as they correspond to eddies that have had the opportunity to stretch and get stronger. To illustrate this phenomenon, Kaneda and Morishita (2013) reported that 33% of the energy dissipation occurs in 5% of the volume in one of the highest Reynolds number direct numerical simulation (DNS) performed to date. One consequence is that the average moments of the energy dissipation $\langle \varepsilon^p(\ell) \rangle$ within a sphere of radius ℓ depends upon the scale ℓ. Self-similarity implies

$$\langle \varepsilon^p(\ell) \rangle \sim \ell^{\tau_p} \quad [6]$$

where the exponents τ_p should again be universal. Kolmogorov's hypothesis that all statistically averaged quantities only depend upon scale and mean dissipation ε implies $\langle \varepsilon^p(\ell) \rangle = \varepsilon^p$, independent of ℓ (i.e., $\tau_p = 0, \forall_p$). If this hypothesis is relaxed to take into account intermittency, the 'refined similarity hypothesis' derived by Kolmogorov (1962) yields a relation between the ζ_p and τ_p exponents:

$$\zeta_p = p/3 + \tau_{p/3} \quad [7]$$

She and Leveque (1994) derived expressions for τ_p and hence for ζ_p that are in excellent agreement with the measurements:

$$\zeta_p = p/9 + 2\left[1 - \left(\frac{2}{3}\right)^{p/3}\right] \quad [8]$$

Note that the –5/3 exponent of k in the expression for $E(k)$ is hardly modified by this extension and that the ζ_3 exponent is always 1, as it can be derived with no adjustable parameter from the Navier–Stokes equation in some conditions (see Frisch, 1995; Kaneda and Morishita, 2013; Kolmogorov, 1941b), yielding Kolmogorov's equation (also called the four-fifths law):

$$S_3(\ell) = -\frac{4}{5}\varepsilon\ell \quad [9]$$

Turbulence can be strongly modified by the presence of global rotation and/or magnetic field. Although we are still lacking a thorough description of turbulence under such conditions, we will unravel and discuss some of its known or inferred properties in **Section 8.06.6** and try to get closer to a description that applies to the Earth's core.

8.06.3 Tools for Turbulence

8.06.3.1 Direct Numerical Simulations

DNSs consist in fully solving the equations of the problem, namely, the Navier–Stokes equation together with the induction and the codensity equations (see **Section 8.06.5.1**). The best Navier–Stokes simulations reach an impressive resolution of 4096^3 (Kaneda and Morishita, 2013). The size of the resulting discrete problem for the Earth's core is such that we cannot hope a DNS at the real parameters anytime soon: from the core size to the Ekman layer thickness, six orders of magnitude in length scale and timescale must be resolved.

The problem is made even worse by the need to take into account the spherical geometry and the coupling with the induction equation. Nevertheless, DNS of the geodynamo have proved very useful, as exposed in **Chapter 8.10**. They clearly demonstrate the role of rotation in the generation of a large-scale magnetic field, dominated by a dipole aligned with the axis of rotation. Furthermore, scaling relationships derived

from these simulations seem to indicate that their output is independent of the precise values of the diffusion coefficients (Christensen and Aubert, 2006), giving hope that relevant asymptotic regimes are attained even though diffusivities are far larger than the values expected for the core.

Some DNS have tackled the question of small-scale turbulence in core situations. Following the theoretical work of Braginsky and Meytlis (1990), StPierre (1996) performed DNS of turbulence in the presence of both rotation and magnetic field. He found that buoyant patches rapidly break up into platelike structures elongated in the directions of the rotation axis and of the prevailing magnetic field. Giesecke (2007) found similar results. However, it is not clear how a turbulent cascade of energy can build upon such structures. Besides, these simulations do not take into account the fact that rotation and magnetic field characteristic times are several orders of magnitude apart in the core (see **Section 8.06.6**).

MHD turbulence is very difficult to model. The magnetic field imposes a strong anisotropy, which can be used to reduce the full MHD equations. Energy spectra for 'weak' and 'strong' MHD turbulence have been obtained this way (see Tobias et al., 2013, for a review).

Even though DNSs are not able to simulate the core, they can offer some insight in the dynamics and, in particular, give hints to support the scenarios that we elaborate based on various studies in different dynamical regimes. **Figures 1** and **2** display a snapshot of a full geodynamo DNS computed for fairly extreme parameters that get closer to core values. It shows thinner elongated coherent structures in the velocity field than in simulations at milder Ekman numbers. It strongly supports the large-scale, high magnetic Reynolds number (*Rm*; see **Table 2**) picture, where the Coriolis force dominates.

8.06.3.2 Laboratory Experiments

The exploration of highly turbulent flows is possible in laboratory experiments. Very long time series are easily obtained. The main problem is often to access the quantities that best document turbulent behavior. Laboratory experiments have played and are still playing an important role in the exploration of the dynamics of geophysical and astrophysical fluids. A review of the experimental results that shed light on core dynamics is given in **Chapter 8.13**.

Early experiments used local intrusive probes and provided key measurements on several features of turbulence. For example, Anselmet et al. (1984) determined the structure exponents ζ_p in a turbulent jet up to $p=10$, providing a strong motivation for theoretical improvements (Frisch, 1995). The first experimental wavenumber energy density spectra for MHD turbulence in an applied magnetic field were measured by Alemany et al. (1979) using velocity probes attached to a grid moving in a column of mercury placed within a solenoid. They found a kinetic energy spectrum $E_u(k)\sim k^{-3}$ demonstrating the strong damping of fluctuations by the applied magnetic field in the low magnetic Reynolds number regime.

Recent experiments rely on optical methods based on particle image velocimetry (PIV), which have evolved into very efficient tools (see Westerweel et al., 2013, for a recent review) and brought new constraints on turbulence in transparent fluids, such as air and water. Let us cite, as an example, the determination of the structure coefficients of Lagrangian velocity increments in a von Kármán flow (Xu et al., 2006) and the structure coefficients of velocity increments in shallow layer rotating turbulence (Baroud et al., 2003). These methods have also been very useful for establishing the idea that the mixing

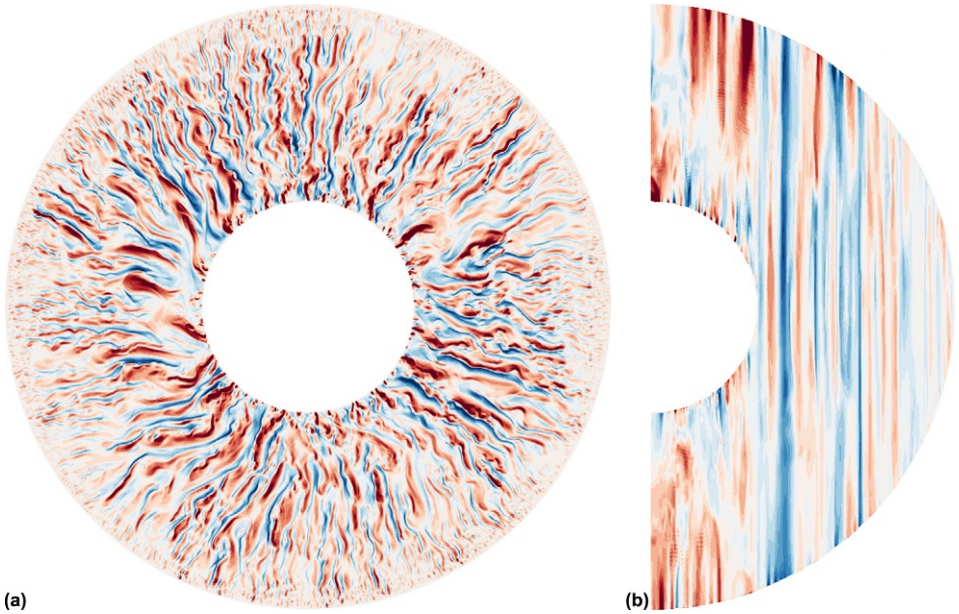

Figure 1 Cylindrical radial velocity component u_s in the equatorial plane (a) and a meridional plane (b). Snapshots from a dynamo DNS at $E=10^{-7}$, $Pm=0.1$, $Pr=1$, and $Ra=2.4\times10^{13}$ (see **Table 2** for the definition of these numbers using ℓ as the radial distance between the inner shell and outer shell), using spherical harmonic expansion up to degree 893 and 1024 radial shells.

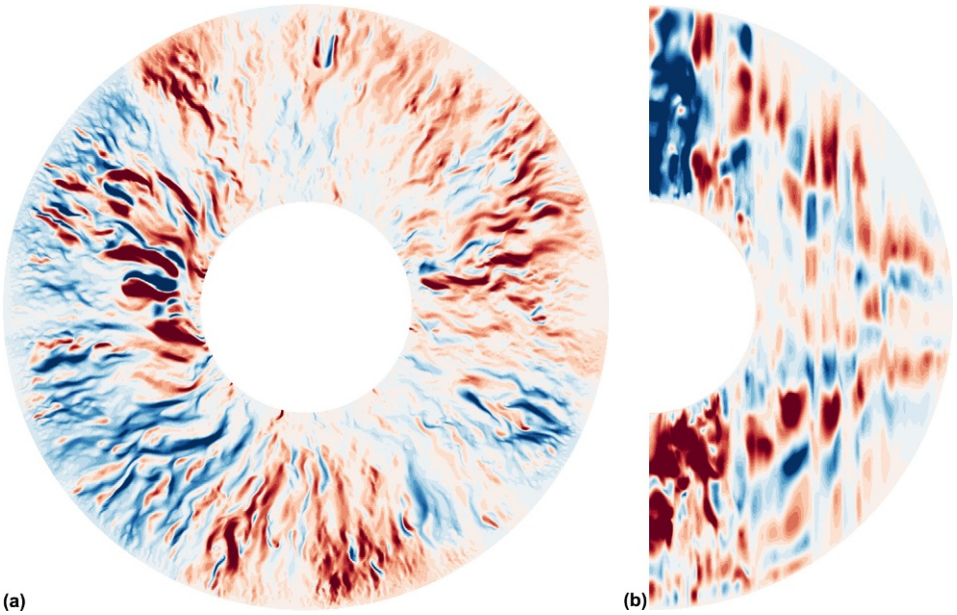

Figure 2 Cylindrical radial magnetic field component B_s in the equatorial plane (a) and a meridional plane (b). Snapshots from a dynamo DNS at $E=10^{-7}$, $Pm=0.1$, $Pr=1$, and $Ra=2.4\times10^{13}$ (see **Table 2** for the definition of these numbers using ℓ as the radial distance between the inner shell and outer shell), using spherical harmonic expansion up to degree 893 and 1024 radial shells.

of potential vorticity (PV) plays a major role in shaping zonal flows in rotating fluids (Aubert et al., 2002). Recently, using a transparent electrolyte and a superconducting magnet, Andreev et al. (2013) demonstrated that PIV methods can be used in MHD experiments.

Advances in handling helium gas at low temperatures have opened a new way for exploring thermal convection at very high Rayleigh numbers. As we will see in **Section 8.06.6.2**, the Rayleigh number measures the vigor of convection. Niemela et al. (2000) reported heat transfer measurements for an amazing range of 11 decades in Rayleigh number from 10^6 to 10^{17}, displaying a very simple power-law dependence of the Nusselt number $Nu=0.124Ra^{0.309}$ over the full range (the Nusselt number measures the convective heat transfer efficiency). They also provide nice evidence for a Kolmogorov $f^{-5/3}$ frequency power spectrum of temperature fluctuations at $Ra=6\times10^{11}$.

For experiments with liquid metals, which are essential for investigating magnetohydrodynamic turbulence, acoustic Doppler velocimetry has proved very useful (Brito et al., 2001, 2011; Stefani et al., 2009). Interestingly, in such experiments, induced magnetic fields resulting from the interaction of the flow with a weak imposed magnetic field, which can be measured outside the experiment, provide an information on the hydrodynamic flow that would be difficult to retrieve otherwise. For example, Kelley et al. (2007) discovered that specific inertial modes were excited in a rotating spherical Couette flow experiment using liquid sodium as a working fluid. These modes appear to be excited by critical layers attached to the Stewartson layer that accommodates the angular velocity jump between the inner sphere and the outer sphere when both rotate (Rieutord et al., 2012).

When a strong dipolar magnetic field is applied in the same Couette geometry, as in the DTS experiment (see Brito et al., 2011), modes are also observed (Schmitt et al., 2008, 2013), but the modes are strongly affected by the Lorentz force. The DTS experiment also demonstrates that turbulence is strongly hampered under the action of both global rotation and a strong magnetic field (Nataf et al., 2008; Nataf and Gagnière, 2008).

The pioneer dynamo experiments of Riga (Gailitis et al., 2001) and Karlsruhe (Stieglitz and Müller, 2001) have not only demonstrated the self-sustained dynamo process in the Lab but also opened the way to using liquid sodium as a working fluid in MHD and dynamo experiments. Several teams across the world have followed their example and set up sodium experiments in which the mean flow is accompanied by fluctuations of a similar amplitude (see Lathrop and Forest, 2011; Verhille et al., 2010, for recent reviews). Spontaneous generation of a magnetic field has thus been observed in the VKS experiment in Cadarache (Monchaux et al., 2007), but only when the impellers are ferromagnetic. A variety of different dynamical regimes have been observed in this device, including spectacular chaotic reversals of the magnetic field (Berhanu et al., 2007). One of the main lessons from these studies is that turbulent fluctuations appear to hinder the dynamo action that the mean flow should produce if it were alone. Besides, ohmic dissipation remains high in these experiments, and Alfvén waves are too damped to play a dynamical role, except when the device is placed in a very strong magnetic field (Alboussiere et al., 2011). Using plasma as a working fluid opens new possibilities, which are under investigation (Spence et al., 2009).

8.06.3.3 Observations

Unfortunately, no observations of the internal geomagnetic field are possible at small scales, mostly because of the crustal field that overprints the small-scale core field. Observations of

turbulence in other systems are thus required to gain insight in what happens in the Earth's core.

Characterization of turbulence in the Earth's atmospheric boundary layer was probably the first target of detailed analyses of turbulence. The first measurements of turbulent fluxes were performed in Australia by the eddy correlation technique (Swinbank, 1951; see Hogstrom, 1996, for a review). All these observations shed light on the universal behavior of turbulence in natural environments, showing, for example, that the von Kármán constant $K=u_*/(z\partial_z u_{\mathrm{H}})$, relating the amplitude of turbulent fluctuations u_* to the vertical gradient of mean horizontal velocity $\partial_z u_{\mathrm{H}}$ in the inertial sublayer, is constant and equal to its laboratory value of 0.4, irrespective of the roughness of the ground, as expected from the scale-invariant properties of universal turbulence (Lo et al., 2005).

Later on, compilations of data from commercial aircraft flights demonstrated that winds and temperature follow Kolmogorov's $k^{-5/3}$ law for wavelengths from a few kilometers up to 400 km, steepening to a k^{-3} law at larger scales (Nastrom and Gage, 1985). Coupling these observations with simulations from general circulation models opens the way to determining the actual energy fluxes responsible for this behavior (Augier and Lindborg, 2013).

Space exploration of the solar system has revealed the fantastic dynamics of the atmospheres of Jupiter and Saturn and opened the way for detailed analyses of their turbulent behavior. The long-term stability of the strong and numerous zonal jets they display remains a strong driver for modeling turbulence on a rotating sphere (see Vasavada and Showman, 2005, for a review).

Combining observations and high-performance numerical modeling, the reanalysis of ocean circulation nicely illustrates the role of quasi-geostrophic mesoscale eddies in the dynamics of the ocean. In particular, zonal motions resulting from the interaction of turbulent eddies have recently been detected (Maximenko et al., 2005).

The solar wind is a great laboratory for MHD turbulence, as reviewed by Bruno and Carbone (2005). Even though it is a collisionless plasma, MHD turbulence is expected for frequencies below 0.1 Hz. Two types of solar winds must be distinguished. The fast wind originates from polar regions of the Sun and has mean velocities about twice as fast as the slow wind coming from equatorial regions. The temporal fluctuations in the solar wind have been measured by several probes starting in the 1960s. The measurements show three regimes in the temporal energy spectrum $E(f)\sim f^{\alpha}$: The lowest frequencies have $\alpha\simeq -1$ for period about a day or longer, while higher frequencies follow $\alpha\simeq -3/2$ for the fast wind and $\alpha\simeq -5/3$ for the slow wind. Finally, at periods around a few seconds, $\alpha\simeq -2$ is found. The transition between the first two regimes is rather sharp and is located around 10–16 hours, depending on the distance from the Sun. The fluctuations are found to be anisotropic, with much weaker fluctuations along the local magnetic field. A strong correlation exists between the velocity and the magnetic fluctuations, especially for the fast wind, showing the predominance of (incompressible) Alfvén waves in solar wind turbulence. At a large distance from the Sun, magnetic field fluctuations are twice more energetic than velocity fluctuations. This observation remains puzzling, although it is also observed in some dynamo simulations.

8.06.3.4 Shell Models

Shell models of turbulence originated in the 1970s, as a tool for accessing the statistical properties of universal turbulence. In these models, structures are ignored, as all fields are projected on a suite of shells of wave number k_n in the spectral domain. The sequence of wave numbers k_n is chosen to be geometric, thus enabling a wide range of length scales to be covered with a limited number of grid points. One takes into account the symmetries and conservation laws that pertain to the type of turbulence under study (2-D or 3-D hydrodynamic turbulence, magnetohydrodynamic turbulence, etc.). The game is then to choose the rules that govern the transfer between shells, which mimic the nonlinear interactions between the various fields of the various shells. The phenomenon of intermittency described earlier in the text can be recovered in shell models.

Shell models have received a lot of attention in the past decade, and extensions to MHD and rotating turbulence have been worked out (see Plunian et al., 2013, for a thorough review). Shell models are particularly appealing for exploring MHD turbulence in fluids with a very small (or very large) magnetic Prandtl number, for which DNSs are hopeless because of the large range of scales to be resolved. The magnetic Prandtl number $Pm=\nu/\eta$ is the ratio of kinematic viscosity over magnetic diffusivity. It is of the order of 10^{-5} for liquid iron in the core. As an example, Plunian and Stepanov (2010) explored how the ratio of magnetic to viscous dissipation varies with the magnetic Prandtl number. They found that, under model assumptions, magnetic dissipation is at least ten times larger than viscous dissipation for core values.

8.06.3.5 Plume Model

In contrast with the approach we just described, David Loper and others focused on buoyant plumes envisioned as the elementary structure at the origin of turbulent motions in the core. The analysis of the dynamics of such plumes in core conditions led David Loper to infer that rising plumes would have dimensions in the range 10–1000 m, typical relative density anomalies between 10^{-10} and 10^{-8}, and upwelling velocities from 10^{-3} to $10^{-1}\,\mathrm{m\,s^{-1}}$, depending on actual core properties. At the base of the convecting outer core, plumes would occupy a fraction of the surface between 10^{-5} and 10^{-1}. The reader is referred to David Loper's chapter (Loper, 2007) in the first edition of the Treatise on Geophysics for a complete description of the plume model.

8.06.4 Parameterization of Turbulence

Numerical simulations are limited by the available memory of the computer and its computing power. The more turbulent the flow, the larger the scale range. Therefore, DNSs that resolve all the spatial scales down to the viscous dissipation scale (the limit of turbulent small scales) cannot reach strongly turbulent regimes. If one could capture the (statistical) effect of turbulent small scales on the larger scales and properly predict the turbulent small-scale state corresponding to the large scales that produce it, we could in principle parameterize the effect of small-scale turbulence.

If several parameterizations for purely hydrodynamic, homogeneous, isotropic turbulence are available and used in hydrodynamic simulations or in the MHD regime at low Rm and low interaction parameter (e.g., Ponty et al., 2005), we should at least question their use for modeling the Earth's core.

On one hand, if we target the dynamics to the small scales inside the Earth's core, we will see that the turbulence inside the Earth's core may never reach the parameter-space region where simple hydrodynamic turbulence takes place (see Section 8.06.6). Thus, we are left with a challenging task: finding a necessarily anisotropic parameterization that depends on the local magnetic field and on the global rotation.

On the other hand, the current numerical geodynamo models do not seem to operate in such a regime, and hydrodynamic turbulence may indeed be important for the small scales in these models. Indeed, even with a magnetic field and a large magnetic diffusivity, part of the flow that is aligned with the magnetic field will not produce electric current and dissipation. Viscosity is the only isotropic dissipation in such systems. Furthermore, the smaller the scale, the smaller the influence of the magnetic field (interaction parameter); hence, the smallest scales may only rely on hydrodynamic turbulence for the energy to reach the viscous dissipation scale.

Here, we wish not to provide a detailed theoretical framework for subgrid-scale modeling, but rather list a few approaches that have been used to perform numerical simulation of the Earth's core. With the previously mentioned limitations in mind, we describe two approaches.

8.06.4.1 Hyperdiffusivities or Eddy Diffusivities

Hyperdiffusivity is the simplest form of parameterization of small-scale turbulence, where the effect of unresolved small scales is expressed as an enhanced diffusivity on the resolved scales. In hydrodynamic turbulence, where the interactions are mostly local (which means that a given scale is mostly influenced by its neighboring scales), such enhanced diffusivity can arguably be restricted to the smallest resolved scales. Although there is no physical justification for the use of hyperdiffusivity, there is a practical one: with increased viscosity at small scales, a numerical simulation is able to dissipate more energy, which would have been the main effect of smaller unresolved scales.

The first geodynamo simulation by Glatzmaier and Roberts (1995) made use of hyperdiffusivity at all scales, which is arguably both a concern and not really a small-scale parameterization, but it allowed to run a full geodynamo model on the computers of the early 1990s. A more reasonable approach is to restrict the use of hyperdiffusivity only at the smaller scales. Following the pioneers, many authors use a hyperdiffusivity of the type $\nu(l)=\nu_0(1+a(l-l_0)^n)$ for $l>l_0$ and $\nu(l)=\nu_0$ for $l\le l_0$, where l is the spherical harmonic degree (angular wave number) and a, l_0, and n are adjustable parameters. It must be emphasized that this is still an isotropic viscosity but its value depends only on l and not on the radial spatial size (for practical reasons). This (historical) formula may seem overly complicated, with three adjustable parameters. A simpler, more elegant form for hyperdiffusivity with self-similarity properties would be

$$\nu(l)=\begin{cases}\nu_0 & \text{for } l\le l_0\\ \nu_0 q^{l-l_0} & \text{for } l\le l_0\end{cases} \quad [10]$$

which has only two independent parameters l_0 and q.

Finally, we want to emphasize that such an approach must be used with care, as it has been shown to have significant effect on the dynamics (Grote et al., 2000).

8.06.4.2 Large Eddy Simulations

Attempts have been made to apply models of hydrodynamic turbulence to model the subgrid scales of the peculiar turbulence occurring inside the Earth's core. A rather successful model is the large eddy simulations (LESs) using a similarity model, where the energy transfer due to the interaction with smaller, unresolved scales is estimated by the transfer that actually occurs between the small but resolved scales of the simulation (e.g., Lesieur, 2008). This has the huge advantage over the eddy-diffusivity technique that it can capture the anisotropic nature of transfer between scales. Although the idea seems interesting, these LES models are still in an early development stage. Indeed, they are constantly compared with higher-resolution DNS, and there are many important tunable parameters (e.g., Buffett, 2003; Chen and Jones, 2008; Matsui and Buffett, 2012). Furthermore, the DNS that they are compared with are far from the dynamical regime expected in the Earth. The presence of boundaries, where turbulence is no more homogeneous, is also a difficulty for LES models.

Currently, LES can be useful to run simulations over a long time period, where the corresponding DNS is feasible but slower. By comparing with a short-term DNS and tuning the subgrid-scale model to reproduce it, we can then trust the LES model for the long-term simulation.

A greater challenge for these models is to actually predict rather than reproduce, which would be a major breakthrough, but it is not clear whether or not they will ever succeed. A key to success might be to ensure that the smallest resolved scales are actually in the low Rm regime, where the self-similar hypothesis is more likely to hold.

8.06.5 Equations, Timescales, and Length Scales

8.06.5.1 Equations

The velocity field $\boldsymbol{u}$ describing the flow of the Earth's liquid core of density ρ is governed by the Navier–Stokes equation including the Coriolis force (due to the rotation rate Ω of the planet), the Lorentz force, and the buoyancy force. It is supplemented with the mass-conservation equation, simplified in the anelastic framework (Gilman and Glatzmaier, 1981; see Chapter 8.03):

$$\partial_t\boldsymbol{u}+(\boldsymbol{u}\cdot\boldsymbol{\nabla})\boldsymbol{u}+2\boldsymbol{\Omega}\times\boldsymbol{u}=-\boldsymbol{\nabla}\Pi+C\boldsymbol{g}+(\boldsymbol{B}\cdot\boldsymbol{\nabla})\boldsymbol{B}/\rho\mu_0+\nu\nabla^2\boldsymbol{u} \quad [11]$$

$$\boldsymbol{\nabla}\cdot(\rho\boldsymbol{u})=0 \quad [12]$$

where Π is a reduced pressure including other potential forces (such as the centrifugal force and magnetic pressure). The evolution of the divergence-free magnetic field $\boldsymbol{B}$ in this liquid metal is governed by the induction equation:

$$\partial_t \boldsymbol{B} + (\boldsymbol{u}\cdot\boldsymbol{\nabla})\boldsymbol{B} = (\boldsymbol{B}\cdot\boldsymbol{\nabla})\boldsymbol{u} + \eta\nabla^2\boldsymbol{B} \quad [13]$$

$$\boldsymbol{\nabla}\cdot\boldsymbol{B} = 0 \quad [14]$$

The evolution of the buoyancy is less well known, as it originates from both chemical and thermal variations, which have different diffusivities. As we are not focusing on the energy injection mechanism details, we can use a single codensity C, with a specified volumetric source term S:

$$\partial_t C + (\boldsymbol{u}\cdot\boldsymbol{\nabla})C = \kappa\nabla^2 C - S \quad [15]$$

There are assumptions behind these equations that we would like to make explicit. For simplicity, the diffusive terms are written as a simple Laplace operator, which implies a homogeneous diffusivity. As the diffusivities are very small, these terms are important only at small scales, while we expect the variations of the diffusivity coefficient to be moderate over the depth of the core. The codensity formulation hides the difference between thermal and chemical diffusivities.

These equations must be completed by boundary conditions. Boundary conditions are important and can control the dynamical state of the system (see, e.g., Sakuraba and Roberts, 2009), but they are thought to have only an indirect effect on the small-scale turbulence.

8.06.5.2 Ordering of Forces in the Earth's Core

For the Earth's core, the order of magnitude of the different terms can be evaluated. We will focus on the scale dependence of this ordering that may help to understand the dynamics of the small scales. From the inversion of the geomagnetic secular variations (see Chapter 8.04), we have an estimate of the large-scale velocity field at the core surface: $U \sim 15$ km year$^{-1} \sim 5\times10^{-4}$ m s^{-1}. More recently, the observation of torsional oscillations by Gillet et al. (2010) has given us an estimate of the magnetic field strength deep inside the core ($B_0 \sim 3\times10^{-3}$ T). The buoyancy force drives the system, but it is hard to assess its strength and compare it to other forces. Indeed, convection tends to smooth the codensity through mixing. We will rather focus on the velocity and magnetic fields as a result from this buoyancy and try to understand how they organize at various scales.

For doing so, we build ℓ-scale dimensionless numbers, which compare the weight of the various terms of the equations at a typical length scale ℓ. This length scale can be related to the wave number k in a Fourier decomposition by $\ell = 2\pi/k$. We find it convenient to express these numbers as ratios of characteristic times, which are functions of ℓ. For example, diffusive phenomena will have timescale τ and length scale ℓ related by

$$\tau_\nu(\ell) = \ell^2/\nu \quad [16]$$

where we have picked here the diffusion of momentum, governed by the kinematic viscosity ν. We can thus define an ℓ-scale *Reynolds number*

$$Re(\ell) = \frac{u(\ell)\ell}{\nu} = \frac{\tau_\nu(\ell)}{\tau_u(\ell)}$$

which compares advection to diffusion of momentum at the ℓ-scale. Other relevant times are listed in Table 1 and will be introduced in the coming sections, while ℓ-scale dimensionless numbers are listed in Table 2.

Table 1 Characteristic times at length scale ℓ

Notation	*Expression*	*Description*
$\tau_\nu(\ell)$	ℓ^2/ν	Viscous time
$\tau_\eta(\ell)$	ℓ^2/η	Magnetic diffusion time
$\tau_\kappa(\ell)$	ℓ^2/κ	Thermal diffusion time
$\tau_D(\ell)$	ℓ^2/D	Compositional diffusion time
$\tau_\rho(\ell)$	$\sqrt{\frac{\ell}{g}\frac{\rho}{\lvert\Delta\rho\rvert}}$	Buoyancy time
t_Ω	$1/\Omega$	Rotation time (independent of ℓ)
$\tau_{\text{Rossby}}(\ell)$	$r_o/\Omega\ell$	Rossby wave propagation time/ bidimensionalization time
$\tau_{\text{Alfvén}}(\ell)$	$\ell\sqrt{\rho\mu_0}/B_0$	Alfvén wave propagation time (large-scale magnetic field)
$\tau_u(\ell)$	$\ell/u(\ell)$	Eddy turnover time, regime-dependent
$\tau_b(\ell)$	$\ell\sqrt{\rho\mu_0}/b(\ell)$	Alfvén wave collision time, regime-dependent

Symbols and properties as defined in **Chapter 8.01** – ρ, ν, k, D, and η (noted λ in **Chapter 8.01**) – are, respectively, the density, kinematic viscosity, thermal diffusivity, compositional diffusivity, and magnetic diffusivity of liquid iron at core conditions. r_0 is the radius of the outer core, g is the gravity, Ω is the angular velocity of the Earth, and B_0 is the intensity of the large-scale magnetic field inside the core. $u(\ell)$ and $b(\ell)$ are the eddy turnover time and magnetic field intensity at length scale ℓ, respectively, which we try to determine for various turbulence scenarios.

8.06.5.2.1 Coriolis force

The ℓ-scale *Ekman number*

$$E(\ell) = \frac{\nu}{\ell^2\Omega} = \frac{t_\Omega}{\tau_\nu(\ell)}$$

compares viscous forces to the Coriolis force. It is the ratio of the rotation time t_Ω over the viscous diffusion time $\tau_\nu(\ell)$. This number is tiny at large scales and reaches unity for scales comparable to the laminar Ekman layer thickness, estimated to be less than a meter in the Earth's core. It is unlikely that turbulence reaches such small scales, because dissipation would be too large (see Section 8.06.6). This means that the Coriolis force is important at every scale, including the dissipative scales.

The ℓ-scale *Rossby number*

$$Ro(\ell) = \frac{u(\ell)}{\ell\Omega} = \frac{t_\Omega}{\tau_u(\ell)}$$

compares eddy entrainment force to the Coriolis force. It is also the ratio of the rotation time over the eddy turnover time at length scale ℓ. For the scale of the whole core, we have $Ro_0 \sim 10^{-6}$, a small value showing the predominance of the Coriolis force at large scales, which will eventually decrease toward smaller scales (if we assume that $u(\ell)/\ell$ increases as ℓ decreases). Depending upon the evolution of the typical velocity $u(\ell)$ with scale ℓ, it may or may not reach values of the order of one or more, which would mark a transition from rotation-dominated turbulence to 3-D turbulence.

Table 2 ℓ-*scale* dimensionless numbers

Notation	*Expression*	*Time ratio*	*Description*
$Re(\ell)$	$\frac{u(\ell)\ell}{\nu}$	$\frac{\tau_\nu(\ell)}{\tau_u(\ell)}$	Reynolds number
$E(\ell)$	$\frac{\nu}{\ell^2\Omega}$	$\frac{t_\Omega}{\tau_\nu(\ell)}$	Ekman number
$Ro(\ell)$	$\frac{u(\ell)}{\Omega\ell}$	$\frac{t_\Omega}{\tau_u(\ell)}$	Rossby number
$Rm(\ell)$	$\frac{u(\ell)\ell}{\eta}$	$\frac{\tau_\eta(\ell)}{\tau_u(\ell)}$	Magnetic Reynolds number
$n(\ell)$	$\frac{b^2(\ell)}{\rho\mu_0 u^2(\ell)}$	$\frac{\tau_u^2(\ell)}{\tau_b^2(\ell)}$	Interaction parameter (small-scale magnetic field)
$N(\ell)$	$\frac{B_0 b(\ell)}{\rho\mu_0 u^2(\ell)}$	$\frac{\tau_u^2(\ell)}{\tau_{\text{Alfven}}(\ell)\tau_b(\ell)}$	Interaction parameter (large-scale magnetic field)
$\Lambda(\ell)$	$\frac{b(\ell)B_0}{\rho\mu_0 u(\ell)\Omega\ell}$	$\frac{\tau_u(\ell)t_\Omega}{\tau_b(\ell)\tau_{\text{Alfven}}(\ell)}$	Elsasser number
$Lu(\ell)$	$\frac{\ell B_0}{\eta\sqrt{\rho\mu_0}}$	$\frac{\tau_\eta(\ell)}{\tau_{\text{Alfven}}(\ell)}$	Lundquist number
$\lambda(\ell)$	$\frac{B_0}{\sqrt{\rho\mu_0}\Omega\ell}$	$\frac{t_\Omega}{\tau_{\text{Alfven}}(\ell)}$	Lehnert (or magnetic Rossby) number
$Ra(\ell)$	$\frac{(-\Delta\rho/\rho)g\ell^3}{\kappa\nu}$	$\frac{\tau_\kappa(\ell)\tau_\nu(\ell)}{\tau_\rho^2(\ell)}$	Rayleigh number
Pr	ν/κ		Prandtl number (independent of ℓ)
Pm	ν/η		Magnetic Prandtl number (independent of ℓ)

One recovers the classical expression of these numbers at the integral scale r_0 by setting $\ell = r_0$. These numbers are also expressed as ratios of characteristic ℓ – scale times, which are defined in **Table 1**.

8.06.5.2.2 Magnetic induction

The ℓ-scale *magnetic Reynolds number*

$$Rm(\ell) = \frac{u(\ell)\ell}{\eta} = \frac{\tau_\eta(\ell)}{\tau_u(\ell)}$$

compares magnetic induction to magnetic diffusion in the induction equation. Evaluated at the largest scale, we have $Rm_0 \sim 10^3$, meaning that a dynamo could take place in the Earth's core. At such scales, the magnetic field has a dynamics of its own and is not a slave of the velocity field. $Rm(\ell)$ decreases with decreasing scale, and when it drops below unity, the magnetic field evolution will be mostly dissipative.

The ℓ-scale *interaction parameter*

$$n(\ell) = \frac{b^2(\ell)}{\rho\mu_0 u^2(\ell)} = \frac{\tau_u^2(\ell)}{\tau_b^2(\ell)}$$

is the ratio of the Lorentz force to the inertial force. When there is a dominant large-scale magnetic field B_0, one can define another interaction parameter:

$$N(\ell) = \frac{B_0 b(\ell)}{\rho\mu_0 u^2(\ell)} = \frac{\tau_u^2(\ell)}{\tau_{\text{Alfven}}(\ell)\tau_b(\ell)}$$

At the largest scale, the ratio of magnetic energy to kinetic energy $N_0 = n_0 \sim 10^4$, which means that the inertial forces are negligible compared with the Lorentz force at large scales.

In small Rm MHD turbulence, the magnetic field is a slave of the velocity field, and the Lorentz force is a linear term. When the magnetic Reynolds number is large, the magnetic field is not a slave of the velocity field and has its own dynamics. Then, the Lorentz force is truly a nonlinear term of the system, and the nonlinear transfer of energy between scales can happen through the Lorentz force. When both the interaction parameters $N(\ell)$ and $Rm(\ell)$ are large, we argue that the nonlinear transfer of energy between scales is dominated by the Lorentz force, while the inertial force plays a negligible role.

At length scales ℓ where $Rm(\ell)$ is small, the induction equation provides an estimate of $b(\ell) \sim u(\ell)B_0\ell/\eta$, where B_0 is the large-scale magnetic field. One can thus build a small-scale interaction parameter $N(\ell \to 0) \sim \ell B_0^2/\eta\rho\mu_0 u(\ell)$. If $Rm(\ell) < 1$, we also have $u(\ell) < \eta/\ell$, so that $N(\ell \to 0) > \ell^2 B_0^2/\eta^2\rho\mu_0 \sim \tau_\eta^2(\ell)/\tau_{\text{Alfvén}}^2(\ell)$. Applying these relations to the Earth's core, we find that $N > 1$ for $\ell > 30$ m. The transition from nonlinear energy transfer dominated by the Lorentz force to an energy transfer dominated by advection may occur at a larger scale than this conservative estimate, but we can safely advocate that most of the nonlinearity of the core dynamics is due to the Lorentz force.

8.06.5.2.3 Lorentz versus Coriolis

We can also compare the Coriolis and Lorentz forces, forming the *Elsasser number*:

$$\Lambda(\ell) = \frac{b(\ell)B_0}{\rho\mu_0 u(\ell)\Omega\ell} = \frac{\tau_u(\ell)t_\Omega}{\tau_b(\ell)\tau_{\text{Alfven}}(\ell)}$$

The large-scale estimate of this ratio gives $\Lambda_0 \sim 0.01$. At scales sufficiently small where $Rm(\ell) < 1$, the low Rm estimate of $b(\ell)$ gives an Elsasser number independent of the length scale: $\Lambda(\ell \to 0) = B_0^2/\rho\mu_0\eta\Omega \sim 10$. This means that the Coriolis force clearly dominates at large scales but progressively yields to the Lorentz force at small scales.

Using the small Rm expression of $\Lambda(\ell)$ in a dynamo regime is inappropriate and results in wrong estimates of the importance of Lorentz and Coriolis forces (Soderlund et al., 2012).

8.06.5.3 Waves and Transients

A thorough description of waves that can propagate in the Earth's core is given in **Chapter 8.09**. If we leave aside sound waves (or seismic waves), there are several other waves that can propagate in our system. First of all, the strong influence of global rotation Ω allows *inertial waves* to exist. They are anisotropic and dispersive, and their group velocity $V_\Omega \sim \Omega\ell$ depends on the length scale ℓ measured in a plane perpendicular to the rotation axis. The propagation of energy by inertial waves occurs mainly along the rotation axis (Davidson et al., 2006), leading to the formation of structures elongated along the rotation axis. The Rossby number, which we have already introduced, also measures the ratio of fluid velocity to inertial wave group velocity.

The presence of the magnetic field allows *Alfvén waves*. Discovered theoretically by Alfvén (1942), these waves couple the velocity field and the magnetic field (see Chapter 8.09). Following the analysis of Tobias et al. (2013), we consider a region at rest with a uniform and constant magnetic field $\boldsymbol{B}_0$. Introducing the Elsasser variables $z^{\pm} = \boldsymbol{u} \pm \boldsymbol{b}/\sqrt{\rho\mu_0}$, where $\boldsymbol{u}$ and $\boldsymbol{b}$ are the velocity and magnetic fluctuations, respectively, the Navier–Stokes and induction equations can be combined to yield

$$(\partial_t \mp \boldsymbol{V}_A \cdot \boldsymbol{\nabla}) z^{\pm} + (z^{\mp} \cdot \boldsymbol{\nabla}) z^{\pm} = -\boldsymbol{\nabla} P + \frac{1}{2}(\nu + \eta)\nabla^2 z^{\pm} + \frac{1}{2}(\nu - \eta)\nabla^2 z^{\mp} \quad [17]$$

In the absence of dissipation ($\nu = \eta = 0$), eqn [17] describes wave-type motions, which propagate in either directions along the $\boldsymbol{B}_0$ field lines, with the Alfvén wave velocity $\boldsymbol{V}_A = \boldsymbol{B}_0/\sqrt{\rho\mu_0}$. In a uniform magnetic field, these waves are nondispersive so that wave packets of any shape propagate without distortion.

These waves are damped by diffusive phenomena, whose importance is measured by the *Lundquist number*:

$$Lu(\ell) = \frac{B_0 \ell}{\sqrt{\rho\mu_0}(\eta + \nu)} = \frac{\tau_{\eta+\nu}}{\tau_{\text{Alfven}}}$$

which compares the diffusive time to the Alfvén propagation time. In liquid metals, where $\eta \gg \nu$, it reduces to $Lu(\ell) = V_A \ell/\eta = \tau_\eta(\ell)/\tau_{\text{Alfvén}}(\ell)$. When $Lu(\ell) < 1$, Alfvén waves are damped and do not exist anymore. In the Earth's core, we have $Lu_0 \sim 10^5$.

The *Alfvén number*

$$A(\ell) = \frac{u(\ell)\sqrt{\rho\mu_0}}{B_0} = \frac{\tau_{\text{Alfven}}(\ell)}{\tau_u(\ell)}$$

measures the ratio of fluid velocity to Alfvén wave speed. It is always small in the core ($A(\ell) < 0.01$), meaning that these waves are dynamically important, at least in the directions perpendicular to the rotation axis.

The ratio of Alfvén to inertial wave speed has been called the *Lehnert number* by Jault (2008) and is also called the magnetic Rossby number in Chapter 8.03:

$$\lambda(\ell) = \frac{B_0}{\sqrt{\rho\mu_0}\Omega\ell} = \frac{t_\Omega}{\tau_{\text{Alfven}}(\ell)}$$

At large scale, $\lambda_0 \sim 10^{-4}$ means that the Taylor columns can form very rapidly (an effect of inertial wave propagation) before the magnetic field can act on the flow (Gillet et al., 2011; Jault, 2008). Once a Taylor column is formed, it can slowly evolve, driven by buoyancy and/or the Lorentz force. At smaller scale, the time to build the Taylor column increases and the columns start to wither. Stationary flow can also escape this Taylor constraint, forming thermal or magnetic winds.

8.06.5.4 What Should Be Considered a Small Scale?

In view of the previous evaluations, there seems to be two main regimes in the core: the high Rm at large scales and the low Rm at small scales. Based on $Rm(\ell)$, the transition happens at a length scale $\ell \sim 10$ km or larger, depending on how $u(\ell)$ evolves with ℓ.

In the high Rm regime, the Coriolis force dominates and balances buoyancy, leading to strongly anisotropic dynamics, with predominance of tall coherent structures elongated along the direction of the rotation axis. The kinetic energy is efficiently converted to magnetic energy, and the transfer between scales is ensured by both the Lorentz force and the induction equation.

In the low Rm regime, the Lorentz force dominates the Coriolis force, which still remains important. The dynamical structures are anisotropic, strongly influenced by the direction of the local magnetic field. A significant part of the kinetic energy is dissipated through Joule heating, but motion along the magnetic field remains almost dissipationless. The interaction parameter is still large so the inertial terms are unlikely to be important for the energy transfer between scales, which happens mainly through the Lorentz force. This regime is probably well described by low Rm rotating MHD turbulence at high interaction parameter.

In this picture, the buoyancy is merely a shadow that provides the driving force. However, the injection of kinetic energy by buoyancy, which happens presumably at small scales, is of particular interest for this problem. In particular, it means that the large scale is possibly the result of a nonlinear cascade of energy due to the Lorentz force, from small scales to large scales.

The next section will detail the mechanisms and try to paint a broad picture of turbulence in the core from large to small scales.

8.06.6 Turbulent Regimes for the Core

The previous section has shown that the relative importance of the various forces depends upon the length scale considered. In this section, we try to infer the actual turbulent regimes that should take place in the Earth's core. We consider as given the various diffusivities and the size and rotation rate of the core. We further assume that the large-scale flow velocity is known, from secular variation inversions (see Chapter 8.04), and that the magnetic field has a dominant large-scale component, whose typical intensity in the core is also known, from the observed velocity of torsional oscillations (Gillet et al., 2010). The actual values we use are listed in Table 3. The questions we address are the following: At what length scale and timescale is the turbulence regime dominated by rotation? By the magnetic field? Can we infer the evolution of flow velocity and small-scale magnetic field in these different regimes? How much energy is dissipated? What is the balance between viscous dissipation and ohmic dissipation? Which waves can propagate?

We perform this exercise step by step, introducing the various ingredients that affect turbulence.

8.06.6.1 τ–ℓ Regime Diagrams

We introduce a τ–ℓ regime diagram that helps retrieve important properties of turbulence and that we will use as a guide when we investigate the effects of rotation and magnetic field on turbulence. It consists in plotting the timescale τ of the relevant physical phenomena as a function of their length scale ℓ.

Figure 3 shows $\tau(\ell)$ versus ℓ for classical hydrodynamic Kolmogorov turbulence, in a log-log plot. For the sake of

illustration, we have assumed that energy is injected at the integral scale ($\ell = r_o$) at a typical timescale $t_{SV} = 300$ years for flow in the core at this length scale. Let us draw the relevant $\tau_u(\ell)$ turnover time of an eddy of radius ℓ. In Kolmogorov's universal turbulence with its $E(k) \simeq \varepsilon^{2/3} k^{-5/3}$ energy density spectrum, the typical eddy turnover time is given by

Table 3 Properties of the core with their numerical values used to draw the figures, as gathered by Peter Olson Chapter 8.01

Property	*Value*	*Unit*	*Description*
κ	5×10^{-6}	$m^2\ s^{-1}$	Thermal diffusivity
D	10^{-9}	$m^2\ s^{-1}$	Chemical diffusivity
ν	10^{-6}	$m^2\ s^{-1}$	Kinematic viscosity
η	1	$m^2\ s^{-1}$	Magnetic diffusivity
r_o	3.48×10^6	m	Radius of the core
M_o	1.835×10^{24}	kg	Mass of the outer core
t_Ω	1.38×10^4	s	Rotation time of the Earth (i.e., $1/2\pi$ day)
t_{SV}	9×10^9	s	r_o-scale core flow time from secular variation inversion (i.e., $\simeq$300 years)
$t_{Alfvén}$	1.4×10^8	s	r_o-scale torsional Alfvén wave time (i.e., $\simeq$4 years)
P	$<10^{13}$	W	Power dissipated in the core

Note that some properties have large uncertainties (see Chapter 8.01). We also define the spin-up time $t_{spin\text{-}up} = r_o/\sqrt{\nu\Omega} \simeq 13000$ years.

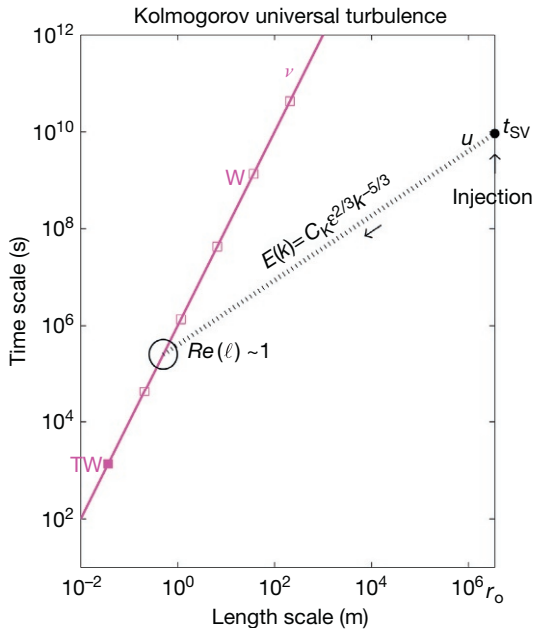

Figure 3 τ–ℓ regime diagram for Kolmogorov's universal hydrodynamic turbulence. Energy cascades from the injection scale (taken here as the integral scale $\ell = r_o$ with timescale $t_{SV} = 300$ years) following Kolmogorov's universal law $\tau_u(\ell) \sim \ell^{2/3} \varepsilon^{-1/3}$ down to the dissipation scale when it intersects the viscous line $\tau_\nu(\ell)$, yielding $Re(\ell) \sim 1$. Viscous dissipation can be read at this intersection point, using values graduated along the $\tau_\nu(\ell)$ line.

$$\tau_u(\ell) \simeq \ell^{2/3} \varepsilon^{-1/3} \qquad [18]$$

since $E(k)k \simeq u^2(\ell)$ and (Note that in this chapter, we will occasionally drop 2π factors and other prefactors for simplicity, since we are mainly dealing with orders of magnitude $k \sim 1/\ell$).

When eddy turnover times are shorter than viscous diffusion time at the same ℓ, fluid motions follow Kolmogorov's cascade downscale until the $\tau_u(\ell)$ line intersects the viscous time line. Intersection points in τ–ℓ regime diagrams correspond to scales at which the regime changes. This intersection corresponds to $Re(\ell) = u(\ell)\ell/\nu \sim 1$, where $Re(\ell)$ is the ℓ-scale Reynolds number, hence the scale at which the regime changes from the inertial range to the diffusive range.

The energy dissipation per unit mass ε is simply deduced from the ratio of the kinetic energy (per unit mass) at this scale divided by the corresponding timescale, yielding $\varepsilon = \ell^2/\tau_\nu^3(\ell) = \nu/\tau_\nu^2(\ell)$. Multiplying by the mass of the liquid outer core $M_o = 1.835 \times 10^{24}$ kg, we obtain the total viscous dissipation, which we have indicated by squares along the $\tau_\nu(\ell)$ viscous line. The squares are a factor of 10^3 apart, and the TW square ($1\ TW = 10^{12}$ W) is filled for reference.

8.06.6.2 Turbulent Convection

Convective motions appear in a fluid layer heated at the bottom and cooled at the top when the temperature gradient is large enough.

8.06.6.2.1 The Rayleigh number

Lord Rayleigh established that the onset of convection is attained when the Rayleigh number Ra_0 reaches a critical value Ra_c, where the Rayleigh number (at the integral scale) is defined as

$$Ra_0 = \frac{(-\Delta\rho/\rho) g r_o^3}{\kappa\nu} \qquad [19]$$

with r_o the thickness of the fluid layer, g the acceleration due to gravity, κ the thermal diffusivity of the fluid, and ν its kinematic viscosity. The $-\Delta\rho/\rho$ term determines the relative density ratio across the layer. It is equal to $\alpha\Delta T$ when the density variations are due to temperature alone, where α is thermal expansivity and ΔT the temperature variation.

It is not so easy to estimate the Rayleigh number in the liquid core, because most of the temperature contrast between the top of the core and its base is due to compression via the equation of state (see Chapter 8.01). This part defines the adiabatic (or isentropic) temperature profile, and only the density variations in excess of it should be included in the $\Delta\rho$ term in the expression of the Rayleigh number. Since heat conducted along the adiabat is large, it is possible that the Rayleigh number is subcritical in part of the core. However, as soon as the density profile departs from the adiabat, the Rayleigh number can get very large.

We will use the τ–ℓ regime diagram of Figure 4 to illustrate this point. One can define a ℓ-scale *Rayleigh number* $Ra(\ell)$ as a thermal diffusion time $\tau_\kappa(\ell)$ times a viscous diffusion time $\tau_\nu(\ell)$ divided by the square of a 'buoyancy time' $\tau_\rho(\ell)$ (which is analogous to the inverse of the buoyancy frequency used in stratified fluids):

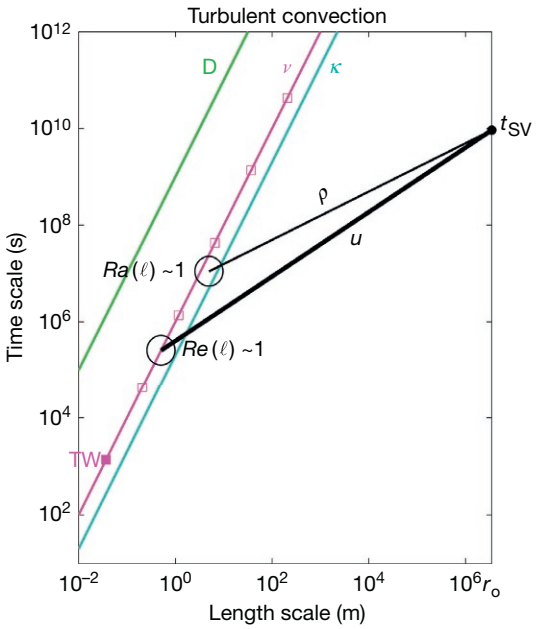

Figure 4 τ–ℓ regime diagram for turbulent thermal convection. The intersection of the 'buoyancy' line $\tau_\rho(\ell)$ with a line at middistance between the viscous line $\tau_\nu(\ell)$ and the thermal diffusion line $\tau_\kappa(\ell)$ defines $Ra(\ell)\sim 1$, where the regime changes from convective at larger scales to diffusive at smaller scales. The $\tau_u(\ell)$ line gives the evolution of the eddy turnover time as a function of ℓ and is here assumed to follow Kolmogorov's law from the integral scale ($\tau_u(r_o)=t_{SV}$) down to the diffusion scale, where the $\tau_u(\ell)$ line intersects the $\tau_\nu(\ell)$ line, yielding $Re(\ell)\sim 1$.

$$Ra(\ell)=\frac{\tau_\kappa(\ell)\tau_\nu(\ell)}{\tau_\rho^2(\ell)} \qquad [20]$$

where $\tau_\rho(\ell)=\sqrt{\frac{\ell}{g}\frac{\rho}{|\Delta\rho|}}$, $\tau_\kappa(\ell)=\ell^2/\kappa$ and $\tau_\nu(\ell)=\ell^2/\nu$.

Using the diffusivities listed in Chapter 8.01 and given again in Table 3, we trace the lines defined by $\tau_\kappa(\ell)$ and $\tau_\nu(\ell)$ in Figure 4.

8.06.6.2.2 Density perturbation

All we know from observations about density perturbations $\Delta\rho/\rho$ is that they are too small to be detected. We pick here a value $\Delta\rho/\rho\simeq 10^{-15}$, which we will justify in the succeeding text, to trace $\tau_\rho(\ell)$. Where $\tau_\rho(\ell)$ is halfway between $\tau_\kappa(\ell)$ and $\tau_\nu(\ell)$ defines the length scale ℓ and corresponding timescale at which $Ra(\ell)\sim 1$. Buoyant fluid parcels with dimensions larger than a few meters will rise with typical rise time of several months. We have also drawn the line $\tau_D(\ell)$ that corresponds to chemical diffusion. We see that chemical (or compositional) convection would start for smaller fluid parcels.

We will see later, when we introduce the role of rotation, that a better value for $\Delta\rho/\rho$ is probably about 10^{-9}. The present value was chosen to be consistent with the hypothesis that large-scale core motions were due to thermal convection, in the absence of rotation and magnetic field. One may then relate the large-scale time t_{SV} to the integral Rayleigh number Ra_0 and thus deduce $\Delta\rho/\rho$. The scaling law for convective large-scale velocity U is not that well known. An ad hoc scaling such as $U\simeq Ra_0^{1/2}\sqrt{\kappa\nu}/r_o$ is not unreasonable in our range of Prandtl and Rayleigh numbers (see Ahlers et al. (2009) for a review) and simply yields $\Delta\rho/\rho\simeq r_o/gt_{SV}^2\sim 10^{-15}$ and $Ra_0\simeq\tau_\kappa(r_0)\tau_\nu(r_0)/t_{SV}^2\sim 10^{17}$.

8.06.6.2.3 Injection and dissipation scales

One could think that the scale ℓ at which $Ra(\ell)\sim 1$ should be the injection scale, in the language of hydrodynamic turbulence. This is not the case in nonrotating convection. Instead, the size of the container appears to be the relevant injection scale, from which energy cascades down to the dissipation scale. More precisely, the classical $k^{-5/3}$ law is retrieved below what is called the Bolgiano scale (after Bolgiano, 1959). The Bolgiano scale appears to be the height of the container in incompressible fluids (Boffetta et al., 2012; Niemela et al., 2000) and the so-called scale height in compressible fluids when the Rayleigh number Ra_0 is larger than 10^{11} (Rieutord and Rincon, 2010). The scale height $H=C_p/\alpha g$ is the height over which density has changed by a factor e under the effect of pressure. In the core, $H\simeq 8900$ km, which is larger than the radius of the core. Therefore, the Bolgiano scale should simply be the radius of the core.

We can then estimate what would be the energy spectrum in the core, if the Earth was not rotating and nonmagnetic. In the τ–ℓ regime diagram of Figure 4, we start from the observed large-scale flow t_{SV} at $\ell=r_o$ and cascade following Kolmogorov's law down to the dissipation scale when the $\tau_u(\ell)$ line intersects the viscous line $\tau_\nu(\ell)$. This happens at a Kolmogorov length scale of about 1 m. We deduce the dissipation per unit mass $\varepsilon=\ell^2/\tau_\nu^3(\ell)=\nu/\tau_\nu^2(\ell)\sim 10^{-17}$ W kg^{-1}, which yields a total viscous dissipation of about 30 MW only.

The idea that buoyancy, which is the driving force of the geodynamo, is available to produce turbulent motions within the core without impeding a specific scale is important to keep in mind.

8.06.6.3 Turbulence in a Rotating Sphere

We have seen in previous chapters that global rotation imposes strong constraints upon flow structures. The Taylor–Proudman theorem implies that the axes of the turbulent eddies are essentially aligned with the axis of rotation of the rotating container. This has led to the idea that turbulence in rotating fluids is essentially two-dimensional. Enabling high-resolution numerical simulations (e.g., Legras et al., 1988) and powerful statistical mechanics approaches (Robert and Sommeria, 1991), 2-D turbulence has been intensively studied early on (Kraichnan and Montgomery, 1980). In the absence of dissipation and forcing, two-dimensionality results in the conservation of the total enstrophy (the integral of the squared vorticity $\int\omega^2$), thereby modifying the classical Kolmogorov cascade into a double cascade: an inverse cascade of energy from the injection scale up to larger length scales with a spectral energy density spectrum $E(k)\sim k^{-5/3}$ and a direct cascade of enstrophy from the injection scale down to smaller length scales with $E(k)\sim k^{-3}$.

However, in a layer at the surface of a rotating sphere, such as the atmosphere, there is an essential difference: strong zonal motions can appear, which are fed by the eddies. Indeed, vortices that move away from the axis of rotation experience a reduction of the Coriolis force, which vanishes at the equator.

This limits the extent of eddies in a latitudinal direction and leads to quasi-geostrophic vortices. On the contrary, azimuthal velocities, which follow geostrophic contours, encounter no resistance, except for viscous friction in the Ekman layers that form at the boundary. These phenomena are nicely displayed in the atmosphere of giant planets, such as Jupiter and Saturn, where strong alternating azimuthal jets circle the planet, entraining and shearing quasi-geostrophic vortices.

Similarly, in a thick layer such as the liquid outer core, columnar vortices that move away from the axis of rotation impinge on the bounding spherical shell. There, the non-penetration condition implies that the velocity component aligned with the cylindrical radius coordinate must convert into a velocity component aligned with the rotation axis, plunging toward the equator from both sides. Such a flow violates the Taylor–Proudman theorem and is therefore inhibited, while azimuthal (zonal) flows are not affected.

Let us examine the τ–ℓ regime diagram of Figure 5 to get a sense of the modifications brought up by rotation in the context of core turbulence. One new timescale stands out: the rotation time of the Earth t_Ω (i.e., $1/2\pi$ day). The intersection of the $\tau_\nu(\ell)$ viscous line with t_Ω defines the thickness of the Ekman layer $\delta_E = \sqrt{\nu/\Omega}$, where Ω is the angular velocity of the Earth. The Ekman layer is about 0.1 m thick. We also introduce the spin-up time $t_{\text{spin-up}} = r_o/\sqrt{\nu\Omega} \simeq 13\,000$ years and draw it in Figure 5. The spin-up time is the time it takes for the core to adjust to a change in the angular velocity of the mantle through viscous coupling, that is, the time it takes for the whole fluid to circulate through the Ekman layer.

8.06.6.3.1 Bidimensionalization and Rossby waves

Inertial waves have periods longer than half a day. They are responsible for implementing the Taylor–Proudman constraint on the flows. Flows at timescales shorter than half a day will not be bidimensionalized. In fact, a blob of vorticity of size ℓ grows into a bidimensional column at a speed equal to $\Omega\ell$ (Davidson, 2013). This means that it takes only a few days for such a blob to convert into an elongated vorticity column, say, ten times longer than wide, whatever the value of ℓ. In a thin layer such as the atmosphere or the ocean, the columns rapidly extend across the entire layer.

However, it is important to realize that in a thick layer such as the liquid outer core, the time required for such a column to reach the core–mantle boundary is given by $\tau_{\text{Rossby}}(\ell) = r_o/\Omega\ell$. The corresponding line is drawn in Figure 5. We have labeled it as the Rossby line, because it also roughly corresponds to the time it takes for a Rossby wave of azimuthal wavelength ℓ to propagate one wavelength. Indeed, the expression of the pulsation of a Rossby wave, as recalled in Chapter 8.09, reads

$$w_{\text{Rossby}} = -2\Omega\frac{\beta k_\varphi}{k^2}$$

with $\beta = \alpha/H_c$, where α is the slope of the spherical shell and H_c the height of the quasi-geostrophic column and k is the wave number of the Rossby wave. Approximating $\alpha \sim 1$ and $H_c \sim r_o$ at midlatitudes and $k \sim k_\varphi$, we retrieve $\tau_{\text{Rossby}}(\ell) \sim r_o/\Omega\ell$.

Above the Rossby line, columns extend across the entire core: motions are quasi-geostrophic (QG). Assuming that ℓ now defines the diameter of the columnar eddies in the equatorial plane, the viscous line $\tau_\nu(\ell)$ is unchanged. However, viscous friction is also present at the ends of the column. There, the velocity drops to zero at the rigid core–mantle boundary. The velocity drop takes place across an Ekman layer of thickness δ_E, thin enough for viscous forces to balance the Coriolis force. The dissipation per unit mass due to viscous friction at the ends of the columns can be written

$$\varepsilon_{QG} = \frac{\ell^2}{\tau_u^2(\ell)\, t_{\text{spin-up}}} \qquad [21]$$

The intersection of the viscous line $\tau_\nu(\ell)$ with the spin-up time marks the length scale at which friction on the walls of a column equals friction at its ends. It occurs for a length $\ell = r_o E_0^{1/4}$, where $E_0 = \nu/\Omega r_o$ is the Ekman number at the integral scale.

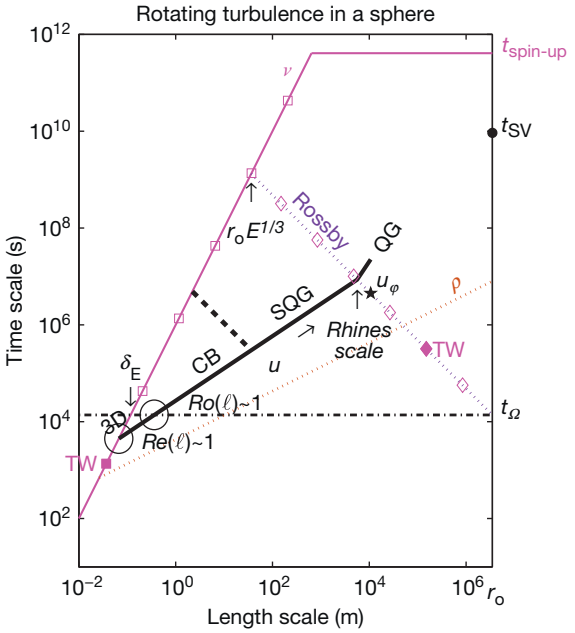

Figure 5 τ–ℓ regime diagram for rotating turbulence in a spherical shell. Rotation yields a specific timescale: t_Ω (dash-dot horizontal line). Its intersection with the viscous line (magenta) yields the Ekman boundary layer thickness δ_E. We also draw a horizontal line for the spin-up time $t_{\text{spin-up}} = r_o/\sqrt{\nu\Omega}$. The dotted line labeled 'Rossby' represents the time $\tau_{\text{Rossby}}(\ell)$ it takes for a Rossby wave to propagate one wavelength ℓ. Its intersection with the viscous line occurs for $\ell = r_o E^{1/3}$, which is the width of convective columns at the onset of convection. The brown dotted line labeled ρ represents the buoyancy line $\tau_\rho(\ell)$. The u_φ star on the Rossby line marks the width (Rhines scale) and velocity of the zonal jets that would make a turn round the Earth in time t_{SV}. The black solid line is the eddy turnover time $\tau_u(\ell)$ line of nonzonal eddies that we infer, starting from the Rhines scale in the quasi-geostrophic (QG) regime. It becomes semi-quasi-geostrophic (SQG) and follows Kolmogorov's slope after crossing the Rossby line and might enter critical balance (CB) at scales smaller than the injection scale (here taken as $r_o E^{1/3}$). The intersection with t_Ω defines $Ro(\ell) \sim 1$. Turbulence becomes three-dimensional (3-D) below the t_Ω line. The intersection with the viscous line defines $Re(\ell) \sim 1$ and provides the amount of viscous dissipation. Viscous dissipation of the zonal and quasi-geostrophic flows occurs in the Ekman layers and is read on the Rossby line, where diamonds are a factor of 10^3 apart, and the terawatt diamond is filled for reference.

We expect that turbulent motions whose timescale and length scale fall in the triangle bounded by the three lines $t_\Omega - \tau_\nu - \tau_{\text{Rossby}}$ will be strongly influenced by rotation with elongated eddies aligned with the rotation axis (z-axis). Those above the $\tau_{\text{Rossby}}(\ell)$ line will be quasi-geostrophic (QG) columnar vortices extending all the way across the liquid core. We find it logical to evaluate on the Rossby line the viscous dissipation due to quasi-geostrophic and zonal motions since below this line, columns will not necessarily reach the surface Ekman layers. QG and zonal flow viscous dissipation $M_o\varepsilon_{QG}$ is thus graduated with diamonds on the Rossby line. The diamonds are a factor of 10^3 apart, and the TW diamond ($1\ \text{TW} = 10^{12}$ W) is filled for reference.

8.06.6.3.2 Zonal flows and potential vorticity

We have seen that truly geostrophic motions (i.e., zonal (or azimuthal) motions in a sphere or a spheroid) behave in a specific way. In contrast to nonaxisymmetric motions, they get organized in winds or jets of a given width. Their lifetime can be extremely long, and they often carry the largest part of the kinetic energy of the flow. Clearly, these bands will limit the maximum size that QG columns can achieve, since they are separated by what appears to be strong barriers. There has been much debate on the origin and characteristics of these bands. One idea has become quite successful, which assesses that bands are the expression of the mixing of potential vorticity (PV) in a staircase fashion (Dritschel and McIntyre, 2008). PV q defined by $q = (w_z + 2\Omega)/H_c$ is an important quantity in rotating fluids because it is conserved when advected by a columnar flow (w_z being the z-component of the vorticity in the rotating frame and H_c the height of the column), when viscous effects are ignored. In a stratified medium with linear density profile, mixing produces a stack of layers in which the density is fairly homogeneous. These layers remain isolated from each other because the sharp density jump across their borders acts as a barrier for small density fluctuations (Phillips, 1972). It is believed that something very similar happens for PV in a rotating fluid in a sphere.

The conservation of PV is also at the origin of Rossby waves. As a column of fluid at rest (outside the cylinder tangent to the inner core) moves away toward the mantle, its height decreases. In order to conserve PV, the column acquires a negative vorticity (in the rotating frame). The opposite holds for a column moving toward high latitude. Both contribute to a prograde, that is, eastward, motion. This wave motion is called a Rossby wave. Note that in shallow layers such as the ocean or atmosphere at the surface of a rotating planet, Rossby waves propagate westward because the planetary vorticity gradient has the opposite sign. The velocity of Rossby waves increases when their wave number decreases. We have drawn the line $\tau_{\text{Rossby}} = r_o/\Omega\ell$ as representing the timescale versus length scale signature of Rossby waves in the τ–ℓ regime diagram of Figure 5.

The intersection of the Rossby line $\tau_{\text{Rossby}}(\ell)$ with the eddy turnover time $\tau_u(\ell)$ defines a Rhines length scale ℓ_{Rhines} while its intersection with the viscous line $\tau_\nu(\ell)$ provides the length scale of thermal Rossby waves $r_o E_0^{1/3}$, which appear at the threshold of convection (Busse, 1970; Jones et al., 2000). The Rhines scale describes how the sphericity of the core stops the inverse cascade of energy from small-scale vortices.

8.06.6.3.3 Possible turbulent regimes

Let us now try to infer what would be the different turbulent regimes encountered in the core if it was nonmagnetic but rotating. Starting from the 'observed' timescale t_{SV} at the largest length scale r_o, we run into a problem: there should be no motion at this scale, since the maximum diameter of columnar eddies is set by the width of zonal bands. We should therefore reinterpret t_{SV} as the typical time a zonal jet takes to circle once around the core. This sets its velocity $u_\varphi = 2\pi r_o/t_{SV}$, which enters the definition of the Rhines scale: $\ell_{\text{Rhines}} \sim \sqrt{u_\varphi r_o/\Omega}$ (Dritschel and McIntyre, 2008). We assume that this defines the width of the zonal jets. The corresponding viscous dissipation can be read on the Rossby line. Guided by observations of the atmosphere of Jupiter, we further assume that the velocity of the eddies at the same scale (their maximum size) will be five times smaller, thus defining the starting point of the turbulent regime diagram we want to construct. Note that actual large-scale zonal velocities are similar to nonzonal velocities in the Earth's core (Hulot et al., 2002; Pais and Jault, 2008) (see the Chapter 8.04).

Above the Rossby line, these eddies are columns extending all the way across the core. The dissipation of these QG vortices can be read at the intersection of the $\tau_u(\ell)$ line with the Rossby line. It is always smaller than that of the zonal jets (because we have assumed eddies have smaller velocities than jets). The inverse energy cascade yields a Kolmogorov-like law for $\tau_u(\ell)$ in that regime. Below the Rossby line, vortices are still very much elongated in the z-direction, but they do not necessarily extend all the way across the core. We label this regime SQG for semi-quasi-geostrophic. In 2-D turbulence, the conservation of enstrophy modifies the turbulent cascade: energy cascades from the injection scale upscale to the largest possible scale (the inverse energy cascade), while enstrophy cascades downscale.

8.06.6.3.4 Below the injection scale

What is the injection scale in our case? Near the onset of convection, it would be the length scale of thermal Rossby waves $r_o E_0^{1/3}$ (Busse, 1970). However, when strong zonal winds are present, they certainly inject energy and enstrophy at their (larger) scale. 2-D turbulence scenarios and quasi-geostrophic numerical models predict a strong decrease of energy for scales below the injection scale. The thick dashed line in Figure 5 displays what would be the τ_u line in the case of an energy spectrum $E(k) \sim k^{-5}$. However, we have seen that rotating turbulence was not strictly 2-D in this regime (below the Rossby line). It has been recently proposed by Nazarenko and Schekochihin (2011) that the flow reaches a 'critical balance' (CB) in this regime that sees the columns progressively shrink in length until 3-D turbulence is reached at $Ro(\ell) \sim 1$ (at the intersection of the $\tau_u(\ell)$ and t_Ω lines). This is what we have drawn in Figure 5, keeping Kolmogorov's slope all the way down to the dissipation scale ($Re(\ell) \sim 1$), where the remaining viscous dissipation can be read.

Note that in our scenario, the $\tau_u(\ell)$ line barely gets below t_Ω, meaning that turbulence remains influenced by rotation almost down to the dissipation scale. Also, note that the total viscous dissipation (zonal and QG plus SQG) is now of the order of 100 GW, compared with 30 MW in the absence of

rotation. As rotation inhibits convection, a larger energy input and larger buoyancy forces are needed to provide the velocities we observe. The $\Delta\rho/\rho$ term can be estimated here by assuming a balance between the buoyancy and the Coriolis forces yielding $\Delta\rho/\rho \simeq 2\Omega r_o/gt_{SV} \sim 10^{-9}$, some six orders of magnitude larger than in the nonrotating case, hence the position of the $\tau_\rho(\ell)$ line in Figure 5.

8.06.6.4 MHD Turbulence

Let us pursue our exercise by building a plausible scenario of turbulence if the core had the magnetic field we observe at large scales but was not rotating.

8.06.6.4.1 Mechanisms of MHD turbulence

Turbulence in the presence of a strong imposed magnetic field is quite different from classical hydrodynamic turbulence. While eddies are the building bricks of hydrodynamic turbulence, it is believed that Alfvén waves are those of magnetohydrodynamic turbulence (Tobias et al., 2013), at least as long as fluid velocities are smaller than the Alfvén speed ($u(\ell) < V_A$) and the Lundquist number is large $Lu(\ell) \gg 1$. In a uniform magnetic field, these waves are nondispersive so that wave packets of any shape propagate without distortion. However, the collision of counterpropagating Alfvén waves does produce some distortion as the waves then propagate along modified field lines. These collisions produce smaller scales to which energy cascades down without dissipation, just like in classical hydrodynamic turbulence, until the dissipation scale is reached. Indeed, the half-sum and half-difference of the energies E^+ and E^- of the Elsasser variables correspond, respectively, to the total energy and cross helicity $\int u \cdot b$, which are both conserved in ideal incompressible MHD.

Two regimes have been identified: weak turbulence, in which the linear term $(V_A \cdot \nabla) z^\pm$ of eqn [17] dominates over the nonlinear term $(z^\mp \cdot \nabla)\, z^\pm$, and strong turbulence when the opposite holds. In weak turbulence, it takes several collisions of wave packets for energy to cascade to smaller scales and the energy spectral density is inferred to scale as $E(k) \sim k^{-2}$, while nonlinear collisions in strong turbulence are more efficient in that respect, yielding $E(k) \sim k^{-3/2}$. The transition occurs when the Alfvén wave collision time $\tau_b(\ell)$ is of the same order as the large-scale Alfvén wave time $t_{Alfvén}$. Turbulence always gets strong at short length scales. Note that in both cases, one expects an equipartition of energy between the velocity and magnetic fluctuations since Alfvén waves are in equipartition. It is also important to realize that the cascade is for length scales perpendicular to the direction of the guide field $\boldsymbol{B}_0$: the wave packets retain their along-field shape. As a consequence, the wave packets become more and more elongated in the guide field direction, somewhat like vortices are elongated along the rotation axis in rotating turbulence, except that the effect gets larger as the length scale gets smaller, in contrast to the rotating case.

8.06.6.4.2 Two scenarios of MHD turbulence

Let us try to sketch the turbulent regimes a magnetized nonrotating Earth would experience. We will discuss two alternative scenarios and use the τ–ℓ regime diagrams of Figures 6 and 7 as a guide. We again consider that we know the values of the diffusivities and draw a new line for magnetic diffusion as $\tau_\eta(\ell) = \ell^2/\eta$. The large-scale starting point for the velocity field is the same as before, deduced from secular variation core flow inversion. We also assume that we know the intensity of the large-scale magnetic field. Indeed, the recent discovery of torsional waves in the Earth's core (Gillet et al., 2010) provides a profile of the *rms* intensity of the s-component of the magnetic field as a function of s, where s is the cylindrical radius.

We infer a typical intensity of $B_0 = 3$ mT, which translates into a large-scale Alfvén wave velocity $V_A = B_0/\sqrt{\rho\mu_0} \simeq 25$ mms^{-1}. Note that, in fact, the velocity of torsional oscillations depends upon the integral of B_s^2 over azimuth and z, so that the contribution of small scales is included in our estimate of B_0. We plot the line $\tau_{Alfvén} = V_A \ell$ in the τ–ℓ regime diagram of Figure 6. At the largest scale ($\ell = r_o$), the corresponding time is about 10^8 s, that is, a few years, some two orders of magnitude smaller that the characteristic time of secular variation. This is just an expression of the fact that magnetic energy is about four orders of magnitude larger than kinetic energy in the Earth's core. Indeed, when expressed in Alfvén velocity, the magnetic field intensity directly compares to flow velocity. The intersection of the $\tau_\eta(\ell)$ and $\tau_{Alfvén}(\ell)$ lines defines the minimum wavelength ℓ Alfvén waves can achieve without being completely dissipated. It corresponds to an ℓ-scale Lundquist number $Lu(\ell) = \tau_\eta(\ell)/\tau_{Alfvén}(\ell) \sim 1$.

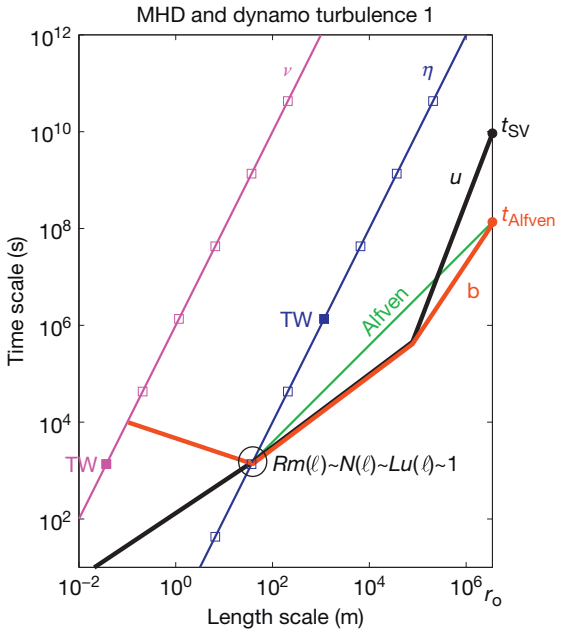

Figure 6 A highly dissipative scenario for magnetohydrodynamic and dynamo turbulence. The timescale of the large-scale magnetic field is $t_{Alfvén}$, deduced from the velocity V_A of torsional oscillations. The green line $\tau_{Alfvén}(\ell)$ gives the time it takes for an Alfvén wave to travel a distance ℓ at this velocity V_A. The red line $\tau_b(\ell)$ measures the strength of the magnetic field at length scale ℓ: it is the characteristic collision time of Alfvén waves. The blue line $\tau_\eta(\ell)$ is the magnetic diffusion line. Ohmic dissipation is graduated with squares along that line. The squares are a factor of 10^3 apart, and the terawatt square is filled. Here, we assume that the τ_u, τ_b, and $\tau_{Alfvén}$ lines all intersect the τ_η line at the same point, where $Rm(\ell) \sim N(\ell) \sim Lu(\ell) \sim 1$, yielding unrealistic ohmic dissipation of millions of TW. The eddy turnover time τ_u continues downscale and intersects the τ_ν line at very small scales, yielding again unrealistic viscous dissipation. This scenario is discarded because it would imply super-Alfvénic velocities.

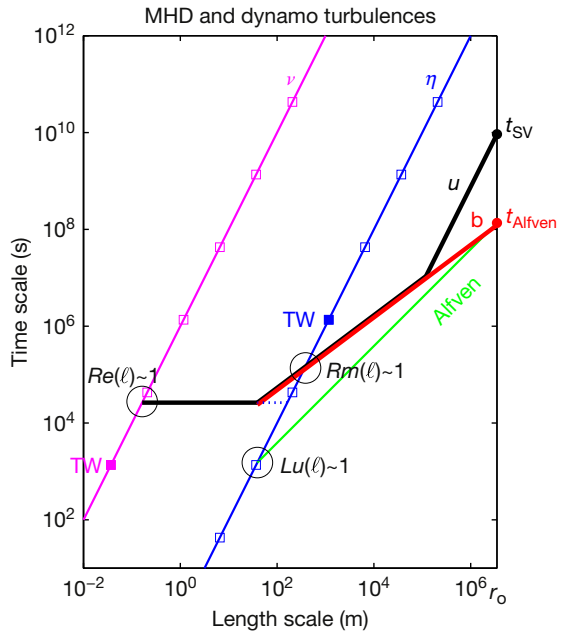

Figure 7 A more realistic scenario for magnetohydrodynamic and dynamo turbulence. In this scenario, we relax the hypothesis that the induction–diffusion balance is achieved at $Rm \sim 1$. Instead, we consider that Alfvén waves can propagate down to a scale ℓ where $Lu(\ell) \sim 1$, that is, at the intersection of the $\tau_\eta(\ell)$ line (blue) with the $\tau_{\text{Alfvén}}(\ell)$ line (green). We assume that the strong turbulence MHD cascade begins at the largest scale r_o. The interaction parameter $N(\ell)$ remains large at all scales, and the flow at small scale is strongly damped by the large-scale magnetic field. Projecting along the blue dashed line yields an ohmic dissipation of about a thousand terawatts, as read on the $\tau_\eta(\ell)$ line.

Where should we plot the lines for the typical velocity field $\tau_u(\ell)$ and for the typical magnetic field $\tau_b(\ell)$ (expressed in Alfvén wave time)? We apply the principles of the MHD turbulence cascade we just described. Assuming equipartition down to the magnetic diffusion scale implies that both the $\tau_u(\ell)$ and $\tau_b(\ell)$ lines should intersect the $\tau_\eta(\ell)$ magnetic diffusion line at the same place in the diagram, which will thus correspond to $Rm(\ell) \sim 1$.

8.06.6.4.3 A highly dissipative scenario

It is then tempting to infer that smaller scales will be in a regime where the small-scale magnetic field results from the diffusion of the magnetic field induced by the interaction of the small-scale velocity field with the large-scale magnetic field. In this diffusive regime, one has $(\boldsymbol{B}_0 \cdot \boldsymbol{\nabla})\boldsymbol{u} \sim \eta \nabla^2 \boldsymbol{b}$, yielding $b \sim uB_0\ell/\eta$, which translates into $\tau_b(\ell) = \tau_{\text{Alfvén}}(\ell)\tau_u(\ell)/\tau_\eta(\ell)$. Since we defined the intersection point by $\tau_u(\ell) = \tau_b(\ell) = \tau_\eta(\ell)$, the intersection should take place where the $\tau_\eta(\ell)$ and $\tau_{\text{Alfvén}}(\ell)$ lines intersect. This intersection thus simultaneously correspond to $Lu(\ell) \sim 1$, $Rm(\ell) \sim 1$, and $N(\ell) \sim 1$, where $N(\ell)$ is the ℓ-scale interaction parameter that measures the effect of the large-scale magnetic field on the velocity field.

At this intersection point, magnetic diffusion takes over and we read the ohmic dissipation $(=M_o\eta/\tau_\eta^2(\ell))$ on the $\tau_\eta(\ell)$ line. It reaches a million terawatts, a value that is clearly unacceptable since no core flux can be larger than our estimate of a total flux from the mantle to the core of 13 TW (see Table 3). The velocity field is probably reduced at this intersection, but what remains should still cascade downscale (Plunian et al., 2013). One can easily check that the interaction parameter decreases as the length scale decreases in this regime, so that hydrodynamic turbulence is recovered with its classical Kolmogorov cascade, as drawn. Figure 6 shows that we finally reach the viscous line $\tau_\nu(\ell)$ for length scales below a millimeter and read a viscous dissipation of a million terawatts again!

There is one problem with this scenario. MHD turbulence above the intersection point at $Rm(\ell) \sim 1$ would be in the strong turbulence regime, for which the energy spectrum is found to be $E(k) \sim k^{-3/2}$ (Tobias et al., 2013), yielding $\tau \sim \ell^{3/4}$, as drawn in Figure 6. This means that the $\tau_u(\ell)$ line is *below* the $\tau_{\text{Alfvén}}(\ell)$ line over a large range of scales, implying that the fluid velocity is larger than the Alfvén speed, which contradicts the hypotheses of Alfvén wave turbulence.

8.06.6.4.4 A more realistic scenario

We thus take into account the latter constraint and require that τ_u and τ_b remain above the Alfvén line. The new scenario we build is drawn in Figure 7. We let the MHD strong turbulence cascade start from the largest scale r_o at time $t_{\text{Alfvén}}$ and assume it goes all the way down to the length scale $\ell \sim \eta\sqrt{\rho\mu_0}/B_0$ for which $Lu(\ell) \sim 1$, at the intersection of the $\tau_\eta(\ell)$ and $\tau_{\text{Alfvén}}(\ell)$ lines. Equipartition is still required, implying that $\tau_u(\ell)$ gets down to times much shorter than t_{SV} to join the $\tau_b(\ell)$ line. We have assumed here a spectrum $E_u(k) \sim k$ for this part, meaning that there is more kinetic energy at small scale than at the integral scale. In contrast with the previous scenario, the interaction parameter $N(\ell) = \tau_u^2(\ell)/\tau_{\text{Alfvén}}(\ell)\tau_b(\ell)$ remains large at all scales, meaning that the large-scale magnetic field strongly influences the flow. Turbulence in the magnetic diffusive regime with a strong applied magnetic field has been explored in laboratory experiments (Alemany et al., 1979). The small scales of the flow are severely damped by the applied magnetic field: the kinetic energy spectrum is $E_u(k) \sim k^{-3}$, which translates into a constant $\tau_u(\ell)$, as drawn in Figure 7. The magnetic energy spectrum is even steeper (not drawn), obeying the induction–diffusion balance. We read an ohmic dissipation of more than a thousand terawatts, which could be much lower though if the strong MHD turbulence spectrum was steeper than $k^{-3/2}$.

Assuming that equipartition at small scale down to the magnetic diffusion scale has a drastic influence on the kinetic and magnetic energy spectra. It is difficult to build scenarios that do not require an unrealistic ohmic dissipation. We will see that rotation can help us recover a more viable scenario.

8.06.6.5 Turbulence in Planetary Cores

The Earth is rotating rather fast. On periods longer than a day, rotation inhibits Alfvén waves (Braginsky, 1970; Jault, 2008). Only geostrophic Alfvén waves, that is, torsional oscillations, are not inhibited. They have indeed been detected in the core (Gillet et al., 2010), and we have used their observed velocity to set our magnetic time $t_{\text{Alfvén}}$ at the integral scale r_o. Quasi-geostrophic Alfvén waves are also possible. But in both cases, the constraint of rotation prevents Alfvén wave collision to be the mechanism by which the magnetic energy cascades down to dissipation.

Using the τ–ℓ regime diagram of Figure 8, let us try to infer what turbulence could look like in the core, taking into account the Earth's rotation and the presence of a strong large-scale magnetic field. The main difference with the previous scenarios is that we do not impose equipartition at small scales. We let the eddy turnover time $\tau_u(\ell)$ decrease with length scale ℓ, assuming a spectrum $E_u(k) \sim k^{-5/3}$ in the dynamo regime. The intersection of the $\tau_u(\ell)$ line with $\tau_\eta(\ell)$ defines the length scale where $Rm(\ell) \sim 1$, below which the flow cannot generate a magnetic field. Below this scale, if the large-scale magnetic field B_0 is dominant, the small-scale magnetic field is obtained by the balance between induction and diffusion and obeys $\tau_b(\ell) = \tau_{\text{Alfvén}}(\ell)\tau_u(\ell)/\tau_\eta(\ell)$. This time, flow velocities remain much lower than Alfvénic speeds. Since $\tau_u(\ell) = \tau_\eta(\ell)$ for $Rm(\ell) \sim 1$, the small-scale magnetic field at $Rm(\ell) \sim 1$ must lie on the Alfvén line. For simplicity, we have thus drawn the $\tau_b(\ell)$ line following the Alfvén line in the dynamo regime.

The interaction parameter $N(\ell) = \tau_u^2(\ell)/\tau_{\text{Alfvén}}(\ell)\tau_b(\ell)$ is very large at all scales, meaning that the large-scale magnetic field strongly influences the flow. Below the scale for which $Rm(\ell) \sim 1$, we thus enter a diffusive regime with a strong applied magnetic field, where Alfvén waves are inhibited by rotation. Following Alemany et al. (1979), we assume a kinetic energy spectrum $E_u(k) \sim k^{-3}$, which translates into a constant $\tau_u(\ell)$, as drawn in Figure 8. The magnetic energy spectrum is even steeper, obeying the induction–diffusion balance.

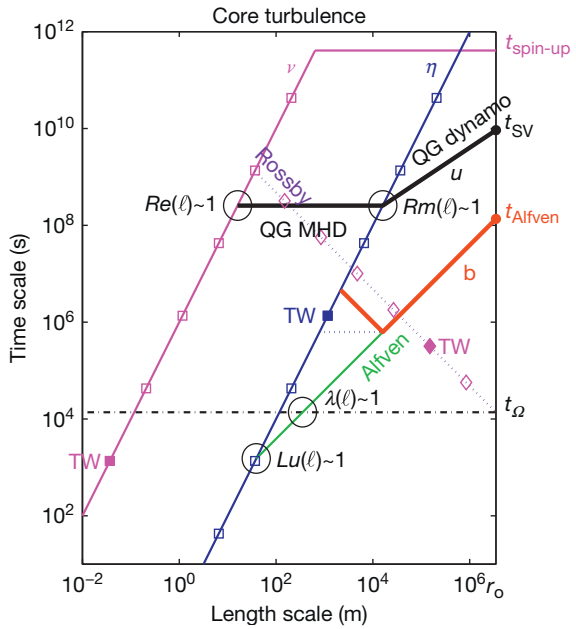

Figure 8 τ–ℓ regime diagram for turbulence in the Earth's core. Both rotation and the magnetic field are taken into account, combining the lines already defined in Figures 5–7. We assume that the kinetic energy density follows a $k^{-5/3}$ law in the quasi-geostrophic dynamo regime. The intersection of the $\tau_u(\ell)$ and $\tau_\eta(\ell)$ lines defines $Rm(\ell) \sim 1$, which marks the transition from the dynamo to the diffusive regime. Quasi-geostrophic (QG) and semi-quasi-geostrophic (SQG) diffusive MHDs govern the following part, with a kinetic energy density spectrum in k^{-3} (yielding a flat $\tau_u(\ell)$ line) and a magnetic energy density spectrum in k^{-5}. Viscous dissipations of the QG (read on the Rossby line) and of the SQG (read on the $\tau_\nu(\ell)$ line) MHD flows amount to a few kilowatts only. Ohmic dissipation is maximum at the length scale ℓ where $Rm(\ell) \sim 1$. Projecting along the blue dashed line yields an ohmic dissipation of a few terawatt, as read on the $\tau_\eta(\ell)$ line. Alfvén waves can be excited and propagate for scales falling on the Alfvén green line between its intersection with t_Ω (which defines $\lambda(\ell) \sim 1$) and that with the magnetic diffusion line (which defines $Lu(\ell) \sim 1$).

Note that in our scenario, the flow is above the Rossby line in the dynamo regime, hence quasi-geostrophic. Most of the nondynamo MHD regime lies above the Rossby line, hence being also quasi-geostrophic (QG). Viscous dissipation can be read along the $\tau_{\text{Rossby}}(\ell)$ line for the quasi-geostrophic MHD flow and on the $\tau_\nu(\ell)$ line for the semi-quasi-geostrophic MHD motions. Both are very small, below the kilowatt range. Ohmic dissipation dominates and mostly occurs at the ℓ-scale where $Rm(\ell) \sim 1$. It can be read along the $\tau_\eta(\ell)$ line, where the dashed blue line intersects, amounting to a few terawatts for the present scenario.

Behind this scenario is the idea that turbulence is very much hindered under the combined constraints of strong magnetic field and fast rotation. The rotating magnetized spherical Couette flow (DTS) experiment provides evidence for this behavior (Nataf and Gagnière, 2008). We end up with a very sluggish core, where the smallest eddies are ten meters in diameter and have turnover times of several years!

Note that the Alfvén line intersects the $\tau_\eta(\ell)$ line below the t_Ω line. This intersection defines $Lu(\ell) \sim 1$, while the intersection of the Alfvén line with the t_Ω line defines $\lambda(\ell) \sim 1$. In that region of the τ–ℓ diagram, it is possible for Alfvén waves to propagate without being hindered by the Earth's rotation (because $\lambda(\ell) > 1$) and without being damped by magnetic diffusion (because $Lu(\ell) > 1$). However, such waves will not be involved in the cascade of energy from large to small scales. Similarly, fluid motions could be excited at timescales shorter than a day (e.g., by tides), but they are not part of the energy cascade.

8.06.7 Summary and Perspectives

Early numerical simulations of the geodynamo have demonstrated the crucial role of rotation in the *generation* of the magnetic field. One of our main messages here is that rotation could also play a key role in limiting the *dissipation* of the magnetic field.

Indeed, the classical scenario of MHD turbulence in the absence of rotation, based on the collision of Alfvén waves, predicts dissipation rates far too large for the core. The constraints brought by rotation prevent Alfvén waves to be the carriers of turbulence. Instead, turbulence gets organized in quasi-geostrophic eddies, strongly elongated along the rotation axis, and strongly damped by the large-scale magnetic field. We end up with a very sluggish core, in which the smallest eddies are ten meters in diameter and have turnover times of several years. The smallest magnetic field structures are even larger, in the kilometer range, but their lifetime might be much shorter (of the order of months). In this scenario, viscous dissipation is negligible, while ohmic dissipation is in the terawatt range. However, one should keep in mind that slightly different scenarios would lead to largely different dissipations.

We note that a planet like Venus, which rotates much more slowly than the Earth (rotation period of 243 days), would not

be in this regime and would not be able to sustain a magnetic field as large as that of the Earth.

The τ–ℓ regime diagram that we introduced is a useful tool for determining the various regimes that can be encountered when going from the large scales down to the dissipative scales. We hope it can guide the construction of appropriate parameterizations of turbulence in LES.

In exploring the various turbulent scenarios, we have noted that key elements were still missing, calling for more experimental and numerical studies. For example, we do not know how to relate quasi-geostrophic and zonal velocities in a convecting sphere. What is the relevant injection scale in these systems? Furthermore, some fundamental differences between the case of the atmosphere of giant planets and that of the core might have been overlooked. Our observation that the time required for a Taylor column to grow and extend across the core is comparable with the propagation time of a Rossby wave questions the validity of quasi-geostrophic modeling of small scales.

MHD and rotating turbulence are even more uncertain. The scenarios we have built are very speculative and await experimental and numerical backing.

What is the prospect of detecting turbulent structures in the core? We have seen that the expected relative density variations are extremely small ($\sim 10^{-9}$), far too small to affect the propagation of seismic waves or the gravity field. However, the velocity of seismic waves can also be modified by rotation, flow velocity, and magnetic field. How important are these effects? Our τ–ℓ diagrams can guide us again. Seismic waves in the core have velocities of about 9 km s^{-1}, yielding a characteristic time of about 400 s at the integral scale r_o. Scattering of seismic waves by turbulent structures roughly scales as their time ratio: strong effects occur when times are comparable. In Figure 8, we see that the time that gets closest to the seismic time is t_Ω: indeed, it is well known that seismic normal modes of the Earth are split by the Coriolis force. The next relevant time is the magnetic Alfvén wave time, but it is already 3 orders of magnitude further away from seismic times, leaving little hope for detection.

Acknowledgments

We thank Dan Lathrop for a fruitful review and Jérôme Noir for spotting an error in an earlier version of our manuscript.

References

Ahlers G, Grossmann S, and Lohse D (2009) Heat transfer and large scale dynamics in turbulent Rayleigh–Benard convection. *Reviews of Modern Physics* 81: 503–537. http://dx.doi.org/10.1103/RevModPhys.81.503.

Alboussière T, Cardin P, Debray F, et al. (2011) Experimental evidence of Alfvén wave propagation in a gallium alloy. *Physics of Fluids* 23: 096601. http://dx.doi.org/10.1063/1.3633090.

Alboussière T, Deguen R, and Melzani M (2010) Melting-induced stratification above the Earth's inner core due to convective translation. *Nature* 466: 744–747. http://dx.doi.org/10.1038/nature09257.

Alemany A, Moreau R, Sulem P, and Frisch U (1979) Influence of an external magnetic field on homogeneous MHD turbulence. *Journal de Mécanique* 18: 277–313.

Alfvén H (1942) Existence of electromagnetic–hydrodynamic waves. *Nature* 150: 405–406. http://dx.doi.org/10.1038/150405d0.

Andreev O, Kolesnikov Y, and Thess A (2013) Visualization of the Ludford column. *Journal of Fluid Mechanics* 721: 438–453. http://dx.doi.org/10.1017/jfm.2013.76.

Anselmet F, Gagne Y, Hopfinger EJ, and Antonia RA (1984) High-order velocity structure functions in turbulent shear flows. *Journal of Fluid Mechanics* 140: 63–89. http://dx.doi.org/10.1017/S0022112084000513.

Aubert J, Jung S, and Swinney HL (2002) Observations of zonal flow created by potential vorticity mixing in a rotating fluid. *Geophysical Research Letters* 29. http://dx.doi.org/10.1029/2002GL015422.

Augier P and Lindborg E (2013) A new formulation of the spectral energy budget of the atmosphere, with application to two high-resolution general circulation models. *Journal of the Atmospheric Sciences* 70: 2293–2308. http://dx.doi.org/10.1175/JAS-D-12-0281.1.

Baroud CN, Plapp BB, Swinney HL, and She ZS (2003) Scaling in three-dimensional and quasi-two-dimensional rotating turbulent flows. *Physics of Fluids* 15: 2091–2104. http://dx.doi.org/10.1063/1.1577120.

Berhanu M, Monchaux R, Fauve S, et al. (2007) Magnetic field reversals in an experimental turbulent dynamo. *Europhysics Letters* 77: 59001. http://dx.doi.org/10.1209/0295-5075/77/59001.

Boffetta G, De Lillo F, Mazzino A, and Musacchio S (2012) Bolgiano scale in confined Rayleigh–Taylor turbulence. *Journal of Fluid Mechanics* 690: 426–440. http://dx.doi.org/10.1017/jfm.2011.446.

Bolgiano R Jr. (1959) Turbulent spectra in a stably stratified atmosphere. *Journal of Geophysical Research* 64: 2226–2229. http://dx.doi.org/10.1029/JZ064i012p02226.

Braginsky SI (1970) Spectrum of oscillations of the Earth's hydro-magnetic dynamo. *Geomagnetism and Aeronomy* 10: 221–233.

Braginsky SI and Meytlis VP (1990) Local turbulence in the Earth's core. *Geophysical and Astrophysical Fluid Dynamics* 55: 71–87. http://dx.doi.org/10.1080/03091929008203556.

Brito D, Alboussière T, Cardin P, et al. (2011) Zonal shear and super-rotation in a magnetized spherical Couette-flow experiment. *Physical Review E* 83: 066310. http://dx.doi.org/10.1103/PhysRevE.83.066310.

Brito D, Nataf HC, Cardin P, Aubert J, and Masson J (2001) Ultrasonic Doppler velocimetry in liquid gallium. *Experiments in Fluids* 31: 653–663. http://dx.doi.org/10.1007/s003480100312.

Bruno R and Carbone V (2005) The solar wind as a turbulence laboratory. *Living Reviews in Solar Physics* 2. http://www.livingreviews.org/lrsp-2005-4.

Buffett BA (2003) A comparison of subgrid-scale models for large-eddy simulations of convection in the Earth's core. *Geophysical Journal International* 153: 753–765. http://dx.doi.org/10.1046/j.1365-246X.2003.01930.x.

Busse FH (1970) Thermal instabilities in rapidly rotating systems. *Journal of Fluid Mechanics* 44: 441–460. http://dx.doi.org/10.1017/S0022112070001921.

Charbonneau P (2005) Dynamo models of the solar cycle. *Living Reviews in Solar Physics* 2. http://www.livingreviews.org/lrsp-2005-2 [on line article] cited [october 2, 2012].

Chen Q and Jones CA (2008) Similarity and dynamic similarity models for large-eddy simulations of a rotating convection-driven dynamo. *Geophysical Journal International* 172: 103–114. http://dx.doi.org/10.1111/j.1365-246X.2007.03621.x.

Christensen UR and Aubert J (2006) Scaling properties of convection-driven dynamos in rotating spherical shells and application to planetary magnetic fields. *Geophysical Journal International* 166: 97–114. http://dx.doi.org/10.1111/j.1365-246X.2006.03009.x.

Davidson PA (2013) Rapidly-rotating turbulence: An experimental perspective. In: Davidson PA, Kaneda Y, and Sreenivasan KR (eds.) *Ten Chapters in Turbulence*, pp. 318–350. Cambridge: Cambridge University Press. http://dx.doi.org/10.1017/CBO9781139032810.009.

Davidson PA, Staplehurst PJ, and Dalziel SB (2006) On the evolution of eddies in a rapidly rotating system. *Journal of Fluid Mechanics* 557: 135–144. http://dx.doi.org/10.1017/S0022112006009827.

Dritschel DG and McIntyre ME (2008) Multiple jets as PV staircases: The Phillips effect and the resilience of eddy-transport barriers. *Journal of the Atmospheric Sciences* 65: 855–874. http://dx.doi.org/10.1175/2007JAS2227.1.

Eymin C and Hulot G (2005) On core surface flows inferred from satellite magnetic data. *Physics of the Earth and Planetary Interiors* 152: 200–220. http://dx.doi.org/10.1016/j.pepi.2005.06.009.

Frisch U (1995) *Turbulence: The Legacy of A.N. Kolmogorov*. Cambridge: Cambridge University Press.

Gailitis A, Lielausis O, Platacis E, et al. (2001) Magnetic field saturation in the Riga dynamo experiment. *Physical Reviews Letters* 86: 3024–3027. http://dx.doi.org/10.1103/PhysRevLett.86.3024.

Giesecke A (2007) Anisotropic turbulence in weakly stratified rotating magnetoconvection. *Geophysical Journal International* 171: 1017–1028. http://dx.doi.org/10.1111/j.1365-246X.2007.03567.x.

Gillet N, Jault D, Canet E, and Fournier A (2010) Fast torsional waves and strong magnetic field within the Earth's core. *Nature* 465: 74–77. http://dx.doi.org/10.1038/nature09010.

Gillet N, Schaeffer N, and Jault D (2011) Rationale and geophysical evidence for quasi-geostrophic rapid dynamics within the Earth's outer core. *Physics of the Earth and Planetary Interiors* 187: 380–390. http://dx.doi.org/10.1016/j.pepi.2012.03.006.

Gilman PA and Glatzmaier GA (1981) Compressible convection in a rotating spherical shell. I – Anelastic equations. II – A linear anelastic model. III – Analytic model for compressible vorticity waves. *The Astrophysical Journal Supplement Series* 45: 335–388. http://dx.doi.org/10.1086/190714.

Glatzmaier GA and Roberts PH (1995) A three-dimensional self-consistent computer simulation of a geomagnetic field reversal. *Nature* 377: 203–209. http://dx.doi.org/10.1038/377203a0.

Grote E, Busse FH, and Tilgner A (2000) Effects of hyperdiffusivities on dynamo simulations. *Geophysical Research Letters* 27: 2001–2004. http://dx.doi.org/10.1029/1999GL011155.

Högström U (1996) Review of some basic characteristics of the atmospheric surface layer. *Boundary-Layer Meteorology* 78: 215–246. http://dx.doi.org/10.1007/BF00120937.

Hulot G, Eymin C, Langlais B, et al. (2002) Small-scale structure of the geodynamo inferred from Oersted and Magsat satellite data. *Nature* 416: 620–623. http://dx.doi.org/10.1038/416620a.

Jault D (2008) Axial invariance of rapidly varying diffusionless motions in the Earth's core interior. *Physics of the Earth and Planetary Interiors* 166: 67–76. http://dx.doi.org/10.1016/j.pepi.2007.11.001.

Jones CA, Soward AM, and Mussa AI (2000) The onset of thermal convection in a rapidly rotating sphere. *Journal of Fluid Mechanics* 405: 157–179. http://dx.doi.org/10.1017/S0022112099007235.

Kaneda Y and Morishita K (2013) Small-scale statistics and structure of turbulence in the light of high resolution direct numerical simulation. In: Davidson PA, Kaneda Y, and Sreenivasan KR (eds.) *Ten Chapters in Turbulence*, pp. 1–42. Cambridge: Cambridge University Press. http://dx.doi.org/10.1017/CBO9781139032810.002.

Kelley DH, Triana SA, Zimmerman DS, Tilgner A, and Lathrop DP (2007) Inertial waves driven by differential rotation in a planetary geometry. *Geophysical and Astrophysical Fluid Dynamics* 101: 469–487. http://dx.doi.org/10.1080/03091920701561907.

Kolmogorov AN (1941a) The local structure of turbulence in incompressible viscous fluid for very large Reynolds number. *Doklady Akademii Nauk SSSR* 30: 299–303.

Kolmogorov AN (1941b) Dissipation of energy in the locally isotropic turbulence. *Doklady Akademii Nauk SSSR* 32: 16–18.

Kolmogorov AN (1962) A refinement of previous hypotheses concerning the local structure of turbulence in a viscous incompressible fluid at high Reynolds number. *Journal of Fluid Mechanics* 13: 82–85. http://dx.doi.org/10.1017/S0022112062000518.

Kraichnan RH and Montgomery D (1980) Two-dimensional turbulence. *Reports on Progress in Physics* 43: 547–619. http://dx.doi.org/10.1088/0034-4885/43/5/001.

Lathrop DP and Forest CB (2011) Magnetic dynamos in the lab. *Physics Today* 64: 40–45. http://dx.doi.org/10.1063/PT.3.1166.

Legras B, Santangelo P, and Benzi R (1988) High-resolution numerical experiments for forced two-dimensional turbulence. *Europhysics Letters* 5: 37–42. http://dx.doi.org/10.1209/0295-5075/5/1/007.

Lesieur M (2008) *Turbulence in Fluids*. Fourth Edition: Springer.

Lo TS, L'vov VS, Pomyalov A, and Procaccia I (2005) Estimating von Karman's constant from homogeneous turbulence. *Europhysics Letters* 72: 943–949. http://dx.doi.org/10.1209/epl/i2005-10323-8.

Matsui H and Buffett BA (2012) Large-eddy simulations of convection-driven dynamos using a dynamic scale-similarity model. *Geophysical and Astrophysical Fluid Dynamics* 106: 250–276. http://dx.doi.org/10.1080/03091929.2011.590806.

Maximenko NA, Bang B, and Sasaki H (2005) Observational evidence of alternating zonal jets in the world ocean. *Geophysical Research Letters* 32. http://dx.doi.org/10.1029/2005GL022728.

Moffatt HK (1961) The amplification of a weak applied magnetic field by turbulence in fluids of moderate conductivity. *Journal of Fluid Mechanics* 11: 625–635. http://dx.doi.org/10.1017/S0022112061000779.

Moffatt HK (1978) *Magnetic Field Generation in Electrically Conducting Fluids*. Cambridge: Cambridge University Press.

Monchaux R, Berhanu M, Bourgoin M, et al. (2007) Generation of a magnetic field by dynamo action in a turbulent flow of liquid sodium. *Physical Review Letters* 98: 044502. http://dx.doi.org/10.1103/PhysRevLett.98.044502.

Nastrom GD and Gage KS (1985) A climatology of atmospheric wavenumber spectra of wind and temperature observed by commercial aircraft. *Journal of the Atmospheric Sciences* 42: 950–960. http://dx.doi.org/10.1175/1520-0469(1985)042<0950:ACOAWS>2.0.CO;2.

Nataf HC, Alboussière T, Brito D, et al. (2008) Rapidly rotating spherical Couette flow in a dipolar magnetic field: An experimental study of the mean axisymmetric flow. *Physics of the Earth and Planetary Interiors* 170: 60–72. http://dx.doi.org/10.1016/j.pepi.2008.07.034.

Nataf HC and Gagnière N (2008) On the peculiar nature of turbulence in planetary dynamos. *Comptes Rendus Physique* 9: 702–710. http://dx.doi.org/10.1016/j.crhy.2008.07.009.

Nazarenko SV and Schekochihin AA (2011) Critical balance in magnetohydrodynamic, rotating and stratified turbulence: Towards a universal scaling conjecture. *Journal of Fluid Mechanics* 677: 134–153. http://dx.doi.org/10.1017/S002211201100067X.

Niemela JJ, Skrbek L, Sreenivasan KR, and Donnelly RJ (2000) Turbulent convection at very high Rayleigh numbers. *Nature* 404: 837–840. http://dx.doi.org/10.1038/35009036.

Obukhov A (1941) Spectral energy distribution in a turbulent spectral energy distribution in a turbulent flow. *Doklady Akademii Nauk SSSR* 32: 22–24.

Pais MA and Jault D (2008) Quasi-geostrophic flows responsible for the secular variation of the Earth's magnetic field. *Geophysical Journal International* 173: 421–443. http://dx.doi.org/10.1111/j.1365-246X.2008.03741.x.

Phillips OM (1972) Turbulence in a strongly stratified fluid—Is it unstable? *Deep Sea Research and Oceanographic Abstracts* 19: 79–81. http://dx.doi.org/10.1016/0011-7471(72)90074-5.

Plunian F and Stepanov R (2010) Cascades and dissipation ratio in rotating magnetohydrodynamic turbulence at low magnetic Prandtl number. *Physical Review E* 82. http://dx.doi.org/10.1103/PhysRevE.82.046311.

Plunian F, Stepanov R, and Frick P (2013) Shell models of magnetohydrodynamic turbulence. *Physics Reports* 523: 1–60. http://dx.doi.org/10.1016/j.physrep.2012.09.001.

Ponty Y, Mininni PD, Montgomery DC, Pinton JF, Politano H, and Pouquet A (2005) Numerical study of dynamo action at low magnetic Prandtl numbers. *Physical Review Letters* 94: 164502. http://dx.doi.org/10.1103/PhysRevLett.94.164502.

Rieutord M and Rincon F (2010) The Sun's supergranulation. *Living Reviews in Solar Physics* 7. http://www.livingreviews.org/lrsp-2010-2 [Online Article]: cited [October 2, 2012].

Rieutord M, Triana SA, Zimmerman DS, and Lathrop DP (2012) Excitation of inertial modes in an experimental spherical Couette flow. *Physical Review E* 86. http://dx.doi.org/10.1103/PhysRevE.86.026304.

Robert R and Sommeria J (1991) Statistical equilibrium states for two-dimensional flows. *Journal of Fluid Mechanics* 229: 291–310. http://dx.doi.org/10.1017/S0022112091003038.

Roberts GO (1972) Dynamo action of fluid motions with two-dimensional periodicity. *Philosophical Transactions of the Royal Society of London, Series A* 271: 411–454. http://dx.doi.org/10.1098/rsta.1972.0015.

Sakuraba A and Roberts PH (2009) Generation of a strong magnetic field using uniform heat flux at the surface of the core. *Nature Geoscience* 2: 802–805. http://dx.doi.org/10.1038/ngeo643.

Schmitt D, Alboussière T, Brito D, et al. (2008) Rotating spherical Couette flow in a dipolar magnetic field: Experimental study of magneto-inertial waves. *Journal of Fluid Mechanics* 604: 175–197. http://dx.doi.org/10.1017/S0022112008001298.

Schmitt D, Cardin P, La Rizza P, and Nataf HC (2013) Magneto-Coriolis waves in a spherical Couette flow experiment. *European Journal of Mechanics B/Fluids* 37: 10–22. http://dx.doi.org/10.1016/j.euromechflu.2012.09.001.

She ZS and Leveque E (1994) Universal scaling laws in fully-developed turbulence. *Physical Reviews Letters* 72: 336–339. http://dx.doi.org/10.1103/PhysRevLett.72.336.

Soderlund KM, King EM, and Aurnou JM (2012) The influence of magnetic fields in planetary dynamo models. *Earth and Planetary Science Letters* 333–334: 9–20. http://dx.doi.org/10.1016/j.epsl.2012.03.038.

Spence EJ, Reuter K, and Forest CB (2009) A spherical plasma dynamo experiment. *Astrophysical Journal* 700: 470–478. http://dx.doi.org/10.1088/0004-637X/700/1/470.

Steenbeck M, Krause F, and Rädler KH (1966) A calculation of the mean electromotive force in an electrically conducting fluid in turbulent motion, under the influence of Coriolis forces. *Zeitschrift für Naturforschung* A21: 369–376.

Stefani F, Gerbeth G, Gundrum T, et al. (2009) Helical magnetorotational instability in a Taylor–Couette flow with strongly reduced Ekman pumping. *Physical Review E* 80: 066303. http://dx.doi.org/10.1103/PhysRevE.80.066303.

Stieglitz R and Müller U (2001) Experimental demonstration of a homogeneous two-scale dynamo. *Physics of Fluids* 13: 561–564. http://dx.doi.org/10.1063/1.1331315.

StPierre MG (1996) On the local nature of turbulence in Earth's outer core. *Geophysical and Astrophysical Fluid Dynamics* 83: 293–306. http://dx.doi.org/10.1080/03091929608208969.

Swinbank WC (1951) The measurement of vertical transfer of heat and water vapour by eddies in the lower atmosphere. *Journal of Meteorology* 8: 135–145. http://dx.doi.org/10.1175/1520-0469(1951)008%3C0135:TMOVTO%3E2.0.CO;2.

Tobias S, Cattaneo F, and Boldyrev S (2013) MHD dynamos and turbulence. In: Davidson PA, Kaneda Y, and Sreenivasan KR (eds.) *Ten Chapters in Turbulence*, pp. 351–404. Cambridge: Cambridge University Press. http://dx.doi.org/10.1017/CBO9781139032810.010.

Vasavada AR and Showman AP (2005) Jovian atmospheric dynamics: An update after Galileo and Cassini. *Reports on Progress in Physics* 68: 1935–1996. http://dx.doi.org/10.1088/0034-4885/68/8/R06.

Verhille G, Plihon N, Bourgoin M, Odier P, and Pinton JF (2010) Laboratory dynamo experiments. *Space Science Reviews* 152: 543–564. http://dx.doi.org/10.1007/s11214-009-9546-1.

Westerweel J, Elsinga GE, and Adrian RJ (2013) Particle image velocimetry for complex and turbulent flows. *Annual Review of Fluid Mechanics* 45: 409–436. http://dx.doi.org/10.1146/annurev-fluid-120710-101204.

Xu H, Bourgoin M, Ouellette NT, and Bodenschatz E (2006) High order Lagrangian velocity statistics in turbulence. *Physical Reviews Letters* 96. http://dx.doi.org/10.1103/PhysRevLett.96.024503.

This page intentionally left blank

8.07 Rotational Dynamics of the Core

A Tilgner, University of Göttingen, Göttingen, Germany

© 2015 Elsevier B.V. All rights reserved.

8.07.1	**Introduction**	183
8.07.1.1	Motivation	183
8.07.1.2	Equations of Motion	185
8.07.1.3	Inertial Oscillations in Infinitely Extended Fluids	186
8.07.1.4	Ekman Layers	187
8.07.2	**Inertial Oscillations in Spherical Shells**	189
8.07.2.1	The Mathematical Problem	190
8.07.2.2	Ray Geometry	190
8.07.2.3	Numerical Simulations	192
8.07.3	**Precession**	193
8.07.3.1	Solutions of the Inviscid Equation of Motion	193
8.07.3.2	Viscous Effects	194
8.07.3.3	Experiments	195
8.07.3.4	Numerical Solutions	197
8.07.3.4.1	Laminar flows	197
8.07.3.4.2	Instability	199
8.07.4	**Tides**	205
8.07.5	**Interaction with Buoyancy and Magnetic Fields**	206
8.07.6	**Summary and Outlook**	209
References		210

Nomenclature

a (m)	Long semiaxis of a spheroid
c (m)	Short semiaxis of a spheroid
d (m)	Distance between the inner and outer boundaries of a spherical shell
E	Ekman number
$e = 1 - c/a$	Ellipticity
E_a	Kinetic energy contained in u_a
e_i, e_o	Ellipticities of the inner and outer boundaries of a spheroidal shell
k	Wave vector
m	Azimuthal wave number
r, θ, φ	Spherical polar coordinates, with θ the colatitude
r_i, r_o	Radii of the inner and outer boundaries of a spherical shell
u	Velocity
u_a	Velocity field antisymmetric with respect to reflection at the origin
u_s	Velocity field symmetrical with respect to reflection at the origin
x, y, z	Cartesian coordinate system with z along the rotation axis
$\hat{z}$	Unit vector along z, $\boldsymbol{\omega}_D = \omega_D \hat{z}$
α	Angle between rotation and precession axes
ν ($m^2\ s^{-1}$)	Kinematic viscosity
Ω	Precession vector
$\boldsymbol{\Omega}$	Ω_P/ω_D
ω	Angular frequency of inertial modes
$\boldsymbol{\omega}_D$ (s^{-1})	Diurnal rotation rate ($\approx 2\pi/24$ h)
$\boldsymbol{\omega}_F$	Rotation vector of fluid in a precessing container
$\boldsymbol{\Omega}_P$ (s^{-1})	Rate of precession

8.07.1 Introduction

8.07.1.1 Motivation

If the mantle was a perfectly rigid shell rotating at a constant angular velocity, the core would rotate with the same angular velocity about the same axis because of viscous entrainment. This chapter deals with perturbations of the simple rigid rotation of the core. The most important perturbations are due to variations of the rotation of the mantle and deformation of the core–mantle boundary (CMB).

There are at least two areas of geophysics for which the rotational dynamics of the core are relevant. First, motions in the core act back on the mantle and affect its rotation. Investigation of the Earth's rotation as a whole obviously requires study of the rotational dynamics of the core in particular. Second, the core motions also generate the magnetic field of the Earth. The flow induced by perturbations of the rotation of the core may contribute to the geodynamo or distort a magnetic field generated by convectively driven flow.

Convection, both thermal and compositional, is a plausible driving mechanism for core motion and ultimately the geodynamo. The structure of buoyancy-driven flows is well documented, and it is in particular established that these flows can produce a dynamo effect. But the energy budget is tight and it could well be that buoyancy is insufficient to power the geodynamo. At any rate, the precession of the rotation axis of the Earth and tidal deformation of the CMB are two effects of which we know that they exist, whereas we do not know with certainty whether the core is convecting, which makes it indispensable to study the response of the rotating core to precession and tides. These two mechanisms share many features, so that precession will be treated in detail, and the ideas developed in this context will then be transposed to the effects of tidal deformation. Both mechanisms have connections with celestial mechanics. A full treatment would require that we also take into account, for example, variations of the lunar orbit, which result from dissipation in the core. But so far, only simpler models have been studied in which the motion or shape of the CMB is prescribed and the response of the core is inquired.

Figure 1 summarizes the problem under study. The mantle rotates about the geographic axis with the rate of diurnal rotation ω_D. The axis of (retrograde) precession is perpendicular to the ecliptic and forms an angle of 23.5° with the geographic axis. The shape of the CMB is assumed spherical or spheroidal (with the geographic axis as axis symmetry). Table 1 collects some relevant numbers.

Other processes have been suggested as possible perturbation of the core's rotation such as earthquakes (Aldridge, 1975). These are certainly less potent than precession and tides. Even the nutations can be neglected compared with precession (Bullard, 1949). There is also the possibility that the inner core and the mantle do not rotate about the same axis or at the same angular velocity, which would force a complicated flow in the outer core. There is no undisputed seismological evidence for a differential rotation between the inner core and the mantle (Laske and Masters, 1999; Souriau and Poupinet, 2000), and gravitational torque acts to resist it (Buffett, 1996). Even if a differential rotation exists, it can only happen as a consequence of motions in the liquid core, so that differential rotation cannot be viewed as a driving mechanism in its own right and it will not be covered in this chapter. A good starting point for the literature on the fluid dynamics of differential rotation is Hollerbach (1998). There has also been an intensive study of libration-induced flows in the past few years. While the fluid mechanics of flows driven by libration are very closely related to the flows driven by precession and tides, libration forcing is virtually inexistent for the Earth and will not be considered in this chapter, even though it may be relevant for other celestial bodies, such as nearly synchronized moons.

As for any other fluid flow, it will be useful to distinguish laminar response from unstable and chaotic flows in which a large-scale motion disintegrates into smaller eddies. It is at present not known which flow regime the Earth's core is in. A laminar flow draws little energy from the motion of the mantle, whereas an unstable flow can dissipate orders of magnitude more power. Only if the flows driven by precession or tides are unstable can the rotational dynamics of the core make a significant contribution to the dynamo process.

Most of this chapter considers the core to be neutrally buoyant. This allows us to look at the peculiarities of rotational effects in isolation and to separate them from buoyancy effects. However, barring an extraordinary coincidence, the core is either stably stratified or convecting. It is important to check which properties of the rotational dynamics may be modified by buoyancy. This will be done towards the end of this chapter (Section 8.07.5).

The topic covered in this chapter suffers from a paucity of directly useful observational data. In fact, Table 1 contains virtually all relevant numbers, that is, the geometry of the core, the astronomical data on the precession of the Earth's axis, and the presumed viscosity and electrical conductivity of the core material. Because no direct observation of the core flow is

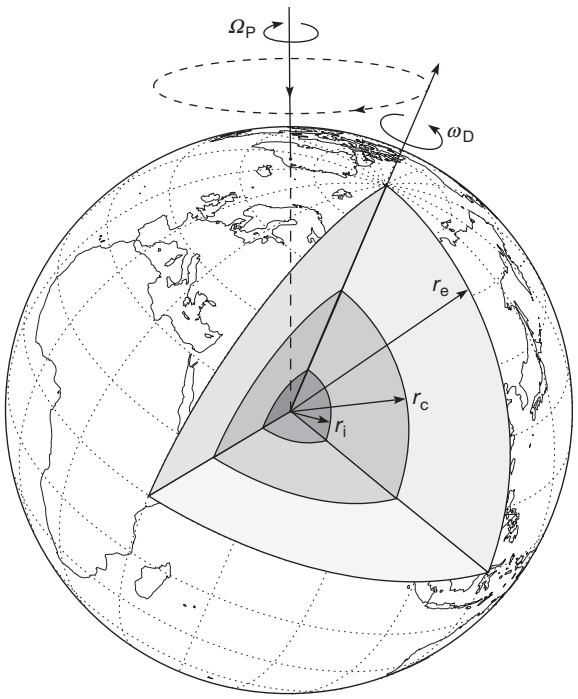

Figure 1 Interior structure of the Earth. The radii of the inner core, r_i, of the core–mantle boundary, r_c, and of the Earth's surface, r_e, are indicated together with the rates of diurnal rotation ω_D and precession Ω_P.

Table 1 Some properties of the Earth

r_i	1220 km
r_c	3480 km
r_e	6370 km
e_{IC}	1/414
e_{CMB}	1/393
Ω_p/ω_D	-1.07×10^{-7}
α	23.5°
ν	10^{-6} m^2 s^{-1}
σ	1.1×10^5 S m^{-1}

The average radii of the inner core, r_i, the core–mantle boundary (CMB), r_c, and the entire Earth, r_e, together with the ellipticities of the inner core and the CMB, e_{IC}, and e_{CMB}, which are taken from Matthews et al. (1991b). The ellipticities are defined with the minor and major axes c and a as $e = 1 - c/a$. The Earth precesses in retrograde direction about the normal to the ecliptic with a period $2\pi/\Omega_P$ of 25 700 years; the diurnal rotation period $2\pi/\omega_D$ equals 1 day. α is the angle between the rotation axis and the normal to the ecliptic. Estimates for the viscosity ν vary widely; see Poirier (1988). The conductivity σ is from Knittle and Jeanloz (1986).

possible, we have to try to deduce that flow from a combination of theory, numerical simulations, and laboratory experiments. Possible connections with observations to be exploited in the future are compiled in the concluding section.

The introductory section presents some general properties of rotating fluids, which will be used later in the chapter. The second section is devoted to inertial modes. These are oscillatory motions in rotating bodies of fluid. Precession excites directly one particular of these modes (the spin-over mode, also called the tilt-over mode) and may excite many more, for instance, through instabilities or interaction with topography. In fact, any perturbation of rotating fluid that is small enough to be described by linearized equations of motion excites superpositions of inertial modes.

The third Section 8.07.1.2 is the largest in this chapter and collects our knowledge about precession-driven flow stemming from theory, experiment, and numerical simulation. The closely connected problem of tidally driven flows is treated in the fourth section. The interaction between buoyancy and magnetic fields, as well as the dynamo effect, is discussed in the fifth section before conclusions and an outlook is given in the sixth section.

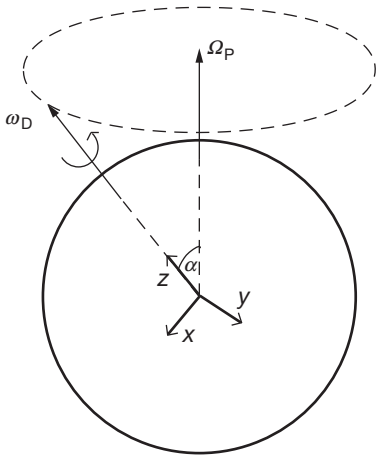

Figure 2 The z-axis is chosen to coincide with the axis of diurnal rotation $\boldsymbol{\omega}_D$, that is, the axis connecting geographic north and south poles. This axis precesses around the precession axis Ω_P. The mantle frame is attached to the core–mantle boundary (CMB). In this frame of reference, the boundaries are at rest but the precession axis is revolving around the z-axis. The precession frame is chosen such that both $\boldsymbol{\omega}_D$ and Ω_P are independent of time, but the boundaries move with velocity $\boldsymbol{\omega}_D \times \boldsymbol{r}$ where $\boldsymbol{r}$ is the position vector of a point on the boundary measured from the origin. Viewed from an inertial system, the tripod x, y, and z of the precession frame is precessing around Ω_P such that Ω_P always remains in the x, z-plane.

8.07.1.2 Equations of Motion

Since we will restrict ourselves to incompressible fluid, the Navier–Stokes equation is the appropriate starting point. This section shows how to use this equation if we want to allow for a variable rotation rate of the mantle.

Two different frames of reference are useful in formulating the equations of motion. The first one is attached to the boundaries and will be called the mantle frame; the second one is chosen such that the precession and rotation axes are stationary and will be called the precession frame; see Figure 2 for definitions. A similar choice has to be made for the tidal problem, where one can opt either for the mantle frame or for a frame in which the tidal bulge is stationary.

We start by deriving the Navier–Stokes equation for an incompressible fluid in an arbitrary frame of reference rotating with the instantaneous angular frequency ω_{ref} relative to inertial space and ask which acceleration is experienced by a fluid particle at position r. The most algorithmic way of obtaining the relation between the acceleration measured in the rotating frame and an inertial frame consists in writing the Euler matrix describing the transformation between the two frames and taking its time derivatives. A more intuitive and shorter derivation uses the relation between time derivatives of vectors in the two frames (Goldstein, 1980) $(\partial/\partial t)_{inert} = (\partial/\partial t)_{rot} + \boldsymbol{\omega}_{ref}\times$. The subscripts specify whether the time dependences are viewed from the inertial or the rotating system. It follows that

$$\left(\frac{\partial}{\partial t}\boldsymbol{r}\right)_{inert} = \left(\frac{\partial}{\partial t}\boldsymbol{r}\right)_{rot} + \omega_{ref}\times\boldsymbol{r}$$

and

$$\left(\frac{\partial^2}{\partial t^2}\boldsymbol{r}\right)_{inert} = \left(\frac{\partial^2}{\partial t^2}\boldsymbol{r}\right)_{rot} + 2\boldsymbol{\omega}_{ref}\times\left(\frac{\partial}{\partial t}\boldsymbol{r}\right)_{rot} + \boldsymbol{\omega}_{ref}\times(\boldsymbol{\omega}_{ref}\times\boldsymbol{r}) + \left(\frac{\partial}{\partial t}\boldsymbol{\omega}_{ref}\right)_{inert}\times\boldsymbol{r}$$

The second and third terms on the right-hand side correspond to the Coriolis and centrifugal forces familiar from uniformly rotating systems; the fourth term is an additional force appearing in nonuniformly rotating frames generally referred to as the Poincaré force. The acceleration in the inertial frame can be deduced from the Navier–Stokes equation for an incompressible fluid with velocity $\boldsymbol{u}_{inert} = [(\partial/\partial t)\boldsymbol{r}]_{inert} = \boldsymbol{u}_{rot} + \boldsymbol{\omega}_{ref}\times\boldsymbol{r}$:

$$\left(\frac{\partial^2}{\partial t^2}\boldsymbol{r}\right)_{inert} = -\frac{1}{\rho}\nabla P + \nu\nabla^2(\boldsymbol{u}_{rot} + \boldsymbol{\omega}_{ref}\times\boldsymbol{r}) + \boldsymbol{f}_{inert}$$
$$= -\frac{1}{\rho}\nabla P + \nu\nabla^2\boldsymbol{u}_{rot} + \boldsymbol{f}_{inert}$$
$$\nabla\cdot\boldsymbol{u}_{inert} = \nabla\cdot\boldsymbol{u}_{rot} = 0$$

ν denotes the viscosity of the fluid, ρ its density, and P the pressure. f_{inert} is a volume force (e.g., the gravitational attraction exerted by the Moon and the Sun) measured in the inertial frame. The aforementioned relations are now assembled to yield the Navier–Stokes equation in the mantle frame. The mantle rotates with a diurnal rate ω_D whose precession is described by the precession vector $\boldsymbol{\Omega}_P$ such that $\boldsymbol{\omega}_{ref} = \boldsymbol{\omega}_D + \boldsymbol{\Omega}_P$ and $[(\partial/\partial t)\omega_{ref}]_{inert} = \boldsymbol{\Omega}_P\times\omega_D$. Dropping subscripts, the equation of motion becomes

$$\frac{\partial}{\partial t}\boldsymbol{u} + (\boldsymbol{u}\nabla)\boldsymbol{u} + 2(\boldsymbol{\omega}_D + \boldsymbol{\Omega}_P)\times\boldsymbol{u} = \nu\nabla^2\boldsymbol{u} - \nabla p - (\boldsymbol{\Omega}_P\times\boldsymbol{\omega}_D)\times\boldsymbol{r} + \boldsymbol{f} \quad \text{(mantle frame)} \qquad [1]$$

with a reduced pressure p, which contains the centrifugal term and the factor $1/\rho$. The no-slip boundary condition at the outer boundary is $\boldsymbol{u} = 0$.

In the precession frame, on the other hand, $\boldsymbol{\Omega}_P$ and $\boldsymbol{\omega}_D$ are stationary such that $\boldsymbol{\omega}_{ref} = \boldsymbol{\Omega}_P$ and the Poincaré force disappears, so that the equation of motion reads

$$\frac{\partial}{\partial t}\boldsymbol{u}+(\boldsymbol{u}\nabla)\boldsymbol{u}+2\boldsymbol{\Omega}_{\mathrm{P}}\times\boldsymbol{u}=\nu\nabla^2\boldsymbol{u}-\nabla p+f\quad\text{(precession frame)}\qquad[2]$$

subject to the condition $\boldsymbol{u}=\boldsymbol{\omega}_{\mathrm{D}}\times r$ at the outer boundary for no-slip boundaries. Analytic work is generally easier in this second frame, but numerical simulations are easier in the first frame because $\boldsymbol{u}$ is small in this frame. The nonlinear term is then less important, and the Courant-Friedrichs-Levy (CFL) condition due to advection is less severe, allowing a larger time step.

The most important point about eqns [1] and [2] is that if f represents gravitational attraction, f derives from a potential and can thus be absorbed in the pressure gradient. Gravitational forces have no influence on the incompressible flow in the cavity of a body whose motion is prescribed. If we consider as given that the Earth executes precessional motion, we do not need to bother about gravitational forces and torques exerted on the core. Equations [1] and [2] with $f=0$ describe the flow in a container precessing on a laboratory bench. Direct application to the Earth's core requires several assumptions chiefly that density variations of the fluid can be ignored (which excludes buoyancy forces) and that all material properties remain constant throughout the liquid core. Magnetic fields will be considered in Section 8.07.5.

It is convenient to rescale all variables so that the equation becomes nondimensional. In the following sections and chapters, time is measured in units of $1/\boldsymbol{\omega}_{\mathrm{D}}$ and the length scale d is chosen either as the radius of the outer boundary or as the gap size between the inner core and the outer boundary if the inner core is taken into account. In these units, the Navier–Stokes equation becomes

$$\frac{\partial}{\partial t}\boldsymbol{u}+(\boldsymbol{u}\nabla)\boldsymbol{u}+2(\hat{\boldsymbol{z}}+\boldsymbol{\Omega})\times\boldsymbol{u}=E\nabla^2\boldsymbol{u}-\nabla p-(\boldsymbol{\Omega}\times\hat{\boldsymbol{z}})\times r\quad\text{(mantle frame)}\qquad[3]$$

where hats denote unit vectors and $\boldsymbol{\Omega}=\boldsymbol{\Omega}_{\mathrm{P}}/\boldsymbol{\omega}_{\mathrm{D}}$. In order to avoid a proliferation of symbols, velocity, length, and time are denoted by the same letters in eqn [1] as their nondimensional counterparts in eqn [3]. The Ekman number E is given by $E=\nu(\boldsymbol{\omega}_{\mathrm{D}}d^2)^{-1}$ and measures in order of magnitude the ratio of viscous to Coriolis forces. Another nondimensional number of interest is the Rossby number $V(\boldsymbol{\omega}_{\mathrm{D}}d)^{-1}$, where V is a typical velocity, which estimates the ratio of the nonlinear term to the Coriolis term. If this number is small, as is the case in many applications, the nonlinear term may be omitted from eqn [3]. We will use this approximation, for example, for the study of inertial modes in Sections 8.07.1.3 and 8.07.2 and for the study of boundary layers in Section 8.07.1.4. In the precession frame (in which the Rossby number is never small), the nondimensional equation of motion is

$$\frac{\partial}{\partial t}\boldsymbol{u}+(\boldsymbol{u}\nabla)\boldsymbol{u}+2\boldsymbol{\Omega}\times\boldsymbol{u}=E\nabla^2\boldsymbol{u}-\nabla p\quad\text{(precession frame)}\qquad[4]$$

8.07.1.3 Inertial Oscillations in Infinitely Extended Fluids

A rotating fluid supports oscillatory motion, the so-called inertial waves, inertial oscillations, or inertial modes. As for all types of waves, boundaries select eigenmodes and resonances for a finite fluid volume. Inertial modes of spherical shells are the topic of Section 8.07.2. It is easiest to explore the distinguishing features of inertial waves in an infinite domain, which we will do in this section.

Consider an unbounded ideal fluid rotating about the z-axis disturbed by motions small enough so that nonlinearities can be neglected in the corotating frame. The nondimensional equation in this frame of reference reads (see eqn [4])

$$\frac{\partial}{\partial t}\boldsymbol{u}+2\hat{\boldsymbol{z}}\times\boldsymbol{u}=-\nabla p,\ \nabla\cdot\boldsymbol{u}=0\qquad[5]$$

We eliminate the pressure by taking the curl of eqn [5]:

$$\frac{\partial}{\partial t}\nabla\times\boldsymbol{u}-2\frac{\partial}{\partial z}\boldsymbol{u}=0\qquad[6]$$

Taking again the curl of eqn [6] one finds with eqn [5]

$$\frac{\partial}{\partial t}\nabla^2\boldsymbol{u}+2\frac{\partial}{\partial z}\nabla\times\boldsymbol{u}=0\qquad[7]$$

$\nabla\times\boldsymbol{u}$ can now be eliminated by cross differentiation between eqns [6] and [7]:

$$\frac{\partial^2}{\partial t^2}\nabla^2\boldsymbol{u}+4\frac{\partial^2}{\partial z^2}\boldsymbol{u}=0\qquad[8]$$

The last equation admits solutions in the form of plane waves $\boldsymbol{u}\propto e^{i(k\cdot r-\omega t)}$ provided that

$$\omega=\pm2\hat{\boldsymbol{k}}\cdot\hat{\boldsymbol{z}}\qquad[9]$$

This dispersion relation shows that $-2\le\omega\le2$ and that ω depends on the direction of propagation of the wave, but not on its wavelength. The phase velocity $\boldsymbol{c}_{\mathrm{p}}$ is given by

$$\boldsymbol{c}_{\mathrm{p}}=\pm2\frac{\hat{\boldsymbol{k}}\cdot\hat{\boldsymbol{z}}}{|\boldsymbol{k}|}\hat{\boldsymbol{k}}\qquad[10]$$

and the group velocity $\boldsymbol{c}_{\mathrm{g}}$ is

$$\boldsymbol{c}_{\mathrm{g}}=\pm2\frac{\hat{\boldsymbol{k}}\times\left(\hat{\boldsymbol{z}}\times\hat{\boldsymbol{k}}\right)}{|\boldsymbol{k}|}\qquad[11]$$

It follows that phase and group velocities are orthogonal; see Figure 3. Their orientations are not independent because $\boldsymbol{c}_{\mathrm{p}}\cdot\hat{\boldsymbol{z}}=\pm2|\hat{\boldsymbol{k}}\cdot\hat{\boldsymbol{z}}|^2/|\boldsymbol{k}|$ and $\boldsymbol{c}_{\mathrm{g}}\cdot\hat{\boldsymbol{z}}=\pm2|\hat{\boldsymbol{k}}\times\hat{\boldsymbol{z}}|^2/|\boldsymbol{k}|$, so that $\mathrm{sgn}(\boldsymbol{c}_{\mathrm{p}}\cdot\hat{\boldsymbol{z}})=\mathrm{sgn}(\boldsymbol{c}_{\mathrm{g}}\cdot\hat{\boldsymbol{z}})$. The peculiar dispersion relation [9] opens the possibility to superpose waves at a particular frequency ω such that they form a localized packet around a surface with normal $\hat{\boldsymbol{n}}$ satisfying $\hat{\boldsymbol{n}}\cdot\hat{\boldsymbol{z}}=\pm\omega/2$. Since the group velocity is perpendicular to $\hat{\boldsymbol{n}}$, the wave motion will stay on that surface. The wave packet will not broaden as time goes on, because the velocity field of the packet at any time t is given by

$$\int f(k)e^{i(\hat{\boldsymbol{n}}k\cdot\boldsymbol{r}-\omega t)}dk=e^{-i\omega t}\int f(k)e^{i\hat{\boldsymbol{n}}k\cdot\boldsymbol{r}}dk$$

where $f(k)$ represents the amplitude of the plane wave with the wave vector $k\hat{\boldsymbol{n}}$. Identical spatial distributions are therefore periodically recovered. In an infinite fluid, the wave motion can be localized in an arbitrarily thin region around the surface. Combinations of waves can be found, which superpose to periodically form jets, shear layers, or a discontinuity in any higher derivative of the velocity field. These singularities can only occur in a periodic motion on surfaces with the appropriate inclination with respect to the rotation axis.

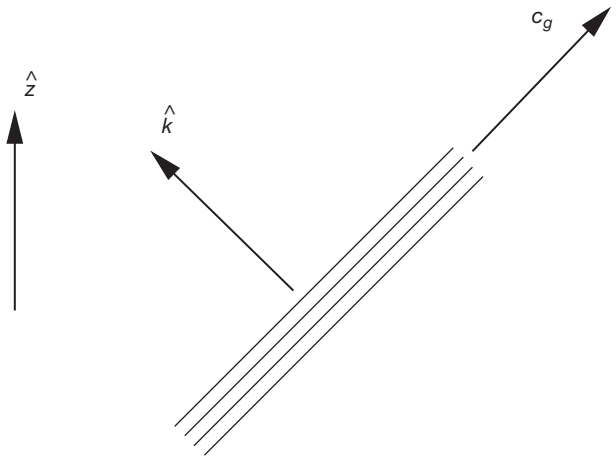

Figure 3 A wave packet indicated by a few wave crests is created by the superposition of plane waves with wave vectors parallel to $\hat{\boldsymbol{k}}$ and angular frequency $\omega = 2\hat{\boldsymbol{k}}\cdot\hat{\boldsymbol{z}}$. The envelope of the packet therefore extends to infinity perpendicular to $\hat{\boldsymbol{k}}$ but is localized in the direction of $\hat{\boldsymbol{k}}$. Individual wave crests propagate along $\hat{\boldsymbol{k}}$, but energy is transported in the direction of the group velocity $\boldsymbol{c}_g$ perpendicular to $\hat{\boldsymbol{k}}$, so that the envelope of the wave packet does not change in time. Reprinted from Tilgner A (2000) Oscillatory shear layers in source driven flows in an unbounded rotating fluid. *Physics of Fluids* 12: 1101–1111.

When inertial waves are reflected off a solid wall, their oscillation frequency stays constant, so that the angle between the wave vector $\boldsymbol{k}$ and the rotation axis $\hat{\boldsymbol{z}}$ is conserved (unlike the familiar situation with light or acoustic waves where the angle between the wave vector and the normal to the reflecting surface is conserved; Greenspan, 1968; Phillips, 1963). The same reflection law must also hold for internal shear layers since these can be represented as a superposition of waves. Some consequences of this unusual reflection law will be explored in **Section 8.07.2**.

A recurrent theme of the following sections is the appearance of inclined internal shear zones in rotating fluids. The term 'shear zone' is meant to encompass simple shear layers and jets, for example. Because of their omnipresence, it is worthwhile to dwell more on the reasons for their existence. It is illuminating to look at the canonical shear layer across which pressure and normal velocity are continuous, but the tangential velocity is not. This model is the standard starting point for an elementary investigation of the Kelvin–Helmholtz instability in nonrotating fluids (Landau and Lifshitz, 1987) in which the surface of discontinuity can have an arbitrary orientation in space. In a rotating system, on the contrary, the orientation of such a surface of discontinuity is not arbitrary because the Coriolis forces on both sides of the discontinuity are different and need to be balanced. Choose Cartesian coordinates x', y', and z' such that $\hat{\boldsymbol{z}}'$ is normal to the surface of discontinuity and forms the angle ϑ with the rotation axis given by $\hat{\boldsymbol{z}} = \cos\vartheta\hat{\boldsymbol{z}}' + \sin\vartheta\hat{\boldsymbol{x}}'$. Denote by $[\cdot]$ the jump experienced by the quantity in square brackets when the plane spanned by the x'- and y'-axes is crossed. From $[p] = 0$ follows $[\partial p/\partial x'] = [\partial p/\partial y'] = 0$. Together with $[u_{z'}] = 0$, the x'- and y'-components of the equation of motion [5] become

$$\frac{\partial}{\partial t}[u_{x'}] = 2\cos\vartheta\,[u_{y'}]$$

$$\frac{\partial}{\partial t}[u_{y'}] = -2\cos\vartheta\,[u_{x'}]$$

If velocities vary in time like $e^{i\omega t}$, this system of equations admits nontrivial solutions only for

$$\omega = \pm 2\cos\vartheta = \pm 2\hat{\boldsymbol{z}}\cdot\hat{\boldsymbol{z}}' \qquad [12]$$

which is identical with the condition derived in eqn [9] if we think of the shear layer as a superposition of inertial waves with wave vectors parallel to $\hat{\boldsymbol{z}}'$.

There is a third mathematical approach. It formalizes the preceding approaches and is only touched upon here because it depends on a whole body of theory on partial differential equations (see Chapters 5 and 6 in Volume 2 of Courant and Hilbert, 1968). Within this general theory, the surfaces on which discontinuities may occur are called characteristic surfaces or characteristics for short. Equation [5] is classified as a hyperbolic equation for $|\omega| < 2$, which implies that inertial waves and internal layers only exist for $|\omega| < 2$. Characteristic surfaces degenerate to lines parallel to the z-axis for $\omega = 0$. The angle between the characteristic surfaces and the rotation axis increases with ω until these surfaces are perpendicular to the z-axis for $|\omega| = 2$. Characteristic surfaces disappear for $|\omega| > 2$ because the equation of motion is then of the so-called elliptic type, which means that flows with $|\omega| > 2$ do not allow for wave propagation and instead resemble potential flows in nonrotating systems. The distinguishing features of rotating flows only appear in the frequency range $|\omega| < 2$. For instance, a disk oscillating in a rotating tank generates inertial waves if the oscillation period of the disk is at least half the rotation period of the tank. If the disk oscillates faster, a flow is set up around the disk, which is related to the potential flow around an oscillating disk in a nonrotating fluid (Reynolds, 1962a,b).

Axisymmetric internal shear layers form conical surfaces around the rotation axis. In the limit $\omega = 0$, the cones become cylinders and occur at the rim of Taylor columns. In the case $\omega = 0$, eqn [6] yields the stronger condition $\partial\boldsymbol{u}/\partial z = 0$ known as the Taylor–Proudman theorem: steady motion in the limit of the small Ekman and Rossby numbers is independent of the z-coordinate. Steady flow (e.g., around obstacles) acquires columnar structure composed of the Taylor columns aligned with the z-axis. Cylindrical, time-independent shear layers have been visualized experimentally numerous times. A few pictures exist also of oscillatory shear layers and their reflections from solid walls (Beardsley, 1970; Greenspan, 1968; McEwan, 1970; Oser, 1958).

8.07.1.4 Ekman Layers

This section looks at motions for which the nonlinear term is still negligible in the mantle frame, but we reinstate the viscous term. Starting from a solution of the inviscid equation of motion, the viscous corrections are to a first approximation confined to thin boundary layers, which accommodate the no-slip boundary conditions. These so-called Ekman layers are of a well-known type omnipresent in rotating fluids.

Boundary layers of course also appear in nonrotating flows and involve a balance between viscous stresses, pressure

gradients, and advection. In a rotating system, the Coriolis force enters into consideration, and we may deduce from dimensional analysis that it introduces an intrinsic length scale, namely, $(\nu/\omega_D)^{1/2}=E^{1/2}d$ with the definitions used in eqn [3], which in most practical circumstances is small compared with the characteristic size of the fluid volume, that is, $E^{1/2}\ll 1$ ($E\approx 10^{-15}$ in the Earth's core). This length scale determines the thickness of the boundary layers at the small Rossby numbers, that is, when advection is negligible. A peculiarity of the Ekman layers is that they usually cause a flow inside the bulk directed perpendicular to the boundaries. This phenomenon is known as the Ekman suction or Ekman pump. In time-dependent flows, the boundary layer approximation from which these conclusions are derived is not valid over the entire surface but breaks down at critical latitudes, as we shall see in the succeeding text. The radial component of velocity is much larger at critical latitudes than elsewhere on the boundary. The steep velocity gradients around critical latitudes extend in the form of internal layers or jets across the entire flow. Since we meet these layers so often throughout this chapter, it is worthwhile going through the mathematics showing that strong flows exist around critical latitudes. The section culminates in Figure 5, which shows the singularity at critical latitudes in one special case.

An elementary treatment of the Ekman layers in stationary flows can be found in many textbooks on fluid mechanics (Acheson, 1990; Kundu and Cohen, 2002). But we are mainly concerned with time-dependent flows in this chapter. A general treatment of the Ekman layers in this case is still possible but rather abstract (Greenspan, 1968). The classical procedure is a formal asymptotic expansion in powers of $E^{1/2}$. It starts with a solution of the inviscid equation and adds to this solution a correction that is significant only near the boundaries. The boundary flow is connected to the bulk flow by matched asymptotics. The boundary layer then requires a correction to the bulk flow, which in turn modifies the boundary layer at a higher order in E. More and more refined solutions are obtained iteratively. To simplify matters, we deduce here the dominant contribution to the boundary layer from a more intuitive approach. We will treat the particular example of the boundary layers of the so-called spin-over mode, which is central to precession-driven flow and which we will also meet in Section 8.07.2.

Assume that the CMB and the inner core are spherical. The inviscid equation of motion then allows the liquid core to spin about an arbitrary axis at an arbitrary angular velocity because there is no coupling between the core and the boundaries. For small but finite viscosity, the interior motion remains close to a rigid rotation. We regard the interior motion as given. Boundary layers form whose structures we are about to compute. For finite viscosity, the inner rotation needs to be maintained by some forcing. We will later see that precession is able to do so.

In the mantle frame, introduce a local coordinate system θ', φ', z' attached to the inner core boundary at colatitude θ with $\hat{\boldsymbol{z}}'$ pointing into the fluid (Figure 4). For definiteness, the equations are derived for the inner core, analogous equations after changes of signs hold at the outer boundary. The local coordinate system is actually redundant for spherical boundaries but helps generalization to other boundary shapes. The rotation of the liquid core is given by $\boldsymbol{\omega}\times\boldsymbol{r}$. We will specify $\boldsymbol{\omega}$ by $\boldsymbol{\omega}=\omega(\sin t\,\hat{\boldsymbol{x}}+\cos t\,\hat{\boldsymbol{y}})$. Note that $\boldsymbol{\omega}$ is stationary in an inertial

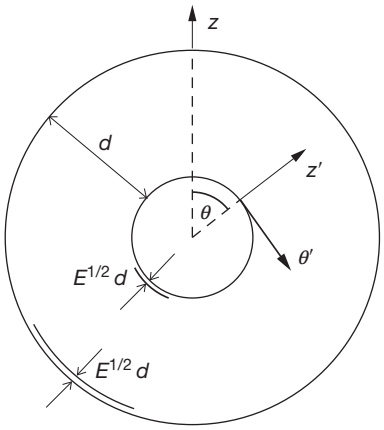

Figure 4 Definition of a local coordinate system. $\hat{\boldsymbol{z}}'$ is normal to the surface and is directed radially for a spherical core. Boundary layers of thickness $E^{1/2}d$ form, where $d=r_o-r_i$ is the gap size of the shell.

frame of reference. This solution obviously violates the no-slip boundary conditions.

Let us restrict ourselves to situations in which the Rossby number is small so that the advection term can be dropped from the momentum eqn [3]. We now look for a correction $\boldsymbol{v}$ such that $\boldsymbol{u}=\boldsymbol{\omega}\times\boldsymbol{r}+\boldsymbol{v}$ satisfies the no-slip boundary conditions, such that $\boldsymbol{v}$ has sizable magnitude only close to the boundaries and such that $\boldsymbol{v}$ is itself a solution of the linearized equation of motion

$$\frac{\partial}{\partial t}\boldsymbol{v}+2\hat{\boldsymbol{z}}\times\boldsymbol{v}=E\nabla^2\boldsymbol{v}-\nabla\tilde{p} \qquad [13]$$

where $\nabla\tilde{p}$ is a pressure gradient, which will also be confined to the boundary layer. We anticipate from the aforementioned dimensional arguments that the thickness of the boundary layer is $\mathcal{O}(E^{1/2})$. In that layer, the variation of velocity with z' is much more rapid than with θ' or φ'. The diffusion term $E\nabla^2\boldsymbol{v}$ then simplifies and becomes $E\partial^2\boldsymbol{v}/\partial z'^2$.

The condition $\nabla\cdot\boldsymbol{v}=0$ implies (see eqn [20]) that $\partial v_{z'}/\partial z'$ (which for a boundary layer of thickness $E^{1/2}$ is in order of magnitude $E^{-1/2}v_{z'}$) is equal to derivatives of $v_{\theta'}$ and $v_{\varphi'}$ with respect to the horizontal coordinates (which are in order of magnitude $v_{\theta'}$ or $v_{\varphi'}$) so that $v_{z'}=\mathcal{O}(E^{1/2}v_{\theta'},E^{1/2}v_{\varphi'})$ and $v_{z'}$ is negligible compared with $v_{\theta'}$ and $v_{\varphi'}$ in the Coriolis term, which becomes $2\boldsymbol{\Omega}\times\boldsymbol{v}\approx 2\cos\theta v_{\varphi'}\hat{\boldsymbol{\theta}}'+2\cos\theta v_{\theta'}\hat{\boldsymbol{\varphi}}'-2\sin\theta v_{\varphi'}\hat{\boldsymbol{z}}'$. Finally, it is useful to introduce the variable $\zeta=E^{-1/2}z'$ so that the balance between the viscous and Coriolis terms in the boundary layers becomes apparent. We now find from eqn [13] using $E\partial^2/\partial z^2=\partial^2/\partial\zeta^2$

$$\begin{aligned}
\frac{\partial}{\partial t}v_{\theta'}-2\cos\theta v_{\varphi'}&=\frac{\partial^2}{\partial\zeta^2}v_{\theta'}+\frac{1}{r_i}\frac{\partial}{\partial\theta'}\tilde{p}\\
\frac{\partial}{\partial t}v_{\varphi'}+2\cos\theta v_{\theta'}&=\frac{\partial^2}{\partial\zeta^2}v_{\varphi'}+\frac{1}{r_i\sin\theta}\frac{\partial}{\partial\varphi'}\tilde{p}\\
\frac{\partial}{\partial t}v_{z'}-2\sin\theta v_{\varphi'}&=\frac{\partial^2}{\partial\zeta^2}v_{z'}+E^{-1/2}\frac{\partial}{\partial\zeta}\tilde{p}
\end{aligned} \qquad [14]$$

together with $\nabla\cdot\boldsymbol{v}=0$. The boundary layer flow is driven by the boundary conditions that $\boldsymbol{v}=-\boldsymbol{\omega}\times\boldsymbol{r}$ for $\zeta=0$ (so that the total velocity is zero on the boundary) and $\boldsymbol{v}=0$ for $\zeta\to\infty$ (in order to recover the inviscid solution at the edge of the boundary layer). This implies $\tilde{p}=$ constant for $\zeta\to\infty$ so that we may

choose $\tilde{p}=0$ for $\zeta\to\infty$, and the z'-component of eqn [14] shows that $\tilde{p}=\mathcal{O}(E^{1/2})$. The pressure can therefore be neglected in the θ'- and φ'-components of the momentum equation, and we arrive at

$$\frac{\partial}{\partial t}\begin{pmatrix}v_{\theta'}\\ v_{\varphi'}\end{pmatrix}+2\cos\theta\begin{pmatrix}-v_{\varphi'}\\ v_{\theta'}\end{pmatrix}=\frac{\partial^2}{\partial\zeta^2}\begin{pmatrix}v_{\theta'}\\ v_{\varphi'}\end{pmatrix} \qquad [15]$$

More explicitly, the boundary condition at $\zeta=0$ is

$$\begin{aligned}v_{\theta'}(\zeta=0)&=-\frac{1}{2}r_i\omega\left(e^{it}e^{i\varphi}+\text{c.c.}\right)\\ v_{\varphi'}(\zeta=0)&=-\frac{1}{2}r_i\omega\cos\theta\left(ie^{it}e^{i\varphi}+\text{c.c.}\right)\end{aligned} \qquad [16]$$

where c.c. stands for complex conjugate. Equation [15] is solved by the ansatz $v_{\theta',\varphi'}=V_{\theta',\varphi'}e^{it}+\text{c.c.}$ and $v_\pm=V_{\theta'}\pm iV_{\varphi'}$ leading to

$$iv_\pm\pm i2\cos\theta v_\pm=\frac{\partial^2}{\partial\zeta^2}v_\pm \qquad [17]$$

These equations admit solutions of the form $v_\pm=v_{\pm0}e^{-\alpha_\pm\zeta}$ with

$$\alpha_\pm=\sqrt{i(1\pm2\cos\theta)} \qquad [18]$$

where the square root is defined such that $\text{Re}\{\alpha_\pm\}>0$ and the boundary condition at infinity is fulfilled automatically. The boundary conditions at $\zeta=0$ determine the final solution:

$$\begin{aligned}v_{\theta'}&=-\frac{1}{2}r_i\left[(1-\cos\theta)\text{Re}\left\{e^{-\alpha_+\zeta}e^{i(\varphi+t)}\right\}\right.\\ &\quad\left.+(1+\cos\theta)\text{Re}\left\{e^{-\alpha_-\zeta}e^{i(\varphi+t)}\right\}\right]\\ v_{\varphi'}&=-\frac{1}{2}r_i\left[(1-\cos\theta)\text{Im}\left\{e^{-\alpha_+\zeta}e^{i(\varphi+t)}\right\}\right.\\ &\quad\left.-(1+\cos\theta)\text{Im}\left\{e^{-\alpha_-\zeta}e^{i(\varphi+t)}\right\}\right]\end{aligned} \qquad [19]$$

$v_{z'}$ is determined by the requirement that $\nabla\cdot\boldsymbol{v}=0$. Since $r_i\gg E^{1/2}d$, the radial coordinate does not vary much across the boundary layer and the representation of $\nabla\cdot\boldsymbol{v}$ in spherical coordinates simplifies to yield

$$\frac{\partial}{\partial z'}v_{z'}=-\frac{1}{r_i\sin\theta}\left(\frac{\partial}{\partial\theta}\sin\theta v_{\theta'}+\frac{\partial}{\partial\varphi}v_{\varphi'}\right) \qquad [20]$$

This equation together with the boundary condition $v_{z'}(z'=0)=0$ fully specifies $v_{z'}$, which will in general be different from zero at the edge of the boundary layer at $\zeta\to\infty$. The nonzero $v_{z'}$ constitutes precisely the Ekman suction and is given by the integral of the right-hand side of eqn [20]:

$$\begin{aligned}E^{-1/2}v_{z'}(\zeta\to\infty)&=\frac{1-\cos2\theta}{2\sin\theta}\text{Re}\left\{\left(\frac{1}{\alpha_+}-\frac{1}{\alpha_-}\right)e^{i(\varphi+t)}\right\}\\ &+\sin\theta\frac{1-\cos\theta}{2}\text{Re}\left\{\frac{i}{\alpha_+^3}e^{i(\varphi+t)}\right\}-\sin\theta\frac{1+\cos\theta}{2}\text{Re}\left\{\frac{i}{\alpha_-^3}e^{i(\varphi+t)}\right\}\end{aligned} \qquad [21]$$

There is a singularity for $1\pm2\cos\theta=0$ where either α_+ or α_- vanishes: $v_{z'}$ diverges at the critical latitudes of $\pm30^\circ$ ($\theta=60$ or 120°). $E^{-1/2}v_{r'}$, which is equal to $E^{-1/2}v_{z'}$ in spherical geometry, is plotted in Figure 5 against θ in the planes $\varphi+t=0$ and $\varphi+t=\pi/2$. The first plane contains $\boldsymbol{\omega}$, whereas the second one is perpendicular to $\boldsymbol{\omega}$.

The singularity is of course not physical. The real boundary layer near the critical latitudes varies rapidly in both the z' and the θ' directions and is therefore much more difficult to treat. A complete theory is still lacking, but Roberts and Stewartson (1963) had shown that one obtains a self-consistent scaling for a boundary layer of thickness $\mathcal{O}(E^{2/5})$ with a lateral extent of $\mathcal{O}(E^{1/5})$ in the θ' direction. The singularity then disappears, but $v_{z'}$ near critical latitudes is still much larger than the $\mathcal{O}(E^{1/2})$ Ekman suction found at a distance from the critical latitudes.

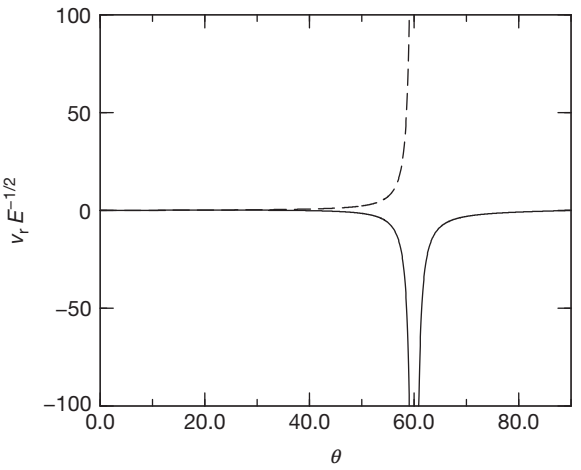

Figure 5 $v_rE^{-1/2}$ at the edge of the inner boundary layer of a spherical shell in the planes $\varphi+t=\pi/2$ (continuous) and $\varphi+t=0$ (dashed) as a function of θ in degrees. Both curves are identical for $\theta>60^\circ$. At the outer boundary, v_r has the opposite sign.

The form of v_r in Figure 5 suggests that a salient feature of the interior correction will be jets (in the plane $\varphi+t=\pi/2$) or shear layers (in the plane $\varphi+t=0$) emanating from critical latitudes. It turns out that these shear zones traverse the entire fluid volume. v_r is time-dependent in the rotating frame of reference, and the shear layer will form an angle with the rotation axis as given by eqn [12]. These shear layers will appear in both experiments and numerical simulations later in this chapter.

The calculation in this section was made for the case of differential rotation, but similar boundary layer effects must occur for any other perturbation of a rotating fluid. Boundary layers of the Ekman type rely on a balance between the Coriolis and viscous forces. The Ekman layers can be substituted with the type of shear layers, which can also exist in the bulk of a rotating fluid at places where the characteristic surfaces are tangential to the boundaries. In the case studied in this section, the inviscid solution depends on time as e^{it} in the mantle frame. Characteristic surfaces then form an angle of 30° with the rotation axis ($\theta=60^\circ$ in eqn [12]) and are tangent to spherical boundaries at latitudes of $\pm30^\circ$, precisely where the Ekman boundary layers break down. The same breakdown occurs for any other time-dependent flow at critical latitudes determined by the frequency of the flow.

8.07.2 Inertial Oscillations in Spherical Shells

Section 8.07.1.3 has shown that plane waves can propagate in a rotating unbounded fluid. In a finite volume, inertial oscillations still occur, though not in the form of plane waves. An

investigation of inertial modes in general is of interest because these oscillations are a useful starting point for the stability analysis of precession or tidally driven flows (Kerswell, 1993b) and in some cases of thermal convection (Zhang, 1993, 1995). It has also been claimed that such modes have been detected with superconducting gravimeters following strong earthquakes (Aldridge and Lumb, 1975; Melchior and Ducarme, 1986), but see Zürn, Richter, Rydelek, and Neuberg (1987) for a critical comment.

More generally, we want to be able to handle arbitrary small perturbations of the rotating core. If the perturbation is small, we can use linearized equations of motion and proceed as for any linear oscillator: The response of the linear system is a superposition of eigenmodes of the system. If we know the eigenmodes, we can easily compute the effect of arbitrary forcings. This is the main motivation for studying inertial modes.

8.07.2.1 The Mathematical Problem

Consider a uniformly rotating body of fluid. If this motion is subject to small perturbations, the nonlinear advection term can be dropped from the Navier–Stokes equation in the rotating frame, which becomes in nondimensional form

$$\frac{\partial}{\partial t}\boldsymbol{u}+2\hat{\boldsymbol{z}}\times\boldsymbol{u}=-\nabla p+E\nabla^2\boldsymbol{u}\ ,\ \nabla\cdot\boldsymbol{u}=0 \qquad [22]$$

together with the boundary condition that $\boldsymbol{u}=0$ on the boundaries. Searching for eigenmodes, we look for solutions in the form $\boldsymbol{u}(r,t)=e^{i\omega t}\boldsymbol{v}(r)$, which leads to

$$i\omega\boldsymbol{v}+2\hat{\boldsymbol{z}}\times\boldsymbol{v}=-\nabla\Phi+E\nabla^2\boldsymbol{v},\quad \nabla\cdot\boldsymbol{v}=0 \qquad [23]$$

with $\boldsymbol{v}=0$ on the boundaries and $p(\boldsymbol{r},t)=e^{i\omega t}\Phi(\boldsymbol{r})$. Equation [23] constitutes a mathematically well-posed eigenvalue problem. The eigenvalues ω have an imaginary part because of viscous damping.

We are mostly interested in the very small Ekman numbers so that we are tempted to put $E=0$ in eqn [23]. The order of the PDE then changes and we have to relax the boundary conditions. We can only impose that the velocity component normal to the boundaries vanishes in an ideal fluid.

Following general fluid dynamic experience, we could naively expect that the solutions for E strictly zero and E different from zero but small are very similar except for thin boundary layers next to solid boundaries. It turns out that in a rotating fluid, ignoring the viscous term leads to great difficulties. In mathematical terms, the problem for $E=0$, even with the relaxed boundary conditions, is ill-posed and in general does not have smooth solutions. The origin of the mathematical problem lies in an overspecification of the boundary conditions. Smooth solutions can only exist for particular shapes of the boundary. For a general treatment of hyperbolic partial differential equations and their admissible boundary conditions, see in particular Courant and Hilbert (1968).

A full sphere (as opposed to a spherical shell) is an example of a geometry, which leads to smooth eigenfunctions. Simple methods for evaluating the eigenvalues and eigenmodes are presented in Greenspan (1968). More recently, even explicit formulas have been found for this geometry (Zhang et al., 2001, 2004). The complete spectrum of eigenfrequencies is known for a full sphere but not for a spherical shell. Viscous effects can be included to the lowest order by computing a boundary layer structure as in Section 8.07.1.4 together with its effects on the interior flow (see Greenspan, 1968). It is not even necessary to include details of the boundary layer structure at critical latitudes. The area around critical latitudes in which the boundary layer differs from a standard Ekman layer and the in- or outflow from the boundary layer scale with E in a way such that their contribution to the total dissipation vanishes for $E\to 0$. Formulas obtained with these approximations are in excellent agreement with experiments (Aldridge and Toomre, 1969) and simulations (Hollerbach and Kerswell, 1995).

The situation is entirely different for a spherical shell. The only smooth inviscid eigenmodes known for this geometry are purely toroidal, that is, they have zero radial velocity so that they are identical with modes of a full sphere. The most important mode of this class is the spin-over mode or tilt-over mode. Imagine a rotating spherical container full of fluid rotating about the same axis as the container. The spin-over mode is excited by impulsively changing the axis of rotation of the container. This operation may be viewed as an elementary step of precession. An ideal fluid is completely unaffected by the motion of the spherical boundaries, so that the fluid (viewed from an inertial frame of reference) continues rotating about its initial axis after the axis of the container has been tipped over. Viewed from a frame of reference attached to the boundaries, however, the axis of rotation of the fluid rotates about the axis of the container with a period equal to the rotation period of the container. With the choice of units leading to eqn [23], this period is 2π. The fluid motion viewed from the mantle frame can be written as being proportional to $\omega_a(\sin t\hat{\boldsymbol{x}}+\cos t\hat{\boldsymbol{y}})\times\boldsymbol{r}+\omega_z\hat{\boldsymbol{z}}\times\boldsymbol{r}$ with arbitrary ω_a and ω_z. The last term is time-independent and an obvious solution of the equation of motion. The bracket can be transformed to $(\sin t\hat{\boldsymbol{x}}+\cos t\hat{\boldsymbol{y}})=e^{i(\varphi+t)}(r/2)(\hat{\boldsymbol{\theta}}+i\cos\theta\hat{\boldsymbol{\varphi}})+\text{c.c.}=\boldsymbol{v}_{so}+\text{c.c.}$ where c.c. denotes complex conjugate. $\boldsymbol{v}_{so}$ is the velocity field of the spin-over mode. The spin-over mode is an inertial oscillation with angular frequency equal to 1. Indeed, it is straightforward to verify that $(\partial/\partial t)\boldsymbol{v}_{so}+2\hat{\boldsymbol{z}}\times\boldsymbol{v}_{so}=\nabla\left(e^{i(\varphi+t)}\frac{i}{2}r^2\sin\theta\cos\theta\right)$, so that v_{so} is a solution of eqn [23] for the eigenfrequency $\omega=1$.

In the two following sections, we will see how the difficulties of the inviscid problem transpire into the solutions of the linearized Navier–Stokes equation.

8.07.2.2 Ray Geometry

We have seen in Section 8.07.1.3 that shear layers can exist in rotating fluids. We expect to find some of those in geometries where no smooth eigenfunctions exist. If we allow for no-slip boundary conditions, we more precisely expect such layers to emanate from critical latitudes. What happens at locations where such a layer meets another part of the boundary?

We have seen in Section 8.07.1.3 that inertial waves of the wave vector $\boldsymbol{k}$ have the angular frequency $\omega=\pm 2|\boldsymbol{k}\cdot\hat{\boldsymbol{z}}|/|\boldsymbol{k}|$, independent of $|\boldsymbol{k}|$. The group velocity is perpendicular to the phase velocity and directed along the characteristics of eqn [22] for $E=0$. The characteristics form the angle ϑ_r with the z-axis such that $\tan\vartheta_r=\pm(4/\omega^2-1)^{-1/2}$. Waves excited at the angular frequency ω can therefore superpose to form rays inclined at angle ϑ_r, and every shear layer may be represented as a

superposition of inertial waves. These waves reflect at boundaries, so that rays or shear layers must do the same. The reflection is very peculiar. Because ω fixes the inclination with respect to the rotation axis and because an oscillation frequency is not modified by a reflection, rays are reflected such that the angle enclosed with the rotation axis remains unchanged.

What happens after multiple reflections? Closed cycles exist at some frequencies in spherical shells. The most important example for us is the case $\omega = 1$, which is relevant for the spin-over mode. Figure 6 shows for a shell with $\eta = r_i/r_o = 0.35$ three independent closed cycles. They all start from critical latitudes. Two rays can emanate from the inner core and one from the CMB. All three lead to closed cycles.

Figure 7 shows numerical simulations of the spin-over mode in a spherical shell with a very small inner core ($r_i/r_o = 0.01$). The closed cycle connected with the CMB at critical latitude is very prominent. Additional features appear in a shell of the Earth-like geometry ($r_i/r_o = 0.35$) (see Figure 8). The ray tangential to the inner core gives rise to a pattern that is clearly recognizable in both Figure 6 and the simulations. On the other hand, the other ray that could come from the critical latitude of the inner core does not show in the numerical results. It is not known at present why one is excited and the other is not. Another view at the layers caused by the inner core is offered by Figure 21.

More interestingly, the unusual reflection law opens the possibility for rays to converge after multiple reflections to caustics, limit cycles, or attractors, examples of which are shown in Figure 9. This process is demonstrated in Figure 10.

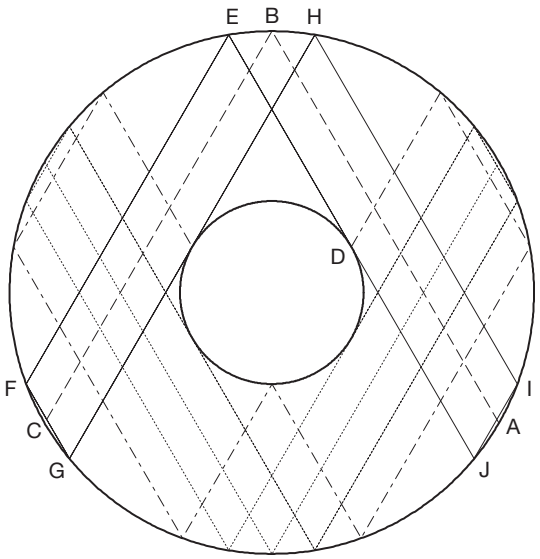

Figure 6 Ray patterns in a spherical shell with $r_i/r_o = 0.35$ for $\omega = 1$. The rotation axis is vertical in this and the following pictures showing meridional cross sections. All rays shown start from critical latitude. The solid line (DEFGHIJ) starts tangentially from the inner core, and the dashed line (ABC) starts from the outer boundary. The dotted line results from the previous two after reflection about the equatorial plane. The dot-dashed line runs along the second characteristic going through the northern critical latitude on the inner core. Its symmetrical counterpart is not included in the figure.

A ray has been started in poleward direction from the inner sphere at northern critical latitude and reflected 1500 times on the boundaries of a spherical shell with $r_i/r_o = 0.35$. For the next 500 reflections, a dot is placed in Figure 10 at the colatitude θ at

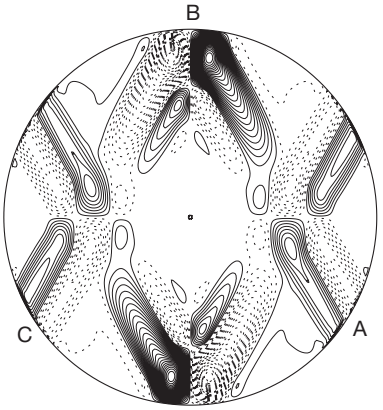

Figure 7 Radial velocity of the spin-over mode for $E = 10^{-6}$ in the meridional plane $\varphi + t = 0$ in the notation of 1.4. In this and all following contour plots, continuous and dashed contour lines indicate positive and negative values of the plotted quantity, respectively. The letters label the same points as in Figure 6.

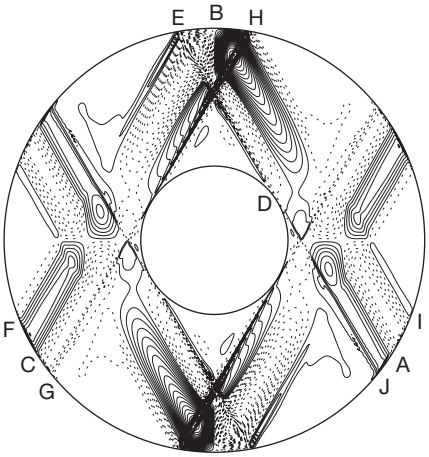

Figure 8 Radial velocity of the spin-over mode in a spherical shell for the same Ekman number and in the same meridional plane as in Figure 7. The letters label the same points as in Figure 6.

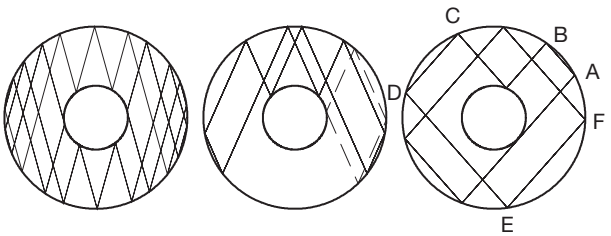

Figure 9 Ray attractors in a shell with $r_i/r_o = 0.35$ for $\omega = 0.532$ (left), $\omega = 0.81$ (center, the dashed line indicates a second attractor), and $\omega = 1.322$ (right). Adapted from Tilgner A (1999) Driven inertial oscillations in spherical shells. *Physical Review E* 59: 1789–1794.

which a reflection off the outer boundary occurs. This procedure is repeated for different ω with a step size $\Delta\omega = 0.002$. For some ω, the ray path covers more or less the entire shell, whereas for the other ω, the ray reaches a periodic orbit.

Note that the shear layer pattern of the spin-over mode in Figure 6 is a closed circuit but not an attractor. Rays starting at nearby critical latitudes are not focused after multiple reflections onto this closed path.

Similar considerations apply to gravity waves in stably stratified fluids. They have the same dispersion relation as inertial waves and can thus also be found on attractors (Maas and Lam, 1995; Maas et al., 1997).

8.07.2.3 Numerical Simulations

Apart from simulations of the spin-over mode, there are also numerical solutions for axisymmetric modes, which are not toroidal. These modes offer a vast terrain for exploration in as far as properties of internal shear layers are concerned. These simulations either directly solve an eigenvalue problem or reproduce the excitation mechanism used in the experiments by Aldridge and Toomre (1969): the rotation rate of a spherical container is modulated sinusoidally in time. The Ekman pumps at the boundary then act at the frequency of the modulation and excite eigenmodes at that frequency. In mathematical terms, consider a spherical shell of gap d filled with fluid of viscosity ν, which rotates about the z-axis with angular velocity $\Omega_0 + \Omega_1 \cos\tilde{\omega}t$. Using for units of time and length $1/\Omega_0$ and d, respectively, one obtains in the frame rotating at the rate Ω_0 about the z-axis eqn [22] as the nondimensional equation of motion. The Ekman number is now defined by $E = \nu/\Omega_0 d^2$. The no-slip boundary conditions require for the fluid velocity $\boldsymbol{u}$ that $\boldsymbol{u} = (\Omega_1/\Omega_0)\cos(\omega t)\,\hat{\boldsymbol{z}} \times \boldsymbol{r}$ at the inner and outer boundaries of radii r_i and r_o with $r_o - r_i = 1$ and $\omega = \tilde{\omega}/\Omega_0$. Ω_1/Ω_0 can be arbitrarily set equal to 1. Only the axisymmetric flow is excited by the driving mechanism considered here so that temporal and spatial dependences are separated by the ansatz $\boldsymbol{u} = \mathrm{Re}\{\boldsymbol{v}(r,\theta)e^{i\omega t}\}$, where Re denotes the real part.

Figure 11 presents a study of the Ekman number dependence at $\omega = 1.32$. The internal layers narrow with decreasing E but retain a finite width so that a perfect agreement with the geometric ray construction is not expected. Indeed, the simple pattern of internal layers at $\omega = 1.32$ (Figure 11) corresponds well to the attractor at $\omega = 1.322$ (Figure 9) but not to the one at exactly $\omega = 1.32$.

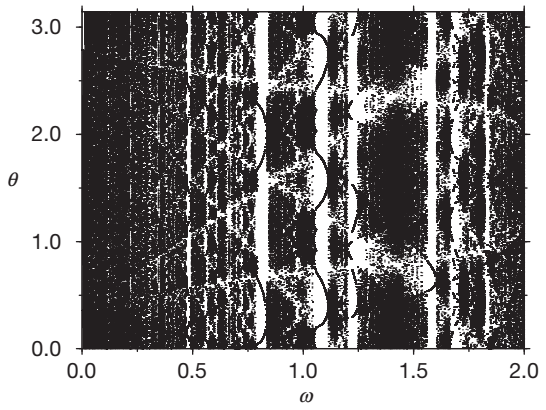

Figure 10 Ray reflections on the outer sphere at colatitude θ as a function of ω.

Many open questions remain concerning the behavior in the limit $E \to 0$. An ongoing research attempts to establish a relation between the attractors of inviscid fluids to the spectrum of eigenfrequencies of flows with the small but finite Ekman numbers (Rieutord et al., 2001). Another task for future research is to determine the stability properties of the shear layers.

Finally, note another important point about the role of critical latitudes. So far, we considered them to be special because the Ekman layers break down at these locations. This is the only mechanism available to generate an internal shear layer in the spin-over mode of a full sphere. But it turns out that for general modes or even for the spin-over mode at the inner core of a spherical shell, internal shear layers preferentially form at critical latitudes even in inviscid fluids. Purely geometric reasons, rather than viscous effects, already single out the critical latitudes. This point has been studied in detail by Stewartson and Rickard (1969) and Rieutord et al. (2001) for discontinuities tangential to the inner sphere in inviscid inertial modes of a spherical shell.

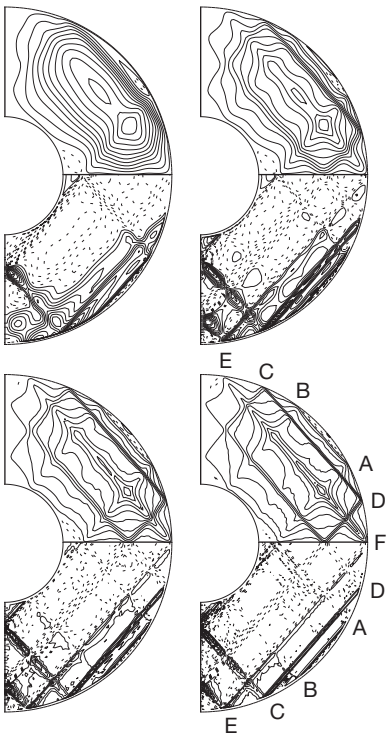

Figure 11 Flow patterns in a shell with $r_i/r_o = 0.35$ driven at $\omega = 1.32$ for the Ekman numbers 10^{-5} (top left), 10^{-6} (top right), 10^{-7} (bottom left), and 10^{-8} (bottom right). The upper half of each panel shows meridional streamlines, and the lower half azimuthal velocity u_φ. The Ekman layers have been removed from the plots of u_φ for clarity. Streamlines are shown at a time at which the instantaneous poloidal energy is maximum; u_φ is shown a quarter cycle of the driving force earlier. The rotation axis is vertical. A few points are labeled as in Figure 9. The remaining points of the attractor nearly coincide with the labeled ones. Adapted from Tilgner A (1999) Driven inertial oscillations in spherical shells. *Physical Review E* 59: 1789–1794.

8.07.3 Precession

In this section, we consider the precessional motion of the mantle as given and ask for the response of the liquid core. In situations where this matters, we will assume that the CMB and the inner core rotate at identical angular velocities about identical axes. The relevant equations of motion are [3] and [4].

8.07.3.1 Solutions of the Inviscid Equation of Motion

Without precession, the fluid settles to a motion of uniform rotation in unison with the rotation of the container. Such a flow has constant vorticity. When the container starts to precess, the liquid tends to maintain its initial motion due to inertia. Viscous and pressure torques exerted by the boundaries on the fluid act to align the vorticity of the flow with the rotation axis of the mantle. As the mantle's axis is continuously moving in inertial space due to precession, this alignment is never quite reached. Let us assume that the flow maintains a spatially uniform but time-dependent vorticity throughout its evolution. Uniform vorticity flows are indeed solutions of the inviscid equation of motion and are commonly called the Poincaré flows. These solutions are derived using the Lagrangian formalism in Poincaré (1910) (parts of which are translated into English in the final pages of the book by Lamb, 1932). A more pedestrian approach is used here (Sloudsky, 1895; Zharkov et al., 1996).

Consider flows that depend linearly on the Cartesian coordinates x, y, and z. To make such a flow fit into an ellipsoid of revolution determined by $(x/a)^2+(y/a)^2+(z/c)^2=1$, stretch the coordinates to transform the ellipsoid into a sphere, assume that the flow is a solid body rotation in that sphere, and transform the coordinates back. In symbols, the stretched velocity vector (u_x/a, u_y/a, and u_z/c) is given by the vector product of any vector $(\tilde{\omega}_x, \tilde{\omega}_y, \tilde{\omega}_z)$ with (x/a, y/a, and z/c):

$$\boldsymbol{u}=\left(\tilde{\omega}_y z\frac{a}{c}-\tilde{\omega}_z y,\ \tilde{\omega}_z x-\tilde{\omega}_x z\frac{a}{c},\ \tilde{\omega}_x y\frac{c}{a}-\tilde{\omega}_y x\frac{c}{a}\right) \qquad [24]$$

It is easy to verify that $\boldsymbol{u}$ is solenoidal and does not penetrate the CMB (or an inner core if it has the same ellipticity as the CMB), but it satisfies neither no-slip nor stress-free boundary conditions and can therefore only be used as a solution of the inviscid Euler equation. These flows have spatially constant vorticity, and the rotation of the fluid $\boldsymbol{\omega}_F$ is given by

$$\boldsymbol{\omega}_F=\frac{1}{2}\nabla\times\boldsymbol{u}=\frac{1}{2}\left(\left(\frac{a}{c}+\frac{c}{a}\right)\tilde{\omega}_x,\left(\frac{a}{c}+\frac{c}{a}\right)\tilde{\omega}_y,\ 2\tilde{\omega}_z\right) \qquad [25]$$

Since the ellipsoid is assumed symmetrical about the z-axis, we are free to choose a coordinate system such that $\Omega_y=0$. The curl of the nonlinear term in the Navier–Stokes equation becomes

$$\begin{aligned}\nabla\times[(\nabla\times\boldsymbol{u})\times\boldsymbol{u}]&=-[(\nabla\times\boldsymbol{u})\cdot\nabla]\boldsymbol{u}\\&=-\left(\tilde{\omega}_z\tilde{\omega}_y\left(\frac{a}{c}-\frac{c}{a}\right),\ \tilde{\omega}_z\tilde{\omega}_x\left(\frac{c}{a}-\frac{a}{c}\right),\ 0\right)\end{aligned} \qquad [26]$$

and the Coriolis term can also be expressed in terms of $\tilde{\omega}_x$, $\tilde{\omega}_y$, and $\tilde{\omega}_z$. Inserting these expressions into eqn [4] with E set to zero and eliminating the $\tilde{\omega}_x$, $\tilde{\omega}_y$, and $\tilde{\omega}_z$ in favor of $\boldsymbol{\omega}_F$ yields the time evolution equation for $\boldsymbol{\omega}_F$:

$$\begin{aligned}\frac{\partial}{\partial t}\omega_{Fx}-\frac{a^2-c^2}{a^2+c^2}\omega_{Fz}\omega_{Fy}-\frac{2a^2}{a^2+c^2}\omega_{Fy}\Omega_z&=0\\ \frac{\partial}{\partial t}\omega_{Fy}+\frac{a^2-c^2}{a^2+c^2}\omega_{Fz}\omega_{Fx}-\omega_{Fz}\Omega_x+\frac{2a^2}{a^2+c^2}\omega_{Fx}\Omega_z&=0\\ \frac{\partial}{\partial t}\omega_{Fz}+\frac{2c^2}{a^2+c^2}\omega_{Fy}\Omega_x&=0\end{aligned} \qquad [27]$$

Assume that precession is started at $t=0$ from a state of uniform rotation. At early times, $\omega_{Fz}\approx 1$ and therefore $\omega_{Fx},\omega_{Fy}=\mathcal{O}(\Omega)$, so that the z-component of eqn [27] yields more precisely $\omega_{Fz}=1-\mathcal{O}(\Omega^2)$.

Let us now consider on the contrary the steady case reached for $t\to\infty$. The z-component requires for $(\partial/\partial t)\boldsymbol{\omega}_F=0$ that $\omega_{Fy}=0$ ($\Omega_x=0$ is a trivial case of no precession at all). This means that $\hat{\boldsymbol{z}}$, Ω and $\boldsymbol{\omega}_F$ all lie in the same plane. The x-component of eqn [27] is thus automatically fulfilled, and the y-component can be rewritten as

$$\omega_{Fx}\left(\frac{a^2-c^2}{a^2+c^2}\omega_{Fz}+\frac{2a^2}{a^2+c^2}\Omega_z\right)=\omega_{Fz}\Omega_x \qquad [28]$$

For any ω_{Fz} different from $\Omega_z 2a^2/(c^2-a^2)$, an ω_{Fx} can be found such that the resulting flow satisfies the Euler equation, nonlinear term included. Viscous boundary layers are necessary in order to select a solution. It is however plausible from physical intuition (and it is confirmed in the succeeding text by solutions of the full Navier–Stokes equation) that ω_{Fz} stays on the order $1-\mathcal{O}(\Omega^2)$ during the evolution from the initial to the final steady state because that state departs little from the initial motion undisturbed by precession. As an alternative argument, it is plausible that ω_{Fz} is the maximum for $\Omega=0$ because both prograde precession and retrograde precession tilt the rotation axis away from its initial position. This again requires $\omega_{Fz}=1-\mathcal{O}(\Omega^2)$. With that assumption, ω_{Fx} can be computed to first order in Ω by setting $\omega_{Fz}=1$ in eqn [28].

Equations [27] and [28] can be expressed in a coordinate-independent form sometimes perceived as more elegant (Malkus, 1971):

$$\boldsymbol{\omega}_F=(\boldsymbol{\omega}_F\hat{\boldsymbol{z}})\hat{\boldsymbol{z}}-\frac{(\boldsymbol{\omega}_F\hat{\boldsymbol{z}})(2+\eta)}{(\boldsymbol{\omega}_F\hat{\boldsymbol{z}})\eta+2(1+\eta)(\Omega\hat{\boldsymbol{z}})}(\Omega\times\hat{\boldsymbol{z}})\times\hat{\boldsymbol{z}} \qquad [29]$$

with $\eta=a^2/c^2-1$. The full solution [24] is the solid body rotation plus a potential flow that is necessary to accommodate the boundary condition:

$$\boldsymbol{u}=\boldsymbol{\omega}_F\times\boldsymbol{r}+\nabla\phi \qquad [30]$$

$$\phi=\frac{-(\boldsymbol{\omega}_F\hat{\boldsymbol{z}})\eta}{(\boldsymbol{\omega}_F\hat{\boldsymbol{z}})\eta+2(1+\eta)(\boldsymbol{\Omega}\hat{\boldsymbol{z}})}(\boldsymbol{\Omega}\times\hat{\boldsymbol{z}})\cdot\boldsymbol{r}(\hat{\boldsymbol{z}}\cdot\boldsymbol{r}) \qquad [31]$$

Figure 12 summarizes the main geometric properties of the Poincaré solution: streamlines lie on ellipsoidal surfaces defined by $(x/a)^2+(y/a)^2+(z/c)^2=$constant. In addition, streamlines are confined to planes perpendicular to $(c\tilde{\omega}_x, c\tilde{\omega}_y, a\tilde{\omega}_z)$, which is different from $\boldsymbol{\omega}_F$. Streamlines are therefore ellipses with identical ellipticities lying in these planes. The normal to these planes is also different from the line running through the centers of the ellipses.

The application to the Earth's parameters ($\Omega_z=\cos 23.5°/(26000\cdot 365)$, $\Omega_x=\sin 23.5°/(26000\cdot 365)$, $c/a=399/400$) of eqn [28] with ω_{Fz} set to 1 leads to $\omega_{Fx}=1.7\times 10^{-5}$. The angle between the rotation axes of the mantle and the core

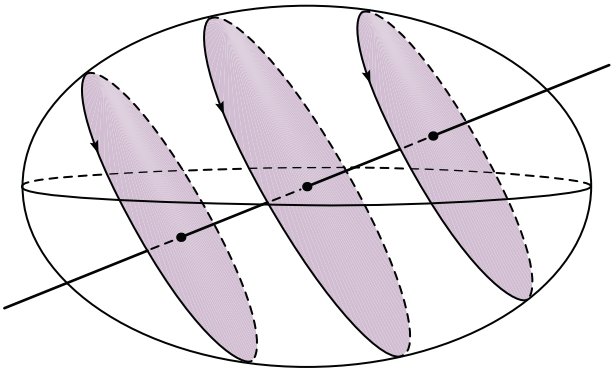

Figure 12 Sketch of the Poincaré flow. Three streamlines are shown together with the normal to the planes to which streamlines are confined.

is therefore 1.7×10^{-5} rad according to eqn [28]. This simple differential rotation leads to rather complicated particle paths of core fluid relative to the mantle (Vanyo, 2004).

8.07.3.2 Viscous Effects

We have seen in the previous section that the inviscid equation of motion does not uniquely determine a solution. If viscosity is taken into account, one needs to find solutions that satisfy the no-slip boundary conditions. The first analytic attempts to include viscous effects represented the full solution as a Poincaré solution modified near the boundaries by a viscous boundary layer (Roberts and Stewartson, 1965; Stewartson and Roberts, 1963). It becomes apparent within this approach that the boundary layers at critical latitudes differ from the viscous layers found elsewhere on the boundary, as was first noticed in Bondi and Lyttleton (1953). A different analysis that is not a perturbation series starting from the Poincaré solution has recently been presented (Zhang et al., 2010). In a linear theory that assumes a zero Rossby number and a small Ekman number, a particular orientation of the Poincaré flow is selected.

Busse (1968) extended the previous theory by including nonlinear effects and determined the flow from an expansion in the Ekman and Rossby numbers. The nonlinear effects introduce two novelties: First, the critical latitudes at which the Ekman layers break down now appear at angles of 60° with respect to the rotation axis of the fluid, not the axis of the container. Second, modifications of the Poincaré solution in the interior of the fluid in the form of a differential rotation appear. This correction is a second-order effect in the sense that its amplitude is proportional to the square of the precession rate. Crucially, however, the correction contains a singularity in the limit of the zero Ekman number: in a spherical container of radius 1, it diverges at a distance cos 30° from the rotation axis of the fluid. One therefore does not recover the Poincaré solution from the full Navier–Stokes equation for an Ekman number tending to zero. This effect originates in a nonlinear interaction within the boundary layer itself (Greenspan, 1969).

The divergence found in the theory has its counterpart in the real system in the form of a cylindrical shear layer coaxial with the rotation axis of the fluid. Experiments have revealed a shear layer at the location predicted by theory and also additional weaker layers (see **Section 8.07.3.3**).

A very simple model introduced by Vanyo and Likins (1972) illustrates how viscous forces select a particular solution. Assume for simplicity that the boundaries are spherical with radii r_i and r_o for the inner core and the outer surface, respectively, and that the core and the mantle execute the same rotational and precessional movement. The Poincaré flow is then a solid body rotation $\boldsymbol{\omega}_F\times\boldsymbol{r}$ with an arbitrary $\boldsymbol{\omega}_F$. In the precession frame, eqn [4] needs to be solved subject to the boundary conditions $\boldsymbol{u}=\hat{\boldsymbol{z}}\times\boldsymbol{r}$ at $r=r_i$, r_o. The simple idea used in Vanyo and Likins (1972) consists in subsuming the viscous effects in a frictional force per unit area proportional to $(\hat{\boldsymbol{z}}-\boldsymbol{\omega}_F)\times\boldsymbol{r}$ acting at the boundaries. In dimensional units, the prefactor is given by $\rho\nu/h$, where h stands for the thickness of the boundary layers, which will have to be chosen empirically. The phenomenological viscous force is simply proportional to the differential rotation between the bulk fluid and the boundaries. There is no symmetry argument that requires the viscous torque to be parallel to $(\hat{\boldsymbol{z}}-\boldsymbol{\omega}_F)$ since $\boldsymbol{\Omega}$ introduces another independent direction. The approximation is nonetheless attractive if we view the boundary layers as a lubricant between the interior fluid and the boundaries. Operating with $\int dV\,\boldsymbol{r}\times$ on eqn [4] yields within the framework of this phenomenology:

$$\frac{d}{dt}\boldsymbol{\omega}_F=\boldsymbol{\omega}_F\times\Omega+\gamma(\hat{\boldsymbol{z}}-\boldsymbol{\omega}_F),\quad \gamma=5\frac{\nu}{\omega_D dh}\frac{r_o^4+r_i^4}{r_o^5-r_i^5} \qquad [32]$$

In the stationary state, $\boldsymbol{\omega}_F$ is given by

$$\boldsymbol{\omega}_F=\frac{\gamma^2}{\gamma^2+\Omega^2}\left(\hat{\boldsymbol{\Omega}}\times\hat{\boldsymbol{z}}\right)\times\hat{\boldsymbol{\Omega}}-\frac{\gamma\Omega}{\gamma^2+\Omega^2}\hat{\boldsymbol{\Omega}}\times\hat{\boldsymbol{z}}+\cos\alpha\,\hat{\boldsymbol{\Omega}} \qquad [33]$$

Independently of the choice of h, one finds for the stationary state $\boldsymbol{\omega}_F\hat{\boldsymbol{z}}=\omega_F^2$ and $\boldsymbol{\omega}_F\cdot\left(\Omega\hat{\boldsymbol{\Omega}}\times\hat{\boldsymbol{z}}\right)<0$. The latter inequality shows that viewed from an inertial frame, the axis of the fluid lags behind the axis of the shell in the precessional motion. At infinitesimal Ω, $\boldsymbol{\omega}_F$ is orthogonal to $\boldsymbol{\Omega}$ and $\hat{\boldsymbol{z}}$. As $|\Omega|$ is increased, $\boldsymbol{\omega}_F$ gradually aligns with $\hat{\boldsymbol{\Omega}}$.

In order to get rid of any adjustable parameters like h, one needs to actually compute the structure of the boundary layers. Busse (1968) determined $\boldsymbol{\omega}_F$ for a spheroid with semiaxes a and c. This calculation is fairly involved and only the result is quoted here:

$$\frac{\boldsymbol{\omega}_F}{\omega_F^2}=\hat{\boldsymbol{z}}+\frac{A\hat{\boldsymbol{z}}\times(\boldsymbol{\Omega}\times\hat{\boldsymbol{z}})+B(\hat{\boldsymbol{z}}\times\boldsymbol{\Omega})}{A^2+B^2} \qquad [34]$$

with $A=0.259(E/\omega_F)^{1/2}/a+(1-c/a)\omega_F^2+\boldsymbol{\Omega}\hat{\boldsymbol{z}}$ and $B=2.62(E\cdot\omega_F)^{1/2}/a$, $E=\nu(\omega_D d^2)^{-1}$. The z-component of eqn [34] reproduces the equation $\boldsymbol{\omega}_F\hat{\boldsymbol{z}}=\omega_F^2$ already obtained in the preceding text. Equation [34] strictly speaking obtains for a full spheroid with semiaxes a and c without an inner core. However, eqn [32] shows that the torque exerted by the inner core on the fluid in a spherical shell with $r_i/r_o=0.35$ is only 2% of the total frictional torque, so that eqn [34] can be reasonably applied to the Earth's core. Equation [34] for $E<10^{-7}$ reproduces the angle of 1.7×10^{-5} already found at the end of **Section 8.07.3.1**. According to eqn [34], the locus of $\boldsymbol{\omega}_F$ approximately sweeps half of a circular cone as Ω is varied; see **Figure 13**.

Noir et al. (2003) arrived at eqn [34] by considering the balance of torques acting on the fluid. They obtain the

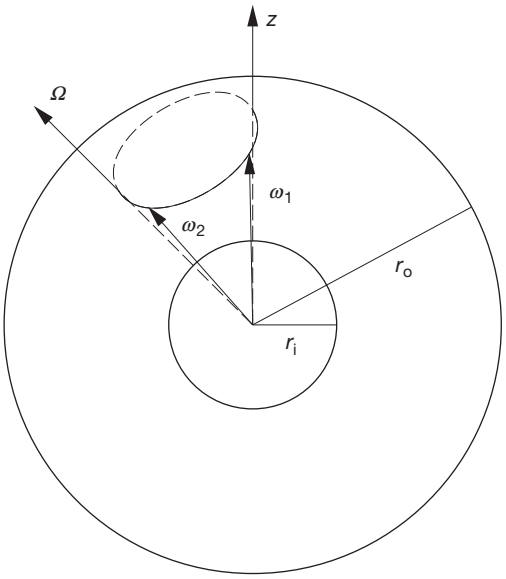

Figure 13 A spherical shell in prograde precession. For infinitesimal precession rates Ω, the rotation of the interior fluid $\boldsymbol{\omega}_1$ is nearly aligned with the z-axis. Viewed from the mantle frame, the fluid rotates with the angular velocity $\boldsymbol{\omega}_1 - \hat{\boldsymbol{z}}$, which is perpendicular to the plane containing $\hat{\boldsymbol{z}}$ and Ω. $\boldsymbol{\omega}_2$ shows a possible rotation vector of the fluid for large Ω. As Ω is increased, the rotation vector varies along a curve as shown and aligns with Ω in the limit of large precession rates. For retrograde precession, the rotation vector of the fluid varies along the dashed curve from $\hat{\boldsymbol{z}}$ to Ω.

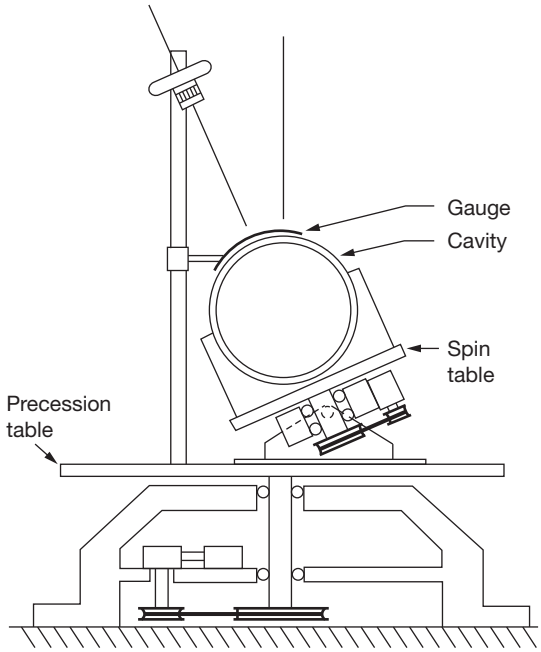

Figure 14 Experimental setup. A transparent ellipsoidal cavity rotates and precesses. A camera pointed along the rotation axis and mounted on the precession table takes pictures of the flow through a transparent gauge. Adapted from Vanyo J (1991) A geodynamo powered by lunisolar precession. *Geophysical and Astrophysical Fluid Dynamics* 59: 209–234, with permission from Taylor & Francis, http://www.tandf.co.uk/journals.

frictional torque from the viscous decay rate of the spin-over mode computed in Greenspan (1968), which allows them to circumvent the most tedious part of the algebra presented in Busse (1968).

Viscous effects ultimately determine how much energy is dissipated by precession. This energy must at least be on the order of 10^{11} W if precession drives the geodynamo. The dissipated energy must be drawn from the rotational motion of the Moon and the Earth. Néron de Surgy and Laskar (1997) had computed the long-term evolution of the Earth including a frictional term of the same form as in eqn [32]. It turns out that a precessional dissipation of nearly 10^{12} W is still compatible with geophysical constraints on the rotation rate.

Precessional forcing certainly has changed during the Earth's history. The obliquity was not constant, though there is controversy about how much it varied (Néron de Surgy and Laskar, 1997; Williams, 1993). The more dramatic variation in precessional forcing comes from the change in distance between the Earth and the Moon. Precessional forcing was of course stronger when the Moon was closer to the Earth.

8.07.3.3 Experiments

Laboratory experiments have historically been our most important tool to gain insight into precession-driven flow. Even with today's computational capabilities, experiments are still superior in several respects, especially concerning the accessible range of the Ekman numbers.

Until recently, experimental diagnosis of precession-driven flow was restricted to torque measurements and optical visualization. Figure 14 shows an experimental apparatus that sets an ellipsoidal container into precessional motion. It consists basically of two superposed turntables. Corotating cameras allow visual observation of dye tracers or flakes suspended in the fluid (normally water). The torque exerted by the motors in order to maintain the precessional motion of the container gives a direct measure of the energy dissipated in the fluid.

Figure 15 summarizes visual observations. At low precession rates, nested cylindrical shear layers appear, which are approximately coaxial with the rotation axis of the fluid. Suspended flakes preferentially align with the shear in these layers but are randomly oriented in regions of low shear. The orientation of the particles is revealed by how they scatter incident light: viewed perpendicular to a plane of illumination, zones of high shear appear bright. When the precession rate is increased, these shear layers seem to develop wavelike instabilities as indicated in Figure 15, and the flow ultimately becomes turbulent at high enough precession rates. The visualization method of course does not allow us to tell whether the shear layers cause the instability or whether their deformation is simply an indicator of instability of different origins. A sudden increase in energy dissipation, and hence in the torque applied by the motors, accompanies the onset of turbulence (Malkus, 1968). A hysteresis loop is observed in the torque when the precession rate is lowered from a value above the onset of turbulence in an ellipsoid of ellipticity 1/10, but none appears in an ellipsoid of ellipticity 1/400 (Vanyo, 1991). The onset of the wavelike instability occurred in one experiment (Malkus, 1968) at $E = 3.6 \times 10^{-6}$ and $\Omega_P/\omega_D = 1/60$ in a

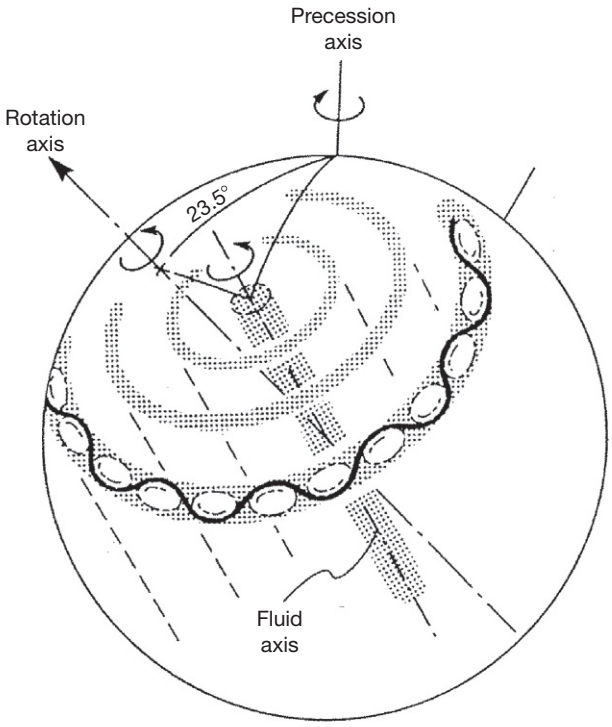

Figure 15 Sketch of visual observations. Adapted from Vanyo J, Lods D, and Wilde P (1994) Precessing mantle, liquid core, and solid core interactions. In: *The 4th SEDI Symposium*, Abstract Book, pp 62–64.

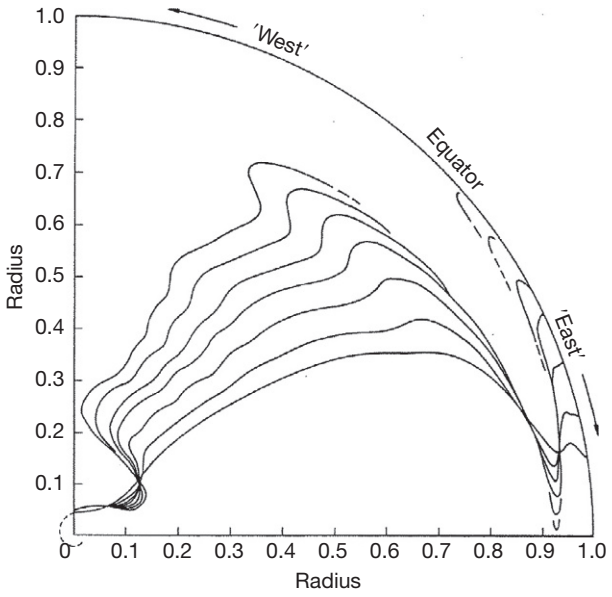

Figure 16 Deformation of a dye streak in the equatorial plane at successive moments in time. The view is from the south pole; west and east are equivalent to retrograde and prograde, respectively. Reprinted from Malkus V (1968) Precession of the earth as the cause of geomagnetism. *Science* 160: 259–264, with permission. Copyright 1968 AAAS.

container of ellipticity 1/25. There are no systematic data available on how this onset depends on the control parameters.

More detail of the structure of the axisymmetric shear layers is given in Figure 16 where the temporal evolution of an initially straight dye line in the equatorial plane is shown. The bulk of the fluid moves in retrograde direction, and the strongest deformation of the dye streak occurs at a radius of about 0.866 (the radius of the boundary being 1). A cylinder at this radius connects the northern to the southern critical latitude ($\cos 30^\circ = 0.866$).

Vanyo et al. (1995) contained numerous photographs of dye tracer visualizations. It transpires that vortices reminiscent of a Kelvin–Helmholtz instability appear on the shear layers. There is also an axial velocity component inside these vortices, so that the flow in the vortices is helical. The gross structure of the helical velocity is not unlike that of buoyancy-driven flow, which adds to the suspicion that the precession-driven flow might act as a dynamo.

The orientation of the velocity in the most prominent shear layer, and the location of that layer, in Malkus' experiment is compatible with the nonlinear theory of Busse. It is not clear at present where the other shear layers come from.

It is also surprising at first that there is no indication in visualizations of the inclined time-dependent shear layers, which have been the topic of Section 8.07.2 (in particular Figures 6 and 7). It is likely that the response time of the suspended flakes is too long to show these layers. Indeed, every flake particle traverses during one rotation period a layer of one sign and the corresponding layer of opposite sign (because the spin-over mode has an azimuthal wave number of 1) so that averaged over one rotation period, there is no reorientation of the particle. Acoustic Doppler anemometry, on the other hand, confirmed the existence of oblique shear layers. Noir et al. (2001a) compared the experimental velocity profiles with numerical simulations and found an agreement for both the shape of the profile and the dependence of the velocities on the control parameters. They concluded that in the Earth's core, the velocity in these layers originating from the CMB is approximately 6×10^{-6} m s^{-1}.

The most basic characterization of precession-driven flow is the orientation of the fluid axis. The first systematic data have been collected by Vanyo and Likins (1971) who compared their results with eqn [33]. A problem with eqn [33] is that it predicts a behavior that is symmetrical between prograde precession and retrograde precession, which is not supported by observation. Pais and LeMouël (2001) reexamined Vanyo's data by fitting them to the theory of Busse, that is, eqn [34], and claimed good agreement. Another study by Noir et al. (2003) showed that discrepancies between experiment and theory remain, which are larger than the experimental errors. Noir et al. (2003) started experimental determinations of the fluid axis of their own using three different methods: tracer particles, pressure measurements, and acoustic Doppler anemometry. Equation [34] is not expected to be universally applicable because it is derived using series developments, which are valid in the limit of the small Ekman numbers, small precession rates, and small ellipticities. Accordingly, Noir et al. (2003) observed deviations at some parameters but found general agreement, even at parameters for which it could not be expected. In particular, there is no reason to doubt that [34] describes very well the behavior of the Earth's core. Numerical simulations in the next section confirm this conclusion.

Consider a sphere rotating in a laboratory about a vertical axis. Unless the laboratory is located at one of the poles, the

Earth's rotation will cause the sphere to precess relative to an inertial frame. The precession rate obtained this way is too small to generate fully turbulent flow, but this simple setup has been used to observe the characteristics of the laminar flow, including the internal shear layers (Boisson et al., 2012; Triana et al., 2012; Vanyo and Dunn, 2000).

Little is known about the structure of precession-driven turbulence. Goto et al. (2007) started a study of turbulence in precessing spheres with spin and precession axes perpendicular to each other. The same configuration of axes was used in a more detailed experiment with a precessing cylinder (Mouhali et al., 2012) in which visualization revealed a predominance of cyclones over anticyclones in the turbulent regime. The cylindrical geometry is of course remote from geophysical applications and fundamentally different from the ellipsoidal geometry in that it does not allow for a laminar constant vorticity solution at nonzero precession rates. Nonetheless, the qualitative features of turbulence are typically independent of boundary shapes, and these experiments are also of interest because they prepare larger experiments, which could lead to a precession-driven laboratory dynamo (Stefani et al., 2012).

8.07.3.4 Numerical Solutions

Experimental progress primarily hinges on the development of new measurement techniques. Anemometry has never been an easy task, but it becomes especially cumbersome in a rotating or even precessing flow. Numerical simulations are attractive in the present context because all quantities of interest can easily be extracted from the data. On the other hand, we cannot simulate the lowest Ekman numbers achievable in experiments.

The most general geometry simulated to date is that of a spheroidal shell in which the minor axes of the inner and outer boundaries coincide with the common rotation axis of the boundaries. Most of the calculations presented here are for equal ellipticities of the inner and outer boundaries so that we state the mathematical problem for this case.

Consider incompressible fluid of kinematic viscosity ν in an ellipsoidal shell rotating with angular frequency ω_D about the z-axis. The shell furthermore executes a precessional motion characterized by the precession vector $\Omega_p\hat{\boldsymbol{\Omega}}_p$ (hats denote unit vectors). The boundaries of the shell are given by

$$\frac{x^2}{a^2}+\frac{y^2}{a^2}+\frac{z^2}{c^2}=1 \qquad [35]$$

$$\frac{x^2}{(\eta a)^2}+\frac{y^2}{(\eta a)^2}+\frac{z^2}{(\eta c)^2}=1 \qquad [36]$$

$\eta<1$ and both boundaries have the same ellipticity $e=1-c/a$. Units of length and time are chosen as $(1-\eta)a$ and $1/\omega_D$, respectively. The equation of motion for the velocity $\boldsymbol{u}(\boldsymbol{r}, t)$ reads in a frame of reference attached to the shell:

$$\frac{\partial}{\partial t}\nabla\times\boldsymbol{u}+\nabla\times\{(2(\hat{\boldsymbol{z}}+\boldsymbol{\Omega})+\nabla\times\boldsymbol{u})\times\boldsymbol{u}\} = E\nabla^2\nabla\times\boldsymbol{u}+2\hat{\boldsymbol{z}}\times\boldsymbol{\Omega} \qquad [37]$$

$$\nabla\cdot\boldsymbol{u}=0 \qquad [38]$$

The Ekman number E is defined by $E=\nu(\omega_D(1-\eta)^2a^2)^{-1}$ and $\boldsymbol{\Omega}=\Omega_p/\omega_D\hat{\boldsymbol{\Omega}}_p$. The precession axis $\hat{\boldsymbol{\Omega}}$ forms the angle $\alpha(0<\alpha<\pi/2)$ with the z-axis and is time-dependent in the chosen system of reference:

$$\hat{\boldsymbol{\Omega}}=\sin\alpha\cos t\,\hat{x}-\sin\alpha\sin t\,\hat{y}+\cos\alpha\,\hat{z} \qquad [39]$$

The boundary conditions require that $\boldsymbol{u}=0$ at $r=r_i$, r_o. For spherical boundaries, $c=a$, $e=0$, and $\eta=r_i/r_o$ where r_i and r_o denote the radii of the inner and outer boundary, respectively.

8.07.3.4.1 Laminar flows

The rotation axis of the fluid, $\boldsymbol{\omega}_F$, is predicted by eqn [34] in the limit of small precession rates, Ekman numbers, and ellipticities. If we want to compare the prediction to numerical simulations, we first need a precise definition of the fluid axis. In the theory, the flow outside the boundary layers is assumed to have constant vorticity. In a sphere, such a flow corresponds to a solid body rotation. We thus seek to extract from the simulated flow a component, which most closely resembles a solid body rotation. This turns out to be quite straightforward because of the numerical method that is usually employed (Tilgner, 1999d). Indeed, it is convenient to numerically solve the Navier–Stokes equation in spherical geometry after decomposing the velocity field $\boldsymbol{u}$ into poloidal and toroidal scalars, ϕ and ψ, by

$$\boldsymbol{u}=\nabla\times\nabla\times(\phi\hat{\boldsymbol{r}})+\nabla\times(\psi\hat{\boldsymbol{r}}) \qquad [40]$$

and to decompose each scalar into spherical harmonics:

$$\phi=r\sum_{l=1}^{\infty}\sum_{m=-l}^{l}\phi_l^m(r,t)P_l^m(\cos\theta)e^{im\varphi}$$
$$\psi=r^2\sum_{l=1}^{\infty}\sum_{m=-l}^{l}\psi_l^m(r,t)P_l^m(\cos\theta)e^{im\varphi} \qquad [41]$$

A solid body rotation of the fluid at radius r is entirely determined by the coefficients $\psi_1^1(r)$ and $\psi_1^0(r)$. The rotation of the fluid at radius r in the mantle frame is given by

$$\boldsymbol{\omega}(r)=-2\mathrm{Re}\{\psi_1^1(r)\}\hat{\boldsymbol{x}}+2\mathrm{Im}\{\psi_1^1(r)\}\hat{\boldsymbol{y}}+\psi_1^0(r)\hat{\boldsymbol{z}} \qquad [42]$$

Re{} and Im{} denote the real and imaginary parts of the quantity in curly brackets, respectively. An average rotation is then defined by $\langle\boldsymbol{\omega}\rangle=(1/V)\int\boldsymbol{\omega}(r)\,dV$, where V is the volume of the shell.

We are now in a position to compare numerical and analytic results. $\boldsymbol{\omega}_F$ determined from eqn [34] with $a=c=r_o$ is given in the precession frame so that we need to compare it with $\langle\boldsymbol{\omega}\rangle+\hat{\boldsymbol{z}}$. Figure 17 shows a polar diagram in which the directions of $\langle\boldsymbol{\omega}\rangle+\hat{\boldsymbol{z}}$ and $\boldsymbol{\omega}_F$ are given. This plot is a 2-D projection of Figure 13. The locus of the directions visited by $\langle\boldsymbol{\omega}\rangle+\hat{\boldsymbol{z}}$ when varying Ω depends on α but not on E according to eqn [34]. This is well verified by the numerical results. Predicted and computed directions differ by angles comparable with the variations of direction of $\boldsymbol{\omega}(r)$ with r and are therefore on the order of the deviations within which a fluid rotation vector can be determined from the numerical data.

Figure 18 compares the kinetic energy of the flow in the mantle frame with the predicted value $(1/2)\int(\boldsymbol{\omega}_F-\hat{\boldsymbol{z}})^2\,dV$. The agreement is fair, and the fractional error would appear even smaller in the precession frame because most of the rotational energy is subtracted out in transforming to the mantle frame, where deviations from solid body rotation are emphasized. The agreement also improves with decreasing E. More comparisons are in Tilgner and Busse (2001) for spherical shells and Lorenzani and Tilgner (2001) for spheroidal shells.

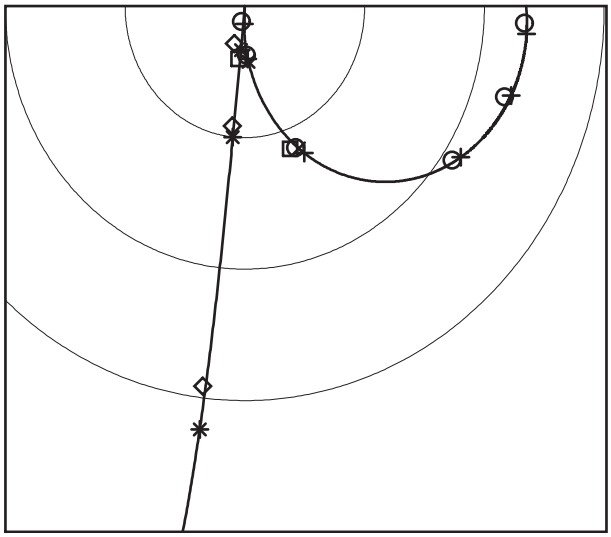

Figure 17 Polar plot showing the orientation of the average rotation of the fluid in a reference frame in which the axes of precession and rotation of the shell are stationary. The thin circles are located at 10°, 20°, and 30° from the north pole. The thick lines show the locus of the directions of the rotation axis of the fluid predicted by eqn [34] for $\alpha = 90°$ (left line) and $\alpha = 23.5°$ (right line), the latter ending at the top right of the figure at the position of the precession axis. Retrograde corresponds to clockwise in this figure. The symbols indicate $E = 10^{-4}$, $\alpha = 23.5°$ (circles), $E = 10^{-5}$, $\alpha = 23.5°$ (squares), and $E = 10^{-4}$, $\alpha = 90°$ (diamonds). The values of Ω can be deduced from **Figure 18** where more data for the same runs are shown; the points close to the pole are for small $|\Omega|$. Near to every data point obtained from direct simulation is another symbol showing the direction calculated with eqn [34] for the same parameter set: Crosses belong to circles, $\times$ to squares, and stars to diamonds. Reprinted from Tilgner A (1999) Magnetohydrodynamic flow in precessing spherical shells. *Journal of Fluid Mechanics* 379: 303–318, with permission from Cambridge University Press.

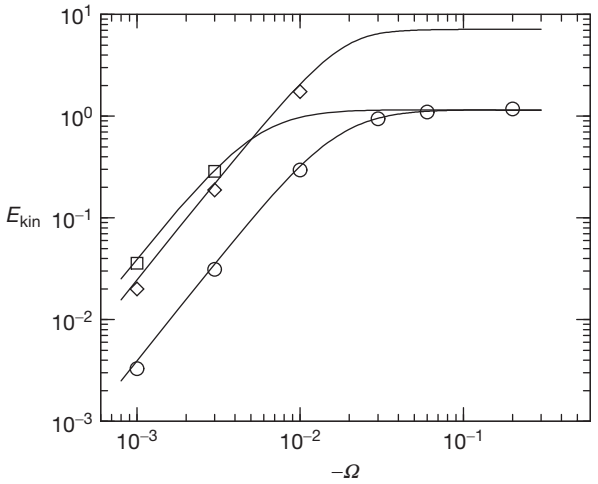

Figure 18 Kinetic energy E_{kin} of the flow in the mantle frame as a function of the (retrograde) precession rate Ω. The symbols indicate $E = 10^{-4}$, $\alpha = 23.5°$ (circles), $E = 10^{-5}$, $\alpha = 23.5°$ (squares), and $E = 10^{-4}$, $\alpha = 90°$ (diamonds). The solid lines show the kinetic energies deduced from eqn [34]. Adapted from Tilgner A (1999) Magnetohydrodynamic flow in precessing spherical shells. *Journal of Fluid Mechanics* 379: 303–318, with permission from Cambridge University Press.

Experiments have revealed oblique conical and cylindrical shear layers. The inclined shear layers are those contained in the spin-over mode and already seen in **Figures 7** and **8**. One of the cylindrical shear layers is predicted by the theory of Busse (1968). These cylinders are coaxial with the rotation axis of the fluid. In order to distil them from the numerical data, we have to plot the zonal component of the velocity axisymmetric about $\boldsymbol{\omega}_F$. This is done in **Figure 19**. The shear layers in the zonal velocity well known from experiments clearly appear in the plots. The exact location of the shear layers depends on both the boundary geometry and the Ekman number. The most precise comparison is possible in **Figure 20** in which the profiles of the zonal velocity in the equatorial plane perpendicular to $\boldsymbol{\omega}_F$ are plotted as a function of radius. The strongest shear layer connects the critical latitudes and the positions of the strongest prograde and retrograde jets correspond exactly to those given in Figure 3 of Malkus (1968). The position of the smaller extrema depends on E and a perfect agreement with Malkus' figure cannot be expected for this part of the profile. As can be deduced from **Figure 20**, the prograde jet becomes stronger with decreasing E. According to Busse (1968), a singularity should develop in the limit $E \to 0$. The Ekman number dependence of the maximum zonal velocity does not follow any simple law valid for the entire interval $10^{-4} < E < 10^{-6}$ but is compatible with a scaling in $E^{-3/10}$ for $10^{-5} < E < 10^{-6}$. Using the scaling in $E^{-3/10}$ down to the Ekman number of the Earth, one finds a velocity of 3×10^{-5} m s^{-1} for the prograde jet inside the core (Noir et al., 2001b).

Figure 20 contains additional structure in the zonal wind, which compares favorably with Malkus' experiment. While we do not understand the origin of these other shear layers, the simulations show that they are not experimental artifacts and that their explanation is hidden in the equation of motion [37].

The simulations, as well as the experiments, had no significant inner core. The effect of an Earth-like inner core has been investigated by Lorenzani and Tilgner (2001). The main cylindrical shear layer is too distant from the inner core to be noticeably modified by it, but a new cylindrical shear layer emerges near the critical latitudes of the inner core.

In as far as the inclined shear layers are concerned, we have reliable theory about the scaling of the velocity with the Ekman number and precession rate for the layer connected with the CMB. This scaling yields a velocity of 6×10^{-6} m s^{-1} when applied to the Earth's core (Noir et al., 2001a).

We are less advanced for the layers associated with the inner core and have to rely on numerics for that case. Tilgner (1999c) reported simulations with free-slip boundary conditions at the CMB and no-slip conditions at the inner core. This isolates the layer connected to the inner core, which is shown in **Figure 21**. The intensity of these shear zones decreases with decreasing E, but the extrapolation to $E = 10^{-15}$ is problematic. The numerical results do not behave according to any simple power law. The Ekman number of the simulation is presumably not small enough yet for the asymptotic regime. One is thus reduced to give an upper bound for the core flow: the radial velocity in the main shear zone will certainly be $< 6.9 \times 10^{-5}$ m s^{-1}.

The Poincaré solution in a shell violates not only no-slip boundary conditions but also the no-penetration boundary condition if inner and outer boundaries have different ellipticities. Based on the experience of **Section 8.07.2**, which has shown that internal layers typically appear even in inviscid solutions in all but the simplest geometries, we may expect

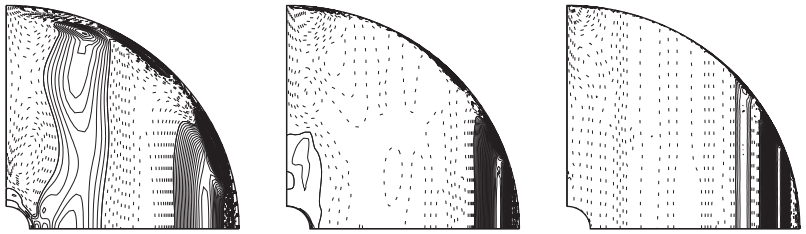

Figure 19 Zonal flow component $u_{\varphi'}$ (where φ' denotes the azimuthal angle with respect to the $\boldsymbol{\omega}_F$-axis) axisymmetric about $\boldsymbol{\omega}_F$, after subtraction of the average rotation of the fluid. $\boldsymbol{\omega}_F$ is pointing upward in all panels. $\eta = 0.1$, $e = 0.04$, $\Omega = -10^{-5}$, and $\alpha = 30^\circ$ in all cases. From left to right, the Ekman number is 10^{-4}, 10^{-5}, and 10^{-6}. Adapted from Lorenzani S and Tilgner A (2001) Fluid instabilities in precessing spheroidal cavities. *Journal of Fluid Mechanics* 447: 111–128, with permission from Cambridge University Press.

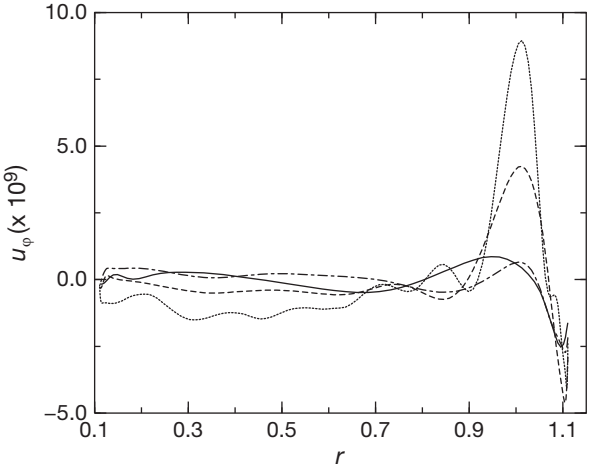

Figure 20 $u_{\varphi'}$ from Figure 19 in the equatorial plane as a function of r for $\Omega = -10^{-5}$, $\alpha = 30^\circ$, and $\eta = 0.1$. The line styles indicate $e = 0.04$, $E = 10^{-4}$ (solid), $e = 0.04$, $E = 10^{-5}$ (dashed), $e = 0.04$, $E = 10^{-6}$ (dotted), and $e = 0$, $E = 10^{-5}$ (dot-dashed). For this last case, $u_{\varphi'}$ has been divided by 100 in order to make the curve fit into the figure. Adapted from Lorenzani S and Tilgner A (2001) Fluid instabilities in precessing spheroidal cavities. *Journal of Fluid Mechanics* 447: 111–128, with permission from Cambridge University Press.

that a difference in ellipticities also brings internal layers into existence.

Simulations of the linearized equations of motion confirm this expectation. This time, the velocities on the characteristic surfaces tangent to the inner core are increasing with decreasing E because one obtains true discontinuities in the inviscid flow, which are smeared out at the finite Ekman number. Simulations yield directly a lower bound for the corresponding layer in the Earth's core of 3.4×10^{-7} m s^{-1}. We have no theory for the Ekman number dependence. The best power law fit to the numerical data suggests a scaling as $E^{-0.17}$. Assuming this is correct, one obtains velocities of 1.2×10^{-5} m s^{-1} for the Earth's core (Tilgner, 1999c). All the different mechanisms therefore seem to generate velocities in the shear zones in the range 10^{-7}–10^{-5} m s^{-1}, which is well below flow velocities deduced from secular variation.

The mechanism based on different ellipticities of the inner core and the CMB is a rather general effect of topography. In fact, the Poincaré flow over topography at the CMB of a height of some 10 km may force larger velocities than those found here, but this possibility remains to be investigated.

8.07.3.4.2 Instability

Instabilities generally break symmetries of the underlying flow. The laminar precession-driven flow is symmetrical with respect to the origin in the sense that $\boldsymbol{u}(\boldsymbol{r}) = -\boldsymbol{u}(-\boldsymbol{r})$. It is therefore useful to separate the full velocity field into symmetrical and antisymmetric components, such that $\boldsymbol{u} = \boldsymbol{u}_a + \boldsymbol{u}_s$ with $\boldsymbol{u}_s = (\boldsymbol{u}(\boldsymbol{r}) - \boldsymbol{u}(-\boldsymbol{r}))/2$ and $\boldsymbol{u}_a = (\boldsymbol{u}(\boldsymbol{r}) + \boldsymbol{u}(-\boldsymbol{r}))/2$. Adding and subtracting the equations for $\partial/\partial t \nabla \times \boldsymbol{u}(\boldsymbol{r})$ and $\partial/\partial t(\nabla \times \boldsymbol{u})(-\boldsymbol{r})$ and noting the fact that the curl of a vector is a pseudovector so that $\nabla \times \boldsymbol{u}_a = \frac{1}{2}[(\nabla \times \boldsymbol{u})(\boldsymbol{r}) - (\nabla \times \boldsymbol{u})(-\boldsymbol{r})]$ and $\nabla \times \boldsymbol{u}_s = \frac{1}{2}[(\nabla \times \boldsymbol{u})(\boldsymbol{r}) + (\nabla \times \boldsymbol{u})(-\boldsymbol{r})]$, one obtains

$$\frac{\partial}{\partial t}\nabla \times \boldsymbol{u}_s + \nabla \times [(\nabla \times \boldsymbol{u}_s) \times \boldsymbol{u}_s + (\nabla \times \boldsymbol{u}_a) \times \boldsymbol{u}_a] + 2\nabla \times ((\hat{\boldsymbol{z}} + \boldsymbol{\Omega}) \times \boldsymbol{u}_s) = E\nabla^2 \nabla \times \boldsymbol{u}_s - 2\boldsymbol{\Omega} \times \hat{\boldsymbol{z}} \quad [43]$$

$$\frac{\partial}{\partial t}\nabla \times \boldsymbol{u}_a + \nabla \times [(\nabla \times \boldsymbol{u}_s) \times \boldsymbol{u}_a + (\nabla \times \boldsymbol{u}_a) \times \boldsymbol{u}_s] + 2\nabla \times ((\hat{\boldsymbol{z}} + \boldsymbol{\Omega}) \times \boldsymbol{u}_a) = E\nabla^2 \nabla \times \boldsymbol{u}_a \quad [44]$$

together with $\nabla \cdot \boldsymbol{u}_a = \nabla \cdot \boldsymbol{u}_s = 0$ and $\boldsymbol{u}_a = \boldsymbol{u}_s = 0$ on the boundaries. Only $\boldsymbol{u}_s$ is forced by precession and $\boldsymbol{u}_a = 0$ is always a possible solution. It is possible that an instability of that solution leaves $\boldsymbol{u}_a = 0$, but an instability is necessary in order to obtain $\boldsymbol{u}_a \neq 0$. The energy E_a contained in the velocity field $\boldsymbol{u}_a$ is therefore a convenient indicator for the onset of an instability. In order to localize instabilities spatially, it is helpful to also introduce the density $\epsilon_a(r)$ of the energy contained in $\boldsymbol{u}_a$ at radius r:

$$\epsilon_a(r) = \frac{1}{4\pi}\int_0^\pi \mathrm{d}\theta \sin\theta \int_0^{2\pi} \mathrm{d}\varphi \, \frac{1}{2}u_a^2 \quad [45]$$

Three different situations are represented in Figure 22. Either only the bulk or only the boundary or both have become unstable. One instability does not seem to affect the other.

Analytic treatment of the stability problem has so far followed one of two strategies. The first approach represents the components of the unstable flow by polynomials and restricts the highest admissible order of the polynomials to a finite number (2 in Kerswell, 1993b and 6 in Wu and Roberts, 2010). The second approach is a linear stability analysis restricted to basic flows, which differ little from a solid body rotation. This chapter will discuss only the second approach in some detail.

8.07.3.4.2.1 Boundary layer instability

Let us first consider the instability localized in the boundary layer. Figure 23 gives an impression of the unstable boundary layer flow. The comparatively small lateral length scales of the

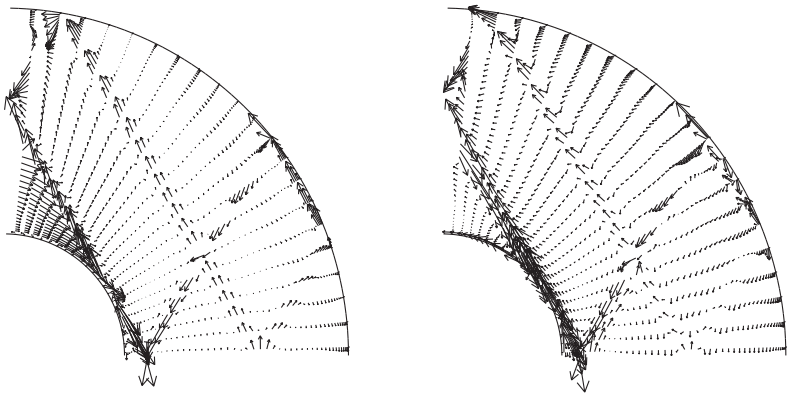

Figure 21 Velocity in meridional planes for $e_i = e_o = 1/400$, $E = 3 \times 10^{-6}$ and stress-free outer and no-slip inner boundaries. $\hat{\boldsymbol{z}}$ is pointing upward; the axis pointing to the right is $\hat{\boldsymbol{\Omega}}$ in the left panel and $\hat{\boldsymbol{z}} \times \hat{\boldsymbol{\Omega}}$ in the right panel. Velocities at equal arrow length are larger in the right panel by a factor 1.24. The mean solid body rotation has been subtracted, and the Ekman layer at the inner core has been removed from the plot. Adapted from Tilgner A (1999) Non-axisymmetric shear layers in precessing fluid ellipsoidal shells. *Geophysical Journal International* 136: 629–636, with permission from Blackwell Publishing.

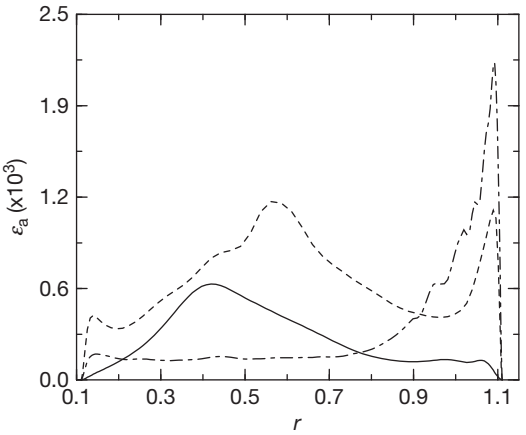

Figure 22 The energy density ϵ_a of the antisymmetric components (eqn [45]) as a function of r for $E = 5 \times 10^{-4}$, $e = 0.1$, $\alpha = 80°$, $\Omega = -0.08$ (solid), $E = 10^{-4}$, $e = 0.04$, $\alpha = 30°$, $\boldsymbol{\Omega} = -0.05$ (dashed), and $E = 10^{-4}$, $e = 0.1$, $\alpha = 80°$, $\Omega = -0.08$ (dot-dashed). The values for the last curve have been divided by ten. $\eta = 0.1$ for all cases. Adapted from Lorenzani S and Tilgner A (2001) Fluid instabilities in precessing spheroidal cavities. *Journal of Fluid Mechanics* 447: 111–128, with permission from Cambridge University Press.

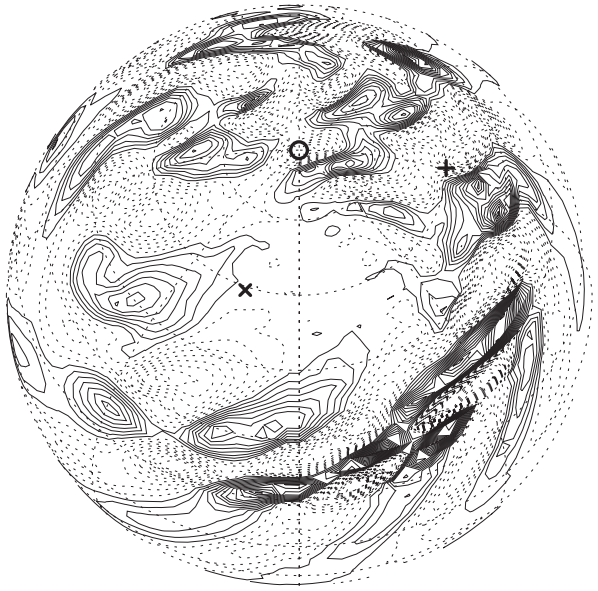

Figure 23 u_{ar} on a surface separated by 0.015 from the outer boundary for $e = 0.04$, $\eta = 0.1$, $E = 10^{-4}$, and $\Omega = -0.03$. The north pole is marked by a circle, the fluid axis by an x, and the precession axis by a $+$. Reprinted from Lorenzani S and Tilgner A (2001) Fluid instabilities in precessing spheroidal cavities. *Journal of Fluid Mechanics* 447: 111–128, with permission from Cambridge University Press.

motions excited by the boundary layer instability become difficult to resolve at more extreme parameters. The development of this instability and ensuing numerical instabilities turn out to be the most serious obstacle on the way to high precession rates at low E. The instabilities of time-independent Ekman layers have already been studied in detail, both numerically and experimentally (Lilly, 1966; Tatro and Mollo-Christensen, 1967). In these studies, the Reynolds and Rossby numbers of the boundary layer emerged as the relevant parameter separating stable from unstable flows. In the present simulation, let us use as the boundary layer thickness the distance from the boundary at which the absolute value of the radial velocity averaged over spheroidal surfaces reaches a maximum. The layer thickness is approximately $1.4 \times E^{1/2}$ in all cases. Based on this thickness and the maximum tangential velocity, the Reynolds numbers of the boundary layer have been computed. The Rossby numbers of the simulated boundary layers lie in between 0.1 and 0.5 and have been estimated as $v_h[2(1+\Omega\cos\alpha)]^{-1}$ where v_h is the maximum tangential velocity at the edge of the boundary layer and $1+\Omega\cos\alpha$ is the total rotation rate about the z-axis. The critical Reynolds number lies somewhere in between 50 and 100, which falls into the range quoted by Tatro and Mollo-Christensen (1967) for time-independent Ekman layers.

Even though the Reynolds number of the boundary layer surely exceeded its critical value in some precession experiments, the Ekman layer instability has never been noted in experiments, which indicates that it stays localized in thin boundary layers also at the parameters typical of experiments. The boundary layers are so thin that an instability within those layers is not easily detectable experimentally.

In the Earth's core, the boundary layers are likely to be unstable. The angle between the Earth's axis of figure and the rotation axis of the core is 1.7×10^{-5}, which leads to velocities at the CMB of up to 4.3 mm s^{-1}. This is one order of magnitude larger than the velocities deduced from the secular variation of the magnetic field. The precessional velocity field varies with the period of 1 day and the mantle of course screens variations of the magnetic field on that timescale. Nonetheless, these large velocities have an influence on the boundary layer dynamics. Based on a critical Reynolds number for the boundary layer of 100 and using $1.4\times E^{1/2}$ for the layer thickness, the Earth's Ekman layer must be unstable if the Ekman number of the Earth's core is $<3.5\times10^{-14}$, which is the case according to current estimates.

8.07.3.4.2.2 Instabilities of the bulk flow

Let us now turn to instabilities of the bulk flow. It is numerically challenging to demonstrate these instabilities. If the boundary layer becomes unstable first, one has to resolve the small-scale structures, which then appear. This considerably slows down the computation. It is therefore best to find sets of parameters where the boundary layers stay stable. The first example that has been reported was for comparatively large Ekman numbers, which then also imply a large Poincaré force to drive the flow vigorously enough. A strong driving is achieved by choosing a large precession rate and a large angle between rotation and precession axes. A large precession rate by itself is not useful because a plateau is reached in the kinetic energy of the flow with increasing $|\Omega|$ (see Figure 18), and at yet larger $|\Omega|$, other inertial modes may become excited (Manasseh, 1992). An angle of about 60° between rotation and precession axes must usually be chosen for computations.

As an example, Figure 24 shows E_a as a function of E at a fixed $|\Omega|$. E_a equals zero for the basic flow; $E_a\neq0$ indicates the onset of a new flow.

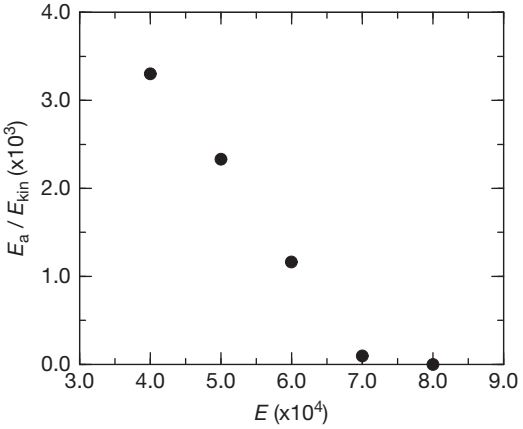

Figure 24 The ratio of the energy contained in the antisymmetric components to the total energy, E_a/E_{kin}, as a function of the Ekman number E for $\Omega=-0.2$ and $\alpha=60°$ in a spherical shell with $r_i/r_o=0.01$.

The simulations of bulk instabilities in precessional flow (Lorenzani and Tilgner, 2001, 2003; Tilgner and Busse, 2001) lead to global instability, which invades the entire fluid volume. It is impossible to connect the origin of instability by mere visual inspection to some particular feature of the underlying laminar flow. We therefore need a more incisive instrument than visualization.

It will prove very useful to spectrally decompose the flow field into components of different azimuthal wave numbers m'. The prime denotes a coordinate system in which the azimuth φ' is measured with respect to the axis of the fluid, not the axis of the container. In order to see why this makes sense, consider the equation governing the linear stability of an ideal fluid driven by precession in the mantle frame:

$$\frac{\partial}{\partial t}\nabla\times\boldsymbol{u}'+2\nabla\times(\hat{\boldsymbol{z}}\times\boldsymbol{u}')+\nabla\times[(\nabla\times\boldsymbol{u}')\times\boldsymbol{u}_0]+\nabla\times[(\nabla\times\boldsymbol{u}_0)\times\boldsymbol{u}']=0 \qquad [46]$$

The total velocity $\boldsymbol{u}$ is the sum of the velocity perturbation $\boldsymbol{u}'$ and the basic flow field $\boldsymbol{u}_0$. If the third and fourth terms are small compared with the Coriolis term, they can be treated as a perturbation, the solution of the unperturbed problem being the inertial eigenmodes. Let us assume that some particular feature of the basic flow triggers the instability and that this feature is characterized by a single wave number m'_0. Cylindrical shear layers, for example, are axisymmetric with respect to $\boldsymbol{\omega}_F$ and thus have $m'_0=0$. In this case, the coefficients in eqn [46] are independent of φ'. In addition, eqn [46] is linear in $\boldsymbol{u}'$ so that $\boldsymbol{u}'$ must have a dependence on φ' in $e^{im'_1\varphi'}$. Axisymmetric shear layers excite unstable flow characterized by a single wave number m'_1.

However, the spin-over mode is a flow with $m'_0=1$. It cannot excite an instability with a single wave number. In the lowest order of a perturbation calculation (outlined in Section 8.07.5), it must excite a pair of eigenmodes of the unperturbed problem. One speaks of a triad resonance when this happens because three entities compose the total flow: the laminar flow $\boldsymbol{u}_0$, which is itself an inertial mode if we identify $\boldsymbol{u}_0$ with the spin-over mode, and the two modes excited by the instability. Let these modes have wave numbers m'_a and m'_b and eigenfrequencies ω_a and ω_b. These modes have time and azimuthal dependences given by $e^{i\left(m'_a\varphi'-\omega_a t\right)}$ and $e^{i\left(m'_b\varphi'-\omega_b t\right)}$. They are coupled by the perturbation only if $|m'_a-m'_b|=1$. The instability thus consists of at least one pair of inertial modes with wave numbers differing by one. Otherwise, the perturbation couplings, that is, the third and fourth terms in eqn [46], would introduce new wave numbers. Equation [46] can impossibly be satisfied if $\boldsymbol{u}'$ consists of a single mode and if $\boldsymbol{u}_0$ is characterized by an m'_0 different from zero. For arbitrary m'_0, the condition $|m'_a-m'_b|=m'_0$ has to be met. A look at a spectrum as a function of m' thus directly gives a hint as to what has caused the instability.

Figure 25 shows an example. The velocity fields corresponding to unstable states have been transformed to the primed coordinate system in which the z'-axis points along $\boldsymbol{\omega}_F$. The field has then been decomposed into spherical harmonics in this new system, and the energy contained in the different spectral components has been plotted against the azimuthal wave number m'. In the example shown in Figure 25, a dominant contribution to $\boldsymbol{u}_a$ occurs at $m'=7$ and 8, whereas $\boldsymbol{u}_s$ differs

little from its shape in stable solutions. It is expected that there is a nonzero contribution from all wave numbers because the spectrum in Figure 25 is for a saturated state and not for an exponentially growing unstable motion. In addition, the prediction that only two wave numbers are populated is only true if the terms involving $\boldsymbol{u}_0$ are infinitesimally small. Nonlinear interactions generate a small peak in the spectrum of $\boldsymbol{u}_s$ at twice the wave number at which the spectrum of $\boldsymbol{u}_a$ peaks.

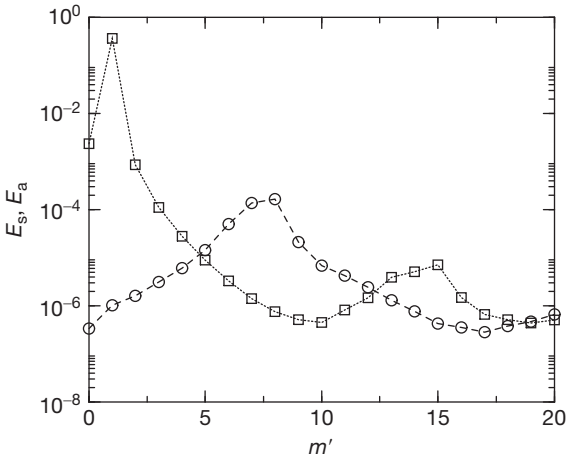

Figure 25 Energy contained in the modes with wave number m' as a function of m' for $\eta = 0.1$, $e = 0.04$, $\alpha = 30°$, $\Omega = -0.03$, and $E = 10^{-4}$. Antisymmetric (circles) and symmetrical (squares) contributions are shown separately. Adapted from Lorenzani S and Tilgner A (2001) Fluid instabilities in precessing spheroidal cavities. *Journal of Fluid Mechanics* 447: 111–128, with permission from Cambridge University Press.

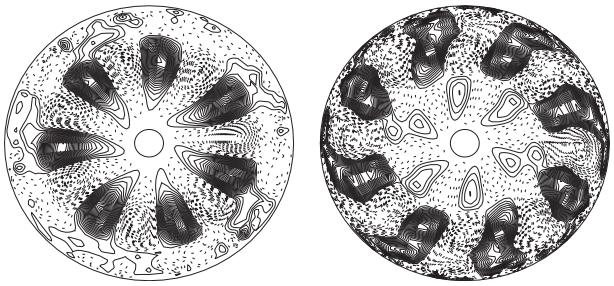

Figure 26 u_{ar} (left) and $u_{az'}$ (right) in the plane perpendicular to $\boldsymbol{\omega}_F$ for the same parameters as in Figure 25. Adapted from Lorenzani S and Tilgner A (2001) Fluid instabilities in precessing spheroidal cavities. *Journal of Fluid Mechanics* 447: 111–128, with permission from Cambridge University Press.

The structure of the instability for the set of parameters used in Figure 25 is clarified in Figures 26 and 27 and summarized in Figure 28. Figures 26 and 27 are snapshots. As time goes on, the $m' = 7$ and 8 patterns rotate independently of each other about the z'-axis. Figure 26 shows $u_{az'}$ and u_{ar} in the plane perpendicular to ω_F. $m' = 7$ appears in u_{ar}, whereas $m' = 8$ dominates $u_{az'}$. The two sets of rolls overlap but are centered at different radii. Figure 27 shows cylindrical cuts at distances from the fluid axis corresponding to these two radii. For $m' = 7$, one finds columnar vortices symmetrical about the equatorial plane of the primed coordinate system, whereas the $m' = 8$ vortices are antisymmetric about this plane.

Figure 28 reproduces these and additional observations in a sketch. Two sets of columnar vortices centered at different distances from the fluid axis exist, with wave numbers differing by one. The entire pattern is antisymmetric with respect to reflection at the origin. Individual rolls in the wave with an odd wave number therefore have equal vorticity in the northern and southern hemispheres. Rolls belonging to the wave with an even wave number on the contrary have opposite vorticities in both hemispheres. The designations north and south refer of course to the primed coordinate system. The axial and azimuthal components in the outer roll pattern are of comparable magnitude, whereas $u_{az'}$ is small in the component with odd m'. $u_{az'}$ reaches its extremal values in between the outer vortices. The same sketch is valid for other parameters, except that the values of m' change.

The axisymmetric shear layers that are so conspicuous in experiments have $m'_0 = 0$. They cannot be the origin of the instability in Figure 25. The inviscid spin-over mode also has $m'_0 = 0$ in a sphere, but its viscous counterpart (with boundary layers, internal shear layers, etc.) has $m'_0 = 1$ and triggers the instability in Figure 25. Two additional features are important in ellipsoidal containers. The first is the ellipticity of the streamlines of the Poincaré solutions sketched in Figure 12. If one considers the unperturbed problem to be the eigenvalue problem in a sphere and if one restricts oneself to small ellipticities of the container so that the elliptic deformation of the streamlines can be treated perturbatively, one will find instabilities involving two modes with wave numbers differing by 2. The second source of instability is introduced by the fact that the elliptical streamlines of the Poincaré flow lie in parallel planes and that there is shear between these planes because the

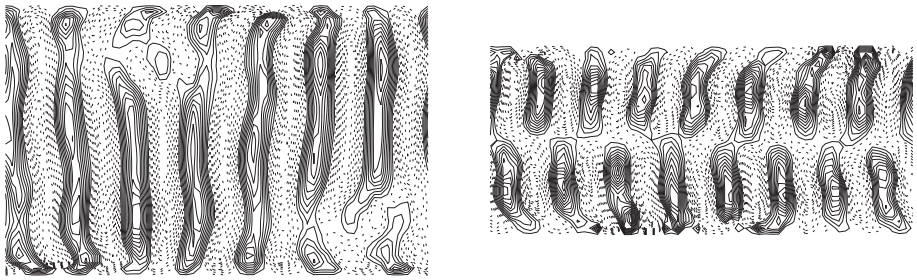

Figure 27 u_{ar} on cylindrical surfaces at distances 0.638 (left) and 0.869 (right) from the $\boldsymbol{\omega}_F$-axis for the same case as in Figures 25 and 26. φ' runs from $-\pi$ to π in going from left to right and θ' is given on the ordinate. Adapted from Lorenzani S and Tilgner A (2001) Fluid instabilities in precessing spheroidal cavities. *Journal of Fluid Mechanics* 447: 111–128, with permission from Cambridge University Press.

line joining the centers of the ellipses is not perpendicular to the plane of the streamlines. This shear couples modes with wave numbers differing by 1. These last two instabilities occur even if viscosity is strictly zero. For this reason, they are classified as inertial instabilities and are more accessible to analytic treatment. Stability criteria are derived in Kerswell (1993b), which show that the instability in **Figure 25** is not due to the elliptical shape of the container, but must be due to viscous corrections to the spin-over mode.

8.07.3.4.2.3 Saturation and turbulence

In order to isolate the two inertial instabilities just mentioned, one must get rid of the viscous boundary layers. This has been done by Lorenzani and Tilgner (2003) by applying free-slip boundary conditions. In this case, a new phenomenon occurs, which is commonly known as resonant collapse: the growing instability does not reach a saturated state but starts to oscillate instead (**Figure 29**). During collapse, a laminar large-scale inertial mode suddenly decays into small-scale turbulence. The small scales draw energy from the large scales, which they dissipate. Once enough energy has been dissipated, the flow becomes laminar and the same instability as before grows once more only to decay into turbulence again. This cycle repeats indefinitely. During the growth phases, the two excited modes have the same qualitative features as those summarized in **Figure 28**. Beyond a certain amplitude of these modes, collapse can occur and E_a returns to small values. **Figure 29** shows an example for parameters far enough beyond the onset of instability so that the variations of the energy are not periodic any more. **Figure 30** demonstrates the appearance and disappearance of small-scale structures in the course of the oscillations.

Laboratory experiments were mostly done with full ellipsoids, but for geophysical applications, the effect of an inner core is of interest. In a simulation with the same parameters as in the preceding text except for an inner core with $\eta = 0.35$, we expect the inner core to cause little change to the resonance conditions because the inertial modes observed without an inner core reach their largest amplitude outside the region now occupied by the inner core. And indeed, the numerical simulation reveals an initial instability with the same pair as before ($m' = 3$ and 4), and the final stage is dominated by the pair $m' = 1$ and 3. However, no collapses occur in this particular case, but small scales remain permanently excited in a statistically stationary state at the end of the run (**Figure 31**).

Lorenzani and Tilgner (2003) had also simulated as closely as possible the experiments of Malkus (1968). It appears from these simulations that the vigorous motions observed in the experiments by Malkus (1968) are likely to be inertial rather than viscous instabilities. This does not exclude the possibility of a viscous instability appearing first at low precession rates. In one case, Malkus had observed a spectacular transition from a chaotic to a fully turbulent flow accompanied by a hysteresis effect (see **Section 8.07.3.3**). Simulations have shown that the sudden increase in turbulence fluctuations and the hysteresis have nothing to do with the onset of a new instability but are rather a manifestation of a reorientation of the vorticity of the underlying Poincaré flow. Turbulence appears at a precession rate at which a reorientation of the fluid axis occurs, too. Quite surprisingly, eqn [34] may have three coexisting solutions, two of which are stable (see Noir et al., 2003). The presence of several solution branches readily explains the hysteresis effect. When the orientation of the basic flow changes abruptly, the strain in the basic flow changes equally abruptly and causes the transition from a more to a less stable flow. We will not consider these effects in any detail here because a catastrophic reorientation as observed in Malkus' experiment is not relevant to the Earth. For $E = 10^{-15}$, $\alpha = 23.5°$, and $e = 1/400$, a similar

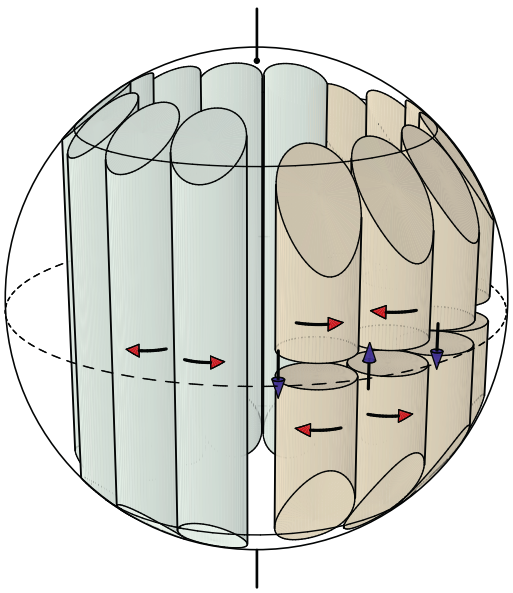

Figure 28 Sketch of the structure of the unstable mode in **Figures 26** and **27**. Reprinted from Lorenzani S and Tilgner A (2001) Fluid instabilities in precessing spheroidal cavities. *Journal of Fluid Mechanics* 447: 111–128, with permission from Cambridge University Press.

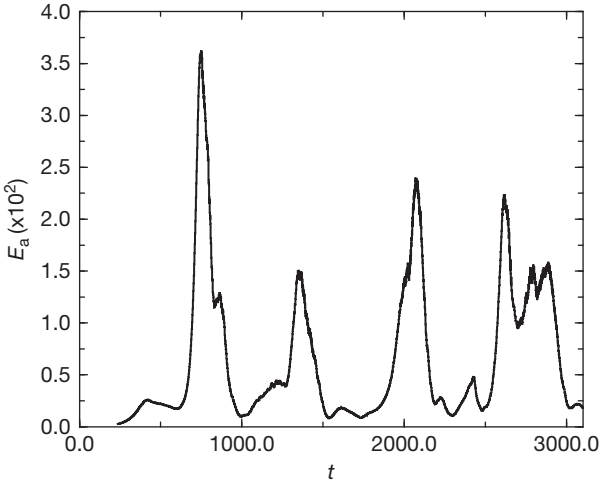

Figure 29 Time evolution of the energy E_a contained in the velocity components antisymmetric with respect to reflection at the origin for $e = 0.06$, $\alpha = 30°$, $\Omega = -0.14$, and $E = 5 \times 10^{-5}$. Adapted from Lorenzani S and Tilgner A (2003) Inertial instabilities of fluid flow in precessing spheroidal shells. *Journal of Fluid Mechanics* 492: 363–379, with permission from Cambridge University Press.

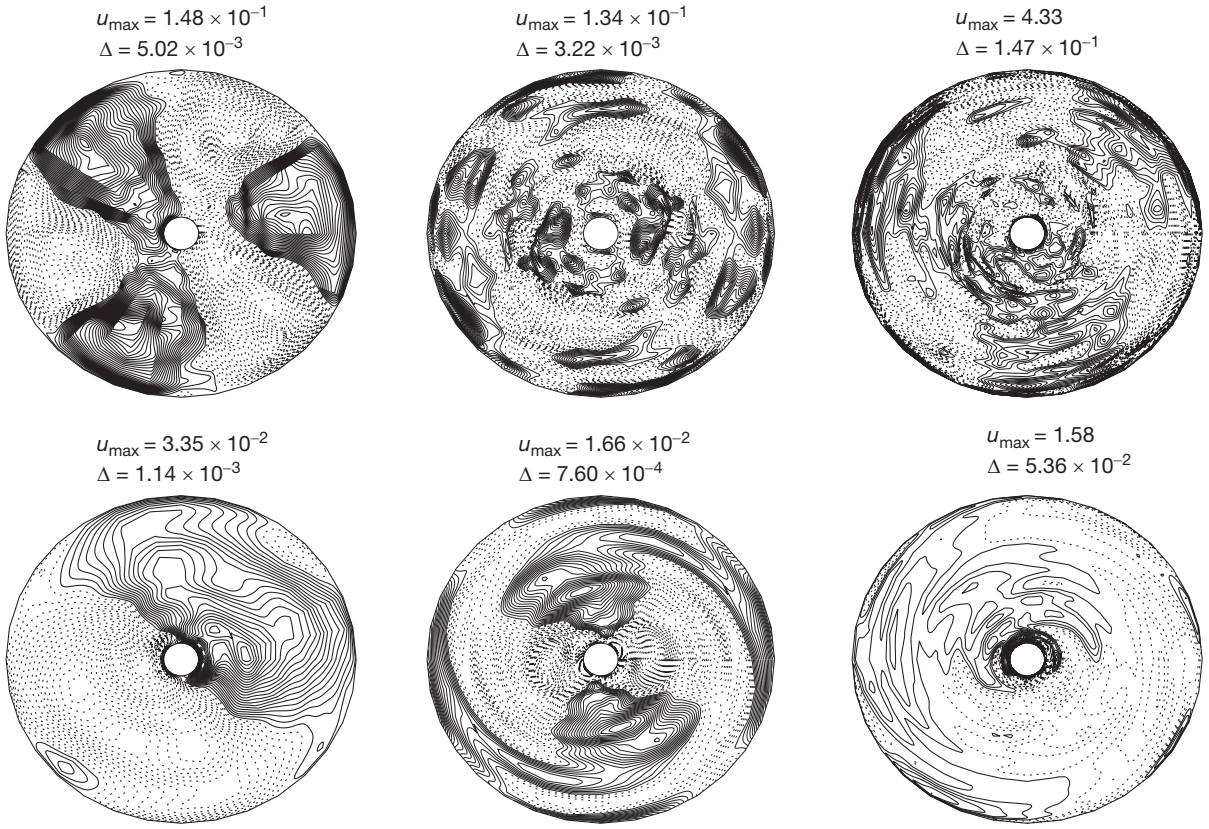
$u_{max} = 1.48 \times 10^{-1}$
$\Delta = 5.02 \times 10^{-3}$
$u_{max} = 1.34 \times 10^{-1}$
$\Delta = 3.22 \times 10^{-3}$
$u_{max} = 4.33$
$\Delta = 1.47 \times 10^{-1}$
$u_{max} = 3.35 \times 10^{-2}$
$\Delta = 1.14 \times 10^{-3}$
$u_{max} = 1.66 \times 10^{-2}$
$\Delta = 7.60 \times 10^{-4}$
$u_{max} = 1.58$
$\Delta = 5.36 \times 10^{-2}$

Figure 30 Pictures of the flow at the times of the first maximum (top) and the first minimum (bottom) in **Figure 29**. The different panels show u_{ar} (left), $u_{az'}$ (middle), and $(\nabla \times \boldsymbol{u}_a)_{z'}$ (right). Adapted from Lorenzani S and Tilgner A (2003) Inertial instabilities of fluid flow in precessing spheroidal shells. *Journal of Fluid Mechanics* 492: 363–379, with permission from Cambridge University Press.

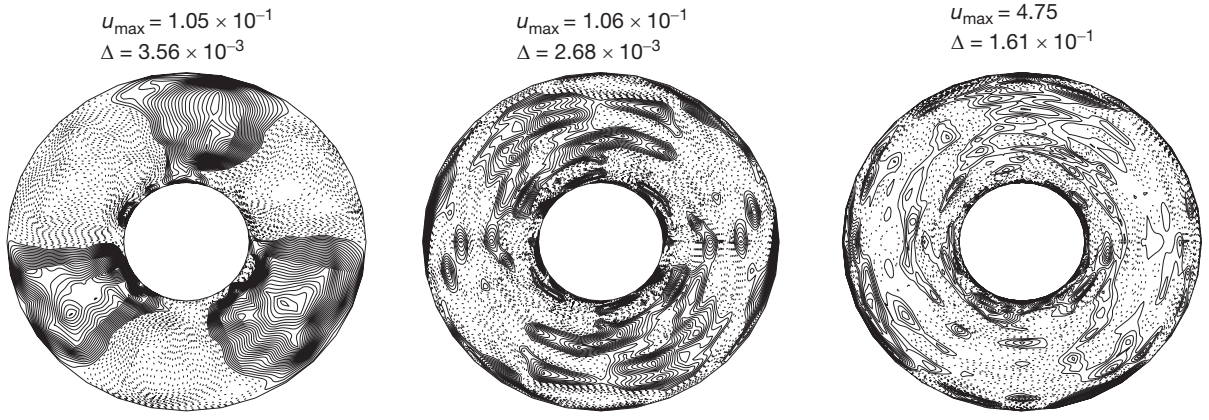

Figure 31 u_{ar} (left), $u_{az'}$ (middle), and $(\nabla \times \boldsymbol{u}_a)_{z'}$ (right) for $e = 0.06$, $\alpha = 30°$, $\Omega = -0.14$, $E = 5 \times 10^{-5}$, and $\eta = 0.35$. Adapted from Lorenzani S and Tilgner A (2003) Inertial instabilities of fluid flow in precessing spheroidal shells. *Journal of Fluid Mechanics* 492: 363–379, with permission from Cambridge University Press.

transition occurs only at $\Omega \approx -10^{-3}$, whereas the actual precession rate of the Earth is $\Omega \approx -10^{-7}$.

8.07.3.4.2.4 Extrapolation to the Earth's core

Two of the instabilities mentioned in this section can be extrapolated to the Earth. First, we expect the Ekman layers in the core to be unstable as mentioned in the preceding text. Then, there are the inertial instabilities. The theory of Kerswell (1993b) has been verified by simulations and can be applied to the core. Unfortunately, according to that theory, the state of precession-driven flow in the Earth's core is uncertain because commonly accepted values of the viscosity of the core put the flow close to its stability limit. Fluid viscosity is one of the least well-constrained material properties of the core. Let us assume

that the core is unstable. The core could then undergo resonant collapses. When collapse occurred in numerical simulations, the growth rate after the collapse was within a factor of 2–3 from the growth rate the same modes have during a linear growth phase starting from a Poincaré solution as described by the perturbation theory. Using the upper bound for the growth rate of an inertial instability given by Kerswell (1993b) applied to Earth's numbers gives a growth rate of 20 000 years^{-1}. Viscosity acts to slow this growth. If collapses play a role in the Earth's core, they could manifest themselves in variations of the magnetic field with a time constant of 20 000 years or longer. There are some indications from paleomagnetic observations for variations that one naively expects in the presence of collapses (Aldridge and Baker, 2003).

On the other hand, we are not able at present to make reasonable guesses concerning the fate of the instabilities due to the axisymmetric shear layers or viscous corrections to the spin-over mode. In all the simulations made so far, the $m'=1$ deviations from a flow with uniform vorticity in the basic state outweigh the $m'=0$ deviations. However, as the Ekman number is decreased, the viscous corrections contributing to the $m'=1$ deviations diminish, whereas the axisymmetric shear layer connecting the critical latitudes becomes more and more singular. An instability of that shear layer is thus plausible at low E. One can determine the typical velocity difference in the $m'=1$ component from visualizations and construct a Rossby number from it. It turns out that this Rossby number increases with the decreasing Ekman number, so that the mechanism related to the $m'=1$ components should remain effective even at the lower Ekman numbers at which the axisymmetric shear layer possibly becomes unstable, too. Since we do not know the stability criterion of these layers, we are not yet able to conclude about the stability of the core flow of the Earth.

8.07.4 Tides

In addition to precession, tidal deformation of the CMB disturbs the rotation of the core flow. Comparatively little space of this chapter is devoted to tidally excited flows despite their potential geophysical significance. This is due to the fact that many ideas on precession-driven flows can be transposed with little modification to tidal flows so that there is not very much new material to present in this section.

We will consider a simple model in which the unperturbed CMB is spherical. Tidal forces deform this boundary into an ellipsoid with the long axis pointing toward the Moon. In this section, all examples will relate to the geometry in which the tidal elongation is perpendicular to the rotation axis, which corresponds to an equatorial tide. Precession is neglected so that tidal effects can be studied in isolation. The orientation of the axis of rotation of the core is not modified by tides. But the streamlines of the core flow, which are circular in the unperturbed core viewed from inertial space, become elliptical due to tidal deformation. Elliptical streamlines also appeared in precession-driven flow (see **Figure 12**) and gave rise to instability. The stability considerations will therefore be very similar for tidal and precessional flows.

The deformation of the boundary in an equatorial tide is characterized by an azimuthal wave number $m=2$. Suppose that the tidal companion is fixed in inertial space. The flow then varies in the mantle frame with a frequency twice the rotation frequency, that is, $\omega=2$ in our dimensionless units. $\omega<2$ if the tidal companion is in prograde rotation.

Let us first look at internal shear layers, which may modify the inviscid picture of **Figure 12**. For $\omega=2$, the group velocity of inertial waves is perpendicular to the rotation axis, and critical latitudes are exactly at the poles. We therefore do not expect a pattern of multiply reflected internal layers as in the precessional case. But nonlinear interactions may start an axisymmetric shear layer at critical latitudes, which in the tidal case degenerates to a line joining the poles. Suess (1971) built an experiment to confirm the existence of such a shear zone. In this experiment, a flexible water-filled sphere was set into rotation. The sphere was deformed into an ellipsoid by a ring surrounding the equator of the sphere. The ring was fixed in the laboratory frame. The experiment confirmed the existence of a shear zone connecting the poles and revealed a second, albeit much weaker, axisymmetric shear layer at half the radius of the sphere. The origin of this second layer is unknown. A more recent experiment (Morize et al., 2010) allowed for a deformation that rotates in the laboratory frame in order to simulate a moon in prograde rotation. Even more axisymmetric shear layers appeared in this case, in line with numerical calculations (Tilgner, 2007b).

We proceed further in the analogy with precession-driven flow and investigate the stability of the flow, ignoring the shear zones just discussed. For small ellipticities, we can again apply the perturbation expansion of **Section 8.07.3.4.2** (see also **Section 8.07.5**). This analysis tells us that tidal distortion couples in triad resonances two inertial modes whose azimuthal wave numbers and frequencies differ by 2. There is also a more intuitive explanation for the instability of tidal flow. Imagine looking at the flow along the rotation axis from inertial space. One then sees elliptical streamlines. Let us represent the elliptical streamlines in a plane $z=$constant with major axes along x and y by the stream function $\Psi=(1+\delta)x^2+(1-\delta)y^2$, where δ measures the deformation from the undeformed stream function x^2+y^2. The corresponding velocity field, $\nabla\times(\Psi\hat{\boldsymbol{z}})$, fits into any container whose boundaries in every plane $z=$constant are ellipses (such as ellipsoids or ellipsoidal cylinders) with a ratio of long and short semiaxes of $[(1+\delta)/(1-\delta)]^{1/2}$. Ψ may be rewritten in the more suggestive form:

$$\Psi=\left(x^2+y^2\right)+\delta\left(x^2-y^2\right) \qquad [47]$$

The first bracket is the stream function in absence of tidal deformation. The second term, proportional to δ, describes hyperbolic streamlines with axes oriented at 45° of the x- and y-axes.

Perturbing vorticity is amplified along the stretching direction of the hyperbolic streamlines. The effect of the stretching is most easily recognized in a deformed cylindrical vortex (instead of a vortex encased in an ellipsoid) infinitely extended along the z-axis with the stream function given by eqn [47]. It is a simple exercise to verify that this vortex is unstable with respect to a perturbation of the form $(-\hat{\boldsymbol{x}}+\hat{\boldsymbol{y}})\times\boldsymbol{r}$, which grows at rate $\delta/2$. Indeed, the equation governing the stability

of the basic flow $\boldsymbol{u}_0 = \nabla \times (\Psi \hat{\boldsymbol{z}})$, namely, eqn [46] in an inertial frame of reference,

$$\frac{\partial}{\partial t}\nabla \times \boldsymbol{u}' + \nabla \times [(\nabla \times \boldsymbol{u}') \times \boldsymbol{u}_0] + \nabla \times [(\nabla \times \boldsymbol{u}_0) \times \boldsymbol{u}'] = 0 \quad [48]$$

is solved by the perturbation $\boldsymbol{u}' = (-\hat{\boldsymbol{x}} + \hat{\boldsymbol{y}}) \times \boldsymbol{r} e^{t \cdot \delta/2}$. This is a solid body rotation stationary in inertial space. In other words, this is a flow of spatially constant vorticity.

In ellipsoids, the simplest unstable mode is also a constant vorticity flow. A potential flow added to the solid body rotation accommodates the boundary conditions. The growth rate of the constant vorticity flow in the ellipsoid depends on the relative sizes of the axes of the ellipsoid. When the vorticity is constant in inertial space, its axis is rotating in the mantle frame with $\omega = 1$. This unstable mode can be represented in the mantle frame as a superposition of the spin-over mode, which varies as $e^{-i(\varphi - t)}$, and its complex conjugate, which varies in $e^{i(\varphi - t)}$. These two modes fulfill the selection rules on wave number and frequency for a triad resonance stated in the next section. Other pairs of modes satisfying the selection rules can be excited as well, but their vorticity is directed parallel to the $(-\hat{\boldsymbol{x}} + \hat{\boldsymbol{y}})$ direction only in the time average. Computations of stability limits and many more fluid dynamic aspects of elliptical instabilities are reviewed in detail in Kerswell (2002).

Several experiments have investigated the instability of elliptically deformed rotating flows, either in cylindrical or in spheroidal geometry (Aldridge et al., 1997, 2007; Eloy et al., 2000; Gledzer and Ponomarev, 1992; Lacaze et al., 2004, 2005; Malkus, 1989; Seyed-Mahmoud et al., 2004). These experiments use one of two methods to realize the required deformation. Most use deformable containers in the same fashion as Suess (1971) (see **Figure 32**). Gledzer and Ponomarev (1992) used an interesting alternative. They spun up fluid in an ellipsoid or a cylinder with ellipsoidal cross section and abruptly stopped the rotation of the container. The fluid continues to rotate due to its inertia and forms a vortex with elliptical streamlines. This vortex is prone to elliptical instability, an example of which is shown in **Figure 33**.

In all cases, excellent agreement with theory has been obtained. After instability, the system settles in a state of one of three possible types, again in analogy with precession. Either a stationary state is reached, or the flow ends in a turbulent and statistically stationary state, or the flow undergoes resonant collapses. There is no understanding or systematic data on which of these three possibilities is realized under which circumstances.

The good agreement between theory and experiment concerning the stability criterion of tidal flow gives us confidence that we can apply this theory to the Earth. From the rotation rate of the Earth and the tidal deformation of the CMB, one computes a growth rate for instabilities in inviscid fluid of approximately 1/(7000 years) (Aldridge et al., 1997). This growth rate is lowered to $10^{-6}\,\text{year}^{-1}$ by viscous damping if the Ekman number of the core is 0.3×10^{-15}. If magnetic dissipation is also taken into account, it is unclear whether the Earth's core is unstable to tidal deformation (Kerswell, 1994), depending mostly on what the precise Ekman number of the core is and on whether the magnetic field is created by the tidal flow itself or by independent convection-driven flow (Cébron et al., 2012).

8.07.5 Interaction with Buoyancy and Magnetic Fields

Up to now, we have only considered neutrally buoyant fluid. This has greatly simplified the analysis and has allowed us some direct comparison with experiments. Eventually, we will have to incorporate thermal and magnetic effects for the geophysical application. Relatively little work has been done in this direction until today so that we are left with many

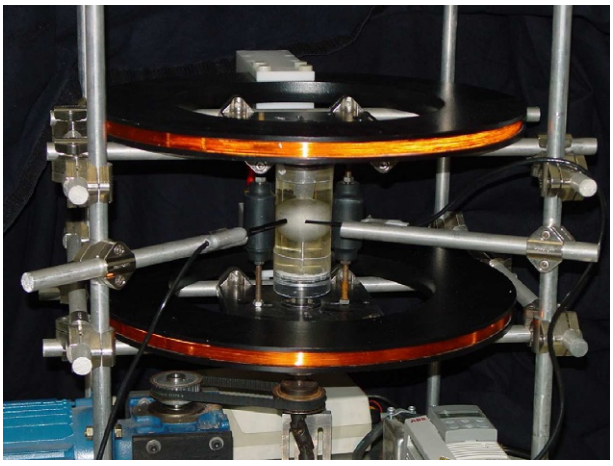

Figure 32 Experimental apparatus for the study of tidal instabilities in use at the 'Institut de Recherche sur les Phénomènes hors Equilibre' in Marseille, France. The fluid under study is in the container of opaque and ellipsoidal appearance in the center of the picture, which is mounted on a rotating shaft and compressed and deformed by two gray cylindrical rollers with their axis parallel to the rotation axis. The rollers are stationary in the laboratory frame. A pair of Helmholtz coils allows the study of induction effects if gallium is used as fluid. Courtesy of L. Lacaze and P. Le Gal, see also Lacaze et al. (2006).

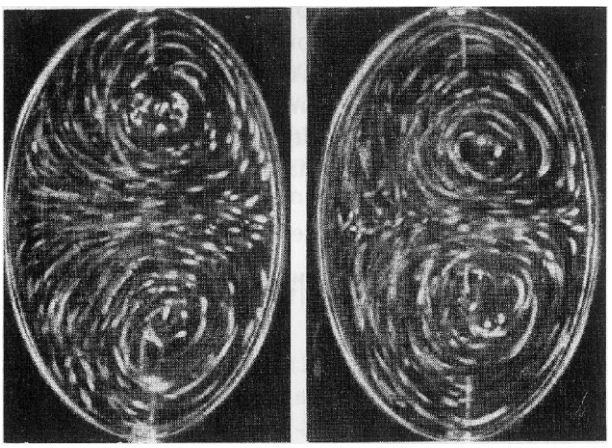

Figure 33 Elliptical instability in an ellipsoid. Streamlines are made visible with suspended particles. A flow with two eddies is excited by the instability. The eddies are time-dependent as evidenced by the two panels, which show the flow a short time interval apart. Reprinted from Gledzer E and Ponomarev V (1992) Instability of bounded flows with elliptical streamlines. *Journal of Fluid Mechanics* 240: 1–30, with permission from Cambridge University Press.

uncertainties. This section reviews the open questions and a few plausible but unproven answers.

As far as thermal effects are concerned, we have to distinguish between the assumptions that the core is convecting or that it is stably stratified. Let us consider the latter possibility first. Stable stratification generally suppresses fluid motion, at least along the density gradient. But it also allows internal waves, which combine with pure inertial waves to form gravitoinertial waves. These waves have properties similar to inertial waves. In particular, discontinuities form on characteristic surfaces, which, however, are not conical any more (Dintrans et al., 1999). The inviscid spin-over mode has no radial component and is thus unaffected by thermal stratification in a sphere. Laminar precession-driven flow cannot differ in any significant way in stable and neutral fluids, so that the instability mechanism through triad resonances can also operate in a stably stratified fluid by coupling gravitoinertial waves. Radial stratification is no impediment to instability (Kerswell, 1993a), but in order to reach equal radial velocity, much more energy must be pumped into the flow compared with the neutral case because of the potential energy stored in the deformation of the background stratification.

If, on the other hand, the core is convecting, the time-averaged temperature distribution equals the adiabatic profile, so that the fluid is on average neutrally buoyant, but perturbations like precession now act on a medium, which is not at rest. This could modify the precession-driven flow through the nonlinear term in the Navier–Stokes equation. The Rossby number (already introduced in Section 8.07.1.2) estimates in order of magnitude the ratio of the nonlinear and Coriolis terms and is $U/(\omega_D L)$ for a motion of typical velocity U and size L in the core, which rotates at the rate ω_D. This number is about 10^{-5} for the whole core using for U velocities deduced from secular magnetic variation and is thus very small. In the first step, let us completely neglect the nonlinear term. Within this approximation, flows driven by different agents superpose linearly. Large-scale structures of inertial modes are therefore unchanged by convection. In particular, the orientation of the fluid axis is unaffected by convection. Dropping the nonlinear term from the Navier–Stokes equation eliminates both the axisymmetric shear layers and the instabilities. We therefore reinstate that term and treat it as a small perturbation. Within this framework, the nonlinear interaction of the (non-axisymmetric) viscous spin-over mode with itself yields an axisymmetric driving term (a Reynolds stress in the language of fluid mechanics), which drives the axisymmetric shear layers. The presence of convective motion adds new contributions to the total axisymmetric driving force but does not remove the one set up by precession. The cylindrical shear layers typical of precession-driven flow thus cannot disappear because of a background of convective motion. At the small scales of the shear zones, L in the expression for the Rossby number becomes small so that the Rossby number can be larger than 1. Significant interaction between convection and precession thus may occur at small scales, in which, for example, convective motion acts like an eddy diffusivity, which broadens shear zones.

We will next show that inertial instabilities of the Poincaré flow also survive in the presence of convection. To see this, it is helpful to have a more formal look at the perturbation calculation mentioned in Section 8.07.3.4.2. Let us start from eqn [46] the linearized inviscid equation of motion valid in the mantle frame for a velocity perturbation $\boldsymbol{u}'$ on top of a basic flow field $\boldsymbol{u}_0$, so that the total velocity is $\boldsymbol{u}_0+\boldsymbol{u}'$. We consider the third and fourth terms to be perturbations compared with the Coriolis term and denote them formally as $\epsilon\mathcal{V}\mathbf{u}'$, where $\mathcal{V}$ is a linear operator acting on $\boldsymbol{u}'$ and ϵ is a bookkeeping parameter that allows us to keep track of the different orders of a perturbation calculation. The uncurled equation eqn [46] becomes

$$\frac{\partial}{\partial t}\boldsymbol{u}'+2\hat{\boldsymbol{z}}\times\boldsymbol{u}'+\nabla p'+\epsilon\mathcal{V}\boldsymbol{u}'=0 \qquad [49]$$

in which $\nabla p'$ is a pressure gradient. Inertial modes with frequency ω_j, which we compactly write as $e^{i\omega_j t}\boldsymbol{\Phi}_j(\boldsymbol{r})$, and their associated pressure p_j are solutions of the unperturbed ($\square=0$) problem:

$$i\omega_j\boldsymbol{\Phi}_j(\boldsymbol{r})+2\hat{\boldsymbol{z}}\times\boldsymbol{\Phi}_j(\boldsymbol{r})+\nabla p_j(\boldsymbol{r})=0 \qquad [50]$$

The $\boldsymbol{\Phi}_j$ are mutually orthogonal (Greenspan, 1968). With the appropriate normalization of the $\boldsymbol{\Phi}_j$, the integral over the fluid volume $\int\boldsymbol{\Phi}_k^*\boldsymbol{\Phi}_j dV=\delta_{j,k}$. We write the solution of eqn [49] as a linear combination of eigenmodes

$$\boldsymbol{u}'=\sum_j c_j(t)e^{i\omega_j t}\boldsymbol{\Phi}_j(r),\quad p'=\sum_j c_j(t)e^{i\omega_j t}p_j(\boldsymbol{r}) \qquad [51]$$

and pose an expansion of the coefficients c_j in ε as

$$c_j=c_j^{(0)}+\epsilon c_j^{(1)}+\epsilon^2 c_j^{(2)}+\cdots \qquad [52]$$

Order ϵ^0 yields $(d/dt)c_j^{(0)}=0$. We obtain at order ϵ^1 by projecting eqn [49] on mode $\boldsymbol{\Phi}_k$ and multiplying by $e^{-i\omega_k t}$:

$$\frac{d}{dt}c_k^{(1)}=-\sum_j c_j^{(0)}e^{i\left(\omega_j-\omega_k\right)t}\int\boldsymbol{\Phi}_k^*\mathcal{V}\boldsymbol{\Phi}_j dV \qquad [53]$$

If we remember that $\boldsymbol{\Phi}_j$ depends on azimuth as $e^{-im_j\varphi}$, we can derive the selection rule on azimuthal wave number for a triad resonance used in Section 8.07.3.4.2 from the requirement that the integral in eqn [53] must be different from 0. Suppose that $\boldsymbol{u}_0$, and hence $\mathcal{V}$, depends on azimuth as $\cos m_0\varphi$. The integral on the right-hand side of eqn [53] contains the term $e^{im_k\varphi}\cos(m_0\varphi)e^{-im_j\varphi}$ whose integral over φ is different from 0 only if $|m_k-m_j|=m_0$. A similar reasoning provides us with a condition on the eigenfrequencies of the two coupled inertial modes. Suppose that $\boldsymbol{u}_0$, and hence $\mathcal{V}$, depends on time as $\cos\omega_0 t$. The right-hand side of eqn [53] then contains two terms, with time dependences $e^{i\left(\omega_j-\omega_k+\omega_0\right)t}$ and $e^{i\left(\omega_j-\omega_k-\omega_0\right)t}$. There is resonance, that is, $c_k^{(1)}$ grows to infinity, if $|\omega_j-\omega k|=\omega_0$. Equation [53] is linear in $\mathcal{V}$ or $\boldsymbol{u}_0$. If $\boldsymbol{u}_0$ contains more than one frequency, only one of them can couple any two inertial modes. It is for this reason that we do not expect convective motion to modify the onset of instabilities found in Section 8.07.3.4.2: in the mantle frame, the precession-driven basic flow has $\omega_0=1$, that is, it varies on a diurnal timescale. Convection on the contrary is believed to vary on much longer timescales of decades or longer. For instance, the turnover time is approximately 1 ky for an eddy spanning the gap between the inner core and the CMB with a flow velocity of 0.1 mm s^{-1}. An instability involving a triad resonance between precession-driven flow and two inertial modes will thus be unaffected by

convection simply because convection is far off that resonance. The same holds true for tidally driven motion. If the tidal companion is fixed in space, the tidal disturbance is characterized by $\omega_0 = 2$ in the aforementioned equations, which is again faster than convective timescales.

As the amplitudes of the unstable modes grow according to eqn [53], the coupling term in eqn [49] will eventually become large and higher orders of perturbation come into play. The unstable modes end in a saturated state or in resonant collapse. At this stage, noteworthy interaction between buoyancy and precession or tides is possible and will have to be investigated in the future.

The argument in the preceding text shows that precessional or tidal instability can grow on top of an already established convective flow by treating a nonlinear term perturbatively. It does not preclude important interactions between thermal stratification and mechanical instability at the level of the linear terms, which means that coexisting thermal stratification and mechanical forcing can stabilize and destabilize each other. Examples for both possibilities are known (Kerswell, 1993a; Le Bars and Le Dizès, 2006). In the context of tidal excitation, both numerical simulations in spheroids (Cébron et al., 2010) and experiments with cylinders (Lavorel and Le Bars, 2010) have demonstrated that a stabilizing thermal gradient can destabilize tidal flow. These studies have also confirmed that triad resonances can grow within established convection flow, and they pointed out that tidal flow contributes to heat transport.

Studies of the influence of magnetic fields involve some arbitrariness since we do not know the magnetic field inside the core. Oblique shear layers also exist in the magnetohydrodynamic case, but they acquire a more oscillatory structure than before. The inertial waves forming the internal shear layers couple to the magnetic field and send off magnetic waves, which occupy a much larger fraction of the fluid volume than the shear layers. At strong enough magnetic fields, these layers also change orientation. This has been observed in numerical simulations in spherical shells (Tilgner, 1999b) and more accurately in infinitely extended fluids (Tilgner, 2000). Kerswell (1994) investigated the damping effect of magnetic fields on instability of tidal flow and concluded that, for Earth's parameters, the magnetic damping is of comparable magnitude as the viscous damping.

The internal shear layers of the spin-over mode dominate the dissipation of that mode, by both viscous dissipation and ohmic dissipation if a magnetic field is present. Buffett (2010) showed that these internal shear layers account for the observed dissipation in Earth's nutations assuming reasonable magnetic field strengths and the fluid viscosity given in **Table 1**. The internal shear layers sufficiently deform the magnetic field so that ohmic dissipation dominates and the observed damping of the nutations can be explained without invoking unplausible fluid viscosities.

Finally, we may wonder whether precession-driven flow itself is capable of generating a magnetic field. The inviscid constant vorticity flow has streamlines confined to parallel planes. Efficient dynamo action requires additional flow components, which can be provided by the Ekman pumps or instabilities. In particular, the instability sketched in **Figure 28** looks promising because it is not unlike the helical columnar structure familiar from rotating convection. Simulations by Tilgner (2005) have shown that both mechanisms indeed modify the constant vorticity flow such that it can sustain magnetic fields at the magnetic Reynolds numbers on the order of the magnetic Reynolds number of the Earth's core. The Ekman pumps by themselves are too weak for field generation in the Earth. It has already been shown by Loper (1975) and Rochester et al. (1975) that energy considerations exclude a geodynamo if the core flow is laminar. But unstable precessional flow remains a plausible alternative to convection-driven flow to explain the geodynamo.

However, precessional flow varies on a diurnal timescale in the mantle frame so that one could expect the magnetic field to do the same, in which case, it would be mostly screened because of the finite conductivity of the mantle. Surprisingly, magnetic field variation in the one simulation available so far occurs mostly on a timescale slower than diurnal. In addition, the dipole moment, which lies near the equatorial plane in that simulation, exhibits random sudden reorientations reminiscent of reversals (see **Figure 34**). Future research will have to tell whether this behavior is typical, whether it persists in the presence of convectively driven motion (in which case, precession might act as a trigger for reversals in dynamos driven by buoyancy), and whether precession-driven dynamos can also produce axial dipoles.

All known precession-driven dynamos in spheres (Tilgner, 2005, 2007a) produce multipolar magnetic fields unlike the dipole-dominated field of the Earth. Wu and Roberts (2009) investigated a precession-driven dynamo in spheroidal geometry and found on the contrary a very smooth magnetic field. Precession-driven dynamos apparently do not generically produce spatially complicated magnetic fields and remain a plausible model for the geodynamo from this point of view.

Since the discovery of precession-driven dynamos in spheres and spheroids, dynamo simulations have also been performed for precessing plane layers (Wu and Roberts, 2008), cubes (Krauze, 2010), and cylinders (Nore et al., 2011). Especially, the cylindrical geometry is of interest for laboratory experiments aiming at demonstrating the dynamo

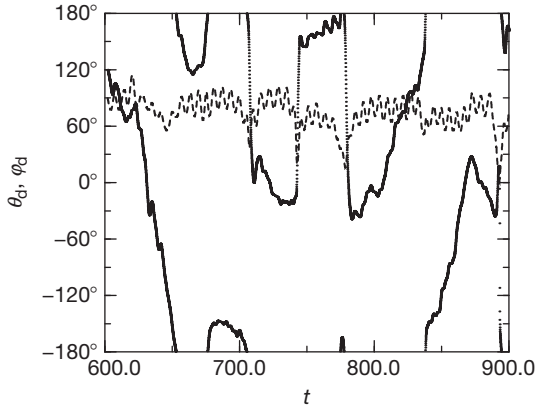

Figure 34 Time series of the polar angles θ_d, the angle between the dipole moment and the rotation axis (dashed line), and φ_d, the angle between the dipole moment and an arbitrary meridian (densely dotted line, appearing continuous for most of the time), for a simulation of a precession-driven dynamo. Reprinted from Tilgner A (2005) Precession driven dynamos. *Physics of Fluids* 17: 034104.

effect in precessing vessels filled with liquid sodium (Gans, 1970; Stefani et al., 2012).

Further consideration of triad resonances driving a dynamo has been inspired by the study of other celestial bodies. The work most directly related to the contents of this chapter is the work by Dwyer et al. (2011) who invoke precession as the possible driving mechanism behind the magnetic field of the early Moon. Similarly, Le Bars et al. (2011) proposed that flow in the Moon's core gone unstable via a triad resonance caused the Moon's magnetic field, but this time, the mechanical driving is provided by collisions rather than a gravitational torque and precession. Receding further from the Earth, Arkani-Hamed et al. (2008) put forward a theory according to which tidal deformation of Mars is responsible for the ancient magnetic field of Mars, the tide being due to an asteroid that stayed long enough close to Mars before falling onto Mars and creating the major impact craters visible on the surface of Mars nowadays.

8.07.6 Summary and Outlook

This chapter has dealt with perturbations of uniform rotation of the liquid core. Because of a lack of direct observations, we have to use a combination of theory, numerical simulations, and laboratory experiments to guide our intuition about core flow. **Section 8.07.2** allowed for arbitrary perturbations as long as the response of the core can be described by linearized equations of motion, that is, the excited amplitude must be small. The following two sections were concerned with perturbations of arbitrary amplitude but of specific type: precession of the axis of rotation of the Earth and tidal deformation of the CMB. The primary response of the core to precession is a rotation of the core about an axis that forms an angle of 1.7×10^{-5} with the axis of rotation of the mantle. This leads to velocities of the core relative to the mantle of up to 4.3 mm s^{-1}, which is much larger than velocities inferred from magnetic secular variation and large enough to cause instability of the boundary layer at the CMB. A summary of numerical values that appeared in **Sections 8.07.3** and **8.07.4** is given in **Table 2**.

A uniformly rotating core is an assumption routinely used in the interpretation of geodetic observations (Matthews et al., 1991a,b). In this context, it is enough to get the core's angular momentum right. Simulations presented in this chapter show that while even the simplest analytic models accurately predict the core's rotation vector, the detailed structure of the actual flow looks quite different from a flow with constant vorticity because the constant vorticity flow does not satisfy all boundary conditions and is prone to instabilities in an ellipsoidal container.

All the flows found in this chapter are marked by internal shear zones. There are two origins for internal shear layers. One is the breakdown of the Ekman layers. Boundary layers in rotating fluids are generally characterized by a balance between the Coriolis and viscous forces. Exceptionally, a different equilibrium is possible when the Coriolis force is balanced by inertia. The scalings of the boundary layer thickness and velocities are then different from the usual Ekman layer. This occurs where shear zones tangential to the boundaries exist. The local accident in the boundary layers starts internal shear layers. These layers become weaker for the decreasing Ekman number at equal bulk rotational energy of the fluid. The situation is different for those shear layers, which are due to the geometry of the boundaries (e.g., inner and outer boundaries of different ellipticities). These layers become more pronounced with the decreasing Ekman number and must turn into singularities in the limit of the zero Ekman number. These shear layers have the largest contribution to dissipation, be it viscous or ohmic dissipation, and must be taken into account in the analysis of Earth's nutations (Buffett, 2010).

Precession and tides provide nonaxisymmetric forcing, which excites directly a nonaxisymmetric flow. Through nonlinear interaction, the flow acquires an axisymmetric component, which typically contains cylindrically shear layers. These layers are very prominent in experimental visualizations.

The velocities in these shear zones are, under all reasonable assumptions, small compared with flow velocities deduced from magnetic secular variation. It is therefore possible that these layers are of little geophysical relevance, unless they are hydrodynamically unstable and excite stronger flow through instabilities. Early experiments nourished the intuition that axisymmetric shear layers are at the origin of instabilities in precession-driven flow. This impression may simply have arisen because of the visualization method employed in the experiments. The condition for stability of these layers is presently unknown, and we cannot conclude about their stability in the core.

Several instability mechanisms have been identified in numerical simulations. First, there is the boundary layer instability alluded to in the preceding text. This instability is confined to the boundary layers and does not modify the flow globally. The bulk of the flow is affected by the second mechanism, which is the triad resonance in which the basic flow excites a pair of inertial modes. Several variants of this mechanism have been found, depending on what component of the flow triggers the instability. Either it can be internal flow caused by viscous interactions at the boundaries or it can be

Table 2 A summary of the best estimates obtained in **Sections 8.07.3** and **8.07.4** for different characteristics of precessing and tidal core flows

Angle between fluid axis and geographic axis	1.7×10^{-5}
Maximal velocity of core fluid relative to mantle	4.3 mm s^{-1}
Velocity in inclined shear layers, connected to the CMB at critical latitudes	6×10^{-6} m s^{-1}
Velocity in inclined shear layers, connected to the inner core at critical latitudes	1.2×10^{-5} m s^{-1}
Axisymmetric prograde jet on the cylindrical surface joining the critical latitudes on the CMB	3×10^{-5} m s^{-1}
Growth rate of inertial instabilities excited by precession	$<(20\ \text{ky})^{-1}$
Growth rate of inertial instabilities excited by tides	$<(7\ \text{ky})^{-1}$

Note that we do not have any estimate for the axisymmetric shear layer attached to the inner core excited by precession.

distortions of the solid body rotation of the core introduced by the shape of the boundaries. Our understanding of the latter type of excitation is good enough, so that we can extrapolate numerical and analytic results to Earth's parameters. It turns out that both precessional excitation and tidal excitation are close to the stability limit. Neither mechanism is clearly above or below the threshold for instability. Any prediction on the stability limit requires knowledge of the viscosity of the core. However, viscosity is one of the least constrained properties of the core.

A phenomenon commonly observed in experiments is the resonant collapse, in which cyclically unstable modes grow and suddenly decay because they draw energy from the basic flow, which then become too weak to sustain the unstable modes. There is no theory yet telling us under which conditions these collapses occur instead of the flow simply reaching a stationary state. We therefore do not know whether to expect such collapses in the core.

The hydrodynamic stability of the core flow is crucial in connection with the geodynamo. A simple rotation cannot generate a magnetic field. The rotation must be perturbed in a nontrivial way. Convection flows notoriously are dynamos, but unstable precession-driven flows are, too.

Most models reviewed in this chapter have neglected buoyancy. Viewed from a frame of reference attached to the mantle, convective flows occur on a much slower timescale than precessional or tidal flow. For this reason, the stability properties of precessional or tidal flows are basically unaltered by coexisting convection.

It can be hoped that simulations coupled with observations of the Earth will allow us to decide which of the aforementioned mechanisms is relevant for the core. For instance, measurements of tidal torques put upper bounds on the energy dissipated in the core due to tidal forcing. Current estimates yield approximately 100 GW for the dissipation in the solid Earth (Ray et al., 1996, 2001), an unknown fraction of which occurs in the mantle. If the full 100 GW were available in the core, it could be enough to drive the geodynamo. At any rate, the dissipation is large enough so that we cannot exclude that tidally driven flow contributes significantly to the core dynamics.

Similarly, dissipation of precession-driven flow must show in changes of orbital parameters of the Earth and the Moon. Changes of the rotation rate of the Earth do not provide us with stringent constraints on precessional dissipation (see **Section 8.07.3.2**), and there is no published work on the effect that this dissipation has on the Moon, which leaves room for future investigation.

Apart from geodetic and astronomical observations, the magnetic field may give interesting indications. The internal shear zones introduced by precession are too weak to be of direct relevance for the geomagnetic field (Busse, 1968; Pais and LeMouël, 2001). But if precession or tides are important, variations of the magnetic field and orbital parameters correlate. It has been claimed that correlations indeed exist between orbital parameters and paleomagnetic intensity and inclination (Channell et al., 1998; Yamazaki and Hirokuni, 2002). However, these claims have been disputed (Valet, 2003). A more robust piece of data is the sequence of reversals. This sequence also seems to reveal a preferred interval between reversals of 100 ky (Consolini and DeMichelis, 2003). The period of 100 ky equals a period at which the eccentricity of the orbit of the Earth changes so that a small modulation of the precession rate with the same period is expected. However, it is far from clear that the amplitude of this modulation is large enough to have any direct effect on the geodynamo. Finally, the magnetic field may carry a signature of resonant collapses, such as slow increases in field intensity followed by sudden decreases. An analysis of the paleomagnetic record by Aldridge and Baker (2003) suggests that events of this type indeed occur.

The sheer magnitude of the flow velocity of the core relative to the mantle induced by precession shows that precession cannot be ignored in a description of core dynamics. Many open questions remain concerning the consequences precession or tides may have on the stability of the bulk of core flow and the geodynamo. Future progress in theory, simulation, and observations will have to tell us how rotational dynamics of the core interact with the geodynamo.

References

Acheson D (1990) *Elementary Fluid Dynamics*. Oxford: Clarendon Press.

Aldridge K (1975) Inertial waves and the Earth's outer core. *Geophysical Journal of the Royal Astronomical Society* 42: 337–345.

Aldridge K and Baker R (2003) Paleomagnetic intensity data: A window on the dynamics of Earth's fluid core? *Physics of the Earth and Planetary Interiors* 140: 91–100.

Aldridge K, Baker R, and Mcmillan D (2007) Rotating parametric instability in early Earth. *Geophysical and Astrophysical Fluid Dynamics* 101: 507–520.

Aldridge K and Lumb L (1975) Inertial waves identified in the Earth's fluid outer core. *Nature* 325: 421–423.

Aldridge K, Seyed-Mahmoud B, Henderson G, and van Wijngaarden W (1997) Elliptical instability of the Earth's fluid core. *Physics of the Earth and Planetary Interiors* 103: 365–374.

Aldridge K and Toomre A (1969) Axisymmetric inertial oscillations of a fluid in a rotating spherical container. *Journal of Fluid Mechanics* 37: 307–323.

Arkani-Hamed J, Seyed-Mahmoud B, Aldridge K, and Baker R (2008) Tidal excitation of elliptical instability in the Martian core: Possible mechanism for generating the core dynamo. *Journal of Geophysical Research* 113: E06003.

Beardsley R (1970) An experimental study of inertial waves in a closed cone. *Studies in Applied Mathematics* 49: 187–196.

Boisson J, Cébron D, Moisy F, and Cortet P-P (2012) Earth rotation prevents exact solid body rotation of fluids in the laboratory. *Europhysics Letters* 98: 59002.

Bondi H and Lyttleton R (1953) On the dynamical theory of the rotation of the Earth: The effect of precession on the motion of the liquid core. *Proceedings of the Cambridge Philosophical Society* 49: 498–515.

Buffett B (1996) Inner core rotation: A test at the worldwide scale. *Geophysical Research Letters* 23: 3803–3806.

Buffett B (2010) Tidal dissipation and the strength of the Earth's internal magnetic field. *Nature* 486: 952–954.

Bullard E (1949) The magnetic field within the Earth. *Proceedings of the Royal Society A* 197: 433–453.

Busse F (1968) Steady fluid flow in a precessing spheroidal shell. *Journal of Fluid Mechanics* 33: 739–751.

Cébron D, Le Bars M, Moutou C, and Le Gal P (2012) Elliptical instability in terrestrial planets and moons. *Astronomy and Astrophysics* 539: A78.

Cébron D, Maubert P, and Le Bars M (2010) Tidal instability in rotating and differentially heated ellipsoidal shell. *Geophysical Journal International* 182: 1311–1318.

Channell J, Hodell D, McNamus J, and Lehman B (1998) Orbital modulation of the Earth's magnetic field intensity. *Nature* 394: 464–468.

Consolini G and DeMichelis P (2003) Stochastic resonance in geomagnetic polarity reversals. *Physical Review Letters* 90: 058501.

Courant R and Hilbert D (1968) *Methoden der Mathematischen Physik*. Berlin: Springer.

Dintrans B, Rieutord M, and Valdettaro L (1999) Gravito-inertial waves in a rotating stratified sphere or spherical shell. *Journal of Fluid Mechanics* 398: 271–297.

Dwyer C, Stevenson D, and Nimmo F (2011) A long-lived lunar dynamo driven by continuous mechanical stirring. *Nature* 479: 212–214.

Eloy C, Le Gal P, and Le Dizès S (2000) Experimental study of the multipolar vortex instability. *Physical Review Letters* 85: 3400–3403.

Gans R (1970) On hydromagnetic precession in a cylinder. *Journal of Fluid Mechanics* 45: 111–130.
Gledzer E and Ponomarev V (1992) Instability of bounded flows with elliptical streamlines. *Journal of Fluid Mechanics* 240: 1–30.
Goldstein H (1980) *Classical Mechanics*. Reading, MA: Addison-Wesley.
Goto S, Ishii N, Kida S, and Nishioka M (2007) Turbulence generator using a precessing sphere. *Physics of Fluids* 19: 061705.
Greenspan H (1968) *The Theory of Rotating Fluids*. Cambridge: Cambridge University Press.
Greenspan H (1969) On the non-linear interaction of inertial modes. *Journal of Fluid Mechanics* 36: 257–264.
Hollerbach R (1998) What can the observed rotation of the Earth's inner core reveal about the state of the outer core? *Geophysical Journal International* 135: 564–572.
Hollerbach R and Kerswell R (1995) Oscillatory internal shear layers in rotating and precessing flows. *Journal of Fluid Mechanics* 298: 327–339.
Kerswell R (1993a) Elliptical instabilities of stratified hydromagnetic waves. *Geophysical and Astrophysical Fluid Dynamics* 71: 105–143.
Kerswell R (1993b) The instability of precessing flow. *Geophysical and Astrophysical Fluid Dynamics* 72: 107–144.
Kerswell R (1994) Tidal excitation of hydromagnetic waves and their damping in the Earth. *Journal of Fluid Mechanics* 274: 219–241.
Kerswell R (2002) Elliptical instability. *Annual Review of Fluid Mechanics* 34: 83–113.
Knittle E and Jeanloz R (1986) High-pressure metallization of FeO and implications for the Earth's core. *Geophysical Research Letters* 13: 1541–1544.
Krauze A (2010) Numerical modeling of the magnetic field generation in a precessing cube with a conducting melt. *Magnetohydrodynamics* 46: 271–280.
Kundu P and Cohen I (2002) *Fluid Mechanics*. San Diego, CA: Academic Press.
Lacaze L, Herreman W, Le Bars M, and Le Gal P (2006) Magnetic field induced by elliptical instability in a rotating spheroid. *Geophysical and Astrophysical Fluid Dynamics* 100: 299–317.
Lacaze L, Le Gal P, and Le Dizès S (2004) Elliptical instability in a rotating spheroid. *Journal of Fluid Mechanics* 505: 1–22.
Lacaze L, Le Gal P, and Le Dizès S (2005) Elliptical instability of the flow in a rotating shell. *Physics of the Earth and Planetary Interiors* 151: 194–205.
Lamb H (1932) *Hydrodynamics*. Cambridge: Cambridge University Press.
Landau L and Lifshitz E (1987) *Fluid Mechanics*. Oxford: Pergamon Press.
Laske G and Masters G (1999) Limits on differential rotation of the inner core from an analysis of the Earth's free oscillations. *Nature* 402: 66–69.
Lavorel G and Le Bars M (2010) Experimental study of the interaction between convective and elliptical instabilities. *Physics of Fluids* 22: 114101.
Le Bars M and Le Dizès S (2006) Thermo-elliptical instability in a rotating cylindrical shell. *Journal of Fluid Mechanics* 563: 189–198.
Le Bars M, Wieczorek M, Karatekin O, Cébron D, and Laneuville M (2011) An impact-driven dynamo for the early moon. *Nature* 479: 215–218.
Lilly D (1966) On the instability of Ekman boundary flow. *Journal of the Atmospheric Sciences* 23: 481–494.
Loper D (1975) Torque balance and energy budget for the precessionally driven dynamo. *Physics of the Earth and Planetary Interiors* 11: 43–60.
Lorenzani S and Tilgner A (2001) Fluid instabilities in precessing spheroidal cavities. *Journal of Fluid Mechanics* 447: 111–128.
Lorenzani S and Tilgner A (2003) Inertial instabilities of fluid flow in precessing spheroidal shells. *Journal of Fluid Mechanics* 492: 363–379.
Maas L, Benielli D, Sommeria J, and Lam F-P (1997) Observation of an internal wave attractor in a confined, stably stratified fluid. *Nature* 388: 557–561.
Maas L and Lam F-P (1995) Geometric focusing of internal waves. *Journal of Fluid Mechanics* 300: 1–41.
Malkus V (1968) Precession of the Earth as the cause of geomagnetism. *Science* 160: 259–264.
Malkus V (1971) Do precessional torques cause geomagnetism? Mathematical Problems in the Geophysical Sciences. *Lectures in Applied Mathematics* 14: 207–228.
Malkus V (1989) An experimental study of global instabilities due to the tidal (elliptical) distortion of a rotating elastic cylinder. *Geophysical and Astrophysical Fluid Dynamics* 48: 123–134.
Manasseh R (1992) Breakdown regimes of inertia waves in a precessing cylinder. *Journal of Fluid Mechanics* 243: 261–296.
Matthews P, Buffet B, Herring T, and Shapiro I (1991a) Forced nutations of the Earth: Influence of inner Core dynamics. 1. Theory. *Journal of Geophysical Research* 96: 8219–8242.
Matthews P, Buffet B, Herring T, and Shapiro I (1991b) Forced nutations of the Earth: Influence of inner core dynamics. 2. Numerical results and comparisons. *Journal of Geophysical Research* 96: 8243–8257.
McEwan A (1970) Inertial oscillations in a rotating fluid cylinder. *Journal of Fluid Mechanics* 40: 603–640.
Melchior P and Ducarme B (1986) Detection of inertial gravity oscillations in the Earth's core with a superconducting gravimeter at Brussels. *Physics of the Earth and Planetary Interiors* 42: 129–134.
Morize C, Le Bars M, Le Gal P, and Tilgner A (2010) Experimental determination of zonal winds driven by tides. *Physical Review Letters* 104: 214501.
Mouhali W, Lehner T, Léorat J, and Vitry R (2012) Evidence for a cyclonic regime in a precessing cylindrical container. *Experiments in Fluids* 53: 1693–1700.
Néron de Surgy O and Laskar J (1997) On the long term evolution of the spin of the Earth. *Astronomy and Astrophysics* 318: 975–989.
Noir J, Brito D, Aldridge K, and Cardin P (2001) Experimental evidence of inertial waves in a precessing spheroidal cavity. *Geophysical Research Letters* 28: 3785–3788.
Noir J, Cardin P, Jault D, and Masson J-P (2003) Experimental evidence of non-linear resonance effects between retrograde precession and the tilt-over mode within a spheroid. *Geophysical Journal International* 154: 407–416.
Noir J, Jault D, and Cardin P (2001) Numerical study of the motions within a slowly precessing sphere at low Ekman number. *Journal of Fluid Mechanics* 437: 283–299.
Nore C, Léorat J, Guermond J-L, and Luddens F (2011) Nonlinear dynamo excitation in a precessing cylindrical container. *Physical Review E* 84: 016317.
Oser H (1958) Experimentelle Untersuchung über harmonische Schwingungen in rotierenden Flüssigkeiten. *Zeitschrift für Angewandte Mathematik und Mechanik* 38: 386–391.
Pais M and LeMouël J (2001) Precession-induced flows in liquid-filled containers and in the Earth's core. *Geophysical Journal International* 144: 539–554.
Phillips O (1963) Energy transfer in rotating fluids by reflection of inertial waves. *Physics of Fluids* 6: 513–520.
Poincaré H (1910) Sur la précession des corps déformables. *Bulletin Astronomique* 27: 321–356.
Poirier J (1988) Transport properties of liquid metals and viscosity of the Earth's core. *Geophysical Journal* 92: 99–105.
Ray R, Eanes R, and Chao B (1996) Detection of tidal dissipation in the solid Earth by satellite tracking and altimetry. *Nature* 381: 595–597.
Ray R, Eanes R, and Lemoine F (2001) Constraints on energy dissipation in the Earth's body tide from satellite tracking and altimetry. *Geophysical Journal International* 144: 471–480.
Reynolds A (1962a) Forced oscillations in a rotating liquid (I). *Zeitschrift für Angewandte Mathematik und Physik* 13: 460–468.
Reynolds A (1962b) Forced oscillations in a rotating liquid (II). *Zeitschrift für Angewandte Mathematik und Physik* 13: 561–572.
Rieutord M, Georgeot B, and Valdettaro L (2001) Inertial waves in a rotating spherical shell: Attractors and asymptotic spectrum. *Journal of Fluid Mechanics* 435: 103–144.
Roberts P and Stewartson K (1963) On the stability of a MacLaurin spheroid of small viscosity. *The Astrophysical Journal* 137: 777–790.
Roberts P and Stewartson K (1965) On the motion of a liquid in a spheroidal cavity of a precessing rigid body. II. *Proceedings of the Cambridge Philosophical Society* 61: 279–288.
Rochester M, Jacobs J, Smylie D, and Chong K (1975) Can precession power the geomagnetic dynamo? *Geophysical Journal of the Royal Astronomical Society* 43: 661–678.
Seyed-Mahmoud B, Aldridge K, and Henderson G (2004) Elliptical instability in rotating spherical fluid shells: Application to Earth's fluid core. *Physics of the Earth and Planetary Interiors* 142: 257–282.
Sloudsky T (1895) De la rotation de la terre supposée fluide à son intérieur. *Bulletin de la Société Impériale des Naturalistes* 9: 285–318.
Souriau A and Poupinet G (2000) Inner core rotation: A test at the worldwide scale. *Physics of the Earth and Planetary Interiors* 118: 13–27.
Stefani F, Eckert S, Gerbeth G, et al. (2012) DRESDYN – A new facility for MHD experiments with liquid sodium. *Magnetohydrodynamics* 48: 103–113.
Stewartson K and Rickard J (1969) Pathological oscillations of a rotating fluid. *Journal of Fluid Mechanics* 35: 759–773.
Stewartson K and Roberts P (1963) On the motion of a liquid in a spheroidal cavity of a precessing rigid body. *Journal of Fluid Mechanics* 17: 1–20.
Suess S (1971) Viscous flow in a deformable rotating container. *Journal of Fluid Mechanics* 45: 189–201.
Tatro P and Mollo-Christensen E (1967) Experiments on Ekman layer instability. *Journal of Fluid Mechanics* 28: 531–543.
Tilgner A (1999a) Driven inertial oscillations in spherical shells. *Physical Review E* 59: 1789–1794.
Tilgner A (1999b) Magnetohydrodynamic flow in precessing spherical shells. *Journal of Fluid Mechanics* 379: 303–318.

Tilgner A (1999c) Non-axisymmetric shear layers in precessing fluid ellipsoidal shells. *Geophysical Journal International* 136: 629–636.
Tilgner A (1999d) Spectral methods for the simulation of incompressible flows in spherical shells. *International Journal for Numerical Methods in Fluids* 30: 713–724.
Tilgner A (2000) Oscillatory shear layers in source driven flows in an unbounded rotating fluid. *Physics of Fluids* 12: 1101–1111.
Tilgner A (2005) Precession driven dynamos. *Physics of Fluids* 17: 034104.
Tilgner A (2007a) Kinematic dynamos with precession driven flow in a sphere. *Geophysical and Astrophysical Fluid Dynamics* 101: 1–9.
Tilgner A (2007b) Zonal wind driven by inertial modes. *Physical Review Letters* 99: 194501.
Tilgner A and Busse F (2001) Fluid flows in precessing spherical shells. *Journal of Fluid Mechanics* 426: 387–396.
Triana S, Zimmermann D, and Lathrop D (2012) Precessional states in a laboratory model of the Earth's core. *Journal of Geophysical Research* 117: B04103.
Valet J-P (2003) Time variations in geomagnetic intensity. *Reviews of Geophysics* 41: 4.
Vanyo J (1991) A geodynamo powered by luni-solar precession. *Geophysical and Astrophysical Fluid Dynamics* 59: 209–234.
Vanyo J (2004) Core–mantle relative motion and coupling. *Geophysical Journal International* 158: 470–478.
Vanyo J and Dunn J (2000) Core precession: Flow structures and energy. *Geophysical Journal International* 142: 409–425.
Vanyo J and Likins P (1971) Measurement of energy dissipation in a liquid-filled, precessing, spherical cavity. *Journal of Applied Mechanics, Transactions of the ASME* 38: 674–682.
Vanyo J and Likins P (1972) Rigid-body approximations to turbulent motion in a liquid-filled, precessing, spherical cavity. *Journal of Applied Mechanics, Transactions of the ASME* 39: 18–24.
Vanyo J, Lods D, and Wilde P (1994) Precessing mantle, liquid core, and solid core interactions, In: *The 4th SEDI Symposium*, Abstract Book, pp 62–64.
Vanyo J, Wilde P, Cardin P, and Olson P (1995) Experiments on precessing flows in the Earth's liquid core. *Geophysical Journal International* 121: 136–142.
Williams G (1993) History of the Earth's obliquity. *Earth-Science Reviews* 34: 1–45.
Wu C and Roberts P (2008) A precessionally-driven dynamo in a plane layer. *Geophysical and Astrophysical Fluid Dynamics* 102: 1–19.
Wu C and Roberts P (2009) On a dynamo driven by topographic precession. *Geophysical and Astrophysical Fluid Dynamics* 103: 467–501.
Wu C and Roberts P (2010) High order instability of the Poincaré solution for precessionally driven flow. *Geophysical and Astrophysical Fluid Dynamics* 105: 287–303.
Yamazaki T and Hirokuni O (2002) Orbital influence on Earth's magnetic field: 100,000 years periodicity in inclination. *Science* 295: 2435–2438.
Zhang K (1993) On coupling between the Poincaré equation and the heat equation. *Journal of Fluid Mechanics* 268: 211–229.
Zhang K (1995) On coupling between the Poincaré equation and the heat equation: Non-slip boundary condition. *Journal of Fluid Mechanics* 284: 239–256.
Zhang K, Chan K, and Liao X (2010) On fluid flows in precessing spheres in the mantle frame of reference. *Physics of Fluids* 22: 116604.
Zhang K, Liao X, and Earnshaw P (2004) On inertial waves and oscillations in a rapidly rotating spheroid. *Journal of Fluid Mechanics* 504: 1–40.
Zhang K, Liao X, Earnshaw P, Liao X, and Busse F (2001) On inertial waves in a rotating fluid sphere. *Journal of Fluid Mechanics* 437: 103–119.
Zharkov V, Molodensky S, Brzezinsky A, Groten E, and Varga P (1996) *The Earth and its Rotation*. Heidelberg: Wichmann.
Zürn W, Richter B, Rydelek P, and Neuberg J (1987) Comment: Detection of inertial gravity oscillations in the Earth's core with a superconducting gravimeter at Brussels. *Physics of the Earth and Planetary Interiors* 49: 176–178.

8.08 Core–Mantle Interactions

BA Buffett, University of California, Berkeley, CA, USA

© 2015 Elsevier B.V. All rights reserved.

8.08.1	Introduction	213
8.08.2	Thermal Interactions	213
8.08.3	Electromagnetic Interactions	217
8.08.4	Mechanical Interactions	218
8.08.5	Chemical Interactions	221
8.08.6	Conclusions	221
References		222

8.08.1 Introduction

Two giant heat engines operate inside the Earth. One powers plate tectonics and accounts for most of the geologic phenomena we observe at the surface. The other operates in the core, where it continually sustains the Earth's magnetic field against persistent ohmic losses. These two heat engines are coupled, primarily through interactions at the boundary between the core and mantle. Transfer of heat, mass, momentum, and electric current across the boundary profoundly affects the dynamics and evolution of both regions on timescales ranging from days to hundreds of millions of years. On short timescales, we observe diurnal wobbles in the Earth's rotation, which are strongly affected by relative motion between the core and the mantle (e.g., Mathews and Shapiro, 1992). This and other types of mechanical interaction influence the flow in the core (e.g., Calkins et al., 2012) and contribute to variations in the length of day (see **Chapter 8.04**). On longer timescales, we expect variations in both the magnitude and spatial distribution of heat flow across the boundary. The resulting thermal interactions influence the vigor and pattern of convection in the core and may alter the frequency of reversals (Glatzmaier et al., 1999; Olson et al., 2010). Electromagnetic interactions are also possible, particularly if the lowermost mantle has a large electrical conductivity. Electric currents near the base of the mantle can generate both large- and small-scale magnetic fields, while the associated Lorentz force contributes to the mechanical interaction. More recent suggestions of chemical reactions between the core and mantle (Brandon and Walker, 2005; Ozawa et al., 2009) raise the intriguing but contentious suggestion that mass has been transferred between the two regions over geologic time. In this chapter, we focus on the consequences of core–mantle interactions for processes in the core. We address a number recent advances in our understanding of thermal, mechanical, electromagnetic, and chemical interactions, as they relate to the dynamics and evolution of the core. We also deal with the role of core–mantle interactions as a means of detecting deep-earth processes at the surface.

8.08.2 Thermal Interactions

Heat flow across the core–mantle boundary (CMB) is a fundamental parameter for the evolution of the core. It controls the rate of cooling and solidification of the core and determines the vigor of convection in the fluid outer core (Nimmo, **Chapter 8.02**). Convection is driven by a combination of thermal and chemical buoyancies as the fluid core cools and solidifies. Chemical buoyancy arises through the exclusion of the light elements from the growing inner core (Braginsky, 1963), whereas thermal buoyancy is generated by latent heat release on solidification (Verhoogen, 1961) and by forming cold, dense fluid in the thermal boundary layer at the top of the core. Each of these buoyancy sources is paced by the CMB heat flow.

The mantle plays an important role in regulating the magnitude of CMB heat flow. The large and relatively sluggish mantle limits heat loss from the core. Estimates of the CMB heat flow are often obtained from inferences of the temperature jump across the thermal boundary layer on the mantle side of the interface (e.g., Lay et al., 2008). Typical values of the heat flow are 6–16 TW, although our present state of knowledge is not sufficient to rule out higher or lower values. Such a broad range of values permit two distinct styles of convection in the core (see **Figure 1**). One style occurs when the CMB heat flow exceeds the conduction of heat along the adiabatic gradient at the top of the core (denoted by Q_{ad}). Convection carries heat in excess of that transported by conduction, requiring a thermal boundary layer on the core side of the boundary. This provides a source of cold, dense fluid to drive convection from the top down into the core. The other regime occurs when the CMB heat flow is less than Q_{ad}. In this case, the mantle is unable to remove the heat carried by conduction down the adiabat. Excess heat accumulates at the top of the core (Gubbins et al., 1982) or is mixed into the interior by flows driven by chemical buoyancy (Loper, 1978). Either of these possibilities eliminates thermal buoyancy production at the top of the core, restricting the buoyancy production to the inner-core boundary region.

Estimates for Q_{ad} have undergone substantial revision in the past few years. Values of Q_{ad} in the range of 5–6 TW are typically obtained when the thermal conductivity is 40–50 W m^{-1} K^{-1}. Higher thermal conductivities from recent theoretical studies (de Koker et al., 2012; Pozzo et al., 2012) yield values of $Q_{ad} = 12$–14 TW. Such a high value could exceed the CMB heat flow. It is also possible that the magnitude of Q_{ad}, relative to the total CMB heat flow, has changed with time. For example, a higher CMB heat flow is likely in the early Earth. Indeed, a higher heat flow

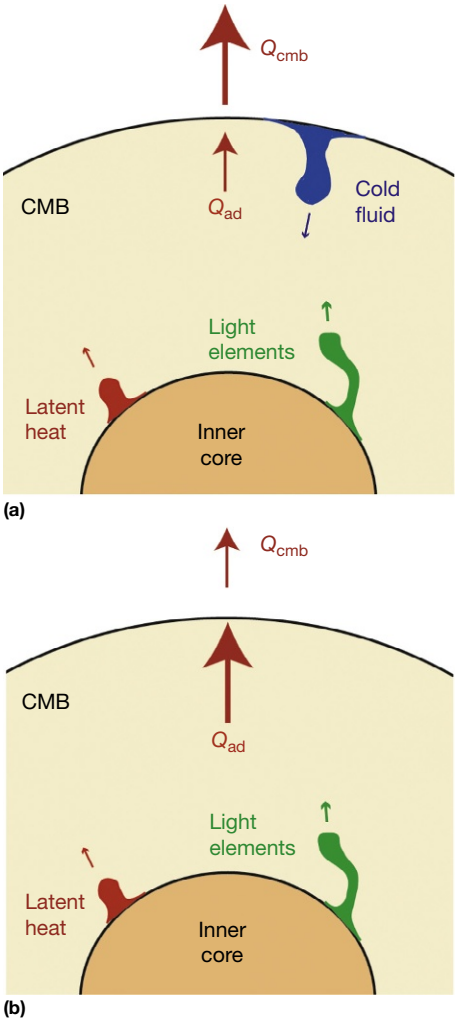

Figure 1 Two distinct styles of convection operate in the core, depending on the relative magnitude of the CMB heat flow, Q_{cmb}, and the heat flow conducted down the adiabat at the CMB, Q_{ad}. a) A thermal boundary layer forms at the top of the core when $Q_{cmb} > Q_{ad}$. Cold and dense fluid at the CMB drives convection from the top. Latent heat and compositional buoyancy from the inner-core boundary drive convection from the bottom. b) The thermal source of buoyancy at the top of the core disappears when $Q_{cmb} < Q_{ad}$. The excess heat that is carried to the CMB by conduction either accumulates at the top or is mixed back into the interior by compositional buoyancy.

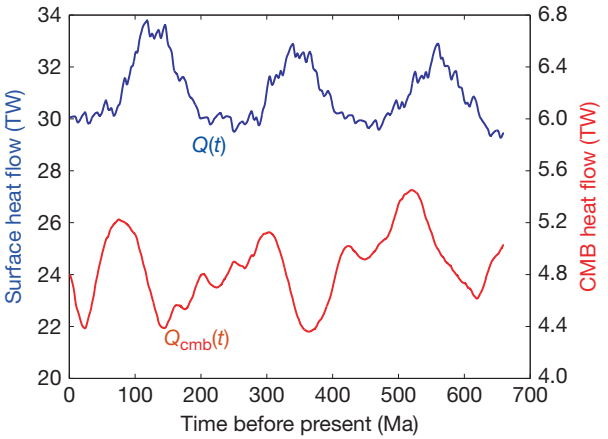

Figure 2 Heat flow at the surface $Q(t)$ and the CMB $Q_{cmb}(t)$ from a numerical convection model with imposed plate motions (Bunge et al., 2003). Plate motion histories over the past 120 Ma are cyclically repeated at earlier times to assess the response with different initial conditions. High heat flow at the surface coincides with times of faster than average plate spreading rates. Increases in heat flow at the CMB occur 50 to 60 Ma later.

may be essential to power the dynamo prior to the formation of the inner core. A switch to bottom-driven convection in the core becomes possible as the Earth cools and the inner core grows.

We might even expect the style of convection to switch intermittently between regimes if the current CMB heat flow is sufficiently close to Q_{ad}. Fluctuations in mantle convection can transiently shift the CMB heat flow above or below Q_{ad}, altering the convective regime.

Evidence for fluctuations in mantle convection can be found in geologic estimates of plate motions. Estimates from the past 120 million years suggest that spreading rates have generally decreased over this time, perhaps by more than 20% (Lithgow-Bertelloni and Richards, 1998; Xu et al., 2006). While the magnitude of this change is debated (Heller et al., 2006; Rowley, 2002), it is clear that modest fluctuations in plate motion can cause thermal interactions with the core. The size and timing of these interactions can be explored by incorporating estimates of plate motions into numerical models of mantle convection (Bunge et al., 2003; McNamara and Zhong, 2005; Zhang and Zhong, 2011). The overall amplitude of CMB heat flow in numerical models can vary widely with the choice of viscosity profile and CMB temperature. However, changes in the rate of plate motion invariably produce changes in the CMB heat flow. **Figure 2** shows the predicted change in heat flow at the surface and at the CMB when plate motions are varied in time according to the calculations of Bunge et al. (2003). (The plate motions over the past 120 Ma are cyclically repeated to extend the record back in time and explore solutions with different initial conditions.) High heat flow at the surface coincides with times of rapid plate spreading. Changes at the CMB are felt about 50–60 Ma later, reflecting the sinking time of subducted lithosphere. A somewhat shorter delay of 30 Ma is reported in the study of Zhang and Zhong (2011). Such a simple correspondence between surface plate speeds and CMB heat flow is probably a crude approximation of the actual dynamics. If the pace of mantle convection is connected with the rates of magnetic reversals, then some incoherence between plate motion and CMB heat flow is required to explain why prolonged periods of dipole stability (i.e., superchrons) are associated with both fast and slow plate speeds (Olson et al., 2013). For the results shown in **Figure 2**, the variation in CMB heat flow is roughly 1 TW, or about 20% about the time-averaged value.

Changes in the CMB heat flow alter the supply of thermal and chemical buoyancies in the outer core. A stratified layer at the top of the core can develop when the heat flow drops below Q_{ad} because the mantle can no longer keep pace with the heat supplied from below by conduction along the adiabat in the core. Excess heat accumulates at the top of the core unless convection in the core can entrain warm fluid back into the

interior. In the absence of entrainment, we expect a warm, stratified layer to grow in response to changes in densities inside and below the stratified layer (Lister and Buffett, 1998). Heat accumulates in the stratified layer, causing the warm fluid to encroach down into the underlying convective region. However, light elements from the inner-core boundary accumulate in the convective region, so the stratified layer gradually becomes heavier in terms of composition. This interplay between the thermal and chemical buoyancies ultimately limits the growth of the stratified layer.

Figure 3 shows two predictions for the thickness of a stratified layer using the model of Lister and Buffett (1998). For the sake of illustration, we adopt the CMB heat flow $Q_{cmb}(t)$ from Figure 2 and consider two conventional values for Q_{ad}. Qualitatively similar results are obtained using the recent theoretical values for Q_{ad} and a higher CMB heat flow, Q_{cmb} ~13–14 TW, from the study of Zhang and Zhong (2011). A lower value, $Q_{ad} = 5$ TW, causes an intermittent stratified layer to develop whenever $Q_{cmb}(t)$ drops below Q_{ad}. A permanent stratified layer develops when $Q_{ad} = 6$ TW, although the thickness of the layer fluctuates in time. In both examples, there is a lag between the time when Q_{cmb} is low and the time when the stratified layer reaches its maximum thickness. This time lag is set primarily by the thermal diffusion time for the stratified layer. We find a relatively thick stratified layer at 100–110 Ma, following a low CMB heat flow at 130 Ma. The low CMB heat flow (in this model) is a consequence of slow plate motions at the surface, 50–60 Ma earlier. The thickest layers are predicted to coincide with the time of maximum surface heat flow, although this result depends on the timescale for variations in the surface heat flow. The existence of a stratified layer in the core might be inferred from observations of variations in the magnetic field, because a stable layer would filter magnetic fluctuations from the underlying convective region (Sreenivasan and Gubbins, 2008). Distinctive features in the field may also develop in the stratified layer through interactions with the convective flow in the underlying region (Zhang and Schubert, 2000). Even more dramatic consequences are possible if the change in CMB heat flow causes the geodynamo to fail. For example, Nimmo and Stevenson (2000) suggested that a transition from plate tectonics to stagnant lid convection on Mars was sufficient to suppress convection throughout the Martian core, causing a termination of the magnetic field.

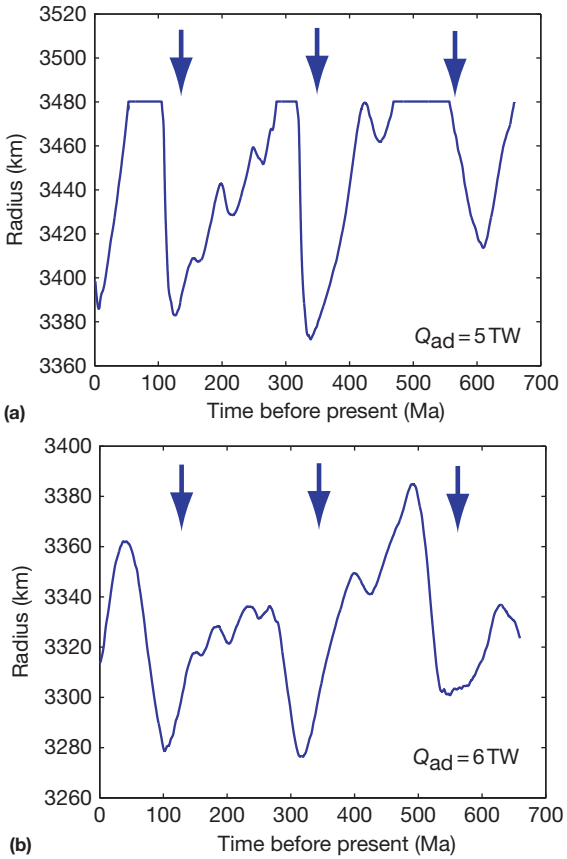

Figure 3 Changes in the radius of a stratified layer in the core in response to variations in CMB heat flow. a) The stratified layer vanishes when the CMB heat flow exceeds the adiabatic heat flow Q_{ad}. Under these conditions the radius of the stratified layer equals the radius of the core (e.g. 3480 km). The stratified layer reappears whenever the CMB heat flow drops below Q_{ad}. b) A persistent stratified layer is present when $Q_{ad} = 6$ TW, although the thickness of the layer varies with time. The arrows indicate the times when the heat flow at the surface is maximum.

Lateral variations in heat flow at the CMB also affect the dynamics of the core. Cold slabs at the base of the mantle are expected to increase the local heat flow by increasing the magnitude of the local temperature gradient at the boundary. This effect seems unavoidable because the low viscosity of the core liquid maintains a nearly constant temperature over the boundary (Bloxham and Jackson, 1990). Small adiabatic variations in temperature over kilometer-scale topography produce temperature variations of roughly 1 K, but these variations are small compared with temperature anomalies of several hundred kelvin or more in the mantle. Consequently, variations in heat flow over the CMB can be inferred from the thermal structure on the mantle side of the boundary. Numerical simulations (Sarson et al., 1997; Zhang and Gubbins, 1993, 1996) and experiments (Sumita and Olson, 1999, 2002) show that lateral variations in heat flow drive fluid motion in the core. In fact, several studies have sought to interpret core flows obtained from secular variation of the magnetic fields in terms of regional variations in heat flow (Bloxham and Gubbins, 1987; Kohler and Stevenson, 1990). Numerical simulations of convection with lateral variations in heat flow reveal a tendency to lock the pattern of convection to the pattern of heat flow at the boundary, although this behavior typically occurs for a narrow range of parameter values. More commonly, the flow is highly time-dependent. The source of the time dependence appears to be a consequence of switching the flow between the horizontal scale of the imposed boundary conditions and the natural scale of convection (Sumita and Olson, 2002; Zhang and Gubbins, 1996).

Similar conclusions are drawn from numerical geodynamo models (Bloxham, 2002; Olson and Christensen, 2002; Sarson et al., 1997). Nonhomogeneous boundary conditions in geodynamo models yield persistent structure in the time-averaged flow (Bloxham, 2002; Davies et al., 2008; Olson and Christensen, 2002), although there can be substantial variation about the average (Bloxham, 2002; Christensen and Olson, 2003). The spatial pattern of the core flow is reflected in the structure of the magnetic field. Models that use seismic

heterogeneity at the base of the mantle to infer the local heat flow have been successful in producing a magnetic field with persistent nondipole structure (see **Figure 4**), similar to that deduced from paleomagnetic observations over the past few million years (Gubbins and Kelly, 1993; Johnson and Constable, 1997, 1998). However, the persistent nondipole structure is not prominent in individual snapshots of the solution; it emerges only after averaging the time-dependent part of the field. So far, it has not been possible to use thermal interactions to explain stationary features in the historical field over the past 300 years (Bloxham, 2002).

Spatial variations in heat flow may also have an important influence on magnetic reversals. The study of Glatzmaier et al. (1999) showed that different patterns of heat flow at the CMB can alter the frequency of magnetic reversals. When the pattern of CMB heat flow is compatible with the natural pattern of convection in the outer core, there is a tendency to produce a stronger dipole field with less time dependence and fewer magnetic reversals. The opposite behavior is observed when the pattern of heat flow and the natural scale of convection are distinct; in this case, much larger variations are observed in the field and reversals appear more frequently. Somewhat surprisingly, the most realistic behavior, in terms of time variations in the virtual geomagnetic pole (VGP), was obtained with uniform boundary conditions. Such a model cannot explain the persistent nondipole structure of the field, so there appear to be other contributing factors. For example, Olson et al. (2010) showed that reversal rates are more sensitive to total heat flow than the spatial variations. High reversal rates correspond to high CMB heat flow, whereas the times of low CMB heat flow could plausibly coincide with extended periods of stable polarity (Driscoll and Olson, 2011).

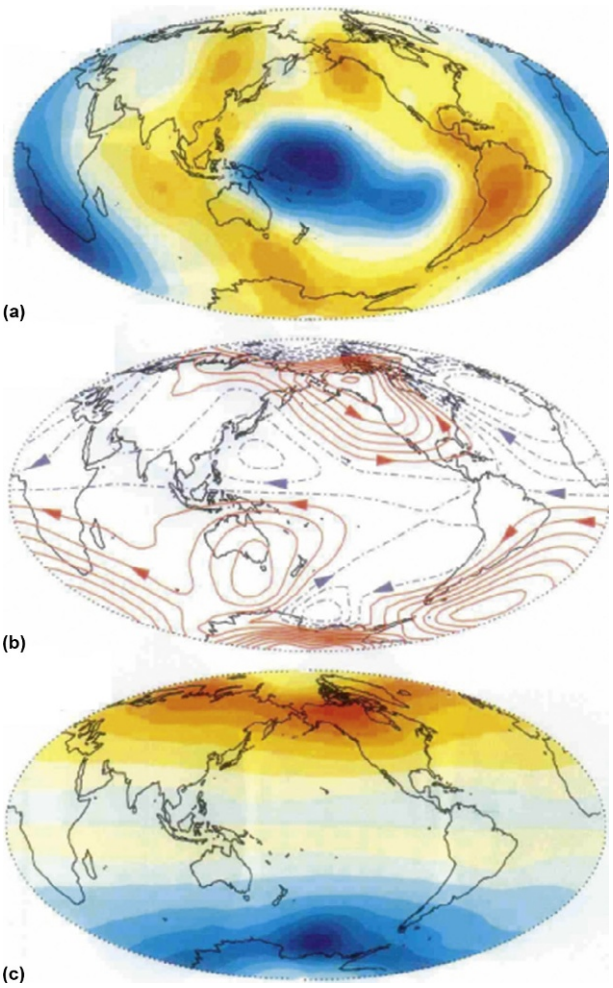

Figure 4 Lateral variations in Q_{cmb} induce flow near the top of the core and alter the time-averaged magnetic field from calculations of Olson and Christensen (2002). a) Lateral variations in boundary heat flow are based on seismic models of velocity heterogeneity near the CMB. b) Toroidal streamlines of steady flow below the CMB are due to imposed heat flow conditions. c) Time-averaged radial magnetic field at CMB reveals nonzonal structure.

Numerical models also suggest that dynamo action fails when lateral variations in heat flow become comparable to the average convective heat flow (Olson and Christensen, 2002). Because a large part of the heat flow at the CMB is carried by conduction along the adiabat, the convective part of the average heat flow could be quite small (or even negative). Lateral variations in heat flow could easily exceed the average convective heat flow, which appears to doom the magnetic field in thermally driven dynamo models. It is not presently known if the dynamo models would still fail if convection was driven primarily by compositional buoyancy. Reconciling the behavior of the field with plausible thermal interactions remains an outstanding challenge.

Another consequence of thermal interactions involves the behavior of the field during a reversal. Compilations of VGPs from transition fields suggest that the VGPs are clustered into one of two preferred longitudes during a reversal (Clement, 1991; Laj et al., 1991). In fact, it is possible for different sites to record different paths for the same reversal because the VGP location is based on the assumption of a dipole field. Nondipole (multipole) components of the field also contribute to the direction of the field at a given site, shifting the VGP location from the position of the actual dipole axis. Different reversal paths emerge from different sites when the multipole components become prominent relative to the dipole. Kutzner and Christensen (2004) investigated the question of preferred reversal paths using a geodynamo model with lateral variations in CMB heat flow. Part of the time-averaged magnetic field in this study included an equatorial dipole, which defines a preferred orientation in longitude. Modeled VGP paths from a large number of sites on the surface sense this orientation, causing a preferred path during reversals. However, the scatter in VGP directions due to multipole components means that the preferred direction emerges only when a large number of sites are averaged. The question of whether preferred reversal paths can be inferred from a small number of sites at the surface remains a contentious issue, both for the models and for the paleomagnetic observations. Additional questions arise because the models are still very far from earthlike conditions. On the other hand, the signatures of thermal core–mantle interactions should be embedded in the flow and field at the top of the core. Identifying these signatures in both observations and models should be an important part of future progress.

8.08.3 Electromagnetic Interactions

Electric currents are induced in the lower part of the mantle as a consequence of dynamo action in the liquid core. Several types of interactions between the core and mantle are possible. One involves the force on current-carrying material, which can transfer momentum between the core and the mantle. This mechanism is commonly proposed to explain variations in the length of day over periods of several decades (e.g., Bullard et al., 1950). A second type of interaction causes a distortion the magnetic field as it diffuses through the mantle toward the surface. The importance of both effects depends on the electrical conductivity of the lower mantle.

Laboratory-based estimates for mantle silicates and oxides, extrapolated to lower mantle conditions, typically yield conductivities of 10 S m^{-1} or less (Xu et al., 2000). Such low values are expected to yield relatively weak currents in the lower mantle and small electromagnetic core–mantle interactions. However, more substantial electromagnetic interactions are possible if the lowermost mantle is not composed entirely of silicates and oxides. Chemical reactions between the core and mantle have been proposed as a mechanism to incorporate iron alloys into the base of the mantle (Knittle and Jeanloz, 1989). The iron alloy may be a reaction product (Jeanloz, 1990) or a result of incorporating core material directly into the mantle (Buffett et al., 2000; Kanda and Stevenson, 2006; Otsuka and Karato, 2012; Petford et al., 2005; Poirier and LeMouel, 1992). A new high-pressure phase of $MgSiO_3$ (Murakami et al., 2004; Oganov and Ono, 2004) may open other possibilities for high electrical conductivities in the lower mantle (Ohta et al., 2010; Ono et al., 2006). Regions of low conductivity may also arise from changes in the partition of iron between the dominant mineral components due to a transition in the spin state of iron in ferropericlase (Badro et al., 2003).

One of the earliest suggestions of electromagnetic core–mantle interaction was motivated by the observation of small fluctuations in the length of day over periods of several decades (Bullard et al., 1950; Rochester, 1962; Roden, 1963). Motion of the core relative to the mantle sweeps lines of magnetic field through the lower mantle, inducing a horizontal electric current. The resulting forces on the core and mantle act to oppose any relative motion. The axial component of the associated torque transfers angular momentum between the core and mantle. Stix and Roberts (1984) were the first to use detailed estimates of flow at the top of the core to determine the electromagnetic torque on the mantle. They predicted variations in the torque that were sufficient to explain the fluctuations in the length of day. However, these variations were superimposed on a steady torque, which had the undesirable effect of causing a steady change in the angular velocity of the core and the mantle. To avoid this effect, they proposed an additional (balancing) torque, which arises when radial electric currents leak across the CMB. The existence of such a current is reasonable, although it cannot be constrained by surface observations. As a result, electromagnetic interactions provide a viable but unproven mechanism for explaining decadal variations in the length of day.

Holme (1998) revisited the question of electromagnetic core–mantle interactions by showing that core flows inferred from measurements of secular variation could not constrain the torque on the mantle (also see Wicht and Jault, 1999). This means that any torque computed from a flow model is largely a product of the assumptions used to resolve the nonuniqueness of the flow rather than the measurements of secular variation. The strategy proposed by Holme (1998) was to determine the flow at the top of the core by fitting the observed secular variation subject to the condition that rearrangement of magnetic flux explains the length-of-day variations. (This calculation did not require any radial current across the CMB.) Plausible core flows were found to explain the variations in the length of day, provided the conductance of the lower mantle was roughly 10^8 S. The necessary conductance could be obtained with a 100 km layer at the base of the mantle and an average conductivity of 10^3 S m^{-1}, although other combinations of thickness and conductivity are possible.

A similar value for the conductance of the lower mantle was obtained from the study of the Earth's nutation (Buffett, 1992). Periodic variations in the direction of the Earth's rotation (nutations) are caused by the lunar and solar tides. The Earth's response to tidal torques includes a differential rotation of the core relative to the mantle, which alters the measured nutation. Electromagnetic interactions cause an additional perturbation by introducing a restoring force that opposes the differential rotation. The associated dissipation due to ohmic loss is detected as a phase lag in the response relative to that predicted for an elastic Earth model (e.g., Mathews and Shapiro, 1992). Comparison of theoretical predictions (Mathews et al., 1991; Wahr, 1981) and observations (Herring et al., 1991) reveals a large discrepancy in the annual nutation, which is particularly sensitive to relative motion between the core and the mantle. Including electromagnetic interactions could eliminate this discrepancy, as long as the conductance of the lower mantle is 10^8 S, comparable to the value required to explain length-of-day variations. However, there is one important distinction. Nutations involve nearly diurnal motion of the core relative to the mantle. (An annual nutation is defined by the period of the beat frequency between the nearly diurnal motion and exactly one cycle per day.) The associated skin depth for magnetic diffusion over diurnal periods limits electric currents to the immediate vicinity of the boundary, so the discrepancies in the nutations are most easily explained by high (10^5–10^6 S m^{-1}) conductivities in a relatively thin (10^2–10^3 m) layer. A variety of mechanisms have been examined to explain (or refute) such a conducting layer at the base of the mantle (Buffett et al., 2000; Kanda and Stevenson, 2006; Knittle and Jeanloz, 1991; Otsuka and Karato, 2012; Petford et al., 2005; Poirier and LeMouel, 1992). While improvements in nutation theory (Koot et al., 2008; Mathews et al., 2002) and observations (Herring et al., 2002) continue to support the existence of a conducting layer, other sources of dissipation have also been proposed. The most likely alternative is viscous dissipation in the liquid core (Buffett, 1992; Deleplace and Cardin, 2006; Koot et al., 2010; Mathews and Guo, 2005), although this explanation requires a viscosity that is roughly four orders of magnitude larger than recent estimates (de Wijs et al., 1998; Zhang and Guo, 2000).

Another type of electromagnetic interaction arises when the electrical conductivity in the lower mantle varies laterally. Steady flow in the core sweeps the radial (poloidal) component of the

magnetic field through the mantle, inducing local electric currents. In a uniform conductor, these currents produce a tangential (toroidal) component of the magnetic field. However, a heterogeneous conductor directs current through the conducting regions. The added complexity in the path of electric current induces a poloidal field, which can strengthen the initial poloidal field. Busse and Wicht (1992) showed that self-sustaining dynamo action is possible in this case, even when the flow in the core is spatially uniform. In effect, the complexity of the conductivity structure replaces the need for complicated fluid motion in a uniform conductor. While the conditions required for self-sustaining dynamo action are unlikely to be realized in the Earth's core, it is possible to induce a small-scale radial field with an amplitude as large as 0.1 mT (Buffett, 1996a). This mechanism can also contribute to the large-scale field at the surface by distorting the unseen toroidal field to produce an observable poloidal component (Koyama et al., 2001). More recent geodynamo simulations with an electrically heterogeneous mantle suggest that the nondipole part of the magnetic field at the Earth's surface can be strongly affected by the distribution of conductivity in the mantle (Chan et al., 2008).

Electromagnetic interactions also accompany time variations in the amplitude of the magnetic field. The largest change in amplitude probably occurs during magnetic reversals. While the general structure of the field during a reversal is not well known, we do know that the axial part of the dipole field vanishes and reappears with the opposite polarity in as little as several thousand years (Clement, 2004; Valet et al., 2012). Rapid time variations in the axial dipole create large-scale electric fields in the lower mantle. When the distribution of electrical conductivity of the mantle is heterogeneous, the resulting currents generate a poloidal field (see **Figure 5**). The structure of the induced field depends on the spatial distribution of electrical conductivity. A large-scale pattern of electrical conductivity with a local conductance of 10^8 S should produce an observable field during a magnetic reversal. Such a mechanism provides an attractive explanation for preferred reversal paths because the geographic location and structure of the induced field are fixed by the distribution of electrical conductivity in the lower mantle. Costin and Buffett (2004) explored this mechanism using a distribution of electrical conductivity that was based on estimates of topography on the CMB (dominantly a degree-2 pattern in spherical harmonics). The main part of the induced field had a nonzonal degree-3 pattern, which was superimposed on a decreasing axial dipole field to predict VGP paths. Preferred paths were caused by the nonzonal part of the field, although the actual location of the preferred paths depended on the location of the observing sites. Costin and Buffett (2004) used the location of sites in the sediment database of Clement (1991) to predict a clustering of reversal paths through the Americas and Asia (see **Figure 6**). This prediction was broadly consistent with inferences drawn from the observations (Clement, 1991).

An interesting test of this prediction is afforded by the current rate of decrease in the dipole field, which is not too different from the average rate of decrease during a reversal (perhaps within a factor of 2 or 3). The induced field is both observable and consistent with historical observations of the field, although it is not currently possible to separate

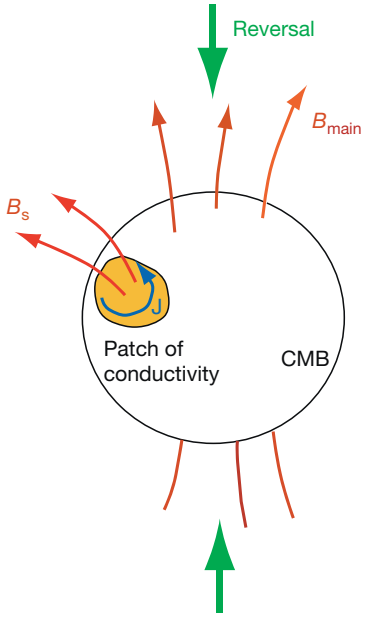

Figure 5 Time variations in the main magnetic field, B_{main}, during reversals induce electric currents J in the conductive regions at the CMB. The electric currents generate a secondary field, B_s, which is superimposed on B_{main}. The resulting distortion of B_{main} can give rise to preferred reversal paths because the location of the secondary field is fixed by the spatial distribution of electrical conductivity near the base of the mantle.

contributions from electromagnetic core–mantle interactions and the underlying variations that originate within the core. This ambiguity is a source of concern because the contribution of electromagnetic core–mantle interactions to the field at the Earth's surface can potentially complicate the way we interpret observations of secular variation.

8.08.4 Mechanical Interactions

Mechanical interactions are commonly invoked to transfer momentum between the core and the mantle. Most attention has focused on mechanisms that account for the observed variations in the length of day over timescales of several decades. Lorentz forces due to electromagnetic interactions offer one possible mechanism, although several other types of mechanical interaction have also been proposed. One such mechanism is due to the flow of the core over topography on the CMB (Hide, 1969). Pressure differences on the leading and trailing sides of bumps on the boundary result in a torque that transfers angular momentum. When seismic estimates of the CMB topography first appeared in the literature (Forte and Peltier, 1991; Morelli and Dziewonski, 1987), it became possible to estimate the pressure (or topographic) torque using models of flow at the top of the core (Hide, 1989; Jault and LeMouel, 1989). Most models of core flow are constrained by assuming a geostrophic force balance in the tangential direction (see **Chapter 8.04**). Under this assumption, the flow field recovered from observations of secular variation can be converted to a pressure field. When that pressure field was

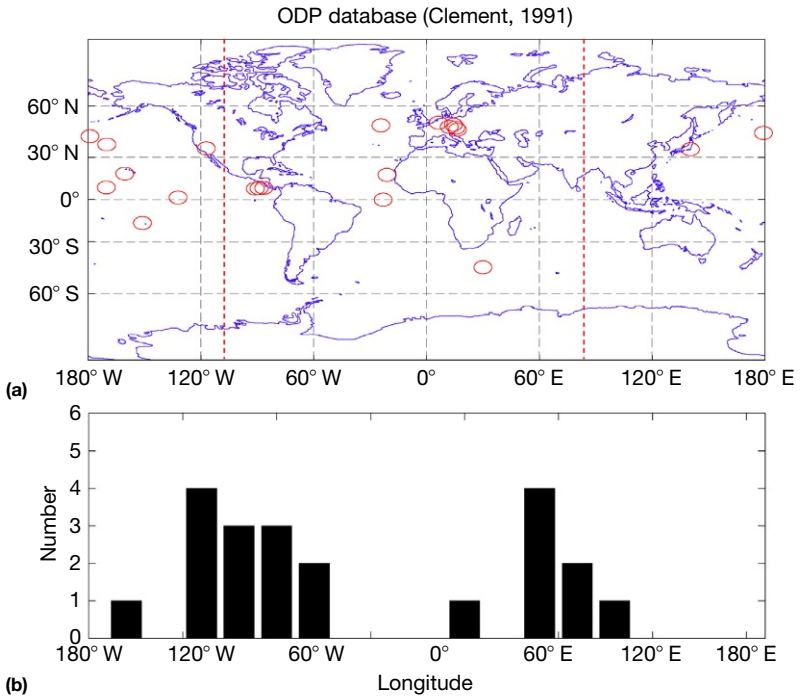

Figure 6 A) Location of samples from the sediment database of Clement (1991) and B) histogram of reversal path longitudes predicted by Costin and Buffett (2004). The spatial distribution of electrical conductivity is based on estimates of the large-scale topography on the CMB. The secondary field induced by this heterogeneous distribution of conductivity causes reversal paths to preferentially pass though the Americas and Asia.

integrated over the boundary with known topography, the resulting torque was too large by several orders of magnitude to explain the observed variation in the length of day (Jault and LeMouel, 1990). A small shift in the position of the topography could greatly reduce the torque, leading to speculations that the pattern of flow was locked by the topography to keep the torque small. Alternatively, it was possible to make small changes to the flow, which eliminated the pressure torque entirely without substantially altering the fit to the secular variation observations (Kuang and Bloxham, 1993). These results demonstrate the sensitivity of the calculation to small errors in either the topography or the flow models.

More problematic is the consistency of calculating a pressure torque using flow models that assume a geostrophic force balance at the top of the core. Geostrophic flow represents a balance between the Coriolis force and pressure gradient. Such a flow can have no time variation because the presence of accelerations implies a departure from geostrophic conditions. There can also be no net torque on the core (or the mantle) because a net torque also implies a change in momentum. Kuang and Bloxham (1997) used this result to show that the pressure torque due to a geostrophic flow must vanish. They did this by demonstrating that the torque associated with the Coriolis force is identically zero. The sum of the pressure and Coriolis torques must vanish if there is no change in momentum in a geostrophic flow, so it follows that the pressure torque is zero. Of course, it is possible that the flow at the top of the core is not geostrophic, so the pressure torque need not vanish. Jault and LeMouel (1999) argued that the geostrophic approximation would still provide a good approximation for the actual pressure field (and hence the pressure torque). However, it is doubtful that a reliable pressure field for mechanical coupling calculations can be recovered from the flow, given the sensitivity of the calculation to small errors.

Other estimates of the pressure torque have been obtained using models of idealized flow over boundary topography (e.g., Anufriyev and Braginsky, 1975, 1977; Moffatt and Dillon, 1976). Pressure in the fluid is perturbed by the flow around the topography. The influence of this perturbation on the boundary topography produces the pressure torque. The amplitude of the pressure torque in these calculations varies as h^2, where h is the height of the topography. One factor of h arises because the perturbation depends on the height of the topography; the second factor of h arises because the integral over the surface for the pressure torque depends on the presence of topography. For boundary topography of a few kilometers at large spatial scales, the resulting pressure torque is probably too small to explain the observed variations in the length of day (e.g., Mound and Buffett, 2005). Similar conclusions have been obtained using numerical geodynamo models that include the influence of boundary topography (Kuang and Chao, 2001). An important aspect of the study by Kuang and Chao (2001) is that they avoid the use of idealized flow and make no assumptions about the structure of the magnetic field. The pressure at the boundary evolves in response to both the underlying convection and the presence of boundary topography. The fact that the pressure torque in these calculations is small would seem to argue against a prominent role for topographic coupling.

Other consequences of fluid pressure on the CMB can be detected at the surface. For example, fluctuations in pressure produce observable changes in both gravity and surface topography (Dumberry and Bloxham, 2004; Fang et al., 1996;

Greff-Lefftz et al., 2004). A typical pressure of 10^3 Pa changes on timescales of several decades as the flow evolves at the CMB. When the mantle responses elastically to the pressure change, the surface displacement can be a few millimeters. The corresponding change in the gravity field is within current the limits of detection (Dumberry and Bloxham, 2004; Greff-Lefftz et al., 2004). Recent interest in this process is motivated by observations of decadal changes in the elliptical part of the gravity field (Cox and Chao, 2002). While it appears that pressure changes in the core are too small to explain the observations of Cox and Chao (2002), current advances in space geodetic observations hold the promise of making the somewhat smaller core processes observable at the Earth's surface.

Gravitational interactions between the core and the mantle cause a different type of mechanical coupling. Convection in both regions creates density anomalies inside the Earth. Gravitational attraction of these density anomalies can result in a transfer of momentum (Jault and LeMouel, 1989; Rubincam, 2003). The distribution of density anomalies in the mantle can be inferred from seismic tomography models by assuming that variations in wave speed are due mainly to temperature (Dziewonski et al., 1977; Hager et al., 1985; Ricard and Vigny, 1989). Unfortunately, a similar procedure is not feasible in the outer core because the density anomalies are far too small to be detected seismically (Stevenson, 1987). An order of magnitude estimate for the density anomalies in the outer core suggests that gravitational interactions could be important (Jault and LeMouel, 1989). However, it is not presently possible to evaluate the torque without knowing the distribution of density anomalies in the outer core.

An alternative source of gravitational interaction occurs between density anomalies in the mantle and the inner core (Buffett, 1996b). The principle source of density heterogeneity in the inner core is caused by topography on the inner-core boundary, which can be estimated by assuming that the boundary tends to adjust over time toward an equipotential surface (see **Chapter 8.12**). (Density anomalies may also occur inside the inner core, but these are probably small compared with the anomalies associated with topography.) In fact, the largest perturbations in the shape of equipotential surfaces in the core are probably due to density anomalies in the mantle, which are large compared with the typical density anomalies in the outer core (e.g., $\Delta\rho/\rho \sim 10^{-8}$). This means that the distribution of density anomalies in the mantle determines the shape of the inner core (see **Figure 7**). Estimates of the gravity perturbations from dynamic geoid studies (Defraigne et al., 1996; Forte et al., 1994) suggest that the peak-to-peak topography on the inner-core boundary is about 100 m or less. When the inner core rotates through the gravitational field of the mantle, a strong gravitational force acts to restore the inner core to its equilibrium position. An equal and opposite force on the mantle is about two orders of magnitude larger than the gravitational force exerted on the mantle by the outer core (Buffett, 1996b), primarily because the density anomalies associated with inner-core topography are much larger (e.g., $\Delta\rho/\rho \sim 10^{-4}$). These large gravitational forces provide a plausible explanation for the decadal variations in the length of day.

Gravitational interactions cannot be solely responsible for fluctuations in the length of day because the moment of inertia of the inner core is so much smaller than that of the mantle.

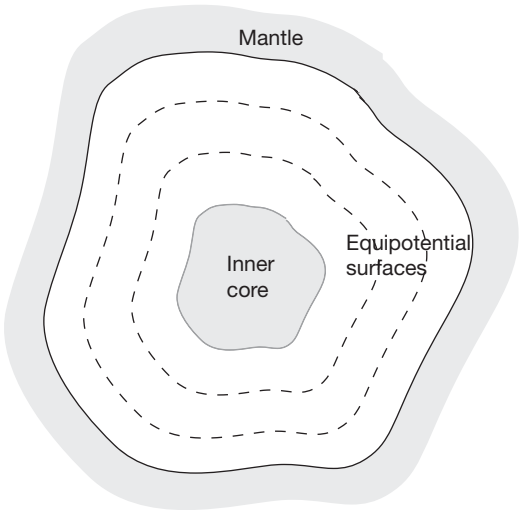

Figure 7 Schematic illustration of the heterogeneous Earth viewed on an equatorial cross section. Density anomalies in the mantle drive flow and perturb the core-mantle boundary. Surfaces of constant potential inside the core are disturbed from axial symmetry by the combined effect of mantle density anomalies and boundary displacements. The inner core adjusts to a hydrostatic state by aligning the boundary with an equipotential surface. This state also minimizes the gravitational potential energy. Rotation of the inner core relative to its equilibrium position produces a mutual gravitational torque on the mantle and inner core.

Instead, the transfer of angular momentum to and from the mantle must rely on changes in the angular momentum of the entire core through a combination of electromagnetic and gravitational torques (Mound and Buffett, 2006). Motions in the fluid outer core are tightly coupled to the inner core by electromagnetic forces on account of the high electrical conductivity on either side of the inner-core boundary. As inner core rotates in response to a strong electromagnetic torque from the fluid core, momentum is transferred to the mantle through the action of the gravitational torque. Tests of this mechanism in numerical geodynamo models yield a torque on the mantle that is sufficient to explain the variations in the length of day (Aubert and Dumberry, 2010; Buffett and Glatzmaier, 2000). It is also possible to explain the length-of-day variations when the fluid motions in the outer core are restricted to the form of torsional oscillations (Dumberry and Mound, 2010; Mound and Buffett, 2005). These oscillations are of interest because the typical period is thought to be compatible with a nominal 60-year variation in the length of day (Braginsky, 1970, 1984). This view has been challenged by a recent detection of torsional oscillations that propagate across the outer core in approximately 4 years (Gillet et al., 2010). Such fast propagation implies a much stronger magnetic field than previously assumed. According to Gillet et al. (2010), these waves recur every 6 years and appear to explain a small-amplitude 6-year variation in the length of day (Abarca del Rio et al., 2000). Alternatively, the 6-year variation might be attributed a gravitational oscillation between the inner core and the mantle (Mound and Buffett, 2006). Corroborating evidence for a gravitationally driven oscillation could be sought in time variations of the gravity field.

8.08.5 Chemical Interactions

It is generally assumed that the core has been chemically isolated from the mantle since the time of core formation. Partial equilibration between liquid iron and silicates establishes the initial composition of the core (e.g., Rubie et al., 2007; Stevenson, 1990). Subsequent transport of mass between liquid iron and silicates is assumed to be insignificant after the core forms. This conventional view is challenged by the studies of Knittle and Jeanloz (1989, 1991), which used diamond-anvil-cell experiments to show that liquid iron reacts with silicates and oxides at high pressure and temperature. The reaction products were thought to include iron alloys, such as FeO and FeSi, and iron-depleted silicate minerals (Goarant et al., 1992; Knittle and Jeanloz, 1989). Mantle minerals in direct contact with the core liquid should quickly establish a local equilibrium because reactions at high temperature are expected to be fast and convective mixing in the core can be relatively efficient (the convective overturn time is probably on the order of 10^3 years). On the other hand, convection in the mantle exposes fresh surfaces of unreacted material more slowly. Jeanloz (1990) suggested that chemical reactions and transport of light elements into the core could have occurred over most of the Earth's history.

Subduction of oxidized ocean crust may also drive reactions by altering chemical conditions at the base of the mantle (Walker, 2005). In either case, chemical reactions could disturb the composition of the core by permitting a flux of mass between the mantle and the core.

Evidence for the core leaking back into the mantle is based on measurements of osmium isotope ratios in lava associated with some hotspots (Brandon et al., 1998; Walker et al., 1995). Enrichment in $^{186}Os/^{188}Os$ and $^{187}Os/^{188}Os$ relative to upper mantle materials has been attributed to small additions of core material to the lower mantle. This core material is subsequently entrained in mantle plumes, where it contributes to lava that is sampled at the surface (see Brandon and Walker, 2005, for a review). Only small amounts of core material are required to perturb the isotopic composition of the mantle because the concentration of Os in the core vastly exceeds that in the mantle, based on partitioning of Os between silicates and liquid metal. However, enrichment in isotopic ratios require a source region with elevated ratios of Pt/Os and Re/Os relative to typical mantle values in order to produce excess ^{186}Os and ^{187}Os through radioactive decay of ^{190}Pt and ^{187}Re. Given the long half-lives involved (e.g., 489 and 42 Ga), the elevated ratios of Pt/Os and Re/Os must be maintained for a very long time to produce the required isotopic enrichment.

Brandon et al. (1998) attributed the elevated ratios of Pt/Os and Re/Os in the liquid core to the growth of the inner core. The initial abundances of Pt, Re, and Os in the core should be close to the chondritic abundances because all of these elements are highly siderophile; most of the initial inventory enters the core with little fractionation. Solidification of the core removes more Os from the liquid core than either Re or Pt (Walker, 2000). This process increases Pt/Os and Re/Os ratios in the outer core above the chondritic ratios. However, experimental estimates for the partitioning of Pt, Re, and Os between liquid and solid iron appear to require an old age for the inner core (Brandon and Walker, 2005), which is incompatible with models for the thermal history of the core (Buffett, 2002; Labrosse et al., 2001). A further complication has arisen with recent measurement of tungsten isotopes in ocean-island basalts that exhibit $^{186}Os/^{188}Os$ and $^{187}Os/^{188}Os$ enrichment (Schersten et al., 2004; Takamasa et al., 2009). So far, there is no evidence for a core signature in tungsten isotopes. On the other hand, Humayun (2011) had proposed a mechanism to elevate ratios of Pt/Os and Re/Os at the base of the mantle after allowing transport of core material across the CMB. This proposal may circumvent the need for an old inner core and avoid difficulties with tungsten isotopes in the mantle. Thus, the role of the core in producing coupled variations in Os isotope ratios remains an open question.

Despite the controversy over isotopic signals from the core, it is difficult to escape the conclusion that some form of chemical interaction is inevitable. Recent experiments on partitioning of major elements between liquid iron and mantle minerals suggest that the core is currently undersaturated in Si and O (Asahara et al., 2007; Ozawa et al., 2008; Sakai et al., 2006; Siebert et al., 2012; Takafuji et al., 2005). For present-day estimates of temperature and bulk mantle composition, the equilibrium concentrations of Si and O in liquid iron should vastly exceed the concentrations required to explain the density deficit of the core relative to pure iron (Tsuno et al., 2013). Transfer of Si and O to the core can produce a buoyant layer at the top of the core (Ozawa et al., 2009), although the vertical extent of such a layer is potentially limited by diffusive transport through the mantle. Most mantle minerals have low diffusivity (Van Orman et al., 2003), but even small amounts of partial melt can substantially enhance diffusivity, eliminating the limitation of mantle-side transport. In this case, a buoyant layer grows by diffusion into the liquid core with modest entrainment by the underlying convection (Buffett and Seagle, 2010).

Cooling over geologic time can substantially alter the solubility of dissolved components. The attendant growth of the inner core can also alter the chemical equilibrium by segregating light elements into the outer core. Eventually, some components in the liquid core may become supersaturated. Stevenson (2007) had argued that Mg is a likely candidate for exsolution because its solubility is relatively low compared with either Si or O. Exsolution could take the form of an immiscible liquid phase (Ito et al., 1995). Alternatively, the excess concentration could drive back reactions at the CMB, removing excess light element and precipitating a solid 'sediment' to the base of the mantle (Buffett et al., 2000). Walker (2005) had also discussed the possibility of electrochemical reactions at the CMB (Kavner and Walker, 2006) and reactions with oxidized oceanic crust. There is no shortage of mechanisms that can cause chemical interactions between the core and the mantle, and there are good reasons for suspecting that many of these operate within the Earth. The challenge lies in quantifying their importance for the evolution and dynamics of the planet.

8.08.6 Conclusions

Interactions between the core and the mantle take many forms. Thermal interaction involves changes in the rate and spatial distribution of heat flow across the CMB. The resulting changes in the vigor and pattern of convection in the core can

dramatically affect the geodynamo and produce observable signals in the magnetic field at the Earth's surface. Electromagnetic interactions are the result of electric currents near the boundary. The consequences are entirely dependent on the electrical conductivity of the lower mantle. A conductance of 10^8 S for the lower mantle is sufficient to explain variations in the length of day and to contribute significantly to the induction of magnetic field inside the Earth. Mechanical interactions are most commonly attributed to the effects of fluid pressure acting on the CMB. While pressure torques are not thought to be the primary mechanism for transferring angular momentum between the core and the mantle, deformations due to fluid pressure on the CMB can cause observable changes in gravity and surface displacement. A more viable explanation for the variations in the length of day at decadal periods involves gravitational interactions, primarily between the inner core and the mantle. Better observations of these gravitational interactions may provide new insights into the non-hydrostatic distribution of mass in the mantle. Chemical interactions of some form appear to be likely, although the details are presently unknown. Advances in high-pressure and high-temperature experiments may soon begin to fill in these details and provide unexpected surprises in the chemical evolution of the core.

References

Abarca del Rio R, Gambis D, and Salstein DA (2000) Interannual signals in length of day and atmospheric angular momentum. *Annales Geophysicae* 18: 347–364.

Anufriyev AP and Braginsky SI (1975) Influence of irregularities of the boundary of the Earth's core on the velocity of the liquid and on the magnetic field. *Geomagnetism and Aeronomy* 15: 754–757.

Anufriyev AP and Braginsky SI (1977) Influence of irregularities of the boundary of the Earth's core on fluid velocity and the magnetic field, II. *Geomagnetism and Aeronomy* 17: 78–82.

Asahara Y, Frost DJ, and Rubie DC (2007) Partitioning of FeO between magnesiowustite and liquid iron at high pressures and temperatures: Implications for the composition of the Earth's outer core. *Earth and Planetary Science Letters* 257: 435–449.

Aubert J and Dumberry M (2010) Steady and fluctuating inner core rotation in numerical geodynamo models. *Geophysical Journal International* 184: 162–170.

Badro J, Fiquet G, Guyot F, et al. (2003) Iron partitioning in Earth's mantle: Toward a deep lower mantle discontinuity. *Science* 300: 789–791.

Bloxham J (2002) Time-independent and time-dependent behaviour of high-latitude flux bundles at the core–mantle boundary. *Geophysical Research Letters* 29: 1854. http://dx.doi.org/10.1029/2001GL014543.

Bloxham J and Gubbins D (1987) Thermal core–mantle interactions. *Nature* 325: 511–513.

Bloxham J and Jackson J (1990) Lateral temperature variations at the core–mantle boundary deduced from the magnetic field. *Geophysical Research Letters* 17: 1997–2000.

Braginsky SI (1963) Structure of F layer and reasons for convection in the Earth's core. *Doklady Akademii Nauk SSSR* 149: 1311–1317.

Braginsky SI (1970) Torsional magnetohydrodynamic vibrations in the Earth's core and variations in length of day. *Geomagnetism and Aeronomy* 10: 1–8.

Braginsky SI (1984) Short-period geomagnetic secular variation. *Geophysical and Astrophysical Fluid Dynamics* 30: 1–78.

Brandon AD and Walker RJ (2005) The debate over core–mantle interaction. *Earth and Planetary Science Letters* 232: 211–225.

Brandon AD, Walker RJ, Morgan JW, Norman MD, and Prichard HM (1998) Coupled Os-186 and Os-187 evidence for core–mantle interaction. *Science* 280: 1570–1573.

Buffett BA (1992) Constraints on magnetic energy and mantle conductivity from the forced nutations of the Earth. *Journal of Geophysical Research* 97: 19581–19597.

Buffett BA (1996a) Effects of a heterogeneous mantle on the velocity and magnetic fields at the top of the core. *Geophysical Journal International* 125: 303–317.

Buffett BA (1996b) Gravitational oscillations in the length of day. *Geophysical Research Letters* 23: 2279–2282.

Buffett BA (2002) Estimates of heat flow in the deep mantle based on the power requirements for the geodynamo. *Geophysical Research Letters* 29: 1566. http://dx.doi.org/10.1029/2001GL014649.

Buffett BA, Garnero EJ, and Jeanloz R (2000) Sediments at the top of the core. *Science* 290: 1338–1342.

Buffett BA and Glatzmaier GA (2000) Gravitational breaking of inner-core rotation in geodynamo simulations. *Geophysical Research Letters* 27: 3125–3128.

Buffett BA and Seagle CT (2010) Stratification of the top of the core due to chemical interactions with the mantle. *Journal of Geophysical Research* 115: B04407.

Bullard EC, Freeman C, Gellman H, and Nixon J (1950) The westward drift of the Earth's magnetic field. *Philosophical Transactions of the Royal Society of London, Series A* 132: 61–92.

Bunge HP, Hagelberg CR, and Travis BJ (2003) Mantle circulation models with variational data assimilation: Inferring past mantle flow and structure from plate motion histories and seismic tomography. *Geophysical Journal International* 152: 280–301.

Busse FH and Wicht J (1992) A simple dynamo caused by conductivity variations. *Geophysical and Astrophysical Fluid Dynamics* 62: 135–144.

Calkins MA, Noir J, Eldredge JD, and Aurnou J (2012) The effects of boundary topography on convection in Earth's core. *Geophysical Journal International* 189: 799–814.

Chan KH, Zhang KK, Li LG, and Liao XH (2008) On the effect of an electrically heterogeneous lower mantle on planetary dynamos. *Physics of the Earth and Planetary Interiors* 169: 204–210.

Christensen UR and Olson P (2003) Secular variation in numerical geodynamo models with lateral variations of boundary heat flow. *Physics of the Earth and Planetary Interiors* 138: 39–54.

Clement BM (1991) Geographical distribution of transitional VGPs: Evidence for non-zonal equatorial symmetry during the Matuyama–Brunhes reversal. *Earth and Planetary Science Letters* 104: 48–58.

Clement BM (2004) Dependence of the duration of geomagnetic polarity reversals on site latitude. *Nature* 428: 637–640.

Costin SO and Buffett BA (2004) Preferred reversal paths caused by a heterogeneous conducting layer at the base of the mantle. *Journal of Geophysical Research* 109: B06101. http://dx.doi.org/10.1029/2003JB002853.

Cox CM and Chao BF (2002) Detection of a large-scale mass redistribution in the terrestrial system since 1998. *Science* 297: 831–833.

Davies CJ, Gubbins D, Ashley AP, and Jimack PK (2008) Time-averaged paleomagnetic field and secular variation: Predictions from dynamo solutions based on lower mantle seismic tomography. *Physics of the Earth and Planetary Interiors* 169: 194–203.

de Koker N, Steinle-Neumann G, and Vicek V (2012) Electrical resistance and thermal conductivity of liquid Fe alloys at high P and T, and the heat flux in Earth's core. *Proceedings of the National Academy of Sciences of the United States of America* 109: 4070–4073.

de Wijs GA, Kresse G, Vocadlo L, et al. (1998) The viscosity of liquid iron at the physical conditions of the Earth's core. *Nature* 392: 805–807.

Defraigne P, Dehant V, and Wahr JM (1996) Internal loading of an inhomogeneous compressible earth with phase boundaries. *Geophysical Journal International* 125: 173–192.

Deleplace B and Cardin P (2006) Viscomagnetic torque at the core mantle boundary. *Geophysical Journal International* 167: 557–566.

Driscoll P and Olson P (2011) Superchron cycles driven by variable core heat flow. *Geophysical Research Letters* 38: L09304.

Dumberry M and Bloxham J (2004) Variations in the Earth's gravity field caused by torsional oscillations in the core. *Geophysical Journal International* 159: 417–434.

Dumberry M and Mound J (2010) Inner core–mantle gravitational locking and the super-rotation of the inner core. *Geophysical Journal International* 181: 806–817.

Dziewonski AM, Hager BH, and O'Connell RJ (1977) Large-scale heterogeneities in the lower mantle. *Journal of Geophysical Research* 82: 239–255.

Fang M, Hager BH, and Herring TA (1996) Surface deformation caused by pressure changes in the fluid core. *Geophysical Research Letters* 23: 1493–1496.

Forte AM and Peltier WR (1991) Mantle convection and core–mantle boundary topography – Explanations and implications. *Tectonophysics* 187: 91–116.

Forte AM, Woodward RL, and Dziewonski AM (1994) Joint inversion of seismic and geodynamic data for models of three-dimensional mantle heterogeneity. *Journal of Geophysical Research* 99: 21857–21877.

Gillet N, Jault D, Canet E, and Fournier A (2010) Fast torsional waves and strong magnetic field within the Earth's core. *Nature* 465: 74–77.

Glatzmaier GA, Coe RS, Hongre L, and Roberts PH (1999) The role of the Earth's mantle in controlling the frequency of geomagnetic reversals. *Nature* 401: 885–890.

Goarant F, Guyot F, Peronneau J, and Poirier JP (1992) High-pressure and high-temperature reactions between silicates and liquid iron alloys in the diamond cell studied by analytical electron microprobe. *Journal of Geophysical Research* 97: 4477–4487.

Greff-Lefftz M, Pais MA, and LeMouel JL (2004) Surface gravitational field and topography changes induced by the Earth's fluid core motions. *Journal of Geodesy* 78: 386–392.

Gubbins D and Kelly P (1993) Persistent patterns in the geomagnetic field over the past 2.5 Myr. *Nature* 365: 829–832.

Gubbins D, Thompson CJ, and Whaler KA (1982) Stable regions in the Earth's liquid core. *Geophysical Journal of the Royal Astronomical Society* 68: 241–251.

Hager BH, Clayton RW, Richards MA, Comer RP, and Dziewonski AM (1985) Lower mantle heterogeneity, dynamic topography and the geoid. *Nature* 313: 541–546.

Heller PL, Anderson DL, and Angevine CL (2006) The middle Cretaceous pulse of rapid sea-floor spreading real or necessary? *Geology* 24: 491–494.

Herring TA, Buffett BA, Mathews PM, and Shapiro II (1991) Forced nutations of the Earth: Influence of inner core dynamics, 3. Very long baseline interferometry data analysis. *Journal of Geophysical Research* 96: 8259–8273.

Herring TA, Mathews PM, and Buffett BA (2002) Modeling of nutation and precession: Very long baseline results. *Journal of Geophysical Research* 107: 2069. http://dx.doi.org/10.1029/2001JB000165.

Hide R (1969) Interaction between Earth's liquid core and mantle. *Nature* 222: 1055–1056.

Hide R (1989) Fluctuations in the Earth's rotation and the topography of the core–mantle interface. *Philosophical Transactions of the Royal Society of London, Series A* 328: 351–363.

Holme R (1998) Electromagnetic core–mantle coupling I. Explaining decadal changes in the length of day. *Geophysical Journal International* 132: 167–180.

Humayun M (2011) A model for osmium isotopic evolution of metallic solids at the core–mantle boundary. *Geochemistry, Geophysics, Geosystems* 12: Q03007. http://dx.doi.org/10.1029/2010GC003281.

Ito E, Morooka K, Ujike O, and Katsura T (1995) Reactions between molten iron and silicate melts at high pressure – Implications for the chemical evolution of the Earth's core. *Journal of Geophysical Research* 100: 5901–5910.

Jault D and LeMouel JL (1989) The topographic torque associated with tangentially geostrophic motion at the core surface and inferences on the flow inside the core. *Geophysical and Astrophysical Fluid Dynamics* 48: 273–296.

Jault D and LeMouel JL (1990) core–mantle boundary shape – Constraints inferred from the pressure torque acting between the core and the mantle. *Geophysical Journal International* 101: 233–241.

Jault D and LeMouel JL (1999) Comment on 'On the dynamics of topographical core–mantle coupling'. *Physics of the Earth and Planetary Interiors* 114: 211–215.

Jeanloz R (1990) The nature of the Earth's core. *Annual Review of Earth and Planetary Sciences* 18: 357–386.

Johnson CL and Constable CG (1997) The time-averaged geomagnetic field: Global and regional biases for 0–5 Ma. *Geophysical Journal International* 131: 643–666.

Johnson CL and Constable CG (1998) Persistently anomalous Pacific geomagnetic fields. *Geophysical Research Letters* 25: 1011–1014.

Kanda RVS and Stevenson DJ (2006) Suction mechanism for iron entrainment into the lower mantle. *Geophysical Research Letters* 33: L02310. http://dx.doi.org/10.1029/2005GL025009.

Kavner A and Walker D (2006) Core/mantle-like interactions in an electric field. *Earth and Planetary Science Letters* 248: 316–329.

Knittle E and Jeanloz R (1989) Simulating the core–mantle boundary – An experimental study of high-pressure reactions between silicates and liquid iron. *Geophysical Research Letters* 16: 609–612.

Knittle E and Jeanloz R (1991) The Earth's core–mantle boundary: Results of experiments at high pressure and temperature. *Science* 251: 1438–1443.

Kohler MD and Stevenson DJ (1990) Modeling core fluid motions and the drift of magnetic-field patterns at the CMB by using topography obtained by seismic inversion. *Geophysical Research Letters* 17: 1473–1476.

Koot L, Dumberry M, Rivoldini A, de Viron O, and Dehant V (2010) Constraints on the coupling at the core–mantle and inner-core boundaries inferred from nutation observations. *Geophysical Journal International* 182: 1279–1294.

Koot L, Rivoldini A, de Viron O, and Dehant V (2008) Estimation of Earth interior parameters from a Bayesian inversion of very long baseline interferometry. *Journal of Geophysical Research* 113: B08414.

Koyama T, Shimizu H, and Utada H (2001) Possible effects of lateral heterogeneity in the D″ layer on electromagnetic variations of core origin. *Physics of the Earth and Planetary Interiors* 129: 99–116.

Kuang W and Bloxham J (1993) On the dynamics of topographical core–mantle coupling. *Geophysical and Astrophysical Fluid Dynamics* 72: 161–195.

Kuang W and Bloxham J (1997) On the dynamics of topographical core–mantle coupling. *Physics of the Earth and Planetary Interiors* 99: 289–294.

Kuang W and Chao BF (2001) Topographic core–mantle coupling in geodynamo modeling. *Geophysical Research Letters* 28: 1871–1874.

Kutzner C and Christensen UR (2004) Simulated geomagnetic reversals and preferred virtual geomagnetic pole paths. *Geophysical Journal International* 157: 1105–1118.

Labrosse S, Poirier JP, and LeMouel JL (2001) The age of the inner core. *Earth and Planetary Science Letters* 190: 111–123.

Laj C, Mazaud A, Weeks R, Fuller M, and Herrero-Bervera E (1991) Geomagnetic reversal paths. *Nature* 351: 447.

Lay T, Hernlund J, and Buffett BA (2008) Core–mantle boundary heat flow. *Nature Geoscience* 1: 25–32.

Lister JR and Buffett BA (1998) Stratification of the outer core at the core–mantle boundary. *Physics of the Earth and Planetary Interiors* 105: 5–19.

Lithgow-Bertelloni C and Richards MA (1998) The dynamics of Cenozoic and Mesozoic plate motions. *Reviews of Geophysics* 36: 27–78.

Loper DE (1978) Some consequences of a gravitationally powered dynamo. *Journal of Geophysical Research* 83: 5961–5970.

Mathews PM, Buffett BA, Herring TA, and Shapiro II (1991) Forced nutations of the Earth – Influence of inner core dynamics, 1. Theory. *Journal of Geophysical Research* 96: 8219–8242.

Mathews PM and Guo JY (2005) Viscoelectromagnetic coupling in precession-nutation theory. *Journal of Geophysical Research* 110: B02402. http://dx.doi.org/10.1029/JB002915.

Mathews PM, Herring TA, and Buffett BA (2002) Modeling of nutation and precession: New nutation series for nonrigid Earth and insights into the Earth's interior. *Journal of Geophysical Research* 107(B4): 2068. http://dx.doi.org/10.1029/2001JB000390.

Mathews PM and Shapiro II (1992) Nutations of the Earth. *Annual Review of Earth and Planetary Sciences* 20: 469–500.

McNamara AK and Zhong SJ (2005) Thermochemical structures beneath Africa and the Pacific Ocean. *Nature* 437: 1136–1139.

Moffatt HK and Dillon RF (1976) Correlation between gravitational and geomagnetic fields caused by interaction of core fluid motion with a bumpy core–mantle interface. *Physics of the Earth and Planetary Interiors* 13: 67–78.

Morelli A and Dziewonski AM (1987) Topography of the core–mantle boundary and lateral homogeneity of the liquid core. *Nature* 325: 638–678.

Mound JE and Buffett BA (2005) Mechanisms of core–mantle angular momentum exchange and the observed spectral properties of torsional oscillations. *Journal of Geophysical Research* 110: B08103. http://dx.doi.org/10.1029/2004JB0035555.

Mound JE and Buffett BA (2006) Detection of a gravitational oscillation in length of day. *Earth and Planetary Science Letters* 243: 383–389.

Murakami M, Hirose K, Kawamura K, Sata N, and Ohishi Y (2004) Post-perovskite phase transition in $MgSiO_3$. *Science* 304: 855–858.

Nimmo F and Stevenson DJ (2000) Influence of early plate tectonics on the thermal evolution and magnetic field of Mars. *Journal of Geophysical Research* 105: 11969–11979.

Oganov AR and Ono S (2004) Theoretical and experimental evidence for a postperovskite phase of $MgSiO_3$ in Earth's D" layer. *Nature* 430: 445–448.

Ohta K, Hirose K, Ichiki M, Shimizu K, Sata N, and Ohishi Y (2010) Electrical conductivities of pyrolitic mantle and MORB materials up to the lowermost mantle conditions. *Earth and Planetary Science Letters* 289: 497–502.

Olson P and Christensen UR (2002) The time-averaged magnetic field in numerical dynamos with non-uniform boundary heat flow. *Geophysical Journal International* 151: 809–823.

Olson P, Coe RS, Driscoll PE, Glatzmaier GA, and Roberts PH (2010) Geodynamo reversal frequency and heterogeneous core–mantle boundary heat flow. *Physics of the Earth and Planetary Interiors* 180: 66–79.

Olson P, Deguen R, Hinnov LA, and Zhong SJ (2013) Controls on geomagnetic reversals and core evolution by mantle convection in the Phanerozoic. *Physics of the Earth and Planetary Interiors* 214: 87–103.

Ono S, Oganov AR, Koyama T, and Shimizu H (2006) Stability and compressibility of the high-pressure phases of Al_2O_3 up to 200 GPa: Implications for the electrical conductivity of the base of the lower mantle. *Earth and Planetary Science Letters* 246: 326–335.

Otsuka K and Karato SI (2012) Deep penetration of molten iron into the mantle caused by a morphological instability. *Nature* 492: 243–246.

Ozawa H, Hirose K, Mitome Y, Bando Y, Sata H, and Ohishi Y (2008) Chemical equilibrium between ferropericlase and molten iron to 134 GPa and implications for the iron content at the bottom of the mantle. *Geophysical Research Letters* 35: L05308.

Ozawa H, Hirose K, Mitome M, Bando Y, Sata N, and Ohishi Y (2009) Experimental study of reaction between perovskite and molten iron to 146 GPa and implications for chemically distinct buoyant layer at the top of the core. *Physics and Chemistry of Minerals* 36: 355–363.

Petford N, Yuen D, Rushmer T, Brodholt J, and Stackhouse S (2005) Shear-induced material transfer across the core–mantle boundary aided by the post-perovskite phase transition. *Earth Planets Space* 57: 459–464.

Poirier JP and LeMouel JL (1992) Does infiltration of core material into the lower mantle affect the observed geomagnetic field? *Physics of the Earth and Planetary Interiors* 99: 1–17.

Pozzo M, Davies C, Gubbins D, and Alfe D (2012) Thermal and electrical conductivity of iron at Earth's core conditions. *Nature* 485: 355–358.

Ricard Y and Vigny C (1989) Mantle dynamics with induced plate tectonics. *Journal of Geophysical Research* 94: 17543–17559.

Rochester MG (1962) Geomagnetic core–mantle coupling. *Journal of Geophysical Research* 67: 4336–4833.

Roden RB (1963) Electromagnetic core–mantle coupling. *Geophysical Journal of the Royal Astronomical Society* 7: 361–374.

Rowley DB (2002) Rate of plate creation and destruction: 180 Ma to present. *Geological Society of America Bulletin* 114: 927–933.

Rubie DC, Melosh HJ, and Nimmo F (2007) Formation of the Earth's core. In: Stevenson D (ed.) *Treatise on Geophysics*, is Elsevier B.V., vol. 9, pp. 51–90.

Rubincam DP (2003) Gravitational core–mantle coupling and the acceleration of the Earth. *Journal of Geophysical Research* 108: 2338. http://dx.doi.org/10.1029/2002JB002132.

Sakai T, Kondo T, Ohltani E, et al. (2006) Interaction between iron and post-perovskite at core–mantle boundary and core signature in plume source region. *Geophysical Research Letters* 33: L15317.

Sarson GR, Jones CA, and Longbottom AW (1997) The influence of boundary region heterogeneity on the geodynamo. *Physics of the Earth and Planetary Interiors* 101: 13–32.

Schersten A, Elliot T, Hawkesworth C, and Norman M (2004) Tungsten isotope evidence that mantle plumes contain no contribution from the Earth's core. *Nature* 427: 234–237.

Siebert J, Badro J, Antonangeli D, and Ryerson FJ (2012) Metal-silicate partitioning of Ni and Co in a deep magma ocean. *Earth and Planetary Science Letters* 321–322: 189–197.

Sreenivasan B and Gubbins D (2008) Dynamos with weakly convecting outer layers: Implications for core–mantle boundary interaction. *Geophysical and Astrophysical Fluid Dynamics* 102: 395–407.

Stevenson DJ (1987) Limits on lateral density and velocity variations in the Earth's outer core. *Geophysical Journal of the Royal Astronomical Society* 88: 311–319.

Stevenson DJ (1990) Fluid dynamics of core formation. In: Newson H and Jones JH (eds.) *The Origin of the Earth*, pp. 231–249. London: Oxford Press.

Stevenson DJ (2007) Core exsolution: A likely consequence of giant impacts and a likely energy source for the geodynamo. *Eos, Transactions American Geophysical Union* 88(52), Fall Meet. Suppl. Abstract U21D02.

Stix M and Roberts PH (1984) Time-dependent electromagnetic core–mantle coupling. *Physics of the Earth and Planetary Interiors* 36: 49–60.

Sumita I and Olson P (1999) A laboratory model for convection in Earth's core driven by a thermally heterogeneous mantle. *Science* 286: 1547–1549.

Sumita I and Olson P (2002) Rotating thermal convection experiments in a hemispherical shell with heterogeneous boundary heat flux: Implications for the Earth's core. *Journal of Geophysical Research* 107(B8): 2169.

Takafuji N, Hirose K, Mitome M, and Bando Y (2005) Solubilities of O and Si in liquid iron in equilibrium with (Mg, Fe)SiO_3 and the light element in the core. *Geophysical Research Letters* 32: L06313.

Takamasa A, Nakai S, Sahoo Y, Hanyu T, and Tatsumi Y (2009) W isotope composition of oceanic island basalts from French Polynesia and their meaning for core–mantle interaction. *Chem. Geol*. 260: 37–46.

Tsuno K, Frost DJ, and Rubie DC (2013) Simultaneous partitioning of silicon and oxygen into the Earth's core during early Earth differentiation. *Geophysical Research Letters* 40: 66–71.

Valet JP, Fournier A, Courtillot V, and Herrero-Bervera E (2012) Dynamical similarity of geomagnetic reversals. *Nature* 490: 89–93.

Van Orman JA, Fei YW, Hauri EH, and Wang JH (2003) Diffusion in MgO at high pressures: Constraints on deformation mechanisms and chemical transport at the core–mantle boundary. *Geophysical Research Letters* 30: 1056. http://dx.doi.org/10.1029/2002GL016343.

Verhoogen J (1961) Heat balance of the Earth's core. *Geophysical Journal of the Royal Astronomical Society* 4: 276–281.

Wahr JM (1981) The forced nutations of an elliptical, rotating, elastic and oceanless Earth. *Geophysical Journal of the Royal Astronomical Society* 64: 705–727.

Walker D (2000) Core participation in mantle geochemistry. *Geochimica et Cosmochimica Acta* 64: 2897–2911.

Walker D (2005) core–mantle chemical issues. *Canadian Mineralogist* 43: 1553–1564.

Walker RJ, Morgan JW, and Horan MF (1995) ^{187}Os enrichment in some plumes: Evidence for core–mantle interaction. *Science* 289: 819–822.

Wicht J and Jault D (1999) Constraining electromagnetic core–mantle coupling. *Physics of the Earth and Planetary Interiors* 111: 161–177.

Xu X, Lithgow-Bertelloni C, and Conrad CP (2006) Global reconstructions of Cenozoic seafloor ages: Implications for bathymetry and sea level. *Earth and Planetary Science Letters* 243: 552–564.

Xu Y, Shankland TJ, and Poe BT (2000) Laboratory-based electrical conductivity in the Earth's mantle. *Journal of Geophysical Research* 105: 27865–27875.

Zhang K and Gubbins D (1993) Convection in a rotating spherical shell with an inhomogeneous temperature boundary condition: Condition at infinite Prandtl number. *Journal of Fluid Mechanics* 250: 209–232.

Zhang K and Gubbins D (1996) Convection in a rotating spherical fluid shell with an inhomogeneous temperature boundary condition at finite Prandtl number. *Physics of Fluids* 8: 1141–1148.

Zhang YG and Guo GJ (2000) Molecular dynamics calculations of the bulk viscosity of liquid iron-nickel alloy and the mechanisms for the bulk attenuation of seismic waves in the Earth's outer core. *Physics of the Earth and Planetary Interiors* 122: 289–298.

Zhang K and Schubert G (2000) Teleconvection: Remotely driven thermal convection in rotating stratified spherical layers. *Science* 290: 1944–1947.

Zhang N and Zhong S (2011) Heat fluxes at the Earth's surface and core–mantle boundary since Pangea formation and their implications for the geomagnetic superchrons. *Earth and Planetary Science Letters* 306: 205–216.

8.09 Waves in the Core and Mechanical Core–Mantle Interactions

D Jault, University Grenoble Alpes/CNRS, Grenoble, France
CC Finlay, DTU Space, Technical University of Denmark, Lyngby, Denmark

© 2015 Elsevier B.V. All rights reserved.

8.09.1	**Motivation**	225
8.09.2	**Competing Constraints from Rotation and Magnetic Fields**	226
8.09.2.1	Small Disturbances from a Quiescent State	226
8.09.2.1.1	Alfvén waves	226
8.09.2.1.2	Inertial waves	226
8.09.2.1.3	Compressibility effects	227
8.09.2.2	Constraint Imposed by Rapid Rotation	228
8.09.2.2.1	Quasi-geostrophic approximations	229
8.09.2.2.2	Wave motion in a quasi-geostrophic system	231
8.09.2.2.3	Axially averaged equations	231
8.09.2.2.4	Magnetic diffusion layer at the top and bottom boundaries	232
8.09.2.2.5	Quasi-geostrophic MHD turbulence	232
8.09.3	**Torsional Waves**	233
8.09.3.1	Taylor's Condition	233
8.09.3.2	The Canonical One-Dimensional Torsional Wave Equation	234
8.09.3.3	Boundary Conditions for the One-Dimensional Torsional Wave Equation	234
8.09.3.4	Inference of the Strength of the Magnetic Field in Earth's Core Interior	235
8.09.3.5	Calculation of Core Angular Momentum Changes	236
8.09.4	**Mechanical Core–Mantle Interactions**	237
8.09.4.1	Geostrophic Contours	237
8.09.4.2	Torsional Waves in the Presence of Topography	239
8.09.4.3	Coupling with the Solid Inner Core	240
8.09.4.3.1	Time-variable geostrophic contours	240
8.09.4.3.2	Gravitational coupling	240
8.09.4.3.3	Electromagnetic coupling	240
8.09.5	**Future Directions – Consistent Approach to the Earth's Core Dynamics**	240
8.09.5.1	Diffusion of the Geomagnetic Signal Through the Weakly Conducting Mantle	240
8.09.5.2	Filtering Through a Stably Stratified Layer Below the CMB	241
8.09.6	**Final Remarks**	242
References		242

8.09.1 Motivation

Various classes of waves are forced in the fluid outer core. Tides and wobbles of the rotation axis drive inertial waves, whereas seismic forcing leads to the propagation of sound waves. However, this chapter focuses mainly on waves that are internally driven. Disturbances initiated in some location within the core propagate as waves until some new equilibrium is found. For example, acoustic waves are instrumental in re-equilibrating the pressure field; they are so fast compared to other waves that they are usually filtered out in models of core dynamics, where it is assumed that pressure information is transmitted instantaneously. More generally, competition between the different possible classes of waves is crucial in determining what the most important dynamical constraints on core motions and magnetic fields are.

There is a second motivation to investigate waves propagating inside the core. Determination of their characteristics can lead to new knowledge concerning the hidden magnetic field and the density profile in the core interior. Recently, the average strength of the magnetic field deep inside the core was estimated from the indirect observation of torsional waves recurring every 6 years or so. In Chapter 5.05, Jackson and Finlay discuss other wave-like features that are apparent in successive images of the radial magnetic field at the core surface over the past 400 years. These disturbances, which remain unexplained, are conspicuous near the equator and drift westward.

Finally, it is usual to separately investigate magnetic induction in the core and in the mantle or, similarly, fluid motions in the core and mechanical core–mantle interactions. However, these phenomena are fundamentally coupled together. Complete models of waves inside the core that are currently in development should include mechanisms of coupling with the mantle. The study of these models expounds the limitations of previous models, which were restricted to either the core or the mantle.

8.09.2 Competing Constraints from Rotation and Magnetic Fields

8.09.2.1 Small Disturbances from a Quiescent State

Comprehensive overviews of waves in the presence of rotation and a magnetic field can be found in Gubbins and Roberts (1987) and Finlay (2008).

8.09.2.1.1 Alfvén waves

Waves arise in a liquid metal permeated by a magnetic field because the Lorentz force tends to oppose the curvature of magnetic field lines. In order to introduce the discussion of these so-called Alfvén waves, we study the case of a uniform, steady magnetic field $\mathbf{B}_0$ (see also Finlay (2007) for a deeper physical insight into the mechanism of Alfvén waves). The reader is referred to **Chapter 8.03** by Roberts where basic magnetohydrodynamic theory, including the derivation of the induction equation from Ohm's law and Maxwell equations, is presented.

The fluid is assumed to be inviscid and perfectly conducting and to have uniform density ρ. The two coupled momentum and induction equations are linearized to obtain

$$\rho\frac{\partial \mathbf{u}}{\partial t} = -\nabla P + \frac{1}{\mu_0}(\mathbf{B}_0\cdot\nabla)\mathbf{B} \qquad [1]$$

$$\frac{\partial \mathbf{B}}{\partial t} = (\mathbf{B}_0\cdot\nabla)\mathbf{u} \qquad [2]$$

where P is a modified pressure, which includes a magnetic pressure term, and μ_0 is the magnetic permeability. Both the magnetic field $\mathbf{B}$ and the velocity field $\mathbf{u}$ are solenoidal:

$$\nabla\cdot\mathbf{u} = \nabla\cdot\mathbf{B} = 0 \qquad [3]$$

Taking the divergence of [1], we obtain

$$\nabla^2 P = 0 \qquad [4]$$

If there are no sources at infinity, $P=0$.

At this point, it is convenient to introduce the quantities $\mathbf{V}_0 = \mathbf{B}_0/\sqrt{\rho\mu_0}$ and $\mathbf{V} = \mathbf{B}/\sqrt{\rho\mu_0}$, which have the dimensions of a velocity. The set of equations [1] and [2] can then be transformed into a wave equation for $\mathbf{V}$,

$$\frac{\partial^2 \mathbf{V}}{\partial t^2} = (\mathbf{V}_0\cdot\nabla)^2\mathbf{V} \qquad [5]$$

and an analogous equation for $\mathbf{u}$ instead of $\mathbf{V}$. It means that fluid or magnetic disturbances transverse to $\mathbf{B}_0$ are propagated in the form of waves. Equations [1] and [2] are both satisfied by solutions of the form

$$\mathbf{u} = \mathbf{f}(\mathbf{x} \pm \mathbf{V}_0 t) \qquad [6]$$

$$\mathbf{V} = \pm\mathbf{f}(\mathbf{x} \pm \mathbf{V}_0 t) \qquad [7]$$

where $\mathbf{f}$ is an arbitrary function and $\mathbf{x}$ is the position vector. The solutions are specified by the initial values of $\mathbf{u}$ and $\mathbf{V}$. Seeking plane wave solutions $\mathbf{u} \propto \exp[\mathrm{i}(\mathbf{k}\cdot\mathbf{x} - \omega t)]$, where $\mathbf{k}$ denotes the wave vector and ω the frequency, we obtain the dispersion relation

$$\omega = \pm(\mathbf{V}_0\cdot\mathbf{k}) = \pm k(\mathbf{V}_0\cdot\mathbf{1}_k) \qquad [8]$$

where $\mathbf{1}_k$ is the unit vector along the direction of $\mathbf{k}$. Thus, the phase speed $c = (\omega/k)$ of the Alfvén waves in the direction of $\mathbf{k}$ is directly given by the Alfvén velocity $\mathbf{V}_0$. The group velocity $\partial\omega/\partial\mathbf{k}$ (i.e., $(\partial\omega/\partial k_x, \partial\omega/\partial k_y, \partial\omega/\partial k_z)$ in Cartesian coordinates (x, y, z)) is defined as the velocity of energy propagation. It is $\mathbf{V}_0$ for all directions of $\mathbf{k}$.

Expressions [6] and [7] show clearly that there is equipartition of energy: the energy density of Alfvén waves is equally distributed among its kinetic $\rho u^2/2$ and magnetic $B^2/2\mu_0 = \rho V^2/2$ components.

Finally, Alfvén waves act as the means of eliminating discontinuities in the tangential components of the magnetic field at the surface of an electrically conducting fluid when there is a magnetic field transverse to the boundary. This effect was first documented by Stewartson (1957) in the case of a perfectly conducting and inviscid fluid half-space abutting a solid and insulating domain. In the presence of kinematic viscosity ν and magnetic diffusivity η, dissipative effects are restricted to a thin boundary layer. The nature of this 'Hartmann' boundary layer depends on the value of the magnetic Prandtl number, $p_\mathrm{m} = \nu/\eta \ll 1$ (Busse et al., 2007, pp 137–138). In the limit $p_\mathrm{m} \ll 1$, which is appropriate for liquid metals, only the velocity field is modified through the boundary layer and to erase the magnetic field discountinuities, Alfvén waves are emitted (Roberts and Scott, 1965). Thus, the dissipation-free interior problem (outside the boundary layer) is required to satisfy not only normal boundary conditions but also tangential ones.

8.09.2.1.2 Inertial waves

Inertial waves are caused solely by rotation. The reader is referred to **Chapter 8.07** by Tilgner for a complete discussion of inertial oscillations in rotating spheres and spherical shells. Once again, an inviscid, incompressible, and infinitely extended fluid is considered. **Chapter 8.07** details how the momentum equation, expressed in a frame of reference rotating with the angular frequency $\mathbf{\Omega}$,

$$\rho\frac{\partial \mathbf{u}}{\partial t} + 2\rho(\mathbf{\Omega}\times\mathbf{u}) = -\nabla p \qquad [9]$$

can be transformed into the equation

$$\frac{\partial^2}{\partial t^2}\nabla^2\mathbf{u} + 4(\mathbf{\Omega}\cdot\nabla)^2\mathbf{u} = 0 \qquad [10]$$

Searching for plane wave solutions, which are suitable for the short-wavelength limit, we obtain the dispersion equation

$$\omega = \pm\frac{2\mathbf{k}\cdot\mathbf{\Omega}}{k} \qquad [11]$$

The frequency ω is independent of the wavelength and the typical period is of the order of the rotation period of the fluid. In contrast to Alfvén waves, inertial waves are strongly dispersive. From eqn [11], the group velocity can be calculated:

$$\mathbf{c}_\mathrm{g} = \pm 2\frac{1_k\times(\mathbf{\Omega}\times 1_k)}{k} \qquad [12]$$

Thus, the energy transport is at right angles to the planes of the constant phase. It can also be shown that the result $|\omega| \le 2\Omega$, obtained here for plane waves in an infinite domain, also holds for inertial oscillations in a contained rotating fluid (Greenspan, 1965).

In the limit $\omega = 0$, which corresponds to $(\mathbf{1}_k\cdot\mathbf{\Omega}) = 0$, there is geostrophic balance between the Coriolis and pressure terms.

From eqn [10], we learn that there is an excitation of inertial waves when the Proudman–Taylor theorem

$$(\mathbf{\Omega}\cdot\nabla)\mathbf{u} = 0 \qquad [13]$$

is violated. In other words, inertial waves will ring until the velocity field is modified in such a way that it satisfies eqn [13]. This state is reached quickly as exemplified by the formation of a 'Taylor' column, named after the famous experiments reported by Taylor (1923), above a disk co-rotating with an infinite body of fluid. In an insightful thought experiment (Davidson, 2001, p. 165; Greenspan, 1968, pp. 192–200), one can imagine a disk of radius r_0 being made to move slowly along the axis of rotation and perpendicular to its own surface at the initial time $t=0$. The axisymmetric fluid velocity is sought as a function of time. The initial value problem can be solved analytically and the solution is given in Greenspan (1968). On each side of the disk and within the axial cylinder C circumscribing the disk, there is a region of increasing size where the fluid particles move with the disk. Outside the cylinder C, the fluid is at rest in the rotating frame of reference. The height of the region moving with the disk increases with time as $\Omega r_0 t$. This finding is consistent with an interpretation in terms of inertial waves as the front velocity corresponds to the group velocity of plane inertial waves, with the wave vector perpendicular to the rotation axis, and a wavenumber of r_0^{-1}. In Earth's core of radius r_c, we expect that Taylor columns of radius l reach the core–mantle boundary (CMB) in both hemispheres after a time of the order $(r_c/l)\Omega^{-1}$.

In a container, the boundaries have significant influence on large-wavelength inertial waves. In the case of the full sphere, implicit solutions for the oscillations and their frequencies were calculated long ago by Bryan (1889). Zhang et al. (2001) relied on the work of Kudlick (1966) to derive explicit solutions for the inertial waves. They paid special attention to the slowest waves, which are almost invariant in the direction parallel to the rotation axis as expected from eqn [11]. They found that the angular frequency of these quasi-geostrophic inertial waves (QGIW) is

$$\omega_R \sim \frac{2\Omega}{m+2}\left(\sqrt{1+\frac{m(m+2)}{N(2N+2m+1)}}-1\right) \qquad [14]$$

where the flow evolves as $\exp[i(m\phi-\omega t)]$ and N increases with the complexity in the s-direction (s, ϕ, z are cylindrical polar coordinates). The sign of ω_R in eqn [14] tells us that the phase of the QGIW waves propagates in the prograde (eastward) direction. For a given m, their frequency decreases as the length scale in the s-direction shortens.

QGIW waves have the character of Rossby waves (hence, the subscript R given earlier), which were first described in the meteorological context. Their mechanism can be visualized by considering a fluid column directed parallel to the rotation axis (**Figure 1**). In the case of the full sphere, the column acquires vorticity when displaced radially inward because it is stretched (Busse, 2002). Conversely, it loses vorticity when shifted outward. Later, eqn [14] is compared with the dispersion equation for Rossby waves after the quasi-geostrophic approximation is introduced (see **Section 8.09.2.2.2**).

When an inner sphere is present, solutions of the inviscid inertial wave equation present singular surfaces (Rieutord et al., 2001). Then, it is necessary to reinstate viscosity to obtain continuous solutions.

8.09.2.1.3 Compressibility effects

The density of the core increases by about 20% from the CMB down to the inner core boundary (ICB). This observation motivates our discussion of compressibility effects. Taking into account compressibility slightly modifies the equations for inertial waves and geostrophic motions. Here, the consequences are illustrated by using a general anelastic framework (Anufriev et al., 2005; Braginsky and Roberts, 1995).

Adiabatic stratification. The anelastic continuity equation is

$$\nabla\cdot(\rho_a\mathbf{u}) = 0 \qquad [15]$$

where ρ_a is the density in an adiabatically stratified reference state. It approximates the conservation of mass equation and governs processes having characteristic time scales, large with respect to acoustic periods, thus eliminating seismic waves from the problem.

In a compressible fluid, pressure variations p cause density variations ρ':

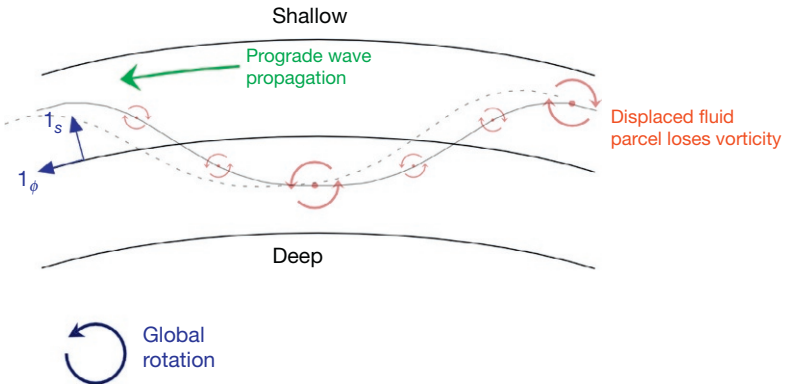

Figure 1 Mechanism of hydrodynamic Rossby waves visualized in the equatorial plane of a spherical shell with large aspect ratio. Vorticity acquired in response to the displacement relative to the rotation axis of axial fluid filaments. Prograde (eastward) propagation of the perturbation.

$$\rho' = p\left(\frac{\partial \rho_a}{\partial p}\right)_{S,\xi} \quad [16]$$

where the entropy S and the composition ξ are kept constant assuming the perturbation to be adiabatic. In the spherically symmetric adiabatic reference state, the pressure and gravitational terms are in hydrostatic balance

$$\frac{dp_a}{dr} = -g\rho_a \quad [17]$$

where $\mathbf{g} = -g\mathbf{1}_r$ is the gravitational acceleration, and eqn [16] transforms into

$$\rho' = -\frac{p}{g\rho_a}\frac{d\rho_a}{dr} \quad [18]$$

The momentum equation

$$\rho_a\frac{\partial \mathbf{u}}{\partial t} + 2\rho_a(\boldsymbol{\Omega}\times\mathbf{u}) = -\nabla p + \rho'\mathbf{g} \quad [19]$$

can then be written as:

$$\rho_a\frac{\partial \mathbf{u}}{\partial t} + 2\rho_a(\boldsymbol{\Omega}\times\mathbf{u}) = -\rho_a\nabla\frac{p}{\rho_a} \quad [20]$$

Assuming a steady state and dropping the first term on the left-hand side, a modified Proudman–Taylor constraint is obtained from eqns [15] and [20]. It holds here only for the components of the velocity field $\mathbf{u}_\perp$ perpendicular to the rotation axis,

$$(\boldsymbol{\Omega}\cdot\nabla)\mathbf{u}_\perp = 0 \quad [21]$$

as a direct consequence of

$$(\boldsymbol{\Omega}\cdot\nabla)\left(\frac{p}{\rho_a}\right) = 0 \quad [22]$$

From [15], we find that the velocity component u_z parallel to the rotation axis depends on z when $u_s \neq 0$:

$$\frac{\partial}{\partial z}(\rho_a u_z) = -u_s\frac{\partial}{\partial s}\rho_a \quad [23]$$

These results hold in the framework of the more complete theory of Braginsky and Roberts (1995), provided that pressure p is replaced by an effective pressure $p+\rho_a U'$ in eqn [22], although their theory accounts for the perturbation U' in the gravitational potential, which has been neglected here.

Gravity waves. Gravity waves arise in the presence of both thermal and compositional density gradients (e.g., Gubbins and Roberts, 1987) when the reference state (p_0, ρ_0) is not exactly adiabatic. The hydrostatic balance [17] holds now for p_0 and ρ_0:

$$\frac{dp_0}{dr} = -g\rho_0(r) \quad [24]$$

We consider radial displacement η_r of a fluid parcel initially at rest, which occurs fast enough to be adiabatic, that is, with negligible heat transfer. The density difference between the displaced parcel and its new environment is:

$$\delta\rho = \eta_r\left[\left(\frac{\partial \rho}{\partial r}\right)_{S,\xi} - \frac{d\rho_0}{dr}\right] \quad [25]$$

and the fluid parcel is subjected to the force $-\delta\rho g\mathbf{1}_r$. Newton's second law gives

$$\rho_0\frac{\partial^2\eta_r}{\partial t^2} = -\delta\rho g \quad [26]$$

The two equations [25] and [26] define the buoyancy (or Brunt–Väisälä) frequency N:

$$N^2 = \frac{g}{\rho_0}\left[\left(\frac{\partial \rho}{\partial r}\right)_{S,\xi} - \frac{d\rho_0}{dr}\right] \quad [27]$$

N is imaginary when the buoyancy exerts a restoring force on the fluid parcel and the stratification is stable. Note that this description does not yet account for the horizontal displacement of matter caused by the rising fluid parcel.

Next, displacement is separated into its radial and horizontal parts, $\delta\mathbf{r} = \eta_r 1_r + \boldsymbol{\eta}_H$. Velocity can be expressed as the rate of change of the displacement of the fluid parcel, that is, $\mathbf{u} = \partial\delta\mathbf{r}/\partial t$. Linearizing about the reference state, the equation of motion may be written as

$$\rho_0\frac{\partial \mathbf{u}}{\partial t} = -\nabla p' + \rho' g \quad [28]$$

Expanding the perturbation variables (pressure p' and displacement $\boldsymbol{\eta}$) as $\exp[i(\mathbf{k}\cdot\mathbf{r} - \omega t)$, where n is the wavenumber in the radial direction and k is the wavenumber in the horizontal direction, the radial and horizontal parts of eqn [28] are

$$-\rho_0\omega^2\eta_r = -inp' - \rho' g \quad [29]$$

$$-\rho_0\omega^2\boldsymbol{\eta}_H = -i\mathbf{k}_H p' \quad [30]$$

Integrating the equation of continuity [15] with respect to time and neglecting $\eta_r d\rho_0/dr$ compared to $n\eta_r\rho_0$ gives

$$n\eta_r + \mathbf{k}_H\cdot\boldsymbol{\eta}_H = 0 \quad [31]$$

Substituting between these yields

$$\rho_0\omega^2\left(1 + \frac{n^2}{k^2}\right)\eta_r = \rho' g \quad [32]$$

From [25] and [27], we also have

$$\rho' g = \rho_0 N^2\eta_r \quad [33]$$

Combining [32] and [33], the dispersion relation for gravity waves is obtained:

$$\omega^2 = \frac{k^2}{k^2 + n^2}N^2 \quad [34]$$

Note that the frequency is always less than N. If the horizontal wavelength of a disturbance is much shorter than its vertical wavelength (i.e., $k^2 \gg n^2$), then the frequency of the gravity waves is simply $\omega = N$, independent of the wavelength.

8.09.2.2 Constraint Imposed by Rapid Rotation

The importance of rotation in a non-magnetized fluid is characterized by the Rossby number Ro, which is defined as the ratio of the advective and Coriolis terms (Vallis, 2006):

$$Ro(l) = \frac{U}{\Omega l} \quad [35]$$

where l is a characteristic length scale in directions at right angles to the axis of rotation and U, a typical velocity. For large-scale dynamics in Earth's core, the term $\mathbf{V}\cdot\nabla\mathbf{V}$ arising from the Lorentz force dominates the advective term $\mathbf{u}\cdot\nabla\mathbf{u}$ and the ratio λ of the magnetic and Coriolis terms is, thus, the appropriate number to characterize the relative importance of rotation:

$$\lambda\,(l) = \frac{V_A}{l\Omega} = \frac{\mathcal{B}}{\sqrt{\mu_0\rho}\,l\Omega} \qquad [36]$$

where $\mathcal{B}$ is a typical magnetic field strength inside the core and V_A, the associated Alfvén wave speed $V_A = \mathcal{B}/\sqrt{\mu_0\rho}$. We refer to λ, where λ is a shorthand for $\lambda(r_c)(=V_A/r_c\Omega)$ and we have taken $l=r_c$ as the Lehnert number for the application to Earth's core. This acknowledges an early theoretical study of magnetohydrodynamic waves in the presence of rotation that identified λ as the key parameter (Lehnert, 1954). The Lehnert number is also the ratio of the periods of inertial and Alfvén waves (Jault, 2008). Other names are used too. In this volume, Paul Roberts introduces λ as the magnetic Rossby number (Ro_m, according to his notation) while Chris Jones, following Christensen and Aubert (2006), denotes it Lo (for Lorentz number). The Lehnert number can also be thought of in terms of a group velocity. It is the ratio of the speeds at which Alfvén and inertial waves carry information and energy.

For wavenumber $k<\lambda^{-1}$, the rapid propagation of inertial waves brings about the formation of Taylor columns; hence, motions with wavenumber $k<\lambda^{-1}$ can be expected to be almost axially invariant (e.g., Staplehurst et al., 2008). For $k>\lambda^{-1}$, Alfvén waves have a higher frequency than inertial waves and small-scale columnar structures have no time to develop. Thus, the length λr_c approximately demarks the scale of the transition between 2D (axially invariant) and 3D dynamics as recently illustrated by Gillet et al. (2011), who documented the change from 2D to 3D dynamics with increasing wavenumber in a spherical shell geometry appropriate to Earth's fluid core (Figure 2).

8.09.2.2.1 Quasi-geostrophic approximations

The quasi-geostrophic framework involves the assumption that the flow is to leading order in geostrophic balance, and that variations in the axial direction are small compared to those in directions at right angles to the rotation axis. It was pioneered in the context of core dynamics by Hide (1966) and formally developed within the context of convection in a rotating annulus by Busse (1970).

We begin with the conservation of momentum in a rotating, electrically conducting, incompressible fluid (see Chapter 8.05, equation [1])

$$\rho\frac{\partial\mathbf{u}}{\partial t} + \rho(\mathbf{u}\cdot\nabla)\mathbf{u} + 2\rho(\boldsymbol{\Omega}\times\mathbf{u}) = -\nabla p + \mathbf{j}\times\mathbf{B} \qquad [37]$$

Buoyancy and viscous forces have been neglected here, so as to focus attention on the interplay between the Coriolis and Lorentz forces.

We treat Earth's core as a spherical container. We proceed to nondimensionalize, using its radius r_c as a typical length scale, $\mathcal{B}$ as a typical magnetic field, $V_A = \mathcal{B}/\sqrt{\mu_0\rho}$ as a typical velocity, ρV_A^2 for the pressure scale, and r_c/V_A for the time scale, to obtain

Figure 2 Quasi-geostrophy of velocities with large scales in directions at right angles to the rotation axis. A meridian slice (snapshot) of the azimuthal velocity extracted from a rapidly rotating dynamo model driven by mass anomaly flux at the two boundaries (see, e.g., Aubert et al., 2009) with $p_m=0.1$ and Ekman number $\nu/\Omega(r_c-r_i)^2=10^{-7}$, leading to Rossby number $Ro\sim6\times10^{-4}$ and Lehnert number $\lambda\sim10^{-3}$. Less and less small scales are filtered out from left to right, illustrating the progressive loss of quasi-geostrophy as the length scale is decreased. Left and middle: scales respectively smaller than $0.1r_c$ and $0.02r_c$ are filtered out. Right: full solution. Personal communication from N. Schaeffer (see also Chapter 8.06).

$$\frac{\partial \mathbf{u}}{\partial t} + (\mathbf{u}\cdot\nabla)\mathbf{u} + 2\lambda^{-1}(\mathbf{1}_z \times \mathbf{u}) = -\nabla p + \mathbf{j} \times \mathbf{B} \qquad [38]$$

where λ is the Lehnert number $\lambda(r_c)$ taking the length scale $l = r_c$ (see [36]). In cylindrical polar coordinates (s, ϕ, z), the shape of its outer boundary is defined by the heights $z = H_c(s)$ above and $z = -H_c(s)$ below the equatorial plane, where $H_c(s) = \sqrt{r_c^2 - s^2}$.

Two different versions of the quasi-geostrophic framework are described here. To begin with, we follow the classical approach proposed by Busse (1970), developed in order to investigate the onset of thermal convection (which occurs far from the equator) in an internally heated, rapidly rotating fluid sphere. It involves expanding the velocity and pressure fields into power series consisting of increasing powers of α, where α is the slope of the outer boundary

$$\alpha(s) = \frac{\mathrm{d}H_c(s)}{\mathrm{d}s} = -\frac{s}{H_c} \qquad [39]$$

For example, the velocity field is expanded as

$$\mathbf{u} = \mathbf{u}_0 + \mathbf{u}_1 + \cdots \qquad [40]$$

where $\mathbf{u}_0 \simeq \mathcal{O}(1)$, $\mathbf{u}_1 \sim \mathcal{O}(\alpha)$, etc. This series will converge provided $|\alpha| \ll 1$. Further assuming that $\lambda \ll 1$ (its value is thought to be $\sim 10^{-4}$ in Earth's core), to leading order there is simply geostrophic balance

$$2\lambda^{-1}(\mathbf{1}_z \times \mathbf{u}_0) = -\nabla p_0 \qquad [41]$$

and $\mathbf{u}_0$ obeys the Proudman–Taylor theorem [13]. To leading order, the quasi-geostrophic flow is, therefore, two-dimensional, without variations in the axial direction. The geostrophic solution [41] is completed by the boundary condition $(\mathbf{1}_z \cdot \mathbf{u}_0) = 0$, which is the rigid boundary condition when there is no boundary slope, as is appropriate for this order.

Since the leading order flow is two-dimensional, it can be written in terms of a scalar stream function Ψ,

$$\mathbf{u}_0 = \nabla \times (\Psi \mathbf{1}_z) = \left(\frac{1}{s}\frac{\partial \Psi}{\partial \phi}, -\frac{\partial \Psi}{\partial s}, 0\right) \quad \text{where} \quad \Psi = -\frac{p_0 \lambda}{2} \qquad [42]$$

Moving to the next order in the expansion provides a prognostic equation, describing the time evolution of the geostrophic flow $\mathbf{u}_0$,

$$\frac{\partial \mathbf{u}^0}{\partial t} + (\mathbf{u}_0\cdot\nabla)\mathbf{u}_0 + 2\lambda^{-1}(\mathbf{1}_z \times \mathbf{u}_1) = -\nabla p_1 + \mathbf{j} \times \mathbf{B} \qquad [43]$$

If there was no magnetic force on the right-hand side of [43], we would find that $\partial p_1/\partial z = 0$ and that the velocity components parallel to the equatorial plane are z-invariant at the first order in α. The reasoning is less straightforward in the presence of a magnetic force (or, for that matter, of a buoyancy term with a nonzero z-component). An equation for the evolution of the axial component of vorticity v

$$v = \mathbf{1}_z \cdot (\nabla \times \mathbf{u}_0) = -\nabla_\perp^2 \Psi$$

where

$$\nabla_\perp^2 = \frac{1}{\mathrm{s}}\frac{\partial}{\partial \mathrm{s}}\left(\mathrm{s}\frac{\partial}{\partial \mathrm{s}}\right) + \frac{1}{\mathrm{s}^2}\frac{\partial^2}{\partial \phi^2} \qquad [44]$$

can, nevertheless, be obtained by taking the z component of the curl of eqn [43]

$$\frac{\mathrm{D}}{\mathrm{v}t} v - 2\lambda^{-1}\frac{\partial u_{1z}}{\partial z} = \mathbf{1}_z \cdot \nabla \times (\mathbf{j} \times \mathbf{B}) \qquad [45]$$

where $\mathrm{D}/\mathrm{D}t = \partial/\partial t + (\mathbf{u}_0 \cdot \nabla)$, and we have made use of the incompressibility condition $\nabla \cdot \mathbf{u}_1 = 0$, which holds at this order since we have already assumed $\nabla \cdot \mathbf{u}_0 = 0$ at the leading order. Next comes a crucial step: averaging over the axial direction $\mathbf{1}_z$. The term $\mathrm{D}v/\mathrm{D}t$ is unchanged, and the term arising from the Coriolis force is readily simplified as follows:

$$-\frac{\lambda^{-1}}{H_c}\int_{-H_c}^{H_c} \frac{\partial u_{1z}}{\partial z}\mathrm{d}z = -2\lambda^{-1}\beta(s)u_{0s} \quad \text{where} \quad \beta(s) = \frac{\alpha}{H_c} \qquad [46]$$

Here, the no-penetration boundary condition at the top and bottom sloping boundaries has been used:

$$\mathbf{u}\cdot(\mathbf{1}_z \mp \nabla H_c) = u_{1z} \mp \alpha u_{0s} = 0 \quad \text{at} \quad z = \pm H_c \qquad [47]$$

Notice that $\mathbf{u}_1$ has been eliminated without specifying its value in the interior.

The resulting axially averaged equation for the evolution of the axial vorticity is

$$-\frac{\mathrm{D}}{\mathrm{D}t} v + 2\lambda^{-1}\beta u_s = -\frac{1}{2H_c}\int_{-H_c}^{H_c} \mathbf{1}_z \cdot \nabla \times (\mathbf{j} \times \mathbf{B})\mathrm{d}z \qquad [48]$$

Although this small α version of the quasi-geostrophic model has proved very successful in studies of thermal convection in a spherical geometry, even in supercritical situations (Gillet and Jones, 2006), using it to study the core dynamics underlying geomagnetic secular variation is problematic on a number of counts. First, it is obviously not correct in the equatorial region where $\alpha \to \infty$. Second, although the z-invariance of QG flows makes the QG apparatus appropriate for continuing into the core interior the surface flows (u_θ, u_ϕ) inverted from geomagnetic data (Pais and Jault, 2008, see **Chapter 8.04**), the flow equation [42] does not obey the no-penetration condition $\mathbf{u}_0 \cdot \mathbf{1}_r = 0$ and so it has to be modified to match the surface flow. Simply adding a z-component u_{1z} such that eqn [47] is obeyed for $\mathbf{u}_0$ is not satisfactory because, then, the total flow is not divergence free. For these reasons, an alternative version of the QG model, which is more accurate where the boundary slope is large, has been sought (Schaeffer and Cardin, 2005). This alternative approach is presented next, following the treatment by Becker and Salmon (1997).

The derivation consists in assuming a priori that $\mathbf{u}_\perp$, the velocity perpendicular to the rotation axis, is z-independent. Requiring $\nabla \cdot \mathbf{u} = 0$, we deduce that u_z varies linearly with z because

$$\frac{\partial u_z}{\partial z} = -\nabla_\perp \cdot \mathbf{u} \qquad [49]$$

which is z-independent. From the no-penetration condition

$$u_z = \pm \mathbf{u}_\perp \cdot \nabla H_c \quad \text{at} \quad z = \pm H_c \qquad [50]$$

(see eqn [47]) we obtain u_z in the interior

$$u_z = \frac{z}{H_c}(\mathbf{u}_\perp \cdot \nabla H_c) \qquad [51]$$

and [49] can be transformed into

$$\nabla\cdot(H_c\mathbf{u}_\perp) = 0 \qquad [52]$$

The z-integrated equatorial velocity $H_c\mathbf{u}_\perp$ can thus be written as a function of a stream function χ and

$$\mathbf{u} = \frac{1}{H_c}\nabla\times(\chi(s,\phi)\mathbf{1}_z) - \frac{z}{H_c^3}\frac{\partial\chi}{\partial\phi}\mathbf{1}_z \qquad [53]$$

The axial vorticity becomes

$$v = -\frac{1}{H_c}\nabla_\perp^2\chi - \frac{s}{H_c^3}\frac{\partial\chi}{\partial s} \qquad [54]$$

Equation [48] thus remains valid, but with new expressions for u_s and v.

8.09.2.2.2 Wave motion in a quasi-geostrophic system

In the absence of the magnetic term on the right-hand side and with β constant, eqn [48] is simply the equation for Rossby waves mentioned in Section 8.09.2.1.2. It is usually derived in the (Cartesian) annulus geometry, in which case the term $\beta\partial\psi/s\partial\phi$ is transformed into $\beta\partial\psi/\partial x$. Rossby waves arise naturally in the perturbation approach outlined earlier. At the leading order, the flow is geostrophic and z-invariant. At the next order, ageostrophy (i.e., deviation from geostrophy) arises because the height of fluid columns parallel to the rotation axis depends on the cylindrical radius. This weak ageostrophy is responsible for the slow prograde wave propagation.

Here, we explore what happens to such Rossby waves in the presence of a simple magnetic field. Following Acheson (1978), we consider a uniform imposed field aligned along the prograde direction in a geometry consisting of a rotating fluid layer between the top and bottom boundaries of a constant slope, that is, unbounded in the cylindrical radial direction. With this setup, neglecting curvature, we are able to work in a local Cartesian coordinate system, with z in the axial direction, x the prograde direction, and y directed toward the rotation axis (i.e., in the direction of increasing fluid depth). Thus, the imposed magnetic field is

$$\mathbf{B}_0 = \mathbf{B}_0\mathbf{1}_x \qquad [55]$$

We make the additional hypothesis that a small magnetic field perturbation will also be axially invariant (as is reasonable when neglecting magnetic diffusion), so it can be represented as the curl of a scalar magnetic potential $A(x, y)$

$$\mathbf{B}(x,y) = \nabla\times(A(x,y)\mathbf{1}_z) \qquad [56]$$

Since the fluid layer is unbounded in the y direction, the layer depth H is used to nondimensionalize length and it is this that appears in the Lehnert number labeled $\lambda_H = B_0/\sqrt{\rho\mu_0}\Omega H$. The linearized equations governing the evolution of small perturbations of the axial vorticity and magnetic field are then

$$\frac{\partial}{\partial t}\nabla_\perp^2\Psi + 2\lambda_H^{-1}\beta\frac{\partial\Psi}{\partial x} = -\frac{\partial}{\partial x}\nabla_\perp^2 A \qquad [57]$$

$$\frac{\partial A}{\partial t} = -\frac{\partial\Psi}{\partial x} \qquad [58]$$

Here, $\nabla_\perp^2 = \partial^2/\partial x^2 + \partial^2/\partial y^2$.

Using trial solutions (Ψ, A) proportional to $\exp[i(k_x x + k_y y - \omega t)]$, and substituting from eqn [58] into eqn [57] to eliminate A, the following quadratic dispersion relation is obtained:

$$\omega^2 + 2\lambda_H^{-1}\frac{\beta k_x}{k^2}\omega - k_x^2 = 0 \quad \text{with } k^2 = k_x^2 + k_y^2 \qquad [59]$$

which permits two solutions

$$\omega = \lambda_H^{-1}\frac{\beta k_x}{k^2}\left(-1 \pm \sqrt{1 + \frac{\lambda_H^2 k^4}{\beta^2}}\right) \qquad [60]$$

When the Lehnert number λ_H is small, the two roots separate, taking the distinct forms

$$\omega_R = -2\lambda_H^{-1}\frac{\beta k_x}{k_2} \quad \text{and} \quad \omega_{MR} = \frac{\lambda_H k_x k^2}{2\beta} \qquad [61]$$

The physical nature of these waves becomes clear on moving back to dimensional units

$$\omega_R = -2\Omega\frac{\beta k_x}{k^2} \quad \text{and} \quad \omega_{MR} = \frac{B_0^2}{\rho_0\mu_0 2\Omega\beta}k_x k^2 \qquad [62]$$

Recall that we have defined our β parameter without including the rotation rate Ω. The solution ω_R corresponds to Rossby waves, and the contribution of the magnetic energy to the total energy of this wave is only $O(\lambda^2)$. The other solution, ω_{MR}, depends fundamentally on both the magnetic field and rotation for its existence. It is known as a magnetic Rossby wave, and it propagates in the opposite direction to the hydrodynamic Rossby wave and with a much lower frequency. It is, therefore, sometimes referred to as the 'slow' wave and is characterized by magnetostrophic balance, inertia being negligible because of the low frequency. In magnetic Rossby waves, time changes in the velocity field occur via time changes in the magnetic field. Hide (1966) argued that in the rotation-dominated, hydromagnetic regime of Earth's core, such waves may be relevant for explaining some aspects of geomagnetic secular variation including the westward motion of magnetic field features. Such features with azimuthal wavenumber $m = 5$ in the equatorial region of the core surface were later discovered by Finlay and Jackson (2003). The section "Magnetic-Coriolis waves" in Finlay et al. (2010) provides a recent review of magnetic Rossby waves including the quest for experimental evidence.

We note here in passing that propagation of hydrodynamic Rossby waves provides a mechanism for establishing a magnetostrophic balance between the Coriolis and magnetic terms in eqn [48].

8.09.2.2.3 Axially averaged equations

In this section, we assume that magnetic surface terms (which appear when we are taking the axial average of the terms arising from the Lorentz force) may be neglected because the magnetic field at the core surface is smaller than that in the core interior. Defining an axial averaging operator

$$\langle X\rangle = \frac{1}{2H_c}\int_{-H_c}^{H_c} X\,dz \qquad [63]$$

and then expanding the terms on the right-hand side of eqn [48] due to the Lorentz force, following Canet et al. (2009) we find

$$-\frac{\mathrm{D}}{\mathrm{D}t}v+2\lambda^{-1}\beta(s)u_s=\left(\frac{1}{s}\frac{\partial}{\partial s}\frac{\partial}{\partial\phi}+\frac{1}{s^2}\frac{\partial}{\partial\phi}\right)\left(\left\langle B_s^2\right\rangle-\left\langle B_\phi^2\right\rangle\right)-\left(\frac{3}{s}\frac{\partial}{\partial s}-\frac{1}{s^2}\frac{\partial^2}{\partial\phi^2}+\frac{\partial^2}{\partial s^2}\right)\left\langle B_sB_\phi\right\rangle \quad [64]$$

Note that the ϕ component of the Navier–Stokes equation, averaged over both the axial and azimuthal directions, directly gives the time evolution of the zonal component of the flow:

$$\frac{\partial\zeta}{\partial t}=\frac{1}{2\pi s^3H_c}\frac{\partial}{\partial s}\left(s^2H_c\left[\oint\left\langle B_sB_\phi\right\rangle\mathrm{d}\phi\right]\right)\quad\text{where}\quad\zeta(s)=u_G(s)/s \quad [65]$$

This is particularly useful when the geometry of the system is restricted to the region ($s\geq r_i$) outside the cylindrical surface tangent to the solid inner core of radius r_i (as in Canet et al. (2009)). Indeed, the vorticity equation [64] leaves the zonal component of the flow undetermined in a multiply connected domain such as a cylindrical annulus (Plaut and Busse, 2002). The subscript G in [65] indicates that axially invariant zonal velocities $u_\phi(s)\mathbf{1}_\phi$ form the geostrophic part of the velocity field in spherical geometry. On the one hand, they satisfy both eqns [41] and [47]. On the other hand, the ageostrophic perturbation u_z is zero if and only if $u_s=0$ (see eqn [47] or eqn [51]). Geostrophic velocities do not contribute to the Coriolis term in the vorticity equation [64]. Given later (see eqn [81]) are the surface terms modifying [65], which have been neglected at this stage. Equation [65] prescribes the evolution of $u_G(s)$ and is key to our later discussion of torsional waves (**Section 8.09.3.2**).

Canet et al. (2009) have also shown that, provided one neglects magnetic diffusion, the induction equation can similarly be axially averaged in order to obtain relations for the evolution of the quadratic quantities $\langle B_s^2\rangle$, $\langle B_\phi^2\rangle$, and $\langle B_sB_\phi\rangle$ that appear in eqn [64]. With the definition [53] for the quasi-geostrophic velocity field, their expression is modified slightly and the following relations obtained:

$$\frac{\partial}{\partial t}\left\langle B_s^2\right\rangle=-H_c(\mathbf{u}\cdot\nabla_\perp)\left(\frac{1}{H_c}\left\langle B_s^2\right\rangle\right)+2\left\langle B_s^2\right\rangle\frac{\partial u_s}{\partial s}+2\frac{\left\langle B_sB_\phi\right\rangle}{s}\frac{\partial u_s}{\partial\phi}$$

$$\frac{\partial}{\partial t}\left\langle B_\phi^2\right\rangle=-\frac{1}{H_c}(\mathbf{u}\cdot\nabla_\perp)\left(H_c\left\langle B_\phi^2\right\rangle\right)+2s\left\langle B_sB_\phi\right\rangle\frac{\partial}{\partial s}\left(\frac{u_\phi}{s}\right)-2\frac{\partial u_s}{\partial s}\left\langle B_\phi^2\right\rangle$$

$$\frac{\partial}{\partial t}\left\langle B_sB_\phi\right\rangle=-(\mathbf{u}\cdot\nabla_\perp)\left\langle B_sB_\phi\right\rangle+s\left\langle B_s^2\right\rangle\frac{\partial}{\partial s}\left(\frac{u_\phi}{s}\right)+\frac{1}{s}\left\langle B_\phi^2\right\rangle\frac{\partial u_s}{\partial_\phi} \quad [66]$$

The coupled equations [64]–[66] govern the time evolution of χ, ζ, $\langle B_s^2\rangle$, $\langle B_\phi^2\rangle$, and $\langle B_sB_\phi\rangle$ in the regions [0, r_c] or [r_i, r_c]. They have to be supplemented by boundary conditions at the two circles delimiting the domain. The no-penetration condition gives $\partial\chi/\partial\phi=0$. The boundary condition for ζ at $s=r_c$ is derived from the fact that the magnetic field that leaves the disk is continuous to a potential field. We give this condition in **Section 8.09.3.3**, where torsional waves are discussed. Additional restrictions on χ, which are also required to ensure continuity of the magnetic field at the boundary with the insulator, have yet to be worked out.

Considerable simplifications of the quasi-geostrophic model [64]–[66] result if one makes the additional hypothesis, introduced earlier in the course of our exposition of Rossby waves, that the magnetic field is also axially invariant:

$$\mathbf{B}(s,\phi)=\nabla\times(A(s,\phi)\mathbf{1}_z) \quad [67]$$

Substitution into the Navier–Stokes and magnetic induction equations yields the simple coupled system

$$\frac{\mathrm{D}}{\mathrm{D}t}\nabla_\perp^2\Psi+\frac{2\lambda^{-1}\beta(\mathrm{s})}{\mathrm{s}}\frac{\partial\Psi}{\partial\phi}=-(\mathbf{B}\cdot\nabla)\nabla_\perp^2\mathrm{A} \quad [68]$$

and

$$\frac{\partial A}{\partial t}=-(\boldsymbol{u}_0\cdot\nabla)A+\frac{1}{S}\nabla_\perp^2\mathrm{A} \quad [69]$$

Here, $S=r_cV_A/\eta$ is known as the Lundquist number, and it describes the ratio between the magnetic diffusion time scale and the Alfvén wave time scale. The assumption of an axial invariant magnetic field is certainly very restrictive. However, it has the advantage of allowing magnetic diffusion to be considered within the QG formalism (in the directions perpendicular to the rotation axis), and the resulting equations are more easily solvable both analytically and numerically, while retaining the essential interplay between the magnetic and velocity fields (see, e.g., Tobias et al., 2007).

8.09.2.2.4 Magnetic diffusion layer at the top and bottom boundaries

The main body of the core has been treated as an inviscid and perfectly conducting fluid in order to derive the coupled vorticity and magnetic equations. Furthermore, the quasi-geostrophic velocity field has been defined in such a way that it obeys the no-penetration condition at the top and bottom of the geostrophic cylinders $z=\pm H_c$. The velocity parallel to the boundary, however, is nonzero (see, e.g., eqn [53]). This situation must be corrected by a viscous (Ekman) boundary layer, with a thickness of $(\nu/\Omega)^{1/2}$. The question thus arises whether there is also a boundary layer for the magnetic field through which its tangential discontinuities can be accommodated.

Such discontinuities are to be expected because the magnetic field components $\mathbf{B}_{||}$ and B_n, parallel and transverse to the boundary, respectively, are related. Provided the domain outside the fluid cavity is treated as an electrical insulator, the magnetic field derives from a unique potential scalar V, $\mathbf{B}=-\nabla V$, with V obeying the Laplace's equation $\nabla^2V=0$. Potential theory then tells us that the specification of the normal component $B_n=-(\nabla V)_n$ at the boundary determines V and, thus, $\mathbf{B}$ uniquely in the outer insulating domain.

In the absence of rotation, any discontinuities of the tangential magnetic field in the boundary layer at the fluid–solid interface are eliminated through the emission of Alfvén waves as long as $\mathbf{B}\cdot\mathbf{n}\neq0$ (see **Section 8.09.2.1.1**). Rapid rotation, however, rigidifies the fluid in the axial direction and hinders the propagation of Alfvén waves normal to the boundary (Backus, 1968, Appendix II). The discontinuities are, accommodated, instead, through a magnetic diffusive boundary layer. Its thickness can be calculated as in a solid conductor. This description holds as long as rapid rotation prevents significant shear from developing in the axial direction.

8.09.2.2.5 Quasi-geostrophic MHD turbulence

Diamond et al. (2007) have discussed β-plane MHD turbulence (eqns [68] and [69]) to clarify the turbulent mixing of momentum and magnetic field in the solar tachocline, where

the dynamics is two-dimensional as the result of a strong stable stratification. They note that quasi-geostrophic turbulence in a spherical shell is characterized by the coexistence of Rossby waves and Alfvén waves at different length scales.

The frequency (eqn [62], left) of Rossby waves to the frequency [8] of Alfvén waves can, indeed, be compared. The wavenumber $k_0=(\beta\Omega/V_A)^{1/2}$ corresponds to the boundary between Alfvénic and Rossby dominated ranges. At large length scales ($k<k_0$), the turbulence is that of a sea of Rossby waves. At small length scales, with wavenumbers above k_0, it can be anticipated that Alfvén waves redistribute equally the energy between the kinetic and magnetic components.

At the beginning of this section, it was noted that a second wavenumber $k_1=\lambda^{-1}=\Omega/V_A$ can be formed from the frequencies of Alfvén and 3D inertial waves. Quasi-geostrophic approximations hold for $k<k_1$, with $k_0\leq k_1$ (see also Chapter 8.06).

8.09.3 Torsional Waves

Torsional waves consist of geostrophic motions. In a spherical shell, geostrophic flows depend only on the distance s to the rotation axis and their velocity can be expressed as $s\zeta(s)\mathbf{1}_\phi$. Any differential rotation ($\mathrm{d}\zeta/\mathrm{d}s\neq 0$) between rigid geostrophic cylinders shears the magnetic field and propagates similarly to Alfvén waves in the direction of either increasing or decreasing s (Figure 3). Estimating the propagation speed of torsional waves gives an estimate of the squared magnetic field strength averaged over the geostrophic cylinders. Torsional waves arise in response to violations of Taylor's condition, which is now introduced.

8.09.3.1 Taylor's Condition

Taylor (1963) considered an incompressible fluid contained in an axisymmetric, rigid, envelope Σ. He investigated the conditions under which there exists a velocity $\mathbf{u}$ in a magnetostrophic balance:

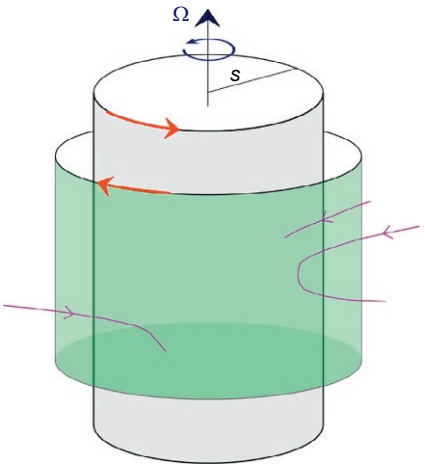

Figure 3 Torsional wave mechanism. All the magnetic field scales contribute to the restoring Lorentz force acting on geostrophic cylinders that is responsible for torsional wave propagation.

$$2\rho(\mathbf{\Omega}\times\mathbf{u})+\nabla p=\mathbf{F},$$

$$\text{with}\quad \mathbf{F}=\mathbf{j}\times\mathbf{B}+\rho'\mathbf{g},\quad \nabla\cdot\mathbf{u}=0,\quad\text{and}\qquad [70]$$

$$\mathbf{u}\cdot\mathbf{n}|_\Sigma=0 \qquad [71]$$

where $\mathbf{n}$ is the unit outward normal to Σ. The necessary and sufficient condition for the existence of a solution is that the inhomogeneity $\mathbf{F}$ is orthogonal to each solution of the adjoint homogeneous problem (where the inner product is defined by the energy norm as in Busse (1970)). The homogeneous part of the equation reduces to a geostrophic balance

$$2\rho(\mathbf{\Omega}\times\mathbf{u})+\nabla p=0 \qquad [72]$$

The solution consists of geostrophic motions $\mathbf{u}_G=1/2\Omega(\mathbf{1}_z\times\nabla p)$. In order to derive the equations for the adjoint homogeneous problem, eqn [72] is multiplied scalarly by the adjoint field $\mathbf{v}$:

$$\forall\mathbf{u},\quad \int\mathbf{v}\cdot(2\rho(\mathbf{\Omega}\times\mathbf{u})+\nabla p)\mathrm{d}V=0$$

$$\forall\mathbf{u},\quad \int-\mathbf{u}\cdot(2\rho(\mathbf{\Omega}\times\mathbf{v}))\mathrm{d}V+\int\mathbf{u}\cdot\nabla\pi\,\mathrm{d}V+\int_\Sigma p(\mathbf{v}\cdot\mathbf{n})\mathrm{d}\Sigma=0 \qquad [73]$$

where eqn [71] has been used to introduce the new term involving π. The adjoint homogeneous problem is simply

$$-2\rho(\mathbf{\Omega}\times\mathbf{v})+\nabla\pi=0 \qquad [74]$$

together with the no-penetration condition ($\mathbf{v}\cdot\mathbf{n}=0$) at the boundary.

As a result, geostrophic motions $\mathbf{u}_G$ are also solutions of the adjoint problem and the following solvability condition has to be satisfied for arbitrary geostrophic motions:

$$\forall\mathbf{u}_G,\quad \iiint\mathbf{u}_G\cdot\mathbf{F}\mathrm{d}V=0 \qquad [75]$$

So far, the derivation remains valid in non-axisymmetric cavities and we use later, in Section 8.09.4.2, the constraint,

$$\forall\mathbf{u}_G,\quad \iiint\mathbf{u}_G\cdot(\mathbf{j}\times\mathbf{B})\mathrm{d}V=0 \qquad [76]$$

derived from the additional assumption $\mathbf{u}_G\cdot\mathbf{g}=0$, which holds when either the buoyancy is neglected or the boundary is axisymmetric. In the latter case, the geostrophic cylinders are circular, $\mathbf{u}_G=s\zeta(s)\mathbf{1}_\phi$, and eqn [76] can be transformed into the constraint originally derived by Taylor (1963),

$$\forall s,\quad \iint_{\Sigma(s)}(\mathbf{j}\times\mathbf{B})_\phi s\,\mathrm{d}\phi\,\mathrm{d}z=0 \qquad [77]$$

where $\Sigma(s)$ denotes the cylindrical surface $s=$constant. Paul Roberts obtains this constraint from a slightly different but fundamentally equivalent approach in the section "MHD geodynamo theory" in Chapter 8.03.

Smylie et al. (1984) generalized the condition [76] to compressible fluids by adopting the subseismic approximation, which is closely related to the anelastic approximation (Rieutord and Dintrans, 2002). It can, indeed, be readily demonstrated that eqn [76] also holds for an anelastic fluid, where

$$2\rho_a(\mathbf{\Omega}\times\mathbf{u})+\rho_a\nabla\frac{p}{\rho_a}=\mathbf{F},\quad\text{with}\quad\nabla\cdot\rho_a\mathbf{u}=0,\quad\mathbf{u}\cdot\mathbf{n}|_\Sigma=0 \qquad [78]$$

provided its solid envelope is axisymmetric. Then, geostrophic motions are again of the form $\mathbf{u}_G = s\zeta(s)\mathbf{1}_\phi$ (see the Proudman–Taylor condition [21] derived in the compressible case) and are solutions of the adjoint homogeneous problem.

When eqn [76] does not hold, it is necessary to reinstate the geostrophic acceleration term in the momentum equation.

8.09.3.2 The Canonical One-Dimensional Torsional Wave Equation

Roberts and Aurnou (2012) have introduced the qualifier 'canonical' in order to refer to the equation for torsional waves in the spherical geometry and in its simplest form, without complications arising from non-axisymmetric terms or from the nonvanishing mantle conductivity. It is remarkable that the equations for torsional waves reduce to a second-order differential equation for the geostrophic angular velocity $\zeta(s,t)$, where the magnetic field enters only through a function of s:

$$\{V_s^2\}(s) = \frac{1}{\rho\mu_0 \hat{\Sigma}_g(s)} \int_{\Sigma_g(s)} B_s^2 s \, dz \, d\phi \qquad [79]$$

where $\hat{\Sigma}_g(s)$ denotes the area of the geostrophic cylinder $\Sigma_g(s)$ of radius s, and density ρ is uniform. The integral in eqn [79] involves all the length scales of the magnetic field.

Braginsky (1970) presented torsional waves as a possible mechanism for the changes in length of day, initially with periods of about 60 years. He gave the original derivation of their equation, which can also be found in Roberts and Soward (1972) and Jault (2003). The equation for the time evolution of the geostrophic velocity is part of the axially averaged equations presented in **Section 8.09.2.2.3**, but there eqn [65] is only approximate. In fact, it is possible to calculate rigorously the boundary terms, which are neglected in eqn [65]. As already mentioned, there is geostrophic acceleration when eqn [77] does not hold, so

$$4\pi\rho H_c \frac{\partial u_G(s)}{\partial t} = \int_{-H_c}^{H} \oint (\mathbf{j}\times\mathbf{B})_\phi \, d\phi \, dz = \frac{1}{\mu_0}\int_{-H_c}^{H_c} \oint \nabla\cdot\left(s\mathbf{B}_M B_\phi\right) d\phi \, dz \qquad [80]$$

where $\mathbf{B}_M$ is the field in the meridional plane $(\mathbf{1}_s, \mathbf{1}_z)$ and H_c, hereafter, is dimensional. Before linearizing, we can separate the last term on the right into volume and surface parts:

$$4\pi\rho\mu_0 H_c \frac{\partial u_G}{\partial t} = \frac{1}{s^2}\frac{\partial}{\partial s}\left(s^2 \int_{-H_c}^{H_c} \oint B_s B_\phi \, d\phi \, dz\right) + \frac{r_c}{H_c}\left(\oint B_r B_\phi \, d\phi(H_c) + \oint B_r B_\phi \, d\phi(-H_c)\right) \qquad [81]$$

The linearization consists in treating the time-dependent quantities as small perturbations of a static basic state. Substituting eqn [66] for $\partial\left(\int_{-H_c}^{H_c} B_s B_\phi \, dz\right)/\partial t$ (with $\mathbf{u}_0 = s\zeta(s)\mathbf{1}_\phi$) into the time derivative of eqn [81], we obtain

$$\frac{\partial^2\zeta}{\partial t^2} = \frac{1}{s^3 H_c}\frac{\partial}{\partial s}\left(s^3 H_c \{V_s^2\}\frac{\partial^2\zeta}{\partial s}\right) + \text{surface terms} \qquad [82]$$

All surface terms depend on the radial magnetic field at the CMB. Assuming that the conductivity of the mantle is weak enough, it is possible to separate these terms into two groups. One introduces a nonlocal coupling between the geostrophic cylinders, regardless of the lower mantle conductivity, when the magnetic field is not symmetrical about the rotation axis. It has been shown, using a realistic model of the magnetic field in the core interior, that this does not affect the propagation of torsional waves much (Jault and Légaut, 2005; Roberts and King, 2013). The other surface terms involve the conductivity of the lower mantle. They cause electromagnetic coupling between the core and the mantle (Dumberry and Mound, 2008).

It is straightforward to generalize eqn [82] to the case of an anelastic fluid core:

$$\frac{\partial^2\zeta}{\partial t^2} = \frac{1}{\mathcal{P}(s)}\frac{\partial}{\partial s}\left(\mathcal{P}(s)\overline{\{V_s^2\}}\frac{\partial\zeta}{\partial s}\right) + \text{surface terms} \qquad [83]$$

with

$$\mathcal{P}(s) = s^3 H_c \bar{\rho}, \; \bar{\rho}(s) = \frac{1}{H_c}\int_0^{H_c} \rho(s,z)\, dz \quad \text{and} \quad \overline{\{V_s^2\}} = \frac{1}{\bar{\rho}\mu_0 \hat{\Sigma}_g(s)}\int_{\Sigma_g(s)} B_s^2 s \, dz \, d\phi \qquad [84]$$

8.09.3.3 Boundary Conditions for the One-Dimensional Torsional Wave Equation

As the propagation of torsional waves is not directly affected by the Coriolis force, the arguments presented earlier (**Section 8.09.2.1.1**) concerning the appropriate boundary conditions, in the absence of rotation, for the coupled momentum and induction equations in the limit of vanishing viscosity and magnetic diffusivity are fully relevant here. Schaeffer et al. (2012) have recently discussed, in this particular context, why the value of the magnetic Prandtl number p_m is crucial, notwithstanding both ν and η are vanishingly small, for the wave reflection at $s = r_c$.

In the relevant limit $p_m \ll 1$, the thin boundary layer involves only the velocity field, and the magnetic field is left unchanged throughout the layer. The boundary conditions for the diffusionless outer problem include a continuity condition for all magnetic field components. If it is assumed that the mantle is electrically insulating, the magnetic field involved in the torsional wave propagation has to match with a potential field at $s = r_c$. At the boundary, the radial electrical currents vanish and the zonal magnetic field is also zero:

$$\mu_0 j_r = \mu_0 j_s = 1_s\cdot(\nabla\times\mathbf{B}) = 0, \quad \oint B_\phi \, d\phi = 0, \quad \text{at } s = r_c \qquad [85]$$

We now seek to transform [85] into a boundary condition on ζ. We develop $\partial j_s/\partial t = 0$ using the frozen flux induction equation for the magnetic field parallel to the boundary (at $s = r_c$)

$$\frac{\partial B_\phi}{\partial t} = -\zeta\frac{\partial B_\phi}{\partial\phi} + sB_s\frac{\partial\zeta}{\partial s} \quad \frac{\partial B_z}{\partial t} = -\zeta\frac{\partial B_z}{\partial\phi} \qquad [86]$$

Thus, we have

$$\forall\phi, \quad \mu_0\frac{\partial}{\partial t}j_s = -s\frac{\partial\zeta}{\partial s}\frac{\partial B_s}{\partial z} = r_c\frac{\partial\zeta}{\partial s}\left(\frac{\partial B_s}{\partial\theta}\right), \quad \left.\frac{\partial\zeta}{\partial s}\right|_{s=r_c}\left(\frac{\partial B_r}{\partial\theta}\right)_{r=r_c,\,\theta=\pi/2} = 0 \qquad [87]$$

Taking the time derivative of the second equation [85], we similarly obtain

$$\left.\frac{\partial \zeta}{\partial s}\right|_{s=r_c} \oint B_r(r_c, \pi/2, \phi)\, \mathrm{d}\phi = 0 \qquad [88]$$

The two equations [87] and [88] yield $\partial\zeta/\partial s = 0$ at $s = r_c$, which, in turn, suffices to ensure that the two constraints [85] remain satisfied.

Interestingly, this result has been obtained without any considerations regarding the vanishing height of the geostrophic cylinders as $s \to r_c$. In this respect, Schaeffer et al. (2012) studied numerically how a geostrophic pulse actually reflects in a spherical cavity at $s = r_c$. For $p_m = 1$, they found that there is no reflection at all as on a vertical wall. For $p_m < 1$, however, the reflection coefficients R on the inside of a spherical boundary and on a wall parallel to the rotation axis differ. In both cases, R increases as $p_m \to 0$ (from $R = 0$ at $p_m = 1$), but the spherical boundary is much less reflective (see their Figure 3). For $p_m = 10^{-3}$, $R \sim 0.8$ in the spherical case.

8.09.3.4 Inference of the Strength of the Magnetic Field in Earth's Core Interior

Several authors have interpreted the zonal and equatorially symmetric part of core surface flows inverted from geomagnetic data as the signature of normal modes of the fluid core consisting of standing torsional waves referred to as torsional oscillations (Bloxham et al., 2002; Zatman and Bloxham, 1997). In these studies, the input flow $u_\phi(\theta,t) = u_\phi(\pi - \theta, t)$ either for the period 1900–90 or for ~1950–2000. To begin with, a few normal modes are fitted to $u_\phi(\theta,t)$. Second, a model of the squared propagation velocity $\{V_s^2\}(s)$ (see definition [79]) is inverted from the periods and the geometry of the normal modes. The period of the modes decreases with the spatial complexity and is about 80 years (i.e., comparable to the 60-year period initially considered by Braginsky) for the mode with the simplest geometry.

The expression of the geostrophic angular velocity $\zeta(s)$ as a combination of normal modes for the time span 1840–1990 (covered by the *gufm1* magnetic field model of Jackson et al. (2000)) has been used by Buffett et al. (2009) to calculate the Green's function, which describes the response of the fluid core to an impulsive excitation. They have obtained source functions, eigenmodes and eigenfrequencies, from their flow model $u_\phi(\theta,t)$.

Estimates of $\{V_s^2\}(s)$ can be translated into magnetic field strengths, which are typically 0.2–0.3 mT (for a basic period of 80 years), about the same as the r.m.s. (root mean square) radial magnetic field at the CMB (0.3 mT). This result is in conflict with the distribution of the magnetic field in numerical simulations of the geodynamo (e.g., Aubert et al., 2009). Such dynamo models display magnetic fields in the core interior with an r.m.s. field amplitude about ten times stronger than the dipole field at the core surface, and imply an intensity of several mT within Earth's core.

Note that there are, of course, other magnetic field changes with both shorter and longer time scales (e.g., Jackson, 2003). Magnetic variations (and length-of-day fluctuations) in the period range 60–80 years have perhaps received most attention because they were the first to be well characterized; this was because of the length and resolution of the time series then available. Roberts et al. (2007) present a more positive viewpoint concerning the 60–80-year signal.

In contrast, Gillet et al. (2010) have recently argued that torsional waves propagate much more rapidly than previously thought. They have attributed both the length-of-day (l.o.d.) and magnetic variations recurring every 6 years to torsional waves emitted periodically from the vicinity of the geostrophic cylinder circumscribing the inner core. As a consequence of the increased propagation velocity of torsional waves, Gillet et al. (2010) have revised upward the r.m.s. strength of the magnetic field in the cylindrical radial direction to approximately 3 mT (Figure 4). The geophysical evidence supporting the new value for the velocity $\{V_s^2\}^{1/2}$ is now outlined.

At frequencies less than 1/5 cycles per year, fluctuations of the atmospheric winds and oceanic currents seem insufficient to cause the observed length-of-day variations (Gross et al., 2004). In fact, a persistent 6-year oscillation in the l.o.d. signal appears more clearly after subtracting contributions to the l.o.d. from the motions in the outer fluid envelope of Earth (Abarca del Rio et al., 2000). This 6-year oscillation was first interpreted as geodetic evidence of gravitational coupling between the laterally heterogeneous mantle and the inner core (Mound and Buffett, 2006). There is also direct evidence for a magnetic signal with the same frequency. Silva et al. (2012) have identified a 6-year periodic signal from the CHAOS3 (1997–2010) and CM4 (1960–2002) geomagnetic field models. These results are consistent with the findings of Gillet et al. (2010), who recovered a 6-year period in the spectrum (over 1925–90) of the l.o.d. variations predicted from their core flow models, which are in phase with the actual l.o.d. changes observed over the same time span.

Provided that the distribution of magnetic energy in the core interior is approximately isotropic, 3 mT r.m.s. strength of the magnetic field in the cylindrical radial direction corresponds to 5 mT typical intensity of the total field (since $3\sqrt{3} \sim 5$). From this value, which agrees approximately with an independent estimate inferred from anomalous dissipation in nutations (Buffett, 2010), it is calculated that the magnetic

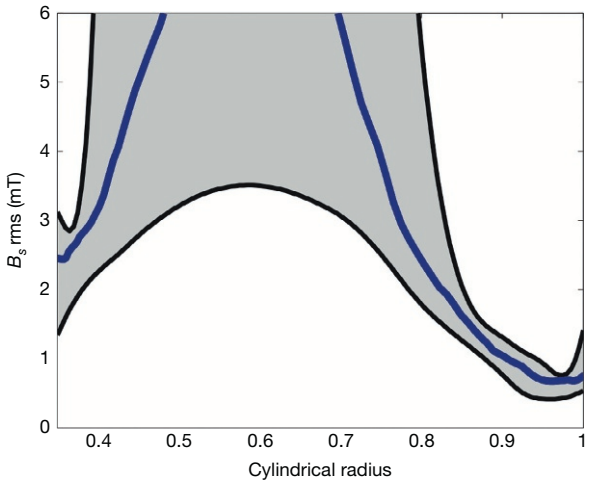

Figure 4 The r.m.s. value of the cylindrical radial magnetic field $B_s(s)$ in the core interior averaged over geostrophic cylinders, as a function of distance to the rotation axis. Reproduced from Gillet, N., Jault, D., Canet, E., Fournier, A., 2010. Fast torsional waves and strong magnetic field within the Earth's core. Nature 465, 74–77.

energy density in the core is about 20 J m^{-3}. The kinetic energy density of large-scale motions, which is about 2×10^{-3} J m^{-3} for a typical velocity 5×10^{-4} m s^{-1}, is thus tiny compared to the total magnetic energy density. This statement is in agreement with the discussion in Section 8.09.2.2.5. At the wavenumber k_0, magnetic and velocity fields have comparable energies. However, for $k<k_0$, $\mathbf{u}\cdot\nabla\mathbf{u}\ll\mathbf{V}\cdot\nabla\mathbf{V}$, and the magnetic energy dominates the kinetic one. According to this picture of Earth's core MHD, transfer of energy between different scales occurs via the magnetic term for $k<k_0$.

Finally, identifying the time evolution of the geostrophic angular velocity $\zeta(s)$ with the propagation of torsional waves constrains the geostrophic shear at $s=r_c$ beneath the equator of the core. As a result, there can be a contradiction between the physical constraint $\partial\zeta/\partial s=0$ at $s=r_c$ (for the case of an insulating mantle) and the core surface flows obtained in kinematic inversions of magnetic data. The difficulty can be traced to the type of the step-by-step approach currently used to model core dynamics. The solution is to invert for the parameters of the torsional waves directly from geomagnetic data and belongs to the realm of data assimilation (Fournier et al., 2010).

8.09.3.5 Calculation of Core Angular Momentum Changes

Presented here is the calculation of the variations in mantle angular momentum, and thus in l.o.d., which compensate the variations in core angular momentum caused by time changes of the geostrophic velocity (Jackson et al., 1993; Jault et al., 1988). Due account is taken of the increase in core density with depth, which does not modify the expression of the geostrophic velocity as $s\zeta(s,t)$ (see eqn [21]) provided that the boundary is symmetrical about the rotation axis.

Mathews et al. (1991) calculated the equatorial moment of inertia A_c of Earth's core from the density profile of the PREM model. They also estimated the dynamical ellipticity e of Earth's core. From these two values, the axial moment of inertia $C_c=A_c/(1-e)$ of the core is found to be about 9.14×10^{36} kg m^2. The moment of inertia C_m of the solid Earth (crust and mantle) is about 7.12×10^{37} kg m^2, whereas the moment of inertia of the solid inner core is comparatively very small, 5.87×10^{34} kg m^2. The inner core is ignored here on the basis of its small angular momentum. In order to calculate the angular momentum carried by geostrophic motions, it is convenient to have an analytical expression for the density profile $\rho(r)$ in the core. To this end, the expression of Labrosse et al. (2001), also used in Chapter 8.02, is adopted:

$$\rho(r)=\rho_c\exp\left(-\frac{r^2}{L_\rho^2}\right) \quad [89]$$

where $\rho_c=1.25\times10^4$ kg m^{-3} is the density at the center and $L_\rho=7.4\times10^6$ m is the length scale for the compression. It is based on the logarithmic equation of state of Poirier and Tarantola (1998) and on the development to the third order of the radius of the gravity profile. Equation [89] is inserted in the expression for the core moment of inertia about the rotation axis:

$$C_c=\iiint r^4\rho(r)\sin^3\theta\,dr\,d\theta\,d\phi \quad [90]$$

with the above values for ρ_c and L_ρ and $C_c=9.15\times10^{36}$ kg m^2 is found to be in good agreement with the value quoted earlier.

The geostrophic velocity $u_G(s)$ is calculated, from magnetic observations, in the mantle rest frame. Thus, the core angular momentum, in an inertial frame is

$$\begin{aligned}\sigma_c&=C_c\Omega(t)+\sigma_c'\\ \sigma_c'&=\iiint\rho(r)s^2u_G(s,t)\,ds\,d\phi\,dz\end{aligned} \quad [91]$$

We insert eqn [89] into [91] and obtain

$$\sigma_c'=2\pi\sqrt{\pi}L_\rho\rho_c\int_0^{r_c}s^2u_G(s)\,\mathrm{erf}\left(\frac{H_c}{L_\rho}\right)\exp\left(-\frac{s^2}{L_\rho^2}\right)ds \quad [92]$$

In the incompressible limit ($L_\rho\to\infty$), we have

$$\sigma_c'=4\pi\rho_c\int_0^{r_c}s^2u_G(s)H_c\,ds=4\pi\rho_cr_c^4\int_0^1x^2\sqrt{1-x^2}u_G(x)dx \quad [93]$$

(with $x=H_c/r_c$) since

$$L_\rho\,\mathrm{erf}\left(\frac{H_c}{L_\rho}\right)\exp\left(-\frac{s^2}{L_\rho^2}\right)=\frac{2H_c}{\sqrt{\pi}}\left(1-\frac{H_c^2+3s^2}{3L_\rho^2}+O\left(\frac{r_c}{L_\rho}\right)^4\right) \quad [94]$$

At the core surface, the geostrophic flow is part of the toroidal flow and can be written as

$$u_G=\nabla\times(Tr)=\sum_{l=0}^{\infty}t_{2l+1}^0\nabla\times\left(P_{2l+1}^0(\cos\theta)r\right),\quad u_G=-\frac{\partial T}{\partial\theta}1_\phi \quad [95]$$

where T is the toroidal scalar and $P_l^0(x)$ is the Legendre polynomial of degree l, and the odd parity stems from the symmetry with respect to the equatorial plane. Thus, not only at the surface (where $\partial P_l^0(\cos\theta/\partial\theta)=P_l^1(\cos\theta)$) but also in the entire volume, as a consequence of geostrophy,

$$u_G=-\sum_{l=0}^{\infty}t_{2l+1}^0P_{2l+1}^1(x) \quad [96]$$

where P_l^1 is the associated Legendre function of degree l and order 1. The functions $(P_{2l+1}^1)l$ form the basis of orthogonal functions over [0,1] for the L^2 inner product.

We then insert

$$x^2\sqrt{1-x^2}=-\frac{1}{5}P_1^1(x)-\frac{2}{15}P_3^1(x) \quad [97]$$

together with eqn [96], in [93] and use

$$\int_0^1P_l^1(x^2)dx=\frac{l(l+1)}{2l+1} \quad [98]$$

to obtain

$$\sigma_c'=\frac{8\pi}{15}\rho_cr_c^4\left(t_1^0+\frac{12}{7}t_3^0\right)=\frac{C_c}{r_c}\left(t_1^0+\frac{12}{7}t_3^0\right) \quad [99]$$

where C_c is also expressed in the incompressible limit ($L_\rho\to\infty$) in order to preserve the consistency of the derivation.

The same steps can be followed to calculate σ_c' at the next orders in $(r_c/L)^2$ analytically. Successive approximations are constructed for σ_c' (as given by eqn [92] and expressions extending eqn [94]) for increasing powers of $(r_c/L_\rho)^2$, from the incompressible result $\sigma_c' = C_c(t_1^0 + 1.714t_3^0)/r_c$ to $\sigma_c' = C_c(t_1^0 + 1.786t_3^0 + 0.0910t_5^0)/r_c$ at the first order and $\sigma_c' = C_c(t_1^0 + 1.777t_3^0 + 0.0789t_5^0 + 0.002t_7^0)/r_c$ at the second order. The direct numerical calculation (substituting expression [96] for u_G in eqn [92]) gives $\sigma_c' = C_c(t_1^0 + 1.776t_3^0 + 0.0796t_5^0 + 0.002t_7^0 + 4.10^{-5}t_9^0 + \cdots)/r_c$. From the rapid convergence of the numerical factors multiplying the coefficients t_{2l+1}^0, we conclude that the incompressible approximation is adequate for the calculation of core angular momentum changes.

Changes in core angular momentum are compensated by changes in mantle angular momentum to preserve the total angular momentum of Earth:

$$(C_m + C_c)\frac{d\Omega}{dt} \sim -\frac{C_c}{r_c}\frac{d}{dt}(t_1^0 + 1.776t_3^0 + 0.080t_5^0 + 0.002t_7^0) \quad [100]$$

The changes in length of day δT (measured in milliseconds) are thus related to the changes in the flow coefficients (measured in kilometers per year) through

$$\delta T \sim 1.232(\delta t_1^0 + 1.776\,\delta t_3^0 + 0.080\,\delta t_5^0 + 0.002\,\delta t_7^0) \quad [101]$$

We recommend using the numerical factor 1.232 instead of 1.138 adopted in most previous investigations of core angular momentum changes. The difference stems from a discrepancy between estimates of C_c.

8.09.4 Mechanical Core–Mantle Interactions

The CMB is not perfectly spherical (see the discussion of the CMB in **Chapter 1.23**). The dynamical ellipticity of the fluid core is one of the parameters entering nutation models, which give an ellipticity value in excess of the hydrostatic value. The extra flattening of the CMB is estimated to be about 400 m (Mathews et al., 2002). This result can constrain 3D geodynamic models of mantle density and seismic wave speeds (Simmons et al., 2010), which in turn give models of the large-scale CMB topography. According to these models, negative topography occurs beneath subducting slabs (in the circum-Pacific region) and positive topography at the base of upwelling regions (Lassak et al., 2010; Soldati et al., 2012; Yoshida, 2008). However, these deviations from a gravity equipotential surface are reduced in the presence of a layer of very low viscosity in the lowermost mantle. An additional source of CMB topography is isostatic compensation of lateral thickness variations in a narrow chemically distinct layer above the CMB. Thus, the amplitude of the CMB models varies with the inclusion of several geodynamic features, which may or may not be present in the actual Earth. To conclude and from a geodynamic perspective, CMB height (valley-to-peak) in the range 1–5 km appears plausible. The most recent seismic models of the CMB topography have amplitudes of ±1.5 km. Both Garcia and Souriau (2000) and Sze and van der Hilst (2003) found that PcP, PKP, and PKKP travel time residuals yield peak-to-peak CMB topography of about 3 km. Then, from a collection of PKiKP-PcP travel times, Koper et al. (2003) argued that the peak-to-peak variations of the outer core thickness do not exceed 4 km. Finally, Koelemeijer et al. (2012) have recently investigated the sensitivity of normal modes to the CMB and its vicinity. They find that the peak-to-peak amplitude of CMB topography has to be smaller than 5 km.

The ICB also probably deviates from a surface of revolution. Buffett (1996) assumed that the ICB corresponds approximately to an equipotential surface of Earth's gravity field. These surfaces are not perfectly spherical because the heterogeneous density distribution in the lower mantle creates gravity anomalies. From mantle convection models and the corresponding degree 2 order 2 gravity components, the peak to peak variations of the equatorial inner core radius are estimated to be 100–200 m. Inner core thermal convection may also cause topography at the ICB above the gravity equipotential surfaces. Mizzon and Monnereau (2013) and Deguen et al. (2013) have investigated this, taking into account dynamically induced melting and freezing of the ICB. They show a rapid transition (as a function of the ratio between the phase change time scale and the viscous relaxation time scale) from a convection mode dominated by a degree 1 component (the translation mode of Monnereau et al. (2010) and Alboussière et al. (2010)) to chaotic plume convection. The scale of the convection is reflected in the scale of the induced ICB topography. The discussion here is mostly concerned with the CMB.

8.09.4.1 Geostrophic Contours

The properties of the geostrophic flow in a container of arbitrary shape have been investigated by Greenspan (1965, 1968) and Soward and Roberts (2007). Let us define the geostrophic contours as the curves drawn on the container surface and tangent to the geostrophic flow. In a container filled with an incompressible fluid, pairs of geostrophic contours on the upper $z = z_T$ and lower $z = z_B$ boundaries are separated by a constant height $z_T - z_B = 2H_c$. These curves are the upper and lower rims of geostrophic cylinders, which are not circular in the presence of topography on the core–mantle interface.

Taking into account both the noncircularity of geostrophic cylinders and the adiabatic stratification $\rho_a(r)$ (see **Section 8.09.2.1.3**) would make the discussion significantly more complicated. Then, the height separating geostrophic streamlines belonging to the same geostrophic cylinder varies with the distance to the rotation axis (see eqn [23]) and geostrophic cylinders do not have a constant height. In the following sections, we keep clear of these subtleties and assume that the density ρ is uniform.

Even though the deviations of the inner and outer boundaries of a nearly spherical shell (such as Earth's fluid core) from a surface of revolution with radii $r = r_i$ and $r = r_c$, respectively, have a small height, there are two regions of the fluid volume where there are no closed geostrophic cylinders. First, the outer boundary may be reentrant in terms of s; it may be locally concave at the equator (Fearn and Proctor, 1992) as illustrated in **Figure 5**. Second, there is a cylindrical volume void of geostrophic surfaces near $s = r_i$ (see **Figure 6**). The discussion of the possible dynamical role of these two regions in the excitation or the attenuation of the torsional waves awaits

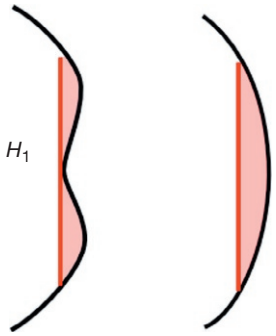

Figure 5 Two meridian slices showing the fluid volume void of geostrophic cylinders (light red) near the outer core equator. The black curve indicates the core–mantle boundary (CMB) and the red curve, a geostrophic cylinder. The figure on the left shows where the CMB is re-entrant. There is no geostrophic contour with height $H_c < H_1$.

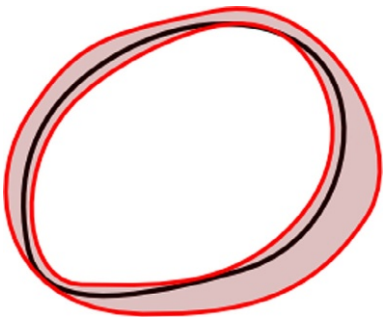

Figure 6 Fluid volume (light red) void of geostrophic cylinders near the inner core equator projected on the equatorial plane. Black curve: projection of the inner core surface. Red curves: geostrophic cylinders closest to the inner core equator. The red inner curve is the projection of the geostrophic cylinder with the largest cross-section above the inner core, and the red outer curve is the projection of the first geostrophic surface circumscribing the inner core.

future studies. We have to leave aside this question. In the following sections, we assume that there are closed geostrophic contours.

The geostrophic velocity and pressure are related by

$$2\rho\Omega\mathbf{u}_G = \mathbf{1}_z \times \nabla p_G \qquad [102]$$

The geostrophic pressure is independent of z.

It is convenient to define a set of curvilinear coordinates (q_1, q_2, q_3) such that the geostrophic cylinders correspond to a constant value of one of the coordinates q_1, as illustrated in Figure 7. It is, thus, natural to use a function of H_c as the new curvilinear coordinate q_1 instead of the distance s to the rotation axis, which is appropriate in containers with symmetry about the rotation axis. We define q_3 as a modification of the cylindrical polar coordinate z such that it is constant $(q_3 = \pm H_c)$ on pairs of geostrophic contours, where geostrophic cylinders intersect the boundary:

$$q_3 = z + H_c - z_T \qquad [103]$$

Then, the unit vector $\mathbf{1}_3$ of the basis remains simply $\mathbf{1}_z$. Following the work of Greenspan (1965) (see also Greenspan, 1968, pp. 43–45), we denote by $\mathbf{n}_T$ and $\mathbf{n}_B$ the unit outward

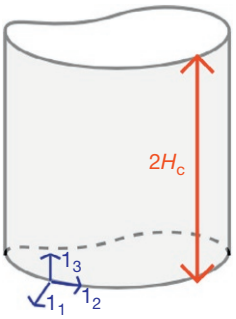

Figure 7 Curvilinear coordinate system (q_1, q_2, q_3). Geostrophic cylinders H_c = constant are coordinate surfaces q_1 = constant. Basis vectors $\mathbf{1}_2$ are tangent to geostrophic contours and $\mathbf{1}_3 = \mathbf{1}_z$.

normals to the outer boundary, respectively, at the top and bottom rims of the geostrophic cylinders. As a consequence of the no-penetration condition $\mathbf{u}\cdot\mathbf{n}_{T,B} = 0$, the vector $\mathbf{n}_T \times \mathbf{n}_B$ is tangent to the geostrophic contours. Thus,

$$\mathbf{1}_2(q_1, q_2) = \frac{\mathbf{n}_T \times \mathbf{n}_B}{|\mathbf{n}_T \times \mathbf{n}_B|} \qquad [104]$$

and $\mathbf{1}_1 = \mathbf{1}_2 \times \mathbf{1}_3$ completes the basis. The coordinate q_2 is chosen so that $\mathbf{1}_1$ and $\mathbf{1}_3$ are tangent to the surfaces of the constant q_2. In this coordinate system, the geostrophic velocity can be written as

$$\mathbf{u}_G = u_G(q_1, q_2)\mathbf{1}_2 \qquad [105]$$

When the container is symmetrical about the equatorial plane ($z_T = H_c$, $z_B = -H_c$, $q_3 = z$), the geostrophic contours are perpendicular to the rotation axis ($\mathbf{1}_2 \cdot \mathbf{1}_3 = 0$), the vectors ($\mathbf{1}_1$, $\mathbf{1}_2$, $\mathbf{1}_3$) form an orthonormal basis, and the curvilinear coordinates (q_1, q_2, q_3) are orthogonal. We shall adopt this simplification. Then the scale factors h_i fully describe the metric tensor:

$$h_i = \left|\frac{\partial \mathbf{r}}{\partial q_i}\right| \qquad [106]$$

where $\mathbf{r}$ is the position vector. Here, the three scale factors $h_1(q_1, q_2)$, $h_2(q_1, q_2)$, and $h_3 = 1$ do not depend on q_3. They replace the set of scale factors ($h_1 = 1$, $h_2 = s$, $h_3 = 1$) for cylindrical polar co-ordinates (s, ϕ, z), used when the container is symmetrical about the rotation axis.

Because $\mathbf{u}_G$ has no component along $\mathbf{1}_1$, the geostrophic pressure depends only on q_1 and eqn [102] reduces to

$$2\rho\Omega h_1 u_G = \frac{\partial p_G}{\partial q_1} \qquad [107]$$

Taking the q_2-derivative of eqn [107], we have

$$\frac{\partial}{\partial q_2}(h_1 u_G) = 0 \qquad [108]$$

The latter equation can also be obtained from the incompressibility condition $\nabla\cdot\mathbf{u} = 0$, which again gives

$$\frac{\partial}{\partial q_2}(h_1 h_3 u_G) = 0 \qquad [109]$$

since the general expression for the divergence in orthogonal curvilinear coordinates is

$$\nabla\cdot\mathbf{u}=\frac{1}{h_1h_2h_3}\left(\frac{\partial}{\partial q_1}(h_2h_3u_1)+\frac{\partial}{\partial q_2}(h_3h_1u_2)+\frac{\partial}{\partial q_3}(h_1h_2u_3)\right) \quad [110]$$

(Morse and Feshbach, 1953, p. 36).

8.09.4.2 Torsional Waves in the Presence of Topography

Sketched out here are possibilities for studying the propagation of torsional waves when the fluid cavity presents deviations from axisymmetry. The derivation of the solvability condition [75] is not contingent on the axisymmetry of the cavity surface (Fearn and Proctor, 1992; Jault, 2003; Soward and Roberts, 2007). It is assumed that the boundary is kept fixed in the rotating frame of reference. For the sake of simplicity, the buoyancy forces are neglected here despite their possible role in this problem. Using eqn [108], eqn [76] can be transformed into

$$\forall q_1,\quad \int_{\Sigma(q_1)}(\mathbf{j}\times\mathbf{B})_2h_2\,\mathrm{d}q_2\,\mathrm{d}z=0 \quad [111]$$

where $\Sigma(q_1)$ is the geostrophic cylinder that is uniquely defined from the constant value taken by the coordinate q_1. Equation [111] generalizes eqn [77]. Fearn and Proctor (1992) remarked, however, that it is misleading to attribute [111] to the need for a torque balance between geostrophic cylinders, which is the definition usually put forward to interpret eqn [77].

When eqn [75] does not hold, as before, it is necessary to restore the geostrophic acceleration term and eqn [80] is generalized to

$$\left(h_1\frac{\partial u_G}{\partial t}\right)(q_1)=\left(s_\rho H_c\oint_{q_1}\frac{h_2}{h_1}\mathrm{d}q_2\right)^{-1}\int_{\Sigma(q_1)}(\mathbf{j}\times\mathbf{B})_2h_2\,\mathrm{d}q_2\,\mathrm{d}q_3 \quad [112]$$

Now the integral on the right-hand side is calculated. It is convenient to write the Lorentz force as

$$\mathbf{j}\times\mathbf{B}=-\frac{1}{2\mu_0}\nabla B^2+\frac{1}{\mu_0}(\mathbf{B}\cdot\nabla)\mathbf{B} \quad [113]$$

since the magnetic pressure term $-\nabla p_m$, with $p_m=B^2/(2\mu_0)$, gives a zero contribution to eqn [112]

$$\int_{-H_c}^{H_c}\left(\oint\frac{1}{h_2}\frac{\partial p_m}{\partial q_2}h_2\,\mathrm{d}q_2\right)\mathrm{d}q_3=0 \quad [114]$$

(p_m is single valued).

Using the expression for the operator $(\mathbf{B}\cdot\nabla)$ in generalized orthogonal coordinates (Morse and Feshbach, 1953, p. 33), we have

$$((\mathbf{B}\cdot\nabla)\mathbf{B})_2=\frac{B_2}{h_2}\frac{\partial B_2}{\partial q_2}+B_3\frac{\partial B_2}{\partial q_3}+\frac{B_1}{h_1}\frac{\partial B_2}{\partial q_1}+\frac{B_1}{h_1h_2}\left(B_2\frac{\partial h_2}{\partial q_1}-B_1\frac{\partial h_1}{\partial q_2}\right) \quad [115]$$

because $h_3=1$ and $\partial h_2/\partial q_3=0$. The first term on the right-hand side gives a zero contribution to the integral of the Lorentz force over a geostrophic cylinder as

$$\oint\frac{B_2}{h_2}\frac{\partial B_2}{\partial q_2}h_2\,\mathrm{d}q_2=0 \quad [116]$$

Then the expression for the divergence [110] can be used to transform eqn [115] into

$$\int_{\Sigma(q_1)}((\mathbf{B}\cdot\nabla)\mathbf{B})_2\mathrm{d}\Sigma=\int_{\Sigma(q_1)}\left(\frac{\partial}{\partial q_3}(B_2B_3)+\frac{1}{h_1h_2^2}\frac{\partial}{\partial q_1}\left(h_2^2B_1B_2\right)+\frac{1}{h_1h_2}\frac{\partial h_1}{\partial qh_2}\left(B_2^2-B_2^1\right)\right)\mathrm{d}\Sigma \quad [117]$$

where the surface element $\mathrm{d}\Sigma$ is $h_2\,\mathrm{d}q_2\,\mathrm{d}q_3$. The z-integral yields a boundary term that can be written as a function of the magnetic field B_n normal to the boundary. Denoting H_c' the derivative of H_c with respect to q_1, the unit outward normal to the CMB, expressed in the basis $(\mathbf{1}_1,\mathbf{1}_2,\mathbf{1}_3)$, is

$$n=\left(H_c'(q_1)^2+h_1^2\right)^{-1/2}\left(H_c'(q_1),0,\pm h_1\right)\quad\text{at}\quad q_3=\pm H_c \quad [118]$$

because the equation of the boundary is $q_3=H_c(q_1)$. After some manipulation, the Lorentz force integrated over $\Sigma(q_1)$ can be written as

$$\begin{aligned}\int_{\Sigma(q_1)}(\mathbf{j}\times\mathbf{B})_2h_2\,\mathrm{d}q_2\,\mathrm{d}q_3=&\frac{1}{\mu_0}\int_{c(q_1)}B_2B_n\frac{1}{h_1}\left(H_c'(q_1)^2+h_2^1\right)^{1/2}h_2\;\mathrm{d}q_2\\&+\frac{1}{\mu_0}\oint\frac{1}{h_1h_2}\frac{\partial}{\partial q_1}\left(h_2^1\int_{-H_c}^{H_c}B_1B_2\,\mathrm{d}q_3\right)\mathrm{d}q_2\\&+\frac{1}{\mu_0}\int_{\Sigma(q_1)}\frac{1}{h_1h_2}\frac{\partial h_1}{\partial q_2}(B_2^2-B_1^2)\mathrm{d}\Sigma\end{aligned} \quad [119]$$

where $C(q_1)$ denotes the two rims of the geostrophic cylinder $\Sigma(q_1)$. The last term disappears in spherical geometry, for which $q_1=s$ and $h_1=1$ and the surfaces $q_2=$constant have zero curvature C

$$C=-\frac{1}{h_1h_2}\frac{\partial h_1}{\partial q_2}=0 \quad [120]$$

Using the identity [108], the frozen flux induction equation gives

$$\begin{aligned}\frac{\partial B_1}{\partial t}&=-\zeta h_1\frac{\partial}{\partial q_2}\left(\frac{B_1}{h_1}\right)\\\frac{\partial B_2}{\partial t}&=-\frac{\zeta}{h_1}\frac{\partial}{\partial q_2}(h_1B_2)+\frac{B_1h_2}{h_1}\frac{\partial\zeta}{\partial q_1}\end{aligned} \quad [121]$$

where the definition of ζ is generalized here as $\zeta=u_c/h_2$.

Since eqn [111] cannot be directly interpreted in terms of torque balance, a short discussion of the topographic torque acting on the mantle is in order. In the presence of CMB topography, the fluid core locally exerts a pressure force akin to the aerodynamic form drag on the solid mantle. It is now shown that the net torquing effect of the geostrophic pressure on the rotation of the mantle is zero. It is convenient to calculate this pressure torque in the coordinate system (q_1, q_2, q_3) because the geostrophic pressure depends only on q_1. The surface element at the CMB is

$$\mathrm{d}\Sigma=\left(H_c'(q_1)^2+h_1^2\right)^{1/2}h_2\,\mathrm{d}q_1\,\mathrm{d}q_2 \quad [122]$$

Since the expression [118] for $\mathbf{n}$, the unit outward normal to the boundary has already been derived, the only missing

ingredient to calculate the axial pressure torque $\Gamma_{p,G}$ acting on the CMB is an expression for $s\mathbf{1}_s$ in the new coordinate system. Let us define

$$s = g(q_1, q_2) \qquad [123]$$

Then

$$\mathbf{1}_s = \frac{1}{h_1}\frac{\partial g}{\partial q_1}\mathbf{1}_1 + \frac{1}{h_2}\frac{\partial g}{\partial q_2}\mathbf{1}_2 \qquad [124]$$

Finally, it is found that the geostrophic pressure $p_G(q_1)$ exerts no torque on the solid walls

$$\begin{aligned}\Gamma_{p,G} &= \int\int_z (s\mathbf{1}_s \times p_G\mathbf{n})\,\mathrm{d}\Sigma \\ &= \int H_c'(q_1)p_G(q_1)\left(\oint g\frac{\partial g}{\partial q_2}\mathrm{d}q_2\right)\mathrm{d}q_1 = 0\end{aligned} \qquad [125]$$

as the contour integral over q_2 in eqn [125] vanishes.

8.09.4.3 Coupling with the Solid Inner Core

8.09.4.3.1 Time-variable geostrophic contours

If there is differential rotation between the inner and outer boundaries of the fluid core, the two boundaries cannot be simultaneously held fixed in the rotating frame of reference. The no-penetration condition then becomes

$$\begin{aligned}\mathbf{u}\cdot\mathbf{n} &= (\boldsymbol{\Omega}_i \times \mathbf{r})\cdot\mathbf{n}, \quad \text{at } r = r_i \\ \mathbf{u}\cdot\mathbf{n} &= (\boldsymbol{\Omega}_o \times \mathbf{r})\cdot\mathbf{n}, \quad \text{at } r = r_c\end{aligned} \qquad [126]$$

where $\boldsymbol{\Omega}_i$ and $\boldsymbol{\Omega}_o$ are the angular velocities of the solid core and the mantle, respectively. This differs from eqn [71] only in the presence of topography. If one boundary is symmetric about the axis of rotation, which implies that $\mathbf{1}_\phi\cdot\mathbf{n} = 0$, choosing the rotation of the other as the rotation of the frame of reference makes eqn [126] time invariant. However, it is not possible to choose the rotating frame of reference such that the two conditions [126] are time-invariant if there is topography on both boundaries. Then, the geostrophic contours are time-variable, which yields new inertial acceleration terms in equations written using the system of coordinates (q_1, q_2, q_3) introduced in Section 8.09.4.1.

8.09.4.3.2 Gravitational coupling

There is possibly a gravitational torque between the solid inner core and the mantle because the solid inner core is denser than the fluid outer core and the mantle is laterally heterogeneous (see Chapter 8.08). Buffett (1996) discovered this mechanism and Mound and Buffett (2005) included it in their study of torsional oscillations. They assumed that there is an equilibrium position where the ICB is an equipotential surface of the gravity field. When the inner core rotates through the gravitational and pressure fields, which can be considered fixed in the mantle reference frame, it experiences both a gravitational and a pressure torque. The two torques would exactly cancel out if the solid and fluid cores had the same density because of the hydrostatic equilibrium.

8.09.4.3.3 Electromagnetic coupling

Any differential rotation between the fluid and solid cores results in a strong restoring electromagnetic torque acting between the two bodies. Indeed, the magnetic field in the core interior is stronger than at its surface and both the inner and the outer cores are good electrical conductors. As a result, the inner core rotation ζ_{IC} is enslaved to the fluid angular velocity. Omitting the other torques acting on the inner core in order to focus on this mechanism, we have

$$C_{IC}\frac{\partial \zeta_{IC}}{\partial t} \approx -\Gamma_{M,IC}\left(\zeta_{IC} - \tilde{\zeta}\right) \qquad [127]$$

where C_{IC} is the axial moment of inertia of the solid inner core, and $\tilde{\zeta}$ is some average of the geostrophic velocity within the cylindrical surface tangent to the inner core that depends on the distribution of the radial magnetic field at the ICB. The factor $\Gamma_{M,IC}$ measures the strength of the electromagnetic coupling, and is proportional to the mean-squared value of the radial field at the ICB. Although they consider eqn [127] from a different viewpoint, Roberts and Aurnou (2012) estimate the time response $C_{IC}/\Gamma_{M,IC}$ for a typical 5 mT radial magnetic field at the ICB and find that it is of the order of a few days. As there is little dissipation involved, electromagnetic coupling with the inner core does not hinder the propagation of torsional waves inward as far as the rotation axis (see Figure 2 of Jault and Légaut (2005)).

Electromagnetic coupling of the fluid and solid core also allows an indirect coupling between the fluid core and the mantle, if it operates in parallel with gravitational coupling between the solid inner core and the mantle (see Section 8.09.4.3.2).

A similar mechanism could also operate at the CMB, provided there was sufficient electrical conductivity in the lowermost mantle. In contrast with the situation at the ICB, electromagnetic coupling at the CMB entails attenuation of the torsional waves. Buffett (1998) and Dumberry and Mound (2008) observe that mantle conduction suppresses the torsional waves before they cross the core if the mantle conductance is large enough to make the electromagnetic torque at the CMB contribute significantly to l.o.d. changes.

Roberts and Aurnou (2012) note that frictional coupling between the fluid and the solid cores may also be important for the reason that their interface is rough if solidification of the inner core occurs through dendritic growth (Deguen, 2012).

8.09.5 Future Directions – Consistent Approach to the Earth's Core Dynamics

8.09.5.1 Diffusion of the Geomagnetic Signal Through the Weakly Conducting Mantle

There is growing seismic evidence that the lowermost mantle is chemically and thermally very heterogeneous (e.g., Lay and Garnero, 2011). A host of 3D structures have been revealed. To cite just one example, dome-like hills sitting on the CMB, up to 100 km high, have been recently imaged using seismic data collected by Earthscope's USArray (Sun et al., 2013). The authors argue that these structures are stabilized at the bottom of the mantle by the addition of a small percentage of Fe-rich oxides. The electrical conductivity of FeO is estimated to be about 9×10^4 S m^{-1} at the pressure and temperature of the CMB, which is much higher than those of other rocks of

the deep mantle (Ohta et al., 2012). Lateral variations of the electrical properties of the lowermost mantle are thus to be expected. They will be very difficult to detect from studies based on the analysis of electrical currents induced in the mantle by varying magnetospheric fields (Kuvshinov, 2012); hence, there is strong motivation for trying, instead, to use the varying core field as the source.

Three types of observations may be used to constrain the mantle conductivity from the bottom. First, the time correlation properties of observatory records and of the geomagnetic coefficient series at Earth's surface may provide us with information about the smoothing of the magnetic signal through the conducting mantle (Gillet et al., 2013; Mandea Alexandrescu et al., 1999). Second, observatory records show abrupt changes in the secular variation of the core field. These events are almost, but not fully, simultaneous at Earth's surface (Alexandrescu et al., 1996). The question has thus arisen whether their different times of occurrence at distinct observatories are caused by the conducting mantle acting as a filter on core signals (Nagao et al., 2003; Pinheiro and Jackson, 2008). Third, changes in the geostrophic flow $\mathbf{u}_G$ throughout the core yield variations in core angular momentum, which can be inferred from observed l.o.d. variations. The flow $\mathbf{u}_G$ also causes the magnetic field outside the core to evolve. Differential delays between magnetic and l.o.d. observations may be ascribable to the conducting mantle (Backus, 1983).

Most work on the transmission of the magnetic field from the core to the mantle has involved a perturbation procedure where the small parameter is the frequency of the core signal. The first order theory gives the zero frequency delay time of the mantle τ_1 (Benton and Whaler, 1983). Backus (1983) extended the theory to the second order and calculated the smoothing time of the mantle. Both Benton and Whaler (1983) and Backus (1983) derived τ_1 as a weighted integral of the mantle conductivity, with a weight vanishing linearly at the CMB,

$$\tau_1 = \frac{\mu_0}{2l+1}\int_{r_c}^{r_e} r\sigma(r)\left(1-\left(\frac{r_c}{r}\right)^{2l+1}\right)\mathrm{d}r \qquad [128]$$

where l is the harmonic degree of the field, σ is the conductivity as a function of radius, and r_e is Earth's radius. The conclusion that the conductivity of the mantle rocks just above the CMB has no influence on the filtering of magnetic signals emanating from the core is drawn directly from the supposedly perfect knowledge of the field at the core surface, whereas the magnetic field at the CMB actually depends on the mantle conductivity.

Considering the conducting mantle as a filter acting on the magnetic field supposedly perfectly known at the core surface has been misleading. We now need to take a step back and to consider the mechanisms behind the production of a magnetic field at the CMB. From coupled models of core dynamics (as discussed in **Sections 8.09.2.2.3** and **8.09.3**) and mantle induction, it will be possible to calculate different quantities (time evolution of l.o.d., geographical distribution of sudden magnetic field changes, auto-correlation of geomagnetic coefficients series), which are measurable. When such direct models are available, solutions of the associated inverse problem will include information on the mantle conductivity, especially near the CMB.

8.09.5.2 Filtering Through a Stably Stratified Layer Below the CMB

A variety of mechanisms may cause a stratified layer to establish at the CMB. It has been suggested that light elements collect at the top of the core either because they are entrained in coherent blobs from the ICB to the CMB (Moffatt and Loper, 1994) or because they migrate down the pressure gradient in the outer core (e.g., Gubbins and Davies, 2013). As another possibility, there are indications from high pressure experiments that the core is undersaturated in oxygen (Buffett and Seagle, 2010; Frost et al., 2010) and silicon (Tsuno et al., 2013) with respect to the mantle, which may have led to the development of an O- and Si-enriched low-density layer beneath the CMB. In addition, the top of the core may be thermally stratified as suggested by recent theoretical ab initio studies (de Koker et al., 2012; Pozzo et al., 2012, 2013), which have revised upward the thermal conductivity of the core and, thus, the amount of heat conducted upward along the adiabat. If the temperature gradient has fallen below the adiabat, the upper part of the core (or a layer at intermediate depth if thermal conductivity increases with depth rapidly enough) is thermally stratified (Gomi et al., 2013; Gubbins et al., 2004).

There is some seismological evidence for stable stratification of the outermost core. Helffrich and Kaneshima (2010) have argued, using observations of SmKS waveforms, that the material at the top of the core is 5.9% less dense than the liquid 300 km below it. This corresponds to a Brunt–Väisälä frequency N in the range of 0.51–1.03 mHz or a ratio of $2\Omega/N \sim 0.1$ for a possible stable layer beneath the CMB.

The preceding sections have given us the tools to briefly discuss the effect of a strongly stratified layer ($N \gg \Omega$) below the core surface of depth D. Following Takehiro and Lister (2001), we consider that the motions in the stratified layer originate from convective motions in the underlying unstable layer, with frequency ω. As in **Section 8.09.2.2.2**, we work in a local Cartesian coordinate system, with x the prograde direction and y directed toward the rotation axis. Here, the z-axis is the gravity axis. In this coordinate system, $\mathbf{\Omega} = \Omega_y\mathbf{1}_y + \Omega_z\mathbf{1}_z$. We further assume that the velocity is proportional to $\exp[\mathrm{i}(k_x x + k_y y + nz - \omega t)]$. Including rotational effects but otherwise similar to eqn [34] given earlier, Takehiro and Lister obtained the dispersion relation

$$\omega^2 = \frac{N^2\left(k_x^2+k_y^2\right) + 4\left(n\Omega_z + k_y\Omega_y\right)^2}{k_x^2+k_y^2+n^2} \qquad [129]$$

which transforms into eqns [11] and [34] in the limiting cases $N=0$ and $\Omega=0$, respectively. When $\omega \ll \Omega, N$, eqn [129] gives the following equation for n:

$$N^2\left(k_x^2+k_y^2\right) + 4n^2(\mathbf{\Omega}\cdot\mathbf{1}_r)^2 \sim 0 \qquad [130]$$

This expression yields the imaginary part of n and, finally, the characteristic penetration depth in the direction parallel to the rotation axis, $\delta \sim \left(2\Omega/\sqrt{k_x^2+k_y^2}N\right)$.

Using the seismological model of Helffrich and Kaneshima (2010) as an example, large length-scale motions with azimuthal wavenumber $m=3$ and lower are predicted to be able to penetrate through the layer, whereas smaller length-scale

features will penetrate less deeply and be attenuated before reaching the CMB.

8.09.6 Final Remarks

Taking into account dynamical effects such as wave motions and restoring forces is helping to resolve several issues concerning the interpretation of geomagnetic data. For example, it is now known that the geostrophic shear $\partial\zeta/\partial s$ at $s=r_c$ is determined by the condition that the magnetic vector is continuous across the CMB. Conversely, away from the core equator, rapid rotation hinders the propagation of Alfvén waves that would eliminate discontinuities in the magnetic field parallel to the CMB. Also, the pressure torque between the core and the mantle cannot be studied independently from the motions that make the pressure change and it is hoped that a consistent model of torsional waves in the presence of CMB topography will soon emerge. Finally, models of induction in the conducting mantle need to be coupled with models of waves in the core or, more generally, of core dynamics, before observations are interpreted in terms of mantle conductivity.

Rapid rotation is the key actor in the story that has been told in this chapter. Because it rigidifies the motions in the direction parallel to the rotation axis, only products of the magnetic field components averaged along the direction parallel to the rotation axis enter the equations for fast and large-scale dynamics. This scale anisotropy between flow variations parallel and perpendicular to the rotation axis has recently motivated the development of another set of reduced equations for flows in the presence of strong rotation that is less restrictive than quasi-geostrophy (Grooms et al., 2010; Julien et al., 2006). In this model, axial variations are small only on an axial scale equal to the scale in the perpendicular direction. It would be worthwhile to generalize the axially averaged equations presented in **Section 8.09.2.2.3** along the same lines.

References

Abarca del Rio R, Gambis D, and Salstein DA (2000) Interannual signals in length of day and atmospheric angular momentum. *Annales Geophysicae* 18: 347–364.

Acheson DJ (1978) Magnetohydrodynamic waves and instabilities in rotating fluids. In: Roberts PH and Soward AM (eds.) *Rotating Fluids in Geophysics*, pp. 315–349. New York: Academic Press.

Alboussière T, Deguen R, and Melzani M (2010) Melting-induced stratification above the Earth's inner core due to convective translation. *Nature* 466: 744–747.

Alexandrescu M, Gibert D, Hulot G, Le Mouël J-L, and Saracco G (1996) Worldwide wavelet analysis of geomagnetic jerks. *Journal of Geophysical Research* 101: 21975–21994.

Anufriev AP, Jones CA, and Soward AM (2005) The Boussinesq and anelastic liquid approximations for convection in the Earth's core. *Physics of the Earth and Planetary Interiors* 152: 163–190.

Aubert J, Labrosse S, and Poitou C (2009) Modelling the palaeo-evolution of the geodynamo. *Geophysical Journal International* 179: 1414–1428.

Backus G (1968) Kinematics of geomagnetic secular variation in a perfectly conducting core. *Philosophical Transactions of the Royal Society of London, Series A* 263: 239–266.

Backus G (1983) Application of mantle filter theory to the magnetic jerk of 1969. *Geophysical Journal of the Royal Astronomical Society* 74: 713–746.

Becker JM and Salmon R (1997) Eddy formation on a continental slope. *Journal of Marine Research* 55: 181–200.

Benton ER and Whaler KA (1983) Rapid diffusion of the poloidal geomagnetic field through the weakly conducting mantle: A perturbation solution. *Geophysical Journal of the Royal Astronomical Society* 75: 77–100.

Bloxham J, Zatman S, and Dumberry M (2002) The origin of geomagnetic jerks. *Nature* 420: 65–68.

Braginsky SI (1970) Torsional magnetohydrodynamic vibrations in the Earth's core and variations in day length. *Geomagnetism and Aeronomy* 10: 1–8.

Braginsky SI and Roberts PH (1995) Equations governing convection in Earth's core and the geodynamo. *Geophysical and Astrophysical Fluid Dynamics* 79: 1–97.

Bryan GH (1889) The waves on a rotating liquid spheroid of finite ellipticity. *Philosophical Transactions of the Royal Society of London, Series A* 180: 187–219.

Buffett BA (1996) Gravitational oscillations in the length of day. *Geophysical Research Letters* 23: 2279–2282.

Buffett BA (1998) Free oscillations in the length of day: Inferences on physical properties near the core–mantle boundary. In: Gurnis M, Wysession ME, Knittle E, and Buffett BA (eds.) *The Core–Mantle Boundary Region*. *Geodynamics Series*, vol. 28, pp. 153–165. American Geophysical Union.

Buffett BA (2010) Tidal dissipation and the strength of the Earth's internal magnetic field. *Nature* 468: 952–955. http://dx.doi.org/10.1038/nature09463.

Buffett BA, Mound J, and Jackson A (2009) Inversion of torsional oscillations for the structure and dynamics of Earth's core. *Geophysical Journal International* 177: 878–890.

Buffett BA and Seagle CT (2010) Stratification of the top of the core due to chemical interactions with the mantle. *Journal of Geophysical Research* 115: B04407. http://dx.doi.org/10.1029/2009JB006751.

Busse FH (1970) Thermal instabilities in rapidly rotating systems. *Journal of Fluid Mechanics* 44: 441–460.

Busse FH (2002) Convective flows in rapidly rotating spheres and their dynamo action. *Physics of Fluids* 14: 1301–1314.

Busse FH, Dormy E, Simitev RD, and Soward AM (2007) Dynamics of rotating fluids. In: Dormy E and Soward AM (eds.) *Mathematical Aspects of Natural Dynamos*, pp. 119–198. Boca Raton, FL: CRC Press.

Canet E, Fournier A, and Jault D (2009) Forward and adjoint quasi-geostrophic models of the geomagnetic secular variation. *Journal of Geophysical Research* 114: B11101. http://dx.doi.org/10.1029/2008JB006189.

Christensen UR and Aubert J (2006) Scaling properties of convection-driven dynamos in rotating spherical shells and application to planetary magnetic fields. *Geophysical Journal International* 166: 97–114.

Davidson PA (2001) *An Introduction to Magnetohydrodynamics*. Cambridge: Cambridge University Press.

Deguen R (2012) Structure and dynamics of Earth's inner core. *Earth and Planetary Science Letters* 333–334: 211–225.

Deguen R, Alboussiere T, and Cardin Ph (2013) Thermal convection in Earth's inner core with phase changes at its boundary. *Geophysical Journal International* 194: 1310–1334. http://dx.doi.org/10.1093/gji/ggt202.

Diamond PH, Itoh SI, Itoh K, and Silvers LJ (2007) β-Plane MHD turbulence and dissipation in the solar tachocline. In: Hughes DW, Rosner R, and Weiss NO (eds.) *The Solar Tachocline*, pp. 213–240. Cambridge: Cambridge University Press.

Dumberry M and Mound JE (2008) Constraints on core–mantle electromagnetic coupling from torsional oscillation normal modes. *Journal of Geophysical Research* 113: B03102. http://dx.doi.org/10.1029/2007/JB005135.

Fearn DR and Proctor MRE (1992) Magnetostrophic balance in non-axisymmetric, nonstandard dynamo models. *Geophysical and Astrophysical Fluid Dynamics* 67: 117–128.

Finlay C (2007) Alfvén waves. In: Gubbins D and Herrero-Bervera E (eds.) *Encyclopedia of Geomagnetism and Paleomagnetism*, pp. 3–6. New York: Springer.

Finlay CC (2008) Waves in the presence of magnetic fields, rotation and convection. In: Cardin Ph and Cugliandolo LF (eds.) *Dynamos*, pp. 403–450. Amsterdam: Elsevier.

Finlay CC, Dumberry M, Chulliat A, and Pais MA (2010) Short timescale core dynamics: theory and observations. *Space Science Reviews* 155: 177–218.

Finlay CC and Jackson A (2003) Equatorially dominated magnetic field change at the surface of Earth's core. *Science* 300: 2084–2086.

Fournier A, Hulot G, and Jault D (2010) An introduction to data assimilation and predictability in geomagnetism. *Space Science Reviews* 155: 247–291.

Frost DJ, Asahara Y, Rubie DC, et al. (2010) Partitioning of oxygen between the Earth's mantle and core. *Journal of Geophysical Research* 115: B02202. http://dx.doi.org/10.1029JB006302.

Garcia R and Souriau A (2000) Amplitude of the core–mantle boundary topography estimated by stochastic analysis of core phases. *Physics of the Earth and Planetary Interiors* 117: 345–359.

Gillet N, Jault D, Canet E, and Fournier A (2010) Fast torsional waves and strong magnetic field within the Earth's core. *Nature* 465: 74–77.

Gillet N, Jault D, Finlay CC, and Olsen N (2013) Stochastic modelling of the Earth's magnetic field: Inversion for covariances over the observatory era. *Geochemistry, Geophysics, Geosystems* 14: 766–786. http://dx.doi.org/10.1002/ggge.20041.

Gillet N and Jones CA (2006) The quasi-geostrophic model for rapidly rotating spherical convection outside the tangent cylinder. *Journal of Fluid Mechanics* 554: 343–369.

Gillet N, Schaeffer N, and Jault D (2011) Rationale and geophysical evidence for quasi-geostrophic rapid dynamics within the Earth's outer core. *Physics of the Earth and Planetary Interiors* 187: 78–88.

Gomi H, Ohta K, Hirose K, et al. (2013) The high conductivity of iron and thermal evolution of the Earth's core. *Physics of the Earth and Planetary Interiors,* 224: 88–103. http://dx.doi.org/10.1016/j.pepi.2013.07.010.

Greenspan HP (1965) On the general theory of contained rotating fluid motions. *Journal of Fluid Mechanics* 22: 449–462.

Greenspan HP (1968) *The Theory of Rotating Fluids*. Cambridge: Cambridge University Press.

Grooms I, Julien K, Weiss JB, and Knobloch E (2010) Model of convective Taylor columns in rotating Rayleigh–Bénard convection. *Physical Review Letters* 104: 224501.

Gross RS, Fukumori I, Menemenlis D, and Gegout P (2004) Atmospheric and oceanic excitation of length-of-day variations during 1980–2000. *Journal of Geophysical Research* 109: B01406. http://dx.doi.org/10.1029/2003JB002432.

Gubbins D, Alfé D, Masters G, Price GD, and Gillan M (2004) Gross thermodynamics of two-component core convection. *Geophysical Journal International* 157: 1407–1414.

Gubbins D and Davies CJ (2013) The stratified layer at the core–mantle boundary caused by barodiffusion of oxygen, sulphur and silicon. *Physics of the Earth and Planetary Interiors* 215: 21–28.

Gubbins D and Roberts PH (1987) Magnetohydrodynamics of the Earth's core. In: Jacobs JA (ed.). *Geomagnetism*, vol. 2, pp. 1–183. New York: Academic Press.

Helffrich G and Kaneshima S (2010) Outer-core compositional stratification from observed core wave speed profiles. *Nature* 468: 807–810. http://dx.doi.org/10.1038/nature09636.

Hide R (1966) Free hydromagnetic oscillations of the Earth's core and the theory of the geomagnetic secular variation. *Philosophical Transactions of the Royal Society of London, Series A* 259: 615–647.

Jackson A (2003) Intense equatorial flux spots on the surface of the Earth's core. *Nature* 424: 760–763.

Jackson A, Bloxham J, and Gubbins D (1993) Time-dependent flow at the core surface and conservation of angular momentum in the coupled core–mantle system. In: Le Mouël J-L, Smylie DE, and Herring T (eds.) *Dynamics of Earth's Deep Interior and Earth Rotation*, pp. 97–107. American Geophysical Union.

Jackson A, Jonkers A, and Walker M (2000) Four centuries of geomagnetic secular variation from historical records. *Philosophical Transactions of the Royal Society of London, Series A* 358: 957–990.

Jault D (2003) Electromagnetic and topographic coupling, and LOD variations. In: Jones CA, Soward AM, and Zhang K (eds.) *Earth's Core and Lower Mantle*, pp. 55–76. Boca Raton, FL: CRC Press.

Jault D (2008) Axial invariance of rapidly varying diffusionless motions in the Earth's core interior. *Physics of the Earth and Planetary Interiors* 166: 67–76.

Jault D, Gire C, and Le Mouël J-L (1988) Westward drift, core motions and exchanges of angular momentum between core and mantle. *Nature* 333: 353–356.

Jault D and Légaut G (2005) Alfvén waves within the Earth's core. In: Soward AM, Jones CA, Hughes DW, and Weiss NO (eds.) *Fluid Dynamics and Dynamos in Astrophysics and Geophysics*, pp. 277–293. Boca Raton, FL: CRC Press.

Julien K, Knobloch E, Milliff R, and Werne J (2006) Generalized quasi-geostrophy for spatially anisotropic rotationally constrained flows. *Journal of Fluid Mechanics* 555: 233–274.

Koelemeijer PJ, Deuss A, and Trampert J (2012) Normal mode sensitivity to Earth's D″ layer and topography on the core–mantle boundary: What we can and cannot see. *Geophysical Journal International* 190: 553–568.

de Koker N, Steinle-Neumann G, and Vlček V (2012) Electrical resistivity and thermal conductivity of liquid Fe alloys at high P and T, and heat flux in Earth's core. *Proceedings of the National Academy of Sciences* 109: 4070–4073.

Koper KD, Pyle ML, and Franks JM (2003) Constraints on aspherical core structure from PKiKP-PcP differential travel times. *Journal of Geophysical Research* 108: 2168. http://dx.doi.org/10.1029/2002JB001995.

Kudlick MD (1966) *On Transient Motions in a Contained Rotating Fluid*. Ph.D. Thesis, Massachussets Institute of Technology, Mathematical Department.

Kuvshinov A (2012) Deep electromagnetic studies from land, sea, and space: Progress status in the past 10 years. *Surveys in Geophysics* 33: 169–209.

Labrosse S, Poirier J-P, and Le Mouël J-L (2001) The age of the inner core. *Earth and Planetary Science Letters* 190: 111–123.

Lassak T, McNamara A, Garnero E, and Zhong S (2010) Core–mantle boundary topography as a possible constraint on lower mantle chemistry and dynamics. *Earth and Planetary Science Letters* 289: 232–241.

Lay T and Garnero E (2011) Deep mantle seismic modeling and imaging. *Annual Review of Earth and Planetary Sciences* 39: 91–123.

Lehnert B (1954) Magnetohydrodynamic waves under the action of the coriolis force. *The Astrophysical Journal* 119: 647–654.

Mandea Alexandrescu M, Gibert D, Le Mouël J-L, Hulot G, and Saracco G (1999) An estimate of average lower mantle conductivity by wavelet analysis of geomagnetic jerks. *Journal of Geophysical Research* 104: 17735–17745.

Mathews PM, Buffett BA, Herring TA, and Shapiro II (1991) Forced nutations of the Earth: Influence of inner core dynamics: 2. Numerical results and comparisons. *Journal of Geophysical Research* 96: 8243–8257.

Mathews PM, Herring TA, and Buffett BA (2002) Modeling of nutation and precession: New nutation series for nonrigid Earth and insights into the Earth's interior. *Journal of Geophysical Research* 107: 2068. http://dx.doi.org/10.1029/2001JB000390.

Mizzon H and Monnereau M (2013) Implication of the lopsided growth for the viscosity of Earth's inner core. *Earth and Planetary Science Letters* 361: 391–401.

Moffatt K and Loper DE (1994) The magnetostrophic rise of a buoyant parcel in the Earth's core. *Geophysical Journal International* 117: 394–402.

Monnereau M, Calvet M, Margerin L, and Souriau A (2010) Lopsided growth of Earth's inner core. *Science* 328: 1014–1017.

Morse PM and Feshbach H (1953) *Methods of Theoretical Physics*. Part I, New York: McGraw-Hill.

Mound JE and Buffett BA (2005) Mechanisms of core–mantle angular momentum exchange and the observed spectral properties of torsional oscillations. *Journal of Geophysical Research* 110: B08103. http://dx.doi.org/10.1029/2004JB003555.

Mound JE and Buffett BA (2006) Detection of a gravitational oscillation in length-of-day. *Earth and Planetary Science Letters* 243: 383–389.

Nagao H, Iyemori T, Higuchi T, and Araki T (2003) Lower mantle conductivity anomalies estimated from geomagnetic jerks. *Journal of Geophysical Research* 108. http://dx.doi.org/10.1029/2002JB001786.

Ohta K, Cohen RE, Hirose K, Haule K, Shimizu K, and Ohishi Y (2012) Experimental and theoretical evidence for pressure-induced metallization in FeO with rocksalt-type structure. *Physical Review Letters* 108: 026403.

Pais MA and Jault D (2008) Quasi-geostrophic flows responsible for the secular variation of the Earth's magnetic field. *Geophysical Journal International* 173: 421–443.

Pinheiro K and Jackson A (2008) Can a 1-D mantle electrical conductivity model generate magnetic jerk differential time delays? *Geophysical Journal International* 173: 781–792.

Plaut E and Busse FH (2002) Low-Prandtl-number convection in a rotating cylindrical annulus. *Journal of Fluid Mechanics* 464: 345–363.

Poirier J-P and Tarantola A (1998) A logarithmic equation of state. *Physics of the Earth and Planetary Interiors* 109: 1–8.

Pozzo M, Davies C, Gubbins D, and Alfè D (2012) Thermal and electrical conductivity of iron at Earth's core conditions. *Nature* 485: 355–358. http://dx.doi.org/10.1038/nature11031.

Pozzo M, Davies C, Gubbins D, and Alfè D (2013) Transport properties for liquid silicon–oxygen–iron mixtures at Earth's core conditions. *Physical Review B* 87: 014110.

Rieutord M and Dintrans B (2002) More concerning the anelastic and subseismic approximations for low-frequency modes in stars. *Monthly Notices of the Royal Astronomical Society* 337: 1087–1090.

Rieutord M, Georgeot B, and Valdetarro L (2001) Inertial waves in a rotating spherical shell: Attractors and asymptotic spectrum. *Journal of Fluid Mechanics* 435: 103–144.

Roberts PH and Aurnou JM (2012) On the theory of core–mantle coupling. *Geophysical and Astrophysical Fluid Dynamics* 106: 157–230. http://dx.doi.org/10.1080/03091929.2011.589028.

Roberts PH and King EM (2013) On the genesis of the Earth's magnetism. *Reports on Progress in Physics* 76: 096801.

Roberts PH and Scott S (1965) On analysis of the secular variation 1. A hydrodynamic constraint: Theory. *Journal of Geomagnetism and Geoelectricity* 17: 137–151.

Roberts PH and Soward AM (1972) Magnetohydrodynamics of the Earth's core. *Annual Review of Fluid Mechanics* 4: 117–154.

Roberts PH, Yu ZJ, and Russell CT (2007) On the 60-year signal from the core. *Geophysical and Astrophysical Fluid Dynamics* 101: 11–35.

Schaeffer N and Cardin Ph (2005) Quasi-geostrophic model of the instabilities of the Stewartson layer in flat and depth-varying containers. *Physics of Fluids* 17: 104111.

Schaeffer N, Jault D, Cardin Ph, and Drouard M (2012) On the reflection of Alfvén waves and its implication for Earth's core modelling. *Geophysical Journal International* 191: 508–516.

Silva L, Jackson L, and Mound J (2012) Assessing the importance and expression of the 6 year geomagnetic oscillation. *Journal of Geophysical Research* 117: B10101, http://dx.doi.org/10.1029/2012JB009405.

Simmons NA, Forte AM, Boschi L, and Grand SP (2010) Gypsum: A joint tomographic model of mantle density and seismic wave speeds. *Journal of Geophysical Research* 115: B12310. http://dx.doi.org/10.1029/2010JB007631.

Smylie DE, Szeto AMK, and Rochester MG (1984) The dynamics of the Earth's inner and outer cores. *Reports on Progress in Physics* 47: 855–906.

Soldati G, Boschi L, and Forte AM (2012) Tomography of core–mantle boundary and lowermost mantle coupled by geodynamics. *Geophysical Journal International* 189: 730–746.

Soward AM and Roberts PH (2007) Taylor's constraint. In: Dormy E and Soward AM (eds.) *Mathematical Aspects of Natural Dynamos*, pp. 419–424. Boca Raton, FL: CRC Press.

Staplehurst PJ, Davidson PA, and Dalziel SB (2008) Structure formation in homogeneous freely decaying rotating turbulence. *Journal of Fluid Mechanics* 598: 81–105.

Stewartson K (1957) The dispersion of a current on the surface of a highly conducting fluid. *Mathematical Proceedings of the Cambridge Philosophical Society* 53: 774–775.

Sun D, Helmberger DV, Jackson JM, Clayton RW, and Bower DJ (2013) Rolling hills on the core–mantle boundary. *Earth and Planetary Science Letters* 361: 333–342.

Sze EKM and van der Hilst RD (2003) Core mantle boundary topography from short period PcP, PKP, and PKKP data. *Physics of the Earth and Planetary Interiors* 135: 27–46.

Takehiro S and Lister JR (2001) Penetration of columnar convection into an outer stably stratified layer in rapidly rotating spherical fluid shells. *Earth and Planetary Sciences Letters* 187: 357–366.

Taylor GI (1923) Experiments on the motion of solid bodies in rotating fluids. *Proceedings of the Royal Society of London A* 104: 213–218.

Taylor JB (1963) The magneto-hydrodynamics of a rotating fluid and the Earth's dynamo problem. *Proceedings of the Royal Society of London* A274: 274–283.

Tobias S, Hughes DW, and Diamond PH (2007) β-Plane magnetohydrodynamic turbulence in the solar tachocline. *The Astrophysical Journal* 667: L113–L116.

Tsuno K, Frost DJ, and Rubie DC (2013) Simultaneous partitioning of silicon and oxygen into the Earth's core during early Earth differentiation. *Geophysical Research Letters* 40: 66–71. http://dx.doi.org/10.1029/2012GL054116.

Vallis GK (2006) *Atmospheric and Oceanic Fluid Dynamics: Fundamentals and Large-Scale Circulation*. Cambridge: Cambridge University Press.

Yoshida M (2008) Core–mantle boundary topography estimated from numerical simulations of instantaneous mantle flow. *Geochemistry, Geophysics, Geosystems* 9: Q07002. http://dx.doi.org/10.1029/2008GC002008.

Zatman S and Bloxham J (1997) Torsional oscillations and the magnetic field within the Earth's core. *Nature* 388: 760–763.

Zhang K, Earnshaw P, Liao X, and Busse FH (2001) On inertial waves in a rotating fluid sphere. *Journal of Fluid Mechanics* 437: 103–119.

8.10 Numerical Dynamo Simulations

UR Christensen and J Wicht, Max-Planck-Institut für Sonnensystemforschung, Göttingen, Germany

© 2015 Elsevier B.V. All rights reserved.

8.10.1	**Introduction**	245
8.10.2	**Basic Formulation of the Magnetohydrodynamic Dynamo Problem**	246
8.10.2.1	Fundamental Ingredients	246
8.10.2.2	Basic Equations and Nondimensional Parameters	247
8.10.2.3	Boundary Conditions and Treatment of Inner Core	248
8.10.2.3.1	Mechanical conditions	248
8.10.2.3.2	Magnetic boundary conditions and inner core conductivity	249
8.10.2.3.3	Thermal boundary conditions and distribution of buoyancy sources	249
8.10.2.4	Miscellaneous Modifications	250
8.10.2.4.1	Modified inertial terms	250
8.10.2.4.2	Compressible models	250
8.10.2.4.3	Dynamos in Cartesian geometry	250
8.10.3	**Numerical Approaches**	250
8.10.3.1	Spectral Methods	250
8.10.3.1.1	Poloidal–toroidal decomposition	251
8.10.3.1.2	Spherical harmonic representation	251
8.10.3.1.3	Radial representation	251
8.10.3.1.4	Spectral equations	252
8.10.3.1.5	Time integration	253
8.10.3.1.6	Evaluation of nonlinear terms	254
8.10.3.1.7	Boundary conditions and inner core	254
8.10.3.1.8	Numerical truncation, hyperdiffusion, and subgrid-scale models	255
8.10.3.2	Local Methods	256
8.10.4	**Model Results**	257
8.10.4.1	Fundamental Aspects	257
8.10.4.1.1	General properties of standard models with dipolar magnetic field	257
8.10.4.1.2	Variations and nondipolar dynamos	259
8.10.4.1.3	Mechanism of magnetic field generation	262
8.10.4.1.4	Taylor state and torsional oscillations	263
8.10.4.1.5	Scaling laws for dynamos	264
8.10.4.2	Comparison with the Geomagnetic Field	266
8.10.4.2.1	Core–mantle boundary field morphology	266
8.10.4.2.2	Magnetic power spectra	268
8.10.4.2.3	Time variability	269
8.10.4.2.4	Comparison with the paleomagnetic field	270
8.10.4.2.5	Mantle influence	271
8.10.5	**Perspectives**	272
References		273

8.10.1 Introduction

It is believed that the Earth's magnetic field is generated by a self-sustained homogeneous dynamo operating in the liquid part of the Earth's iron core. Thermal and compositional buoyancy forces drive a convective circulation of the electrically conducting fluid. Assuming that a magnetic field already exists, electrical currents are induced in the moving fluid. When the magnetic field associated with these currents has the strength and geometry suitable for the induction process so that there is no further need for a field of external origin, we speak of a self-sustained dynamo. Technical dynamos in cars or power plants are self-sustained but rely for their operation on the guiding of the electrical currents by the complex arrangements of wires. In contrast, the geodynamo operates in a sphere whose conductivity is approximately uniform. In the decades from 1950 to 1990, dynamo theory has shown that homogeneous dynamo action is possible in principle and has elucidated the basic requirements (see **Chapter 8.03**). However, models that reproduce the detailed properties of the geomagnetic field had to wait until the numerical simulation of magnetohydrodynamic (MHD) flow has become mature enough.

While earlier models had shown that three-dimensional self-consistent geodynamo simulations are possible in principle, the year 1995 brought a final breakthrough. Glatzmaier and Roberts (1995a,b) and Kageyama and Sato (1995) showed

 http://dx.doi.org/10.1016/B978-0-444-53802-4.00145-7

that such models can indeed explain several properties of the geomagnetic field, including reversals. Since then, a large number of dynamo models have been published. In many of them, the magnetic field properties closely match those of the geomagnetic field in terms of spatial spectra and magnetic field morphology, secular variation, and sometimes the characteristics of dipole reversals. Scientists progressively use dynamo models as a tool to explain specific properties of the geomagnetic field even though some conditions in the models differ strongly from those in the Earth's core. All models assume a far too large viscosity in order to suppress small-scale turbulence that cannot be resolved with the available computational means. On the other hand, the magnetic Reynolds number, Rm, which describes the ratio of advection of magnetic field to magnetic diffusion, is only of order 10^3 in the geodynamo. This value is moderate in comparison with that for dynamos in other astrophysical systems and is accessible to direct numerical simulation. The ability to run numerical models at the correct value of the magnetic Reynolds number is probably the key for the success of geodynamo modeling. Whether the suppression of small flow scales seriously corrupts the essential physics of the dynamo process remains an open question.

In this chapter, we review the progress in geodynamo modeling since 1995. Earlier reviews addressing numerical dynamo simulations have been given by Kono and Roberts (2002), Glatzmaier (2002), Wicht and Tilgner (2010), Jones (2011), and Christensen (2011). They usually concentrated on specific aspects of dynamo modeling, such as the comparison with geomagnetic field properties, the fundamental physical processes operating in dynamos, and the approximations and limitations of present models and the prospects to overcome them in the future. Here, we try to give a fairly complete account on the results of dynamo modeling with regard to all these issues. We will assume that the reader is familiar with the basic concepts of MHDs, rotating fluids, and dynamo theory, which are discussed in earlier chapters (see **Chapters 8.05** and **8.03**) and in some of the review papers mentioned in the preceding text.

We restrict the discussion to direct numerical simulations of the full MHD dynamo problem. In this case, the coupled equations of magnetic induction and of flow of a conducting fluid influenced by the electromagnetic Lorentz force are solved. Aside from the MHD dynamo models, there are several simpler approaches to the dynamo problem that have been extensively studied in the past but that received less attention for geodynamo applications after reliable solutions to the full dynamo problem have become available. We briefly mention the concepts of kinematic dynamo models, mean-field theory, and magnetoconvection without discussing the results in detail. In the kinematic dynamo problem, the fluid flow is analytically prescribed and unaffected by the magnetic field. Kinematic dynamos (see **Chapter 8.03**, Section 8.03.3) have played an important role for establishing that spherical homogeneous dynamos are possible. More recently, they are only occasionally studied in the context of the geodynamo (e.g., Gubbins, 2008). The so-called mean-field dynamo models (see **Chapter 8.03**, Section 8.03.5) are based on a separation of scales, for both the flow $\mathbf{u}$ and the magnetic field $\mathbf{B}$. The interaction of small unresolved scales of $\mathbf{u}$ and $\mathbf{B}$ plays an important role for generating a large-scale magnetic field. Since the details of the small-scale turbulence are poorly known, simple parameterizations are employed to describe this induction process. Today, the main application of mean-field dynamo modeling is in astrophysics, where the magnetic Reynolds number is very large. We will address it in so far as it provides a context for understanding magnetic field generation mechanisms in MHD models. The term magnetoconvection (see **Chapter 8.05**, Section 8.05.5) describes a system that is governed by the full set of MHD equations for a convection-driven flow. However, the magnetic field is not self-sustained but is imposed by boundary conditions, although it can be modified by the flow. Magnetoconvection modeling is employed to understand how electromagnetic forces affect the flow in cases where the magnetic field cannot be expected to be self-sustained or where a specific configuration of the magnetic field is desired.

In **Section 8.10.2**, we present the fundamental MHD equations in a simple but probably adequate form for modeling the geodynamo. We proceed to describe the various modifications of the basic equations and their boundary conditions that have been employed by different authors. In **Section 8.10.3**, we discuss numerical schemes for solving the MHD equations in a sphere. Readers less interested in the technical aspects of dynamo modeling can skip this section. Most modelers have used some variant of a spectral transform method, in which the variables are expanded in spherical harmonic functions in the angular variables. Nonlinear terms in the equations are calculated on grid points, which require repeated transformations between the spectral representation and the grid representation. Other numerical methods based on a purely local description are slowly emerging. In the main part of this chapter, we try to give a rather complete review of the modeling results obtained since 1995. **Section 8.10.4** consists of two main parts. First, we discuss the more fundamental questions addressed in geodynamo simulations, such as the mechanism of magnetic field generation and the influence of the various nondimensional model parameters. In the second part, we discuss models geared to explain different properties of the geomagnetic field. In **Section 8.10.5**, we end the discussion by trying to give a perspective of how dynamo modeling may develop in the foreseeable future.

8.10.2 Basic Formulation of the Magnetohydrodynamic Dynamo Problem

8.10.2.1 Fundamental Ingredients

There is a general consensus that a successful self-consistent model of the geodynamo requires several basic ingredients. (1) A plausible mechanism for driving the flow of an electrically conducting fluid must be part of the model. In almost all published models, this is assumed to be thermal and/or compositional convection (but see Tilgner (2005) and **Chapter 8.07**, Section 8.07.5, for dynamo models driven by precession). (2) Cowling's theorem (see **Chapter 8.03**, Section 8.03.3.5) prohibits simplified two-dimensional solutions to the dynamo problem; hence, the fluid flow and the magnetic field must be modeled in three dimensions. Spherical geometry is essential to reproduce the global, dipole-dominated magnetic field of the Earth. (3) The model system must be rotating because Coriolis forces are essential for structuring the flow in a

way that is conducive for dynamo action and the emergence of a dipole-dominated magnetic field.

Other properties of the Earth's core are usually assumed not to play a primary role. In most models, the effects of compressibility on the density and the radial thermal structure of the core are ignored. Instead, the Boussinesq approximation is applied, in which density changes due to temperature or compositional variations enter only through a buoyancy term in the Navier–Stokes equation (see **Chapter 8.05**, Section 8.05.2.5). In this respect, models for the geodynamo differ strongly from dynamo models for gas planets or stars. All material properties are taken to be constant. Most models consider a rotating fluid shell bounded at the inner radius r_i and outer radius r_o (see **Figure 1**). The region outside the shell (the mantle) is usually assumed to be insulating, while the solid inner core is modeled as an electrical conductor with the same conductivity as the outer core. However, in many simple models, the inner core has been treated as an insulator.

One of the simplest dynamo models that can be constructed along these lines has been used to define a benchmark for numerical codes (Christensen et al., 2001). In the following section, we will use the setup and the definitions of the benchmark dynamo as starting point. We will then proceed to discuss various modifications used in other dynamo models.

8.10.2.2 Basic Equations and Nondimensional Parameters

Following the considerations mentioned earlier, the standard set of equations consists of the Navier–Stokes equation, including the Coriolis and Lorentz force terms; the condition that the velocity field $\mathbf{u}$ is divergence-free; a transport equation for temperature T or composition; and the induction equation for the magnetic field $\mathbf{B}$. The latter results from Maxwell's equations, ignoring displacement currents, and Ohm's law. The physical background of these equations is discussed, for example, in Gubbins and Roberts (1987), Braginsky and Roberts (1995), or **Chapter 8.05**, Section 8.05.2. The equations must be complemented by appropriate boundary conditions. A simple choice is that $\mathbf{u}$ vanishes on the boundaries (impenetrable no-slip boundaries); T is fixed on the outer boundary and inner boundary to T_o and $T_o + \Delta T$, respectively; and $\mathbf{B}$ matches appropriate fields for $r < r_i$ and $r > r_o$. These external fields must have a form that excludes sources outside the dynamo region (see **Chapter 8.03**, Section 8.03.3.1).

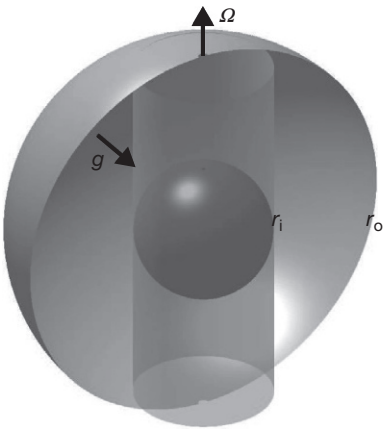

Figure 1 Basic geometry for a dynamo operating in a fluid shell rotating with angular frequency Ω. The inner core tangent cylinder is shown by the transparent surface.

Most modelers treat the equations in nondimensional form, with some notable exceptions where physical variables are used (Glatzmaier and Roberts, 1995a,b, 1997). However, there is no unique or generally accepted way to scale the equations. As a consequence, different sets of nondimensional control parameters are employed. For convection-driven dynamos, there are basically four independent control parameters. In the definition of the dynamo benchmark study, the fundamental length scale is the thickness $D = r_o - r_i$ of the spherical shell, time t is scaled by the viscous diffusion time D^2/ν with ν the kinematic viscosity, temperature is scaled by ΔT, and magnetic induction is scaled by $(\rho\mu\lambda\Omega)^{1/2}$ with ρ the density, μ the magnetic permeability, λ the magnetic diffusivity, and Ω the rotation rate. This leads to the following set of nondimensional equations:

$$E\left(\frac{\partial \mathbf{u}}{\partial t} + \mathbf{u}\cdot\nabla\mathbf{u}\right) + 2\hat{\mathbf{z}}\times\mathbf{u} + \nabla\Pi = E\nabla^2\mathbf{u} + \mathrm{Ra}\frac{r}{r_o}T + \frac{1}{Pm}(\nabla\times\mathbf{B})\times\mathbf{B} \quad [1]$$

$$\frac{\partial \mathbf{B}}{\partial t} - \nabla\times(\mathbf{u}\times\mathbf{B}) = \frac{1}{Pm}\nabla^2\mathbf{B} \quad [2]$$

$$\frac{\partial T}{\partial t} + \mathbf{u}\cdot\nabla T = \frac{1}{Pr}\nabla^2 T + \varepsilon \quad [3]$$

$$\nabla\cdot\mathbf{u} = 0, \quad \nabla\cdot\mathbf{B} = 0 \quad [4]$$

The unit vector $\hat{\mathbf{z}}$ indicates the direction of the rotation axis. We assume that gravity is a linear function of radius, $g(r) = g_o r/r_o$, where g_o is the value on the outer boundary. Π is the nonhydrostatic pressure and ε the volumetric heating rate. The four nondimensional control parameters are the Ekman number

$$E = \frac{\nu}{\Omega D^2} \quad [5]$$

a modified Rayleigh number

$$Ra = \frac{\alpha g_o \Delta T D}{\nu\Omega} \quad [6]$$

the Prandtl number

$$Pr = \frac{\nu}{\kappa} \quad [7]$$

and the magnetic Prandtl number

$$Pm = \frac{\nu}{\lambda} \quad [8]$$

Here, κ is the thermal diffusivity and α is the thermal expansivity.

Variants of the nondimensional equations and control parameters result from different choices for the fundamental scales. For the length scale, often, r_o is chosen instead of D. Other natural scales for time are the magnetic or the thermal diffusion time and the rotation period. There are also different options for scaling the magnetic field strength. The prefactor of two, which is retained in the Coriolis term in eqn [1], is often incorporated into the definition of the Ekman number. When the thermal boundary condition is in terms of a specified heat flux F instead of a fixed temperature contrast, temperatures can

be scaled by $F/(kD)$, with thermal conductivity k, and by replacing ΔT in eqn [6] with this expression, a flux-based Rayleigh number is obtained. The conventional Rayleigh number for a fixed temperature contrast

$$R = \frac{\alpha g_o \Delta T D^3}{\kappa \nu} \qquad [9]$$

is related to the modified Rayleigh number used here by $Ra = \mathrm{RE}/Pr$. Although the control parameters and the place where they appear in the nondimensional equations differ for the various ways of scaling, they can usually be written as simple combinations of the four parameters that have been introduced earlier. The conversion between different forms of the control parameters can involve complicated numerical factors (Kono and Roberts, 2002).

Characteristic properties of the solution are usually expressed in terms of nondimensional diagnostic parameters. In the context of the geodynamo, the two most important ones are the magnetic Reynolds number Rm and the Elsasser number Λ. Usually, the rms values of the velocity u_{rms} and of the magnetic field B_{rms} inside the spherical shell are taken as characteristic values. The magnetic Reynolds number

$$Rm = \frac{u_{\mathrm{rms}} D}{\lambda} \qquad [10]$$

can be considered as a measure for the flow velocity and describes the ratio of advection of the magnetic field to magnetic diffusion. Other characteristic nondimensional numbers related to the flow velocity are the (hydrodynamic) Reynolds number

$$Re = \frac{u_{\mathrm{rms}} D}{\nu} \qquad [11]$$

which measures the ratio of inertial forces to viscous forces, and the Rossby number

$$\mathrm{Ro} = \frac{u_{\mathrm{rms}}}{\Omega D} \qquad [12]$$

a measure for the ratio of inertial to Coriolis forces. The Elsasser number

$$\Lambda = \frac{B_{\mathrm{rms}}^2}{\mu_o \lambda \rho \Omega} \qquad [13]$$

measures the ratio of Lorentz to Coriolis forces and is equivalent to the square of the nondimensional magnetic field strength in the scaling chosen here.

Typical values for the control parameters and the nondimensional numbers characterizing the flow and magnetic field in the Earth's core and in dynamo simulations with a dipole-dominated field are listed in Table 1. Here, the Rayleigh number is normalized by its critical value Ra_c for the onset of convection without a magnetic field. The distinction between weakly and strongly driven models is discussed in Section 8.10.4.1.1; the differences between them go beyond the choice of the Rayleigh number.

8.10.2.3 Boundary Conditions and Treatment of Inner Core

8.10.2.3.1 Mechanical conditions

In the simplest model, the fluid shell is treated as a container with rigid, impenetrable, and corotating walls. This implies that within the rotating frame of reference, all velocity components vanish at r_o and r_i. Kuang and Bloxham (1997) argued that, because the Ekman number has a far larger value in the model than it has in the core, the no-slip boundary leads to excessively large Ekman-layer effects, and they suggested that it is preferable to eliminate the viscous Ekman layer entirely. Hence, they replaced the condition of zero horizontal velocity by one of the vanishing viscous shear stresses (free-slip condition). The influence of mechanical boundary conditions is discussed in Section 8.10.4.1.2.

There is no a priori reason why the inner core should corotate with the mantle. Some models allow for differential rotation of the inner core and mantle with respect to the reference frame (e.g., Glatzmaier and Roberts, 1995a, 1996b; Kuang and Bloxham, 1997). The change of rotation rate is determined from the net torque. Viscous and electromagnetic torques and torques due to gravitational coupling between density heterogeneities in the mantle and in the inner core contribute (see Section 8.10.3.1.7). Neglecting the gravitational torque, Glatzmaier and Roberts (1996b) found that the inner core rotates with a few degrees per year by coupling to a mean prograde (eastward) flow near the inner core boundary. Following this modeling result, seismic evidence for differential

Table 1 Order of magnitude of parameters in the core and in dynamo models

	Control parameters			
	Ra/Ra_c	E	Pm	Pr
Core	$\gg 1$	$10^{-15}-10^{-14}$	$10^{-6}-10^{-5}$	$0.1-1$
Weakly driven models	$1-10$	$>10^{-4}$	>1	1
Strongly driven models	$10-100$	$10^{-6}-10^{-4}$	$10^{-1}-10^{3}$	$0.025-10^{3}$
	Diagnostic parameters			
	Rm	Re	Ro	Λ
Core	10^3	10^8-10^9	$\approx 10^{-7}$	$0.1-10$
Weakly driven models	$40-100$	<30	$10^{-2}-10^{-1}$	$0.3-10$
Strongly driven models	10^2-10^3	<2000	$3\times10^{-4}-10^{-2}$	$0.1-100$

rotation of similar order had been claimed, but later seismological studies concluded that differential rotation rates are much smaller (e.g., Mäkinen and Deuss, 2011; Zhang et al., 2005). Subsequent dynamo simulations also showed smaller values of inner core rotation, in particular when gravitational coupling of the mantle and inner core was taken into account (Buffett and Glatzmaier, 2001). Aubert and Dumberry (2011) studied in dynamo models the parameter dependence of inner core differential rotation and concluded that its steady part becomes very small for an Earth-like value of the Ekman number, whereas superimposed oscillatory fluctuations can lead to larger instantaneous rotation rates.

8.10.2.3.2 Magnetic boundary conditions and inner core conductivity

When assuming an electrically insulating mantle and inner core, the magnetic field inside the fluid shell matches continuously to a potential field in both the exterior and the interior regions. When a spectral numerical method based on spherical harmonic functions is adopted, these conditions are easy to satisfy (**Section 8.10.3.1.7**). This is not the case when local numerical methods are used (**Section 8.10.3.2**). In several of these models, a condition of vanishing horizontal magnetic field components has been used (Harder and Hansen, 2005; Kageyama and Sato, 1995, 1997a; Li et al., 2002). Allowing only for a nonzero radial field component at the boundary (sometimes called the 'quasivacuum condition') has no physical foundation. However, the solution obtained with this condition seems qualitatively similar to that obtained with the appropriate condition for a truly insulating exterior region (Harder and Hansen, 2005). The quasivacuum condition may therefore be acceptable as a numerical convenience in studies where details of the external field structure are of no interest.

Treating the inner core as an insulator is obviously not realistic either, and in a number of models, it has the same electrical conductivity as the fluid shell. In this case, an equation equivalent to eqn [2] must be solved for the inner core, where the velocity field simply describes the solid-body rotation of the inner core with respect to the reference frame. At the inner core boundary, a continuity condition for the magnetic field and the horizontal component of the electric field apply. Results from a simplified mean-field dynamo model (Hollerbach and Jones, 1993) suggested that the finite conductivity of the inner core plays an essential role for stabilizing the dipole polarity of the dynamo field, which would reverse far more frequently in the absence of a conducting inner core. In a suite of magnetohydrodynamic models including some in which the dipole field reverses, Wicht (2002) found only minor differences between cases with insulating and with conducting inner core when everything else was equal. In contrast, Dharmaraj and Stanley (2012) reported that inner core conductivity strengthens the dipole dominance and reduces the number of reversals in their model. They attributed the difference to the results by Wicht (2002) mainly to their use of fixed heat flux instead of fixed temperatures in the thermal boundary condition.

In some models (Glatzmaier and Roberts, 1995a; Kuang and Bloxham, 1999), the mantle is not treated as an insulator, but a thin layer of moderate conductivity is assumed at its bottom. The main purpose is to allow for mechanical coupling of the mantle and the fluid core by electromagnetic torques. The effects of the conducting layer on the dynamo process itself have not been studied systematically, but are presumably small.

8.10.2.3.3 Thermal boundary conditions and distribution of buoyancy sources

In the present Earth, convection is thought to be driven by a combination of thermal and compositional buoyancy, the latter arising from the release of the light alloying element(s) upon solidification of the inner core (Lister and Buffett, 1995; Loper, 1978) (see also **Chapter 8.02**). Sources of heat are the release of latent heat of inner core solidification and the secular cooling of the outer and inner core, which can effectively be treated like a heat source. Experimental evidence for the possible presence of radioactive elements in the core, such as potassium, is controversial (Corgne et al., 2007; Rama Murthy et al., 2003). The heat loss from the core is controlled by the convecting mantle, which effectively imposes a condition of fixed heat flux at the core–mantle boundary on the dynamo. The heat flux is spatially and temporally variable. The timescale is that of mantle convection, which is several tens to a hundred million years, hence much longer than relevant timescales for the dynamo process. Therefore, in geodynamo models, the temporal variation is generally ignored (except in Driscoll and Olson, 2009b), but in several models, the spatial variability is accounted for (see **Section 8.10.4.2.5**).

In many geodynamo models, convection is driven by an imposed fixed temperature contrast between the inner and the outer boundaries, setting $\varepsilon = 0$ in eqn [3]. This condition has been used for simplicity and has no physical basis, but it had been assumed that the nature of the thermal boundary condition has little influence on the dynamo. However, work by Sakuraba and Roberts (2009) and Hori et al. (2010, 2012) showed that it can have a strong effect on the scale of the flow and the geometry of the magnetic field (see **Section 8.10.4.1.2**). The physically appropriate form of boundary condition for the inner boundary is less clear than it is for the outer boundary. A possible translational motion of the inner core may lead to hemispheric melting of iron and the formation of a stably stratified layer surrounding the inner core (e.g., Alboussiere et al., 2010). Such complexities have not yet been studied in dynamo models.

The rate of inner core growth and the associated compositional flux from the inner core boundary depend directly on the heat loss to the mantle (Lister and Buffett, 1995). The distinction between compositional buoyancy and thermal buoyancy becomes dynamically important when the respective diffusivities differ (double-diffusive convection). Double diffusive dynamos have been studied numerically in the context of Mercury's core under the assumption of a stabilizing thermal gradient and a destabilizing compositional gradient (Manglik et al., 2010). When both gradients are unstable, as is probably the case in the Earth's core, usually the effective (turbulent) diffusivities are assumed to be similar. For equal values of the diffusivities, the light element concentration and the temperature, weighted with their contributions to the buoyancy force, can be combined into a single variable, which is sometimes termed 'codensity.' It satisfies an equation that is formally

equivalent to eqn [3] (Braginsky and Roberts, 1995; Davies and Gubbins, 2011; Kutzner and Christensen, 2004). Hence, there is no fundamental distinction between compositional convection and thermal convection. The governing equations are often written in terms of temperature, but with the understanding that compositional convection is also implied. The main distinction lies in the distribution of sources and sinks of the buoyant agent. For pure thermal convection powered by secular cooling and radiogenic heat, the sources are volumetrically distributed, and the core–mantle boundary represents the sink. In the case of pure compositional convection, the inner core boundary is the source, and the sink is distributed throughout the outer core (negative ε in eqn [3], representing the homogeneous mixing of the excess concentration of light element into the fluid body), with a zero flux condition on the outer boundary. The general case of thermocompositional convection with a given distribution of internal and bottom driving is obtained by setting the inner boundary flux, the outer boundary flux, and ε to appropriate values (e.g., Aubert et al., 2009). The influence of the mode of driving convection on the magnetic field is discussed in **Section 8.10.4.1.2**.

8.10.2.4 Miscellaneous Modifications

8.10.2.4.1 Modified inertial terms

In some models, the inertial term in eqn [1] has been neglected (Glatzmaier and Roberts, 1995a,b) or has been treated in a simplified way by retaining only its axisymmetric component (Glatzmaier and Roberts, 1996a; Kuang and Bloxham, 1997, 1999). The reason for ignoring inertial forces is, aside from the simplification, that they are considered to be much smaller in the Earth's core than the dominant Coriolis and Lorentz forces. The rationale for retaining axisymmetric inertial terms is that for differential motion of cylinders coaxial to the rotation axis, inertia is believed to be the only way to balance in the Earth's core residual electromagnetic torques acting on these cylinders, which gives rise to torsional oscillations (TOs) (see **Section 8.10.4.1.4**). However, while inertial forces may perhaps play a small role under conditions of the Earth's core, it is not clear that this is also true for the nominal parameter values of the dynamo models. Unfortunately, no direct comparison of the same model with and without (full) inertial terms is available. An open question is if current dynamo models containing the (full) inertia terms give too much influence to inertia compared to the geodynamo.

8.10.2.4.2 Compressible models

While most geodynamo models assume the flow to be incompressible and employ the Boussinesq approximation, those by Glatzmaier and Roberts (1996a) (and subsequent models of these authors) take the density stratification and other non-Boussinesq effects, such as the dissipative contributions to the heat equation, into account. In these models, the anelastic approximation is used, which differs from the fully compressible formulation by suppressing sound waves. A systematic study by Gastine et al. (2012) showed that the magnetic field becomes nondipolar for density contrasts that exceed a factor of four. If the weak density stratification in the Earth's outer core by a factor of 1.2 has a significant effect is unclear, but could be possible (Evonuk and Samuel, 2012).

8.10.2.4.3 Dynamos in Cartesian geometry

Spherical geometry is essential for reproducing the appropriate topology of the magnetic field and has a strong influence on the shape of the flow. However, for plane layer geometry, more efficient numerical methods are available, which allow simulations at more realistic parameter values, for example, lower values of the Ekman number. Although the Cartesian models cannot represent direct models of the geodynamo, they allow to address fundamental questions concerning the force balance and the dynamic regime. Plane-layer dynamos have been studied by St. Pierre (1993), Rotvig and Jones (2002), Stellmach and Hansen (2004), and Cattaneo and Hughes (2006) at Ekman numbers (defined by eqn [5]) as low as 10^{-6}. Stellmach and Hansen (2004) found in their dynamos that at an Ekman number of order 10^{-4}, the presence of a magnetic field has only a weak influence on the scale of the flow. At 10^{-6}, it promotes significantly larger flow scales than those that occur for nonmagnetic convection, as expected for the so-called strong-field dynamo regime (see **Chapter 8.05**, in particular Section 8.05.5.3). Furthermore, they found a robust example for a subcritical dynamo, where the self-sustained magnetic field is necessary for convection to occur at all (see also St. Pierre, 1993). In spherical shell dynamos, these effects have not been demonstrated so far.

8.10.3 Numerical Approaches

We will focus on outlining the principles of spectral methods that have been employed for most of the dynamo simulations to date. The quest to compute at more realistic parameters values makes massive parallel computing inevitable. Several researchers have therefore developed codes based on local methods that promise a better performance on multiprocessor systems. **Section 8.10.3.2** offers a brief overview of these new developments.

8.10.3.1 Spectral Methods

Spectral approaches are well established for solving differential equations and were first applied to the dynamo problem by Bullard and Gellman (1954). The originally employed Galerkin approaches (Bullard and Gellman, 1954; Zhang and Busse, 1989, 1990) have been superseded by the more efficient pseudospectral methods. For geodynamo simulations, these have been introduced by Glatzmaier and Roberts (1995a) (based on earlier developments for modeling stellar dynamos; Glatzmaier, 1984) and have been adopted subsequently by many other dynamo modelers.

In this approach, the unknowns are expanded into complete sets of functions in radial and angular directions. Chebyshev polynomials and spherical harmonic functions are the common choice. This allows to express all partial derivatives analytically. Employing orthogonality relations of spherical harmonic functions and using collocation or finite differencing methods in radius then lead to algebraic equations that are integrated in time with a mixed implicit/explicit scheme. The nonlinear terms and the Coriolis force are evaluated in grid space rather than in spectral space. Although this approach

requires costly numerically transformations between the two representations, the resulting decoupling of all spherical harmonic modes leads to a net gain in computational speed. Before explaining these methods in more detail, we introduce the poloidal–toroidal decomposition.

8.10.3.1.1 Poloidal–toroidal decomposition

Representing the magnetic field in spherical coordinates (r, θ, ϕ) by a poloidal and a toroidal part,

$$\mathbf{B}(r,\theta,\phi) = \nabla\times\nabla[\hat{\mathbf{r}}g(r,\theta,\phi)] + \nabla[\hat{\mathbf{r}}h(r,\theta,\phi)] \qquad (14)$$

guarantees that its divergence vanishes (eqn [4]). Three unknown field components are replaced by two scalar fields, the poloidal potential g and the toroidal potential h. This decomposition is unique, aside from an arbitrary radial function $f(r)$ that can be added to g or h without affecting $\mathbf{B}$. An analogous decomposition represents the flow field $\mathbf{u}$ by poloidal and toroidal potentials v and w in the Boussinesq approximation assumed here.

The two scalar potentials of a divergence-free vector field can be extracted from the radial component and the radial component of its curl:

$$\hat{\mathbf{r}}\cdot\mathbf{B} = -\Delta_H g \qquad [15]$$

$$\hat{\mathbf{r}}\cdot(\nabla\times\mathbf{B}) = -\Delta_{\mathrm{H}} h \qquad [16]$$

The operator Δ_{H} denotes the horizontal part of the Laplacian:

$$\Delta_{\mathrm{H}} = \frac{1}{r^2\sin\theta}\frac{\partial}{\partial\theta}\sin\theta\frac{\partial}{\partial\theta} + \frac{1}{r^2\sin^2\theta}\frac{\partial^2}{\partial^2\phi} \qquad [17]$$

8.10.3.1.2 Spherical harmonic representation

Spherical harmonic functions Y_{lm} are a natural choice for the horizontal expansion in colatitude θ and longitude ϕ:

$$Y_{lm}(\theta,\phi) = P_{lm}(\cos\theta)\mathrm{e}^{im\phi} \qquad [18]$$

where l and m denote degree and order, respectively, and P_{lm} is an associated Legendre function. Different normalizations are in use. Here, we adopt a complete normalization so that the orthogonality relation reads

$$\int_0^{2\pi}\mathrm{d}\phi\int_0^{\pi}\sin\theta\mathrm{d}\theta Y_{lm}(\theta,\phi)Y_{l'm'}(\theta,\phi) = \delta_{ll'}\delta_{mm'} \qquad [19]$$

For example, the spherical harmonic representation of the magnetic poloidal potential $g(r,\theta,\phi)$, truncated at degree and order L, then reads

$$g(r,\theta,\phi) = \sum_{l=0}^{L}\sum_{m=-l}^{l} g_{lm}(r)Y_{lm}(\theta,\phi) \qquad [20]$$

with

$$g_{lm}(r) = \frac{1}{\pi}\int_0^{\pi}\mathrm{d}\theta\sin\theta g_m(r,\theta)P_{lm}(\cos\theta) \qquad [21]$$

$$g_m(r,\theta) = \frac{1}{2\pi}\int_0^{2\pi}\mathrm{d}\phi g(r,\theta,\phi)e^{-im\phi} \qquad [22]$$

The potential $g(r,\theta,\phi)$, is a real function so that $g^*_{lm}(r) = g_{l,-m}(r)$, where the asterisk denotes the complex conjugate. Thus, only coefficients with $m\geq 0$ have to be considered. The same kind of expansion is made for the toroidal magnetic potential, the velocity potentials, pressure, and temperature (or codensity).

Equations [21] and [22] define a two-step transform from the longitude/latitude representation to spherical harmonic representation $(r,\theta,\phi)\rightarrow(r,l,m)$. Equation [20] formulates the inverse procedure $(r,l,m)\rightarrow(r,\theta,\phi)$. Fast Fourier transforms can be employed in longitudinal direction, requiring (at least) $N_\phi = 2L+1$ evenly spaced grid points ϕ_i. Several authors have developed fast Legendre transforms that could be employed in latitudinal direction (Healy et al., 2004; Lesur and Gubbins, 1999; Schaeffer, 2012; Spotz and Swarztrauber, 2001). While not as efficient as FFTs, they could nevertheless help further speed up dynamo calculations, a potential that has not been explored so far. Most spectral codes to date rely on Gauss–Legendre quadrature (Abramowitz and Stegun, 1984) for evaluating integral [21]:

$$g_{lm}(r) = \frac{1}{N_\theta}\sum_{j=1}^{N_\theta} w_j g_m(r,\theta_j)P_{lm}(\cos\theta_j) \qquad [23]$$

where θ_j are the N_θ Gaussian quadrature points defining the latitude grid and w_j are the respective weights. Prestored values of the associated Legendre functions at grid points θ_j in combination with an FFT in ϕ provide the inverse transform [20] (Spotz and Swarztrauber, 2001). Generally, $N_\phi = 2N_\theta$ is taken, which provides isotropic resolution in the equatorial region (**Figure 2**). Choosing $L = [min(2N_\theta, N_\phi) - 1]/3$ prevents aliasing errors.

8.10.3.1.3 Radial representation

Different approaches have been employed for representing the radial variation of the unknowns. In some codes, a spectral representation is used only for the dependence on the angular variables, and a finite difference scheme is employed in the radial direction (e.g., Kuang and Bloxham, 1999). Here, we concentrate on schemes that also expand radial dependencies into complete sets of functions. Series of trigonometric functions (Wicht and Busse, 1997; Zhang and Busse, 1988) allow to automatically fulfill the boundary condition, but Chebyshev polynomials $C(x)$ are a more common choice. The polynomial of degree n is defined by

$$C_n(x) = \cos(n\arccos(x)), \quad -1\leq x\leq 1 \qquad [24]$$

When truncating at degree N, the radial expansion of the poloidal magnetic potential reads

$$g_{lm}(r) = \sum_{n=0}^{N} g_{lmn}C_n(r) \qquad [25]$$

with

$$g_{lmn} = \frac{2-\delta_{n0}}{\pi}\int_{-1}^{1}\frac{dx g_{lm}(r(x))C_n(x)}{\sqrt{1-x^2}} \qquad [26]$$

The Chebyshev definition space $(-1\leq x\leq 1)$ is usually mapped linearly onto radius $(r_{\mathrm{i}}\leq r\leq r_{\mathrm{o}})$ by

$$x(r) = 2\frac{r-r_{\mathrm{i}}}{r_{\mathrm{o}}-r_{\mathrm{i}}} - 1 \qquad [27]$$

Nonlinear mapping can be employed to modify the radial dependence of the grid-point density (Tilgner, 1999).

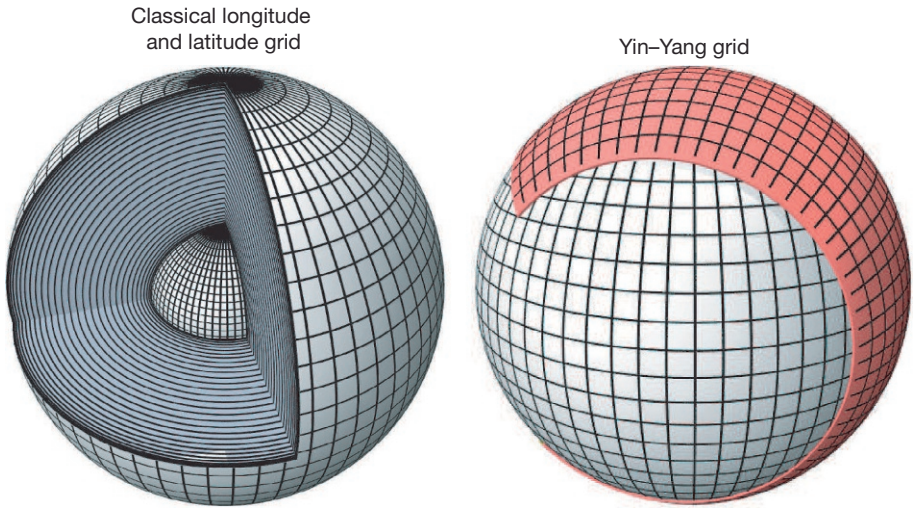

Figure 2 Comparison of the classical longitude/latitude grid and the Yin–Yang grid that has been used in conjunction with finite difference methods by Kageyama and Yoshida (2005). The latter avoids the highly inhomogeneous coverage in the polar region by reusing the low-latitude band to cover the whole spherical surface.

When choosing the N_r extrema of C_{N_r-1} as radial grid points,

$$x_k = \cos\left(\pi\frac{(k-1)}{N_r-1}\right), \quad k=1,2,\ldots,N_r \qquad [28]$$

the values of the Chebyshev polynomials at these points are simply given by cosine functions:

$$C_{nk} = C_n(x_k) = \cos\left(\pi\frac{n(k-1)}{N_r-1}\right) \qquad [29]$$

This particular choice has two advantages. For one, the grid points become denser towards the inner radius and outer radius and better resolve potential boundary layers. In addition, FFTs can be employed to switch between grid representation [26] and Chebyshev representations [25], rendering this procedure a fast Chebyshev transform. Choosing $N_r > N$ provides radial dealiasing.

Figure 2 shows the distribution of grid points, which becomes denser at the shell boundaries and towards the rotation axis. While the former is a desired effect, the latter may lead to numerical problems that we will address in Section 8.10.3.2.

8.10.3.1.4 Spectral equations

We have now introduced the necessary tools for deriving the spectral equations. Taking the radial components of the Navier–Stokes eqn [1] and the induction eqn [2] provides evolution equations for the poloidal potentials $v(r,\theta,\phi)$ and $g(r,\theta,\phi)$. The radial component of the curl of these equations provides evolution equations for the toroidal counterparts $w(r,\theta,\phi)$ and $h(r,\theta,\phi)$. Expanding all potentials in spherical harmonics and Chebyshev polynomials, multiplying with Y^*_{lm}, and integrating over spherical surfaces (while making use of the orthogonality relation [19]) result in equations for the expansion coefficients v_{lmn}, g_{lmn}, w_{lmn}, h_{lmn}, p_{lmn}, and T_{lmn}, respectively.

The two evolution equations for the poloidal and toroidal flow potentials are

$$E\frac{l(l+1)}{r^2}\left[\left(\frac{\partial}{\partial t}+\frac{l(l+1)}{r^2}\right)C_n - C_n''\right]v_{lmn} + C_n' p_{lmn} - Ra\frac{r}{r_o}C_n T_{lmn} = \int \mathrm{d}\Omega Y^*_{lm}\hat{\mathbf{r}}\cdot\mathbf{F} \qquad [30]$$

and

$$E\frac{l(l+1)}{r^2}\left[\left(\frac{\partial}{\partial t}+\frac{l(l+1)}{r^2}\right)C_n - C_n''\right]w_{lmn} = \int \mathrm{d}\Omega Y^*_{lm}\,\hat{\mathbf{r}}\cdot\nabla\times\mathbf{F} \qquad [31]$$

Here, $\mathrm{d}\Omega$ is the spherical surface element. We use the summation convention for the Chebyshev index n. Radial derivatives of Chebyshev polynomials are denoted by primes. The action of the horizontal Laplacian [17] on spherical harmonics has been expressed analytically by

$$\Delta_H Y_{lm} = -\frac{l(l+1)}{r^2}Y_{lm} \qquad [32]$$

We note that the terms on the left-hand side of eqns [30] and [31], resulting from the viscous term, the pressure gradient, the buoyancy term, and the explicit time derivative, completely decouple in spherical harmonic degree and order. Terms that do not decouple, namely, Coriolis force, Lorentz force, and advection of momentum, are collected on the right-hand side of eqns [30] and [31] into the forcing term $\mathbf{F}$:

$$\mathbf{F} = -2\hat{\mathbf{z}}\times\mathbf{u} - E\mathbf{u}\cdot\nabla\mathbf{u} + \frac{1}{\mathrm{Pm}}(\nabla\times\mathbf{B})\times\mathbf{B} \qquad [33]$$

Resolving $\mathbf{F}$ into potential functions is not required. Its numerical evaluation is discussed in Section 8.10.3.1.6.

The pressure remains an additional unknown in the equation for the poloidal potential [30]. Hence, one more equation involving v_{lmn} and p_{lmn} is required. It is obtained by taking the horizontal divergence of the Navier–Stokes eqn [1], providing

$$E\frac{l(l+1)}{r^2}\left[\left(\frac{\partial}{\partial t}+\frac{l(l+1)}{r^2}\right)C_n'-C_n''-\frac{2l(l+1)}{r^3}C_n\right]v_{lmn}+\frac{l(l+1)}{r^2}C_n p_{lmn}$$
$$=-\int \mathrm{d}\Omega Y_{lm}^{*}\nabla_{\mathrm{H}}\cdot\mathbf{F} \qquad [34]$$

As an alternative, eqn [30] can be replaced by an equation obtained by applying the operator $(\hat{\mathbf{r}}\cdot\nabla\times\nabla\times)$ to the Navier–Stokes equation. This procedure provides an equation for the poloidal flow potential that eliminates the pressure. However, it also increases the radial order of the differential equation, which may lead to additional numerical complications (Hollerbach, 2000; Tilgner, 1999).

The equations for the poloidal and toroidal magnetic field coefficients read

$$\frac{l(l+1)}{r^2}\left[\left(\frac{\partial}{\partial t}+\frac{1}{Pm}\frac{l(l+1)}{r^2}\right)C_n-\frac{1}{Pm}C_n''\right]g_{lmn}=\int \mathrm{d}\Omega Y_{lm}^{*}\hat{\mathbf{r}}\cdot\mathbf{D} \qquad [35]$$

and

$$\frac{l(l+1)}{r^2}\left[\left(\frac{\partial}{\partial t}+\frac{1}{Pm}\frac{l(l+1)}{r^2}\right)C_n-\frac{1}{Pm}C_n''\right]h_{lmn}$$
$$=\int \mathrm{d}\Omega Y_{lm}^{*}\hat{\mathbf{r}}\cdot\nabla\times\mathbf{D} \qquad [36]$$

with the dynamo term

$$\mathbf{D}=\nabla\times(\mathbf{u}\times\mathbf{B}) \qquad [37]$$

The last spectral equation concerns the temperature field and is given by

$$\frac{1}{Pr}\left[\left(Pr\frac{\partial}{\partial t}+\frac{l(l+1)}{r^2}\right)C_n-\frac{2}{r}C_n'-C_n''\right]T_{lmn}$$
$$=-\int \mathrm{d}\Omega Y_{lm}^{*}\,\mathbf{u}\cdot\nabla T \qquad [38]$$

We have now derived a full set of equations ([30], [31], [35], [36], [34], and [38]), each describing the evolution of a single spherical harmonic mode of the six unknown fields (assuming that the terms on the right-hand side are given). Each equation couples $N+1$ Chebyshev coefficients for a given spherical harmonic mode (l, m). Typically, a collocation method is employed to solve for the Chebyshev coefficients. This means that the equations are required to be exactly satisfied at $N-1$ grid points defined by eqns [27] and [28]. Excluded are the points $r=r_{\mathrm{i}}$ and $r=r_{\mathrm{o}}$, where the boundary conditions provide additional constraints on the set of Chebyshev coefficients (see **Section 8.10.3.1.7**).

8.10.3.1.5 Time integration

The strong nonlinearities in the equations generally demand either higher-order time-stepping methods (Kageyama and Yoshida, 2005), multistep algorithms (Clune et al., 1999; Glatzmaier, 1984; Hollerbach, 2000), or iterative schemes (Harder and Hansen, 2005; Hejda and Reshetnyak, 2003). Implicit time-stepping schemes offer increased stability and allow for larger time steps (Hejda and Reshetnyak, 2003; Wicht and Busse, 1997; Zhang and Busse, 1988). However, fully implicit approaches have the disadvantage that the nonlinear terms couple all spherical harmonic modes. The potential gain in computational speed is therefore lost at higher resolution, where one very large matrix has to be dealt with rather than a set of much smaller ones. Similar considerations hold for the Coriolis force, one of the dominating forces in the system and therefore a prime candidate for implicit treatment. However, the Coriolis term couples modes (l, m, n) with ($l+1$, m, n) and ($l-1$, m, n) and also couples poloidal and toroidal flow potentials. An implicit treatment of the Coriolis term therefore also results in a much larger (albeit sparse) inversion matrix. Most authors (Clune et al., 1999; Glatzmaier, 1984; Matsui and Okuda, 2004) consequently prefer a mixed implicit/explicit algorithm. Here, we describe the one suggested by Glatzmaier (1984).

Nonlinear and Coriolis terms, collected on the right-hand side of equations ([30], [31], [35], [36], [34], and [38]), are treated explicitly with a second-order Adams–Bashforth scheme. Terms collected on the left-hand side are time-stepped with an implicit modified Crank–Nicolson algorithm. While the equations are coupled radially, they decouple for all spherical harmonic modes. But note that the poloidal flow potential eqn [31] and the pressure eqn [34] are coupled for a given spherical harmonic mode.

As an example, we derive the time-stepping equation for the poloidal magnetic potential of degree l and order m, denoting the explicit nonlinear term at radial grid point r_k with

$$D_{klm}(t)=\int \mathrm{d}\Omega Y_{lm}^{*}\hat{\mathbf{r}}\cdot\mathbf{D}(t,r_k,\theta,\phi) \qquad [39]$$

After discretization of the partial time derivative, $\partial g_{lmn}/\partial t=(g_{lmn}(t+\delta t)-g_{lmn}(t))/\delta t$ where δt is the time step, we can formulate the left-hand side of eqn [35] as a matrix multiplication. The matrices $\mathbf{A}$ and $\mathbf{G}$ are defined by

$$A_{kn}=\frac{l(l+1)}{r_k^2}\frac{1}{\delta t}C_{nk} \qquad [40]$$

and

$$G_{kn}=\frac{l(l+1)}{r_k^2}\frac{1}{Pm}\left(\frac{l(l+1)}{r_k^2}C_{nk}-C_{nk}''\right) \qquad [41]$$

where $C_{nk}=C_n(r_k)$. The matrices depend on l but not on m. Advancing time from t to $t+\delta t$ is then a matter of solving

$$(A_{kn}+\alpha G_{kn})g_{lmn}(t+\delta t)=(A_{kn}-(1-\alpha)G_{kn})g_{lmn}(t)+\frac{3}{2}D_{klm}(t)$$
$$-\frac{1}{2}D_{klm}(t-\delta t) \qquad [42]$$

The classical Crank–Nicolson scheme is obtained for $\alpha=0.5$, but Glatzmaier (1984) reported that a slightly larger weight of $\alpha=0.6$ helps to stabilize the time integration. Since the stability requirements limiting δt will usually change during a computational run, the time step should be adjusted accordingly. The matrix $\mathbf{G}$ remains unchanged, but $\mathbf{A}$ has to be updated whenever δt is changed. This, in turn, requires a new triangulation of matrix $A_{kn}+\alpha G_{kn}$, which is then stored for subsequent time steps until the next adjustment of δt is in order. Courant's condition (Press et al., 2003) offers a guideline concerning the size of δt, demanding that δt should be smaller than the advection time between two grid points. Strong Lorentz forces require an additional stability criterion that is obtained by replacing the flow speed by the Alfvén velocity in a modified Courant's criterion (Christensen et al.,

1999). The explicit treatment of the Coriolis force requires that the time step is limited to a fraction of the rotation period, which may be the relevant criterion at low Ekman number when flow and magnetic field remain weak. Non-homogeneous grids and other numerical effects generally require an additional safety factor in the choice of δt.

8.10.3.1.6 Evaluation of nonlinear terms

Detailing the evaluation of the Coriolis force term and the nonlinear terms is beyond the scope of this chapter, but we outline a few key issues. The nonlinear terms can in principle be calculated in spherical harmonic space. Several early dynamo simulations followed this approach (Bullard and Gellman, 1954; Phillips and Ivers, 2003; Wicht and Busse, 1997; Zhang and Busse, 1990), but the respective representations are cumbersome to formulate and numerically very expensive to evaluate when the number of involved modes becomes large. The vast majority of recent codes therefore rely on pseudospectral (or spectral transform) methods, where the nonlinear terms are evaluated in grid space rather than in spectral space. However, the spatial derivatives required in the nonlinear terms are best calculated in spectral space. This is done by multiplication with im for the derivative with respect to ϕ, by precomputing radial derivatives of the Chebyshev polynomials at grid points, by using the expression [32] for the action of the horizontal Laplacian, and by employing recurrence relations (Abramowitz and Stegun, 1984) for the latitudinal derivatives of the Legendre polynomials. The pseudospectral method requires back and forth transformations between the spherical harmonic and the grid representation at each time step. In particular, the relatively slow Legendre transforms make this the most time-consuming part of pseudospectral codes.

8.10.3.1.7 Boundary conditions and inner core

Since the system of equations is formulated on a radial grid, boundary conditions can simply be satisfied by replacing the collocation equation at grid points r_i and r_o with appropriate expressions. The condition of zero radial flow on the boundaries implies

$$C_n(r)v_{lmn} = 0 \quad \text{at } r = r_\mathrm{i}, r_\mathrm{o} \qquad [43]$$

Note that the summation convention with respect to radial modes n is used again. The no-slip condition requires that the horizontal flow components also have to vanish, provided the two boundaries are at rest. This condition is fulfilled when

$$C_n'(r)v_{lmn} = 0 \quad \text{at } r = r_\mathrm{i}, r_\mathrm{o} \qquad [44]$$

and

$$C_n(r)w_{lmn} = 0 \quad \text{at } r = r_\mathrm{i}, r_\mathrm{o} \qquad [45]$$

for all harmonic modes (l, m). The two conditions [43] and [44] replace the poloidal flow potential eqn [30] and the pressure eqn [34], respectively, at the collocation points r_i and r_o.

If the inner core and mantle are allowed to react to torques, a condition based on conservation of angular momentum replaces condition [45] for mode $(l=1,\ m=0)$ (Hollerbach, 2000):

$$\mathbf{I}\frac{\partial}{\partial t}\omega = \mathbf{\Gamma} \qquad [46]$$

The tensor $\mathbf{I}$ denotes the moment of inertia of inner core or mantle, respectively; ω is the mantle or inner core rotation rate relative to that of the reference frame; and $\mathbf{\Gamma}$ is the respective torque. Viscous, magnetic, and gravitational torques have been considered (Aurnou et al., 1996; Buffett, 1997; Buffett and Glatzmaier, 2001; Wicht, 2002; Xu and Szeto, 1994). Generally, it is assumed that the gravitational interaction between the oblateness of the Earth's mantle and the polar flattening of the inner core causes very large restoring forces that minimize any deviations between the mantle and the inner core rotation axes (Buffett, 1996; Xu and Szeto, 1998). All authors therefore consider only inner core rotation about the polar axis.

Free-slip boundary conditions require that the viscous stress vanishes, which in turn implies that the nondiagonal components $e_{r\phi}$ and $e_{r\theta}$ of the strain-rate tensor vanish. Translated to the spectral representation, this requires

$$\left[C_n''(r) - 2\frac{1}{r}C_n'(r)\right]v_{lmn} = \left[C_n'(r) - 2\frac{1}{r}C_n(r)\right]w_{lmn} = 0 \qquad [47]$$

Magnetic boundary conditions at the interface with an insulating mantle or insulating inner core are similarly implemented. The toroidal magnetic field cannot enter any insulator and therefore has to vanish at the boundary

$$C_n(r)h_{lmn} = 0 \quad \text{at} \quad r = r_\mathrm{i} \quad \text{and/or} \quad r = r_\mathrm{o} \qquad [48]$$

Matching conditions for the poloidal magnetic field with a source-free external potential field require that the following equations are satisfied at the boundary grid points:

$$C_n'(r)g_{lmn} - C_n(r)\frac{l+1}{r}g_{lmn} = 0 \quad \text{at} \quad r = r_\mathrm{i} \qquad [49]$$

$$C_n'(r)g_{lmn} + C_n(r)\frac{l}{r}g_{lmn} = 0 \quad \text{at} \quad r = r_\mathrm{o} \qquad [50]$$

If the inner core is modeled as an electrical conductor, a simplified dynamo equation has to be solved in which the fluid flow is replaced by the solid-body rotation of the inner core. The latter is described by a single toroidal flow mode $(l=1,\ m=0)$. The resulting nonlinear terms can be expressed by a simple spherical harmonic expansion, where the superscript I denotes values in the inner core and ω_I its differential rotation rate:

$$\int \mathrm{d}\Omega Y_{lm}^{*}\hat{\mathbf{r}}\cdot\nabla\times\left(\mathbf{u}^\mathrm{I}\times\mathbf{B}^\mathrm{I}\right) = -i\omega_\mathrm{I}m\frac{l(l+1)}{r^2}g_{lm}^\mathrm{I}(r) \qquad [51]$$

$$\int \mathrm{d}\Omega Y_{lm}^{*}\hat{\mathbf{r}}\cdot\nabla\times\nabla\times\left(\mathbf{u}^\mathrm{I}\times\mathbf{B}^\mathrm{I}\right) - i\omega_\mathrm{I}m\frac{l(l+1)}{r^2}h_{lm}^\mathrm{I}(r) \qquad [52]$$

The expensive back and forth transformations between spherical harmonic and grid representation are therefore not required for advancing the inner core magnetic field in time.

In the inner core, the magnetic potentials are again conveniently expanded into Chebyshev polynomials. The Chebyshev variable x spans the whole diameter of the inner core, so that grid points are dense near the inner core boundary but sparse in the center. The mapping is given by

$$x(r) = \frac{r}{r_i} \quad (-r_i, \leq r, \leq r_i) \qquad [53]$$

Each point in the inner core is thus represented twice, by grid points (r, θ, ϕ) and $(-r, \pi - \theta, \phi + \pi)$. Since both representations must be identical, this imposes a symmetry constraint that can be fulfilled when the radial expansion comprises only polynomials of even order (Hollerbach, 2000):

$$g^{\mathrm{I}}_{lm}(r) = \left(\frac{r}{r_i}\right)^{l+1} \sum_{i=0}^{M-1} g^{\mathrm{I}}_{lm2i} C_{2i}(r) \qquad [54]$$

An equivalent expression holds for the toroidal potential in the inner core. FFTs can again by employed efficiently for the radial transformation, using the M extrema of $C_{2M-1}(r)$ with $x > 0$ as grid points.

The sets of spectral magnetic field equations for the inner core and the outer core are coupled via continuity equations for the magnetic field and the horizontal electric field. Continuity of the magnetic field is assured by (1) continuity of the toroidal potential, (2) continuity of the poloidal potential, and (3) continuity of the radial derivative of the latter. Continuity of the horizontal electric field demands (4) that the radial derivative of the toroidal potential is continuous, provided that the horizontal flow and the electrical conductivity are continuous at the interface. These four conditions replace the spectral eqns [35] and [36] on the outer core side and eqns [51] and [52] on the inner core side. Employing free-slip conditions or allowing for electrical conductivity differences between inner core and outer core leads to more complicated and even nonlinear matching conditions (Schubert and Zhang, 2001).

8.10.3.1.8 Numerical truncation, hyperdiffusion, and subgrid-scale models

It is numerically unfeasible to resolve the whole spectrum of different length scales and timescales present in the geodynamo. For example, turbulent eddies in the core can be expected to have a size down to 10 m, whereas the grid spacing in the currently best resolved models is several tens of kilometers. Dynamo models are therefore forced to run with thermal and viscous diffusivities much higher than the molecular values to damp the smaller scales that cannot be represented with the computing resources at hand. The magnetic diffusivity is the only exception where realistic values can be used. These increased diffusivities are sometimes rationalized as a parameterization of turbulent transport properties on the subgrid-scale level and are then referred to as eddy or turbulent diffusivities (see **Chapter 8.05**, Section 8.05.5.2.4). Note, however, that the turbulent diffusivities in the Earth's core are likely still several orders of magnitude smaller than in typical dynamo models and, being determined by the complex turbulent dynamics, may also be anisotropic (Braginsky and Roberts, 1995). The important question is whether the effects we aspire to model are still correctly represented in the resolved scales.

In a spectral code, the resolution is determined by the truncation level (L, N) of the expansion. We can give the truncation a physical interpretation by assuming that the diffusion of the unresolved scales is practically infinite. Spectra of magnetic and kinetic energy are often taken to judge if the resolution is sufficient. The energy should clearly decay from the dominant mode toward the tail of the spectrum. A decay over several orders a magnitude is regarded desirable, but tests with different levels of truncation have indicated that the general properties of the solution do not change significantly when the drop in the energy spectra exceeds a factor of 50 (Christensen et al., 1999; Kutzner and Christensen, 2002).

Several dynamo models have invoked hyperdiffusivities to ensure numerical stability at values of the Ekman number and the Rayleigh number that would normally require much higher levels of truncation than could be afforded (Glatzmaier and Roberts, 1995a,b, 1996a; Kuang and Bloxham, 1997, 1999; Sakuraba and Kono, 1999; Stanley and Bloxham, 2004, and some other papers of these authors). This typically means that the action of the Laplacians in some or all of the diffusive terms in eqns [1]–[3] is amplified by a factor that more strongly damps small spatial scales in the flow, magnetic field, or temperature field, respectively. Hyperdiffusion is generally implemented in the spherical harmonic representation with an amplification factor that increases with spherical harmonic degree l.

The argument for using scale-dependent hyperdiffusivities is that the smaller resolved scales in the solution are expected to interact more strongly with the unresolved scales than the larger components. It is assumed that the main effect of this interaction is to transfer energy to the unresolved scales, which is parameterized by enhancing the diffusivities for the smaller resolved scales. However, the use of hyperdiffusivity has been criticized on various grounds. First, there is no guideline how to choose the amplification factor. Second, in its usual form, hyperdiffusivity is anisotropic in the sense that the value of diffusivity is sensitive to the horizontal scale but is independent on the scale in the radial direction.

While the use of hyperviscosity allows simulations at lower values of the Ekman number than would be possible with the use of regular viscosity, one must keep in mind that the nominal value of the Ekman number refers to the viscosity experienced by the largest scale in the flow (sometimes, this value has been termed the 'headline' Ekman number). Intermediate scales in the flow may actually be more relevant for the dynamo. The effective Ekman number at these scales is larger than the nominal value and is in fact of an order where simulations are possible with regular viscosity. When comparing fully resolved simulations with cases using hyperdiffusivity, several authors report significant differences that at least argue against an arbitrary choice of the amplification factor (Grote et al., 2000a; Roberts and Glatzmaier, 2000; Zhang and Jones, 1997). It remains an open question to what extent hyperdiffusivities not only affect the small-scale components of the solution but also change the overall character of the dynamo. Most modelers that use hyperdiffusivities consider them as a 'necessary evil' (Glatzmaier, 2002), which should be abandoned as more powerful computational resources allow for high spatial resolution or which should be replaced by a more sophisticated parameterization of subgrid-scale processes that has a better basis.

To understand how the action of the unresolved subgrid scales could influence the dynamo dynamics, we have to consider the nonlinear interactions. They are responsible for the energy transfer between different length scales. Turbulence theory is mostly concerned with a cascade that transfers the energy from the large scale of energy injection to the small scale where energy is ultimately dissipated away. But the cascade can

also work in the opposite direction, particularly when strong rotational constraints play a role. Reynolds stresses, a statistical correlation of small-scale momentum advection, are a prominent example of such an inverse cascade. They likely drive the fierce zonal winds observed at the surface of the gas planets (Christensen, 2001; Gastine and Wicht, 2012; Heimpel et al., 2005). Rather than using more or less arbitrary turbulent diffusivities, subgrid-scale methods, sometimes called large eddy simulations, try to parameterize the energy transfer between numerically resolved and unresolved scales based on the interaction within the resolved scales. Several publications show the potential of this approach (Chen and Jones, 2008; Matsui and Buffett, 2005; Matsushima, 2006; Nelson et al., 2013). A full application in a 3-D spherical planetary dynamo simulation, however, is still missing.

8.10.3.2 Local Methods

In recent years, several authors have invested in developing new dynamo codes based on methods that we summarize under the term 'local' here: finite differences, finite elements, finite volume or control volume, and spectral element methods. There are several reasons for a local approach. (1) They permit a more flexible decomposition of the spherical shell allowing for local grid refinements and for deviations from spherical symmetry. (2) Some local methods are simpler to implement and all are more straightforward to parallelize than spectral schemes. (3) Local methods avoid the need for performing Legendre transforms at every time step, which are computationally expensive when the number of modes becomes large.

Spherical coordinates and longitude/latitude grids are the obvious choice for solving problems in spherical domains. However, the grid is highly anisotropic at higher latitudes where cell sizes decrease rapidly toward the poles. This anisotropy can cause numerical instabilities, and painfully small time steps may be required in some schemes to fulfill Courant's criterion near the rotation axis (Hejda and Reshetnyak, 2003). This is less of a problem when convection close to the rotation axis stays weak but can become an issue at higher Rayleigh numbers.

Local methods, on the other hand, allow for very flexible domain decompositions, which are the very reason for their success in complex industrial applications. However, complicated decompositions, nonorthogonal subdomains, and locally varying coordinate systems are penalized with higher code complexity and additional numerical costs (Harder and Hansen, 2005). Choosing a decomposition is a question of finding the best compromise for the specific problem and the specific geometry.

Finite element methods decompose the spherical shell into a number of subvolumes or cells (Chan et al., 2001, 2007; Matsui and Okuda, 2004). Galerkin methods are applied to each individual cell, expanding the unknowns in linear (Matsui and Okuda, 2004), quadratic (Chan et al., 2001), or higher-order functions. Hybrid solutions, using Fourier expansions in longitude and a spectral element decompositions in the meridional plane (Fournier et al., 2005), have been implemented for thermal convection in a rotating sphere and can be extended to the dynamo problem. Using higher-order spectral representation within the meridional cells defines the so-called spectral element schemes (Fournier et al., 2004). All finite-element applications circumvent possible instabilities in the polar region by providing a nearly even coverage of the spherical surface.

Finite difference methods approximate derivatives by differences of functional values on neighboring grid points. Dynamo models by Kuang and Bloxham (1999), Dormy et al. (1998), and Willis et al. (2007) apply finite differences in radial direction only. Earlier implementations of the finite difference method in all three dimensions (Kageyama and Sato, 1995, 1997a; Kageyama et al., 1993) retained the latitude/longitude grid. FFT-based low-pass filters were employed to circumvent numerical instabilities in the polar region due to the grid anisotropy. A newer and more elegant approach manages to combine advantages of the classical decomposition with the flexibility of finite difference applications in a so-called Yin–Yang grid shown in **Figure 2**. The Yin subgrid uses a longitude/latitude decomposition at low to intermediate latitudes where the coverage is nearly isotropic but omits a strip in longitude. The same grid geometry is used again in the Yang counterpart to cover higher latitudes and the remaining longitudes. Two simple rotations about the z-axis and an equatorial axis convert Yin to Yang. Both sections overlap, implying some computational overhead of about 6% at high resolution.

Another way to circumvent the pole-instability problem is finite-volume schemes (Harder and Hansen, 2005; Hejda and Reshetnyak, 2003). These methods combine a decomposition into volume cells with staggered grids, and rather than solving the differential equations directly, they are expressed in conservative form by integration over each volume cell. Gauss' theorem is then employed to convert the integrals into fluxes over the cell boundaries. Temperature and pressure are evaluated in cell centers, while normal flow and magnetic field components are computed on cell surfaces. The volume of each cell controls its relative importance in the solution, thus rendering cells close to the pole almost negligible in a longitude/latitude grid.

Spectral methods offer two significant advantages: Derivatives are easily calculated with high accuracy, and, most notably in the context of dynamo simulations, the formulation of magnetic boundary conditions at the interface with an external insulator (eqns [48]–[50]) is straightforward. A larger number of grid points (meaning a larger number of unknowns) are required in local methods to gain accuracies comparable with pseudospectral schemes (Christensen et al., 2001). As far as the magnetic boundary condition is concerned, local methods either apply artificial boundary conditions (see **Section 8.10.2.3.2**) or explicitly solve for the field in the outer region. Since the insulating region is purely diffusive, significantly less computational effort is necessary than for solving the dynamo equation in the shell. The additional numerical costs seem acceptable (Chan et al., 2001, 2007; Kageyama and Yoshida, 2005; Matsui and Okuda, 2004).

Most local codes do not employ the poloidal–toroidal decomposition [14] of flow and magnetic field. When primitive variables, that is, velocity and magnetic field components, are used, continuity and $\nabla \cdot \mathbf{B} = 0$ have to be enforced explicitly. The three components of the Navier–Stokes equation and the

continuity equation form a system of four equations to determine four unknowns, three flow components, and the pressure. The latter should be 'corrected' to enforce $\nabla \cdot \mathbf{u} = 0$ in Boussinesq codes or continuity of mass flux in compressible schemes (Harder and Hansen, 2005). For example, an auxiliary pseudopressure gradient ∇q can be incorporated into the dynamo equation (Chan et al., 2007). Solving $\nabla^2 q = 0$ at each time step in conjunction with a starting condition $\nabla \cdot \mathbf{B} = 0$ guarantees that $\mathbf{B}$ remains divergence-free at all times. Note that this numerical trick does not affect the curl of the dynamo equation. It is thus compliant with Maxwell's equations (Chan et al., 2001; Harder and Hansen, 2005) and simply takes advantage of the inherent gauge freedom.

The expected parallelization efficiency is one of the main incentives for using local rather than spectral methods. Parallelization of a spectral code comes at the cost of a significant communication overhead since the whole solution has to be broadcast twice at every time step, each processor communicating with all other processors (Clune et al., 1999). An efficient parallelization of spectral codes is more demanding than for local schemes but is nevertheless possible, at least on parallel computers of medium size and high communication bandwidth. Reported parallelization efficiencies are 84% on 64 processors of an IBM p575 shared-memory system, where memory access rather than interprocessor communication is the limiting factor; about 80% on 128 processors of a distributed memory T3E with a highly optimized code (Clune et al., 1999); and 66% on 512 processors of the Earth Simulator, which has a mixed shared/distributed architecture (Takahashi et al., 2005). Recent efforts in optimizing the ASH code (Clune et al., 1999) have succeeded to yield efficient parallelization on thousands of processors (Featherstone, 2012).

For codes based on local methods, parallelization is a simple matter of assigning a separate subdomain of the sphere to each processor. Differential operators require information from neighboring cells only, which amounts to much less overall communication than for spectral methods. A peak performance of 46% has been reported on 4096 processors for the Yin–Yang finite-element code running on the Earth Simulator (Kageyama and Yoshida, 2005).

Comparing performances of different codes on different architectures is a daunting task, in particular when absolute runtime or computer availability is also considered. It seems fair to say that, while local methods have the potential of running more efficiently than spectral methods on very large parallel systems, spectral methods still keep the pace even on thousands of processors. A more detailed comparison of different methods can be found in Wicht et al. (2009).

8.10.4 Model Results

Numerical dynamo models have been studied for different purposes. In some cases, the main aim was to understand the physical principles that shape the fluid flow and lead to the generation of a magnetic field. Other models strove at reproducing certain properties of the geomagnetic field and elucidating the specific conditions for their occurrence. Often, these two aims have been combined. In this section, we will first treat the more fundamental aspects and then proceed to a detailed comparison of model results with the geomagnetic field.

8.10.4.1 Fundamental Aspects

8.10.4.1.1 General properties of standard models with dipolar magnetic field

We will first consider the 'standard' model setup and choice of boundary conditions adopted by the majority of modelers. It comprises no-slip boundaries and driving of convection predominantly by a buoyancy flux from the inner core. These dynamos often generate a magnetic field dominated by the axial dipole, in particular when they are weakly driven. By 'weak driving,' we mean primarily that the Rayleigh number does not far exceed the critical value for the onset of (nonmagnetic) convection, typically by a factor of less than 10. 'Strongly driven dynamos,' which are more than ten times supercritical, can also be dipolar. But depending on the convective vigor, restrictions apply on the possible choices of other control parameters (see **Table 1**), in particular the Ekman number, when one aims at obtaining a dipole-dominated field. This point will be discussed in the succeeding text and in **Section 8.10.4.1.2**. Of course, a gradual transition exists between weakly and strongly driven dynamos, and there is no strict dichotomy.

A sufficiently large value of the magnetic Reynolds number $Rm \approx 50$ is needed for self-sustained dynamo action. In weakly driven models, this can only be achieved when the magnetic Prandtl number is significantly larger than one. In many weakly driven models, a fairly high value of the Ekman number ($E > 10^{-4}$) has been assumed. The flow pattern and the magnetic field are relatively large-scaled in such cases, and high spatial resolution is not required.

One of the simplest models had been selected for a benchmark comparison study, and its properties have been quantitatively verified by a number of independent numerical codes (Christensen et al., 2001). It is one of the few known dynamo solutions that are quasistationary in the sense that the only time dependence consists of a steady drift of the pattern in longitude. The magnetic Reynolds number is only 39, one of the lowest values for which a self-sustained dynamo has been found. **Figure 3** shows various aspects of the solution. It exhibits a fourfold symmetry in longitude and mirror symmetry with respect to the equator. Even a slight change in the control parameters breaks the symmetry of the solution and leads to a chaotic time variation. However, aside from the larger complexity and presence of smaller spatial scales, the general pattern of the flow and the magnetic field is broadly similar to those of the benchmark solution in many models with weak driving for a rather broad range of control parameters (e.g., Christensen et al., 1999; Kageyama and Sato, 1997a).

When characterizing the flow, the region inside and outside the tangent cylinder must be distinguished. The tangent cylinder is an imaginary cylinder parallel to the rotation axis that touches the inner core at the equator (**Figure 1**). In the weakly driven models, the flow is organized in nearly geostrophic convection columns outside the tangent cylinder (**Figure 4**). The term 'geostrophic' refers to a flow that is controlled by the balance of Coriolis and pressure gradient force and whose velocity field does ideally not change in the direction of the

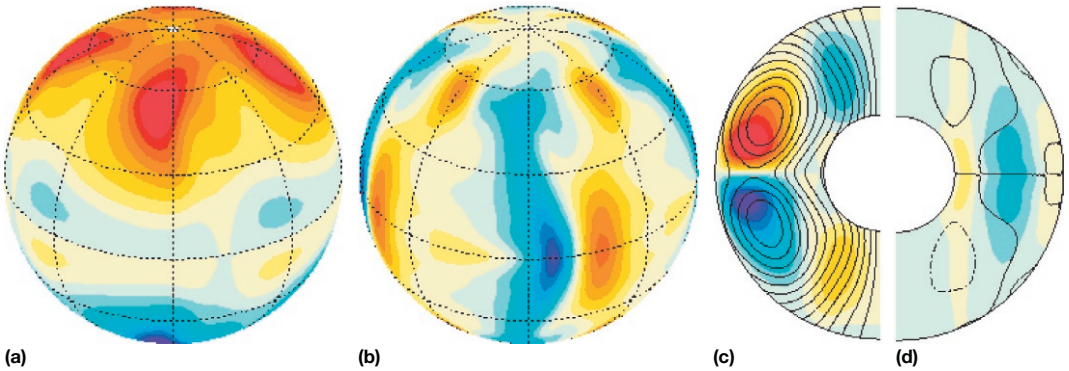

Figure 3 The benchmark dynamo model with insulating inner core, no-slip boundaries with fixed temperatures, $Ra = 100$ ($1.8 \times$ critical), $E = 10^{-3}$, $Pr = 1$, and $Pm = 5$. (a) Radial magnetic field at the outer radius; (b) radial velocity at $0.83r_o$; (c) axisymmetric magnetic field, eastward toroidal field in red, westward in blue, and field lines of the poloidal field; (d) axisymmetric flow, reddish colors for eastward flow, bluish westward, and streamlines for meridional circulation.

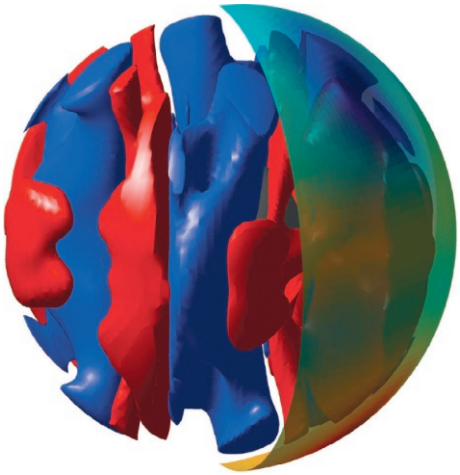

Figure 4 Isosurfaces of positive (red) and negative (blue) vorticity $\omega_z = \hat{\mathbf{z}} \cdot \nabla \times \mathbf{u}$ for the benchmark dynamo.

rotation vector. The particle motion in these columns is helical: superimposed on the vortex motion around the column, there is a (nongeostrophic) flow along the column axis, which converges towards the equatorial plane in cyclonic vortices and diverges away from the equatorial plane in anticyclonic vortices. In the case of weakly driven convection, there is little motion inside the tangent cylinder.

In many weakly driven dipolar models, the magnetic field on the outer boundary is concentrated into flux bundles centered near 60° latitude, which coincide with downwelling flow below the boundary (**Figure 3(a)** and **3(b)**). Weaker inverse flux spots, whose polarity is opposite to the dominant polarity in their hemisphere, occur in pairs north and south of the equator. In the interior of the shell, the axisymmetric part of the poloidal magnetic field has a typical bull's-eye pattern, and the axisymmetric toroidal field consists of two flux bundles of opposite polarity outside the inner core tangent cylinder near the equatorial plane (**Figure 3(c)**). The axisymmetric flow (**Figure 3(d)**) is weak.

In strongly driven models, the control parameters are somewhat closer to Earth values although still different by orders of magnitude (see **Table 1**). Christensen et al. (1999) and Christensen and Aubert (2006) found that at sufficiently high Rayleigh number, standard dynamos no longer generate a dipole-dominated magnetic field. Rather, the magnetic field on the outer boundary is dominated by a mixture of higher-degree components (multipolar dynamo). The value of Ra/Ra_c at which dipolar dynamos break down rises with the inverse Ekman number. Hence, strongly driven dynamos require a low Ekman number, typically less than 10^{-4}, when the emphasis is on models with a dipolar field that can be compared to the geodynamo. The magnetic Prandtl number can be around one or smaller in strongly driven models. The magnetic Reynolds number, which in the weakly driven models are typically of order one hundred or less, can reach values up to one thousand and therefore matches the likely Earth value (Christensen and Tilgner, 2004). Such models require larger computational resources, and fewer of these cases have been published (e.g., Christensen and Aubert, 2006; Sakuraba and Roberts, 2009; Takahashi et al., 2005). A special case are models employing hyperdiffusivities (see **Section 8.10.3.1.8**), which use strong convective driving and a low value of the Ekman number, but suppress small spatial scales.

With regular diffusivities, the strongly driven solutions contain much more small-scale structure than the weakly driven models (**Figure 5**). This is also reflected in the magnetic energy spectrum (**Figure 6**), which in the strongly driven case has a flat distribution from degree four to approximately degree 20 before it starts to fall off. In the benchmark case, the spectral power drops rapidly with harmonic degree beyond $l = 8$. Nonetheless, the dipole contribution to the magnetic energy stands out in both cases. Also, some morphological aspects of the flow and magnetic field pattern are not dissimilar in the strongly driven models from those in cases with weak driving. This comprises the organization of the flow outside the tangent cylinder in nearly geostrophic columns, the concentration of magnetic flux on the outer boundary in high-latitude patches, and the occurrence of inverse flux spots at low latitude. An important difference is that at higher Rayleigh number, vigorous flow occurs also inside the tangent cylinder. Upwelling flow is often found at or nearby the polar axis (Glatzmaier and Roberts, 1995b; Olson et al., 1999; Sreenivasan and Jones,

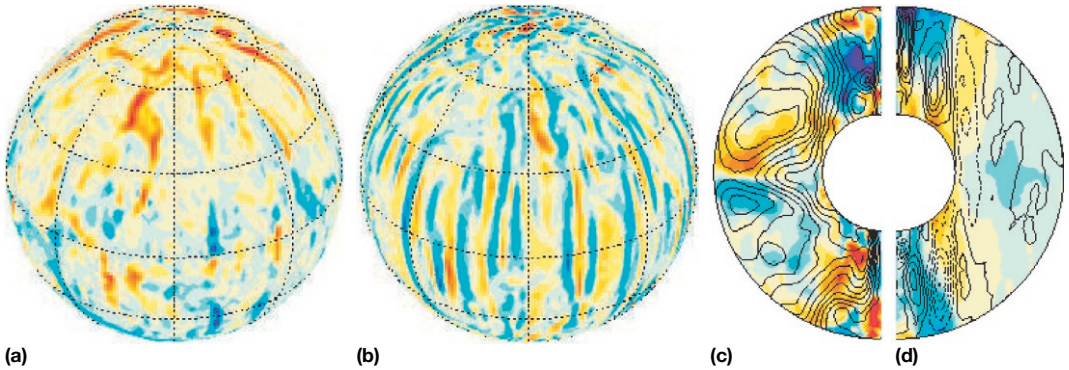

Figure 5 Strongly driven dynamo model, $Ra = 3600$ (42× critical), $E = 3 \times 10^{-5}$, $Pr = 1$, and $Pm = 2.5$. Snapshot of (a) radial magnetic field at the outer radius, (b) radial velocity at 0.93 r_o, (c) axisymmetric magnetic field, and (d) axisymmetric flow. Details as in **Figure 3**.

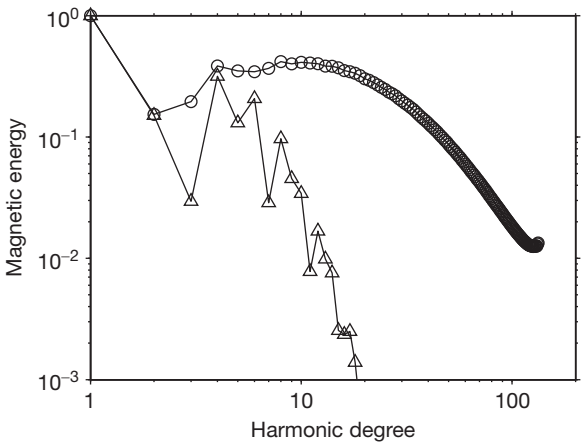

Figure 6 Spectrum of magnetic energy inside the conducting shell as function of harmonic degree for the benchmark model (triangles) and the strongly driven case shown in **Figure 5** (circles). In the latter case, a time-averaged spectrum is shown. The spectra have been normalized by the $\ell = 1$ component.

2005, 2006a). Due to a thermal wind mechanism (which means a flow governed by a balance of buoyancy and Coriolis forces), the warm rising plume is associated with a westward vortex flow near the outer shell boundary and an eastward vortex near the inner core boundary. **Figure 5(d)** shows this general pattern but also that some complexity exists in the details. The magnetic flux escaping from the fluid shell inside the tangent cylinder region is relatively weak. In the strongly driven cases, the axisymmetric toroidal magnetic field is more pronounced inside than outside the tangent cylinder. Outside the tangent cylinder, it is dominated by a pair of azimuthal flux bundles near the equatorial plane, as it is in the weakly driven models.

In both weakly and strongly driven models, the Elsasser number Λ, describing the strength of the magnetic field, is found to be roughly of order one. The strength of Earth's field at the core–mantle boundary corresponds to $\Lambda \approx 0.1$, and reasonable assumptions lead to the conclusion that the mean field strength inside the core is an order of magnitude larger. Hence, on an order of magnitude scale, the models reproduce the geomagnetic field strength. However, the actual values of Λ in different models, particularly the strongly driven ones, cover a fairly large range from $\Lambda = 0.1$ to $\Lambda = 100$ (Christensen and Aubert, 2006). Values of $\Lambda \geq 1$ are usually associated with a balance between Coriolis force and Lorentz force on the flow. However, a comparison of nonmagnetic convection and dynamo solutions at otherwise identical parameter values shows not much differences in the structure of geostrophic convection columns (Soderlund et al., 2012), suggesting that Λ may not be the appropriate parameters to describe the influence of magnetic forces in dynamos.

In strongly driven dynamos, the flow and the magnetic field fluctuate chaotically with time (**Figure 7**). The partitioning of kinetic or magnetic energy into the toroidal and poloidal and the axisymmetric and nonaxisymmetric components is of interest with a view on the field generation mechanism. When the standard spectral method is employed, it is easily calculated and has been reported by several authors (e.g., Christensen et al., 1999; Grote et al., 1999; Simitev and Busse, 2005). In the types of dynamos discussed earlier, the magnetic energy is rather evenly divided between the toroidal field and the poloidal field. The axisymmetric contribution is large in the weakly driven dynamos; in the benchmark case, it contributes 88% to the poloidal field and 55% to the toroidal field. These figures drop with increasing magnetic Reynolds number and are 16% (poloidal) and 7% (toroidal) for the case shown in **Figures 5** and **7**. The axisymmetric toroidal magnetic field is usually weaker than the axisymmetric poloidal field. Most of the kinetic energy is contributed by the nonaxisymmetric toroidal (~60%) and nonaxisymmetric poloidal (~30%) parts, which reflects the dominance of columnar convection. The axisymmetric toroidal flow (differential rotation) contributes typically of the order 10% or less (but see next section). The energy in the axisymmetric poloidal flow (meridional circulation) is usually tiny.

8.10.4.1.2 Variations and nondipolar dynamos

Some published dynamos differ in their magnetic field pattern or flow structure from the cases described earlier. According to the symmetry properties of the magnetic field with respect to the equatorial plane, a dipolar and a quadrupolar family of dynamos are distinguished (Zhang and Gubbins, 1993). In the former case, the B_r and the B_ϕ components are antisymmetric about the equator, and the B_θ component is symmetric. These

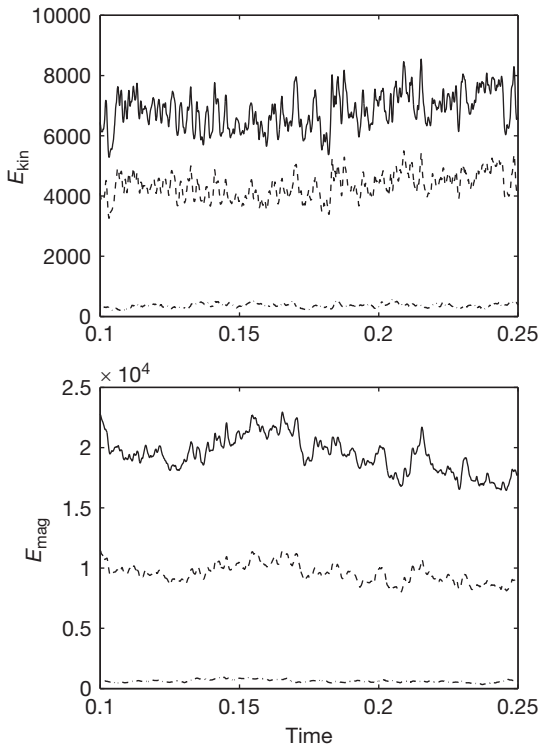

Figure 7 Time series of the kinetic energy density E_{kin} and magnetic energy density E_{mag} for the case shown in **Figure 5**. Full lines indicate total energies, broken lines the toroidal part, and dash-dotted lines the axisymmetric toroidal contribution.

symmetries are reversed for the quadrupolar family. Although the field of an axial dipole and that of an axial quadrupole show the respective symmetries, the classification does not necessarily imply the dominance of one or the other harmonic contribution. When we speak of a dipolar dynamo (in contrast to a dynamo belonging to the dipole family), we mean that it has a dominant axial dipole component. Weakly driven dynamos models often obey one or the other symmetry. The benchmark dynamo, for example, belongs to the dipolar symmetry family. Strongly driven models are not perfectly symmetric.

Ishihara and Kida (2000) reported dynamo solutions dominated by the equatorial dipole, which have been studied more extensively by Aubert and Wicht (2004). They are found at Rayleigh numbers just beyond the onset of dynamo action and are members of the quadrupolar dynamo family. When the Rayleigh number is increased to slightly more supercritical values, the equatorial solution becomes unstable. The axial dipole solution representing the complementary symmetry family takes over. The increase in meridional circulation associated with the larger Rayleigh number seems to favor the axial dipole configuration (Aubert and Wicht, 2004; Tilgner, 2004).

At a rather large Ekman number of order 10^{-2}, Wicht and Olson (2004) found dynamos with a strong meridional circulation and lack of geostrophic columns, which exhibit quasi-periodic dipole reversals. But the more standard type with columnar flow also exists also at such large values of the Ekman number (Driscoll and Olson, 2009a; Katayama et al., 1999).

Grote et al. (2000b) and Simitev and Busse (2005) performed an extensive survey of parameter space for dynamos with stress-free boundaries, varying in particular the Prandtl number and the magnetic Prandtl number in a wide range (see also Busse and Simitev, 2005a,b; Grote and Busse, 2001). The flow in these models is driven partly by internal heat sources and has usually a columnar structure. While some of their dynamos, particularly those at high Pr and high Pm, have magnetic fields dominated by a stable axial dipole component, they also find dynamos with a different magnetic field geometry. At moderate to low values of the magnetic Prandtl number, the dynamos have predominantly quadrupolar magnetic field symmetry or are of a hemispheric type, where the magnetic field generation process operates only in the northern or southern hemisphere. The field structure in these dynamos frequently oscillates in a nearly periodic manner. This is also the case for some of their dipolar dynamos, which may show periodic reversals (Busse and Simitev, 2005b). Busse and Simitev (2006) explained them in terms of dynamo (Parker) waves, whose periods agree with predictions of a simple mean-field dynamo wave theory.

In models of nonmagnetic rotating convection with stress-free boundaries, a strong zonal flow outside the tangent cylinder is excited, which may carry most of the kinetic energy. Grote and Busse (2001) described the so-called relaxation oscillation, in which convective flow is virtually absent most of the time. Nearly periodic bursts of convection occur when the zonal flow is sufficiently diminished by viscous friction. The energy of the zonal flow is replenished by the associated inertial effects (Reynolds stresses), which in turn suppresses the convection (see also Christensen, 2002). However, in the presence of a self-sustained magnetic field, in particular a strong dipolar field, the zonal flow is inhibited and usually no longer dominates over other flow components. Relaxation oscillations are suppressed and convection becomes more efficient in terms of the net heat transport (Grote and Busse, 2001). Aubert (2005) showed that the weaker zonal flow in a dipolar dynamo model outside the tangent cylinder differs also in shape and excitation mechanism from the nearly geostrophic zonal flow found in nonmagnetic models. In the dynamo, it obeys a thermal find balance and contours of equal azimuthal velocity tend to align with the axisymmetric field lines, which minimizes Maxwell's stresses associated with shearing of the field lines.

For stress-free boundaries, bistability of dynamo solutions is found for a substantial parameter range: depending on the initial condition for the magnetic field, either a strong dipolar field or a weaker multipolar field persists (Gastine et al., 2012; Schrinner et al., 2012; Simitev and Busse, 2009). Also, the zonal flow is markedly different in the two solution branches, with a rather weak thermal wind-driven flow in the dipolar branch and strong geostrophic zonal flow, similar to that in nonmagnetic convection, in the multipolar branch. In models with rigid boundaries, where strong zonal flows are suppressed by friction in the Ekman boundary layer, at least at values of the Ekman number that are accessible to numerical simulations, bistability is hardly found. So far, only two examples have been reported by Christensen and Aubert (2006) and Duarte et al. (2013). In general, strong dipolar magnetic fields and strong zonal flow are mutually exclusive. The dynamo

models of Kuang and Bloxham (1997, 1999) with stress-free boundaries are exceptional in the sense that a very strong zonal flow, which carries 80% of the kinetic energy, coexists with a strong magnetic field whose poloidal part is dominated by the axial dipole component. Also, in the low-Ekman-number models by Kageyama et al. (2008) and Miyagoshi et al. (2010), a strong zonal flow in a hardly convecting outer region (far from the rotation axis) coexists with a strong dipolar field generated by nearly geostrophic sheetlike convective flow closer to the axis. These two sets of models differ in some assumptions from the standard setup, which may explain the differences. In the former case, hyperdiffusivities are employed and nonaxisymmetric inertial terms are neglected. In the latter non-Boussinesq models, an ideal gas equation of state is used and gravity decreases strongly with radius rather than to increase outward.

In models with no-slip boundaries, Kutzner and Christensen (2000, 2002) found that driving convection by a significant contribution of internal heating favors dynamos creating a quadrupolar or multipolar magnetic field, whereas dipolar fields are preferred when the source of buoyancy is concentrated at the inner core boundary, as in the case of compositional convection. However, dipole-dominated solutions for internally heated dynamos have also been found (Grote et al., 2000b; Sakuraba and Kono, 1999). The thermal boundary condition on the outer boundary plays an important role for the mode selection in internally heated dynamos, with a fixed temperature condition promoting multipolar magnetic fields, whereas a fixed flux condition leads to a dipole-dominated field (Hori et al., 2010). Also, for dynamos with bottom heating, the choice of flux conditions instead of fixed temperature (or codensity) has a significant influence on the solution, promoting, for example, larger scales in the flow and the magnetic field (Hori et al., 2012; Sakuraba and Roberts, 2009). In bottom-heated cases, the choice of boundary condition at the inner boundary seems more influential than that for the outer boundary (Hori et al., 2012). When convection is driven very strongly at a high supercritical Rayleigh number, the dipolar solution breaks down in favor of a multipolar one, irrespective of the distribution of buoyancy sources and the nature of the boundary conditions. **Figure 8** illustrates the magnetic field structure on the outer boundary of such a dynamo.

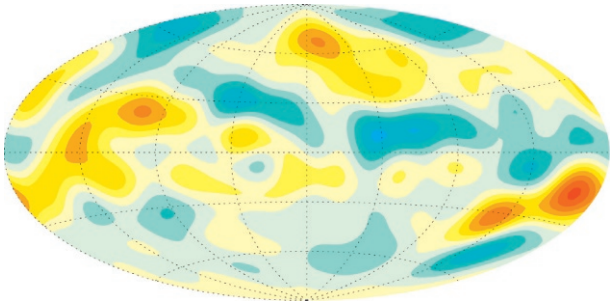

Figure 8 Snapshot of the magnetic field at the outer boundary of a dynamo model with $Ra = 3600$, $E = 3 \times 10^{-5}$, $Pm = 0.5$, and $Pr = 1$. Only the large-scale part up to harmonic degree and order 12 is shown. The dipole contribution is weak. When either Pm is increased to one or Ra is decreased to 2400, the axial dipole contribution to the field becomes dominant.

Sreenivasan and Jones (2006b) studied the influence of inertial forces by covarying in a set of dynamo models the parameters in such a way that the relative weight of the inertial term in the governing equations changes, whereas the weight of all others forces remains unaffected. Strengthening the inertial forces leads to weaker and less dipolar magnetic fields. Christensen and Aubert (2006) demonstrated that the role of inertial forces is rather universal in controlling the type of dynamo solution. Balancing the inertial term against the Coriolis term in the Navier–Stokes equation, they defined as characteristic parameter measuring their ratio a local (scale-dependent) Rossby number $Ro_\ell = u_{\rm rms}/(\Omega\ell)$, where ℓ is the characteristic length scale of the flow. They showed that, independent of the values of the various control parameters, dipolar dynamos are obtained when Ro_ℓ is below a critical value of about 0.12 and multipolar ones above this value, for cases with no-slip boundaries and driving of convection by fixed temperatures on both boundaries. Also, for other thermal boundary conditions and modes of driving convection, the local Rossby number has been found to be an appropriate ordering parameter, but the critical value for the breakdown of dipolar solutions depends somewhat on the exact conditions (Aubert et al., 2009). For dynamos with stress-free boundary conditions, Ro_ℓ remains a relevant ordering parameter in the sense that the dipolar branch breaks down beyond a critical value close to that for no-slip boundaries, while dipolar and multipolar dynamos coexist below the critical value (Gastine et al., 2012; Yadav et al., 2013a).

A contrasting view on the cause of the dipolar–multipolar transition is given by Soderlund et al. (2012), who calculated the relative contribution of various forces in the Navier–Stokes equation for their dynamo models and argued that the ratio of inertial forces to viscous forces, rather than inertial forces to Coriolis forces, controls the transition.

Dynamos that have dipole-dominated fields for most of the time but show occasional polarity reversals are found in a transitional parameter range between dipolar and multipolar solutions, that is, for values of Ro_ℓ near the critical one (Driscoll and Olson, 2009a; Kutzner and Christensen, 2002; Olson and Christensen, 2006). Olson and Christensen (2006) proposed a relation linking Ro_ℓ to the fundamental control parameters. Based on this scaling law, they suggested that Ro_ℓ in the geodynamo is close to the transition point between the dipolar and the nondipolar regimes and that this may be the reason why Earth shows stochastic reversals.

Inertial forces become larger when convection is driven more strongly. Their adverse influence on dipole field generation can be balanced by enhancing the rotational force. This explains why strongly driven dipolar dynamos need a low value of the Ekman number. It also explains why dipolar dynamos at low magnetic Prandtl number, which obviously need strong driving in order to reach a supercritical value of the magnetic Reynolds number, are only found when also the Ekman number is low. Christensen et al. (1999) and Christensen and Aubert (2006) determined that the minimum value of the magnetic Prandtl number at which dipolar dynamos exist varies with the Ekman number as

$$Pm_{\rm min} \simeq 450E^{3/4} \qquad [55]$$

8.10.4.1.3 Mechanism of magnetic field generation

Several authors have analyzed numerical dynamo solutions in order to clarify the fundamental mechanisms by which the magnetic field is maintained. The term 'mechanism' can be understood in different ways. Often, it refers to the process that generates axisymmetric poloidal field from axisymmetric toroidal field and vice versa, with the mediation of non-axisymmetric field components. Conceptually, this analysis follows closely the mean-field dynamo theory (Chapter 8.03, Section 8.03.4), taking the axisymmetric components as the mean magnetic field and the nonaxisymmetric parts as the fluctuating or small-scale part.

The mechanism is more easily elucidated in weakly driven dynamos, where the flow outside the tangent cylinder is organized in well-defined geostrophic columns with negative helicity in the northern hemisphere and positive helicity in the southern hemisphere. In columnar convection, the helicity (defined as $H=\mathbf{u}\cdot\nabla\times\mathbf{u}$) is coherent within each hemisphere, meaning a systematic correlation of local velocity and local vorticity. Kageyama and Sato (1997b) described the mechanism how the columnar convection cells convert an axisymmetric toroidal field, which is eastward in the northern hemisphere and westward in the southern hemisphere, into the poloidal field of an axial dipole. The process is illustrated in Figure 9(a) showing schematically three steps in the evolution of an initially purely azimuthal field, indicated by two field lines. The field lines are advected by the flow, represented by two geostrophic columns and the superimposed ageostrophic circulation (indicated by open arrows). They are distorted and twisted into a poloidal field geometry following the scheme of the classical Parker loop (see Chapter 8.03, Section 8.03.2.6). An identical field geometry is generated in other pairs of convection columns, and overall, the field has a significant mean meridional component with dipole geometry. In the terminology of mean-field electrodynamics, the axisymmetric poloidal field is generated by an α-effect, although the helical eddies in the flow are rather large-scaled in contrast to the usual assumption of scale separation in mean-field theory. This mechanism for poloidal field generation seems to operate in all published numerical dynamo models with columnar convection. Sreenivasan and Jones (2011) found that the Lorentz force modifies the columnar flow in a way that increases its helicity, in particular when the magnetic field is dipolar and less so for a quadrupolar field, which can explain why the dipolar field geometry seems to be preferred over the quadrupolar geometry.

The axisymmetric toroidal field can, in principle, be produced by an α-effect acting on the dipole field or through shearing it by differential rotation in the mean zonal flow (ω-effect). Depending on which mechanism dominates for the creation of the toroidal mean field, dynamos are classified as α^2-dynamos or $\alpha\omega$-dynamos (see Chapter 8.03, Section 8.03.5.2). The strong axisymmetric toroidal field inside the tangent cylinder that is found in many strongly driven dynamo models (e.g., Glatzmaier and Roberts, 1995a) is clearly due to shearing of poloidal field by the thermal wind circulation (compare Figure 5), that is, an ω-effect. The origin of the toroidal field outside the tangent cylinder is more controversial and may indeed differ between dynamo models. Olson et al. (1999) suggested that it is created by the columnar flow through a mechanism similar to the one that creates the poloidal field. This is illustrated in Figure 9(b), showing the evolution of an initially straight poloidal field line that is advected in the flow. The two nearly azimuthal segments of the field line in the final configuration, which run in opposite direction north and south of the equator, combine with the

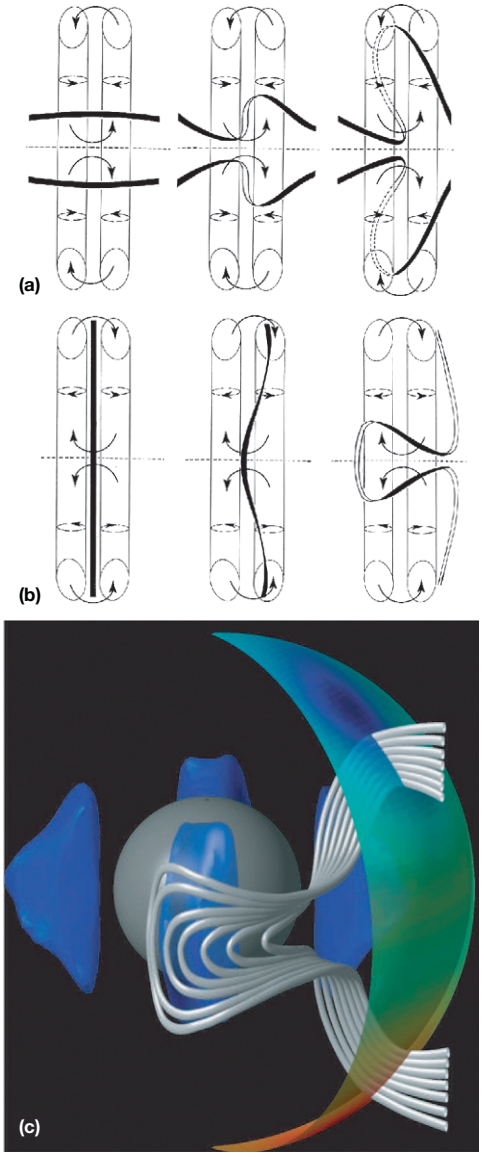

Figure 9 (a) Cartoon showing in a time sequence of the conversion of azimuthal field into poloidal field by columnar convection. The broken line indicates the equatorial plane. Superimposed on the columnar circulation is an ageostrophic flow along the column axis and between the columns; this combination implies negative helicity in the northern hemisphere and positive helicity in the southern hemisphere. (b) Illustration of the generation of axisymmetric toroidal field from poloidal field by columnar convection. (c) Field line bundle in the benchmark dynamo model entering/emerging through one of the high-latitude flux concentrations on the outer boundary (compare Figure 3). The gray sphere in the center is the inner core and isosurfaces of anticyclonic vorticity $\omega_z<0$ are shown in blue. (a) and (b) are reproduced from Olson P, Christensen UR, and Glatzmaier GA (1999). Numerical modeling of the geodynamo: Mechanism of field generation and equilibration. *Journal of Geophysical Research* 104, 10383–10404 with permission by AGU.

identical field configuration in other pairs of convection columns to form the global axisymmetric toroidal field. Note that the final field configuration in Figure 9(a) and 9(b) is similar when it is properly phase-shifted and represents conceptually the actual field-line geometry found in the benchmark dynamo model (Figure 9(c)).

Schrinner et al. (2005, 2007) and Schrinner (2011) investigated the induction process in weakly driven dynamo models in more detail in a mean-field context. They confirmed that basically an α^2-mechanism operates, but they also show that simple mean-field models based on an isotropic α-effect are not adequate. Olson et al. (1999) studied the role of the ω-effect in their dynamo models by isolating the contribution to the generation of the mean axisymmetric toroidal field by shearing of the poloidal field in gradients of the azimuthal circulation. Because outside the tangent cylinder this contribution was found to be largely anticorrelated with the toroidal magnetic field, the ω-effect was ruled out as its main source. Schrinner et al. (2012) found that the ω-effect is the source of the axisymmetric toroidal field in the multipolar branch of dynamo solutions, but not in the dipolar branch.

However, for some dipolar dynamo models, evidence for an essential role of the ω-effect has been presented. Kageyama and Sato (1997a) found that their dynamo did not operate when the zonal flow was artificially suppressed, even though its contribution to the total kinetic energy is rather small. Buffett and Bloxham (2002) addressed the conversion of energy in the model of Kuang and Bloxham (1997, 1999) with stress-free boundaries, in which the axisymmetric toroidal flow component is dominant. They demonstrated that the source term for the axisymmetric toroidal magnetic energy closely matches a particular sink term for the axisymmetric toroidal kinetic energy, which represents the work done against Lorentz forces. This shows clearly that the toroidal magnetic field is generated by the ω-effect in this particular dynamo model. Simitev and Busse (2005) monitored in their dynamo models several 'interaction integrals' that quantify the source for the various magnetic field components in terms of the interaction of different components of the velocity field and magnetic field. They found that the axisymmetric toroidal magnetic field is mainly sustained by the interaction of the axisymmetric toroidal flow with the axisymmetric poloidal field, that is, an ω-effect.

Ishihara and Kida (2002), Aubert et al. (2008b), and Takahashi and Shimizu (2012) studied the field generation mechanism in dipolar dynamo models from a different angle by monitoring characteristic 3-D magnetic field-line structures and the associated magnetic energy density. They identified regions where stretching of magnetic field lines converts kinetic energy into magnetic energy. They found that field-line stretching is closely associated with the columnar helical flow illustrated in Figure 9 and that the intense magnetic flux bundles generated in this way contribute to the axisymmetric poloidal and the axisymmetric toroidal field, which supports an α^2-mechanism.

In summary, an α-effect associated with the helical flow in convection columns generates the axial dipole field in all models that do have a strong dipole. The role of differential rotation for the generation of the axisymmetric toroidal magnetic field seems to differ in various dynamo models. Somewhat surprisingly, this does not necessarily imply strong differences in the structure of the poloidal magnetic field that is observable outside the dynamo region.

Using the velocity field of full MHD dynamo models as input for a kinematic dynamo calculation, Schrinner et al. (2010) surprisingly found that dipolar dynamos are 'kinematically stable.' A 'test field' is advanced in time by solving the magnetic induction equation for the given flow, but it does not react back on the flow. For the flow obtained from multipolar dynamos, a test field (that is not aligned with the actual magnetic field) is found to grow exponentially in time, that is, only the actual magnetic field quenches the velocity field in a way that limits its growth (see also Cattaneo and Tobias, 2009). However, for a flow taken from a dipolar dynamo, even if it fluctuates chaotically with time, the test field does neither grow nor decay but eventually aligns with the actual magnetic field (at an arbitrary amplitude that depends on the initial condition). Schrinner et al. (2010) interpreted this behavior by arguing that the azimuthally and temporally averaged mean-field dynamo operator, which describes the induction of axisymmetric magnetic field by the given flow, has a single dominant eigenmode in case of dipolar dynamos. This mode is (nearly) neutrally stable, whereas all other eigenmodes are strongly damped. In the case of multipolar dynamos, the different eigenmodes have similar growth rates and compete with each other.

8.10.4.1.4 Taylor state and torsional oscillations

Since Ekman number and Rossby number are small for the Earth's core (see Table 1), the geodynamo is thought to operate in a magnetostrophic regime where only Coriolis force, pressure gradient, buoyancy, and Lorentz force contribute to the first-order force balance in the Navier–Stokes equation [1]. The relative motion of the so-called geostrophic cylinders (GCs), concentric cylinders aligned with the rotation axis, then obeys an interesting particular dynamics (see also Chapter 8.04, Section 8.04.5).

Neither pressure gradients nor buoyancy contributes to the azimuthal acceleration of these cylinders. Since in addition the integrated azimuthal Coriolis forces also vanish, the Lorentz force integral taken over the surface of a GC with radius s

$$\tau(s) = \frac{1}{Pm}\int_{GC} \mathrm{d}S\hat{\phi}\cdot[(\nabla\times\mathbf{B})\times\mathbf{B}] \qquad [56]$$

remains the only first-order contribution in this particular force balance and should therefore also be small (Taylor, 1963). More precisely, the locally strong Lorentz force contributions must cancel to the extent that the integral reaches the level of the second-order force contributions, that is, of inertial or viscous forces. The integral τ is commonly called the Taylor integral and the limit $\tau \to 0$ as $E \to 0$ and $Ro \to 0$ defines the Taylor state.

Temporal variations in magnetic field or flow inevitably introduce deviations from the (approximated) Taylor state at some cylindrical radius s. The then sizable Lorentz forces accelerate the respective GC, causing shear in the azimuthal flow. This leads to the production of azimuthal magnetic field by stretching the field component B_s perpendicular to the rotation axis, and the associated magnetic restoring forces result in torsional

oscillations (TOs) that travel toward the inner and outer boundary. TOs can be thought of as one-dimensional Alfvén waves with a characteristic propagation speed of $U_A = B_s/(\rho\mu)^{1/2}$.

Using the conservative estimate of 0.5 mT for the field strength in the core leads to timescales D/U_A in the range of decades. Oscillations with such periods have indeed been identified in the secular variation signal (Dickey and de Viron, 2009; Zatman and Bloxham, 1997, 1999) and may be responsible for geomagnetic jerks (Bloxham et al., 2002) (see also **Chapter 8.04**, Section 8.04.5.3). A more recent detection of traveling waves with a period of 6 years implies a mean internal field of about 2 mT (Gillet et al., 2010a,b), which is compatible with values suggested by extrapolating numerical dynamo simulations (see **Section 8.10.4.1.5**). Dumberry and Mound (2008) pointed out that TOs may be significantly damped by electromagnetic core–mantle coupling and that the observed timescales may rather reflect the excitation mechanism, that is, the inertial dynamics in a more general sense.

Busse and Simitev (2005a) and Takahashi et al. (2005) demonstrated that in their dynamo models, the Lorentz torques on GCs are much larger than their viscous counterparts, which is a prerequisite for Taylor state and TOs. Wicht and Christensen (2010), however, were the first to clearly identify TOs in their dynamo simulations (**Figure 10**). As expected, these specific motions become a more significant part of the azimuthal and axisymmetric dynamics in the simulations once viscous forces assume a secondary role for $E \leq 3 \times 10^{-5}$. In addition, a relatively low Rayleigh number is required to minimize Reynolds stresses, a particular inertia contribution that results from the correlation of small-scale flow components that feed energy into zonal flows via nonlinear momentum advection. Because of the weak inertial effects (low values of the local Rossby number Ro_ℓ), however, such models would never undergo magnetic field reversals. In addition, the spatial field complexity and the general temporal behavior remain too simple compared to observation (see **Section 8.10.4.2**). This suggests that inertial effects may also play a more important role in the Earth's core than the Rossby number implies and that Reynolds stresses may significantly contribute to the secular variation signal interpreted as TOs (Christensen and Aubert, 2006; Wicht and Christensen, 2010).

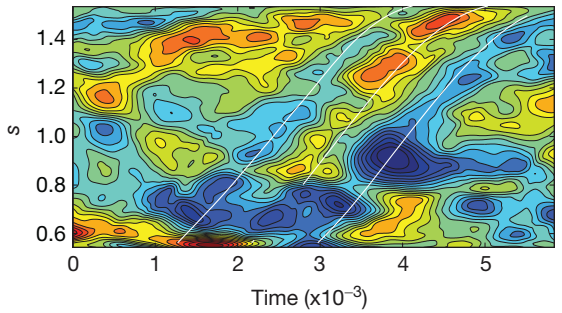

Figure 10 Azimuthal velocity of geostrophic cylinders in a dynamo model at $E = 3 \times 10^{-6}$ and $Ro_\ell = 0.02$. The x-axis shows time in units of the magnetic diffusion time; the y-axis is the cylindrical radius s spanning the region outside the tangent cylinder. White lines mark the path that the waves should take when traveling with the local Alfvén speed. The good agreement confirms that the observed waves are indeed torsional oscillations.

Wicht and Christensen (2010) also pointed out that TOs are generally more difficult to identify in dynamo simulations than in the geomagnetic signal. The reason is that the Alfvén Mach number, the ratio of the typical convective flow velocity to the Alfvén wave speed, is around 0.1 or smaller in the Earth's core but typically of order one in the numerical models. TOs thus propagate clearly faster than the typical convective flow in the Earth's core and are therefore easier to identify than in the simulations where the timescales are similar.

Schaeffer et al. (2012) demonstrated that the reflection of TOs at the outer boundary depends on the magnetic Prandtl number. For Pm values around one, typical for numerical dynamo simulations, the torsional Alfvén waves are absorbed, which is indeed consistent with the simulation results (**Figure 10**). In the geophysical limit of very small Pm, however, the waves are reflected and can cross the core several times before being damped away. Magnetic Prandtl numbers significantly smaller than one thus seem required to more realistically model TOs in the numerical simulations. Since this requires Ekman numbers $E \leq 10^{-6}$, the respective simulations would be extremely costly. Schaeffer et al. (2012) showed that stress-free outer boundary conditions also yield the correct reflection behavior even at larger Pm values. While this offers an easier option for the numerical simulations, it comes at the costs of adopting an unphysical boundary condition. The potential consequences remain to be explored.

8.10.4.1.5 Scaling laws for dynamos

Scaling laws that relate the characteristic properties of convection-driven dynamos in rotating spherical shells, such as the flow velocity or the magnetic field strength, to the control parameters are of fundamental interest. On the one hand, well-established scaling laws are an essential part of a comprehensive dynamo theory. On the other hand, they allow to make predictions for the strength of Earth's paleofield at times when parameters were different than today or to put the properties of the geodynamo in context with dynamos in other planets. In the past, heuristic scaling laws have been presented that were often based on the assumption of a magnetostrophic force balance (see Christensen, 2010, for an overview). Using numerical geodynamo simulations for deriving (or testing) scaling laws started with Christensen and Tilgner (2004), Aubert (2005), and Christensen and Aubert (2006). Because the dynamo properties depend on four control parameters (when the inner core radius and the nature of the boundary conditions are fixed), this enterprise could only start when a large number of results covering a sufficient region of the parameter space had become available.

It was found that an essential step for obtaining simple scaling laws is the introduction of parameters that are independent of any of the three diffusivities that enter into the dynamo problem. As fundamental control parameter, Christensen (2002) defined a modified Rayleigh number that depends on the advected heat flux Q_{adv}:

$$Ra_Q^* = \frac{1}{4\pi r_o r_i} \frac{\alpha g_o Q_{adv}}{\rho c \Omega^3 D^2} \qquad [57]$$

The relation to the conventional Rayleigh R number (eqn [9]) and the modified Rayleigh number Ra (eqn [6]) is

$$Ra_Q^* = Ra(Nu-1)\frac{E^2}{Pr} = R(Nu-1)\frac{E^3}{Pr^2} \quad [58]$$

where $Nu = QD/(4\pi r_o r_i \rho c \kappa \Delta T)$ is the Nusselt number, that is, the ratio of heat flow Q to the heat flow in a conductive state. Note that Ra_Q^* is proportional to the (nondimensional) power generated by buoyancy forces. The characteristic properties of the solution also need to be scaled in a way that does not involve diffusivities. For example, the mean flow velocity is expressed by the Rossby number.

Aubert (2005) studied how the velocity of the mean zonal flow (the axisymmetric component of u_ϕ) depends on Ra_Q^*. In the case of nonmagnetic rotating convection, he found that the zonal flow is mainly driven by inertial effects (Reynolds stresses) and the corresponding Rossby number Ro_{zonal} depends on both Ra_Q^* and the Ekman number. In contrast, in his dynamo cases, the zonal flow arises from a thermal wind effect and its amplitude is found to be a simple function of Ra_Q^*, independent of the parameters E, Pr, and Pm that describe the influence of diffusivities:

$$Ro_{zonal} \simeq Ra_Q^{*1/2} \quad [59]$$

In a more extensive study, Christensen and Aubert (2006) derived scaling laws for the global velocity, described by the Rossby number Ro; the efficiency of heat transport, described by a modified Nusselt number $Nu^* = (Nu-1)EPr^{-1}$; and the magnetic field strength, expressed by the Lorentz number $Lo = B_{rms}/[(\mu\rho)^{1/2}\Omega D]$. They found the latter parameter more useful for describing the magnetic field strength than the conventional Elsasser number (eqn [13]). Christensen and Aubert (2006) used a large set of dynamo models with fixed temperature boundary conditions and restricted their analysis to dynamos with a dipole-dominated magnetic field. They found the following best-fitting scaling laws:

$$Nu^* = 0.074 Ra_Q^{*0.53} \quad [60]$$

$$Ro = 0.85 Ra_Q^{*0.41} \quad [61]$$

$$Lo/f_{ohm}^{1/2} = 0.91 Ra_Q^{*0.34} \quad [62]$$

Based on the idea that the magnetic field strength is determined by the power available to balance ohmic dissipation, a correction factor $f_{ohm}^{1/2}$ has been introduced in eqn [62], where f_{ohm} is the relative contribution of ohmic dissipation to the total dissipation. f_{ohm} is thought to be close to one in the Earth's core. The numerical results fit the scaling law for the modified Nusselt number very well for the dipolar dynamo solutions. However, when inertial forces dominate compared to rotational forces, the dependence of the Nusselt number becomes weaker and more similar to that of turbulent nonrotating convection (King et al., 2010). The fits for the Rossby and Lorentz numbers are decent, the latter being shown in **Figure 11**. The values of the exponents in eqns [60]–[62] are empirical and may be slightly different in the truly asymptotic limit $E \to 0$, that is, being simple rational numbers.

Olson and Christensen (2006) examined a broader set of models, also including nondipolar dynamos, to find a scaling relation for the dipole moment as the main observable for magnetic fields of planets other than Earth. As long as the magnetic field is dipole-dominated, they found that a Lorentz number that characterizes the mean dipole strength at the outer boundary of the dynamo region scales like $Lo_{dip} = \gamma Ra_Q^{*1/3}$, with $\gamma = 0.1 - 0.2$. In the nondipolar regime, the average field inside the dynamo is somewhat weaker and the external dipole field is substantially weaker, but eqn [62] still holds with the same exponent and a smaller prefactor (Christensen, 2010). Aubert et al. (2009) found that basically the same scaling laws are obeyed by dynamos with fixed flux boundary conditions, with internal heating, or with different relative size of the inner core, and Yadav et al. (2013a,b) showed this for dynamos with free-slip boundaries, density stratification, or radial variations in the diffusivities. Takahashi et al. (2008) and Stelzer and Jackson (2013) reanalyzed dipolar dynamos with fixed temperature boundary conditions. The best-fitting exponents found in these studies are very similar to the original values of Christensen and Aubert (2006), in the range 0.41–0.44 for the Rossby number and around 1/3 for the Lorentz number.

The fit of the numerical results for the Rossby number and the Lorentz number can be improved by assuming a weak additional influence of the magnetic Prandtl number (Christensen and Aubert, 2006; Stelzer and Jackson, 2013). The Ekman number and the hydrodynamic Prandtl number do not seem to have a significant effect. The exponents for the dependence on the magnetic Prandtl number are moderate, for the best fit to the Lorentz number; Christensen and Aubert (2006) found a value of 0.11 and Stelzer and Jackson (2013) found 0.15. But the rather large extrapolation from model

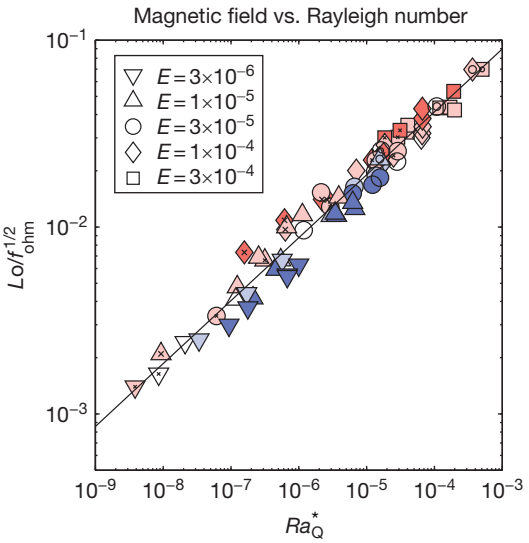

Figure 11 Lorentz number (nondimensional magnetic field strength) corrected for the fraction of ohmic dissipation versus modified Rayleigh number for 72 dynamo models that generate a dipole-dominated magnetic field. The Ekman number is indicated by the shape of the symbol; the magnetic Prandtl number is color-coded ($Pm > 3$ dark red, $1 < Pm \leq 3$ light red, $Pm = 1$ white, $0.3 \leq Pm < 1$ light blue, and $Pm < 0.3$ dark blue). Prandtl numbers other than one are indicated by a large cross ($Pr = 10$), small cross ($Pr = 3$), small circle ($Pr = 0.3$), or large circle ($Pr = 0.1$) inside the main symbol. Adapted from Christensen UR and Aubert J (2006) Scaling properties of convection-driven dynamos in rotating spherical shells and applications to planetary magnetic fields. *Geophysical Journal International* 166, 97–114 with permission by Blackwell.

values of $Pm \sim O(1)$ to core values $\sim O(10^{-6})$ implies that a Prandtl number dependence would have a significant impact.

Using a somewhat more limited set of model results, Christensen and Tilgner (2004) derived a scaling law for the ohmic dissipation time τ_{ohm}, defined as magnetic energy divided by the rate of ohmic dissipation. They found it to depend on the magnetic Reynolds number according to

$$\tau_{\text{ohm}} = 1.74\,\tau_{\text{dipole}} Rm^{-1}, \qquad [63]$$

where $\tau_{\text{dipole}} = r_o^2/(\pi^2\lambda)$ is the dipole decay time. Again, an additional dependence on the magnetic Prandtl number could improve the fit to the model data. Christensen and Tilgner (2004) also determined the ohmic dissipation time for the Karlsruhe laboratory dynamo experiment, in which the magnetic Prandtl number has the small value of a liquid metal, and found it to agree much better with the scaling law eqn [63] than with a more complex one involving Pm. They suggested that a weak dependence of the dynamo properties on the magnetic Prandtl number at values $Pm \sim 1$ may disappear at $Pm \ll 1$. The Pm-independent scaling law would then better represent conditions in the Earth's core. Christensen and Aubert (2006) speculated that this may also apply to the scaling of other properties, like the mean field strength (Lorentz number). Later analyses of the ohmic dissipation time for a larger set of dynamo results (Christensen, 2010; Stelzer and Jackson, 2013) arrived at a slightly weaker dependence on Rm together with a weak influence of E and Pm.

Christensen and Tilgner (2004) (see also Lhuillier et al., 2011) found that the characteristic timescale for the magnetic secular variation in numerical dynamo models (scaled by the magnetic diffusion time) is inversely proportional to the magnetic Reynolds number (see **Section 8.10.4.2.3**). They used this dependence to estimate a characteristic flow velocity in the Earth's core of 0.5 mm s^{-1}, which resulted with their assumed value for the electrical conductivity of 6×10^{-5} Sm^{-1} in a magnetic Reynolds number of approximately 1000. With the recent upward revision of core conductivity (de Koker et al., 2012; Pozzo et al., 2012), this could rise to $Rm \approx 2,500$.

Christensen (2010) discussed the possible theoretical background for the empirically derived scaling laws. An interesting point is the independence of the magnetic field strength [62] on the rotation rate for an exponent of exactly 1/3. Davidson (2013) took this independence as a starting point, and assuming a MAC balance (balance of magnetic, Archimedean, and Coriolis forces), he arrived at an exponent of 4/9 for the Rossby number scaling, very close to the value derived in the simulations. For the ohmic dissipation time, he found a dependence on $Rm^{-3/4}$, slightly weaker but not far from the numerical results. Some progress in the theoretical understanding of the scaling laws has been made, yet a complete and consistent theory is still missing.

Christensen and Aubert (2006) applied eqn [61] to estimate a value of order 10^{-13} for the modified Rayleigh number Ra_Q^* in the Earth's core, using as input the velocity value mentioned earlier inferred from secular variation. For this value, eqn [62] predicts a magnetic field strength in the core of 1.2 mT. The estimate of Ra_Q^* and hence the buoyancy flux obtained in this way is on the low side. Assuming a larger core flow velocity due to the contribution of hidden smaller scales (Finlay and Amit, 2011) would conform with larger values, resulting in a mean core magnetic field up to 3 mT. These values are in agreement with constraints on the field strength inside the core from torsional waves (Gillet et al., 2010a,b) or the observed damping of inner core nutations under the assumption that it is mostly caused by the ohmic dissipation due to field distortion at narrow shear layers (Buffett, 2010). Christensen et al. (2009) compared the predictions of a generalized form of the scaling law for magnetic field strength with the observed field strength of Jupiter and with that of rapidly rotating stars. The good agreement supports a rather wide range of validity of the scaling law and reinforces its applicability to the geodynamo.

The scaling laws that involve a dependence on the magnetic Prandtl number severely underpredict the field strength in the Earth's core (Christensen and Aubert, 2006). Clarifying the role of the magnetic Prandtl number and providing a better theoretical foundation for the scaling laws remains a task for the future.

8.10.4.2 Comparison with the Geomagnetic Field

Many dynamo simulations reproduce the first-order properties of the geomagnetic field: dipole dominance and the correct order of magnitude of global field strength. A more detailed comparison is thus necessary to assess how realistically the different simulations model the geodynamo process. We have to content ourselves with comparing the field above the core surface, since there is little or no information about the geomagnetic field inside the core. This task is difficult for dynamo modelers and geomagnetists alike, since the Earth's magnetic field varies on a large range of timescales, reaching from reversal-rate variations over several tens of million years to geomagnetic jerks representing annual changes. In addition, details of the spatial structure of the field are known to some degree for the recent field but are increasingly less resolved when going back in time. Since **Chapter 8.11** is devoted to reversals and excursion, we concentrate here on timescales from decadal to millennium variations.

In order to compare dimensionless simulations to geomagnetic properties, we have fixed the magnetic diffusion time D^2/λ to 122 kyr by assuming an electrical conductivity of $\sigma = 6 \times 10^5$ Sm^{-1}. This amounts to a dipole decay time of 29 kyr. The field strength is calculated by adopting Earth's rotation rate and a core density of $\rho = 1.1 \times 10^4$ kg m^{-3}. Note that recent ab initio calculation suggests a higher electrical conductivity (Pozzo et al., 2012) that would increase the magnetic diffusion time to about 250 kyr and the dipole decay time to 60 kyr.

8.10.4.2.1 Core–mantle boundary field morphology

How well do we know the geomagnetic field at the top of the dynamo region? Even today, with several satellites measuring the magnetic field with previously unknown precision, there are significant inherent limitations. While the Gauss decomposition separates magnetic fields of external and internal origin, it does not allow to distinguish between Earth's crustal field and the field produced by the dynamo process. Some separation of the two is possible nevertheless, based on two properties of the geomagnetic field. While the dynamo field varies on geologically short timescales, the crustal

magnetization can be regarded stationary in comparison. Furthermore, the crustal field is of smaller scale, leaving the core field at scales below degree 14 basically uncontaminated (Maus et al., 2006). Additional precaution is needed when downward continuing field measurements to the core–mantle boundary, making it necessary to regularize or 'damp' contributions beyond roughly $l=12$ (Bloxham and Gubbins, 1985; Finlay et al., 2012). Within these limitations, modern field models (Maus et al., 2006; Olsen, 2002) provide a global representation of the present geomagnetic field at the core–mantle boundary up to degree and order 14.

Figure 12 compares the radial magnetic field for the year 1990 in the GUFM1 model (Jackson et al., 2000) with two dynamo simulations. While we have selected snapshots that closely match the geomagnetic field, most features are typical for dynamo models in the respective regimes. The longitude is arbitrary in the simulations. Continental contours have been included as a measure for relative size and orientation of magnetic structures. Figure 12(b) and 12(c) depicts a model at a relatively low Ekman number of $E=3\times10^{-5}$. Panel (c) shows the full numerical resolution, while panel (b) shows the same solution subject to a simulated 'crustal' filter that damps contributions beyond degree 12 and excludes contributions beyond degree 14. Figure 12(d) displays the filtered field for a reversing dynamo at $E=3\times10^{-4}$ (Kutzner and Christensen, 2002).

There are many similarities between the geomagnetic field and the simulations apart from the obvious dipole dominance and the approximate agreement in the field strength: weaker field inside the tangent cylinder, strong normal polarity flux lobes close to the tangent cylinder, and pairwise inverse field patches around the equator. 'Normal' and 'inverse' refer to radial magnetic field directions parallel or antiparallel to the dominant dipole direction. The reversing dynamo also possesses inverse field patches inside the tangent cylinder and at midlatitudes in the southern hemisphere, very similar to today's field configuration. While these similarities are truly remarkable, the comparison also reveals discrepancies typical for many dynamo simulations. For example, in the reversing dynamo model, the dipole is significantly less pronounced than in the present geomagnetic field (see also Figure 13). Another deviation concerns the field in the equatorial region. North–south aligned pairs of inverse magnetic field patches dominate the equatorial region in typical dynamo simulations, in particular in the reversing numerical model, but we find mainly normal polarity patches in this region in today's and probably also the historic magnetic field (Finlay, 2005). Wicht and Tilgner (2010) demonstrated that low-Ekman-number simulations tend to replicate this specific feature better.

Note that the simulation in Figure 12(c) shows many small-scale field structures described by spherical harmonic degrees beyond 14. These structures become even smaller for lower Ekman and larger Rayleigh numbers. Field patches that nicely resemble geomagnetic features when subjected to the crustal filter turn out to be enlarged images of much narrower and significantly more complex small-scale features.

In the dynamo simulations, flux maxima and minima have been associated with downwellings and upwellings in the convective flow (Christensen et al., 1998; Kutzner and Christensen, 2004; Olson et al., 1999). The convergent flow associated with downwellings collects magnetic field lines and thereby enhances the already present background field. The divergent flow connected to upwellings has the opposite effect. Intense flux lobes close to the tangent cylinder that are created by downwellings inside cyclonic convection columns and the low field strength around the pole caused by polar upwellings

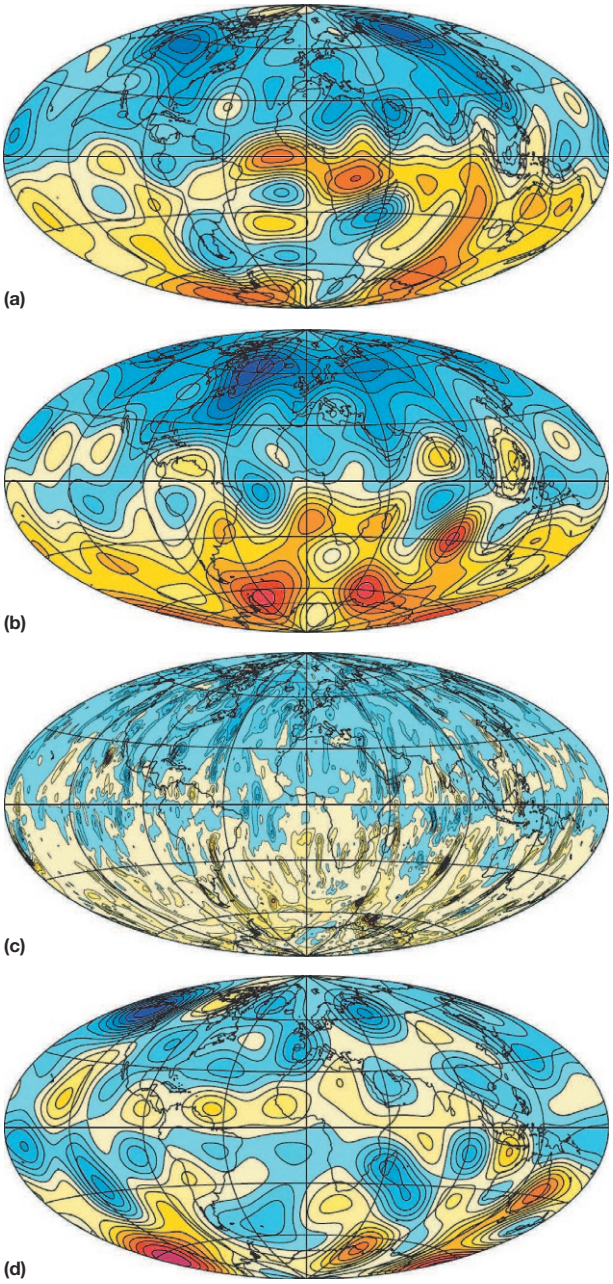

Figure 12 Comparison of the radial magnetic field at the core–mantle boundary for the 1990 GUFM1 model (Jackson et al., 2000) and two different dynamo simulations. (b, c) Present a model at $E=3\times10^{-5}$, $Ra=42\times Ra_c$, $Pm=1$, and $Pr=1$. Spectral filtering similar to the one employed in GUFM1 has been used in (b); (c) B_r at full numerical resolution up to spherical harmonic degree and order 133. The dipole is very stable in this model. (d) The filtered magnetic field of a reversing dynamo at $E=3\times10^{-4}$, $Ra=26\times Ra_c$, $Pm=3$, and $Pr=1$ (Wicht, 2002). We have selected a snapshot during a stable polarity interval.

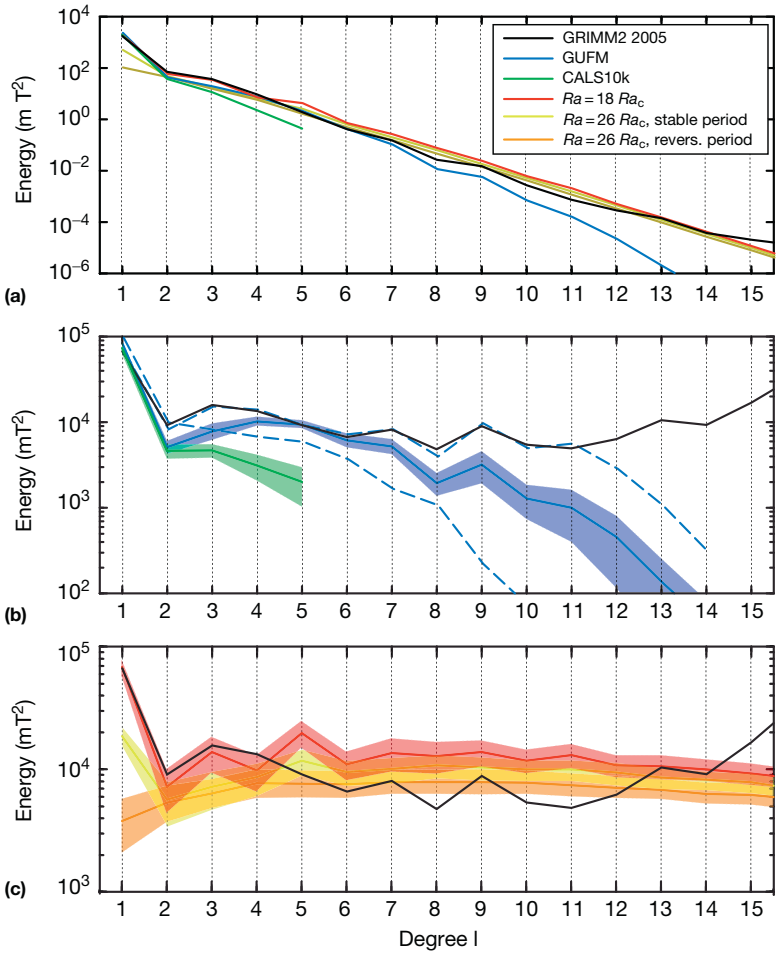

Figure 13 Comparison of time-averaged geomagnetic power spectra for different geomagnetic field models and dynamo simulations. (a) Spectra at Earth surface. (b) Geomagnetic models at core–mantle boundary. Colored bands in the width of the standard deviation indicate time variability. (c) Comparison of the geomagnetic GRIMM2 spectrum with spectra from dynamo simulations at the core–mantle boundary. See text for more explanation.

are prominent examples for these effects. In addition, upwellings create 'dipolar' pairs, consisting of an inverse and a normal polarity patch, by pushing out horizontal field lines toward the exterior. Diffusion takes over close to the outer boundary to finally bring the pair to the CMB (Bloxham, 1986; Christensen et al., 1998). The latter effect could be responsible for the inverse patches identified in the recent geomagnetic field.

Christensen et al. (2010) and Wicht et al. (2011) more closely analyzed the parameter dependence of the time-averaged field morphology in numerical models concerning its similarity to the geomagnetic field. Both concluded that even models at relatively large Ekman numbers can be surprisingly Earth-like provided the Rayleigh number is large enough to yield sufficient spatial and temporal complexity. Christensen et al. (2010) reported that the magnetic Ekman number $E_\lambda = E/Pm$ has to be smaller than 10^{-4} for an Earth-like morphology. In addition, the magnetic Reynolds number should reach at least about 200 with larger values being required at lower E_λ. These results suggest that increasing the magnetic Prandtl number instead of decreasing the Ekman offers an alternative and numerically more affordable path toward more Earth-like models. This path, however, will not lead from nonreversing to reversing dynamos since enhanced temporal variability and specifically reversals require larger Rayleigh numbers (Wicht et al., 2011).

8.10.4.2.2 Magnetic power spectra

The spatial resolution of geomagnetic field models decreases when we go back in time. Historic field models mainly rely on data from geomagnetic observatories and on measurements taken by mariners. They cover up to four centuries (Bloxham and Jackson, 1992; Jackson et al., 2000) and provide Gauss coefficients up to degree 14 in 2.5 year intervals. However, the spatial resolution lies below degree 14 in the earlier epochs of these models due to decreasing data coverage, limited data quality, and the lack of intensity measurements prior to the 1830s. Archaeomagnetic and paleomagnetic data allow to construct field models spanning several thousand years (Hongre et al., 1998; Korte and Constable, 2003, 2005, 2011). The latest models cover the past 10 000 years with a spatial resolution equivalent to degree $l = 4$ and temporal resolution of about 100 years (Korte et al., 2011).

The time dependence of the resolution makes it difficult to decide which of today's smaller magnetic field features are

typical and should therefore be replicated by a realistic dynamo model. Rather than comparing more snapshots of geomagnetic and simulated models for various epochs, we proceed with analyzing magnetic power spectra W_l that describe the magnetic energy density carried by each spherical harmonic degree l (Mauersberger–Lowes spectrum). Figure 13 compares magnetic power spectra of the GRIMM2 model for the year 2005 (Lesur et al., 2010a) (black), time-averaged spectra of the historic GUFM1 model (Jackson et al., 2000) (blue), the archaeomagnetic CALSK10 model (Korte et al., 2011) (green), and geodynamo simulations. Panel (a) shows the spectra at a radial level equivalent to the Earth's surface. Here, differences are hard to discern since all spectra decay similarly with the exception of the time-averaged GUFM1 model where the higher harmonics are obviously subject to stronger damping. Panel (b) visualizes the difference of the three geomagnetic field models at the core–mantle boundary (cmb). Colored bands show the width of the respective standard deviations and illustrate time variability. We have added GUFM1 spectra for the two bounding years of this model, 1590 (lower dashed blue line) and 1990 (upper dashed blue line). The significantly stronger decay of the 1590 model reflects the inferior resolution in earlier years. Differences between the higher harmonic contributions in the 1990 GUFM1 and the 2005 GRIMM2 model indicate the stronger damping of the former. The degree 18 GRIMM2 model is overly optimistic concerning the reliability of magnetic field coefficients beyond degree 12. The lower energy of higher moments in the CALSK10 model is possibly biased by low resolution and strong damping. The larger time variations, on the other hand, are a likely consequence of the longer averaging interval, 10 000 years instead of 400 years for GUFM1 (Korte et al., 2011).

Figure 13(c) compares time-averaged spectra from dynamo simulations with the GRIMM2 spectrum at the cmb. We have again selected models at parameters $E=3\times10^{-4}$, $Pr=1$, and $Pm=3$ for two different Rayleigh numbers: $Ra=18\times Ra_c$ (red, averaged over 64 kyr), representing the stable dipole regime, and $Ra=26\times Ra_c$, representing the reversing case shown in Figure 12. Two spectra for the latter cover a stable polarity interval (yellow, averaged over 43 kyr) and a period during which the dipole is weak and reverses several times (orange, averaged over 46 kyr). The comparison demonstrates that dynamo simulations in the dipole-dominated regime (red and yellow) are well capable of reproducing the dipole moment and the power spectrum of the present geomagnetic field.

A specific feature reproduced by the dynamo simulations is the relatively low geomagnetic quadrupole contribution that lies clearly below the octupole contribution. Maxima at $l=3$ and $l=5$ in the simulation reflect the latitudinal differentiation into the regions inside and outside the tangent cylinder described in Section 8.10.4.1.1 and into the band of inverse field around the equator (Figure 12). Olson and Christensen (2002) reported that the time-averaged octupole is significantly more pronounced in their numerical simulations than in paleomagnetic models (Section 8.10.4.2.4). However, the differentiation becomes weaker when the Rayleigh number is increased. The observable part of the model spectrum is essentially white during unstable periods (orange curve in a Figure 13) with the exception of particularly low dipole and quadrupole contributions. The field seems to lose its large-scale coherence.

8.10.4.2.3 Time variability

A simple global measure for the typical timescales associated with the field contribution of spherical harmonic degree l can be derived from the magnetic power spectrum W_l and the power spectrum of magnetic field variations $\dot{W}_l$:

$$\tau_l^{\mathrm{SV}} = \left(W_l/\dot{W}_l\right)^{1/2} \qquad [64]$$

In dynamo models, τ_l is inversely proportional to the magnetic Reynolds number, as already discussed in Section 8.10.4.1.5, and also to the spherical harmonic degree l (Christensen and Olson, 2003; Christensen and Tilgner, 2004; Christensen et al., 2012; Lhuillier et al., 2011). Based on a set of dynamo simulations, Christensen and Tilgner (2004) derived the scaling

$$\tau_l^{\mathrm{SV}} = 21.7\,\tau_{\mathrm{dipole}}(Rm\,l)^{-1} \qquad [65]$$

Hongre et al. (1998) reported that τ_l^{SV} is typically of the order of a few hundred years in archaeomagnetic data and, like in the numerical models, decreases as l^{-1}. While some authors suggest a somewhat different exponent (Lesur et al., 2008; Olsen et al., 2006) for models of the present geomagnetic field, a detailed statistical analysis by Lhuillier et al. (2011) indicates that the simpler inverse proportionality remains compatible with the data. Equation [65] allows to estimate the Earth's magnetic Reynolds number based on the typical timescales of roughly four centuries and yields $Rm\approx10^3$.

The high quality of modern satellite data has increased the confidence that also the secular acceleration, the second time derivative of the geomagnetic field, can be estimated with sufficient precision (Gillet et al., 2010a,b). A secular acceleration spectrum $\ddot{W}_l$ allows to define the respective timescale:

$$\tau_l^{\mathrm{SA}} = \left(\dot{W}_l/\ddot{W}_l\right)^{1/2} \qquad [66]$$

which is bound to be shorter than its secular variation counterpart. Degrees $l=2$ to $l=8$ are regarded as trustworthy and all provide roughly the same timescale of $\tau_l^{\mathrm{SA}}\approx10$ year (Christensen et al., 2012; Holme et al., 2011). Degree $l=1$ suffers from an incomplete external field model, while an insufficient temporal/spatial resolution compromises the higher degrees. Christensen et al. (2012) found the secular acceleration timescale in their dynamo simulations to be roughly independent of the spherical harmonic degree up to $l\approx8$. The respective timescale of approximately 10 years is very similar to the geomagnetic one for models with Earth-like values of Rm. For larger degrees, however, τ_l^{SA} drops as l^{-1} in the models, just like the secular variation timescale. The acceleration behavior at large l is explained by flow advection of the changing magnetic field, whereas the 10-year timescale at low l directly reflects the timescale of flow acceleration (Christensen et al., 2012).

While dynamo simulations do a good job in reproducing the statistical properties of geomagnetic field variability, the actual structural pattern of variation is a more difficult issue. The westward drift is a long-standing feature in the historic magnetic field and describes the motion of magnetic structures along the equator in the Atlantic hemisphere (see, e.g., Finlay and Jackson, 2003). On longer timescales, however, the drift is a complex function of latitude and time (Dumberry and Finlay, 2007; Wardinski and Korte, 2008).

Westward and eastward drifts at low latitudes are present in several dynamo simulations (Glatzmaier and Roberts, 1996a; Kuang and Bloxham, 1997) and advection and wave propagation can be the causes (Christensen and Olson, 2003; Kono et al., 2000; Rau et al., 2000). Both mechanisms may contribute, one or the other being dominant at different times. Aubert (2005) analyzed time-averaged zonal flows for a suite of dynamo simulations (see **Section 8.10.4.1.5**) and found it generally very similar to the flow inferred from present-day secular variation (Hulot et al., 2002).

A fast eastward zonal flow inside the north polar cap of the tangent cylinder and its somewhat weaker southern counterpart seem typical for the geomagnetic secular variation of more recent epochs (Amit and Olson, 2004, 2006; Hulot et al., 2002; Olson and Aurnou, 1999). These vortices were first described by Glatzmaier and Roberts (1995b) and can be found in many dynamo simulations (e.g., Aubert, 2005; Sreenivasan and Jones, 2006a). Their origin is the thermal wind associated with hot plumes rising from the inner core boundary (see **Section 8.10.4.1.1**).

Progress has also been made in the understanding of long timescale variations. Constable and Johnson (2005) stacked data from different sources to cover geomagnetic dipole variations from timescale of centuries to tens of million years. A Fourier analysis reveals four distinct frequency ranges: (1) an ultralow-frequency (UF) band with timescales longer than 10 Myr representing mainly the presence of superchrons, (2) a low-frequency (LF) band with timescales between 0.1 and 10 Myr typical for reversal and excursion rates, (3) a transitional (TF) band with timescales between 1 kyr and 0.1 Myr reflecting typical paleosecular variations and durations of reversals and excursions, and (4) a high-frequency (HF) band with timescales between a century and a millennium covering typical secular variation.

The power decreases with frequency f and most of the energy is contained in the LF and TF bands. Since the UF band covers only the very long fluctuation, its 'color' is hard to judge, but the LF band clearly seems to be white, that is, the power does not depend on the frequency. Sakuraba and Hamano (2007) extended the analysis by also including historic and recent field models and suggested slopes of $f^{-5/3}$ for the TF and $f^{-11/3}$ for the HF bands. The former value is compliant with the classical inertial range turbulence. They also present a dynamo simulation that shows similar slopes in both bands. Since the simulation ran too short and showed no reversals, UF and LF bands are not covered and the slope in the TF band remains ambiguous.

Olson et al. (2012) combined several dynamo simulations to cover a broader frequency range. The low resolution required at higher Ekman numbers $E \geq 10^{-3}$ allows for long integration times including hundreds of reversals. Lower Ekman number simulations, on the other hand, may better reflect the high-frequency behavior but are numerically too expensive for covering the longer timescales. Since the model parameters are generally not realistic, several ways of rescaling the dimensionless simulations can be used. Both the magnetic diffusion time and the convective overturn time are directly relevant for the dynamo process and therefore seem viable timescale options. Olson et al. (2012) demonstrated that the latter does a better job in collapsing the dipole moment frequency spectra from different dynamo models. The combined spectra are largely compliant with the findings of Constable and Johnson (2005) and show the four distinct bands with similar frequency slopes.

8.10.4.2.4 Comparison with the paleomagnetic field

Scarcity and uncertain dating of paleomagnetic data permit only statistical field models covering the past 5 Myr (Constable and Johnson, 1999; Constable and Parker, 1988; Hatakeyama and Kono, 2002; Johnson and Constable, 1995, 1997; Johnson et al., 2008; Kelly and Gubbins, 1997; Kono and Tanaka, 1995). Constable and Parker (1988) suggested that each Gauss coefficient may be treated as an independent normally distributed random variable assuming that the dynamo works as a so-called giant Gaussian process. The statistical paleomodel is then defined by mean and standard deviation of the Gauss coefficients, the latter serving as a measure for the amplitude of the paleosecular variation. This approach allows to disregard the severe dating uncertainties.

Most statistical paleosecular models indicate that all mean coefficients vanish except for the dominant axial dipole, the axial quadrupole, and possibly also the axial octupole. The latter two amount only to a few percent of the axial dipole. Since mantle influence may play an important role in determining the time-averaged paleofield, we will discuss this issue in **Section 8.10.4.2.5**. Constable and Parker (1988) proposed a particularly simple statistical secular variation model where the standard deviation only depends on degree l. This model was later modified to account for the observed latitudinal dependence of the scatter in the virtual geomagnetic pole (see Hulot et al. (2010) and references therein).

Paleomagnetists commonly express directional data obtained at a specific site by the position (longitude, latitude) that a virtual geomagnetic (north) pole (VGP) would assume in a purely dipolar field. The angular standard deviation around the mean VGP position is called VGP scatter. When averaged in longitude and over latitudinal bands, the VGP scatter shows a very distinct latitude dependence (**Figure 14**), rising from about 12° at the equator to about 20° at higher latitudes

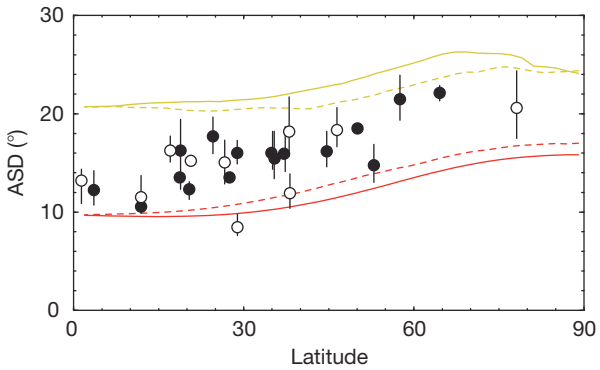

Figure 14 Azimuthally averaged angular standard deviation of the VGP position (ASD) after Kono and Roberts (2002) (symbols with error bars) and for the stable (red) and reversing (yellow) dynamos shown in **Figure 13**. Closed symbols and solid lines (open symbols, dashed lines) denote northern hemisphere (southern hemisphere) results. In the reversing simulation, transitional VGPs further away than 45° from either pole have been disregarded in the analysis.

(Kono et al., 2000). This dependence could not be reproduced by the models of Glatzmaier et al. (1999), where no significant latitudinal variation is found. The models of Sakuraba and Kono (1999), Wicht (2005), and Christensen and Olson (2003) show the correct latitudinal variation, but the variation amplitude is too high in the former two dynamos and too low in the latter. **Figure 14** displays values of the angular standard deviation (ASD) of the VGP for the two numerical dynamo models whose spectra are shown in **Figure 13**. We have averaged over time spans of 120 and 500 kyr, respectively, for sites on a one by one degree grid. The paleomagnetic ASD values shown for comparison are based on datasets spanning 5 Myr with a much scarcer coverage in time and space (Kono et al., 2000). The latitude dependence is nicely reproduced and the amplitudes now embrace the paleomagnetic values, being too low for $Ra = 18 \times Ra_c$ and too high for $Ra = 26 \times Ra_c$. Numerical models thus also seem capable of reproducing the correct variation amplitude provided the Rayleigh number is chosen accordingly.

An analysis of the dynamo simulation by Sakuraba and Kono (1999) suggests that an increased standard deviation in the g_{21} and h_{21} coefficients leads to the latitude dependence (Kono et al., 2000). This is also a favored explanation for the statistical paleomagnetic models, superseding the original assumption that the standard deviation only depends on degree l (Hulot and Gallet, 1996).

8.10.4.2.5 Mantle influence

The sluggish convection in Earth's mantle determines the power available to drive the dynamo by controlling the heat flux through the core–mantle boundary. Besides the total flux, also, the horizontal variations matter. As long as the longitudinal symmetry is not broken, any nonaxisymmetric dynamo feature should average out over time, leaving a mean magnetic field that only depends on latitude. The growing evidence for persistent nonaxisymmetric features in the geomagnetic field and also a north–south asymmetry is commonly explained with the laterally inhomogeneous outer boundary heat flux imprinted by the lower mantle.

Since the mantle evolves on timescales of tens of million years, its thermal structure can be regarded as stationary on typical dynamo timescales. The sizable lateral temperature variations in the lower mantle adjust to the practically constant temperature at the top of the core over a thermal boundary layer at the bottom of the mantle. Combining models of the lower mantle thermal structure with estimates for the boundary layer thickness provides lateral variations in the radial temperature gradients and thus a heat flux pattern at the core–mantle boundary (cmb). Information about the temperature structure can be deduced from seismic tomography models. The interpretation is complicated by the fact that the seismic velocities depend not only on temperature but also on composition and possible phase transitions (postperovskite and partial melt) (Amit and Choblet, 2009). Details may be a matter of debate, but the heat flux pattern is clearly dominated by Y_{22}, the spherical harmonic function of degree $l = 2$ and order $m = 2$. Estimates suggest that the variation amplitude amounts to about 30% of the superadiabatic heat flux but larger peak values seem possible (Aubert et al., 2007).

A growing number of numerical models adopt a 'tomographic' outer boundary heat flux pattern to elucidate its impact on the dynamo process. The first attempt by Glatzmaier et al. (1999) mainly addressed the influence on the reversal rate and is discussed in **Chapter 8.11** along with subsequent work on reversals. Here, we consider the impact of heterogeneous heat flux on magnetic field and core flow structure.

A particularly prominent nonaxisymmetric feature is the intense magnetic flux 'lobes' underneath Canada and Siberia that are evident in the recent (**Figure 12**) and historic magnetic field and can also be discerned in time-averaged archaeomagnetic (Korte and Constable, 2006; Korte et al., 2011) and paleomagnetic models (Johnson et al., 2008; Kelly and Gubbins, 1997). A corresponding pair of southern flux lobes is present in the recent, the historic, and likely also the archaeomagnetic fields (Korte and Holme, 2010; Korte et al., 2011). The position of the flux lobes seems to fluctuate considerably on a millennial timescale around the long-term mean position (Amit et al., 2010, 2011; Korte and Holme, 2010). Single lobes can also disappear for some time, and there are periods where three lobes may have been present in the northern hemisphere (Korte and Holme, 2010).

As already discussed earlier, even with a homogenous outer boundary condition, dynamo simulations tend to produce similar flux lobes at comparable latitudes. The longitude remains arbitrary but can be surprisingly persistent even on a millennial timescale (Wicht et al., 2011). Continuity on the million year scale, however, is best explained by a nonaxisymmetric outer boundary heat flux pattern (Bloxham, 2002; Olson and Christensen, 2002). Tomographic pattern can perfectly lock the solutions to the mantle, but only at unrealistically small Rayleigh numbers where the time dependence is generally weak (Gubbins et al., 2007; Sreenivasan, 2009; Sreenivasan and Gubbins, 2008; Willis et al., 2007). In the more strongly driven simulations by Amit et al. (2010), the lobes show a variability reminiscent of that in the archaeomagnetic field (Amit et al., 2011; Korte and Holme, 2010). The location and number of flux lobes in the time-averaged field, however, depend on the model parameters (Amit et al., 2010). Sreenivasan and Gubbins (2008) and Sreenivasan (2009) reported that a weakly convecting or even stably stratified outer layer allows to more effectively lock the solution to the mantle. The existence of such a layer has been suggested by several authors on different grounds (e.g., Gubbins and Davies (2013) and references therein). For example, recently revised thermal conductivity estimates imply that the outer part of the Earth's core may be subadiabatic (Pozzo et al., 2012).

The secular variation seems to be significantly lower in the Pacific than in the Atlantic hemisphere in the historic (Jackson et al., 2000), the archaeomagnetic (Korte and Constable, 2006), and possibly also the paleomagnetic fields. Using a tomographic cmb heat flux pattern, Bloxham (2002) and Christensen and Olson (2003) indeed found reduced secular variation where the flux is lower than average underneath the Pacific. However, Christensen and Olson (2003) pointed out that the zonal variation in secular variation amplitude is quite weak in the models and significantly smaller than the latitudinal variation that features prominently in paleomagnetic VGP scatter.

The present and historic magnetic spectra show a particularly weak quadrupole contribution. On the archaeomagnetic

and paleomagnetic timescale, however, the axisymmetric quadrupole amounts to a few percent of the axial dipole. Axial dipole and quadrupole belong to the two different equatorial symmetry families (see **Section 8.10.4.1.1**). The presence of both these families suggests that the dynamo is operating differently in the northern hemisphere than in the southern hemisphere. On a shorter timescale, this may simply reflect normal dynamic fluctuation. Persistence on a longer timescale, however, requires a breaking of the equatorial symmetry, and the cmb heat flux pattern once more seems a likely candidate. Since the dominant Y_{22} pattern is equatorially symmetric, other secondary contributions have to do the job. Olson and Christensen (2002) ran simulations with different heat flux patterns and reported that only a pure degree $l=1$ and order $m=0$ type yields a significant time-averaged quadrupole component while a topographic pattern fails to do so. McMillan et al. (2001) arrived at the same conclusion based on simulations by Glatzmaier et al. (1999). The persistent octupole component discussed for some paleomagnetic models (Hulot et al., 2010) on the other hand is typical for dynamo simulations even with homogeneous outer boundary heat flux (Olson and Christensen, 2002). It is mostly the expression of the weakened field inside the tangent cylinder and the flux lobes discussed earlier.

Aubert et al. (2007) used numerical dynamo simulations to explore the influence of different cmb heat flux patterns on the fluid motion at the top of the free stream, that is, just underneath the Ekman boundary layer. They reported that, like for homogeneous boundary conditions (Aubert, 2005), the time-averaged flow is governed by the thermal wind balance and therefore roughly follows the temperature structure at the top of the core (see also Sreenivasan, 2009). How closely this temperature structure matches the imposed cmb heat flux structure and how deeply its influence penetrates into the core depend on the simulations parameters. For example, smaller Rayleigh numbers and larger heat flux variation amplitudes promote a closer match and deeper penetration. The azimuthal shift between both structures, reported earlier by Gibbons and Gubbins (2000) and Olson and Christensen (2002), seems to depend on the Péclet number, the ratio of thermal diffusion time to overturn time. Aubert et al. (2007) suggested that the shift vanishes in the large Péclet number regime relevant for Earth.

The results from Aubert et al. (2007) also indicate that the time-averaged core flow based on historic magnetic field models may already reveal some mantle influence. This implies vice versa that the time-averaged flow at the top of the free stream can be inferred from the cmb heat flux pattern. Tests show that this roughly works in certain regions but fails for other (Amit and Choblet, 2009, 2012; Amit et al., 2008). However, the many uncertainties and assumptions entering this problem make it difficult to judge the validity of this approach.

Coupling to the mantle thermal structure may also explain two other interesting observations. Aubert et al. (2008a) demonstrated that a tomographic cmb heat flux pattern can result in a quasipersistent flow cyclone that more efficiently cools one side of the inner core. This resulting hemispheric difference in inner core growth may lead to differences in the iron grain matrix that could potentially explain the seismic inhomogeneities in the outer 100 km of the inner core. The second observation that can be explained by a tomographic heat flux pattern is a preference of virtual magnetic poles to follow two distinct latitude bands during reversals (Gubbins and Love, 1998). Dynamo simulations by Coe et al. (2000) and Kutzner and Christensen (2004) show that the tomographic heat flux pattern promotes a concentration at the same bands identified in the paleomagnetic data. These bands represent regions of increased heat flux causing stronger magnetic up- and downwellings and thus more pronounced magnetic flux concentrations. Magnetic directional data therefore tend to point to this region when the dipole is weak during reversals.

The available results already indicate that using a tomographic pattern may be essential for replicating the detailed structure of the geomagnetic field and its secular variation. However, the parameter dependence reported by several authors indicates that more numerical studies are required to elucidate the impact of the cmb heat flux pattern on the dynamo process. Scanning, for example, different Ekman and Rayleigh numbers may ultimately allow to extrapolate the effects to Earth.

8.10.5 Perspectives

Numerical geodynamo models have had a remarkable success in matching geomagnetic field properties, to an extent that was not dreamed of twenty years ago. They produce dipole-dominated magnetic fields of the right strength, reproduce the observed temporal variability and field morphology, and show reversal behavior similar to that deduced from paleomagnetism.

However, not all models perform equally well. The values of fundamental control parameters cannot match Earth values, and in the first geodynamo models, their values had been chosen rather arbitrarily or according to the numerical feasibility. More recently, progress has been made in establishing scaling laws that relate characteristic dynamo properties to the control parameters. The results are encouraging and suggest that, despite large parameter discrepancies, the models may fall into the same dynamic regime as the actual geodynamo. So far, these laws are partly empirical and their range of validity remains unclear. To better consolidate them, simulations at more extreme parameter values, such as Ekman numbers $E<10^{-6}$ and magnetic Prandtl numbers $Pm\ll 1$, are needed, which will require tremendous computational resources.

We must also develop a better theoretical understanding of the force balance in the dynamo models and compare it to the expected balance in the Earth's core. How important is viscous friction in the dynamo models and at which Ekman number will its influence become negligible? Do small unresolved scales act mainly as an energy sink, or do they play a significant role for the induction process? What determines the magnetic field variations on the decadal timescale? Are there essential differences between dynamos operating at a magnetic Prandtl number of order one and those working at a very low value of Pm? To answer such questions and to consolidate the theoretical basis of the scaling laws remains a task for the future.

In addition to better understanding convection-driven dynamos in the most basic setup, the consequences of various 'real

Earth' complications need to be explored. How does the interplay of compositional and thermal buoyancy (double-diffusive convection) affect the dynamo? Are Boussinesq models basically adequate, or do non-Boussinesq effects such as fluid compressibility and the redistribution of thermal energy by ohmic heating have a sizable impact? What are the most appropriate boundary and coupling conditions at the core–mantle boundary and the inner core boundary (e.g., is the flux of light element at the inner core boundary heterogeneous?), and how does this affect the dynamo? Are there stably stratified layers at the top of the Earth's core (e.g., because of a significantly subadiabatic thermal gradient) or above the inner core (e.g., because of melting of iron on one side of the inner core), and how does this affect the dynamo, in particular with respect to observable properties of the geomagnetic field? This list of open questions is certainly far from exhaustive.

Earth is not the only magnetic planet in the solar system. It would strengthen the confidence in the geodynamo models tremendously if it could be shown that the models can reproduce the field strength and geometry of other planets, after adaptation to the specific conditions in these objects. So far, a comparative dynamo theory covering the diversity of planetary magnetic fields is in its infancy (Stanley and Glatzmaier, 2010) (see also **Chapter 10.07**).

Up to now, geodynamo modeling has been used as a tool for understanding the principal properties of the geomagnetic field. An exciting perspective for the future is that actual observations of the field can be used in a data assimilation context to construct models that better represent the underlying dynamic state not only close to the core–mantle boundary but also at depth. Data assimilation can also help to improve predictions for the magnetic field evolution over the next couple of decades. First steps in this direction have been taken (Aubert, 2013; Fournier et al., 2010); see also **Chapter 5.02**.

References

Abramowitz M and Stegun IA (1984) *Pocketbook of Mathematical Functions*. Thun: Verlag Harry Deutsch.

Alboussière T, Deguen R, and Melzani M (2010) Melting-induced stratification above the Earth's inner core due to the convective translation. *Nature* 466: 744–747.

Amit H, Aubert J, and Hulot G (2010) Stationary, oscillating or drifting geomagnetic flux patches? *Journal of Geophysical Research* 115, B07108.

Amit H, Aubert J, Hulot G, and Olson P (2008) A simple model for mantle-driven flow at the top of Earth's core. *Earth, Planets and Space* 60: 845–854.

Amit H and Choblet G (2009) Mantle-driven geodynamo features—Effects of post-perovskite phase transition. *Earth, Planets and Space* 61: 1255–1268.

Amit H and Choblet G (2012) Mantle-driven geodynamo features—Effects of compositional and narrow D″ anomalies. *Physics of the Earth and Planetary Interiors* 190: 34–43.

Amit H, Korte M, Aubert J, Constable C, and Hulot G (2011) The time-dependence of intense archeomagnetic flux patches. *Journal of Geophysical Research* 116, B12106.

Amit H and Olson P (2004) Helical core flow from geomagnetic secular variation. *Physics of the Earth and Planetary Interiors* 147: 1–25.

Amit H and Olson P (2006) Time-average and time-dependent parts of core flow. *Physics of the Earth and Planetary Interiors* 155: 120–139.

Aubert J (2005) Steady zonal flows in spherical shell dynamos. *Journal of Fluid Mechanics* 542: 53–67.

Aubert J (2013) Flow throughout the Earth's core inverted from geomagnetic observations and numerical dynamo models. *Geophysical Journal International* 192: 1537–1556.

Aubert J, Amit H, and Hulot G (2007) Detecting thermal boundary control in surface flows from numerical dynamos. *Physics of the Earth and Planetary Interiors* 160: 143–156.

Aubert J, Amit H, Hulot G, and Olson P (2008a) Thermochemical flows couple the Earth's inner core growth to mantle heterogeneity. *Nature* 454: 758–760.

Aubert J, Aurnou J, and Wicht J (2008b) The magnetic structure of convection-driven numerical dynamos. *Geophysical Journal International* 172: 945–956.

Aubert J and Dumberry M (2011) Steady and fluctuating inner core rotation in numerical geodynamo models. *Geophysical Journal International* 184: 162–170.

Aubert J, Labrosse S, and Poitou C (2009) Modelling the paleo-evolution of the geodynamo. *Geophysical Journal International* 179: 1414–1429.

Aubert J and Wicht J (2004) Axial versus equatorial dynamo models with implications for planetary magnetic fields. *Earth and Planetary Science Letters* 221: 409–419.

Aurnou JM, Brito D, and Olson PL (1996) Mechanics of inner core superrotation. *Geophysical Research Letters* 23: 3401–3404.

Bloxham J (1986) The expulsion of magnetic flux from the Earth's core. *Philosophical Transactions of the Royal Society of London* 87: 669–678.

Bloxham J (2002) Time-independent and time-dependent behaviour of high-latitude flux bundles at the core–mantle boundary. *Geophysical Research Letters* 39: 1854.

Bloxham J and Gubbins D (1985) The secular variation of Earth's magnetic field. *Nature* 317: 777–781.

Bloxham J and Jackson A (1992) Time-dependent mapping of the magnetic field at the core–mantle boundary. *Journal of Geophysical Research* 97: 19537–19563.

Bloxham J, Zatman S, and Dumberry M (2002) The origin of geomagnetic jerks. *Nature* 420: 65–68.

Braginsky SI and Roberts PH (1995) Equations governing convection in Earth's core and the geodynamo. *Geophysical and Astrophysical Fluid Dynamics* 79: 1–97.

Buffett BA (1996) Gravitational oscillations in the length of day. *Geophysical Research Letters* 23: 2279–2282.

Buffett BA (1997) Geodynamic estimates of the viscosity of the Earth's inner core. *Nature* 388: 571–573.

Buffett BA (2010) Tidal dissipation and the strength of the Earth's internal magnetic field. *Nature* 468: 952–954.

Buffett BA and Bloxham J (2002) Energetics of numerical geodynamo models. *Geophysical Journal International* 149: 211–224.

Buffett BA and Glatzmaier GA (2001) Gravitational braking of inner-core rotation in geodynamo simulations. *Geophysical Research Letters* 27: 3125–3128.

Bullard EC and Gellman H (1954) Homogeneous dynamos and terrestrial magnetism. *Proceedings of the Royal Society of London A* 247: 213–278.

Busse FH and Simitev R (2005a) Convection in rotating spherical fluid shells and its dynamo states. In: Soward AM, Jones CA, Hughes DW, and Weiss NO (eds.) *Fluid Dynamics and Dynamos in Astrophysics and Geophysics*, pp. 359–392. New York: Taylor and Francis.

Busse FH and Simitev R (2005b) Dynamos driven by convection in rotating spherical shells. *Astronomische Nachrichten* 326: 231–240.

Busse FH and Simitev RD (2006) Parameter dependences of convection-driven dynamos in rotating spherical fluid shells. *Geophysical and Astrophysical Fluid Dynamics* 100: 341–361.

Cattaneo F and Hughes DW (2006) Dynamo action in a rotating convective layer. *Journal of Fluid Mechanics* 553: 401–418.

Cattaneo F and Tobias SM (2009) Dynamo properties of the turbulent velocity field of a saturated dynamo. *Journal of Fluid Mechanics* 621: 205–214.

Chan KH, Zhang K, Li L, and Liao X (2007) A new generation of convection-driven spherical dynamos using EBE finite element method. *Physics of the Earth and Planetary Interiors* 163: 251–265.

Chan KH, Zhang KK, Zou J, and Schubert G (2001) A non-linear, 3-D spherical α^2 dynamo using a finite element method. *Physics of the Earth and Planetary Interiors* 128: 35–50.

Chen QN and Jones CA (2008) Similarity and dynamic similarity models for large-eddy simulations of a rotating convection-driven dynamo. *Geophysical Journal International* 172: 103–114.

Christensen UR (2001) Zonal flow driven by deep convection in the major planets. *Geophysical Research Letters* 28: 2553–2556.

Christensen UR (2002) Zonal flow driven by strongly supercritical convection in rotating spherical shells. *Journal of Fluid Mechanics* 470: 115–133.

Christensen UR (2010) Dynamo scaling laws: Applications to the planets. *Space Science Reviews* 152: 565–590.

Christensen UR (2011) Geodynamo models: Tools for understanding properties of earth's magnetic field. *Physics of the Earth and Planetary Interiors* 187: 157–169.

Christensen UR and Aubert J (2006) Scaling properties of convection-driven dynamos in rotating spherical shells and applications to planetary magnetic fields. *Geophysical Journal International* 166: 97–114.

Christensen UR, Aubert J, Busse FH, et al. (2001) A numerical dynamo benchmark. *Physics of the Earth and Planetary Interiors* 128: 25–34.

Christensen UR, Aubert J, and Hulot G (2010) Conditions for Earth-like geodynamo models. *Earth and Planetary Science Letters* 296: 487–496.

Christensen UR, Holzwarth V, and Reiners A (2009) Energy flux determines magnetic field strength of planets and stars. *Nature* 457: 167–169.

Christensen UR and Olson P (2003) Secular variation in numerical geodynamo models with lateral variations of boundary heat flow. *Physics of the Earth and Planetary Interiors* 138: 39–54.

Christensen UR, Olson P, and Glatzmaier GA (1998) A dynamo model interpretation of geomagnetic field structures. *Geophysical Research Letters* 25: 1565–1568.

Christensen UR, Olson P, and Glatzmaier GA (1999) Numerical modeling of the geodynamo: A systematic parameter study. *Geophysical Journal International* 138: 393–409.

Christensen UR and Tilgner A (2004) Power requirement of the geodynamo from ohmic losses in numerical and laboratory dynamos. *Nature* 429: 169–171.

Christensen UR, Wardinski I, and Lesur V (2012) Time scales of geomagnetic secular acceleration in satellite field models and geodynamo models. *Geophysical Journal International* 190: 243–254.

Clune TC, Eliott JR, Miesch MS, Toomre J, and Glatzmaier GA (1999) Computational aspects of a code to study rotating turbulent convection in spherical shells. *Parallel Computing* 25: 361–380.

Coe RS, Hongre L, and Glatzmaier GA (2000) An examination of simulated geomagnetic reversals from a paleomagnetic perspective. *Philosophical Transactions of the Royal Society of London A* 358: 1141–1170.

Constable CG and Johnson CL (1999) Anisotropic paleosecular variation models: Implication for geomagnetic field observables. *Physics of the Earth and Planetary Interiors* 115: 35–51.

Constable C and Johnson C (2005) A paleomagnetic power spectrum. *Earth and Planetary Science Letters* 153: 61–73.

Constable CG and Parker RL (1988) Statistics of the geomagnetic secular variation for the past 5 m.y. *Journal of Geophysical Research* 93: 11569–11581.

Corgne A, Keshav S, Fei YW, and McDonough WF (2007) How much potassium is in the Earth's core? New insights from partitioning experiments. *Earth and Planetary Science Letters* 256: 567–576.

Davidson PA (2013) Scaling laws for planetary dynamos. *Geophysical Journal International* 195: 67–74. http://dx.doi.org/10.1093/gji/ggt167.

Davies CJ and Gubbins D (2011) A buoyancy profile for the Earth's core. *Geophysical Journal International* 187: 549–563.

de Koker N, Steinle-Neumann G, and Vlček V (2012) Electrical resistivity and thermal conductivity of liquid Fe alloys at high P and T, and heat flux in the Earth's core. *Proceedings of the National Academy of Sciences* 109: 4070–4073.

Dharmaraj G and Stanley S (2012) Effect of inner core conductivity on planetary dynamo models. *Physics of the Earth and Planetary Interiors* 212–213: 1–9.

Dickey JO and de Viron O (2009) Leading modes of torsional oscillations within the Earth's core. *Geophysical Research Letters* 36: 15302.

Dormy E, Cardin P, and Jault D (1998) MHD flow in a slightly differentially rotating spherical shell, with conducting inner core, in a dipolar magnetic field. *Earth and Planetary Science Letters* 158: 15–24.

Driscoll P and Olson P (2009a) Effects of buoyancy and rotation on the polarity reversal frequency of gravitationally driven numerical dynamos. *Geophysical Journal International* 178: 1337–1350.

Driscoll P and Olson P (2009b) Polarity reversals in geodynamo models with core evolution. *Earth and Planetary Science Letters* 282: 24–32.

Duarte L, Gastine T, and Wicht J (2013) Anelastic dynamo models with variable electrical conductivity: An application to gas giants. *Physics of the Earth and Planetary Interiors* 222: 22–34.

Dumberry M and Finlay CC (2007) Eastward and westward drift of the Earth's magnetic field for the last three millennia. *Earth and Planetary Science Letters* 254: 146–157.

Dumberry M and Mound JE (2008) Constraints on core–mantle electromagnetic coupling from torsional oscillation normal modes. *Journal of Geophysical Research* 113: 3102.

Evonuk M and Samuel H (2012) Simulating rotating fluid bodies: When is vorticity generation via density stratification important? Earth Planet. *Science Letters* 317–318: 1–7.

Featherstone N (2012) Scaling the pseudo-spectral mountain: Spherical anelasticity at 10,000 cores. AGU Fall Meeting, San Francisco, Oral contribution.

Finlay CC (2005) Hydromagnetic waves in Earth's core and their influence on geomagnetic secular variation. Ph.D. thesis, School of Earth and Environment, University of Leeds.

Finlay CC and Amit H (2011) On flow magnitude and field-flow alignment at Earth's core surface. *Geophysical Journal International* 186: 175–192.

Finlay CC and Jackson A (2003) Equatorially dominated magnetic field change at the surface of Earth's core. *Science* 300: 2084–2086.

Finlay CC, Jackson A, Gillet N, and Olsen N (2012) Core surface magnetic field evolution 2000–2010. *Geophysical Journal International* 189: 761–781.

Fournier A, Bunge H-P, Hollerbach R, and Vilotte J-P (2004) Application of the spectral-element method to the axisymmetric Navier–Stokes equation. *Geophysical Journal International* 156: 682–700.

Fournier A, Bunge H-P, Hollerbach R, and Vilotte J-P (2005) A Fourier-spectral element algorithm for thermal convection in rotating axisymmetric containers. *Journal of Computational Physics* 204: 462–489.

Fournier A, Hulot G, Jault D, et al. (2010) An introduction to data assimilation and predictability in geomagnetism. *Space Science Reviews* 155: 247–291.

Gastine T, Duarte L, and Wicht J (2012) Dipolar versus multipolar dynamos: The influence of the background density stratification. *Astronomy and Astrophysics* 546: A19.

Gastine T and Wicht J (2012) Effects of compressibility on driving zonal flow in gas giants. *Icarus* 219: 428–442.

Gibbons SJ and Gubbins D (2000) Convection in the Earth's core driven by lateral variations in the core–mantle boundary heat flux. *Geophysical Journal International* 142: 631–642.

Gillet N, Jault D, Canet E, and Fournier A (2010a) Fast torsional waves and strong magnetic fields within the Earth's core. *Nature* 465: 74–77.

Gillet N, Lesur V, and Olsen N (2010b) Geomagnetic core field secular variation models. *Space Science Reviews* 155: 129–145.

Glatzmaier GA (1984) Numerical simulation of stellar convective dynamos. 1. The model and methods. *Journal of Computational Physics* 55: 461–484.

Glatzmaier GA (2002) Geodynamo simulations—How realistic are they? *Annual Review of Earth and Planetary Sciences* 30: 237–257.

Glatzmaier GA, Coe RS, Hongre L, and Roberts PH (1999) The role of the Earth's mantle in controlling the frequency of geomagnetic reversals. *Nature* 401: 885–890.

Glatzmaier GA and Roberts PH (1995a) A three-dimensional convective dynamo solution with rotating and finitely conducting inner core and mantle. *Physics of the Earth and Planetary Interiors* 91: 63–75.

Glatzmaier GA and Roberts PH (1995b) A three-dimensional self-consistent computer simulation of a geomagnetic field reversal. *Nature* 337: 203–209.

Glatzmaier GA and Roberts PH (1996a) An anelastic evolutionary geodynamo simulation driven by compositional and thermal convection. *Physica D* 97: 81–94.

Glatzmaier GA and Roberts PH (1996b) Rotation and magnetism of Earth's inner core. *Science* 274: 1887–1891.

Glatzmaier GA and Roberts PH (1997) Simulating the geodynamo. *Contemporary Physics* 38: 269–288.

Grote E and Busse FH (2001) Dynamics of convection and dynamos in rotating spherical fluid shells. *Fluid Dynamics Research* 28: 349–368.

Grote E, Busse FH, and Tilgner A (1999) Convection-driven quadrupolar dynamos in rotating spherical shells. *Physical Review E* 60: 5025–5028.

Grote E, Busse FH, and Tilgner A (2000a) Effects of hyperdiffusivities on dynamo simulations. *Geophysical Research Letters* 27: 2001–2004.

Grote E, Busse FH, and Tilgner A (2000b) Regular and chaotic spherical shell dynamos. *Physics of the Earth and Planetary Interiors* 117: 259–272.

Gubbins D (2008) Implications of kinematic dynamo studies for the geodynamo. *Geophysical Journal International* 173: 79–91.

Gubbins D and Davies CJ (2013) The stratified layer at the core–mantle boundary caused by barodiffusion of oxygen, sulphur and silicon. *Physics of the Earth and Planetary Interiors* 215: 21–28.

Gubbins D and Love JJ (1998) Preferred VGP paths during geomagnetic polarity reversals: Symmetry considerations. *Geophysical Research Letters* 25: 1079–1082.

Gubbins D and Roberts P (1987) Magnetohydrodynamics of the Earth's core. In: Jacobs JA (ed.) *Geomagnetism*, vol. 2, pp. 1–183. London: Academic Press.

Gubbins D, Willis AP, and Sreenivasan B (2007) Correlation of Earth's magnetic field with lower mantle thermal and seismic structure. *Physics of the Earth and Planetary Interiors* 162: 256–260.

Harder H and Hansen U (2005) A finite-volume solution method for thermal convection and dynamo problems in spherical shells. *Geophysical Journal International* 161: 522–532.

Hatakeyama T and Kono M (2002) Geomagnetic field model for the last 5 Myr: Time-averaged field and secular variation. *Physics of the Earth and Planetary Interiors* 133: 181–215.

Healy DM Jr., Kostelec PJ, and Rockmore D (2004) Towards safe and effective high-order Legendre transforms with application to FFTs for the 2-sphere. *Advances in Computational Mathematics* 21: 59–105.

Heimpel MH, Aurnou JM, and Wicht J (2005) Simulation of equatorial and high-latitude jets on Jupiter in a deep convection model. *Nature* 438: 193–196.

Hejda P and Reshetnyak M (2003) Control volume method for the dynamo problem in the sphere with the free rotating inner core. *Studia Geophysica et Geodaetica* 47: 147–159.
Hollerbach R (2000) A spectral solution of the magneto-convection equations in spherical geometry. *International Journal for Numerical Methods in Fluids* 32: 773–797.
Hollerbach R and Jones CA (1993) A geodynamo model incorporating a finitely conducting inner core. *Physics of the Earth and Planetary Interiors* 75: 317–327.
Holme R, Olsen N, and Bairstow FL (2011) Mapping geomagnetic secular variation at the core–mantle boundary. *Geophysical Journal International* 186: 521–528.
Hongre L, Hulot G, and Khokhlov A (1998) An analysis of the geomagnetic field over the past 2000 years. *Physics of the Earth and Planetary Interiors* 106: 311–335.
Hori K, Wicht J, and Christensen UR (2010) The effect of thermal boundary conditions on dynamos driven by internal heating. *Physics of the Earth and Planetary Interiors* 182: 85–97.
Hori K, Wicht J, and Christensen UR (2012) The influence of thermo-compositional boundary conditions on convection and dynamos in a rotating spherical shell. *Physics of the Earth and Planetary Interiors* 196–197: 32–48.
Hulot G, Eymin C, Langlais B, Mandea M, and Olson N (2002) Small-scale structure of the geodynamo inferred from Ørsted and Magsat satellite data. *Nature* 416: 620–623.
Hulot G, Finlay CC, Constable CG, Olsen N, and Mandea M (2010) The magnetic field of planet Earth. *Space Science Reviews* 152: 159–222.
Hulot G and Gallet Y (1996) On the interpretation of virtual geomagnetic pole (VGP) scatter curves. *Physics of the Earth and Planetary Interiors* 95: 37–53.
Ishihara N and Kida S (2000) Axial and equatorial magnetic dipoles generated in a rotating spherical shell. *Journal of the Physical Society of Japan* 69: 1582–1585.
Ishihara N and Kida S (2002) Dynamo mechanism in a rotating spherical shell: Competition between magnetic field and convection vortices. *Journal of Fluid Mechanics* 465: 1–32.
Jackson A, Jonkers ART, and Walker MR (2000) Four centuries of geomagnetic secular variation from historical records. *Philosophical Transactions of the Royal Society of London* A358: 957–990.
Johnson CL and Constable CG (1995) Time averaged geomagnetic field as recorded by lava flows over the past 5 Myr. *Geophysical Journal International* 122: 489–519.
Johnson CL and Constable CG (1997) Time averaged geomagnetic field: Global and regional biases for 0–5 Myr. *Geophysical Journal International* 131: 643–666.
Johnson CL, Constable CG, Tauxe L, et al. (2008) Recent investigations of the 0–5 Ma geomagnetic field recorded by lava flows. *Geochemistry, Geophysics, Geosystems* 9: Q04032.
Jones CA (2011) Planetary magnetic fields and fluid dynamos. *Annual Review of Fluid Mechanics* 43: 583–614.
Kageyama A, Miyagoshi T, and Sato T (2008) Formation of current coils in geodynamo simulations. *Nature* 454: 1106–1109.
Kageyama A and Sato T (1995) Computer simulation of a magnetohydrodynamic dynamo. II. *Physics of Plasmas* 2: 1421–1431.
Kageyama A and Sato T (1997a) Dipole field generation by an MHD dynamo. *Plasma Physics and Controlled Fusion* 39: 83–92.
Kageyama A and Sato T (1997b) Velocity and magnetic field structures in a magnetohydrodynamic dynamo. *Physics of Plasmas* 4: 1569–1575.
Kageyama A, Watanabe K, and Sato T (1993) Simulation study of a magnetohydrodynamic dynamo: Convection in a rotating shell. *Physics of Fluids B* 24: 2793–2806.
Kageyama A and Yoshida M (2005) Geodynamo and mantle convection simulations on the Earth Simulator using the Yin-Yang grid. *Journal of Physics: Conference Series* 16: 325–338.
Katayama JS, Matsushima M, and Honkura Y (1999) Some characteristics of magnetic field behavior in a model of MHD dynamo thermally driven in a rotating spherical shell. *Physics of the Earth and Planetary Interiors* 111: 141–159.
Kelly P and Gubbins D (1997) The geomagnetic field over the past 5 million years. *Geophysical Journal International* 128: 315–330.
King E, Soderlund K, Christensen U, Wicht J, and Aurnou J (2010) Convective heat transfer in planetary dynamo models. *Geochemistry, Geophysics, Geosystems* 11: Q06016.
Kono M and Roberts PH (2002) Recent geodynamo simulations and observations of the geomagnetic field. *Reviews of Geophysics* 40: 1013.
Kono M, Sakuraba A, and Ishida M (2000) Dynamo simulation and palaeosecular variation models. *Philosophical Transactions of the Royal Society of London* 358: 1123–1139.
Kono M and Tanaka H (1995) Mapping the Gauss coefficients to the pole and the models of paleosecular variation. *Journal of Geomagnetism and Geoelectricity* 47: 115–130.
Korte M and Constable CG (2003) Continuous global geomagnetic field models for the past 3000 years. *Physics of the Earth and Planetary Interiors* 140: 73–89.
Korte M and Constable CG (2005) Continuous geomagnetic field models for the past 7 millennia: 2. CALS7K. *Geochemistry, Geophysics, Geosystems* 6: Q02H16.
Korte M and Constable CG (2006) Centennial to millennial geomagnetic secular variations. *Geophysical Journal International* 167: 43–52.
Korte M and Constable CG (2011) Improving geomagnetic field reconstructions for 0–3 ka. *Physics of the Earth and Planetary Interiors* 188: 247–259.
Korte M, Constable C, Donadini F, and Holme R (2011) Reconstructing the Holocene geomagnetic field. *Earth and Planetary Science Letters* 312: 497–505.
Korte M and Holme R (2010) On the persistence of geomagnetic flux lobes in global Holocene field models. *Physics of the Earth and Planetary Interiors* 182: 179–186.
Kuang W and Bloxham J (1997) An Earth-like numerical dynamo model. *Nature* 389: 371–374.
Kuang W and Bloxham J (1999) Numerical modeling of magnetohydrodynamic convection in a rapidly rotating spherical shell: Weak and strong field dynamo action. *Journal of Computational Physics* 153: 51–81.
Kutzner C and Christensen UR (2000) Effects of driving mechanisms in geodynamo models. *Geophysical Research Letters* 27: 29–32.
Kutzner C and Christensen UR (2002) From stable dipolar to reversing numerical dynamos. *Physics of the Earth and Planetary Interiors* 131: 29–45.
Kutzner C and Christensen UR (2004) Simulated geomagnetic reversals and preferred virtual geomagnetic pole paths. *Geophysical Journal International* 157: 1105–1118.
Lesur V and Gubbins D (1999) Evaluation of fast spherical transforms for geophysical application. *Geophysical Journal International* 139: 547–555.
Lesur V, Wardinski I, Hamoudi M, and Rother M (2010) The second generation of the GFZ reference internal magnetic model: GRIMM-2. *Earth, Planets and Space* 62: 765–773.
Lesur V, Wardinski I, Rother M, and Mandea M (2008) GRIMM: The GFZ reference internal magnetic model based on vector satellite and observatory data. *Geophysical Journal International* 173: 382–394.
Lhuillier F, Fournier A, Hulot G, and Aubert J (2011) The geomagnetic secular variation timescale in observations and numerical dynamo models. *Geophysical Research Letters* 38: L09306.
Li J, Sato T, and Kageyama A (2002) Repeated and sudden reversals of the dipole field generated by spherical dynamo action. *Science* 295: 1887–1890.
Lister JR and Buffett BA (1995) The strength and efficiency of thermal and compositional convection in the geodynamo. *Physics of the Earth and Planetary Interiors* 91: 17–30.
Loper DE (1978) Some thermal consequences of the gravitationally powered dynamo. *Journal of Geophysical Research* 83: 5961–5970.
Makinen AM and Deuss A (2011) Global seismic body wave observations of temporal variations in the Earth's inner core, and implications for its differential rotation. *Geophysical Journal International* 187: 355–370.
Manglik A, Wicht J, and Christensen UR (2010) A dynamo model with double diffusive convection for Mercury's core. *Earth and Planetary Science Letters* 289: 619–628.
Matsui H and Buffett BA (2005) Sub-grid scale model for convection-driven dynamos in a rotating plane layer. *Physics of the Earth and Planetary Interiors* 153: 74–82.
Matsui H and Okuda H (2004) Treatment of the magnetic field for geodynamo simulations using the finite element method. *Earth, Planets and Space* 56: 945–954.
Matsushima M (2006) Reexamination of a scale-similarity model for the subgrid-scale flux in the Earth's core. *Geophysical and Astrophysical Fluid Dynamics* 100: 363–377.
Maus S, Rother M, Stolle C, et al. (2006) Third generation of the Potsdam Magnetic Model of the Earth (POMME). *Geochemistry, Geophysics, Geosystems* 7: Q07008.
McMillan DG, Constable CG, Parker RL, and Glatzmaier GA (2001) A statistical analysis of magnetic fields from some geodynamo simulations. *Geochemistry, Geophysics, Geosystems* 2: 11. http://dx.doi.org/10.1029/2000GC000130.
Miyagoshi T, Kageyama A, and Sato T (2010) Zonal flow formation in the Earth's core. *Nature* 463: 793–796.
Nelson NJ, Brown BP, Brun AS, Miesch MS, and Toomre J (2013) Magnetic wreaths and cycles in convective dynamos. *Astrophysical Journal* 762: 73.
Olsen N (2002) A model of the geomagnetic field and its secular variation for epoch 2000 estimated from Ørsted data. *Geophysical Journal International* 149: 454–462.
Olsen N, Lühr H, Sabaka TJ, et al. (2006) Chaos—A model of the geomagnetic field derived from CHAMP, Ørsted and SAC-C magnetic satellite data. *Geophysical Journal International* 166: 67–75.
Olson P and Aurnou J (1999) A polar vortex in the Earth's core. *Nature* 402: 170–173.
Olson P and Christensen UR (2002) The time-averaged magnetic field in numerical dynamos with nonuniform boundary heat flow. *Geophysical Journal International* 151: 809–823.

Olson P and Christensen UR (2006) Dipole moment scaling for convection-driven planetary dynamos. *Earth and Planetary Science Letters* 250: 561–571.

Olson P, Christensen UR, and Driscoll PE (2012) From superchrons to secular variation: A broadband dynamo frequency spectrum for the geomagnetic dipole. *Earth and Planetary Science Letters* 319–320: 75–82.

Olson P, Christensen UR, and Glatzmaier GA (1999) Numerical modeling of the geodynamo: Mechanism of field generation and equilibration. *Journal of Geophysical Research* 104: 10383–10404.

Phillips CG and Ivers DJ (2003) Strong field anisotropic diffusion models for the Earth's core. *Physics of the Earth and Planetary Interiors* 140: 13–28.

Pozzo M, Davies C, Gubbins D, and Alfe D (2012) Thermal and electrical conductivity of iron at Earth's core conditions. *Nature* 485: 355–358.

Press WH, Teukolsky SA, Vetterling WT, and Flannery BP (2003) *Numerical Recipes*, 2nd ed., vol. 1. Cambridge: Cambridge University Press.

Rama Murthy V, van Westrenen W, and Fei Y (2003) Experimental evidence that potassium is a substantial radioactive heat source in planetary cores. *Nature* 423: 163–165.

Rau S, Christensen UR, Jackson A, and Wicht J (2000) Core flow inversions tested with numerical dynamo models. *Geophysical Journal International* 141: 485–497.

Roberts PH and Glatzmaier GA (2000) A test of the frozen-flux approximation using a new geodynamo model. *Philosophical Transactions. Royal Society of London* 358: 1109–1121.

Rotvig J and Jones CA (2002) Rotating convection-driven dynamos at low Ekman number. *Physical Review E* 66: 056308.

Sakuraba A and Hamano Y (2007) Turbulent structure in Earth's fluid core inferred from time series of geomagnetic dipole moment. *Geophysical Research Letters* 34: 15308.

Sakuraba A and Kono M (1999) Effect of the inner core on the numerical simulation of the magnetohydrodynamic dynamo. *Physics of the Earth and Planetary Interiors* 111: 105–121.

Sakuraba A and Roberts PH (2009) Generation of a strong magnetic field using uniform heat flux at the surface of the core. *Nature Geoscience* 2: 802–805.

Schaeffer N (2012) Efficient Spherical Harmonic Transforms aimed at pseudo-spectral numerical simulations. *Geochemistry, Geophysics, Geosystems* 14: 751–758.

Schaeffer N, Jault D, Cardin P, and Drouard M (2012) On the reflection of Alfvén waves and its implication for Earth's core modeling. *Geophysical Journal International* 191: 508–516.

Schrinner M (2011) Global dynamo models from direct numerical simulations and their mean-field counterparts. *Astronomy and Astrophysics* A108: 121.

Schrinner M, Petitdemange L, and Dormy E (2012) Dipole collapse and dynamo waves in global direct numerical simulations. *Astrophysical Journal* 752: 121.

Schrinner M, Radler K-H, Schmitt D, Rheinhardt M, and Christensen U (2005) Mean-field view on rotating magnetoconvection and a geodynamo model. *Astronomische Nachrichten* 326: 245–249.

Schrinner M, Radler K-H, Schmitt D, Rheinhardt M, and Christensen U (2007) Mean-field concept and direct numerical simulation of rotating magnetoconvection and the geodynamo. *Geophysical and Astrophysical Fluid Dynamics* 101: 81–116.

Schrinner M, Schmidt D, Cameron R, and Hoyng P (2010) Saturation and time dependence of geodynamo models. *Geophysical Journal International* 182: 675–681.

Schubert G and Zhang K (2001) Effects of an electrically conducting inner core on the planetary and stellar dynamos. *Astrophysical Journal* 557: 930–942.

Simitev R and Busse FH (2005) Prandtl-number dependence of convection-driven dynamos in rotating spherical fluid shells. *Journal of Fluid Mechanics* 532: 365–388.

Simitev R and Busse FH (2009) Bistability and hysteresis of dipolar dynamos generated by turbulent convection in rotating spherical shells. *Europhysics Letters* 85: 19001.

Soderlund KM, King E, and Aurnou JM (2012) The influence of magnetic fields in planetary dynamo models. *Earth and Planetary Science Letters* 333–334: 9–20.

Spotz WF and Swarztrauber PN (2001) A performance comparison of associated Legendre projections. *Journal of Computational Physics* 168: 339–355.

Sreenivasan B (2009) On dynamo action produced by boundary thermal coupling. *Physics of the Earth and Planetary Interiors* 177: 130–138.

Sreenivasan B and Gubbins D (2008) Dynamos with weakly convecting outer layers: Implications for core–mantle boundary interaction. *Geophysical and Astrophysical Fluid Dynamics* 102: 395–407.

Sreenivasan B and Jones CA (2005) Structure and dynamics of the polar vortex in the Earth's core. *Geophysical Research Letters* 32, L20301.

Sreenivasan B and Jones CA (2006a) Azimuthal winds, convection and dynamo action in the polar regions of planetary cores. *Geophysical and Astrophysical Fluid Dynamics* 100: 319–339.

Sreenivasan B and Jones CA (2006b) The role of inertia in the evolution of spherical dynamos. *Geophysical Journal International* 164: 467–476.

Sreenivasan B and Jones CA (2011) Helicity generation and subcritical behaviour in rapidly rotating dynamos. *Journal of Fluid Mechanics* 633: 5–30.

St. Pierre MG (1993) The strong-field branch of the Childress-Soward dynamo. In: Proctor MRE, et al. (eds.) *Solar and Planetary Dynamos*, 329–337.

Stanley S and Bloxham J (2004) Convective-region geometry as the cause of Uranus' and Neptune's unusual magnetic fields. *Nature* 428: 151–153.

Stanley S and Glatzmaier G (2010) Dynamo models for planets other than Earth. *Space Science Reviews* 152: 617–650.

Stellmach S and Hansen U (2004) Cartesian convection-driven dynamos at low Ekman number. *Physical Review E* 70: 056312.

Stelzer Z and Jackson A (2013) Extracting scaling laws from numerical dynamo models. *Geophysical Journal International* 193: 1265–1276.

Takahashi F, Matsushima M, and Honkura Y (2005) Simulations of a quasi-Taylor state geomagnetic field including polarity reversals on the Earth simulator. *Science* 309: 459–461.

Takahashi F, Matsushima M, and Honkura Y (2008) Scale variability in convection-driven MHD dynamos at low Ekman number. *Physics of the Earth and Planetary Interiors* 167: 168–178.

Takahashi F and Shimizu H (2012) A detailed analysis of a dynamo mechanism in a rotating spherical shell. *Journal of Fluid Mechanics* 701: 228–250.

Taylor JB (1963) The magneto-hydrodynamics of a rotating fluid and the Earth's dynamo problem. *Proceedings of the Royal Society of London* 274: 274–283.

Tilgner A (1999) Spectral methods for the simulation of incompressible flows in spherical shells. *International Journal for Numerical Methods in Fluids* 30: 713–724.

Tilgner A (2004) Small Scale Kinematic Dynamos: Beyond the a-Effect. *Geophysical and Astrophysical Fluid Dynamics* 98: 225–234.

Tilgner A (2005) Precession-driven dynamos. *Physics of Fluids* 17: 034104.

Wardinski I and Korte M (2008) The evolution of the core-surface flow over the last seven thousands years. *Journal of Geophysical Research* 113: 5101.

Wicht J (2002) Inner-core conductivity in numerical dynamo simulations. *Physics of the Earth and Planetary Interiors* 132: 281–302.

Wicht J (2005) Palaeomagnetic interpretation of dynamo simulations. *Geophysical Journal International* 162: 371–380.

Wicht J and Busse FH (1997) Magnetohydrodynamic dynamos in rotating spherical shells. *Geophysical and Astrophysical Fluid Dynamics* 86: 103–109.

Wicht J and Christensen UR (2010) Torsional oscillations in dynamo simulations. *Geophysical Journal International* 181: 1367–1380.

Wicht J and Olson P (2004) A detailed study of the polarity reversal mechanism in a numerical dynamo model. *Geochemistry, Geophysics, Geosystems* 5: Q03H10.

Wicht J, Stellmach S, and Harder H (2009) Numerical models of the geodynamo: From fundamental Cartesian models to 3D simulations of field reversals. In: Glassmeier KH, Soffel H, and Negendank JFW (eds.) *Geomagnetic Field Variations*, pp. 107–158. Berlin: Springer.

Wicht J, Stellmach S, and Harder H (2011) Numerical dynamo simulations: From basic concepts to realistic models. In: Freeden W, Nashed M, and Sonar T (eds.) *Handbook of Geomathematics*, pp. 459–502. Berlin/Heidelberg/New York: Springer.

Wicht J and Tilgner A (2010) Theory and modeling of planetary dynamos. *Space Science Reviews* 152: 501–542.

Willis AP, Sreenivasan B, and Gubbins D (2007) Thermal core–mantle interaction: Exploring regimes for locked dynamo action. *Physics of the Earth and Planetary Interiors* 165: 83–92.

Xu S and Szeto AMK (1994) Gravitational coupling in the Earth's interior revisited. *Geophysical Journal International* 118: 94–100.

Xu S and Szeto AMK (1998) The coupled rotation of the inner core. *Geophysical Journal International* 133: 279–297.

Yadav RK, Gastine T, and Christensen UR (2013a) Scaling laws in spherical shell dynamos with free-slip boundaries. *Icarus* 225: 185–193.

Yadav RK, Gastine T, Christensen UR, and Duarte LDV (2013b) Consistent scaling laws in anelastic spherical shell dynamos. *Astrophysical Journal* 774: 6.

Zatman S and Bloxham J (1997) Torsional oscillations and the magnetic field within the Earth's core. *Nature* 388: 760–761.

Zatman S and Bloxham J (1999) On the dynamical implication of models of B_s in the Earth's core. *Geophysical Journal International* 138: 679–686.

Zhang K and Busse FH (1988) Finite amplitude convection and magnetic field generation in a rotating spherical shell. *Geophysical and Astrophysical Fluid Dynamics* 44: 33–53.

Zhang K and Busse FH (1989) Convection driven magnetohydrodynamic dynamos in rotating spherical shells. *Geophysical and Astrophysical Fluid Dynamics* 49: 97–116.

Zhang K and Busse FH (1990) Generation of magnetic fields by convection in a rotating spherical fluid shell of infinite Prandtl number. *Physics of the Earth and Planetary Interiors* 59: 208–222.

Zhang K and Gubbins D (1993) Convection in a rotating spherical fluid shell with an inhomogeneous temperature boundary condition at infinite Prandtl number. *Journal of Fluid Mechanics* 250: 209–232.

Zhang K and Jones CA (1997) The effect of hyperviscosity on dynamo models. *Geophysical Research Letters* 24: 2869–2872.

Zhang J, Song X, Li Y, Richards PG, Sun X, and Waldhauser F (2005) Inner core differential motion confirmed by earthquake waveform doublets. *Science* 309: 1357–1360.

This page intentionally left blank

8.11 Magnetic Polarity Reversals in the Core

GA Glatzmaier and RS Coe, University of California, Santa Cruz, CA, USA

© 2015 Elsevier B.V. All rights reserved.

8.11.1	Introduction	279
8.11.2	Observations	279
8.11.3	Models	286
8.11.4	Conclusions	293
References		293

8.11.1 Introduction

Paleomagnetic observations have provided much information about the nature of geomagnetic dipole reversals and three-dimensional (3D) magnetohydrodynamic (MHD) computer models are beginning to provide insight to the reversal mechanism. Reversals typically take 2000–12 000 years to occur – one to two orders of magnitude shorter than the dipole-dominated, stable polarity epochs between reversals. However, the durations of both the polarity transitions and epochs vary greatly. The average reversal frequency appears to depend on the degree of equatorial symmetry of the nonaxial dipole (NAD) field (i.e., the total field minus the axial dipole term) and may have been greatly reduced prior to ~1 Ga. Virtually all records document lowered intensity during reversals, but they differ in complexity of transitional direction change. At least some reversals have highly complex transition paths. In addition, stable polarity epochs are often punctuated by large directional excursions and reduced intensity that occur more frequently than reversals and may be regarded as failed reversals. A statistical bias of transition poles for preferred geographical regions that correlate with lower-mantle tomography has been claimed, and such bias has been produced in dynamo simulations employing laterally varying heat flux at the core–mantle boundary (CMB). Higher-fidelity records at multiple locations over the globe are needed to establish how the field varies in time and space during reversals and to provide guidance for computer modeling. No external trigger is necessary for reversals, which occur as a natural result of the very nonlinear dynamo process; that is, the flow, field, and thermodynamic variables of the Earth's outer fluid core all depend on time and space and on each other in a chaotic way. The more realistic computer simulations suggest that MHD instabilities continually occur but only one in many attempts results in a complete reversal of the magnetic dipole field and that these successful reversals often have different morphologies and durations. Computer models have provided new insights into the mechanism of the geodynamo and its reversals, but much better spatial resolution, lower viscosity, and longer simulations are needed to reveal and understand the complex turbulent processes that underlie the polarity reversal phenomenon.

8.11.2 Observations

The observational evidence for evaluating and improving geodynamo simulations comes from direct observations of the geomagnetic field over the past few centuries and from the paleomagnetism of magnetic materials, such as rocks, fired artifacts, adobe, and even pigments from paintings, over the rest of geologic time (see **Chapters 5.01–5.07**; see also **Chapters 5.08–5.14**). Thus, for information about most geomagnetic behavior, we rely upon the results of paleomagnetic studies. These show us that the Earth's magnetic field has been dominantly dipolar in the past, as it is today. Moreover, to a reasonable approximation, it averages to axial dipolar over a few tens of thousands of years (e.g., Merrill, 1996). This is demonstrated for the past 150 My by the agreement between plate reconstructions based on marine magnetic anomalies and paleomagnetic apparent polar wander paths (Besse and Courtillot, 2002). The preponderance of paleomagnetic evidence suggests that dipolar dominance was typical earlier as well (McElhinny, 2004), perhaps even during much of the Precambrian, but Precambrian evidence is sparse and equivocal (Dunlop and Yu, 2004). To the second order, however, a small but significant departure from dipolar of the time-averaged field has long been noted (Wilson, 1971). Averaged over the past 5 My, the departure can be represented as an axial quadrupole contribution that is 3–5% of, and the same sign as, the axial dipole (Johnson et al., 2008; McElhinny, 2004). The comparison of paleomagnetic and plate–tectonic continental reconstructions suggests that a 3% axial quadrupole component may have been typical over the past 200 My (Besse and Courtillot, 2002).

The other salient feature of the field is that it reverses polarity. Geologically speaking, reversals occur very quickly. Even for the most recent, Matuyama–Brunhes reversal, which occurred 0.78 Ma, the error in age for the best-dated transitional basalt flows is comparable to the transition duration (Singer et al., 2005). For this reason, the duration of reversals must be obtained from sedimentary records, using the stratigraphic thicknesses of the transition zones and estimates of the deposition rate. From 30 selected records of the last four reversals, Clement (2004) found that the average time for the field to change direction from one polarity to the other was 7000 years (**Figure 1**). These reversals, so defined, tended to occur more quickly at low latitudes than at mid-to-high latitudes, with individual durations ranging from 2000 to 12 000 years. This regionally varying behavior implies that the transitional field has a large nondipolar component.

In detail, reversal records display a wide variety of field behavior (Coe and Glen, 2004). Almost all exhibit large intensity drops during transition, but their directional behavior

 http://dx.doi.org/10.1016/B978-0-444-53802-4.00146-9

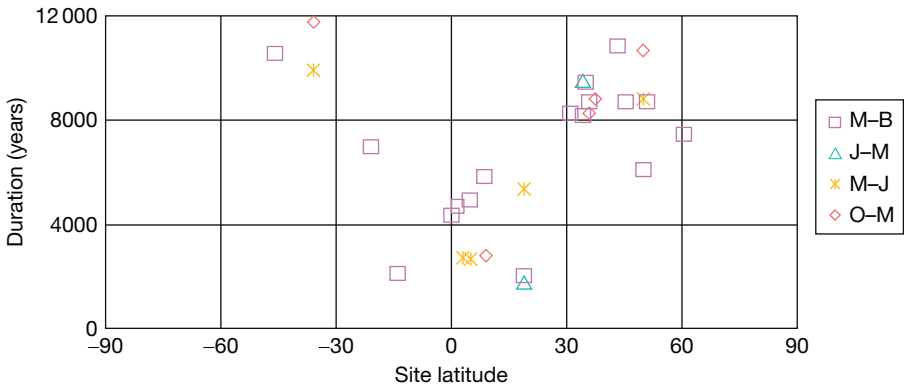

Figure 1 The duration of directional change from one stable polarity to the other during the last four reversals, as determined from transition-zone thickness and estimated deposition rate in sedimentary sections. Note that the duration so defined increases with latitude. This method may underestimate the duration of complex reversals by designating early or late instability as unrelated pre- or posttransition excursions. M–B, Matuyama–Brunhes; J–M, Jaramillo–Matuyama; M–J, Matuyama–Jaramillo; O–M, Olduvai–Matuyama. Adapted from Clement BM (2004) Dependence of the duration of geomagnetic polarity reversals on site latitude. *Nature* 428: 637–640.

varies greatly. The most detailed, high-deposition-rate lava-flow records and sedimentary records show that at least some reversals are complex, with episodes of oscillatory and rapid field change (**Figures 2(a)** and **3**). Often, the field reverses briefly but relapses to intermediate directions one or more times before finally attaining stable opposite polarity. This behavior complicates the estimation of duration. For instance, if one includes an early unsuccessful swing to normal polarity in the Matuyama–Brunhes transition, its duration is about 18 000 years (**Figure 4**), three times longer than if one considers that swing to be an unrelated precursor (Singer et al., 2005). Inclusion of the precursory swing in direction seems reasonable, in light of the complex transition paths of **Figures 2(a)** and **3**. Even excluding the precursor, high-resolution sediment records show that this transition is complex, with multiple large swings of the field direction (Channell and Lehman, 1997). Some dynamo simulations have also produced long, complex reversal transitions – for example, the second reversal during the tomographic simulation of Glatzmaier et al. (1999) (see case 'h' of **Figure 14** and Coe and Glen, 2004; Figure 7 and Plate 1).

Despite the striking differences in high-resolution reversal records, a recent study by Valet et al. (2012) boldly advances the hypothesis that all polarity transitions are governed by a common underlying process in which the dipole field collapses and regenerates three times in close succession (**Figure 5(a)** and **5(b)**). During each phase of low dipole intensity, the remaining nondipole field produces highly variable directions between normal and reversed polarity. The first phase is a precursor in which the dipole regenerates in its original polarity, the second phase is the transit to opposite polarity, and the third phase is a rebound in which the dipole decays and regenerates in its recently achieved opposite polarity. In support of their conceptual model, they consider only the most detailed lava-flow transition zones, thereby avoiding possible problems of smoothing and other artifacts of magnetic recording in sedimentary records, and require that they occur in stratigraphically ordered volcanic sequences with full-polarity normal and reversed flows above and below. Furthermore, they assume that the average interval between successive flows for each record, though quite different from one record to another, is more or less constant within a single record. This allows them to stack the records as shown in **Figure 5(a)**, rescaling the lava-flow numbers to a common correlation number by lining up the records at the first transitional flow, stretching or compressing each of them so that they also line up at the final transitional flow or at some other distinctive point in the records, and plotting the lava-flow correlation number versus reversal angle for each record. Observations and modeling of recent field variability from archeomagnetic records lead to estimates of ~2.5 ky or less for the precursor and rebound and ~1 ky for the transit. Their estimate of 5–6 ky for the duration of an entire reversal accords well with most estimates, including the average duration of 7 ky of Clement (2004), but of course not with the 2–12 ky latitudinal variability (see **Figure 1**). It also fits with the durations of reversals exhibited in many dynamo simulations (e.g., Glatzmaier et al., 1999; Kutzner and Christiansen, 2004; Olson et al., 2011), though there are significant exceptions (e.g., simulation (h) of **Figure 14** where the second reversal takes four to five times longer). Six of the seven records in **Figure 5(a)** exhibit some degree of directional rebound (reversal angle in excess of 30°), whereas only three records show a precursor. However, one of those shown in **Figure 5(a)** without a precursor (Steens Mountain) is not an exception because there are actually three successive lava flows a little below the transit zone that do have paleomagnetic reversal angles slightly >30° (Mankinen et al., 1985; Table 1 lavas B70–72). Moreover, in the lava-flow section slightly below the transit zone in the Hawaii 0.78 My record, radioisotopic dating has revealed an ~100 ky hiatus (Coe et al., 2004), which can explain the discrepancy with the Tahiti 0.78 My record that does display a precursory mode.

Despite its apparent success, how generally applicable this three-phase model is to reversals will require further testing. Dynamo simulations have produced numerous exceptions to the rule, with transition paths that are too simple or too complex, but what is needed are more high-resolution

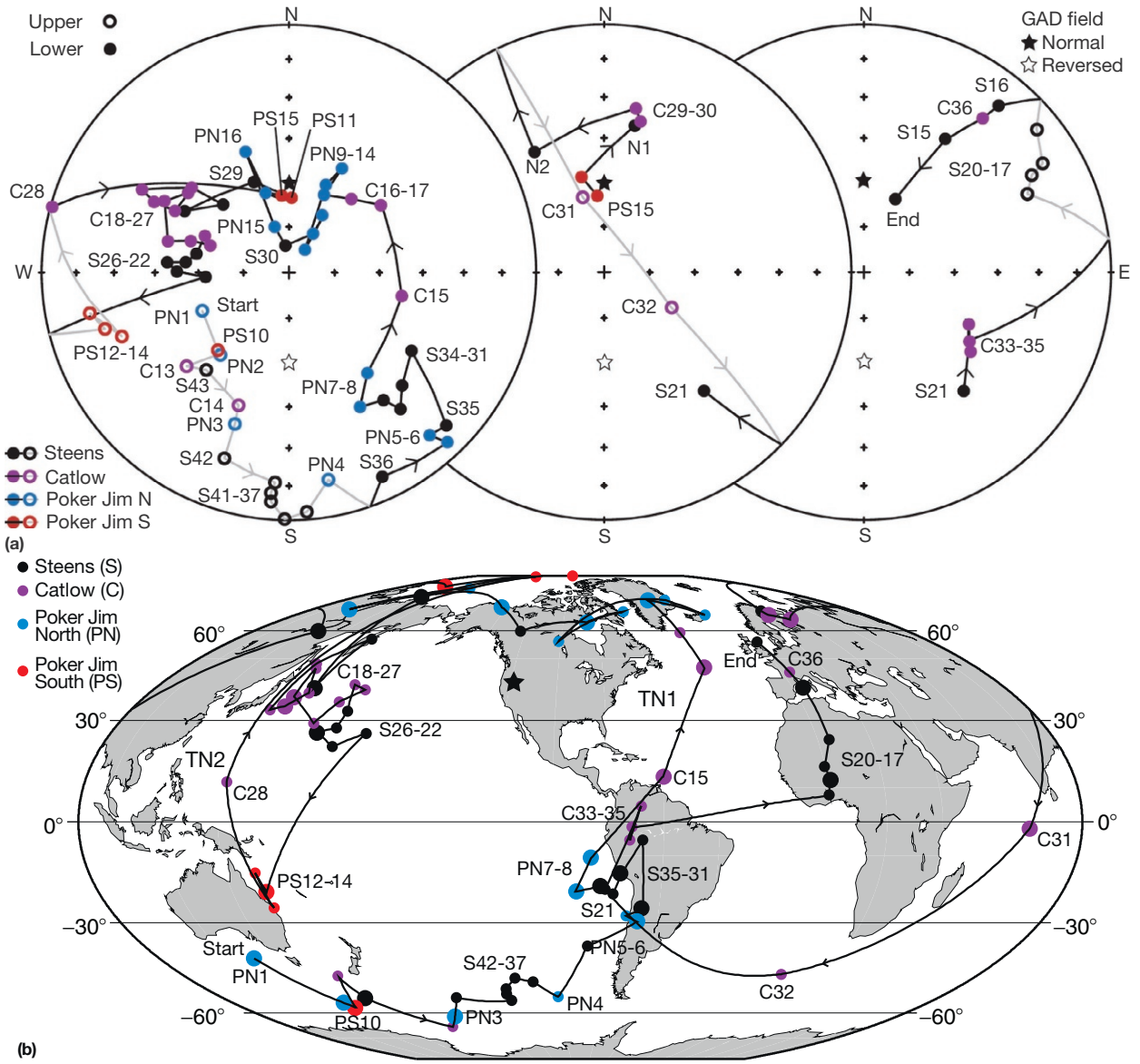

Figure 2 (a) Composite directional record of the 16.7 Ma Steens Mountain reversal recorded in four sections of superposed lava flows in SE Oregon (Jarboe et al., 2011). Arrows indicate the progression of time, and open (solid) symbols indicate upward (downward)-pointing directions. Note the increased complexity of the transition path when new directions found at Poker Jim Ridge (north and south) and Catlow Peak are spliced into the earlier record from Steens Mountain of Mankinen et al. (1985) and Camps et al. (1999). Open and closed stars are the reversed and normal axial dipole directions for that region. (b) The transition path of virtual geomagnetic poles (VGPs) for the Steens Mountain reversal derived from the composite directional record of Figure 2(a) (Jarboe et al., 2011). Some of the stop-and-go character of much of the path, with clusters of VGPs separated from each other by sizable gaps, probably reflects the episodic nature of volcanic eruptive activity, but the clusters around the west coast of South America and in the northwestern Pacific Ocean may represent significant lengths of time (see text).

paleomagnetic reversal records of the full-field vector, intensity, and direction. The most detailed one available currently is the Steens volcanic record, with an apparent resolution two or more times that of the other detailed volcanic records (**Figure 5(c)**) and considerable paleointensity data (Prévot et al., 1985). It exhibits the additional complexity of two closely spaced directional rebounds rather than only one (**Figure 2**), but intensity data are lacking to show whether or not the field recovered its strength during the interval between the directional rebounds.

In the search for some kind of systematics to the tangle of reversal transition paths, various authors have long proposed that there is a tendency for transitional virtual geomagnetic poles (VGPs) to cluster geographically in preferred longitudinal bands or patches on Australasia and the Americas and to avoid the Central Pacific Basin (Clement, 1991; Hoffman, 1992; Hoffman and Mochizuki, 2012; Hoffman and Singer, 2004; Laj et al., 1991; Love, 2000), though the statistical significance of this tendency has been disputed (McFadden et al., 1993; Merrill and McFadden, 1999; Prévot and Camps,

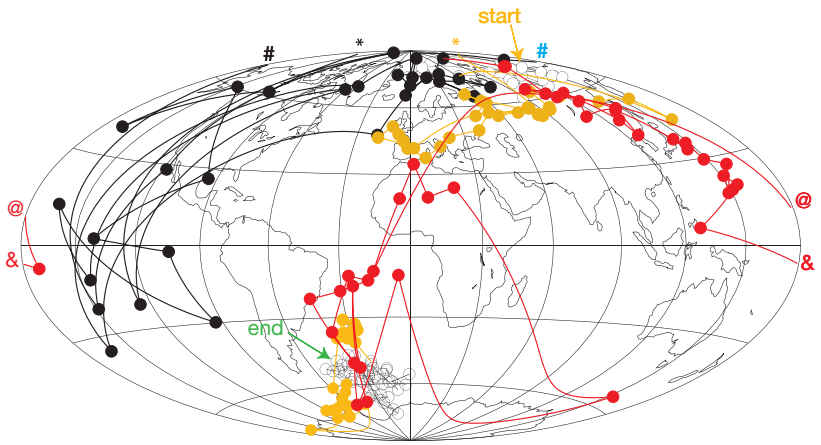

Figure 3 The Gauss–Matuyama (2.58 Ma) reversal record of VGPs recorded in sediments deposited in Searles Lake, California (Glen et al., 1999). Note the highly complex VGP path, with initial and final excursions in orange, multiple rapid oscillations in black, and main reversing phase including two large swings from high to equatorial latitudes in red.

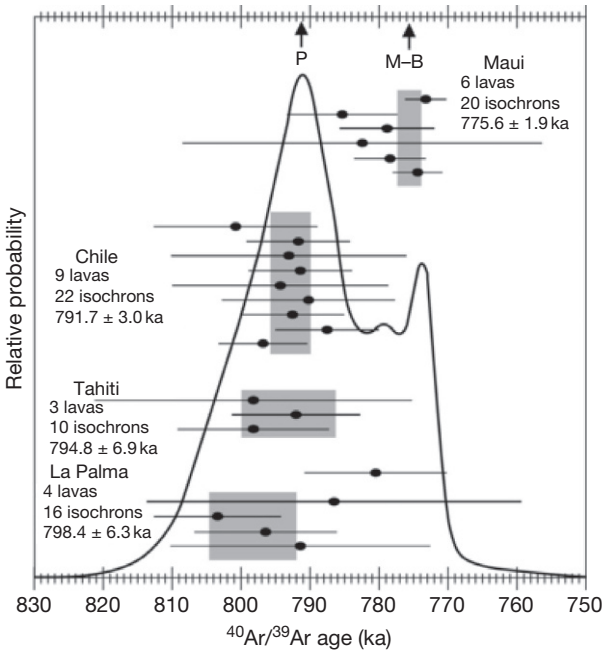

Figure 4 Ar/Ar ages of 23 transitionally magnetized lava flows from four widely spaced localities that record transitional field directions attributed to the most recent Matuyama–Brunhes (M–B) reversal. Gray bands show the weighted mean age and 2σ uncertainty for each lava sequence. The ages of the lavas from Maui and the uppermost flow from La Palma correspond to the accepted age of the M–B reversal from sedimentary cores (Tauxe et al., 1996), whereas those of the others correspond to what has been termed the M–B precursor (P) (Hartl and Tauxe, 1996). The probability density curve indicates that these lavas together span a minimum of 18 ky, a period about three times longer than the conventionally cited M–B duration. Adapted from Singer BS, Hoffman KA, Coe RS, et al. (2005) Structural and temporal requirements for geomagnetic field reversal deduced from lava flows. *Nature* 434: 633–636.

1993; Valet et al., 1992, 2012). If true, the long timescale would suggest the influence of the lowermost mantle. The preferred areas do correlate with large-scale seismic tomography, overlying regions in the lower mantle of higher than average P- and S-wave velocity (e.g., Grand, 2002). Assuming that higher seismic velocity signifies regions with lower than average lower-mantle temperature, convective downwelling in the core could be localized there and concentrate poloidal flux lines. Transitional VGP preference would then be expected (Gubbins and Coe, 1993) and has been produced by some dynamo simulations employing appropriate heat-flux boundary conditions at the CMB (Coe et al., 2000; Kutzner and Christensen, 2004; Olson and Christensen, 2002).

The Steens reversal record (**Figure 2(b)**) does not exhibit a longitudinal band or bands, but rather a series of clusters of VGPs, raising the question whether the clusters record standstills in the field or episodic volcanism. It is well known that eruptive activity is generally episodic, but the two most prominent VGP clusters of the Steens record, in western South America and the western Pacific, are each represented by multiple flows from sections 60 to 80 km apart. Moreover, the chemistry of the flows differs significantly both within and between sections, and the South American cluster is visited twice, both early and late in the record. Rather than brief bursts of volcanism, lingering of the VGP for appreciable periods of time seems a better explanation for these clusters. This in turn suggests geographic preference, which is consistent with the higher than average S-wave velocities detected beneath them in the lowermost mantle (Grand, 2002).

There are clusters of VGPs at these locations in some other polarity transitions (see Jarboe et al., 2011 for examples), as would be expected if clustering is due to the effect of low-temperature anomalies in the lowermost mantle, but that raises the question why there are VGP paths for plenty of other polarity transitions that do not display clustering in these regions (e.g., see Figure 1 in Valet et al., 2012). Some of these transitions do have VGP clusters in other places (e.g., Glen et al., 1999; Hoffman and Mochizuki, 2012; Jarboe et al., 2011) such as around Australia and eastern North America, both of which are characterized by fast lower-mantle shear-wave anomalies, but sometimes also in northern Africa, which paradoxically is underlain by slow shear-wave velocities (Grand, 2002). Support for transitional VGP clustering is also sought in the vertical component of the modern NAD field – that remaining after

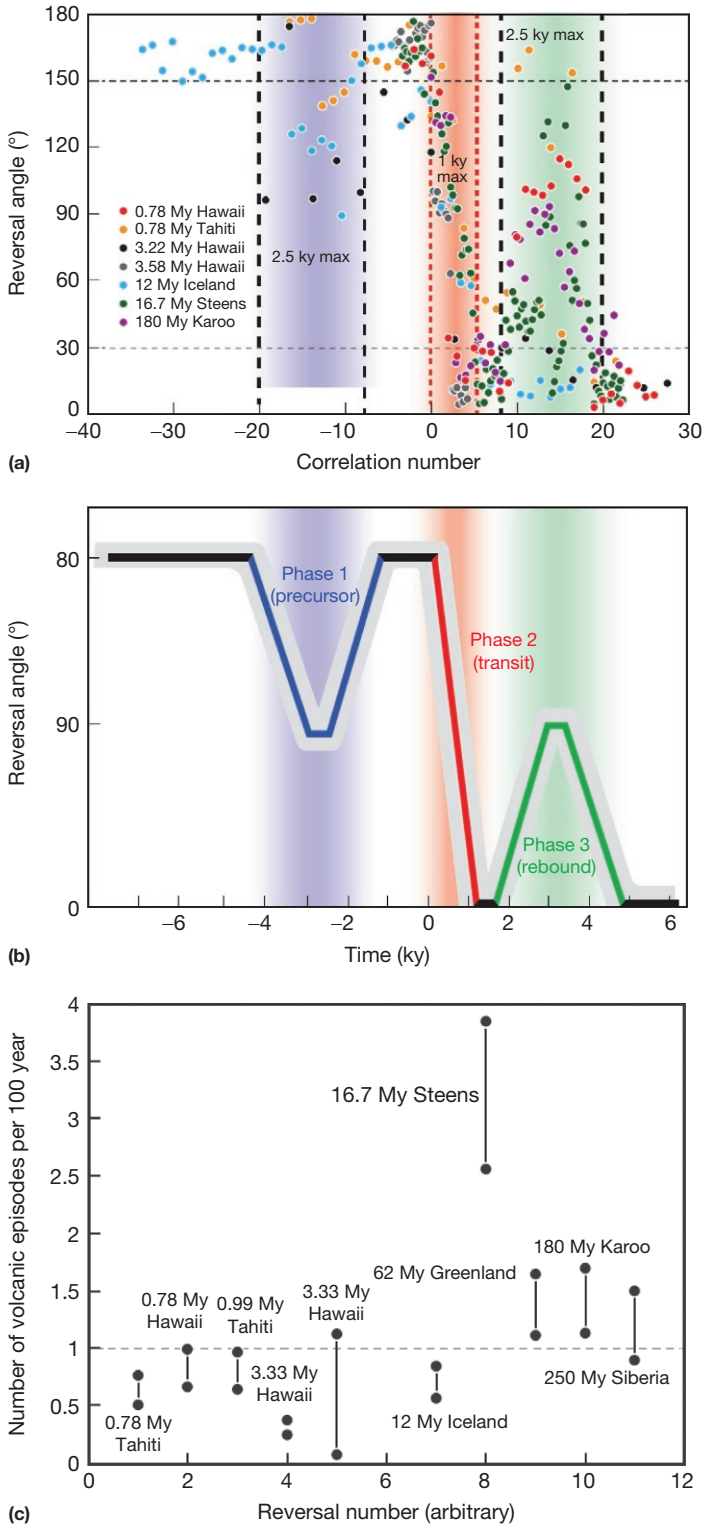

Figure 5 Sequential lava-flow numbers for the most complete, stratigraphically ordered lava-flow reverse-to-normal polarity transition records are rescaled to a common correlation number by assuming that the polarity transitions have a common duration. In (a), the correlation number is plotted versus reversal angle for these records and suggests that an underlying structure involving three phases of field instability might be common to reversal transitions, as shown in (b) and discussed in the text. (c) The degree of detail of the reversal records is indicated by the number of distinct field directions recorded by groups of sequential lava flows in the transition zone. Adapted from Valet JP, Fournier A, Courtillot V, and Herrero-Bervera E (2012) Dynamical similarity of geomagnetic field reversals. *Nature* 90: 89–94.

subtraction of the axial dipole field, which exhibits strong downward-directed anomalous patches in eastern North America and the southern Atlantic Ocean and an upward-directed patch in the Australasian region (Hoffman and Mochizuki, 2012; Figure 4). These flux patches cause clustering of VGPs of the modern NAD field in eastern North America and the southern Atlantic regions and also in the region antipodal to Australasia. Under the assumption that these modern flux patches are caused by lower-mantle anomalies, as proposed by Hoffman and Singer (2008), then they would be expected to persist for tens of millions of years and produce VGP clustering of the paleomagnetic transitional field in these regions or their antipodes, depending on whether the patches contained upward or downward flux. A problem is that these six regions where one could expect flux patches under this scenario occupy a very appreciable proportion of the total area in which a VGP would be classified as transitional. Thus, the degree to which transitional VGP clusters demonstrate statistically significant geographic preference caused by lower-mantle anomalies remains difficult to assess rigorously.

Earth's reversals occur aperiodically, in fact almost randomly, but the mean duration appears to change progressively over long time intervals (Figure 6(a)). As determined from dating rocks of known magnetic polarity and from analyzing the record of marine magnetic anomalies produced by sea-floor spreading, from 0 to 165 Ma, the field reversed on average about two times per million years, but over 10 My intervals the average reversal rate varied from highs of at least five per million years to a low of 0. During the interval from 124 to 83 Ma, the so-called Cretaceous Normal Superchron (CNS), no true polarity reversals have been unequivocally demonstrated. Two other superchrons have been documented in the past 550 My, the Kiaman Reversed and the Moyero Reversed superchrons (Pavlov and Gallet, 2005) in Permo-Carboniferous and Ordovician time, respectively (Figure 6(b)).

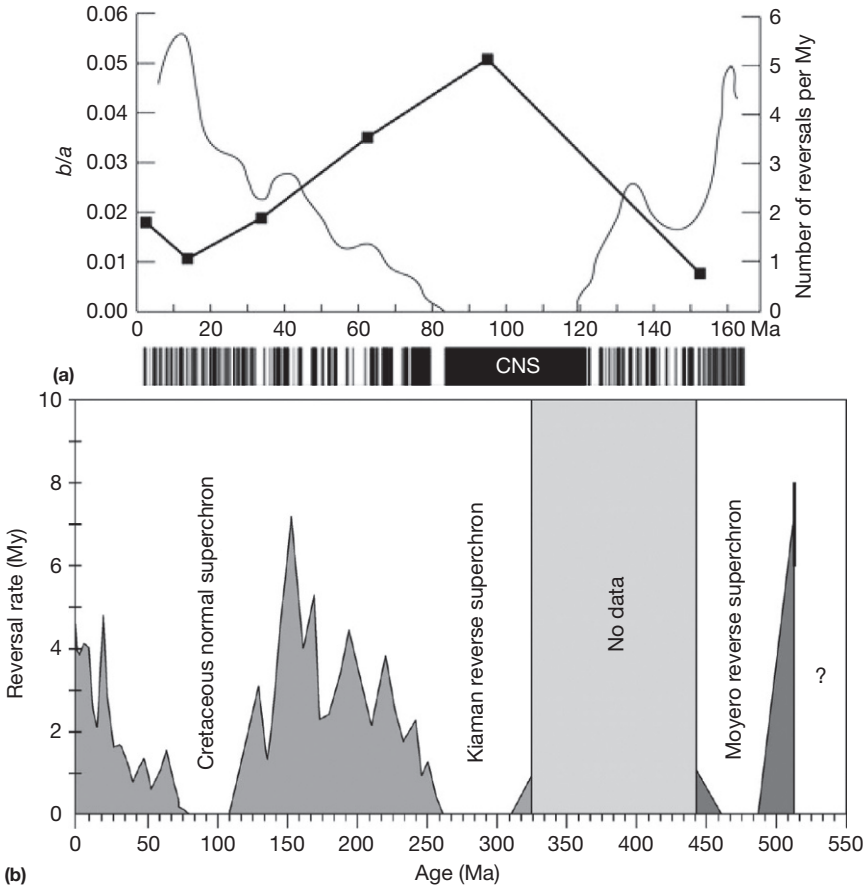

Figure 6 (a) Smoothed reversal rate (thin wavy line) corresponding to normal and reversed chrons (black and white bars) of the geomagnetic polarity timescale (Ogg et al., 2004). The rate goes to zero in the Cretaceous Normal Superchron, from 83 to 118 Ma. The squares denote *b*/*a*, a relative measure of the average ratio of the antisymmetric to symmetrical parts of the geomagnetic field (excluding the axial dipole) as a function of time in the past, inferred from paleomagnetic secular variation using the results of McFadden et al. (1991). These demonstrate a strong inverse correlation between *b*/*a* and reversal rate. We note that recent studies (see Ogg, 2004) suggest even higher reversal rates from 155 to 165 Ma than shown here ($\sim$10 My^{-1}) (adapted from Coe RS and Glatzmaier GA (2006) Symmetry and stability of the geomagnetic field. *Geophysical Research Letters* 33: L21311. http://dx.doi.org/10.1029/2006GL027903). (b) In the last 550 My, there are two well-documented superchrons when no true polarity reversals have been unequivocally documented and a third, the Moyero Reversed Superchron, that has been proposed more recently (adapted from Pavlov V, Gallet Y (2005) A third superchron during the Early Paleozoic. *Episodes* 28: 1–7).

From the analysis of the latitudinal variation of paleomagnetic secular variation recorded by lava flows over the past 150 My, McFadden et al. (1991) proposed that average reversal rate is related to symmetry of the NAD field: A higher degree of symmetry of the field about the equator, as expressed by its spherical harmonic gauss coefficients, correlates with more frequent reversals (**Figure 6(a)**). For example, the equatorial dipolar and axial quadrupolar harmonics of the field are symmetrical and the axial octupolar harmonic is antisymmetric (Merrill, 1996). The analysis of the Glatzmaier et al. (1999) dynamo simulations supports this idea: **Figure 7** shows that the most stable, nonreversing simulation (case 'e' of **Figure 14**) has far more energy associated with antisymmetric than with symmetrical gauss coefficients (Coe and Glatzmaier, 2006). More recently, a new analysis of the latitude dependence of secular variation for an expanded set of lava flows erupted during the CNS reaffirms this correlation between lower reversal rate and higher antisymmetric harmonic content of the field (Biggin et al., 2008a). In addition, an insightful synthesis of new and previous studies of Permo-Carboniferous red beds came to a similar conclusion for the Kiaman Reversed Superchron (Haldan et al., 2009).

Relatively little is known for sure about the ancient, Precambrian geomagnetic field, but there is evidence indicating that it existed as early as 3.40–3.45 Ga (Tarduno et al., 2010), and the earliest documented reversal occurred around 3.2 Ga (Layer et al., 1998). Several attempts have been made to apply the same secular variation approach applied in the preceding text to make inferences about reversal frequency in the Precambrian. A dynamo simulation with a solid inner core that is only one-quarter of its size today (Roberts and Glatzmaier, 2001) produced an even more antisymmetric NAD field (Coe and Glatzmaier, 2006), hinting that reversals may have been much less common in the distant geologic past when the Earth's inner core was smaller (see **Chapter 8.02**). Limited paleomagnetic evidence available documenting reversals in several thick sections of rocks older than 1 Ga and less than 2.8 Ga suggested an average reversal rate five to ten times less than the well-documented rate of ~1.7 per million years for the 0–150 Ma interval (Coe and Glatzmaier, 2006, and references therein), although large temporal gaps between these sections and likely large hiatuses could make this estimate unrepresentative. But two later studies of Precambrian secular variation in lavas and dikes between 1.1 and 2.8 Ga provide additional indirect support for a slower Precambrian reversal rate by inferring a greater degree of antisymmetry of the average field relative to the modern field (Biggin et al., 2008b; Smirnov et al., 2011). Most recently, on the basis of their magnetostratigraphic findings from Siberia and those of Elston et al. (2002) from North America, Gallet et al. (2012) suggested that the field before ~1 Ga was characterized by a greater proportion of superchrons that are bounded abruptly by periods of high reversal frequency, but the average reversal rate estimated from 1 to 2.8 Ga is nonetheless much lower than from 0 to 150 Ma. Thus, the emerging consensus (see Nimmo vol. 8 *Energetics of the Core* and vol. 9 *Thermal and Compositional Evolution of the Core*) that inner-core nucleation occurred relatively recently in earth history, around 1 Ga or even later, is consistent with the observations suggesting significantly different, on-average lower reversal frequency during Mesoproterozoic and Neoarchean time. Although these observations are uncertain, the computer simulations of the geodynamo mentioned earlier in the text support a lower reversal frequency with a smaller solid inner core. The main reason for this model result is the deep-shell geometry of the fluid outer core; that is, a smaller inner core provides less obstruction within the fluid core and therefore weaker instabilities in the global flow and field (see **Section 8.11.3**).

In addition to reversals, which entail a switch from one well-established polarity state to stable opposite polarity, the geomagnetic field has undergone many brief excursions to reduced intensity and reversed or nearly reversed directions, some of which have been detected around the globe. These might represent failed reversal attempts. During the past 0.78 My of today's normal polarity epoch when global simultaneity of brief field fluctuations is easier to establish, there have been eight or more excursions (**Figure 8**) (Champion et al., 1988; Guyodo and Valet, 1999; Lund et al., 2006). They are generally distinguished from complete polarity reversals by their short duration of ~1–10 000 years. In the paleomagnetic and sea-floor magnetic anomaly records, their classification is somewhat arbitrary (Acton et al., 2006): It is difficult to draw a line between failed reversals and very short true reversals on the one hand and

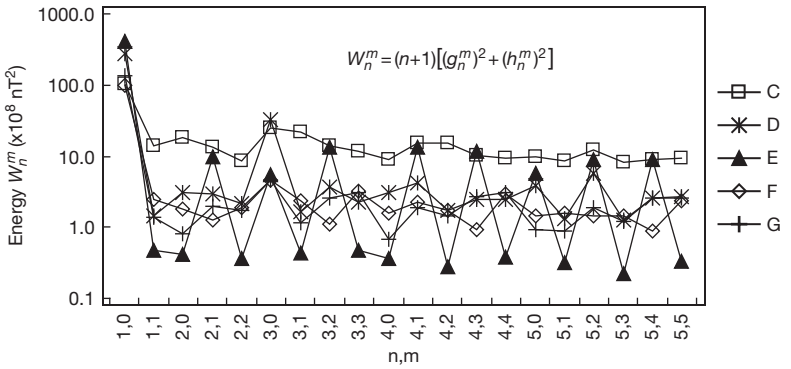

Figure 7 Time-averaged spatial energy density W_n^m at the CMB associated with each harmonic degree and order up to $n,m = 5,5$ for five of the simulations of Glatzmaier et al. (1999) that are shown in **Figure 14**. The terms associated with gauss coefficients g_n^m and h_n^m are antisymmetric about the equator when $(n+m)$ is odd and are symmetrical about the equator when $(n+m)$ is even. Note that the most stable case, E, heavily favors antisymmetric energy terms (with $n+m$ odd), as does generally the second most stable case D. Adapted from Coe RS and Glatzmaier GA (2006) Symmetry and stability of the geomagnetic field. *Geophysical Research Letters* 33: L21311. http://dx.doi.org/10.1029/2006GL027903.

unusually large directional secular variation on the other. However, in dynamo simulations, failed reversals can be unambiguously defined as excursions for which the field deep in the core maintains its original polarity throughout the time of intermediate and reversed directions at the surface of the Earth, as illustrated in Figure 9 (Glatzmaier et al., 1999).

8.11.3 Models

Although the magnetic dipole reversal mechanism is still poorly understood, mathematically it is easy to see why there can be two oppositely directed magnetic basins of attraction. Given a solution to the set of equations that govern the

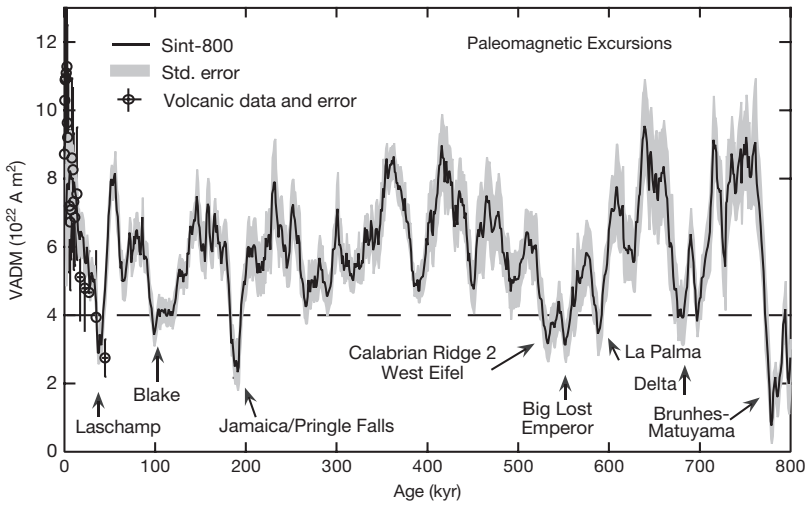

Figure 8 Excursions of the geomagnetic field since the last reversal (Brunhes–Matuyama), as indicated by deep minima in the Earth's dipole moment (VADM). Results are from a global stack of records of relative paleointensity data derived from marine sedimentary cores, normalized to fit volcanic absolute paleointensity results. Adapted from Guyodo Y and Valet JP (1999) Global changes in intensity of the Earth's magnetic field during the past 800 kyr. *Nature* 399: 249–252.

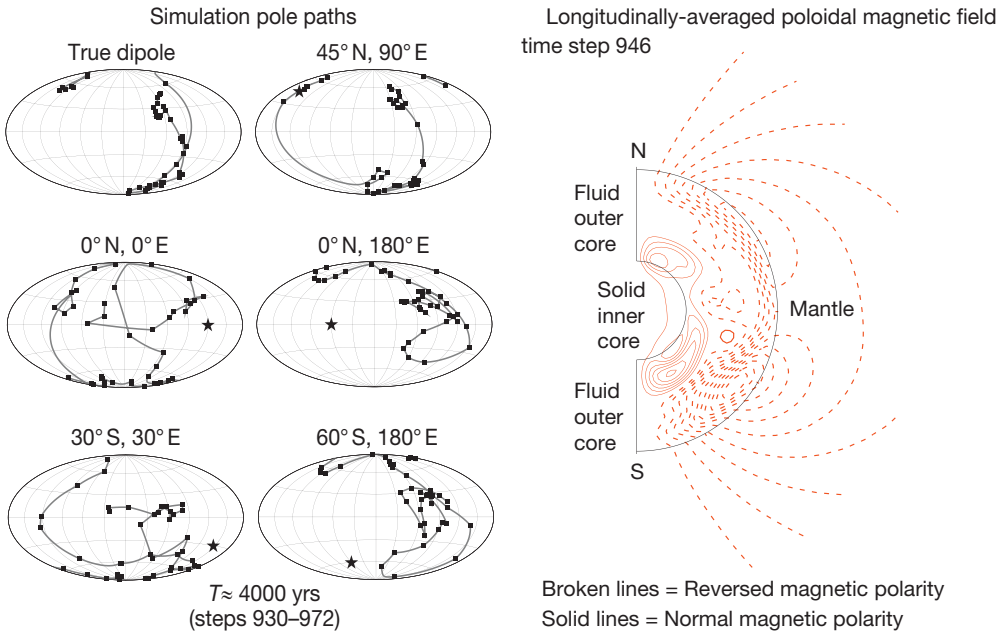

Figure 9 A failed reversal during case 'c' simulation of Glatzmaier et al. (1999) that occurred around 88 000 years in the record of **Figure 14(c)**. Left: True dipole path and VGP paths for five locations around the globe. Right: Longitudinally averaged poloidal flux in the outer core at the midpoint of the directional excursion shows that while the field reversed in most of the outer core and above, it retained the original normal polarity close to the inner core and within it. Note that each plotted time step represents about 100 years and 3500 numerical time steps.

thermodynamics and MHD for a convective dynamo (i.e., fluid flow, magnetic field, and thermodynamic variables), completely reversing the magnetic field everywhere would also satisfy the same set of equations; that is, reversing the sign of the magnetic field vector everywhere will not change the Lorentz force or Joule heating because the field is quadratic in these terms. It will also not affect the magnetic induction or conservation equations because the field, although linear in these two equations, appears in every term.

Reversals of the dipolar part of the magnetic field were originally studied using 2D axisymmetric models of the mean magnetic fields. These models are kinematic, that is, the fluid flow is prescribed or parameterized instead of being part of the solution. Only the longitudinally averaged part of the magnetic field is calculated (see **Chapter 8.03**). This method continues to be employed in the solar community to study the periodic reversals associated with the sunspot cycle (e.g., Bonanno et al., 2006) and in the geophysics community to study the aperiodic paleomagnetic reversals (e.g., Giesecke et al., 2005). Such models prescribe the two main ingredients for a self-sustaining dynamo: the 'alpha effect,' which twists toroidal (longitudinally directed) magnetic field into poloidal (radially and latitudinally directed) field, and the 'omega effect,' which shears poloidal field into toroidal field. The alpha effect can also act on poloidal field to generate (or destroy) toroidal field. The alpha prescription in these models parameterizes the effects of helical fluid flow and the omega prescription represents the effects of differential rotation (i.e., the variation of angular velocity with radius and latitude). Replacing these complicated, nonlinear, 3D, time- and spatially dependent processes with 2D and usually time-independent functions greatly simplifies the problem. These studies formed a basis for understanding convective dynamos. The simplifications and assumptions built into these models greatly reduce the complexity and computational expense and therefore can provide good statistics because of the long times that can be simulated. Unfortunately with this approach, one cannot reconstruct what the 3D dynamics must be that maintains the prescribed alpha and omega effects. Discovering and understanding the details of the dynamo mechanisms require a self-consistent solution of the full set of nonlinear 3D equations that represent conservation of mass, momentum, energy, magnetic flux, and magnetic induction (see **Chapters 8.05** and **8.08**).

Early, self-consistent MHD models of the solar dynamo were developed by Gilman (1983) and Glatzmaier (1985). Instead of prescribing the alpha and omega effects parametrically, they solved a full set of MHD equations for the 3D time-dependent fluid flow, thermodynamics, and magnetic field in a rotating spherical shell that served as an analog of convection and magnetic field generation in the solar interior. The resulting solutions maintained a differential rotation at the surface, very similar to that observed on the Sun, and a magnetic field that continuously and periodically reversed as a 'dynamo-wave' propagating in latitude, somewhat similar to the large-scale fields observed on the solar surface. However, the coarse spatial resolution, which was barely affordable at that time, forced the simulated fluid flows to be unrealistically laminar. Later, it was found that the differential rotation below the surface predicted by these early models was not consistent with the profile inferred from helioseismology. Computers today provide much better spatial resolution, which allows the simulations to be at least weakly turbulent. This changes the style of the dynamics (from large convective cells to small convective plumes), the transport of angular momentum and therefore the pattern of differential rotation, the generation of vorticity and helicity, and ultimately the dynamo mechanism. However, the solar dynamo is still far from being well understood.

The original 3D MHD geodynamo models were developed in the early 1990s. Surprisingly perhaps, the challenge then was not to produce reversals, but to stop them from occurring too frequently. These were strongly convective and rotationally dominant (high Rayleigh number and low Ekman number) dynamos that were quite unstable. In addition, the solid inner core (see **Chapter 8.10**) was originally approximated as an insulator (for numerical simplicity) because most people at that time felt the small inner core would have little effect on the dynamo in the outer fluid core. However, when Hollerbach and Jones (1993) showed that a finite-conducting inner core in their 2D 'mean-field dynamo model' stabilizes their solution, Glatzmaier and Roberts (1995) made the inner core conducting in their 3D MHD model and obtained a relatively stable, dipole-dominated dynamo (**Figure 10**) that, after a couple of magnetic diffusion times, produced an isolated dipole reversal (**Figure 11**). The large insulating inner core in their original (frequently reversing) model obstructed the flow, whereas their new conducting inner core provided an anchor for the field via magnetic torque, which resulted in a solution still time-dependent but not continuously reversing. As

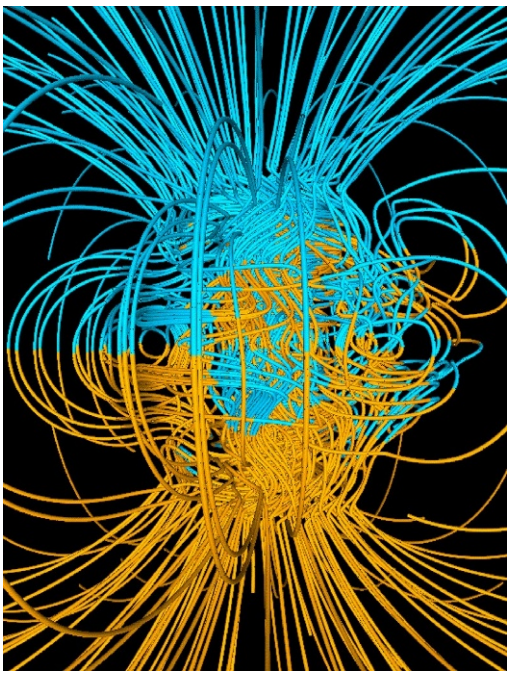

Figure 10 A snapshot of the simulated geomagnetic field produced by Glatzmaier and Roberts (1995). A set of magnetic lines of force illustrated the 3D structure of the field, which is intense and complicated inside the fluid core and smooth and dipole-dominated outside the core. The rotation axis of the model Earth is vertical in the illustration and yellow lines represent outward-directed field and blue lines represent inward-directed field. The field is sheared around the 'tangent cylinder' to the inner-core equator.

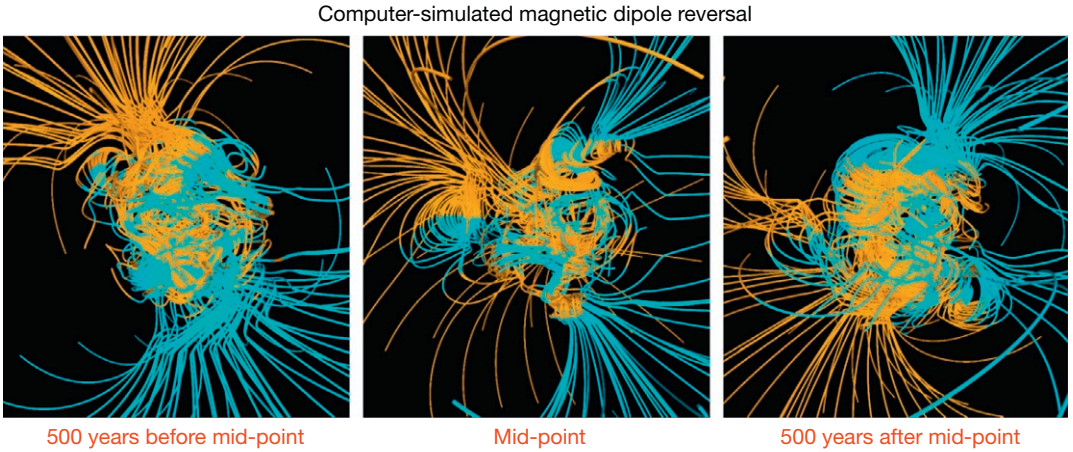

Figure 11 Three snapshots of a simulated magnetic field (as in **Figure 10**) at 500 years before the midpoint in the dipole reversal, at the midpoint, and at 500 years after the midpoint.

mentioned in the preceding text, tests with a much smaller conducting inner core (less flow obstruction) produced a more stable and more antisymmetric magnetic field (Coe and Glatzmaier, 2006; Roberts and Glatzmaier, 2001), which suggests that the reversal frequency may have been very low in the distant past (see **Chapter 8.02**).

It has been nearly two decades since that first spontaneous magnetic dipole reversal was found in a 3D MHD self-consistent computer simulation of the geodynamo (Glatzmaier and Roberts, 1995). Since then, several groups around the world have developed similar geodynamo models (see **Chapter 8.08**), some of which also produce magnetic reversals (Busse, 2002; Kageyama et al., 1999; Kida et al., 1997; Kutzner and Christensen, 2002; Reshetnyak and Steffen, 2005; Sarson and Jones, 1999; Takahashi et al., 2005; Wicht, 2002). The various MHD geodynamo models employ different sets of parameters, boundary conditions, numerical methods, and spatial resolution (Glatzmaier, 2002); therefore, a detailed comparison is difficult. Yet many of the results have features quite similar to geomagnetic and paleomagnetic observations. Reviews have been written that qualitatively compare the results to the paleomagnetic reversal record (e.g., Dormy et al., 2000; Kono and Roberts, 2002).

Reversing MHD dynamo simulations fall loosely into three categories: (1) periodic dynamo waves, for which the field continuously reverses (Busse, 2002; Kida et al., 1997); (2) reversals possibly triggered by large-scale plume events, fluctuations in the axisymmetric meridional circulation, or changes in kinetic and magnetic energies (Kageyama et al., 1999; Reshetnyak and Steffen, 2005; Sarson and Jones, 1999; Wicht and Olson, 2004); and (3) those with relatively long epochs of varying durations between reversals of varying durations and with more frequent failed reversals (Glatzmaier et al., 1999; Kutzner and Christensen, 2002; Takahashi et al., 2005). For the simulations of category (3), the reversals occur through the combined nonlinear action of many small-scale fluctuations.

The early solar dynamo models (Gilman, 1983; Glatzmaier, 1985) produced periodic and continuously occurring solar reversals via an alpha–omega dynamo-wave mechanism. The more recently simulated reversals of Kida et al. (1997) and Busse (2002) also appear to be global-scale dynamo waves driven by laminar convection. However, as discussed in the preceding text, paleomagnetic reversals do not continuously occur; that is, the epochs between reversals are long (~10 magnetic dipole diffusion times) compared with the typical duration of a reversal (~0.1–0.5 magnetic dipole diffusion time). (A geomagnetic dipole diffusion time is 20 000 years.) They are also aperiodic; that is, the lengths of these epochs are highly irregular (**Figure 6**). In addition, failed reversals (or excursions) are much more frequent than full reversals (**Figure 8**). Several of the early MHD dynamo simulations produced qualitatively similar sequences of full and failed dipole reversals (Glatzmaier et al., 1999; Kageyama et al., 1999; Sarson and Jones, 1999).

It appears that the progression through the three categories of simulations is correlated with the vigor of the convection (i.e., the Rayleigh and Reynolds numbers) and the relative effect of rotation (i.e., the Ekman and Rossby numbers) (see **Chapters 8.03**, **8.05**, and **8.08**). Assuming the rotation rate, electrical conductivity, heat flux, and dimensions of the Earth's core, the smaller the prescribed thermal and viscous diffusivities, the more turbulent the flow and the closer these nondimensional numbers approach Earth-like values and the more Earth-like the reversals appear. However, the character and frequency of the reversals also likely depend on several other model specifications: the ratio of buoyancy and Coriolis forces, the pattern of the heat flux over the CMB, and the relative size of the solid inner core.

Wicht and Olson (2004), for example, studied a weak-field, slowly rotating, large-scale convective dynamo, which produced a series of quite regular (periodic) reversals with periods long relative to the duration of a reversal but short relative to a magnetic diffusion time (**Figure 12**). These results are more Earth-like than the continuously reversing dynamo-wave solutions because of their relatively long, stable epochs between the reversals; however, the process is still periodic, that is, the durations of the epochs do not vary randomly as the Earth's do (**Figure 6**). Reversed-polarity magnetic flux is generated when convective plumes twist the field; this reversed flux is then advected throughout the outer core by the dominant meridional circulation. However, Lorentz forces have very little effect on the flow in their simulations; that is, the solutions

are nearly kinematic. The main advantage of this approach is the ease of analysis; that is, the reversal mechanism is large scale and the reversal frequency is high and constant. However, the reversal mechanism may not be very Earth-like.

Kutzner and Christensen (2002) studied more strongly convective and more rotationally dominant cases. They found that convective dynamos with small Rayleigh numbers (i.e., small convective driving for a given rotation rate) tend to be stable and have a dominant axial dipole; large Rayleigh numbers produce frequently reversing dynamos and less dipolar fields. The cases that fall within a narrow region of parameter space between these two regimes have longer and more irregular times between reversals and therefore appear more Earth-like (**Figure 13**). Increased reversal frequency with increased convective driving relative to the effects of rotation seems quite reasonable. Polarity reversals in dynamo simulations tend to be initiated by chaotic modifications in the dominant fluid flow pattern, like the differential rotation, that is maintained by Coriolis forces organizing the structure of convectively driven flow. These temporary flow modifications twist and shear the existing magnetic field in ways that are slightly different than the usual dynamo mechanism; this destroys the original polarity and begins to generate the new polarity. Such perturbations in the flow need to continue long enough for the original polarity to be completely destroyed and replaced by a global field with the new polarity. The tendency for such modifications in the flow is greater when the chaotic effects of the convection are greater than the organized effects of the rotation.

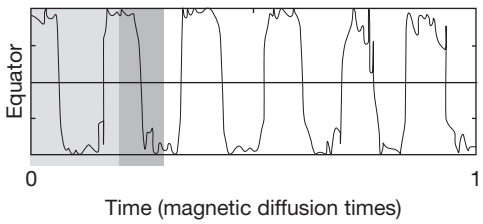

Figure 12 The magnetic pole latitude (at the surface) versus time (in magnetic diffusion times, here estimated as 80 000 years). Adapted from Wicht J and Olson P (2004) A detailed study of the polarity reversal mechanism in a numerical dynamo model. *Geochemistry, Geophysics, Geosystems* 5. http://dx.doi.org/10.1029/2003GC000602.

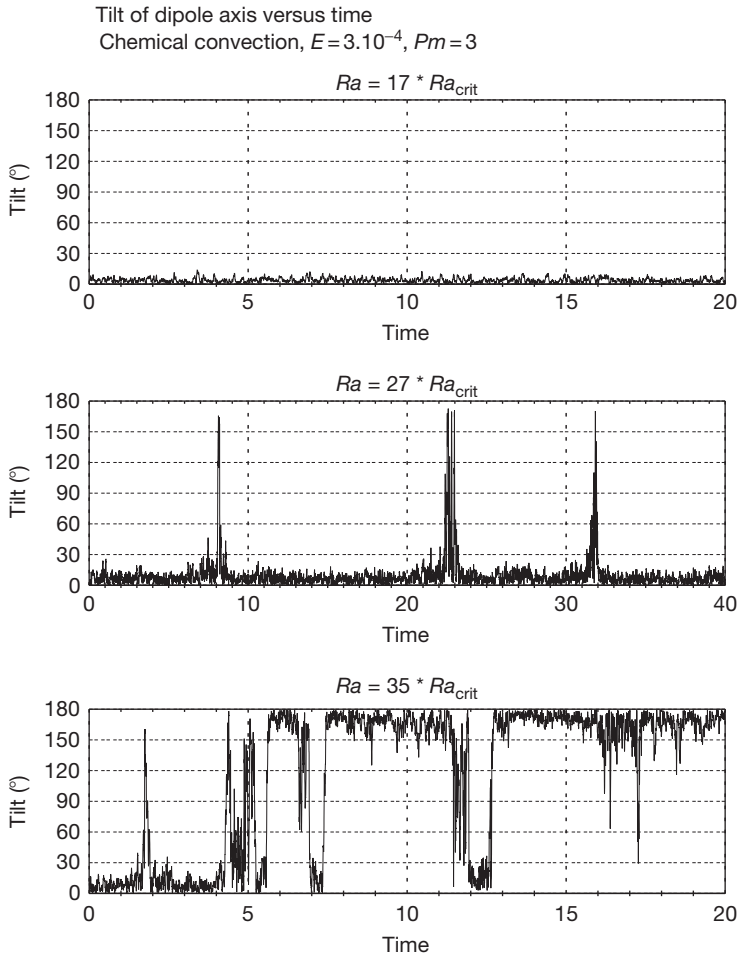

Figure 13 Three time series of a simulated field. The top row is for a low Rayleigh number, which is stable. The middle row is for a higher Rayleigh number, which has failed reversals. The bottom row is for a still higher Rayleigh number, which shows dipole reversals and failed reversals. Each row shows the dipole colatitude at the surface versus time (in magnetic diffusion times, here estimated as 80 000 years). Adapted from Kutzner C and Christensen U (2002) From stable dipolar to reversing numerical dynamos. *Physics of the Earth and Planetary Interiors* 121: 29–45.

Several other groups have since studied this reversal-tendency dependence on the relative effects of convection and rotation by analyzing many long dynamo simulations (e.g., Christensen and Aubert, 2006; Driscoll and Olson, 2009; Lhuiller et al., 2013; Olson and Christensen, 2006; Olson et al., 2010, 2011). They all basically agree that in parameter space, a transitional regime exists between one dominated by rotation, characterized by a dominantly dipolar field structure (above the CMB) that does not reverse, and one dominated by convection, characterized by a multipolar field structure with a frequently reversing dipole. Dynamo simulations in this transitional parameter regime have long stable dipole-dominated chrons separated by relatively short reversals, which sometimes are very complex involving failed reversals (Lhuiller et al., 2013; Olson et al., 2011). These studies suggest that the Earth's dynamo sits in an extension of this transitional regime where the effects of convection and rotation are comparable but both are many orders of magnitude greater than what they are for any of these computer-simulated dynamos. Although quite possible, such a huge extrapolation in parameter space is necessarily uncertain because the characteristics of a dynamo mechanism depend not only on the ratio of the convective to rotational effects but also on the absolute amplitudes of these two fundamental dynamo ingredients.

Glatzmaier et al. (1999) chose strongly convective, rotationally dominant, cases to test the sensitivity of convective dynamos to the pattern of the heat-flux boundary condition on the CMB (**Figure 14**), presumably imposed by mantle convection. Their model differs from all other geodynamo models by solving the equations of motion within the anelastic approximation instead of the Boussinesq approximation (see **Chapters 8.03**, **8.05**, and **8.08**). That is, in their model, the variation of density with depth is taken into account and both compositional and thermal buoyancy are computed. In addition, more self-consistent thermal and compositional boundary conditions are applied at the inner-core boundary. They found that forcing greater heat flux through the CMB in the polar and equatorial regions, as opposed to midlatitude, produces a strong, stable, axial dipole, whereas the opposite CMB heat-flux pattern produces frequent reversals (see **Chapter 8.12**). Of the eight cases they tested, their Earth-like tomographic heat-flux case (h) and their homogeneous heat-flux case (g) appear most Earth-like in terms of the long and irregular times between reversals and the relatively short and highly variable reversal durations. In addition, like the Earth, case 'h' has more frequent failed reversals than successful reversals. The system seems to be continually trying to reverse via MHD instabilities but only after many attempts are the conditions favorable for the new polarity to continue to grow and the old polarity to be fully destroyed (**Figure 15**). This continuing process of trying to reverse occurs in these simulations at roughly the frequency at which failed reversals occur in the Earth, which is similar to the frequency that regular full reversals occur in the Wicht and Olson (2004) simulations (**Figure 12**). As mentioned earlier in the text, Coe and Glatzmaier (2006) (Figure 7) show that, for the cases tested by Glatzmaier et al. (1999), low reversal and excursion frequencies and high field intensities are associated with magnetic fields at the CMB that are mainly antisymmetric with respect to the equator (i.e., more like an axial dipole field instead of an axial quadrupole field).

Several other dynamo simulation studies with similar patterns of heterogeneous CMB heat flux have since been made; these span many more magnetic diffusion times and produce more reversals per case than does the Glatzmaier et al. (1999) study. However, some of the conclusions from these later studies conflict with those of Glatzmaier et al. (1999). For example, Kutzner and Christensen (2004) and Olson et al. (2010) found that reducing the CMB heat flux in the equatorial region reduces the resulting reversal and excursion frequencies in their dynamo simulations and found that their reversal frequencies are fairly insensitive to the relative amount of CMB heat flux in the polar regions or to the nonaxisymmetry of the heat-flux boundary condition. In particular, the most stable (i.e., nonreversing) case of Glatzmaier et al. (1999) is their case E (**Figure 14(e)**), which has an axisymmetric CMB heat flux peaking in both the equatorial and polar regions; this case also maintains the highest field intensity, dipolarity, and axial antisymmetry (Table 1 of Coe and Glatzmaier, 2006). In contrast, this CMB heat-flux pattern produces relatively high reversal and excursion frequencies in the simulations by Kutzner and Christensen (2004) and by Olson et al. (2010). The three studies do, however, agree that a CMB heat-flux pattern like that of case D in **Figure 14(d)** (i.e., high CMB heat flux in the polar regions and low flux in the equatorial region) produces a lower reversal frequency than the one like that of case C, which has the opposite CMB heat-flux pattern of case D imposed. This may suggest that the region of parameter space sampled by Glatzmaier et al. (1999) is more sensitive to the heat flux in the polar regions, whereas that sampled by Kutzner and Christensen (2004) and Olson et al. (2010) is more sensitive to the heat flux in the equatorial region. Kutzner and Christensen (2004) and Olson et al. (2010) also investigated what effect the prescribed amplitude of the spatial variations in the CMB heat flux has on the reversal frequency in their simulations; both studies found little effect.

Another issue, for which various simulation studies have produced conflicting conclusions, is the effect of a finitely conducting solid inner core on the frequency of dipole reversals. As mentioned in the preceding text, Glatzmaier and Roberts (1995) found that an insulating inner core in their early simulations produced a reversal frequency much greater than that seen in the paleomagnetic reversal record and that making their inner core electrically conducting reduced their reversal frequency. The long magnetic diffusion time of the inner core (a couple thousand years), relative to the shorter convective turnover time of the outer core (a couple hundred years), tends to anchor the original polarity and increase the time fluid flow modifications in the outer core need to persist in order to achieve a successful reversal. That is, like the stabilizing effects of rotation mentioned previously in the text, the conducting inner core inhibits changes in the global magnetic field structure that convection attempts to cause. However, two subsequent dynamo simulation studies produced conclusions about the effects of a conducting inner core on the frequency of magnetic reversals that differ from those of Glatzmaier and Roberts (1995) and Glatzmaier et al. (1999). Wicht (2002) found very little difference between his insulating inner-core case and his conducting inner-core cases. Lhuiller et al. (2013), on the other hand, found that the conductivity of the inner core does have a significant effect, but the opposite of that found by Glatzmaier and Roberts (1995); that

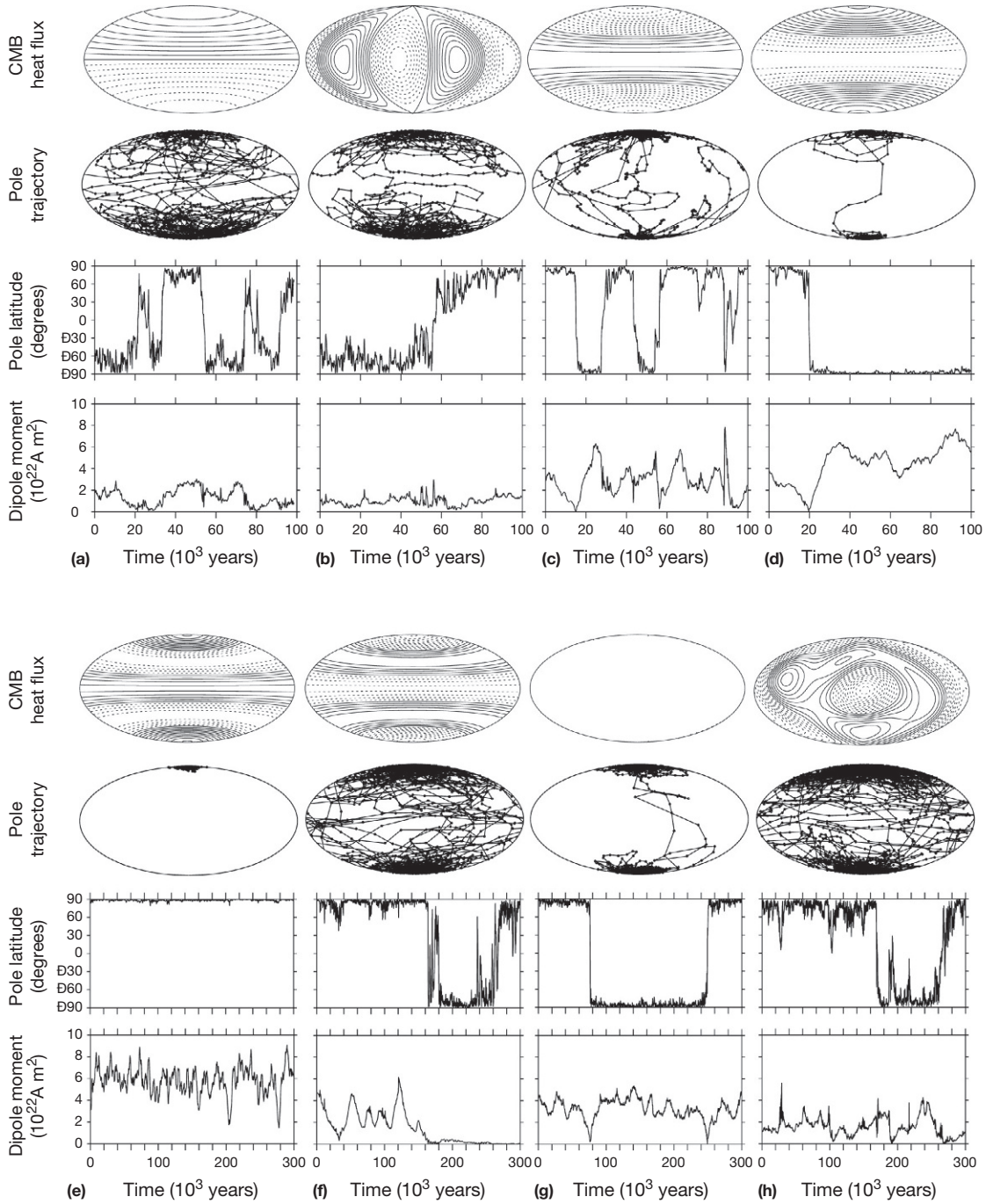

Figure 14 Eight dynamo simulations with different imposed patterns of radial heat flux at the CMB. The top row shows the patterns of CMB heat flux. Solid contours represent greater heat flux out of the core relative to the mean; broken contours represent less. Case 'g' has a uniform CMB heat flux and case 'h' has a pattern based on seismic tomography, assuming that lower sound speed corresponds to warmer mantle and therefore smaller heat flux out of the core. The second row shows the trajectory of the south magnetic pole of the dipole part of the field outside the core, spanning the times indicated in the plots; the marker dots are about 100 years apart. The plots in the third and fourth rows show the south magnetic pole latitude and the magnitude of the dipole moment (in units of 10^{22} Am^2) versus time (in units of 1000 years). Reproduced from Glatzmaier GA, Coe RS, Hongre L, and Roberts PH (1999) The role of the Earth's mantle in controlling the frequency of geomagnetic reversals. *Nature* 401: 885–890, with permission from *Nature*.

is, Lhuiller et al. (2013) found that their insulating inner-core cases have a smaller reversal frequency than their conducting inner-core cases. Lhuiller et al. (2013) provided a detailed statistical analysis, based on empirical probability distribution functions of their simulated results, that illustrates how their insulating inner-core case is much more likely to be in one of the two stable axial dipole polarity states than in an unstable transition state. Their conducting inner-core cases, on the other hand, show a higher probability of being in the transition state, that is, they have higher reversal and failed reversal frequencies.

A related issue is how the size of a conducting solid inner core affects the reversal frequency. Dynamo simulations by Roberts and Glatzmaier (2001) that investigate the past, present, and future of the geodynamo suggest that the Earth's magnetic field in the distant past, when the solid inner core was smaller or did not yet exist, may have been more strongly dominated by the axial dipole and less likely to experience dipole reversals than it is today; this trend is suggested to continue into the distant future. The reason for this is that a smaller inner core provides less obstruction between hemispheres for fluid flow and magnetic field, resulting in weaker perturbations to the global flow and field. As discussed in Section 8.11.2, paleomagnetic observations, though sparse, appear to support a lower average reversal rate from 1 to 2.8 Ga than during the well-documented interval from 0 to 150 Ma. Olson et al. (2013) recently conducted a more ambitious study of how the evolution of the Earth's mantle and core has affected the dipole reversal frequency over the Phanerozoic, including the issue of superchrons. They do a series of dynamo simulations representing different times during the past half billion years by setting the dynamo control parameters for each epoch to reflect the evolutionary changes in the CMB heat flux, inner-core size, inner-core boundary compositional flux, and the Earth's rotation rate. Two scenarios are tested to prescribe the CMB heat flux at the various epochs the dynamo is run during the simulated evolution. One scenario uses a reconstruction of the Earth's history of mantle convection, including tectonic plate motions, based on a 3D mantle convection simulation. The other assumes a time-independent pattern of CMB heat flux based on today's hot-spot locations and seismic shear-wave heterogeneity of the lower mantle. They find that their time-dependent CMB heat flux scenario produces a decreasing reversal frequency with age (in rough agreement with the findings of Roberts and Glatzmaier (2001)) and produces a slow cycle of reversal frequency, that is, superchrons. Their time-independent CMB heat-flux scenario does not have these tendencies.

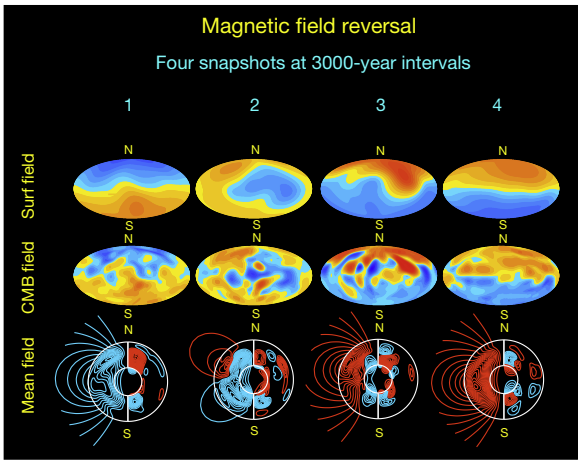

Figure 15 A sequence of snapshots of the longitudinally averaged magnetic field through the interior of the core and of the radial component of the field at the CMB and at what would be the surface of the Earth, displayed at roughly 3000-year intervals, spanning the first dipole reversal of case 'h' in Figure 14. In the plots of the average field, the small circle represents the inner-core boundary and the large circle is the CMB. The poloidal field is shown as magnetic field lines on the left-hand sides of these plots (blue is clockwise and red is counterclockwise). The toroidal field direction and intensity are represented as contours (not magnetic field lines) on the right-hand sides (red is eastward and blue is westward). Hammer (equal area) projections of the entire CMB and surface are used to display the radial field (with the two different surfaces displayed as the same size). Reds represent outward-directed field and blues inward-directed field. The surface field, which is typically an order of magnitude weaker, was multiplied by 10 to enhance the color contrast. Adapted from Glatzmaier GA, Coe RS, Hongre L, and Roberts PH (1999) The role of the Earth's mantle in controlling the frequency of geomagnetic reversals. *Nature* 401: 885–890.

As computational resources continue to improve, simulations using much smaller (i.e., more realistic) diffusivities become possible. Takahashi et al. (2005) produced some of the most realistic geodynamo simulations to date by using much larger Rayleigh numbers and smaller Ekman numbers, that is, smaller, more realistic viscous, thermal, and magnetic diffusivities. Several dipole reversals occurred with a highly variable reversal frequency (Figure 16). They also show that the internal dynamics of the fluid core changes significantly when the viscous forces become much smaller than the Coriolis (rotational) and Lorentz (magnetic) forces, which underscores the importance of reaching the very low viscosity (turbulent) regime if one wishes to simulate and understand the dynamo mechanism in the Earth's core.

Considerable progress has been made over the past two decades in our understanding of the geodynamo through the use of 3D MHD dynamo simulations. However, although the various dynamo simulation studies do agree on some things, several issues, like how CMB heat-flux patterns and the conductivity of the solid inner core affect the geodynamo reversal frequency, are still unresolved. These discrepancies are

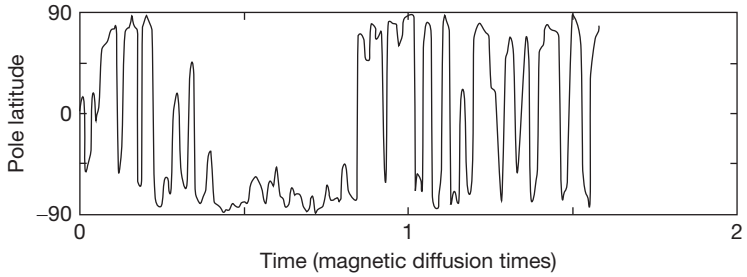

Figure 16 The magnetic pole latitude (at the surface) versus time (in magnetic diffusion times, here estimated as 200 000 years). Adapted from Takahashi F, Matsushima M, and Honkura Y (2005) Simulations of a quasi-Taylor state geomagnetic field including polarity reversals on the Earth Simulator. *Science* 309: 459–461.

partly due to the differences in dynamo model approximations. Some assume a constant background density; some account for density stratification. Some simulate only thermal convection or only compositional convection; some define a codensity that approximates the combination of the two; some treat both separately, each making its own contribution to buoyancy and to the flux at the inner-core and outer-core boundaries. Some treat the solid inner core as an insulator; some treat it as a conductor, but may or may not allow it to freely rotate in response to the viscous and magnetic torques on it.

However, the main reason for the disagreement among simulation studies is likely due to the approximations those designing the dynamo simulations are forced to make because parallel supercomputers are not yet fast enough to simulate global MHD convective dynamos in a parameter regime that would closely approximate the strong rotationally dominant turbulence that exists in the Earth's low-viscosity fluid outer core. That is, all 'geodynamo' simulations to date have some control parameters, like viscosity, set to values far from what would produce realistic flows and fields. The various studies choose different ways to do this. For example, most studies choose viscous, thermal, compositional, and magnetic diffusivities that are all roughly equal to the magnetic diffusivity of the Earth's core, instead of setting the viscous, thermal, and compositional diffusivities to more realistic values orders of magnitude smaller. They define 'time' based on the correct (20 000-year) magnetic diffusion time, which is proportional to the square of the radius of the Earth's core divided by its magnetic diffusivity. However, the ratio of viscous to rotational effects, that is, the Ekman number, in all dynamo simulations, especially those used to analyze long simulated times required for reversal studies, is forced (for computational reasons) to be many orders of magnitude larger than it is for the Earth's fluid core. Therefore, the rotational period in these models is four to five orders of magnitude longer than the Earth's rotational period of 1 day. An alternative (Glatzmaier and Roberts, 1995; Glatzmaier et al., 1999) is to use not only the Earth's correct magnetic diffusion time but also its actual 1-day rotation period. To do this (with current computers) requires using a smaller Ekman number and a viscous diffusivity much larger than the Earth's magnetic diffusivity (instead of smaller than it). The smaller Ekman number requires a much smaller numerical time step (because of an inertial oscillation constraint proportional to the rotation period of the model core) and a larger Rayleigh number, which requires much greater spatial resolution. This, in turn, significantly increases the computational resources required to simulate a magnetic diffusion time; but 'time' then is geophysically realistic for the two major forces in the problem: Coriolis (i.e., rotational) and Lorentz (i.e., magnetic). Obviously, neither way of coping with the lack of sufficient computational power should be expected to produce realistic geodynamo simulations (Glatzmaier, 2002); and it is not surprising that these different choices result in somewhat different conclusions about what controls the reversal frequency of the geodynamo.

A goal for future dynamo simulations (Glatzmaier, 2002) is to be able to run with a viscous diffusivity no greater than the magnetic diffusivity of the Earth's core ($2\ m^2\ s^{-1}$) and at the rotation period of 1 day, which would mean an Ekman number of 10^{-9}, about three orders of magnitude smaller than what can be done today in a global 3D dynamo simulation. Efforts are currently being made to improve or completely rewrite dynamo codes to take advantage of future supercomputers on which hundreds of thousands of processors will be able to work efficiently in parallel on a dynamo simulation that runs for months at a time simulating the geodynamo at a high enough spatial resolution and temporal resolution to capture strong turbulence and for a long enough simulated time to study reversals.

8.11.4 Conclusions

Our understanding of geomagnetic reversals has improved considerably over the years with paleomagnetic studies and geodynamo simulations. Paleomagnetic observations now provide considerable constraints on the time-averaged field and the character of reversals, some of which have been matched to first order in some dynamo simulations. Nonetheless, more 'ground truthing' observations and more realistic simulations are needed to discover the details of the reversal mechanism in the Earth's core and what influences its range of variation.

In terms of observations, longer, more reliable, and more detailed records of paleomagnetic field behavior are needed, especially early in the Earth's history. This of course will take considerable time and effort.

In terms of models, geodynamo simulations need to be more turbulent and rotationally dominant. Laminar flows are certainly easier to produce and analyze; but it is unlikely that the large-scale convection cells seen in such studies produce a reversal mechanism representative of that in the Earth's turbulent outer core. The same conclusion has been reached in the solar dynamo community. In addition, much longer simulations are needed to gather better statistics on the types and frequencies of reversals. Finally, the sensitivities to several model specifications, like density stratification, boundary conditions, compositional buoyancy, inner-core conductivity, and diffusion coefficients, need to be tested. These modeling goals all require significant amounts of computing resources and, as in the past, compromises will need to be made as we wait for computer hardware and codes to improve. Support for this research was provided by NSF CSEDI and Geophysics programs.

References

Acton G, Guyodo Y, and Brachfeld S (2006) The nature of a cryptochron from a paleomagnetic study of chron C4r.2r recorded in sediments off the Antarctic Peninsula. *Physics of the Earth and Planetary Interiors* 156: 213–222.

Besse J and Courtillot V (2002) Apparent and true polar wander and the geometry of the geomagnetic field over the last 200 Myr. *Journal of Geophysical Research* 107(6–1): 6–31.

Biggin AJ, Strik GHMA, and Langereis CG (2008a) Evidence for a very-long-term trend in geomagnetic secular variation. *Nature Geoscience* 1: 395–398.

Biggin AJ, Van Hinsbergen DJJ, Langereis CG, Straathof GB, and Deenen MHL (2008b) Geomagnetic secular variation in the Cretaceous Normal Superchron and in the Jurassic. *Physics of the Earth and Planetary Interiors* 169: 3–19.

Bonanno A, Elstner D, and Belvedere G (2006) Advection-dominated solar dynamo model with two-cell meridional flow a positive alpha-effect in the tachocline. *Astronomische Nachrichten* 327: 680–685.

Busse FH (2002) Convective flows in rapidly rotating spheres and their dynamo action. *Physics of Fluids* 14: 1301–1314.

Camps P, Coe RS, and Prevot M (1999) Transitional geomagnetic impulse hypothesis: Geomagnetic fact or rock-magnetic artifact? *Journal of Geophysical Research* 104: 17747–17758.

Champion DE, Lanphere MA, and Kuntz MA (1988) Evidence for a new geomagnetic reversal from lava flows in Idaho: Discussion of short polarity reversals in the Brunhes and late Matuyama polarity chrons. *Journal of Geophysical Research* 93: 11667–11680.

Channell JET and Lehman B (1997) The last two geomagnetic polarity reversals recorded in high-deposition-rate sediment drifts. *Nature* 389: 712–715.

Christensen U and Aubert J (2006) Scaling properties of convection-driven dynamos in rotating spherical shells and applications to planetary magnetic fields. *Geophysical Journal International* 166: 97–114.

Clement BM (1991) Geographical distribution of transitional VGPs – Evidence for non-zonal equatorial symmetry during the Matuyama–Brunhes geomagnetic reversal. *Earth and Planetary Science Letters* 104: 48–58.

Clement BM (2004) Dependence of the duration of geomagnetic polarity reversals on site latitude. *Nature* 428: 637–640.

Coe RS and Glatzmaier GA (2006) Symmetry and stability of the geomagnetic field. *Geophysical Research Letters* 33: L21311. http://dx.doi.org/10.1029/2006GL027903.

Coe RS and Glen JMG (2004) The complexity of reversals. In: Channell JET, Kent DV, Lowrie W, and Meert JG (eds.) *Timescales of the Internal Geomagnetic Field*. *Geophysical Monograph Series*, vol. 145, pp. 221–232. Washington, DC: AGU.

Coe RS, Hongre L, and Glatzmaier GA (2000) An examination of simulated geomagnetic reversals from a palaeomagnetic perspective. *Philosophical Transactions of the Royal Society of London, Series A* 358: 1141–1170.

Coe RS, Singer BS, Pringle MS, and Zhao X (2004) Matuyama–Brunhes reversal and Kamikatsura event on Maui: Paleomagnetic directions, 40Ar/39Ar ages, and implications. *Earth and Planetary Science Letters* 222: 667–684.

Dormy E, Valet J-P, and Courtillot V (2000) Numerical models of the geodynamo and observational constraints. *Geochemistry, Geophysics, Geosystems* 1: 1–42. http://dx.doi.org/10.1029/2000GC000062.

Driscoll P and Olson P (2009) Effects of buoyancy and rotation on the polarity reversal frequency of gravitationally-driven numerical dynamos. *Geophysical Journal International* 178: 1337–1350.

Dunlop DJ and Yu Y (2004) Intensity and polarity of the geomagnetic field during Precambrian time. In: Channell JET, Kent DV, Lowrie W, and Meert JG (eds.) *Timescales of the Internal Geomagnetic Field*. *Geophysical Monograph Series*, vol. 145, pp. 85–100. Washington, DC: AGU.

Elston DP, Enkin RJ, Baker J, and Kisilevsky DK (2002) Tightening the Belt: Paleomagnetic-stratigraphic constraints on deposition, correlation, and deformation of the Middle Proterozoic (ca. 1.4 Ga) Belt-Purcell Supergroup, United States and Canada. *Geological Society of America Bulletin* 114: 619–638.

Gallet Y, Pavlov V, Halverson G, and Hulot G (2012) Toward constraining the long-term reversing behavior of the geodynamo: A new "Maya" superchron 1 billion years ago from the magnetostratigraphy of the Kartochka Formation (southwestern Siberia). *Earth and Planetary Science Letters* 339–340: 117–126.

Giesecke A, Rudiger G, and Elstner D (2005) Oscillating alpha-squared-dynamos and the reversal phenomenon of the global geodynamo. *Astronomische Nachrichten* 326: 693–700.

Gilman PA (1983) Dynamically consistent nonlinear dynamos driven by convection in a rotating spherical shell. II: Dynamos with cycle and strong feedbacks. *Astrophysical Journal Supplement Series* 53: 243–268.

Glatzmaier GA (1985) Numerical simulations of stellar convective dynamos. II: Field propagation in the convection zone. *Astrophysical Journal* 291: 300–307.

Glatzmaier GA (2002) Geodynamo simulations – How realistic are they? *Annual Review of Earth and Planetary Sciences* 30: 237–257.

Glatzmaier GA, Coe RS, Hongre L, and Roberts PH (1999) The role of the Earth's mantle in controlling the frequency of geomagnetic reversals. *Nature* 401: 885–890.

Glatzmaier GA and Roberts PH (1995) A three-dimensional self-consistent computer simulation of a geomagnetic field reversal. *Nature* 377: 203–209.

Glen JMG, Coe RS, and Liddicoat JC (1999) A detailed record of paleomagnetic field change from Searles Lake, California: 2. The Gauss Matuyama polarity reversal. *Journal of Geophysical Research* 104: 12883–12894.

Grand SP (2002) Mantle shear-wave tomography and the fate of subducted slabs. *Philosophical Transactions of the Royal Society of London A* 360: 2475–2491.

Gubbins D and Coe RS (1993) Longitudinally confined geomagnetic reversal paths from non-dipolar transition fields. *Nature* 362: 51–53.

Guyodo Y and Valet JP (1999) Global changes in intensity of the Earth's magnetic field during the past 800 kyr. *Nature* 399: 249–252.

Haldan MM, Langereis CG, Biggin AJ, Dekkers MJ, and Evans ME (2009) A comparison of detailed equatorial red bed records of secular variation during the Permo-Carboniferous Reversed Superchron. *Geophysical Journal International* 177: 834–848. http://dx.doi.org/10.1111/j.1365-246X.2009.04124.x.

Hartl P and Tauxe L (1996) A precursor to the Matuyama–Brunhes transition-field instability as recorded in pelagic sediments. *Earth and Planetary Science Letters* 138: 121–135.

Hoffman KA (1992) Dipolar reversal states of the geomagnetic field and core mantle dynamics. *Nature* 359: 789–794.

Hoffman KA and Mochizuki N (2012) Evidence of a partitioned dynamo reversal process from paleomagnetic recordings in Tahitian lavas. *Geophysical Research Letters* 39: L06303. http://dx.doi.org/10.1029/2011GL050830.

Hoffman KA and Singer BS (2004) Regionally recurrent paleomagnetic transitional fields and mantle processes. In: Channell JET, Kent DV, Lowrie W, and Meert JG (eds.) *Timescales of the Internal Geomagnetic Field*. *Geophysical Monograph Series*, vol. 145, pp. 233–243. Washington, DC: AGU.

Hoffman KA and Singer BS (2008) Magnetic source separation in Earth's outer core. *Science* 321: 1800. http://dx.doi.org/10.1126/science.1159777.

Hollerbach R and Jones CA (1993) Influence of the Earth's core on geomagnetic fluctuations and reversals. *Nature* 365: 541–543.

Jarboe NA, Coe RS, and Glen JM (2011) Evidence from lava flows for complex polarity transitions: The new composite Steens Mountain reversal record. *Geophysical Journal International* 186: 580–602.

Johnson CL, Constable CG, Tauxe L, et al. (2008) Recent investigations of the 0–5 Ma geomagnetic field recorded by lava flows. *Geochemistry, Geophysics, Geosystems* 9: Q04032. http://dx.doi.org/10.1029/2007GC001696.

Kageyama A, Ochi MM, and Sato T (1999) Flip–flop transitions of the magnetic intensity and polarity reversals in the magnetohydrodynamic dynamo. *Physical Review Letters* 82: 5409–5412.

Kida S, Araki K, and Kitauchi H (1997) Periodic reversals of magnetic field generated by thermal convection in a rotating spherical shell. *Journal of the Physical Society of Japan* 66: 2194–2201.

Kono M and Roberts PH (2002) Recent geodynamo simulations and observation of the geomagnetic field. *Reviews of Geophysics* 40: 1013. http://dx.doi.org/10.1029/2000RG000102.

Kutzner C and Christensen U (2002) From stable dipolar to reversing numerical dynamos. *Physics of the Earth and Planetary Interiors* 121: 29–45.

Kutzner C and Christensen UR (2004) Simulated geomagnetic reversals and preferred virtual geomagnetic pole paths. *Geophysical Journal International* 157: 1105–1118.

Laj C, Mazaud A, Weeks R, Fuller M, and Herrero-Bervera E (1991) Geomagnetic reversal paths. *Nature* 351: 447.

Layer PW, Lopez-Martinez M, Kroner A, York D, and McWilliams M (1998) Thermochronometry and palaeomagnetism of Archaean Nelshoogte Pluton, South Africa. *Geophysical Journal International* 135: 129–145.

Lhuiller F, Hulot G, and Gallet Y (2013) Statistical properties of reversals and chrons in numerical dynamos and implications for the geodynamo. *Physics of the Earth and Planetary Interiors* 220: 19–26.

Love JJ (2000) Statistical assessment of preferred transitional VGP longitudes based on palaeomagnetic lava data. *Geophysical Journal International* 140: 211–221.

Lund S, Stoner JS, Channell JET, and Acton G (2006) A summary of Brunhes paleomagnetic field variability recorded in ocean drilling program cores. *Physics of the Earth and Planetary Interiors* 156: 194–204.

Mankinen EA, Prévot M, Grommé CS, and Coe RS (1985) The Steens Mountain (Oregon) geomagnetic polarity transition.1: Directional history, duration of episodes, and rock magnetism. *Journal of Geophysical Research* 90: 393–416.

McElhinny M (2004) Geocentric axial dipole hypothesis: A least squares perspective. In: Channell JET, Kent DV, Lowrie W, and Meert JG (eds.) *Timescales of the Internal Geomagnetic Field*. *Geophysical Monograph Series*, vol. 145, pp. 1–12. Washington, DC: AGU.

McFadden PL, Barton CE, and Merrill RT (1993) Do virtual geomagnetic poles follow preferred paths during geomagnetic reversals? *Nature* 361: 342–344.

McFadden PL, Merrill RT, McElhinny MW, and Lee S (1991) Reversals of the Earth's magnetic field and temporal variations of the dynamo families. *Journal of Geophysical Research* 96: 3923–3933.

Merrill RT (1996) *The Magnetic Field of the Earth*, 531 pp. San Diego, CA: Academic Press.

Merrill RT and McFadden PL (1999) Geomagnetic polarity transitions. *Reviews of Geophysics* 37: 201–226.

Ogg JG (2004) The Jurassic period. In: Gradstein FM, Ogg JG, and Smith AG (eds.) *A Geologic Time Scale*, pp. 307–343. Cambridge: Cambridge University Press.

Ogg JG, Agterberg FP, and Gradstein FM (2004) The Cretaceous period. In: Gradstein FM, Ogg JG, and Smith AG (eds.) *A Geologic Time Scale*, pp. 344–383. Cambridge: Cambridge University Press.

Olson P and Christensen UR (2002) The time-averaged magnetic field in numerical dynamos with nonuniform boundary heat flow. *Geophysical Journal International* 151: 809–823.

Olson P and Christensen UR (2006) Dipole moment scaling for convection-driven planetary dynamos. *Earth and Planetary Science Letters* 250: 561–571.

Olson PL, Coe RS, Driscoll PE, Glatzmaier GA, and Roberts PH (2010) Geodynamo reversal frequency and heterogeneous core–mantle boundary heat flow. *Physics of the Earth and Planetary Interiors* 180: 66–79.

Olson PL, Deguen R, Hinnov LA, and Zhong S (2013) Controls on geomagnetic reversals and core evolution by mantle convection in the Phanerozoic. *Physics of the Earth and Planetary Interiors* 214: 87–103.

Olson PL, Glatzmaier GA, and Coe RS (2011) Complex polarity reversals in a geodynamo model. *Earth and Planetary Science Letters* 304: 168–179.

Pavlov V and Gallet Y (2005) A third superchron during the Early Paleozoic. *Episodes* 28: 1–7.

Prévot M and Camps P (1993) Absence of preferred longitude sectors for poles from volcanic records of geomagnetic reversals. *Nature* 366: 53–57.

Prévot M, Mankinen EA, Coe RS, and Grommé CS (1985) The Steens Mountain (Oregon) geomagnetic polarity transition. 2. Field intensity variations and discussion of reversal models. *Journal of Geophysical Research* 90: 10417–10448.

Reshetnyak M and Steffen B (2005) A dynamo model in a spherical shell. *Numerical Methods and Programming* 9: 27–34.http://www.num-meth.srcc.msu.su.

Roberts PH and Glatzmaier GA (2001) The geodynamo, past, present, and future. *Geophysical and Astrophysical Fluid dynamics* 94: 47–84.

Sarson GR and Jones CA (1999) A convection driven geodynamo reversal model. *Physics of the Earth and Planetary Interiors* 111: 3–20.

Singer BS, Hoffman KA, Coe RS, et al. (2005) Structural and temporal requirements for geomagnetic field reversal deduced from lava flows. *Nature* 434: 633–636.

Smirnov AV, Tarduno JA, and Evans DAD (2011) Evolving core conditions ca. 2 billion years ago detected by paleosecular variation. *Physics of the Earth and Planetary Interiors* 187: 225–231.

Takahashi F, Matsushima M, and Honkura Y (2005) Simulations of a quasi-Taylor state geomagnetic field including polarity reversals on the Earth Simulator. *Science* 309: 459–461.

Tarduno JA, Cottrell RD, Watkeys MK, et al. (2010) Geodynamo, solar wind, and magnetopause 3.4 to 3.45 billion years ago. *Science* 327: 1238–1240.

Tauxe L, Herbert T, Shackleton NJ, and Kokk YS (1996) Astronomical calibration of the Matuyama–Brunhes boundary: Consequences for magnetic remanence acquisition in marine carbonates and the Asian loess sequences. *Earth and Planetary Science Letters* 140: 133–146.

Valet JP, Fournier A, Courtillot V, and Herrero-Bervera E (2012) Dynamical similarity of geomagnetic field reversals. *Nature* 90: 89–94.

Valet JP, Tucholka P, Courtillot V, and Meynadier L (1992) Palaeomagnetic constraints on the geometry of the geomagnetic field during reversals. *Nature* 356: 400–407.

Wicht J (2002) Inner-core conductivity in numerical dynamo simulations. *Physics of the Earth and Planetary Interiors* 132: 281–302.

Wicht J and Olson P (2004) A detailed study of the polarity reversal mechanism in a numerical dynamo model. *Geochemistry, Geophysics, Geosystems* 5: 1–23. http://dx.doi.org/10.1029/2003GC000602.

Wilson RL (1971) Dipole offset: The time-averaged palaeomagnetic field over the past 25 million years. *Geophysical Journal of the Royal Astronomical Society* 22: 491–504.

This page intentionally left blank

8.12 Inner Core Dynamics

I Sumita, Kanazawa University, Kanazawa, Japan
M Bergman, Bard College at Simon's Rock, Great Barrington, MA, USA

© 2015 Elsevier B.V. All rights reserved.

8.12.1	**Introduction**	297
8.12.2	**Core Composition and Phase Diagram, Crystal Structure, and Thermal Conductivity of Iron**	298
8.12.2.1	Composition of the Core	298
8.12.2.2	Phase Diagram of Iron Alloy	299
8.12.2.3	Crystal Structure of Iron	300
8.12.2.4	Thermal Conductivity of the Core	301
8.12.3	**Solidification of the Inner Core**	301
8.12.4	**Grain Size and Rheology in the Inner Core**	302
8.12.5	**Origin of Inner Core Elastic Anisotropy**	304
8.12.5.1	An Overview	304
8.12.5.2	Anisotropy of hcp Iron	304
8.12.5.3	Dynamical Models	305
8.12.5.4	Solidification Texturing Models	307
8.12.6	**Origin of Other Inner Core Seismic Structures**	308
8.12.6.1	Properties and Structure of the ICB and the 'F-Layer'	308
8.12.6.2	Inner Core Attenuation and Scattering	309
8.12.6.3	Hemispheric and Depth Variation of Seismic (Isotropic) Velocity, Attenuation, Elastic Anisotropy, and Attenuation Anisotropy	309
8.12.7	**Inner Core Rotation**	311
8.12.7.1	An Overview	311
8.12.7.2	Electromagnetic Coupling	311
8.12.7.3	Gravitational Coupling	311
8.12.7.4	Combined Coupling	312
8.12.8	**Summary**	312
References		312

8.12.1 Introduction

With a radius of just over 1200 km, the Earth's solid, central inner core is only 30% smaller than the moon. Its dynamics are fascinating and, for planet Earth, possibly unique. The inner core boundary (ICB) is a solid–liquid phase boundary, where the geotherm crosses the liquidus temperature of the iron alloy that comprises the Earth's core. The solidity of the inner core is a consequence of the melting temperature gradient being steeper than the geothermal gradient, as a result of the effects of pressure on the liquidus temperature. In smaller planets and satellites, the entire core may be solid. As the Earth cools and solidification proceeds, the radius of the ICB increases with time. There is a considerable uncertainty in the parameters required for calculating precisely the core's thermal history, but recent best estimates place the age of the inner core at < 1 billion years (see Chapter 8.02). Many of the dynamical processes that take place in the inner core are likely to be related to its growth, which in turn is strongly controlled by the pattern of heat transfer in the outer core or, in other words, the climate of the outer core. Although the inner core, outer core, and mantle are all dynamically coupled, both thermally and mechanically, the effects of coupling are particularly important for the inner core because of its relatively small volume. This implies that the inner core may act as a recorder of the geodynamic processes occurring not only in the outer core but also in the mantle.

The study of inner core dynamics has been motivated by a wide range of observations and inferences, many coming from seismology. Geodynamics has attempted to explain the origin of these inner core properties and attributes, such as elastic anisotropy and high attenuation. Another set of observations that has given us insight into the inner core comes from geomagnetism. For example, inner core solidification has been proposed to be an important candidate for the energy source to drive the geodynamo, and it may affect long-term variations of the strength of the geomagnetic dipole. In addition, motion of the inner core is thought to affect geodetic observations of polar motion.

In this chapter, we review the current understanding of the dynamical processes that operate in the inner core. First, we review the current knowledge of the composition of the inner core and its phase relations. These are important for estimating the compositional buoyancy that helps drive convection in the outer core and for understanding the process through which the inner core is solidifying. Next, we present a discussion on the grain size and stress in the inner core, which are important in controlling the mechanism and timescale of deformation and hence the strain rate and viscosity. This is followed by a critical examination of the models proposed for the origin of

inner core elastic anisotropy, one of the most intriguing features of the inner core. These models require knowledge of the stable phase and elasticity of iron under inner core conditions, which remain uncertain. We also review the origin of other properties inferred of the inner core, such as high attenuation, attenuation anisotropy, and the radial and lateral heterogeneity of seismic properties. Finally, we discuss the mechanisms of inner core super-rotation and translation, further consequences of the dynamical coupling between the inner core and the outer core.

The inner core is a difficult part of our planet to study: the temperature and pressure are difficult to achieve in the lab, remote observations from seismology and geomagnetism are noisy and tricky to interpret, and the dynamical regime is so unlike any other that it is a challenge for theoreticians. Nevertheless, there has been progress. Some of the interesting works since the last edition include seismological findings of sharp, non-spherically symmetric boundaries within the inner core and increasing evidence for a decrease in the P-wave velocity gradient at the base of the outer core that is suggestive of a dense fluid layer; a reevaluation of thermal convection in the inner core that suggests that it could be stratified and have an unusual translational mode that could be responsible for both east–west asymmetry in the inner core and the dense fluid layer; numerical calculations that show that mantle heterogeneities could also be responsible for the east–west asymmetry and a dense fluid layer; a second reevaluation of inner core thermal convection due to revised higher estimates of the thermal conductivity of iron under core conditions; and the possibility of compositional convection in the inner core. This chapter will cover these and other new progress in the field in addition to providing the background work that led to these advances.

8.12.2 Core Composition and Phase Diagram, Crystal Structure, and Thermal Conductivity of Iron

This section examines the composition and phase diagram of the core; in particular, how they impact the solidification and deformation of the Earth's inner core. We also examine briefly the crystal structure of iron under inner core conditions, as well as its thermal conductivity, the latter being important for understanding the dynamical regime of Earth's inner core. See Jeanloz (1990) and Poirier (1994) for detailed reviews on the composition of the core, Boehler (1996a,b) for a review of the pressure–temperature phase diagram of iron (evidence for the existence of the various solid phases and the variation of the melting temperature with pressure), and (**Chapter 2.06**) for a comprehensive discussion of the mineralogy of Earth's core.

8.12.2.1 Composition of the Core

The composition of the core remains 'an uncertain mixture of all the elements' (Birch, 1952). The average density of the Earth, the solar abundance of the elements, and the presence of iron meteorites, thought to be remnants of planetoid cores, all point to the core containing elemental iron (Birch, 1952). Comparison with iron meteorites (Brown and Patterson, 1948; Buchwald, 1975) suggests that the core also contains about 8% nickel by mass. Because nickel has a density similar to that of iron (Stacey and Davis, 2008), its presence in the core is difficult to detect seismically, and furthermore, little theoretical or experimental work on the partitioning of nickel has been carried out.

More studies have been aimed at the composition of the less-dense alloying components in the core and their partitioning upon solidification. Early static compression experiments extrapolated to core conditions (Birch, 1952; Bridgman, 1949) and shock compression experiments (McQueen and Marsh, 1966) showed that iron–nickel alloys under core pressures are about 6–10% more dense than the outer core (Bullen, 1949), implying that less-dense alloying components must be present. More recent calculations using first principles and molecular dynamics (Laio et al., 2000) confirm that liquid iron at 330 GPa and 5400 K is about 6% more dense than the seismic Earth model PREM in the core (Dziewonski and Anderson, 1981), and calculations based on lattice potential theory lean toward a 10% deficit (Shanker et al., 2004).

Iron meteorites contain FeS (troilite) inclusions, suggesting that FeS may alloy with iron in the core (Mason, 1966), and experiments show that sulfur has an affinity for liquid iron–nickel alloys, at least in the range 2–25 GPa and 2073–2623 K (Li and Agee, 2001). Iron–sulfur–silicon liquids have been found to be miscible above 15 GPa at 2343 K (Sanloup and Fei, 2004). Cosmochemical arguments have been made that the mantle is depleted in sulfur relative to its chondritic abundance by two orders of magnitude and that the missing sulfur could reside in the core (Murthy and Hall, 1970). However, since sulfur is volatile, this line of argument has been questioned (Ringwood, 1977).

FeO is absent in iron meteorites because at atmospheric pressure, it is soluble by $<0.1\%$ by mass in solid iron and its solubility increases only slightly above the liquidus (Ringwood, 1977). However, its solubility increases with temperature and pressure as it becomes metallic, so that it could be present in the core (Ringwood and Hibberson, 1990). On the other hand, Huang et al. (2011) found from shock wave data that oxygen in the outer core cannot simultaneously match the observed density and seismic velocity profiles. Other possible alloying components include iron silicate (Fe_xSi_{1-x}), Fe_3C, and FeH (Fukai, 1984; Georg et al., 2007; Lin et al., 2002; MacDonald and Knopoff, 1958; Okuchi, 1997; Wood, 1993), all likely to be metallic under core pressures. Abundance and volatility during condensation from the nebula, the mode of core formation, and solubility in iron during core formation presumably determined the composition of less-dense elements in the core. See McDonough (2003) for a comprehensive discussion of light elements in the core.

The inner core is more dense than the outer core, by about $600\ \mathrm{kg\ m^{-3}}$ according to the seismic Earth model PREM (Dziewonski and Anderson, 1981) and $550 \pm 50\ \mathrm{kg\ m^{-3}}$ according to a model by Masters and Shearer (1990). Part of this difference, perhaps $200\ \mathrm{kg\ m^{-3}}$, can be attributed to iron being more dense in the solid phase (Laio et al., 2000; Stacey and Davis, 2008). The rest is attributed to the less-dense alloying components partitioning into the outer core during solidification of the core. This partitioning has important consequences for the thermodynamics, fluid dynamics, and metallurgy of the core (see **Section 8.12.3**; also **Chapter 8.02**).

The seismically inferred density increase at the ICB, above that due to the phase transition, can be explained if the core is an iron-rich alloy. However, unless the solidus slope is vertical in a phase diagram, some nonzero fraction of the less-dense alloying components will fractionate into the inner core as it solidifies. Jephcoat and Olson (1987) extrapolated the density of pure iron to inner core conditions and found that it is too dense to explain the inner core seismic data, suggesting that the inner core also contains some light alloy, equivalent to 3–7% sulfur by mass. Similarly, Laio et al. (2000) had calculated that solid iron under the conditions at the ICB is 2–3% more dense than given by PREM (Dziewonski and Anderson, 1981) and Lin et al. (2005) confirmed this experimentally by studying the sound velocities of pure iron at high pressure and temperature. Stixrude et al. (1997) calculated that the mass fraction of the less-dense element depends on which less-dense element and compound are present (for instance, FeS vs. FeS_2). However, all estimates indicate that the density jump at the ICB exceeds the 200 kg m^{-3} expected for the phase transition alone, implying that light elements are segregating into the outer core.

Sherman (1995) found that oxygen partitions almost completely into the outer core, so that while it could be responsible for the density jump beyond that due to the phase transition, it could not be the cause of the inner core being less dense than pure iron under inner core conditions. One caveat to this could be if there is a significant liquid fraction still present in the inner core (as much as 8%; Vocadlo, 2007), though this seems unlikely on dynamical grounds since melt is likely to get squeezed out (Sumita et al., 1996). Thus, sulfur is likely to be a necessary component of the core, though it may partition equally between inner and outer cores (Alfe et al., 2000), it by itself cannot explain the density jump at the ICB. Kuwayama et al. (2009) found experimentally that the solubility of silicon in hexagonal close-packed (hcp) iron increases with pressure, perhaps as high as 9.9%.

Geochemists have examined the question of radioactive isotopes in the core, particularly U^{238}, Th^{232}, and K^{40}. Although the presence of radioactive heat had long been proposed as a source of energy for the geodynamo (Bullard, 1950; Gubbins et al., 1979), the presence of heat-producing isotopes has long been questioned, as there is little experimental evidence for their solubility in liquid iron under core conditions (McDonough, 2003). Paleomagnetic evidence suggests that the Earth's magnetic field is at least 3.2 billion years old (McElhinny and Senanayake, 1980; Tarduno et al., 2007). Since the compositional buoyancy provided by inner core solidification helps drive the dynamo, the inner core may be as old as the dynamo. However, thermal calculations (Labrosse et al., 2001) suggest that such an old inner core is incompatible with the rate at which the inner core is currently growing, especially in light of recent estimates of core thermal conductivity (see **Section 8.12.2.4**). A resolution to this problem may be the presence of K^{40} in the core (Gessmann and Wood, 2002; Murthy et al., 2003), which, with a half-life of 1.25 billion years, would have been an important heat source earlier in the Earth's history, allowing a slow rate of inner core growth. Another possibility is that the power requirements of the dynamo are less than previously thought (Christensen and Tilgner, 2004), mitigating the need for an old inner core and hence radioactive heat sources. In light of all these uncertain possibilities, the presence of radioactive elements in the core and the age of the inner core remain open questions.

8.12.2.2 Phase Diagram of Iron Alloy

Considerable work has been done in determining the alloy phase diagram of the core and the crystal structure of iron under inner core pressure and temperature conditions. In a binary system with end members A and B, where each pure solid exists only in a single solid phase (crystal structure) and where A and B are miscible in the liquid phase, as is likely in the outer core (Alfe et al., 1999; Helffrich and Kaneshima, 2004), three types of phase diagrams are possible. Which type of phase diagram exists for a given system is determined by the minimum in Gibbs free energy:

$$G = H - TS \qquad [1]$$

where H is the enthalpy, T is the temperature, and S is the entropy. If the crystal structures are the same, and the atomic sizes are similar, then A and B may be completely miscible in the solid state and in the liquid state ($\Delta H = 0$ upon mixing). Liquid and solid are then both ideal solutions, and only two phases, liquid and solid, are possible in the temperature-composition field (**Figure 1**).

If the change in enthalpy upon mixing in the solid state is nonzero, then the solid is a real solution. If $\Delta H > 0$, atoms A and B are incommensurate, because of either a differing crystal structure, atomic size, or both. In this case, it is energetically favorable for the mixture to remain a liquid to a temperature below that of the pure solid melting temperatures. Accompanying the melting point depression is a miscibility gap in the solid at low temperatures such that two solid phases coexist. If ΔH is large enough, the miscibility gap can extend up to the liquid phase (Porter and Easterling, 1992). In this situation, the lower entropy associated with two separate solid phases, an A-rich α-phase and a B-rich β-phase (rather than randomly mixed atoms in a single phase), is made up for by the lower enthalpy that results from A and B existing primarily in separate phases.

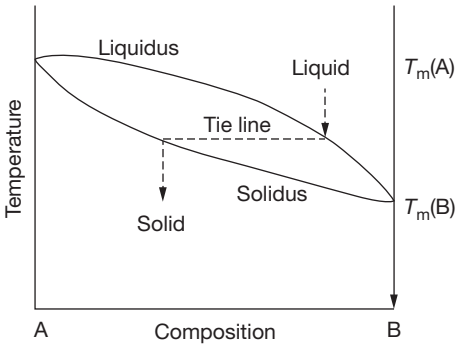

Figure 1 Phase diagram for a binary system (A,B) exhibiting complete solubility in both the liquid and solid phases (the enthalpy of mixing, ΔH, equals zero), so that both the liquid and solid phases are ideal solutions. The liquidus represents the temperature at which liquid of a given composition solidifies. A horizontal tie line at that temperature connects to the solidus, which gives the composition of the solid. The space between the curves represents the width of the phase loop, which is a measure of the compositional difference between the liquid and solid.

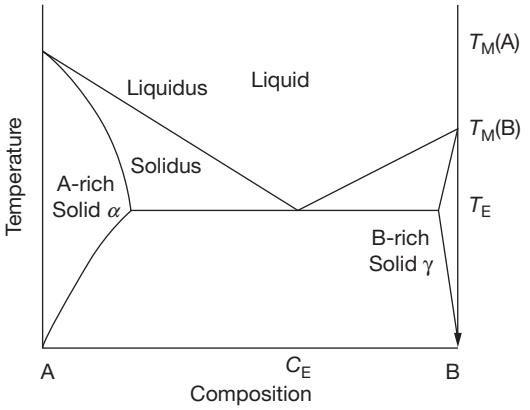

Figure 2 Phase diagram for a binary system exhibiting complete solubility in the liquid phase. where $\Delta H > 0$ in the solids, the solids are real solutions. Because $\Delta H > 0$ in the solids, the system remains liquid to lower temperatures than the melting temperature of pure A or pure B (T_M(A) or T_M(B)). ΔH is sufficiently positive that the miscibility gap in the solid phase extends up to the liquid phase. Such a phase diagram represents a eutectic system. Two solid phases, A-rich α-phase and B-rich γ-phase, exist at all temperatures beneath the eutectic temperature T_E, the lowest temperature at which liquid can be in equilibrium with solid. At T_E, the composition of the liquid is C_E.

Such a system exhibits a eutectic phase diagram (Figure 2), and there exists a eutectic composition that has a minimum melting temperature. Due to the entropic contribution, B will have nonzero solubility in the A-rich α-phase, and vice versa, but such a solid solution is not ideal. Examples of this type of phase behavior are ubiquitous, including model laboratory systems sodium chloride–water, ammonium chloride–water, lead–tin, and zinc–tin.

In a binary system with $\Delta H > 0$, it is also possible for stable solid phases other than those of pure A and pure B to exist. When such intermediate phases are present (as is common with iron alloys), a more complex phase diagram results. Other solidification reactions such as peritectic solidification can result. However, the essential solidification structure of the alloy is similar to that of a eutectic system (Porter and Easterling, 1992).

If $\Delta H < 0$, it is energetically favorable for a solid phase to form, so that a maximum in the melting temperature occurs for some intermediate composition. Such a solid is known as an ordered alloy because the atoms arrange themselves in a particular structure known as a superlattice. Ordered alloys often occur only within a certain compositional range. There is no experimental evidence that any of the possible core alloy components form an ordered alloy with iron under inner core conditions.

At low pressures, Fe–FeS forms a eutectic with a melting point depression of 600 K from that of iron. However, Boehler (1996a) had presented evidence showing that the melting point depression decreases with increasing pressure, based on experiments reaching pressures up to 62 GPa, still much lower than the 330 GPa at the ICB. This suggests that Fe–FeS may form an ideal solid solution at inner core pressures. This does not preclude an iron-enriched inner core, provided that the liquidus and solidus are sufficiently separated in composition (the phase loop in Figure 1 is wide) and the melting temperature of iron is higher than that of FeS, at core pressures. The latter may well be the case (Anderson and Ahrens, 1996; Boehler, 1992). However, Alfe et al. (2000) found from ab initio calculations that the concentration of sulfur in the solid state is very near to that of the liquid state. Such a similarity in composition would seem to have difficulty in explaining the excess density jump at the ICB. (The similarity indicates that the liquidus and solidus are close in composition. While this suggests an ideal solid solution, a eutectic system could still be a possibility if a significant fraction of the inner core has not yet cooled to the eutectic temperature; Fearn et al., 1981.)

On the other hand, FeO alone may not be able to explain the presence of a less-dense component in the inner core. Sherman (1995), also using first-principles calculations, showed that the concentration of oxygen in the solid state is very low at inner core pressures. However, Alfe et al. (1999) suggested that the concentration could be higher for other assumed crystal structures, and Stixrude et al. (1997) were able to explain the inner core density with FeO present in solid solution with pure iron rather than as a mixture of separate phases.

Since the composition of the core remains uncertain, the phase diagram is also uncertain, but in spite of these uncertainties, it is likely that a binary phase diagram captures the salient features of core solidification.

8.12.2.3 Crystal Structure of Iron

Understanding the solid phase(s) of pure and alloyed iron under inner core conditions is central to interpreting the seismic anisotropy of the inner core (see Section 8.12.5). Figure 3 summarizes the phase boundaries of iron. Under atmospheric pressure and room temperature, pure iron takes on a body-centered cubic (bcc) crystal structure (the α-phase). At higher temperatures, it undergoes a phase transformation to a face-centered cubic (fcc) crystal structure (the γ-phase), and before melting, it undergoes an entropy-driven phase transformation to another bcc crystal structure (the δ-phase). At high pressure, pure iron transforms to a phase with a higher packing density, the hcp ϵ-phase. It has generally been thought that this is the stable phase of pure iron under inner core conditions, and experiments using as high as 273 GPa and 4490 K (Sakai et al., 2011) and 377 GPa and 5700 K (Tateno et al., 2010) confirm this. Though there have been some reports of a double hcp phase (the β-phase; Saxena et al., 1993), the experimental inference for this has been questioned (Kubo et al., 2003; Vocadlo et al., 1999).

There have been several studies examining whether ε-iron could transform to a bcc phase (Belonoshko et al., 2003; Komabayashi and Fei, 2010; Matsui and Anderson, 1997; Ross et al., 1990), and a recent work suggests that impurities might stabilize the bcc phase of iron under inner core conditions (Cote et al., 2008a,b; Dubrovinsky et al., 2007; Vocadlo et al., 2003; Zhang and Oganov, 2010). However, the energy differences between the different phases are very small (Vocadlo et al., 2008), with some studies also suggesting that the fcc phase could be most stable (Cote et al., 2010; though Vocadlo et al. (2006) found nickel stabilizes the hcp phase), so clearly, more work, both experimental and theoretical, needs to be

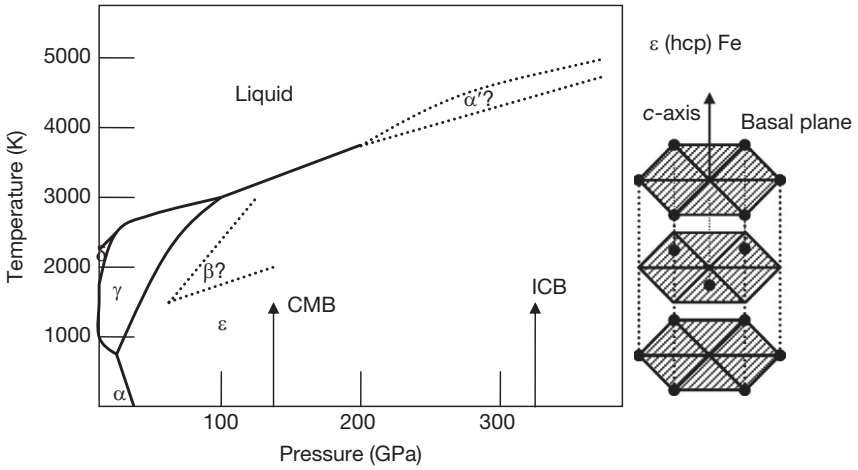

Figure 3 Summary of the phase boundaries of iron. The uncertainty of the boundaries increases with temperature and pressure, and the existence of the double hcp β-phase and bcc α′-phase is uncertain. To the right is the crystal structure of the hcp ϵ-phase.

done. One might speculate that the energy differences are so small that the inner core could be a region of mixed phases, which could be the cause of the increasingly complex pattern of anisotropy inferred by seismologists (see **Chapter 1.23** and **Section 8.12.6**). Although molecular dynamics calculations show that bcc iron under inner core conditions could have a single crystal elastic anisotropy as great as 12% (Belonoshko et al., 2008), it is not obvious that the high symmetry of the cubic phases could lead to the primarily cylindrical anisotropy that is observed in the inner core.

8.12.2.4 Thermal Conductivity of the Core

Although it is a bit of an aside from the main thrust of this chapter, the thermal conductivity plays a pivotal role for the dynamical state of the inner core (as well as for the outer core and mantle and for the generation of the geomagnetic field; see **Chapter 8.02**), and there has been recent work on the subject that we briefly review here. Stacey and Loper (2007) used extrapolations of resistivity measurements of shock-compressed iron and iron–silicon alloys and the Wiedemann–Franz law relating the electrical and thermal conductivities in metals, to estimate the thermal conductivity of the inner core to be about $28\,\mathrm{W\,m^{-1}\,K^{-1}}$, lower than an oft-used estimate of $63\,\mathrm{W\,m^{-1}\,K^{-1}}$ (Stacey and Anderson, 2001). However, Sha and Cohen (2010), de Koker et al. (2012), and Pozzo et al. (2012) used first-principles calculations to find that the thermal conductivity could be as high as $150–200\,\mathrm{W\,m^{-1}\,K^{-1}}$ for iron alloys under inner core conditions. These calculations are consistent with the results from diamond-anvil-cell experiments (Hirose et al., 2011) that reach conditions appropriate to the top of the outer core, though Konopkova et al. (2011) obtained a lower value, $32\,\mathrm{W\,m^{-1}\,K^{-1}}$, at a lower temperature, 2000 K.

8.12.3 Solidification of the Inner Core

Although hottest at its center, the inner core is solidifying directionally outward due to the effect of pressure on the liquidus slope. A flat solid–fluid interface can become morphologically unstable (Mullins and Sekerka, 1963, 1964) due to constitutional supercooling (Porter and Easterling, 1992; Rutter, 1958). This occurs when rejection of solute during solidification of an alloy leads to a solute boundary layer in the fluid with a scale thickness D/V, where D is the solute diffusivity and V is the inner core growth velocity. If the gradient of the local freezing temperature (the liquidus)

$$\mathrm{d}T_\mathrm{L}/\mathrm{d}z = \Delta T/(D/V) \qquad [2]$$

where ΔT is the temperature difference between the liquidus and solidus, exceeds the actual temperature gradient in the fluid, $\mathrm{d}T/\mathrm{d}z$, then freezing is predicted ahead of the flat solid–fluid interface (see **Figure 4**). This results in the growth of a solid perturbation into the fluid.

Morphological instability due to constitutional supercooling typically results in dendritic growth of solute-poor solid, with interdendritic, solute-rich pockets. Dendrites oriented close to the direction of heat flow grow most rapidly (dendrites also grow in particular crystallographic directions, the key to solidification texturing). Directionally solidified alloys exhibit columnar crystals, elongated in the direction of dendritic growth (Porter and Easterling, 1992). The mushy zone is the mixed solid–liquid region during dendritic growth. Mushy zones are ubiquitous features in directionally solidifying metallic alloys, organic systems, and aqueous salt solutions on both sides of the eutectic, though they are less common in silicates because of the low entropy associated with faceted dendrites (Jackson, 1958; Miller and Chadwick, 1969).

Loper and Roberts (1981) extended the condition for morphological instability to include the effect of pressure variations on the liquidus, estimating that the inner core growth rate is nearly 500 times supercritical. In essence, the argument for morphological instability of the ICB rests on the small temperature gradient $\mathrm{d}T/\mathrm{d}z$ near the ICB, in spite of the inner core growth velocity V also being very small. Fearn et al. (1981) suggested that the center of the Earth could exceed the eutectic temperature, so that the entire inner core would be in a mushy state.

Loper and Roberts (1978, 1980) also examined the thermodynamics of a slurry, which is a general mixed phase region.

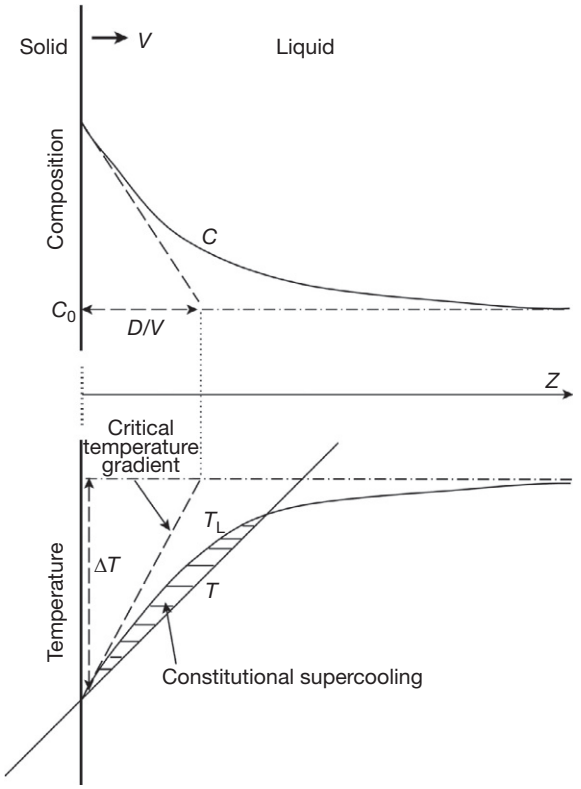

Figure 4 Dendritic growth in directionally solidifying alloys can occur when the liquid is constitutionally supercooled. Adjacent to the solid is a solute boundary layer of scale thickness D/V, where D is the solute diffusivity and V is the growth rate of the solid. The solute concentration C in the boundary layer is enriched relative to its value C_0 far from the solid. This enrichment depresses the equilibrium freezing temperature T_L by an amount ΔT from its value far from the solid. If the temperature T in the liquid is less than T_L, then solid is predicted ahead of the solid–liquid interface, a condition known as constitutional supercooling. The criterion for constitutional supercooling is that the temperature gradient in the liquid, $dT/dz < \Delta T/(D/V)$. Adapted from Porter DA and Easterling KE (1992) *Phase Transformations in Metals and Alloys*. London: Chapman and Hall.

They considered an inner core formed by downward precipitation of heavy, iron-rich particles. Shimizu et al. (2005) later considered the possibility that the inner core might in part grow by precipitation rather than dendritic growth, so that the region near the ICB might be a slurry layer rather than a mushy layer. They found, however, that morphological instability is likely for all realistic values of the liquidus concentration slope.

Morse (1986, 2002) had questioned the prediction of a mushy inner core on other grounds – the assumption that heat and solute near the ICB are removed only by diffusion. Loper and Roberts (1981) ignored the effect of convection, arguing that it must become small near the boundary, but Morse (1986, 2002) suggested that convection at the base of the outer core reduces the solute buildup, making the inner core growth rate nearly five orders of magnitude less than that needed for morphological instability. However, Deguen et al. (2007) found that for plausible phase diagrams of Earth's core, morphological instability of the ICB is likely in spite of advective transport of solute away from the ICB.

Section 8.12.5.4 summarizes the seismic evidence for solidification structures in the inner core. There is also meteoritic evidence, although this evidence is ambiguous because of the relative lack of data and the large extrapolation from a meteorite to a planetary core. Iron meteorites such as those from the Cape York shower exhibit compositional gradients that are too large to result from the general fractionation of a planetoid core but instead are more likely due to microsegregation between secondary and tertiary dendrite arms (Esbensen and Buchwald, 1982; Haack and Scott, 1992). Moreover, the FeS (troilite) nodules in meteorites are elongated and oriented, suggesting interdendritic pockets of melt during directional solidification (Esbensen and Buchwald, 1982).

8.12.4 Grain Size and Rheology in the Inner Core

The rheology of iron at core conditions governs the style and rate of deformation in the inner core. For timescales longer than the Maxwell relaxation time

$$\tau = \eta/G \qquad [3]$$

the inner core can be considered to behave as a viscous fluid. Here, η is the viscosity and G is the rigidity. Current estimates of inner core viscosity span a large range, of the order 10^{13}–10^{21} Pa s, but even if the upper limit applies, the inner core is less viscous than the mantle, because it is closer to its melting temperature. With a rigidity on the order of 10^{11} Pa (Dziewonski and Anderson, 1981), τ is between 10^2 and 10^{10} s, which is far shorter than mantle timescales. Constraints from rheology come from theoretical and empirical laws of mineral physics and from elastic and anelastic properties of seismic waves at various frequencies. Here, we review the viscous properties followed by the elastic and anelastic properties.

Viscosity relates the stress σ to the strain rate $d\varepsilon/dt$. The general form of the strain rate in a solid can be expressed as

$$d\varepsilon/dt = A(DGb)/(kT)(b/d)^p(\sigma/G)^n \qquad [4]$$

where D is the diffusion coefficient, b is the Burgers vector, k is Boltzmann's constant, T is temperature, d is the grain size, and p, n, and A are dimensionless constants (Van Orman, 2004).

Deformation occurs under imposed stress either by the diffusive movement of vacancies and atoms or from slipping of lattice by dislocations (Poirier, 1985). Both of these mechanisms of deformation coexist, but the mechanism that gives the larger strain rate under a given stress becomes the predominant one. At high-stress conditions, power law creep ($p=0$, $n=3$–5) gives the largest strain rate under a given stress. The nonlinear dependence of strain rate on stress results because the dislocation density increases with applied stress.

At low-stress conditions, both dislocation (Harper–Dorn creep) and diffusion creeps are possible. For large grain size, a Newtonian-type dislocation creep (Harper–Dorn creep, with $p=0$, $n=1$) dominates over diffusion creep. A Newtonian dependence is interpreted to arise from dislocation density that is independent of stress. One interpretation for the stress-independent dislocation creep was provided by Wang et al. (2002), who suggested that dislocation density results from the sum of two stresses: the applied stress and the Peierl's

stress required to move the dislocations. For low-stress conditions, Peierl's stress dominates, and the dislocation density becomes independent of applied stress. For small grain size, a Newtonian diffusion creep becomes faster. This is because the smaller grain size yields a larger spatial gradient of density of vacancies or atoms, which causes the deformation. There are two types of diffusion creeps: one where diffusion occurs within the lattice (Nabarro–Herring creep: $p=2$, $n=1$) and the other where diffusion occurs along the grain boundaries (Coble creep: $p=3$, $n=1$). The activation energy for grain boundary diffusion is smaller than that for lattice diffusion (Poirier, 1985), so for the high-temperature conditions of the inner core, Nabarro–Herring creep is more important.

These regimes of deformation are summarized in the form of deformation mechanism maps for various materials of interest (Frost and Ashby, 1982; also, see **Table 1** for a general summary of the various high-temperature deformation mechanisms). Deformation mechanism maps are often constructed as a function of homologous temperature, T/T_m (where T_m is the melting temperature), and normalized stress, σ/G. A compilation of data has shown that materials with the same crystal structure and similar bonding have similar deformation mechanism maps (Frost and Ashby, 1982), so hcp metals can be used as an analog of hcp iron to estimate the constants in eqn [4]. Homologous temperature of the inner core is high (>0.9), so we are left with estimating the magnitude of stress and grain size in order to estimate the viscosity of the inner core.

Several studies have sought to identify and quantify sources of stress in the inner core (see also **Section 8.12.5**). For instance, Jeanloz and Wenk (1988) considered a nonadiabatic large-scale degree-one flow in the inner core. They assumed a temperature variation of about 1 K with a length scale of 1000 km and estimated that a buoyancy stress of about 10^4 Pa would arise. Together with the deformation mechanism of iron (Frost and Ashby, 1982), they estimated a viscosity of 10^{10}–10^{16} Pa s. This leads to a very large strain rate of the order of 10^{-9} s^{-1} or an equivalent flow velocity of about 10^{-3} m s^{-1}, which is comparable to the outer core flow velocity and is unrealistically fast.

Yoshida et al. (1996) considered an anisotropic inner core growth and obtained a strain rate of the order of 10^{-18} s^{-1}. Such a small strain rate is a result of a very slow growth rate of the inner core. They considered power law creep and Nabarro–Herring (diffusion) creep as possible candidates. From evaluating the stress needed to cause this strain rate, they showed that diffusion creep occurs for a grain size <6 m and a power law creep occurs if the grain size is larger than 6 m, though there are uncertainties in the parameter values used. As an additional condition, they assumed that dynamical recrystallization governs the grain size, which yields a smaller grain size for larger stress. Using these constraints, they obtained a grain size of 5 m, which is marginally in the diffusion creep regime and a viscosity of 3×10^{21} Pa s. In another model, they applied a Maxwell relaxation model to seismic attenuation data and estimated the viscosity to be $>10^{16}$ Pa s.

Reaman et al. (2011) incorporated the effect of grain growth as the inner core grows with time. Assuming the initial crystal size of the order of 1 cm, which grows in proportion to square root of time, they estimated how the deformation mechanism and the viscosity change with depth below the ICB. Using typical stress levels of 10–10^4 Pa estimated from previous works, they estimated that Nabarro–Herring creep will dominate at the shallow parts. As the grains grow, however, the viscosity increases, and eventually, dislocation creep, which does not depend on the grain size, becomes the faster deforming mechanism and dominates. According to their estimate, the inner core becomes rheologically layered with viscosity increasing with depth. In addition, they argue that dislocation creep becoming the dominant deformation mechanism in the deeper inner core is responsible for the increasing anisotropy with depth.

Bergman (1998, 2003) examined the issue of grain size in the inner core. One constraint on grain size comes from assuming that the frequency-dependent inner core attenuation (see **Section 8.12.6.2**) arises from scattering (e.g., Cormier and Li, 2002; Cormier et al., 1998). Under this assumption, the grain size is large, of the order of a seismic body wavelength, that is, 100 m–1 km (Bergman, 1998). Calvet and Margerin (2008) estimated a grain size of 400 m using multiple scattering modeling. It is also possible to estimate the grain size from extrapolation of dendrite size obtained from laboratory experiments (although by six orders of magnitude!). Due to the slow cooling rate in the inner core, the grain-size estimate is of the order of a few hundred meters (Bergman, 2003). It is perhaps interesting to note that there have been a few piano-sized iron meteorites, thought to be remnants of planetoid cores, and that from the uniformity of their Widmanstätten patterns, they have cooled from single crystals, though of course, their histories are unknown.

Van Orman (2004) argued that Harper–Dorn creep is the dominant deformation mechanism in the inner core. This mechanism occurs at low-stress and large-grain-size conditions, a regime not considered by Yoshida et al. (1996). For the low stress level in the inner core, Van Orman (2004)

Table 1 High temperature deformation mechanisms

	p = *0 (grain size-independent)*	p = *2*	p = *3*
$n=1$ (Newtonian)	Harper–Dorn creep (dislocation density independent of stress) Low stress Large grain size	Nabarro–Herring creep (diffusion within lattice) Low stress	Coble creep (diffusion along grain boundaries) Low stress Small grain size
$n=3$–5	Power law creep (dislocation density increases with stress) High stress		

showed that power law creep is unlikely and that Harper–Dorn creep would occur for grain sizes exceeding 10–30 μm. In this likely case, the estimated viscosity becomes 10^{10}–10^{12} Pa s, which is quite small. The deformation mechanism in the inner core thus remains unclear.

An attempt to constrain the inner core viscosity from nutation observations has been made by Koot and Dumberry (2011). Here, they showed that the observation of Earth's nutation can be explained by electromagnetic coupling at the ICB and the viscous deformation within the inner core, if the viscosity is in the range of $2–7 \times 10^{14}$ Pa s.

It is important to note that the aforementioned estimates are for solid iron. The presence of melt within the inner core might drastically reduce the viscosity, so that the aforementioned estimates should be taken as an upper limit. In addition, the presence of melt would promote diffusion of atoms along grain boundaries and cause pressure solution-type creep (which is similar to Coble creep), thus resulting in a grain-size dependence.

8.12.5 Origin of Inner Core Elastic Anisotropy

8.12.5.1 An Overview

Inner core elastic anisotropy, where P-waves travel about 3% faster in the polar direction than parallel to the equatorial plane, with a larger degree of anisotropy in the deeper inner core, is well established from seismic body waves and free oscillations (see **Chapter 1.23** and **Section 8.12.6**). The most plausible interpretation, based on the analogy with mantle anisotropy, is that it results from the lattice-preferred orientation of the hcp iron that comprises the inner core. Alternatively, it could be due to shape-preferred orientation of melt pockets (Singh et al., 2000). Seismology has also shown that there is an attenuation anisotropy, where P-waves in the polar direction are more attenuated (see **Section 8.12.5.4**; Creager, 1992; Song and Helmberger, 1993; Souriau and Romanowicz, 1996, 1997; Yu and Wen, 2006).

A variety of models have been proposed to explain the origin of inner core elastic anisotropy. We can classify them into two categories. The first category consists of dynamical models, which assume that the crystals align as a result of plastic deformation within the inner core. The second set of models assumes that the inner core texture forms during solidification from the liquid outer core. **Table 2** lists the advantages and drawbacks of each of the models together with the primary limiting factors. In the next subsection, we summarize the anisotropic properties of hcp iron and its style of slip under dislocation creep, followed by a review of the two categories of models for understanding inner core elastic anisotropy.

8.12.5.2 Anisotropy of hcp Iron

The anisotropy of hcp iron at inner core conditions was first estimated from analog hcp metals. Wenk et al. (1988) considered Ti at room conditions to be a good analog for the inner core because it has a similar c/a ratio and ratio of linear compressibility as hcp iron. They concluded that P-waves should be faster in the c-axis direction. Sayers (1989) analyzed several hcp metals and arrived at the same conclusion. These estimates were based on room temperature values. Bergman (1998) argued, based on the temperature dependence of the elastic constants of hcp metals, that the magnitude of anisotropy of hcp iron would become even larger at core temperatures.

First-principles calculations and high-pressure experiments have made direct determination of elastic constants possible

Table 2 Models for inner core anisotropy

Mechanism	*First reference*	*Advantages*	*Drawbacks*	*Primary limiting factors*
Deformation models				
Inner core thermal convection	Jeanloz and Wenk (1988)	Analogy with mantle	Uncertainty of inner core thermal convection	Solid viscosity, thermal conductivity
Preferential equatorial solidification due to outer core convection	Yoshida et al. (1996)	Explains relation of fast axis with spin axis, preferential solidification observed in lab experiments	Low stress levels so that texture may take age of IC to develop	Outer core heat flow anisotropy, inner core growth rate
Radial component of Maxwell stress	Karato (1999)	Anisotropy reflects magnetic field, larger stress level	Stress likely to be balanced by other stresses	Magnetic field strength and pattern
Azimuthal component of Maxwell stress	Buffett and Wenk (2001)	Can sustain flow	Requires c-axis to be slow, depth dependence?	Magnetic field strength and pattern
Joule heating	Takehiro (2011)	Can sustain flow	Assumes a simple magnetic field pattern	Magnetic field strength and pattern
Solidification models				
Paramagnetic susceptibility	Karato (1993)	Novel	Iron under inner core conditions not likely to be paramagnetic	Anisotropy of paramagnetic susceptibility
Anisotropic heat flow due to outer core convection	Bergman (1997)	Observed in lab, simple depth dependence, may also explain attenuation anisotropy	Requires c-axis to be fast, effects of deformation?	Outer core heat flow anisotropy

None of the models by themselves can easily explain latitudinal variations or abrupt changes with depth.

(Steinle-Neumann et al., 2003). Stixrude and Cohen (1995) calculated elastic constants of hcp iron at core pressures (but 0 K), again finding the *c*-axis fast, by about 4% for compressional waves. These calculations were then extended to high temperatures by Steinle-Neumann et al. (2001), who found that the sense of P-wave anisotropy reversed from that at 0 K, so that the *a*-axis of a single crystal is 10–12% faster than the *c*-axis at high temperature. According to Steinle-Neumann et al. (2001), the seismic inference of a 3% fast P-wave velocity in the polar direction can thus be explained by 1/3 alignment of *a*-axes (or basal planes) in the polar direction. However, calculations by Gannarelli et al. (2003) did not find a reversal of the sense of anisotropy nor did experiments by Antonangeli et al. (2006). On the other hand, Vocadlo et al. (2009) found the reversal of anisotropy with temperature and indicated that hcp iron becomes nearly isotropic near its melting temperature, which Sha and Cohen (2010) found at pressures and temperatures of the inner core. Accordingly, the anisotropic property of hcp iron is not settled (see **Chapter 2.06**). Experimental determination of the elastic constants by Mao et al. (1998, 1999) inferred a bulk modulus and rigidity similar to previous values, but with the fast axis lying at an angle intermediate between the *c*- and *a*-axes.

If the preferred orientation of hcp iron occurs by dislocation creep, a critical issue is whether the predominant slip plane is basal or prismatic. Poirier and Price (1999) applied the criterion derived by Legrand (1984) to determine whether basal or prismatic slip dominates in hcp iron. To distinguish between the various slip regimes, Legrand (1984) defined a parameter R as

$$R = (c_{66} \cdot \gamma_B)/(c_{44} \cdot \gamma_P) \quad [5]$$

where c_{66} and c_{44} are elastic constants and γ_B and γ_P are the stacking fault energies in the basal and prism planes, respectively. Legrand (1984) showed that when $R < 1$, the primary slip system is basal and when $R > 1$, it is prismatic. Using ab initio calculations, Poirier and Price (1999) calculated the stacking fault energies for hcp iron, and using the published elastic constants for 0 K hcp iron, they found that R becomes 0.37–0.43, indicating that hcp iron slips predominantly on the basal plane. This result is also obtained when the elastic constants of Steinle-Neumann et al. (2001) or Sha and Cohen (2010) are used.

Wenk et al. (2000b) conducted high-pressure deformation experiments of hcp iron in a diamond anvil, at pressures of up to 220 GPa. By imposing a uniaxial nonhydrostatic stress, they found that *c*-axes align parallel to the axis of the diamond cell. Comparing with the results from plasticity theory, they found that basal slip is dominant in determining the overall preferred orientation even if prismatic slip is favored over basal slip.

8.12.5.3 Dynamical Models

The key issues for a dynamical origin of the preferred orientation are the source and pattern of stress and the mechanism of alignment. The first of the dynamical models was by Jeanloz and Wenk (1988), who proposed that preferred orientation of hcp iron is caused by inner core convection driven by internal heat sources. By evaluating the radiogenic heat generation in the inner core, they concluded that the Rayleigh number in the inner core is supercritical. They showed that if a spherical harmonic degree $l = 1$ convection exists in the inner core (note that they assumed an impermeable boundary; the translative mode (Alboussiere et al., 2010) discussed in **Section 8.12.6** results from a permeable boundary due to melting and solidification), then the resulting simple shear flow in the equatorial region yields a *c*-axis alignment of about 45° from the polar direction. Averaging such a crystal alignment and using the elastic constants of Ti, Jeanloz and Wenk obtained a fast P-wave in the polar direction. There are, however, several issues with this model. First, the amount of radiogenic heat is highly uncertain so that thermal convection in the inner core may not occur. Thermal history calculations generally do not yield thermal convection in the inner core because the geothermal gradient in the inner core becomes smaller than the adiabat (due to the slow growth rate of the inner core), which allows sufficient time for the inner core to cool (Sumita et al., 1995; Yoshida et al., 1996; Yukutake, 1998). Also, this model does not explain why a degree 1 convection pattern with a symmetry axis corresponding to the rotation axis should be preferred. Later, numerical studies of thermal convection in the inner core were carried out by Weber and Machetel (1992) and Wenk et al. (2000a). In the latter study, preferred orientation of hcp iron under a polar downwelling and an equatorial upwelling was calculated, which resulted in a fast P-wave in the polar direction.

The possibility of thermal convection within the inner core has been reconsidered by Buffett (2009) and Cottaar and Buffett (2012). They showed that the temperature gradient within the growing inner core becomes superadiabatic, and therefore, thermal convection is possible at the early stages of inner core growth. The shape of the inner core becomes elliptical due to centrifugal forces. Buffett (2009) used a perturbation method and showed that at the onset of convection, a degree 1 thermal convection occurs with its symmetry axis aligned to the rotational axis. Accordingly, it is possible that as thermal convection ceases with inner core growth, the final convective pattern takes the $l = 1$ pattern.

A different explanation for an inner core flow pattern with an axis coinciding with the rotation axis was given by Yoshida et al. (1996). They argued that the inner core growth should be of zonal degree 2 because of the columnar convection in the outer core, which transports heat more efficiently from low latitudes of the inner core. This causes the inner core to grow faster near the equator (see **Figure 5**). Experiments conducted by Bergman et al. (2005) show this effect in a rotating hemisphere of salt water solidifying from the center. However, because of the density difference between the inner and outer cores, the inner core must deform isostatically to maintain its spherical shape and an overall stress field with uniaxial tension in the polar direction results. Using the elastic constants of Stixrude and Cohen (1995) and Kamb's theory of preferred orientation by recrystallization under stress (Kamb, 1959), Yoshida et al. (1996) showed that this model can explain the observed inner core anisotropy. Sumita and Yoshida (2003) used the same model with the elastic constants of Steinle-Neumann et al. (2001) and found that *a*-axes aligning in the polar direction can explain the sense of anisotropy. One problem with this model is that the stress resulting from anisotropic

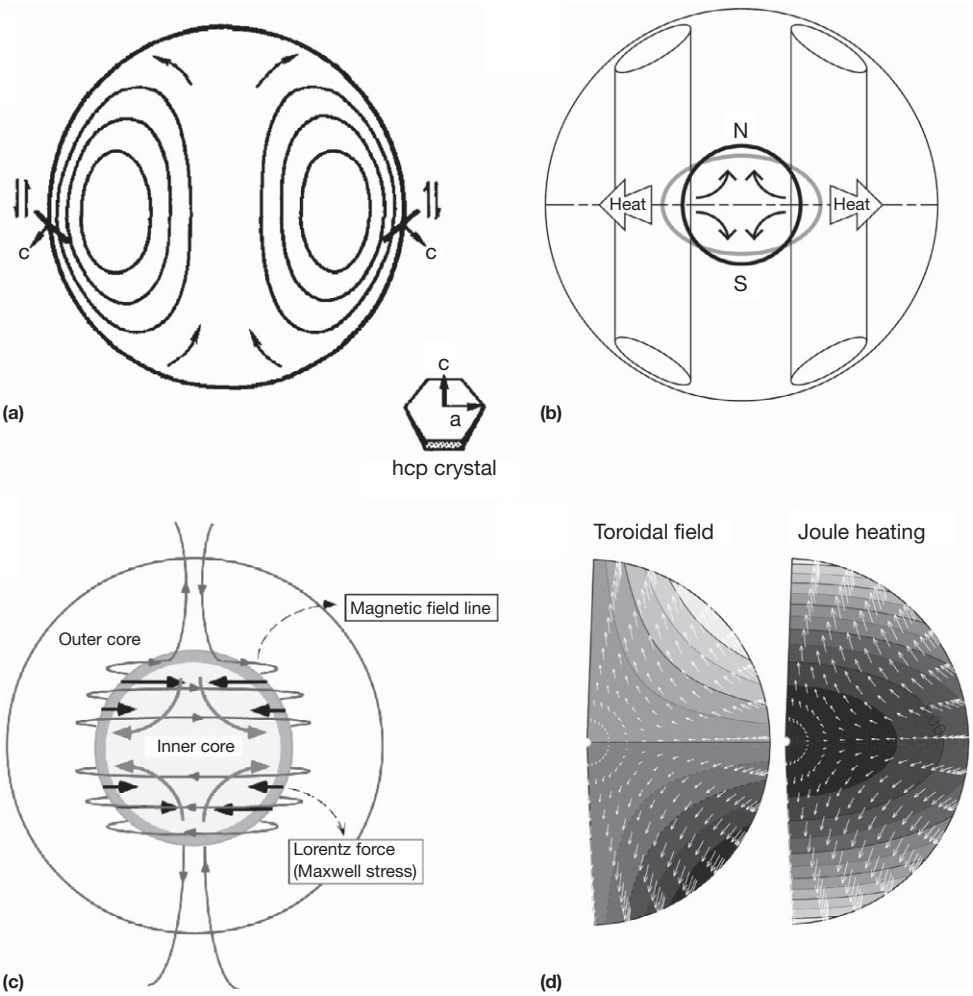

Figure 5 Some dynamical models exhibiting a radial flow in the inner core. In these models, such flow is considered to be responsible for the preferred orientation of crystals. (a) An internally heated inner core can convect. A degree 1 mode is the first unstable mode (adapted from Jeanloz R (1990) The nature of the Earth's core. *Annual Review of Earth and Planetary Sciences* 18: 357–386). (b) Convection in a rapidly rotating, spherical fluid shell such as the outer core is more efficient at transporting heat perpendicular to the rotation axis. This leads to an inner core that solidifies more oblately than the gravitational equipotential. A solid-state flow results, and the stress may lead to a recrystallization texture (adapted from Yoshida S, Sumita I, and Kumazawa M (1996) Growth model of the inner core coupled with outer core dynamics and the resulting elastic anisotropy. *Journal of Geophysical Research* 101: 28085–28103). (c) Maxwell stresses resulting from the magnetic field in the outer core can squeeze the inner core, causing a flow. Here, a toroidal magnetic field is shown to cause such flow. In this model, the flow pattern depends on the magnetic field pattern of the outer core (adapted from Karato S (1999) Seismic anisotropy of the Earth's inner core resulting from flow induced by Maxwell stresses. *Nature* 402: 871–873). (d) A heterogeneous distribution of Joule heating in the inner core can generate a flow. The left figure shows the toroidal magnetic field (light – positive and dark – negative) with arrows indicating the electric current field. The right figure shows the Joule heating (lighter areas with larger values) with arrows indicating the flow field (adapted from Takehiro S (2011) Fluid motions induced by horizontally heterogeneous Joule heating in the Earth's inner core. *Physics of the Earth and Planetary Interiors* 184: 134–142, with permission).

growth is quite small due to the slow growth rate of the inner core. As a result, preferred orientation would take a geologically long time (on the order of 10^9 years) to develop. The applicability of Kamb's theory under the presence of dislocations is also uncertain.

Deguen and Cardin (2009) conducted a similar calculation as in Yoshida et al. (1996) obtaining a flow in the anisotropically growing inner core. Here, they incorporated the effects of compositional stratification in the inner core. They showed that as the inner core grows, the stratification causes the flow to become confined to the uppermost part of the inner core, suggesting that anisotropy deeper in the inner core is a remnant of earlier dynamics or solidification and that texture nearer the ICB is due to active tectonics. In Deguen et al. (2011), the preferred orientation of iron crystals in an anisotropically growing inner core was calculated assuming a dislocation creep model. The resulting anisotropy is in reasonable agreement with seismological observations, but no quantitative comparison was made. Deguen and Cardin (2011) and Cottaar and Buffett (2012) further studied thermochemical convection in a growing inner core. The calculations indicate that at present, it is possible that convection in the inner core may be ongoing or has ceased due to either a decrease in the cooling rate or a compositional stabilization. In a convecting inner core, small-scale motions

become particularly dominant if the inner core viscosity becomes $< 10^{19}$ Pa s. In addition, the symmetry axis of convection does not necessarily coincide with the rotation axis.

Another difficulty for thermal convection arises from new, higher estimates for the thermal conductivity of iron under core conditions (see **Section 8.12.2.4**). Gubbins et al. (2013) had suggested that the inner core may in fact not be compositionally stable, which could resurrect convection in the inner core, though they would argue against stratified convection. Their argument rests on the possibility that the partition coefficient of light elements might decrease as the inner core grows (Alfe et al., 2002), so that the inner core becomes compositionally unstable even as the outer core becomes more enriched in light elements. Another factor in compositionally destabilizing the inner core is the presence of the iron-enriched F-layer at the base of the outer core (see **Section 8.12.6.1**). The verdict remains out on convection in the inner core.

Karato (1999) argued that Maxwell stresses resulting from the geomagnetic field generated in the outer core could also induce flow in the inner core, by radially squeezing the inner core at the ICB. In this model, a toroidal magnetic field of $B = 10^{-2}$–10^{-1} T results in Maxwell stresses $\sigma = 10^{2}$–10^{4} Pa. Since the induced flow pattern in the inner core is controlled by the magnetic field pattern in the outer core, this model predicts that the inner core anisotropy reflects the magnetic field pattern. However, Buffett and Bloxham (2000) questioned whether the Maxwell stresses can actually drive a radial flow in the inner core or whether they are simply balanced by other stresses. They considered the balance between magnetic, pressure, and buoyancy stresses and showed that these stresses would not equilibrate because of the incompatibility between thermodynamic and hydrostatic equilibrium conditions at the ICB. As a result, they predicted that viscous flow would occur, but they also showed this flow to be weak and confined near the ICB. As a result, they concluded that the radial component of the Maxwell stress is unsuitable for causing preferred orientation.

Buffett and Wenk (2001) used the elastic constants by Steinle-Neumann et al. (2001) and considered the Lorentz force tangential to the inner core. They calculated the resulting anisotropy that forms under an inner core shear flow. The resulting stress in this model becomes quite small, of the order of several Pa. Assuming both basal and prismatic slips to occur for hcp iron, they showed that the *c*-axes become parallel to the equatorial plane, which is consistent with the seismic inferences, if the *c*-axis of hcp iron under inner core conditions is indeed the slow direction. Since the Maxwell stress decreases with the distance from the ICB, the alignment becomes weak with depth, so that an explanation is needed to produce a stronger anisotropy with depth. Another issue is that the stress field depends strongly on the morphology of the magnetic field, which is not known well.

Takehiro (2011) proposed that the horizontally heterogeneous Joule heating in the inner core can drive the flow, an example of which is shown in **Figure 5(d)**. Here, a degree 2 toroidal magnetic field at the ICB is accompanied by a poloidal electric current, which results in a larger Joule heating at the poles. As a result, upwelling occurs at the poles and downwelling occurs at the equatorial region. Balancing the convective heat flux with the Joule heating, he estimated that the flow generates a stress of the order of 1–10^{2} Pa for a viscosity of 10^{17} Pa s, which is comparable to or larger than the stress estimated from previous models.

To summarize, the condition of thermodynamic equilibrium at the ICB is important in evaluating the flow pattern in the inner core, as the analysis of Buffett and Bloxham (2000) showed. Since the flow pattern in the outer core, the solidification at the ICB, and the pattern and magnitude of Maxwell stresses are all coupled, a self-consistent model of inner core anisotropy needs to properly incorporate all of these effects.

8.12.5.4 Solidification Texturing Models

The second category of models to explain the origin of inner core anisotropy invokes solidification. Karato (1993) proposed that hcp iron may have a paramagnetic susceptibility and would align during solidification under a magnetic field, hence resulting in a preferred orientation. However, this model predicts larger anisotropy near the ICB, which is inconsistent with the observations. Furthermore, theoretical studies show hcp iron to be nonparamagnetic at core pressures (Söderlind et al., 1996; Steinle-Neumann et al., 1999).

A solidification texturing during directional cooling was shown by Bergman (1997) to be a possible mechanism for understanding inner core elastic anisotropy. The directional cooling occurs perpendicular to the rotation axis, as a result of the pattern of convection in the outer core, as suggested by Yoshida et al. (1996), later demonstrated in experiments by Bergman et al. (2005). Solidification experiments on tin-rich alloys exhibit dendrites that grow in a particular crystallographic direction controlled by the direction of heat flow, resulting in elastic anisotropy. This result was extended to hcp zinc alloys by Bergman et al. (2000). Hence, the direction of heat flow becomes a preferred crystallographic direction (**Figure 6**). The geometry of the crystal growth results in an increase in

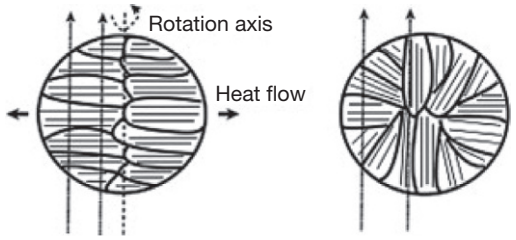

Figure 6 A solidification texturing model resulting in a preferred orientation of crystals. Heat flow perpendicular to the rotation axis leads to dendritic growth in the cylindrically radial direction. The heavier lines represent columnar crystals; the lighter lines primary dendrites. The left panel represents a longitudinal cross section; the right panel an equatorial cross section. North–south seismic rays (left panel), represented by the dotted arrows, are always perpendicular to the growth direction of dendrites. The component of rays perpendicular to the rotation axis (right panel) that is parallel to the growth direction of dendrites increases with turning depth in the inner core. This is the origin of the depth dependence associated with solidification texturing of the inner core. (Such geometric depth dependence becomes less strong for rays not turning on the equatorial plane.) Adapted from Bergman MI (1997) Measurements of elastic anisotropy due to solidification texturing and the implications for the Earth's inner core. *Nature* 389: 60–63.

anisotropy with depth. The effect of fluid flow on solidification texturing of hcp zinc alloys was examined by Bergman et al. (2003). In agreement with the solidification of hcp sea ice, the experiments showed that the fluid flow causes transverse texturing, indicating that alignment is sensitive to the direction of fluid flow and that of heat flow.

Brito et al. (2002) conducted directional solidification experiments using liquid (pure) gallium and measured the resulting anisotropy of the polycrystalline gallium. They found that for all cases, crystals elongated parallel to the imposed thermal gradient that determined the direction of crystal growth and that other factors such as turbulence and magnetic field have little influence. They also found that the preferred orientation of crystals is controlled primarily by the presence of seed grains and that this strongly affects the amount of anisotropy. Seeding has been observed to have more of an effect on the texture of solidifying fresh water than salt water (Weeks and Wettlaufer, 1996). Unresolved issues with solidification texturing include whether conduction will dominate over convection as regards heat transport in the outer core, the role of postsolidification deformation in modifying the solidification texture, whether the observed depth dependence can be explained by the simple depth dependence predicted by geometry, and the uncertainty as to the sense of fastest wave propagation in hcp iron under inner core conditions.

8.12.6 Origin of Other Inner Core Seismic Structures

In this section, we review other seismic structures of the inner core and their geodynamic interpretations.

8.12.6.1 Properties and Structure of the ICB and the 'F-Layer'

The ICB has been found to be seismically sharp, with a transition thickness of <5 km (Cummins and Johnson, 1988). Such a sharp ICB may be explained, in spite of dendritic growth of the inner core, by a rapid increase in solid fraction of partial melt with depth, which might result from convection within the mushy layer (Loper, 1983; Worster, 1991) or from compaction (Sumita et al., 1996). It has been proposed that the inner core radius may depend on frequency, if the ICB is a diffuse boundary defined by the relaxation time equivalent to the period of a seismic wave (Anderson, 1983). However, this has not been substantiated, which indicates that the ICB is probably not a gradual transition from the outer core to the inner core. There is also a discrepancy on the density jump at the ICB (see **Chapter 1.23**) that might yield clues as to the nature of the ICB. Krasnoshchekov et al. (2005) found considerable lateral variability in the amplitude of waves reflected off the ICB, which they interpret as the ICB having a 'mosaic' structure with thin patches of partial melt interspersed with regions with a sharp transition between solid and fluid.

Over the years, the lowermost layer of the outer core has received considerable attention, and its presence is likely intimately related to inner core dynamics. Historically, this layer had been known as the 'F-layer' and was marked by a decrease in P-wave velocity. Braginsky (1963) suggested a slurry layer to explain the F-layer, but when the original seismic evidence for the layer was found to be due to scattering in the mantle's D″ layer (Haddon and Cleary, 1974), and it was realized that the core was likely on the iron-rich side of the eutectic, such a layer was abandoned. However, in recent years, the F-layer has been found to have a small to zero P-wave velocity gradient compared to PREM (Kaneshima et al., 1994; Song and Helmberger, 1992, 1995; Souriau and Poupinet, 1991). There is some evidence that this 150–200 km thick layer might also have high attenuation (Zou et al., 2008), which has been interpreted as perhaps a glassy layer (Cormier, 2009).

Gubbins et al. (2008) have revisited a slurry layer in an effort to create a stably stratified, iron-rich, dense layer that could explain the reduced velocity gradient, though it is still not clear that such a slurry layer is likely on metallurgical grounds (see **Section 8.12.3**). Alboussiere et al. (2010) suggested another way to achieve a dense fluid layer above the ICB: the inner core might be convecting in a translative mode whereby it is melting on one side and freezing on the other (**Figure 7**). Of course, the net inner core is growing radially outward, though the translation rate may exceed the growth rate by some ten times. In experiments, they show that the net growth and accompanying release of light elements allow for convection through the dense layer so as to stir the geodynamo but that the melting can provide the iron-rich dense fluid to comprise the F-layer. However, the translative mode requires a relatively high inner core viscosity, $>3\times10^{18}$ Pa s (see **Section 8.12.4**); else, the convection takes the more usual form associated with an effectively impermeable boundary (Deguen et al., 2013). Moreover, if the thermal conductivity of iron under core conditions is as high as some recent estimates (see **Section 8.12.2.4**), then inner core thermal convection may be unlikely, though compositional convection may be possible (see **Section 8.12.5.3**). Gubbins et al. (2011)

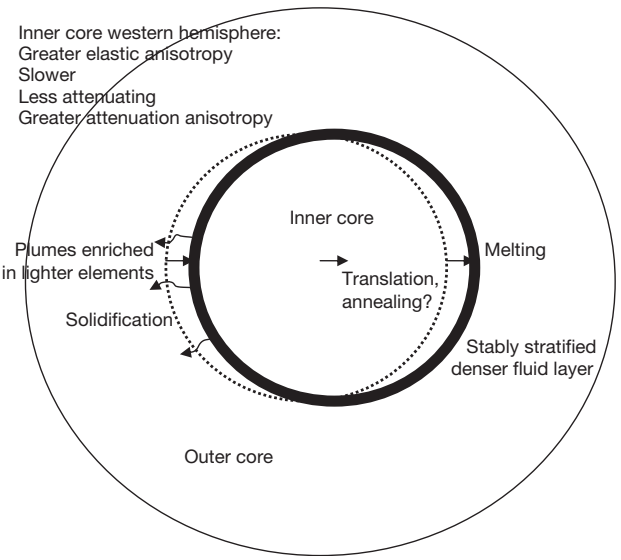

Figure 7 The inner core may be translating eastward, driven by convection. As it does so, it solidifies in the west, releasing plumes enriched in lighter elements, and melts in the east, resulting in an iron-enriched layer that is more dense than the overlying outer core. The asymmetry could be the cause for the differing seismic properties between the hemispheres in the inner core. Adapted from Bergman MI (2010) An inner core slip-sliding away. *Nature* 466: 697–698.

suggested another means of producing melting of some region of the inner core, and hence the dense fluid layer, while maintaining net growth: numerical calculations suggest that variations in the thermal heat flux at the core–mantle boundary could persist to the ICB and be sufficiently large so as to allow localized heat flow into the inner core.

8.12.6.2 Inner Core Attenuation and Scattering

Knowledge of seismic attenuation in the inner core could give earth scientists considerable insight into the nature of the inner core, but at present, the depth and frequency dependence of the seismic quality factor in compression Q_α or in shear Q_β remain uncertain (Masters and Shearer, 1990). At body-wave frequencies (1 Hz), Q_α in the upper inner core is quite low, about 200, increasing to 440–1000 deeper into the inner core (Cormier, 1981; Doombos, 1983; Souriau and Roudil, 1995). Using normal modes, Widmer et al. (1991) found Q_β to be even lower, about 120. Little depth resolution is available from the normal-mode data.

Taken together, these studies could indicate a frequency dependence of attenuation or high attenuation in compression, but mineral physicists are not in agreement. Mao et al. (1998) found that the aggregate shear wave speed of hcp iron extrapolated from 220 GPa and room temperature to inner core conditions is about 15% greater than that in the inner core (Dziewonski and Anderson, 1981), suggesting near-melting softening. However, some studies (Jackson et al., 2000; Laio et al., 2000; Steinle-Neumann et al., 2001) found a Poisson's ratio for hcp iron under inner core conditions comparable to that from PREM, suggesting that the high Poisson's ratio of the inner core is an intrinsic property of hcp iron at high temperature.

Attenuation in the inner core can result from intrinsic relaxation and diffusion mechanisms and from scattering. As seismic waves travel, they cause an adiabatic pressure perturbation, which causes a temperature change and, potentially, freezing and melting. These cause thermal and compositional diffusion and result in attenuation. Loper and Fearn (1983) derived an expression for frequency-dependent attenuation due to diffusion. Under this mechanism, attenuation increases with melt fraction, with peak attenuation at the timescale corresponding to thermal and compositional diffusion.

Singh et al. (2000) evaluated the attenuation for the case where liquid can flow in the interconnected space of a solid matrix, as a result of the pressure variations arising from the propagation of seismic waves. In the seismic frequency range of interest, their results showed an attenuation peak at a viscosity of around 250 Pa s, many orders of magnitude less than that likely in the inner core (see **Section 8.12.4**), so that attenuation from this mechanism is negligibly small. Singh et al. (2000) also found that fluid inclusions can lower the shear wave velocity, a result confirmed by Vocadlo (2007), which could explain the anomalously low S-wave velocity in the inner core (Cao et al., 2005; Dziewonski and Anderson, 1981). However, the amount of partial melt required, some 8%, may be unrealistically high (Sumita et al., 1996), and Belonoshko et al. (2007) found that grain boundaries and defects may account for the low S-wave velocity. Calvet and Margerin (2008) also found that the effective S-wave velocity in an aggregate can be up to 15% less than the average in a single crystal.

Another interesting finding is the coda waves following the inner core-reflected wave (PKiKP) (e.g., Vidale and Earle, 2000). One interpretation is that these are caused by strong scatterers with a scale length of about 2 km in the outermost 300 km of the inner core (Vidale and Earle, 2000). They may alternatively be due to reverberation effects near the ICB (Poupinet and Kennett, 2004), though Peng et al. (2008) argue that they can only be produced by volumetric scatterers within the inner core. Laboratory experiments indicate that there are at least three length scales associated with solidification that could be relevant to scattering: the grain size, the spacing between dendrites, and the spacing between the chimneys of the upwelling in the mushy layer (e.g., Tait et al., 1992). Reverberation near the ICB might be caused by waves trapped in a low-Q mushy zone between the high-Q outer core and the deeper inner core.

Scattering can give rise to an apparent Q that is lower than the intrinsic material value. This has been explored by Cormier (1981) and Cormier and Li (2002) for 10–30 km wavelength body waves. Bergman (1998) and Cormier et al. (1998) also examined whether anisotropic scattering as a result of columnar crystal growth might also be responsible for an attenuation anisotropy (Creager, 1992; Oreshin and Vinnik, 2004; Souriau and Romanowicz, 1996, 1997; Yu and Wen, 2006), where waves traveling parallel to the fast rotation axis exhibit smaller amplitudes and more complex waveforms. Anisotropic scattering has been observed in directionally solidified hcp zinc alloys (Bergman et al., 2000). Like the elastic anisotropy, the attenuation anisotropy may also have a hemispheric variation. On the other hand, some studies have shown that there are regions without such attenuation anisotropy (Helffrich et al., 2002).

8.12.6.3 Hemispheric and Depth Variation of Seismic (Isotropic) Velocity, Attenuation, Elastic Anisotropy, and Attenuation Anisotropy

Next, we turn to radially and laterally heterogeneous structures in the inner core. Recent seismological studies have revealed that there exist small (less than the average 3% difference in anisotropic velocity) large-scale longitudinal and radial variations in average P-wave (isotropic) velocity and lateral and radial variations in attenuation. There are also such variations in elastic and attenuation anisotropy. See **Chapter 1.23** for a more comprehensive review.

It has been found that the eastern hemisphere has a larger isotropic velocity and a smaller Q (Cao and Romanowicz, 2004; Niu and Wen, 2001; Tanaka and Hamaguchi, 1997; Wen and Niu, 2002). The isotropic velocity and Q may also have a strong depth dependence, with a high velocity and strongly scattering layer in the upper 30 km of the eastern hemisphere, perhaps due to a higher concentration of light elements (Waszek and Deuss, 2011). Cao and Romanowicz (2004) found a hemispheric variation of the depth dependence of Q, increasing with depth in the eastern hemisphere but decreasing with depth in the western hemisphere.

The western hemisphere has a larger elastic and attenuation anisotropy (Creager, 1999; Tanaka and Hamaguchi, 1997; Yu and Wen, 2006), though these too likely have depth

dependences (Irving and Deuss, 2011), with lateral variations of the anisotropies typically decreasing with depth. Normal modes also show east–west variations of the elastic anisotropy (Deuss et al., 2010). In general, elastic anisotropy has been found to increase with depth (Creager, 1992, 2000), with some studies finding a 100–200 km isotropic layer at the top of the western hemisphere of the inner core and thicker, some 400 km, in the eastern hemisphere (Garcia and Souriau, 2000), whereas other studies find a 50 km thick isotropic layer at the top of the western hemisphere above a more anisotropic region, but no isotropic layer in the eastern hemisphere and rather a lower level of elastic anisotropy throughout that hemisphere (Waszek and Deuss, 2011).

The lateral and radial boundaries between these regions are clearly still uncertain, as is the sharpness of the transitions, the latter of which is important for interpreting these features and understanding the dynamics of the inner core. Song and Helmberger (1998) first suggested a sharp and laterally variable boundary between an isotropic upper inner core and an anisotropic lower inner core. The sharpness of any transitions in the inner core has been questioned (Leyton et al., 2005), though Waszek and Deuss (2011) found a sharp boundary between the eastern and the western hemispheres.

Finally, the seismic structure of the deepest inner core is yet more difficult to infer from body waves due to the lack of a reference phase, but some observations suggest that the central 200 km of the inner core may be distinctly different from other parts of the inner core, with a different sense of anisotropy (Beghein and Trampert, 2003; Ishii and Dziewonski, 2002, 2003), perhaps suggesting a phase transition from hcp to bcc iron.

It is a challenge to understand the cause of even homogeneous elastic anisotropy in the inner core, but it is even more difficult to understand the radial and lateral heterogeneities of the isotropic velocity, attenuation, and elastic and attenuation anisotropies, though presumably, these hold the clue to it all and hence toward an understanding of inner core dynamics. Sharp boundaries may be particularly difficult to explain, other than by phase transitions. The origin of these features likely involves some combination of the mechanisms discussed here and in **Section 8.12.5** or ones not yet explored such as a positive feedback mechanism, for example, one involving an anisotropic thermal conductivity.

Hemispheric structure may be produced by long-term lateral variation in outer core convection controlled by the thermally heterogeneous mantle (Sumita and Olson, 1999, 2002). For instance, Bergman et al. (2003, 2005) found that fluid flow in the melt can affect the solidification texture, and Aubert et al. (2008) combined the results of these experiments in a numerical calculation to suggest that hemispheric differences in the inner core could be due to long-term mantle control, though the details remain somewhat uncertain. For instance, Cormier (2007) suggested that if the eastern hemisphere were more actively solidifying, it would tend to have grains elongated more in the cylindrically radial direction that would lead to more scattering and higher attenuation. More rapid solidification in the eastern hemisphere would also lead to a porous inner core because there is insufficient time to expel liquid by compaction, leading to a low P-wave velocity there. This is opposite to what is observed, but perhaps, the presence of more light elements mitigates a more porous region.

On the other hand, if the western hemisphere were solidifying more rapidly and if the inner core elastic anisotropy results from preferential growth (Bergman, 1997) or deformation resulting from such growth (Yoshida et al., 1996), then the western hemisphere might have a larger elastic anisotropy, as observed. As previously discussed, Gubbins et al. (2011) suggest that heterogeneous mantle control over outer core convection could not only produce hemispheric variations on inner core dynamics and hence structure but also produce hemispheric melting of the inner core, leading to the F-layer. In any case, long-term mantle control to explain hemispheric variations requires that the inner core be locked to the mantle (Buffett, 1996b), implying that seismologists are inferring an inner core oscillation rather than a rotation (see **Section 8.12.7**). Future observations should resolve this issue.

Another means of producing hemispheric variations is the translative mode of inner core convection (Alboussiere et al., 2010) discussed in **Section 8.12.6.1** and shown in **Figure 7**. In addition to being a means to produce the F-layer, this mode obviously results in east–west differences. For instance, Monnereau et al. (2010) predicted that as inner core material solidifies in the west and moves eastward, it anneals and coarsens, resulting in higher isotropic P-wave velocity and more attenuation (for seismic body wavelengths) in the eastern hemisphere. Bergman et al. (2010) showed further that directionally solidified alloys can lose their texture as they anneal, which would result in weaker elastic and attenuation anisotropies in the eastern hemisphere, also as observed. However, Al-Khatatbeh et al. (2013) showed that alloys do not always lose their texture as they anneal, and in any case, Deguen et al. (2013) discussed that the translative mode requires a viscosity $>3\times10^{18}$ Pa s and a sufficiently low thermal conductivity, though it is also possible that the translative mode could result from compositional convection (Gubbins et al., 2013). A sharp boundary between the hemispheres is a particular challenge for the inner core translation model, however, as one would expect the transition of seismic properties to be smoothly varying.

Several possible explanations can be given for the cause of larger anisotropy with depth. A smaller anisotropy at shallow parts can arise from random alignment in the horizontal plane or from alignment such that the symmetry axis (c-axis for hcp) is in the radial direction. The former can result from the slow kinetics of crystal alignment, the geometry of solidification texturing (Bergman, 1997; see **Figure 6**), or the fluid flow in the outer core and the latter from a principal stress axis in the radial direction at shallow depths. Such a stress field may arise from electromagnetic stresses or from compaction. Deguen and Cardin (2009, 2011) suggest that the depth dependence of the elastic anisotropy could result from convective stratification, so that, for instance, the deeper inner core might retain an older texture, whereas the more shallow inner core texture reflects current dynamics. Sharp boundaries might result more naturally in this model, but in order to produce hemispheric differences, the model would need to be combined with another mechanism. Similarly, Cottaar and Buffett (2012) suggest that the depth variations could result in changes in the convective regime.

Attenuation in the deep inner core has been found to be smaller, which may be explained by a smaller liquid fraction or from a larger grain size.

8.12.7 Inner Core Rotation

8.12.7.1 An Overview

Inner core rotation relative to the mantle was first proposed on theoretical grounds by Gubbins (1981) and then found to occur, on the order of degrees per year, in numerical dynamos by Glatzmaier and Roberts (1995a,b). Shortly thereafter, Song and Richards (1996) inferred that the tilted symmetry axis of inner core anisotropy is rotating eastward about the spin axis, at a rate of 1.1° per year, and Su et al. (1996) found a rate as high as 3° per year. However, using a lateral anisotropy gradient rather than the tilted symmetry axis, Creager (1997) limited the differential rotation to 0.2–0.3° per year. In these studies, there is a trade-off between the rate of superrotation and the level of anisotropy and symmetry axis tilt or the anisotropy gradient. Vidale et al. (2000) examined the PKiKP coda from nuclear tests, which eliminates trade-offs associated with event mislocations, to also infer a differential rotation rate of 0.2° per year. However, using the splitting of core-sensitive normal modes, Laske and Masters (1999) preferred no rotation, though the data allow a maximum inner core superrotation of 0.2–0.3° per year. Numerical dynamos with a better resolution and without hyperdiffusion also predict a modest prograde inner core rotation of about 0.1° per year, which further decreases to 0.02 per year when gravitational coupling is included (Buffett and Glatzmaier, 2000). There have been controversial seismological issues (Souriau and Poupinet, 2003), and a recent study using a globally extended data set (Makinen and Deuss, 2011) does not support superrotation. On the other hand, studies using earthquakes with similar waveforms (Zhang et al., 2005) and using different events at the same station (Song and Poupinet, 2007) continue to support superrotation. If the inner core is superrotating, the hemispheric seismic structure seems difficult to form. Recently, Waszek et al. (2011) showed that the boundary of the hemispheric structure shifted eastward with depth and proposed that this is consistent with an extremely slow superrotation of 0.1–1° per million years. Here, we review mechanisms that can cause and inhibit inner core rotation.

8.12.7.2 Electromagnetic Coupling

Various torques can act on the inner core and these can make the inner core rotate. Electromagnetic torque was considered by Gubbins (1981) and was also the driving mechanism in the numerical dynamos by Glatzmaier and Roberts (1995a,b). Electromagnetic torque originates from the restoring force caused by the outer core flow that stretches the magnetic field lines. It is expressed as (Rochester, 1962)

$$\Gamma = 1/\mu_0 \int B_r B_\phi r \sin\theta \mathrm{d}S \qquad [6]$$

where μ_0 is the magnetic permeability and B_r and B_ϕ are the radial and azimuthal fields at the ICB, respectively. Quantitative estimates of inner core rotation from electromagnetic torque were given by Gubbins (1981). He showed that when an electromagnetic torque of 10^{19} N m is applied to the inner core, it would rotate and approach a steady angular velocity of about 0.13° per year and induce a toroidal magnetic field of about 80 gauss. He also showed that an oscillatory motion with a period of about 10 years is possible.

The mechanism of inner core rotation in the numerical dynamos by Glatzmaier and Roberts (1995a,b) was analyzed in Glatzmaier and Roberts (1996). They showed that the electromagnetic coupling caused by the thermal wind within the inner core tangent cylinder was the primary cause. Within the tangent cylinder, upwellings form above the polar region and downwellings near the equator. This meridional circulation causes eastward flow near the inner core and westward flow near the core–mantle boundary, by conservation of angular momentum. The eastward flow, coupled with the magnetic field, results in an electromagnetic coupling between the outer core flow and the inner core and spins up the inner core.

An analytic model of inner core rotation driven by the thermal wind was also derived by Aurnou et al. (1996). Assuming that the temperature inside the tangential cylinder is higher than the temperature outside, they showed that the resulting eastward thermal wind, coupled with the magnetic field, can quantitatively explain the inner core superrotation. This model was extended in Aurnou et al. (1998) by numerically calculating the resulting inner core rotation from electromagnetic coupling for three different outer core flow patterns. This work confirmed that the thermal wind can efficiently couple inner core rotation to outer core flow.

8.12.7.3 Gravitational Coupling

Mass anomalies in the mantle can deform the inner core. When the inner core rotates relative to the mantle, a misalignment of the inner core topography relative to the mantle mass anomaly causes a gravitational restoring force to the inner core. This torque was shown to become quite large, of the order of 10^{21} N m, by Buffett (1996b). Although there are uncertainties in the mass anomaly within the mantle, this estimate indicates that a gravitational torque can exceed the electromagnetic torque by orders of magnitude and thus lock the inner core to the mantle to inhibit rotation. Such gravitational coupling between the mantle and the inner core can cause an exchange of angular momentum between them and result in length-of-day variations (Buffett, 1996a,b).

Gravitational torque can become small if the inner core topography cannot become as high as that caused by the mass anomaly of the mantle. If this torque becomes smaller than the electromagnetic torque, the inner core may rotate. Buffett (1997) showed that it is possible to constrain the viscosity of the inner core if the inner core is rotating under the gravitational torque. One case is when the viscosity of the inner core is so small that the inner core can deform rapidly and thus misalignment of the mantle mass anomaly and inner core topography does not occur. The other case is when the viscosity of the inner core is so high that the inner core is slow to deform and thus the inner core topography becomes small. For this case, however, because of high viscosity, once it becomes locked to the mantle, it would become unable to

rotate again. From the aforementioned constraints, the inner core viscosity was found to become $< 10^{16}$ Pa s or $> 10^{20}$ Pa s.

Dumberry (2010) proposed a new mechanism of inner core rotation driven by a gravitational torque. The inner core growth can become longitudinally heterogeneous due to heat flux variations in the outer core caused by the mantle convection. As a result, the shape of the inner core misaligns with the gravitational potential, and a gravitational torque will act to spin the inner core.

8.12.7.4 Combined Coupling

Estimates of electromagnetic torque have large uncertainty because the strength of the toroidal field inside the core cannot be observed. Aurnou and Olson (2000) calculated the inner core rotation under the combined effects of electromagnetic, gravitational, and viscous torques. Among these torques, the viscous torque was found to be very small. When the electromagnetic and gravitational torques are comparable, the inner core rotation showed time-dependent features. A more general case of inner core rotation, where the inner core was also allowed to tilt, was studied by Xu et al. (2000).

Incorporation of the combined effects of gravitational torque and viscous deformation of the inner core into a numerical geodynamo calculation was done by Buffett and Glatzmaier (2000), who demonstrated that the gravitational torque can significantly suppress inner core rotation.

Dumberry and Mound (2010) theoretically analyzed the oscillatory motion of the inner core. They constrained the magnitude of the gravitational and electromagnetic coupling to be compatible with the inner core differential rotation rate inferred from seismic observations. Aubert and Dumberry (2011) conducted a detailed parameter study of the inner core superrotation including the viscous, magnetic, and gravitational torques and obtained a scaling law of superrotation as a function of Ekman number. Extrapolating to the core conditions, the scaling predicts a steady superrotation of few degrees per million years, upon which a large fluctuation of about 0.1° per year is superimposed.

8.12.8 Summary

The inner core remains a difficult part of our planet to study. In every way, it presents challenges: for mineral physicists, the extreme pressures and temperatures are difficult to reach in the lab; for seismologists, the 5200 km of overburden obfuscates inner core signals; and for geodynamicists, the wide variety and interaction of possible phenomena and the large uncertainty of physical parameters complicate interpretation. Nevertheless, progress continues along multiple fronts: observational scientists will become more proficient at extracting signals; experimentalists will continue to make technical improvements to achieve the extreme conditions of the inner core and to design appropriate analog experiments and derive scaling laws by varying the parameters; computational scientists will go where experimentalists cannot; and theoreticians will make progress in coupling data from all disciplines. Further progress toward understanding the inner core will require a multi- and interdisciplinary effort. We also expect that geodynamicists will continue to simulate yet unknown observations, such as was the case with inner core superrotation. Perhaps, it should have been possible to have predicted inner core elastic anisotropy prior to its discovery! Formulating testable models by geodynamicists is one of the key directions to the study of the inner core.

It is always dangerous to make specific predictions about the directions a field of study will take (one is reminded of Roberts (1988) statement that worrying about the inner core is "like worrying about the size of the tip when one can't pay the bill"), but we will nevertheless try. The composition of the light elements of the core is likely to remain uncertain – there are too many ways to put the puzzle together. This means that the phase diagram of the core will also remain uncertain. It does not mean, however, that there will be no progress toward understanding such important issues as the partitioning of elements between the inner and outer cores and the light elements' effects on the melting temperature. On the other hand, it seems reasonable that we will make progress toward understanding the stable phases(s) of pure and alloyed iron under inner core conditions. Likewise, we expect that the current uncertainty concerning the elastic constants of hcp iron and its thermal conductivity under inner core conditions will get sorted out. Similarly, if there is another stable phase of iron in the inner core, we will determine its elastic properties.

Inner core seismology is difficult, but not intractable. Over time, we will come to some agreement concerning the elastic and anelastic properties of the inner core. Of particular interest will be the geographic distributions of the isotropic velocity, the elastic anisotropy, the bulk attenuation, and the attenuation anisotropy and the sharpness of inner core transitions. One thing seems certain: like the rest of the Earth, the inner core is not simple and featureless. In some ways, this makes it less interesting – there is no one simple physical mechanism that can explain all the data. Ultimately, though, it shows that the inner core too exhibits the rich array of phenomena that makes earth science challenging and interesting. We predict that geodynamicists will take up the challenge to cross disciplines and come to understand the origin of inner core anisotropy, in all of its detail, as well as other interesting seismic properties that we dig up. We also predict that the inner core will continue to surprise us and hold keys to understanding long-standing problems in the earth sciences, such as magnetic field generation and reversals and the history of the core.

References

Alboussiere T, Deguen R, and Melzani M (2010) Melting-induced stratification above the Earth's inner core due to convective translation. *Nature* 466: 744–747.

Alfe D, Gillan MJ, and Price GD (2000) Constraints on the composition of the Earth's core from *ab initio* calculations. *Nature* 405: 172–175.

Alfe D, Gillan MJ, and Price GD (2002) Ab initio chemical potentials of solid and liquid solutions and the chemistry of the Earth's core. *Journal of Chemical Physics* 116: 7127–7136.

Alfe D, Price GD, and Gillan MJ (1999) Oxygen in the Earth's core: A first-principles study. *Physics of the Earth and Planetary Interiors* 110: 191–210.

Al-Khatatbeh Y, Bergman MI, Lewis DJ, Mason Z, Zhu L, and Rosenstock S (2013) Annealing of directionally solidified alloys revisited: No loss of texture during translation of Earth's inner core. *Physics of the Earth and Planetary Interiors* 223: 32–39.

Anderson DL (1983) A new look at the inner core of the Earth. *Nature* 302: 660.

Anderson WW and Ahrens T (1996) Shock temperatures and melting in iron sulfides at core pressures. *Journal of Geophysical Research* 101: 5627–5642.

Antonangeli D, Merkel S, and Farber DL (2006) Elastic anisotropy in hcp metals at high pressure and the sound wave anisotropy of the Earth's inner core. *Geophysical Research Letters* 33: L24303. http://dx.doi.org/10.1029/2006GL028237.

Aubert J, Amit H, Hulot G, and Olson P (2008) Thermochemical flows couple the Earth's inner core growth to mantle heterogeneity. *Nature* 454: 758–761.

Aubert J and Dumberry M (2011) Steady and fluctuating inner core rotation in numerical geodynamo models. *Geophysical Journal International* 184: 162–170.

Aurnou JM, Brito D, and Olson PL (1996) Mechanics of inner core super-rotation. *Geophysical Research Letters* 23: 3401–3404.

Aurnou JM, Brito D, and Olson PL (1998) Anomalous rotation of the inner core and the toroidal magnetic field. *Journal of Geophysical Research* 103: 9721–9738.

Aurnou J and Olson P (2000) Control of inner core rotation by electromagnetic, gravitational and mechanical torques. *Physics of the Earth and Planetary Interiors* 117: 111–121.

Beghein C and Trampert J (2003) Robust normal mode constraints on inner core anisotropy from model space search. *Science* 299: 552–555.

Belonoshko AB, Ahuja R, and Johansson B (2003) Stability of the body-centered-cubic phase of iron in the Earth's inner core. *Nature* 424: 1032–1034.

Belonoshko AB, Skorodumova NV, Davis S, Osiptsov AN, Rosengren A, and Johansson B (2007) Origin of the low rigidity of the Earth's inner core. *Science* 316: 1603–1605.

Belonoshko AB, Skorodumova NN, Rosengren A, and Johansson B (2008) Elastic anisotropy of Earth's inner core. *Science* 319: 797–800.

Bergman MI (1997) Measurements of elastic anisotropy due to solidification texturing and the implications for the Earth's inner core. *Nature* 389: 60–63.

Bergman MI (1998) Estimates of the Earth's inner core grain size. *Geophysical Research Letters* 25: 1593–1596.

Bergman MI (2003) Solidification of the Earth's core. In: Veronique D, Kenneth C, Stephan Z, and Shun-Ichiro K (eds.) *Earth's Core: Dynamics, Structure, Rotation*. *Geodynamics Series*, vol. 31, pp. 105–127. Washington, DC: American Geophysical Union. http://dx.doi.org/10.1029/31GD08.

Bergman MI (2010) An inner core slip-sliding away. *Nature* 466: 697–698.

Bergman MI, Agrawal S, Carter M, and Macleod-Silberstein M (2003) Transverse solidification textures in hexagonal close-packed alloys. *Journal of Crystal Growth* 255: 204–211.

Bergman MI, Giersch L, Hinczewski M, and Izzo V (2000) Elastic and attenuation anisotropy in directionally solidified (hcp) zinc and the seismic anisotropy in the Earth's inner core. *Physics of the Earth and Planetary Interiors* 117: 139–151.

Bergman MI, Lewis DJ, Myint IH, Slivka L, Karato SI, and Abreu A (2010) Grain growth and loss of texture during annealing of alloys, and the translation of Earth's inner core. *Geophysical Research Letters* 37: L22313. http://dx.doi.org/10.1029/2010GL045103.

Bergman MI, Macleod-Silberstein M, Haskel M, Chandler B, and Akpan N (2005) A laboratory model for solidification of Earth's core. *Physics of the Earth and Planetary Interiors* 153: 150–164.

Birch F (1952) Elasticity and constitution of the Earth's interior. *Journal of Geophysical Research* 57: 227–286.

Boehler R (1992) Melting of the Fe–FeO and Fe–FeS systems at high pressures: Constraints on core temperatures. *Earth and Planetary Science Letters* 111: 217–227.

Boehler R (1996a) Fe–FeS eutectic temperatures to 620 kbar. *Physics of the Earth and Planetary Interiors* 96: 181–186.

Boehler R (1996b) Melting temperature of the Earth's mantle and core: Earth's thermal structure. *Annual Review of Earth and Planetary Sciences* 24: 15–40.

Braginsky SI (1963) Structure of the F-layer and reasons for convection in Earth's core. *Doklady Akademii Nauk SSSR, English Translation* 149: 1311–1314.

Bridgman PW (1949) Linear compression to 30,000 kg/cm^2, including relatively incompressible substances. *Proceedings of the American Academy of Arts and Sciences* 77: 187–234.

Brito D, Elbert D, and Olson P (2002) Experimental crystallization of gallium: Ultrasonic measurements of elastic anisotropy and implications for the inner core. *Physics of the Earth and Planetary Interiors* 129: 325–346.

Brown H and Patterson C (1948) The composition of meteoritic matter: III. Phase equilibria, genetic relationships, and planet structures. *Journal of Geology* 56: 85–111.

Buchwald VF (1975) *Handbook of Iron Meteorites*. vol. 1. Berkeley, CA: University of California Press.

Buffett BA (1996a) Gravitational oscillations in the length of day. *Geophysical Research Letters* 23: 2279–2282.

Buffett BA (1996b) A mechanism for decade fluctuations in the length of day. *Geophysical Research Letters* 23: 3803–3806.

Buffett BA (1997) Geodynamic estimates of the viscosity of the Earth's inner core. *Nature* 388: 571–573.

Buffett BA (2009) Onset and orientation of convection in the inner core. *Geophysical Journal International* 179: 711–719.

Buffett BA and Bloxham J (2000) Deformation of Earth's inner core by electromagnetic forces. *Geophysical Research Letters* 27: 4001–4004.

Buffett BA and Glatzmaier GA (2000) Gravitational braking of inner core rotation in geodynamo simulations. *Geophysical Research Letters* 27: 3125–3128.

Buffett BA and Wenk H-R (2001) Texturing of the Earth's inner core by Maxwell stresses. *Nature* 413: 60–63.

Bullard EC (1950) The transfer of heat from the core of the Earth. *Monthly Notices of the Royal Astronomical Society* 6: 36–41.

Bullen KE (1949) Compressibility–pressure hypothesis and the Earth's interior. *Monthly Notices of the Royal Astronomical Society, Geophysical Supplement* 5: 355–368.

Calvet M and Margerin L (2008) Constraints on grain size and stable iron phases in the uppermost inner core from multiple scattering modeling of seismic velocity and attenuation. *Earth and Planetary Science Letters* 267: 200–212.

Cao A and Romanowicz B (2004) Hemispherical transition of seismic attenuation at the top of the Earth's inner core. *Earth and Planetary Science Letters* 228: 243–253.

Cao A, Romanowicz B, and Takeuchi N (2005) An observation of PKJKP: Inferences on inner core shear properties. *Science* 308: 1453–1455.

Christensen UR and Tilgner A (2004) Power requirement of the geodynamo from Ohmic losses in numerical and laboratory dynamos. *Nature* 429: 169–171.

Cormier VF (1981) Short-period PKP phase and the anelastic mechanism of the inner core. *Physics of the Earth and Planetary Interiors* 24: 291–301.

Cormier VF (2007) Texture of the uppermost inner core from forward- and back-scattered seismic waves. *Earth and Planetary Science Letters* 258: 442–453.

Cormier VF (2009) A glassy lowermost outer core. *Geophysical Journal International*. http://dx.doi.org/10.1111/j.1365-246X.2009.04283.x.

Cormier VF and Li X (2002) Frequency-dependent seismic attenuation in the inner core. 2: A scattering and fabric interpretation. *Journal of Geophysical Research* 107(B12): 2362.

Cormier VF, Li X, and Choy GL (1998) Seismic attenuation of the inner core: Viscoelastic or stratigraphic? *Geophysical Research Letters* 25: 4019–4022.

Cote AS, Vocadlo L, and Brodholt JP (2008a) Light elements in the core: Effects of impurities on the phase diagram of iron. *Geophysical Research Letters* 35: L05306. http://dx.doi.org/10.1029/2007GL032788.

Cote AS, Vocadlo L, and Brodholt JP (2008b) The effect of silicon impurities on the phase diagram of iron and possible implications for the Earth's core structure. *Journal of Physics and Chemistry of Solids* 69: 2177–2181.

Cote AS, Vocadlo L, Dobson DP, Alfe D, and Brodholt JP (2010) Ab initio lattice dynamics calculations on the combined effect of temperature and silicon on the stability of different iron phases in the Earth's inner core. *Physics of the Earth and Planetary Interiors* 178: 2–7.

Cottaar S and Buffett B (2012) Convection in the Earth's inner core. *Physics of the Earth and Planetary Interiors* 198–199: 67–78.

Creager KC (1992) Anisotropy of the inner core from differential travel times of the phases PKP and PKIKP. *Nature* 356: 309–314.

Creager KC (1997) Inner core rotation rate from small-scale heterogeneity and time-varying travel times. *Science* 278: 1284–1288.

Creager KC (1999) Large-scale variations in inner core anisotropy. *Journal of Geophysical Research* 104: 23127–23139.

Creager KC (2000) Inner core anisotropy and rotation. In: Karato S-I, Stixrude L, and Lieberman R, et al. (eds.) *Mineral Physics and Seismic Tomography from the Atomic to Global Scale*, pp. 89–114. Washington, DC: American Geophysical Union.

Cummins P and Johnson LR (1988) Synthetic seismograms for an inner core transition of finite thickness. *Geophysical Journal* 94: 21–34.

de Koker N, Steinle-Neumann G, and Vlcek V (2012) Electrical resistivity and thermal conductivity of liquid Fe alloys at high P and T, and heat flux in Earth's core. *Proceedings of the National Academy of Sciences of the United States of America* 109: 4070–4073.

Deguen R, Alboussiere T, and Brito D (2007) On the existence and structure of a mush at the inner core boundary of the Earth. *Physics of the Earth and Planetary Interiors* 164: 36–49.

Deguen R, Alboussiere T, and Cardin P (2013) Thermal convection in Earth's inner core with phase change at its boundary. *Geophysical Journal International* 194(3): 1310–1334.

Deguen R and Cardin P (2009) Tectonic history of the Earth's inner core preserved in its seismic structure. *Nature Geoscience* 2: 419–422.

Deguen R and Cardin P (2011) Thermochemical convection in Earth's inner core. *Geophysical Journal International* 187: 1101–1118.

Deguen R, Cardin P, Merkel S, and Lebensohn RA (2011) Texturing in Earth's inner core due to preferential growth in its equatorial belt. *Physics of the Earth and Planetary Interiors* 188: 173–184.

Deuss A, Irving JCE, and Woodhouse JH (2010) Regional variation of inner core anisotropy from seismic normal mode observations. *Science* 328: 1018–1020.

Doombos DJ (1983) Observable effects of the seismic absorption band in the Earth. *Geophysical Journal of the Royal Astronomical Society* 75: 693–711.

Dubrovinsky L, Dubrovinskaia N, Narygina O, et al. (2007) Body-centered cubic iron–nickel alloy in Earth's core. *Science* 316: 1880–1883.

Dumberry M (2010) Gravitationally driven inner core differential rotation. *Earth and Planetary Science Letters* 297: 387–394.

Dumberry M and Mound J (2010) Inner core–mantle gravitational locking and the super-rotation of the inner core. *Geophysical Journal International* 181: 806–817.

Dziewonski AM and Anderson DL (1981) Preliminary reference Earth model. *Physics of the Earth and Planetary Interiors* 25: 297–356.

Esbensen KH and Buchwald VF (1982) Planet (oid) core crystallization and fractionation – Evidence from the Agpalilik mass of the Cape York iron meteorite shower. *Physics of the Earth and Planetary Interiors* 29: 218–232.

Fearn DR, Loper DE, and Roberts PH (1981) Structure of the Earth's inner core. *Nature* 292: 232–233.

Frost HH and Ashby MF (1982) *Deformation Mechanism Maps*, 166 pp. Tarrytown, NY: Pergamon.

Fukai Y (1984) The iron–water reaction and the evolution of the Earth. *Nature* 308: 174–175.

Gannarelli CM, Alfe S, and Gillan MJ (2003) The particle-in-cell model for ab initio thermodynamics: Implications for the elastic anisotropy of the Earth's inner core. *Physics of the Earth and Planetary Interiors* 139: 243–253.

Garcia R and Souriau A (2000) Inner core anisotropy and heterogeneity level. *Geophysical Research Letters* 27: 3121–3124.

Georg RB, Halliday AN, Schauble EA, and Reynolds BC (2007) Silicon in the Earth's core. *Nature* 447: 1102–1106.

Gessmann CK and Wood BJ (2002) Potassium in the Earth's core? *Earth and Planetary Science Letters* 200: 63–78.

Glatzmaier GA and Roberts PH (1995a) A three-dimensional self-consistent computer simulation of a geomagnetic field reversal. *Nature* 377: 203.

Glatzmaier GA and Roberts PH (1995b) A three-dimensional convective dynamo solution with rotating and finitely conducting inner core and mantle. *Physics of the Earth and Planetary Interiors* 91: 63.

Glatzmaier GA and Roberts PH (1996) Rotation and magnetism of the Earth's inner core. *Science* 274: 1887–1891.

Gubbins D (1981) Rotation of the inner core. *Journal of Geophysical Research* 86: 11695–11699.

Gubbins D, Alfe D, and Davies CJ (2013) Compositional instability of Earth's solid inner core. *Geophysical Research Letters* 364: 37–43. http://dx.doi.org/10.1002/grl.50186.

Gubbins D, Masters TG, and Jacobs JA (1979) Thermal evolution of the Earth's core. *Geophysical Journal of the Royal Astronomical Society* 59: 57–99.

Gubbins D, Masters G, and Nimmo F (2008) A thermochemical boundary layer at the base of Earth's outer core and independent estimate of core heat flux. *Geophysical Journal International* 174: 1007–1018.

Gubbins D, Sreenivasan B, Mound J, and Rost S (2011) Melting of the Earth's inner core. *Nature* 473: 361–363.

Haack H and Scott ERD (1992) Asteroid core crystallization by inward dendritic growth. *Journal of Geophysical Research* 97: 14727–14734.

Haddon RAW and Cleary JR (1974) Evidence for scattering of seismic PKP waves near the mantle–core boundary. *Physics of the Earth and Planetary Interiors* 8: 211–234.

Helffrich G and Kaneshima S (2004) Seismological constraints on core composition from Fe–O–S liquid immiscibility. *Science* 306: 2239–2242.

Helffrich G, Kaneshima S, and Kendall J-M (2002) A local, crossing-path study of attenuation and anisotropy of the inner core. *Geophysical Research Letters* 29(12): 1568. http://dx.doi.org/10.1029/2001GL014059.

Hirose K, Gomi H, Ohta K, Labrosse S, and Hernlund J (2011) The high conductivity of iron and thermal evolution of the Earth's core. *Mineralogical Magazine* 75: 1027 (abstract).

Huang H, Fei Y, Cai L, et al. (2011) Evidence for an oxygen-depleted liquid outer core of the Earth. *Nature* 479: 513–516.

Irving JCE and Deuss A (2011) Hemispherical structure in inner core velocity anisotropy. *Journal of Geophysical Research* 116: B04307. http://dx.doi.org/10.1029/2010JB007942.

Ishii M and Dziewonski AM (2002) The innermost inner core of the Earth: Evidence for a change in anisotropic behavior at the radius of about 300 km. *Proceedings of the National Academy of Sciences* 99(22): 14026–14030.

Ishii M and Dziewonski AM (2003) Distinct seismic anisotropy at the center of the Earth. *Physics of the Earth and Planetary Interiors* 140: 203–217.

Jackson KA (1958) Mechanism of growth. In: Maddin R, et al. (eds.) *Liquid Metals and Solidification*, pp. 174–186. Cleveland, OH: American Society for Metals.

Jackson I, Fitzgerald JD, and Kokkonen H (2000) High temperature viscoelastic relaxation in iron and its implication for the shear modulus and attenuation of the Earth's inner core. *Journal of Geophysical Research* 105: 23605–23634.

Jeanloz R (1990) The nature of the Earth's core. *Annual Review of Earth and Planetary Sciences* 18: 357–386.

Jeanloz R and Wenk H-R (1988) Convection and anisotropy of the inner core. *Geophysical Research Letters* 15: 72–75.

Jephcoat A and Olson P (1987) Is the inner core of the Earth pure iron? *Nature* 325: 332–335.

Kamb WB (1959) Theory of preferred crystal orientation developed by crystallization under stress. *Journal of Geology* 67: 153–170.

Kaneshima S, Hirahara K, Ohtaki T, and Yoshida Y (1994) Seismic structure near the inner core–outer core boundary. *Geophysical Research Letters* 21(2): 157–160.

Karato S (1993) Inner core anisotropy due to the magnetic field induced preferred orientation of iron. *Science* 262: 1708–1711.

Karato S (1999) Seismic anisotropy of the Earth's inner core resulting from flow induced by Maxwell stresses. *Nature* 402: 871–873.

Komabayashi T and Fei Y (2010) Internally consistent thermodynamic database for iron to the Earth's core conditions. *Journal of Geophysical Research* 115: B03202. http://dx.doi.org/10.1029/2009JB006442.

Konopkova Z, Lazor P, Goncharov AF, and Struzhkin VV (2011) Thermal conductivity of hcp iron at high pressure and temperature. *High Pressure Research* 31: 228–236.

Koot L and Dumberry M (2011) Viscosity of the Earth's inner core: Constraints from nutation observations. *Earth and Planetary Science Letters* 308: 343–349.

Krasnoshchekov DN, Kaazik PB, and Ovtchinnikov VM (2005) Seismological evidence for mosaic structure of the surface of the Earth's inner core. *Nature* 435: 483–487.

Kubo A, Ito E, Katsura T, et al. (2003) *In situ* X-ray observation of iron using Kawai-type apparatus equipped with sintered diamond: Absence of β phase up to 44 GPa and 2100 K. *Geophysical Research Letters* 30: 1126. http://dx.doi.org/10.1029/2002GL016394.

Kuwayama Y, Sawai T, Hirose K, Sata N, and Ohishi Y (2009) Phase relations of iron–silicon alloys at high pressure and high temperature. *Physics and Chemistry of Minerals* 36: 511–518.

Labrosse S, Poirier J-P, and Le Mouel J-L (2001) The age of the inner core. *Earth and Planetary Science Letters* 190: 111–123.

Laio A, Bernard S, Chiarotti GL, Scandolo S, and Tosatti E (2000) Physics of iron at Earth's core conditions. *Science* 287: 1027–1030.

Laske G and Masters G (1999) Rotation of the inner core from a new analysis of free oscillations. *Nature* 402: 66–69.

Legrand B (1984) Relations entre la structure el′ectronique et la facilite de glissement dans les metaux hexagonaux compacts. *Philosophical Magazine* 49: 171–184.

Leyton F, Koper KD, Zhu L, and Dombrovskaya M (2005) On the lack of seismic discontinuities in the inner core. *Geophysical Journal International* 162: 779–786.

Li J and Agee CB (2001) Element partitioning constraints on the light element composition of the Earth's core. *Geophysical Research Letters* 28: 81–84.

Lin J-F, Heinz DL, Campbell AJ, Devine JM, and Shen G (2002) Iron–silicon alloy in Earth's core? *Science* 295: 313–315.

Lin J-F, Sturhahn W, Zhao J, Shen G, Mao H-K, and Hemley RJ (2005) Sound velocities of hot dense iron: Birch's law revisited. *Science* 308: 1892–1894.

Loper DE (1983) Structure of the inner core boundary. *Geophysical and Astrophysical Fluid Dynamics* 22: 139–155.

Loper DE and Fearn DR (1983) A seismic model of a partially molten inner core. *Journal of Geophysical Research* 88: 1235–1242.

Loper DE and Roberts PH (1978) On the motion of an iron-alloy core containing a slurry: I. General theory. *Geophysical and Astrophysical Fluid Dynamics* 9: 289–321.

Loper DE and Roberts PH (1980) On the motion of an iron-alloy core containing a slurry: II. A simple model. *Geophysical and Astrophysical Fluid Dynamics* 16: 83–127.

Loper DE and Roberts PH (1981) A study of conditions at the inner core boundary of the Earth. *Physics of the Earth and Planetary Interiors* 24: 302–307.

MacDonald GJF and Knopoff L (1958) The chemical composition of the outer core. *Journal of Geophysics* 1: 1751–1756.

Makinen AM and Deuss A (2011) Global seismic body-wave observations of temporal variations in the Earth's inner core, and implications for its differential rotation. *Geophysical Journal International* 187: 355–370.

Mao HK, Shu J, Shen G, Hemley RJ, Li B, and Singh AK (1998) Elasticity and rheology of iron above 220 GPa and the nature of the Earth's inner core. *Nature* 396: 741–743.
Mao HK, Shu J, Shen G, Hemley RJ, Li B, and Singh AK (1999) Correction: Elasticity and rheology of iron above 220 GPa and the nature of the Earth's inner core. *Nature* 399: 280.
Mason B (1966) Composition of the Earth. *Nature* 211: 616–618.
Masters TG and Shearer PM (1990) Summary of seismological constraints on the structure of the Earth's core. *Journal of Geophysical Research* 95: 21691–21695.
Matsui M and Anderson OL (1997) The case for a body-centered cubic phase (α') for iron at inner core conditions. *Physics of the Earth and Planetary Interiors* 103: 55–62.
McDonough WF (2003) Compositional model for the Earth's core. In: Holland HD and Turekian KK (eds.) *The Mantle and Core*. *Treatise on Geochemistry*, vol. 2, pp. 547–568. Oxford: Pergamon.
McElhinny MW and Senanayake WE (1980) Paleomagnetic evidence for the existence of the geomagnetic field 3.5 Ga ago. *Journal of Geophysical Research* 85: 3523–3528.
McQueen RG and Marsh SP (1966) Shock-wave compression of iron–nickel alloys and the earth's core. *Journal of Geophysical Research* 71: 1751–1756.
Miller WA and Chadwick GA (1969) The equilibrium shapes of small liquid droplets in solid–liquid phase mixtures: Metallic h.c.p. and metalloid systems. *Proceedings of the Royal Society of London Series A* 312: 257–276.
Monnereau M, Calvet M, Margerin L, and Souriau A (2010) Lopsided growth of Earth's inner core. *Science* 328: 1014–1017.
Morse SA (1986) Adcumulus growth of the inner core. *Geophysical Research Letters* 13: 1557–1560.
Morse SA (2002) No mushy zones in the Earth's core. *Geochimica et Cosmochimica Acta* 66(12): 2155–2165.
Mullins WW and Sekerka RF (1963) Morphological stability of a particle growing by diffusion or heat flow. *Journal of Applied Physics* 34: 323–329.
Mullins WW and Sekerka RF (1964) Stability of a planar interface during solidification of a dilute binary alloy. *Journal of Applied Physics* 35: 444–451.
Murthy VR and Hall HT (1970) The chemical composition of the Earth's core: Possibility of sulfur in the core. *Physics of the Earth and Planetary Interiors* 2: 276–282.
Murthy VR, van Westrenen W, and Fei Y (2003) Experimental evidence that potassium is a substantial radioactive heat source in planetary cores. *Nature* 423: 163–165.
Niu F and Wen L (2001) Hemispherical variations in seismic velocity at the top of the Earth's inner core. *Nature* 410: 1081–1084.
Okuchi T (1997) Hydrogen partitioning into molten iron at high pressures: Implications for Earth's core. *Science* 278: 1781–1784.
Oreshin SI and Vinnik LP (2004) Heterogeneity and anisotropy of seismic attenuation in the inner core. *Geophysical Research Letters* 31: L02613. http://dx.doi.org/10.1029/2003GL018591.
Peng Z, Koper KD, Vidale JE, Leyton F, and Shearer P (2008) Inner core fine-scale structure from scattered waves recorded by LASA. *Journal of Geophysical Research* 113: B09312. http://dx.doi.org/10.1029/2007JB005412.
Poirier J-P (1985) *Creep of Crystals*. New York: Cambridge University Press.
Poirier J-P (1994) Light elements in Earth's outer core: A critical review. *Physics of the Earth and Planetary Interiors* 85: 319–337.
Poirier J-P and Price GD (1999) Primary slip system of epsilon-iron and anisotropy of the Earth's inner core. *Physics of the Earth and Planetary Interiors* 110: 147–156.
Porter DA and Easterling KE (1992) *Phase Transformations in Metals and Alloys*. London: Chapman and Hall.
Poupinet G and Kennett BLN (2004) On the observation of high frequency PKiKP and its coda in Australia. *Physics of the Earth and Planetary Interiors* 146: 497–511.
Pozzo M, Davies C, Gubbins D, and Alfe D (2012) Thermal and electrical conductivity of iron at Earth's core conditions. *Nature* 485: 355–358.
Reaman DM, Daehn GS, and Panero WR (2011) Predictive mechanism for anisotropy development in the Earth's inner core. *Earth and Planetary Science Letters* 312: 437–442.
Ringwood AE (1977) Composition of the core and implications for the origin of the Earth. *Geochemical Journal* 11: 111–135.
Ringwood AE and Hibberson W (1990) The system Fe–FeO revisited. *Physics and Chemistry of Minerals* 17: 313–319.
Roberts PH (1988) Future of geodynamo theory. *Geophysical and Astrophysical Fluid Dynamics* 44: 3–31.
Rochester MG (1962) Geomagnetic core–mantle coupling. *Journal of Geophysical Research* 67: 4833–4836.
Ross M, Young DA, and Grover R (1990) Theory of the iron phase diagram at Earth core conditions. *Journal of Geophysical Research* 95: 21713–21716.
Rutter JW (1958) Imperfections resulting from solidification. In: Maddin R, et al. (eds.) *Liquid Metals and Solidification*, pp. 243–262. Cleveland, OH: American Society for Metals.
Sakai T, Ohtani E, Hirao N, and Ohishi Y (2011) Stability field of the hcp-structure for Fe, Fe–Ni, and Fe–Ni–Si alloys up to 3 Mbar. *Geophysical Research Letters* 38: L09302. http://dx.doi.org/10.1029/2011GL047178.
Sanloup C and Fei Y (2004) Closure of the Fe–S–Si liquid miscibility gap at high pressure. *Physics of the Earth and Planetary Interiors* 147: 57–65.
Saxena SK, Shen G, and Lazor P (1993) Experimental evidence for a new iron phase and implications for Earth's core. *Science* 260: 1312–1314.
Sayers CM (1989) Seismic anisotropy of the inner core. *Geophysical Research Letters* 16: 270–276.
Sha X and Cohen RE (2010) Elastic isotropy of ε-Fe under Earth's core conditions. *Geophysical Research Letters* 37: L10302. http://dx.doi.org/10.1029/2009GL042224.
Shanker J, Singh BP, and Srivastava SK (2004) Volume–temperature relationship for iron at 330 GPa and the Earth's core density deficit. *Physics of the Earth and Planetary Interiors* 147: 333–341.
Sherman DM (1995) Stability of possible Fe–FeS and Fe–FeO alloy phases at high pressure and the composition of the Earth's core. *Earth and Planetary Science Letters* 132: 87–98.
Shimizu H, Poirier J-P, and Le Mouel J-L (2005) On crystallization at the inner core boundary. *Physics of the Earth and Planetary Interiors* 151: 37–51.
Singh SC, Taylor MAJ, and Montagner J-P (2000) On the presence of liquid in Earth's inner core. *Science* 287: 2471–2474.
Söderlind P, Moriarty JA, and Wills JM (1996) First-principles theory of iron up to Earth-core pressures: Structural, vibrational and elastic properties. *Physical Review B: Condensed Matter* 53: 14063–14072.
Song X and Helmberger DV (1992) Velocity structure near the inner core boundary from waveform modeling. *Journal of Geophysical Research* 97(B5): 6573–6586.
Song X and Helmberger DV (1993) Anisotropy of the Earth's inner core. *Geophysical Research Letters* 20: 285–288.
Song X and Helmberger DV (1995) A P wave velocity model of Earth's core. *Journal of Geophysical Research* 100(B7): 9817–9830.
Song XD and Helmberger DV (1998) Seismic evidence for an inner core transition zone. *Science* 282: 924–927.
Song X and Poupinet G (2007) Inner core rotation from event-pair analysis. *Earth and Planetary Science Letters* 261: 259–266.
Song XD and Richards PG (1996) Observational evidence for differential rotation of the Earth's inner core. *Nature* 382: 221–224.
Souriau A and Poupinet G (1991) The velocity profile at the base of the liquid core from PKP(BC + C_{diff}) data: An argument in favour of radial inhomogeneity. *Geophysical Research Letters* 18(11): 2023–2026.
Souriau A and Poupinet G (2003) Inner core rotation: A critical appraisal. In: Dehant V, et al. (eds.) *Earth's Core: Dynamics, Structure, Rotation*. *Geodynamics Series*, vol. 31, pp. 65–82. Washington, DC: AGU. http://dx.doi.org/10.1029/31GD06.
Souriau A and Romanowicz B (1996) Anisotropy in inner core attenuation: A new type of data to constrain the nature of the solid core. *Geophysical Research Letters* 23(1): 1–4.
Souriau A and Romanowicz B (1997) Anisotropy in the inner core: Relation between P-velocity and attenuation. *Physics of the Earth and Planetary Interiors* 101: 33–47.
Souriau A and Roudil P (1995) Attenuation in the uppermost inner core from broad-band GEOSCOPE PKP data. *Geophysical Journal International* 123: 572–587.
Stacey FD and Davis PM (2008) *Physics of the Earth*, 4th edn. Cambridge: Cambridge University Press.
Stacey FD and Anderson OL (2001) Electrical and thermal conductivities of Fe–Ni–Si alloy under core conditions. *Physics of the Earth and Planetary Interiors* 124: 153–162.
Stacey FD and Loper DE (2007) A revised estimate of the conductivity of iron alloy at high pressure and implications for the core energy budget. *Physics of the Earth and Planetary Interiors* 161: 13–18.
Steinle-Neumann G, Stixrude L, and Cohen RE (1999) First-principles elastic constants for the hcp transition metals Fe, Co and Re at high pressure. *Physical Review B* 60: 791–799.
Steinle-Neumann G, Stixrude L, Cohen RE, and Gulseren O (2001) Elasticity of iron at the temperature of the Earth's inner core. *Nature* 413: 57–60.
Steinle-Neumann G, Stixrude L, and Cohen RE (2003) Physical properties of iron in the inner core. In: Dehant V, et al. (eds.) *Earth's Core: Dynamics, Structure, Rotation*. *Geodynamics Series*, vol. 31, pp. 213–232. Washington, DC: AGU. http://dx.doi.org/10.1029/31GD10.
Stixrude L and Cohen RE (1995) High-pressure elasticity of iron and anisotropy of the Earth's inner core. *Science* 267: 1972–1975.
Stixrude L, Wasserman E, and Cohen RE (1997) Composition and temperature of Earth's inner core. *Journal of Geophysical Research* 102: 24729–24739.
Su WJ, Dziewonski AM, and Jeanloz R (1996) Planet within a planet: Rotation of the inner core. *Science* 274: 1883–1887.

Sumita I and Olson P (1999) A laboratory model for convection in Earth's core driven by a thermally heterogeneous mantle. *Science* 286: 1547–1549.

Sumita I and Olson P (2002) Rotating thermal convection experiments in a hemispherical shell with heterogeneous boundary heat flux: Implications for the Earth's core. *Journal of Geophysical Research* 107. http://dx.doi.org/10.1029/2001JB000548.

Sumita I, Yoshida S, Hamano Y, and Kumazawa M (1995) A model for the structural evolution of the Earth's core and its relation to the observations. In: Yukutake T (ed.) *The Earth's Central Part: Its Structure and Dynamics*, pp. 231–261. Tokyo: Terra Scientific.

Sumita I, Yoshida S, Kumazawa M, and Hamano Y (1996) A model for sedimentary compaction of a viscous medium and its application to inner core growth. *Geophysical Journal International* 124: 502–524.

Sumita I and Yoshida S (2003) Thermal interactions between the mantle, outer and inner cores, and the resulting structural evolution of the core. In: Dehant V, Kenneth C, and Shun-Ichiro K, et al. (eds.) *Earth's Core: Dynamics, Structure, Rotation*. *Geodynamics Series*, vol. 31, pp. 213–232. Washington, DC: AGU. http://dx.doi.org/10.1029/31GD14.

Tait S, Jahrling K, and Jaupart C (1992) The planform of compositional convection and chimney formation in a mushy layer. *Nature* 359: 406–408.

Takehiro S (2011) Fluid motions induced by horizontally heterogeneous Joule heating in the Earth's inner core. *Physics of the Earth and Planetary Interiors* 184: 134–142.

Tanaka S and Hamaguchi H (1997) Degree one heterogeneity and hemispherical variation of anisotropy in the inner core from PKP(BC)–PKP(DF) times. *Journal of Geophysical Research* 102: 2925–2938.

Tarduno JA, Cotrell RD, Watkeys MK, and Baruch D (2007) Geomagnetic field strength 3.2 billion years ago recorded by single silicate crystals. *Nature* 446: 657–660.

Tateno S, Hirose K, Ohishi Y, and Tatsumi Y (2010) The structure of iron in Earth's inner core. *Science* 330: 359–361.

Van Orman JA (2004) On the viscosity and creep mechanism of Earth's inner core. *Geophysical Research Letters* 31: L20606. http://dx.doi.org/10.1029/2004GL021209.

Vidale JE, Dodge DA, and Earle PS (2000) Slow differential rotation of the Earth's inner core indicated by temporal changes in scattering. *Nature* 405: 445–448.

Vidale JE and Earle PS (2000) Fine-scale heterogeneity in the Earth's inner core. *Nature* 404: 273–275.

Vocadlo L (2007) Ab initio calculations of the elasticity of iron and iron alloys at inner core conditions: Evidence for a partially molten inner core? *Earth and Planetary Science Letters* 254: 227–232.

Vocadlo L, Alfe D, Gillan MJ, Wood IG, Brodholt JP, and Price GD (2003) Possible thermal and chemical stabilization of body-centered-cubic iron in the Earth's core. *Nature* 424: 536–539.

Vocadlo L, Brodholt J, Alfe D, Price GD, and Gillan MJ (1999) The structure of iron under the conditions of the Earth's inner core. *Geophysical Research Letters* 26: 1231–1234.

Vocadlo L, Dobson DP, and Wood IG (2006) An ab initio study of nickel substitution into iron. *Earth and Planetary Science Letters* 248: 132–137.

Vocadlo L, Dobson DP, and Wood IG (2009) Ab initio calculations of the elasticity of temperature at inner core pressure. *Earth and Planetary Science Letters* 288: 534–538.

Vocadlo L, Wood IG, Alfe D, and Price GD (2008) Ab initio calculations on the free energy and high P–T elasticity of face centered cubic iron. *Earth and Planetary Science Letters* 268: 444–449.

Wang JN, Wu JS, and Ding Y (2002) On the transitions among different creep regimes. *Materials Science and Engineering A* 334: 275–279.

Waszek L and Deuss A (2011) Distinct layering in the hemispherical seismic velocity structure of Earth's upper inner core. *Journal of Geophysical Research* 116: B12313. http://dx.doi.org/10.1029/2011JB008650.

Waszek L, Irving J, and Deuss A (2011) Reconciling the hemispherical structure of Earth's inner core with its super-rotation. *Nature Geoscience* 4: 264–267.

Weber P and Machetel P (1992) Convection within the inner core and thermal implications. *Geophysical Research Letters* 19: 2107–2110.

Weeks WF and Wettlaufer JS (1996) Crystal orientations in floating ice sheets. In: Arsenault RJ, Cole D, and Gross T, et al. (eds.) *The Johannes Weertman Symposium*, pp. 337–350. Zimbabwe: The Minerals, Metals, & Materials Society.

Wen L and Niu F (2002) Seismic velocity and attenuation structures in the top of the Earth's inner core. *Journal of Geophysical Research* 107(B11): 2273. http://dx.doi.org/10.1029/2001JB000170.

Wenk H-R, Baumgardner JR, Lebenson RA, and Tome CN (2000a) A convection model to explain anisotropy of the inner core. *Journal of Geophysical Research* 105: 5663–5677.

Wenk H-R, Matthies S, Hemley RJ, Mao H-K, and Shu J (2000b) The plastic deformation of iron at pressures of the Earth's inner core. *Nature* 405: 1044–1047.

Wenk H-R, Takeshita T, Jeanloz R, and Johnson GC (1988) Development of texture and elastic anisotropy during deformation of hcp metals. *Geophysical Research Letters* 15: 76–79.

Widmer R, Masters G, and Gilbert F (1991) Spherically symmetric attenuation within the Earth from normal mode data. *Geophysical Journal International* 104: 541–553.

Wood BJ (1993) Carbon in the core. *Earth and Planetary Science Letters* 117: 593–607.

Worster MG (1991) Natural convection in a mushy layer. *Journal of Fluid Mechanics* 224: 335–359.

Xu S, Crossley D, and Szeto AMK (2000) Variations in length of day and inner core differential rotation from gravitational coupling. *Physics of the Earth and Planetary Interiors* 117: 95–110.

Yoshida S, Sumita I, and Kumazawa M (1996) Growth model of the inner core coupled with outer core dynamics and the resulting elastic anisotropy. *Journal of Geophysical Research* 101: 28085–28103.

Yu W and Wen L (2006) Inner core attenuation anisotropy. *Earth and Planetary Science Letters* 245: 581–594.

Yukutake T (1998) Implausibility of convection in the Earth's inner core. *Physics of the Earth and Planetary Interiors* 108: 1–13.

Zhang F and Oganov AR (2010) Iron silicides at pressures of the Earth's inner core. *Geophysical Research Letters* 37: L02305. http://dx.doi.org/10.1029/2009GL041224.

Zhang J, Song X-D, Li Y, Richards PG, Sun X, and Waldhauser F (2005) Inner core differential motion confirmed by earthquake waveform doublets. *Science* 309: 1357–1360.

Zou Z, Koper KD, and Cormier VF (2008) The structure of the base of the outer core inferred from seismic waves diffracted around the inner core. *Journal of Geophysical Research* 113: B05314. http://dx.doi.org/10.1029/2007JB005316.

8.13 Experiments on Core Dynamics

P Cardin, University Grenoble Alpes/CNRS, Grenoble, France; Université Joseph-Fourier, Grenoble, France
P Olson, Johns Hopkins University, Baltimore, MD, USA

© 2015 Elsevier B.V. All rights reserved.

8.13.1	**Introduction**	317
8.13.2	**Rotational Dynamics**	318
8.13.2.1	Formation of Taylor Columns	318
8.13.2.2	Inertial Modes	319
8.13.2.3	Viscous Layers	320
8.13.2.3.1	Ekman boundary layers	320
8.13.2.3.2	Stewartson layers	320
8.13.2.4	Nonlinear Effects	321
8.13.2.4.1	Nonlinear resonance of the Poincaré mode	321
8.13.2.4.2	Geostrophic zonal motions in precession experiments	321
8.13.2.4.3	Libration experiments	322
8.13.2.4.4	Parametric instabilities	322
8.13.2.4.5	Quasigeostrophic turbulence	324
8.13.3	**Thermal Convection in a Rapidly Rotating Spherical Shell**	324
8.13.3.1	Experimental Conditions	324
8.13.3.2	Onset of Convection	325
8.13.3.3	Developed Convective States	325
8.13.3.4	Liquid Metal Experiments	326
8.13.3.5	Heat Flux Measurements	326
8.13.3.6	Zonal Flows	327
8.13.3.7	Compositional Convection	328
8.13.4	**Magnetohydrodynamics**	329
8.13.4.1	Hartmann Layers	329
8.13.4.2	Internal Magnetic Layers	329
8.13.4.3	Pseudodiffusive Magnetic Columns	330
8.13.4.4	Turbulence under the Influence of a Magnetic Field	331
8.13.4.5	Magnetoconvection in Rotating Fluids	331
8.13.4.6	Magneto Inertial Waves	331
8.13.5	**Experimental Dynamos**	332
8.13.5.1	The Riga Dynamo	332
8.13.5.2	The Karlsruhe Dynamo	334
8.13.5.3	The VKS Experiments	335
8.13.5.4	Turbulence and Dynamo Onset	336
Acknowledgments		337
References		337

8.13.1 Introduction

Laboratory experiments on the dynamics of the Earth's core are usually designed to understand the basic fluid and solid mechanical processes that affect the geodynamo, the evolution of the core, and its interaction with the mantle. As a rule, their intent is not to reproduce the full complexity of the core, because laboratory fluid experiments, like numerical simulations, are subject to many limitations. First and foremost, the volume of the working fluids is limited. The linear dimensions in fluid experiments range from centimeters to a few meters at most, a full six orders of magnitude smaller than the linear dimensions of the core. Second, a restricted range of physical properties of the working fluids are available. Water is generally the preferred fluid for nonmagnetic experiments, whereas gallium or sodium is used in situations where magnetic fields and electric currents are required. Both of these liquids have viscous, thermal, and magnetic diffusivities that are reasonably close to the core values. However, in spite of the overall match of their transport properties, there is still a mismatch between experiments using these fluids and the core.

Two important physical attributes that distinguish experiments on the core from experiments on the Earth's mantle, for example, are the background solid-body rotation and the magnetic field, which are critical in the core but are unimportant in the solid, poorly conducting silicate portions of the Earth. In laboratory experiments, the rotation and the magnetic field are generally imposed on the fluid and are limited to upper values around ≈ 1000 rpm and ≈ 1 T, respectively. These physical parameters, along with the diffusivities, enter into the definitions of two of the critical dimensionless numbers that characterize the dynamics of the core, the Ekman number E and the

Hartmann number *Ha*. Because of the dependence on length scale, rotation and magnetic field strength, both of these numbers assume unrealistic values in experiments, even though they are sometimes closer to the core in experiments than in numerical simulations.

One major advantage that laboratory experiments offer is their ability to naturally include the nonlinear effects and the associated instabilities that accompany large-amplitude forcing in fluids. One major disadvantage is the difficulty of obtaining full global measurements of highly variable quantities. As a rule, experimental flows have to be understood using a finite number of local-based measurements. Under these circumstances, it is often difficult to get a general understanding of the system without the help of theory or an accompanying numerical simulation. Lastly, it often is difficult to demonstrate asymptotic behavior using a single experimental apparatus, as it is generally impractical to vary the dimensionless parameters widely enough in a given apparatus. Because of this limitation, it is usually necessary to repeat even very successful experiments using different fluids and different setups and then make careful intercomparisons of their results. The next section in this chapter will describe how the planetary rotation influences the flow in the core. The following section describes experiments on thermal convection in rapidly rotating spheres. The next sections treat the magnetic influence on the dynamics of electrically conducting fluids, including fluids with convection and rotation. As we shall see, too little is known from experiments of the dynamics in situations where all of these effects are present simultaneously. Finally, we review some of the recent results of experimental dynamos.

8.13.2 Rotational Dynamics

The Coriolis acceleration derived from the basic solid-body rotation of the Earth plays a major role in the dynamics of the liquid core. In this section, we examine several simple experiments that feature the Coriolis acceleration and give physical insight into how it influences fluid motion in the core, in situations where magnetic fields are not as important. Later, we examine magnetic effects on fluid motion, and then we examine situations where the effects of rotation and magnetic fields are present simultaneously.

8.13.2.1 Formation of Taylor Columns

Consider the motion in a cylindrical vessel filled with water on a table rotating at angular velocity Ω (i.e., period of rotation T). The top of the water is a free surface and the bottom is a flat rigid boundary. Centered in the bottom boundary is a circular disk made of a porous material (cf. Figure 1). When solid-body rotation is established in the fluid, a uniform suction is suddenly started at the disk. As a result of the suction, water is removed from the tank, and the resulting inward, converging flow is deflected into a cyclonic vortex by the Coriolis effect. The growing vortex is seen in the pictures (Figure 2) by the azimuthal shear that marks its edges. This shear tends to align flakes suspended in the fluid in the azimuthal direction; these produce the black regions seen in the images. The progressive growth of the vortex along the direction of the axis of rotation gives birth to an elongated flow structure called a Taylor column (Taylor, 1923). In this case, the formation of the Taylor column lasts only a few periods of rotation. The mechanism for its growth is the propagation of inertial waves originating near the porous disk. The group velocity at which energy propagates by inertial waves is given by (See Chapter 8.07):

$$v_g = \frac{2}{k^3} k(\Omega k)$$

Assuming the wave number $k \approx \pi/d$ and propagation perpendicular to the rotation axis, we find that the rise time is $Th/4d \approx 33$ s, in good agreement with the observations (Figure 2). We verified experimentally that the growth rate of the Taylor column is independent of both the height of the fluid

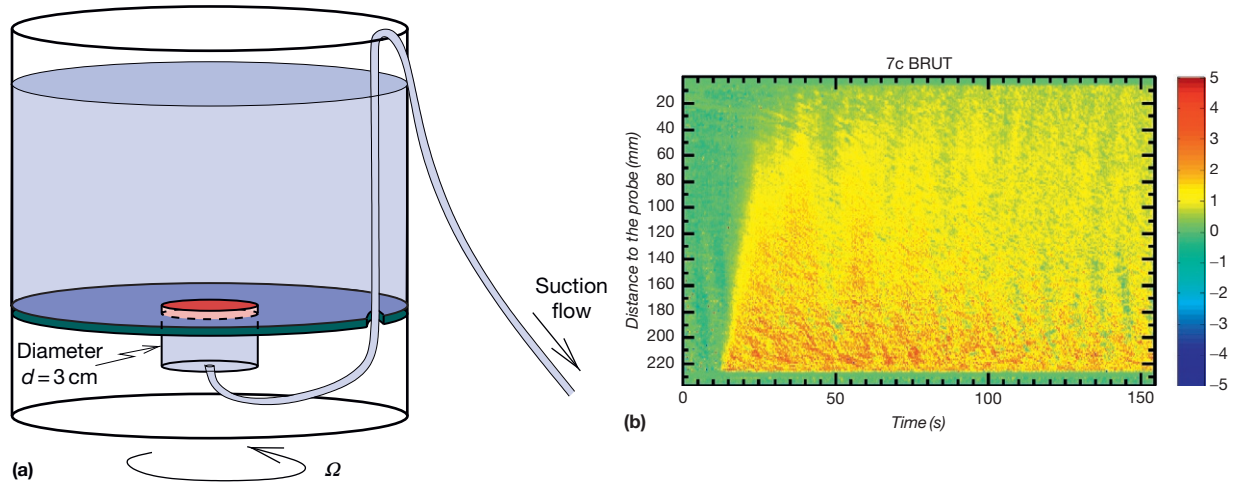

Figure 1 a: Sketch of a cylindrical tank of water on a rotating platform. The diameter and the height of water are both $h = 20$ cm. The diameter of the porous disk at the base of the tank is $d = 3$ cm. The period of rotation of the turning table is $T = 9$ s. The water in the tank is allowed to spin up to a state of solid-body rotation, and then, a small amount of water is removed or injected through the porous disk. b: Space–time evolution of the resulting axial component of the velocity, obtained using ultrasonic Doppler velocimetry from a probe located at the surface of the fluid and pointing toward the porous disk located at 220 mm. The color scale gives the axial velocity in mm s^{-1}.

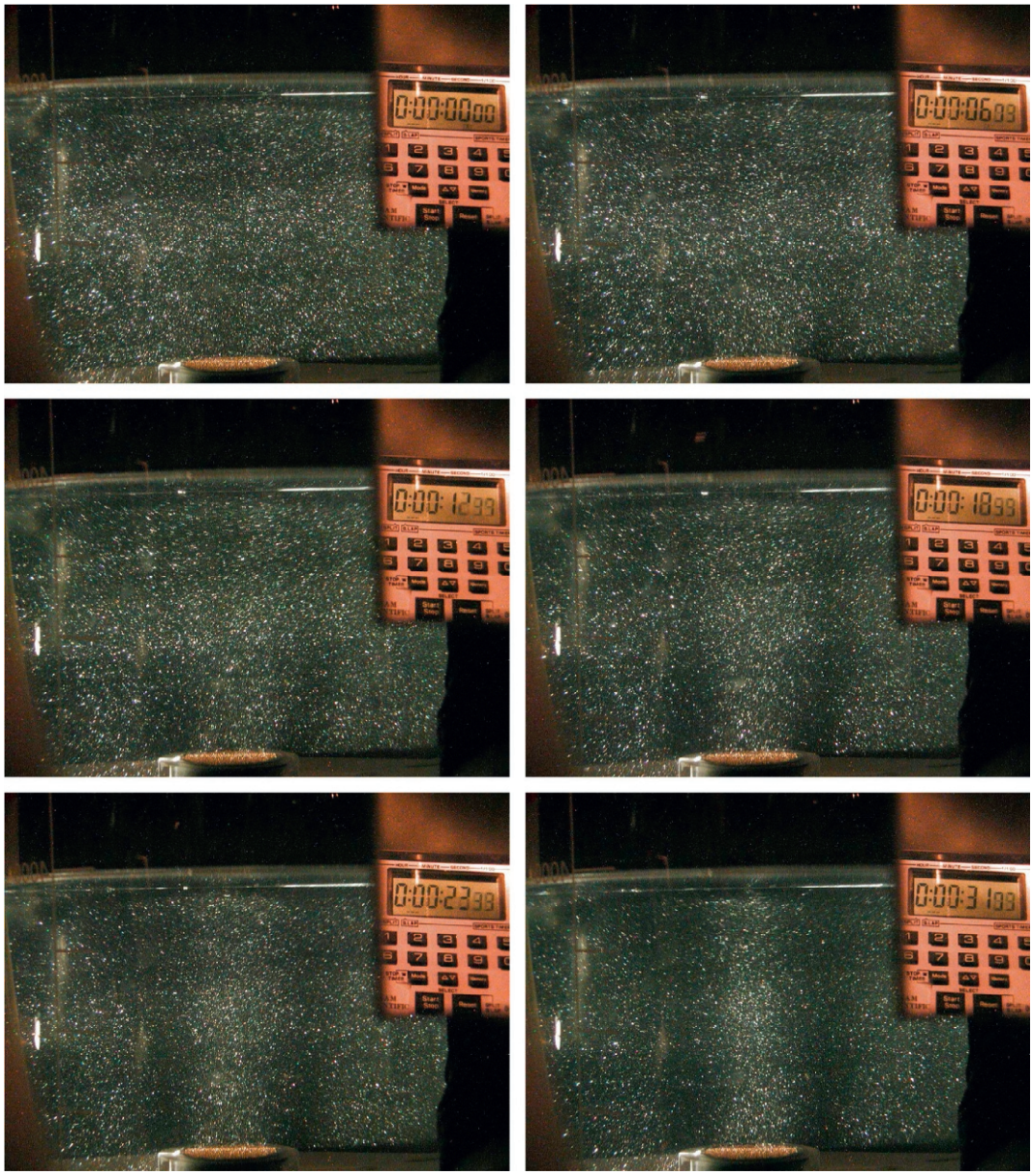

Figure 2 Visualization of the formation of a Taylor column in Kalliroscope fluid. The injection rate is 7×10^{-7} m^3 s^{-1} and the period of rotation of the platform is $T = 20$ s.

and the diameter of the tank. However, we find that it is proportional to the diameter of the suction area. Although the formation of the column is the result of the propagation of inertial waves in the fluid, the final state of the flow is columnar and almost two-dimensional (2-D) and is called *geostrophic*.

The formation process can also be seen in the spatiotemporal diagram of the z-component of the velocity at the center of the Taylor column measured by ultrasonic Doppler velocimetry and shown in **Figure 1** (the velocimetry technique is described in Brito et al., 2001). These measurements reveal many propagating structures, which consist of superimposed inertial waves with different wave numbers. After the formation of the Taylor column, Doppler measurements show a linear dependence of the axial component and an invariance of the tangential component of the velocity with the height, as predicted for a geostrophic column. Applying these results to the outer core, the time needed to reach the final 2-D columnar state is inversely proportional to the transverse length scale of the flow (i.e., the column diameter). Small-scale columns may therefore not be geostrophic. A typical column diameter that corresponds to this condition may be estimated by equating the turnover time of convective structure d/V to the time of formation of the column $Th/4d$. With $V = 10^{-3}$ ms^{-1}, $h = 10^6$ m, we find that scales lower than 5 km are not geostrophic in the Earth's core.

8.13.2.2 Inertial Modes

In cavities, such inertial waves may resonate and form inertial modes, which have been clearly identified (Aldridge and Toomre, 1969). Recent experiments (Kelley et al., 2007; Rieutord et al.,

2012) have shown that the spherical Couette flow (between two concentric differentially rotating spheres) excites inertial modes detected by resonances (eigenfrequencies) of pressure or passive magnetic field measurements at the outer boundary. In close comparison with numerical calculations, the observed oscillations are interpreted as nonaxisymmetric, retrograde, equatorially antisymmetric inertial modes. In these turbulent experiments, it is still unclear what the nature of their excitation is and why only equatorially antisymmetric modes are present.

8.13.2.3 Viscous Layers

After the formation of the Taylor column by inertial waves, the flow continues to evolve in time, although at a slower rate. The rate of evolution and the amplitude of the flow are no longer controlled by inertial waves, but instead become controlled by viscous effects concentrated in two types of shear layers: boundary viscous layer called Ekman layers and internal shear layers called Stewartson layers. Both layers may play important roles in the core.

8.13.2.3.1 Ekman boundary layers

Ekman layers are boundary layers in which there is a balance between the viscous force and the Coriolis acceleration. They are typically quite thin. For example, in the Taylor column experiment just described, the thickness of a laminar Ekman layer is of order $\sqrt{\nu/\Omega}$, that is, ≈ 1 mm. Accordingly, it is generally very difficult to study them experimentally. In the Earth's core, the predicted thickness of the laminar Ekman layer is of the order of 1 m. Nevertheless, they have a finite range of stability, and in some situations, they play an important role in the larger-scale dynamics.

Early experiments by Faller (1963) have identified two types of instabilities in laminar Ekman layers, which occur at local Reynolds numbers (defined in terms of the thickness of the Ekman layer and the velocity at the top of the layer) of 125 and 55 (called types I and II, respectively). Lingwood (1997) had explained these instabilities in term of convective instabilities, and the predictions of a linear stability theory based on this interpretation agree with the experimental results. According to these results, purely laminar Ekman layers in the core could be marginally unstable, because their local Reynolds numbers $\left(V/\sqrt{\nu\Omega}\right)$ are around 100. Assuming a molecular viscosity of $\nu = 10^{-6}\ \mathrm{m^2\,s^{-1}}$ for the fluid in the outer core gives a typical velocity of $10^{-3}\ \mathrm{ms^{-1}}$ to trigger boundary layer instabilities, slightly larger than velocities at the top of the core inferred from the geomagnetic field secular variation (see Eymin and Hulot, 2005 and Volume 5 of this Treatise).

Ekman boundary layers produce a pumping effect on the fluid outer core that acts perpendicular to the core–mantle and inner–outer core boundaries. Ekman pumping has it origin in the requirement for mass conservation in the Ekman boundary layer (Greenpan, 1968). Although the velocity induced by the Ekman pumping is quite small, a factor $E^{1/2}$ smaller than the free stream velocities parallel to the boundary, it nevertheless can have a large influence on geostrophic flows. Ekman pumping tends to suppress the jump of vorticity between the fluid and the boundary, for example. In rotating spin-up, where a fluid adjusts to changes in the rotation rate of its container, Ekman pumping is the mechanism that accelerates the core of the fluid to the new rotation rate. Using a ultrasonic Doppler velocimetry, we have measured azimuthal velocity in the bulk of a rotating sphere during a spin-up experiment and checked the linear theory of Greenspan (Greenpan, 1968) up to Rossby number ($\Delta\Omega/\Omega$) of 0.3 (Brito et al., 2004). The Greenspan theory is valid for nonmagnetic planetary cores ($Ro \ll 1$) if one considers only geostrophic motions with longer periods than 1 day.

Ekman layers may include singularities, particularly on curved surfaces (Stewartson and Roberts, 1963). For stationary Ekman layers in spherical shells, the singularity occurs at the critical latitude of 0° in the equatorial region where the rotation vector is parallel to the layer. For oscillating flows with pulsations between 0 and 2Ω, where Ω is angular velocity of the rotating system, the critical latitude moves from the equator to the pole in both hemispheres, the amount depending on the pulsation frequency. Ekman layer singularities have been observed experimentally in precessing experiments (Noir et al., 2001a) where they lead to the formation of internal shear layers in the fluid that are aligned along characteristic surfaces (Kerswell, 1995). Noir et al. (2001a) had measured these time-oscillating detached shear layers in a precessing experiment using Doppler velocimetry. They are generally invisible with flakes or dye because they oscillate at frequencies close to the container frequency (exactly at the container frequency in the (Noir et al., 2001a) experiment). This internal shear layer consists of a main jet connected to the Ekman layer singularity and alternating jets parallel to the main one (Noir et al., 2001b). Its spatiotemporal structure may be understood in terms of inertial waves propagating inside the fluid (see **Chapter 8.07**). Application to the liquid outer core, if we ignore the action of the magnetic field and other nonlinear effects, suggests this mechanism will generate inertial waves of wavelength 20 km with typical velocity of $V = 6 \times 10^{-6}\ \mathrm{ms^{-1}}$.

8.13.2.3.2 Stewartson layers

Stewartson layers (Stewartson, 1957) are internal shear layers located along the edges of Taylor columns, as in **Figure 1**. Compared with Ekman boundary layers, Stewartson layers have a much larger thickness, proportional to $E^{1/4}\,L$, where $E = \nu/\Omega L^2$ is the Ekman number, ν the kinematic viscosity, Ω the rotation rate, and L a typical length scale. Their dynamics is complicated by the presence of a nested asymptotic sublayer of thickness $E^{1/3}\,L$. The classical experimental method for producing Stewartson shear layers is to apply a differential rotation to a disk in a cylinder of fluid in solid-body rotation. Hide and Titman (1967) studied the stability of these layers and found that at a critical value of the Rossby number $\Delta\Omega/\Omega$, geostrophic vortices develop inside the Stewartson layer. They obtained very different results for positive versus negative Rossby numbers, a result that has been confirmed by new experiments (Früh and Read, 1999) but is still not well understood. Nevertheless, Früh and Read (1999) demonstrated that the onset of this instability is dictated by the local Reynolds number, which is a measure of the shear across the layer, and scales like $E^{1/4}\,L$ relative to the molecular dissipation ν/L^2. The critical value of this local Reynolds number is around 19.

We have studied the stability of Stewartson layers in a spherical Couette experiment (Schaeffer and Cardin, 2005) consisting of a rotating spherical shell with a differentially

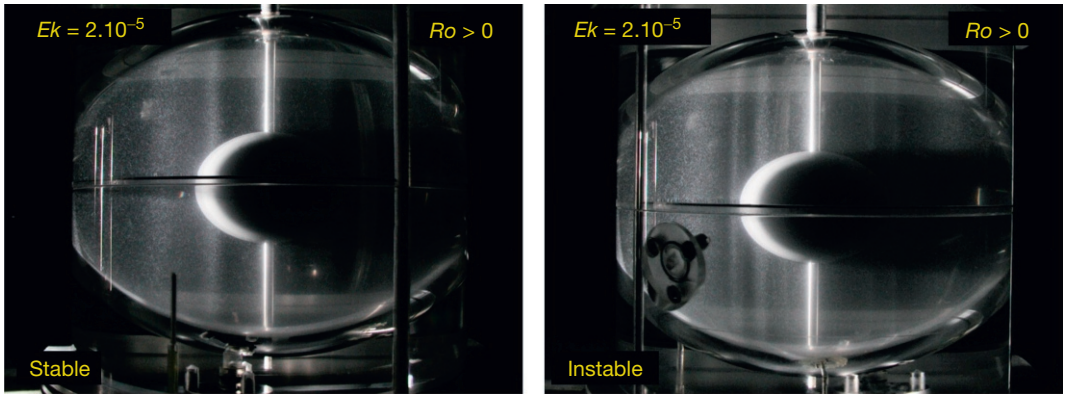

Figure 3 Instability of a Stewartson layer in a Couette shear flow between differentially rotating spheres. Reproduced from Schaeffer N (2004) *Instabilités, Turbulence et Dynamo Dans une Couche de Fluide Cisaille en Rotation Rapide*. PhD Thesis, Université Joseph Fourier Grenoble.

rotating inner core. Figure 3 shows photographs of the Stewartson layer below and above the threshold of instability, respectively. Because of the spherical geometry, the unstable Stewartson layer generates Rossby waves. Generation of these Rossby waves (Hide, 1966) relies on the variation of the height of a column as the column moves radially away or toward the rotation axis. When a fluid column moves outward, its height is reduced by the spherical outer boundary, and conservation of mass requires the cross-sectional area of the column to increase. By conservation of angular momentum, this causes a decrease in its vorticity, a consequence of the Kelvin circulation theorem. Symmetry considerations dictate that an inward motion generates a cyclonic vortex and an outward motion generates an anticyclonic vortex. With a spherical outer boundary, these waves propagate in the prograde azimuthal direction. Columnar Rossby waves have been measured experimentally using ultrasonic Doppler techniques. Figure 4 shows spatiotemporal diagrams of the radial velocity in the equatorial plane. The Rossby wave fills the whole shell with spiral arms. It is propagating in time in the prograde direction. The onset of these waves is controlled by the critical Rossby number ($\Delta\Omega/\Omega$), which in this geometry is of the order of $\beta E^{1/2}$ where $\beta = \frac{1}{h}\frac{\mathrm{d}h}{\mathrm{d}s}$ and where h is the height of the column and s the cylindrical radius. In terms of local Reynolds number, this relationship can be written as $\beta E^{-1/4}$, which explicitly contains a dependence on the global rotation rate, in contrast with the situation in the experiment by Früh and Read (1999) made in a flat geometry. In the absence of a magnetic field, any variation of the period of the inner core larger than 10^{-2} s will generate Rossby waves at the tangent cylinder, but the presence of magnetic fields strongly affects the Stewartson layer at the tangent cylinder and also affects wave generation there (Dormy et al., 1998).

8.13.2.4 Nonlinear Effects

Many nonlinear effects have been observed in rotating fluid experiments. One important source of the kinetic energy for nonlinear motions is precession. As described in detail in Chapter 8.07, the axis of rotation of the solid Earth precesses with a period of about 26 000 years, and the response of the fluid core to the precession consists of a solid-body rotation about an axis that lags the rotation of the solid by a small angle, the so-called Poincaré response, plus other more complex flows.

8.13.2.4.1 Nonlinear resonance of the Poincaré mode

The pioneering work of Malkus (1968) was the first to verify experimentally that the linear response of the fluid to precession is a component of solid-body rotation about an equatorial axis, as predicted by Poincaré (1910). The overall solid-body rotation of the fluid is slightly tilted away from the minor axis of the spheroid and the two axes form an angle θ, which can be measured in laboratory (Vanyo et al., 1995) and compared to the theoretical viscous correction to the Poincaré mode direction predicted by Busse (1968). In our experiments (Noir et al., 2001b, 2003), we have observed jumps of the angle θ by varying continuously the retrograde precession forcing as shown in Figure 5. This effect can be understood as a nonlinear resonance between the gravest (lowest frequency) fundamental inertial mode in the spheroidal cavity and the precession.

In the course of its evolution, the physical parameters of the Earth's rotation have changed with time. Periodic resonances between the tilt-over mode and different nutations (annual, semiannual, and others) should have produced large-amplitude excursions of the axis of rotation of the liquid core and affect global geodynamics (Greff-Lefftz and Legros, 1999). For these resonances, nonlinear theory reduces to the linear analysis used in Greff-Lefftz and Legros (1999), but for larger forcings (e.g., as for the Bradley nutation), the nonlinear resonance condition applies (Figure 6).

8.13.2.4.2 Geostrophic zonal motions in precession experiments

Precession experiments exhibit very nicely the characteristic cylindrical flow structures of rotation-dominated fluids. The flake images in Figure 7 show some of these structures. The shear zones in these images correspond to stationary geostrophic azimuthal motions superimposed on the Poincaré mode. These motions were measured quantitatively the first time by Malkus (1968) and his measurements have subsequently been confirmed. In our experiments, dye has been injected in the fluid, and using a camera attached to spheroid, we followed the deformation of the dye patch and the results

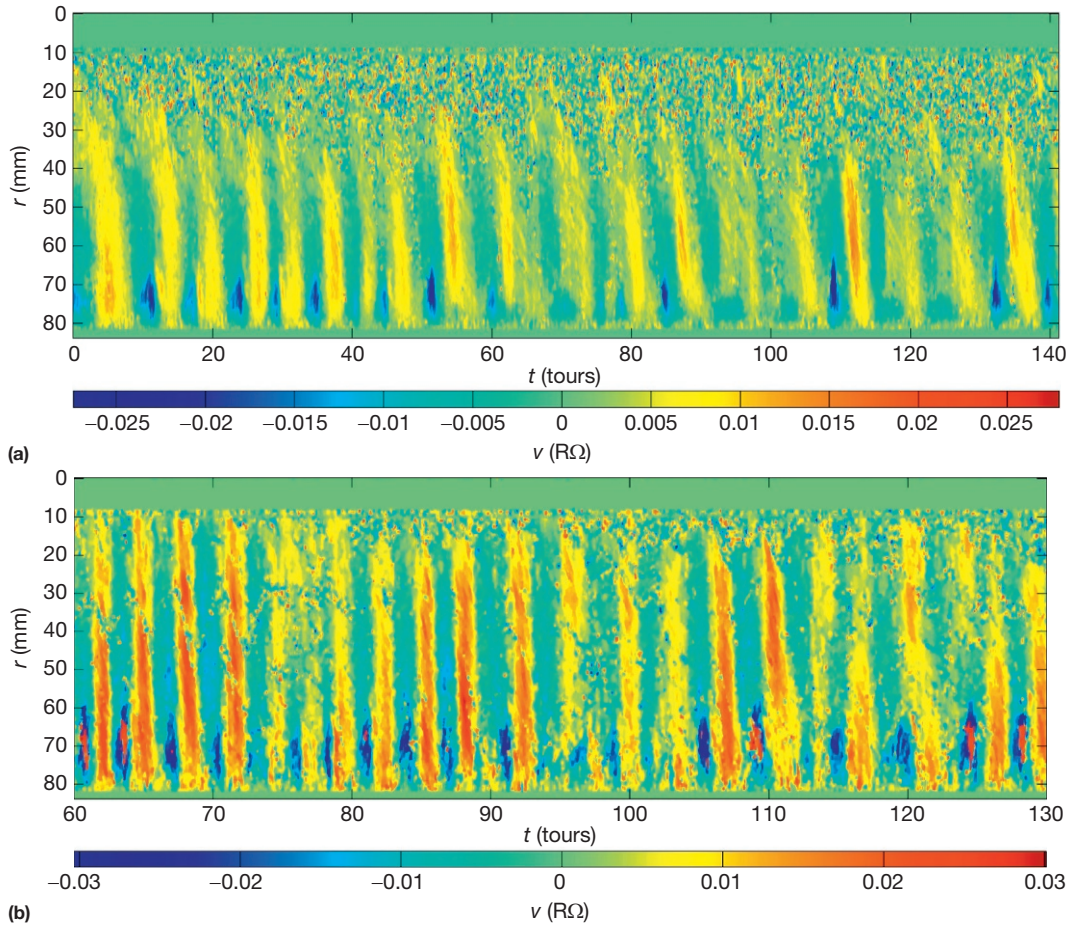

Figure 4 Propagation of a Rossby wave in a rotating spherical Couette flow. Time evolution of the radial velocity in the equatorial region (colors are indicative of the velocity amplitude). r is the distance from the rotation axis to the ultrasonic probe. The differentially rotating inner core is located at $r=80$ mm. The velocity is plotted in nondimensional units of $R\Omega$. The Ekman number is $E=2.1\times10^{-5}$. Upper: $Ro=\Delta\Omega/\Omega=0.17$ (just above critical). Lower: $Ro=0.68$.

confirm Malkus' findings (Figure 6). Apart from small variations, the primary motion consists of a cylinder of fluid that is rotating faster than the Poincaré mode and located at a radius of 0.9. Noir et al. (2001b) proposed to explain these geostrophic motions as nonlinear effect in the Ekman layer singularity, while Hollerbach and Kerswell (1995) proposed that they result from nonlinear interactions of inertial waves in volume. Our spherical numerical simulation reproduces the cylindrical shear layers with the correct wavelength (see Figure 6) but the amplitude is incorrect by a factor 3. This discrepancy is still unsolved. Even with this discrepancy, these results allow us to estimate the amplitude ($\approx10^{-5}$ ms^{-1}) and the size (≈20 km) of the stationary geostrophic cylinders in the outer core, which are predicted to be located at 30° in the absence of magnetic field (Noir et al., 2001a).

8.13.2.4.3 Libration experiments

Several planets have a time periodic axial rotation rate, known as libration, that results from gravitational interactions with an orbital partner. In the presence of a liquid core, the librating outer shell drives a flow in the liquid layer by various mechanisms including topographic, gravitational, electromagnetic, and viscous processes. Recent experimental studies (Noir et al., 2010, 2012) have shown that viscous coupling can generate complex internal dynamics. It has been shown that longitudinal libration in an axisymmetric container can drive inertial modes in the bulk of the fluid as well as boundary layer centrifugal instabilities in the form of Taylor–Görtler rolls (Calkins et al., 2010; Noir et al., 2010), and their nonlinear interaction within the Ekman boundary layers generates a steady, axisymmetric flow, called zonal flow (Noir et al., 2012; Sauret et al., 2010).

8.13.2.4.4 Parametric instabilities

Elliptic and shear instabilities may be present in precession experiments and also may be present in the core (Kerswell, 2002). These instabilities develop from a resonance between two inertial wave modes and a background shear flow. All these ingredients are present in tidally driven flows and precessing flows (see Chapter 8.07). As shown by Malkus (1989), in a cylindrical experiment, the parameters can be tuned so as to

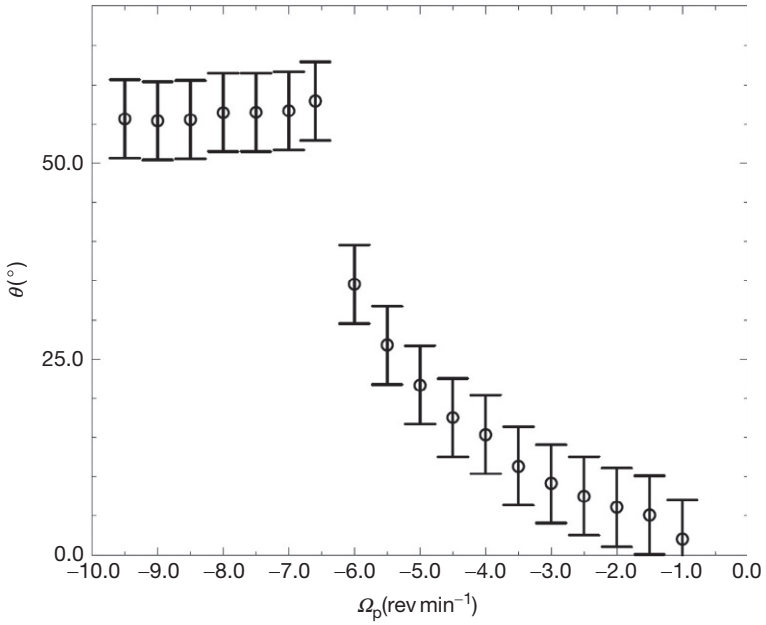

Figure 5 Rapid variations of the position of the axis of the Poincaré mode in a precessing experiment. The obliquity of the experimental spheroid is $\alpha = 20^\circ$ and the rotation of the spheroid is 300 rpm. The angle between the minor axis of the spheroid and the Poincaré axis is plotted against the rotation rate Ω_p of the precession. Around the value $\Omega_p = -6.2$ rpm, a jump is observed. Reproduced from Noir J, Jault D, and Cardin P (2001a) Numerical study of the motions within a slowly precessing sphere at low Ekman number. *Journal of Fluid Mechanics* 437: 283–299.

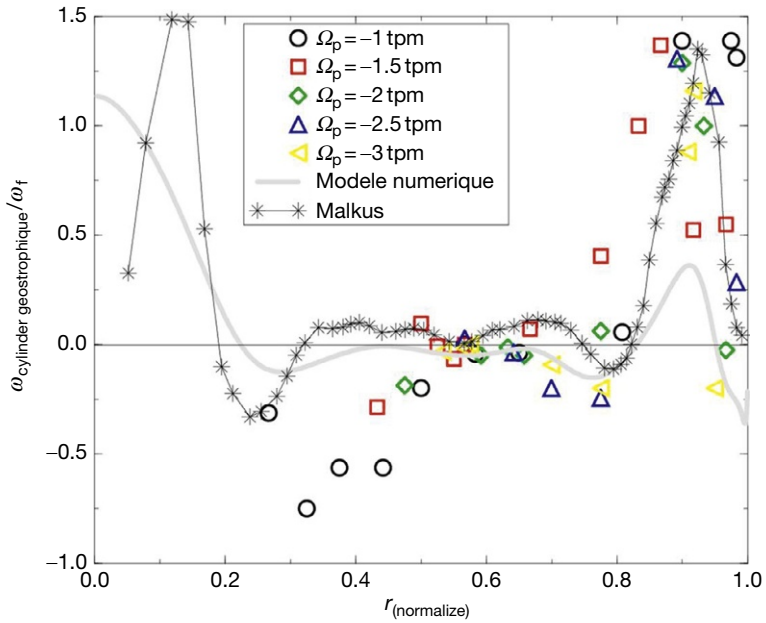

Figure 6 Amplitude of the geostrophic motions normalized by the angular velocity of the Poincaré mode versus the distance along the major axis of the spheroid for different forcings (measured by dye injection and transport). The obliquity of the spheroid is $\alpha = 20^\circ$ and its rotation is 212 rpm. The black solid line with stars shows the results of Malkus (1968) and the gray solid line shows the numerical results of Noir et al. (2001b).

get sudden, catastrophic events called elliptical instabilities. The elliptical instability first grows linearly (Kerswell, 2002) and then nonlinearly, destabilizing the background flow to small-scale turbulence, which grows until it reaches viscous saturation (Eloy et al., 2000). Lacaze et al. (2004) had observed elliptical instabilities in spheroidal geometry and their experimental findings agree with the theoretical prediction. Significantly, elliptical instabilities are observed to produce large-amplitude motions and turbulence even in situations where the forcing is small, as is the case for the tidal forcing of the core (Le Bars et al., 2010) or with an inner core (Aldridge et al., 2007). But intermittent turbulent regimes similar to

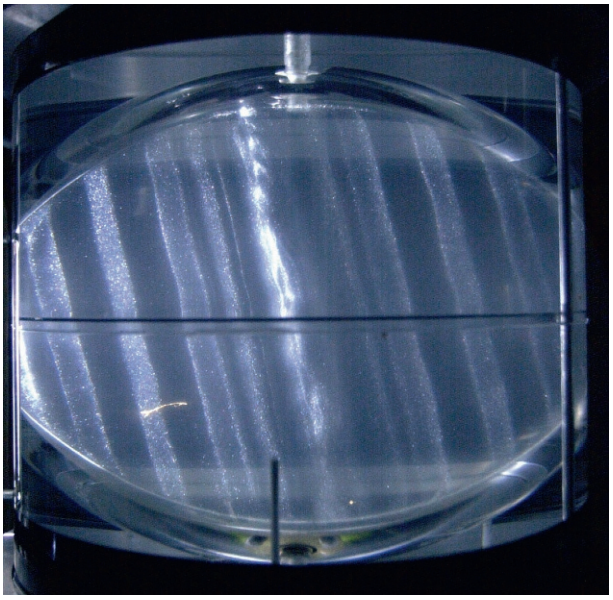

Figure 7 Side view of a meridional plane (illuminated by flakes reflection) of a precessing flow. The obliquity of the spheroid is $\alpha = 20^\circ$, and the rotation of spheroid is 300 rpm. The precessing table spins progradely with an angular velocity of 10 rpm. Cylindrical shear zones denote the presence of concentric geostrophic zonal flows (description of the experimental setup in Noir et al., 2003).

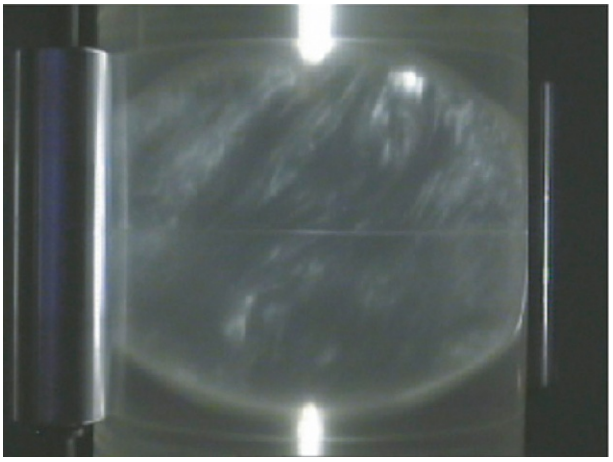

Figure 8 Turbulent flow in a meridional cross section in a rotating oblate spheroid of water (Ekman number $E = 10^{-5}$; eccentricity $e = 0.06$) deformed by two orbiting rollers 180° apart representing tidal forcing, after Le Bars et al. (2010). The turbulence is driven by the elliptical instability (description of the experimental setup in Le Bars et al., 2010).

those observed in tidal experiments have not yet been observed in precessing experiments. Perhaps, the vertical oscillation of the axis of rotation of the fluid in **Figure 7** is the spherical equivalents of the structures observed in tidal experiments eight. Without a better understanding of the turbulent breakdown of the spherical elliptical instabilities in precessing or tidally driven experiments, any application to planetary cores would be highly speculative (Aldridge and Baker, 2003; Thouveny et al., 2008; **Figure 8**).

8.13.2.4.5 Quasigeostrophic turbulence

As the forcing increases, rotating flows become turbulent, through instabilities originating in the fluid volume and by boundary layer instabilities. Ultimately, this turbulence becomes 3-D, but for moderate forcings, the turbulence remains nearly geostrophic. According to the Taylor–Proudman constraint, it is possible for columnar flow to become turbulent in planes perpendicular to the axis of rotation long before it becomes turbulent in the axial direction. Ekman pumping and topographic effects (or β-effect) both strongly influence this quasigeostrophic turbulence, which differs from 2-D turbulence as generally studied by physicists (Tabeling, 2002). For β-plane geometry flows, Rhines (1975) predicted a dominant turbulent scale $\sqrt{U/\beta}$ and scaling dependence for the spectra of kinetic energy. Zonal jets in giant planets are thought to be the result of the inverse cascade of kinetic energy from small scales to the so-called Rhines' scale (k^{-5} law where k is the wave number). Many experiments have tried to check Rhines' theory, using turbulence in β-plane flows. Here, we present two of these. A group in Texas led by H. Swinney (see, e.g., Aubert et al., 2002) studied the inverse cascade and the formation the zonal jets in a cylindrical β tank with injected fluid at the bottom by small tubes. Using the large Coriolis table at Grenoble, Read et al. (2004) studied the same process by injecting a spray of salty water onto the top of their 10 m rotating tank. Both experiments showed evidence of azimuthal axisymmetric flows, but neither was able to precisely measure the power-law variation of the spectra, which is often very difficult to retrieve experimentally. In a spherical shell, the β-effect varies with cylindrical radius and there is also a discontinuity at the tangent cylinder of the inner core. These variations cannot be neglected in deriving the expected Rhines' scale and may cause spherical shell turbulence to differ considerably from the character of β-plane turbulent flows. This is another topic that would benefit from additional experimental investigation.

8.13.3 Thermal Convection in a Rapidly Rotating Spherical Shell

8.13.3.1 Experimental Conditions

Apart from space experiments made in the microgravity environment of Earth orbit (Egbers et al., 1999; Hart et al., 1986), all laboratory investigations of rotating spherical convection in planetary cores rely on the centrifugal force as a substitute for the radial gravity force. It is not difficult for centrifugal acceleration to dominate over laboratory gravity in a rotating apparatus. For a typical experimental size of 10 cm, a spin rate in excess of 100 rpm is required to fulfill this condition. It is perhaps surprising that the centrifugal acceleration can adequately model the spherical gravity of a planet for rotating fluid mechanics, but experiments have shown it can (Busse, 1970). The centrifugal acceleration varies linearly with the cylindrical radius, like the component of the central gravity perpendicular to the axis of rotation of a planet with a uniform density. The difference in direction (outward vs. inward) between the two accelerations is taking into account by a reverse temperature gradient (cooler at the center) in the experiments, which leads to buoyancy (Archimedean) forces having their proper

orientation in the experiment. The analogy is further strengthened because in a rotating planet, the axial component of the central gravity is mainly balanced by pressure forces, a consequence of the Taylor–Proudman constraint. Thermal convection is produced experimentally in spherical shells by imposing thermal boundary conditions at the inner and outer boundaries, the higher temperature on the outer boundary for the reasons given in the preceding text (Carrigan and Busse, 1983). If the boundary temperatures are uniform, then the temperature varies on surfaces of constant centrifugal potential in the direction of the axis of rotation. This results in an ageostrophic buoyancy force perpendicular to the surface of the cylinder. A thermal wind (an ageostrophic azimuthal flow) is therefore produced to balance this buoyancy force in the experiment, an effect that is practically zero in the Earth's core. The amplitude of this spurious flow given by the thermal wind balance, which can be written as

$$\frac{\partial u_\phi}{\partial z} = \frac{1}{2}\alpha\Omega s\frac{\partial T}{\partial z}$$

where z is the coordinate along the axis of rotation, s the cylindrical radius, α the thermal expansion, and Ω the rotation rate of the sphere. The maximum velocity of this thermal wind is located on the vicinity of the inner core equator and is given by Carrigan and Busse (1983):

$$u_\phi = \frac{\alpha\Omega\Delta T}{2}$$

where ΔT is the imposed temperature difference between the inner and outer boundary. It represents an azimuthal flow of 2 mm s^{-1} for a rotation of 100 rpm with 1 K of temperature difference ($\alpha = 2\times10^{-4}$ K^{-1} for water).

8.13.3.2 Onset of Convection

Pioneering experiments by Busse and Carrigan (1976) have shown that the onset of thermal convection in a rapidly rotating sphere may be described by propagating thermal Rossby waves (Busse, 1970), which consist of columns of alternating positive and negative vorticity aligned with the axis of rotation and propagating in the prograde direction just outside the tangent cylinder of the inner core. Busse and his colleagues performed the first quantitative determination of the onset of convection in rotating annulus with a constant slope for bottom and top boundaries (Busse and Carrigan, 1974) and a spherical shell, using water as the working fluid and flake visualization (Carrigan and Busse, 1983). Their results agree relatively well with the theoretically predicted $E^{-1/3}$ asymptotic law for the critical Rayleigh number for convective onset at low Ekman number. Cordero and Busse (1992) determined the critical parameters for convective onset in a rotating hemispheric shell using temperature measurements. Laboratory gravity was used with the centrifugal acceleration in these experiments to generate paraboloidal surfaces of potential of gravity as close as possible to spherical surfaces in a 'southern' hemisphere geometry. They also took into account the thermal wind effect in determining the critical frequency of the thermal Rossby waves. In addition, they observed the spiral structure of the convection columns and transitions to quasi-periodic states and chaos (Cordero, 1993). Following these initial studies, many discrepancies between theoretical, numerical, and experimental determinations of the onset of convection in rotating spherical shells were subsequently discovered. Using an approximate method to solve the linear stability problem, Jones et al. (2000) showed how to resolve some of the discrepancies between theoretical and numerical results. Dormy et al. (2004) completed the comparative study between numerical and analytic approaches, especially for the differential heating case. A close comparison with experimental data is often not easy, but E. Dormy has computed the critical parameters for the Cordero and Busse (1992) experiment and has come up with a critical frequency of ω_c/Ω of 2.2×10^{-3} instead of 2.6×10^{-3} found experimentally (E. Dormy, personal communication).

8.13.3.3 Developed Convective States

The convective flow remains columnar in a rotating sphere above the threshold for convective onset provided the amplitude of the buoyancy forces remains smaller than the Coriolis forces. Cardin and Olson (1994) had performed experiments up to 50 times the critical Rayleigh number in water. We observed that the critical Rossby waves disappear above the onset. Numerous columnar vortices fill the spherical shell with a quasigeostrophic form of turbulent convection (**Figure 9**). In this regime, strong thermal plumes generate retrograde vortices at the inner core boundary prolongated outward by prograde spiraled ribbon-shaped street of retrograde vortices. The structures that characterize fully developed rotating convection have been clearly observed by Sumita and Olson (2000) in a hemispheric experiment with water. Just beyond the onset of convection, Rossby waves tend to fill the sphere, and the azimuthal number of convective features increases along a radius. Consequently, radial bifurcations or trees are observed in the field of flow (cf. **Figure 10**). This bifurcation is understood as an effect of the increase of the boundary slope (β-effect) with the cylindrical radius, which controls the azimuthal wave number of the convection. As the thermal forcing becomes stronger (more than eight times critical), the Rossby waves are expelled toward the outer portion of the spherical shell, where the large slope strongly inhibits radial motion (**Figure 10**) as the innermost part of the convection becomes more turbulent. This regime has been called 'dual convection.' Aubert et al. (2003) argued that this transition between inertial regimes and Rossby wave regimes is controlled by a local Reynolds number, the ratio of turnover time, and the Rossby wave period.

Quantitative measurements of the radial velocity in rapidly rotating convection have been made using the ultrasonic Doppler velocimetry (Aubert et al., 2001, 2003; Brito et al., 2001; Gillet et al., 2007a). A typical space–time diagram is shown in **Figure 11**. Thermal convection tends to be stronger in the vicinity of the inner cylinder, for the reasons discussed earlier. The time average of the rms radial velocity shows a maximum close to the inner cylinder (**Figure 12**). Following Cardin and Olson (1994) and Aubert et al. (2001) proposed that the maximum of measured radial velocity can be matched to a scaling law $(\alpha g Q/\rho C_p \Omega^3 D^4)^{2/5}$ where Q is the heat flux, α the thermal expansion, g the acceleration of gravity, ρ the density, C_p the heat capacity, Ω the rotation rate, and D the

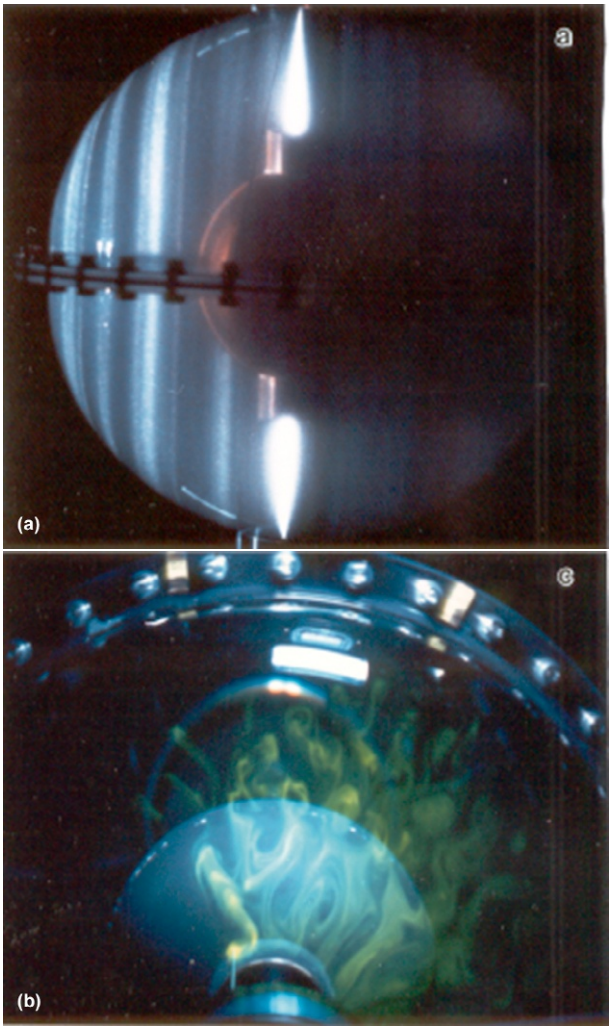

Figure 9 Experimental results on the structure of thermal convection at 50 times critical. Left: Side view of chaotic convection using a light beam and flakes inside the fluid. Right: Top view showing equatorial section of the columns and their organization using fluorescein dye released at the north pole of the inner core. Rotation is anticlockwise (more details in Cardin and Olson, 1994).

gap. This scaling results from a balance between Archimedean (buoyancy), inertial, and Coriolis forces (plus some other assumptions). The quality and the range of the experimental data may allow for other scalings. The typical radial size of the columns in Figure 11 is between 10 and 20 mm, not far from the critical size at the onset (15 mm) for these experimental parameters. It has proved to be difficult to measure any change in vortex size over the range of accessible experimental control parameters, although there is some expectation on theoretical grounds to observe larger vortices fed by the inverse cascade of energy in 2-D turbulence as the Rayleigh number increases. Rhines (1975) also suggested that the inverse cascade stops at the scale $\propto\sqrt{U_{\mathrm{conv}}/\beta}$, which correspond to the balance between the Reynolds stresses and the vortex stretching in the vorticity equation. Higher rotation rate experiments are needed to study the evolution of the size of the vortices and other turbulent effects.

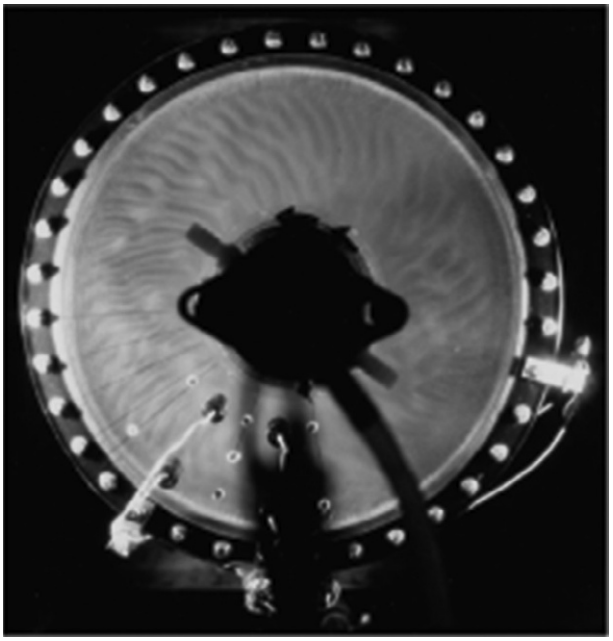

Figure 10 Experimental results on the structure of thermal convection at six times critical in a rapidly rotating hemispheric shell. Top view showing equatorial section of the columns seen by flakes reflection. Rotation is anticlockwise (more details in Sumita and Olson, 2000).

8.13.3.4 Liquid Metal Experiments

Using a liquid metal as the working fluid allows experimental study of thermal convection at low Prandtl number ($P=\nu/\kappa$ where ν is the kinematic viscosity and κ the thermal diffusivity), which is the regime of interest for core dynamics in terms of this parameter. Even if liquid metals (gallium and sodium) have a somewhat lower Prandtl number ($P\approx 0.025$) than expected for the liquid iron at core conditions ($P\approx 0.1$), they are a better model than water ($P\approx 7$), and they have the critical property that their thermal diffusivity is much larger than their viscosity. Liquid metals are not easy to use because they are opaque, and because of their very high thermal conductivity, high heat flux is needed to initiate the thermal convection. At Rayleigh numbers only four times critical, convective velocities are much larger than corresponding ones in water (Aubert et al., 2001, 2003; Gillet et al., 2007a), and Reynolds numbers as large as 2000 have been obtained (cf. Figure 12). Measured radial velocities seem to follow the scaling law described earlier for water (Aubert et al., 2001), but the size of the vortices is larger in the gallium experiment and the inertial convection region (the vortices) occupies about 2/3 of the gap. The Rossby wave convection is pushed outward and may be responsible for large variations of the Root Mean Square (RMS) velocity in the profile (at large radius) shown in Figures 12 and 13.

8.13.3.5 Heat Flux Measurements

As the strength of the buoyancy forces increases relative to the strength of the rotational constraint, the columnar structure of the convection becomes less regular and the convective flow becomes more and more 3-D. Clearly, the characteristics of

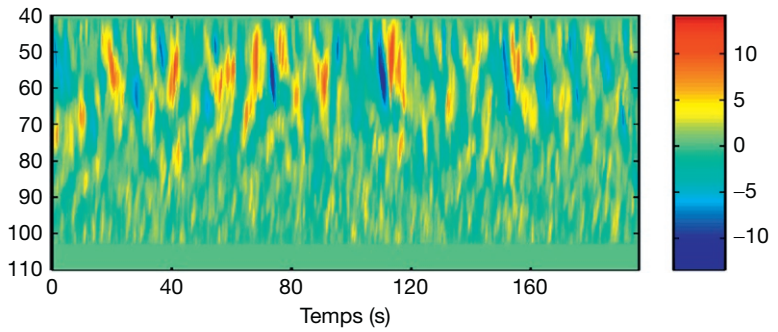

Figure 11 Experimental results on the structure of thermal convection for 40 times the critical Rayleigh number, with $E = 6.5 \times 10^{-6}$ and $P = 7$. Abscissa is time in s, ordinate is the depth in the spherical shell, outer sphere is at 110 mm, and the inner cylinder is located at 40 mm. Colors represent the radial velocity in mm s^{-1} (red is outward, blue inward). Strong anticyclones moving retrograde close the inner cylinder appear as a time oscillation (blue red) (as in (110, 50) region) (more details in Gillet et al., 2007a).

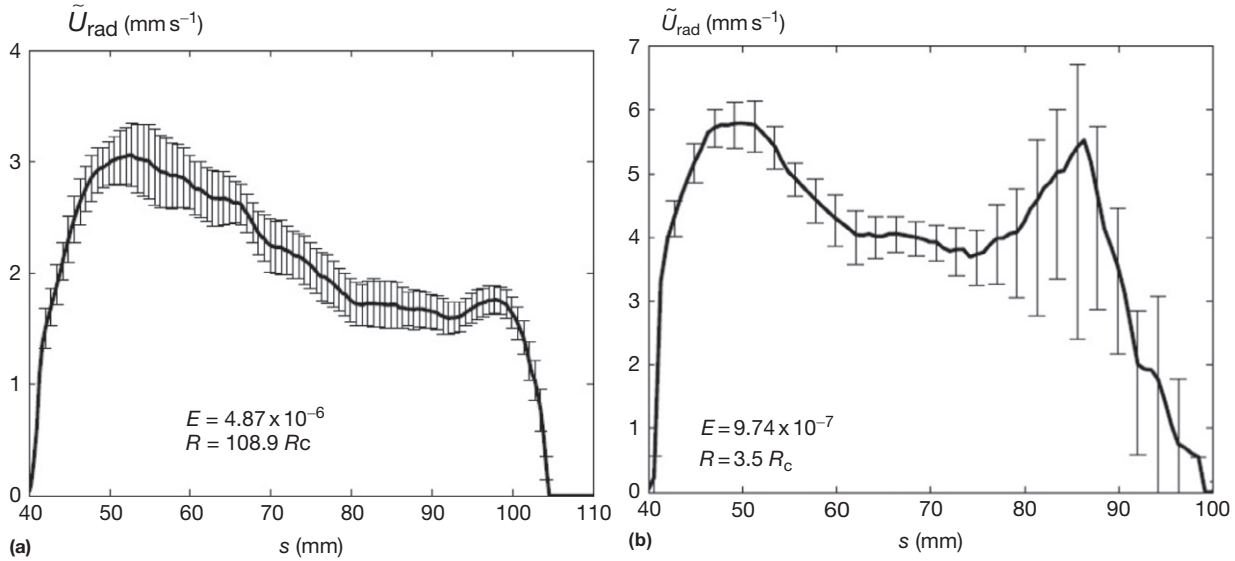

Figure 12 Experimental measurement of the radial convective velocity versus the radius. Left: In water for $Ra = 102Ra_c$, $E = 4.5 \times 10^{-6}$, $P = 7$. Right: In Gallium for $Ra = 3.5Ra_c$, $E = 7.9 \times 10^{-7}$, $P = 0.025$ (more details in Gillet et al., 2007a).

heat transport depend on the degree of columnar structure, and we are interested to determine where the boundary between columnar and noncolumnar convection lies and, by extrapolation, determine where Earth's core and other planetary cores are with respect to this boundary. Temperatures are generally easy to measure in experiments and can give much information on the dynamics (amplitude, fluctuations, transport, etc.). Sumita and Olson (2000, 2003) performed a series of experiments with water and silicon oil to measure the ratio between the Nusselt number (measure of the convective heat flux) and the Rayleigh number in the hemispheric shell setup. Thermal convection experiments in rotating water-filled cylinders by King et al. (2009) provide evidence that, at least for heat transport characteristics, rotationally dominated convection is limited to situations where the viscous Ekman layer is thinner than the thermal boundary layer. This interpretation is still in discussion (Zhong et al., 2009) as bulk mechanisms are invoked to interpret the transition. For nonrotating convection, a 2/7 power law relationship between the Nusselt number and the Rayleigh number is often found experimentally, whereas for rapidly rotating plane layer convection, it is found that $Nu \propto (Ra/Ra_{crit})^{6/5}$ with $Ra_{crit} \propto E^{-4/3}$. Based on this difference, King et al. (2012) contended that geostrophy begins to break down when $RaE^{3/2}$ is much > 1.

8.13.3.6 Zonal Flows

Azimuthal mean flows are almost always observed in rotating spherical experiments, and they were detected in the early rotating annulus experiments in Busse and Hood (1982). Cardin and Olson (1994) and Sumita and Olson (2000) reported a slow retrograde azimuthal transport of dye injected around the inner core (cf. **Figure 9**) at Rayleigh numbers above a few times critical. Using ultrasonic measurements, Aubert et al. (2001) reported the first quantitative measurements of zonal flows for water and gallium. This study has been augmented by Gillet et al. (2007a) using more precise measurements (typical examples are shown in **Figure 14**). A larger zonal flow is present in the gallium experiment compared to the water experiments. This difference is the result of much

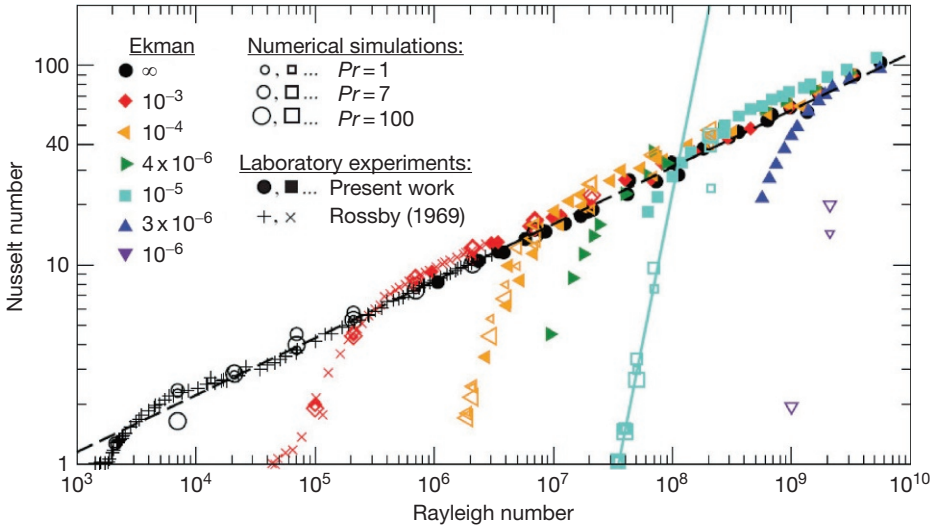

Figure 13 Nusselt number versus Rayleigh number for cylindrical rotating experiments with water and sucrose solution by King et al. (2012). The dashed black line corresponds to a 2/7 power law, while the cyan blue line corresponds to a 6/5 one.

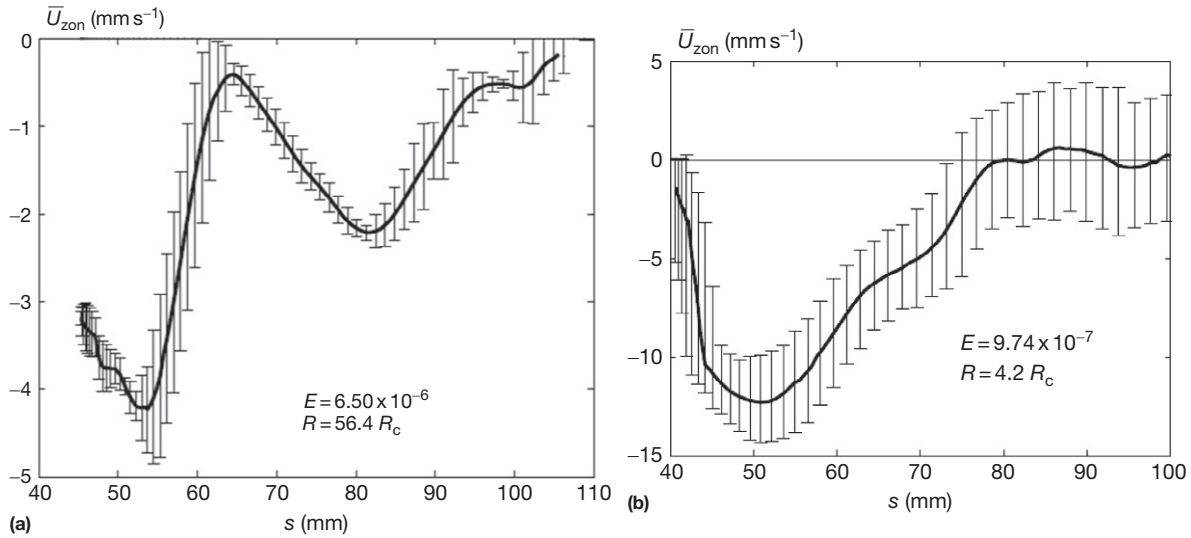

Figure 14 Experimental measurement of the zonal velocity versus the radius in rotating convection. Left: In water for $Ra = 102Ra_c$, $E = 4.5 \times 10^{-6}$, $P = 7$. Right: In Gallium for $Ra = 3.5Ra_c$, $E = 7.9 \times 10^{-7}$, $P = 0.025$ (more details in Gillet et al., 2007a).

stronger convective velocities in low Prandtl number liquid metal experiment, which is combined with the nonlinear effect associated with the axisymmetric geostrophic flow. Just above the onset of convection, we expect the zonal flow to increase quadratically with the convective velocity (as in the water experiment in Aubert et al., 2001). For larger forcings, Gillet et al. (2007a) proposed a 4/3 power-law scaling, based on Rhines' scales for the size of the zonal and nonaxisymmetric flows. In the case of gallium experiment, the presence of the large zonal flow strongly affects the organization of thermal convection, even just above the onset (Plaut and Busse, 2002).

Additional effects arise when the forcing is not uniform. Sumita and Olson (2002) studied the effect of a heterogeneous boundary heat flux on the dynamics. For some conditions, they observed the formation of large-scale spiraling front with a jet. The jet traverses the entire fluid shell, all the way from the outer to the inner boundary in some cases. This front is stationary with respect to the thermal boundary heterogeneity, and it separates two distinct types of large-scale flow, which is superposed on a small-scale flow consisting of thermal convective vortices.

8.13.3.7 Compositional Convection

Cardin and Olson (1992) modeled compositional convection in the outer core by the release of denser fluid (a mixture of water and sugar) at the inner spherical surface of a rotating spherical shell filled with pure water. They observed very thin, tenuous plumes, which moved radially from the inner boundary to the outer boundary. An analysis in terms of buoyancy

fluxes (compositional vs. thermal) led to the proposal that the dynamics are mainly dominated by thermal convective structures, in spite of the fact that the compositional buoyancy is larger.

8.13.4 Magnetohydrodynamics

We now consider the action of the Lorentz force on the dynamics of a nonrotating, electrically conducting fluid. The experiments of this type are substantially more difficult, as they entail the problems of handling liquid metals and the problems of producing and controlling strong magnetic fields. The role of the magnetic forces in these experiments is somewhat analogous to the rotational constraint in the previous experiments, and the analogy extends to the formation of boundary layers and magnetic columns. Ultimately, however, we are interested in systems where rotation and magnetic field are both present.

8.13.4.1 Hartmann Layers

In the presence of a magnetic field, diffusive magnetic layers called Hartmann layers form at the interfaces between materials with different electric properties (Hartmann and Lazarus, 1937; Moreau, 1990). In a Hartmann layer of thickness $Ha^{-1}L = \frac{\sqrt{\mu\rho\eta\nu}}{B}$, the Lorentz forces are in balance with the viscous forces. Murgatroyd (1953) found that the friction factor in those Hartmann layers is a function of the ratio of the Reynolds number (Re) to the Hartmann number (Ha), which is equivalent to a local Reynolds number defined in terms of the thickness of the Hartmann layer. The stability of the viscomagnetic Hartmann layer has been studied experimentally by Moresco and Alboussière (2004), and the transition to turbulence (and vice versa, the transition to laminar flow) has been found to occur at a local Reynolds number of 380 (±10%) (see **Figure 15**). The experimentally determined critical value of the local Reynolds number is two orders of magnitude smaller than the one deduced from linear stability analysis, which implies that nonlinear effect plays an important role in the stability of Hartmann layers. It is also possible that the roughness of the boundary itself plays an important role in destabilizing the Hartmann layers, which are very thin in many experimental situations (sometimes as thin as 3 μm).

The stability of the secondary type of Hartmann layer, which is oriented parallel to the magnetic field (with characteristic thickness $Ha^{-1/2}L$), has been examined by Burr et al. (2000). Above the critical Reynolds number ($2000 < Re < 5000$), elongated vortices with their axes aligned with the imposed magnetic field appear above the boundary layer. In the absence of strong rotational effects, magnetic Hartmann boundary layers at the core–mantle boundary are expected to be stable, given the typical speeds of flow in the core inferred from geomagnetic secular variation.

8.13.4.2 Internal Magnetic Layers

Free-standing, detached diffusive magnetic layers may exist in the interior of an electrically conducting fluid. As with Stewartson shear layers, they occur in specific geometries such as a spherical shell, which makes them of interest for core dynamics. Dormy et al. (1998) found them numerically in a linear spherical Couette flow with in imposed dipolar magnetic field. As in Hartmann layers, the viscous and magnetic forces are in balance in the shear layer, and this equilibrium generates a superrotating toroidal jet embedded by the imposed magnetic field lines. The thickness of the jet is $Ha^{-1/2}L$ (Dormy et al., 2002) and the amplitude of the superrotation is limited. The electric boundary conditions can change the shape and the amplitude of these internal shear layers (Hollerbach, 2000). A superrotating jet has been observed in the Derviche Tourneur Sodium (DTS) experiment in Grenoble (Nataf et al., 2006). DTS is a liquid sodium experiment to study the properties of flow in the regime where both rotation and magnetic field play an important role in the dynamics (Cardin et al., 2002). The experiment consists of a rotating spherical shell (with a core-like radius ratio of 0.35) with a differentially rotating inner core. The Couette flow in the spherical shell is subject to a strong dipolar magnetic field imposed by a permanent magnet located inside the inner core. We have found experimental evidences of superrotation (cf. **Figure 16**) that features an equatorial inner region rotating faster than the inner core in the presence (Nataf et al., 2006) of bulk rotation (rotation of the

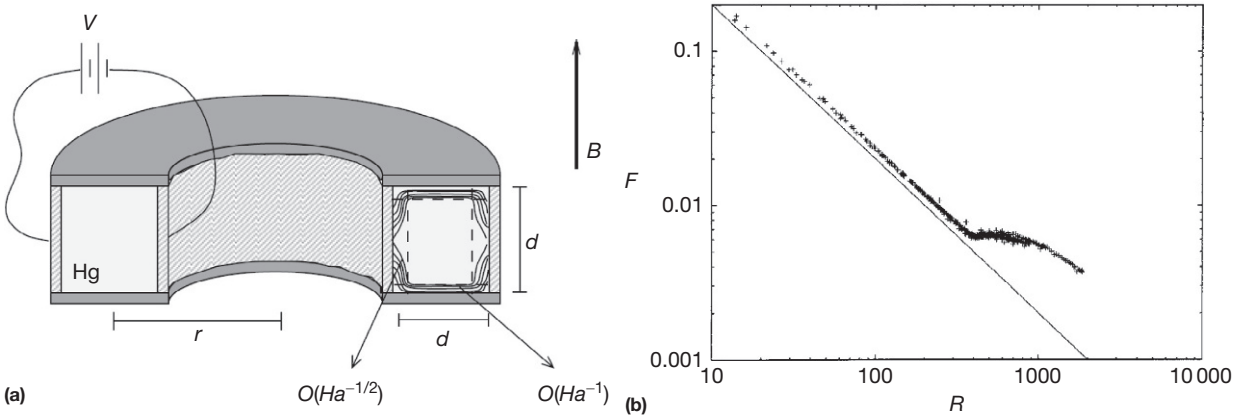

Figure 15 Experimental study of the stability of the Hartmann layers. A flow of liquid mercury ($d = 1$ cm) is produced by an imposed electric current in an imposed vertical magnetic field B (up to 13 T). The Hartmann boundary layer becomes unstable at a local Reynolds number of 380. Reproduced from Moresco P and Alboussière T (2004) Experimental study of the instability of the Hartmann layer. *Journal of Fluid Mechanics* 504: 167–181.

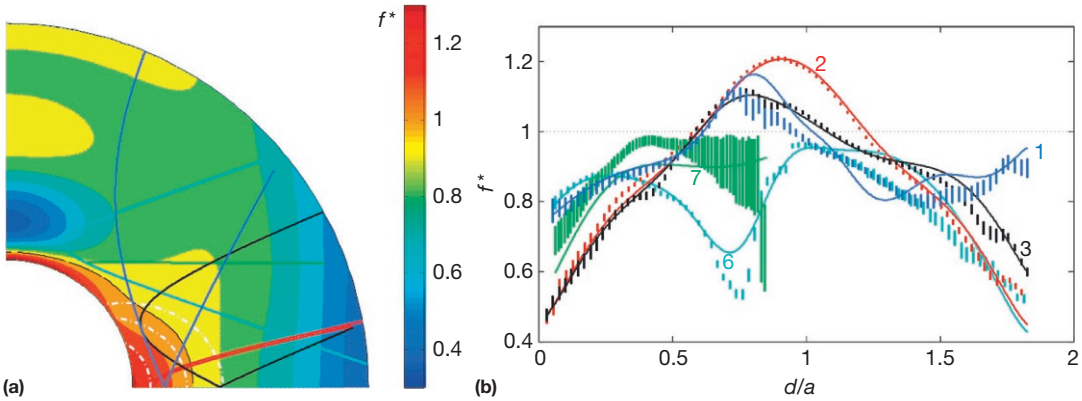

Figure 16 Experimental evidence of superrotation in the DTS experiment. (a) Right: Reconstructed isovalue map of fluid angular velocity for an inner core velocity of 3 Hz assuming axisymmetry and equatorial symmetry of the averaged flow. The Ferraro law applies in the superrotating area (red and orange) as the contours of the angular velocity follow the magnetic field lines (in white dashed lines). (b) Comparison between the measured profiles of Doppler velocity (errors bars) and the synthetic profiles (solid lines) for corresponding color rays plotted in (a) with the same color code. More details in Brito et al. (2011).

outer sphere) or its absence (Brito et al., 2011). **Figure 16** shows Doppler measurements of the angular velocity in the spherical shell across the outer sphere. The maximum in the measured angular velocity is larger than the imposed angular velocity of the inner core, which demonstrates the presence of superrotation. A comparison with nonlinear numerical results (computed at lower forcing) confirms that the maximum of superrotation is located close to the equator of the inner sphere in the experiments, whereas it occurs close to magnetic field line attached to equator of the outer boundary in the linear calculations. Strong nonlinear effects are evidently responsible for shifting the superrotation crescent inward where the magnetic field is the strongest.

This superrotation flow in the vicinity of the magnetized inner sphere is understood as the consequence of a magnetostrophic balance in the presence of rotation (Dormy et al., 1998; Nataf et al., 2008) or as a consequence of the Ferraro law of isorotation on magnetic field lines (Brito et al., 2011). The transition from a Ferraro regime in the interior to a geostrophic regime, where inertial forces predominate, in the outer regions takes place where the local Elsasser number is about one (the Elsasser number is a dimensionless number, which measures the ratio between the magnetic forces and the inertial forces). The induced magnetic field has been measured outside the spherical shell. A peak of strong amplification of magnetic field has been observed when the fluid rotation rate is almost equal and opposite to the outer sphere rotation rate. The fluid is then almost at rest in the laboratory frame, and the Taylor–Proudman constraint vanishes, enabling a strong meridional flow. We suggest that dynamo action might be favored in such a situation (Nataf et al., 2008).

8.13.4.3 Pseudodiffusive Magnetic Columns

Through the Lorentz force, the presence of a magnetic field tends to make the flow field anisotropic, elongating the dynamic structures along the field lines. This elongation occurs by two different processes – the Joule dissipation and Alfvén wave propagation (Loper and Moffatt, 1993; Moreau, 1990; Shimizu and Loper, 1997). The effect of these two is to deform an initially isotropic perturbation (such as spherical blob) into a columnar structure, elongated parallel to the local magnetic field direction. The theory behind the effect is fully described in **Chapter 8.06**. Any motion of a conducting fluid across the magnetic field lines induces eddy (Foucault) electric currents and also causes Joule dissipation, which tend to suppress such a transverse flow. Sreenivasan and Alboussière (2002) had performed experiments to study the formation of a magnetic column (a 2-D vortex) from a 3-D flow structure. They observed anisotropic decay of a vortex created by an impulse of electric current. The vortex velocity is small enough to be in the regime where the induced magnetic field is negligible compared with the imposed magnetic field (i.e., the magnetic Reynolds number is less than unity). For strong magnetic fields (i.e., the interaction parameter N, measuring the ratio between Lorentz and nonlinear forces, is greater than one), they observed an exponential decay of the kinetic energy until the column reaches the other boundary. This is interpreted as the formation of a magnetic column by the pseudodiffusive process of Joule currents flowing in the direction of the magnetic field. At larger magnetic fields (large Lindquist number), we expect the formation of the columns to be driven by Alfvén waves; however, to our knowledge, the experimental formation of magnetic columns by this particular mechanism has never been reported. In the core, elongated fluid columns can be formed by either of the two propagating wave processes we have described – fluid disturbances propagating as inertial waves along the direction of the rotation axis and Alfvén waves propagating along the magnetic field lines. To compare the relative strength of these two processes in the core, we estimate the Lehnert number λ (Cardin et al., 2002), which is the ratio of their respective group velocities,

$$\lambda = \frac{B}{\sqrt{\mu_0 \rho} \Omega L}$$

For small λ (as in the core), a rapid disturbance will generate quasigeostrophic columns in a few days by inertial wave propagation. At longer periods of time, the motion will

correspond to a balance between the Coriolis and the Lorentz forces (the magnetostrophic balance). It is possible that short-period events in the geomagnetic secular variation could be interpreted as motions of this type. Experiments are needed to confirm how this process might work in the core.

8.13.4.4 Turbulence under the Influence of a Magnetic Field

Experiments on magnetohydrodynamic (MHD) turbulence have been made to study fundamental properties of the turbulence under the action of a strong magnetic field. Although there are many well-known applications of MHD turbulence in metallurgy and related subjects, the number of such experiments that have been applied to the core is relatively small. The statistical properties of MHD turbulence are often characterized by their magnetic and kinetic spectra. Kinetic energy spectra are deduced from time measurements of pressure, while magnetic energy spectra are inferred from the variations of one component of the magnetic field. Often, both measurements are made in the same location. Time spectra are sometimes converted into spatial spectra under the hypothesis of ergodicity (which is true only in homogeneous turbulence and could be wrong in the core), or the so-called Taylor assumption, which applies to turbulence transported in a mean flow. In experiments at small Rm and in the presence of a weak external magnetic field $\left(\frac{\sigma B^2 R}{\rho U} \ll 1\right)$, the magnetic field can be considered as a passive vector in the flow, and magnetic energy spectra typically exhibit a 11/3 power exponent in the inertial regime in this situation (Bourgoin et al., 2002), which is related to the classical Kolmogorov exponent $(-5/3)$ of the kinetic energy spectra. For stronger magnetic fields $\left(\text{i.e.,} \frac{\sigma B^2 R}{\rho U} > 1\right)$, Alemany et al. (1979) found a -5 power exponent for the magnetic energy spectra and a -3 power exponent for the kinetic energy spectra in an experiment of free decay of grid-generated turbulence in mercury. The two distinct results at different strengths of the applied magnetic field were subsequently confirmed by Messadek and Moreau (2002).

8.13.4.5 Magnetoconvection in Rotating Fluids

When acting separately, both rotation and magnetic field tend to stabilize an electrically conducting fluid layer against thermal convection. However, in a classic paper, Chandrasekar (1968) used marginal stability analysis to show that the stability to thermal convection can be reduced when both effects are present together. A local minimum in the critical Rayleigh number is possible when the Coriolis and the Lorentz forces are both large and are of comparable magnitude (i.e., when the ratio of these two forces, the Elsasser number, is of order one). Nagakawa (1957) observed this local stability minimum in his study of a horizontal plane of liquid mercury heated from below and put in a strong vertical magnetic field. More recently, Aurnou and Olson (2001) had made a comprehensive set of thermal convective experiments in horizontal layer of liquid gallium subject to uniform rotation and a uniform vertical magnetic field. Aurnou and Olson (2001) focused on the relationship between Nusselt and Rayleigh numbers at various Ekman and Elsasser numbers. As expected, they found that the convection is inhibited by rotation and magnetic field acting separately, but they did not find regimes of enhanced convection under the dual action of rotation and magnetic field. This is possibly due to the limited parameter regime sampled in these experiments, in which the minimum in stability was missing. Gillet et al. (2007b) performed magnetoconvection experiments in a rotating spherical shell with liquid gallium. Strong electric currents on the axis of rotation were used to induce a toroidal magnetic field with a quasicylindrical geometry. Again, the magnetic field was evidently too weak in this experiment to observe the decrease of the critical Rayleigh number with the Elsasser number. The results of Gillet et al. (2007b) agree with the variations of the critical parameters deduced from a quasigeostrophic numerical approach at low Elsasser number. The concept introduced by Chandrasekar (1968) that magnetic fields and rotation may simultaneously destabilize a fluid is potentially very important for the geodynamo and other planetary dynamos, as it opens the possibility of subcritical dynamo action liquid cores. Experimental studies with larger magnetic fields would be valuable in this context, to investigate thermal convection at low Prandtl and magnetic Prandtl numbers in regimes where Coriolis and Lorentz forces are comparable and dominant in the system.

8.13.4.6 Magneto Inertial Waves

In the DTS experiment (rotating spherical Couette flow of liquid sodium in a strong dipolar magnetic field; Nataf et al., 2006, see **Section 8.13.4.2**), we have also detected propagating disturbances that travel along parallels of the spherical shell (Schmitt et al., 2008). Detailed analysis of electric potentials and the induced magnetic field measured at the outer sphere indicate the azimuthal wave numbers, the propagation velocities, the equatorial symmetry, and the latitudinal variations of the oscillations (Schmitt et al., 2013). These fluctuations correspond to the hydromagnetic waves described by Hide (1966) and Schmitt et al. (2008), which correspond to a hybrid of Alfvén waves and inertial waves. **Figure 17** shows the power spectra of the radial fluctuating magnetic field at the outer boundary for different latitudes. The even part of the radial field is dominated by modes with $m=1$ (within the range 5–12 Hz) and $m=3$ (22–30 Hz) azimuthal numbers, while $m=2$ modes (15–21 Hz) are dominant for the odd part. In both cases, other minor peaks are present (shown by arrows) with a modulation with the latitude for the same m. Their source of excitation on the hydromagnetic waves in DTS is not very well understood even if the outer turbulent layer may be suspected (Figueroa et al., 2013; Schmitt et al., 2013). With the help of numerical model, experimental modes have been identified, and it was found that the excited modes are mainly dominated by the inertial forces except in the vicinity of the magnetized inner core where the magnetic forces dominate.

These magnetoinertial waves are also called MC waves (magnetocoriolis waves) and have been seen by Nornberg et al. (2010) in an MHD experiment firstly dedicated to the quest of magnetorotational instabilities (MRI) in Princeton. MRI, which apply mainly to astrophysical situations, are also magnetoinertial phenomenon, but in these instabilities, centrifugal forces are the main inertial ingredient instead of the Coriolis forces. Quasi-MRI have been observed in the PREMISE experiment in Dresden, which imposes a helical magnetic field in a Taylor–Couette experiment (Stefani et al., 2007).

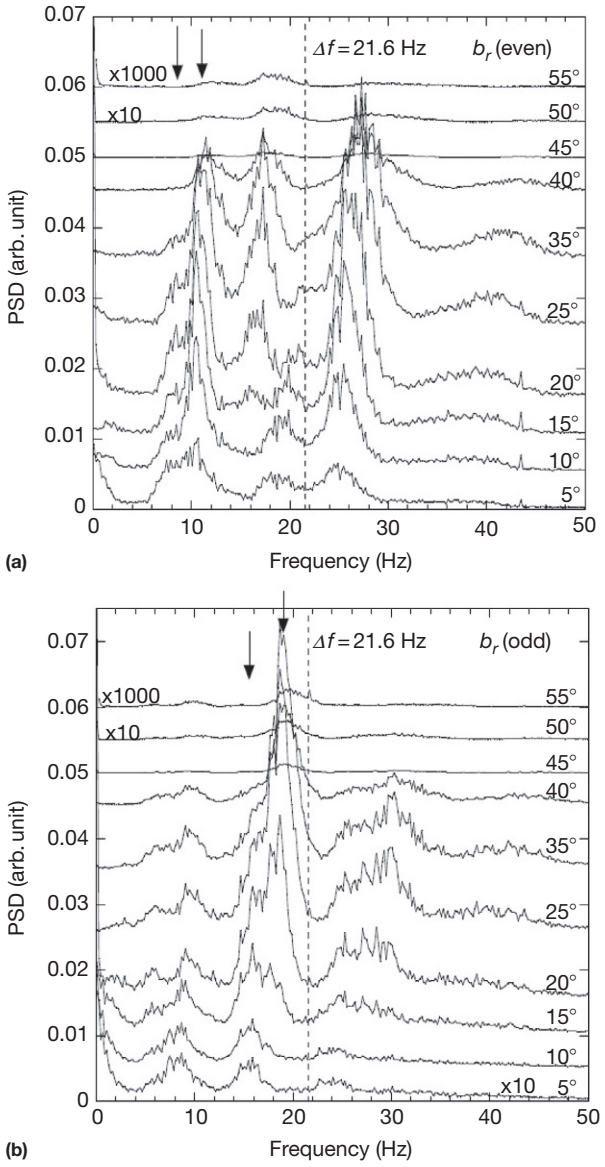

Figure 17 Symmetrized power spectral densities of radial fluctuating magnetic field, at various latitudes ranging from 5° (bottom) to 55° (a) even part, (b) odd part; each curve is shifted vertically by a constant value, for sake of clarity; dashed line shows the forcing rate $\Delta f = 21.6$ Hz. More details in Schmitt et al. (2013).

8.13.5 Experimental Dynamos

According to the magnetic induction equation (see **Chapter 8.03**), the magnetic Reynolds number ($R_m = UL/\eta$, where U and L are typical velocity and length and η the magnetic diffusivity) is the critical parameter to initiate dynamo action in an electrically conducting fluid. For velocity fields with suitable symmetry properties (i.e., fluid motions with helicity), kinematic dynamo studies have shown that critical magnetic Reynolds numbers between 10 and 100 are necessary to reach dynamo conditions (Dudley and James, 1989; see also **Chapter 8.03**. Such magnetic Reynolds numbers are not easy to produce in a laboratory experiment. The best electric conductor among the common fluids is molten sodium, with a magnetic diffusivity $\eta = 0.09\ \mathrm{m^2\ s^{-1}}$ at 120 °C (see Nataf, 2003 for physical properties). Even though its use requires special safety (and administrative!) procedures and also requires control at relatively high operating temperatures (the melting temperature of sodium is 98 °C), it remains the only practical fluid to use in experimental dynamo modeling. To reach high magnetic Reynolds numbers in the relatively small volume of an experiment, very high fluid velocities are needed (more precisely, very high gradients of velocity are needed, since solid-body rotation does not count here). Numerically, velocities of order 10 m s^{-1} are needed even in relatively large size containers, 1 m or larger. As we have seen before, thermal convection velocities in laboratory experiment are too small for this, by two orders of magnitude or more, so a thermally convective dynamo experiment remains an impractical goal. Instead, the approach has been to achieve very high velocities in liquid sodium containers in which the fluid is driven mechanically by powerful motors. A large amount power (>100 kW) is needed to produce such high velocities, even allowing for the fact that the density of liquid sodium is relatively low. The main advantages that experiments offer for modeling dynamo action in planetary cores stem from their transport properties, which are closer to the Earth's core than most numerical dynamos. The magnetic Prandtl number of liquid sodium ($Pm = \nu/\eta \approx 10^{-5}$) is comparable to the magnetic Prandtl number of liquid iron. Compare these with present numerical dynamo models, which encounter difficulties with magnetic Prandtl numbers smaller than about 0.1 (see **Chapter 8.10**). It is easy to understand that small-scale feature and rapid time variations of the flow depend strongly on the values of the diffusion coefficients in the fluid. In addition, liquid metals tend to easily produce highly turbulent dynamos, since the Reynolds number is Pm^{-1} times greater than the magnetic Reynolds number. Presumably, this is one of the reasons why numerical modeling is limited to magnetic Prandtl numbers close to one. At this stage, experimental dynamo modeling remains far removed from the conditions of the core, in terms of the geometry, the source of motions, and the strength of planetary rotation. However, today's dynamo experiments are just the beginning. The priority up until now has been to obtain self-generation; the next goal is to increase their geophysical realism.

8.13.5.1 The Riga Dynamo

In 2000, the Riga group headed by Prof. Agris Gailitis culminated a 30-year effort when they achieved self-excitation of a magnetic field in a liquid sodium experiment (Gailitis et al., 2003). Their experimental apparatus was specially designed to produce the flows of the kinematic dynamo theory of Ponomarenko (1973) at relatively low critical magnetic Reynolds number (Gailitis et al., 2003). As shown in **Figure 18**, the apparatus consists of three coaxial stainless steel cylinders, each 3 m long. Liquid sodium is accelerated downward by a helicoid propeller located at the top of the inner cylinder and returns to the top by a vertical flow in the larger-diameter cylindrical shell. The liquid sodium in the outermost cylinder is at rest and acts to increase the magnetic diffusion time of the system. At fast rotation rates of the propeller (>1900 rpm,

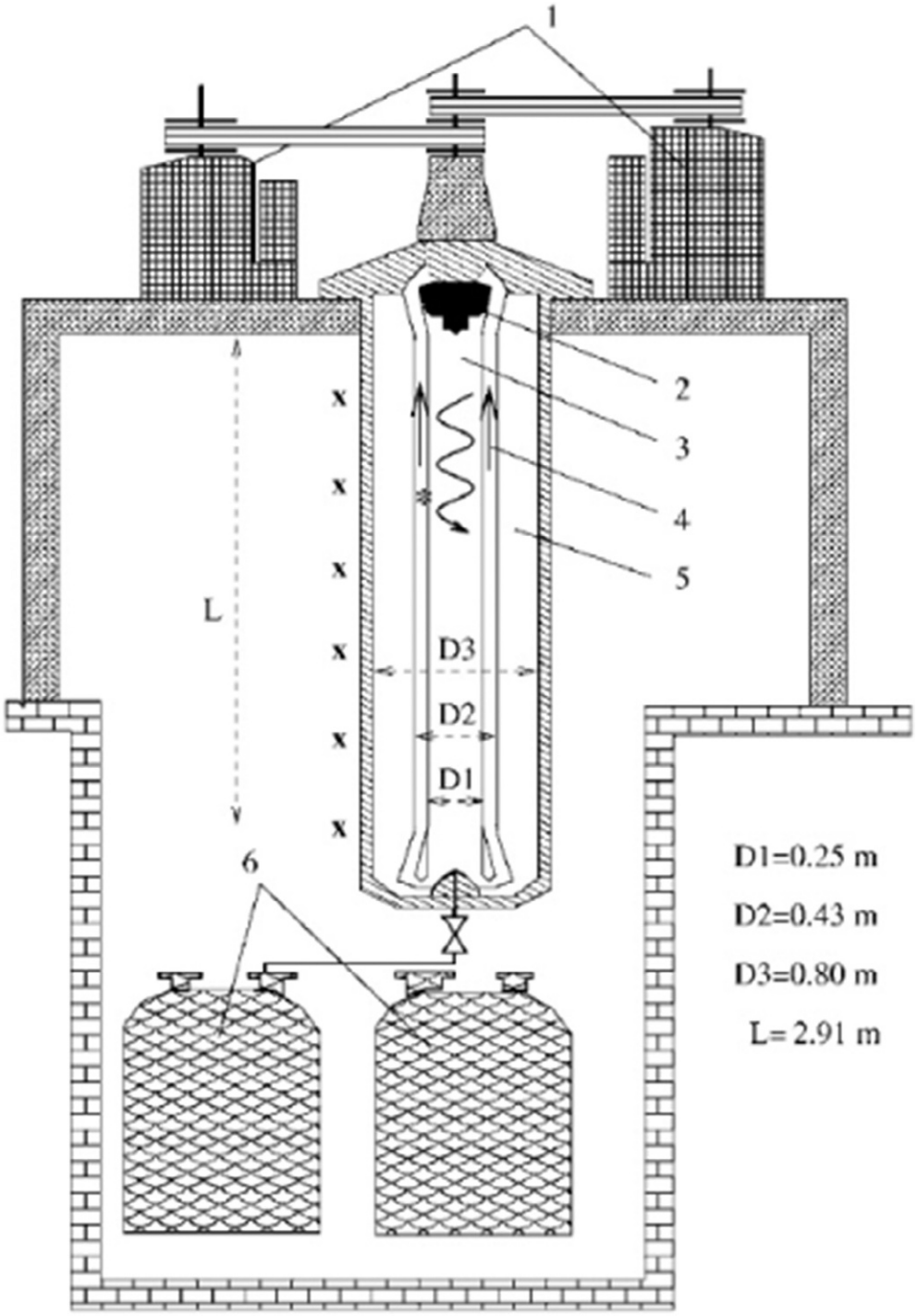

Figure 18 The Riga dynamo facility. Main parts of the apparatus include 1, two motors (55 kW each); 2, propeller; 3, helical flow region; 4, backflow region; 5, sodium at rest; 6, sodium storage tanks; *, position of the fluxgate sensor; x, positions of the six Hall sensors. Reproduced from Gailitis A, Lielausis O, Dement'ev S, et al. (2000) Detection of a flow induced magnetic field eigenmode in the riga dynamo facility. *Physical Review Letters* 84: 4365–4368.

corresponding to a magnetic Reynolds number of about 20 based on the radius of the inner cylinder), an oscillating self-sustained magnetic field was observed. Below and above the onset, the frequency of this magnetic field is very close to the kinematic dynamo model predictions (cf. Figure 19). The experimental growth rate below the onset of dynamo action (determined by the study of an imposed external magnetic field) is also very close to the appropriate prediction of 2-D kinematic dynamo calculations (cf. Figure 19). Following a step increase in the velocity, the dynamo-induced magnetic

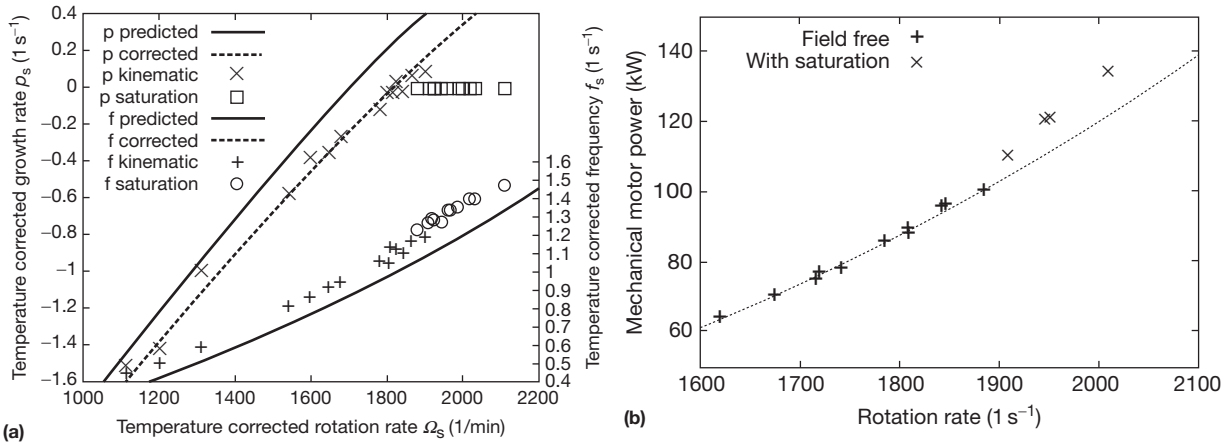

Figure 19 Results of the Riga dynamo experiment. Left: Measured growth rates p and frequencies f for different rotation rates in the kinematic and the saturation regime, compared with the numerical predictions (reproduced from Gailitis A, Lielausis O, Platacis E, Gerbeth G, and Stefani F (2003) The riga dynamo experiment. *Surveys in Geophysics* 24: 247–267). Right: Motor power below (+) and within (x) the dynamo regime. The motor power scales as the third power of the rotation rate (dashed line) of the propeller below the dynamo onset. Reproduced from Gailitis A, Lielausis O, Platacis E, et al. (2001) Magnetic field saturation in the riga dynamo experiment. *Physical Review Letters* 86: 3024–3027.

field increases exponentially with time, with a growth rate in agreement with the numerical kinematic dynamo model predictions. The field grows until it reaches a saturation level of a few milliteslas. Saturated states have been maintained for several minutes (compared to the magnetic diffusion time of order 1 s), leaving no doubt about the presence of a self-sustained magnetic field (Gailitis et al., 2003).

The power dissipated in the dynamo regime is shown in Figure 19. There is a clear deviation from the Ω^3 law expected from simple hydraulic arguments and observed below the onset (Gailitis et al., 2001). An increase of 10 kW is needed to sustain the dynamo and compensate the Joule dissipation of the electric currents supporting the magnetic field. This level of power consumption matches the dissipation predicted for a magnetic field with the geometry of the least stable magnetic eigenmode and with the experimentally observed amplitude. In the saturated state, the azimuthal fluid flow is expected to be weaker away from the propeller, and this effect would dictate the level of saturation (Gailitis et al., 2003). Velocity measurements are required to quantify the action of the Lorentz forces on the flow. Using ultrasound Doppler velocimetry, the first tests have shown that the sodium that was expected to be at rest in outer cylinder is in fact in motion during dynamo action (F. Stefani, private communication).

8.13.5.2 The Karlsruhe Dynamo

A second successful dynamo experiment was made in 2000, this time in Karlsruhe. Featuring a design inspired by the early kinematic dynamo models of Roberts (1972) and Busse (1992), the apparatus consists of an array of 52 stainless steel spin generators, as shown in Figure 20. Each spin generator consists of two parts: a central tube of 10 cm of diameter where the motion approximates a Poiseuille flow and a surrounding outer cylinder where the liquid sodium follows a helical flow path constrained by a series of blades. Liquid sodium is circulated through these

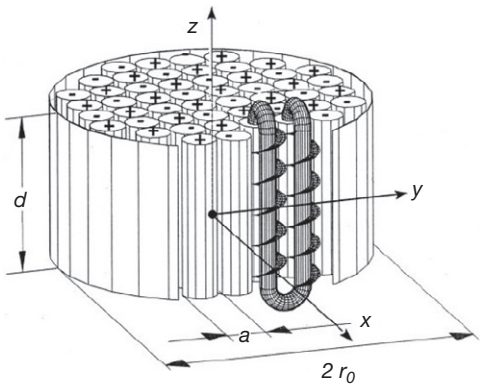

Figure 20 Sketch of the Karlsruhe dynamo apparatus. An array of 52 spin (helical flow) generators are enclosed inside a 1.7 m diameter stainless steel cylinder. Liquid sodium is pumped through the generator array. Dimensions: $a = 0.21$ m, $r_0 = 0.85$ m, $d = 0.703$ m . Reproduced from Müller U, Stieglitz R and Horanyi S (2004) A two-scale hydromagnetic dynamo experiment. *Journal of Fluid Mechanics* 498: 31–71.

pipes by three remote MHD pumps with power 210 kW. This experiment has two different scales: the spin generator scale and the modulus scale, which is ten times larger. This scale separation makes it suitable for applications of dynamo mean field theories (Rädler and Brandenburg, 2003). For volume rates larger than ≈ 100 m^3 h^{-1}, the authors observed a self-sustained stationary magnetic field of a few milliteslas for long periods of time (more than 1 h) (Müller et al., 2006). The experimental onset agrees quite well with kinematic dynamo results of Tilgner (1997) and with mean field theory results of Rädler et al. (1998) as shown in Figure 21 even if the experimental threshold is 10% lower than the predicted values.

Outside the modulus, the large-scale magnetic field is mainly a dipole with its axis perpendicular to the direction of the channels (Müller et al., 2004), in agreement with numerical and theoretical models. As predicted, the magnetic field has

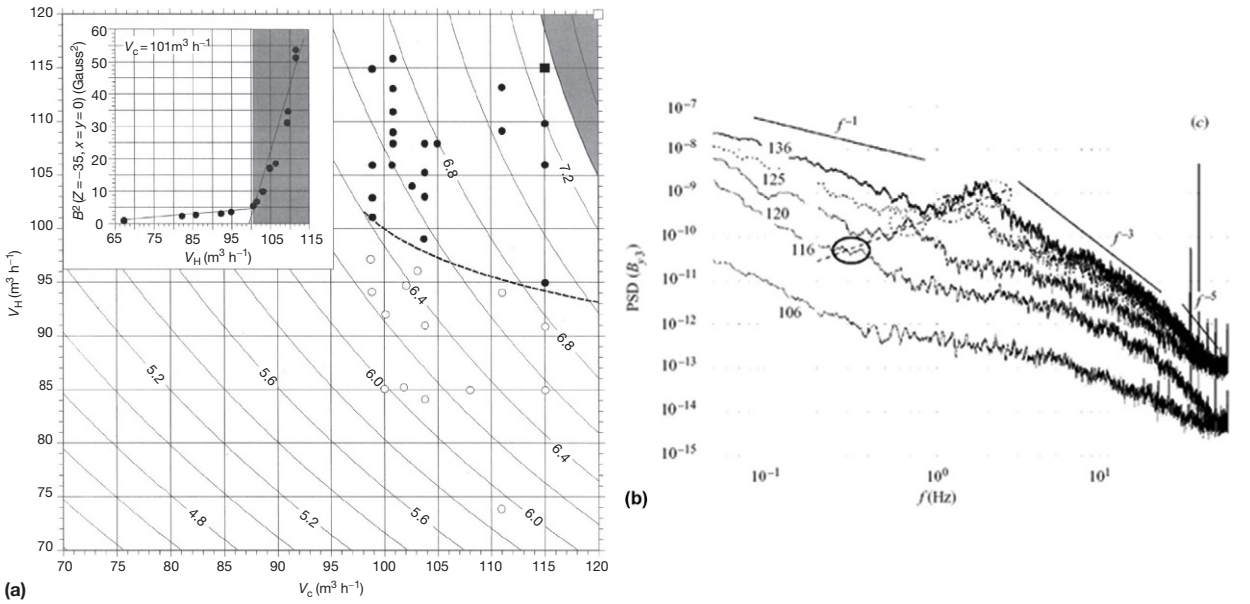

Figure 21 Results of the Karlsruhe dynamo experiment. a: Stability diagram for the onset of dynamo action as a function of the central flow rate V_C and the helical flow rates V_H. The filled dots denote experimentally measured dynamo action; open dots denote nondynamo states. The dashed line indicates the experimentally obtained marginal stability curve, defined by a regression of the steep increase of the magnetic energy ($\approx B^2$) with V_H (see subgraph in the upper left). The gray-marked domain specifies the flow rate domain for the existence of a dynamo as calculated by Radler. The isolines show the values of a modified magnetic Reynolds number according to the mean field model of Radler. The two squared symbols indicate Tilgner's calculations for onset of dynamo action (Tilgner, 1997). b: Power spectral density (PSD) for the components by for five different volumetric flow rates of operation at the center of the modulus. $V_H = 100$ m^3 h^{-1} and for five central volumetric flow rates $V_C = 106$, 116, 120, 125, 136 m^3 h^{-1}. Reproduced from Müller U, Stieglitz R and Horanyi S (2004) A two-scale hydromagnetic dynamo experiment. *Journal of Fluid Mechanics* 498: 31–71.

a staircase structure in the direction of the channels, but two preferred directions of the equatorial dipole were found (instead of arbitrary many directions, as predicted theoretically). Müller et al. (2004) showed that these two preferred directions are controlled by an external magnetic field and permanent magnetic fields. The magnetic field along the central axis of the modulus has been measured. The geometry agrees quite well with the numerically predicted eigenmode, but some loss of symmetry has been observed (Müller et al., 2006). In the center region, field intensities up to 40 mT have been measured, ten times greater than the values of the magnetic field outside the device. Saturation of the magnetic field can be understood in this experiment as a back reaction of the Lorentz forces on the fluid flow. Müller et al. (2006) measured up to a 13% decrease on the amplitude of the velocity in the central pipe above the dynamo onset. More interestingly, they also reported an increase of the fluctuations of the velocity field around its mean (rms) value as the experiment reaches dynamo conditions. Generally, in MHD, the presence of the magnetic field reduces the turbulent fluctuations of the velocity field. The authors associate the fluctuations of velocity field with the fluctuations of the magnetic field, which become more and more energetic as the dynamo becomes more supercritical Müller et al. (2006). This effect can be seen in magnetic field spectra, which exhibit a maximum at moderate frequency (1 Hz). The frequency of this maximum shifts to higher values as the flow rate increases above the value for dynamo onset. These spectra show two trends around the peak, one with an f-1 variation at lower frequency and another with an f-3 variation at larger frequencies. At very large frequencies, the authors claim a f-5 dependency.

8.13.5.3 The VKS Experiments

A French collaboration has built the VKS experiment in Cadarache (the French Atomic Agency), consisting of a Van Karman swirling flow of liquid sodium (volume = 50 l) in a cylindrical vessel. The flow is generated by two counterrotating propellers driven by 300 kW power motors. A wide variety of MHD experiments were initially tried (Bourgoin et al., 2002), culminating in a 2007 experiment in which a large and persistent magnetic field was measured (Monchaux et al., 2007; Ravelet et al., 2008) in which the impellers (disks with curved blades) were consisted of soft ferromagnetic iron. Otherwise identical experiments using stainless steel blades failed to produce dynamo action. Clearly, the ferromagnetic elements in the experiment play a crucial role in the magnetic field induction process (Berhanu et al., 2010). Subsequent investigations (Gissinger et al., 2008; Guervilly and Brummell, 2012; Verhille et al., 2010) have sought to quantify the importance of the boundary conditions in the dynamo process, in order to understand the effect of ferromagnetic pieces in VKS. These studies have shown that high magnetic permeability boundary conditions tend to lower the critical magnetic Reynolds number in the VKS geometry but the contribution of the remanent

magnetic field from the soft iron impellers has proved difficult to model.

The geometry of the large induced magnetic field in the VKS experiment is predominantly axisymmetric, with a strong toroidal magnetic component (Monchaux et al., 2007), contrary to what was predicted by kinematic dynamos for this geometry (Ravelet et al., 2005). This is now understood to be an α-effect derived from the induction of the spiraling flow between the blades of the impellers (Laguerre et al., 2008), but the detailed mechanisms of magnetic field generation and saturation still need to be clarified. A diverse set of dynamic regimes are observed (Figure 22) in situations where the forcing (i.e., the rotation of the impellers) is not symmetrical. Most dramatically, magnetic field reversals have been observed (Berhanu et al., 2007; Ravelet et al., 2008). A phenomenological analogy with paleomagnetic reversals of the geodynamo has been explored (Petrelis et al., 2009), but the correspondence in terms of timescales remains a source of uncertainty. However, the temporal behavior of the VKS field is suggestive of the generic behavior of low-dimensional dynamic systems, despite the high degree of turbulence in the VKS flow (Berhanu et al., 2010). Typically, reversal regimes are observed at the boundary between stationary and oscillating regimes. Furthermore, it is found that the time between successive reversals is essentially random, consistent with the notion that VKS reversals are connected via turbulent fluctuations of the system, which drive the dynamic system away from its equilibrium states. We note that random reversal regimes are extremely localized in the phase diagram of the VKS experiment (denoted as 'period divergence' in Figure 22). If this same behavior characterizes geomagnetic reversals, it would imply that the geodynamo has remained in the same locale in its parameter space for most if not all of geologic time.

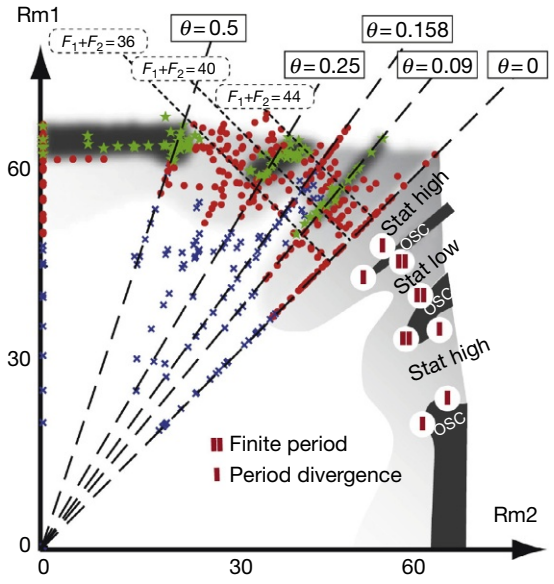

Figure 22 Phase diagram of the VKS experiments in terms of the magnetic Reynolds numbers of the two impellers. The sum of the rotation rates of the impellers ($F1+F2$) is shown as short dashed lines. The intensity of the forcing, parameterized by $F1+F2$, controls the transition to a sustained magnetic field via a supercritical bifurcation to a stationary state. For some values of the asymmetry parameter $\theta=(F1F2)/(F1+F2)$, time-dependent regimes develop. Two qualitatively different transitions between oscillatory and stationary regimes are reported, involving a strong and a weak divergence of the period of oscillations, respectively. Random reversal regimes are observed in 'period divergence' areas between these regimes. These dynamic transitions can be interpreted as a low-dimensional interaction of two dynamo modes. Reproduced from Berhanu M, Verhille G, Boisson J, et al. (2010) Dynamo regimes and transitions in the VKS experiment. *European Physical Journal B* 77(4): 459–468.

8.13.5.4 Turbulence and Dynamo Onset

The magnetic Prandtl number is the ratio of the viscosity to the magnetic diffusivity of the fluid. The magnetic Prandtl number of liquid metals is typically very low, with its value in the outer core not too different from liquid sodium, 5×10^{-6}. A magnetic Reynolds number of a few tens as required for dynamo action implies an ordinary Reynolds number larger than 10^7 in dynamo experiments and also in the core. Consequently, properly scaled dynamo experiments are necessarily turbulent, and for the same reason, the geodynamo is also turbulent, although the turbulence in the outer core has special characteristics (see Chapter 8.06). The two successful dynamo experiments have overcome the turbulence problem by very precise control of the flow (e.g., constrained by guiding pipes), reducing the effects of turbulence, which are usually undesirable. For instance, in the Riga dynamo, Gailitis et al. (2000) estimated the level of turbulence to be $<10\%$ and the corresponding increase of the critical magnetic Reynolds number only 1%. Similar levels of turbulence have been observed in Karlsruhe experiment (Müller et al., 2006). On the other hand, failed dynamo experiments in Maryland (Peffley et al., 2000; Sisan et al., 2003; Zimmerman et al., 2011), Cadarache (Berhanu et al., 2010; Bourgoin et al., 2002) and Wisconsin (Limone et al., 2012; Spence et al., 2006) are based on less constrained, more turbulent flows and have not reached the critical value of the magnetic Reynolds number. The presence of turbulence in these less constrained experiments has raised their effective critical magnetic Reynolds numbers above the predictions of numerical kinematic dynamos based on purely laminar flow (Laval et al., 2006; Limone et al., 2012; Marié et al., 2003; Nornberg et al., 2006; Ponty et al., 2005; Ravelet et al., 2005).

All of these experiments reveal how the flow induces magnetic fields from the interaction of the turbulence with the imposed magnetic field. For instance, the exponential decay rate of the magnetic field after shutdown provides information on the growth rate of the induced magnetic field (Peffley et al., 2000) and gives some information on how far the experiment is from dynamo onset. Time-averaged large-scale flows also have been observed to induce magnetic fields in different direction than the applied field, an example of the Ω (Brito et al., 1995; Lehnert, 1958; Spence et al., 2006) or Parker effect (Volk et al., 2005). The induction effects due to small-scale turbulent fluctuations and their contribution to the mean induction, the so-called α-effect, have also been studied experimentally. In Perm, Stepanov et al. (2006) investigated induction mechanisms in a screw flow of gallium in a toroidal channel with screw diverters during a spin-down process. Their measurements yielded a low upper bound on the α-effect compared to the predictions from dimensional analysis. The

studies of the no-screw (no diverter) spin-down flow of liquid sodium or liquid gallium lead to give an experimental evidence of a turbulent magnetic diffusivity (Noskov et al., 2012). In January 2013, as this chapter was written, the College Park experiment (Couette spherical shell of 3 m of diameter) had run but no self-sustained magnetic field has been observed yet.

Acknowledgments

Thanks to Thierry Alboussière, Julien Aubert, Jonathan Aurnou, Daniel Brito, Nicolas Gillet, Dominique Jault, Henri-Claude Nataf, Jérôme Noir, and Nathanaël Schaeffer.

References

Aldridge K and Baker R (2003) Paleomagnetic intensity data: A window on the dynamics of Earth's fluid core? *Physics of the Earth and Planetary Interiors* 140: 91–100.

Aldridge K, Baker R, and Mcmillan D (2007) Rotating parametric instability in early Earth. *Geophysical and Astrophysical Fluid Dynamics* 101(5–6): 507–520.

Aldridge KD and Toomre A (1969) Axisymmetric inertial oscillations of a fluid in a rotating spherical container. *Journal of Fluid Mechanics* 37: 307–323.

Alemany A, Moreau R, Sulem PL, and Frisch U (1979) Influence of an external magnetic field on homogeneous MHD turbulence. *Journal de Mécanique* 18: 277–313.

Aubert J, Brito D, Nataf H-C, Cardin P, and Masson J-P (2001) A systematic experimental study of rapidly rotating spherical convection in water and liquid gallium. *Physics of the Earth and Planetary Interiors* 128: 51–74.

Aubert J, Gillet N, and Cardin P (2003) Quasigeostrophic models of convection in rotating spherical shells. *Geochemistry, Geophysics, Geosystems* 4: 1. http://dx.doi.org/10.1029/2002GC000456.

Aubert J, Jung S, and Swinney HL (2002) Observations of zonal flow created by potential vorticity mixing in a rotating fluid. *Geophysical Research Letters* 29: 1–23.

Aurnou JM and Olson PL (2001) Experiments on Rayleigh Bénard convection, magnetoconvection and rotating magnetoconvection in liquid gallium. *Journal of Fluid Mechanics* 430: 283–307.

Berhanu M, Monchaux R, Fauve S, et al. (2007) Magnetic field reversals in an experimental turbulent dynamo. *EPL* 77(5).

Berhanu M, Verhille G, Boisson J, et al. (2010) Dynamo regimes and transitions in the VKS experiment. *European Physical Journal B* 77(4): 459–468.

Bourgoin M, Marié L, Pétrélis F, et al. (2002) Magnetohydrodynamics measurements in the von Kármán sodium experiment. *Physics of Fluids* 14: 3046.

Brito D, Alboussiere T, Cardin P, et al. (2011) Zonal shear and super-rotation in a magnetized spherical Couette-flow experiment. *Physical Review E* 83(6, Part 2).

Brito D, Aurnou J, and Cardin P (2004) Turbulent viscosity measurements relevant to planetary core–mantle dynamics. *Physics of the Earth and Planetary Interiors* 141: 3–8.

Brito D, Cardin P, Nataf H-C, and Marolleau G (1995) Experimental study of a geostrophic vortex of gallium in a transverse magnetic field. *Physics of the Earth and Planetary Interiors* 91: 77–98.

Brito D, Nataf H-C, Cardin P, Aubert J, and Masson J-P (2001) Ultrasonic Doppler velocimetry in liquid gallium. *Experiments in Fluids* 31: 653–663.

Burr U, Barleon L, Müller U, and Tsinober A (2000) Turbulent transport of momentum and heat in magnetohydrodynamic rectangular duct flow with strong sidewall jets. *Journal of Fluid Mechanics* 406: 247–279.

Busse FH (1968) Steady fluid flow in a precessing spheroidal shell. *Journal of Fluid Mechanics* 33: 739–751.

Busse FH (1970) Thermal instabilities in rapidly rotating systems. *Journal of Fluid Mechanics* 44: 441–460.

Busse F (1992) Dynamo theory of planetary magnetism and laboratory experiments. *Springer Proceedings in Physics* 69: .

Busse FH and Carrigan CR (1974) Convection induced by centrifugal buoyancy. *Journal of Fluid Mechanics* 62: 579–592.

Busse FH and Carrigan CR (1976) Laboratory simulation of thermal convection in rotating planets and stars. *Science* 191: 81–83.

Busse FH and Hood LL (1982) Differential rotation driven by convection in a rapidly rotating annulus. *Geophysical and Astrophysical Fluid Dynamics* 21: 59–74.

Calkins MA, Noir J, Eldredge JD, and Aurnou JM (2010) Axisymmetric simulations of libration-driven fluid dynamics in a spherical shell geometry. *Physics of Fluids* 22(8): 086602.

Cardin P, Brito D, Jault D, Nataf H-C, and Masson J-P (2002) Towards a rapidly rotating liquid sodium dynamo experiment. *Magnetohydrodynamics* 38: 177–189.

Cardin P and Olson P (1992) An experimental approach to thermochemical convection in the Earth's core. *Geophysical Research Letters* 19: 1995–1998.

Cardin P and Olson P (1994) Chaotic thermal convection in a rapidly rotating spherical shell: Consequences for flow in the outer core. *Physics of the Earth and Planetary Interiors* 82: 235–259.

Carrigan CR and Busse FH (1983) An experimental and theoretical investigation of the onset of convection in rotating spherical shells. *Journal of Fluid Mechanics* 126: 287–305.

Chandrasekar S (1968) *Hydrodynamic and Hydromagnetic Stability*. New York: Clarendon Press.

Cordero S (1993) Experiments on convection in a rotating hemispherical shell: Transition to chaos. *Geophysical Research Letters* 20: 2587–2590.

Cordero S and Busse FH (1992) Experiments on convection in rotating hemispherical shells –Transition to a quasi-periodic state. *Geophysical Research Letters* 19: 733–736.

Dormy E, Cardin P, and Jault D (1998) MHD flow in a slightly differentially rotating spherical shell, with conducting inner core, in a dipolar magnetic field. *Earth and Planetary Science Letters* 160: 15–30.

Dormy E, Jault D, and Soward AM (2002) A super-rotating shear layer in magneto-hydrodynamic spherical Couette flow. *Journal of Fluid Mechanics* 452: 263–291.

Dormy E, Soward AM, Jones CA, Jault D, and Cardin P (2004) The onset of thermal convection in rotating spherical shells. *Journal of Fluid Mechanics* 501: 43–70.

Dudley ML and James RW (1989) Time-dependent kinematic dynamos with stationary flows. *Proceedings of the Royal Society of London A* 425: 407–429.

Egbers C, Brasch W, Sitte B, Immohr J, and Schmidt J-R (1999) Estimates on diagnostic methods for investigations of thermal convection between spherical shells in space. *Measurement Science and Technology* 10: 866–877.

Eloy C, Le Gal P, and Le dizès S (2000) Experimental study of the multipolar vortex instability. *Physical Review Letters* 85: 3400–3403.

Eymin C and Hulot G (2005) On core surface flows inferred from satellite magnetic data. *Physics of the Earth and Planetary Interiors* 152: 200–220.

Faller AJ (1963) An experimental study of the instability of the laminar Ekman boundary layer. *Journal of Fluid Mechanics* 15: 560–576.

Figueroa A, Schaeffer N, Nataf HC, and Schmitt D (2013) Modes and instabilities in magnetized spherical Couette flow. *Journal of Fluid Mechanics* 716: 445–469.

Früh W-G and Read PL (1999) Experiments on a barotropic rotating shear layer. Part 1. Instability and steady vortices. *Journal of Fluid Mechanics* 383: 143–173.

Gailitis A, Lielausis O, Dement'ev S, et al. (2000) Detection of a flow induced magnetic field eigenmode in the riga dynamo facility. *Physical Review Letters* 84: 4365–4368.

Gailitis A, Lielausis O, Platacis E, Gerbeth G, and Stefani F (2003) The riga dynamo experiment. *Surveys in Geophysics* 24: 247–267.

Gailitis A, Lielausis O, Platacis E, et al. (2001) Magnetic field saturation in the riga dynamo experiment. *Physical Review Letters* 86: 3024–3027.

Gillet N, Brito D, Jault D, and Nataf H-C (2007a) Experimental and numerical study of convection in a rapidly rotating spherical shell. *Journal of Fluid Mechanics* 580: 83–121.

Gillet N, Brito D, Jault D, and Nataf H-C (2007b) Experimental and numerical study of magnetoconvection in a rapidly rotating spherical shell. *Journal of Fluid Mechanics* 580: 123–143.

Gissinger C, Iskakov A, Fauve S, and Dormy E (2008) Effect of magnetic boundary conditions on the dynamo threshold of von Karman swirling flows. *EPL* 82(2).

Greenpan H (1968) *The Theory of Rotating Fluids*. Cambridge, UK: Cambridge University Press.

Greff-Lefftz M and Legros H (1999) Core rotational dynamics and geological events. *Science* 286: 1707–1709.

Guervilly C and Brummell NH (2012) Self-consistent simulations of a von Karman type dynamo in a spherical domain with metallic walls. *Physical Review E* 86(4, Part 2).

Hart JE, Glatzmaier GA, and Toomre J (1986) Space-laboratory and numerical simulations of thermal convection in a rotating hemispherical shell with radial gravity. *Journal of Fluid Mechanics* 173: 519–544.

Hartmann J and Lazarus F (1937) Experimental investigations on the flow of mercury in a homogeneous magnetic field. *Det Kgl Danske Videnskabernes Selskab Mathematisk Fysiske Meddelelser* 15: 1–45.

Hide R (1966) Free hydromagnetic oscillations of the Earth's core and the theory of the geomagnetic secular variation. *Proceedings of the Royal Society of London A* 259: 615–650.

Hide R and Titman C (1967) Detached shear layers in a rotating fluid. *Journal of Fluid Mechanics* 29: 39–60.

Hollerbach R (2000) Magnetohydrodynamic flows in spherical shells. *Arkiv for Fysik* 549: 295.

Hollerbach R and Kerswell RR (1995) Oscillatory internal shear layers in rotating and precessing flows. *Journal of Fluid Mechanics* 298: 327–339.

Jones CA, Soward AM, and Mussa AI (2000) The onset of thermal convection in a rapidly rotating sphere. *Journal of Fluid Mechanics* 405: 157–179.

Kelley DH, Triana SA, Zimmerman DS, Tilgner A, and Lathrop DP (2007) Inertial waves driven by differential rotation in a planetary geometry. *Geophysical and Astrophysical Fluid Dynamics* 101(5–6): 469–487.

Kerswell RR (1995) On the internal shear layers spawned by the critical regions in oscillatory Ekman boundary layers. *Journal of Fluid Mechanics* 298: 311–325.

Kerswell RR (2002) Elliptical instabilities. *Annual Review of Fluid Mechanics* 34: 83–113.

King EM, Stellmach S, and Aurnou JM (2012) Heat transfer by rapidly rotating Rayleigh–Benard convection. *Journal of Fluid Mechanics* 691: 568–582.

King EM, Stellmach S, Noir J, Hansen U, and Aurnou JM (2009) Boundary layer control of rotating convection systems. *Nature* 457(7227): 301–304.

Lacaze L, Le Gal P, and Le Dizès S (2004) Elliptical instability in a rotating spheroid. *Journal of Fluid Mechanics* 505: 1–22.

Laguerre R, Nore C, Ribeiro A, Léorat J, Guermond J-L, and Plunian F (2008) Impact of impellers on the axisymmetric magnetic mode in the vks2 dynamo experiment. *Physical Review Letters* 101: 104501.

Laval J-P, Blaineau P, Leprovost N, Dubrulle B, and Daviaud F (2006) Influence of turbulence on the dynamo threshold. *Physical Review Letters* 96(20): 204503.

Le Bars M, Lacaze L, Le Dizes S, Le Gal P, and Rieutord M (2010) Tidal instability in stellar and planetary binary systems. *Physics of the Earth and Planetary Interiors* 178(1–2): 48–55.

Lehnert B (1958) An experiment on axisymmetric flow of liquid sodium in a magnetic field. *Arkiv for Fysik* 13: 109–116.

Limone A, Hatch DR, Forest CB, and Jenko F (2012) Facilitating dynamo action via control of large-scale turbulence. *Physical Review E* 86: 066315.

Lingwood RJ (1997) Absolute instability of the Ekman layer and related rotating flows. *Journal of Fluid Mechanics* 331: 405–428.

Loper D and Moffatt K (1993) Small-scale hydromagnetic flow in the Earth's core: Rise of a vertical buoyant plume. *Geophysical and Astrophysical Fluid Dynamics* 68: 177–202.

Malkus WVR (1968) Precession of the Earth as the cause of geomagnetism. *Science* 160: 259–264.

Malkus WVR (1989) An experimental study of the global instabilities due to the tidal (elliptical) distortion of a rotating elastic cylinder. *Geophysical and Astrophysical Fluid Dynamics* 48: 123–134.

Marié L, Burguete J, Daviaud F, and Léorat J (2003) Numerical study of homogeneous dynamo based on experimental von Kármán type flows. *European Physical Journal B* 33: 469–485.

Messadek K and Moreau R (2002) An experimental investigation of MHD quasi-two-dimensional turbulent shear flows. *Journal of Fluid Mechanics* 456: 137–159.

Monchaux R, Berhanu M, Bourgoin M, et al. (2007) Generation of a magnetic field by dynamo action in a turbulent flow of liquid sodium. *Physical Review Letters* 98(4).

Moreau R (1990) *Magnetohydrodynamics*. Dordrecht, The Netherlands: Kluwer.

Moresco P and Alboussière T (2004) Experimental study of the instability of the Hartmann layer. *Journal of Fluid Mechanics* 504: 167–181.

Müller U, Stieglitz R, and Horanyi S (2004) A two-scale hydromagnetic dynamo experiment. *Journal of Fluid Mechanics* 498: 31–71.

Müller U, Stieglitz R, and Horanyi S (2006) Experiments at a two-scale dynamo test facility. *Journal of Fluid Mechanics* 552: 419–440.

Murgatroyd W (1953) Experiments on magneto-hydrodynamic channel flow. *Philosophical Magazine* 44: 1348–1354.

Nagakawa Y (1957) Experiments on the instability of a layer of mercury heated from below and subject to the simultaneous action of a magnetic field and rotation. *Proceedings of the Royal Society of London A* 242: 81–88.

Nataf H-C (2003) Dynamo and convection experiments. In: *Earth's Core and Lower Mantle*, pp. 153–179. London: Taylor and Francis.

Nataf HC, Alboussiere T, Brito D, et al. (2006) Experimental study of super-rotation in a magnetostrophic spherical Couette flow. *Geophysical and Astrophysical Fluid Dynamics* 100(4–5): 281–298.

Nataf HC, Alboussiere T, Brito D, et al. (2008) Rapidly rotating spherical Couette flow in a dipolar magnetic field: An experimental study of the mean axisymmetric flow. *Physics of the Earth and Planetary Interiors* 170(1–2): 60–72.

Noir J, Brito D, Aldridge K, and Cardin P (2001) Experimental evidence of inertial waves in a precessing spheroidal cavity. *Geophysical Research Letters* 28: 3785–3788.

Noir J, Calkins M, Lasbleis M, Cantwell J, and Aurnou J (2010) Experimental study of libration-driven zonal flows in a straight cylinder. *Physics of the Earth and Planetary Interiors* 182(12): 98–106.

Noir J, Cardin P, Jault D, and Masson J-P (2003) Experimental evidence of nonlinear resonance effects between retrograde precession and the tilt-over mode within a spheroid. *Geophysical Journal International* 154: 407–416.

Noir J, Cbron D, Bars ML, Sauret A, and Aurnou J (2012) Experimental study of libration-driven zonal flows in non-axisymmetric containers. *Physics of the Earth and Planetary Interiors* 204205: 1–10.

Noir J, Jault D, and Cardin P (2001) Numerical study of the motions within a slowly precessing sphere at low Ekman number. *Journal of Fluid Mechanics* 437: 283–299.

Nornberg MD, Ji H, Schartman E, Roach A, and Goodman J (2010) Observation of magnetocoriolis waves in a liquid metal taylor-couette experiment. *Physical Review Letters* 104: 074501.

Nornberg MD, Spence EJ, Kendrick RD, Jacobson CM, and Forest CB (2006) Intermittent magnetic field excitation by a turbulent flow of liquid sodium. *Physical Review Letters* 97(4): 044503.

Noskov V, Denisov S, Stepanov R, and Frick P (2012) Turbulent viscosity and turbulent magnetic diffusivity in a decaying spin-down flow of liquid sodium. *Physical Review E* 85: 016303.

Peffley NL, Cawthorne AB, and Lathrop DP (2000) Toward a self-generating magnetic dynamo: The role of turbulence. *Physical Review E* 61: 5287–5294.

Petrelis F, Fauve S, Dormy E, and Valet J-P (2009) Simple mechanism for reversals of Earth's magnetic field. *Physical Review Letters* 102(14).

Plaut E and Busse F (2002) Low Prandtl number convection in a rotating cylindrical annulus. *Journal of Fluid Mechanics* 464: 345–363.

Poincaré R (1910) Sur la précession des corps déformables. *Bulletin Astronomique* 27: 321–356.

Ponomarenko Y (1973) On the theory of hydromagnetic dynamo. *Journal of Applied Mechanics and Technical Physics* 14: 775.

Ponty Y, Mininni PD, Montgomery DC, et al. (2005) Numerical study of dynamo action at low magnetic Prandtl numbers. *Physical Review Letters* 94(16): 164502.

Rädler K-H, Apstein E, Reinhardt M, and Schüler M (1998) The Karlsruhe dynamo experiment, a mean field approach. *Studia Geophysica et Geodaetica* 42: 224–231.

Rädler K-H and Brandenburg A (2003) Contributions to the theory of a two-scale homogeneous dynamo experiment. *Physical Review E* 67(2): 026401.

Ravelet F, Berhanu M, Monchaux R, et al. (2008) Chaotic dynamos generated by a turbulent flow of liquid sodium. *Physical Review Letters* 101(7).

Ravelet F, Chiffaudel A, Daviaud F, and Léorat J (2005) Toward an experimental von Kármán dynamo: Numerical studies for an optimized design. *Physics of Fluids* 17: 7104.

Read P, Yamazaki YH, Lewis SR, et al. (2004) Jupiter's and Saturn's convectively driven banded jets in the laboratory. *Geophysical Research Letters* 31.

Rhines P (1975) Waves and turbulence on a beta-plane. *Journal of Fluid Mechanics* 69: 417–443.

Rieutord M, Triana SA, Zimmerman DS, and Lathrop DP (2012) Excitation of inertial modes in an experimental spherical Couette flow. *Physical Review E* 86: 026304.

Roberts GO (1972) Dynamo action of fluid motions with two-dimensional periodicity. *Philosophical Transactions of the Royal Society of London* 271: 411–454.

Sauret A, Cbron D, Morize C, and Le Bars M (2010) Experimental and numerical study of mean zonal flows generated by librations of a rotating spherical cavity. *Journal of Fluid Mechanics* 662: 260–268.

Schaeffer N and Cardin P (2005) Quasigeostrophic model of the instabilities of the Stewartson layer in flat and depth-varying containers. *Physics of Fluids* 17: 4111.

Schmitt D, Alboussière T, Brito D, et al. (2008) Rotating spherical Couette flow in a dipolar magnetic field: Experimental study of magneto-inertial waves. *Journal of Fluid Mechanics* 604: 175–197.

Schmitt D, Cardin P, La Rizza P, and Nataf HC (2013) Magneto-Coriolis waves in a spherical Couette flow experiment. *European Journal of Mechanics B-Fluids* 37: 10–22.

Shimizu H and Loper DE (1997) Time and length scales of buoyancy-driven flow structures in a rotating hydromagnetic fluid. *Physics of the Earth and Planetary Interiors* 104: 307–329.

Sisan DR, Shew WL, and Lathrop DP (2003) Lorentz force effects in magneto-turbulence. *Physics of the Earth and Planetary Interiors* 135: 137–159.

Spence EJ, Nornberg MD, Jacobson CM, Kendrick RD, and Forest CB (2006) Observation of a turbulence-induced large scale magnetic field. *Physical Review Letters* 96(5): 055002.

Sreenivasan B and Alboussière T (2002) Experimental study of a vortex in a magnetic field. *Journal of Fluid Mechanics* 464: 287–309.

Stefani F, Gundrum T, Gerbeth G, Ruediger G, Szklarski J, and Hollerbach R (2007) Experiments on the magnetorotational instability in helical magnetic fields. *New Journal of Physics* 9.

Stepanov R, Volk R, Denisov S, Frick P, Noskov V, and Pinton J-F (2006) Induction, helicity, and alpha effect in a toroidal screw flow of liquid gallium. *Physical Review E* 73(4): 046310.

Stewartson K (1957) On almost rigid rotation. *Journal of Fluid Mechanics* 3: 17–26.

Stewartson K and Roberts PH (1963) On the motion of a liquid in a spheroidal cavity of a precessing rigid body. *Journal of Fluid Mechanics* 17: 1–20.

Sumita I and Olson P (2000) Laboratory experiments on high Rayleigh number thermal convection in a rapidly rotating hemispherical shell. *Physics of the Earth and Planetary Interiors* 117: 153–170.

Sumita I and Olson P (2002) Rotating thermal convection experiments in a hemispherical shell with heterogeneous boundary heat flux: Implications for the Earth's core. *Journal of Geophysical Research* 107: 1–5.

Sumita I and Olson P (2003) Experiments on highly supercritical thermal convection in a rapidly rotating hemispherical shell. *Journal of Fluid Mechanics* 492: 271–287.

Tabeling P (2002) Two-dimensional turbulence: A physicist approach. *Physics Reports* 362: 1–62.

Taylor G (1923) Experiments on the motion of solid bodies in rotating fluids. *Proceedings of the Royal Society of London A* 104: 213–218.

Thouveny N, Bourles DL, Saracco G, Carcaillet JT, and Bassinot F (2008) Paleoclimatic context of geomagnetic dipole lows and excursions in the Brunhes, clue for an orbital influence on the geodynamo? *Earth and Planetary Science Letters* 275(3–4): 269–284.

Tilgner A (1997) Predictions on the behaviour of the Karlsruhe dynamo. *Acta astronomica* et geophysica *Universitatis Comenianae* 19: 51–62.

Vanyo JP, Wilde P, Cardin P, and Olson P (1995) Experiments on precessing flows in the Earth's liquid core. *Geophysical Journal International* 121: 136–142.

Verhille G, Plihon N, Bourgoin M, Odier P, and Pinton J-F (2010) Induction in a von Karman flow driven by ferromagnetic impellers. *New Journal of Physics* 12.

Volk R, Odier P, and Pinton J-F (2006) Fluctuation of magnetic induction in von kármán swirling flows. *Physics of Fluids* 18(8), http://dx.doi.org/10.1063/1.2265009.

Zhong J-Q, Stevens RJAM, Clercx HJH, Verzicco R, Lohse D, and Ahlers G (2009) Prandtl-, Rayleigh-, and Rossby-number dependence of heat transport in turbulent rotating rayleigh-bénard convection. *Physical Review Letters* 102: 044502.

Zimmerman DS, Triana SA, and Lathrop DP (2011) Bi-stability in turbulent, rotating spherical Couette flow. *Physics of Fluids* 23(6): 065104.